Conference
on Modelling Fluid Flow (CMFF'22)
Radisson Blu Béke Hotel August 30 – September 2, 2022 Budapest / Hungary

Conference on Modelling Fluid Flow CMFF'22
The 18th event of the International Conference Series
on Fluid Flow Technologies held in Budapest since 1959

Conference Proceedings

Edited by J. Vad

Department of Fluid Mechanics / Faculty of Mechanical Engineering
Budapest University of Technology and Economics 2022

Proceedings of the Conference on Modelling Fluid Flow
CMFF'22

Edited by J. Vad

Department of Fluid Mechanics,
Budapest University of Technology and Economics
2022 Budapest, Hungary

ISBN 978-963-421-881-4

Published by the Department of Fluid Mechanics
Budapest University of Technology and Economics
H-1111 Budapest, Bertalan L. u . 4-6., Hungary
www.ara.bme.hu Phone: +36-1-463-4072

Conference on Modelling Fluid Flow (CMFF'22)
The 18th International Conference on Fluid Flow Technologies
Budapest, Hungary, August 30-September 2, 2022

APPLICATION OF HYBRID RANS/VMS MODELING TO ROTATING MACHINES

Florian MIRALLES[1], Bastien SAUVAGE[2], Stephen WORNOM[3], Bruno KOOBUS[4], Alain DERVIEUX[5],

[1] Corresponding Author. IMAG, Univ. Montpellier, CNRS, Place Eugène Bataillon, 34090 Montpellier, France. E-mail: florian.miralles@umontpellier.fr
[2] Univ. Côte d'Azur/INRIA Projet Ecuador, Sophia-Antipolis, France, E-mail: Bastien.Sauvage@inria.fr
[3] IMAG, Univ. Montpellier, CNRS, Montpellier, France. E-mail: stephen.wornom@inria.fr
[4] IMAG, Univ. Montpellier, CNRS, Montpellier, France. E-mail: bruno.koobus@umontpellier.fr
[5] Lemma, Biot, France, and Univ. Côte d'Azur/INRIA Projet Ecuador, Sophia-Antipolis, France, E-mail: alain.dervieux@inria.fr

ABSTRACT

The proposed communication deals with hybrid RANS-LES modeling. The target application is the study of flows around rotating machines like helicopters and drones. In fine, the simulations should provide accurate estimates concerning the noise emission. Each of these flows can involve mean and high Reynolds turbulent regions with detached eddies and with thin laminar and turbulent boundary layers. A hybrid model, like DDES, is then mandatory, with possibly an improved resolution of LES regions, which are mainly turbulent wakes. It is then interesting to apply there a more sophisticated LES model than the LES part of DDES. In our study, we use there the Dynamic variational multiscale model (DVMS). In the other regions, a DDES or simply a RANS modeling is applied. In both cases a two-equation closure is chosen. After a discussion of the modeling ingredients, we shall present a comparison of the RANS, LES, and hybrid models for two series of flows. Although computed by many researchers, flows around cylinders remain difficult to predict. The comparison will continue with a flow around a cross shaped mixing device rotating inside a cylinder.

Keywords: hybrid turbulence models, variational multiscale model for LES, chimera method, cylinder flow, rotating machine, unstructured grids

NOMENCLATURE

$\underline{W}$	$[-]$	flow variables
ρ	$[kg/m^3]$	density
$\underline{u}$	$[m/s]$	velocity vector
E	$[J/m^3]$	total energy per unit volume
k	$[m^2/s^2]$	turbulence kinetic enery
ε	$[m^2/s^3]$	dissipation rate of k
$\underline{W}_h$	$[-]$	discrete flow variables
$\underline{W'}_h$	$[-]$	small resolved scales of $\underline{W}_h$
$\langle\ \rangle$	$[-]$	Reynolds average
$\underline{F}$	$[-]$	convective and diffusive fluxes
$\underline{\tau}^{\text{RANS}}$	$[-]$	RANS closure term
$\underline{\tau}^{\text{LES}}$	$[-]$	LES closure term
$\underline{\tau}^{\text{DDES}}$	$[-]$	DDES closure term
ν	$[m^2/s]$	kinematic viscosity of the fluid
ν_t	$[m^2/s]$	turbulent kinematic viscosity
$\overline{C}_d$	$[-]$	mean drag coefficient
C'_l	$[-]$	r.m.s. of the lift coefficient
$\overline{C}_{p_b}$	$[-]$	mean base pressure coefficient
$\overline{\theta}$	$[deg.]$	mean separation angle
Δ	$[m]$	LES filter width
l_{RANS}	$[m]$	RANS turbulence length scale
μ_{SGS}	$[kg/m/s]$	LES eddy viscosity
μ_{RANS}	$[kg/m/s]$	RANS eddy viscosity

1. INTRODUCTION

In this paper, hybrid models are evaluated for the simulation of massively separated flows around fixed and moving geometries, with the objective of applying them to aeroacoustic problems involving complex industrial flows at high Reynolds numbers. For this purpose, the turbulence models need to behave preferentially like large eddy simulation models (LES) in order to introduce little dissipation and thus better capture the small scales and the fluctuations of the unsteady flows considered. However, these flows involve very thin boundary layers, which current computers and softwares cannot compute in LES mode, only in RANS mode. To accommodate both needs, LES and RANS, the hybrid turbulence approach, combining LES and RANS in a somewhat zonal manner, is considered by many research teams.

In this work, beside the classical Delayed Detached Eddy Simulation model (DDES, [1]), we study an approach which combines zonally this last model and the dynamic variationnal multiscale model (DVMS, [2]). In this hybrid DDES/DVMS approach [3], the DVMS model is preferentially activated in the wake regions where this latter model introduces less dissipation than the LES component of DDES. A hybrid RANS/DVMS model [4], where the RANS component is Goldberg's $k-\varepsilon$ model [5], is also applied in this study. A smooth blending function, which is based on the value of a blending parameter, is employed in these hybrid strategies, for switching from RANS to DVMS or DDES to DVMS. In [4], these models are applied to flows around a cylinder at moderate Reynolds number, starting from Reynolds number 20000.
In many industrial cases, and particularly cases with rotating geometries like propellers, the Reynolds number is much higher.

In the present paper, these hybrid models are applied to the flow around a circular cylinder in the supercritical regime, namely at Reynolds numbers 1 million and 2 million. At Reynolds number 1 million, the supercritical regime shows turbulent flow separation on both the upper and lower surface of the cylinder with a laminar-turbulent transition in the boundary layers located between the stagnation point and the separation one. At Reynolds number 2 million, the high transition regime shows a fully turbulent boundary layer on one side of the cylinder, and a partially laminar, partially turbulent boundary layer on the other side. This benchmark, which contains many characteristics encountered in industrial flows, is challenging due to the complex physics of the flow and the considered high Reynolds numbers, and remains a difficult calculation to perform. The second application concerns the flow at Reynolds number 1.8 million around a cross shaped mixing device rotating inside a cylinder.

This work is part of a cooperation program with Keldysh Institute of Applied Mathematics of Moscow focussing on the "Efficient simulation of noise of rotating machines", see e.g. [6, 7, 8].

The remainder of this paper is organized as follows. Section 2 presents the hybrid turbulence models used in this work. Section 3 describes the numerical scheme. In Section 4, applications are presented. The obtained results are analyzed and compared with those obtained in other numerical studies and with experimental data. Finally, concluding remarks are drawn in Section 4.

2. TURBULENCE MODELING

2.1. RANS

First, we want to specify that RANS stands for unsteady RANS throughout the document.

In this work, and as far as the closure of the RANS equations is concerned, we use the low Reynolds $k-\varepsilon$ model proposed in Goldberg et al.[5]. This model was designed to improve the predictions of the standard $k-\varepsilon$ one for adverse pressure gradient flows, including separated flows. For the sake of brevity, the equations of this model are not recalled in this document.

2.2. LES-like model: DVMS

In this section, we present the DVMS model which is preferred to the classical LES approach in our hybrid strategies because of some specific properties, as will be specified hereafter, that allow this model to have a better behavior in some regions of the flow, such as shear layers and wakes.

The Variational Multiscale (VMS) model for the large eddy simulation of turbulent flows has been introduced in [9] in combination with spectral methods. In [2], an extension to unstructured finite volumes is defined. This method is adapted in the present work. Let us explain this VMS approach in a *simplified context*. Assume the mesh is made of two embedded meshes. On the fine mesh we have a P^1-continuous finite-element approximation space V_h with the usual basis functions Φ_i vanishing on all vertices but vertex i. Let V_{2h} represents its embedded coarse subspace. Let V'_h be the complementary space: $V_h = V_{2h} \oplus V'_h$. The space of *small scales* V'_h is spanned by only the fine basis functions Φ'_i related to vertices which are not vertices of V_{2h}. Let us denote the compressible Navier-Stokes equations by:
$\frac{\partial \underline{W}}{\partial t} + \nabla \cdot \underline{F}(\underline{W}) = \underline{0}$ where $\underline{W} = (\rho, \rho\underline{u}, E)$.
The VMS discretization writes for $\underline{W_h} = \sum \underline{W}_i \Phi_i$:

$$\left(\frac{\partial \underline{W}_h}{\partial t}, \Phi_i\right) + \left(\nabla \cdot \underline{F}(\underline{W}_h), \Phi_i\right) = -\left(\underline{\tau}^{LES}(\underline{W}_h{}'), \Phi_i{}'\right) \quad (1)$$

For a test function related to a vertex of V_{2h}, the RHS vanishes, which limits the action of the LES term to small scales. *In practice*, embedding two unstructured meshes V_h and V_{2h} is a constraint that we want to avoid. The coarse level is then built from the agglomeration of vertices/cells as sketched in Fig. 1. It remains to define the model term $\underline{\tau}^{LES}(\underline{W}'_h)$. This

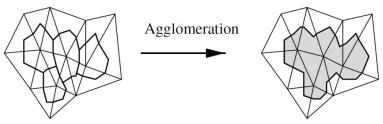

Figure 1. Building the VMS coarse level

term represents the subgrid-scale (SGS) stress term, acting only on small scales W'_h, and computed from the small scale component of the flow field by applying either a Smagorinsky [10] or a WALE SGS model [11], the constants of these models being evaluated by the Germano-Lilly dynamic procedure [12, 13]. The resulting model is denoted DVMS in this paper. It has been checked [14] that combining VMS and dynamic procedure effectively brings improved predictions.

A key property of the VMS formulation is that the modeling of the dissipative effects of the unresolved structures is only applied on the small resolved scales, as sketched in Fig. 2. This property is not satisfied by LES models which damp also the other resolved scales. Important consequences are that a VMS model introduces less dissipation than its LES counterpart (based on the same SGS model) and that the backscatter transfer of energy from smallest scales to large scales is not damped by the model. These VMS models then generally allow a better behavior near walls, in shear layers and in the presence of large coherent structures.
Moreover, in this work, the dynamic procedure, which provides a tuning of the SGS dissipation in space and time, is combined with the VMS approach, which limits its effects to the smallest resolved scales, so that the resulting DVMS model enjoys synergistic effects.

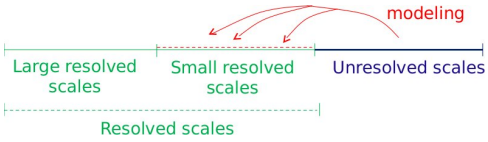

Figure 2. VMS principle.

2.3. DDES model

The DDES approach used in this work is based on the Goldberg's $k-\varepsilon$ model [5]. In other words, this RANS model is introduced in the DDES formulation [1] by replacing the $D_k^{\text{RANS}} = \rho\varepsilon$ dissipation term in the k equation by $D_k^{\text{DDES}} = \rho\frac{k^{3/2}}{l_{\text{DDES}}}$ where

$$l_{\text{DDES}} = \frac{k^{3/2}}{\varepsilon} - f_d \max(0, \frac{k^{3/2}}{\varepsilon} - C_{\text{DDES}}\Delta)$$
$$\text{with} \quad f_d = 1 - \tanh((8r_d)^3)$$
$$\text{and} \quad r_d = \frac{\nu_t + \nu}{\max(\sqrt{u_{i,j}u_{i,j}}, 10^{-10})K^2 d_w^2}.$$

K denotes the von Karman constant ($K = 0.41$), d_w the wall-normal distance, $u_{i,j}$ the x_j-derivative of the ith-component of the velocity u, and the model constant C_{DDES} is set to the standard value 0.65.

2.4. Hybrid RANS/DVMS

The central idea of the hybrid RANS/DVMS model [3] applied in this study is to combine the mean flow field obtained by the RANS component with the application of the DVMS model wherever the grid resolution is adequate. In this hybrid model, the $k-\varepsilon$ model of Goldberg (subsection 2.1) is used as the RANS component. First, let us write the semi-discretization of the RANS equations :

$$\left(\frac{\partial\langle\underline{W}_h\rangle}{\partial t}, \Phi_i\right) + \left(\nabla\cdot\underline{F}(\langle\underline{W}_h\rangle), \Phi_i\right) = -\left(\underline{\tau}^{\text{RANS}}(\langle\underline{W}_h\rangle), \Phi_i\right).$$

A natural hybridation writes:

$$\left(\frac{\partial\underline{W}_h}{\partial t}, \Phi_i\right) + \left(\nabla\cdot\underline{F}(\underline{W}_h), \Phi_i\right) =$$
$$-\theta\left(\underline{\tau}^{\text{RANS}}(\langle\underline{W}_h\rangle), \Phi_i\right) - (1-\theta)\left(\underline{\tau}^{\text{LES}}(\underline{W}_h'), \Phi_i'\right)$$

where $\underline{W}_h$ denotes now the hybrid variables and θ is the blending function which varies between 0 and 1 and is defined by:

$$\theta = 1 - f_d(1 - \tanh(\xi^2))$$
$$\text{with} \quad \xi = \frac{\Delta}{l_{\text{RANS}}} \quad \text{or} \quad \xi = \frac{\mu_{\text{SGS}}}{\mu_{\text{RANS}}},$$

the shielding function f_d being defined as in Subsection 2.3.
The blending function θ allows for a progressive switch from RANS to LES (DVMS in our case) where the grid resolution becomes fine enough to resolve a significant part of the local turbulence scales or fluctuations, i.e. computational regions suitable for LES-like simulations. Additionally, this blending function, thanks to the shielding function f_d, prevents the activation of the LES mode in the boundary layer. By way of example, the isocontours of the blending function θ for the flow past a circular cylinder are shown in Fig. 3. We can see in particular that in the boundary layer the RANS model is activated, while in the wake the LES approach is recovered.

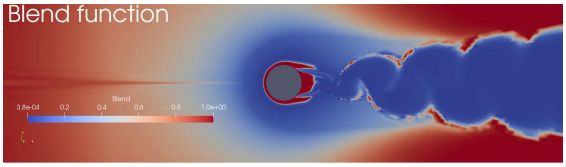

Figure 3. Isocontours of the blending function for the circular cylinder benchmark (Re= 10^6): for $\theta = 1$ (in red) the RANS model is activated, wherever $0 < \theta < 1$ additional resolved fluctuations are computed, and in the limit $\theta \to 0$ (in blue) the LES approach (DVMS in this work) is recovered.

2.5. Hybrid DDES/DVMS

The key idea of the proposed hybrid DDES/DVMS model [4] is to use the DVMS approach instead of the LES component of DDES in locations where this component is expected to be activated, especially in wake regions where the DVMS approach allows more accurate prediction.

Assuming that the semi-discretization of the DDES equations writes:

$$\left(\frac{\partial\underline{W}_h}{\partial t}, \Phi_i\right) + \left(\nabla\cdot\underline{F}(\underline{W}_h), \Phi_i\right) = -\left(\underline{\tau}^{\text{DDES}}(\underline{W}_h), \Phi_i\right),$$

the hybrid equations are then defined by:

$$\left(\frac{\partial \underline{W}_h}{\partial t}, \Phi_i\right) + \left(\nabla \cdot \underline{F}(\underline{W}_h), \Phi_i\right) = -\theta\left(\underline{\tau}^{\mathrm{DDES}}(\underline{W}_h), \Phi_i\right) - (1-\theta)\left(\underline{\tau}^{\mathrm{LES}}(\underline{W}'_h), \Phi'_i\right)$$

where $\underline{W}_h$ denotes the hybrid variables and θ is the blending function defined as in the previous subsection.

3. NUMERICAL DISCRETIZATION

3.1. Numerical scheme

The governing equations are discretized in space using a mixed finite-volume/finite-element method applied to unstructured tetrahedral grids. The adopted scheme is vertex-centered, i.e. all degrees of freedom are located at the vertices. The diffusive terms are discretized using P1 Galerkin finite-elements on the tetrahedra, whereas finite-volumes are used for the convective terms. The numerical approximation of the convective fluxes at the interface of neighboring cells is based on the Roe scheme [15] with low-Mach preconditioning [16]. To obtain second-order accuracy in space, the Monotone Upwind Scheme for Conservation Laws reconstruction method (MUSCL) [17] is used, in which the Roe flux is expressed as a function of reconstructed values of W at each side of the interface between two cells. A particular attention has been paid to the dissipative properties of the resulting scheme, since this is a key point for its successful use in LES, and therefore in simulations performed with a hybrid turbulence model. The numerical dissipation provided by the scheme used in the present work is made of sixth-order space derivatives [18] and thus is concentrated on a narrow-band of the highest resolved frequencies. This is expected to limit undesirable damping of the large scales by numerical dissipation. Moreover, a parameter γ directly controls the amount of introduced numerical viscosity and can be explicitly tuned in order to reduce it to the minimal amount needed to stabilize the simulation. Time advancing is carried out through an implicit linearized method, based on a second-order accurate backward difference scheme and on a first-order approximation of the Jacobian matrix [19]. The resulting numerical discretization is second-order accurate both in time and space. It should be noted that the spatial discretization used in this work leads to a superconvergent approximation, i.e. the accuracy can be well above second-order for some Cartesian meshes. One can also add that the objective is not a higher-order convergence but a strong reduction of dissipation and a certain reduction of the dispersion in the general case of a non-Cartesian (but not too irregular) mesh.

3.2. Mesh adaptation for rotating machines

Our numerical model has been extended to rotor-stator simulation with a Chimera technique.

The Chimera method aims at solving partial differential equations by decomposition into subdomains with overlap in order to avoid having to use a global mesh. This method allows the communication between the computational subdomains thanks to the overlapping of the subdomains. In our case we consider a decomposition in two domains as shown in Fig. 4, a fixed domain in red and a rotating domain in blue. For computations we start by locating the boundary nodes of domain 1 in domain 2, and reciprocally we locate the boundary nodes of domain 2 in domain 1, then the aerodynamic values of each boundary node are determined by interpolation and each domain performs its calculation with the new interpolated values.

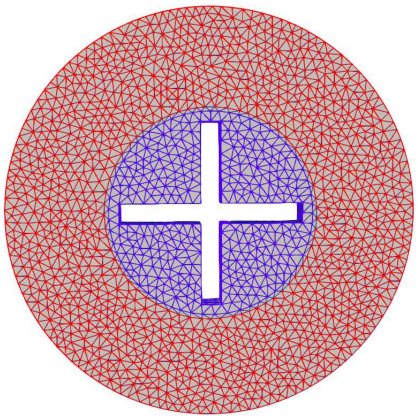

Figure 4. Definition of rotor and stator from an initial mesh : in red, the stator, in blue the rotor, and in gray, the overlap region.

A mesh adaptation loop based on a metric depending of the Mach number has been combined with the Chimera algorithm. The Transient Fixed Point mesh adaptation algorithm [20, 21, 22] is applied to each domain from a metric field evaluated on the whole domain.

4. APPLICATIONS

4.1. Flow past a cylinder

The predictions of the flow around a circular cylinder are presented. Two Reynolds numbers, 10^6 and 2×10^6, based on the cylinder diameter, D, and on the freestream velocity, are considered. Only a few numerical investigations have been performed for Reynolds numbers higher than 10^6. This interval is inside the supercritical regime which appears at Reynolds number higher than 2×10^5 and for which the separation becomes turbulent [23].

The computational domain is such that $-15 \leq (x, y)/D \leq 15$, and $-1 \leq z/D \leq 1$ where x, y and z denote the streamwise, transverse and spanwise directions respectively, the cylinder axis being located at $x = y = z = 0$. The mesh contains 4.8 millions nodes.

The Steger-Warming conditions [24] are imposed

at the inflow and outflow. The flow is assumed to be periodic in the spanwise direction. The inflow Mach number is set to 0.1 so that the compressibility effects can be considered as negligible. The free-stream turbulence intensity is below 1%. In order to control the computational costs, a wall law is applied in the close vicinity of the wall. For accuracy purpose, the Reichardt analytical law [25], which gives a smooth matching between linear, buffer and logarithmic regions, is chosen. As the y^+ normalized distance is generally subject to large variations in complex flows, the wall law is combined with low Reynolds modeling which locally damps the fully turbulent model in regions in which the wall law does not cover the buffer zone.

Reynolds number 10^6

The behavior of the hybrid models presented in Section 2 are first investigated in terms of flow bulk coefficients. From Table 1, it can be noted that the predictions of these coefficients are globally in good agreement with the experimental data and the numerical results in the literature. The lift time fluctuations are nevertheless better predicted by the RANS/DVMS model compared to the other two hybrid models. This good behavior is confirmed by the correct prediction of the distribution of the mean pressure coefficient, see Fig. 5. On the other hand, it can be observed from Table 1 and Fig. 5 that Smagorinsky and WALE SGS models give globally comparable results. It is also worth noting that the RANS model predicts rather well the bulk coefficients.
Fig. 6 shows instantaneous isocontours of the vorticity magnitude for each of the turbulence models used for this benchmark. As one might expect, the unsteady RANS model is more dissipative and captures less flow detail than the hybrid models, with in particular a much more damped and regular wake.

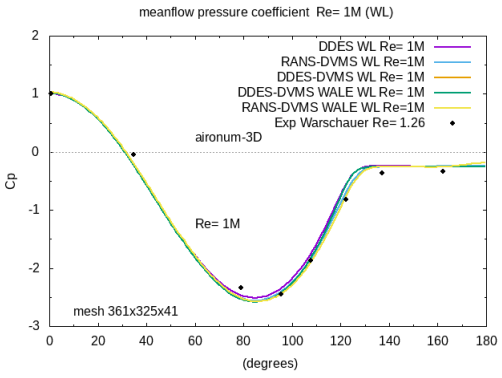

Figure 5. Distribution of the mean pressure coefficient over the cylinder surface. Comparison between experimental data and numerical results at Reynods number 10^6.

Table 1. Bulk coefficients of the flow around a circular cylinder at Reynolds number 10^6. The subscripts S and W holds respectively for Smagorinsky and WALE SGS models.

	$\overline{C}_d$	C'_l	$-\overline{C}_{pb}$	$\overline{\theta}$
Present simul.				
RANS	0.20	0.02	0.20	130
DDES	0.20	0.04	0.22	138
DDES/DVMS$_S$	0.20	0.02	0.22	135
DDES/DVMS$_W$	0.20	0.02	0.26	132
RANS/DVMS$_S$	0.25	0.09	0.25	132
RANS/DVMS$_W$	0.26	0.11	0.22	134
Other simul.				
RANS [26]	0.40	-	0.41	-
LES [26]	0.31	-	0.32	-
LES [27]	0.27	0.12	0.28	108
Measurements				
Exp. [28]	-	0.24	0.33	-
Exp. [29]	0.22	-	-	-
Exp. [30]	0.25	0.32	-	-
Exp. [31]	-	-	-	130
Exp. [32]	0.2-0.4	0.1-0.15	0.2-0.34	-

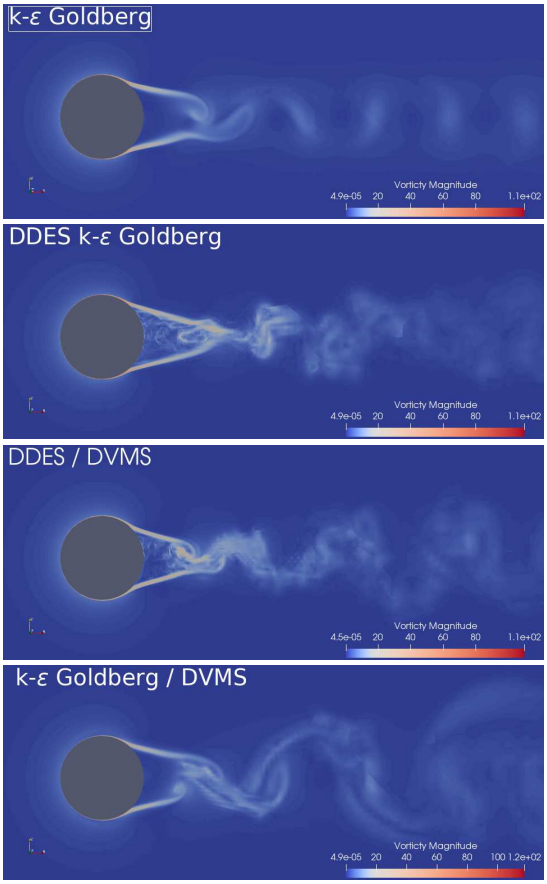

Figure 6. Circular cylinder, Re= 10^6: instantaneous isocontours of the vorticity magnitude. From top to bottom: RANS, DDES, DDES/DVMS and RANS/DVMS.

Reynolds number 2×10^6

The main outputs obtained by the RANS, DDES, DDES/DVMS and RANS/DVMS models are summed up in Table 2. Regarding the two hybrid models using the DVMS approach, only the results obtained with the Smagorinsky SGS model are shown, the WALE SGS model giving very similar results. It can be noticed that all models overpredict the separation angle, and that the fluctuations of the lift coefficient are overpredicted by the RANS and DDES/DVMS model. The RANS/DVMS approach gives on the whole the most satisfactory results. In Fig. 7, which shows the distribution of the mean pressure coefficient, the numerical results obtained with both hybrid models RANS/DVMS and DDES/DVMS are in very good agreement with the experimental results, in particular RANS/DVMS.

Table 2. Bulk coefficients of the flow around a circular cylinder at Reynolds number 2×10^6. The subscript S holds for Smagorinsky SGS model.

	$\overline{C}_d$	C'_l	$-\overline{C}_{pb}$	$\overline{\theta}$
Present simul.				
RANS	0.26	0.066	0.30	128
DDES	0.28	0.038	0.27	132
DDES/DVMS$_S$	0.26	0.070	0.35	130
RANS/DVMS$_S$	0.24	0.030	0.30	132
Other simul.				
LES/TBLE [33]	0.24	0.029	0.36	105
Measurements				
Exp. [28]	0.26	0.033	0.40	105
Exp. [29]	0.32	0.029	-	-

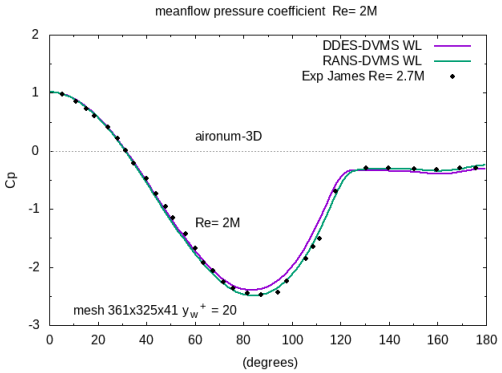

Figure 7. Distribution of the mean pressure coefficient over the cylinder surface. Comparison between experimental data and numerical results at Reynods number 2×10^6.

4.2. Flow around a rotating cross

We present a preliminary computation obtained with the combination of the mesh adaptation, the Chimera approximation and the DDES model. They are used for simulating the mixing process obtained with the rotation of a cross in a cylindric box. The Reynolds number is 1.8 million, based on the thickness of the blades. The number of vertices of the initial mesh is 10.466. After two turns, and five mesh adaptations, the number of vertices of the adapted mesh is 1.05 million.

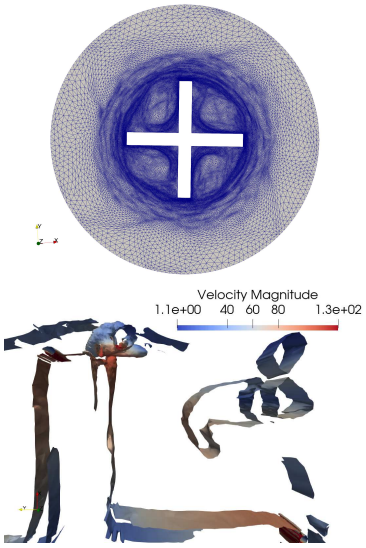

Figure 8. DDES computation of a rotating mixing device with a mesh adaptative Chimera approach (horizontal cut). View of the mesh and of Q-factor (colored with velocity magnitude) after the vertical upper blade.

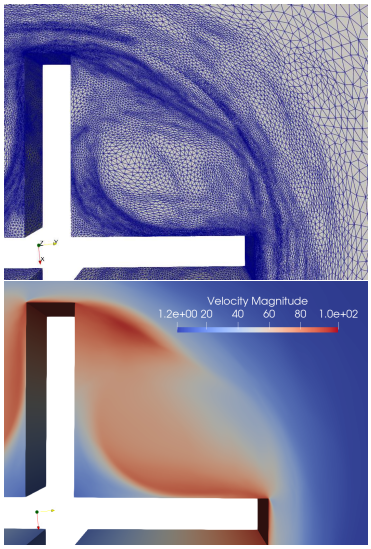

Figure 9. DDES computation of a rotating mixing device with a mesh adaptative Chimera approach (horizontal cut). Partial view of the mesh and velocity magnitude.

In Fig. 8a, we present a view of this final adapted mesh. Mesh size normal to the cylinder is yet not small enough to allow the creation of strong non-2D features. This is verified from the examination of the

Q-factor, Fig. 8b. Fig. 9 shows details of mesh and velocity magnitude. It seems from this first calculation that despite the hign Reynold number, the flow separates at blade angle is a rather stable mode.

5. CONCLUSION

Several hybrid strategies, based on the DDES, RANS and DVMS models, are first evaluated for the simulation of the supercritical flow around a circular cylinder. This benchmark is characterized by turbulent boundary-layer separation. The cylinder flow is first computed at Reynolds 10^6. The predictions of the main flow parameters are in overall good agreement with experimental data and the results of simulations in the literature, especially the RANS/DVMS model. A second series of computations of the flow past a circular cylinder is carried out at Reynolds 2×10^6. The predictions obtained by the hybrid models used to perform this benchmark are a little less accurate compared to the previous Reynolds number, more specifically for the mean separation angle which is overestimated. Again, the RANS/DVMS model is the hybrid model among those applied which gives the best results overall. It is also to be noted that the pressure distribution is well predicted by the hybrid models for both Reynolds numbers, especially by the RANS/DVMS model. Then, the DDES formulation is applied to the flow around a rotating cross inside a cylinder with a Reynolds number of 1.8×10^6. Preliminary results using mesh adaptation with meshes of 1 million vertices show that separations are more stable than in the flows around the cylinder. RANS/DVMS computations are planned. The new tool is also being applied to other rotating devices like propellers and will produce mesh adapted results for these geometries in a near future.

ACKNOWLEDGEMENTS

This work was supported by the ANR NORMA project, grant ANR-19-CE40-0020-01 of the French National Research Agency. The authors gratefully acknowledge GENCI for granted access to HPC resources through CINES (grants 2020-A0092A05067 and 2021-A0102A06386) and IDRIS (grant 2021-A0112A05067).

REFERENCES

[1] Spalart, P. R., Deck, S., Shur, M. L., Squires, K. D., Kh., S. M., and Travin, A. K., 2006, "A new version of detached-eddy simulation, resistant to ambiguous grid densities", *Theoritical and Computational Fluid Dynamic*, Vol. 20(3), pp. 181–195.

[2] Koobus, B., and Farhat, C., 2004, "A variational multiscale method for the large eddy simulation of compressible turbulent flows on unstructured meshes-application to vortex shedding", *Comput Methods Appl Mech Eng*, Vol. 193, pp. 1367–1383.

[3] Moussaed, C., Salvetti, M. V., Wornom, S., Koobus, B., and Dervieux, A., 2014, "Simulation of the flow past a circular cylinder in the supercritical regime by blending RANS and variational-multiscale LES models", *Journal of Fluids and Structures*, Vol. 47, pp. 114–123.

[4] Itam, E., Wornom, S., Koobus, B., and Dervieux, A., 2018, "Combining a DDES model with a dynamic variational multiscale formulation", *12th International ERCOFTAC Symposium on Engineering Turbulence Modelling and Measurements (ETMM12)*, La Grande Motte, France.

[5] Goldberg, U., Peroomian, O., and Chakravarthy, S., 1998, "A wall-distance-free $k - \varepsilon$ model with Enhanced Near-Wall Treatment", *Journal of Fluids Engineering*, Vol. 120, pp. 457–462.

[6] Garanzha, V. A., and Kudryavtseva, L. N., 2020, "Moving deforming mesh generation based on quasi-isometric functional", *Lecture Notes in Computational Science and Engineering, WoS, Scopus-Q1*.

[7] Bakhvalov, P. A., and Kozubskaya, T. K., 2021, "On using artificial viscosity in edge-based schemes on unstructured grids", *Mathematical Models and Computer Simulations*, Vol. 13 (4), pp. 705–715.

[8] Duben, A. P., Kozubskaya, T. K., Rodionov, P. V., and Tsvetkova, V. O., 2021, "EBR schemes with curvilinear reconstructions of variables in the near-wall region", *Computational Mathematics and mathematical physics*, Vol. 61 (1), pp. 1–16.

[9] Hughes, T. J. R., Mazzei, L., and Jansen, K. E., 2000, "Large eddy simulation and the variational multiscale method", *Comput Vis Sci*, Vol. 3, pp. 47–59.

[10] Smagorinsky, J., 1963, "General circulation experiments with the primitive equations", *Monthly Weather Review*, Vol. 91(3), pp. 99–164.

[11] Nicoud, F., and Ducros, F., 1999, "Subgrid-scale stress modelling based on the square of the velocity gradient tensor", *Flow, Turbulence and Combustion*, Vol. 62, pp. 183–200.

[12] Germano, M., Piomelli, U., Moin, P., and Cabot, W., 1991, "A dynamic subgrid-scale eddy viscosity model", *Phys Fluids A*, Vol. 3 (7), pp. 1760–1765.

[13] Lilly, D. K., 1992, "A proposed modification of the Germano subgrid-scale closure method", *Phys Fluids*, Vol. A4, p. 633.

[14] Moussaed, C., Wornom, S., Salvetti, M. V., Koobus, B., and Dervieux, A., 2014, "Impact of dynamic subgrid-scale modeling in variational multiscale large-eddy simulation of bluff body flows", *Acta Mechanica*, Vol. 225, pp. 3309–3323.

[15] Roe, P. L., 1981, "Approximate Riemann solvers parameters vectors and difference schemes", *J Comput Phys*, Vol. 43, pp. 357–372.

[16] Guillard, H., and Viozat, C., 1999, "On the behaviour of upwind schemes in the low Mach number limit", *Comput Fluids*, Vol. 28, pp. 63–86.

[17] Van Leer, B., 1977, "Towards the ultimate conservative scheme. IV: a new approach to numerical convection", *J Comput Phys*, Vol. 23, pp. 276–299.

[18] Camarri, S., Salvetti, M. V., Koobus, B., and Dervieux, A., 2004, "A low diffusion MUSCL scheme for LES on unstructured grids", *Comput Fluids*, Vol. 33, pp. 1101–1129.

[19] Martin, R., and Guillard, H., 1996, "A second-order defect correction scheme for unsteady problems", *Comput Fluids*, Vol. 25(1), pp. 9–27.

[20] Alauzet, F., Frey, P. J., George, P.-L., and Mohammadi, B., 2007, "3D transient fixed point mesh adaptation for time-dependent problems: Application to CFD simulations", *J Comp Phys*, Vol. 222, pp. 592–623.

[21] Alauzet, F., Loseille, A., and Olivier, G., 2016, "Multi-Scale Anisotropic Mesh Adaptation for Time-Dependent Problems", *RR-8929*, INRIA.

[22] Guégan, D., Allain, O., Dervieux, A., and Alauzet, F., 2010, "An L^{∞}-L^{p} mesh adaptive method for computing unsteady bi-fluid flows", *Int J Numer Meth Eng*, Vol. 84 (11), pp. 1376–1406.

[23] Sumer, B. M., and Fredsoe, J., 2006, *Hydrodynamics Around Cylindrical Structures*, World Scientific.

[24] Steger, J., and Warming, R. F., 1981, "Flux vector splitting for the inviscid gas dynamic equations with applications to finite difference methods", *J Comp Phys*, Vol. 40, pp. 263–293.

[25] Hinze, J., 1959, *Turbulence*, McGraw-Hil.

[26] Catalano, P., Wang, M., Iaccarino, G., and Moin, P., 2003, "Numerical simulation of the flow around a circular cylinder at high Reynolds numbers", *Int J Heat Fluid Flow*, Vol. 24, pp. 463–469.

[27] Kim, S.-E., and Mohan, L. S., 2005, "Prediction of unsteady loading on a circular cylinder in high Reynolds number flows using large eddy simulation", *Proceedings of OMAE 2005: 24th International Conference on Offshore Mechanics and Artic Engineering, june 12-16, Halkidiki, Greece, OMAE 2005-67044*.

[28] Shih, W. C. L., Wang, C., Coles, D., and Roshko, A., 1993, "Experiments on flow past rough circular cylinders at large Reynolds numbers", *J Wind Eng Indust Aerodyn*, Vol. 49, pp. 351–368.

[29] Schewe, G., 1995, "On the force fluctuations acting on a circular cylinder in crossflow from subcritical up to transcritical Reynolds numbers", *Journal of Fluid Mechanics*, Vol. 133, pp. 265–285.

[30] Szechenyi, E., 1975, "Supercritical Reynolds number Simulation for Two-dimensional flow over circular cylinders", *J Fluid Mech*, Vol. 70, pp. 529–542.

[31] Goelling, B., 2006, "Experimental investigations of separating boundary-layer flow from circular cylinder at Reynolds numbers from 10^5 up to 10^7; Three-dimensional vortex flow of a circular cylinder", G. Meier, and K. Sreenivasan (eds.), *Proceedings of IUTAM Symposium on One Hundred Years of Bloundary Layer Research*, Springer, The Netherlands, pp. 455–462.

[32] Zdravkovich, M. M., 1996, "Different modes on vortex shedding: an overview", *Journal of Fluid and Structures*, Vol. 10(5), pp. 427–437.

[33] Sreenivasan, A., and Kannan, B., 2019, "Enhanced wall turbulence model for flow over cylinder at high Reynolds number", *AIP Advances*, Vol. 095012.

Conference on Modelling Fluid Flow (CMFF'22)
The 18th International Conference on Fluid Flow Technologies
Budapest, Hungary, August 30-September 2, 2022

NUMERICAL SIMULATION OF A CONFINED BACKWARD-FACING STEP FLOW USING HYBRID TURBULENCE MODELS IN OPENFOAM

Wim MUNTERS[†,1], Lilla KOLOSZAR[1], Philippe PLANQUART[1]

[1] Department of Environmental and Applied Fluid Dynamics. von Karman Institute for Fluid Dynamics. Waterloosesteenweg 72, 1640 Sint-Genesius-Rode, Belgium.
[†]Corresponding author. Email: wim.munters@vki.ac.be

ABSTRACT

To date, numerical simulation of separated flows remains challenging, with hybrid RANS–LES turbulence models promising to deliver scale-resolving accuracy at acceptable computational cost. Here, we investigate hybrid turbulence models readily available in OpenFOAM, and benchmark their performance to Reynolds-averaged approaches and turbulence-resolving high-fidelity reference data for a confined backward-facing step flow at low Reynolds number. Results show that scale-adaptive simulation techniques do not produce resolved turbulence and fail to outperform the baseline Reynolds-averaged simulations for the considered case. In contrast, detached-eddy variants do resolve turbulence in the separated shear layer, yet some configurations suffer from modelled-stress depletion. A grid coarsening study compares the degradation of accuracy for each approach, showcasing robustness of the standard Reynolds-averaged approach and, surprisingly, the relatively good performance of full large-eddy simulations even at coarse resolutions.

Keywords: Backward-facing step, Detached Eddy Simulation, Hybrid turbulence modelling, Large-eddy simulation, OpenFOAM, Scale-adaptive simulation

1. INTRODUCTION

Hybrid turbulence models, in which different modeling strategies are applied throughout the simulation domain, have historically been used primarily for high-Reynolds number external flows around airfoils and obstacles with massive separation in fields such as aerospace and ground transportation [1, 2]. Since the late 1990s, a large amount of different hybrid models based on Reynolds-Averaged Navier–Stokes (RANS) and Large-Eddy Simulation (LES) models have been developed based on various techniques for hybridization. Recent overviews of the general approach and state-of-the-art methods can be found, e.g., in [3]. Although they have been used with success in many studies, several weaknesses have also become apparent over the years. For example, spurious switching to LES zones in insufficiently destabilized regions has been known to produce so-called modeled stress depletion (MSD), in which neither modeled (RANS) nor resolved (LES) turbulence produces sufficient mixing close to transition zones [1]. Furthermore, studies using hybrid turbulence models for internal flows at low to medium Reynolds numbers have been more scarce to date. Even though such cases benefit from (partial) scale resolution, effects of viscosity and confinement have the potential to attenuate massive separation effects as observed in high-Reynolds external flows, which can be challenging for hybrid methods [1].

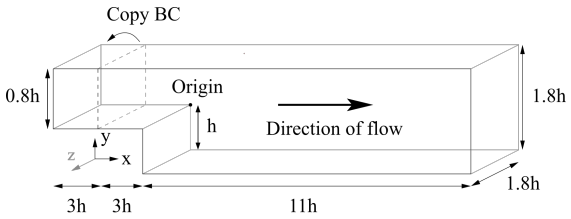

Figure 1. Sketch of the BFS domain. Figure adapted from [4]

Here, we investigate hybrid turbulence models available in OpenFOAM, and benchmark their performance to fully Reynolds-averaged approaches, LES with partial scale resolution, and direct numerical simulations (DNS) resolving all turbulence scales. The benchmark is performed for a confined backward-facing step flow at low Reynolds number. Hybrid models considered in the study are the scale-adaptive simulation model (SAS) and variants of the detached-eddy simulation model (DES).

2. CASE DESCRIPTION

We investigate an incompressible backward-facing step (BFS) flow, characterized by an inlet channel with a sudden step expansion. This expan-

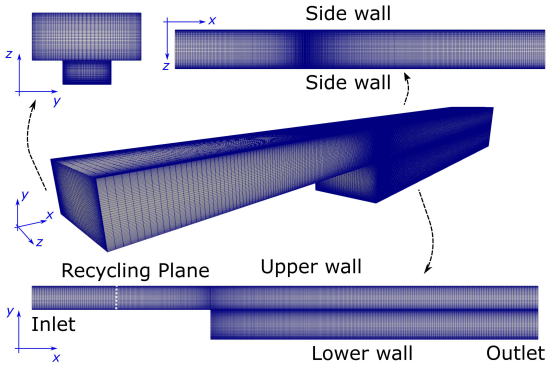

Figure 2. Overview of the baseline simulation grid.

sion results in adverse pressure gradients and a large-scale separated shear layer (SSL) downstream of the step, which in turn causes anisotropy and recirculation. Although the geometry is simple, these flow phenomena justify the BFS as a standard test case for turbulence models. We specifically focus on the reference BFS presented by Oder et al. [5]), for which a DNS database is available. A sketch of the considered BFS geometry is presented in Figure 1. Except for in- and outlet, all boundaries are solid walls, hence the BFS is confined. Upstream of the step, a recycling condition produces a fully developed channel flow with an inlet velocity $\langle u_{in} \rangle$. The flow is characterized by a relatively low Reynolds number Re = 6400, based on $\langle u_{in} \rangle$ and step height h.

3. SIMULATION METHODOLOGY

3.1. Numerical setup

Incompressible simulations are compared for different turbulence models readily available in OpenFOAM v2012 [10, 11]. To this end, simulations are performed on an identical baseline simulation grid suitable for all turbulence modeling strategies considered, as illustrated in Figure 2. The wall resolution is chosen to resolve the viscous sublayers such that $y^+ = u_\tau y/\nu \approx 1$ averaged over solid surfaces, with u_τ the local friction velocity, y the first cell-center height off the wall, and ν the viscosity. The overall grid is further built with uniform stretching using the `simpleGrading` tool, such that resolution of large eddies remains supported throughout the domain, resulting in a grid of about 3.7 million cells. Initial tests showed that this grid supports LES in which about 94% of the turbulence in the domain is resolved, whereas the remaining 6% is accounted for by the subgrid-scale model. Matching the DNS reference setup, the inlet applies a 'mapped condition' which introduces the solution at the recycling plane back at the inlet, resulting in a periodic channel flow between inlet and recycling plane. Walls are treated with no-slip conditions (no wall functions are used), zero-gradient pressure, and appropriate fixed-value conditions for turbulence model quantities. At the outlet, a reference pressure value is fixed, whereas other flow quantities are subject to zero-gradient and zero-backflow conditions. Steady cases are solved using the simpleFoam solver, whereas the pisoFoam solver is used for transient simulations. Unsteady simulations are initialized using a steady RANS solution. Subsequently, simulations are advanced in time until a statistically stationary state is observed, after which statistical sampling is performed over a time horizon of about 50 domain flow-throughs.

3.2. Turbulence modeling

Baseline RANS and LES are performed as lower and upper limits of expected attainable performance by the hybrid models. The RANS uses the $k-\omega$ SST turbulence model [6], whereas the LES uses a high-fidelity dynamic k sub-grid scale model [7]. Both models rely on a prognostic equation for the modeled turbulent kinetic energy k. This prognostic equation contains a destruction term which is inversely proportional to a modeled turbulence length scale d. In this way, smaller values for d result in a reduction of modeled k, in turn yielding lower eddy viscosity ν_t. The main difference in governing equations of unsteady RANS and LES lies in the how d is defined. In RANS it depends solely on the solution as, e.g.,

$$d_{\mathrm{SST}} = k^{0.5}/(0.09\omega) \tag{1}$$

for the $k-\omega$ SST model. For LES on the other hand it is directly sensitized to the local grid resolution Δ as $d_{\mathrm{LES}} = C_{\mathrm{LES}}\Delta$ instead, with C_{LES} a constant in the order of 1 (dependent on local flow variables in dynamic formulations). In this way, on finer LES grids the foregoing ν_t reduction destabilizes the numerical solution to facilitate resolution of large eddies.

A first hybrid setup consists of the $k-\omega$ SST SAS turbulence model [8]. The SAS methodology can be viewed as an extension to unsteady RANS for which, in addition to the standard $k-\omega$ SST length scale d_{SST}, the underlying turbulence model is provided with a second independent von-Kármán length scale d_{vK} based on the ratio of first and second-order velocity gradients. This allows to automatically reduce ν_t in regions of strong shear and inherent instability, thus promoting eddy resolution based solely on the properties of the numerical solution.

In contrast, the other three hybrid setups considered in this work lean more towards an LES approach, in which the grid resolution Δ plays a direct role in the turbulence model. More specifically, three variants of DES methods are considered. Firstly, we consider the $k-\omega$ SST DES developed by Strelets [2], which defines a length scale

$$d_{\mathrm{DES}} = \min\left(d_{\mathrm{SST}}, C_{\mathrm{DES}}\Delta\right). \tag{2}$$

Note that this results in DES adhering to the smallest of either the RANS or the LES length scale formulation[1], thus promoting LES behavior on sufficiently

[1] In practice, C_{DES} slightly differs from C_{LES} to accommodate different zones in the $k-\omega$ SST model.

Table 1. Overview of simulation cases.

Case	Resolution of large eddies	Turbulence model	Modeled turbulence length scale
RANS	None	$k-\omega$ SST [6]	$d_{\mathrm{SST}} = k^{0.5}/(0.09\omega)$
LES	Everywhere (down to grid scale Δ)	k (dynamic) [7]	$d_{\mathrm{LES}} = C_{\mathrm{LES}}\Delta$
SAS	Hybrid: based on solution	$k-\omega$ SST SAS [8]	$d_{\mathrm{SAS}} = d_{\mathrm{SST}}/d_{vK}$
DES	Hybrid: based on solution + grid	$k-\omega$ SST DES [2]	$d_{\mathrm{DES}} = \min(d_{\mathrm{SST}}, d_{\mathrm{LES}})$
DDES	Hybrid: DES + boundary-layer shielding	$k-\omega$ SST DDES [9]	$d_{\mathrm{DDES}} \approx d_{\mathrm{SST}}$ (close to walls) $\approx d_{\mathrm{DES}}$ (away from walls)
IDDES	Hybrid: DDES + WMLES features	$k-\omega$ SST IDDES [9]	$d_{\mathrm{IDDES}} \approx d_{\mathrm{SST}}$ (close to walls) $\approx d_{\mathrm{DES}}$ (away from walls) (+ log-layer modifications)

fine grids. Secondly, the $k-\omega$ SST Delayed DES formulation proposed by Gritskevitch *et al.* [9] is used. DDES defines a shielding function f_d, which is used to avoid spurious grid-induced transition to scale-resolving regimes in attached boundary layers, a problem which is known to severely impact accuracy in standard DES. The length scale is further defined as

$$d_{\mathrm{DDES}} = d_{\mathrm{SST}} - f_d \max\left(d_{\mathrm{SST}} - C_{\mathrm{DES}}\Delta\right), \qquad (3)$$

with $f_d \approx 0$ close to walls, hence $d_{\mathrm{DDES}} \approx d_{\mathrm{SST}}$ and $f_d \approx 1$ away from them, resulting in $d_{\mathrm{DDES}} \approx d_{\mathrm{DES}}$. Third, the $k-\omega$ SST Improved DDES model is employed [9], which features slight modifications of DDES in the log layer close to solid boundaries to make it more amenable wall-modeled LES (WMLES) operation. Note that all turbulence models mentioned above are readily available in OpenFOAM v2012 and are used in their default configuration. Simulation cases for all 6 turbulence models considered here are summarized in Table 1.

4. RESULTS ON BASELINE GRID

In this section, we show the performance of the different turbulence models and compare them to each other and to the reference DNS data, with specific focus on the hybrid models. Firstly, we set the baseline performance by comparing the full RANS and LES approaches in Sect. 4.1. Next, we discuss the behavior of the different hybrid setups in Sect. 4.2. Finally, we discuss the overall performance of all methods in Sect. 4.3

4.1. Setting the bar: RANS and LES

A qualitative view of the flow fields in LES and RANS is shown in Figure 3. It can be seen that, while the RANS streamwise velocity is smooth and time-averaged by construction (a), the LES counterpart (b) features turbulent structures throughout the domain. Looking at the time-averaged vertical velocities in (c) and (d), the 3D structure of the fields is very different, especially in the downstream vicinity of the step.

Profiles of flow quantities along the domain midplane are compared to DNS data in Figure 4. For the horizontal velocity $\overline{u}$ (a), it can be seen that the turbulent channel profiles from DNS are matched well by both RANS and LES. However, downstream of

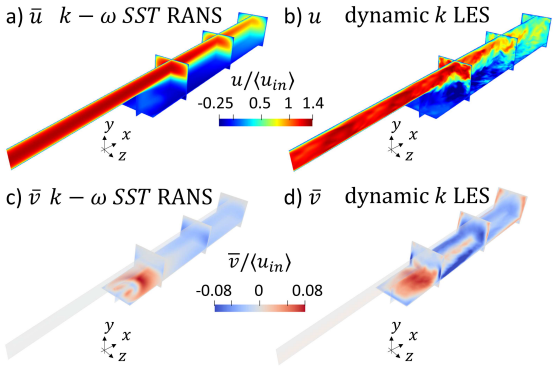

Figure 3. Flow field visualization for RANS (left, a, c) and LES (right, b, d) of streamwise velocity u (top, a, b) and vertical velocity v (bottom, c, d). All except (b) illustrate time-averaged quantities.

the step, RANS shows significant deviations from the DNS whereas LES retains a good match throughout the domain. More specifically, the backflow velocity in the separation bubble close to the step ($1 \le x/h \le 3$) is significantly underpredicted by RANS, whereas the flow velocity in the top right part of the domain is overpredicted ($3 \le x/h \le 11, 0 \le y/h \le 0.8$). Turning to the vertical velocity $\overline{v}$ in panel (b), it is seen that the LES achieves an acceptable match with the DNS data. Even though the velocity is lower than the DNS data for $4 \le x/h \le 10, -1 \le y/h \le 0$, the overall shape of the profile is retained. In contrast, RANS only matches the DNS profile at $x/h = 2$, while the S-shaped profiles observed in DNS and LES are not found at all in the RANS solution.

In addition to the mean-flow quantities discussed above, Figure 4c) contains profiles of the resolved and modeled time-averaged turbulent kinetic energy $\overline{k}$. LES achieves a good match with DNS, although slight overpredictions are observed for $2 \le x/h \le 4, -1 \le y \le 0$. Furthermore, the LES seems highly resolved, i.e., sub-grid modeled components are much smaller than the resolved components. Regarding the modeled turbulence in RANS, we see the largest discrepancies with DNS are observed in the SSL close to the step, where turbulence is generally underpredicted. Downstream, the match with DNS is

improved, although it remains worse than the LES.

In summary, we conclude here that LES is able to match the DNS data throughout the entire domain, whereas RANS exhibits significant discrepancies downstream of the step. This observation is in line with the motivation for using hybrid RANS/LES turbulence models, as large-eddy scale resolution in the downstream zone could hence be capable of increasing overall accuracy.

4.2. Behavior of hybrid methods

4.2.1. SAS

Figure 5 shows a snapshot of streamwise velocity u (a) as well as the time-averaged vertical velocity (b). A first observation is that the streamwise velocity snapshot is free of any resolved turbulence fluctuations. Next, the vertical velocity in the case of SAS exhibits a similar structure as that in RANS shown in Figure 3c), which was discussed to match poorly with the DNS reference. Also upon investigation of the midplane profiles, which are not further shown here, the SAS was found to be nearly identical to RANS. Summarizing, in the current setup, SAS fails to resolve any turbulence and does not improve model fidelity over a standard RANS.

4.2.2. DES

As shown in Figure 6, the DES qualitatively behaves much like the LES from Figure 3(b,d), including a domain filled with turbulent fluctuations for the snapshot and a similar structure in vertical velocity as observed in the LES. Figure 7 illustrates the time-averaged RANS / LES indicator function, which is defined based on the modeled turbulence lengthscale (see Table 1) with the `DESModelRegions` function in OpenFOAM. It can be seen that the majority of the midplane is consistently treated as LES, while regions very close to the wall turn to a RANS approach. Only the region closely downstream of the step exhibits some switching between RANS and LES. Apart from the latter, the DES thus behaves very similar to a WMLES. This further explains the observations in midplane profiles in Figure 8, showing strong similarity between LES and DES, except very close to the step, where DES underpredicts both the vertical velocity $\overline{v}$ and the turbulence kinetic energy $\overline{k}$.

4.2.3. DDES

DDES has been originally designed to avoid the transition to LES mode in wall-attached boundary layers. Figure 9a) indicates that the channel region does not contain any fluctuations, and that the onset of scale resolution is delayed to the far downstream region of the SSL. The RANS / LES indicator function shown in Figure 10 indeed reveals a hybrid domain division into a RANS zone in the upstream channel and top-wall attached boundary layer, whereas the SSL is treated with LES. This domain partitioning is highly desirable, since RANS was shown to work well in such regions and expected to allow significant grid coarsening, whereas LES should enhance fidelity in the SSL. However, when comparing the vertical velocity structure in Figure 9b), we see that neither of the expected structures observed before in RANS or LES is attained.

Further looking at midplane profiles in Figure 8, DDES produces a poor match with DNS / LES. The expected recirculation zone ($0 \leq x/h \leq 6, -1 \leq y/h \leq 0$) appears to be almost stagnant with no recirculation predicted by DDES. Furthermore, the vertical velocity is very much underpredicted in this zone, which seems to be compensated by far too large negative vertical velocities in the outlet zone ($x/h \geq 8$). Focusing on turbulence profiles in Figure 8c), it becomes clear that DDES is suffering from severe MSD in the expected recirculation zone. Even though the model has turned to an LES formulation here (thus without support of a RANS turbulence model), this zone is turbulence-deficient without any resolved scales to take up the turbulent mixing effects. Possibly the relatively low Reynolds number is delaying transition at the separation point.

4.2.4. IDDES

IDDES was developed as a DDES formulation that would be more amenable to WMLES. Figure 11 shows the flow field to be very similar to fields from LES and DES (which was shown to behave as WMLES). Interestingly, the shielding functions do not prohibit LES zones in the upstream channel flow, but do created a RANS zone immediately adjacent to the step separation point as shown in Figure 12. Midplane profiles shown in Figure 11 further confirm the affinity to LES results.

4.3. Discussion

In the previous sections, a qualitative discussion and comparison of the flow fields of the considered models was performed. A comparison between steady RANS and LES showed that large-eddy resolution in the SSL allows to significantly improve the overall match with DNS data, justifying that the current BFS setup is suitable for testing the performance of locally scale-resolving hybrid methods.

Results obtained from the hybrid simulation indicated that for the current case their behavior can be classified in three groups. Firstly, SAS resembles a steady RANS field, with virtually no scale resolution and similar flow field characteristics. Secondly, DES and IDDES behave like WMLES, where the entire domain is simulated as an LES zone, except for regions in the direct wall vicinity. Thirdly, DDES exhibits a more classical hybrid domain subdivision, in which only the SSL is an LES zone, whereas the inlet channel and top wall are predominantly RANS. This latter configuration is promising, as it turns to scale resolution only in the region where RANS clearly struggles to match the DNS data. The different behavior between DDES and IDDES (which are formulated in a relatively similar manner) is an interesting

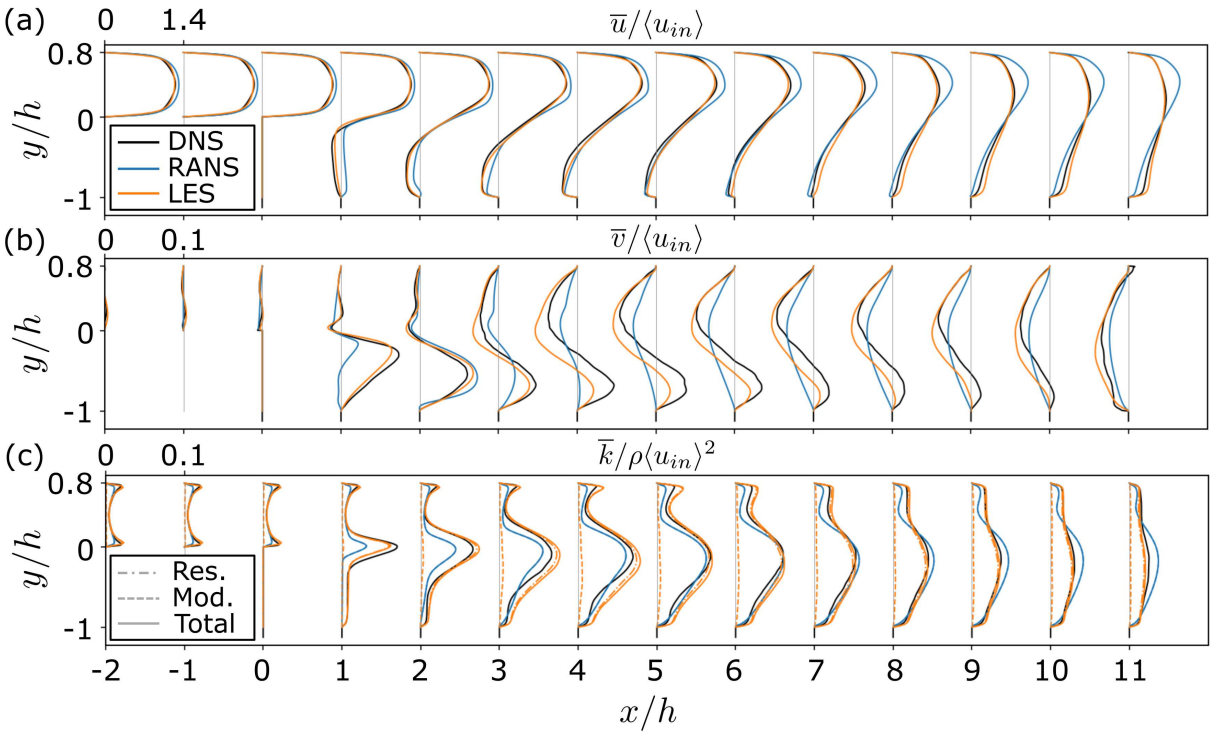

Figure 4. Profiles along midplane for DNS, RANS, and LES. (a) Streamwise velocity component $\overline{u}$. (b) Vertical velocity component $\overline{v}$. Turbulent kinetic energy $\overline{k}$. Dashed, dot-dashed, and full lines indicated modeled, resolved and total (modeled + resolved) components. (Modeled and resolved components in DNS and RANS respectively are zero by definition and not further shown).

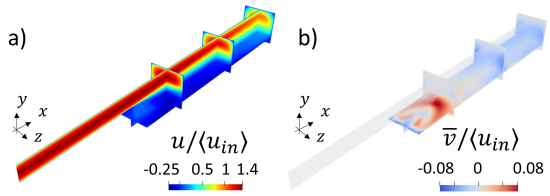

Figure 5. Flow field visualization for SAS. a) Streamwise velocity snapshot u. b) Time-averaged vertical velocity $\overline{v}$.

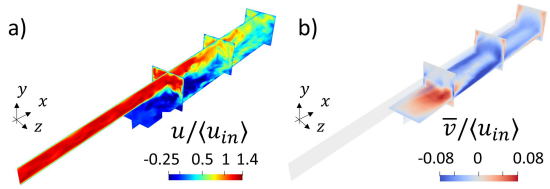

Figure 6. Flow field visualization for DES. a) Streamwise velocity snapshot u. b) Time-averaged vertical velocity $\overline{v}$.

Figure 7. RANS/LES indicator function along the midplane for the DES setup.

observation, possibly indicating a sensitive bifurcation in the behavior of these methods for this setup.

Table 2 provides a quantitative comparison of all considered turbulence models based on the relative mean absolute error (MAE) of profiles with respect to DNS shown in the discussions above. A first observation is that the vertical velocity $\overline{v}$ generally exhibits the largest error. Next, we see that general qualitative observations from previous sections are reaffirmed here, i.e. LES has the lowest MAE overall for every variable, whereas RANS shows significantly larger MAE than LES. SAS does not significantly improve the accuracy in comparison to RANS, while the WMLES-like behavior of DDES and IDDES result in important error reduction, more specifically for $\overline{u}$ and $\overline{v}$ Finally, DDES, even though it shows a promising RANS / LES domain partition, has the poorest accuracy of all simulations, caused by the MSD resulting from a delayed transition of the separated shear layer downstream of the step.

A recurring observation throughout Sect. 4 has been the different structure of both vertical and backflow velocity close to the step, which suggests a different organization of the recirculation and reattachment in the different simulations. To quantify this, we compute the time- and spanwise-averaged wall shear stress $\overline{\tau}$ at the bottom surface downstream of the step as

$$\overline{\tau}/\rho = \frac{1}{TL_z}\int_0^{L_z}\int_0^{T} \tau_{\text{wall}}(x,z,t)/\rho \,\mathrm{dt}\,\mathrm{dz}, \qquad (4)$$

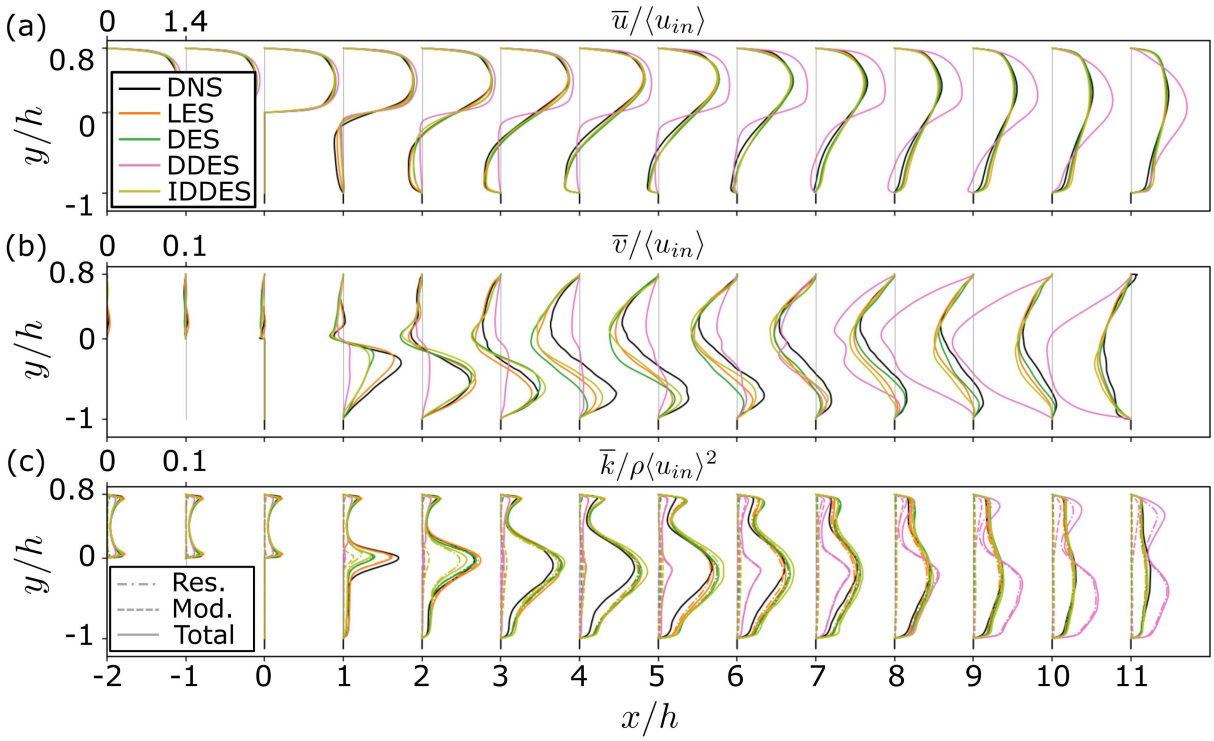

Figure 8. Profiles along midplane for DNS, LES, and DES variants. (a) Streamwise velocity component $\overline{u}$. (b) Vertical velocity component $\overline{v}$. Turbulent kinetic energy $\overline{k}$. Dashed, dot-dashed, and full lines indicated modeled, resolved and total (modeled + resolved) components.

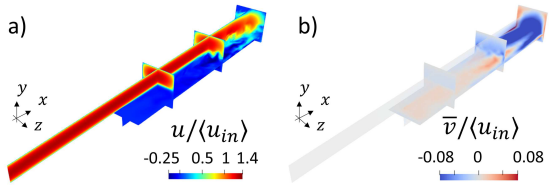

Figure 9. Flow field visualization for DDES. a) Streamwise velocity snapshot u. b) Time-averaged vertical velocity $\overline{v}$.

Figure 10. RANS/LES indicator function along the midplane for the DDES setup.

which is plotted as a function of streamwise location in Figure 13. The zero-crossing of $\overline{\tau}$ represents a spanwise-averaged reattachment point. LES, DES, and IDDES, reaffirm their resemblence and fidelity by closely matching the reattachment point observed in the reference DNS. Also, RANS and SAS are both shown to severely overpredict the size of the recirculation bubble, with RANS reattaching at $x/h \approx 11$, and SAS not reattaching at all. DDES finally shows a different recirculation structure from any of the other models, caused by the MSD mentioned above.

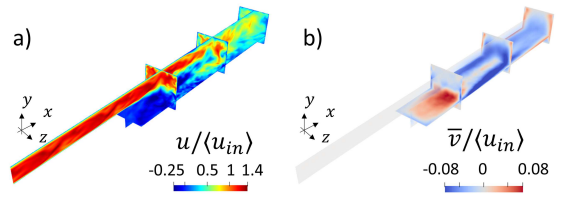

Figure 11. Flow field visualization for IDDES. a) Streamwise velocity snapshot u. b) Time-averaged vertical velocity $\overline{v}$.

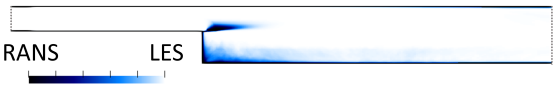

Figure 12. RANS/LES indicator function along the midplane for the IDDES setup.

5. GRID RESOLUTION SENSITIVITY

An important note to make on the results presented in the previous section is they are all performed on a fine mesh suitable for highly-resolved LES, as shown by the minor contribution of sub-grid LES terms e.g. in Figure 4. Therefore, the computational cost of all simulations (except for the steady RANS) is roughly equal. However, an appeal of hybrid and RANS methods is that they potentially retain their accuracy on more affordable meshes, since RANS zones are more robust to coarse resolutions than LES.

For this reason, we present a grid study here, and

Table 2. Relative mean absolute error of mid-plane profiles compared to DNS reference [5]. Best and worst values for every variable are indicated in boldfaced and underlined text respectively.

Model	$\overline{u}$	$\overline{v}$	$\overline{k}$
RANS	7.3%	16.0%	9.0%
SAS	9.7%	15.5%	8.9%
DES	3.9%	12.9%	7.2%
DDES	<u>12%</u>	<u>32.0%</u>	<u>22.7%</u>
IDDES	4.1%	12.2%	8.7%
LES	**2.8%**	**8.8%**	**5.5%**

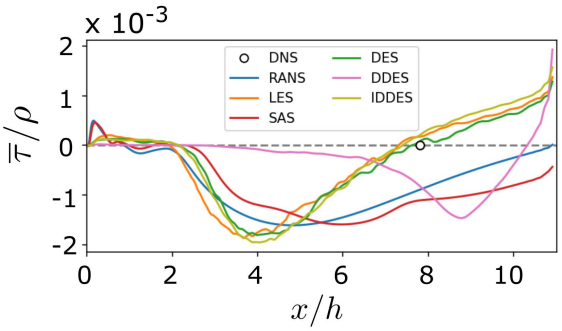

Figure 13. Time- and spanwise-averaged wall shear stress for RANS, LES, SAS, DES, DDES, and IDDES. DNS reattachment shown with circle.

quantify error sensitivity of different turbulence models to grid coarsening. The study is performed with 6 coarsened grids (C1 – C6), where the baseline grid resolution is reduced by 20% in all spatial directions, resulting in an overall reduction of degrees of freedom by a factor about 2 per coarsening step, or a total reduction of about 160 over the entire range.

A first observation from Table 3 (top) is the insensitivity of RANS error of about 9.6% to the grid resolution over the large range of coarsening. On the other side of the spectrum, we see that LES shows an expected decrease in accuracy with grid coarsening, as fewer turbulent scales can be resolved by the grid and have to be accounted for by the subgrid-scale model. Based on the current error metric, the crossover point, where RANS attains similar or superior accuracy over LES, lies around a resolution between the C3 grid and C4 grid. It was found that, around this point, the domain-integrated fraction of resolved to total turbulent kinetic energy in LES is about 80% for these grids, corresponding with the general 80% rule-of-thumb for a proper LES. These are promising observations especially for the LES-like hybrid methods DES, DDES and IDDES, as grid coarsening could convert LES zones to RANS zones, and it is observed that in RANS zones the grid resolution, and hence the computational cost, can significantly reduced without sacrificing accuracy.

However, investigation of the hybrid performance shows that this promise remains unfulfilled, as none of the hybrid methods can retain accuracy higher than the RANS baseline error of 9.6% upon grid coarsening. DDES remains very poor for all grids considered. DES exhibits a sharp error increase for grid C2. Further investigation showed this was caused by a laminarization of the inlet channel in LES mode. Indeed, Table 3 (bottom) shows that DES retains its WMLES character and does not switch to RANS zones, even at the coarsest grids. IDDES shows a gradual increase in errors due to a switch towards the configuration with RANS at inlet and walls, and LES in the SSL. However, in this mode IDDES suffers from MSD, resulting in large errors.

The observations in the current section allow to draw important conclusions regarding the hybrid methods considered in this report for the current low-Reynolds number BFS flow. Although for LES-suited grids DES and IDDES improve the match with DNS data compared to the baseline RANS by running in WMLES mode, these improvements are not retained upon grid coarsening. SAS and DDES never succeed to surpass RANS accuracy. Note that some of these observations can be linked to the relatively low Reynolds number of the current setup. We verified that, at higher Reynolds numbers the foregoing problems are somewhat mitigated, yet not fully resolved. This is omitted here due to space limitations.

6. SUMMARY

We have investigated hybrid turbulence models for a confined BFS flow at low Reynolds number. Simulations were performed using RANS, LES, and hybrid SAS and DES variants. Results were compared to existing high-fidelity DNS data. A first set of simulations was performed on a fine simulation grid. A comparison between RANS and LES showed that partial scale resolution allows to significantly improve the overall match with DNS, justifying the current BFS setup is suitable for testing the performance of locally scale-resolving hybrid methods. Results obtained from the hybrid simulations indicate that, for the current case, their behavior can be classified in three groups, with SAS resembling RANS, DES and IDDES behaving like WMLES, and DDES showing a more promising hybrid domain partition.

A quantitative comparison revealed that the (WM)LES type models DES and IDDES emerge as the higher-fidelity hybrid turbulence models. In contrast, SAS and DDES fail to consistently improve over RANS. Especially the recirculation structure and associated reattachment point are very ill-predicted by the SAS and DDES, whereas DES and IDDES closely adhere to the LES and DNS. While SAS does not qualitatively distinguish itself from RANS, the DDES suffers from MSD caused by a lack of both resolved and modeled turbulence in the zone close to the step.

A grid coarsening study was performed to quantify the error degradation of all models, as well as the switching behavior between RANS and LES

Table 3. Top: *Averaged error metric* for sensitivity study including baseline (B) and coarsened grids (C1 – C6). Degrees of freedom per grid are shown in parenthesis. Best and worst errors for every grid indicated in boldfaced and underlined text respectively. Bottom: *Domain LES fraction* for DES, DDES, and IDDES. Boldfaced text indicates configuration with RANS at inlet and walls combined with LES in SSL

	B	C1	C2	C3	C4	C5	C6
Averaged error metric	(3.7M)	(1.9M)	(942k)	(465k)	(230k)	(106k)	(52k)
RANS	9.6%	9.8%	9.9%	9.8%	**9.9%**	**9.5%**	**9.5%**
SAS	10.4%	10.8%	11.2%	11.3%	10.3%	9.9 %	9.9%
DES	7.3%	10.8%	23.0%	21.9%	21.3%	20.9%	19.1%
DDES	20.1%	18.3%	21.9%	17.4%	18.0%	18.0%	17.6%
IDDES	8.0%	10.4%	12.0%	11.7%	15.9%	16.6%	14.6%
LES	**6.2%**	**8.2%**	**8.7%**	**9.5 %**	11.5%	12.4%	13.3%
Domain LES fraction	B	C1	C2	C3	C4	C5	C6
DES	87%	86%	56%	57%	57%	61%	67%
DDES	**41%**	**38%**	56%	**31%**	**30%**	**31%**	**27%**
IDDES	88%	87%	85%	**33%**	**36%**	**34%**	**26%**

zones for DES and its variants. The grid study showed that, although its error metrics continuously worsen with coarsening, LES retains superior accuracy over RANS except for very coarse grids. However, none of the hybrid methods retained their improvements over RANS for coarsened grids.

In conclusion, it was shown that, for the current setup, the considered hybrid methods only perform adequately if the grid allows them to run in WMLES mode throughout the entire domain, and that attempts to reduce computational cost with regard to a full LES invariably lead to a strong increase in error for the hybrid models. However, also more promising observations were made, mainly that DDES and IDDES are capable of automatically dividing the domain into desirable RANS and LES zones, and that higher Reynolds numbers appear to promote scale development closer to the step.

We close with suggestions for future research. A similar investigation for significantly higher Reynolds numbers will clarify whether current models automatically improve by earlier natural scale development. Also, it would be interesting to see whether scale development is promoted by perturbations close to the separation point, or whether such immediate development can only be attained by resolved turbulence in the channel, which triggers a bypass-type transition in the SSL. Finally, it is important to note that we only considered ready-to-use standard hybrid techniques available in OpenFOAM v2012. It would be interesting to further assess the behavior of more advanced hybrid models that promise rapid transition in separated flows for the current BFS setup [12].

ACKNOWLEDGEMENTS

The authors thank Jure Oder and Matilde Fiore for discussions and help with the DNS data. This work has been performed in context of the PATRICIA project, which has received funding from European Union's Horizon 2020 Research and Innovation programme under grant agreement No. 945077.

REFERENCES

[1] Spalart, P. R., 2009, "Detached-eddy simulation", *Annual review of fluid mechanics*, Vol. 41, pp. 181–202.

[2] Strelets, M., 2001, "Detached eddy simulation of massively separated flows", *39th Aerospace sciences meeting and exhibit*, p. 879.

[3] Chaouat, B., 2017, "The state of the art of hybrid RANS/LES modeling for the simulation of turbulent flows", *Flow, turbulence and combustion*, Vol. 99 (2), pp. 279–327.

[4] Tiselj, I., and Oder, J., 2019, "Direct Numerical Simulation of a Backward-Facing Step.", *Technical Deliverable of Euratom RIA SESAME project*.

[5] Oder, J., Shams, A., Cizelj, L., and Tiselj, I., 2019, "Direct numerical simulation of low-Prandtl fluid flow over a confined backward facing step", *International Journal of Heat and Mass Transfer*, Vol. 142, p. 118436.

[6] Menter, F. R., Kuntz, M., and Langtry, R., 2003, "Ten years of industrial experience with the SST turbulence model", *Turbulence, heat and mass transfer*, Vol. 4 (1), pp. 625–632.

[7] Kim, W.-W., and Menon, S., 1995, "A new dynamic one-equation subgrid-scale model for large eddy simulations", *33rd Aerospace Sciences Meeting and Exhibit*, p. 356.

[8] Egorov, Y., and Menter, F., 2008, "Development and application of SST-SAS turbulence model in the DESIDER project", *Advances in Hybrid RANS-LES Modelling*, Springer, pp. 261–270.

[9] Gritskevich, M. S., Garbaruk, A. V., Schütze, J., and Menter, F. R., 2012, "Development of DDES and IDDES formulations for the k-ω shear stress transport model", *Flow, turbulence and combustion*, Vol. 88 (3), pp. 431–449.

[10] OpenCFD OpenFOAM v2012, available at `https://develop.openfoam.com/Development/openfoam/-/releases/OpenFOAM-v2012`, accessed: 24 May 2022.

[11] Weller, H. G., Tabor, G., Jasak, H., and Fureby, C., 1998, "A tensorial approach to computational continuum mechanics using object-oriented techniques", *Computers in Physics*, Vol. 12 (6), pp. 620–631.

[12] Shur, M. L., Spalart, P. R., Strelets, M. K., and Travin, A. K., 2015, "An enhanced version of DES with rapid transition from RANS to LES in separated flows", *Flow, turbulence and combustion*, Vol. 95 (4), pp. 709–737.

Conference on Modelling Fluid Flow (CMFF'22)
The 18th International Conference on Fluid Flow Technologies
Budapest, Hungary, August 30 -September 2, 2022

EFFECT OF SHEAR RATE ON POLYMER-INDUCED FLOCCULATION FOR BEHAVIOURAL MODIFICATION TECHNIQUES

Lee MORTIMER[1], Michael FAIRWEATHER[2]

[1] Corresponding Author. School of Chemical and Process Engineering, Faculty of Engineering and Physical Sciences, University of Leeds. Leeds LS2 9JT, United Kingdom. E-mail: l.f.mortimer@leeds.ac.uk
[2] School of Chemical and Process Engineering, Faculty of Engineering and Physical Sciences, University of Leeds. Leeds LS2 9JT, United Kingdom. E-mail: m.fairweather@leeds.ac.uk

ABSTRACT

A novel potential-based model for resolving polymer-particle interaction is presented and used to study the effect of shear rate on the adsorption dynamics of polymer chains onto a stationary particle surface. The polymeric phase is modelled as a sequence of bead-spring components using Langevin dynamics with the finite extensible nonlinear elastic potential to represent the molecular interactions within the polymer chain. The effects of steric interactions and the Kratky-Porod bending rigidity potential are also included in the calculations. Particles are modelled as computational spheres which interact sterically with the polymer beads through a modified, truncated Lennard-Jones potential. Dependencies of conformation properties such as the mean radius of gyration and end-to-end distance on the diffusion coefficient, bending rigidity and the shear flow rate are discussed and their implications on the collision cross section for polymer-particle interactions are considered. Polymer-particle adsorption events are studied, and it is shown that low shear encourages full adsorption at the point of collision, whereas increased shear hinders it, with moderate shear causing shorter tail-like structures upon adsorption. The findings of this study are of importance to the development of behavioural modification techniques where bulk system parameters are tuned to obtain a desired behaviour.

Keywords: Adsorption, Brownian dynamics, multiphase flows, polymeric flows, polymer-particle interaction, shear flows

NOMENCLATURE

D	[m^2 s^{-1}]	Diffusion coefficient
D_p	[m]	Particle diameter
K_B^*	[-]	Bending rigidity
K_F^*	[-]	FENE potential strength
K_{LJT}^*	[-]	LJT potential strength
k_B	[J K^{-1}]	Boltzmann constant
m_b	[kg]	Bead mass
N_A	[-]	Number of adsorbed beads
N_B	[-]	Number of beads in chain
N_T	[-]	Number of tail beads
$\boldsymbol{r}_i$	[m]	Bead position vector
$\boldsymbol{r}_i^*$	[-]	Polymer position vector
R_0^*	[-]	Maximum FENE bond length
T	[K]	Temperature
V_i	[J]	Total bead interaction potential
$V_{i,B}^*$	[-]	Bending potential
$V_{i,F}^*$	[-]	FENE potential
$V_{i,P}^*$	[-]	LJT potential
$V_{i,W}^*$	[-]	WCA potential
$V_{0,P}^*$	[-]	LJT potential shift
V_W^*	[-]	Wall potential
We	[-]	Weissenberg number
δr^*	[-]	Bead separation
δr_{max}^*	[-]	Maximum separation for WCA
δt^*	[-]	Verlet integration timestep
δy^*	[-]	Wall penetration distance
ξ	[kg s^{-1}]	Bead drag coefficient
$\boldsymbol{\eta_i}(t)$	[s$^{-1/2}$]	Brownian noise term
σ_b	[m]	Bead diameter
τ_b	[s]	Bead timescale
θ_i	[-]	Polymer chain angle

Subscripts and Superscripts

FENE	Finitely extensible nonlinear elastic
LJT	Lennard-Jones (truncated)
WCA	Weeks-Chandler-Anderson
i	Bead in polymer chain
x, y, z	Cartesian coordinates
< >	Timewise mean
$\bar{}$	Polymer chain mean
*	Non-dimensional units

1. INTRODUCTION

The addition of small concentrations of high-molecular-weight polymers to particle-laden flows to separate non-settling fine solids from aqueous suspensions is a promising technique to instigate settling, suitable for many industrial challenges and requirements such as filtration and thickening [1-3]. Despite demonstration in laboratory-scale rigs and wastewater flows, the dynamics leading to flocculation in such systems are still poorly understood [4]. In such applications, natural flocculants are usually combined with synthetic polymers to tailor the additive properties to those required for maximum efficiency, with the process of doing so referred to as behavioural modification. However, without the ability to predict the system parameters which best exhibit a required outcome, these techniques are still performed inefficiently. Furthermore, the potential to use polymers in sensitive systems such as nuclear waste processing flows depends upon on the development of improved understanding and demonstrable effectiveness. In recent decades, the application of various polymeric-phase modelling techniques [5] has uncovered remarkable behaviours in simple interacting systems such as stagnant tanks [6], as well as in shear and turbulent flows [7].

Monte-Carlo modelling has shown that the resulting polymer-particle structure is highly dependent on the strength of the interaction potentials [8], with the relative proportion of trains to tails and loops increasing with interaction strength. Similar studies also indicate that the polymer chain length is an important parameter when predicting the critical adsorption point [9]. Despite reasonable progress in recent studies, many questions remain unanswered surrounding the dynamics leading to polymer-particle bridging and subsequent flocculation, particularly so in non-stagnant systems, where shear has been shown to play an important role in polymer conformation [10]. Polymers within shear flows have been shown experimentally to undergo both elongational and rotational mechanisms which lead to tumbling motions, increasing the complexity of polymer-particle interaction behaviour [11]. This study aims to use nonequilibrium Langevin dynamic simulations to elucidate the fundamentals of polymer-particle interaction and adhesion within shear flows, as well as the way in which chemical or bulk properties (such as ionic strength which modulates the molecular interaction potentials and shear rate which affects the conformity of the polymer chain) affect the dynamics of adhesion, bridging and subsequent flocculation.

The development of the present technique also provides a foundation to study more complex rheological flows through interaction with the fluid stress tensor based on local polymer conformation. This allows for further study of processes such as drag reduction and viscoelasticity.

2. METHODOLOGY

In the present work, Langevin dynamics is used to simulate polymers as macromolecular chains of interacting beads (monomers), as employed in various Brownian dynamic studies [12-14]. The position vector $\boldsymbol{r}_i$ of each bead (referenced using subscript i) in a polymer chain evolves by obeying the following Newtonian equation of motion [5]:

$$m_b \frac{d^2\boldsymbol{r}_i}{dt^2} = -\boldsymbol{\nabla} V_i - \xi\left(\frac{d(\boldsymbol{r}_i)}{dt} - \boldsymbol{u}_{F,i}\right) + \sqrt{2k_B T\xi}\,\boldsymbol{\eta}_i(t). \tag{1}$$

Here, m_b represents the mass of the bead, t is time, V_i is the total interaction potential calculated at the bead's current position, ξ is the drag coefficient, $\boldsymbol{u}_{F,i}$ is the local fluid velocity, k_B is the Boltzmann constant, T is the temperature and $\boldsymbol{\eta}_i(t)$ is a Brownian noise term satisfying $\langle \eta_{ia}(t)\rangle = 0$ and $\langle \eta_{ia}(t)\eta_{ib}(t')\rangle = \delta_{a,b}\delta(t-t')$. If a constant bead diameter is used, σ_b, then time may be nondimensionalised using the Brownian bead timescale $\tau_b = \sqrt{m_b\sigma_b/k_B T}$, and space using the bead diameter. Further introducing the diffusion coefficient, $D = k_B T/\xi$, allows us to rewrite Eq. (1) as:

$$\frac{d^2\boldsymbol{r}_i^*}{dt^{*2}} = -\boldsymbol{\nabla} V_i^* - \frac{1}{D}\left(\frac{d\boldsymbol{r}_i^*}{dt^*} - \boldsymbol{u}_{F,i}^*\right) + \sqrt{\frac{2}{D}}\,\boldsymbol{\eta}_i^*(t^*), \tag{2}$$

where variables superscripted with $(*)$ represent nondimensional terms.

The contributions to the overall interaction potential for the beads are given by:

$$V_i^* = V_{i,F}^* + V_{i,B}^* + V_{i,W}^* + V_{i,P}^*. \tag{3}$$

The first term $V_{i,F}^*$ represents the bonds between the monomers using the finitely extensible nonlinear elastic (FENE) spring force described using the potential:

$$V_{i,F}^*(\delta r^*) = -\frac{K_F^* R_0^{*2}}{2}\ln\left[1 - \left(\frac{\delta r^*}{R_0^*}\right)^2\right], \tag{4}$$

where $\delta r^* = |\boldsymbol{r}_{i+1}^* - \boldsymbol{r}_i^*|$ is the bead separation, K_F^* is the FENE energy scale and R_0^* is the maximum FENE bond length. This interaction potential is only included in the calculation of neighbouring beads in the chain of monomers. The second term is used to model the effects of polymer bending rigidity observed in real polymers, wherein acute polymer

angles are less favoured energetically due to molecular constraints. The Kratky-Porod potential is given by:

$$V_{i,B}^*(\theta_i) = K_B^*(1 + \cos(\theta_i), \quad (5)$$

where θ_i is the angle formed by two neighbouring separation vectors, i.e. $\theta_i = \cos^{-1}(\hat{\boldsymbol{n}}_{i+1} \cdot \hat{\boldsymbol{n}}_i)$ with $\hat{\boldsymbol{n}}_i = (\boldsymbol{r}_i^* - \boldsymbol{r}_{i+1}^*)/|\boldsymbol{r}_i^* - \boldsymbol{r}_{i+1}^*|$. K_B represents the strength of the bending rigidity. The penultimate term in Eq. (3) represents steric interactions between polymer beads and is given by a Weeks-Chandler-Anderson (WCA) potential:

$$V_{i,W}^*(\delta r^*) = 1 + 4\left[\left(\frac{1}{\delta r^*}\right)^{12} - \left(\frac{1}{\delta r^*}\right)^{6}\right], \quad (6)$$

which contributes to the total potential for all pairs of monomers within a maximum distance δr_{max}^*. The final term represents interaction with a dispersed particulate phase. Particles are represented by rigid body isotropic spheres of constant diameter, $D_P = 5\sigma_b$. In all simulations considered here the particle remains fixed at the midpoint of the domain. Polymer beads close to the particle are able to interact sterically. The polymer-particle interaction potential is a truncated Lennard-Jones (LJT) potential which takes the form [14]:

$$V_{i,P}^*(\delta r^*) = K_{LJT}^*\left[\left(\frac{1}{\delta r^* - s^*}\right)^{12} - 2\left(\frac{1}{\delta r^* - s^*}\right)^{6}\right] + V_{0,P}^*, \quad (7)$$

with the term $V_{0,P}^*$ representing shifting the interaction potential such that $V_{i,P}^*(\delta r^* > 5) = 0$, given as:

$$V_{0,P}^*(\delta r^*) = K_{LJT}^*\left[\left(\frac{1}{2.5}\right)^{12} - 2\left(\frac{1}{2.5}\right)^{6}\right]. \quad (8)$$

To solve Eqs. (2-8), the Verlet-velocity integration method was employed with constant timestep δt^*. For shear flows, the shear rate is parameterised by the Weissenberg number based on the bead timescale, $We = \tau_b du/dy = du^*/dy^*$. The domain in all cases is a $90 \times 30 \times 90$ computational channel cell, with periodic conditions in the streamwise (x^*) and spanwise (z^*) directions, and a wall potential at the extents of the y^*direction, with form:

$$V_W^*(\delta y^*) = 10.0\delta y^{*2}, \quad (9)$$

with δy^* the wall penetration distance. The domain is illustrated in Figure 1. In the case of shear flows, the lower wall ($y^* = 0$) possesses a constant streamwise velocity of $u_x^* = 0$ everywhere on the wall, and the top wall is kept at $u_x^* = 30We$, with the gradient constant within the domain. The particle diameter is fixed at $D_P^* = 10$.

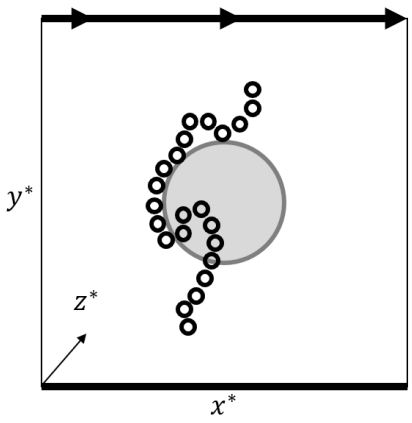

Figure 1. Overview of polymer-particle adsorption event within cell. Particle is represented by the large grey circle, while polymer beads represented by small white circles. Thick black arrowed lines represent direction and magnitude of shear flow

3. RESULTS AND DISCUSSION

We first consider the tuneable parameters in our model, of which there are many. The number of beads in a polymer chain is fixed at $N_B = 32$. To complement previous studies [13], both the FENE potential and the maximum FENE bond length are fixed, with $K_F^* = 30$ and $R_0^* = 1.6$. The impact of these parameters on the components of the individual bead-bead interaction potentials as well as their total as a function of separation distance is illustrated in Figure. 2. Here, a stable minimum is observed at just below $\delta r^* = 1.0$, which would be the equilibrium separation without the influence of Brownian forces or fluid interaction.

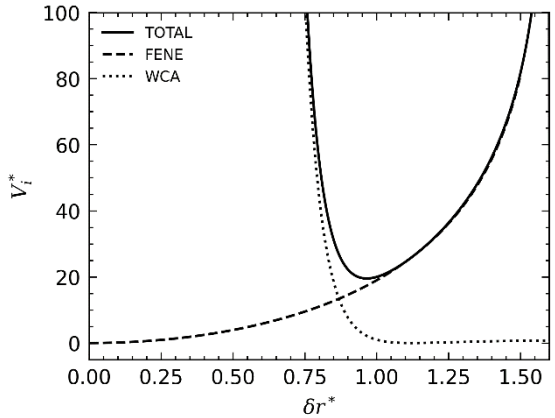

Figure 2. Interaction potentials for neighbouring polymer beads with $K_F^* = 30$ and $R_0^* = 1.6$

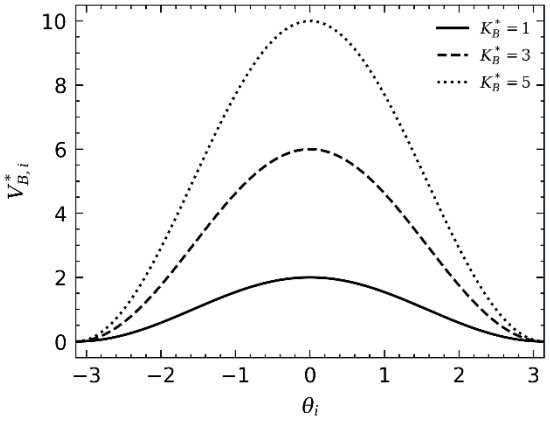

Figure 3. Effect of bending rigidity, K_B^*, on interaction potential for neighbouring polymer beads

The effect of the bending rigidity strength on the full potential as a function of chain angle is also illustrated in Figure 3. For increased strengths, the minima at more obtuse angles becomes more stable, hence less bending between the polymer beads is expected leading to more straightened-out conformities.

Initial simulations were performed under quiescent conditions in order to determine how the bending rigidity, K_B^*, affects the conformity of the polymer. The effect of variation of the diffusion coefficient, D, was also considered, which determines the extent of damping within the system. For all simulations presented here, Monte-Carlo techniques were employed, meaning that multiple instances of the same simulation were performed with measurables averaged over all instances. For the quiescent simulations, 1000 samples were obtained with individual polymers injected into a stagnant cell and allowed to disperse freely. The timestep remained constant at $\delta t^* = 0.005$.

The effect of K_B^* and D on the temporal evolution of the mean end-to-end polymer chain distance is illustrated in Figure 4. The system exhibits the greatest elongational behaviour when both the bending rigidity and the diffusion coefficient are greatest, with the increase in D having the greatest effect when compared to the overdamped $D = 0.5$ system. In the other two cases, at $K_B^* = 3$ and $K_B^* = 1$, the variation of diffusion coefficient had the opposite effect, meaning that the larger coefficient systems exhibited lower polymer end-to-end separations. This is likely due to the dominance of the Brownian term in Eq. (2) leading to more compact conformity states where bending rigidity plays a less important role. This is clear for the low damping system with $K_B^* = 3$ and $K_B^* = 1$ where the eventual mean end-to-end distance vectors are very similar.

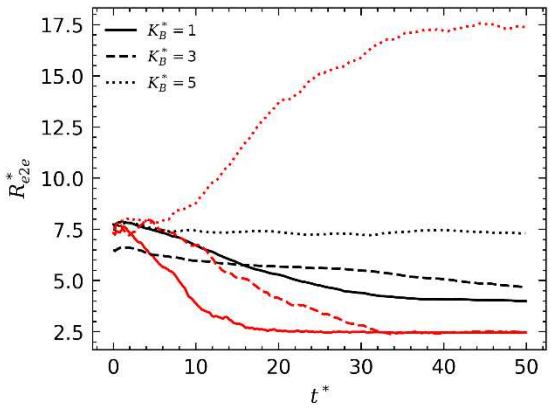

Figure 4. Effect of bending rigidity, K_B^*, and diffusion coefficient, D, on temporal evolution of end-to-end polymer chain distance in quiescent conditions. Black: $D = 0.5$, Red: $D = 5$

The mean radius of gyration associated with a polymer chain was calculated using:

$$R_{0,i}^* = \sqrt{\frac{1}{N_B}\sum_i (\boldsymbol{r}_i^* - \bar{\boldsymbol{r}}^*)^2}, \tag{10}$$

with $\boldsymbol{r}_i^*$ the position of bead i and $\bar{\boldsymbol{r}}^*$ the mean bead position. The temporal evolution of the mean of this quantity is illustrated in Figure 5. Once again, the system with the high diffusion coefficient and bending rigidity exhibited large radii of gyration and the greatest deviation between the damped and undamped cases.

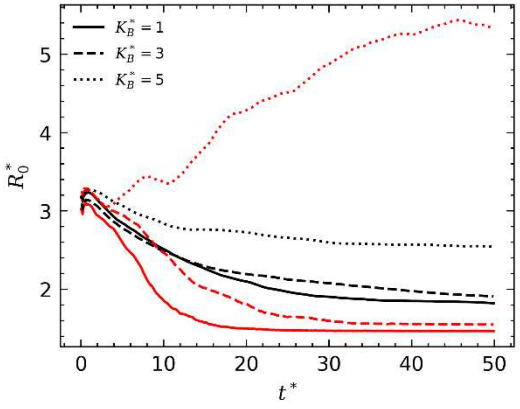

Figure 5. Effect of bending rigidity, K_B^*, and diffusion coefficient, D, on temporal evolution of polymer chain radius of gyration under quiescent conditions. Black: $D = 0.5$, Red: $D = 5$

From Figs. 5 and 4 it is clear that polymers in these cases are stretching and forming long elongated strands. For lower bending rigidities, varying the diffusion coefficient has a much more pronounced effect than varying the rigidity, with the most curled-

up polymers occurring in the undamped, low rigidity case. Here beads are able to visit locations close to the polymer centre of volume during their random diffusion, with little tendency to extend away from their neighbouring beads.

To investigate the effect of Weissenberg number, We, on the conformation properties of polymers, subsequent simulations were performed in a shear flow within the domain outlined in Fig. 1. This time, the diffusion coefficient and bending rigidity were set constant at $K_B^* = 1$ and $D = 5$ (i.e. the most curled polymers under quiescent conditions) in order to isolate stretching effects due to shear. Root beads were initially injected into a random location within the domain and allowed to 'grow' randomly ensuring that the following bead was located on a surrounding unit sphere. Grown beads were also not allowed to overlap.

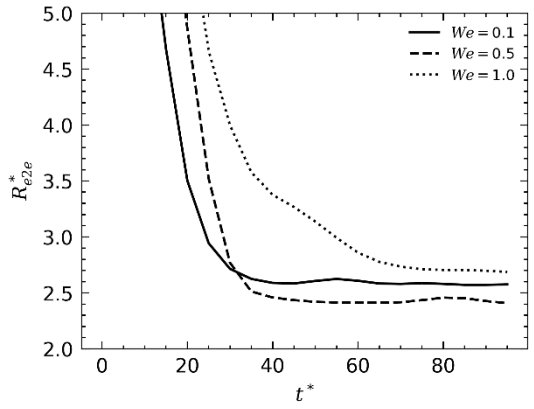

Figure 6. Effect of Weissenberg number, We, on temporal evolution of end-to-end polymer chain distance under shear flow conditions

The temporal evolution of the mean end-to-end distance as a function of We is illustrated in Figure 6. This property is maximised for the highest shear rate, meaning the velocity gradient across the polymer chain induces stretching. Interestingly, for the midrange shear, R^*_{e2e} is actually reduced. Tumbling behaviour was observed, consistent with previous studies [15], which counteracted the extensional behaviour associated with the shear, wherein chains would begin to extend and then, due to the torque applied by the variation in fluid velocity across the chain, would begin to rotate. When the chains are orientated streamwise there is no longer any velocity gradient across the polymer and hence the curling mechanisms can occur, bringing the two ends of the polymer closer together. At the lowest shear rate, this curling dynamic is dominant (as in the quiescent flows) but the polymer chain contracts in on itself across the full chain, offering greater distance between the start and end beads. In Figure 7, the effect on the radius of gyration of the resulting conformities is clear. For high Weissenberg number, the polymers sample more elongated states, with intermediate distances between beads generally larger. Even though the mean end-to-end distance is lowest for $We = 0.5$, the radius of gyration remains moderate, which implies slightly elongated spherical conformities (which was confirmed by visual inspection of the systems). Finally, for low Weissenberg number, R_0^* remains low, as the chains form tightly bound conformities.

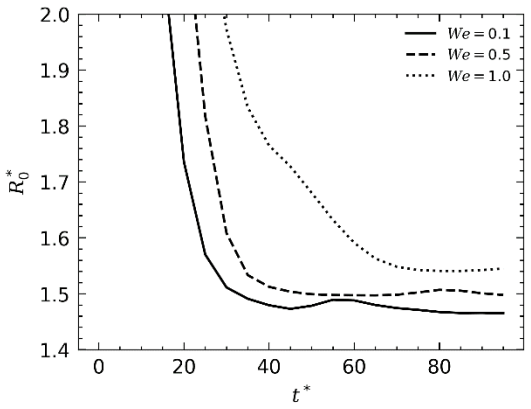

Figure 7. Effect of Weissenberg number, We, on temporal evolution of polymer chain radius of gyration under shear flow conditions

If an applied shear flow causes the polymer radius of gyration to increase, it is expected that the collision cross section between polymers and particles would increase for flocculation applications. However, it is also known from the literature that there exists competition between coagulation and fragmentation, which depends highly on the shear rate [16]. To elucidate further the dynamics at the point of polymer-particle impact and interaction, the effect of Weissenberg number on the adsorption of polymer chains onto a spherical particle was also studied. In these simulations, a single particle was fixed in the centre of the domain, with bead-particle interactions governed by the LJT force as in Eq. (7). Parameters for these simulations are presented in Table 1.

Table 1. Polymer-particle adsorption simulation parameters

Parameter	Value
We	0.1, 0.5, 1.0
R_0^*	1.6
D	5
K_F^*	30.0
K_B^*	1.0
K_P^*	10.0
δt^*	0.005
N_B	32

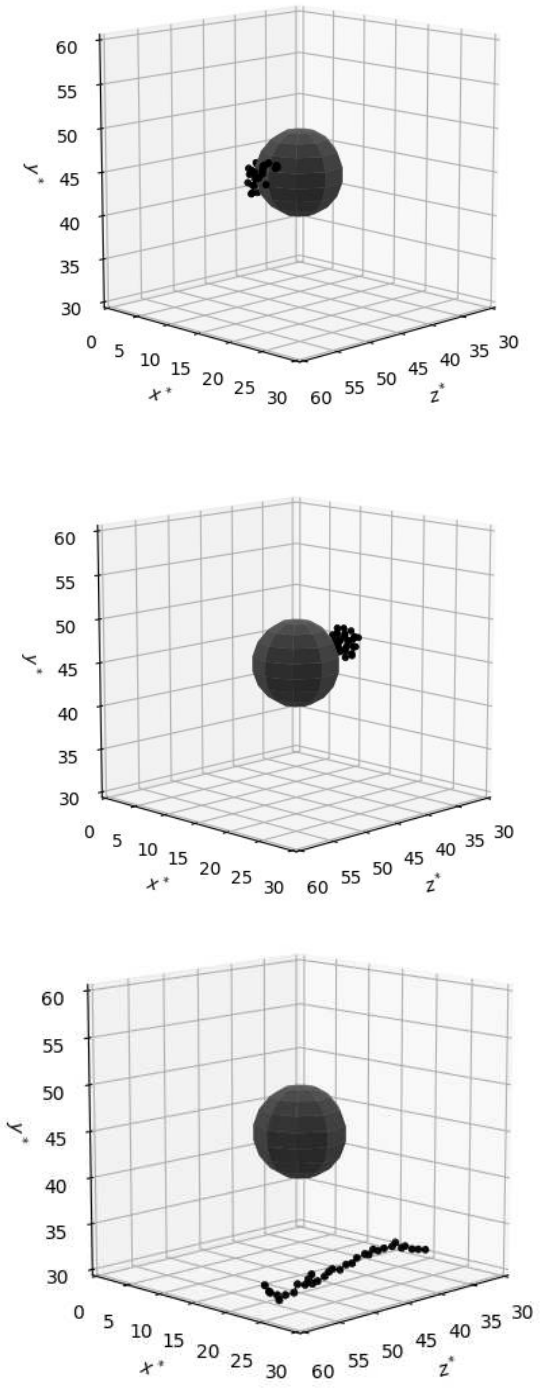

Figure 8. Instantaneous snapshots of $t^* = 15$. Effect of We on eventual polymer adsorption state is indicated with $We = 0.1$ (upper), $We = 0.5$ (middle) and $We = 1.0$ (lower)

In each Monte-Carlo instantiation, a single polymer was injected in a random location with a conformation chosen at random from the samples obtained in the polymer-only systems. This initial position means that the shear flow would direct the polymer towards the particle in time. This chosen setup aims to capture a single polymer-particle interaction event typical of those taking place in shear and turbulent flows. Once injected, the simulation is allowed to evolve for a set amount of time ($t^* = 15$). The final positions of each bead were then recorded, with some instances ending with polymer-particle adsorption and some without.

Examples of three typical eventualities for each Weissenberg number are presented in Figure. 8. The top plot demonstrates the low shear ($We = 0.1$) simulation, where most of the beads have clearly adsorbed onto the surface of the particle. Given the spherical 'ball' nature of the conformity of these polymers, collisions with the particle are likely and the lack of flow strength allows the chain to unravel across the particle. The middle plot illustrates a typical medium shear example, where some beads in the polymer chain have successfully adsorbed onto the particle, but the full polymer remains curled and has not fully unravelled. Finally, in many cases at high shear, $We = 1.0$, the polymers are unsuccessful in adsorbing onto the particle. In some cases temporary adsorption was observed, but the shear flow was strong enough to remove the polymer from the particle.

To further quantify the extent of polymer bead adsorption, an adsorption condition is defined such that the surface-to-surface distance between a bead and the particle is lower than an arbitrary value $\sigma_A = 2$. Table 2 shows the percentage of instantiations resulting in at least one polymer bead remaining adsorbed onto the particle surface. For low shear, over half the interactions resulted in adsorption, whereas as the Weissenberg number increases, the occurrence of adsorption becomes increasingly unlikely. In the case of $We = 1.0$, the shear is too strong for beads to remain bound to the particle surface, and it is likely that any instances of adsorption at the sample time was due to their random walk being close to the particle.

Table 2. Adsorption efficiency dependence on Weissenberg number

We	% Adsorption
0.1	67.4
0.5	37.6
1.0	12.1

To further examine the conformity of the chain at the particle surface, the probability density function for the number of adsorbed beads in each polymer chain, N_A, sampled over all 100 Monte-Carlo instances is *presented* in Figure 9. Starting with the low shear rate system, these interactions exhibited the most $N_A = N_B = 32$ (i.e. full adsorption) events where all beads in the chain remained bound to the surface. The distribution is also fairly uniform, and so there existed some interactions where only a few of the beads fully adsorbed and others where the chain failed to adsorb

at all. As the shear rate increases, the number of fully adsorbed chains is reduced and the number of chains in the region where fewer than half of the beads adsorb increases. This is indicative of tail- and train-like adsorption behaviour, where the particle has a polymer chain attached, with a free end or loop still subject to fluid dispersion. Finally, the high shear system peaks at $N_A = 0$ indicating the dominance of events with no adsorption, however, there did still exist a few events exhibiting tail- and train-like behaviour.

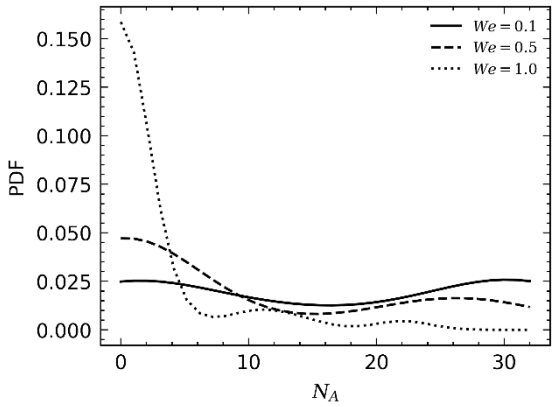

Figure 9. Probability density function of the number of adsorbed beads N_A. Effect of Weissenberg number is illustrated

Lastly, to further quantify the existence of tails within the adsorbed state, N_T is defined as the number of 'tail' beads within a polymer chain which are connected to a 'free' end as well as an adsorbed bead. Connected in this case refers to an eventual neighbour further down the chain in either direction. The distribution of the number of tail beads in our adsorbed states is presented in Figure. 10.

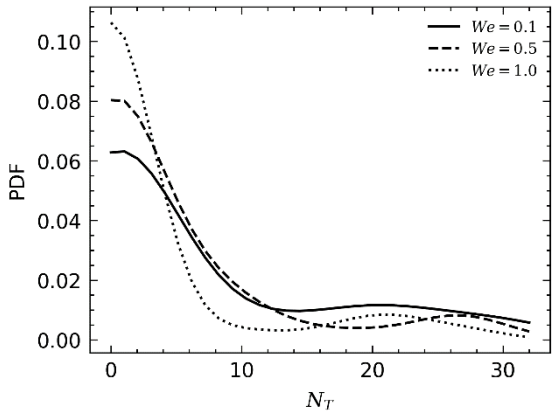

Figure 10. Probability density function of the number of tail beads N_T. Effect of Weissenberg number is illustrated

Evidently, tails formed generally had $N_T < 10$ and were more common in the high shear systems because in the $We = 0.1$ system most beads were adsorbed onto the particle. It is also interesting that a secondary wide peak forms around $N_T = 20$ which likely corresponds to polymers with two tails and an adsorption region. Similar analysis of train-like (sequences of adsorbed beads) and loop-like (sequences of unadsorbed beads but attached at either end) behaviour was performed which indicated trains forming with low shear.

4. CONCLUSIONS

A novel potential-based particle-polymer simulation adsorption simulation technique has been developed in order to explore the fundamentals of flocculation and polymer-surface interaction. The polymeric phase has been modelled using the FENE bead-spring approach and time-evolved using Langevin dynamics. Interactions within the polymer chain as well as the Kratky-Porod bending rigidity potential have been included in the calculations. The particle phase was modelled as a finite-size computational sphere, which interacts sterically with the polymer beads through a modified truncated Lennard-Jones potential.

From Monte-Carlo studies of quiescent flows it was shown that polymers exhibit the greatest extensional behaviour when both the diffusion coefficient and the chain rigidity is high. For undamped systems, the influence of rigidity is very low beneath $K_B^* = 3$, whereas for damped systems, the parameter affects the eventual radius of gyration and mean end-to-end distance vector, with increased rigidity leading to more elongated conformities.

Studies of polymers in shear showed that for high shear rates, chains were longer and possessed a larger radius of gyration. For medium shear, the polymers would undergo tumbling motion and the end-to-end distance vector would be reduced while their radius of gyration remained moderate. Finally, for the low shear system, conformities were generally ball-like and both properties were low.

Monte-Carlo simulations of shear flows in the presence of a single stationary particle were also performed to determine mechanisms for adsorption. Most adsorption took place in the low shear rate system, with beads able to resist the flow and unravelling across the particle surface. For the medium shear rate, some beads were able to adsorb onto the particle, forming tails and trains which increase the effective flocculation radius of the particle. For high shear rate, most beads were unable to adsorb onto the particle, with those successful often being removed later in the simulation. This is an interesting phenomenon for understanding the conditions which lead to most effective flocculation and should be studied further. Another important parameter to consider is the polymer-particle LJT interaction strength, which can be influenced by modifying the ionic strength of the solution. In doing so, the effects of shear which reduce adsorption

could be counterbalanced by stronger attraction between the polymer and the particles. Using the techniques described in this paper, multi-particle simulations may also be performed to observed the way in which, and under what conditions, two or more particles begin to flocculate. Finally, the polymer contribution to the fluid stress tensor may also be included for study of more complex rheological measurements such as drag reduction, viscoelasticity and turbulence modulation [17-18].

ACKNOWLEDGEMENTS

The authors are grateful for funding from the UK Engineering and Physical Sciences Research Council through the TRANSCEND (Transformative Science and Engineering for Nuclear Decommissioning) project (EP/S01019X/1).

REFERENCES

[1] Lockwood, A. P. G., Peakall, J., Warren, N. J., Randall, G., Barnes, M., Harbottle, D., and Hunter, T. N., 2021, "Structure and Sedimentation Characterisation of Sheared Mg $(OH)_2$ Suspensions Flocculated with Anionic Polymers", *Chem Eng Sci,* Vol. 231, 116274.

[2] Vajihinejad, V., Gumfekar, S. P., Bazoubandi, B., Najafabadi, Z. R., and Soares, J. B. P., 2019, "Water Soluble Polymer Flocculants: Synthesis, Characterization, and Performance Assessment", *Macromol Mater Eng,* Vol. 304, 1800526.

[3] Lee, C. S., Robinson, J., and Chong, M. F., 2014, "A Review on Application of Flocculants in Wastewater Treatment", *Process Saf Environ Prot,* Vol. 92, pp. 489-508.

[4] Dickinson, E., and Eriksson, L., 1991, "Particle Flocculation by Adsorbing Polymers", *Adv Colloid Interface Sci*, Vol. 34, pp. 1-29.

[5] Öttinger, H. C., 2012, *Stochastic Processes in Polymeric Fluids: Tools and Examples for Developing Simulation Algorithms*, Springer-Verlag.

[6] Smith, D. E., Babcock, H. P., and Chu, S., 1999, "Single-Polymer Dynamics in Steady Shear Flow", *Science*, Vol. 283, pp. 1724-1727.

[7] Fu, Z., and Kawaguchi, Y., 2013, "A Short Review on Drag-Reduced Turbulent Flow of Inhomogeneous Polymer Solutions", *Adv Mech Eng*, Vol. 5, 432949.

[8] Li, C. Y., Cao, W. P., Luo, M. B., and Li, H., 2016, "Adsorption of Polymer on an Attractive Nano-Sized Particle", *Colloid Polym Sci*, Vol. 294, pp. 1001-1009.

[9] Li, H., Qian, C. J., and Luo, M. B., 2012, "Simulation of a Flexible Polymer Tethered to a Flat Adsorbing Surface", *J Appl Polym Sci*, Vol. 124, pp. 282-287.

[10] He, G. L., Messina, R., and Löwen, H., 2010, "Statistics of Polymer Adsorption Under Shear Flow", *J Chem Phys*, Vol. 132, 124903.

[11] He, G. L., Messina, R., Löwen, H., Kiriy, A., Bocharova, V., and Stamm, M., 2009, "Shear-Induced Stretching of Adsorbed Polymer Chains", *Soft Matter*, Vol. 5, pp. 3014-3017.

[12] Doyle, P. S., Shaqfeh, E. S., and Gast, A. P., 1998, "Rheology of Polymer Brushes: A Brownian Dynamics Study", *Macromolecules*, Vol. 31, pp. 5474-5486.

[13] Brackley, C. A., 2020. "Polymer Compaction and Bridging-Induced Clustering of Protein-Inspired Patchy Particles", *J Phys Condens Matter*, Vol. 32, 314002.

[14] Li, C. Y., Luo, M. B., Li, H., and Cao, W. P., 2017, "Simulation Study on the Conformational Properties of an Adsorbed Polymer on a Nanoparticle", *Colloid Polym Sci*, Vol. 295, pp. 2251-2260.

[15] Chopra, M., and Larson, R. G., 2002, "Brownian Dynamics Simulations of Isolated Polymer Molecules in Shear Flow Near Adsorbing and Nonadsorbing Surfaces", *J Rheol*, Vol. 46, pp. 831-862.

[16] Spicer, P. T., and Pratsinis, S. E., 1996, "Shear-Induced Flocculation: The Evolution of Floc Structure and the Shape of the Size Distribution at Steady State", *Water Res*, Vol. 30, pp. 1049-1056.

[17] White, C. M. and Mungal, M. G., 2008. "Mechanics and prediction of turbulent drag reduction with polymer additives". *Annu. Rev. Fluid Mech*, Vol 40, pp. 235-256.

[18] Smith, G. D., Bedrov, D., Li, L., and Byutner, O., 2002. "A molecular dynamics simulation study of the viscoelastic properties of polymer nanocomposites". *J Chem Phys*, Vol 117, pp. 9478-9489.

Conference on Modelling Fluid Flow (CMFF'22)
The 18th International Conference on Fluid Flow Technologies
Budapest, Hungary, August 30 -September 2, 2022

ANALYSIS OF THE REPEAT COLLISION EFFECT IN SIMULATED PARTICLE-LADEN FLOWS WITH AND WITHOUT AGGLOMERATION

David RUPP[1], Lee MORTIMER[2], Michael FAIRWEATHER[3]

[1] Corresponding Author. School of Chemical and Process Engineering, Faculty of Engineering and Physical Sciences, University of Leeds. Leeds LS2 9JT, United Kingdom. E-mail: pmdr@leeds.ac.uk
[2] School of Chemical and Process Engineering, Faculty of Engineering and Physical Sciences, University of Leeds. Leeds LS2 9JT, United Kingdom. E-mail: l.f.mortimer@leeds.ac.uk
[3] School of Chemical and Process Engineering, Faculty of Engineering and Physical Sciences, University of Leeds. Leeds LS2 9JT, United Kingdom. E-mail: m.fairweather@leeds.ac.uk

ABSTRACT

Direct numerical simulation, facilitated by the spectral element method, has been used to study collisions and agglomeration in particle-laden fluid flows through a channel at shear Reynolds number$Re_\tau = 300$. The particulate phase is simulated using Lagrangian particle tracking and a stochastic technique. Curiously, the implementation of agglomeration in the deterministic approach caused a major reduction in the particle collision rate. To determine the cause of this effect, analysis of the collision rate across the channel for different particle properties was performed. For systems without agglomeration, collisions between particles tended to be located on consistent streamlines, occurring between single pairs of particles. A numerical analysis of this effect confirmed the result, where inter-particle collisions across the channel mostly took place between non-unique particle pairs, i.e. particle pairs which collide more than once within a short timeframe. This repeat collision effect was weakest towards the channel walls, and a dependency on the size of the turbulent eddies within the channel was observed. Repeat collisions are shown to be almost eliminated with the addition of the agglomeration mechanism. The impact of this effect on the accuracy of the stochastic technique is discussed, and modifications are suggested to account for the repeat collisions. Even with these the collision rate was exaggerated compared to the deterministic approach.

Keywords: Particle-laden flows, agglomeration, collision, DNS, LPT, stochastic method.

NOMENCLATURE

C_D	[-]	Drag coefficient
C_L	[-]	Lift coefficient
d_p^*	[-]	Particle diameter
e_n^{*2}	[-]	Coefficient of restitution
$\boldsymbol{f}_i$	[-]	Body forces on cell i
$\boldsymbol{f}_{PG}$	[-]	Pressure gradient force
$\boldsymbol{f}_{2W}^{*i}$	[-]	Two-way coupling force
H^*	[-]	Hamaker constant
M_{VM}	[-]	Virtual or added mass term
p^*	[-]	Pressure
P_{coll}	[-]	Collision probability
r_p^*	[-]	Particle radius
Re_B	[-]	Bulk Reynolds number
Re_τ	[-]	Shear Reynolds number
t^*	[-]	Time
u_η	[-]	Kolmogorov velocity scale
$\boldsymbol{u}^*$	[-]	Fluid velocity vector
$\boldsymbol{u}_S^*$	[-]	Slip velocity
$\boldsymbol{u}_F^*$	[-]	Fluid velocity
U_B	[m s^{-1}]	Fluid bulk velocity
V_i^*	[-]	Volume of a computational cell
$\boldsymbol{x}_P^*$	[-]	Particle position
δ	[m]	Channel half-height
δ_0^*	[-]	Minimum contact distance
ε	[m^2 s^{-2}]	Turbulence energy dissipation rate
η	[-]	Kolmogorov length scale
ν	[m^2 s^{-1}]	Kinematic viscosity
ρ_F	[kg m^{-3}]	Fluid phase density
ρ_P	[kg m^{-3}]	Particle phase density
$\boldsymbol{\tau}^*$	[-]	Deviatoric stress tensor
$\boldsymbol{\omega}_F^*$	[-]	Fluid vorticity

Subscripts and Superscripts

DNS	Direct numerical simulation
DSMC	Direct simulation Monte Carlo
LES	Large eddy simulation
LPT	Lagrangian particle tracker
SEM	Spectral element method
x, y, z	Cartesian coordinates
*	Non-dimensional units

1. INTRODUCTION

Accurate simulation of particle-laden flows is of fundamental importance to any area of industry that will at some point be required to transport a fluid-solid multiphase component of its process or waste to a new location. Multiphase flow simulations are frequently performed in industries which refine and transport chemicals, such as agriculture [1], pharmaceuticals [2], and mineral processing [3]. The core electrical energy generation methods, coal, oil and gas, are also obvious examples that handle multiphase flows [4]. Without informed optimisation, industrial processes can be inefficient, unsafe and costly, due to the amount of maintenance required, or the need for part replacement, which can often be hazardous. This is particularly true of the nuclear waste processing industry where exposure to radioactive or otherwise dangerous materials is possible.

The dynamic properties and complex mechanisms of turbulent wall-bounded flows demand high levels of mathematical accuracy for the purpose of making predictions of chaotic behaviour. A minute change in initial conditions will inextricably lead to differing results. In the case of experimental studies, this sensitivity to initial conditions can lead to unreliable reproducibility, for said conditions are tremendously difficult to isolate, more so as the Reynolds number increases. For a more accurate representation of the flow, methods such as large eddy simulation (LES) and direct numerical simulation (DNS) are available. Both of these methods involve constructing a mesh for resolving small scale effects with high accuracy, and then solving the Navier-Stokes equations at all the relevant scales.

Traditionally, the Lagrangian particle tracking method has been used to simulate the movement of particles and the collisions thereof. In this case, particles are modelled as computational spheres and a suitably integrated force-balance equation of motion is used to advect them. This method, whilst accurate, suffers from similar computational constraints to DNS, where collision calculations become unfeasible for large particle numbers, often required for the representation of industrial flows.

One alternative to the Lagrangian method of colliding particles is the stochastic method [5], for which complexity scales with the number of particles, rather than the number squared. The method calculates the likelihood of a particular particle colliding through the generation of a fictitious collision partner, which is representative of the local particle phase properties, so that no information is required on the actual position and direction of motion of the surrounding real particles [5]. This then resolves the correct number of collisions for the flow based on the collision probability and the averaged statistics of the particles in the same region.

This study investigates this methodology in conjunction with a channel flow geometry where both inter-particle collisions and agglomeration are considered. It assesses an unexpected condition that the implementation of agglomeration causes, with the stochastic method, an excessively high collision rate, and determines a cause and potential solution.

2. METHODOLOGY

To simulate the continuous phase, a spectral element method (SEM) is used to determine the action of the fluid. The SEM is a hybrid of the finite element method and the spectral method. Combining the accuracy of the spectral method with the generality of the finite element method leads to a much more flexible technique for solving the incompressible Navier-Stokes equations. The code employed, Nek5000 [6], has been extensively tested and validated, and contains efficient parallelisation capabilities as well as the flexibility to include an effective particle phase model. The SEM is implemented by dividing the fluid domain into smaller elements, the number and shape of which are determined by the geometry of the domain and by the intended resolution of the program, with enough flexibility to accommodate common and indeed uncommon fluid domains. This work used DNS, so the elements used have an upper bound for size, which is ideally no greater than 15 times the Kolmogorov length scale [7]. The non-dimensionalised Navier-Stokes equations can be stated as:

$$\frac{d\boldsymbol{u}^*}{dt^*} + (\boldsymbol{u}^* \cdot \nabla)\boldsymbol{u}^* = -\nabla p^* + \frac{1}{Re_B}\nabla \cdot \boldsymbol{\tau}^* + f_i \qquad (1)$$

$$\nabla \cdot \boldsymbol{u}^* = 0 \qquad (2)$$

Here, $\boldsymbol{u}^*$ is the fluid velocity vector, which has been non-dimensionalised in terms of the bulk velocity U_B, and t^* is an expression of non-dimensionalised time, $t^* = tU_B/\delta$, where δ is half the height of the channel. p^* is a non-dimensionalised pressure term, $p^* = p/\rho_F {U_B}^2$, where ρ_F is the density of the continuous phase. Re_B is the bulk Reynolds number given by $\delta U_B/v$, and $\boldsymbol{\tau}^*$ is the non-dimensionalised deviatoric stress tensor, $\boldsymbol{\tau}^* = (\nabla \boldsymbol{u}^* + \nabla \boldsymbol{u}^{*T})$. The final term, f_i, represents body forces on cell i, given by $\boldsymbol{f}_i = \boldsymbol{f}_{PG} + \boldsymbol{f}_{2W}^{*i}$. The flow is driven by a constant pressure gradient term $\boldsymbol{f}_{PG} = (Re_\tau/Re_B)^2\hat{\boldsymbol{x}}$, with $\hat{\boldsymbol{x}}$ a unit vector in the streamwise direction. The term $\boldsymbol{f}_{2W}^{*i}$ represents two-way momentum exchange between the fluid and particulate phases.

These equations were solved by Nek5000 for an initially turbulent fluid flow in a channel geometry of $12 \times 2 \times 6$ non-dimensional distance units where the 12 (x^*) and 6 (z^*) dimensions had continuous, periodic boundaries, and the 2 (y^*) dimension was

wall-bounded with a no-slip condition. At $Re_\tau = 300$ this was simulated using a $32 \times 32 \times 32$ element mesh with spectral discretization order $N = 7$, i.e. a total of 11.2M elements.

In order to model the dispersed particle phase of a multiphase flow, a Lagrangian particle tracker (LPT) was first employed which was developed in conjunction with the Nek5000 code used in this study. The Lagrangian particle tracking routine tracks individual particles as computational spheres, and time-evolves their velocity and position synchronously with the Eulerian fluid flow model, operating over the same timesteps and representing the fluid-particle interactions by solving the non-dimensional equations of motion described below:

$$\frac{\partial \boldsymbol{x}_P^*}{\partial t^*} = \boldsymbol{u}_P^* \tag{3}$$

$$\frac{\partial \boldsymbol{u}_P^*}{\partial t^*} = \frac{1}{M_{VM}} \left[\underbrace{\frac{3 C_D |\boldsymbol{u}_s^*|}{4 d_p^* \rho_P^*} \boldsymbol{u}_s^*}_{Drag} + \underbrace{\frac{3}{4} \frac{C_L}{\rho_P^*} (\boldsymbol{u}_s^* \times \boldsymbol{\omega}_F^*)}_{Lift} + \underbrace{\frac{1}{2 \rho_P^*} \frac{D \boldsymbol{u}_F^*}{D t^*}}_{Virtual\ Mass} + \underbrace{\frac{1}{\rho_P^*} \frac{D \boldsymbol{u}_F^*}{D t^*}}_{Pressure\ Gradient} \right] \tag{4}$$

The fourth order Runge-Kutta method, also known as RK4 [8], was used to solve these equations for each particle within every time-step in the Lagrangian particle tracker. Here, d_p^* and ρ_P^* are respectively the diameter and density of the particle, and, after being non-dimensionalised, $\boldsymbol{u}_s^*$, $\boldsymbol{u}_F^*$ and $\boldsymbol{\omega}_F^*$ are the slip velocity, fluid velocity and vorticity, with C_D and C_L being the coefficients of drag and lift.

For increased volume fraction flows where collision effects are dominant, the effect of the particles on the fluid must be considered. The two-way coupling momentum exchange term is included in the final term of Eq. (1) to account for this:

$$\boldsymbol{f}_{2W}^{*i} = \frac{1}{V_i^*} \sum_j \frac{\partial \boldsymbol{u}_{P\,j}^*}{\partial t^*} \tag{5}$$

where V_i^* is the volume of a computational cell, and j is a function applied to each particle in that cell.

The deterministic particle interactions were treated as hard sphere collisions, with collision times smaller than the LPT timestep, and additional interparticle forces were either ignored as negligible, or partially implemented as part of the agglomeration mechanism. To reduce computational demand, the domain was reduced into smaller cells, with only particles in the same cell considered as potential collision partners. The non-dimensional radii of the particles considered in this study were $r_p^* = 0.005$ and 0.01 (equivalent to 100 μm and 200 μm particles, with Stokes numbers, in water, of 0.31 and 1.25, respectively) .

A deterministic energy-balance method was used to calculate the energetic collision conditions under which an agglomerate forms, as used by Njobuenwu and Fairweather [9]. This is given as:

$$\boldsymbol{u}_{P,rel}^{*2} - \frac{(1 - e_n^{*2}) \left(\boldsymbol{u}_{P,rel}^* . \hat{\boldsymbol{n}} \right)^2}{\left| \left(\boldsymbol{u}_{P,rel}^* . \hat{\boldsymbol{n}} \right) \right|} \leq \frac{H^*}{6 \delta_0^{*2}} \left[\frac{6(1 - e_n^{*2})}{\pi^2 \rho_P^* \sigma^*} \left(\frac{d_{P,i}^{*3} + d_{P,j}^{*3}}{d_{P,i}^{*2} d_{P,j}^{*2} \left(d_{P,i}^* + d_{P,j}^* \right)} \right) \right] \tag{6}$$

where H^* is the non-dimensional Hamaker constant, given by $H^* = H / \rho_F U_B^2 \delta^3$, $\delta_0^* = \delta_0 / \delta$ is the minimum contact distance, also non-dimensionalised, and e_n^{*2} is the normal coefficient of restitution. $\hat{\boldsymbol{n}}$ is a unit vector pointing between the colliding particle pair and $\boldsymbol{u}_{P,rel}^{*2}$ is the relative velocity between the colliding particles. Upon collision, if the condition stated in the equation is satisfied, the particles are considered to combine into a spherical agglomerate with radius calculated such that the new volume is equivalent to the summed volume of its constituents.

Rupp et al. [10] introduced a modified stochastic technique for use in channel flows, which employs advective theory as derived by Saffman and Turner [11]. This calculates the particle collision rate within a given strata of a flow, a cell encompassing the entirety of the channel in the streamwise and spanwise dimensions, and a small section in the wall-normal dimension, matching the fluid elements used. The probability of collision for a particle is given as:

$$P_{coll} = \left(\frac{8\pi}{15} \right)^{1/2} n_p (d_p)^3 \left(\frac{\varepsilon}{\nu} \right)^{1/2} \Delta t \tag{7}$$

where ε is the turbulence kinetic energy dissipation rate, ν is the kinematic viscosity, and n_p and d_p are the particle number density and the diameter. Two classes of particle were simulated using both the deterministic and stochastic techniques. Further simulations were perfomed for both cases with the agglomeration mechanism active. As will be made apparent in the discussion section, modifications were required to be made to the code where the stochastic technique was employed in a model with agglomeration. These modifications were based on observations made by Wang et al. [12], where the below equation relates to the change in the collision rate due to certain interparticle effects such as the accumulation effect:

$$\frac{\Gamma}{\Gamma_0} = 4.85 \frac{\eta}{r} g(r) \frac{\langle |w_r| \rangle}{u_\eta} \tag{8}$$

Here, η and u_η represent, respectively, the Kolmogorov length and velocity scales, r is the radius, and $g(r)$ is a statistical function of the radius known as the radial distribution at contact which directly measures the accumulation effect. $\langle|w_r|\rangle$ represents the Lagrangian pair relative velocity statistics of particles and is a measure of the turbulent transport effect.

3. RESULTS AND DISCUSSION

The baseline case for this study was a four-way coupled deterministic simulation of a turbulent channel flow without agglomeration. This was performed for particles of radii $r_p^* = 0.005$ and 0.01 at quantities of 300k and 2.2M. The results of these simulations were previously compared with the outcomes using the direct simulation Monte Carlo (DSMC) stochastic technique, showing good agreement [10]. Simulations using the agglomeration mechanism generated useful results surrounding both the impact of particles on the fluid as well as the rate of particulate aggregation in simple wall-bounded flows. In general, the effect of agglomeration on the mean fluid streamwise velocities and the normal and shear stresses was small over the simulation time considered. Of the cases considered, the system with the most significant change was the channel populated with the higher radius $r_p^* = 0.01$ particles, with results shown in Figs. 1 and 2.

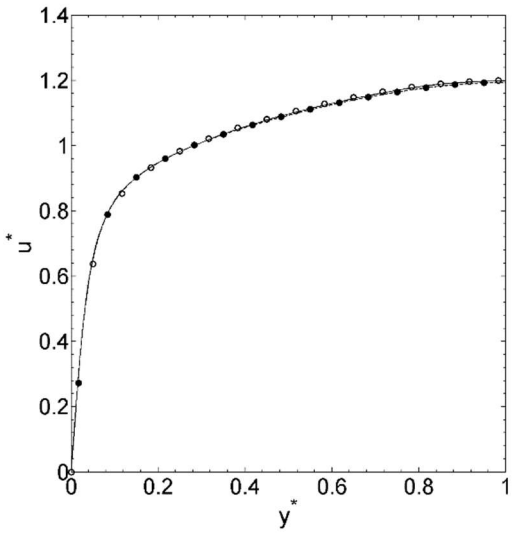

Figure 1. Mean streamwise velocities, u^*, for fluid flows with 300k, 200µm particles. Fluid values from the simulation — with and - - - without agglomeration, and particle values ● with and ○ without agglomeration.

The inclusion of high Stokes number particles can be seen to have affected the overall particle statistics slightly, and the fluid statistics less so (with little difference visible between the lines with and without agglomeration). Previous studies by the authors in this geometry and Reynolds number have shown the mean streamwise velocity to be resistant to change, and likewise here the streamwise particle velocity shown in Fig. 1 is seen to be minimally impeded towards the centre of the channel.

The normal and shear stresses, displayed in Fig. 2, are likewise minimally affected. A notable change is in the spanwise fluid velocity at $0.3 < y^* < 0.7$, a region shown in previous studies to be particularly affected by changes in the particle Stokes number [13].

Figure 3 is a plot of the evolution of agglomerates over time for the high concentration case (where aggregation is most significant), and demonstrates the formation of agglomerates containing as many as 40 single particles by $t^* = 150$. Thus, the lines, ranging from top to bottom in the plot, are for single particles, and then for agglomerates with 2, 3, 4 ... 10 particles, followed by particles with 15, 20 ... 40 particles.

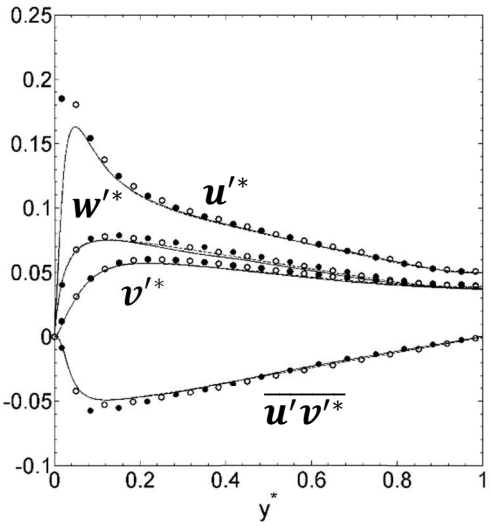

Figure 2. Normal and shear stresses, $u'^*, v'^*, w'^*, \overline{u'v'^*}$, for fluid flows with 300k, 200µm particles. Fluid values from the simulation — with and - - - without agglomeration, and particle values ● with and ○ without agglomeration.

Having demonstrated the DSMC stochastic technique for the prediction of collisions in previous work, the model was now incorporated into the overall model which employed the additional post-collision agglomeration mechanism. However, this resulted in an immediate upturn in agglomeration when compared to the deterministic interaction flow, to the point where the simulation could not handle the effects on the fluid flow from the sudden appearance of many high Stokes number particles created by agglomeration.

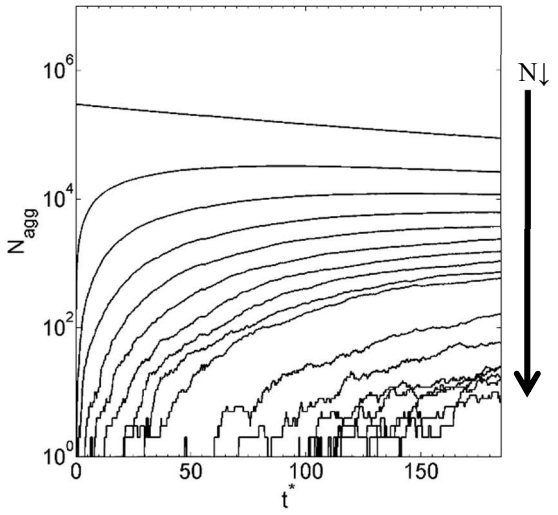

Figure 3. Number, N_{agg}, of differently sized agglomerates for 2.2M, 100µm deterministic particles with sizes N = 1, 2, 3 … 9 and 10, 15, … 50 (top to bottom).

Since the stochastic technique had up to this point been consistent with the deterministic as far as the collision rate was concerned, this effect was of interest. It was initially theorised to be because of an underestimation in the collision energy, or some other peculiarity of the stochastic technique. Even a small change in collision rate would quickly accumulate to a large change in the effects of agglomeration, and the stochastic technique did exhibit an increased collision rate compared to the deterministic approach. This increase was further determined to be a small part of the effect. What was quickly ascertained was that the collision rate dropped substantially when agglomeration was implemented for the deterministic simulation of particles, with Table 1 showing the scale of this decrease to be of at least an order of magnitude.

Investigating the cause of the change in collision rate was carried out through analysis of the collision location within the channel. The locations of collisions taking place over the course of 100 simulation timesteps were recorded and are illustrated in Fig. 4. For the purpose of easier visualisation, a sector of the channel was chosen that was one half of the total length, width and breadth of the entire geometry.

Each individual point in the figure represents the location of a collision between two particles. These positions tend to form dotted lines, particularly towards the centreline of the channel. These would appear to indicate multiple collisions occurring in the same relative places over the course of the simulation. The fact that these lines follow fluid streamlines is indicative of this, and indeed what is being observed here is particles that are confined to the same fluid eddies colliding with each other repeatedly.

Table 1. Comparisons of deterministic collision rates per bulk time unit for cases with and without agglomeration.

Case	$300k, r_p^* = 0.005$	$2.2M, r_p^* = 0.005$	$300k, r_p^* = 0.01$
Collisions without agglomeration	2,218	160,847	10,447
Collisions with agglomeration	214	10,299	1,707

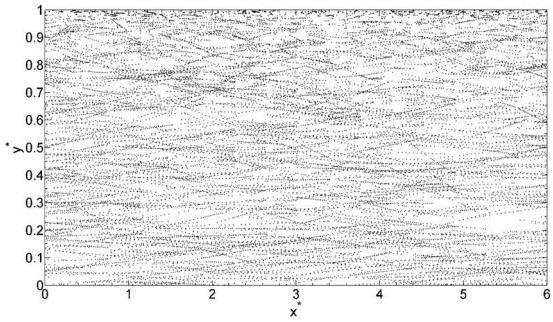

Figure 4. Visualisation of the location (plotted as dots) of deterministic collisions in the $x^* - y^*$ plane for a section of a channel flow in which the 300k, 100µm particle case is being simulated with four-way coupling.

A numerical analysis of this effect was performed, shown in Fig. 5. The identities of the two particles colliding were recorded for a selection of collisions from the deterministic simulation without agglomeration, for the three different cases considered over a hundred timesteps. A unique collision here is defined from these identities, counted as the first time a particular pair of particles had collided during those timesteps.

Comparing the numbers of unique collisions across the channel to the total number within that section showed that the majority of non-unique collisions (shown in Fig. 5) take place at the centre of the channel, where the turbulent eddies are most stable. The simulation with the lowest radius and particle number had the lowest collision rate overall, and this makes it something of an outlier, with non-unique collisions being far more likely to occur than for any two given particles to encounter each other for the first time.

The $r_p^* = 0.01$ case also has some unique properties, with an increase in non-unique collisions in the wall regions. This is caused by turbophoresis moving high speed particles to those regions. Overall, a higher collision rate caused by either particle size or number increasing has the effect of

increasing the rate of unique collisions, though the collision rate is still dominated by particles that are kept in close proximity by localised fluid effects.

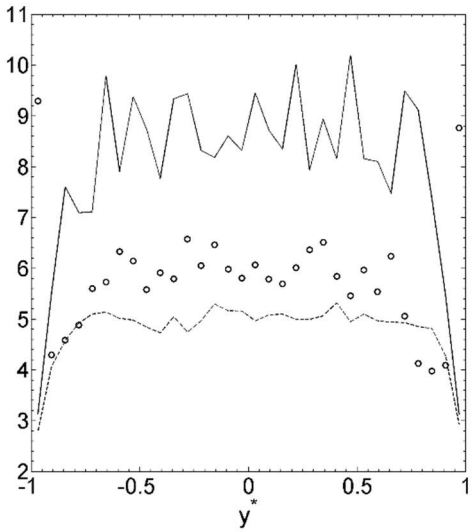

Figure 5. Proportion of deterministic collisions taking place across the channel which are not unique for three particle cases simulated in this study. — $N_p = 300k, r_p^* = 0.005$; - - - $N_p = 2.2M, r_p^* = 0.005$; ○ $N_p = 300k, r_p^* = 0.01$.

Particles under these conditions, due to continuous proximity and repeated chances for collision, would agglomerate with greater frequency when this is considered as a factor in the simulation. With the existence of particles in similar local fluid regions becoming a non-factor, the collision rate drops quickly and stabilises at a much lower value than predicted by the four-way coupled simulation without agglomeration. This can be seen in Fig. 6, which shows the collision rate over time.

Here, each case displays an initial spike of collisions. This is an artifact of the initial conditions, which took particle statistics from an already settled flow without agglomeration, but illustrates an effect larger than the reduction in collision rate over time as more and more particles agglomerate. The case with the large radius particles is the only one where the collision rate changes comparably.

The stochastic simulation of the four-way coupled system, however, considers only the advective forces on the particles, and their sizes in the calculation of collision rate. This does not quickly change with the implementation of agglomeration, and as a result the collision rate remains a close match to the first set of values in Table 1, rather than the correct second set. This in turn results in a high agglomeration rate that swiftly results in absurdly large particles and makes the simulation of limited value.

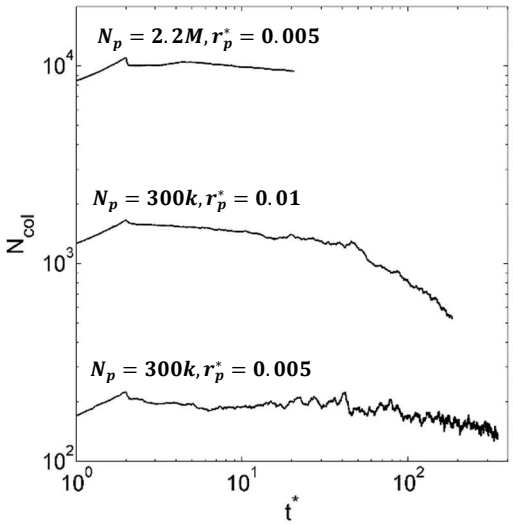

Figure 6. Temporal evolution of number of collisions per timestep for the three deterministic cases colliding with agglomeration.

Wang et al. [12] described the effects known as the accumulation effect and the turbulent transport effect. These were potential candidates for the cause of the repeat collision effect that has been observed in this study, so calculations for the magnitude of these effects were implemented into the formulas the stochastic technique uses for the collision rate. This had the desired effect of reducing the rate of collision, and therefore agglomeration, but as Figs. 7 and 8 show, this reduction was not equal to the size of the effect.

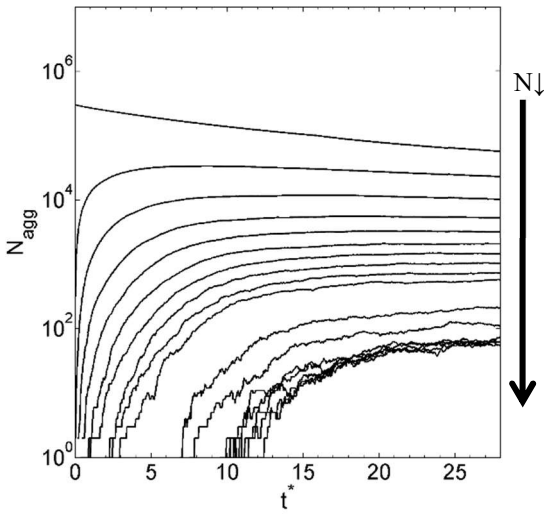

Figure 7. Number, N_{agg}, of differently sized agglomerates for 2.2M, 100μm stochastic particles with sizes N = 1, 2, 3 … 9 and 10, 15, … 50 (top to bottom).

Here it can be seen that even the "improved" stochastic technique is still overpredicting the

collision rate, with the size 40 agglomerates occurring at around $t^* = 10$, rather than $t^* = 150$ as occurred for the corresponding deterministic case in Fig. 3.

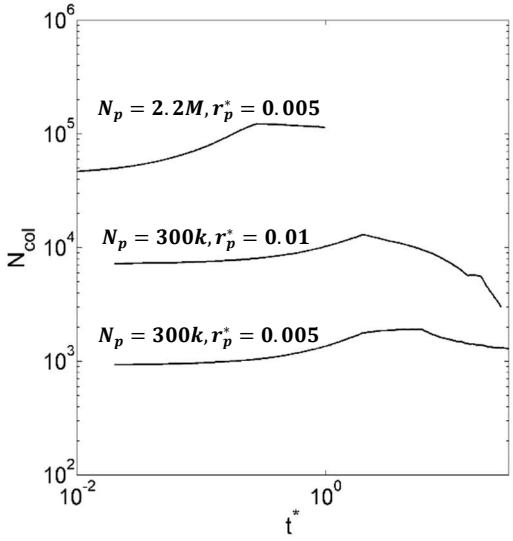

Figure 8. Temporal evolution of number of collisions per timestep for the three stochastic cases colliding with agglomeration.

For the higher concentration case the agglomeration rate was significant enough that the timestep had to be reduced substantially for the simulation to not diverge due to high-Stokes number particle interaction with the fluid. This is why the logarithmic time axis starts earlier for the high concentration case in Fig. 8.

Table 2. Comparisons of deterministic and stochastic runtimes and collision rates for cases with and without agglomeration.

Case	$300k, r_p^* = 0.005$	$2.2M, r_p^* = 0.005$	$300k, r_p^* = 0.01$
Deterministic runtime	2.43	17.75	3.09
Deterministic collisions/t*	214	10,299	1,707
Stochastic runtime	2.19	13.41	2.53
Stochastic collisions/t*	1,895	72,862	15,291

Table 2 shows the collision rates for the modified stochastic technique to be less than an order of magnitude greater, which is an improvement over the unmodified technique, however there is still a clear need for improvement.

The stochastic technique does however reduce the computational demand as claimed, shown in the same table, where the compute time/timestep is normalised by a one-way coupled simulation of the $300k, r_p^* = 0.005$ case. Each case studied was faster where the stochastic technique was used, meaning that further improvements to the technique can be expected to pay dividends in simulation time.

4. CONCLUSIONS

This study investigated the impact of stochastic particle agglomeration on previously studied four-way coupled particle-laden channel flows, with a focus on a repeated collision effect which cause inaccuracies in the agglomeration rate. With agglomeration implemented, the simulation of particle-laden channel flows gains versatility, in that aggregation can be captured. For this particular geometry and the particles Stokes numbers considered, the effect of the particles on the fluid was small, with the most significant results, from the higher Stokes number case, shown here.

While applying the agglomeration mechanism to a previously successful stochastic DSMC technique, an inconsistency emerged which led to an investigation into what is termed the repeat collision effect. This effect turned out to be a direct result of fluid streamlines in the bulk flow confining low Stokes number particles to close proximity, which would then collide repeatedly, skewing the number of reported collisions.

The stochastic technique, previously observed to match this reported number of collisions, did not account for the agglomeration of the confined particles, leaving isolated agglomerates with a magnitude lower collision rate. It therefore agglomerated particles at an inordinate rate with a devastating effect on the accuracy of the simulation.

An attempt was made to rectify this through modifications based on a study of the accumulation and turbulent transport effects, and this had some success, reducing the collision and agglomeration rates, though not enough to make the simulation accurate.

As improvements to the stochastic technique for handling inter-particle collisions are ongoing, it is expected that further work on this technique will lead to a more effective solution to the repeat collision effect. In the meantime, the stochastic technique has proven an effective way to reduce computational cost in cases where its inconsistencies can be resolved.

Further work also needs to consider the relationship between the coefficient of restitution and the repeat collision effect, as the agglomeration chance per collision was near to unity for this study, and this is what drove the deviations between collision rates with and without agglomeration.

ACKNOWLEDGEMENTS

D.R. would like to thank the Engineering and Physical Sciences Research Council in the UK, and the National Nuclear Laboratory, who funded the work described as part of the EPSRC Centre for Doctoral Training in Nuclear Fission – Next Generation Nuclear.

REFERENCES

[1] Lee, I. B., Bitog, J. P. P., Hong, S.W., Seo, I. H., Kwon, K. S., Bartzanas, T., Kacira, M., 2013, "The past, present and future of CFD for agro-environmental applications." *Computers and Electronics in Agriculture*, Vol. 93, pp. 168-183.

[2] Chakravarti, A., Patankar, N. A., Panchagnula, M. V., 2019, "Aerosol transport in a breathing alveolus." *Physics of Fluids*, Vol. 31, 121901.

[3] Guha, D., Ramachandran, P.A., Dudukovic, M. P., 2007, "Flow field of suspended solids in a stirred tank reactor by Lagrangian tracking." *Chemical Engineering Science*, Vol. 62, pp. 6143-6154.

[4] Raynal, L., Augier, F., Bazer-Bachi, F., Haroun, Y., Pereira da Fonte, C., 2016 "CFD applied to process development in the oil and gas industry – A review." *Oil & Gas Science and Technology*, Vol. 71, 42.

[5] Sommerfeld, M., 2001, "Validation of a stochastic Lagrangian modelling approach for col nter-particle collisions in homogeneous isotropic turbulence", *International Journal of Multiphase Flow*, Vol. 27, pp. 1829-1858.

[6] Fischer, P. F., Lottes, J. W., Kerkemeier, S. G., 2008, Nek5000. http://nek5000.mcs.anl.gov.

[7] Moser, R. D., Moin, P., 1984, "Direct numerical simulation of curved turbulent channel flow." *NASA Technical Memorandum* 85974

[8] Süli, E., Mayers, D., 2003, *An Introduction to Numerical Analysis*, Cambridge University Press.

[9] Njobuenwu, D.O., Fairweather, M., 2017, "Simulation of deterministic energy-balance particle agglomeration in turbulent liquid-solid flows." *Physics of Fluids*, Vol. 29, 083301.

[10] Rupp, D. A., Mortimer, L. F., Fairweather, M., 2021, "Development of an effective stochastic collision method for use in four-way coupled turbulent flows." Proc. *13th International ERCOFTAC Symposium on Engineering Turbulence Modelling and Measurements*, Rhodes, Greece, Paper 13.

[11] Saffman, P. G., Turner, S. J., 1956, "On the collision of drops in turbulent clouds." *Journal of Fluid Mechanics*, Vol. 1, pp. 16-30.

[12] Wang, L. P., Wexler, A. S, Zhou, Y., 2000, "Statistical mechanical description and modelling of turbulent collision of inertial particles." *Journal of Fluid Mechanics*, Vol. 415, pp.117-153.

[13] Rupp, D. A., Njobuenwu, D. O., Fairweather, M., 2018, "Particle volume fraction effects in simulations of turbulent channel flows." In: Proc. *12th International ERCOFTAC Symposium on Engineering Turbulence Modelling and Measurements*, Montpellier, France.

Conference on Modelling Fluid Flow (CMFF'22)
The 18th International Conference on Fluid Flow Technologies
Budapest, Hungary, August 30-September 2, 2022

APPROXIMATE DECONVOLUTION MODEL FOR TWO-DIMENSIONAL DECAYING HOMOGENEOUS ISOTROPIC TURBULENCE USING HIGH ORDER DISCRETIZATION SCHEMES

Lena CABAN[1], Agnieszka WAWRZAK[1], Artur TYLISZCZAK[1]

[1] Department of Thermal Machinery, Faculty of Mechanical Engineering and Computer Science, Czestochowa University of Technology. Armii Krajowej 21, 42-201 Czestochowa, Poland, E-mail: lena.caban@pcz.pl, agnieszka.wawrzak@pcz.pl, artur.tyliszczak@pcz.pl

ABSTRACT

The paper presents the results of numerical simulations of a two-dimensional homogenous isotropic turbulent flow carried out using the direct numerical simulation (DNS) and large eddy simulation (LES) methods. In the latter case, the classical Smagorinsky model and the Approximate Deconvolution Method (ADM) are used to model the sub-grid terms. In ADM the unfiltered variables are obtained from the iterative van Cittert method and are used to directly calculate the sub-grid tensor. The vorticity-stream function formulation of the Navier-Stokes equation is used in this work. We focus on the accuracy and dependence of ADM on the type of the filter (explicit, compact), its order, number of the iterations during the deconvolution procedure and the order of derivative discretization. Comparisons with DNS data are performed taking into account the basic quantities, e.g. the total energy, variance, and also higher order statistical moments (skewness and kurtosis). We found that when a high-order discretization method is used the ADM with compact difference type filtering schemes is more accurate than using the classical finite difference type filters.

Keywords: approximate deconvolution model, decaying homogeneous isotropic turbulence, high-order methods, large-eddy simulation

1. INTRODUCTION

Two-dimensional (2D) turbulence is not an ideal model of real turbulent flow. It does not occur in nature or in laboratory, but it finds applications in analysis of geophysical flows, such as oceanic and atmospheric phenomena, as well as in astronomy and plasma physics [1, 2, 3]. It is also important for understanding fully developed three-dimensional (3D) turbulence, although the behavior of its energy cascade is different than in real 3D flows [4, 5, 6]. In the latter case, the energy is transferred from large scales to smaller ones by the vortex stretching mechanism that does not exist in a 2D turbulent flow. In this case, according to the Kraichnan-Batchelor-Leith (KBL) theory, a reverse energy transfer takes place.

Direct numerical simulation (DNS) of such a complex phenomenon as turbulence requires a large amount of computing resources and is usually very time consuming. A common approach is to use large eddy simulations (LES), in which only large-scale vortices are directly calculated, while the effect of small sub-grid scales is modeled. The LES equations are formally defined with the low-pass filter operator that separates these scales. So far, various approaches to modeling the interactions of scales and the closure of the LES system have been presented [7]. A relatively novel one is the Approximate Deconvolution Model (ADM) introduced by Stolz and Adams [8]. The ADM uses the repeated filtering to approximate the unfiltered flow variables and then applies them to the unknown sub-grid terms to close the LES system. Initially, ADM was successfully applied in 3D turbulent flow modeling [9, 10, 11, 12]. Then it was used to model 2D turbulence in large-scale ocean circulation problems [13, 14] as well as to small-scale atmospheric boundary layer [15, 16, 17]. Recently, Boguslawski et al. [18] applied ADM based on the Wiener deconvolution method for 2D homogenous isotropic turbulence. San et al. [19] performed a detailed sensitivity analysis of the low-pass spatial filters for ADM-LES of homogeneous incompressible 3D flows using 2nd order finite difference discretization scheme. They considered various types of filters such as box filters, compact difference filters (CDF), known also as Padé-type filters, differential and hyper-differential filters. San and Staples [20] also tested various high-order numerical schemes such as explicit and compact finite differences, Arakawa scheme, dispersion-relation-preserving scheme, and the Fourier-Galerkin pseudospectral scheme for DNS of homogeneous

isotropic 2D decaying turbulent flows. In the present work, we continue this research applying different filters and discretization methods and perform comparisons not only for basic quantities (e.g. a total energy, variance) but also for higher-order statistical moments, i.e. skewness and kurtosis.

2. GOVERNING EQUATIONS

The dimensionless vorticity-stream function formulation of the Navier-Stokes equations for 2D incompressible flows can be written as follows:

$$\frac{\partial \omega}{\partial t} + u\frac{\partial \omega}{\partial x} + v\frac{\partial \omega}{\partial y} = \frac{1}{\mathrm{Re}}\left(\frac{\partial^2 \omega}{\partial x^2} + \frac{\partial^2 \omega}{\partial y^2}\right) \tag{1}$$

$$\frac{\partial^2 \psi}{\partial x^2} + \frac{\partial^2 \psi}{\partial y^2} = -\omega \tag{2}$$

where ω is the vorticity, ψ is the stream function, $u = \frac{\partial \psi}{\partial y}$, $v = -\frac{\partial \psi}{\partial x}$ are the velocity components and Re is the Reynolds number.

Denoting by G the filter kernel in physical space, the filtering of a general variable f is determined by the convolution operation $\bar{f} = G * f$, where $\int_{-\infty}^{\infty} G(\xi)\,\mathrm{d}\xi = 1$. Thus, applying the filtration operation to the equations (1) and (2) gives:

$$\frac{\partial \bar{\omega}}{\partial t} + \bar{u}\frac{\partial \bar{\omega}}{\partial x} + \bar{v}\frac{\partial \bar{\omega}}{\partial y} = \frac{1}{\mathrm{Re}}\left(\frac{\partial^2 \bar{\omega}}{\partial x^2} + \frac{\partial^2 \bar{\omega}}{\partial y^2}\right) + \tau_{\mathrm{SGS}} \tag{3}$$

$$\frac{\partial^2 \bar{\psi}}{\partial x^2} + \frac{\partial^2 \bar{\psi}}{\partial y^2} = -\bar{\omega} \tag{4}$$

where $\bar{u} = \frac{\partial \bar{\psi}}{\partial y}$, $\bar{v} = -\frac{\partial \bar{\psi}}{\partial x}$ and

$$\tau_{\mathrm{SGS}} = -\left(\overline{u\frac{\partial \omega}{\partial x}} + \overline{v\frac{\partial \omega}{\partial y}}\right) + \left(\bar{u}\frac{\partial \bar{\omega}}{\partial x} + \bar{v}\frac{\partial \bar{\omega}}{\partial y}\right) \tag{5}$$

is the sub-grid term which cannot be directly computed because the unfiltered variables u, v, and ω are unknown. The standard closure for this sub-grid term is usually based on the sub-grid viscosity, whereas in the ADM approach it is computed using the approximate unfiltered quantities.

3. APPROXIMATE DECONVOLUTION MODEL

In this paper, the ADM is based on the so-called iterative van Cittert deconvolution method [21], which applied for a general variable $\bar{f}$ can be written as:

$$f^* = \underbrace{\sum_{n=0}^{N_{\mathrm{ADM}}} (I - G)^n}_{G_a^{-1}} \bar{f} \tag{6}$$

where I is the identity operator and G_a^{-1} is the approximate inverse filter. With the deconvolution model, the unclosed sub-grid term can be closed as follows:

$$\tau_{\mathrm{SGS}} = -\underbrace{\left(\overline{u^*\frac{\partial \omega^*}{\partial x}} + \overline{v^*\frac{\partial \omega^*}{\partial y}}\right)}_{\mathrm{ADM}} + \left(\bar{u}\frac{\partial \bar{\omega}}{\partial x} + \bar{v}\frac{\partial \bar{\omega}}{\partial y}\right) \tag{7}$$

where u^*, v^*, and ω^* are the reconstructed variables.

In practical LES, the exact form of the filter function G is unknown. It is a combination of an implicit filter combined with mesh spacing and the filters induced by the numerical discretization of the first and second derivatives (G_I) [22]. In this paper, we do not attempt to precisely define the effective filter G_e such that $G_e = G_I G$. Moreover, the filter used in the ADM may be completely different from the LES filter. In this paper, however, we only consider the ideal situation when these two filters are equal and we focus on the effect of discretization on the simulation results. We consider two types of LES filters which are based on the explicit and compact filtering methods.

3.1. Explicit and compact filters

For simplicity, we consider a 1D periodic domain $[0, L]$ consisting of K uniformly distributed nodes $x_i = h(i-1)$, for $i = 1, \ldots, K$, with the mesh spacing $h = L/K$. The formulas derived for the 1D domain can be directly applied to 2D and 3D cases along separate lines in each direction.

The general formula for the explicit finite difference filtering (FDF) schemes can be written as:

$$\bar{f}_i = \frac{1}{2}\sum_{j=0}^{N_c} b_j^c \left(f_{i+j} + f_{i-j}\right) \tag{8}$$

and for the implicit compact filters (CDF) as:

$$\bar{f}_i + \sum_{k=1}^{M_c} a_k^c \left(\bar{f}_{i+k} + \bar{f}_{i-k}\right) = \frac{1}{2}\sum_{j=0}^{N_c} b_j^c \left(f_{i+j} + f_{i-j}\right) \tag{9}$$

where $\bar{f}_i$ are the filtered values at nodes x_i, f_i are the known discrete function values. The filters coefficients a_k^c and b_j^c can be calculated from the following system of $N_c + 1$ equations for FDF schemes:

$$\begin{cases} \sum\limits_{j=0}^{N_c} b_j^c = 1 \\ \sum\limits_{j=1}^{N_c} j^{2i} b_j^c = 0 \ \text{ for } \ i = 1, ..., N_c - 1 \\ T(\pi) = 0 \end{cases} \tag{10}$$

and from $M_c + N_c$ equations for CDF schemes:

$$\begin{cases} 1 + 2\sum\limits_{k=1}^{M_c} a_k^c = \sum\limits_{j=0}^{N_c} b_j^c \\ \sum\limits_{k=1}^{M_c} 2k^{2i} a_k^c = \sum\limits_{j=1}^{N_c} j^{2i} b_j^c \ \text{ for } \ i = 1, ..., N_c - 1 \\ T(\pi) = 0 \\ (\mathrm{d}^l T(\omega)/d\omega^l)(\pi) = 0 \ \text{ for } \ l = 2k, k = 1, ..., M_c - 1 \end{cases} \tag{11}$$

where

$$T(\omega) = \hat{G}_{(M_c,N_c)}(\omega) = \frac{\sum_{j=0}^{N_c} b_j^c \cos(j\omega)}{1 + 2\sum_{k=1}^{M_c} a_k^c \cos(k\omega)}, \quad (12)$$

is the filter kernel associated with CDF schemes (9) in Fourier space, known as the transfer function, and $\omega = 2\pi n/K$, for $0 \le n \le K/2$, is the so-called scaled wavenumber in the range $[0, \pi]$. In the case of FDF schemes that can be considered as CDF with $M_c = 0$, the formula (12) is reduced to the nominator. The highest possible order of filtration for the assumed stencils of Eqs. (8) and (9) is equal to $(2N_c)$ and $2(M_c + N_c - 1)$, respectively. This is achieved when all the coefficients a_k^c and b_j^c are explicitly determined from the expansions of f and $\bar{f}$ into the Taylor series and additional constraints for the transfer function. Figure 1. shows the transfer functions of some FDF and CDF schemes used in this work. Here, we only compare the results using second order filtering schemes with $M_c = 0, N_c = 1$, denoted as $G_{(0,1)}$ and with $M_c = 1, N_c = 1$, denoted by $G_{(1,1)}$.

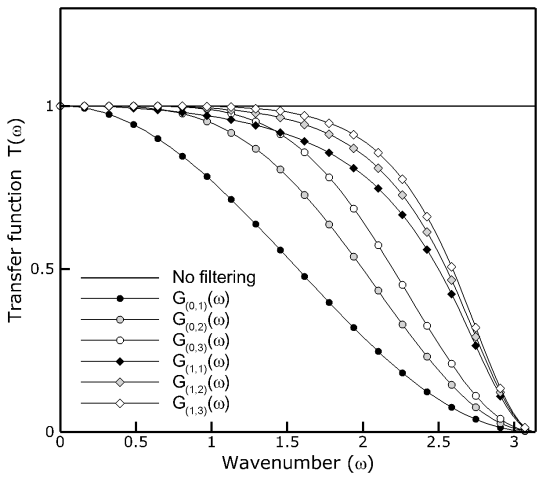

Figure 1. Transfer functions of G

4. NUMERICAL METHODS

The objective of this work is to test and evaluate the ADM model for 2D incompressible flow using explicit and compact high-order discretization methods and compare the results using the pseudospectral method. In this section, we briefly discuss the spatial discretization and temporal integration methods we use.

4.1. Spatial discretization methods

The general formula for the approximation of the first and second order derivatives using explicit finite difference (FD) and compact difference (CD) discretization schemes can be written as follows:

$$f_i' + \sum_{k=1}^{M} a_k \left(f_{i-k}' + f_{i+k}'\right) = \frac{1}{h}\sum_{j=1}^{N} b_j \left(f_{i+j} - f_{i-j}\right) \quad (13)$$

$$f_i'' + \sum_{k=1}^{M} a_k \left(f_{i-k}'' + f_{i+k}''\right) = \frac{1}{h^2}\sum_{j=1}^{N} b_j \left(f_{i+j} - 2f_i + f_{i-j}\right) \quad (14)$$

where FD schemes are obtained for $M = 0$. The highest possible order of approximation for given stencils M and N on the left and right-hand side of Eqs. (13) and (14) is equal to $2M + 2N$. This is obtained when all coefficients a_k and b_j are determined directly from the Taylor series expansions. The coefficients a_k and b_j can be derived from the following systems of $M + N$ equations:

$$\begin{cases} 1 + 2\sum_{k=1}^{M} a_k = 2\sum_{j=1}^{N} j^r b_j \\ \sum_{k=1}^{M} \left(\prod_{l=1}^{r} (2i+l)\right) k^{2i} a_k = \sum_{j=1}^{N} j^{2i+r} b_j \end{cases} \quad (15)$$

where the second equation is for $i = 1, ..., N + M - 1$. The case with $r = 1$ corresponds to the first order derivative approximation and $r = 2$ to the second order. Table 1 shows the discretization schemes we use in this work, along with their corresponding orders.

Table 1. Spatial discretization schemes and corresponding them approximation orders.

	FD scheme	CD scheme
2^{nd} order	$M = 0, N = 1$	-
4^{th} order	$M = 0, N = 2$	$M = 1, N = 1$
6^{th} order	$M = 0, N = 3$	$M = 1, N = 2$
8^{th} order	$M = 0, N = 4$	$M = 1, N = 3$
10^{th} order	$M = 0, N = 5$	$M = 1, N = 4$
12^{th} order	-	$M = 2, N = 4$
20^{th} order	-	$M = 4, N = 6$

4.2. Temporal integration method

As we mainly concentrate on the accuracy of the spatial discretization methods and ADM, we use a fourth-order Runge-Kutta (RK) time integration scheme with a small time step $\Delta t = 5.0 \times 10^{-4}$. Taking into account Eq. (3) written as:

$$\frac{d\omega}{dt} = D(u, v, \omega) \quad (16)$$

where $D(u, v, \omega)$ is a discrete operator of spatial derivatives, the fourth-order RK scheme can be is

defined as:

$$\begin{aligned}
\omega^{(1)} &= D\left(u^n, v^n, \omega^n\right) \\
\omega^{(2)} &= D\left(u^n + \tfrac{\Delta t}{2}u^{(1)}, v^n + \tfrac{\Delta t}{2}v^{(1)}, \omega^n + \tfrac{\Delta t}{2}\omega^{(1)}\right) \\
\omega^{(3)} &= D\left(u^n + \tfrac{\Delta t}{2}u^{(2)}, v^n + \tfrac{\Delta t}{2}v^{(2)}, \omega^n + \tfrac{\Delta t}{2}\omega^{(2)}\right) \\
\omega^{(4)} &= D\left(u^n + \Delta t u^{(3)}, v^n + \Delta t v^{(3)}, \omega^n + \Delta t \omega^{(3)}\right) \\
\omega^{n+1} &= \omega^{(n)} + \tfrac{\Delta t}{6}\left(\omega^{(1)} + 2\omega^{(2)} + 2\omega^{(3)} + \omega^{(4)}\right)
\end{aligned} \tag{17}$$

where for $k = 1, 2, 3$ the velocity components $u^{(k)}$, $v^{(k)}$ are obtained from Eq. (4).

5. RESULTS

We consider a 2D periodic domain with the dimensions $L_x \times L_y = 2\pi \times 2\pi$. The flow field is initialized as a homogeneous isotropic turbulence (HIT) in accordance with the method suggested by San et al. [20], with the Taylor and Kolmogorov length scales equal to $l_t = 0.022L_x$ and $\eta = 0.00236L_x$, respectively. In two-dimensional turbulence, the inertial range in the energy spectrum is proportional to k^{-3}, where $k = |\underline{k}| = \sqrt{k_x^2 + k_y^2}$ is a wavenumber in Fourier space. The initial energy spectrum is given by the formula

$$E(k) = \frac{a_s}{2}\frac{1}{k_p}\left(\frac{k}{k_p}\right)^{2s+1} \exp\left[-\left(s + \frac{1}{2}\right)\left(\frac{k}{k_p}\right)^2\right] \tag{18}$$

in which the maximum value of initial energy spectrum is obtained for k_p, $a_s = \frac{(2s+1)^{s+1}}{2^s s!}$, and s is a shape parameter. As in [20], we take $k_p = 12$ and $s = 3$. The initial vorticity distribution is defined as

$$|\tilde{\omega}(\underline{k})|\sqrt{\frac{k}{\pi}E(k)}e^{i\zeta(\underline{k})} \tag{19}$$

where $\zeta(\underline{k}) = \xi(\underline{k}) + \eta(\underline{k})$ is the phase function, and $\xi(\underline{k}), \eta(\underline{k}) \in [0, 2\pi]$ are independent random values.

The results obtained using the ADM model described above are compared with the classical Smagorinsky model and filtered DNS data. In the Smagorinsky model, the sub-grid term is defined as

$$\tau_{\mathrm{SGS}} = \nu_t\left(\frac{\partial^2\omega}{\partial x^2} + \frac{\partial^2\omega}{\partial y^2}\right) \tag{20}$$

where $\nu_t = (C_s\Delta)^2\sqrt{\bar{S}_{ij}\bar{S}_{ij}}$ is the non-dimmensional turbulent viscosity, C_s is the Smagorinsky constant, Δ is the filter width and S_{ij} is the strain rate tensor.

The simulations were carried out for the Reynolds number Re = 1000. The exemplary DNS results were obtained on the mesh with 1025^2 nodes and the results of the classical LES or applying ADM were obtained on the mesh consisting of 257^2 nodes. The total simulation time was $t = 10$ seconds.

The initial vorticity field and its evolution over time in the HIT configuration in the case of DNS is shown in Figure 2. At the time moment $t = 0$, large scale vortices do not exist. It can be seen that initially only small-scale turbulent structures are present. Over the time they form larger vortical structures and decay under the influence of the viscous forces.

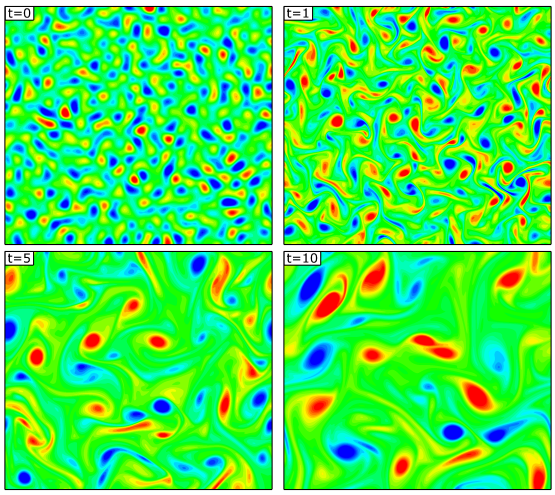

Figure 2. Vorticity contours in HIT configuration at various time moments.

In DNS and LES with the Smagorinsky model the 6th order CD scheme was used with $M = 1$ and $N = 2$ in Eqs. (13) and (14). The computations performed with ADM were performed with various FD, CD schemes and also pseudospectral discretization method. The results obtained using the ADM are compared with the results of DNS and also with those achieved without any model on the mesh consisting of 256^2 nodes .

Figure 3 shows the comparison of the energy spectrum for filtered values of DNS, classical Smagorinsky model and ADM with $N_{\mathrm{ADM}} = 2$ using 2nd order FDF and CDF schemes and various discretization methods at time $t = 5$ seconds. It can be seen that in all cases the total energy of the flow predicted by both LES and ADM agrees relatively well with the filtered DNS solution.

However, there are significant differences for the higher central moments, such as variance, skewness and kurtosis, as shown in Figures 4 to 6. In these cases, the ADM provides much more accurate results compared to the classical LES. From the Figs. 4 to 6 we can also see that the ADM with CDF schemes is much more accurate than with FDF schemes.

Moreover, the results obtained without the subgrid model using the pseudospectral method diverges from DNS data. This is because the mesh 256^2 does not ensure a sufficient resolution and, as the pseudospectral method is not dissipative, it turns out to be unstable. It can be seen that the ADM stabilizes it correctly. Figure 7 shows the comparison of the vorticity fields at the time moment $t = 10$ for ADM with 2nd order FDF and CDF schemes and for 'No model' using the pseudospectral method with DNS vorticity field. It is worth noting that only the ADM with the

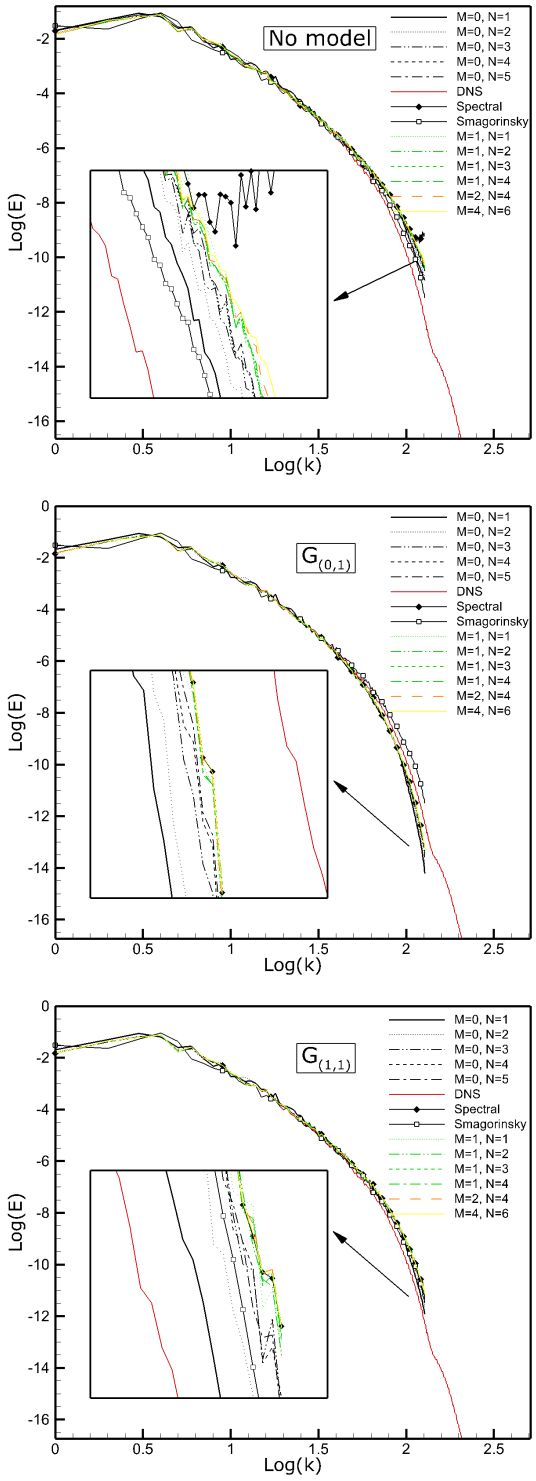

Figure 3. Energy spectra at time $t = 5$

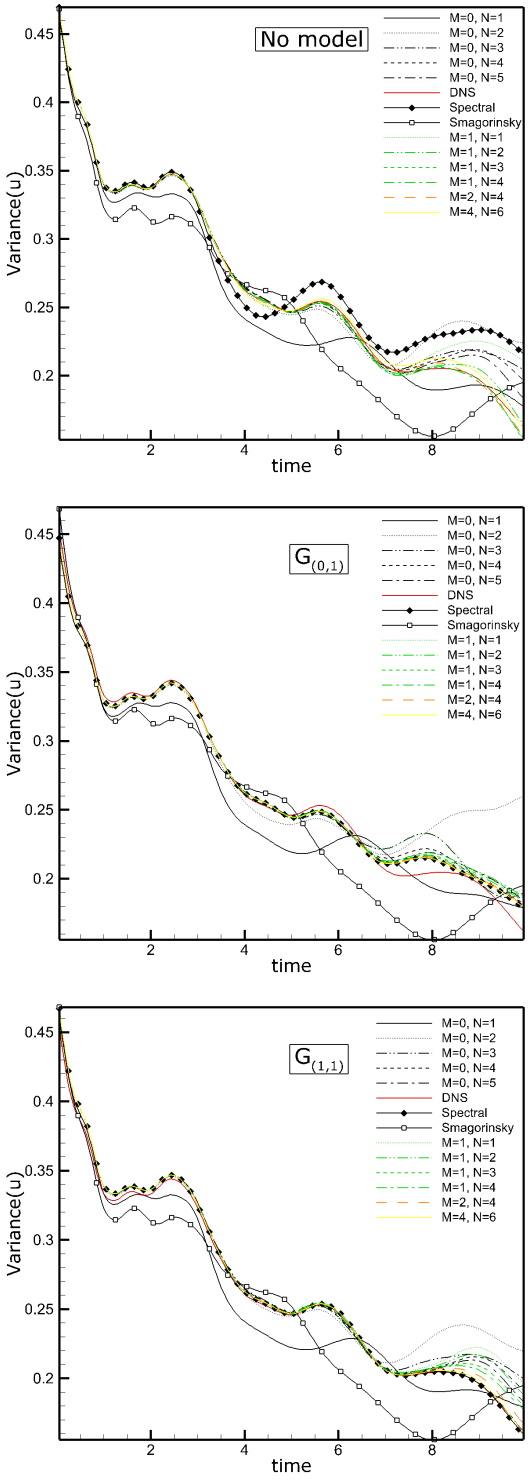

Figure 4. Variance of the u variable

pseudospectral CDF scheme almost perfectly agrees with DNS. As shown in [23], the higher the order of the CD discretization scheme, the results are closer to the spectral solutions.

6. SUMMARY

In this paper, we applied the Approximate Deconvolution Model (ADM) for numerical modeling a two-dimensional homogeneous isotropic turbulent flow. We analysed the effect of ADM accuracy and its dependence on the type of filter (explicit, compact) and its order. We also performed an analysis

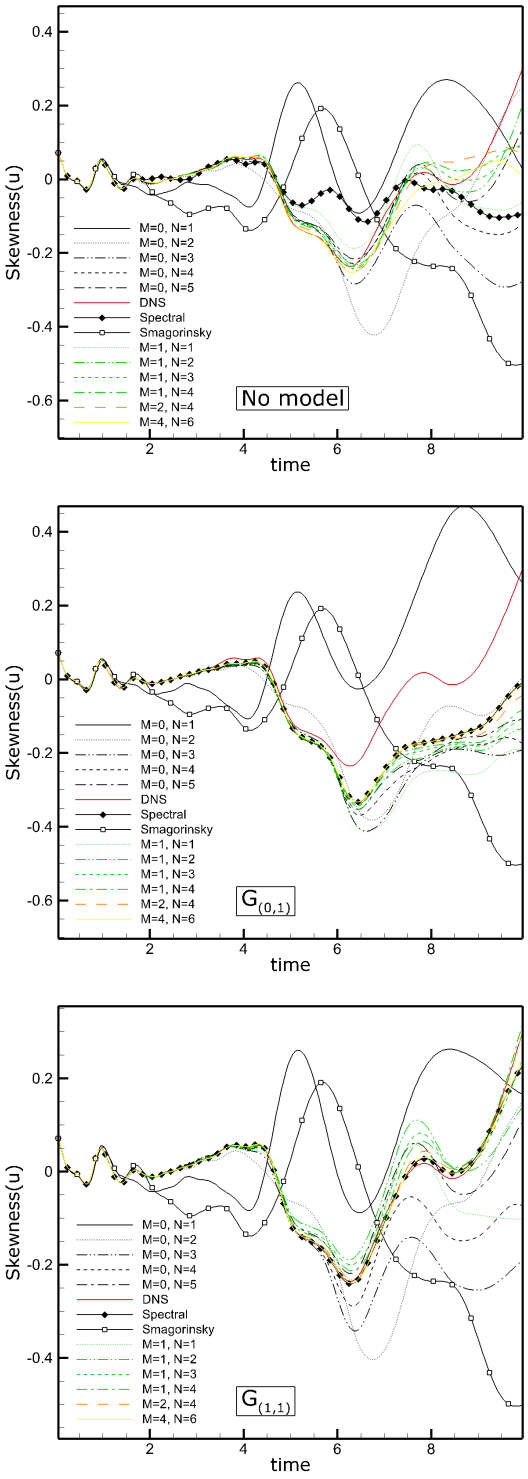

Figure 5. Skewness of the u variable

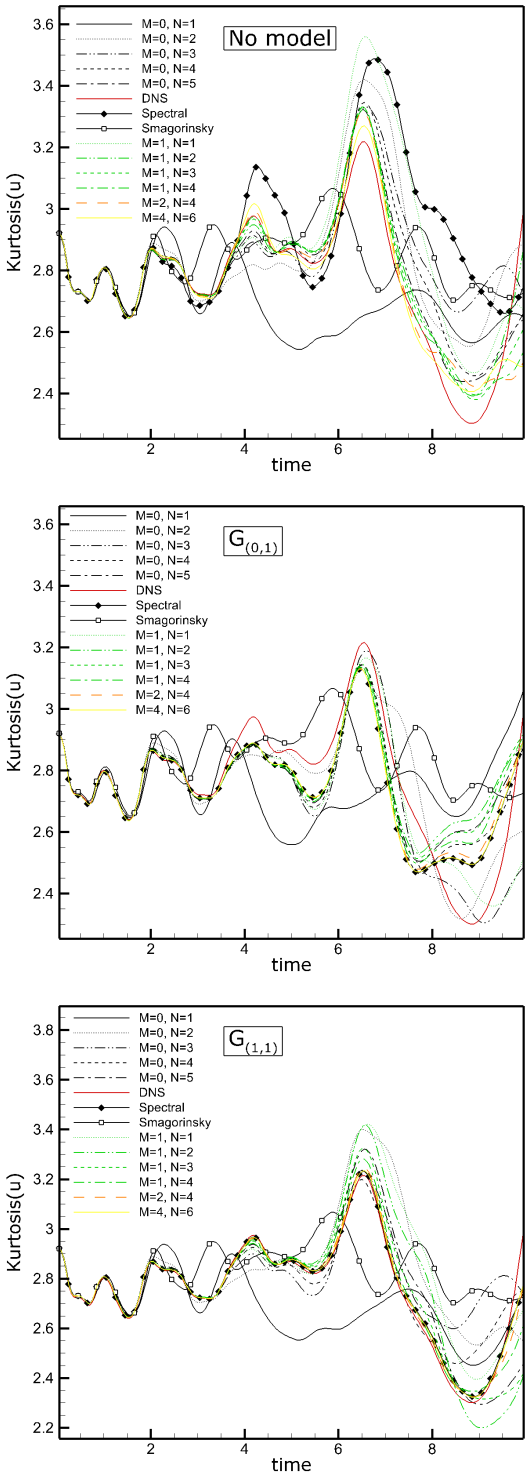

Figure 6. Kurtosis of the u variable

of ADM's dependence on various spatial discretization methods, such as explicit finite difference and compact difference schemes, as well as the Fourier pseudospectral method.

The results obtained using the ADM model were compared with the classical Smagorinsky model and the DNS data. It has been observed that the use of a higher order compact discretization scheme with the ADM model leads to nearly spectral accuracy. It was found that in such cases the ADM based on the compact filters is more accurate than using the classical finite difference type filters.

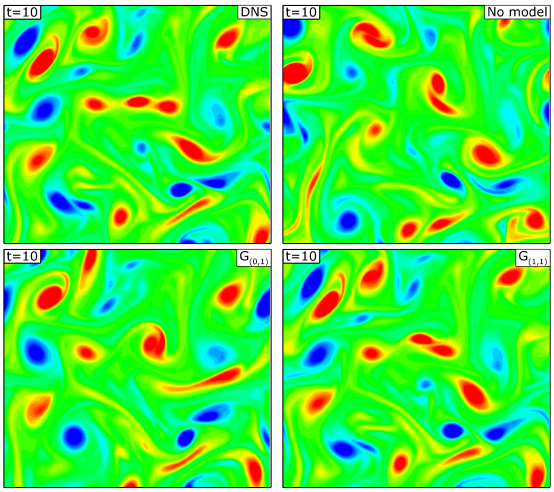

Figure 7. Vorticity contours in HIT configuration obtained in the simulations using DNS (upper left figure), 'no-model' approach (upper right), ADM with 2nd order FDF (lower left) and CDF (lower right).

ACKNOWLEDGEMENTS

This work was supported by the National Science Centre, Poland (Grant no. 2018/29/B/ST8/00262) and statutory funds of Czestochowa University of Technology BS/PB 1-100-3011/2021/P. The authors acknowledge Prof. Bernard J. Geurts for fruitful discussions stimulating this work within the framework of the International Academic Partnerships Programme No. PPI/APM/2019/1/00062 sponsored by National Agency for Academic Exchange (NAWA).

REFERENCES

[1] Danilov S. D., Gurarie D., 2000, "Quasi-two-dimensional turbulence", *Physics-Uspekhi*, Vol. 43 (9), pp. 863–900.

[2] Tabeling, P., 2002, "Two-dimensional turbulence - a physicist approach", *Physics Reports*, Vol. 362 (1), pp. 1–62.

[3] Boffetta G., Ecke R. E, 2012, "Two-Dimensional Turbulence", *Annual Review of Fluid Mechanics*, Vol. 44 (1), pp. 427–451.

[4] Kraichnan, R. H., 1967, "Inertial Ranges in Two-Dimensional Turbulence", *Physics of Fluids*, Vol. 10 (7), pp. 1417–1423.

[5] Batchelor, G. K., 1969, "Computation of the Energy Spectrum in Homogeneous Two-Dimensional Turbulence", *Physics of Fluids*, Vol. 12 (12), pp. 233–239.

[6] Leith, C. E., 1971, "Atmospheric Predictability and Two-Dimensional Turbulence", *Journal of the Atmospheric Sciences*, Vol. 28 (2).

[7] Sagaut, P., 2006, *Large Eddy Simulation for Incompressible Flows*, Springer, Berlin, Heidelberg.

[8] Stolz S., Adams N. A., 1999, "An approximate deconvolution procedure for large-eddy simulation", *Physics of Fluids*, Vol. 11 (7), pp. 1699–1701.

[9] Stolz S., Adams N. A., Kleiser L., 2001, "The approximate deconvolution model for large-eddy simulations of compressible flows and its application to shock-turbulent-boundary-layer interaction", *Physics of Fluids*, Vol. 13 (10), pp. 2985–3001.

[10] Stolz S., Adams N. A., Kleiser, L., 2001, "An approximate deconvolution model for large-eddy simulation with application to incompressible wall-bounded flows", *Physics of Fluids*, Vol. 13 (4), pp. 997–1015.

[11] Schlatter P., Stolz S., Kleiser L., 2004, "LES of transitional flows using the approximate deconvolution model", *International Journal of Heat and Fluid Flow*, Vol. 25 (3), pp. 549–558.

[12] Domaradzki J. A., Adams N. A., 2002, "Direct modelling of subgrid scales of turbulence in large eddy simulations", *Journal of Turbulence*, Vol. 3 (24), pp. 1–19.

[13] San O., Staples A. E., Wang Z., Iliescu T., 2011, "Approximate deconvolution large eddy simulation of a barotropic ocean circulation model", *Ocean Modelling*, Vol. 40 (2), pp. 120–132.

[14] San O., Staples A. E., Iliescu T., 2013, "Approximate deconvolution large eddy simulation of a stratified two-layer quasi-geostrophic ocean model", *Ocean Modelling*, Vol. 63, pp. 1–20.

[15] Chow F. K., Street R. L., Xue M., Ferziger J. H., 2005, "Explicit Filtering and Reconstruction Turbulence Modeling for Large-Eddy Simulation of Neutral Boundary Layer Flow", *Journal of the Atmospheric Sciences*, Vol. 62 (7), pp. 2058–2077.

[16] Chow F. K., Street R. L., 2009, "Evaluation of Turbulence Closure Models for Large-Eddy Simulation over Complex Terrain: Flow over Askervein Hill", *Journal of Applied Meteorology and Climatology*, Vol. 48 (5), pp. 1050–1065.

[17] Zhou B., Chow F. K., 2011, "Large-Eddy Simulation of the Stable Boundary Layer with Explicit Filtering and Reconstruction Turbulence Modeling", *Journal of the Atmospheric Sciences*, Vol. 68 (9), pp. 2142–2155.

[18] Boguslawski A., Wawrzak K., Paluszewska A., Geurts B. J., 2021, "Deconvolution of induced spatial discretization filters subgrid modeling in LES: application to two-dimensional turbulence", *Journal of Physics Conference Series*, Vol. 2090 (1), p. 012064.

[19] San O., Staples A. E., Iliescu T., 2014, "A posteriori analysis of low-pass spatial filters for approximate deconvolution LES of homogeneous incompressible flows", *International Journal of Computational Fluid Dynamics*, Vol. 29 (1), pp. 40–66.

[20] San O., Staples A. E., 2012, "High-order methods for decaying two-dimensional homogeneous isotropic turbulence", *Computers and Fluids*, Vol. 63, pp. 105–127.

[21] van Cittert P.H., 1931, "Zum Einfluß der Spaltbreite auf die Intensitätsverteilung in Spektrallinien. II", *Zeitschrift für Physik*, Vol. 69, pp. 298–308.

[22] Geurts B.J, van der Bos F., 2005, "Numerically induced high-pass dynamics in large-eddy simulation", *Physics of Fluids*, Vol. 17 (12), p. 125103.

[23] Caban L., Tyliszczak A., 2022, "High-order compact difference schemes on wide computational stencils with a spectral-like accuracy", *Computers and Mathematics with Applications*, Vol. 108, pp. 123–140.

Conference on Modelling Fluid Flow (CMFF'22)
The 18th International Conference on Fluid Flow Technologies
Budapest, Hungary, August 30 -September 2, 2022

ON THE USAGE OF TIP APPENDAGES FOR FLOW CONTROL IN AIR-COOLED CONDENSERS

Lorenzo TIEGHI[1*], Alessandro CORSINI[1], Giovanni DELIBRA[1], Johan van der SPUY[2], Francesco Aldo TUCCI[1]

[1]Department of Mechanical and Aerospace Engineering, Faculty of Industrial and Civil Engineering, Sapienza University of Rome, Rome, Italy.
[2]Department of Mechanical & Mechatronic Engineering, Faculty of Mechanical Engineering, Stellenbosh University, Cape Town, South Africa
[*]Corresponding Author, e-mail: lorenzo.tieghi@uniroma1.it. Tel.: +39 06 445 85234

ABSTRACT

Air cooled condensers (ACCs) are commonly found in power plants working with concentrated solar power or in steam power plants operated in regions with limited water availability. In ACCs the flow of air is driven toward the heat exchangers by axial fans that are characterized by large diameters and operate at very high mass flow rates near-zero static pressure rise. Given the overall requirements in steam plants these fans are subjected to inflow distortions, unstable operations and have high noise emissions.
Previous studies show that leading edge bumps in the tip region of axial fans effectively reduce the sound pressure levels without affecting the static efficiency of the fan. Nevertheless, the effects of such treatment in terms of flow patterns and heat exchanging in the whole ACC system were not investigated.
In this work, the effect of leading-edge bumps on the flow patterns is analyzed. Two RANS simulations were carried out using OpenFOAM on a simplified model of the air-cooled condenser. The fans are simulated using a frozen rotor approach. Turbulence modelling relies on the RNG k-epsilon model. The fan is characterized by a diameter of 7.3 m and a 333 m^3/s of volumetric flow rate at the design point. The presence of the heat exchanger is modelled using a porous media approach.
The comparison between the flow fields clearly exert that the modified blade is responsible for the redistribution of radial velocities in the rotor region. This drastically reduces the losses related to the installation of the fan in a real configuration.
Keywords: air cooled condensers, CFD, flow control, inflow distortion, leading edge appendages.

NOMENCLATURE

ACC		Air-Cooled Condenser
P	[kW]	Fan power
Q	[m^3/s]	Volume flow rate
U	[m/s]	blade velocity
c	[m/s]	absolute velocity
w	[m/s]	relative velocity
Δp_{TTS}	[Pa]	total-to-static pressure rise

Subscripts and Superscripts

r	radial
x	axial

1. INTRODUCTION

Condensers in steam power plants can be either water- or air- cooled. Usually, the first solution is preferred because it guarantees higher overall efficiency given the lower ancillary operational costs involved and a more compact solution. However, some power plants require air-cooled condensers, usually because of the lack of cooling water near the installation site. That is the case of concentrated solar power (CSP) plants with a bottoming Rankine cycle, as CSP are commonly installed in desertic areas, or large steam plants like [1], that are installed in desertic areas near largely populated cities.

For this work, we will refer to air-cooled condensers (ACC) and their typical arrangement and in particular to the design of fans inside these units. The ACC assembly comprises a series of cooling units (>400 in the plant shown in Figure 1) where large axial fans feed fresh air to a series of heat exchangers, where the steam condensates. The

typical arrangement, shown in, is that of a A-frame condenser unit with the fan inlet placed several meters above the ground and the heat exchangers on top of the fan.

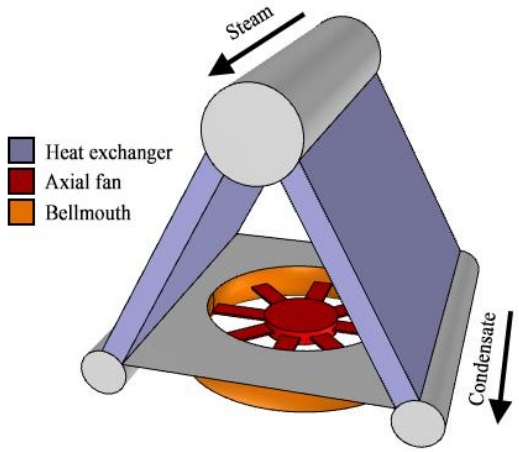

Figure 1: A-frame arrangement for an ACC unit

These fans are operated with very high-volume flow rates (250 to 400+ m^3/s) and very low static pressure rise (100 to 300 Pa). This unusual combination results in a design characterized by large diameter (6-12m), low hub ratio (0.25-0.4) and rotational velocity between 100-200 rpm. Being so large and mounted on very high (>30m) structures to provide a sufficiently wide inflow, these fans are often characterized by a large and irregular tip clearance due to assembly issues that eventually reflect on fan efficiency [2].

Operations of these fans is also critical as efficiency drops when working with a lateral wind condition, in sandy environments or with extreme environmental temperature. In these conditions, the volume dilatation of the structures can in fact impact significantly on tip gap, with possible effects on fan efficiency, vibrations, mechanical failures, and noise emissions. Noise is in fact among the problems of large ACCs array due to the high number of fans involved [3][4].

Among the possible strategies available to fan designers to tackle part of these problems, sinusoidal serrations were proposed to control trailing edge separation, evolution of the tip leakage vortex and control noise. Developed from biomimicry assumptions on the hydrodynamics of the humpback whale fin tubercles [5], this leading edge modifications were found to change the dynamics of separation and loss of lift capability in NACA 4 digit modified airfoils. This capability derived by the counter-rotating vortices shed from the serrations at the leading edge, that at very high angles of attack (where the airfoil is supposed to operate in stalled conditions) result in controlling trailing edge separation and limiting it in span-wise positions that correspond to the trough of the leading edge serration. Later studies, based on unsteady computations, revealed that a secondary motion arises in spanwise direction, with secondary phenomena resulting in a secondary shedding frequency that involves the whole blade span [6]. The separation control capability of leading edge serrations was exploited in modified axial fan geometries to control the development of the tip leakage vortex along the suction side of the rotor, resulting in a controlled stall dynamics [7]. Moreover, when dealing with noise, experimental and numerical findings [8][9] show how sinusoidal leading edges results in a change of the acoustic signature of the fan.

In the framework of H2020 MinwaterCSP project [10], we designed a fan for ACC that is now in operations at Stellenbosh University. This fan is running in an ACC unit in real conditions and is characterized by limitations that during operations can result in distorted inflow conditions and reduction of the volume flow rate. In particular this is a consequence of the nearby university buildings and of a water channel that flows below the test rig. Among the MinwaterCSP requirements for this fan there was a request for a low noise design as in real ACCs the hundreds of units can in fact results in health issues for people and fauna. In this case, however, the real problem comes from the proximity of the university and the presence of staff and students. For these reasons and given the background on leading edge serrations mentioned above, we here present a preliminary study of the effects of the modified geometry on the aerodynamics of this fan.

2. NUMERICAL METHODOLOGY

2.1. Computational Domain

The computational domain is chosen based on the experimental apparatus that is described in [2]. It describes a full-scale A-type air cooled condenser [11]**Errore. L'origine riferimento non è stata trovata.**. This ACC experimental configuration include a grid downstream of the fan, that was modelled using a porous media.

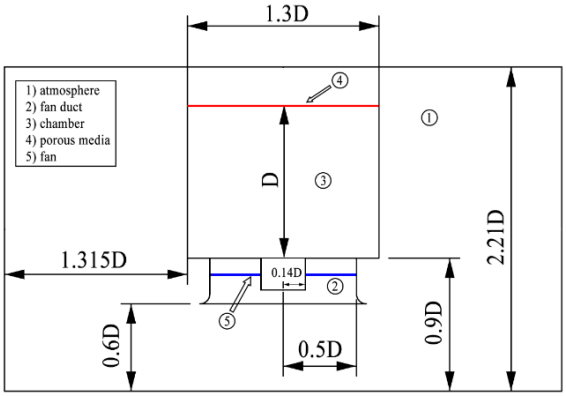

Figure 2 – Front view of the numerical domain

The structural supports to the exchanger are not included in the final model, their effect being neglectable from an aerodynamic point of view. The domain, normalized by the rotor diameter D, is reported in Figure 2.

The domain is symmetric with respect to the fan, therefore each of the four lateral boundaries is located at 1.315D from the exchanger walls.

2.1. Fan Description

The fan is an eight-blade low-speed axial fan. Rotor diameter is 7.3 m, with a hub-to-tip ratio equal to 0.284. Tip clearance is set to 0.2% of the blade tip chord. The rotational speed of the fan is 151 rpm. The fan provides 105 Pa of total-to-static pressure at the nominal volumetric flow rate of 333 m^3/s. The design process of both the fan and its modified version are reported in [12]. The leading edge bumps are designed by varying the blade chord of +/-5%, following a sinusoidal low in the last 25% of the blade span. The original blade, here labeled as *datum* fan, and its modified version, here labeled as *whale* fan, are shown in Figure 3.

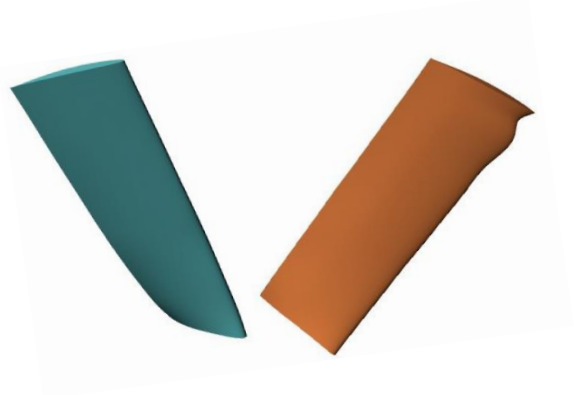

Figure 3 - Datum (left) and whale (right) fan geometries

2.3. Computational Grid

The computational grid was generated for both geometries using the *snappyHexMesh* utility of the OpenFOAM v2106 library. The base grid entails 0.8M cells with unity aspect ratio and a cell size of approximately 0.13m. The grid is sequentially refined in the whole exchanger and in the rotor region, as shown in Figure 4.

Due to the large computational domain, the grid was designed for high Reynolds computation. Therefore, the wall spacing was set to achieve a y^+=100 on the first layer of cells.

A grid sensitivity analysis on the datum fan configuration was performed using total-to-static pressure rise and convergence parameter. Results are shown in Figure 5, showing that a grid refinement of 20M cells is sufficient for this setup.

In particular, 2M cells are used to model the external atmosphere, 15M in the rotor region and 3M cells in the exchanger. A visualization of the grids on the whale fan rotors is provided in Figure 6.

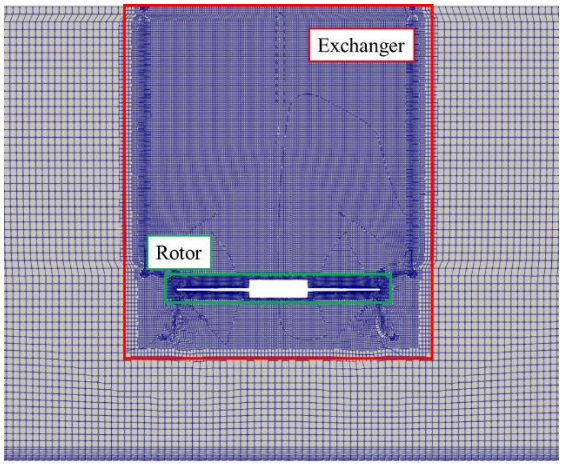

Figure 4 - Grid refinements

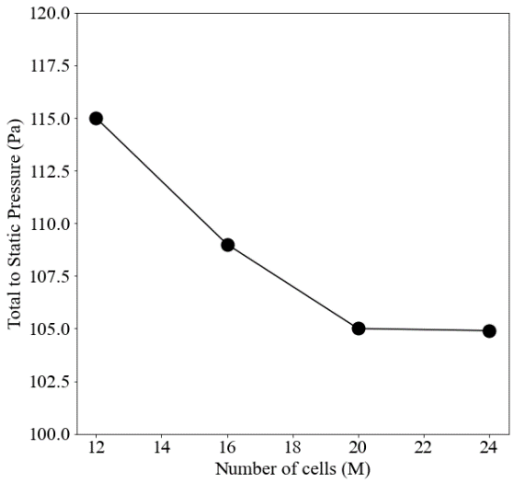

Figure 5 - TTS pressure as a function of the number of cells, datum blade

2.4. Porous media setup

The porous media is modelled using the parabolic Darcy-Forchheimer relationship. The 10 cm thick, porous region in the exchanger is responsible of a pressure loss that is calculated according to:

$$\frac{\partial p}{\partial x_j} = -\frac{\mu}{\kappa} U_j - \frac{\mu}{\kappa_1} U_j^2 \qquad (1)$$

where κ and κ_1 are respectively the Darcy and Forchheimer coefficients. This pressure gradient acts as sink term in the momentum equation. The coefficients of Eq. (1) where derived from the geometry of the squared grid in the test-rig that has a characteristic length of 5 cm, following the methodology reported in [13]. Since the flow is characterized by a predominant axial direction, the coefficients in orthogonal directions are set to 10^{10}.

2.5. Numerical setup

Turbulence modelling relies on the RNG k-epsilon model [14]. The steady computations are based on a frozen rotor approach and the incompressible equations are solved using the SIMPLE solver. Convergence was assessed by the torque of the fan and the velocity in probes up- and downstream of the fan. The linearized systems of equations were solved using a smoothSolver for all the quantities, except for pressure, that was solved using a conjugate gradient solver. Tolerance for convergence was set to 10^{-6} for all quantities except pressure, that was set to 10^{-4}.

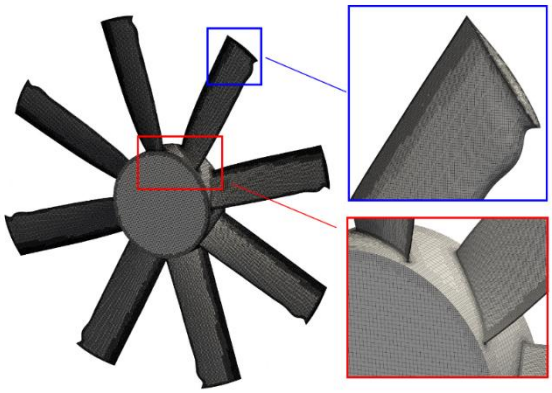

Figure 6 - Mesh of the fan and details of the grid at blade tip and hub, whale fan design2.6. Boundary conditions

A scheme of the boundary condition is reported in Figure 7. The terrain is treated as a rough wall, with relative thickness of 0.1. The mass flow rate is imposed on the lateral boundaries, equal to 25% of the duty point of the fan. Atmosphere is treated as a slip wall for numerical stability of the simulation. At the outflow of the fan, total pressure is imposed, with zeroGradient (zG) condition on velocity. On all solid surfaces, standard wall functions for turbulent kinetic energy, dissipation rate and turbulent viscosity are used.

.

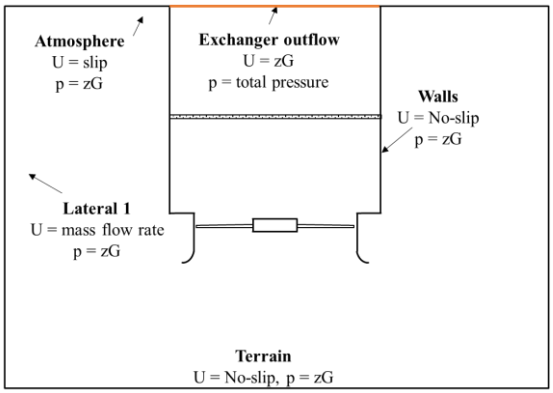

Figure 7 - Scheme of boundary conditions, front view

3. RESULTS

For a preliminary assessment of the accuracy of computations, a comparison of TTS pressure and TTS efficiency are shown in Table 1. Pressure is averaged over two planes at 1.6 D and 1.8 D from the terrain. Numerical computations results show that the pressure rise capability of the two fans in ISO conditions is practically the same, with slightly worst efficiency of the whale fan, confirming the conclusions in [15]. However, the installation inside the ACC setup leads to different behavior: the datum geometry in fact shows a reduction of the pressure rise capability of 32%, with a negligible change in power adsorbed, while the whale fan has a reduction of pressure rise capability and power consumption of about 10%.

Table 1. Validation of CFD results

Arrangement		Q	Δp_{TTS}	Power
-	-	m^3/s	Pa	kW
Datum	ACC	333	95	61.7
	Single Rotor	333	140	60.4
Whale	ACC	333	123.8	56
	Single Rotor	333	137.6	62

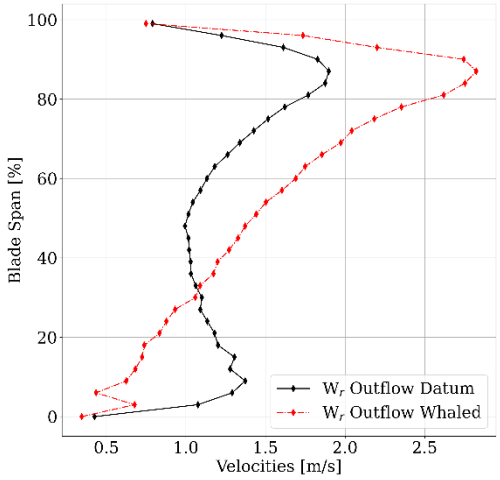

Figure 8 – Radial velocity at the outlet of the datum fan (black) and the whale fan (red)

This change in performance is associated to a higher work capability of the tip region and a change into the spanwise behavior of the flow. This is shown in Figure 8, where the whale fan shows a linear trend from root to 85% of the span, while the datum geometry has a higher radial velocity value at the root of the blade and then a lower value from 1/3 of the blade span.

The change in performance can be associated mainly to the effect of the leading-edge modification on the development of the tip leakage vortex. As shown in Figure 9 in fact at the through of the sinusoidal leading edge the flow accelerates and reaches a relative velocity of over 70 m/s. The

resulting jet released by this region of the rotor delays the development of the tip leakage vortex with respect to the datum fan. In fact, in the datum geometry the leaking starts at about 10% of the chord of the tip section, with a secondary vortex being released at about 50% of the chord.

On the whale rotor only this second structure is present, due to the counter rotating flow released by the modified leading edge that blocks the development of the first leaking structure.

This is better seen in Figure 10 and Figure 11 where relative velocity and pressure contours are plotted on an iso-radius surface at 99% of the blade span. In both figures the trace of the tip leakage vortex system is clearly recognizable, with a delayed development for the whale rotor geometry

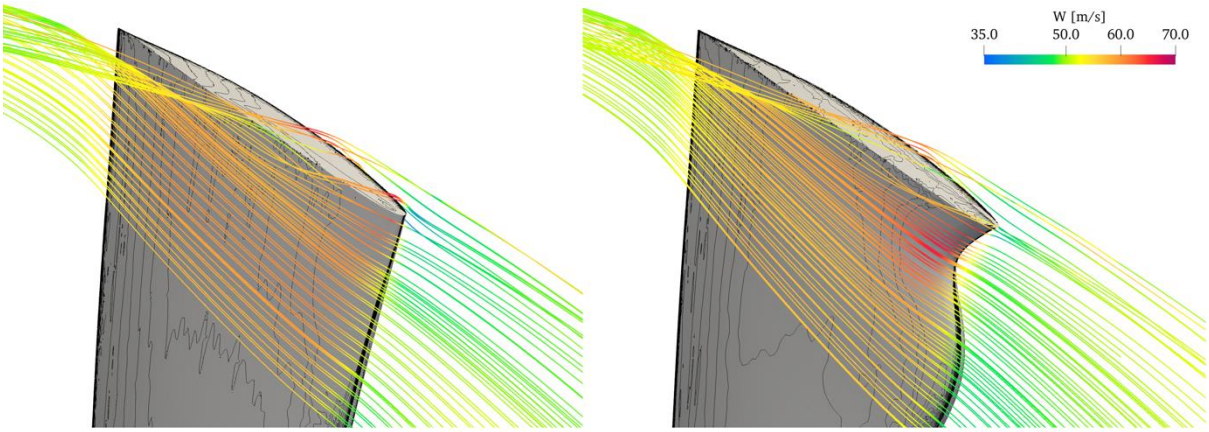

Figure 9 – Relative velocity streamlines on the tip region for datum (left) and whale (right) fan colored with relative velocity

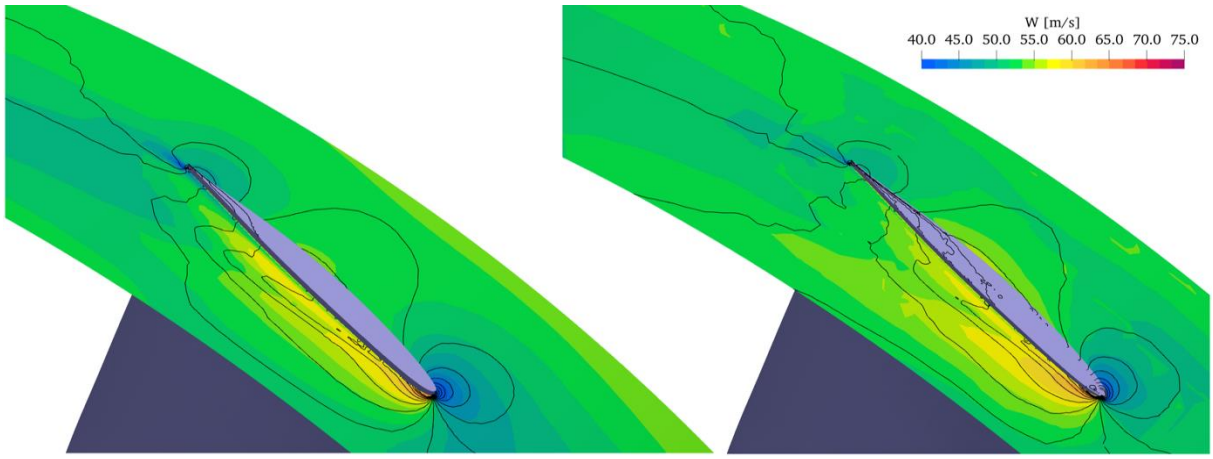

Figure 10 - Relative velocity contours on iso-radius surface at 99% of the blade span for datum (left) and whale (right) fan

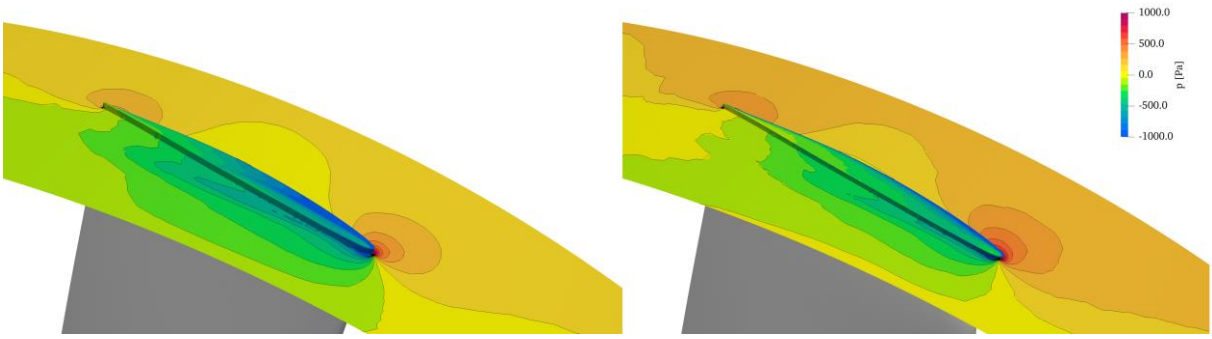

Figure 11 - Relative contours on iso-radius surface at 99% of the blade span for datum (left) and whale (right) fan

5. CONCLUSIONS

Following the conclusions of previous works on modified fan rotors with sinusoidal leading edges, we tested this flow control solution on an air-cooled condenser fan for steam power plants.

In ISO arrangements show that the original blade and the whale blade have similar performance in both total-to-static pressure rise capability and adsorbed power. When fitted in the ACC however there is a clear improvement as the whale fan have a loss of pressure rise with respect to the ISO arrangement that of about 11%, against a loss of 32% for the datum blade. Also, the absorbed power is reduced of 10% while the datum fan has negligible difference with respect to ISO conditions.

The different behavior was then related to a radial redistribution of the flow induced by the modified rotor and its capability to control and contrast the development of the tip-leakage vortex on the suction side of the rotor. These findings are similar to those shown in [5].

REFERENCES

[1] Fourie, N., Van Der Spuy, S. J., & Von Backström, T. W. (2015). Simulating the effect of wind on the performance of axial flow fans in air-cooled steam condenser systems. Journal of Thermal Science and Engineering Applications, 7(2), 021011.

[2] Van der Spuy, S. J., Els, D. N. J., Tieghi, L., Delibra, G., Corsini, A., Louw, F. G., ... & Meyer, C. J. (2021, June). Preliminary Evaluation of the 24 Ft. Diameter Fan Performance In the MinWaterCSP Large Cooling Systems Test Facility. In Turbo Expo: Power for Land, Sea, and Air (Vol. 84898, p. V001T10A005). American Society of Mechanical Engineers.

[3] Van der Spuy, S. J., von Backström, T. W., & Kröger, D. G. (2009). Performance of low noise fans in power plant air cooled steam condensers. Noise Control Engineering Journal, 57(4), 341-347.

[4] Angelini, G., Bonanni, T., Corsini, A., Delibra, G., Tieghi, L., & Volponi, D. (2018). On surrogate-based optimization of truly reversible blade profiles for axial fans. Designs, 2(2), 19.

[5] Corsini, A., Delibra, G., & Sheard, A. G. (2013). On the role of leading-edge bumps in the control of stall onset in axial fan blades. Journal of fluids engineering, 135(8).

[6] Zhang, M. M., Wang, G. F., & Xu, J. Z. (2013). Aerodynamic control of low-Reynolds-number airfoil with leading-edge protuberances. AIAA journal, 51(8), 1960-1971.

[7] Corsini, A., Delibra, G., & Sheard, A. G. (2014). The application of sinusoidal blade-leading edges in a fan-design methodology to improve stall resistance. Proceedings of the Institution of Mechanical Engineers, Part A: Journal of Power and Energy, 228(3), 255-271.

[8] Biedermann, T. M., Kameier, F., & Paschereit, C. O. (2019). Successive aeroacoustic transfer of leading-edge serrations from single airfoil to low-pressure fan application. Journal of Engineering for Gas Turbines and Power, 141(10).

[9] Biedermann, T. M., Chong, T. P., Kameier, F., & Paschereit, C. O. (2017). Statistical–empirical modeling of airfoil noise subjected to leading-edge serrations. AIAA Journal, 55(9), 3128-3142.

[10] The MinWaterCSP Project - http://www.minwatercsp.eu

[11] Kirstein, C., von Backström, T. and Kröger, D. (2005). Flow Through a Solar Chimney Power Plant Collector-to-Chimney Transition Section. International Solar Energy Conference. DOI: 10.1115/ISEC2005-76011.

[12] Volponi, D., Bonanni, T., Tieghi, L., Delibra, G., Wilkinson, M., van der Spuy, J. and von Backström, T. (2018). CFD Simulation Results for the MinWaterCSP Cooling Fan. DOI: 10.13140/RG.2.2.22031.89768.

[13] Idelchik, Isaak E. "Handbook of hydraulic resistance." wdch (1986)

[14] Yakhot, V. S. A. S. T. B. C. G., Orszag, S. A., Thangam, S., Gatski, T. B., & Speziale, C. (1992). Development of turbulence models for shear flows by a double expansion technique. Physics of Fluids A: Fluid Dynamics, 4(7), 1510-1520.

[15] Tieghi, L., Delibra, G., Corsini, A., & Van Der Spuy, J. (2020). Numerical investigation of CSP air cooled condenser fan. In E3S Web of Conferences (Vol. 197, p. 11010). EDP Sciences.

Conference on Modelling Fluid Flow (CMFF'22)
The 18th International Conference on Fluid Flow Technologies
Budapest, Hungary, August 30-September 2, 2022

EFFECT OF LEAKAGE ON THE PERFORMANCE OF THE VANELESS DIFFUSER OF A CENTRIFUGAL PUMP MODEL

Meng FAN[1], Antoine DAZIN[1], Francesco ROMANO[1], Gérard BOIS[1]

[1] Univ. Lille, CNRS, ONERA, Arts et Métiers Institute of Technology, Centrale Lille, UMR 9014-LMFL-Laboratoire de Mécanique des Fluides de Lille - Kampé de Fériet, F-59000, Lille, France

ABSTRACT

An analysis of a pump vaneless diffuser model is presented with a particular focus on the leakage effect between the impeller outlet and diffuser inlet section. RANS and URANS simulations are conducted for three different leakage configurations. The $k-\omega$ SST turbulence model is used, carrying out the simulation by the open-source software OpenFOAM. Results obtained for each numerical configuration are analyzed and discussed. Comparison with experimental results corresponding to one of the tested configurations is also presented. They show that the leakage flow slightly influences the overall pump performance and more specifically the vaneless diffuser one. When considering the real flow rate obtained by CFD, including leakage effects, comparison with the experimental results get closer both for the overall pump and for the vaneless diffuser performances. A special focus on the instability onset in the vaneless diffuser is also proposed for each leakage configuration which leads to selecting the best way to reproduce experimental behavior from an adequate CFD approach and correct boundary conditions.

Keywords: numerical simulation, performance, instability

NOMENCLATURE

δ	$[-]$	relative error
Δp	$[Pa]$	pressure difference
ν_T	$[-]$	eddy viscosity
ω_{imp}	$[rad/s]$	angular velocity
ρ	$[kg/m^3]$	air density
b	$[m]$	diffuser width
H_b	$[m]$	outflow domain height
L	$[m]$	radial gap value
N	$[rpm]$	rotational speed
p	$[Pa]$	static pressure
Q	$[m^3/s]$	pump flow rate
Q_d	$[m^3/s]$	pump design flow rate
R	$[m]$	radius
Re	$[-]$	pump Reynolds number
Z	$[-]$	number of blades

Subscripts

1	impeller inlet
2	impeller outlet
3	diffuser inlet
4	diffuser outlet
C	centrifugal pump
D	diffuser
$D1$-$D9$	related to the nine evenly distributed probes along the radial direction over the shroud side of the diffuser
I	impeller
$S1$-$S4$	related to the probes placed at $\theta = 0,\ \pi/2,\ \pi,\ 3\pi/2$ on the inlet pipe

1. INTRODUCTION

Centrifugal pumps are widely used in many domains such as irrigation, water supply, cooling systems, and pumping stations. However, the operating range of pumps is affected by the occurrence of unstable phenomena. Among them, rotating stall can affect the vaneless diffuser of the pump when operating at a partial flow rate. This has been already described and analyzed by several authors in radial flow pumps and compressors like Jansen et al. [1, 2], Senoo et al. [3], Fringe et al. [4], and Sundström et al. [5]. Even if this phenomenon is now well described, the effect of the leakage flow at diffuser inlet on the rotating stall onset and dynamic has never been investigated. Detailed information on the pump model geometry can be found in Wuibaut et al. [6]. This model set-up uses air as working fluid and its dimensions are determined using similarity laws parameters, i.e same specific speed and specific radius of the initial pump working with water. To get a sufficiently high pump Reynolds number value of $Re = \omega_{imp} R^2/\nu = 5.48 \times 10^5$, based on the impeller outlet radius and a rated angular speed of $\omega_{imp} = 125$ rad/s, the air pump model's main dimensions are listed in table 1.

The present case study has been experimentally

SHF impeller characteristics	
Tip intlet radius	R_1 = 141.1mm
Outlet radius (experiment)	R_2 = 256.6mm
Outlet radius (simulations)	R_2 = 257.5mm
Outlet width	b_2 = 38.5mm
Number of blades	$Z = 7$
Outlet blade angle	β_{2c} =22.5°
Design flowrate(1200 rpm)	$Q_d = 0.236\text{m}^3/\text{s}$
Reynolds number	$Re = {R_2}^2\omega_{imp}/\nu$
(Q/Q_d = 1.0, N = 1200 rpm)	$= 5.52\times10^5$
Vaneless diffuser characteristics	
Inlet radius (experiment)	R_3 = 257.1mm
Inlet radius (case A)	R_3 = 257.5mm
Inlet radius (case B and C)	R_3 = 260.075mm
Outlet radius	R_4 = 385.5mm
Constant width	b_3 = 38.5mm

Table 1. Main geometrical characteristics of the impeller and diffuser

and analytically investigated in previous works by Dazin et al. [7, 8], and by Heng et al. [9, 10] and [11], even though the effects of the leakage flow have been neglected. Some attempts to include leakage effects in CFD investigation have been presented by Dupont et al. [12] and Pavesi et al. [13] to partially explain overall mean performance discrepancies between experiments and numerical results, but with a vaned diffuser configuration. In the present paper, three different leakage configurations are numerically analyzed using RANS and URANS approaches and compared with experimental performance results on the whole pump and the vaneless diffuser itself. The limitations of the numerical methods employed on this pump model are pointed out combined with the effects of each leakage configuration.

2. METHODOLOGY

2.1. Computational Domain

The three different tested configurations are shown in figure 1. They are respectively called "case A", "case B", and "case C".

- Case A corresponds to a simplified configuration for which there is no leak between the impeller and the vaneless diffuser (see fig. 1 (a)).

- Case B corresponds to a usual pump configuration that allows leakage flow from outlet to inlet sections of the impeller. Consequently, a radial gap $L = R_3 - R_2$ is introduced as shown in fig. 1 (b).

- Case C, given in fig. 1 (c), is quite close to the experimental set-up with the same value of the radial gap value L. The inlet axial gap that separates the inlet tube and the rotating impeller is neglected.

The overall CFD domains include the inlet pump pipe domain (radius R_1 and pipe lenght $10R_1$). The outlet pump domain that is represented by an external cylinder of height H_b and external radius R_b. An outflow box dimension of $H_b/b_3 = 15$ and outlet radius $R_b/R_3 = 3$, is placed after the diffuser outlet section.

2.2. Problem Formulation and Mesh

The flow in a centrifugal pump is incompressible and three-dimensional. Turbulence, rotation of the impeller, the shape of the blades, centrifugal force, and Coriolis force lead to complex flow phenomena in the centrifugal pump. In this study, the flow in the pump is described by the Reynolds averaged Navier-Stokes equations, either in steady (RANS) or unsteady (URANS) form. The URANS equations are

$$\frac{\partial(\mathbf{u})}{\partial t} + (\mathbf{u}\cdot\nabla)\mathbf{u} + \nabla p = \nabla\cdot(2\nu\mathbf{S} - \boldsymbol{\tau}), \quad \nabla\cdot\mathbf{u} = 0, \quad (1)$$

where $\mathbf{u} = \mathbf{u}(\mathbf{x}, t)$ denotes the mean part of the velocity vector, $\mathbf{u} = (u_1, u_2, u_3)$, $p = p(\mathbf{x}, t)$ denotes the mean part of the kinematic pressure, ν is the constant kinematic viscosity, $\mathbf{x}$ is the position vector, t denotes time, $\mathbf{S} = \frac{1}{2}(\nabla\mathbf{u} + \nabla^T\mathbf{u})$ is the mean rate of the strain tensor with the components

$$S_{ij} = \frac{1}{2}\left(\frac{\partial u_i}{\partial x_j} + \frac{\partial u_j}{\partial x_i}\right), \quad (2)$$

and $\boldsymbol{\tau}$ is the Reynolds stress tensor.

For the (U)RANS simulation, the Reynolds stress tensor is modeled by an eddy-viscosity approach containing two conservation equations for the turbulent properties ϕ. Depending on the model type, the placeholder ϕ can be the turbulent kinetic energy k, the turbulent dissipation ϵ or the turbulent specific dissipation rate ω, respectively:

$$\frac{\partial(\phi)}{\partial t} + (\mathbf{u}\cdot\nabla)\phi = P_\phi + \nabla\cdot(D_\phi\nabla\phi) + E_\phi. \quad (3)$$

Different turbulence models contain the terms for production P, diffusion D, and dissipation E. The eddy viscosity ν_T can be deduced from the calculated turbulence quantities as $\nu_T \sim k^2/\epsilon$ or $\nu_T \sim k/\omega$ [14]. The shear-stress transport $k-\omega$ SST turbulent model is used to simulate the turbulent flow in this study.

The computational mesh for the whole domain is multi-block-structured and has several refinement zones to capture the flow field in detail in areas of interest. The mesh is finest near the walls and is gradually coarser further away from the walls. The finer block-structured mesh of the short inlet pipe, impeller, and vaneless diffuser regions with a zoomed view of the refined zones in the impeller and diffuser domain is illustrated in fig. 2 (a) and fig. 2 (b). While a coarser mesh is used in the long inlet pipe and the outflow box regions. In the model scale, the numerical simulations have y+ values of approximately 1 near the walls in the short inlet pipe, impeller, and diffuser regions. The corresponding y+ value near

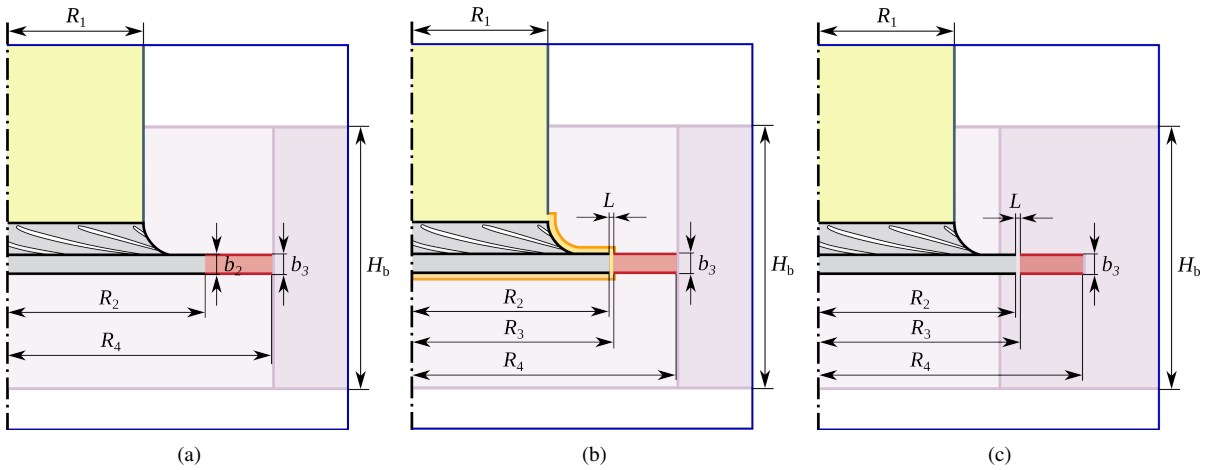

Figure 1. Schematic of the (a) case A, (b) case B, and (c) case C of the centrifugal pump.

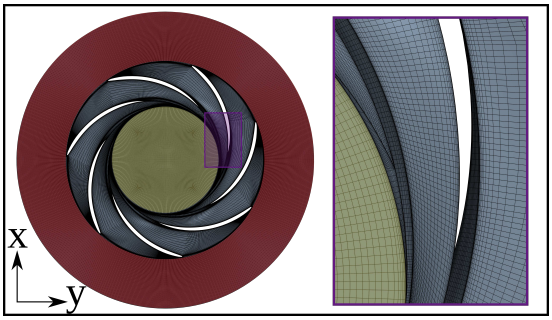

(a)

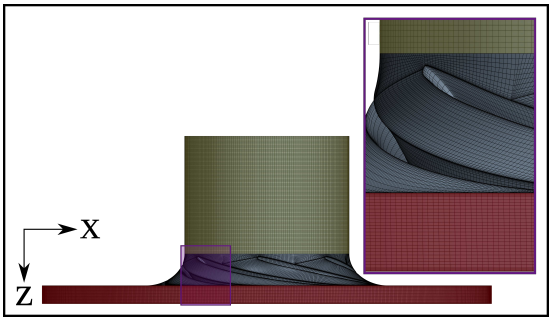

(b)

Figure 2. Top (a) and side (b) view of a typical mesh of case A employed for carrying out the three-dimensional URANS simulations.

the long pipe wall is less than 10 since the mesh for this region is coarser. The mesh is generated by the commercial software ANSYS ICEM CFD and then converted to the format that OpenFoam uses based on the mesh converter library `fluent3DmesToFoam`.

A grid number independence verification was carried out with four schemes. As shown in tab. 2, the predicted performance of the pump at the design condition with different grid resolutions are compared. The relative error of the predicted pump performance increases with the increase of grids sizes and then decreased to 0.93%. Therefore, a total mesh number of 2.3 million for the numerical domain were selected.

Case	Grid number	PSI	δ
1	617691	0.3843	1.75%
2	1118819	0.3864	2.30%
3	2316400	0.3742	0.93%
4	5406783	0.3777	–

Table 2. Grid independence verification data. δ is the relative error computed with respect to the finest grid, i.e. $\delta = |\mathrm{PSI}_{\mathrm{Case\ 4}} - \mathrm{PSI}_{\mathrm{Case\ *}}|/|\mathrm{PSI}_{\mathrm{Case\ 4}}|$, where the asterisk denotes either Case 1, 2 or 3.

2.3. Numerics in OpenFOAM

All the numerical simulations were carried out using the open-source software OpenFOAM. The solver `simpleFoam` which enables the addition of MRF (Multiple Reference Frame) zones is applied for RANS simulations. While a transient solver `pimpleFoam` with dynamic mesh handling is applied for URANS simulations. In this simulation work, the temporal discretization term makes use of a second-order `backward` differencing scheme, named backward. The gradient term was discretized using the discretization method `Gauss` with linear interpolation where the discretization scheme is `Gauss` means gaussian interpolation of second order. The momentum divergence term was discretized using the second-order `linearUpwind` scheme, which is a blend of linear and upwind schemes. The linear scheme is used for `Interpolation` terms, where Gauss linear corrected scheme is used for Laplacian terms.

A Dirichlet type boundary condition named `flowRateInletVelocity` is chosen for the inlet boundary condition. We specify the inlet velocity corresponding to a pre-set value of inlet flow rate Q. And the static pressure $p = 0$ Pa is set for the outlet. The noslip wall boundary is used for fixed walls, and the `rotatingWallVelocity` boundary condi-

tion which specifies a rotational velocity is used for rotating walls.

To exclude the startup phase of the flow from the simulations, the RANS simulation results are used as initial values for URANS. The rotational speed was chosen as 125 rad/s and a time step was chosen as Δt, corresponding to 0.5° of the impeller revolution. The simulation results lead to an averaged Courant number for the whole domain of 0.0075 at the design flow rate. For RANS simulations, 10000-time steps were simulated. For URANS simulations, 70 rotating revolutions were simulated and all the results presented in this paper are corresponding to the last time step.

2.4. Experimental Set-ups

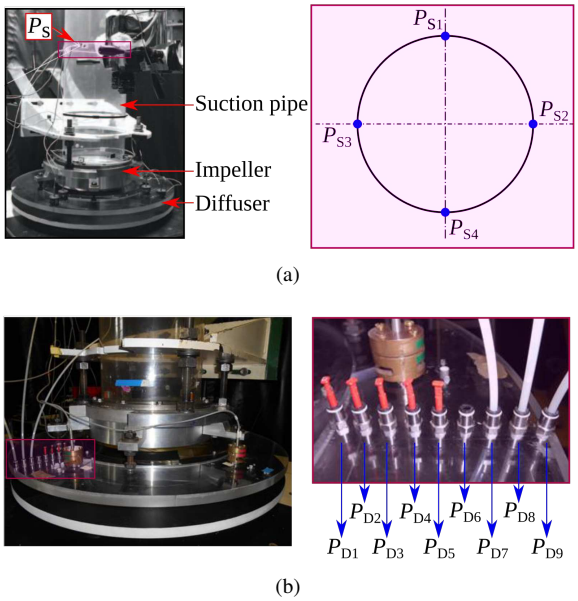

Figure 3. (a) Static pressure taps' locations at the pump inlet pipe. (b) Wall static pressure taps and microphones' locations installed on the vaneless diffuser.

The experimental set-up is briefly described here and is shown on fig. 3. It includes the transparent inlet pipe, the radial impeller, and the vaneless diffuser. The inlet pipe length is equivalent to the one of the numerical inlet domain. A set of replaceable diaphragms (with different inlet diameters), placed in a tank located before the inlet pipe section, are used to adjust the flow rate Q. No volute exists downstream the vaneless diffuser to ensure axisymmetric outlet boundary conditions corresponding to atmospheric pressure. To obtain diffuser pressure recovery, the set-up is equipped with nine steady wall pressure taps along with the diffuser shroud (equally spaced from R = 264 mm to 384 mm). The corresponding measurement uncertainty is evaluated at ± 2 Pa. Several flow rates values between Q/Q_d = 0.26 and 1.53 are chosen for a fixed rotational speed of N = 1200 rpm. Q_d denotes the design flow rate.

3. RESULTS

3.1. Pump Performance

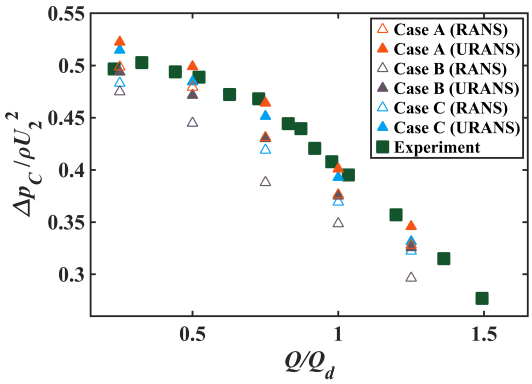

(a)

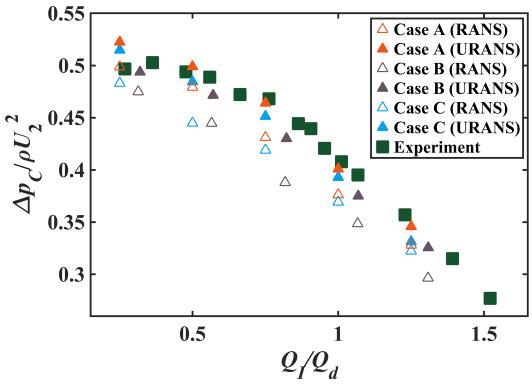

(b)

Figure 4. (a) Overall pump performance versus reduced pump flow rate Q. (b) Overall pump performance versus reduced impeller flow rate Q_I. Δp_C denotes the static pressure difference between the inlet and the outlet sections of the centrifugal pump; ρ denotes the density of the air.

The pump performance curves obtained by the RANS and URANS simulations are compared with the experimental results as shown in fig. 4 (a). As expected, the URANS simulation results are in better agreement with the experimental ones, as they captured the slowest scales of the time-dependent dynamics. Looking at the results of the three different configurations, the performance curve of case C, which is the same geometrical configuration as the experimental set-up, is the closest to the experimental results over the whole operating range. The performance curve of case A is slightly above the experimental results. Most of the experimental results are between the numerical results of cases A and C. Concerning case B, the pressure difference between the impeller outlet and inlet section leads to a leakage flow going out at the impeller-diffuser radial gap, feeding back the impeller inlet plane. This results in an increment of the flow rate in the impeller. Besides, an approximated flow leakage value is estimated through the inlet axial gap in front of

the impeller as already proposed by Heng [11], who modify the experimental impeller flow rate Q_I which is slightly larger than Q. This effect is taken into account and the corrected performance curves of case C and experiment, based on the impact of the flow rate increment in the impeller, are plotted in fig. 4 (b). The corresponding simulation results of case C get closer to the experimental ones.

3.2. Impeller Performance

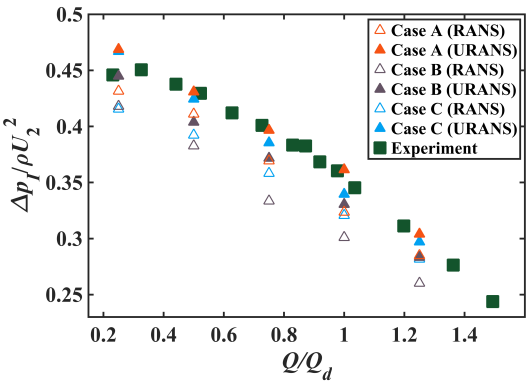

(a)

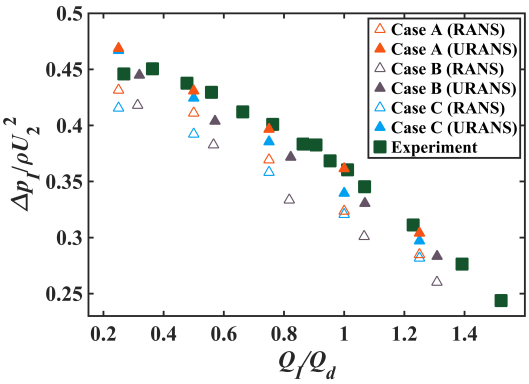

(b)

Figure 5. (a) Impeller performance versus reduced pump flow rate Q. (b) Impeller performance versus the reduced impeller flow rate Q_I. Δp_I denotes the static pressure difference between the inlet and the outlet impeller sections.

Fig. 5 (a) shows the impeller performance curve obtained with the RANS and URANS approaches. The impeller performance curves are very similar to the whole pump performance curves with the same trend. However, the simulation results of the impeller performance are closer to the experimental results of the whole pump performance. This means that the pump performance is mainly dominated by the impeller performance. The shifted impeller performance curves, based on the flow rate correction method mentioned before, are shown in fig. 5 (b). The corrected results show that excepting a flow rate change, the leakage flow does not have a big impact on the impeller performances.

3.3. Diffuser Performance

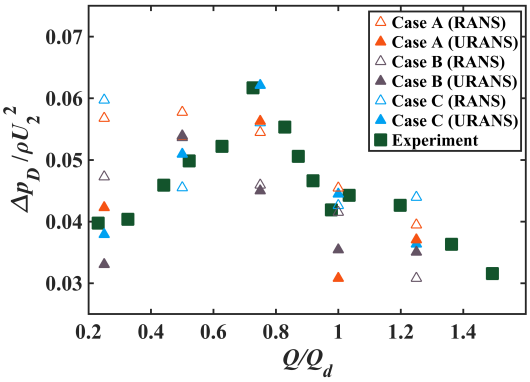

(a)

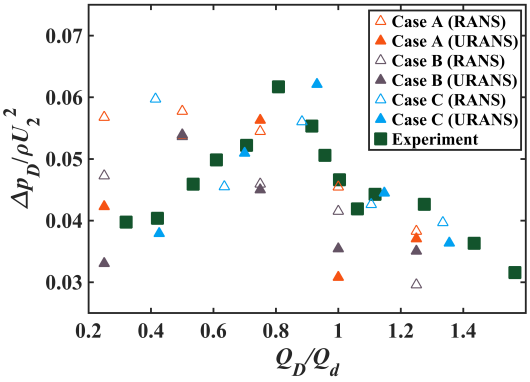

(b)

Figure 6. (a) Diffuser pressure recovery versus reduced pump flow rate Q. (b) Diffuser pressure recovery versus reduced diffuser flow rate Q_D. Δp_D denotes the static pressure difference between the inlet and the outlet sections of the vaneless diffuser.

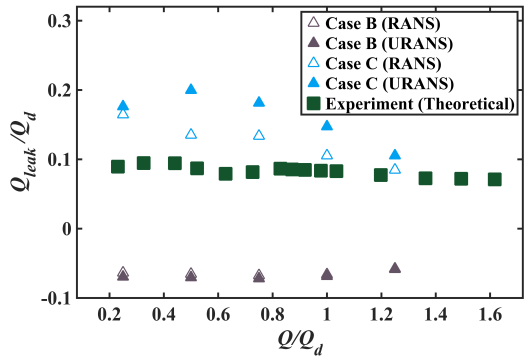

Figure 7. Plotting of the leakage flow rates Q_{leak} versus the flow rate of the pump Q.

Fig. 6 (a) shows the comparison of the diffuser performance obtained by the RANS and URANS simulations for several flow rate Q values. Both the RANS and URANS simulation results look acceptable under large flow rates. The real flow rate inside the diffuser Q_D is higher than the flow rate Q used

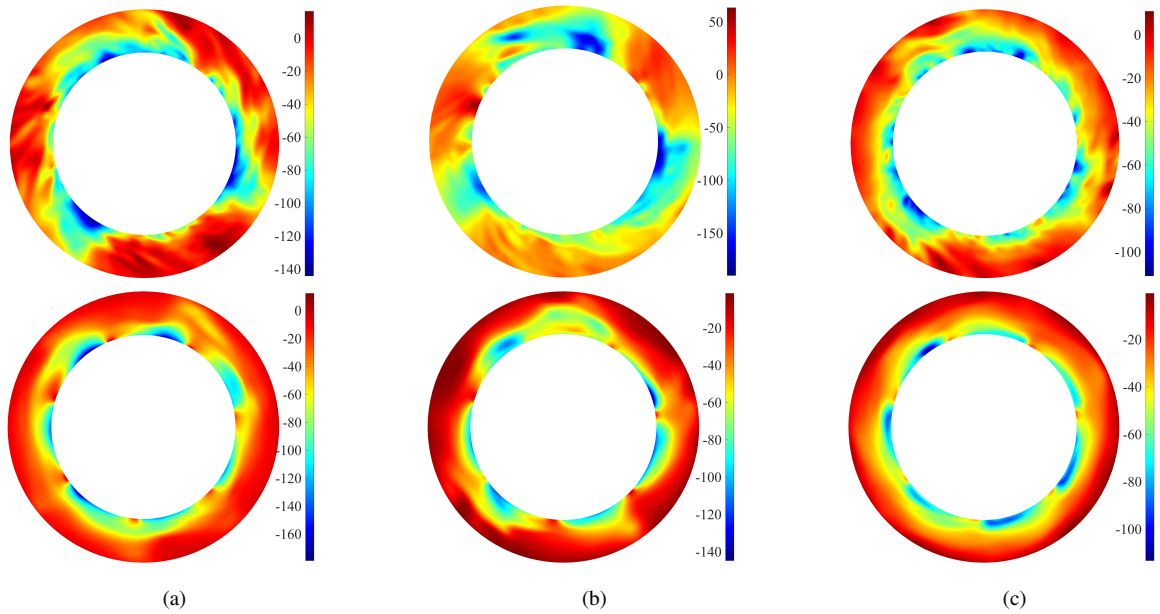

(a) (b) (c)

Figure 8. Instantaneous color maps of the static pressure p (pa) at the mid-height of the diffuser at the flow rate $Q/Q_d = 0.25$ obtained by the URANS (top figures) and RANS (bottom figures) for: (a) case A, (b) case B, and (c) case C.

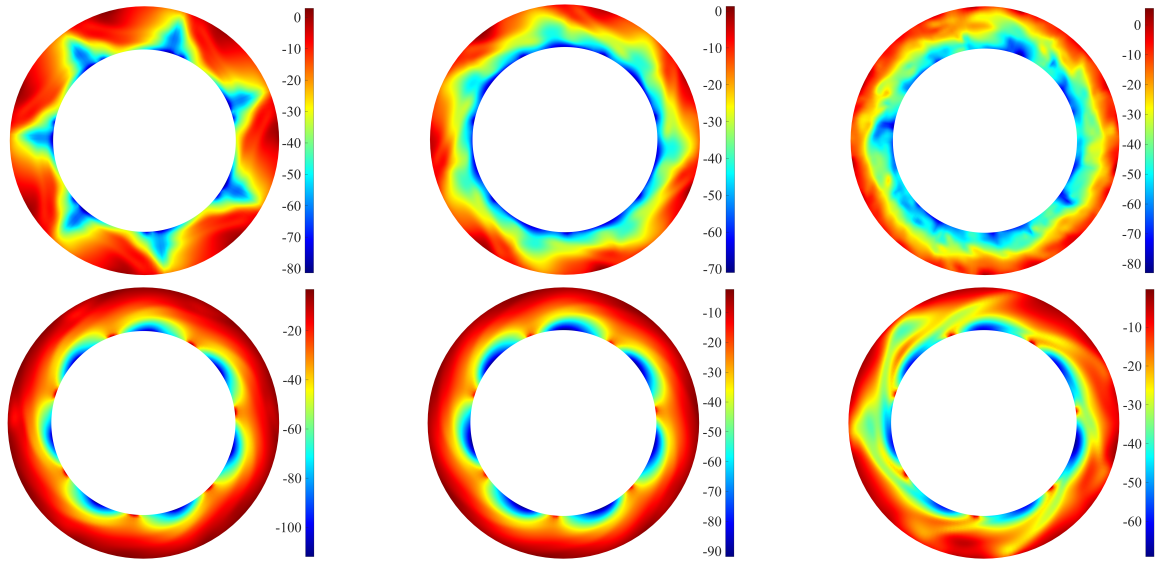

(a) (b) (c)

Figure 9. Instantaneous color maps of the static pressure p (pa) at the mid-height of the diffuser at the flow rate $0Q/Q_d = 1.00$ obtained by the URANS (top figures) and RANS (bottom figures) for: (a) case A, (b) case B, and (c) case C.

on fig. 6 (a). The corresponding flow rate increment, obtained by the numerical simulations in the vaneless diffuser, is due to the leakage caused by the pressure difference between the diffuser inlet and the atmospheric pressure. Fig. 7 gives the estimated leakage flow rate ratio that was first obtained from experiments by Heng et al. [9, 10, 11] and the one obtained from CFD. The diffuser performance curves are consequently shifted as plotted on the fig. 6 (b); it shows that simulation results obtained for case C are now in a better agreement with the experimental results.

However at the smallest flow rate, the RANS simulation results are very different compared with the URANS results. This is due to the rotating stall phenomena occurring in the vaneless diffuser that was already detected in previous works. Such an instability cannot be captured properly by the steady calculations. This can be seen on fig. 8 (a), 8 (b)

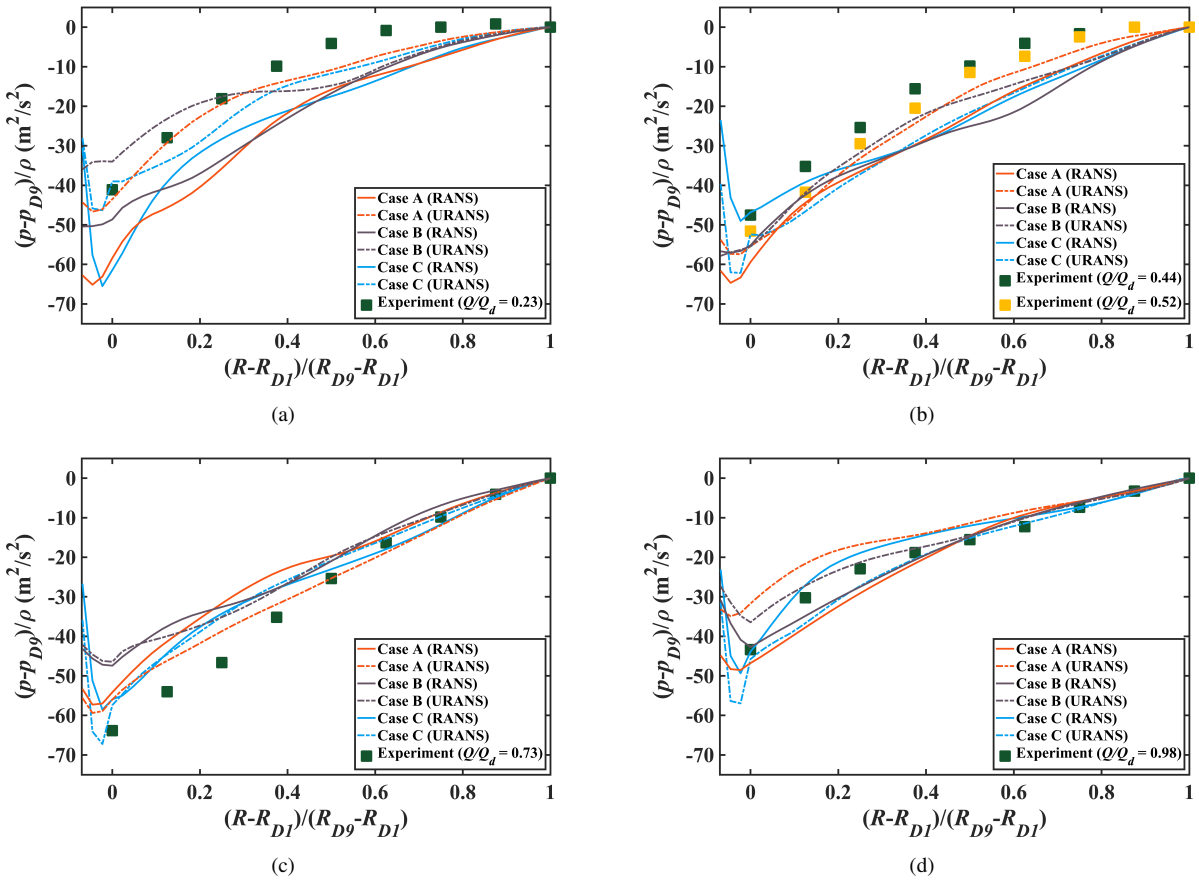

Figure 10. Diffuser radial pressure recovery distributions for different flow rates. (a) $Q/Q_d = 0.25$**, (b)** $Q/Q_d = 0.50$**, (c)** $Q/Q_d = 0.75$**, (d)** $Q/Q_d = 1.00$**.**

and 8 (c). They show the static pressure maps at mid height section between hub to shroud obtained by the numerical simulations for $Q/Q_d = 0.25$, using URANS (top figures) and RANS (bottom figures) for each three cases A, B and C respectively. Three stall cells can be observed very clearly in the case A and case B of the URANS results which well corresponds to the PIV study carried out by Dazin in 2011 [8] in previous investigations.

For the cases A and B at the design flow rate $Q/Q_d = 1.00$, the numerical diffuser performance is still very different from the experiment. This is due to another instability developing at the design flow rate and enhancing the impeller wake inside the diffuser (see fig. 9). A peculiar seven-periodic pattern is observed in the vaneless diffuser far from the diffuser inlet for case A and case B looking at the URANS results. Such instability is normally tamed down by the leakage flow in case C, which results in better performance close to design conditions. As the RANS simulations cannot capture the time dependent instability for case A and case B at the design flow rate, they over-predict the diffuser performance.

The radial distributions of the pressure recovery are plotted in fig. 10, for all three configuration cases (A, B and C) at four different flow rates. The non-dimensional radial position equals zero at the first radial location of the experimental wall pressure tap in the vaneless diffuser $D1$. The negative radial value corresponds to the region where strong jet and wake mixture usually occurs just after the impeller outlet section. This is the reason why URANS results can better capture the corresponding large local pressure losses corresponding to negative pressure recovery with large gradients.

For $Q/Q_d = 0.25$ (fig. 10 (a)), the RANS simulation cannot correctly predict the diffuser pressure recovery owing to the rotating stall. As the flow rate increases, for $Q/Q_d = 0.50$ to $Q/Q_d = 0.75$ (respectively fig. 10 (b) and fig. 10 (c)), both URANS and RANS simulation results are a good agreement with the experiments.

At the design flow rate $Q/Q_d = 1.00$ (fig. 10 (d)), an important difference can be observed between the RANS and URANS simulations. This is attributed to the instability development that was previously pointed out in the previous section for case A and B.

4. CONCLUSIONS

Performances on a pump model using air as working fluid is numerically and experimentally investigated with a focus on the vaneless diffuser characteristics. Three different geometrical configurations have been tested for the RANS and URANS

simulations for the analysis of the leakage effects and make more precise comparisons with experimental results.

The leakage flow can significantly affect the flow characteristics depending on the volume flow rate at the impeller inlet. The simulation results show little influence of the leakage on the global performance and impeller performance, but show a significant impact on the diffuser behavior.

When correctly taking the local leakage effects into account:

- The comparisons between numerical predictions and experiments are significantly improved. URANS approach is always better than RANS one, mainly for the vaneless diffuser performance analysis.
- For off-design low flow rates, like for Q/Q_d = 0.25, three-stall-cells structures can be observed for the configuration that corresponds to the experimental one. Moreover, a different instability is observed to develop at the design flow rate Q/Q_d = 1.00. A more precise analysis of such a complex phenomenon will be performed in future works.

ACKNOWLEDGEMENTS

We kindly acknowledge the GENCI (grand équipement national de calcul intensif) for the numerical resources granted to conduct this study under the project A0102A01741. Furthermore, we appreciate the support of the China Scholarship Council for the doctoral students of M. Fan (CSC student number 201908320328).

REFERENCES

[1] Jansen, W., 1964, "Rotating Stall In a Radial Vaneless Diffuser", *Journal of Basic Engineering-Transactions of the ASME*, Vol. 86(4), pp. 750–758.

[2] Jansen, W., 1964, "Steady Fluid Flow in A Radial Vaneless Diffuser", *Journal of Basic Engineering-Transactions of the ASME*, Vol. 86(3), pp. 607–617.

[3] Senoo, Y., and Kinoshita, Y., 1977, "Influence of Inlet Flow Conditions and Geometries of Centrifugal Vaneless Diffusers on Critical Flow Angle for Reverse Flow", *ASME Journal of Fluids Engineering*, Vol. 99(1), pp. 98–103.

[4] Frigne, P., and Van Den Braembussche, R., 1984, "A Theoretical Model for Rotating Stall In the Vaneless Diffuser of A Centrifugal Compressor", *Journal of Engineering for Gas Turbines and Power*, Vol. 106, pp. 468–474.

[5] Sundström, E., Mihăescu, M., Giachi, M., Belardini, E., and Michelassi, V., 2017, "Analysis of Vaneless Diffuser Stall Instability in A Centrifugal Compressor.", *International Journal of Turbomachinery, Propulsion and Power*, Vol. 2(4), p. 19.

[6] Wuibaut, G., Dupont, P., Caignaert, G., and Stanislas, M., 2000, "Experimental Analysis of Velocities in the Outlet Part of A Radial Flow Pump Impeller and the Vaneless Diffuser using Particle Image Velocimetry", *Proceedings of the XX IAHR Symposium (Charlotte USA)*, Charlotte, USA, pp. 6–9.

[7] Dazin, A., Coutier-Delgosha, O., Dupont, P., Coudert, S., Caignaert, G., and Bois, G., 2008, "Rotating Instability in the Vaneless Diffuser of A Radial Flow Pump", *Journal of Thermal Science*, Vol. 17, pp. 368–374.

[8] Dazin, A., 2011, "High-speed Stereoscopic PIV Study of Rotating Instabilities in A Radial Vaneless Diffuser", *Experiments in Fluids*, Vol. 51, pp. 83–93.

[9] Heng, Y. G., Dazin, A., Ouarzazi, M. N., and Si, Q. R., 2016, "Experimental Study and Theoretical Analysis of the Rotating Stall in a Vaneless Diffuser of Radial Flow Pump", *IOP Conference Series: Earth and Environmental Science*, Vol. 49, p. 032006.

[10] Heng, Y. G., Dazin, A., and Ouarzazi, M. N., 2017, "Linear Stability Analysis of Rotating Stall in A Wide Vaneless Diffuser", *Proceedings of 12th European Conference on Turbomachinery Fluid dynamics & Thermodynamics*, Stockholm, Sweden, Vol. EUROPEAN TURBOMACHINERY SOCIETY, pp. ETC2017–301.

[11] Heng, Y. G., Dazin, A., Ouarzazi, M. N., and Si, Q. R., 2018, "A Study of Rotating Stall in A Vaneless Diffuser of Radial Flow Pump", *Journal of Hydraulic Research*, Vol. 56(4), pp. 494–504.

[12] Dupont, P., Bayeul-Laine, A. C., Dazin, A., and Bois, G., 2014, "Leakage Flow Simulation in A Specific Pump Model", *IOP Conference Series: Earth and Environmental Science*, Montreal, Canada, Vol. 22, pp. 1–10.

[13] Pavesi, G., Dazin, A., Cavazzini, G., Caignaert, G., Bois, G., and Guido, A., 2011, "Experimental and Numerical Investigation of Unforced unsteadiness in a Vaneless Radial Diffuser", *9th european conference on turbomachinery-fluid dynamics and thermodynamics*, Istanbul, Turkey, pp. 625–636.

[14] Kratzsch, C., Timmel, K., Eckert, S., and Schwarze, R., 2015, "URANS Simulation of Continuous Casting Mold Flow: Assessment of Revised Turbulence Models", *Steel Research International*, Vol. 86(4), pp. 400–410.

Conference on Modelling Fluid Flow (CMFF'22)
The 18th International Conference on Fluid Flow Technologies
Budapest, Hungary, August 30 -September 2, 2022

PERFORMANCE PREDICTION AND CFD ANALYSES OF A VARIABLE-PITCH AXIAL FLOW FAN

Chan LEE[1], Hyun Gwon KIL[2], Eui Jong NOH[3] , Sang Ho YANG[4]

[1] Corresponding Author. Department of Mechanical Engineering, Faculty of Mechanical Engineering, University of Suwon. Hwaseong, South Korea, Tel.: +82 31 220 2219, E-mail: clee@suwon.ac.kr
[2] Department of Mechanical Engineering, Faculty of Mechanical Engineering, University of Suwon. E-mail: hgkil@suwon.ac.kr
[3] Department of Mechanical Engineering, Student, University of Suwon.
[4] Research Lab., Vice President, Samwon E&B, Siheung, South Korea

ABSTRACT

Axial flow fans have been widely used for the air-conditioning and the ventilation systems of industrial, commercial and residential sectors, and their performance and efficiency are being improved by variable-pitch operation. The present paper investigates the effect of three dimensional blading design method of axial flow fan on fan performance and efficiency under variable-pitch operation. The three dimensional blade geometry of an axial flow fan is designed by free vortex, combined vortex or controlled blading design method. The three fan models designed by the different blading design methods are examined on the variable-pitch fan operations by comparing their performance predictions by streamline curvature method with the flow field analyses by CFD technique and measurement by chamber-type test facility of a existing fan model. From the comparison results, combined vortex design method is superior to the other competing desugn methods in the aspect of wide range of flow capacity while free vortex design or controlling blading design method is more proper to improve fan efficiency.

Keywords: Axial flow fan, CFD modeling, Fan blading design method, Fan performance prediction, Variable-pitch fan operation

NOMENCLATURE

C_L	[-]	section lift coefficient
p_T	[Pa]	total pressure
r	[m]	radial distance
$\underline{V}$	[m/s]	absolute flow velocity
α	[$deg.$]	absolute flow angle
σ	[-]	solidity
ρ	[kg/m^3]	density of air
Ω	[-]	angular frequency

Subscripts and Superscripts

m	mean value
1, 2	blade inlet, blade outlet
θ	tangential direction
'	blade design value

1. INTRODUCTION

As fans are important elements of air conditioning and ventilation systems in industrial, commercial, and residential sectors, it is very urgent and essential to reduce the power consumption of fans in each field. For this reason, recently, there is a need to develop the fan capable of operating in wide range and with high efficiency, and fan rotation speed control method using inverter has already been applied and variable-pitch fan operation method is being actively applied to axial fan application systems. Many researches have been being conducted on the designs and analyses of variable-pitch fans for achieving high efficiency over wide flow capacity range[1]. Wallis proposed a fan blading design method of variable-pitch fan by using the correlations of flow angle and section lift coefficient[2]. According to the Howden fan development study[3], the determination of spanwise blade angle distribution is very critical design issue of variable-pitch fan and should be optimized through applying various design methods and verifying their effects by measurement and CFD modeling. Spuy and Backstrom[4] also applied an optimization procedure to minimize exit kinetic energy of variable-pitch rotor-only axial fan, and then designed optimal spanwise fan blade angle distribution.

Thus, this paper conducted design studies and flow analyses, performance predictions for examining the effects of different 3D blading design methods of axial fan on fan performance and

efficiency during variable-pitch operation. Furthermore, based on the selelcted appropriate blading design method, an design optimization is conducted for maximizing total efficicny of variable-pitch fan and the optimal fan is verified by CFD method.

2. FAN DESIGN AND PERFORMANCE PREDICTION METHOD

In the case of variable-pitch fan, there is the remarkable change in incidence angle of air flow due to the change in setting angle of varible-pitch rotor blade. Since the flow rate, pressure, and efficiency of fan are significantly affected due to this incidence angle change, in order to ensure wide flow range and high efficiency of variable-pitch fan, it is necessary to design rotor blade sections to effectively respond to the changes in incidence angle[5].

Therefore, using the FANDAS code as Korean fan design program, the present study employs three different blading design methods, free vortex design(FVD), combined vortex design (CVD) and controlled blading design (CBD), to design and stack blade sections of variable-pitch fan. Table 1 summarizes the design rules of the three design methods to determine the tangential velocity distribution and then the blade angles of fan rotor blade outlet[2,5,6].

Table 1 Design rules of three design methods

Design Method	Design rule	Remark
Free Vortex Design (FVD)	$V_{\theta 2} = \frac{a}{r}$	$\frac{\Delta p_T}{\rho \Omega} = a$
Combined Vortex Design(CVD)	$V_{\theta 2} = \frac{a}{r} + br$	$\frac{\Delta p_T}{\rho \Omega} = a + br_m^2$
Controlled Blading Design(CBD)	Adjust and control the spanwise distributions of blade stagger and camber angles of ξ(r) and θc(r).	Wallis(1981), Mckenzie(1997): C_L is given on each blade section, and then the corresponding α_1' and α_2' are determined $C_L = \frac{2cos\alpha_m}{\sigma}(tan\alpha_1 - tan\alpha_2)$

Before the application of the FANDAS code to new variable-pitch fan design, the reliability and prediction accuracy in the design and performance prediction of the FANDAS code are verified. First verification examples are three automotive cooling fans which are designed by different blading design methods of the FANDAS code. The rotation speed of the three fan models is 1940 rpm, and the chord length of the fans varies from 0.049 m (hub) to 0.078 m (tip), and the number of blades is 7[8]. The shapes of the three fan blades are shown and compared in Fig. 1. For the CFD modeling of three fan models, unstructured mesh systems on chamber type flow domain are constructed with about 1 million elements and high mesh quality. On the mesh system shown in Fig. 2, numerical calculations are conducted on the three fan models by the ANSYS CFX code[9] with frozen rotor scheme and k-ω SST turbulence models. The airflow passing over the blade surface calculated by the CFD technique is also depicted in Fig. 2. Performance predictions by the CFD simulations are conducted on three fan models designed by the FVD, the CVD and the CBD methods. In addition, for a fan model designed by the CBD method, a performance test is performed in an outlet chamber set-up facility with multiple nozzles according to AMCA standard.

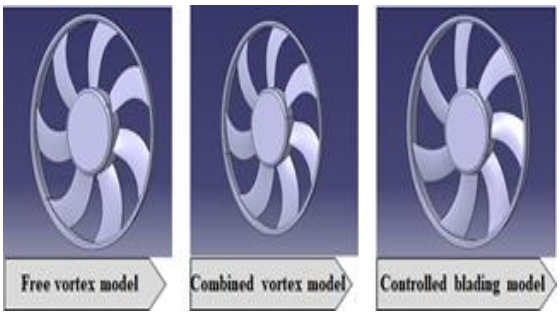

Fig. 1 Three different fan design models

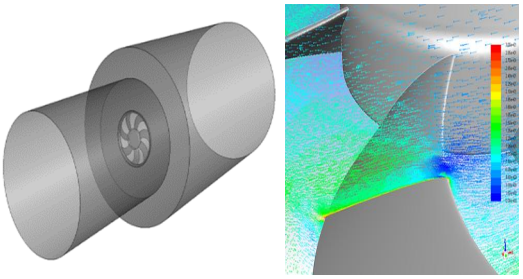

Fig. 2 Computational domain in fan

Fig. 3 shows the comparison between the static pressure curves by the FANDAS code prediction, the CFD calculation and the measurement results. It can be seen in Fig. 3 that the CFD calculation results for the CBD fan are well agreed with the measurement results and the prediction accuracy of the present CFD method is excellent. Fig. 3 also shows the FANDAS prediction, the CFD calculation and the measurement results are well agreed over the entire flow range of the FVD, the CVD and the CBD fans.

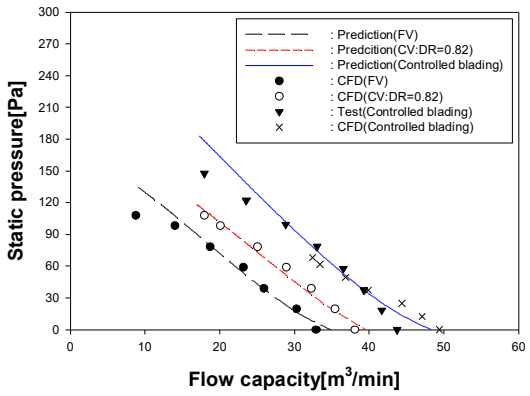

Fig. 3 Static pressure curves of three fan models

Fig. 4 also shows that the efficiency prediction results of the FANDAS code are relatively well consistent with the CFD and the measurement results. From these results of Figs. 3 and 4, it is judged that the FANDAS code is very suitable for designing 3D fan blade shapes and predicting the fan performance regardless of fan blade design method.

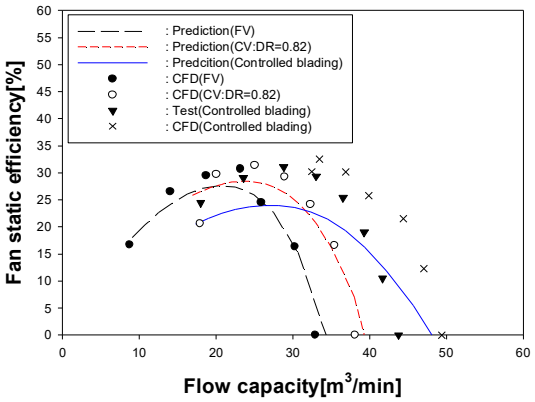

Fig. 4 Efficiency curves of three fan models

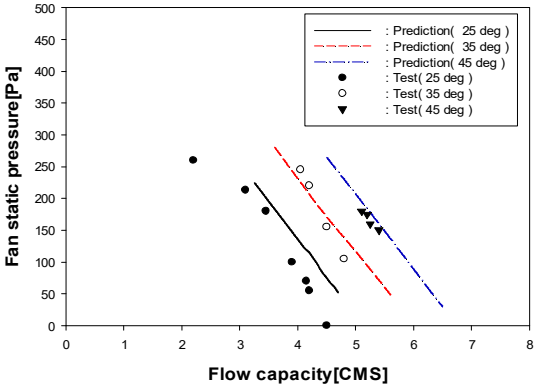

Fig. 5 Static pressure curves of variable-pitch fan

Fig. 5. shows the comparison between the FANDAS prediction and the measurement of a variable-pitch air-conditioning fan as second verification example(refer to Fig. 6). This fan is designed by the CBD method with the tip diameter of 0.63 m, the hub to tip ratio of 0.23, 1440 RPM and F-series airfoil thickness distribution. As shwon in Fig. 5, the FANDAS code predcition is favorably compared with the measurement of pressure curves of fan under variable-pitch operation. The results of Fig. 5 imply that the FANDAS code is also suitable for predicting fan performance at variable-pitch operation.

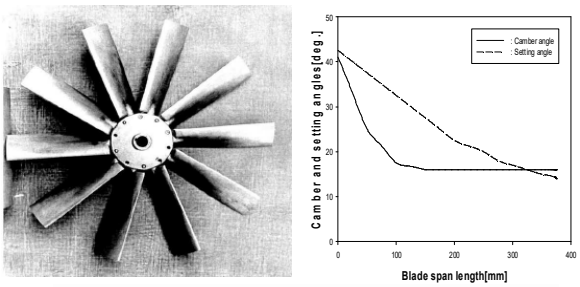

Fig. 6 Air-conditioning fan and its blade angles

3. VARIABLE-PITCH FAN DESIGNS BY DIFFERENT BLADING DESIGN METHODS

In order to examine and compare the effects of three different fan blading design methods, axial flow type jet fans are newly designed by applying the FANDAS code with the same design requrements and parameters. Three new fan models by the FVD, the CVD and the CBD methods are also compared with an exsiting model of the Samwon E&B of Fig. 7, which is designed by reverse-engineering method.

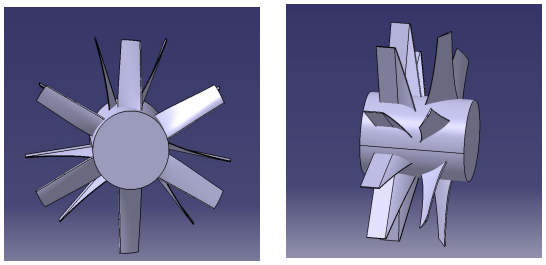

Fig. 7 Geometry of existing fan model

The variations of the setting and camber angles of the designed fans along blade span are shown in Fig. 8. It can be seen that the setting and camber angles of the CVD are somewhat gently compared to the FVD and the CBD results.

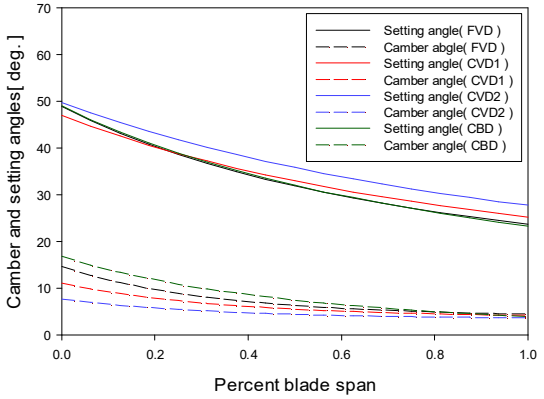

Fig. 8 Setting and camber angles of jet fan models

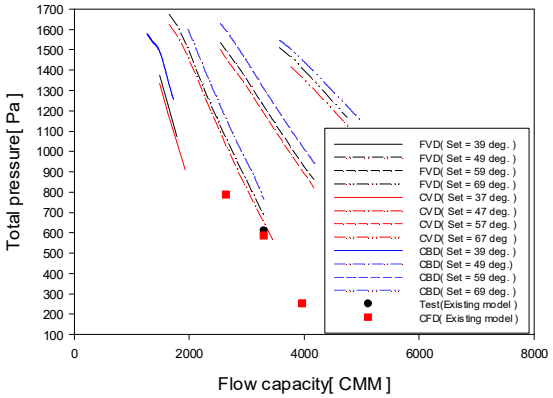

Fig. 9 Pressure curves of three jet fan models

Figs. 9 and 10 show the changes in total pressure and total efficiency according to the flow rate of the three jet fan models. As shown in Fig. 8, as the design hub setting angle (47, 49 degrees) of the rotor blade is reduced and increased, the flow rate range of the fan is significantly reduced. When the setting angle is reduced compared to the design value, the slope of the total pressure curve rapidly increases and the flow rate range is significantly reduced. Fig. 10 shows that the total efficiency decreases when the fan is used outside the design setting angle. It is noted that the FANDAS efficiency prediction is based on pure thermodynamic calculation, so tends to be somewhat higher than the actual value based on shaft power.

In addition, comparing the results of the three fan blade design methods, it can be seen that the CVD and the CBD methods are advantageous in terms of operating range, while the FVD and the CBD method are advantageous in terms of efficiency. As shown in Figs. 9 and 10, three fan models desined by the FVD, the CVD and the CBD methods shows superior performance and efficiency to the existing one.

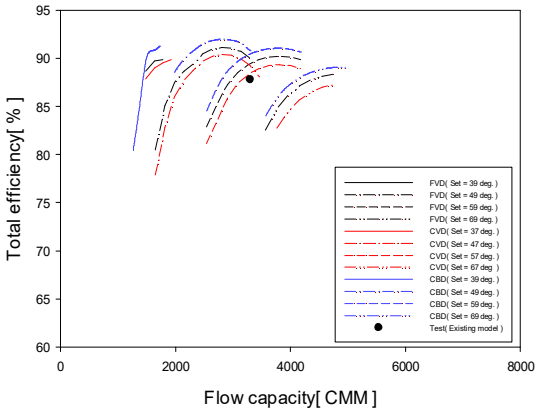

Fig. 10 Efficiency curves of three jet fan models

To sum up the whole results of Figs. 8, 9 and 10, it can be concluded that the CBD is more appropriate method than the FVD and the CVD in the aspects of fan operation range and efficiency.

4. OPTIMAL DESIGN OF A VARIABLE-PITCH FAN BY USING THE CBD METHOD

Based on the CBD method of the FANDAS code and the design result of section 3 of this paper as initial solution, a design optimization problem is constructed and solved with optimization algorithm of the PIAnO code[10] for maximum total efficiency of fan. In this optimal design problem, total 19 design variables including 10 blade section camber and setting angles are selected and 11 design constraints are used (refer to Fig. 11). After several iterations, all the design variables and constrains are converged and optimal design solution is achieved. Fig. 12 shows the 3-D geometries of rotor and stator blades of optimal fan.

Fig. 11 Optimization design scheme of axial fan

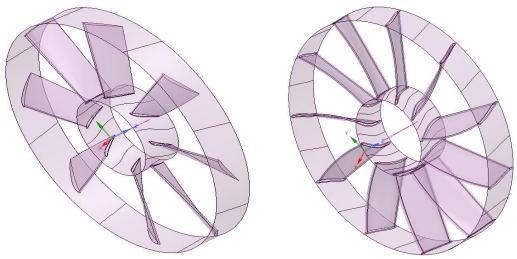

Fig. 12 Optimal variable-pitch fan design
(left: rotor blade, right: stator blade)

In order to verify the optimal fan design, CFD modeling is made with the unstructured mesh system of duct type flow domain of optimal fan shown in Fig. 13 and numerial computations are carried out by the ANSYS CFX code with frozen rotor scheme and k-ω SST turbulence models.

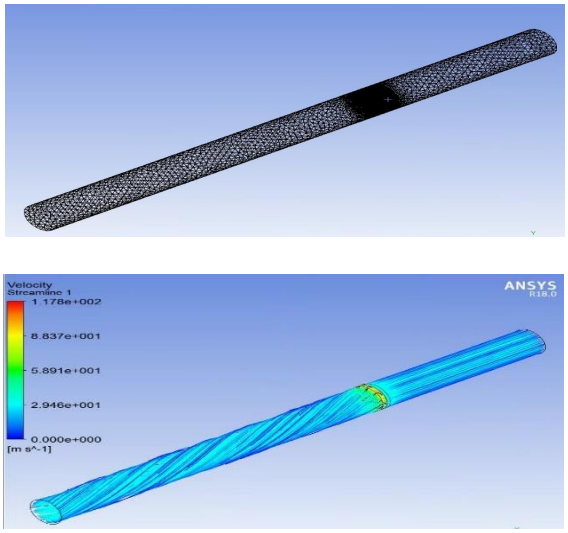

Fig. 13 Mesh system and streamlines of optimal fan model

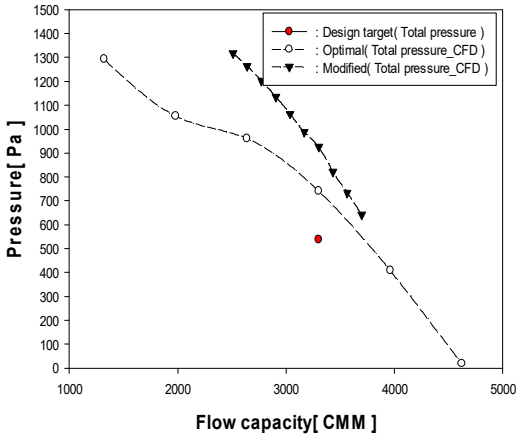

Fig. 14 Total pressure curves of fan models

Fig. 14 shows the predicted total pressure curves of optimal and modified fan models. Modified model is a derivative fan which can be easily constructed through some modification of setting angles of designed blade element sections. Because the CBD method determines and combines several blade section designs to form 3-D fan blade geometry, it is very flexible to design another new fan model by the setting combination of blade sections. As shown in Fig. 14, optimal fan model shows much higher total pressure at design point than the design target of 540 Pa and wide operation range from 1200 to 4600 CMM. Modified fan model also shows remarkable total pressure improvement compared with the optimal one through some setting angle modification.

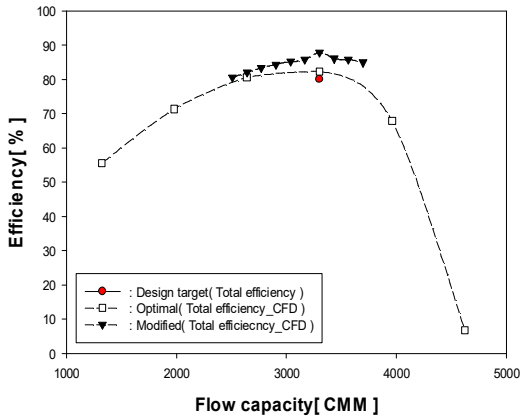

Fig. 15 Total efficiency curves of fan models

Total efficiency curves of optimal and modified fan models are predicted and compared in Fig. 15. As shown in Fig. 15. The efficiency predicted by CFD technique is based on shaft power. The design-point efficiency of optimal fan model is around 83% and higher than the design target of 80%, and the efficiency of modified fan model is much higher the design target of 80%. Total efficiencies of optimal and modified fan models are also maintained above 80% in wide range of flow capacity. Predicted fan power curves are plotted and compared in Fig. 16. The power of optimal fan is much lower than the design target of 55 kW at design point and maintained as lower level than 55 kW over entire flow capacity range.

From the CFD results of Figs. 14, 15 and 16, fan design optimization by the FANDAS code with the CBD method gives high performance and efficiency fan model which can operate in wide operation range and may be sutiable for variable-pitch operation.

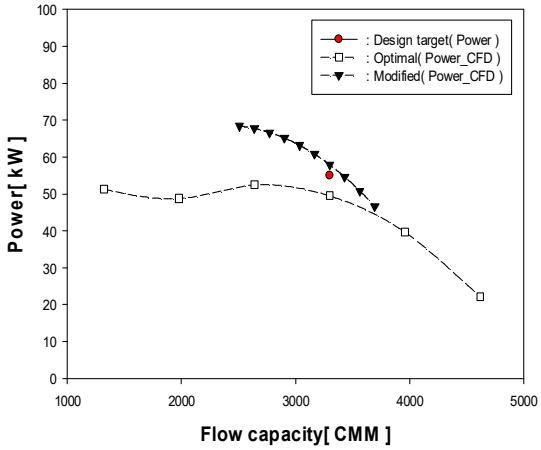

Fig. 16 Power curves of fan models

5. CONCLUSIONS

The present study examines the effects of three different fan blading design methods (the FVD, the CVD and the CBD) on fan performance, efficiency and operation range. From the design study results, the CBD is shown to be superior to the FVD and the CVD in the design of variable-pitch fan with wide operation range and high efficiency. Based on the CBD method, optimal design of a variable-pitch fan is conducted for maximizing fan total efficiency with multiple design variables and constraints. Optimal fan model shows larger total pressure, higher total efficiency and lower power than the design target values, and can be easily modified for obtaining another new fan model because of the design flexibility of the CBD method.

ACKNOWLEDGEMENTS

This work was supported by the Korea Institute of Energy Technology Evaluation and Planning (KETEP) grant funded by the Korea government Ministry of Trade, Industry & Energy(MOTIE), Republic of Korea. (No. 2021202080026B)

REFERENCES

[1] Wright, T., and Gerhart, P. M., 2009, *Fluid Machinery: Application, Selection and Design*, 2nd edition, CRC Press.

[2] Wallis, R. A., 1983, *Axial Flow Fans and Ducts*, 2nd edition, John Wiley & Sons.

[3] van der Spuy, S. J., 1997, "Design of a Low-Noise Rotor-Only Axial Flow Fans," *Master Thesis of Mechanical Engineering, University of Stellanbsch.*

[4] van der Spuy, S. J. and von Backstrom, T.W., 2002, "Performance of rotor-only axial fans designed for minimum exit kinetic energy," *R & D Journal, vol. 18, no.3, pp.63-69*

[5] Lee, C., 2021,"A Performance Prediction Method of the Axial Flow Fans with Blade Sweep," *KSFM Journal, vol. 24, no.5, pp.24-29.*

[6] Dixon, S. L., 1998, *Fluid Mechanics and Thermodynamics of Turbomachinery,* 4th edition, Buterworth & Heinemann.

[7] McKenzie, A. B., 1997, *Axial Flow Fans and Compressors*, Ashgate.

[8] Lee, C., 2016, *Development of an integrated computer program for designing, performance, and noise analysis of axial flow fans for automobile,* Technical report, Hanon systems.

[9] ANSYS Inc., 2011*, ANSYS CFX manual*, ANSYS Release 16.0

[10] PIDOTEC, 2022, *PIAnO manual*

Conference on Modelling Fluid Flow (CMFF'22)
The 18th International Conference on Fluid Flow Technologies
Budapest, Hungary, August 30-September 2, 2022

COMPARISON STUDY OF THE $k - k_L - \omega$ AND $\gamma - Re_\theta$ TRANSITION MODELS IN THE OPEN WATER PERFORMANCE PREDICTION OF A RIM-DRIVEN THRUSTER

Bao LIU[1], Maarten VANIERSCHOT[2], Frank BUYSSCHAERT[3]

[1] Department of Mechanical Engineering, Group T Leuven Campus, KU Leuven, Leuven, Belgium. E-mail: bao.liu@kuleuven.be
[2] Corresponding Author. Department of Mechanical Engineering, Group T Leuven Campus, KU Leuven, Leuven, Belgium. E-mail: maarten.vanierschot@kuleuven.be
[3] Department of Mechanical Engineering, Bruges Campus, KU Leuven, Bruges, Belgium. E-mail: frank.buysschaert@kuleuven.be

ABSTRACT

The present work examines the capabilities of two transition models implemented in ANSYS Fluent in the open water performance prediction of a rim-driven thruster (RDT). The adopted models are the three equation $k - k_l - \omega$ and the four equation $\gamma - Re_\theta$ models. Both models are first tested on a ducted propeller. The numerical results are compared with available experimental data and a good correlation is found for both. Simulations employing both transition models are then carried out on a four-bladed rim-driven thruster model and the results are compared with the $k - \omega$ SST turbulence model. It is observed that the streamline patterns on the blade surface are significantly different between the transition and fully turbulent models. The transition models can reveal a laminar region on the blade while the $k - \omega$ SST model assumes the flow is entirely turbulent, resulting in a considerable difference in torque prediction. It is noted that unlike the $k - \omega$ SST model, the transition models are quite sensitive to the free stream turbulence quantities such as turbulent intensity and turbulent viscosity ratio, as these quantities determine the onset of the transition process. Finally, the open water performance of the RDT and the structure of the flow field are also presented and discussed.

Keywords: transition model, rim-driven thruster, open water performance

NOMENCLATURE

δ_{ij}	$[-]$	Kronecker delta
ϵ	$[m^2/s^3]$	dissipation rate of turbulent kinetic energy
γ	$[-]$	intermittency
Re	$[-]$	Reynolds number
Re_θ	$[-]$	momentum thickness Reynolds number
$\mathrm{Re}_{\theta t}$, $\widetilde{\mathrm{Re}}_{\theta t}$	$[-]$	transition onset momentum thickness Reynolds number
μ	$[kg/(m \cdot s)]$	dynamic viscosity
μ_t	$[kg/(m \cdot s)]$	turbulent or eddy viscosity
ν	$[m^2/s]$	kinematic viscosity
ω	$[1/s]$	specific dissipation rate of turbulent kinetic energy
ρ	$[kg/m^3]$	fluid density
$\rho\overline{u_i'u_j'}$	$[N/m^2]$	Reynolds stress
τ_w	$[N/m^2]$	wall shear stress
C_f	$[-]$	skin friction coefficient
C_p	$[-]$	pressure coefficient
D	$[m]$	propeller diameter
d	$[m]$	wall distance
J	$[-]$	advance coefficient
k/k_T	$[m^2/s^2]$	turbulent kinetic energy
K_{Qp}	$[-]$	propeller torque coefficient
K_{Qr}	$[-]$	rim torque coefficient
K_{Td}	$[-]$	duct thrust coefficient
K_{Tp}	$[-]$	propeller thrust coefficient
K_{Tr}	$[-]$	rim thrust coefficient
k_L	$[m^2/s^2]$	laminar kinetic energy
n	$[1/s]$	rotational speed
p	$[Pa]$	dynamic pressure
v	$[m/s]$	representative velocity
v_a	$[m/s]$	advance velocity

Subscripts and Superscripts

PS, SS	pressure side, suction side
T, Q	thrust, torque

1. INTRODUCTION

Computational Fluid Dynamics (CFD) has become a very powerful tool in analyzing engineering problems in recent decades, such as the performance prediction of marine propellers. The widest application is achieved by solving the Reynolds-Averaged Navier-Stokes (RANS) equations because compared

to other approaches, such as Direct Numerical Simulation (DNS) or Large Eddy Simulation (LES), the RANS method is much cheaper with still a reasonable accuracy. To solve the Reynolds stress terms in the RANS equations, turbulence models based on the Boussinesq hypothesis are introduced. Amongst them, the most popular ones are the $k-\epsilon$ and $k-\omega$ models. Since these turbulence models are built on the assumption that the resolved flow field is fully turbulent, they are incapable of predicting transition phenomena which are frequently encountered in physical problems. In order to improve the potential of the currently existing turbulence models in resolving transitional flows, a lot of efforts have been made to develop models which can predict the transition process from laminar to turbulence. There are generally two approaches: one is to couple transition correlations, which are obtained from available experimental data, into the turbulence models; the other one is to solve additional transport equations to account for the transitional effects. However, even if a transition model is successfully developed, it is still questionable whether it can be implemented into modern CFD codes which are usually based on unstructured grids and parallel execution, as most transition models are still using non-local variables or integral terms. Single-point models which use only local variables are required for general application. In ANSYS Fluent, there are two transition models available, i.e. the three equation $k-k_L-\omega$ and four equation $\gamma-Re_\theta$ models. Both models introduce additional transport equations to include the transitional effects in flows.

The present work aims to test the capabilities of these two transition models in the hydrodynamic characteristics prediction of a rim-driven thruster (RDT). As confirmed in the research of Kuiper [1], for a propeller of model scale, there is often a large area of laminar flow on both sides of the blade surface. In order to investigate the potential reason for discrepancy between simulations and experiments, especially at a high loading condition, Wang [2] employed the Loci/CHEM flow solver to study a marine propeller 5168 using the $k-k_L-\omega$ transition model. The SST $k-\omega$ turbulence model was also used for comparison. The simulation results were analyzed and compared with experimental data. It was found that the transition model showed better performance in resolving the flow field and therefore improved the prediction accuracy, while the standard SST $k-\omega$ model indicated excessive dissipation of vortex cores. Pawar [3] investigated the propeller of an Autonomous Underwater Vehicle (AUV) which often operates at low Reynolds numbers. The global and local hydrodynamic characteristics of an open and ducted propeller are investigated with the $\gamma-Re_\theta$ transition model. The results demonstrated that the transition model was able to predict the complex flow physics such as leading-edge separation, tip leakage vortex, and the separation bubble on the outer surface of the duct.

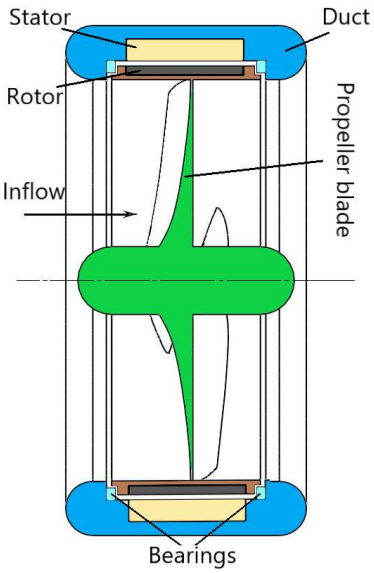

Figure 1. Schematic layout of an RDT

An RDT resembles a ducted propeller in structural design as both contain a propeller and duct. But unlike for a ducted propeller, there is no tip clearance on the RDT propeller. Instead, a gap channel is formed by the rim and duct surfaces. The schematic of an RDT layout is presented in Figure 1 [4]. According whether there is a central hub, the RDT can be roughly classified into the hub type and the hub-less type (Figure 2). Both types have their own advantages and disadvantages [5]. For example, the hub type RDT has a greater structural strength and bearings can be installed in the hub to reduce friction, while the hubless type has a simpler structure and higher hydrodynamic efficiency. Due to the appealing potential the RDT possesses, many researches have been conducted on the modeling and evaluation of RDTs using both fully turbulent RANS models [4, 6, 7, 8, 9, 10] as well as transition models [11]. For the model-scale RDT, the flow on the propeller often tends to be in the laminar or transitional regime. Therefore, transitional modeling is required to better resolve the boundary layer in order to achieve improved hydrodynamic performance prediction. Nevertheless, a detailed comparison between different transition models is still lacking and this study tries to fill this knowledge gap. The structure of the paper is organized as follows: firstly a brief description of the transition models used in this study is presented, then some validation studies are carried out to test the capabilities of those models, followed by the results and discussion of the RDT simulations.

2. NUMERICAL MODELING

The RANS equations for incompressible Newtonian fluids are given as

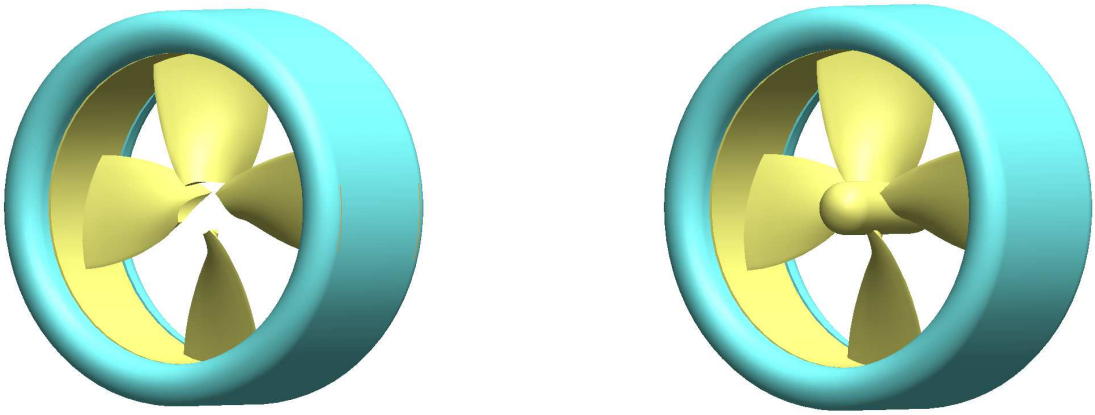

(a) Hub-less type **(b) Hub type**

Figure 2. RDT categorization based on the structural design

$$\frac{\partial u_i}{\partial x_i} = 0, \tag{1}$$

$$\rho\left(\frac{\partial u_i}{\partial t} + u_j\frac{\partial u_i}{\partial x_j}\right) = -\frac{\partial p}{\partial x_i} + \mu\frac{\partial^2 u_i}{\partial x_j \partial x_j} + \frac{\partial}{\partial x_j}\left(-\rho\overline{u_i' u_j'}\right),$$

where ρ is the fluid density, x_i and u_i $(i, j = 1, 2, 3)$ are the spatial coordinate and mean velocity component respectively, t is the flow time, p is the pressure, μ is the dynamic viscosity and $-\rho\overline{u_i' u_j'}$ is the Reynolds stress term. For incompressible Newtonian flows, the Reynolds stress can be related to the mean strain rate and eddy viscosity as follows

$$-\rho\overline{u_i' u_j'} = \mu_t\left(\frac{\partial u_i}{\partial x_j} + \frac{\partial u_j}{\partial x_i}\right) - \frac{2}{3}\rho k\delta_{ij}, \tag{2}$$

where μ_t is the turbulent viscosity, k the turbulent kinetic energy and δ_{ij} the Kronecker delta. The formulation of closure to the above equations is called turbulence modeling. Currently the most popular turbulence models in industrial applications are the two-equation ones, like the $k-\epsilon$ model. This model has gone through many modifications to improve and extend its applicability. It has great capabilities for free-shear flows but behaves poorly in flows with an adverse pressure gradient. To tackle this issue, the $k-\omega$ model by was proposed, which has better performance for flows with weak adverse pressure gradient. Again, several updates have been made to this model to enhance its performance.

2.1. $k-\omega$ SST model

The $k-\omega$ SST turbulence model developed by Menter [12] is an improved version of the original $k-\omega$ model. It has robust near wall treatment and the ability to compute flows with moderate adverse pressure gradients. The transport equations for the turbulent kinetic energy k and the specific turbulent dissipation rate ω are given in [12].

2.2. $\gamma - Re_\theta$ transition model

The $\gamma - Re_\theta$ transition model is a correlation-based transition model using local variables, which contains two additional transport equations, i.e. for the intermittency γ and the transition onset momentum thickness Reynolds number $\widetilde{Re}_{\theta t}$. The additional transport equations are not used to model the transition physics but to provide a framework to which empirical correlations can be made for specific cases. The intermittency is a measure of the flow if it is laminar or turbulent: $\gamma = 0$ means fully laminar flow and $\gamma = 1$ means fully turbulent flow. Therefore, the intermittency equation is used to trigger the local transition process. The second quantity is the transition onset Reynolds number $Re_{\theta t}$, which is used to account for the non-local influence of turbulence intensity on the boundary layer, as well as to relate the empirical correlation to the onset criteria in the intermittency equation. Finally the intermittency function is coupled with the original $k-\omega$ SST model, which is used to turn on the production term of the turbulent kinetic energy downstream of the transition location and the equation for the $\widetilde{Re}_{\theta t}$ can pass the information on the free-stream conditions into the boundary layer. The formulated equations for the intermittency γ and transition momentum thickness Reynolds number $\widetilde{Re}_{\theta t}$ are given as:

$$\rho\left(\frac{\partial \gamma}{\partial t} + \frac{\partial\left(u_j\gamma\right)}{\partial x_i}\right) = P_\gamma - E_\gamma + \frac{\partial}{\partial x_i}\left[\left(\mu + \frac{\mu_t}{\sigma_f}\right)\frac{\partial \gamma}{\partial x_j}\right] \tag{3}$$

$$\rho\left(\frac{\partial \widetilde{\mathrm{Re}}_{\theta t}}{\partial t} + \frac{\partial u_j \widetilde{\mathrm{Re}}_{\theta t}}{\partial x_j}\right) = P_{\theta t} + \frac{\partial}{\partial x_j}\left[\sigma_{\theta t}\left(\mu + \mu_t\right)\frac{\partial \widetilde{\mathrm{Re}}_{\theta t}}{\partial x_j}\right] \tag{4}$$

where P_γ, E_γ are source terms which control the production and destruction of the intermittency, σ_f is a model constant equal to 1, $P_{\theta t}$ is the production term

that is designed to relate the transported scalar $\widetilde{\mathrm{Re}}_{\theta t}$ to the local empirical $\mathrm{Re}_{\theta t}$ outside the boundary layer, and $\sigma_{\theta t}$ is a model constant equal to 10. The detailed definitions of the above terms can be found in [13]. The effective intermittency γ_{eff}, obtained by solving the above equations, is incorporated into the transport equations for k and ω in the $k-\omega$ SST model.

2.3. $k - k_L - \omega$ model

Unlike the $\gamma - Re_\theta$ model, the $k - k_L - \omega$ model is a physics-based model. Three additional transport equations are solved to account for the effects of pre-transition fluctuations, including the bypass and natural transitions. In this model, the concept of laminar kinetic energy k_L is employed, which represents the velocity fluctuations in the pre-transitional regions. With the increase of turbulence intensity in the freestream, the mean velocity profiles in these regions are distorted and more intensive streamwise fluctuations can take place, which finally break down and result in transition. This occurs when the characteristic time-scale for turbulence production is smaller than the viscous diffusion timescale of the pre-transitional fluctuations. It is assumed that the production of k_L is a result of the interaction between the Reynolds stresses and the mean shear where the total energy of k_L and k_T is constant, which means that when transition occurs, the energy is transferred from k_L to k_T. The three additional transport equations for k_T, k_L and ω are given as:

$$\frac{Dk_T}{Dt} = P_{k_T} + R_{BP} + R_{NAT} - \omega k_T - D_{k_T} + \frac{\partial}{\partial x_j}\left[\left(\nu + \frac{\alpha_T}{\sigma_k}\right)\frac{\partial k_T}{\partial x_j}\right] \tag{5}$$

$$\frac{Dk_L}{Dt} = P_{k_L} - R_{BP} - R_{NAT} - D_L + \frac{\partial}{\partial x_j}\left[\nu\frac{\partial k_L}{\partial x_j}\right] \tag{6}$$

$$\frac{D\omega}{Dt} = C_{\omega 1}\frac{\omega}{k_T}P_{k_T} + \left(\frac{C_{\omega R}}{f_W} - 1\right)\frac{\omega}{k_T}(R_{BP} + R_{NAT}) - C_{\omega 2}\omega^2 + C_{\omega 3} f_\omega \alpha_T f_W^2 \frac{\sqrt{k_T}}{d^3} + \frac{\partial}{\partial x_j}\left[\left(\nu + \frac{\alpha_T}{\sigma_\omega}\right)\frac{\omega}{x_j}\right] \tag{7}$$

The various terms in the model equations represent production, destruction, and transport mechanisms, where P_{k_T}, D_{k_T} are respectively the production and destruction of turbulent kinetic energy, R_{BP}, R_{NAT} represent the effect of bypass and natural transitions, C_ω, and σ_ω are model constants, f_ω, f_W are the damping functions, and α_T is the effective diffusivity. The detailed definitions of the above terms can be found in [14].

2.4. Solution strategy

The SIMPLE (Semi-Implicit Method for Pressure Linked Equation) algorithm is adopted for the pressure and velocity coupling. Second-order upwind schemes are used for the discretization of momentum and turbulence terms. Moreover, the Moving Reference Frame (MRF) approach is employed to handle the rotation of the propeller. The MRF method is a steady-state approximation for the analysis of situations involving domains that are rotating relatively to each other. The governing equations for the flow in the selected rotating zone are solved in a relative rotating frame. To characterise the performance of the propeller, the following hydrodynamic coefficients are defined:

$$J = \frac{v_a}{nD}, \tag{8}$$

$$K_\mathrm{T} = \frac{\mathrm{T}}{\rho n^2 D^4}, \tag{9}$$

$$K_\mathrm{Q} = \frac{\mathrm{Q}}{\rho n^2 D^5}, \tag{10}$$

$$\eta = \frac{J}{2\pi}\frac{K_\mathrm{T}}{K_\mathrm{Q}}, \tag{11}$$

$$C_p = \frac{p - p_\infty}{\frac{1}{2}\rho v^2}, \tag{12}$$

$$C_f = \frac{\tau_w}{\frac{1}{2}\rho v^2}, \tag{13}$$

which represent the advance coefficient, the thrust and torque coefficients, the efficiency, the pressure and the skin friction coefficients respectively. The representative velocity $v = \sqrt{v_a^2 + (0.7\pi n D)^2}$, v_a is the advance velocity, T is the torque, D the propeller diameter, n the rotational speed and the shear stress $\tau_w = \mu \frac{\partial u}{\partial y}\big|_{y=0}$, with u the flow velocity along the blade surface and y is the normal distance.

3. RESULTS AND DISCUSSION

3.1. Test cases

3.1.1. Flow over a flat plate

To test the capabilities of the $\gamma - Re_\theta$ and $k - k_L - \omega$ transition models, a benchmark test case is examined, namely the flow over a flat plate without pressure gradient. The computational domain and boundary

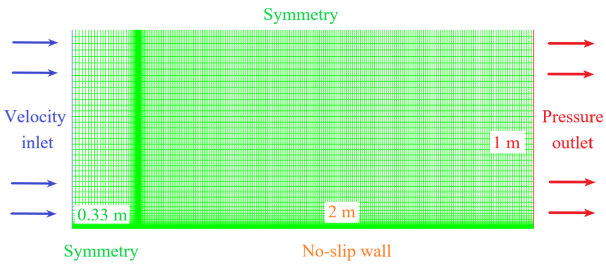

Figure 3. Definition of computational domain, mesh and boundary conditions

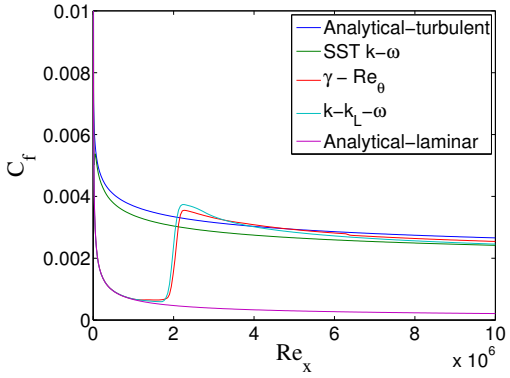

(a) TI=1%, TVR=10

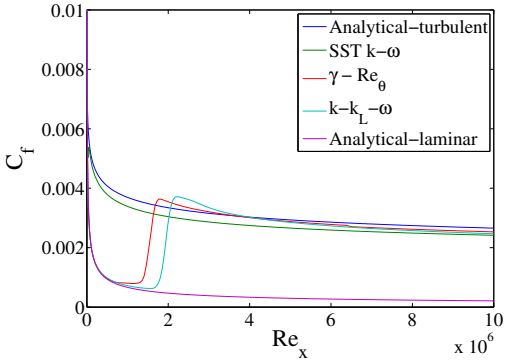

(b) Tu=1%, TVR=100

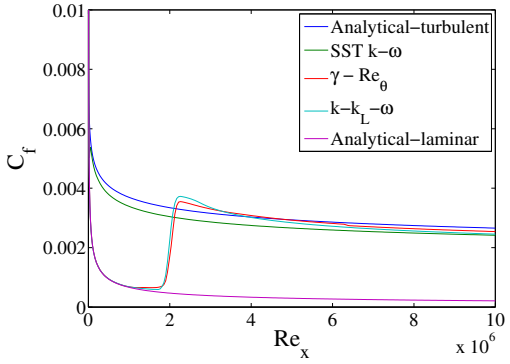

(c) TI=5%, TVR=10

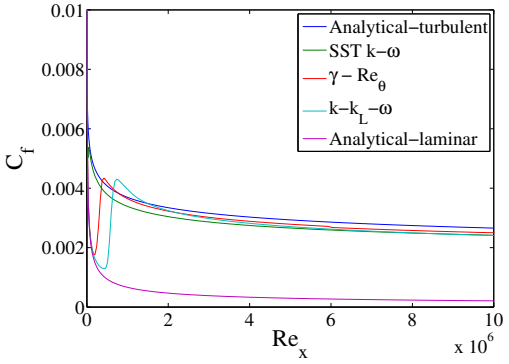

(d) Tu=5%, TVR=100

Figure 4. Influence of inlet parameters on the onset of transition process on a flat plate

conditions are shown in Figure 3. The flat plate has a length of 2 m and is placed 0.33 m downstream the inlet, as indicated by the black circle. A symmetry boundary condition is used to guide the uniform flow from the inlet to the plate. A pressure outlet is adopted at the end of the plate, while a no-slip boundary condition is used for the plate itself.

The transition onset is generally based on the disturbance strength in the boundary layer, which is determined by the flow properties of the free-stream, like turbulence intensity (TI). When the flow develops, there would be a decay in TI, and the turbulent viscosity ratio (TVR) reflects the decaying speed. Therefore different combinations of turbulent intensity and turbulent viscosity ratio are assessed and the results are given in Figure 4. Re_x is the Reynolds number determined by the position on the plate along the flow direction. In this figure, the gray and blue lines represent the analytical solutions for laminar and turbulent flows respectively. From the results it is observed that the values for turbulent intensity and turbulent viscosity ratio can influence the location of transition onset. Because higher turbulent viscosity ratio will reduce the decay of the turbulent intensity, resulting in an earlier onset of the transition process. Therefore, to accurately evaluate a solution for a practical problem, appropriate assessment of there values at the inlet is very important. Generally both transition models can robustly reflect the flow physics.

3.1.2. Open water performance of a ducted propeller

Another test case is conducted for a ducted propeller, where open water tests are available. Figure 5 provides a comparison between the two transition models and experimental measurements obtained from [15]. A good correlation is found between both

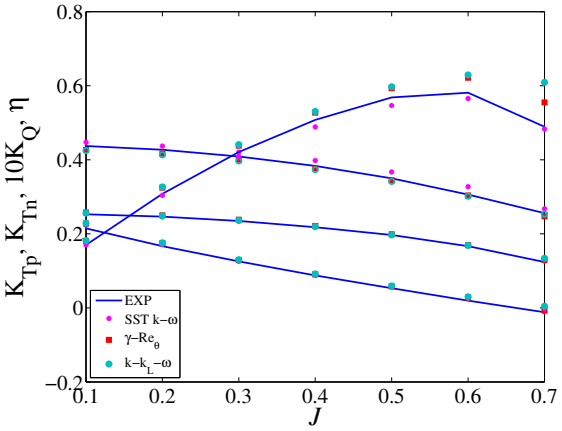

Figure 5. Comparison of open water performance of the ducted propeller between CFD results and experimental data

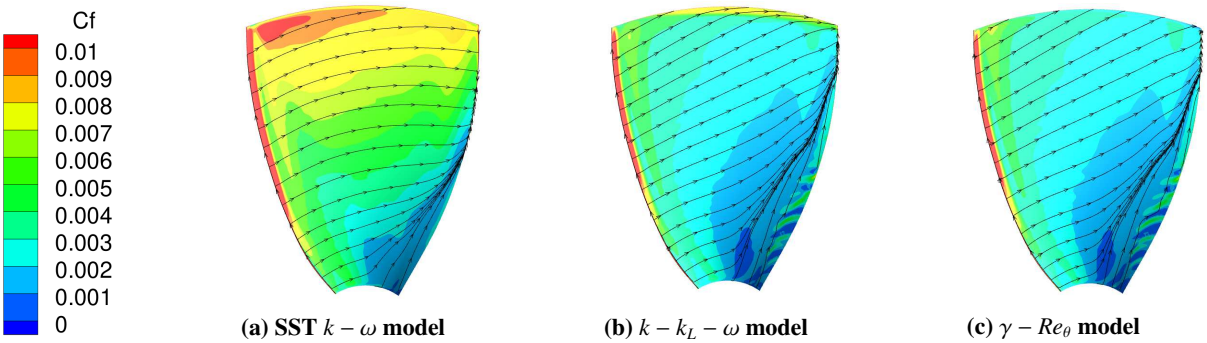

(a) SST $k-\omega$ model **(b) $k-k_L-\omega$ model** **(c) $\gamma-Re_\theta$ model**

Figure 6. Comparison of flow patterns on the blade surface using different models

transition models and experimental data. It is noted that the propeller and duct thrust predicted by the $\gamma - Re_\theta$ transition model are quite close to those obtained by the $k-\omega$ SST turbulence model. The major difference is found for the propeller torque prediction, where the $k-\omega$ SST model gives higher values for propeller torque under all advance coefficients. To find out the reasons, the components of thrust and torque are compared respectively as provided in Table 1, which gives a comparison between the result from the $k-\omega$ SST model and the $\gamma - Re_\theta$ model. It can be observed that pressure is the dominating factor both in thrust and torque and that the difference in torque prediction between the two models is mainly caused by the shear stress. As the transition model gives lower values for skin friction, a slightly higher thrust and a lower torque are expected.

3.2. Open water performance of the RDT

In this section, the simulation results using the fully turbulent and transition models are presented and analyzed for the open water performance of an RDT. To better understand the transition process, different propeller speeds are considered as the Reynolds number needs to be high enough to trigger the transitional effects in the model. Revolution rates of 10 rps and 20 rps are investigated and the Reynolds number at the propeller section of $r/R = 0.7$ is 5.07×10^5 and 1.14×10^6 respectively.

3.2.1. Flow patterns on the propeller

The distribution of skin friction coefficient C_f on the pressure and suction side of the propeller blade with constrained streamlines by all three models is provided in Figure 6. The pattern of the streamlines

Table 1. Contribution of pressure and shear forces to the thrust (T) and torque (Q) of the propeller at $J = 0.1$

	SST $k-\omega$ model		$\gamma - Re_{\theta t}$ model	
	T (N)	Q ($N \cdot m$)	T (N)	Q ($N \cdot m$)
Pressure	93.31	3.69	93.76	3.73
Shear	-1.94	0.41	-0.86	0.17
Total	91.37	4.1	92.9	3.9

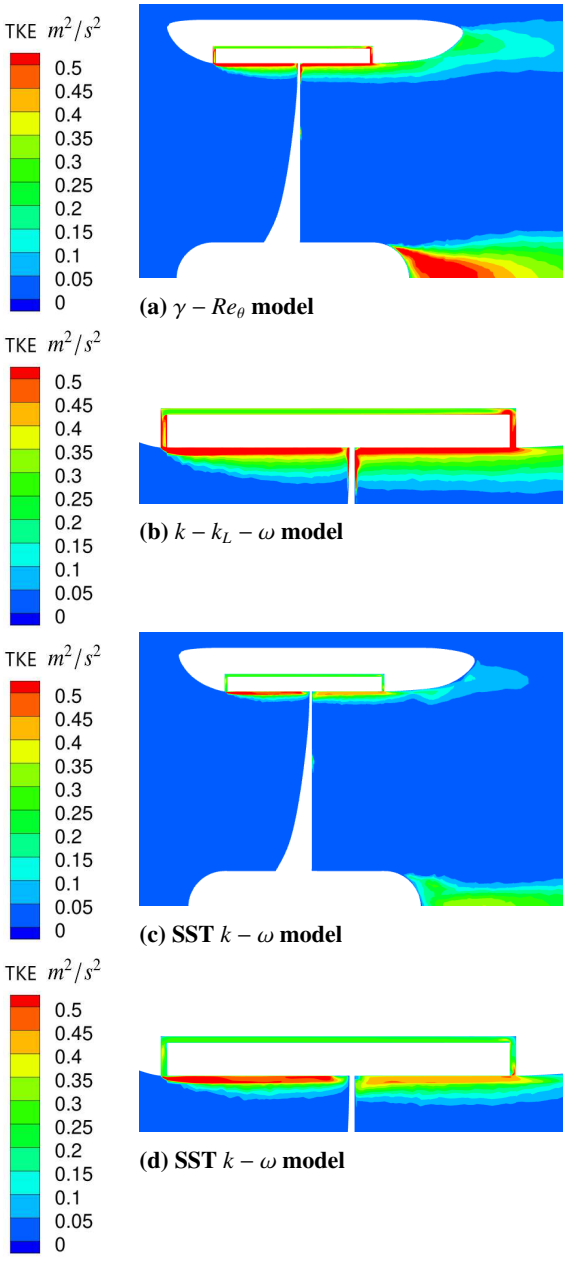

(a) $\gamma - Re_\theta$ model

(b) $k-k_L-\omega$ model

(c) SST $k-\omega$ model

(d) SST $k-\omega$ model

Figure 7. Comparison of turbulent kinetic energy (TKE) distribution near the propeller using the $k-k_L-\omega$ and $\gamma - Re_{\theta t}$ model

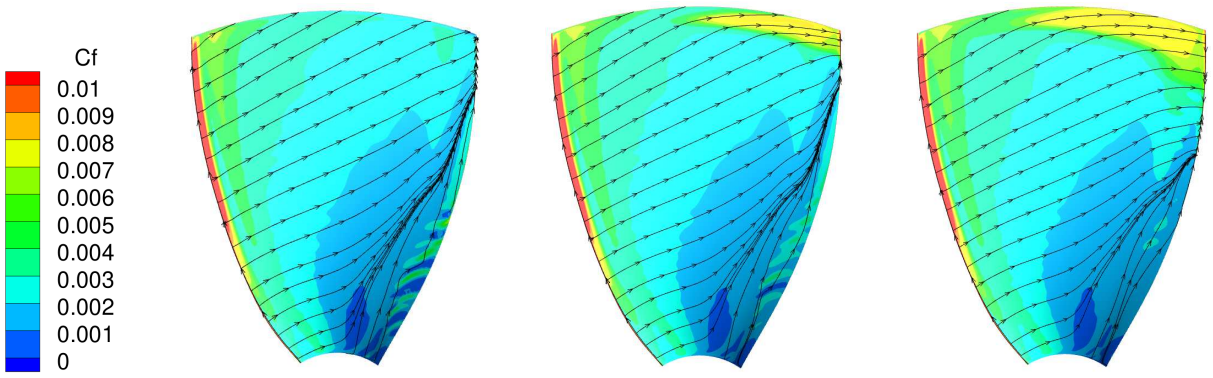

(a) TI=5% and TVR=10 **(b) TI=5% and TVR=100** **(c) TI=5% and TVR=200**

Figure 8. Influence of TI and TVR on the transition process using the $\gamma - Re_\theta$ model

is an indication of the flow regime over the blade. As the direction of the streamline is a result of inertial and centrifugal force, the streamline is always deflected to the dominant force. When the flow is turbulent, the inertial force has greater influence compared to the centrifugal force, therefore the streamline is forced to go along the tangential direction over the blade. However, in the case of a laminar flow, the opposite phenomenon can be observed, and the streamline is outwardly oriented.

The difference in streamline patterns can be clearly observed between the turbulence model and transition models. Moreover, the skin friction is obviously larger in the turbulent flow than in the laminar flow. Because a greater wall shear stress is achieved in the turbulent boundary layer, where the velocity gradient at the wall is steeper. The skin friction distribution on the blade surface predicted by two transition models are quite close, except the difference found at the blade tip. The $k - k_L - \omega$ models gives higher values for C_f, and there is obviously a change in the direction of the streamlines, indicating the flow is changing from a laminar to a turbulent regime. Figure 7 provides a comparison of kinetic energy distribution near the blade by two transition models. There is clearly more turbulent kinetic energy (TKE) production at the blade tip region by the $k - k_L - \omega$, resulting in the change in flow regime. In Table 2, the thrust and torque of different components predicted by two models are compared. The $\gamma - Re_\theta$ model gives higher values for propeller thrust and torque in both pressure and shear forces. However, since there is currently no experimental data available for the RDT, it is hard to conclude which model has higher accuracy in performance prediction.

Table 2. Contribution of pressure and shear forces to the thrust (T) and torque (Q) of the propeller at $J = 0.5$

	$k - k_L - \omega$ model		$\gamma - Re_{\theta t}$ model	
	Pressure	Shear	Pressure	Shear
T_p (N)	26.832	-0.568	31.388	-0.556
T_d (N)	1.512	-0.488	0.808	-0.368
T_r (N)	6.028	-0.564	6.82	-0.248
Q_p $(N \cdot m)$	0.692	0.048	0.792	0.06
Q_r $(N \cdot m)$	0	0.5	0	0.464

3.2.2. Influence of Reynolds number

As discussed above, the turbulence model assumes the boundary layer on the blade is always fully turbulent, despite the fact that there might be transitional flows locally. By comparison, the transition models have the potential to capture this phenomenon. However, it is also observed in previous work that the streamlines are almost all directed outwardly, i.e. the the flow is in laminar regime over the entire blade surface. And this also explains the negligible difference in performance prediction when changing the TI and TVR values at the inlet. As the Reynolds number is below the critical value, the transitional effects are not yet activated. Therefore, to further investigate how the onset of transition is related to the turbulent intensity, a higher rotational propeller rotational rate is considered.

The influence of turbulence intensity of the freestream on the transition process on the blade surface is presented in Figure 8. Three combinations of TI and TVR values are investigated. The TI at the inlet is set constant, therefore the fluctuations close to the thruster are based on the TVR. The higher values of TVR reduce the decay of TI, resulting in an earlier onset of transition. It is clearly observed that with the increase of TVR, the turbulent effect becomes more pronounced at the blade tip, which is indicated by a larger skin friction. It is also noted that the $k - k_L - \omega$ model is not as sensitive to these inlet parameters as the $\gamma - Re_\theta$, and the skin friction distribution and streamline pattern are very close under different disturbances.

4. CONCLUSION

Laminar to turbulent transition flows are often observed on marine propellers at model scales. Accurately resolving this flow phenomenon can significantly improve the performance prediction of the

propeller. In this work, the capabilities of the $k - k_L - \omega$ and $\gamma - Re_\theta$ transition models implemented in the ANSYS Fluent flow solver are tested for the performance prediction of a rim-driven thruster. Different test cases are firstly conducted to ensure the quality of the numerical simulations. From the validation study using the ducted propeller, it is concluded that the transition models exhibit better performance than the turbulence model. The predicted thrusts of propeller and duct, which are mainly based on pressure contribution, are quite close using different models. However, the propeller torque is exceptional. When there is a transitional flow, the transition models give lower values for torque due to smaller shear stress prediction. This is a result of the laminar boundary layer and the streamlines in this situation are more outwardly oriented due to centrifugal acceleration. The comparison between the $k - k_L - \omega$ and $\gamma - Re_\theta$ transition models in hydrodynamic performance prediction of an RDT is then conducted. From the results it is found that there is a small difference between the two models. The $k-k_L-\omega$ predicts more local turbulent regions such as the blade tip, and therefore the skin friction is higher in this region than that of the $\gamma-Re_\theta$ model. The $\gamma-Re_\theta$ model predicts higher propeller thrust, especially for the pressure component, but it is at present not certain which model is more accurate. More research is required for verification.

ACKNOWLEDGEMENTS

The authors would like to thank the China Scholarship Council (CSC) for their financial support for the first author (Grant No. 201806950010). The computational resources and services used in this work were provided by the VSC (Flemish Supercomputer Center), funded by the Research Foundation - Flanders (FWO) and the Flemish Government - department EWI.

REFERENCES

[1] Kuiper, G., 1981, "Cavitation Inception on Ship Model Propeller", Ph.D. thesis, Delft University of Technology.

[2] Wang, X., and Walters, K., 2012, "Computational Analysis of Marine-Propeller Performance Using Transition-Sensitive Turbulence Modeling", *J Fluids Eng*, Vol. 134, p. 071107.

[3] Pawar, S., and Brizzolara, S., 2019, "Relevance of Transition Turbulent Model for Hydrodynamic Characteristics of Low Reynolds Number Propeller", *Appl Ocean Res*, Vol. 87, pp. 165–178.

[4] Liu, B., and Vanierschot, M., 2021, "Numerical Study of the Hydrodynamic Characteristics Comparison between a Ducted Propeller and a Rim-Driven Thruster", *Appl Sci-Basel*, Vol. 11, p. 4919.

[5] Yan, X. P., Liang, X. X., Wu, O. Y., Liu, Z. L., Liu, B., and Lan, J. F., 2017, "A Review of Progress and Applications of Ship Shaft-less Rim-Driven Thrusters", *Ocean Eng*, Vol. 144, pp. 142–156.

[6] Dubas, A. J., Bressloff, N. W., and Sharkh, S. M., 2015, "Numerical modelling of rotor–stator interaction in rim driven thrusters", *Ocean Eng*, Vol. 106, pp. 281–288.

[7] Song, B. W., Wang, Y. J., and Tian, W. L., 2015, "Open water performance comparison between hub-type and hubless rim driven thrusters based on CFD method", *Ocean Eng*, Vol. 103, pp. 55–63.

[8] Cai, M. J., Yang, C. J., Wu, S. J., Zhu, Y. S., and Xie, Y., 2015, "Hydrodynamic analysis of a rim-driven thruster based on RANS method", *OCEANS 2015-MTS/IEEE Washington*, pp. 1–5.

[9] Gaggero, S., 2020, "Numerical design of a Rim-driven thruster using a RANS-based optimization approach", *Appl Ocean Res*, Vol. 94, p. 101941.

[10] Cao, Q. M., Z., W. X., H., T. D., and W., H. F., 2015, "Study of gap flow effects on hydrodynamic performance of rim driver thrusters with/without pressure difference", *J Hydrodynam B*, Vol. 30, pp. 485–494.

[11] Liu, B., Vanierschot, M., and F., B., 2022, "Effects of transition turbulence modeling on the hydrodynamic performance prediction of a rim-driven thruster under different duct designs", *Ocean Eng*, Vol. 256, p. 111142.

[12] Menter, F. R., 1994, "Two-Equation Eddy-Viscosity Turbulence Models for Engineering Applications", *AIAA J*, Vol. 32, pp. 1598–1605.

[13] Menter, F. R., Langtry, R. B., Likki, S. R., Suzen, Y. B., Huang, P. G., and Völker, S., 2006, "A Correlation-Based Transition Model Using Local Variables—Part I: Model Formulation", *J Turbomach*, Vol. 128, pp. 413–422.

[14] Walters, D. K., and Cokljat, D., 2008, "A Three-Equation Eddy-Viscosity Model for Reynolds-Averaged Navier—Stokes Simulations of Transitional Flow", *J Fluids Eng*, Vol. 130.

[15] Oosterveld, M. W. C., 1970, *Wake adapted ducted propellers*, H. Veenman & Zonen, Wageningen, The Netherlands.

Conference on Modelling Fluid Flow (CMFF'22)
The 18th International Conference on Fluid Flow Technologies
Budapest, Hungary, August 30-September 2, 2022

EFFICIENT PIV MEASUREMENTS IN THE INTERIOR OF COMPLEX, TRANSPARENT GEOMETRIES

Mirko EBERT[1], Christin VELTEN[2], Katharina ZÄHRINGER[2], Christian LESSIG[1]

[1] Corresponding Author. Institute for Simulation and Graphics, Department of Computer Science, Otto-von-Guericke-Universität Magdeburg. Universitätsplatz 2, 39106 Magdeburg, Germany. E-mail: {mirko.ebert | christian.lessig}@ovgu.de
[2] Lehrstuhl für Strömungsmechanik und Strömungstechnik, Fakultät für Verfahrens- und Systemtechnik, Otto-von-Guericke-Universität Magdeburg. E-mail: {christin.velten | katharina.zaehringer }@ovgu.de

ABSTRACT

In many industrial applications, such as packed beds and combustion engines, gas flows through complex geometries play an important role. The measurement of these is therefore of considerable importance, e.g. for process monitoring and optimization. Spatially and temporally highly resolved measurements of these flows are, however, often difficult since no direct optical access to the interior is possible, rendering techniques such as PIV inapplicable. Transparent geometry, e.g. from glass, restores optical access but it leads to severe optical distortions in captured images, again preventing the use of standard techniques. We present an efficient and robust numerical algorithm to reconstruct gas flow velocity vector fields in the interior of complex, transparent geometry from PIV measurements. A complete simulation of PIV experiments, which allows, e.g., to optimize an experimental setup without building hardware, is also introduced. We validate our PIV reconstruction technique with simulated experiments as well as real-world PIV measurements in a complex bulk reactor.

Keywords: PIV, ray tracing, flow velocity measurement in transparent packed bed

1. INTRODUCTION

Particle image velocimetry (PIV) is a well established technique to obtain spatially and temporally highly resolved velocity field measurements of gaseous flows [1]. Since PIV is based on imaging the flow, it requires the investigation region to be optically accessible. This, however, is not easily satisfied in many applications where there is complex flow geometry. One example are bulk reactors where immersed particles play a fundamental role for the overall dynamics but these also block the line of sight to many flow regions of interest.

In this article, we present an efficient and robust numerical technique for PIV-based flow velocity measurements in complex environments. We assume that geometries that would block the line of sight are of transparent material, e.g. glass. This ascertains optical access but also causes strong optical distortions in captured PIV images, rendering standard PIV calculation techniques inapplicable. In our work, we resolve this by numerically computing the undistorted PIV image that would have been obtained for the flow with its tracer particles in a geometry that has no optical effect.

We obtain the undistorted image with a two step technique. First, we reconstruct the light field, which describes the light energy density as a function of position and direction, on the PIV investigation plane. This is accomplished using an inverse light transport simulation of a computer model of the experimental setup that uses the distorted PIV image as light source. With the light field available, a forward optical simulation in an empty environment yields the undistorted PIV image, which can be used with standard PIV vector field calculation techniques. Our approach is nontrivial since the problem is a priori ill-posed and we discuss how it can, nonetheless, robustly yield corrected images and high fidelity vector fields.

We demonstrate the efficacy of our technique using, firstly, simulated PIV experiments, in which case the ground truth vector field is precisely known, and, secondly, real PIV experiments in a complex bulk reactor. We also investigate how regions where no vector field reconstruction is possible can be minimized with multi-camera PIV setups.

The remainder of the article is structured as follows. After discussing related work in Sec. 1, we present in Sec. 2 our numerical technique to enable PIV in optically complex environments. In Sec. 3 we verify our technique with simulated PIV experiments and in Sec. 4 we present results for real ones in a bulk reactor. The paper concludes in Sec. 5 where we also discuss future work.

Related Work The measurement of flow fields in complex geometries is challenging since optical methods, such as PIV or PTV (particle tracking velocimetry), are not directly applicable. Using transparent geometry, e.g. of glass, restores optical access. However, it also induces strong optical distortions, for example due to strongly curved or angled transparent surfaces, which render standard techniques for flow field calculation inapplicable.

In liquids, refractive index matching (RIM), where the refractive index of the flow liquid is matched to that of the immersed, transparent geometry, can be employed to counterbalance the distortion. This was used in conjunction with optical methods to compute flow vector fields in packed beds for example in [2, 3, 4, 5]. In gaseous flows, however, RIM is inapplicable due to the large difference between refractive indices.

Invasive techniques, such as endoscopic PIV, provide an alternative approach for flow measurements when optical access from the outside is not possible. This was used, for example, to analyze velocity fields of water flows in the porous space of packed beds [6, 7]. The insertion of probes into a flow can, however, have a significant effect on its behavior.

For simple optical setups, e.g. when the experimental apparatus is viewed through a slightly curved window, optical distortions can be corrected for by careful calibration [8, 9]. Kováts et al. [10] demonstrated that this is still applicable in more challenging configurations with a single layer of hollow spheres. These authors used multi-step calibration with the interstices and the spheres being considered separately.

For large optical distortions, more sophisticated methods than careful calibration are required. Kang et al. [11] developed a correction for the flow field inside a droplet using ray tracing. Some terms in their algorithm were found to be erroneous by Minor et al. [12] who corrected these. Later, Zha et al. [13] used ray tracing for distortion correction of flow measurements in a transparent diesel motor cylinder.

For complex particle beds, the use of ray tracing to correct for optical distortions was first demonstrated by Martins et al. [14, 15]. We will spell out the implicit assumptions in this work, extend it to scale better to more complex setups, and allow for the recovery of larger areas of the flow fields.

2. PIV IN OPTICALLY COMPLEX ENVIRONMENTS

We consider PIV setups with complex geometry that is transparent at least in the line of sight of the measurement camera. Optical access to the flow is then still available but the transparent geometry causes strong distortions in captured PIV images that lead to incorrectly computed vector fields when standard techniques for PIV vector field calculation are used; see the experimental results in Fig. 6. Our approach to obtain the true vector fields is to reconstruct the light field $\ell(x, \omega)$ on the PIV investigation plane and then simulate the image formation process as if no distorting geometry would be present, see Fig. 1 for an overview. This yields a corrected PIV image that can be used with standard approaches for PIV vector field calculations.

Although the light field $\ell(x, \omega)$ can in principle be obtained by tracing the measured light intensity $I(u)$ from the PIV images back through the experimental setup, the computation is ill-posed since the measurement on the camera reduces the $5D$ function $\ell(x, \omega)$ that depends on position x and direction ω to the $2D$ intensity $I(u)$, averaging the contributions coming from different directions and projecting it onto the two-dimensional image plane.[1] The reconstruction is furthermore compounded by the need for a minute alignment between experiment and simulation as well as magnification effects that can cause the projection of large regions of the PIV investigation plane onto a small number of pixels.

In the following, we will detail our numerical technique that, despite the difficulties, allows for the computation of corrected PIV images and, through this, the accurate calculation of vector fields with PIV in optically complex environments. We will first consider the light field reconstruction and then the alignment between experiment and simulation.

2.1. Light field reconstruction

To obtain a corrected PIV image that allows for the use of standard PIV software, we require knowledge of the light field $\ell(x, \omega)$ on the investigation plane P at the time when the image is taken. The available information for the reconstruction is, however, only the distorted PIV measurement, i.e. the two-dimensional intensity function $I(u) : \mathcal{I} \to \mathbb{R}$ on the image plane $\mathcal{I}$. A reconstruction is, therefore, only possible when additional assumptions about the light field are made.

We will assume, firstly, that the distorted PIV image was captured with a pinhole camera model so that the contributions to $I(u)$ for fixed $u \in \mathcal{I}$ come from a single direction only and, secondly, that the light field $\ell(x, \omega)|_P$ on the PIV investigation plane is isotropic and has no angular dependence, i.e. $\ell(p) = \ell(x, \omega)|_P$ with $p \in P$.

The pinhole camera, with focal length and lens distortion as parameters, is fitted to best match the real camera in the experiment, see Sec. 2.2 for details. This provides a good approximation, as is corroborated by Fig. 2 that shows a pixel-accurate agreement between the geometries in a photograph and a computer-generated image with the fitted pinhole camera.

An isotropic light field ignores the strong anisotropy in the Mie scattering of the tracer particles.

[1] By the symmetry of the light field, which corresponds to the constancy of $\ell(x, \omega)$ along light rays, the function is, in fact, only four-dimensional; the reconstruction problem remains, however, ill-posed.

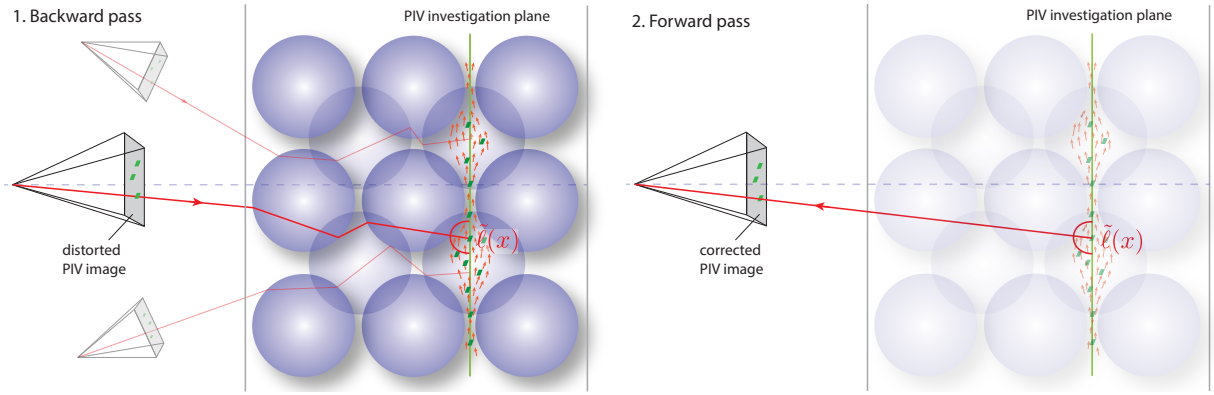

Figure 1. Conceptual depiction of our reconstruction algorithm with spheres as transparent flow geometry. In the forward pass, the captured PIV image is used as a light source and with a ray tracing light transport simulation through the experimental setup, an approximation $\tilde{\ell}(x) = \tilde{\ell}(x, \omega)$ of the light field on the PIV investigation plane is reconstructed. The use of multiple PIV cameras is also possible and this can lead to improved reconstructions of $\tilde{\ell}(x)$. After the reconstruction of $\tilde{\ell}(x)$, the undistorted PIV image is reconstructed by forward ray tracing with $\tilde{\ell}(x)$ as light source and with the distorting geometry removed from the experimental setup, which is easily realized numerically. Standard PIV software can then be used to compute the flow vector field.

This effect is nevertheless considerably reduced in a camera arrangement, where the scattered light is collected over a range of angles, depending on the distance (which is rather large in our case) and aperture of the camera, as well as in a field of particles where multi-scattering takes place [1]. Furthermore, what is used for the velocity field determination is, however, only the relative position of tracer particles in an image pair, with the magnitude Fourier-averaged over an interrogation window. In this sense the assumption of an isotropic light field can be understood as an analogue of the binarization that is sometimes performed as image pre-processing before PIV. In more complex camera setups, e.g. those considered in Sec. 3.1, an anisotropic light field might be beneficial or necessary. This will be the subject of future work.

With the above assumptions, the mapping of the $2D$ function $I(u)$ to the $2D$ function $\ell(p)$ is well posed. In particular, an approximation $\tilde{\ell}(p)$ to $\ell(p)$ can be obtained by tracing light rays backwards from the camera with the distorted PIV image as source until the rays intersect P, see Fig. 1, left. By the reversibility of light transport, pointwise values $\ell(p)$ are obtained by reflecting and refracting the rays through the scene and scattering these according to the Fresnel equations [16]. We record all $\ell(p)$ which, when interpolated, provide the approximation $\tilde{\ell}_P$. The corrected PIV image I_c, which allows for the use of standard PIV calculations for determining the flow velocity field, is then obtained by simulating the image formation process for an experimental setup with $\tilde{\ell}(x)$ as light source and with all distorting geometry removed, see Fig. 1, right.

It is possible to consider the above computation as a mapping $M : I \to I_c$ from the distorted PIV image I to the corrected one I_c, side-stepping an explicit computation of $\tilde{\ell}$. This was followed in [14, 15]. However, the approach scales quadratically in the number of pixels, so that for state-of-the-art camera resolutions with $O(10^7)$ or more pixels, the mapping M requires tens of gigabytes of storage. Furthermore, since on modern compute hardware the bottleneck is usually memory transfer and not computations, performing the ray tracing for every image that is to be reconstructed is in practice faster than applying a precomputed mapping.

2.2. Alignment of Experimental Setup and Simulation

A precise alignment between simulation and experiment is critical for an accurate correction of distorted images. We thereby currently presume that an accurate 3D model of the experimental setup exists, e.g. because it served as input to its manufacturing, so that the alignment reduces to calibrating the camera. Following the approach in computer vision [17], we separate this calibration into an intrinsic part, which determines the camera parameters that best match a pinhole camera model and which corrects for lens distortion, and an extrinsic one, which accounts for the rigid alignment of the camera with respect to the experimental setup. Among other things, this separation has the advantage that different numerical techniques can be used for the different parts, which we exploit in our approach. Both calibrations are performed in the experimental setup prior to the flow measurement.

For the intrinsic calibration, we experimented with the OpenCV library [18] as well as with the commercial PIV software DaVis from LaVision. We obtained the best results with a combination of both when the focal length and the optical center are determined with the DaVis calibration and the lens dis-

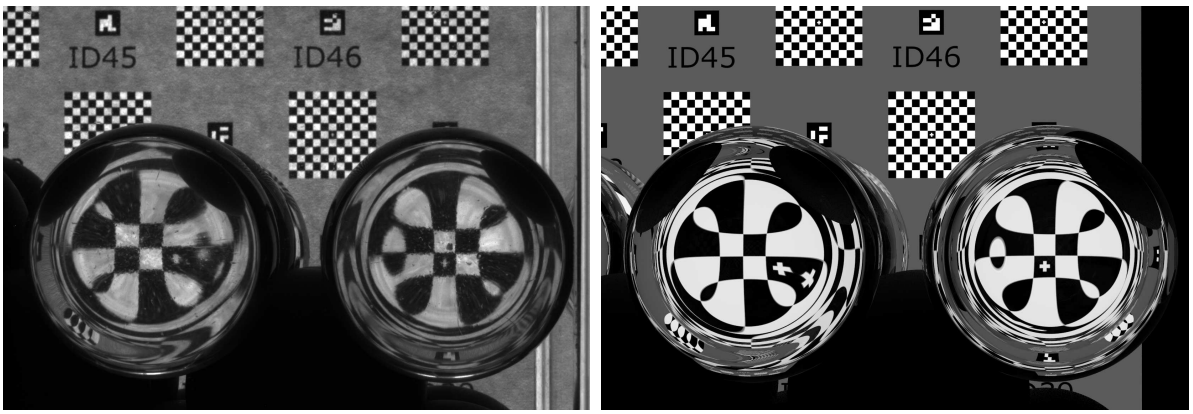

Figure 2. Comparison between photograph of an experimental setup without a flow (left) and computer-generated image of it (right). A good agreement with a pixel-accurate alignment of the geometry can be observed.

tortion subsequently in OpenCV.

For extrinsic calibration, we use AruCo markers that integrated into the experimental setup (cf. Fig. 2) so that we have always a sufficient number of markers in the field of vision. The markers consist of a barcode that allows for their unique identification and they are placed at non-colinear, known positions in the experimental setup, see Fig. 2. Using a geometric description of the relative marker positions, standard libraries, e.g. [18], can be used to obtain an estimation of the camera position relative to these. For us, this provides the position of the camera and its orientation with respect to the experimental setup. The camera's position would also be available from the setup itself, at least up to measurement uncertainties, but not the orientation, which is critical for an accurate reconstruction [14].

To verify the accuracy of the calibration we compare for each experimental run a computer-generated image of the corresponding experimental setup with a photograph, both without flow to facilitate the comparison. An example is shown in Fig. 2. As can be seen there, a good agreement is achieved and an overlay of the images verifies that one has a pixel-accurate alignment of the geometry. An even closer match of the images could be obtained by also simulating depth-of-field but since this does not facilitate PIV reconstruction we do not perform the expensive additional computations. Fig. 2 also shows that for our concrete setup the computer model is sufficiently accurate for the light transport simulation. However, at least locally a strong sensitivity to errors in the computer model exists for both the geometry and parameters such as the refractive index. A quantitative analysis of the sensitivity will be pursued in future work.

2.3. Implementation

Our implementation of the light transport simulation is based on the open source ray tracing software pbrt [19], which provides a flexible and efficient Monte Carlo light transport simulator designed for research. Some modifications to the software were necessary to adapt it for our purposes. The most important ones are a textured area light source, which is used for the captured PIV image; an implementation of a pinhole camera with lens distortion, which matches the model of OpenCV; a surface material that represents the reconstructed light field in the scene; and extending the light ray representation in the software so that it has information about the ray's origin and destination. In our implementation, we also do not explicitly record $\tilde{\ell}$ but exploit that the forward pass (cf. Fig. 1) is very simple and allows one to directly compute the corrected image I_c. For an experimental setup with 12 visible spheres, the computation time of I_c from a given distorted PIV image I at a resolution of 1000×1000 pixels is 6.5 s on a 12 core processor with 2.2 GHz.

The pbrt-based implementation of the light transport simulation is complemented by python code for the calibration as well as the necessary data conversion between the different parts of the processing pipeline.

3. SIMULATED PIV EXPERIMENTS

In this section, we consider the validation of the computational pipeline introduced in Sec. 2 with simulated PIV experiments to obtain insight on the influence of different parameters, like geometric tolerances and camera orientation and position. While the present work provides only first steps in this direction, it will in the future help with the design and and planning of experiments. This allows us to compare to a known ground truth and also to control and separate different error sources. In Sec. 3.1 we detail the principle methodology for this and in Sec. 3.2 the concrete realization as well as the obtained results are discussed. We also demonstrate that simulated PIV experiments can help to minimize difficulties in the experiments and reconstructions, which is considerably more efficient when done numerically than with real experiments.

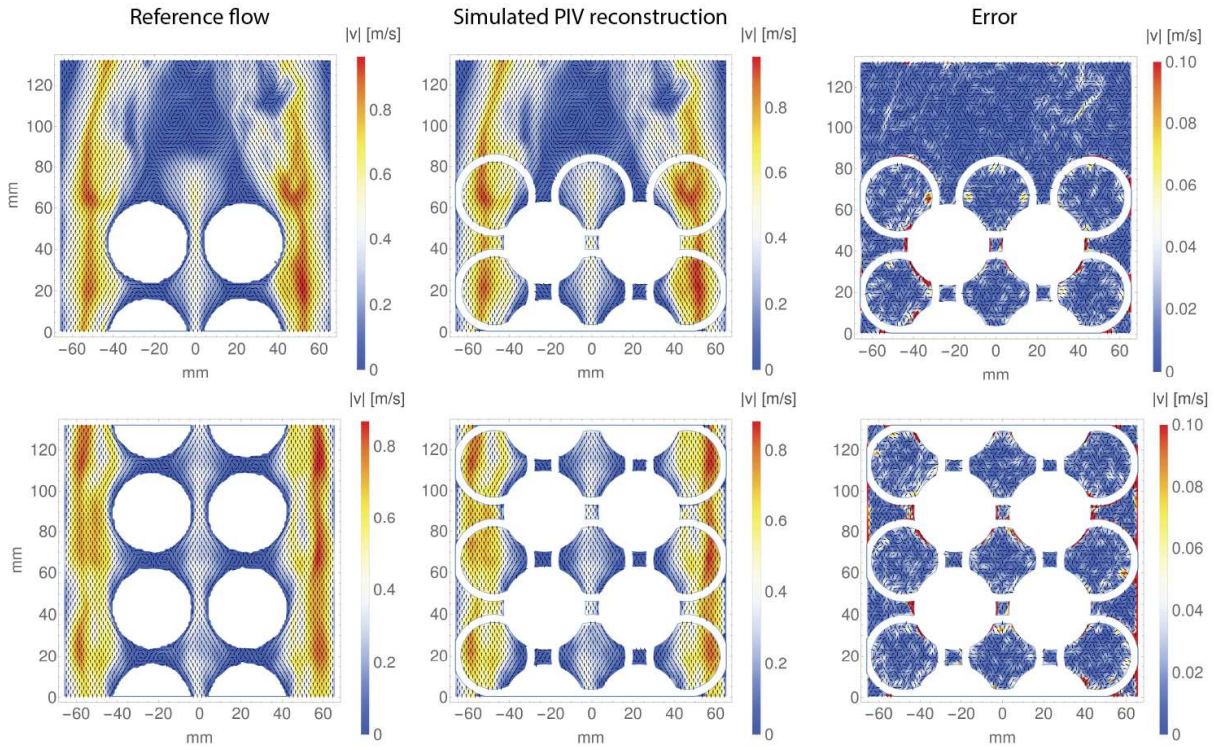

Figure 3. CDF simulated reference (left), calculated flow vector fields (center), and difference (right) for the top layer (top) and eleventh layer (bottom) of the packing in the bulk reactor in Fig. 4. In each case, the virtual PIV investigation plane was horizontally behind two layers of spheres of the 3×3 layout and thus cut through the spheres of the subjacent layer, resulting in the circular regions where even in the reference no vector field is defined. The error is the difference between the reference and the computed vector field.

3.1. Simulation of PIV experiments

The input for the simulated PIV experiments is a 3D computer model of the experimental setup as well as a simulation of the flow through it. Trajectories of PIV tracer particles along the flow are obtained by integrating the fluid vector field numerically from random but well distributed initial conditions for the time between the two PIV images (e.g. 10^{-4} s). The particles at their start and end positions are stored in images that represent the laser sheet of the PIV investigation plane at the two different times, with particle sizes chosen to be optimal for PIV evaluation. The images corresponding to the PIV laser sheet are subsequently used as light source for a light transport simulation through the computer model of the experimental setup (with the full geometry) to determine the distorted PIV images that would have been captured by a measurement camera.

After the distorted PIV images have been obtained, the computations proceed as described in Sec. 2 to reconstruct corrected images.

3.2. Validation

For validation, we used a preliminary computer model of the bulk reactor in the experiments of Sec. 4, shown in Fig. 4, with a flow simulation in it performed with the Lattice-Boltzmann code ALBORZ [20]. For time integration of virtual PIV tracer particles, the classical Runge-Kutta-4 scheme was employed. We currently use a pinhole camera to capture simulated PIV images, although more complex and realistic models are possible [21]. Vector fields were calculated from corrected, simulated PIV images using the commercial PIV software DaVis from LaVision. Since all geometric parameters are exactly known, no alignment between (virtual) experiment and simulation, as described in Sec. 2.2, was necessary.

Calculated flow vector fields for two different measurement positions in the bulk reactor (surface on top and eleventh layer on bottom) are shown in Fig. 3, center, and the reference flow field from the simulation in Fig. 3, left. Minor artifacts, for example in the interstices between the particles where fine vortical structures are not fully resolved, can be observed by comparing both columns. Overall, however, an accurate reconstruction of the flow field is obtained.

In the right column of Fig. 3, the differences between reference flow field and simulated PIV are depicted. The white circular regions in Fig. 3 result from very strong optical distortions at the rim of the spheres in front of the measurement plane. Through the distortion, the corresponding regions on the PIV investigation plane are mapped onto a single or a small number of pixels on the camera image, rendering reconstruction impossible. Therefore, the regions

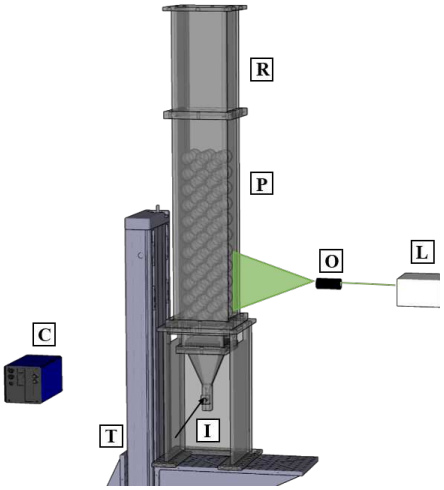

Figure 4. Experimental Setup consisting of a bulk reactor (R), the bcc-packing (P), the air inlet (I), the laser Quantel Q-smart Twins 850 (L), the camera (C), the light sheet optics (O) and a 3D-traversing system (T).

are masked for PIV vector field calculations to avoid that the distortions affect larger neighborhoods.

PIV vector field calculations from the simulated experiments and with ray tracing corrected particle images lead to an average uncertainty of $2.211 \cdot 10^{-5}$ m/s. This demonstrates that very few errors are introduced by the simulation and correction method. The good results are partially a consequence of the lack of imperfections and misalignments that are unavoidable in real-world experiments. However, in our opinion, this demonstrates an advantage of the simulation since the different components of a real setup can be studied independently and the errors introduced by these can be delineated (for the components and effects that are present in the necessarily simplified simulation). In particular, the integration of, for example, an imperfect camera or alignment errors into the simulation is easily possible.

3.3. Reduction of Non-Reconstructable Regions

In this section, we use the PIV simulation to investigate how to minimize regions where vector field reconstruction is impossible due to a very large optical distortion, see the rings in Fig. 3 as well as the discussion above. Simulated PIV experiments provide here the advantage that alternatives can be explored significantly more efficiently than with a physical experimental setup.

To minimize non-reconstructable regions, we consider the use of multiple cameras for the PIV measurement. The setup is analogous to that in Fig. 4 but with five synchronized cameras, three of which are in the same plane as the original one and two in an elevated position, see Fig. 1. We compute virtual PIV measurement through these cameras analogous to Sec. 3.1 by performing a light transport simulation for each of them, yielding five simulated PIV images. For the reconstruction of the isotropic light field $\tilde{\ell}(p)$ on the investigation plane, we can now utilize the five PIV measurements and this provides the principal advantage of the multi-camera setup. In particular, each of the five images is used as source for a backward light transport pass as described in Sec. 2.1 and the contributions from the different cameras are accumulated into $\tilde{\ell}(p)$, yielding a more accurate approximation to the original light field $\ell(p)$. This is demonstrated in Fig. 5 for the first configuration in Fig. 3, which corresponds to the surface layer of the packing in the bulk reactor. The regions where no reconstruction was possible previously are completely removed. Some additional artifacts appear in the calculated vector fields that result from multiple reflections and induced poor optical quality in the corrected PIV image. A weighted combination of the different cameras in a multi-camera setup, which will likely allow one to remove the artifacts, will be investigated in future work.

4. PHYSICAL PIV EXPERIMENTS

Next to the simulated PIV experiments presented in the last section, we evaluated our reconstruction algorithm also with preliminary real experiments with a physical realization of the bulk reactor also used in the simulations.

4.1. Experimental Setup

The experimental setup is shown in Fig. 4. A bulk reactor (R) holds a packing of body centered cubic d = 40 mm polypropylene precision spheres and N-BK7 ball lenses (P), which are used in the measurement regions to generate optical access. In the first layer 3×3 spheres are arranged. By moving the reactor, which is placed on a 3D traversing unit (T), the required measurement position and alignment can be generated with the help of a ray tracing calibration target, which is placed on the rear side of the reactor. The measurement plane is created by a light sheet optic (O) and a Quantel Q-smart Twins 850 laser (L). For detection of the measurement signal, coming from illuminated liquid Di-Ethyl-Hexyl-Sebacat (DEHS) tracer particles, an Imager LX 8M Camera (C) from LaVision is used. The tracer particles enter together with the pressurized air controlled by a Bronkhorst Mass-Stream Controller (D-6371) through the reactor inlet (I). Particle fields are recorded with a frequency of $f = 1.67$ Hz. Before the correction is computed as described in Sec. 2, a calibration is applied to the images with the commercial software DaVis from LaVision. The software is also used for vector field calculation from the distortion-corrected images.

4.2. Vector Field Calculation

In this experiment, surface measurements above nine layers of spheres are carried out. The measurement plane is in the centre between the second and third sphere in the camera viewing direction. The

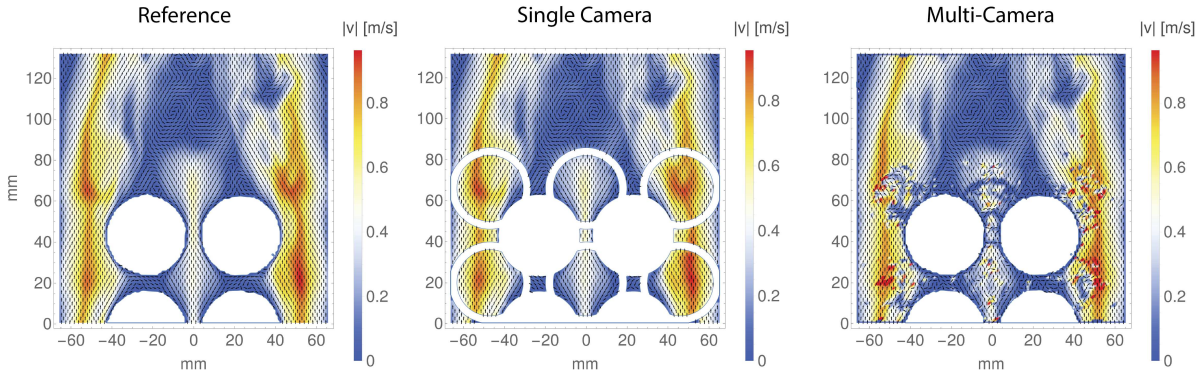

Figure 5. CFD simulated reference flow field (left), and reconstructed vector fields (center and right) for the surface of the packing in the bulk reactor of Fig. 4. In the center is the result for a PIV setup with one camera, which yields circular regions that cannot be reconstructed due to very large optical distortions. In the five camera setup on the right a reconstruction of these regions is possible, although some additional artifacts appear.

flow field of the surrounding can be calculated easily by direct application of standard PIV evaluation with a cross-correlation method, with multi-pass calculation and a decreasing size of the interrogation window from 64×64 to 32×32 pixels with 50% overlap. This leads to the vector fields shown in Fig. 6, top row, for particle Reynolds number $\mathrm{Re_P} = 200$ and $\mathrm{Re_P} = 300$ without (first and third column) and with (second and fourth column) ray tracing based correction. The particle Reynolds number is based on the sphere diameter and a theoretical porosity of a bcc-packing of $\phi = 0.32$.

Even without correction (first and third column) a vector field can be calculated in the distorted region behind the center sphere, although it is corrupted by effects like mirroring and magnification. Due to these and the shadows of the underlying layer of spheres blocking the light sheet, no measurement signal is obtained in the lower region behind the spheres. To obtain the real velocity field, the ray tracing based correction is applied and the resulting images are afterwards evaluated by the same standard PIV calculation as presented above.

After the correction (second and fourth column) the surrounding flow field matches very well the flow behind the centre sphere, where optical distortions were maximal. Directly above the center sphere a region with higher velocities appears, leading to a recirculation zone. Considering the higher velocities in the centre and lower velocities closer to the rim regions of the sphere, the flow fields behind the outer spheres match this condition very well. Unfortunately, the rim region of the spheres cannot be reconstructed completely due to high optical distortions, cf. Sec. 3, leading to the masked white half ring.

The averaged relative uncertainties based on the averaged uncertainty from the uncertainty fields shown in the lower row of Fig. 7 divided by the averaged velocity from the absolute velocity fields are in the range of 2.3% to 3.6%. The presentation of relative uncertainty fields is not practical because of the recirculation zones in the centre of the field, leading to unreasonable high relative uncertainties by division of velocities close to 0 m/s. Comparing the uncertainty fields of the distorted and the corrected data shows no significant difference since only the uncertainty of the PIV evaluation itself is considered by this method. The error of the correction method can only be determined properly by the use of known synthetic reference data, like presented before.

5. CONCLUSION AND FUTURE WORK

In this work, we presented a computationally efficient numerical technique to perform PIV in complex environments with transparent geometry. We validated the technique with simulated PIV experiments, where we obtained good agreement with the known ground truth solutions, and with real experiments in a complex bulk reactor, where high quality velocity fields were obtained. We also demonstrated that simulated PIV experiments are of utility in their own right by using it to investigate how multiple cameras can improve reconstructions.

Next to work on the real experiments with the bulk reactor in Fig. 4, we want to extend our numerical technique into multiple directions. We want to use our simulated PIV experiments to better understand the different sources of errors that occur in physical experiments and devise strategies to minimize these. For this, we also want to use more complex camera models [21]. The principle challenge there is to develop a camera calibration that can robustly account for the additional parameters. Numerical optimization of the computer model to better match the physical experimental setup could also help to improve our technique. Another important direction for future work is a sensitivity analysis of our approach, in particular with respect to errors in the computer model as well as the calibration.

We also want to extend our preliminary results on multi-camera PIV. Importantly, the artifacts that

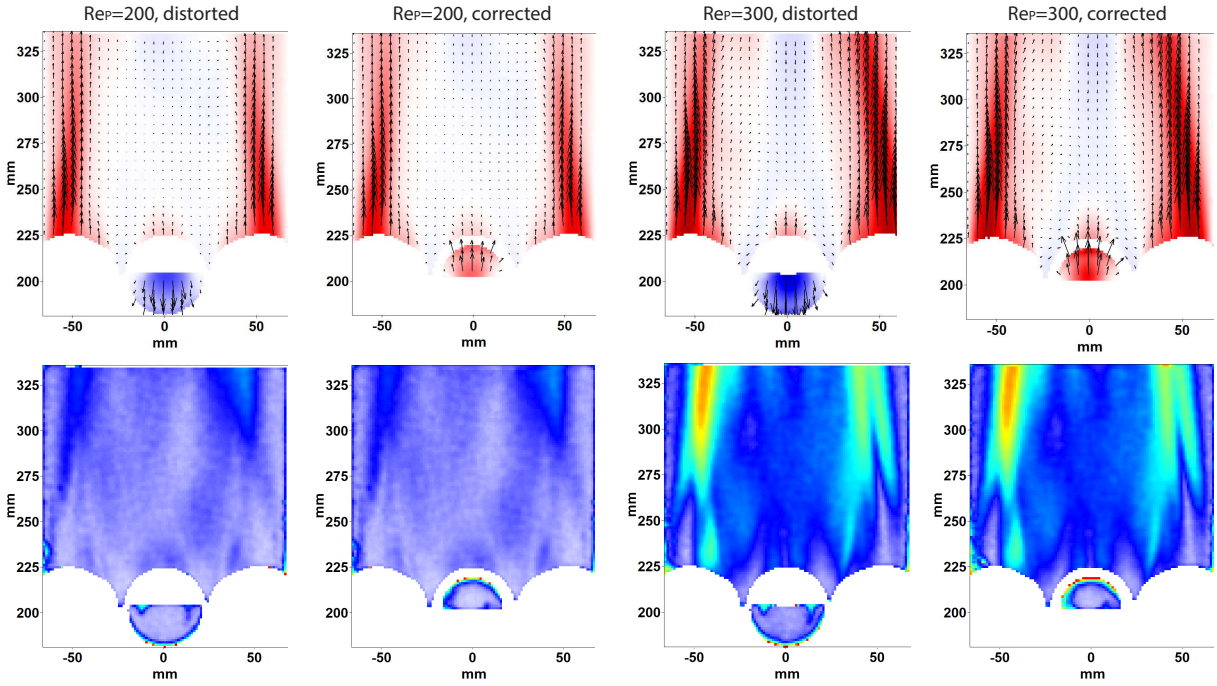

Figure 6. Averaged vertical velocity component V_y as color gradient and entire vector field as overlay for particle Reynolds numbers 200 and 300 above nine layers of spheres calculated by distorted and corrected images (top row) and PIV uncertainty fields below.

are currently visible need to be reduced or avoided. This will likely be possible by appropriately weighting the contributions from different cameras. Interesting is thereby how many cameras are needed and if a sophisticated reconstruction procedure can potentially reduce the number of cameras to not unduly increase the experimental work. The use of multiple cameras also allows one to compute an approximation $\tilde{\ell}(x, \omega)$ to the light field on the PIV investigation plane with angular dependence and we want to investigate if this improves vector field reconstruction. A related direction is the use of a plenoptic camera instead of multiple separate ones. This could increase reconstruction quality and also avoid the considerable challenge that calibration of multiple individual cameras poses in real experiments.

In the future, we also want to publicly release our computational pipeline, including integrations into standard CAD and modeling software.

ACKNOWLEDGEMENTS

Funded by the Deutsche Forschungsgemeinschaft (DFG, German Research Foundation) – Project-ID 422037413 – TRR 287. We thank Ali Husseini and Feng Huang for the the ALBORZ simulation through the bulk reactor that was used in Sec. 3.

REFERENCES

[1] Raffel, M., Willert, C., Scarano, F., Kähler, C. J., Wereley, S. T., and Kompenhans, J., 2018, *Particle Image Velocimetry - A Practical Guide*, Vol. 1, Springer Verlag, URL `https://elib.dlr.de/119724/`.

[2] Budwig, R., 1994, "Refractive index matching methods for liquid flow investigations", *Experiments in Fluids*, Vol. 17 (5), pp. 350–355.

[3] Hassan, Y. A., and Dominguez-Ontiveros, E., 2008, "Flow visualization in a pebble bed reactor experiment using PIV and refractive index matching techniques", *Nuclear Engineering and Design*, Vol. 238 (11), pp. 3080–3085.

[4] Wiederseiner, S., Andreini, N., Epely-Chauvin, G., and Ancey, C., 2010, "Refractive-index and density matching in concentrated particle suspensions: a review", *Experiments in Fluids*, Vol. 50 (5), pp. 1183–1206.

[5] Borrero-Echeverry, D., and Morrison, B. C. A., 2016, "Aqueous ammonium thiocyanate solutions as refractive index-matching fluids with low density and viscosity", *Experiments in Fluids*, Vol. 57 (7).

[6] Tani, N., Kondo, H., Mori, M., Hishida, K., and Maeda, M., 2002, "Development of fiberscope PIV system by controlling diode laser illumination", *Experiments in Fluids*, Vol. 33 (6), pp. 752–758.

[7] Blois, G., Smith, G. H. S., Best, J. L., Hardy, R. J., and Lead, J. R., 2011, "Quantifying the dynamics of flow within a permeable bed using time-resolved endoscopic particle imaging velocimetry (EPIV)", *Experiments in Fluids*, Vol. 53 (1), pp. 51–76.

[8] Willert, C., 1997, “Stereoscopic digital particle image velocimetry for application in wind tunnel flows”, *Measurement Science and Technology*, Vol. 8 (12), pp. 1465–1479.

[9] Soloff, S. M., Adrian, R. J., and Liu, Z.-C., 1997, “Distortion compensation for generalized stereoscopic particle image velocimetry”, *Measurement Science and Technology*, Vol. 8 (12), pp. 1441–1454.

[10] Kováts, P., Thévenin, D., and Zähringer, K., “Experimentelle Untersuchung von Strömungsfeldern in den Zwischenräumen grober Schüttungen”, .

[11] Kang, K. H., Lee, S. J., Lee, C. M., and Kang, I. S., 2004, “Quantitative visualization of flow inside an evaporating droplet using the ray tracing method”, *Measurement Science and Technology*, Vol. 15 (6), pp. 1104–1112.

[12] Minor, G., Oshkai, P., and Djilali, N., 2007, “Optical distortion correction for liquid droplet visualization using the ray tracing method: further considerations”, *Measurement Science and Technology*, Vol. 18 (11), pp. L23–L28.

[13] Zha, K., Busch, S., Park, C., and Miles, P. C., 2016, “A novel method for correction of temporally- and spatially-variant optical distortion in planar particle image velocimetry”, *Measurement Science and Technology*, Vol. 27 (8), p. 085201.

[14] Martins, F. J. W. A., da Silva, C. C., Lessig, C., and Zähringer, K., 2018, “Ray-Tracing Based Image Correction of Optical Distortion for PIV Measurements in Packed Beds”, *JAOP: Journal of Advanced Optics and Photonics*, Vol. 1 (2), pp. 71–94, URL `http://www.techscience.com/doi/10.3970/jaop.2018.903.870.html`.

[15] Martins, F. J. W. A., da Silva, A. C., Lessig, C., and Zähringer, K., 2018, “Ray-Tracing Based Image Correction of Optical Distortions Caused by Transparent Spheres for Application in PIV”, *19th International Symposium on the Application of Laser and Imaging Techniques to Fluid Mechanics*, Lisbon.

[16] Born, M., and Wolf, E., 1999, *Principles of Optics: Electromagnetic Theory of Propagation, Interference and Diffraction of Light*, Cambridge University Press, Cambridge, seventh edn.

[17] Hartley, R., and Zisserman, A., 2003, *Multiple View Geometry in Computer Vision*, Cambridge University Press, New York, NY, USA, 2 edn., ISBN 0521540518.

[18] Bradski, G., 2000, “OpenCV”, *Dr Dobb’s Journal of Software Tools*.

[19] Pharr, M., and Humphreys, G., 2010, *Physically Based Rendering: From Theory to Implementation*, Morgan Kaufmann Publishers Inc., San Francisco, CA, USA, second edn.

[20] Hosseini, S. A., 2020, “Development of a lattice Boltzmann-based numerical method for the simulation of reacting flows”, Ph.D. thesis, université Paris-Saclay.

[21] Kolb, C., Mitchell, D., and Hanrahan, P., 1995, “A Realistic Camera Model for Computer Graphics”, *Proceedings of SIGGRAPH ’95*, ACM Press, New York, New York, USA, ISBN 0897917014, pp. 317–324, URL `http://portal.acm.org/citation.cfm?id=218380.218463`.

Conference on Modelling Fluid Flow (CMFF'22)
The 18th International Conference on Fluid Flow Technologies
Budapest, Hungary, August 30-September 2, 2022

MODELING ELECTROHYDRODYNAMICALLY ENHANCED DRAG IN CHANNEL AND PIPE FLOWS USING ONE-DIMENSIONAL TURBULENCE

Marten KLEIN[1], Juan Alí MEDINA MÉNDEZ[1], Heiko SCHMIDT[1]

[1] Chair of Numerical Fluid and Gas Dynamics, Faculty of Mechanical Engineering, Electrical and Energy Systems, Brandenburg University of Technology (BTU) Cottbus-Senftenberg. Siemens-Halske-Ring 15A, D-03046, Cottbus, Germany. Tel.: +49 355 69-5127, Fax: +49 355 69-5127, E-mail: marten.klein@b-tu.de (M. Klein), medinjua@b-tu.de (J. A. Medina Méndez), heiko.schmidt@b-tu.de (H. Schmidt)

ABSTRACT

The joint modeling of flow hydrodynamics and electrokinetics is a relatively unexplored area of turbulent flow research. We address a lack of available models for electrohydrodynamic (EHD) turbulent flow utilizing a lower-order approach, the stochastic One-Dimensional Turbulence (ODT) model. ODT is constructed on the principles of the direct energy cascade of Navier–Stokes turbulence, with key emphasis on the accurate resolution of the small molecular transport scales within a notional line-of-sight. We investigate two canonical flow configurations to demonstrate the applicability of the model in the simulation of EHD flows. First, we investigate EHD effects in zero-pressure-gradient turbulent boundary layers by two-way coupled model application to plane Couette flow of a dilute electrolyte. Second, we apply the one-way coupled model to EHD-enhanced gas flow through a vertical pipe with an inner concentric electrode, where electric fields are generated by means of a corona discharge and the corresponding effect of a continuum ionic charge density field.

Keywords: EHD turbulence, multiphysical boundary layers, one-dimensional turbulence, stochastic modeling, turbulent drag enhancement

1. INTRODUCTION

Electrohydrodynamic (EHD) flows are encountered in various technical applications. As an overview of research-led EHD applications we cite examples of electrostatic precipitation [1], EHD-enhancement of heat and mass transfer [2, 3], turbulent drag [4], hydrogen production in water electrolysis [5], plasma-assisted combustion [6], among others. For numerical simulations of such devices, it is crucial to accurately and economically model entangled hydrodynamic and electrokinetic processes down to and even below the Kolmogorov and Batchelor scales [7]. One of the key issues for accurate modeling of EHD flows is the correct representation of nonlocal and nonlinear interactions between the fluid flow, charge-carrier distributions, and electric fields. These interactions may cause a departure of the turbulence dynamics, e.g., from K41 [8] to electrokinetic turbulence [9]. Indeed, on some EHD regimes, turbulence may appear even at very low Reynolds numbers, e.g., when the electric body forces substitute the role of external inertial forces, and the former are in a large ratio with respect to the viscous forces [10]. Direct Numerical Simulations (DNSs) should be the method of preferred choice for unraveling the physics presents in EHD flows. However, DNSs are, even to this day, limited in terms of their heavy computational overload, i.e., limited to moderate Reynolds numbers [11]. Needless to say, diffusive sub-grid-scale parameterizations used in Reynolds-averaged Navier–Stokes (RANS) or large-eddy simulations (LES), specifically in the presence of walls, are of limited applicability in EHD flows. This is because turbulent drag modifications are nonuniversal and, depending on the flow regime, related to flow laminarization or turbulence regeneration by the action of spatially varying body forces (e.g. [12, 13]) that require new modeling strategies.

Alternative to averaged and filter-based turbulence models, we address issues in turbulent EHD flows with a dimensionally reduced stochastic modeling approach, the so-called One-Dimensional Turbulence (ODT) model [14]. The model has the capability to capture detailed statistics of simultaneous scalar and momentum transport in the vicinity of a wall (e.g. [15]) and complex mixing processes in the bulk (e.g. [16]). In general, ODT aims to resolve all relevant scales of the flow but only for a one-dimensional (1-D) domain that represents a notional line-of-sight. A stochastic process is used to mimic the effects of turbulent stirring motions, whereas deterministic molecular diffusion, electric drift currents, Coulomb forces, and boundary conditions, are directly resolved. For the present standalone application to wall-bounded EHD turbulence,

the ODT domain is aligned with the wall-normal coordinate. This allows to resolve details of wall-normal transport processes and to capture variable momentum sources [16] and nonhomogeneous electric fields [17] if needed.

The rest of this paper is organized as follows. Section 2 gives an overview of the ODT model formulations for multiphysical wall-bounded flows with an extension to EHD flows. Section 3 collects key results partitioned into two-way coupled EHD Couette flow of dilute electrolytes and one-way coupled EHD-enhanced vertical pipe flow with an inner concentric electrode. Last, in Section 4, we summarize the two case studies.

2. FLOW MODEL FORMULATION

2.1. Overview of the ODT model

In decaying isotropic turbulence seen on a line-of-sight through the turbulent flow (the ODT line), piecewise-transformations on scalar profiles, or triplet maps, induce an increase in the rate of strain, which is characteristic of turbulent eddies. Symbolically, the effect of the triplet map $f(y)$ on an instantaneous profile of the property field $\psi(y)$ is denoted as the transformation $\psi(y) \rightarrow \psi(f(y))$ (in a y-oriented wall-normal domain of a Cartesian coordinate system) [14]. The triplet map microscopically models turbulence phenomenology. It takes a property profile along a selected size l interval, compresses the profile to $l/3$, pastes two copies of this profile to fill again, and flips the central copy to ensure continuity.

Such mapping events are stochastically sampled from unknown distribution functions with the aid of a Poisson process (e.g. [18]). Based on assumed distribution functions for the mapping event size l and location y_0, an efficient thinning-and-rejection method is used for probabilistic selection, in which the rate of implementation of the mappings is calculated in accordance with the local turbulence time-scale (eddy turnover time τ). The latter is obtained from the available energy of the current flow state. Under absence of body forces, the available energy follows from the velocity shear across a size-l interval around location y_0 [14] since the eddy kinetic energy, l^2/τ^2, is proportional to the squared eddy velocity, u_K^2. This scale velocity is modified when eddy-available potential energy and viscous effects are taken into account as detailed below. A factor of proportionality that controls the rate of implemented mapping events is included in the model as a rate parameter, C. The kinetic energy and the rate-of-strain are related by means of an equivalent turbulent diffusivity. The implementation of a given map at fixed turbulent diffusivity then favors the sampling of further mappings. This is the model representation of the turbulent kinetic energy cascade [14].

The set of operations comprising the sampling process and the mappings themselves is known as an eddy event. For decaying isotropic turbulence, there are still two other elements required in the model to complete a consistent dynamic picture of turbulence. One is a mechanism for viscous transport implementation, and the other one is a mechanism for turbulence kinetic energy (TKE) dissipation. Both are a consequence of the viscous momentum flux, which is implemented in a direct way in ODT, by resolving the corresponding numerical fluxes in the 1-D domain after an eddy event has been sampled [14]. This leads to the formulation of a symbolic 1-D partial differential equation (PDE) for a scalar velocity component ψ in ODT. Specialized to Cartesian coordinates in a temporal ODT formulation, this is

$$\frac{\partial \psi}{\partial t} = M - \frac{\partial F(\psi)}{\partial y}. \tag{1}$$

Here, $F(\psi)$ is the model-resolved flux of ψ, e.g., $F(\psi) = -\sigma\,(\partial\psi/\partial y)$ for molecular diffusive gradient fluxes in which σ is a kinematic diffusion coefficient. $M = M(C, y, f(y))$ represents discrete mapping effects that punctuate deterministic evolution of the conserved scalar $\psi(y, t)$ at discrete times. The mapping effects depend on the selected physical mapping $f(y)$, which models turbulent microstructure, and a turbulent eddy rate parameter C. Note that there is an alternative spatial ODT formulation, which is generally treated as a reinterpretation of the parabolic temporal ODT formulation. Details on the spatial formulation are omitted here, but these can be found in other ODT publications [19, 20, 21].

2.2. Model formulation for temporally developing planar wall-bounded flow

The presence of walls introduces a wall-normal-position dependence on the turbulent scalar transport. Close to the wall, viscous transport is dominantly one-dimensional, aligned with the wall-normal direction. Away from the wall, viscous transport may have a more inherent three-dimensional (3-D) character, although the turbulent transport may dominate instead. The transition between the near-wall and away-from-the-wall behavior is controlled in ODT in practical terms by the model parameter Z. The latter defines a viscous penalty by setting a lower limit below which eddy implementation is suppressed [22]. This imposes the dominance of the viscous transport.

Another important dynamical feature in wall-bounded flows is the anisotropy of the velocity statistics. In this context, the role of the turbulent pressure transport is the redistribution of the TKE among the Reynolds stress components [23]. In ODT, this pressure-scrambling effect is modeled with the aid of a kernel function $K(y) = y - f(y)$ [22]. Eddy events are modified to implement mappings, as well as the kernel effects for velocity components, such that $\psi(y) \rightarrow \psi(f(y))$ for a conserved scalar, and $u_i(y) \rightarrow u_i(f(y)) + c_i K(y)$ for the Cartesian velocity components u_i, $i = 1, 2, 3$. As detailed in [22], c_i is a kernel coefficient calculated based on the available energy and a model parameter $\alpha \in [0, 1]$ that controls the efficiency of inter-component kinetic energy

redistribution, such that

$$c_i = \frac{1}{\int_{y_0}^{y_0+l} \rho K^2 \,\mathrm{d}y} \Bigg(u_{i,K} + \mathrm{sgn}\left(u_{i,K}\right) \times \sqrt{(1-\alpha)\, u_{i,K}^2 + \frac{\alpha}{2}\left(u_{j,K}^2 + u_{k,K}^2\right)} \Bigg). \tag{2}$$

Here, $u_{i,K} = \int_{y_0}^{y_0+l} \rho u_i(f(y)) K(y) \,\mathrm{d}y$, where ρ is the uniform density, and (i, j, k) permutations of $(1, 2, 3)$.

The expression for τ, or in this case τ^{-2}, considering $u_{i,K}$ as the available kinetic energy for redistribution, as well as the viscous penalty factor, is based on [22],

$$\tau^{-2} = \frac{2K_0}{\int_{y_0}^{y_0+l} \rho K^2(y) \,\mathrm{d}y} \times \left(\frac{K_0 \sum_i u_{i,K}^2}{2 \int_{y_0}^{y_0+l} \rho K^2(y) \,\mathrm{d}y} - \frac{Z}{2} \frac{\mu_{\mathrm{eddy}}^2}{\rho_{\mathrm{eddy}} l^2} \int_{y_0}^{y_0+l} \mathrm{d}y \right). \tag{3}$$

Here, $K_0 = \left(l^2 \int_{y_0}^{y_0+l} \mathrm{d}y \right)^{-1} \int_{y_0}^{y_0+l} K^2(y) \,\mathrm{d}y$, which converges to $4/27$ in the continuum kernel limit. Additionally, μ_{eddy} and ρ_{eddy} are weighted averages of the dynamic viscosity and the density within the eddy range $[y_0, y_0 + l]$. The density and dynamic viscosity of the fluid are assumed as constants, and of uniform value.

Eddy events are sampled in time on the basis of an acceptance probability P_a, following a Poisson process. The value of P_a for a selected candidate eddy event is calculated as in [14] based on the current flow state. Considering the rate parameter C, the acceptance probability is given by

$$P_a = C \frac{\Delta t_s}{\tau} \frac{1}{l^2 \chi(l, y_0)} < 1. \tag{4}$$

Here, Δt_s is a sampling time interval that needs to be able to resolve any possible eddy turnover time τ. Hence, we select $\Delta t_s < \tau$, which is adapted dynamically in the implementation (see [22]). Furthermore, $\chi(l, y_0)$ is a presumed joint probability density function (JPDF) of eddy event sizes and locations which is used to obtain reasonable candidate events. Oversampling and rejection guarantees that ODT simulation results are insensitive to the exact choice of this JPDF.

After an eddy event is implemented, the deterministic evolution is comparable to that in Eq. (1). With the model resolved viscous flux $F_i(u_i) = -\nu \left(\partial u_i / \partial y\right)$, mapping (M_i) and kernel, as well as momentum sources for the selected component i, we obtain

$$\frac{\partial u_i}{\partial t} = M_i + K_i + S_i + \nu \frac{\partial^2 u_i}{\partial y^2}. \tag{5}$$

This expression incorporates now symbolically the effects of the kernel, and of the energy redistribution among velocity components, by means of the term $K_i(C, Z, \alpha, u, f(y))$. S_i is a source term for the i-th velocity component to be integrated together with the viscous flux, e.g., a fixed pressure gradient (FPG).

2.3. Extension to spatially developing flow with variable density effects

The model formulation presented in Section 2.2 considers the temporal change of scalar profiles along a line-of-sight through the turbulent flow, and is generally referenced as T-ODT. An extension of the model to capture streamwise fluxes of spatially evolving flows (e.g., boundary-layer-type flows) has been presented in [14, 24] and is denoted by S-ODT. More importantly, [24] also present a variable-density formulation for low Mach number flows. In both variable-density T-ODT and S-ODT, a second kernel function $J(y) = |K(y)|$ is introduced in order to facilitate enforcement of physical conservation properties.

For variable-density flow, the various integral expressions above receive the mapped mass density such that $\rho \rightarrow \rho(f(y))$. In variable density T-ODT, the calculation of the available kinetic energy $u_{i,K}$ changes accordingly. The fractions $u_{i,K} \Big/ \int_{y_0}^{y_0+l} \rho K^2(y) \,\mathrm{d}y$ and $u_{i,K}^2 \Big/ \left(2 \int_{y_0}^{y_0+l} \rho K^2(y) \,\mathrm{d}y\right)$ in Eqs. (2) and (3), change to $P_i/(2S)$ or $P_i^2/(4S)$, respectively, where, as in [24],

$$P_i = u_{i,K} - H \int_{y_0}^{y_0+l} [\rho u_i](f(y))\, J(y) \,\mathrm{d}y, \tag{6}$$

$$S = \frac{H^2+1}{2} \int_{y_0}^{y_0+l} \rho(f(y))\, K^2(y) \,\mathrm{d}y - H \int_{y_0}^{y_0+l} \rho(f(y))\, J(y)\, K(y) \,\mathrm{d}y, \tag{7}$$

$$H = \frac{\int_{y_0}^{y_0+l} \rho(f(y))\, K(y) \,\mathrm{d}y}{\int_{y_0}^{y_0+l} \rho(f(y))\, J(y) \,\mathrm{d}y}. \tag{8}$$

In the S-ODT model, the streamwise change of the scalar profiles in the line-of-sight through turbulence is studied. Two variants arise in this case. One is the conservative boundary-layer formulation [24], and another the non-conservative wall-constrained internal-flow formulation [20]. Essentially, in S-ODT, all integrals in Eqs. (6–8), as well as the integrand of $\int_{y_0}^{y_0+l} \rho K^2(y) \,\mathrm{d}y$ in the prefactor in Eq. (3), receive an additional multiplication by $u(f(y))$, the mapped streamwise advecting velocity (see [20, 24] for details). The time-scale τ changes to a streamwise length-scale ξ, and the temporal sampling Δt_s changes to a streamwise sampling Δx_s [24]. Symbolically, the S-ODT equivalent of Eq. (5) has a modified left-hand side and reads

$$u \frac{\partial u_i}{\partial x} = M_i + K_i + S_i + \nu \frac{\partial^2 u_i}{\partial y^2}. \tag{9}$$

2.4. Extensions to cylindrical geometry

An additional model extension, or a generalization of the T-ODT and S-ODT formulations for both Cartesian and cylindrical flows, considering a dynamically adaptive mesh, was presented in [19]. The cylindrical formulation replaces the planar coordinate y for the radial coordinate r, while any line-integral $\int(\cdot)\,\mathrm{d}y$ in all of the equations presented so far, changes to a surface radial integral of the form $\int(\cdot)\,r\,\mathrm{d}r$. Eqs. (1) and (9) also consider a change in the form of the gradient flux. The generalized scalar conservation equation, Eq. (1), becomes

$$\frac{\partial\psi}{\partial t} = M(C,Z,r,f(r)) - \frac{1}{r}\frac{\partial\left(rF(\psi)\right)}{\partial r}, \tag{10}$$

where $F(\psi) = -\sigma\,(\partial\psi/\partial r)$ for the model resolved radial molecular diffusive flux. The specific form of the viscous flux for every velocity component in the cylindrical coordinate system is given in [20].

Note that [20] also introduces a variable-density formulation in which the density is treated as an active scalar, coupled with the evolution of the temperature. The temperature and density states are coupled by the ideal gas law and the divergence condition during the deterministic evolution between subsequent eddy events. This procedure is the equivalent of the enforcement of mass and energy conservation.

2.5. Incorporation of EHD effects

Incorporation of EHD effects is done by the implementation of an appropriate form of the Coulomb forces and by the account of the change in electrostatic potential energy in the ODT eddy sampling procedure. The Coulomb force density is given by $\rho_f E_i$, which is a body force that can be implemented in the ODT momentum equations, e.g., Eq. (9) (in such case, per unit mass density of the fluid). Here, $\rho_f = e(n_+c_+ - n_-c_-)$, is the continuum density of free charges due to positively (+) and negatively (−) charged scalars (i.e., electrochemical species or tracers) with concentration $c_\pm$ and valence $n_\pm$ multiplying the unit charge e on an electron, and by Faraday's law for nonmagnetic media, the electric field is given by $E_i = -\partial\Phi/\partial x_i$, where Φ denotes the total electrostatic potential and $(x_i) = (x,y,z)^{\mathrm{T}}$ the Cartesian coordinates. The concentrations $c_\pm$ obey individual scalar conservation equations similar to Eq. (1), but also other formulations specializing to electron an ion currents are possible. Coulomb forces acting perpendicular to the ODT line are treated straightforwardly as momentum sources [17] that drive turbulence by an increase of velocity shear, whereas those acting along the ODT line affect the eddy rate analogous to gravity [14, 25] as detailed below.

The main goal for the present application cases is capturing leading-order EHD effects that are associated with a modification of the boundary-layer dynamics. Hence, the developed 'minimal flow model' shall be able to capture wall-normal contributions to nonuniversal EHD turbulence circumventing computation of 3-D electric fields. For the stand-alone ODT application to EHD channel and pipe flows considered here, it is assumed that all property fields are not only statistically but also momentarily approximately homogeneous in the lateral directions. Available reference DNS [4] indicate that this assumption is reasonable for the background mean state justifying application to cases with weak fluctuations.

The transfer of electrostatic potential energy to kinetic energy of the flow, or *vice versa*, is the mechanism for implementation of the effects of the work performed by the flow against Coulomb forces by a notional eddy turnover, represented as the instantaneous application of the triplet map $f(y)$ for the wall-normal coordinate y. For the application cases analyzed here, only the effects of a resolved electric field along the ODT line are considered, thus any electrostatic potential energy involved in the formulation is due to the resolved E_2 component of the electric field. Non-resolved components E_1 and E_3, that are zero on average for the cases at hand, are neglected. In that sense, there is no *direct* contribution to the mean kinetic energy by $\rho_f E_i$, given that the modeled effect is simply seen as a modification of the pressure gradient in the line direction. Any EHD-enhancement (or loss), is then a consequence of a modified fluctuating pressure transport, which is modeled in ODT by the kernel kinetic energy redistribution. This is the formulation equivalent of a modification in the Reynolds stress tensor components, which is conceptually comparable to the discussion in [26] on the effect of electric body forces.

The form of the change in electrostatic potential energy, ΔE_{pot}, results from the work performed on the fluid due to the energy release from the pre-mapped to the post-mapped state analogous to buoyancy [14, 25]. ΔE_{pot} has to be added within the square bracket of Eq. (3) for EHD-enhanced sampling. Likewise, it requires a multiplication by $4S$ under the square root of Eq. (2) for potential energy redistribution due to the ODT kernel. Specializing to Cartesian coordinates, we have

$$\Delta E_{\mathrm{pot}} = -\int_{y_0}^{y_0+l} \Big[\rho_f(f(y))\,\Phi(\rho_f(f(y))) - \rho_f(y)\,\Phi(\rho_f(y))\Big]\,\mathrm{d}y. \tag{11}$$

In addition to this equation and the solution of Eq. (5), the 1-D conservation equation for ρ_f, and the Nernst–Planck equation, are solved together with the 1-D representation of Gauss' law for the electric potential, $\partial(\epsilon E_i)/\partial x_i = \rho_f$, as well as Faraday's law, $E_i = -\partial\Phi/\partial x_i$, for a known electric permittivity ϵ and the dynamically resolved component $i = 2$, which is acting along the ODT line and energetically influences turbulent eddy implementations.

The above considerations yield two different types of EHD coupling. In the one-way coupling case, the Nernst–Planck equation reduces to a zero-

divergence condition for the electric current density [27]. This results then in a uniform electric current density along the ODT line (planar Cartesian case). Electroquasistatic fields are calculated before hand and remain fixed during the simulation. In the case of two-way coupling, the Nernst–Planck equations are similar to Eq. (1). An explicit numerical solver is used in which the model resolved instantaneous profile of $\Phi(y)$ is obtained by numerical solution of a 1-D Poisson equation by application of the Thomas algorithm whenever $\rho_f(y)$ has changed.

3. RESULTS

Turbulent electroconvection exhibits different flow regimes that may be categorized by the relative strengths of the Coulomb, viscous, and inertial forces. In addition, the relaxation processes of free electric charges and their coupling to electric fields within the working fluid need to be taken into account. Typical applications are heat transfer enhancement (e.g. [3]) due to weak coupling and flow control (e.g. [4]) due to strong coupling. Below, we begin with the strongly coupled regime for plane Couette flow of a dilute electrolyte. After that, we turn to the weakly coupled regime for vertical pipe flow with an inner concentric electrode.

3.1. Drag enhancement in turbulent EHD Couette flow

In this section we consider a simple model for strongly coupled wall-bounded EHD turbulence in a Couette-type flow of a dilute electrolyte. The flow configuration is sketched in Figure 1 and corresponds with that in [4]. The top wall is moving and held at a different voltage relative to the bottom one. No-slip isopotential zero-flux wall-boundary conditions are prescribed. The T-ODT model set-up uses $C = 10$, $Z = 600$, $\alpha = 2/3$ as in [28]. The electrolytes considered have neutral bulk charge and consist of two identical ionic scalar species $\psi = c_\pm$ with the same valence and mobility but opposite charge. The model-resolved deterministic ion fluxes in accordance with Eq. (1) thus have diffusive and drift contributions so that

$$F_\pm(c_\pm) = -D\frac{\partial c_\pm}{\partial y} \mp \frac{Dc_\pm}{V_T}\frac{\partial \Phi}{\partial y}. \tag{12}$$

In analogy to [4], scaling of the Poisson–Nernst–Planck and Navier–Stokes equations (or the dimensionally reduced ODT representation of them) yields five dimensionless control parameters that define the flow state: the bulk Reynolds number, $\mathrm{Re} = Uh/\nu$, the ionic Schmidt number, $\mathrm{Sc} = \nu/D$, the dimensionless voltage, $\hat{V} = 2V/V_T$, which is varied across the range 0–40, the fixed coupling constant, $\beta = \epsilon V_T^2/(\rho\nu D) = 0.5$, and the fixed normalized Debye layer thickness, $\lambda_D/h = \sqrt{\epsilon V_T/(2\rho c_0 e h^2)} = 0.01$. In these expressions, U denotes the prescribed wall velocity magnitude, h the channel half-height, $V_T = k_B T/e$ the thermal voltage, D the kinematic diffusivity of the ions in the electrolyte, and c_0 the uniform initial concentration of the univalent ion species, respectively, in addition to the other physical parameters introduced above.

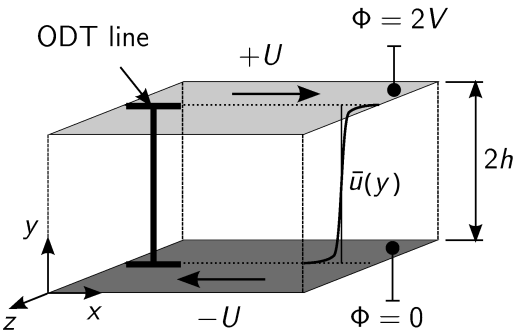

Figure 1. Sketch of the EHD Couette configuration with temporally developing flow. The one-dimensional computational domain (ODT line) is fixed in space and approximately taken as closed system in order to facilitate utilization of ODT as stand-alone tool.

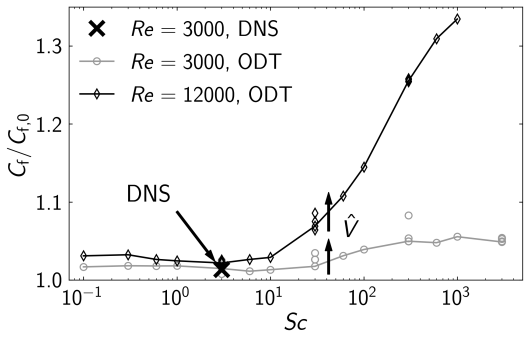

Figure 2. ODT prediction of the turbulent drag enhancement as function of Sc **for various** Re **and** $\hat{V}$ **for fixed** $\beta = 0.5$ **and** $\lambda_\mathrm{D}/h = 0.01$**, as well as fixed ODT model parameters. Connected symbols are for** $\hat{V} = 10$**. For fixed** Sc**, the drad increases with** $\hat{V}$ **(arrows). Reference DNS (×) is from [4].**

Note that Re is the only direct control parameter for the flow regime. $\hat{V}$ is an additional control parameter that parameterizes the internal energy and thus takes the role of an equation of state. The three remaining parameters are related to the electrolyte: Sc gives the ratio of the viscous and scalar (ionic) diffusion coefficients; λ_D/h is a relative measure of electric charge separation that also determines the electric and ionic layers at the electrodes; and β expresses the strength of typical Coulomb forces in units of typical viscous forces. In a concentrated (dilute) ionic liquid (e.g. [29]), dielectric polarization is strong (weak) so that the dielectric permittivity is large (small). For constant electric charge on the ions, the Debye length has to increase (decrease) with β so that we do not consider β a variable control parameter. Instead it is kept fixed at $\beta = 0.5$ [4].

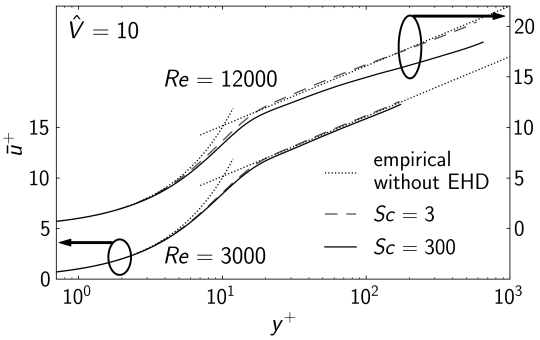

Figure 3. Dimensionless mean velocity defect $\bar{u}^+(y^+)$ for various Re **(vertically shifted) and** Sc **with $\hat{V} = 10$, $\beta = 0.5$, $\lambda_D/h = 0.01$, and fixed ODT model parameters. The empirical law of the wall (dotted; see, e.g., [32]) for hydrodynamic flow without EHD effects is given for orientation.**

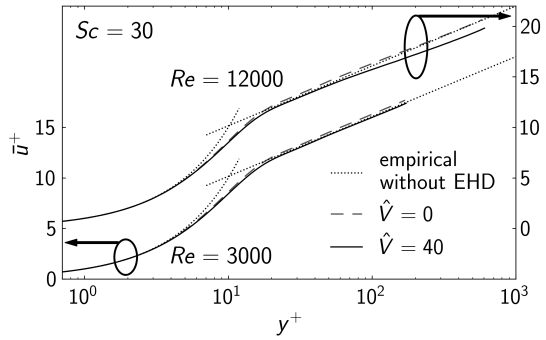

Figure 4. Dimensionless mean velocity defect $\bar{u}^+(y^+)$ for various Re **(vertically shifted) and $\hat{V}$ with** Sc = 30 **analogous to Fig. 3.**

Figure 2 shows the skin friction drag coefficient C_f, which is, for Couette flow, evaluated based on the Reynolds-averaged streamwise velocity profile, $\bar{u}(y) = \overline{u(y,t)}$, as

$$C_f = 2\frac{u_\tau^2}{U^2} \quad \text{with} \quad u_\tau = \sqrt{\nu \left|\frac{\mathrm{d}\bar{u}}{\mathrm{d}y}\right|_{\text{wall}}}. \tag{13}$$

ODT pre-simulations conducted for $\hat{V} = 0$ (absence of EHD effects; not shown here) agree with corresponding purely hydrodynamic reference experiments [30] within 2–5% yielding $C_{f,0} \approx 5.9 \times 10^{-3}$ for Re = 3000 and $C_{f,0} \approx 4.7 \times 10^{-3}$ for Re = 12,000, respectively. This level of agreement is also exhibited by the EHD-enhanced cases at Sc $\simeq$ 1 that only mildly overestimate available reference DNS as shown in Fig. 2. In fact, present ODT results suggest that the turbulent drag is largely insensitive to EHD effects for Sc $\lesssim$ 10.

A significant increase of the turbulent drag can be seen in Fig. 2 for Sc $\gtrsim$ 30 up to $\approx$ 30% for Sc $\geq$ 300 at Re = 12,000 investigated. The magnitude of the effect increases with Sc, Re, and $\hat{V}$. Interestingly, ODT predicts a regime change for the critical Schmidt number $\mathrm{Sc}_{\mathrm{crit}} \simeq 30$, which agrees with an inferred value of $\mathrm{Sc}_{\mathrm{crit}} \sim O(10)$ suggested by [4] based on DNS, albeit it remained elusive if drag increases or decreases due to enhanced coupling. In any case, the ODT prediction suggests that Re must be large enough so that the turbulent scaling cascade is broad enough to be sensibly influenced by EHD effects [31].

Figures 3 and 4 show wall-normal profiles of the dimensionless mean velocity deficit $\bar{u}^+$ over the dimensionless boundary layer coordinate y^+ given by

$$\bar{u}^+ = \frac{|\bar{u} - u_{\text{wall}}|}{u_\tau}, \quad y^+ = \frac{y u_\tau}{\nu}. \tag{14}$$

ODT simulation results are shown for various Re, Sc, and $\hat{V}$ in order to assess which region of the boundary layer is influenced by EHD effects. The hydrodynamic law of the wall (e.g. [32]) is given for orientation for the intersecting viscous sub and log layers, $\bar{u}^+(y^+) = y^+$ for $y^+ < 5$ and $\bar{u}^+(y^+) = \kappa^{-1} \ln y^+ + B$ with $\kappa = 0.39$ and $B = 4.2$ for $y^+ > 30$, respectively. ODT results for $\hat{V} = 0$ (without EHD effects) reproduce the sub and log layer exactly, though with some deficit in the buffer layer at around $y^+ \simeq 30$ when compared with reference data [4] (not shown here for clarity). For finite $\hat{V} \gtrsim O(10)$, boundary layer similarity is broken first in the bulk and outer layer for the ODT simulations with Re = 12,000 and Sc = 30. For further increasing Sc or $\hat{V}$, the entire log region is affected while near-wall similarity is exactly maintained for $y^+ < 10$ and approximately maintained for $10 < y^+ < 100$. Decreasing $\bar{u}^+$ for increasing Sc or $\hat{V}$ reflects the increase in u_τ due to which C_f increases so that the trends in Figs. 3 and 4 are consistent with those in Fig. 2.

Altogether, the results obtained demonstrate that ODT is a lower-order but high-fidelity flow model that is able to predict sensible mean effects in two-way coupled EHD turbulence for at least moderately high Re and Sc. This regime is presently inaccessible to DNS and not faithfully treatable with LES or RANS due to the inapplicability of modeling assumptions involved. A 3-D extension of the stochastic model (e.g., based on ODTLES [33, 34] or AME [35]) and dedicated reference experiments are needed in order to asses the 1-D model prediction in order to clarify its applicability to EHD turbulence.

3.2. Drag enhancement in turbulent EHD vertical pipe flow

In this section we present the results for a one-way coupled EHD pipe flow simulation with an inner concentric electrode, which resembles the experimental electrostatic precipitator (ESP) device of [36]. In the following, we slightly extend a recent comprehensive ODT study [21] on pipe flow ESP, which was conducted by two of the authors and that addresses the application case and modeling in more detail.

A sketch of the flow configuration is shown in

Figure 5. In the ODT simulations, the radially oriented S-ODT line is advected upwards with the flow through the ESP, i.e., this is a spatial ODT formulation. The cylindrical pipe flow is subject to an electric field induced by a (positive) corona discharge originated at the electrode. We only consider one-way coupled electric fields which are not modified by fluctuations in ρ_f, yet equally affect the stochastic random sampling as described in Sec. 2.5. Electric charges (positive ions in air) are assumed as a continuum phase. For details on the generation of the electroquasistatic (EQS) fields and on the general implementation, please refer to [21] or [37]. In addition to the electrostatic potential energy formulation used during eddy events, we also incorporate the Joule heating as a source term to resolve during the deterministic advancement of the temperature equation, see [21, 37].

The objective of the simulations is the evaluation of the friction drag, which is represented in [36] by the Darcy friction factor,

$$f_D = -\frac{4R}{\rho_b U_b^2}\frac{\mathrm{d}\overline{p}}{\mathrm{d}z}, \tag{15}$$

where R is the outer radius of the cylindrical pipe ESP. The mean flow is axially symmetric due to geometry. Hence, $\mathrm{d}\overline{p}/\mathrm{d}z$ can be obtained from the Reynolds-averaged momentum equations, neglecting turbulent correlations of the molecular dynamic viscosity. Indeed, the wall pressure difference, between the outlet and the inlet of a pipe section of finite length Δ, can be calculated as

$$\begin{aligned}\Delta p_w = &\\ &-\frac{2}{R^2}\Delta\left(\int_0^R \langle\rho u_1 u_1\rangle\, r\,\mathrm{d}r - R^2\left(\langle\mu\rangle\frac{\partial\langle u_2\rangle}{\partial r}\right)\Big|_R\right)\\ &-\frac{2}{R^2}\Delta\left(\int_0^R \langle\mu\rangle\frac{\partial\langle u_2\rangle}{\partial r}\, r\,\mathrm{d}r\right) - \frac{2}{R}\int_0^{B_{\mathrm{TS}}}\tau_w \mathrm{d}z\\ &-\frac{J_R}{\beta_f},\end{aligned} \tag{16}$$

where Δ refers to a difference between the location of the outlet (i.e., $z = B_{\mathrm{TS}}$) and the inlet (i.e., $z = 0$) of the simulated device. J_R is the uniform radially weighted electric current density, which is obtained from the voltage-current values given as an input to the simulation, and β_f is the mobility of the free ionic charges. Eq. (16) allows an approximation of the average pressure gradient required for Eq. (15) as $\mathrm{d}\overline{p}/\mathrm{d}z \approx \Delta p_w / B_{\mathrm{TS}}$.

Figure 6 shows the ensemble average of the inlet profiles used in the S-ODT simulations. Two different types of profiles are used based on the geometry of the experimental device. Unlike a traditional pipe flow, the configuration in Fig. 5 includes an internal electrode boundary, which imposes a no-slip condition at the electrode. Note that the sketch provided in Fig. 5 corresponds to the test section of the experimental device, see [36]. The device possesses an entry section, which is supposed to provide

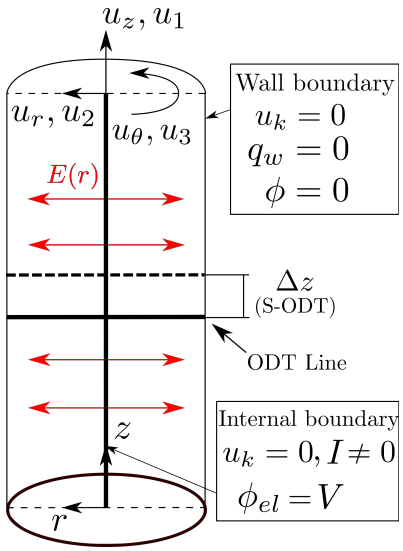

Figure 5. Sketch of the spatially developing EHD vertical pipe flow. The ODT line is advected upwards with the momentary axial velocity during a simulation run. $I \neq 0$ refers to the electrical current needed to inject charge carriers at the axis by a corona discharge.

a fully developing flow at the inlet of the test section. However, a verification of the hydrodynamic entry length L_H (see [39]) performed for one of the Reynolds number cases in [36], $\mathrm{Re}_b = 4000$, shows that L_H is larger than the sum of both device entry and test section lengths. Therefore, we evaluate both fully developed turbulent inlet profiles (generated with a cylindrical T-ODT formulation), as well as equivalent turbulent flow profiles achieving a target developing f_D value. The latter is calculated according to the actual entry and test section lengths, and the formula provided in [39].

Figure 7 shows the results for the evaluation of f_D. The experimental device has radius $R = 1.6 \times 10^{-2}$ m, test section length $B_{\mathrm{TS}} = 1.02$ m, and entry section length $B_{\mathrm{entry}} = 1.59$ m. The inner concentric electrode of the device has radius $R_{\mathrm{elec}} = 1.25 \times 10^{-4}$ m, and length $B_{\mathrm{elec}} = 2.05$ m. The inlet gas flow is assumed at atmospheric pressure with uniform fluid properties (Prandtl number $\mathrm{Pr}_{\mathrm{air}} \simeq 0.71$) at a temperature $T_0 = 300.15$ K. The inlet flow has a bulk velocity $U_b = 2$ m/s, and associated $\mathrm{Re}_b = 4000$. We evaluate three different Masuda numbers: $\mathrm{Md} \approx 1.97 \times 10^4$, 1.27×10^5, and 3.17×10^5, on top of the neutral (no EHD) pipe flow condition. The Masuda number (e.g. [40, 41]) is here defined as $\mathrm{Md} = \epsilon_0\, \Phi_{\mathrm{el}}\, (\Phi_{\mathrm{el}} - \Phi_{\mathrm{on}}) \,/\, (\rho_0 \nu_0^2)$, where ϵ_0 is the vacuum electrical permittivity, ρ_0 and ν_0 the reference mass density and kinematic viscosity of the gas, respectively, $\Phi_{\mathrm{el}} = V$ the electrode operating voltage, and Φ_{on} the corona-discharge onset voltage (both voltages are measured in the experiments) relative to the grounded pipe with voltage $\Phi_{\mathrm{pipe}} = 0$.

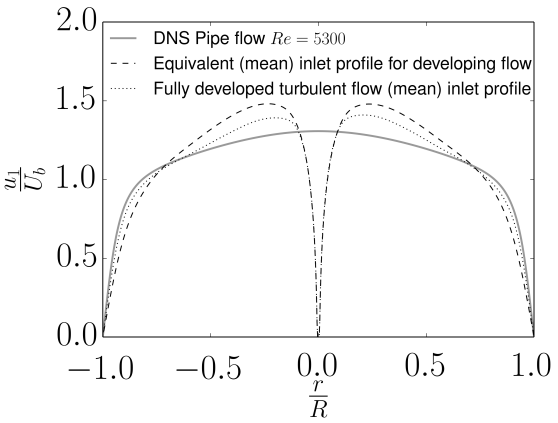

Figure 6. Ensemble average of initial (inlet) conditions for the evaluated Re = 4000 **pipe flow (see description in text). The reference DNS is from [38] and shown for comparison.**

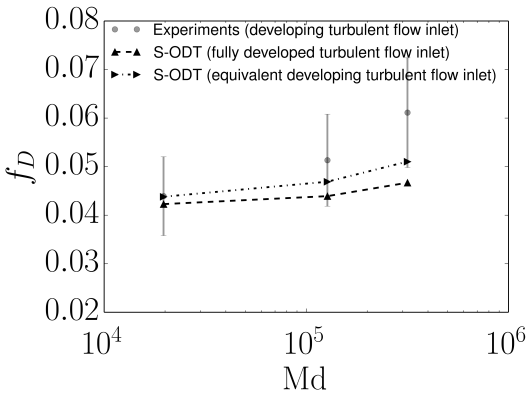

Figure 7. ODT prediction of the enhancement of the Darcy friction factor f_D with the dimensionless EHD body force (Masuda number Md**). Reference experiments are from [36].**

Despite the friction factor evaluation being simply an integral quantity of the flow, the results obtained by the ODT simulations (see Fig. 7) are worth commenting due to the multiphysical nature of the application. This is neither an application that can be easily evaluated by DNS nor treated faithfully with LES or RANS. ODT provides small-scale resolution and dynamical complexity by capturing relevant physical processes at feasible cost. The relative contributions to the pressure gradient according to Eq. (16) are thus model predictions. It has been verified that the largest contribution to $\mathrm{d}\overline{p}/\mathrm{d}z$ is due to the wall shear stress τ_w, and in second place, by the average kinetic energy gradient. The latter is the reason why the utilization of developing flow inlet conditions are necessary to obtain a model prediction that reasonably captures the reference experiments.

4. SUMMARY

EHD turbulence denotes a chaotic flow that is influenced by inertial, viscous, and Coulomb forces across a range of scales. Dynamical processes are nonuniversal and reach down to the Kolmogorov scale [8], η_K, and Batchelor scales [42], $\mathrm{Sc}^{-1/2}\eta_K$, placing a strong burden on numerical simulation and modeling. For EHD turbulence it has been shown recently that the smallest scales for the flow kinetic energy and, hence, also high-Sc transported scalars are not the Kolmogorov and Batchelor scales, but new characteristic EHD scales [7, 13]. These emerging scales can be even smaller than the Kolmogorov and Batchelor scale increasing the cost of numerical simulation of EHD turbulence. In applications, like membraneless redox flow [43] and liquid metal [44] batteries, but alao in wire-plate precipitators [17], EHD flows are confined so that velocity and scalar boundary layers, in particular Debye layers, at domain walls and internal interfaces have to be resolved. Resolution and predictability requirements are addressed here by utilizing the stochastic One-Dimensional Turbulence (ODT) model for regime-overreaching numerical investigation of wall-bounded EHD-enhanced flows.

For two-way coupled EHD Couette flow, ODT predicts EHD-enhanced outer layer turbulence that nonlocally affects the entire turbulent boundary layer. Turbulent drag increases for $\mathrm{Re} \gtrsim 10^4$ and $\mathrm{Sc} \gtrsim 30$ suggesting that charge carriers have to be immobile enough to get stirred down to the turbulent microscales in order to yield strong interactions between hydrodynamics and electrokinetics. Present ODT results suggest that at least $\sqrt{\mathrm{Sc}} \gtrsim 5$ (based on the Batchelor scale) times smaller length scales are needed in the transported electric scalar than in the velocity field.

In one-way coupled vertical EHD pipe flow with a coaxial central electrode, ODT hints at transient effects in a developing turbulent flow. Turbulent drag is enhanced by an EHD-based amplification of the rate of change of the turbulent kinetic energy as revealed by an analysis of the contributions to the pressure drop per unit pipe length. Based on boundary-layer similarity, we assert that the mechanism is at work for the radial direction in the EHD gas-phase pipe flow is similar to that in EHD Couette flow of an ionic liquid.

Altogether, ODT is a self-contained, dimensionally reduced flow model that combines fidelity, predictability, and numerical efficiency. We have demonstrated its applicability to EHD-enhanced flows for future application as sub-filter-scale model.

ACKNOWLEDGEMENTS

H.S., J.M., and M.K. acknowledge support by the European Regional Development Fund (EFRE), Grant no. StaF 23035000. Furthermore, M.K. acknowledges support by the BTU Graduate Research School (Conference Travel Grant).

REFERENCES

[1] Robinson, M., 1968, "Turbulent Gas Flow and Electrostatic Precipitation", *J Air Pollut Control Assoc*, Vol. 18 (4), pp. 235–239.

[2] Laohalertdecha, S., Naphon, P., and Wongwises, S., 2007, "A review of electrohydrodynamic enhancement of heat transfer", *Renewable Sustainable Energy Rev*, Vol. 11 (5), pp. 858–876.

[3] Bacher, C., and Riebel, U., 2021, "Electrohydrodynamically enhanced mass transfer in a wetted-wall column", *Chem Eng Res Des*, Vol. 167, pp. 183–197.

[4] Ostilla-Mónico, R., and Lee, A. A., 2017, "Controlling turbulent drag across electrolytes using electric fields", *Faraday Discuss*, Vol. 199, pp. 159–173.

[5] Shiva Kumar, S., and Himabindu, V., 2019, "Hydrogen production by PEM water electrolysis – A review", *Mater Sci Energy Technol*, Vol. 2 (3), pp. 442–454.

[6] Ju, Y., and Sun, W., 2015, "Plasma assisted combustion: Dynamics and chemistry", *Prog Energy Combust Sci*, Vol. 48, pp. 21–83.

[7] Zhao, W., and Wang, G., 2019, "Cascade of turbulent energy and scalar variance in DC electrokinetic turbulence", *Physica D: Nonlin Phen*, Vol. 399, pp. 42–50.

[8] Kolmogorov, A. N., 1941, "The local structure of turbulence in incompressible viscous fluid for very large Reynolds numbers", *Dok Akademii Nauk SSSR*, Vol. 30, pp. 299–303.

[9] Zhao, W., and Wang, G., 2017, "Scaling of velocity and scalar structure functions in AC electrokinetic turbulence", *Phys Rev E*, Vol. 95 (2), 023111.

[10] Storey, B. D., 2005, "Direct numerical simulation of electrohydrodynamic flow instabilities in microchannels", *Phys D: Nonlin Phen*, Vol. 211 (1), pp. 151–167.

[11] Duraisamy, K., Iaccarino, G., and Xiao, H., 2019, "Turbulence Modeling in the Age of Data", *Annu Rev Fluid Mech*, Vol. 51 (1), pp. 357–377.

[12] Pandey, S., Chu, X., Weigand, B., Laurien, E., and Schumacher, J., 2020, "Relaminarized and recovered turbulence under nonuniform body forces", *Phys Rev Fluids*, Vol. 5, p. 104604.

[13] Zhao, W., and Wang, G., 2021, "A tentative study of the transport of energy and other scalar quantities in forced turbulence driven by $\nabla^n A$-type volume forces", *J Hydrodyn*, Vol. 33 (6), pp. 1271–1281.

[14] Kerstein, A. R., 1999, "One-dimensional turbulence: Model formulation and application to homogeneous turbulence, shear flows, and buoyant stratified flows", *J Fluid Mech*, Vol. 392, pp. 277–334.

[15] Klein, M., Schmidt, H., and Lignell, D. O., 2022, "Stochastic modeling of surface scalar-flux fluctuations in turbulent channel flow using one-dimensional turbulence", *Int J Heat Fluid Flow*, Vol. 93, 108889.

[16] Klein, M., Zenker, C., and Schmidt, H., 2019, "Small-scale resolving simulations of the turbulent mixing in confined planar jets using one-dimensional turbulence", *Chem Eng Sci*, Vol. 204, pp. 186–202.

[17] Medina Méndez, J. A., Schmidt, H., and Riebel, U., 2019, "Towards a one-dimensional turbulence approach for electrohydrodynamic flows", *11th Int. Symp. Turbul. Shear Flow Phen. (TSFP11)*, Southampton, UK, pp. 1–6, ID 265.

[18] Papoulis, A., and Pillai, S. U., 2002, *Probability, Random Variables, and Stochastic Processes*, McGraw-Hill, New York, 4th edn.

[19] Lignell, D., Lansinger, V. B., Medina Méndez, J. A., Klein, M., Kerstein, A. R., Schmidt, H., Fistler, M., and Oevermann, M., 2018, "One-dimensional turbulence modeling for cylindrical and spherical flows: model formulation and application", *Theor Comput Fluid Dyn*, Vol. 32 (4), pp. 495–520.

[20] Medina Méndez, J. A., Klein, M., and Schmidt, H., 2019, "One-Dimensional Turbulence investigation of variable density effects due to heat transfer in a low Mach number internal air flow", *Int J Heat Fluid Flow*, Vol. 80, 108481.

[21] Medina Méndez, J. A., Bacher, C., Riebel, U., and Schmidt, H., 2022, "Electrohydrodynamically-enhanced drag in a vertical pipe-flow with a concentric electrode: A One-Dimensional Turbulence study", *European Journal of Mechanics – B/Fluids*, Vol. 95, pp. 240–251.

[22] Kerstein, A. R., Ashurst, W. T., Wunsch, S., and Nilsen, V., 2001, "One-dimensional turbulence: Vector formulation and application to free-shear flows", *J Fluid Mech*, Vol. 447, pp. 85–109.

[23] Lee, K., Venugopal, V., and Girimaji, S. S., 2016, "Pressure-strain energy redistribution in compressible turbulence: Return-to-isotropy versus kinetic-potential energy equipartition", *Phys Scr*, Vol. 91 (8), 084006.

[24] Ashurst, W. T., and Kerstein, A. R., 2005, "One-dimensional turbulence: Variable-density formulation and application to mixing layers", *Phys Fluids*, Vol. 17 (2), 025107.

[25] Wunsch, S., and Kerstein, A. R., 2005, "A stochastic model for high-Rayleigh-number convection", *J Fluid Mech*, Vol. 528, pp. 173–205.

[26] Davidson, J. H., and Shaughnessy, E. J., 1986, "Turbulence generation by electric body forces", *Exp Fluids*, Vol. 4 (1), pp. 17–26.

[27] Melcher, J. R., 1981, *Continuum electromechanics*, Vol. 2, MIT press Cambridge.

[28] Klein, M., and Schmidt, H., 2020, "Towards a stochastic model for electrohydrodynamic turbulence with application to electrolytes", *Proc Appl Math Mech*, Vol. 20, e202000128.

[29] Lee, A. A., Vella, D., Perkin, S., and Goriely, A., 2015, "Are room-temperature ionic liquids dilute electrolytes?", *J Phys Chem Lett*, Vol. 6 (1), pp. 159–163, pMID: 26263105.

[30] Robertson, J. M., 1959, "On turbulent plane Couette flow", *Sixth Midwestern Conference on Fluid Mechanics*, University of Texas, Austin, pp. 169–182.

[31] Klein, M., and Schmidt, H., 2021, "Investigating Schmidt number effects in turbulent electroconvection using one-dimensional turbulence", *Proc Appl Math Mech*, Vol. 21, e202100147.

[32] Pope, S. B., 2000, *Turbulent Flows*, Cambridge University Press, ISBN 978-0521598866.

[33] Gonzalez-Juez, E., Schmidt, R. C., and Kerstein, A. R., 2011, "ODTLES simulations of wall-bounded flows", *Phys Fluids*, Vol. 23, p. 125102.

[34] Glawe, C., Medina M., J. A., and Schmidt, H., 2018, "IMEX based multi-scale time advancement in ODTLES", *Z Angew Math Mech*, Vol. 98, pp. 1907–1923.

[35] Kerstein, A. R., 2022, "Reduced numerical modeling of turbulent flow with fully resolved time advancement. Part 1. Theory and physical interpretation", *Fluids*, Vol. 7 (2), 76.

[36] Nelson, D. A., Ohadi, M. M., Zia, S., and Whipple, R. L., 1990, "Electrostatic effects on pressure drop in tube flows", *Int J Heat Fluid Flow*, Vol. 11 (4), pp. 298–302.

[37] Medina Mendez, J. A., 2020, "Application of the One-Dimensional Turbulence model to electrohydrodynamically enhanced internally forced convective flows", Ph.D. thesis, Brandenburgische Technische Universität Cottbus-Senftenberg, Cottbus, Germny.

[38] Khoury, G. K. E., Schlatter, P., Noorani, A., Fischer, P. F., Brethouwer, G., and Johansson, A. V., 2013, "Direct Numerical Simulation of Turbulent Pipe Flow at Moderately High Reynolds Numbers", *Flow, Turbul Comb*, Vol. 91 (3), pp. 475–495.

[39] Abraham, J. P., Sparrow, E. M., and Tong, J. C. K., 2008, "Breakdown of Laminar Pipe Flow into Transitional Intermittency and Subsequent Attainment of Fully Developed Intermittent or Turbulent Flow", *Numer Heat Transfer, Part B*, Vol. 54 (2), pp. 103–115.

[40] Masuda, S., and Matsumoto, Y., 1974, "Motion of a microcharge particle within electrohydrodynamic field", *Elect Eng Jpn*, Vol. 94 (6), pp. 20–26.

[41] Masuda, S., and Hosokawa, S., 1995, "Electrostatic precipitation", J.-S. Chang, A. Kelly, and J. Crowley (eds.), *Handbook of electrostatic processes*, Marcel Dekker New York, pp. 441–480.

[42] Batchelor, G. K., 1959, "Small-scale variation of convected quantities like temperature in turbulent fluid. Part 1. General discussion and the case of small conductivity", *J Fluid Mech*, Vol. 5, pp. 113–133.

[43] Ruiz-Martín, D., Moreno-Boza, D., Marcilla, R., Vera, M., and Sánchez-Sanz, M., 2022, "Mathematical modelling of a membrane-less redox flow battery based on immiscible electrolytes", *Appl Math Model*, Vol. 101, pp. 96–110.

[44] Kolesnichenko, I., Frick, P., Eltishchev, V., Mandrykin, S., and Stefani, F., 2020, "Evolution of a strong electrovortex flow in a cylindrical cell", *Phys Rev Fluids*, Vol. 5, p. 123703.

Conference on Modelling Fluid Flow (CMFF'22)
The 18th International Conference on Fluid Flow Technologies
Budapest, Hungary, August 30 -September 2, 2022

EFFECTS OF TIP LEAKAGE VORTEX CAVITATION ON FLOW FIELD UNDER CAVITATION INSTABILITY

Youngkuk YOON[1], Seung Jin SONG[2]

[1] Department of Mechanical Engineering, Seoul National University. 1 Gwanak-ro, Gwanak-gu, Seoul, Korea. Tel.: +82 2 880 1701, E-mail: truesky1218@snu.ac.kr
[2] Corresponding Author, Department of Mechanical Engineering, Seoul National University. 1 Gwanak-ro, Gwanak-gu, Seoul, Korea. Tel.: +82 2 880 1667, E-mail: sjsong@snu.ac.kr

ABSTRACT

Cavitation instabilities induce axial and circumferential vibration, and noise in turbopump inducers. Therefore, the purpose of the present study is to investigate the mechanism of the cavitation instability. Flow field near the two-bladed inducer leading edge under alternate blade cavitation was experimentally investigated by using particle image velocimetry (PIV). It was found that the tip leakage vortex cavitation draws the flow toward its region of collapse and induce negative angle of attack change to the adjacent blade. Also, this cavity-blade interaction was shown to be the main cause of the alternate blade cavitation. It was further shown that this cavity-blade interaction is the strongest when the cavity collapse occurs in the inducer throat area under which the pressure perturbation due to alternate blade cavitation is the largest.

Keywords : cavitation instability, inducer, PIV

NOMENCLATURE

c*	[m]	inducer throat chordwise length
α	[DEG]	incidence angle
$\Delta\alpha$	[DEG]	change in incidence angle
σ	[-]	cavitation number
ϕ	[-]	flow coefficient

1. INTRODUCTION

Inducer cavitation instabilities cause serious noise and vibration which can lead to a failure of propulsion system. Therefore, their types and identification have gained much attention. For example, Tsujimoto et al. [1] observed various cavitation instabilities which occurred in three-bladed inducer and categorized them into local instabilities such as super-synchronous rotating cavitation and global instabilities such as cavitation surge. Also, Cervone et al. [2] experimentally observed a cavitation instability called alternate blade cavitation with two-bladed inducer. These various cavitation instabilities have different frequency and spatial mode characteristics which can be identified via Fourier transformation and circumferential unsteady pressure measurements.

To predict the cavitation instability and to analyse its mechanism, various models have been suggested. Tsujimoto et al. [3] used an actuator disk method to predict rotating cavitation. In the method, quasi-steady lumped parameters such as mass flow gain factor and cavitation compliance are introduced, and it was shown that the mass flow gain factor plays a key role in the cavitation instability. Also, Watanabe et al. [4] and Horiguchi et al. [5] performed stability analysis using singularity method. They predicted various cavitation instabilities including forward and backward propagating rotating cavitation. However, the above methods cannot adequately reflect the 3-D nature of the inducer cavitation, which is mostly composed of tip leakage vortex cavitation (TLVC). Therefore, 3-D numerical approach and experiments have been conducted to investigate the cavitation instability mechanism. Kang et al. [6] conducted 3-D numerical simulation and showed that cavitation instabilities begin to occur when the cavity on a blade interacts with the adjacent blade leading edge. Kim and Song [7] performed an experimental investigation on rotating cavitation and showed that the cavitation decreases the incidence angle of the following blade via particle image velocimetry (PIV) and high-speed visualization. However, even though these studies proposed the mechanism of cavity-blade interaction for the cavitation instability, only few selected cases have been examined in the research.

Therefore, in the present research, the interaction between cavity and the flow field is investigated under various operating condition for two-bladed inducer. PIV was used to quantify the change in velocity field around blade leading edge

and, furthermore, the cavity-blade interaction under alternate blade cavitation.

2. EXPERIMENTAL SETUP

Experiments have been performed with Seoul National University Water Tunnel (SNUWT, Figure 1). SNUWT is composed of a water tank, electric heater, flow meter, booster pump, control valve, and an inducer test section to control flow coefficient and cavitation number independently. Also, a filtration chamber prevents the particle with size larger than 1 micron from entering the test facility. A detailed description of the facility is given in Kim and Song [7].

To determine the cavitation number and to identify cavitation instability, steady and unsteady pressure measurement were conducted. Four pneumatic pressure sensors (Druck PMP 5073) were mounted at inlet and outlet of the inducer, and five unsteady pressure transducers (Kulite HKM-375) were flush-mounted at the inducer inlet casing. Also, for PIV, inducer casing was made of transparent acryl. Litron L 200-15 PIV laser and Phantom v2640 camera were used for the flow field measurement.

A Two-bladed inducer was examined in the present research (Figure 2). Details about the inducer can be found in [8]. All the experiments were conducted under design flow coefficient, and the cavitation number was lowered from non-cavitating condition to near super-cavitating condition which showed severe alternate blade cavitation.

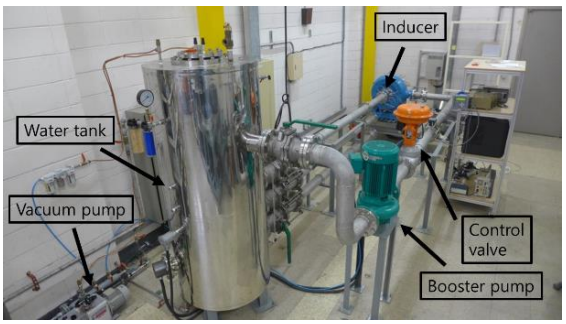

Figure 1. Seoul National University Water Tunnel

3. EXPERIMENT RESULTS AND DISCUSSION

To quantify the blade-cavity interaction, firstly, the flow field near blade leading edge under non-cavitating condition was obtained and averaged over region of interest as shown in Figure 3.

The background image of the Fig. 3 is the raw image under continuous lighting filmed with high-speed camera. Also, the overlapped particle images are taken under pulsed laser lighting and the green vectors are resulting velocity vectors. The red dotted box shows the area over which the velocity vectors are averaged to determine the mean velocity vector near blade leading edge.

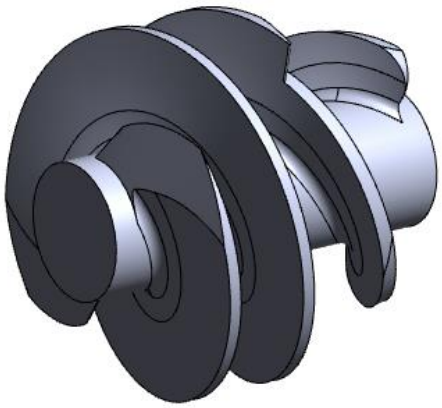

Figure 2. Geometry of the test inducer

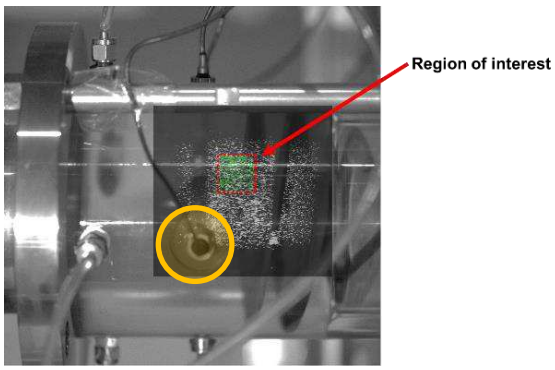

Figure 3. PIV region of interest

Then, at cavitating condition, the same calculation is proceeded and the difference between mean velocity vectors is obtained. Under alternate blade cavitation, leading edges of the two blades are treated separately due to asymmetry of cavity. Finally, these velocity differences are converted to change in angle of attack in rotating frame ($\Delta\alpha$). In the present study, $\Delta\alpha$ was used to represent the cavity-blade interaction.

In the present study, the occurence of the alternate blade cavitation is examined via unsteady pressure measurement at the inducer casing inlet. At 0.15D, where D is the inducer casing diameter, upstream of the inducer tip leading edge, unsteady pressure transducer is flush-mounted, which is highlighted as an orange circle in Fig. 3, and sampled at 2,000 sampes per second. During experiment, inlet pressure, and therefore, cavitation number is decreased. While decreasing the cavitation number, the unsteady pressure signal, whose DC component is filetered, is Fourier-transformed to examine the alternate blade cavitation. Figures 4 and 5 show the typical Fourier transformation results under equal-length cavitation (symmetrical development of the cavitation without cavitaiton instability) and alternate blade caviation. In both cases, peak is observed at normalized frequency of 2, due to the

blade passing frequency of the two-bladed inducer. If the system is under alternate blade cavitation as shown in Fig. 5, normalized frequency of 1 (which equals the shaft rotating frequency) is excited due to the asymmetry of the alternate blade cavitation. Figure 6 visualizes the asymmetry of cavity development under alternate blade cavitation. Both long and short cavities are developed on different blades, and this asymmetric pattern is attached to the blade and remains stationary in the rotating frame. Therefore, not only the blade passing frequency, the shaft rotating frequency is also strongly excited. This peak at normalized frequency of 1 is used to judge whether the alternate bladce cavitaiton occurs and its magnitude can be used to represent the strength of the instability. In the experiment, the magnitude of the Fourier coefficient and the difference between two cavity lengths show the same trend, and thus they were both used to represent the magnitude of the alternate blade cavitation.

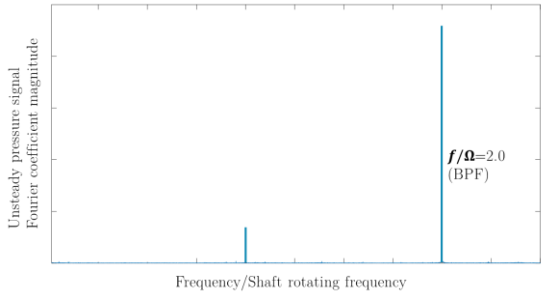

Figure 4. Typical frequency traces under equal-length cavitation

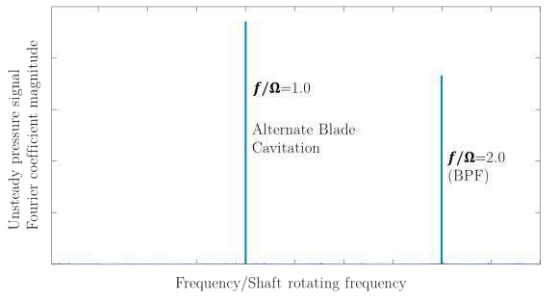

Figure 5. Typical frequency traces under two-bladed inducer alternate blade cavitation

Due to the strong axial flow induced by the collapsing cavity, Δα has negative sign in most of the situation. Figures 7, 8, and 9 shows the flow field vector plot at the PIV region of interest under non-cavitating condition and alternate blade cavitation. In Figs. 8 and 9, both blades 1 & 2 are shown to compare the effect of the larger cavity and the smaller cavity. In Fig. 7, it can be seen that the backflow is developed near the blade leading edge due to adverse pressure gradient of the inducer. In Fig. 8, similar flow structure is developed near the blade 1 leading edge (blades are numbered as 1 and 2, corresponding the blade with larger cavity and smaller cavity under alternate blade cavitation, respectively). Therefore, the smaller cavity induced at blade 2 is not enough developed to interact with the leading edge of the following blade.

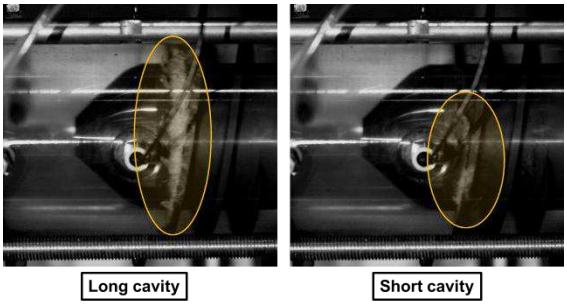

Figure 6. Visualization of alternate blade cavitation

However, as can be seen in Fig. 9, strong axial flow is developed at the blade 2 leading edge. This is due to cavity collapse near the blade 2 leading edge. While the cavity developed at blade 1 is large enough to interact with the following blade leading edge, it collapses due to high pressure downstream and drags the surrounding fluid to create strong axial flow. This axial flow decreases the incidence of the following blade and inhibits the cavity development.

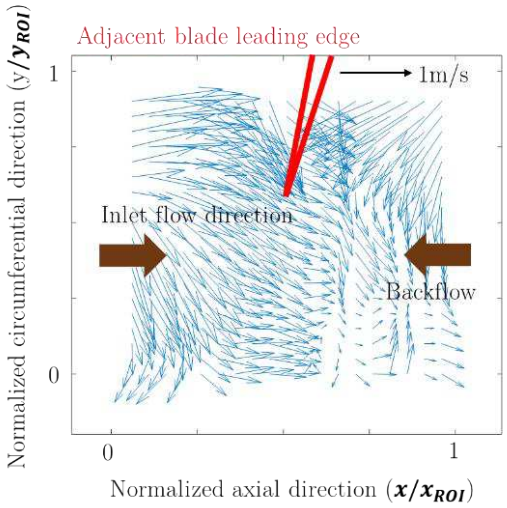

Figure 7. Flow field near blade leading edge at non-cavitating condition

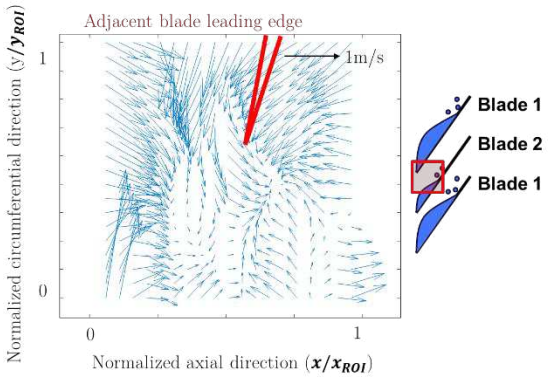

Figure 8. Flow field near blade 1 leading edge under alternate blade cavitation

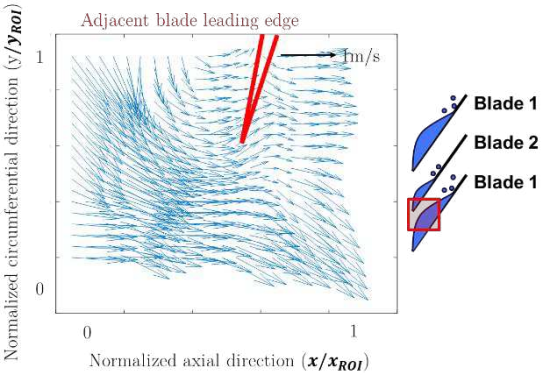

Figure 9. Flow field near blade 2 leading edge under alternate blade cavitation

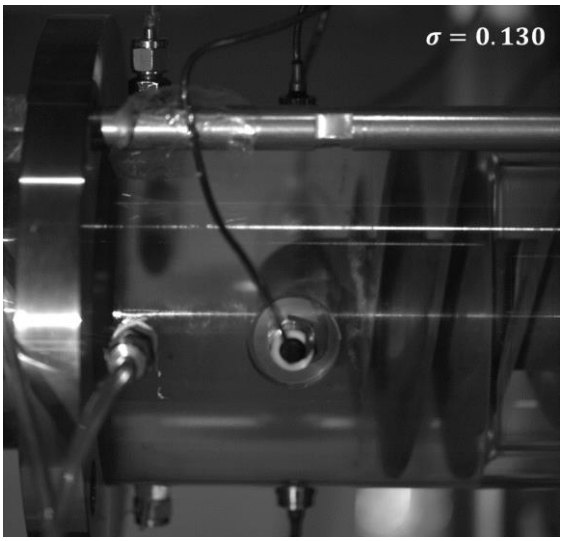

Figure 10. High-speed visualization of the cavity at $\sigma = 0.130$

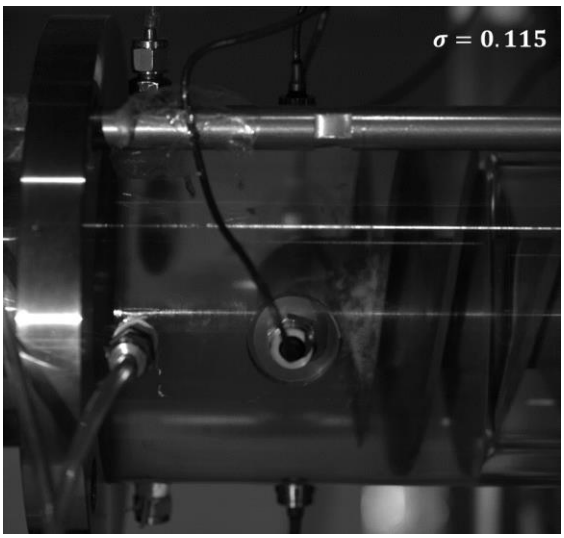

Figure 11. High-speed visualization of the cavity at $\sigma = 0.115$

The existence of the critical cavity length which enables the cavity to interact with the following blade leading edge can also be confirmed with early stages of the cavity development. At $\sigma = 0.115$ and 0.130, normalized cavity length (see Figure 12) is less than 0.5 and the cavity is developed in the form of equal cavity length (same cavity is developed at both blades). Figures 10 and 11 show the visualization of the cavity in both cases. From the figures, it can be seen that the cavities are not enough to reach the following blade leading edge and no impact is exerted on the incidence angle. With respect to the following blade, those cavities are the same with non-cavitating condition.

Fig. 12 summarize the experiment results under various cavitation numbers. The abscissa is the cavitation number which is defined as follows:

$$\sigma = \frac{p_{inlet} - p_v}{\frac{1}{2}\rho U^2}. \quad (1)$$

If the cavitation number decreases, the difference between the inlet pressure and the vapor pressure decreases, and the system becomes more susceptible to cavitation. The ordinate is the normalized cavity length, which is the length of the TLVC normalized by the inducer throat chord length as shown in the right inset of Fig. 12. As the cavitation number gets lower than 0.11, the cavity length graph bifurcates and shows maximum difference at around $\sigma = 0.08$. This represents the alternate blade cavitation region where the two blades have different cavity lengths. The longer cavity length is represented with red line and the shorter one is with the blue line. Fig. 12 shows that, after the alternate blade cavitation onset, the magnitude (or the difference between two cavity

lengths) increases until certain cavitation number and then again decreases.

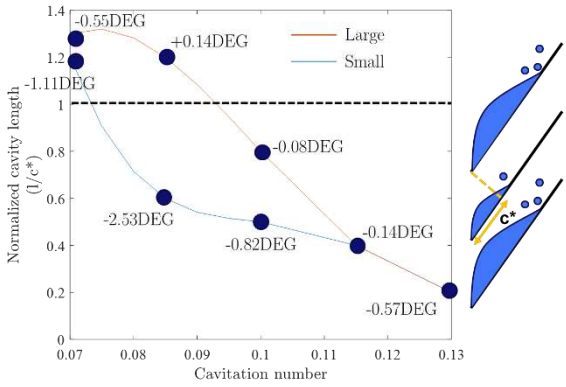

Figure 12. Cavity length and change in angle of attack under various cavitation number

Also shown in Fig. 12 as dark blue dots and captions are $\Delta\alpha$s at the given cavitation number and blade. Firstly, it can be seen in Figs. 8 and 9 that the alternate blade cavitation occurs due to uneven incidence for each blade. While the cavity on the red branch is large enough to interact with the leading edge of the following blade, it induces strong axial flow and, therefore, decreases the incidence angle of the following blade. Thus, the blade loading of the following blade, which is denoted as the blue branch, decreases and TLVC extent also decreases. Furthermore, by comparing the measured $\Delta\alpha$s at various cavitation number, changing magnitude of the alternate blade cavitation (whose trend is also observed by Huang et al. [9]) can be explained.

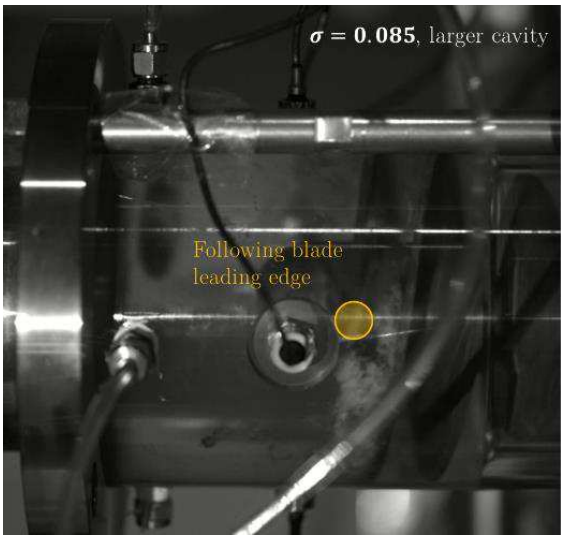

Figure 13. Visualization of the cavity at $\sigma = 0.085$

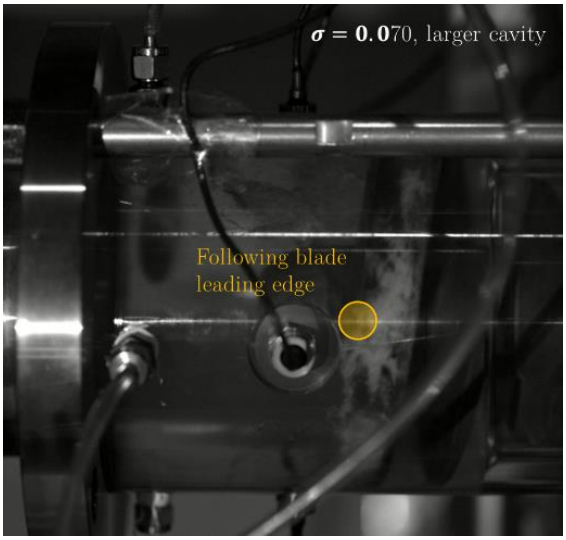

Figure 14. Visualization of the cavity at $\sigma = 0.070$

The magnitude of the alternate blade cavitation is the largest when the normalized length of the larger cavity is around 1. Before and after that point, decrease in angle of attack due to the larger cavity (which is $\Delta\alpha$ denoted on the blue branch) becomes smaller. Hence, it can be said that the magnitude of $\Delta\alpha$ is maximized when the normalized cavity length is near 1 ($l \approx c^*$). As the cavitation number decreases, the cavity length will increase, and the resulting magnitude of $\Delta\alpha$ and alternate blade cavitation increases until the cavity length reaches c*. After that, $\Delta\alpha$, and the alternate blade cavitation, will decrease.

Physically, maximized $\Delta\alpha$ at $l \approx c^*$ can be explained by the position of cavity collapse. While the collapse of the cavity bubble at the TLVC trailing edge induces large axial flow and decreases the incidence of the following blade, the position of the TLVC trailing edge plays a key role as proposed by Kang et al. [6]. Therefore, if the position of the cavity collapse coincides with the leading edge of the following blade, $\Delta\alpha$ is maximized and the alternate blade cavitation becomes the strongest. This can be more clearly seen in the Figures 13 and 14. Fig. 13 shows the larger cavity at $\sigma = 0.085$, and Fig. 14 shows larger cavity at $\sigma = 0.070$. At $\sigma = 0.085$, most of the cavities collapse near the leading edge of the following blade. However, at $\sigma = 0.070$, TLVC further extends until l/c*=1.3 and much less cavities collapse near the leading edge of the following blade. This reduces the induced axial flow and, accordingly, the incidence angle of the following blade less decreased.

4. SUMMARY AND CONCLUSIONS

In this study, the interaction between cavity and the following blade is experimentally investigated and quantified using particle image velocimetry and high-speed visualization of cavity. It was shown that

the collapse of the TLVC decreases the incidence of the following blade and, therefore, decreases its TLVC extent. Due to this interaction, alternate blade cavitation occurs. Also, the observed trend of alternate blade cavitation magnitude is explained by $\Delta\alpha$s at various cavitation number. It can be seen that the cavity-blade interaction is maximized when the normalized cavity length is around 1 and cavity collapses near the following blade leading edge, also when the alternate blade cavitation is the strongest.

ACKNOWLEDGEMENTS

This work was supported by BK21+ Program and Seoul National University Institute of Advanced Machines and Design (SNU-IAMD).

REFERENCES

[1] Tsujimoto, Y., Yoshida, Y., Maekawa, Y., Watanabe, S., and Hashimoto, T., 1997, "Observations of Oscillating Cavitation of an Inducer", *ASME J Fluids Engineering*, Vol. 119, pp. 775-781.

[2] Cervone, A., Bramanti, C., Rapposelli, E., Torre, L., and d'Agostino, L., 2006, "Experimental Characterization of Cavitation Instabilities in a Two-Bladed Axial Inducer", *AIAA J Propulsion and Power*, Vol. 22, pp. 1389-1395.

[3] Tsujimoto, Y., Kamijo, K., and Yoshida, Y., 1993, "A Theoretical Analysis of Rotating Cavitation in Inducers", *ASME J Fluids Engineering*, Vol. 115, pp. 135-141.

[4] Watanabe, S., Sato, K., Tsujimoto, Y., and Kamijo, K., 1999, "Analysis of Rotating Cavitation in a Finite Pitch Cascade Using a Closed Cavity Model and a Singularity Method", *ASME J Fluids Engineering*, Vol. 121, pp. 834-840.

[5] Horiguchi, H., Watanabe, S., and Tsujimoto, Y., 2000, "A Linear Stability Analysis of Cavitation in a Finite Blade Count Impeller", *ASME J Fluids Engineering*, Vol. 122, pp. 798-805.

[6] Kang, D., Yonezawa, K., Horiguchi, H., Kawata, Y., and Tsujimoto, Y., 2009, "Cause of Caviation Instabilities in Three Dimensional Inducer", *Int J Fluid Machinery and Systems*, Vol. 2, pp. 206-214.

[7] Kim, J., and Song, S. J., 2019, "Visualization of Rotating Cavitation Oscillation Mechanism in a Turbopump Inducer", *ASME J Fluids Engineering,* Vol. 141, pp. 091103.

[8] Yoon, Y., Kim, J., and Song, S. J., 2022, "Identification of Inducer Cavitation Instabilities Using High-Speed Visualization", *Experimental Thermal and Fluid Science*, Vol. 132, pp. 110548.

[9] Huang, J.-D., Aoki, M., and Zhang, J.-T., "Alternate Blade Cavitation on Inducer", *JSME International J Series B Fluids and Thermal Engineering,* Vol. 41, pp. 1-6.

Conference on Modelling Fluid Flow (CMFF'22)
The 18th International Conference on Fluid Flow Technologies
Budapest, Hungary, August 30-September 2, 2022

Numerical study of vortex-induced vibration of a circular cylinder subject to oscillatory flow at high Keulegan-Carpenter numbers

Dániel DOROGI[1], Efstathios KONSTANTINIDIS[2], László BARANYI[3]

[1] Corresponding Author. Department of Fluid and Heat Engineering, Institute of Energy Engineering and Chemical Machinery, Faculty of Mechanical Engineering and Informatics, University of Miskolc. H-3515 Miskolc-Egyetemváros. Tel.: +36 46 565 111, E-mail: daniel.dorogi@uni-miskolc.hu
[2] Department of Mechanical Engineering, University of Western Macedonia, Greece. E-mail: ekonstantinidis@uowm.gr
[3] Department of Fluid and Heat Engineering, Institute of Energy Engineering and Chemical Machinery, Faculty of Mechanical Engineering and Informatics, University of Miskolc, Hungary. E-mail: laszlo.baranyi@uni-miskolc.hu

ABSTRACT

This work investigates the vortex-induced vibration of a circular cylinder placed perpendicular to a uniform oscillatory flow at the Keulegan-Carpenter number values of 500, i.e. in the drag-dominated regime. The cylinder was allowed to vibrate in the direction transverse to the oscillatory flow. The non-dimensional forms of the governing equations for fluid flow and cylinder motion were solved in a non-inertial reference frame using an in-house finite-difference code. Simulations were conducted for a system with mass ratio of 2 with zero structural damping. The maximum Reynolds number and maximum reduced velocity are set to 150 and 5, respectively. It is shown that the cylinder response comprises high-frequency vortex-induced vibrations and low-frequency wave-induced oscillations. Plots of the phase-averaged vibration amplitude and fluid force as functions of the time-dependent reduced velocity display strong hysteresis. It is further shown that the phase-averaged amplitude over the deceleration stage follows quite closely the path traced by data points from steady-flow tests. However, the fluid forces that drive the motion are markedly different over a large part of the time-dependent reduced velocity domain for oscillatory and steady flows.

Keywords: drag-dominated range, Keulegan-Carpenter number, oscillatory flow, vortex-induced vibration

NOMENCLATURE

$\mathcal{D}$	[−]	dilation, non-dimensionalised by U_m/D
A^*	[−]	vibration amplitude non-dimensionalised by D
$C_{x,y}$	[−]	magnitudes of non-dimensional fluid forces in x and y directions
D	[m]	cylinder diameter
$F^*_{x,y}$	[−]	fluid forces in x and y directions non-dimensionalised by $\frac{1}{2}\rho U_m^2 D$
K_C	[−]	Keulegan-Carpenter number, $K_C = U_m/(f_o D)$
R	[−]	radius non-dimensionalised by D
Re	[−]	Reynolds number, $U_m D/\nu$
U	[−]	velocity of the uniform stream non-dimensionalised by U_m
U_m	[−]	magnitude of the stream velocity
U_r	[−]	reduced velocity, $U_m/(f_n D)$
c	[kg/s]	structural damping
f_n	[s^{-1}]	natural frequency of the cylinder in vacuum
f_o	[s^{-1}]	frequency of the uniform stream
f^*_y	[−]	vibration frequency non-dimensionalised by U_m/d
$f^*_{C_{x,y}}$	[−]	frequencies of fluid forces in x and y directions non-dimensionalised by U_m/d
k	[N/m]	spring stiffness
m	[kg/m]	mass of the cylinder per unit length
p	[−]	pressure non-dimensionalised by ρU_m^2
t	[−]	time non-dimensionalised by D/U_m
$u,\ v$	[−]	velocities in x and y directions non-dimensionalised by U_m
$x,\ y$	[−]	Cartesian coordinates non-dimensionalised by D
y_c	[−]	cylinder displacement non-dimensionalised by D

μ	[−]	mass ratio, $4m/(\rho D^2\pi)$
ν	[m^2/s]	kinematic viscosity of the fluid
ρ	[kg/m^3]	fluid density
ζ	[−]	structural damping ratio, $c/(2\sqrt{km})$

Subscripts and Superscripts

1, 2	on the cylinder surface, at the outer boundary of the domain
c	refers to cylinder response (y_c)
x, y	streamwise, transverse
$\widetilde{\dots}$	dimensional quantity ($\widetilde{U}$)

1. INTRODUCTION

Vortex-induced vibration (VIV) of bluff structural elements is a practical fluid-structure interaction (FSI) mechanism playing a significant role for example in offshore platforms, risers, offshore wind turbines or high slender buildings. Due to its importance, this phenomenon has been thoroughly investigated in the past decades using both laboratory experiments and numerical simulations; the most significant review papers are Bearman [1, 2], Sarpkaya [3] and Williamson and Govardhan [4].

The majority of the FSI researches have investigated the case of an elastically supported circular cylinder placed into a uniform free stream [5, 6, 7]. However, engineering structures are often exposed to waves; FSI studies on waves include [8, 9, 10]. Waves are usually modelled using a uniform oscillatory flow, where the velocity of the stream can be written as $\widetilde{U}(t) = U_m \sin(2\pi f_o t)$, where t is the time, U_m and f_o are the magnitude and frequency of the stream velocity, respectively. The Keulegan-Carpenter number $K_C = U_m/(f_o D)$ and the Reynolds number $Re = U_m D/\nu$ are the dimensionless groups used to characterise the incoming stream, where D is the cylinder diameter and ν is the kinematic viscosity of the fluid.

In VIV, generally the cylinder can move in two directions, i.e. streamwise with and transverse to the free stream [10, 11]. However, researchers often consider one-degree-of-freedom cylinder motion. Williamson [8] constructed an analytical approach to predict streamwise-only VIV of a circular cylinder. The author solved the equation of cylinder motion together with Morison *et al*. [12]'s formulation for the streamwise fluid force. Williamson [8] found that the predicted response compares well with experimental results. Anagnostopulos and Illiadis [13] and Taheri *et al*. [14] investigated a similar problem using two-dimensional (2D) computational fluid dynamics (CFD) simulations.

Transverse-only vortex-induced vibrations have been found to be more important, because the oscillation amplitudes are higher in this directions than those in the streamwise direction. Sumer and Fredsøe [9] experimentally investigated the VIV of a circular cylinder in the Keulegan-Carpenter number range of $K_C = 5 - 100$. They showed that when increasing K_C above 5 the cylinder undergoes high-amplitude vibrations with the amplitude depending on the value of the reduced velocity $U_r = U_m/(f_n D)$, where f_n is the natural frequency of the cylinder in vacuum. In contrast to the VIV response in a uniform free stream, lock-in/synchronisation occurs over several 'sections' in the U_r domain. McConnel and Jiao [15] observed similar characteristics in their experimental results. Zhao *et al*. [16] carried out extensive 2D simulations for $K_C = 10$ and 20. They found that in the reduced velocity domain of $U_r < 8$ the frequency spectra of cylinder displacement contains one dominant peak at twice the flow oscillation frequency. However, above $U_r = 8$ Zhao *et al*. [16] identified multiple peaks, which are the whole number multiples of the frequency of the main stream. Zhao *et al*. [17] found similar features, i.e. multiple frequency peaks in the cylinder response, using three-dimensional computations.

The studies mentioned above have been limited to low Keulegan-Carpenter number values, i.e. $K_C < 100$; no results exist at high K_C values. In this study transverse-only VIV of a circular cylinder placed into an oscillatory flow is investigated at the high Keulegan-Carpenter number value of $K_C = 500$ by means of 2D finite-difference computations. The maximum reduced velocity, maximum Reynolds number, mass ratio and structural damping ratio values are fixed at $U_r = 5, Re = 150, \mu = 2$ and $\zeta = 0$, respectively. Since the difference between K_C and U_r is large, the cylinder response might be expected to be strongly modulated. The main objective of this study is to develop a methodology to analyse the oscillation amplitude and frequency and fluid forces acting on the cylinder.

2. METHODOLOGY

The two-dimensional flow of the Newtonian incompressible constant property fluid is governed by the two components of the Navier-Stokes equations written in a non-inertial reference frame attached to the vibrating cylinder, the continuity equation and the pressure Poisson equation. The non-dimensional forms of these equations are written as follows:

$$\frac{\partial u}{\partial t} + u\frac{\partial u}{\partial x} + v\frac{\partial u}{\partial y} = -\frac{\partial p}{\partial x} + \frac{1}{Re}\nabla^2 u + \dot{U}, \tag{1}$$

$$\frac{\partial v}{\partial t} + u\frac{\partial v}{\partial x} + v\frac{\partial v}{\partial y} = -\frac{\partial p}{\partial y} + \frac{1}{Re}\nabla^2 v - \ddot{y}_c, \tag{2}$$

$$\mathcal{D} = \frac{\partial u}{\partial x} + \frac{\partial v}{\partial y} = 0, \tag{3}$$

$$\nabla^2 p = 2\left(\frac{\partial u}{\partial x}\frac{\partial v}{\partial y} - \frac{\partial u}{\partial y}\frac{\partial v}{\partial x}\right) - \frac{\partial \mathcal{D}}{\partial t}, \tag{4}$$

where t is the dimensionless time, x and y are the non-dimensional Cartesian coordinates in the streamwise and transverse directions, respectively, u and v are the non-dimensional streamwise and transverse velocity components of the fluid, p is the non-

dimensional pressure, $\mathcal{D}$ is the dilation and $\ddot{y}_c$ is the non-dimensional acceleration of the cylinder in the transverse direction. In this study the cylinder diameter D and the magnitude of the stream velocity U_m are used as length and velocity scales, respectively. Although the dilation is zero by Eq. (3), $\partial\mathcal{D}/\partial t$ is kept in Eq. (4) to reduce numerical errors [18]. In Eq. (1) $U = \sin(2\pi t/K_C)$ is the non-dimensional velocity of the fluid stream, where $K_C = U_m/(f_o D)$ is the Keulegan-Carpenter number based on the flow oscillation frequency f_o. In Eqs. (1) and (2) $Re = U_m D/\nu$ is the maximum Reynolds number, where ν is the kinematic viscosity of the fluid, and in these equations the overdot represents differentiation with respect to time. The transverse acceleration component of the cylinder in Eq. (2) is obtained by solving Newton's second law of cylinder motion. This equation in non-dimensional form is written as follows:

$$\ddot{y}_c + \frac{4\pi\zeta}{U_r}\dot{y}_c + \left(\frac{2\pi}{U_r}\right)^2 y_c = \frac{2}{\pi\mu}F_y^*(t), \qquad (5)$$

where y_c, $\dot{y}_c$ and $\ddot{y}_c$ are the non-dimensional cylinder displacement, velocity and acceleration, respectively, $U_r = U_m/(f_n D)$ is the maximum reduced velocity, where f_n is the natural frequency of the cylinder in vacuum, ζ and μ are the structural damping ratio and the mass ratio, respectively, and $F_y^*(t)$ is the non-dimensional sectional fluid force acting on the cylinder.

The physical domain of the computations is considered to be an area confined between two concentric circles: R_1 is the non-dimensional radius of the cylinder surface, while R_2 is that of the outer surface. On $R = R_1$ no-slip boundary conditions are applied for u and v, while for the fluid pressure a Neumann-type condition is used. On $R = R_2$, the pressure gradient is set to zero, while the two velocity components are chosen to be $u = U(t)$ and $v = -\dot{y}_c(t)$.

In order to achieve high degree of accuracy the physical domain is transformed to a computational domain on which an equidistant grid is generated; the mesh is boundary-fitted on the physical plane [19]. The transformed governing equations with boundary conditions are solved using an in-house CFD code based on the finite difference method [19, 7, 20]. The spatial derivatives are approximated using fourth-order accurate central difference schemes except for the convective terms, which are discretised by applying a modified third-order upwind difference scheme. Eqs. (1) and (2) are integrated with respect to time using the explicit Euler approach, while the fourth-order explicit Runge-Kutta method is implemented for the time discretisation of Eq. (5). The successive over-relaxation method is used to solve the linear system resulting from the discretisation of the pressure Poisson equation while satisfying the continuity equation in each time step.

The number of grid points in the peripheral and radial directions are set to 361 and 314, respectively,

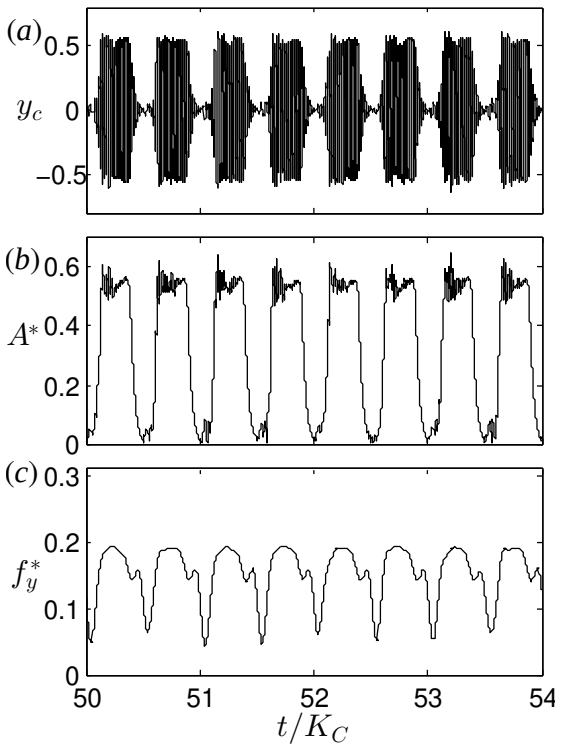

Figure 1. Time histories of (a) cylinder displacement y_c, (b) amplitude A^* and (c) frequency f_y^* of cylinder oscillation

the radius ratio R_2/R_1 is chosen to be 240 and the dimensionless time step is fixed at $\Delta t = 0.0005$. The currently applied CFD code has been extensively validated against data in the literature for stationary cylinder, forced cylinder oscillation and vortex-induced vibration cases [19, 7, 20].

3. RESULTS AND DISCUSSION

In this study two-dimensional CFD computations are carried out in order to investigate vortex-induced vibrations of a circular cylinder placed into the high-Keulegan-Carpenter-number (and thus slowly-varying) oscillatory flow of $K_C = 500$. The maximum Reynolds number, maximum reduced velocity and mass and structural damping ratio values are fixed at $Re = 150$, $U_r = 5$ $\mu = 2$ and $\zeta = 0$, respectively. Figure 1 shows the non-dimensional cylinder displacement y_c and its amplitude A^* and frequency f_y^* against time. Note that time histories in this and subsequent figures correspond to the time interval $t/K_C = 50 - 54$, i.e. over 4 periods of the oscillatory flow. The cylinder displacement displays intervals of high-amplitude between intervals of low-oscillation amplitude in each flow cycle (see Fig. 1a). By applying the Hilbert transform [6] to the displacement signal it is possible to obtain the time-dependent amplitude and frequency of the cylinder, shown in Fig. 1b and 1c, respectively. As can be seen in Fig. 1b the time-dependent amplitude varies approximately between zero and 0.6. The maximum value is close

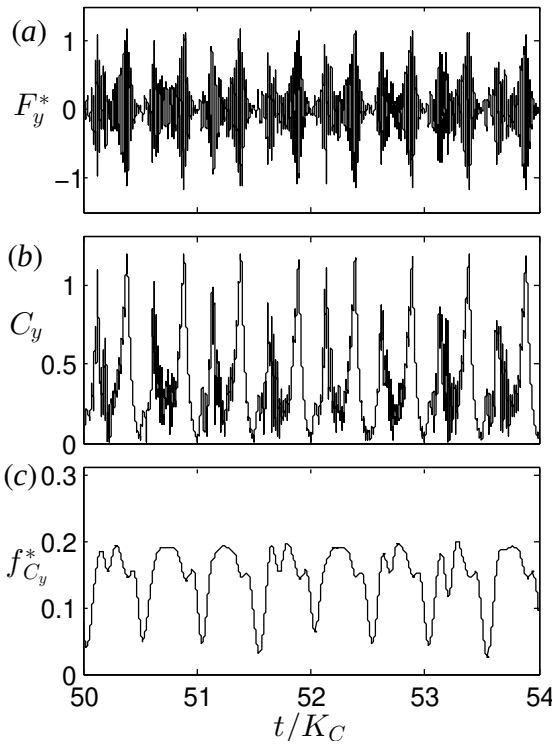

Figure 2. Time histories of (*a*) transverse fluid force F_y^*, (*b*) and magnitude C_y and (*c*) frequency $f^*_{C_y}$ of F_y^*

to the peak amplitude of transverse response in uniform free stream at low Reynolds numbers in the unsteady laminar regime [21, 22]. As shown in Fig. 1*c*, the time-dependent vibration frequency varies from a minimum value of approximately 0.05 up to 0.20. The maximum value (i.e. 0.2) corresponds to the reciprocal of the maximum reduced velocity U_r^{-1}. It is interesting to note that neither $A^*(t)$ nor $f_y^*(t)$ displays smooth harmonic-like variations (see discussion of phase-averaging below).

Figure 2 shows the time histories of the transverse fluid force F_y^*, i.e. the motion-driving force, and the magnitude C_y and frequency $f^*_{C_y}$ of the force signal obtained using the Hilbert transform. As can be seen Fig. 2*b*, the time-dependent magnitude of F_y^* fluctuates between a minimum value of approximately zero and a maximum value slightly above 1.0. It might be noted that fluctuations in the time-dependent force magnitude occur at four times the frequency of flow oscillation due to peaking twice each time the flow speed increases either in the positive or the negative direction. Despite being essentially periodic, fluctuations in $C_y(t)$ have rather stochastic cycle-to-cycle variations, which are also evident in the time history of its frequency $f^*_{C_y}(t)$ (see Fig. 2*c*).

Figure 3 shows the frequency of the driving force against the frequency of cylinder vibration in the time interval $50K_C \leq t \leq 54K_C$, i.e. the period analysed

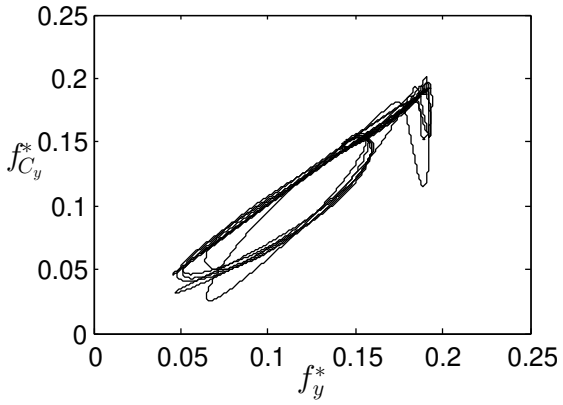

Figure 3. Time-dependent frequency of cylinder vibration against the frequency of transverse fluid force within the non-dimensional time interval $50K_C \leq t \leq 54K_C$

in Figs. 1 and 2. It can be seen that the driving force and the cylinder have the same frequency over part of the flow oscillation. However, $f^*_{C_y}(t)$ and $f_y^*(t)$ are different over another part of the flow oscillation; the elliptical-like trajectory suggests that there is a definite relationship between them. In addition, there also exist deviations from the elliptical-like trajectory, which might be attributed to the stochastic cycle-to-cycle variations in the behaviour of the system.

Figure 4*a* shows the time history of the fluid force acting in the direction of the main flow. The streamwise fluid force F_x^* displays fluctuations in the period of flow oscillation and overriding high-frequency fluctuations that appear at intervals near its peak magnitude. The low- and high-frequency fluctuations are separated from each other using a low-pass filter in order to analyse the streamwise force more thoroughly. The low-frequency force component F^*_{xf} shown in Fig. 4*b* displays very repeatable oscillations. This component can be modelled very accurately using Morison *et al.*'s equation [12] but this is not explored further here.

The high-frequency component is obtained by subtracting the low-frequency component from the total force $F_x^* - F^*_{xf}$ and the resulting signal is shown in Fig. 4*c* (black line). Then, the time-dependent magnitude $C_x(t)$ and frequency $f^*_{C_x}(t)$ of the streamwise force are obtained by applying the Hilbert transform to the high-frequency signal. The resulting time histories are plotted in Fig. 4*c* (red line) and 4*d*, respectively. It can be seen in Fig. 4*c* that $C_x(t)$ displays a variation similar to that of $A^*(t)$, i.e. intervals of high amplitudes interspersed intervals of low-amplitude. As can be seen in Fig. 4*d*, the maximum of $f^*_{C_x}$ is approximately 0.4, which is roughly the twice the peaks of f_y^* or $f^*_{C_y}$ (see Figs. 1*c* and 2*c*). This finding is consistent with the results from VIV in uniform free stream; in those cases the frequency of the F_x^* is always twice the frequency of F_y^* [21].

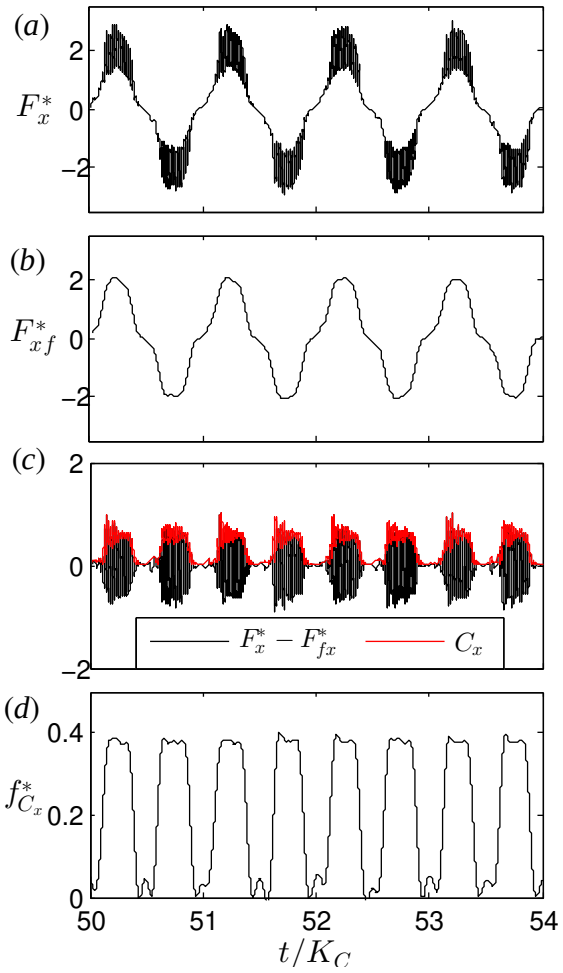

Figure 4. Time histories of (*a*) streamwise fluid force F_x^*, (*b*) low-frequency component of force F_{xf}^*, (*c*) high-frequency component of F_x^* and its magnitude C_x and (*d*) frequency of the high-frequency force component $f_{C_x}^*$

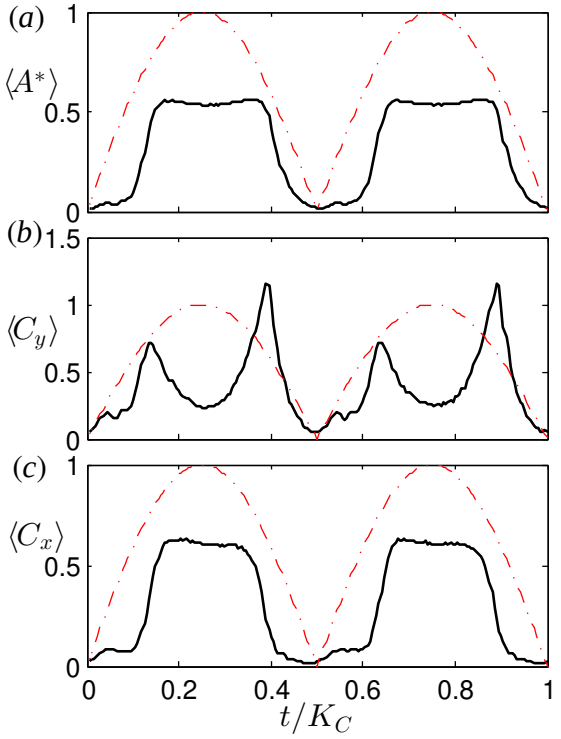

Figure 5. Phase-averaged (*a*) amplitude of cylinder displacement, (*b*) transverse fluid force and (*c*) streamwise fluid force. The red dashed line represents $|U(t)|$.

In addition, it is interesting to note that the minimum value of $f_{C_x}^*$ is approximately zero; this contrasts with the variation of $f_{C_y}^*$ (see Fig. 2*c*).

The displacement and force signals over 100 flow cycles were phase averaged using 200 non-overlapping bins, each containing 5000 data points. Phase-averaged results for the response amplitude $\langle A^* \rangle$ are shown in Fig. 5*a*. It can be seen that the amplitude response is high during the part of high-speed flow. Remarkably, $\langle A^* \rangle$ increases and decreases much more abruptly than the flow speed and attains two local maxima; one during the flow deceleration stage ($t/K_C = 0 - 0.25$) and another during the flow acceleration stage ($t/K_C = 0.25 - 0.5$). These local maxima are accompanied by marked increases in the phase-averaged magnitude of the transverse force $\langle C_y \rangle$, as can be seen in Fig. 5*b*. During the deceleration stage the driving force leads the motion, whereas force and motion are almost in phase during the acceleration stage. Furthermore, the local peak in $\langle C_y \rangle$ is much higher (nearly double) during the acceleration stage than during the deceleration stage. These observations signify fundamental differences in the mechanisms related to flow-induced vibration during different parts of the flow-oscillation cycle. On the other hand, the variation of the phase-averaged magnitude of the streamwise force $\langle C_x \rangle$ is very similar to that of $\langle A^* \rangle$, as can be seen in Fig. 5*c*.

Additional simulations are conducted for the case when the cylinder is placed into a uniform free stream. For simplicity we will refer to this case as 'steady-VIV'. The parameters of these computations (i.e. the Reynolds number and reduced velocity) are chosen so as to correspond to the conditions at selected points of the oscillatory flow. Figure 6 provides comparisons of the phase-averaged results in oscillatory flow against steady-VIV data. It can be seen that the time-dependent amplitude response over the deceleration stage in oscillatory flow (see red curves in Fig. 6) follows quite closely the path traced by the steady-VIV amplitude as a function of the time-dependent reduced velocity $U_r^*(t) = \widetilde{U}/(f_n D)$. At the peak reduced velocity (i.e. $U_r^*(t) = U_r$), results for both oscillatory-VIV and steady-VIV almost coincide, including the magnitude of the fluid forces. However, during the acceleration stage (blue), the response amplitude is markedly higher in oscillatory-VIV than in steady-VIV and a hysteresis loop is formed in the plot of $\langle A^* \rangle$ as a function of $U_r^*(t)$.

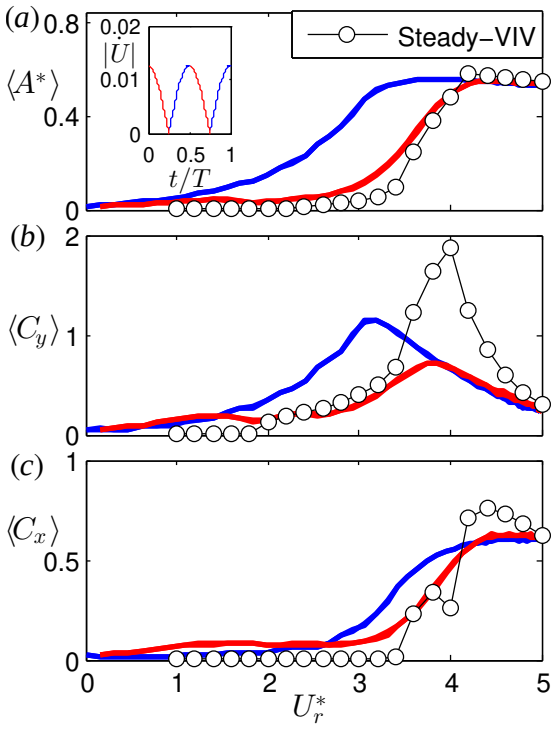

Figure 6. Comparison of results for oscillatory-VIV (coloured lines) with corresponding steady-VIV data (black circles+lines). The insert shows the stages of flow acceleration (blue) and deceleration (red) in absolute values for oscillatory-VIV

Similar trends can be observed in the variation of the magnitude of the unsteady fluid forces (high-frequency components). Furthermore, it is interesting to observe the marked differences in the magnitude of the transverse force near $U_r^*(t) = 4$, where $\langle C_y \rangle$ for steady-VIV is more than twice its value for oscillatory-VIV, despite the fact that the amplitude is almost the same for both cases.

4. CONCLUSIONS

In this study vortex-induced vibrations of a circular cylinder placed into a high-Keulegan-Carpenter-number (i.e. $K_C = 500$) oscillatory flow is investigated by means of two-dimensional finite-difference simulations. The maximum Reynolds number, the maximum reduced velocity and the mass and structural damping ratios are fixed at the values of $Re = 150$, $U_r = 5$, $\mu = 2$ and $\zeta = 0$, respectively.

The time-dependent magnitude and frequency of the signals (i.e. cylinder displacement and fluid forces) are obtained from Hilbert transform of the high-frequency (filtered) signals. The oscillation amplitude and the magnitude of the streamwise fluid force follow similar trends: in each flow oscillation cycle a time interval of high amplitudes is between intervals of low-amplitudes. In contrast, the magnitude of the transverse fluid force fluctuates at twice the frequency of the oscillation amplitude. The maximum frequency of the cylinder displacement and transverse fluid force are approximately 0.2, which is identical to the reciprocal value of the maximum reduced velocity U_r^{-1}. However, the peak frequency of the streamwise fluid force is approximately 0.4, i.e. close to the value of $2U_r^{-1}$.

Plots of the phase-averaged vibration amplitude and fluid forces (calculated based on 100 flow oscillation cycles) display strong hysteresis behaviour, which is unexpected given the very slow variation of the flow speed. This highlights the strongly nonlinear dynamics of vortex-induced vibration. The simulation results from the oscillatory flow are compared with the corresponding steady-VIV results (i.e. cases when the cylinder is placed into a uniform free stream). Although the amplitude of cylinder vibration and the magnitude of the streamwise fluid force compare relatively well, higher discrepancies are found in the magnitude of the transverse fluid force.

ACKNOWLEDGEMENTS

DD and LB was supported by the European Union and the Hungarian State, co-financed by the European Regional Development Fund in the framework of the GINOP-2.3.4-15-2016-00004 project, aimed to promote the cooperation between the higher education and the industry.

REFERENCES

[1] Bearman, P., 1984, "Vortex Shedding from Oscillating Bluff Bodies", *Annual Review of Fluid Mechanics*, Vol. 16, pp. 195–222.

[2] Bearman, P., 2011, "Circular Cylinder Wakes and Vortex-Induced Vibrations", *Journal of Fluids and Structures*, Vol. 27 (5-6), pp. 648–658.

[3] Sarpkaya, T., 2004, "A Critical Review of the Intrinsic Nature of the Vortex-Induced Vibrations", *Journal of Fluids and Structures*, Vol. 19 (4), pp. 389–447.

[4] Williamson, C., and Govardhan, R., 2004, "Vortex-Induced Vibration", *Annual Review of Fluid Mechanics*, Vol. 36, pp. 413–455.

[5] Khalak, A., and Williamson, C., 1999, "Motions, Forces and Mode Transitions in Vortex-Induced Vibrations at Low Mass-Damping", *Journal of Fluids and Structures*, Vol. 13 (7-8), pp. 813–851.

[6] Konstantinidis, E., Zhao, J., Leontini, J., Lo Jacono, D., and Sheridan, J., 2020, "Phase Dynamics of Effective Drag and Lift Components in Vortex-Induced Vibration at Low Mass–Damping", *Journal of Fluids and Structures*, Vol. 96, p. 103028.

[7] Dorogi, D., and Baranyi, L., 2020, "Identification of Upper Branch for Vortex-Induced Vibration of a Circular Cylinder at $Re = 300$", *Journal of Fluids and Structures*, Vol. 98, p. 103135.

[8] Williamson, C. H. K., 1985, "In-Line Response of a Cylinder in Oscillatory Flow", *Applied Ocean Research*, Vol. 7 (2), pp. 97–106.

[9] Sumer, B. M., and Fredsøe, J., 1997, "Transverse Vibrations of an Elastically Mounted Cylinder Exposed to an Oscillating Flow", *Journal of Offshore Mechanics and Arctic Engineering*, Vol. 110, pp. 387–394.

[10] Lipsett, A. W., and Williamson, I. D., 1994, "Response of a Cylinder in Oscillatory Flow", *Journal of Fluids and Structures*, Vol. 8 (7), pp. 681–709.

[11] Domenichini, F., 2002, "Quasiperiodicity and Chaos in the Dynamics of an Elastically Mounted Circular Cylinder", *European Journal of Mechanics-B/Fluids*, Vol. 21 (3), pp. 341–354.

[12] Morison, J., Johnson, J., and Schaaf, S., 1950, "The Force Exerted by Surface Waves on Piles", *Journal of Petroleum Technology*, Vol. 2 (5), pp. 149–154.

[13] Anagnostopoulos, P., and Iliadis, G., 1998, "Numerical Study of the Flow Pattern and the In-Line Response of a Flexible Cylinder in an Oscillating Stream", *Journal of Fluids and Structures*, Vol. 12 (3), pp. 225–258.

[14] Taheri, E., Zhao, M., Wu, H., and Tong, F., 2020, "Numerical Investigation of Streamwise Vibration of an Elastically Mounted Circular Cylinder in Oscillatory Flow", *Ocean Engineering*, Vol. 209, p. 107300.

[15] McConnell, K. G., and Jiao, Q., 1986, "The In-Line Forces Acting on an Elastically Mounted Cylinder Oscillating in Still Water", *Experimental Mechanics*, Vol. 26 (1), pp. 66–70.

[16] Zhao, M., Cheng, L., and An, H., 2012, "Numerical Investigation of Vortex-Induced Vibration of a Circular Cylinder in Transverse Direction in Oscillatory Flow", *Ocean Engineering*, Vol. 41, pp. 39–52.

[17] Zhao, M., Pearcey, T., Cheng, L., and Xiang, Y., 2017, "Three-Dimensional Numerical Simulations of Vortex-Induced Vibrations of a Circular Cylinder in Oscillatory Flow", *Journal of Waterway, Port, Coastal, and Ocean Engineering*, Vol. 143 (4), p. 04017007.

[18] Harlow, F. H., and Welch, J. E., 1965, "Numerical Calculation of Time-Dependent Viscous Incompressible Flow of Fluid with Free Surface", *The Physics of Fluids*, Vol. 8 (12), pp. 2182–2189.

[19] Baranyi, L., 2008, "Numerical simulation of flow around an orbiting cylinder at different ellipticity values", *Journal of Fluids and Structures*, Vol. 24 (6), pp. 883–906.

[20] Konstantinidis, E., Dorogi, D., and Baranyi, L., 2021, "Resonance in Vortex-Induced In-Line Vibration at Low Reynolds Numbers", *Journal of Fluid Mechanics*, Vol. 907, p. A34.

[21] Singh, S., and Mittal, S., 2005, "Vortex-Induced Oscillations at Low Reynolds Numbers: Hysteresis and Vortex-Shedding Modes", *Journal of Fluids and Structures*, Vol. 20 (8), pp. 1085–1104.

[22] Govardhan, R., and Williamson, C., 2006, "Defining the Modified Griffin Plot in Vortex-Induced Vibration: Revealing the Effect of Reynolds Number Using Controlled Damping", *Journal of Fluid Mechanics*, Vol. 561, pp. 147–180.

Conference on Modelling Fluid Flow (CMFF'22)
The 18th International Conference on Fluid Flow Technologies
Budapest, Hungary, August 30-September 2, 2022

Direct Numerical Simulation of the Wake Flow of a Miniature Vortex Generator and its Interaction with a Laminar Boundary Layer

Maarten VANIERSCHOT[1], András SZABÓ[2], Péter Tamás NAGY[2], György PAÁL[2]

[1] Corresponding Author. KU Leuven, Department of Mechanical Engineering, Group T Leuven campus, Celestijnenlaan 300, B-3001 Heverlee, Belgium. Tel.: +32 16 301072, E-mail: maarten.vanierschot@kuleuven.be
[2] Department of Hydrodynamic Systems, Faculty of Mechanical Engineering, Budapest University of Technology and Economics. E-mail: aszabo@hds.bme.hu

ABSTRACT

Miniature vortex generators (MVGs) are an attractive technology to delay laminar to turbulent transition or to postpone flow separation of laminar boundary layers. Despite the appearance of several recent studies, much more work still needs to be done to optimize these MVGS or to study their interaction with a boundary layer flow. Therefore, in this study we perform Direct Numerical Simulations (DNS) to study the complex three dimensional wakes generated by a pair of triangular and rectangular winglets and their interaction with a laminar boundary layer flow. Vortex identification using the Q-criterion shows the existence of a strong pair of counter-rotating vortices. Next to this primary vortex pair, much weaker secondary vortices can also be found, induced by the winglet geometry. For five Blasius profiles with different boundary layer thicknesses, the strength, radius and position of the main vortex pair is characterized. The generated output profiles of this study can be used as an input for solving the boundary region equations further downstream and together with a BiGlobal stability analysis, the effectiveness of the MVGs in the suppression of Tollmien-Schlichting waves can be examined.

Keywords: Boundary layer interaction, DNS, Miniature Vortex Generators, Wake flow

NOMENCLATURE

p	$[Pa]$	pressure
R	$[m]$	radius
r	$[m]$	distance from the vortex center
R^2	$[-]$	coefficient of determination
r_f	$[-]$	refinement ratio
U, V, W	$[m/s]$	streamwise, wall normal, spanwise velocity component
u_i	$[m/s]$	velocity component in the i-direction
U_∞	$[m/s]$	freestream velocity
V_m	$[m/s]$	velocity magnitude
x, y, z	$[m]$	streamwise, wall normal, spanwise coordinate
δ	$[m]$	boundary layer thickness
Γ	$[m^2/s]$	circulation
ν	$[m^2/s]$	kinematic viscosity
ρ	$[kg/m^3]$	density

Subscripts and Superscripts

c	vortex center
θ	polar coordinate

1. INTRODUCTION

The application of streamwise streaks to a boundary layer flow can increase the transitional Reynolds number as these streaks can dampen the formation of Tollmien-Schlichting waves, since it is well-known that these waves can undergo secondary instabilities, leading to a transition to turbulence of the boundary layer [1]. Hence, suppressing them can shift the transition location downstream and therefore reduce the skin friction drag. Nevertheless, if the streak amplitude is too large, an inflectional instability of the boundary layer occurs, bypassing the classical transition mechanism [2]. Therefore, special care must be taken in the generation of streamwise streaks. From a practical point of view, the streaks can be generated by applying structural disturbances in the boundary layer, such as for instance cylinders or bumps. However, care must be taken as their wakes might also exhibit unsteady behavior, reducing the effectiveness [3]. A promising technology to generate high amplitude streaks are winglets, the so-called Miniature Vortex Generators (MVGs) [4],[5],[6]. They are implemented in pairs to gen-

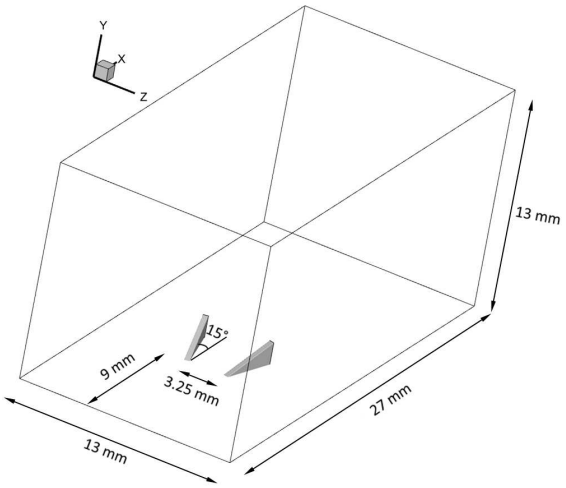

Figure 1. Schematic view of the numerical domain for the triangular MVGs

erate a counter rotating vortex pair. MVGs can be triangular or rectangular in shape and they have been studied extensively. Nevertheless, a detailed comparison of the flow field generated by rectangular or triangular MVGs is still lacking, as is also the influence of the boundary layer thickness on the flow structures in their wakes. To fill this knowledge gap, this study compares the flow fields generated by triangular and rectangular MVGs and studies their wake structure as a function of the boundary layer thickness. The generated output profiles of this study can be used as an input for BiGlobal stability analyses, where the effectiveness of the MVGs in the suppression of Tollmien-Schlichting waves can be examined [7].

2. NUMERICAL SETUP

2.1. MVG geometry

The MVG configuration in this study is based on the work of Siconolfi et al. [8]. A schematic view of the triangular MVG configuration is shown in Figure 1. The numerical domain is a rectangular box with length $X = 27$ mm, height $Y = 13$mm and width $Z = 13$mm, where the x-axis is the flow direction and the origin of the cartesian coordinate system is located at the inlet of the domain on the bottom wall, halfway the spanwise direction. The MVGs are placed in the center of a cross-sectional plane at a distance of 9mm from the inlet. The MVGs have a length of 3.25 mm, a width of 0.3 mm and a height of 1.3 mm. The distance between the MVG pair is 3.25 mm and they are placed under an angle of 15° with the flow direction. These MVGs are placed in pairs along the spanwise direction with a distance of 13 mm between them.

2.2. Governing equations

In this study, the steady state 3D Navier-Stokes equations for Newtonian fluids are solved. The equations, representing the conservation of mass and momentum are given by

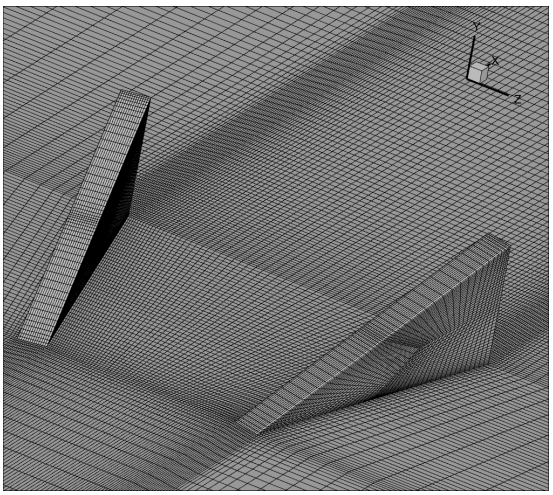

(a) Triangular MVG pair

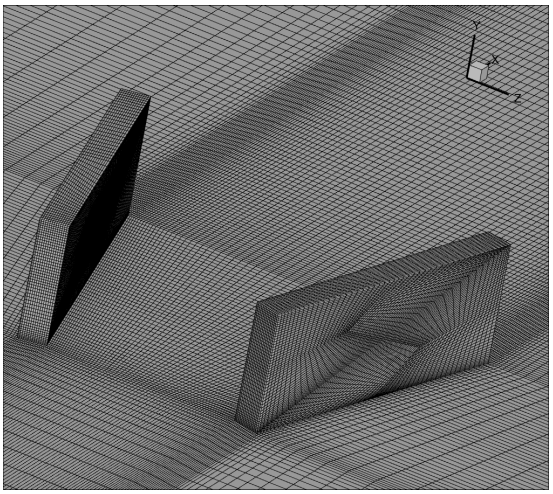

(b) Rectangular MVG pair

Figure 2. Details of the surface mesh of the MVG pair.

$$\frac{\partial u_j}{\partial x_j} = 0 \text{ and} \tag{1}$$

$$u_j \frac{\partial u_i}{\partial x_j} = -\frac{1}{\rho}\frac{\partial p}{\partial x_i} + \nu \frac{\partial^2 u_i}{\partial x_j \partial x_j}, \tag{2}$$

where u_i is a velocity component, ν is the kinematic viscosity, ρ is the density and p is the pressure. In this study, the governing fluid is air at standard temperature and pressure with a density $\rho = 1.225\, kg/m^3$ and a kinematic viscosity of $\nu = 1.4607\, mm^2/s$. The equations are solved using Ansys Fluent 18.2. The numerical grid is hexahedrally structured and constructed using PointWise. The total number of cells is around 2 million. A view of the surface mesh of the rectangular and triangular MVGs is shown in Figure 2. To maintain a similar grid structure between the two types, the rectangular winglet is divided in two triangles.

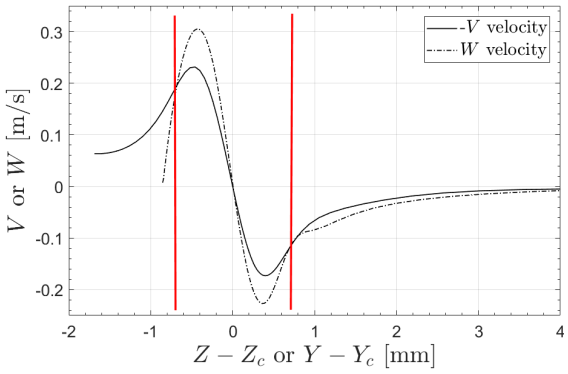

Figure 3. Horizontal and vertical velocity profiles through the center of the vortex in a cross-sectional plane x =22 mm

2.3. Boundary conditions

At the inlet, a fully developed Blasius velocity profile in the wall normal coordinate (y) is adopted and uniform in the spanwise direction (z). The freestream velocity is $U_\infty = 7.7$ m/s and the boundary layer thicknesses simulated are $\delta = 0$, 0.65, 1.3, 2.6 and 3.25 mm, giving a Reynolds number based on the thickness between 0 and 1713. At the outlet, a pressure boundary condition is applied where the gauge pressure is set at 0 Pa. On the side walls, periodic boundary conditions are applied and the top boundary is a symmetry plane.

2.4. Solution strategy

The QUICK (Quadratic upstream interpolation for convective kinematics) discretization scheme for momentum is adopted, while the pressure is discretised by the PRESTO! scheme [9, 10]. The segregated SIMPLEC (Semi-Implicit Method for Pressure Linked Equations-Consistent) is used for pressure velocity coupling. For each simulation, the residuals levels drop down to double precision machine accuracy before the iterations are stopped.

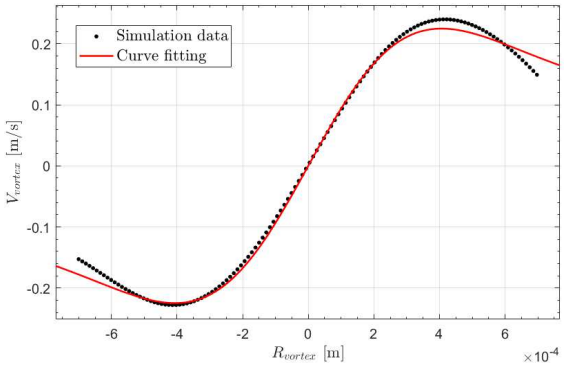

Figure 4. Average of the horizontal and vertical velocity profiles through the center of the vortex in a cross-sectional plane x =22 mm

2.5. Vortex characterisation

In order to determine the characteristics of each vortex pair generated by the MVGs, a Batchelor vortex is fitted to the velocity profiles along a horizontal and vertical line through the vortex center in a plane at $x = 22$ mm. An example of such numerically obtained profiles is shown in Figure 3. Although the difference between the local velocity maximum location of V and W is very small, it can be clearly seen that the vortex is slightly asymmetric due to effects of the bottom wall and the other vortex of the pair. Therefore, the fitted Batchelor vortex is applied to the average of both profiles between ±0.7 mm from the center (red lines in the figure). An example of such an averaged profile is shown in Figure 4.
The velocity profile of a Batchelor vortex is given by

$$V_\theta(r,\theta) = \frac{\Gamma}{2\pi r}\left[1 - \exp\left(-r^2/R_c^2\right)\right], \tag{3}$$

where V_θ is the V component for a horizontal profile or the W component for a vertical profile, r is the distance from the vortex center, Γ the circulation and R_c the radius of the vortex. The fitted Batchelor vortex based on the 2 profiles given in Figure 3 is shown by the red curve in Figure 4. The R^2 value is 0.9971 for this particular profile and the lowest value found in this study was 0.98, showing a Batchelor vortex profile is a very good fit for both the rectangular and triangular MVGs.

3. RESULTS

3.1. Mesh independency study

To estimate the discretisation error, the Grid Convergence index (GCI) method developed by Roache is employed [11]. The relative error between different meshes is calculated as

$$\epsilon = \frac{\phi_1 - \phi_2}{\phi_1}, \tag{4}$$

where ϕ is a certain flow quantity and the subscript 1 refers to the coarser mesh and 2 refers to the finer mesh. The GCI on the coarse mesh can be calculated as

$$GCI = 3\epsilon\frac{r_f^p}{r_f^p - 1}, \tag{5}$$

where r_f is the refinement ratio in one direction ($r_f = \sqrt{2}$ in this study) and p is the order of the discretisation scheme, which is 3 in this case. Three different grids, a coarse, medium and fine mesh were

Table 1. Number of cells for the three meshes employed in the grid convergence study

coarse mesh	medium mesh	fine mesh
2,009,421	5,715,812	16,075,368

Table 2. Location, strength and radius of the vortex pair of the triangular MVG for the three meshes employed in a cross-sectional plane x =22 mm

	coarse mesh	medium mesh	fine mesh
$Y_c\ [mm]$	0.8539	0.8529	0.8528
$Z_c\ [mm]$	1.6436	1.6424	1.6434
$\Gamma\ [mm^2/s]$	802	787	814
$R_o\ [mm]$	0.3624	0.3539	0.3637

adopted for which Table 1 shows the number of grid cells of each. The values of the location, strength and radius of the right vortex of the pair is shown in Table 2. The results show a non-monotonic convergence and the GCI of Y_c for the coarse mesh is 0.4% and for the medium mesh it is 0.04%, while for Z_c the GCI is 0.2% for both the coarse and medium meshes. The difference between the values for the circulation and radius is larger, but they fall well within the 95% confidence interval of the fitting parameters of Eq. 3, which is about 4% .

3.2. Flow field structure

The flow field structure of the MVGs is shown in Figure 5 for a boundary layer thickness $\delta = 0$ at the inlet. The black surfaces denote zero streamwise velocity, hence recirculation zones, and vortical structures are visualised using the Q criterion [12]. Both MVGs generate a counter rotating vortex pair which is not aligned with the flow direction. However, the vortex pair generated by the rectangular pair spreads more compared to the triangular one. The structure of the flow field of the rectangular MVGs is also more complex compared to the triangular ones. In the former, apart from the primary counter rotation vortex pair, a secondary vortex pair is also present. Moreover, a horse shoe vortex is formed near the leading edge of the rectangular MVG, which is a typical structure observed in bluff body flows [13]. Looking at the wake structure, the wake of the rectangular MVG is also much more complicated. At the leading edge, a small recirculation zone can be observed, which is not present in the triangular MVG, as the triangular surface of the latter allows the air to flow smoothly around the MVG. The angle of attack of 15° induces separation on the inner side of the MVG pair. For the rectangular MVG, this wake is much larger (comparing Figure 6a with Figure 6b) and as a result, the drag coefficient of the triangular MVG, $C_D = 1.32$, is much smaller than the one for the rectangular MVG, $C_D = 2.58$. This large discrepancy is caused by a domination of the pressure drag due to separation over the viscous drag as the former is 4 times higher compared to the latter.

The flow field structure of both MVGs for a boundary layer thickness $\delta = 3.25$ mm ($\delta/h = 2.5$) is shown in Figure 7. Comparison with Figure 5 shows the large influence of the boundary layer thickness on

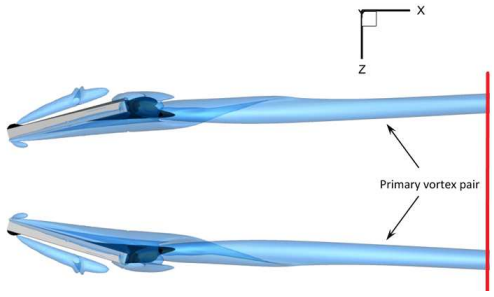

(a) Triangular MVGs

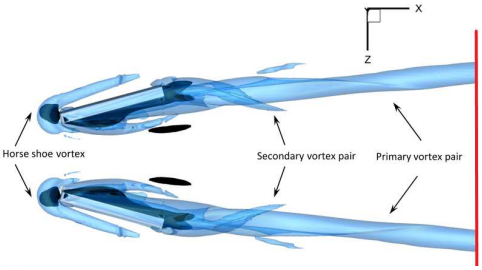

(b) Rectangular MVGs

Figure 5. Top view of the structure of the flow field of the MVGs for a boundary layer with thickness δ = 0 mm. The black isosurface denotes zero streamwise velocity, while the vortical structures are visualised with blue isosurfaces of Q = 8×10^6 1/s

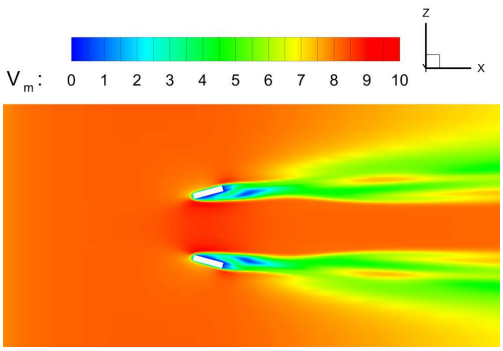

(a) Triangular MVGs

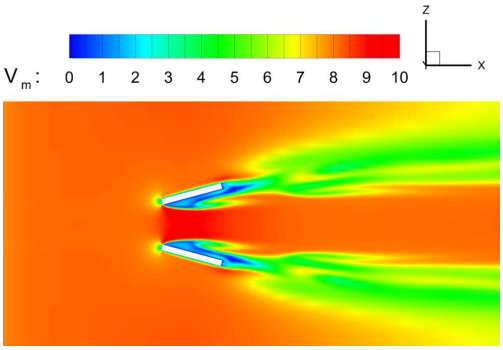

(b) Rectangular MVGs

Figure 6. Velocity magnitude in a cross-sectional plane at half the height of the MVG for a boundary layer with thickness δ = 0 mm.

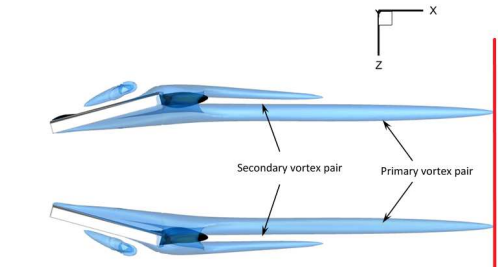

(a) Triangular MVGs

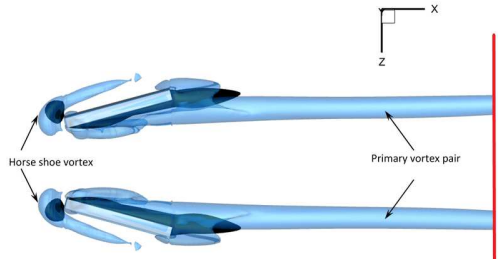

(b) Rectangular MVGs

Figure 7. Top view of the structure of the flow field of the MVGs for a boundary layer with thickness δ = 3.25 mm (δ/h = 2.5). The black isosurface denotes zero streamwise velocity, while the vortical structures are visualised with blue isosurfaces of Q = 8×10^5 1/s

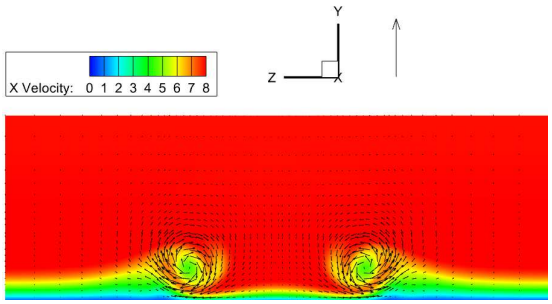

(a) Triangular MVGs

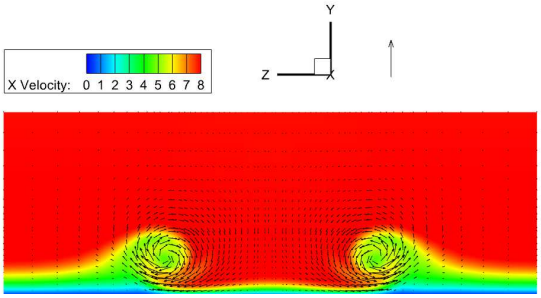

(b) Rectangular MVGs

Figure 9. Details of the vortex pair at a cross-sectional plane at x = 22 mm for a boundary layer of thickness δ = 0 mm. The length of the reference vector is 5 m/s

the flow field. Comparing Figures 5a and 7a shows

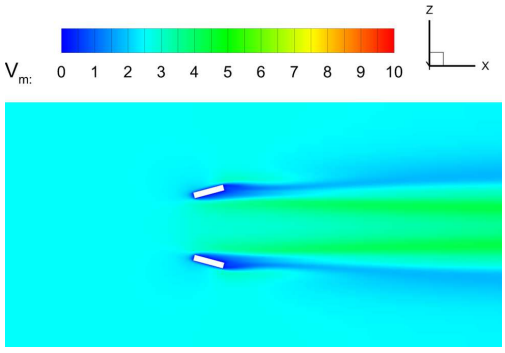

(a) Triangular MVGs

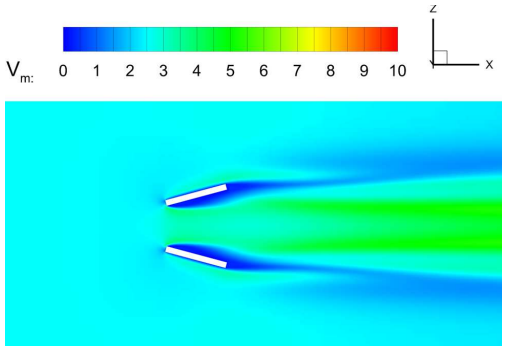

(b) Rectangular MVGs

Figure 8. Velocity magnitude in a cross-sectional plane at half the height of the MVG for a boundary layer with thickness δ = 3.25 mm.

a secondary vortex pair for the triangular MVG for δ = 3.25 mm (δ/h = 2.5). For the rectangular MVG, the complexity of the flow field is reduced and the secondary vortex pair is no longer present. Nevertheless, the horse shoe vortex at the leading edge is still present. Similar to δ = 0 mm, the drag coefficient of the triangular MVG, C_D = 0.24, is much smaller than the one for the rectangular MVG, C_D = 0.56. This large discrepancy is again caused by a domination of the pressure drag due to separation (Figure 8) over the viscous drag, although it is only 2 times higher instead of 4 for δ = 0 mm. Nevertheless, as the wake is smaller (comparison of Figure 8 with Figure 6), the drag coefficient is significantly lower than for δ = 0 mm.

3.3. Far field of the MVGs

The far field structure behind the MVGs, at a cross-sectional plane x = 22 mm (depicted by the red lines in Figures 5 and 7) for a boundary layer thickness δ = 0 mm is shown in Figure 9. The MVGs significantly reduce the boundary layer thickness in the region between the vortex pair, both for the rectangular and triangular MVGs. This reduction in thickness is much less if the boundary layer thickness at the inlet is increased, as shown in Figure 10.

3.4. Influence of the boundary layer thickness

As seen from Figures 5 and 7, the boundary layer thickness has a significant influence on the structure of the flow field and hence the characteristics of the

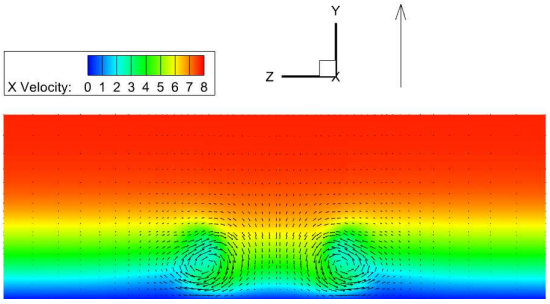

(a) Triangular MVGs

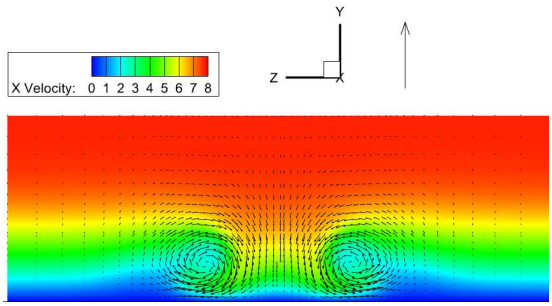

(b) Rectangular MVGs

Figure 10. Details of the vortex pair at a cross-sectional plane at x = 22 mm for a boundary layer of thickness δ = 3.25 mm. The length of the reference vector is 2 m/s

vortex pair. The location, strength and radius of the triangular MVG pair is shown in Table 3 and of the rectangular pair in Table 4. The values are obtained from a curve fit of Eq. 3 to the average velocity profiles of the horizontal and vertical direction through the vortex center. As the boundary layer thickness increases, the strength of the vortex pair decreases, as also the distance between the pair. This is related to the decrease in pressure difference between the front and rear side of the MVG as the incoming velocity profile along the height of the MVG decreases since the boundary layer thickness at the location of the MVG pair increases. A decrease in pressure difference generates a vortex pair, similar to the wingtip vortices in airplane wings, which is less strong. Moreover, the rectangular MVGs generate a stronger vortex pair compared to the triangular MVGs.

4. CONCLUSIONS

In this study, direct numerical simulations of the fluid flow around rectangular and triangular Mini-

Table 3. Vortex center, strength and radius of the vortex pair of the triangular MVG in a cross-sectional plane x =22 mm

δ	0	0.5h	h	2h	2.5h
Y_c $[mm]$	0.863	0.856	0.834	0.847	0.854
Z_c $[mm]$	2.11	1.97	1.83	1.68	1.64
Γ $[mm^2/s]$	3971	3038	2172	1106	802
R_c $[mm]$	0.322	0.299	0.314	0.336	0.362

Table 4. Vortex center, strength and radius of the vortex pair of the rectangular MVG in a cross-sectional plane x = 22 mm

δ	0	0.5h	h	2h	2.5h
Y_c $[mm]$	0.941	0.928	0.911	0.891	0.907
Z_c $[mm]$	2.55	2.38	2.18	1.85	1.76
Γ $[mm^2/s]$	5923	5364	4470	2366	1789
R_c $[mm]$	0.346	0.357	0.392	0.455	0.486

ature Vortex Generators (MVGs) in a flat plate boundary layer flow are performed. The wake structure is analysed as a function of the boundary layer thickness δ. It is shown that the rectangular MVGs generate a more complex flow field for small δ, while the triangular MVGs have a more complex flow field for large δ. The vortex pair generated by the rectangular MVGs is also stronger than the triangular one. As δ increases, the vortex pair becomes less strong and the distance between the cores decreases. With the results in this study, the generated output profiles at x = 22 mm can be used as an input for solving the boundary region equations further downstream and together with a BiGlobal stability analysis, the effectiveness of the MVGs in the suppression of Tollmien-Schlichting waves can be examined.

ACKNOWLEDGEMENTS

The authors wish to thank KU Leuven and Budapest University of Technology and Economics for financing this research through grant No. CELSA/21/024.

REFERENCES

[1] Herbert, T., 1988, "Secondary Instability of Boundary-layers", *Annu Rev Fluid Mech*, Vol. 20, pp. 487–526.

[2] Brandt, L., and Henningson, D., 2002, "Transition of Streamwise Streaks in Zero-pressure-gradient Boundary Layers", *J Fluid Mech*, Vol. 472, pp. 229–262.

[3] Loiseau, J.-C., Robinet, J.-C., and Cherubini, S. end Leriche, E., 2014, "Investigation of the Roughness-induced Transition: Global Stability Analyses and Direct Numerical Simulations", *J Fluid Mech*, Vol. 760, pp. 175–211.

[4] Fransson, J., and Talamelli, A., 2012, "On the Generation of Steady Streamwise Streaks in Flat-plate Boundary Layers", *J Fluid Mech*, Vol. 698, pp. 211–234.

[5] Shahinfar, S., Sattarzadeh, S., Fransson, J., and Talamelli, A., 2012, "Revival of Classical Vortex Generators now for Transition Delay", *Phys Rev Lett*, Vol. 109, p. 074501.

[6] Shahinfar, S., Fransson, J., Sattarzadeh, S., and Talamelli, A., 2013, "Scaling of Streamwise

Boundary Layer Streaks and their Ability to Reduce Skin-friction Drag", *J Fluid Mech*, Vol. 733, pp. 1–32.

[7] Szabó, A., Nagy, P., Vanierschot, M., and Paál, G., 2022, "Stability Analysis of a Streaky Boundary Layer generated by Miniature Vortex Generators", *to appear in: Proceedings of the 18th International Conference on Fluid Flow Technologies (CMFF22)*, Budapest, Hungary.

[8] Siconolfi, L., Camarri, S., and Fransson, J., 2015, "Stability Analysis of Boundary Layers Controlled by Miniature Vortex Generators", *J Fluid Mech*, Vol. 784, pp. 596–618.

[9] Leonard, B., 1979, "A Stable and Accurate Convective Modelling Procedure based on Quadratic Upstream Interpolation", *Comput Methods Appl Mech Eng*, Vol. 19, pp. 59–98.

[10] Patankar, S., 1980, *Numerical Heat Transfer and Fluid Flow*, Hemisphere, Washington DC.

[11] Roache, P., 1994, "Perspective: a Method for Uniform Reporting of Grid Refinement Studies", *J Fluids Eng*, Vol. 116, pp. 405–413.

[12] Jeong, J., and Hussain, F., 1995, "On the Identification of a Vortex", *J Fluid Mech*, Vol. 285, pp. 69–94.

[13] Carr, I., and Plesniak, M., 2017, "Surface obstacles in pulsatile flow", *Experiments in Fluids*, Vol. 58, p. 152.

Conference on Modelling Fluid Flow (CMFF'22)
The 18th International Conference on Fluid Flow Technologies
Budapest, Hungary, August 30-September 2, 2022

A WALL MODEL FOR HIGH-FIDELITY LARGE-EDDY SIMULATION

Lukas UNGLEHRT[1], Johannes KREUZINGER[2], Michael MANHART[3]

[1] Professorship of Hydromechanics, TUM School of Engineering and Design, Technical University of Munich. Arcisstr. 21, 80333 München, Germany. Tel.: +49 289 28565. E-mail: lukas.unglehrt@tum.de
[2] Kreuzinger und Manhart Turbulenz GmbH. E-mail: j.kreuzinger@km-turbulenz.de
[3] Professorship of Hydromechanics, TUM School of Engineering and Design, Technical University of Munich. E-mail: michael.manhart@tum.de

ABSTRACT

We present a novel wall model for well resolved large-eddy simulation (LES) of complex flows. The model is based on a Taylor series expansion of the velocity and pressure profiles in wall-normal direction. The derivatives are determined from the near-wall asymptotics of the Navier-Stokes equations. We take a cubic polynomial for the velocity profile and a linear function for the pressure profile and impose a collocation constraint at a fluid point normal to the wall. This results in an evolution equation for the wall shear stress.

The accuracy of the wall model is assessed with both an a-priori and an a-posteriori approach for the oscillatory Stokes boundary layer and a Falkner-Skan boundary layer. Finally, we apply the model for a LES of turbulent channel flow.

Keywords: boundary layer equations, large eddy simulation, direct numerical simulation, wall model

NOMENCLATURE

U	$[m/s]$	velocity outside the boundary layer
$\Delta x, \Delta y, \Delta z$	$[m]$	cell size
$a, \tilde{a}$	$[1/s]$	velocity gradient
f	$[-]$	stream function
h	$[m]$	channel half-height
p	$[Pa]$	pressure
u, w	$[m/s]$	wall-parallel velocity components
u_τ	$[-]$	friction velocity
v	$[m/s]$	wall-normal velocity component
x, z	$[m]$	wall-parallel coordinates
y	$[m]$	wall-normal coordinate
$\Delta x^+, \Delta y^+, \Delta z^+$	$[-]$	cell size in wall units
$\underline{n}$	$[-]$	wall-normal unit vector
$\underline{u}$	$[m/s]$	velocity vector
$\underline{\underline{I}}$	$[-]$	identity matrix
β	$[-]$	Falkner-Skan parameter
δ_s	$[m]$	Stokes boundary layer thickness $\sqrt{2\nu/\Omega}$
η	$[-]$	dimensionless wall-normal coordinate
η_s	$[-]$	dimensionless wall-normal coordinate
μ	$[Pa \cdot s]$	dynamic viscosity
ν	$[m^2/s]$	kinematic viscosity
Ω	$[1/s]$	frequency
ρ	$[kg/m^3]$	density
$\underline{\tau}_w$	$[Pa]$	wall shear stress vector

Subscripts and Superscripts

$+$	in wall units, i.e. normalised with ν and u_τ
0	amplitude of an oscillation
p	at an interpolation point close to the wall
w	at the wall ($y = 0$)

1. INTRODUCTION

In the simulation of turbulent flow, there exist three principal simulation paradigms. The Reynolds-averaged Navier-Stokes (RANS) equations supplemented with a suitable turbulence model for the Reynolds stresses can be used to approximately compute the time-average velocity field and higher order statistics like the turbulent kinetic energy. The large-eddy simulation (LES) approach explicitly resolves the large, energetic turbulent scales of motion on the numerical grid and only models the stresses arising from the unresolved motion (sub-grid scale or SGS stresses). While the LES comes at a higher computational expense, it is generally considered more reliable for complex flow configurations. The direct numerical simulation resolves all turbulent length and time scales and does not require a turbulent or SGS model. Its accuracy and reliability comes with very large computational costs which inhibits its application at high Reynolds numbers.

In wall-bounded turbulent flow and in flow around bluff bodies, a high grid resolution is necessary in all three simulation paradigms to resolve thin laminar boundary layers or the viscous sublayer of turbulent boundary layers. The wall shear stress

is determined by this viscosity-dominated near wall flow and its accurate prediction is necessary to obtain quantitatively correct results or, e.g. when smooth flow separations are present, even a qualitatively correct flow topology.

In LES, two approaches have been developed to address this problem: wall modeled LES and wall-resolved LES. In wall modeled LES, the wall shear stress is either computed via an assumed velocity profile ("wall function") or by solving a dedicated differential equation on the wall. The former approach commonly relies on the logarithmic velocity profile of turbulent boundary layers or extensions thereof [1]. In the latter approach, some authors solve Reynolds-averaged Navier-Stokes (RANS) equations with a turbulence model on a zonally embedded refined grid near the wall [2, 3]. The velocity boundary conditions for the RANS equations are supplied by the LES and in turn the wall shear stress for the LES results from the RANS solution. In a similar spirit, a wide variety of hybrid RANS/LES models have been developed in which the length-scale of the RANS turbulence model is chosen depending on the grid. The resulting modeled stresses are a mixture between Reynolds stresses and SGS stresses. An example for this is the so-called Detached Eddy Simulation [4]. In wall-resolved LES, the wall shear stress is computed by applying a finite difference approximation. Therefore, high resolutions of approximately one wall unit are required near the wall. The advantage of this approach is that the modeling error is limited to the sub-grid scale model. An intermediate approach between the two paradigms can be realised by blending the wall function with a linear approximation of the velocity profile. For example, the Werner-Wengle wall function [5] uses a linear approximation of the velocity profile if the wall-nearest grid point is below 12 wall units and a $\frac{1}{7}$-th power law at larger wall distances. Based on the grid resolution near the wall, this model results in a wall modeled or a wall-resolved LES. Breuer et al. [6] have extended this model by incorporating pressure gradient effects.

In complex flow configurations where laminar boundary layers, transition to turbulence or flow separation and reattachment may occur, wall functions and RANS-based models have a large uncertainty as the underlying model assumptions – e.g. the presence of a turbulent equilibrium boundary layer – do not always hold in the flow [7, 8]. On the other hand, wall-resolved LES of high-Reynolds number flow can have a prohibitive computational cost, e.g. [9].

In this contribution, we present a wall model for LES that is derived directly from the Navier-Stokes equations under the boundary layer assumptions. The aim of this model is to provide an accurate approximation to the wall shear stress using only information that is available in the wall-nearest cell. In a high-fidelity wall-resolved LES, this allows to choose a coarser grid resolution near the wall while maintaining the predictive quality in complex flow configurations.

2. DERIVATION OF THE WALL MODEL

In this section, we demonstrate how our wall model can be derived. In the first step, the velocity and pressure gradient profiles are approximated by a Taylor series in the wall-normal coordinate.

In the second step (see Sec. 2.1), we determine relations among the expansion coefficients by inserting the expansions into the incompressible Navier-Stokes equations with no-slip conditions. For two-dimensional flow, Dallmann and Gebing [10] have derived such relations from the Taylor series of the streamfunction. Moreover, they recognised that within the region of convergence of the Taylor series of the streamfunction, the velocity field is completely determined by the wall shear stress, the wall pressure and the initial conditions. Consequently, all derivatives occurring in the expansion can be expressed in terms of the wall shear stress and the wall pressure. Also based on the work of [10], Shrikhande [11] investigated the possibility of reconstructing the velocity field from wall shear stress and wall pressure data. They demonstrated their method for various canonical flows and simulations of idealised aircraft wake vortices. They found that the Taylor series converges fast close to the wall and slowly far from the wall. In the present work, we consider the inverse problem – reconstructing the wall shear stress from a known velocity and pressure gradient. We also apply the above derivation to the boundary layer equations to obtain a simplified form of the wall model (see Sec. 2.2).

In the third step (see Sec. 2.3), we truncate the polynomial expansions and impose a collocation condition at a fluid point off the wall. This results in a system of partial differential equations for the wall shear stress with a source term which is a function of quantities at the collocation point. Finally, we discuss the properties of the wall model and possible generalisations (see Sec. 2.4).

2.1. Compatibility conditions from the Navier-Stokes equations

First, the velocity profile is expanded into a Taylor series in the wall distance y:

$$u = u_\mathrm{w} + \left.\frac{\partial u}{\partial y}\right|_\mathrm{w} y + \left.\frac{\partial^2 u}{\partial y^2}\right|_\mathrm{w} \frac{y^2}{2} + \left.\frac{\partial^3 u}{\partial y^3}\right|_\mathrm{w} \frac{y^3}{6} + O(y^4) \quad (1)$$

From the definition of the wall shear stress, the first derivative can be identified as

$$\left.\frac{\partial u}{\partial y}\right|_\mathrm{w} = \frac{\tau_{\mathrm{w}x}}{\mu} \quad (2a)$$

Inserting the Taylor expansion into the momentum equation and grouping by powers of y, we obtain the following expressions for the higher wall-normal de-

rivatives of the velocity profile at the wall:

$$\left.\frac{\partial^2 u}{\partial y^2}\right|_{\mathrm{w}} = \frac{1}{\mu}\left.\frac{\partial p}{\partial x}\right|_{\mathrm{w}} \tag{3a}$$

$$\left.\frac{\partial^3 u}{\partial y^3}\right|_{\mathrm{w}} = \frac{1}{\rho\nu^2}\frac{\partial \tau_{\mathrm{w}x}}{\partial t} - \frac{1}{\mu}\left(2\frac{\partial^2 \tau_{\mathrm{w}x}}{\partial x^2} + \frac{\partial^2 \tau_{\mathrm{w}z}}{\partial x\,\partial z}\right) \tag{3b}$$

The former relation is the trace of the wall-parallel momentum equation and represents the well known *compatibility condition at the wall* [12], whereas the latter relation (3b) is the trace of the y-derivative of the wall-parallel momentum equation and has been obtained by Dallmann and Gebing [10] in its two-dimensional form using the streamfunction.

As the pressure gradient at the wall is generally unknown, it must be extrapolated from the field. A Taylor expansion of the pressure in wall-normal direction gives

$$\frac{\partial p}{\partial x} = \left.\frac{\partial p}{\partial x}\right|_{\mathrm{w}} + \left(\frac{\partial^2 \tau_{\mathrm{w}x}}{\partial x^2} + \frac{\partial^2 \tau_{\mathrm{w}z}}{\partial x\,\partial z}\right) y + O(y^2) \tag{4}$$

where the wall-normal momentum and the continuity equation were used. As the pressure gradient is multiplied with y^2 in the Taylor expansion of the velocity, the overall approximation error of the velocity remains of order $O(y^4)$.

Please note that similar expressions can be obtained for the w-component by interchanging x and z, u and w, and $\tau_{\mathrm{w}x}$ and $\tau_{\mathrm{w}z}$. These have been omitted for the sake of brevity.

2.2. Compatibility conditions from the boundary layer equations

For high Reynolds number flow, we can apply the simplifications of boundary layer theory. We can neglect the wall-parallel derivatives in the viscous term as well as the wall-normal variation of the pressure. Based on these assumptions, we obtain the modified relations

$$\left.\frac{\partial^3 u}{\partial y^3}\right|_{\mathrm{w}} = \frac{1}{\rho\nu^2}\frac{\partial \tau_{\mathrm{w}x}}{\partial t} \tag{5}$$

for the third derivative of the velocity and

$$\frac{\partial p}{\partial x} = \left.\frac{\partial p}{\partial x}\right|_{\mathrm{w}} \tag{6}$$

for the pressure gradient.

2.3. Closure of the wall model

In order to close the equation, we neglect the $O(y^4)$ terms in equation (1) and impose a collocation condition at position y_{p}: $u(y_{\mathrm{p}}) = u_{\mathrm{p}}$. We obtain a differential equation for the wall shear stress:

$$\frac{\partial \tau_{\mathrm{w}x}}{\partial t} = -\frac{6\nu}{y_{\mathrm{p}}^2}\tau_{\mathrm{w}x} + \frac{6\rho\nu^2}{y_{\mathrm{p}}^3}(u_{\mathrm{p}} - u_{\mathrm{w}}) - \frac{3\nu}{y_{\mathrm{p}}}\left.\frac{\partial p}{\partial x}\right|_{\mathrm{p}} \tag{7}$$

As a consequence of the boundary layer assumptions, the equation is local and does not contain wall-parallel derivatives of the wall shear stress. This simplifies the implementation of the model considerably.

Instead of a collocation condition, a cell average value could be imposed to close the wall model [6]. Depending on the properties of the numerical scheme of the flow solver, this approach could be advantageous.

2.4. Discussion

The cubic wall model (7) forms part of a hierarchy of Taylor polynomial approximations starting with the linear and quadratic approximations

$$\tau_{\mathrm{w}x} = \frac{\mu}{y_{\mathrm{p}}}(u_{\mathrm{p}} - u_{\mathrm{w}}) \tag{8}$$

$$\tau_{\mathrm{w}x} = \frac{\mu}{y_{\mathrm{p}}}(u_{\mathrm{p}} - u_{\mathrm{w}}) - \frac{y_{\mathrm{p}}}{2}\left.\frac{\partial p}{\partial x}\right|_{\mathrm{p}} \tag{9}$$

with the latter suggested by [13]. Equation (9) is included in (7) as the steady state solution. Models of higher order can be derived by determining more terms in the Taylor expansions of velocity and pressure. These models feature a quadratic nonlinearity of the wall shear stress and an elliptic equation along the wall that determines the curvature of the pressure profile.

We see the main application of our model in the simulation of complex wall bounded flows for which the assumption of a classical turbulent boundary layer does not hold. An example for this is the flow around a wall-mounted cylinder where the wall shear stress follows a laminar boundary layer scaling [8]. However, since the wall model is based on a cubic polynomial, we expect that the model derived from the Navier-Stokes equations could be also applied as a wall boundary condition for high-order finite difference and finite volume codes.

In the computation of turbulent flow, an advantage of the proposed methodology is that the wall model is formulated in terms of the instantaneous wall shear stress. Consequently, the deficiency of the wall function approach that the instantaneous velocity profile is assumed to be of the same form as the mean velocity profile, is avoided. As the cubic wall model is derived solely from the pressure and viscous terms, the interpolation point y_{p} is constrained to lie in the viscous sublayer. This could be alleviated by using a higher order polynomial and by including a sub-grid scale model (e.g. the WALE model [14]) into the derivation of the compatibility conditions.

Using a variation of constants formula, it can be shown that the cubic contribution of the wall model results in a smoothing of the quadratic model (9):

$$\tau_{\mathrm{w}x} = \int_0^t \frac{6\nu}{y_{\mathrm{p}}^2} e^{-\frac{6\nu(t-t')}{y_{\mathrm{p}}^2}} \left(\frac{\mu}{y_{\mathrm{p}}}(u_{\mathrm{p}} - u_{\mathrm{w}}) - \frac{y_{\mathrm{p}}}{2}\left.\frac{\partial p}{\partial x}\right|_{\mathrm{p}}\right) \mathrm{d}t' + \tau_{\mathrm{w}x}|_{t=0}\, e^{-\frac{6\nu t}{y_{\mathrm{p}}^2}} \tag{10}$$

Consequently, the wall model has an exponentially decaying memory. The wall shear stress follows velocity and pressure fluctuations with a frequency below $6\nu/y_{\mathrm{p}}^2$, whereas higher frequencies are damped.

3. ANALYTICAL VALIDATION

In this section, we assess the accuracy of the wall model (7) when the exact velocity and pressure fields are assumed to be known. The difference between the modeled and the exact wall shear stress is expanded into a Taylor series in terms of the distance of the interpolation point y_p. For comparison, we also assess the accuracy of using linear and quadratic wall functions.

3.1. Stokes boundary layer

As a first test case, we choose the oscillatory Stokes boundary layer. It is an analytical solution of the Navier-Stokes equations in a semi-infinite domain bounded by a wall oscillating harmonically in its tangent plane. We consider the flow in the coordinate frame moving with the wall which leads to the appearance of an oscillatory pressure gradient $\underline{\nabla} p = -\rho\, U_0\, \sin(\Omega t)\, \underline{e}_x$. After the transient has decayed, the solution results as

$$u(t,y) = U_0 \left[e^{-\eta_\mathrm{s}} \cos\left(\Omega t - \eta_\mathrm{s}\right) - \cos\left(\Omega t\right) \right] \tag{11}$$

with the normalised coordinate $\eta_\mathrm{s} = y/\delta_\mathrm{s}$ and the boundary layer thickness $\delta_\mathrm{s} = \sqrt{2\nu/\Omega}$ [12]. The wall shear stress can be obtained as

$$\tau_{\mathrm{w}x} = \mu \sqrt{\frac{\Omega}{\nu}} U_0 \sin\!\left(\Omega t - \frac{\pi}{4}\right) \tag{12}$$

and it advances the outer flow by a quarter of a period.

We evaluate the linear, quadratic and cubic model for the velocity field (11) and perform a Taylor series expansion in y_p. For the linear model (8), we obtain

$$\tau_{\mathrm{w}x,\mathrm{lin}} - \tau_{\mathrm{w}x} = -\frac{\rho \Omega U_0}{2} \sin(\Omega t)\, y_\mathrm{p} + O(y_\mathrm{p}^2)\,, \tag{13}$$

for the quadratic model (9), we obtain

$$\begin{aligned} \tau_{\mathrm{w}x,\mathrm{quad}} - \tau_{\mathrm{w}x} = -\frac{\rho \Omega U_0}{6} \sqrt{\frac{\Omega}{\nu}} \sin\!\left(\Omega t + \frac{\pi}{4}\right) y_\mathrm{p}^2 \\ + O(y_\mathrm{p}^3)\,, \end{aligned} \tag{14}$$

and for the cubic model (7), we obtain

$$\tau_{\mathrm{w}x,\mathrm{cub}} - \tau_{\mathrm{w}x} = -\frac{\rho \Omega^2 U_0}{24\,\nu} \cos(\Omega t)\, y_\mathrm{p}^3 + O(y_\mathrm{p}^4)\,. \tag{15}$$

The a-priori value of the wall shear stress from the cubic wall model is therefore third-order accurate in the wall distance of the interpolation point y_p.

3.2. Falkner-Skan boundary layer

The Falkner-Skan boundary layer [12] is a self-similar solution to the laminar boundary layer equations for flow around a wedge. The solution is characterised by the parameter β; the interior angle of the wedge is given as $\beta\pi$. For $\beta = 0$ and $\beta = 1$, the Falkner-Skan solution corresponds to the Blasius boundary layer and the plane stagnation point flow, respectively.

The solution to the Falkner-Skan boundary layer is given as

$$u(x,y) = U(x) f'(\eta) \tag{16}$$

with the similarity variable

$$\eta = y \sqrt{\frac{1}{2-\beta} \frac{U(x)}{\nu x}}\,. \tag{17}$$

The dimensionless stream function $f(\eta)$ satisfies the differential equation

$$f''' + f f'' + \beta(1 - f'^2) = 0 \tag{18}$$

with $f(0) = 0$, $f'(0) = 0$ and $f'(\infty) = 1$. The exact wall shear stress is given as

$$\tau_{\mathrm{w}x} = \mu U(x) \sqrt{\frac{1}{(2-\beta)} \frac{U(x)}{\nu x}}\, f''_\mathrm{w} \tag{19}$$

where $f''_\mathrm{w} = f''(0)$ is solely a function of β.

We evaluate the linear and quadratic wall function as well as the steady state of the wall model (7) and perform a Taylor expansion. For the linear wall function, the error results as

$$\tau_{\mathrm{w}x,\mathrm{lin}} - \tau_{\mathrm{w}x} = -\frac{\beta}{2-\beta} \frac{\rho U(x)^2}{2x}\, y_\mathrm{p} + O(y_\mathrm{p}^2) \tag{20}$$

which is first-order accurate in the distance of the interpolation point y_p. For the quadratic wall function as well as for the cubic wall model, we obtain

$$\begin{aligned} \tau_{\mathrm{w}x,\mathrm{quad}} - \tau_{\mathrm{w}x} &= \tau_{\mathrm{w}x,\mathrm{cub}} - \tau_{\mathrm{w}x} \\ &= \frac{2\beta - 1}{(2-\beta)^2} f''^2_\mathrm{w} \frac{\rho U(x)^3}{24 \nu x^2}\, {y_\mathrm{p}}^3 + O(y_\mathrm{p}^4)\,. \end{aligned} \tag{21}$$

The a-priori value of the wall shear stress of the cubic wall model is again third-order accurate in y_p. As the flow is steady, the time derivative of the wall shear stress is zero and the predictions of the quadratic and cubic model are the same.

4. NUMERICAL VALIDATION

In this section, we investigate the accuracy of the wall model (7) when the velocity field is unknown and the evaluation of the wall model is coupled to the direct numerical simulation or large-eddy simulation of the velocity and pressure fields. This approach permits to assess feedback effects between the wall model and the flow solution. We compare the predictive performance of the linear approximation (8) and our model (7) depending on the grid resolution.

4.1. Description of the flow solver

The simulations were performed using our in-house code MGLET [15]. It uses a second-order central finite volume scheme on a block-structured Cartesian grid with a staggered arrangement of variables [16]. The time integration employs a third-order low-storage explicit Runge-Kutta scheme [17] and the divergence-free constraint of the velocity field is enforced in every substep by solving a Poisson equation for a correction pressure [18].

Flow in complex geometries is treated using

a cut-cell immersed boundary method based on [19, 20]. This discretisation preserves the skew-symmetry of the convective term and the positive-definiteness of the diffusive term. The time step restriction due to the small cells that occur invariably as a complex geometry intersects a Cartesian grid is circumvented with a merging strategy.

4.2. Implementation details

In the following, we comment on some noteworthy aspects of the coupling of the wall model into our flow solver. The wall shear stress appears explicitly as a momentum flux in the finite volume balance of the cut-cells. For each cut-cell, the velocity vector and pressure gradient are interpolated to a point at a wall-normal distance of $y_\mathrm{p} = \Delta y$ and the wall-normal component is removed from both vectors [21]. Then, either the linear wall function (8) or our wall model is used to compute the wall shear stress vector from the tangential velocity and pressure gradient. Please note that the linear wall function is the default second-order approximation of the diffusive term [21]. We use a vectorial form of the wall model (7) derived from the boundary layer equations:

$$\begin{aligned}\frac{\partial \underline{\tau}_\mathrm{w}}{\partial t} = &-\frac{6\nu}{y_\mathrm{p}^2}\underline{\tau}_\mathrm{w} + \frac{6\rho\nu^2}{y_\mathrm{p}^3}\left[\underline{\underline{I}} - \underline{n}\otimes\underline{n}\right](\underline{u}_\mathrm{p} - \underline{u}_\mathrm{w}) \\ &-\frac{3\nu}{y_\mathrm{p}}\left[\underline{\underline{I}} - \underline{n}\otimes\underline{n}\right]\underline{\nabla p}\Big|_\mathrm{p}\end{aligned} \tag{22}$$

We integrate this equation using the same explicit Runge-Kutta scheme as for the momentum equation. The coupling is implemented by simply updating the values at the beginning of each stage of the Runge-Kutta scheme.

For the present choice of the wall distance y_p of the interpolation point the stability of the time integration scheme is not affected. In particular, the critical ratio $6\nu\Delta t/y_\mathrm{p}^2 = 6\nu\Delta t/\Delta x^2$ that can be obtained from the decay constant of the wall model is equal to the diffusion number of a cubic open fluid cell.

4.3. Stokes boundary layer

We simulated the oscillatory Stokes boundary layer flow (11) on a domain $[0, 31\,\delta_\mathrm{s}]$. A no-slip boundary condition is applied at the bottom and a slip boundary condition is applied at the top. We use a cell size of $0.05\,\delta_\mathrm{s}$, $0.1\,\delta_\mathrm{s}$, …, $3.2\,\delta_\mathrm{s}$. The flow was started from rest and the calculation was performed until $\Omega t = 50$. Due to the slow decay of the transient and our explicit time integration scheme, it was not economical to simulate the flow until a steady oscillation was reached. Instead, we compare the solution to the analytical solution of [22] for the transient flow in response to a sinusoidal pressure gradient.

Fig. 1 shows the convergence of the velocity field $u(y,t)$ to the analytical solution in the L^2 norm computed over space and time. The velocity is interpolated linearly between the grid points. We observe a second order convergence of the solution for both the linear wall function (as expected) and the cubic wall

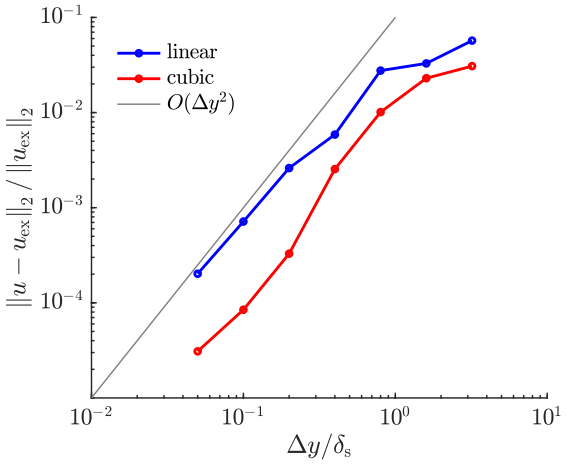

Figure 1. Convergence of the velocity field $u(y,t)$ for the transient Stokes boundary layer in the space-time L^2-norm.

model. The error for the cubic wall model (22) is approximately a third to half of the error for the linear wall function. Notably, the cubic wall model maintains an advantage over the linear wall function also for very coarse grids. For the same error, the wall model allows to coarsen the grid by a factor of 2.

4.4. Plane stagnation point flow

In this section, we investigate the accuracy of the wall model for the plane stagnation point flow (a Falkner-Skan boundary layer with $\beta = 1$) which is an exact semi-analytic solution of the Navier-Stokes equations [12]. This flow has the property that the boundary layer thickness is constant in space. This allows us to choose a constant grid resolution of the boundary layer. Furthermore, the plane stagnation point flow is prototypical for stagnation points that appear in flow around bluff bodies. As the boundary layer is often thinnest at the stagnation point, the resolution of this flow can dictate the overall grid resolution requirements.

The flow was simulated in a rectangular domain of height $12\sqrt{\nu/a}$ and width $36\sqrt{\nu/a}$. At the top of the domain, we applied a constant inflow velocity $v = -ay$ with a Neumann boundary condition for the velocity u. At the left ($x = 0$), we apply a symmetry boundary condition. At the bottom ($y = 0$), we apply the wall shear stress from the wall function or wall model. At the right, we assign a constant pressure $p = 0$ (this is inconsistent with the analytical solution). We varied the cell size in powers of 2 from $\Delta y/\delta_{99} = 0.0161$ to 0.514. At the coarsest grid resolution, the boundary layer is therefore contained in only two cells.

The corresponding analytical solution is derived from the potential flow with $u = \tilde{a}x$ and $v = -\tilde{a}y$ and

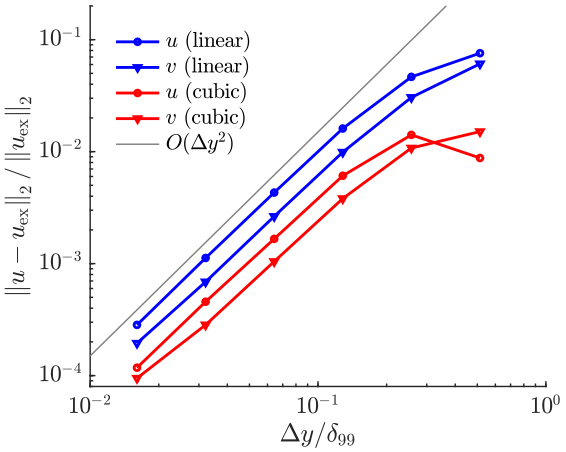

Figure 2. Convergence of the velocity profiles $u(y)$ and $v(y)$ at $x = \sqrt{\nu/\tilde{a}}$ for the plane stagnation point flow in the L^2-norm computed over the y-direction.

has the form

$$u(x, y) = \tilde{a} x f'(\eta) \tag{23a}$$

$$v(x, y) = -\sqrt{\tilde{a}\nu}\, f(\eta) \tag{23b}$$

where the dimensionless stream function $f(\eta)$ is a solution to the Falkner-Skan equation (18) for $\beta = 1$. Due to the displacement effect of the boundary layer, the constant $\tilde{a}$ must be chosen differently from the value a in the simulation. We set a value $\tilde{a} = 1.0556\, a$ that is derived from the requirement that the analytical solution matches the inflow profile of the simulation. In particular, the constant $\tilde{a}$ is a solution to

$$\sqrt{\tilde{a}/a}\, f\left(12\sqrt{\tilde{a}/a}\right) = 12 \tag{24}$$

Fig. 2 shows the convergence of the velocity profiles at $x = \sqrt{\nu/\tilde{a}}$ in the L^2-norm computed over the y-coordinate. It is apparent that the wall model significantly improves the prediction of the velocity field. In particular, at the coarsest grid resolution the cubic wall model is approximately as accurate as the linear wall function with a grid refined by a factor of 4.

4.5. Turbulent channel flow

In order to verify the correctness and robustness of the wall model (22) and to establish resolution requirements in turbulent flow, we performed LES of turbulent flow in a plane channel at a Reynolds number $Re_\tau = \frac{u_\tau h}{\nu} = 180$ with the friction velocity $u_\tau = \sqrt{\tau_w/\rho}$ and the half-height h. As reference data we use the direct numerical simulation (DNS) of [23]. The length of the domain is chosen like in [24] as $4\pi h$ in streamwise (x) and $2\pi h$ in spanwise (z) direction and the y-coordinate goes from $-h$ to h. The flow is driven by a constant pressure gradient. The sub-grid stresses are modelled with the WALE-viscosity model of Nicoud and Ducros [14].

We consider three grid resolutions for which the viscous sublayer is marginally resolved. At the coarsest resolution, the grid has a uniform cell size of $\Delta x^+ = \frac{u_\tau \Delta x}{\nu} = 24$ wall units in the streamwise, $\Delta y^+ = 6$ wall units in the wall-normal and $\Delta z^+ = 12$ wall units in the spanwise directions. At the intermediate resolution, the grid has a cell size of $\Delta x^+ = 18$, $\Delta y^+ = 4.5$ and $\Delta z^+ = 9$ wall units and at the finest resolution, the cell sizes are $\Delta x^+ = 12$, $\Delta y^+ = 3$ and $\Delta z^+ = 6$ wall units. Consequently, the interpolation point that is used to compute the wall shear stress lies at a distance of $y_p^+ = 6$, $y_p^+ = 4.5$ and $y_p^+ = 3$ wall units, respectively. Flow statistics were collected over approximately 50 flow-through times and further averaged over the x- and z-direction.

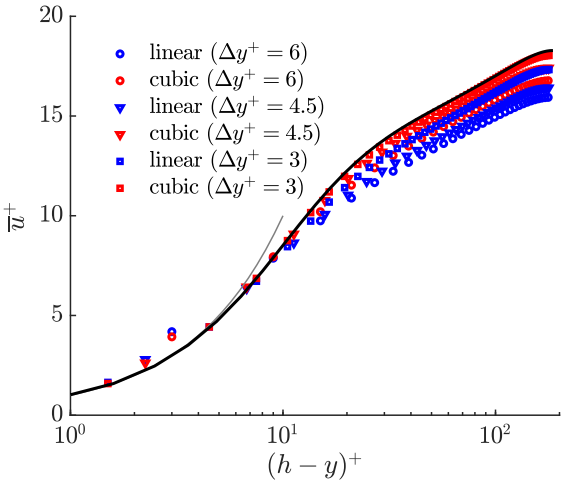

Figure 3. Mean velocity profile inside the turbulent channel flow for $Re_\tau = 180$. The symbols represent the velocity profiles obtained from our LES, the black line represents the DNS by Hoyas and Jiménez [23]. The grey line displays the linear law of the wall $u^+ = y^+$.

Fig. 3 shows the profile of the mean streamwise velocity $\overline{u}$ normalised with wall units (i.e. ν and u_τ) over the wall distance. We can see that the simulation results with the wall model show a significant improvement over the results computed with the linear law of the wall. For example, the results of the wall model at $\Delta y^+ = 4.5$ (red triangles) are approximately identical to the results obtained with the linear wall function at $\Delta y^+ = 3$ (blue squares). Furthermore, the results from the wall model at y_p^+ lie very close to the DNS reference. Please note that the wall shear stress is computed by interpolating the velocity to y_p – in the present grid configuration that means taking the average value between the two velocities closest to the wall – and then imposing either the linear wall function (indicated by the dotted line) or feeding the value into the wall model. Therefore, the velocity closest to the wall overshoots the linear law of the wall at the coarse grid resolution.

Fig. 4 shows the profile of the Reynolds shear stress $-\overline{u'v'}$ normalised with wall units (i.e. ν and

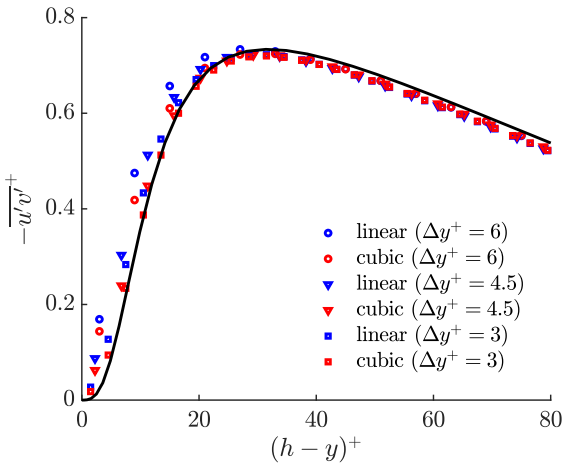

Figure 4. Reynolds shear stress profile inside the turbulent channel flow for $Re_\tau = 180$. The symbols represent the velocity profiles obtained from our LES, the black line represents the DNS by Hoyas and Jiménez [23].

u_τ) over the wall distance. Again, the wall model exhibits a marked improvement over the linear law of the wall particularly in the buffer layer.

It follows from the near-wall behaviour of the velocity that at leading order in the wall distance $h - y$ the Reynolds shear stress only depends on the wall shear stress fluctuation field (cf. Smits et al. [25]):

$$-\overline{u'v'} \approx \frac{1}{2\mu^2}\overline{\tau'_{wx}\left(\frac{\partial \tau'_{wx}}{\partial x} + \frac{\partial \tau'_{wz}}{\partial z}\right)}(h-y)^3 \qquad (25)$$

Therefore, the improved prediction of the Reynolds shear stress near the wall directly reflects a better prediction of the wall shear stress fluctuations.

The improvement in the mean velocity profile is mainly attributed to the inclusion of the pressure gradient which at this relatively low Reynolds number dominates the near wall part of the buffer layer. The more accurate Reynolds shear stress further improves the prediction.

For higher Reynolds numbers, the contribution of the pressure gradient to the mean velocity profile decreases with $1/Re_\tau$ [26]. In light of the findings of Smits et al. [25], we expect that including the time derivative of the wall shear stress into the wall model remains important also for high Reynolds numbers.

5. CONCLUSION

A wall model was derived based on a cubic Taylor polynomial for the velocity profile and a linear profile for the pressure. The wall-normal velocity derivatives were expressed in terms of the wall shear stress and the wall pressure using relations obtained from the Navier-Stokes [10] or boundary layer equations. By imposing a collocation constraint for the velocity at a point off the wall, we obtained an ordinary differential equation for the wall shear stress.

We first conducted an a-priori investigation in which the wall shear stress was computed from a known velocity profile. For the oscillatory Stokes boundary layer and the Falkner-Skan boundary layer, we found that our wall model converges to the exact wall shear at third order in the distance of the interpolation point. We observed that for small distances from the wall, the model has a superior accuracy than a linear approximation when a pressure gradient is present and a superior accuracy than both a linear and a quadratic approximation [13] when the flow is unsteady.

In a second step, we performed a-posteriori tests for which the wall model was coupled to a flow solver. For the same test cases, we observed that the wall model achieves the same accuracy as the linear wall function for half the grid resolution. Use of the wall model resulted in reasonably accurate solutions when there are two or more cells over the 99% boundary layer thickness. Finally, we performed wall-resolved LES of a turbulent channel flow at $Re_\tau = 180$ at various grid resolutions for which the interpolation point lies within the viscous sublayer. We found that the wall model achieves the same accuracy as the linear wall function for two thirds of the grid resolution.

In conclusion, the present wall model can deliver significant gains in accuracy at the same grid resolution (or significant savings in grid points at the same accuracy) for LES that marginally resolve boundary layers or the viscous sublayer in turbulent flow.

Future work might combine the present model with the model of Breuer et al. [6] by replacing their quadratic approximation of the velocity profile within the viscous sublayer with the cubic approximation derived in sections 2.1–2.3. It could also be interesting to investigate other velocity profiles than the Taylor polynomials. As already noted by [11], the monomial basis could be replaced by a different function basis with a higher approximation power, e.g. rational functions.

ACKNOWLEDGEMENTS

The authors gratefully acknowledge the computational and data resources provided by the Leibniz Supercomputing Centre (`www.lrz.de`).

REFERENCES

[1] Shih, T.-H., Povinelli, A., Liu, N.-S., Potapczuk, G., and Lumley, J. L., 1999, "A Generalized Wall Function", *Technical Memorandum 19990081113*, NASA.

[2] Balaras, E., and Benocci, C., 1994, "Subgrid Scale Models in Finite Difference Simulations of Complex Wall Bounded Flows", *Applications of Direct and Large Eddy Simulation, AGARD*, Chania, Greece, Vol. 551, pp. 2.1–2.6.

[3] Cabot, W., and Moin, P., 2000, "Approximate Wall Boundary Conditions in the Large-Eddy Simulation of High Reynolds Number Flow",

Flow, Turbulence and Combustion, Vol. 63 (1), pp. 269–291.

[4] Spalart, P., Jou, W.-H., Strelets, M., and Allmaras, S., 1997, "Comments on the Feasibility of LES for Wings, and on a Hybrid RANS/LES Approach", *Proceedings of First AFOSR International Conference on DNS/LES*, Greyden Press.

[5] Werner, H., and Wengle, H., 1993, "Large-eddy simulation of turbulent flow over and around a cube in a plate channel", F. e. a. Durst (ed.), *Turbulent Shear Flows 8*, Springer, Berlin, pp. 155–168.

[6] Breuer, M., Kniazev, B., and Abel, M., 2007, "Development of Wall Models for LES of Separated Flows Using Statistical Evaluations", *Computers & Fluids*, Vol. 36 (5), pp. 817–837.

[7] Schanderl, W., Jenssen, U., and Manhart, M., 2017, "Near-Wall Stress Balance in Front of a Wall-Mounted Cylinder", *Flow, Turbulence and Combustion*, Vol. 99, pp. 665–684.

[8] Jenssen, U., Schanderl, W., Strobl, C., Unglehrt, L., and Manhart, M., 2021, "The Viscous Sublayer in Front of a Wall-Mounted Cylinder", *Journal of Fluid Mechanics*, Vol. 919, p. A37.

[9] Schanderl, W., and Manhart, M., 2016, "Reliability of wall shear stress estimations of the flow around a wall-mounted cylinder", *Computers and Fluids*, Vol. 128, pp. 16–29.

[10] Dallmann, U., and Gebing, H., 1994, "Flow Attachment at Flow Separation Lines", G. H. Schnerr, R. Bohning, W. Frank, and K. Bühler (eds.), *Fluid- and Gasdynamics*, Acta Mechanica, Springer, Vienna, ISBN 978-3-7091-9310-5, pp. 47–56.

[11] Shrikhande, G., 2012, "Assessment of Taylor-series Model for Estimation of Vortex Flows Using Surface Stress Measurements", Master's thesis, Michigan State University.

[12] Schlichting, H., and Gersten, K., 2006, *Grenzschicht-Theorie*, Springer, Berlin Heidelberg, ISBN 978-3-540-23004-5.

[13] Manhart, M., Peller, N., and Brun, C., 2008, "Near-Wall Scaling for Turbulent Boundary Layers with Adverse Pressure Gradient", *Theoretical and Computational Fluid Dynamics*, Vol. 22 (3), pp. 243–260.

[14] Nicoud, F., and Ducros, F., 1999, "Subgrid-Scale Stress Modelling Based on the Square of the Velocity Gradient Tensor", *Flow, Turbulence and Combustion*, Vol. 62 (3), pp. 183–200.

[15] Manhart, M., Tremblay, F., and Friedrich, R., 2001, "MGLET: A Parallel Code for Efficient DNS and LES of Complex Geometries", *Parallel Computational Fluid Dynamics 2000*, North-Holland, Amsterdam, ISBN 978-0-444-50673-3, pp. 449–456.

[16] Harlow, F. H., and Welch, J. E., 1965, "Numerical Calculation of Time-Dependent Viscous Incompressible Flow of Fluid with Free Surface", *The Physics of Fluids*, Vol. 8 (12), pp. 2182–2189.

[17] Williamson, J., 1980, "Low-Storage Runge-Kutta Schemes", *Journal of Computational Physics*, Vol. 35 (1), pp. 48–56.

[18] Chorin, A. J., 1968, "Numerical Solution of the Navier-Stokes Equations", *Mathematics of Computation*, Vol. 22 (104), pp. 745–762.

[19] Dröge, M., and Verstappen, R., 2005, "A New Symmetry-Preserving Cartesian-Grid Method for Computing Flow Past Arbitrarily Shaped Objects", *International Journal for Numerical Methods in Fluids*, Vol. 47 (8-9), pp. 979–985.

[20] Cheny, Y., and Botella, O., 2010, "The LS-STAG Method: A New Immersed Boundary/Level-Set Method for the Computation of Incompressible Viscous Flows in Complex Moving Geometries with Good Conservation Properties", *Journal of Computational Physics*, Vol. 229 (4), pp. 1043–1076.

[21] Meyer, M., Devesa, A., Hickel, S., Hu, X. Y., and Adams, N. A., 2010, "A Conservative Immersed Interface Method for Large-Eddy Simulation of Incompressible Flows", *Journal of Computational Physics*, Vol. 229 (18), pp. 6300–6317.

[22] Liu, C.-M., and Liu, I.-C., 2006, "A Note on the Transient Solution of Stokes' Second Problem with Arbitrary Initial Phase", *Journal of Mechanics*, Vol. 22 (4), pp. 349–354.

[23] Hoyas, S., and Jiménez, J., 2006, "Scaling of the Velocity Fluctuations in Turbulent Channels up to Reτ=2003", *Physics of Fluids*, Vol. 18 (1), p. 011702.

[24] Kim, J., Moin, P., and Moser, R., 1987, "Turbulence Statistics in Fully Developed Channel Flow at Low Reynolds Number", *Journal of Fluid Mechanics*, Vol. 177, pp. 133–166.

[25] Smits, A. J., Hultmark, M., Lee, M., Pirozzoli, S., and Wu, X., 2021, "Reynolds Stress Scaling in the Near-Wall Region of Wall-Bounded Flows", *Journal of Fluid Mechanics*, Vol. 926.

[26] Pope, S. B., 2000, *Turbulent Flows*, Cambridge University Press, Cambridge; New York, ISBN 978-0-521-59125-6 978-0-521-59886-6.

Conference on Modelling Fluid Flow (CMFF'22)
The 18th International Conference on Fluid Flow Technologies
Budapest, Hungary, August 30 -September 2, 2022

SUITABILITY OF A PROFILE WITH TUBERCLES FOR AXIAL PUMPS - INVESTIGATION USING FLOW SIMULATION

Mareen DERDA[1], Ferdinand NEUMANN[2], Paul Uwe THAMSEN[3]

[1] Corresponding Author. Department of Fluid System Dynamics, Institute of Fluid Dynamics and Technical Acoustics, Technische Universität Berlin. Straße des 17. Juni 135, 10623 Berlin, Germany. Tel.: +49 30 314 27832, E-mail: mareen.derda@tu-berlin.de
[2] E-mail: ferdinand.neumann@campus.tu-berlin.de
[3] Department of Fluid System Dynamics, Institute of Fluid Dynamics and Technical Acoustics, Technische Universität Berlin., E-mail: paul-uwe.thamsen@tu-berlin.de

ABSTRACT

Even if wind tunnel tests and simulations have confirmed that tubercles can influence the behaviour of a profile, research in the field of axial pumps has so far been lacking. However, previous studies cannot be transferred to the application in axial pumps, since the requirements for the profile geometry as well as the Reynolds number range differ. The present study aims to address this research gap by performing a CFD simulation with a profile common for axial pumps, the Goe11K, testing four different tubercle configurations. At the same time, this simulation is a preliminary study for experimental tests.

The results show that certain tubercle configurations improve the behaviour of the profile in the post-stall area, i.e. increase the lift of the profile at large angles of attack (α). In general, the curve of the profiles with tubercles runs more evenly, without the drastic drop in lift. This improved property comes at the expense of lower maximum lift and increased drag at lower α. With regard to the use in axial pumps, it can be concluded that there are advantages particularly in the partial load range. That could ultimately enlarge the operation range of an axial pump.

Keywords: axial pumps, CFD, tubercles

NOMENCLATURE

A	[m]	tubercle amplitude
c	[m]	chord length
c_D	[-]	coefficient of drag
c_L	[-]	coefficient of lift
d_A	[mm]	outer pump diameter
k	[J/kg]	turbulent kinetic energy
L	[m]	characteristic length
n	[$1/min$]	rotational speed
Δp	[$kg/m \cdot s^2$]	pressure difference to ambiance
Re	[-]	Reynolds number
u	[m/s]	freestream velocity
w	[m]	tubercle wavelength
$y+$	[-]	dimensionless wall distance
α	[°]	angle of attack
ν	[m^2/s]	kinematic viscosity
ρ	[kg/m^3]	density
ω	[$1/s$]	specific dissipation rate

1. INTRODUCTION

Previous research by Fish et al. [1] and many others have already shown that sinusoidal wing leading edges, modeled after the leading edge of humpback whale fins and called tubercles, can strongly influence flow behaviour. The earlier study has shown that the tubercles change the stall and post-stall behaviour of a wing resulting in a smoother flow separation and an increased post-stall lift [1].

However, the known research on the application of tubercles in pumps is limited and non-existent for axial pumps. Due to the different profile selection, results from existing studies cannot be relied on when designing axial pump blades with tubercles. Therefore, this study aims to address that research gap by using CFD-methods on an infinite vane with a Goe11K, a profile commonly used in axial pumps, within a Reynolds number region of $Re = 1.5 \cdot 10^6$ and an α range from 0° to 24°. Since axial pumps represent a wide area of application and therefore an important area of research, this is a first step towards the investigation of the suitability of tubercled profiles for axial pumps. Based on this, experimental investigations are to be carried out.

2. STATE OF RESEARCH

2.1. Basic Mechanism of Tubercles

In the previous research literature, four mechanisms of action of tubercles are mainly distinguished. The first effect was mentioned by van Nierop et al. [2]. It was claimed that the pressure

distribution on the wing in flow direction, which is different behind tubercle tips and valleys, influences the separation behaviour. Due to a higher pressure gradient behind the tubercle valleys the flow separates there first while still staying attached behind the tips. This contributes to the smoother separation characteristics of a tubercled wing.

The second effect was mentioned by Miklosovic et al. [3]. The resulting vortices behind the tubercle valleys are thought to increase the momentum exchange between boundary layer and freestream near the trailing edge of the wing, resulting the flow staying attached in these regions at higher α. This working mechanism is comparable to the one of "vortex generators".

A third working mechanism was mentioned by Pedro et al. [4]. The vortices, which appear behind tubercle valleys, work as a barrier against spanwise flow on a wing like wing fences. Therefore, on finite wings tubercles reduce the expansion of separation zones along the wingspan resulting in an increased lift at high α, where parts of a finite wing are already stalled. It must be noted that this effect only shows in experiments and simulations with finite wings with changing profile contour along the span. As a result, those phenomena will not occur in the presented simulation approach, where the wing profile does not change along the span. Therefore, no spanwise pressure gradient and no changeable separation behaviour along wingspan can be expected, which tubercles could potentially help reducing.

The fourth effect was described by Custodio [5]. The author argues that the vortices accelerate the flow on the wing, resulting in lower pressure and lift often called "vortex lift".

2.2. Influence of Tubercles on the Behaviour of a Profile

The before mentioned study by Miklosovic et al. [3] has shown, how tubercles can improve the flow around a wing. In their research a finite wing with a NACA 0012 profile, with a maximum thickness of 12% at 30% chord length, was tested in a wind tunnel at a Reynolds number range from $Re = 1.35 \cdot 10^5$ up to $Re = 5 \cdot 10^5$. The Reynolds number is defined as the ratio of inertial forces to viscous forces and can be calculated with Eq. (1).

$$Re = \frac{u \cdot L}{\nu} \tag{1}$$

The wing with tubercles showed an increased maximum lift by 6% and a decreased drag up to 32% at high α. In addition, the stall characteristic of the wing was smoother on the wing with tubercles than on the one without. At low α the tubercles did not show a change in lift and drag when compared with the non-modified wing.

A study by Cai et al. [6] tested the influence of tubercles on an infinite wing with a NACA 63_4-021 profile at Reynolds number $Re = 2 \cdot 10^5$ using CFD-methods. The results in this research show a different influence of the tubercles on wing performance. At high α, where the flow on the unmodified wing is still attached, the tubercled wing has an increased drag and reduced lift. The tubercles show an improved flow behaviour only in the region of separated flow, where drag is like the unmodified wing while lift is increased.

Those two studies highlight, that the influence of tubercles on the wing characteristics is not the same for all applications, but rather depend on parameters like the selected airfoil, Reynolds number and test setup.

The influence of tubercles on flow characteristics also depends on the geometry of the tubercles defined by the amplitude A and the wavelength w. Both parameters are annotated in Figure 1 for better understanding.

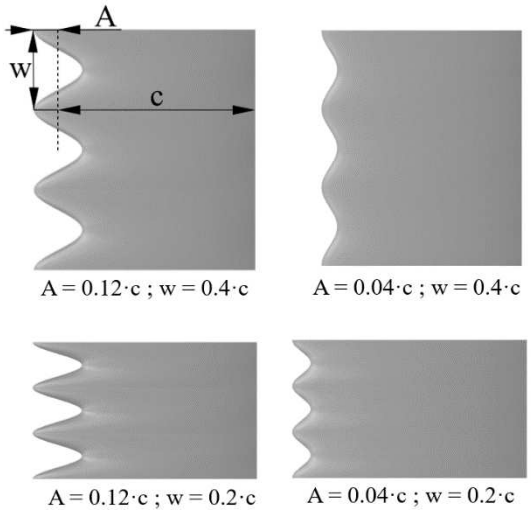

Figure 1. Selected tubercle configurations

Studies by Johari [7] and Hansen et al. [8] demonstrate that with higher amplitudes the flow around the wing is more influenced by the tubercles and therefore lift and drag are changed more compared to a wing without tubercles. This can be seen in the study by Johari [7] where a small amplitude of $A = 0.025 \cdot c$ only reduces maximum lift slightly and improves post-stall lift by a small amount while versions with a high amplitude of $A = 0.12 \cdot c$ have a higher reduction of maximum lift but also higher lift in the post-stall regime.

The influence of the tubercle wavelength does not appear to be as decisive as that of the amplitude. Also, no general rule for the influence of the wavelength can be found in the studies presented here. However, at high wavelengths such as e.g. $w = 0.86 \cdot c$ tested by Hansen et al. [8], the flow behaviour on the wing tends to be very similar to that on the unmodified wing.

2.3. Hypotheses

Even if research findings to date cannot be directly transferred to the application in axial pumps, due to the completely different profile requirements, hypotheses related to the subject of the study can still be derived. These are:

1. The profiles with tubercles do not reach the maximum lift coefficient c_L of the profile without tubercles but show better lift behavior in the post-stall area.
2. The drag coefficient c_D of the profiles with tubercles will be slightly higher for angles without flow separation compared to the reference wing.
3. The lift behavior of the profile with tubercles depends on the configuration used.
    a. Smaller amplitudes result in higher maximum lift, but only minor improvements in the post-stall area.
    b. Larger amplitudes result in lower maximum lift, but better post-stall behavior.
4. A smoother stall characteristic can be expected on the tubercled wings than on the baseline wing.

These hypotheses are to be examined in the present study using a CFD simulation.

3. METHOD

As already mentioned, previous research findings cannot be transferred, among other things due to the different profile requirements for axial pumps. Therefore, the profile selection and the selection of the tubercle configurations to be simulated are discussed here first before the setup of the CFD simulation is described.

3.1. Profile Selection and Selected Configurations

The essential profile requirements for axial pumps include slimness combined with a high thickness reserve reducing the suction peak at the leading edge and therefore making the pump vanes less prone to cavitation. Furthermore, a high maximum glide ratio in the design point is desired for a high efficiency of the pump [9]. The chosen Goe11K is shown in Figure 2.

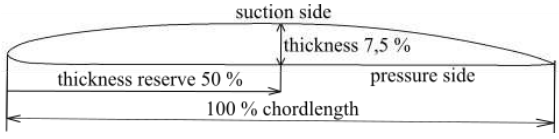

Figure 2. Selected profile Goe11K

This profile meets these requirements [10] and was already used in axial pumps at the Department of Fluid System Dynamics at the Technical University of Berlin, so previous test results can be compared.

Four configurations of tubercled wings and the baseline version were simulated to investigate a variety of different designs while keeping computational efforts at a reasonable level. A preselection of amplitudes and wavelengths was made considering the analysis made by Hansen et al. [8]. From these studies the configurations were selected to stay within a presumably promising range. Four configurations were created by combining two amplitude values with two values for the wavelength. The selected amplitudes are $A = 0.04 \cdot c$ and $A = 0.12 \cdot c$ and the wavelengths $w = 0.2 \cdot c$ and $w = 0.4 \cdot c$. The leading edge of the baseline wing was taken as the axis around which the defined sinus curve oscillates. This was done to ensure that the projected wing area on the modified wings is the same as on the reference. The four resulting configurations can be seen in Fig. 1. With those wings a wide range of amplitude-to-wavelength-ratios A/w is covered. Reaching from $A/w = 0.1$ for the smoothest up to $A/w = 0.6$ for the sharpest tubercles. Each of the four configurations and the reference profile without tubercles were simulated in the α range from 0° to 24°, with 3° intervals each, with a Reynolds number of $Re = 1.5 \cdot 10^6$.

3.2. CFD Setup

The CFD model was set up with the use of OpenFOAM and according to general information and guidelines on CFD setup e.g. from Schwarze [11]. The presented CFD model reflects an instationary and incompressible flow state and makes use of the RANS-approach. Turbulence in the domain is modelled using the kωSST-model as described in [11], a two-equation-model, which reflects turbulence in the freestream and the boundary layer well. Due to the addition of only two new variables, the turbulent kinetic energy k, and the specific dissipation ratio ω, computation time is kept at a reasonable level while still achieving a good depiction of turbulence in the domain. Because of those properties, it is industrial standard and used in this paper.

The calculation domain (cf. Figure 3) was designed to reflect an infinite vane. Therefore, both sidewalls where set to a symmetry condition.

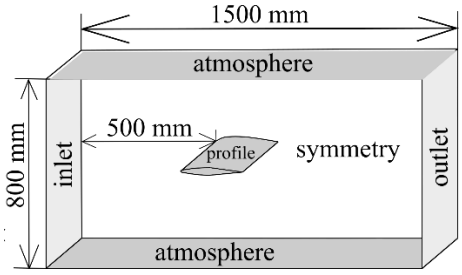

Figure 3. Calculation domain

The created mesh is an unstructured mesh consisting of roughly two million cells. The freestream cells are tetraeders while the boundary layers around the wing are resolved using prism layers. The resolved boundary layers were needed to ensure accurate drag and lift predictions.

Solving was done using the solver pisoFoam, which uses the PISO-algorithm. For discretisation of convective terms, the selected scheme was Gauss linear upwind, for the diffusive terms Gauss linear limited 1 was chosen and for gradient terms the Gauss linear scheme was applied. For the temporal discretization the Crank Nicolson scheme was applied with a blending factor of 0.7.

3.3 Mesh study

A mesh study was carried out to ensure that the results are independent from the mesh. To investigate the influence of the mesh resolution on the results, four different resolutions were tested with the baseline wing at $\alpha = 6°$ using the unsteady setup described above. To change the resolution of the mesh, multiple parameters like growth rate of the cells and first layer thickness of the prism layers and thereby $y+$ were adapted. For good results the requirement $y+ < 5$ should be reached in all cells at the wall to keep the cells within the viscous sublayer [11].

Table 1. Overview of the Mesh Study

Cell Count in Million	max y+	c_D [-]	c_L [-]
0.52	8.809	0.0281	0.998
1.42	7.942	0.0235	1.005
2.195	6.01	0.0194	1.007
4.210	3.74	0.0191	0.993

Table 1 shows the time-averaged force coefficients and the maximum $y+$ value for the mesh study. It was found that a poor mesh resolution has a considerable influence on the calculated drag. Between the two highest resolutions the drag value does not vary more than two percent which makes the occurring error tolerable. The maximum $y+$ for this resolution is above five. To save computation time the resolution with around two million cells was nonetheless selected for this study, because only around 0.5% of the cells on the wing surface had a $y+$ value above five.

The constructed simulation model was validated by comparing the simulated lift and drag behaviour of the Goe11K baseline profile with profile data from Riegels [10]. The results, seen in Figure 4, show good agreement for lift and reasonable agreement for drag.

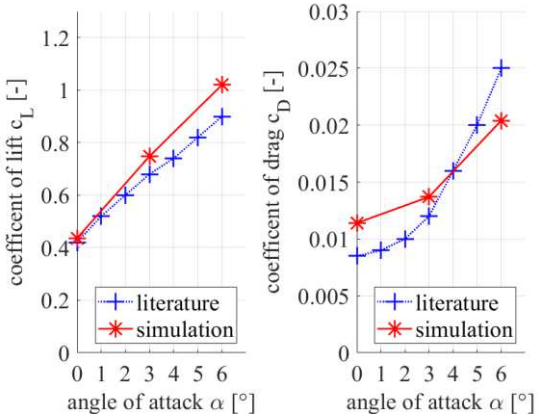

Figure 4. Comparison between simulation results and literature data

4. RESULTS

First, the results of the simulation are presented using the calculated coefficients, after which a qualitative evaluation is carried out using the simulated pressure distribution.

4.1. Quantitative Evaluation

Figure 5 shows the results for the lift coefficients c_L of all tubercle versions and the base wing from the simulation over the simulated α range from 0° to 24°. As can be seen the lift of the baseline wing increases with α up to 18°, where maximum lift of $c_L = 1.6$ is reached. A further increase of α leads to flow separation at the leading edge of the wing. The maximum achievable lift through tubercle configurations is only $c_L = 1.2$. Depending on the tubercle configuration, this corresponds to a maximum loss of lift of about 35%. Furthermore, it was found that all tubercle configurations show a smoother separation behaviour than the baseline.

Apart from that, all tubercle configurations have a higher lift coefficient c_L in the post-stall area than the reference wing. The lift improvement in the post-stall area is the biggest at $\alpha = 21°$ where the tubercles improve lift up to 20%.

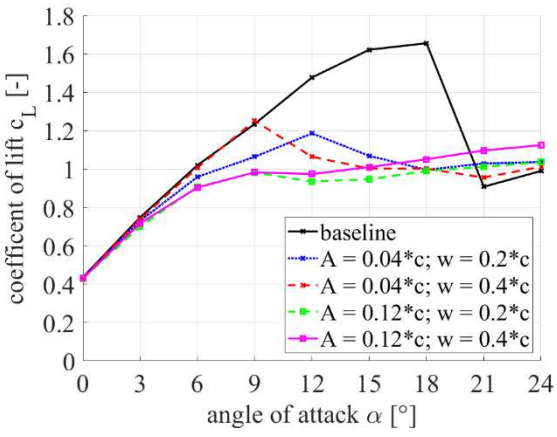

Figure 5. Calculated coefficient of lift c_L for tubercled configurations and baseline

Figure 6 shows the coeffient of drag c_D calculated in the simulations for all versions with modified leading edge and the reference wing plotted over the α range. It is visible that the drag of all configurations between 9° and 18° is higher than on the unmodified wing. In the post-stall-region of the base wing, three of the four tested tubercle configurations achieve lower drag than the unmodified wing.

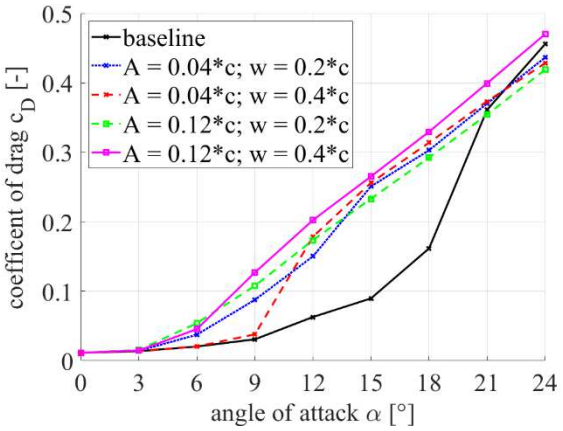

Figure 6. Calculated coefficient of drag for tubercled configurations and baseline

The quantitative evaluation has shown, that the aerodynamical coefficients are heavily influenced by the application of tubercles. The next section is going to determine the reasons for this changed flow behaviour.

4.2. Qualitative Evaluation

In this section the flow around the tubercled wing is analysed using pictures created in post-processing of the simulation. The investigation is started at a low α and is going to describe the changes in the flow field when increasing α to and also beyond the separation angle of the reference wing.

Figure 7 compares the pressure distribution on the suction side of the basewing (the upper wing in Fig. 7) with that of one selected configuration for $\alpha = 3°$. For this comparison the surface is coloured by the local pressure, where blue symbolises low pressures and orange high pressures. The reference wing has a uniform pressure distribution along the whole width while on the tubercled wing a higher negative pressure can be observed in the tubercle valleys than on the tips. The observed negative pressure also exceeds the suction peak of the reference wing.

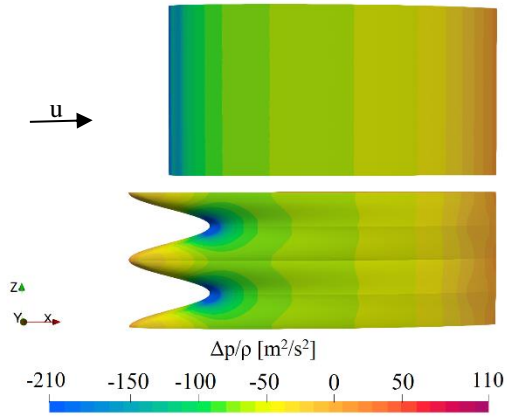

Figure 7. Pressure distribution on the base wing and the tubercle configuration with $A = 0.12 \cdot c$ and $w = 0.2 \cdot c$ at $\alpha = 3°$

When looking at the simulation results it was found that on the simulated wings with the amplitude of $A = 0.12 \cdot c$ a pair of vortices, which can be seen in Figure 8, starts to develop only behind the tubercle valleys on the suction side at $\alpha = 6°$ and above. Fig. 8 shows the surface of the selected tubercle configuration, which is coloured depending on the local pressure. In addition, streamlines are shown in grey to highlight the flow above the wing and to show the vortex behind the tubercle valley. These vortices, although they create some negative pressure and hence vortex lift at the surface, are the reason for the reduction in lift, since the vortex lift is less than the lift present on the wings with fully attached flow, and also the reason for the increase in drag observed in Figures 5 to 6 for these configurations. The vortices mentioned grow when increasing α.

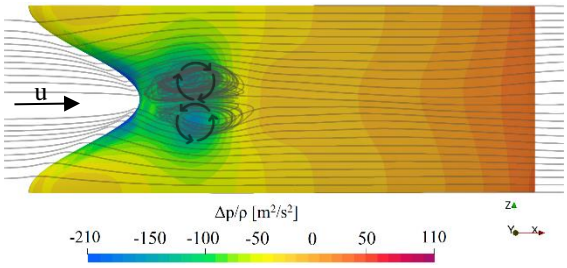

Figure 8. Pair of vortices on the configuration with $A = 0.12 \cdot c$ and $w = 0.2 \cdot c$ at $\alpha = 6°$

Regarding the separation behaviour it was found that some configurations already lose c_L compared to the baseline wing at $\alpha = 6°$ resulting from the mentioned vortices. However, the flow on the configuration with the lowest amplitude-to-wavelength ratio of $A/w = 0.1$, which is the version with the smoothest tubercles, stays completely attached until $\alpha = 9°$. At $\alpha = 12°$ the flow on a major part of this wing is separated, as shown in Figure 9, but a high negative pressure is still present on the tubercle tips.

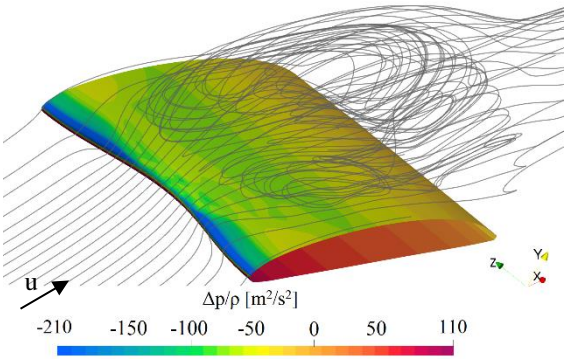

Figure 9. Flow on the configuration with $A = 0.04 \cdot c$ and $w = 0.4 \cdot c$ at $\alpha = 12°$

The flow on the reference wing remains attached up to an $\alpha = 18°$. While increasing α the suction pressure on the leading edge increases to very high values. Regarding these high simulated negative pressures, it should be mentioned, that cavitation could appear at those points when used in water, which strongly influences the behaviour of a pump.

Above $\alpha = 18°$ the wing without tubercles stalls and as a result the achieved lift is rapidly reduced. In comparison the flow on the tubercled wings is still attached at small parts of the wing behind the tubercle tips (cf. Figure 10) at these high α.

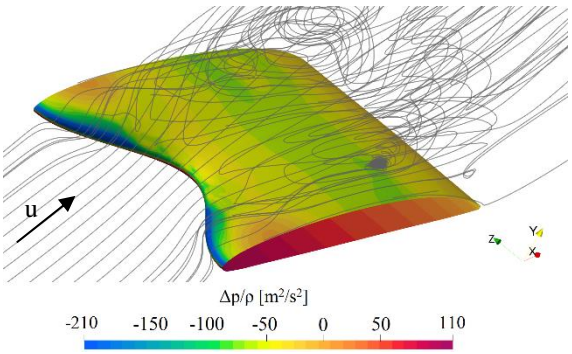

Figure 10. Partly attached flow on the tubercled wing with $A = 0.12 \cdot c$ and $w = 0.2 \cdot c$ at $\alpha = 21°$

5. DISCUSSION

The simulation results show that for the selected profile, setup and Reynolds number improvements in post-stall lift can be found, while there is a loss at lower α. Therefore, the first hypothesis is confirmed. However, the magnitude of this trend has been underestimated and appears large compared to the literature e.g. [6]. The loss in lift in the pre-stall region of around 35% is large while the improvement in post-stall is smaller with around 10% to 20%. The best tested configuration is the one with the amplitude of $A/c = 0.12$ and the wavelength of $w/c = 0.4$. While the loss of this version at low angles is comparable to the version with the same tubercle amplitude, the lift is the highest for all tubercle configuration from $\alpha = 18°$ upwards.

Regarding the second hypothesis, which stated that drag values in the area of adjacent flow should be slightly higher for the tubercled versions, it can be argued that again the overall trend follows this hypothesis but the extent to which the drag is increased is, with around 50% increase compared to the baseline, greater than expected. Therefore, the hypothesis can not be verified because only a minor increase in drag was expected, but the results showed a rather significant increase.

The differing results compared to the literature can be attributed to multiple factors.

Firstly, the chosen Goe11K profile is with a thickness of 7.5% chord slimmer than profiles described in literature. It is designed to achieve a high glide ratio at low α. This leads to a significant increase in drag when vortices start to appear behind the tubercle valleys at $\alpha = 6°$, where the drag of two tubercled configurations is more than doubled (cf. Fig. 6). Secondly the approach of an infinite wing does not show the benefit of tubercles created through spanwise flow suppression, which can be seen when comparing results from Miklosovic et.al. [3] and Cai et.al. [6]. When using the infinite wing model, the third working mechanism of tubercles (see chapter 2.) does not improve flow around the wing, because no spanwise flow appears due to the absence of a spanwise pressure gradient or spanwise forces, that could be suppressed. However, the infinite wing approach more closely reflects the conditions in an axial flow pump than a finite wing because the casing suppresses the formation of tip vortices. Thirdly, a study by Dropkin et al. [12] has shown that the maximum lift on a tubercled wing does not increase in the same way the maximum lift of an unmodified wing does at higher Reynolds numbers. Therefore, the selected Reynolds number of $Re = 1.5 \cdot 10^6$, which is high compared to most studies on tubercle application, results in a larger difference in maximum lift between base wing and tubercle configurations. Lastly, it must be noted that the lift on the base wing at high α from 12° to 18° can partly be attributed to the simulated high negative pressures. When using tubercles in an axial pump with water as the pumping medium those high negative pressures could lead to cavitation on the leading edge and therefore lift would be reduced. As a result, the difference in lift between tubercle configurations and baseline wing at those α might be smaller in reality.

The third hypothesis, which claimed that the lift behaviour depends on the selected tubercle configuration, is confirmed when looking at the simulation results. The versions with a smaller amplitude follow the lift slope of the unmodified wing up to $\alpha = 9°$ and achieve a higher maximum lift in the pre-stall area of the baseline than the version with higher amplitude. Furthermore, on these configurations a sudden decrease in lift can be found at $\alpha = 9°$ or $\alpha = 12°$. This is due to the fact, that at

those α a vast area of the wing stalls, decreasing lift. This effect cannot be observed on the tubercle configurations with the higher amplitude. The lift does not increase as much as on the other versions at low α but also does not drop noticeably at any α. This is due to the smoother separation behaviour on those wings. In the post-stall region only the version with the wavelength of $w/c = 0.4$ has a better lift value than the configurations with the lower amplitude. This might be due to the fact, that the amplitude-to-wavelength ratio on the configuration with $A/c = 0.12$ and $w/c = 0.2$ might be too high.

The fourth hypothesis, dealing with the stall characteristic, can also be accepted. The separation behaviour on the tubercled versions is indeed smoother than on the baseline wing. While no tubercled versions shows a rapid lift decrease like the baseline does, the lift on the versions with the small amplitude of $A/c = 0.04 \cdot c$ does drop slightly at $\alpha = 9°$ resp. $\alpha = 12°$. In contrast the lift curve for the wings with the higher tubercle amplitude do not show a drop in lift at any α.

6. CONCLUSION

From the simulation results and from the studies presented in chapter 2 it can be concluded that the benefit of tubercles comes in operation points where a flow separation on unmodified wings/blades is likely. For axial pumps this is the case in operation points well below the design point. In the simulation it was shown that an optimized tubercle configuration can improve lift at those points by 20%, while maintaining similar drag values. This is because tubercles not only delay flow separation by energizing the boundary layer at the trailing edge, but also confine appearing separation zones locally. As a result, on larger parts of the blades the flow should stay attached for longer.

In addition, the application of tubercles would also most likely reduce or completely erase the phenomenon called “rotation stall” described in [9], where a stalled region rotates in opposite direction to the blades. This is because of the smoother separation characteristics of the tubercled blades compared to the version with conventional leading edge.

Concerning Reynolds number, it can be concluded, that the selected Reynolds number of $Re = 1.5 \cdot 10^6$, which was chosen based on an existing pump with an outer diameter of $d_A = 149\ mm$, an average chord length of around $c = 100\ mm$ and a rotational speed of $n = 2865\ rpm$ in the design point, reduces the positive effect of the tubercles. The use of tubercles in axial pumps with a lower Reynolds number, due to a smaller chord length of the blades or a lower rotational speed, could be more advantageous.

In the design point, which would be at around $\alpha = 3°$, where the highest glide ratio is achieved on the reference wing, lift and drag on the tubercle configurations are not changed by much, the maximum glide ratio is reduced from 54 to around 50 depending on the selected configuration. However, when increasing α the efficiency and lift of the unmodified wing cannot be achieved with tubercles. Compared to studies shown in chapter 2 the difference between unmodified and tubercled wings is bigger in the presented simulation. Reasons for that were described to be the profile selection, Reynolds number and the model of the infinite wing. Regarding profile selection, tubercles seem to be less effective on profiles needed for axial flow pumps than on thicker profiles used for other applications. In the matter of the selected infinite wing model, it is true that axial pump blades do not show a free tip like on e.g. airplane wings, where spanwise flow is to be expected, because of the casing around the blades. However, crossflow can nonetheless be expected to a certain extend because of centrifugal forces or partial flow separation on the blades.

Another important influence on axial pumps is cavitation. It was already briefly mentioned in the discussion, that the appearance of cavitation might change results. However, the simulation was not set up to cover this phenomenon and therefore the influence of cavitation could not be investigated on. Research by Johari [7] suggests that tubercles influence cavitation behaviour depending on the selected configuration. In this study [7] a wing with a NACA 63_4-021was tested with different tubercle configurations at $Re = 7.2 \cdot 10^5$ and a range of α from 12° to 24°. For versions with low amplitudes and higher wavelengths the cavitation characteristics is similar to that of the baseline wing. On the whole leading edge of the wing sheet cavitation appears and increases in size with higher α. On configurations with higher amplitudes and smaller wavelength cavitation appears earlier then on the baseline wing but is confined to the regions behind the tubercle valleys for all α. Sheet cavitation did not appear on those wings. Because only the area behind the tubercle valleys is affected by cavitation on these wings, lift can still be created on the tubercle tips. Since the simulation has shown that a major part of the lift is created in the affected region it remains unclear whether the total lift created by these configurations under cavitation conditions really is higher than on an unmodified wing.

Nonetheless, it is likely that the evenly lift behaviour due to the smoother separation of the wings with tubercles enlarges a pump's operating range, with benefits in the application.

Overall, tubercles on axial pumps are expected to bring overall improvement, if a wide operation range, good efficiency and suction head are required, especially at low speed well below the operation point.

7. SUMMARY AND OUTLOOK

Due to missing research on the application of tubercles in axial pumps the aim of this study was to determine possible influences of tubercles when used on axial pump vanes. The Goe11K profile was selected for the simulation because it is a slim profile with a high thickness reserve and consequently well suited for the use in axial pumps.

The Reynolds number was chosen to be $Re = 1.5 \cdot 10^6$ based on an existing axial pump tested previously. Four tubercled wings where selected based on the results of earlier studies [7, 8] covering a good spectrum of amplitudes and wavelengths. The simulation was set up as a transient and incompressible CFD-simulation in OpenFOAM. using the model approach of an infinite wing. This set up was selected to keep computational effort at a reasonable level making it possible to investigate four tubercle configurations at a large α range. A mesh independence study was carried out to make sure results are not reliant on the discretisation of the domain. The simulation results show only small improvements in the post-stall area due to the leading-edge tubercles, while a significant reduction in maximum lift in the pre-stall area was observed. This was attributed to the selected Reynolds number, profile selection and infinite wing model. In the discussion an aspect outside the simulation model "rotation stall" was considered as well. Leading to the conclusion that the benefit of tubercles at lower Reynolds numbers might be higher than in the simulation. Furthermore, the simulation results showed that the tubercled wings have a smoother separation behaviour. This gain leading to a wider operation range still comes at a cost of lower lift and higher drag in the design point.

Despite that, it was argued that tubercles could improve axial pumps used at lower Reynolds numbers when a fitting tubercle configuration is selected and a good suction head is needed at low speeds, well below the design point.

Further studies should investigate whether these results can be transferred to applications in axial pumps as expected or whether other effects that have not yet been considered, such as centrifugal forces, dominate the flow. For this purpose, a test bench according to DIN EN ISO 9906 is currently being set up at the Department of Fluid System Dynamics at the Technical University of Berlin. This will be used to investigate the extent to which tubercles on the front edge of the blades of an axial three-bladed pump impeller with the Goe11K profile used in the simulation change the efficiency, the head, the power consumption, and the cavitation behaviour.

REFERENCES

[1] Fish, F. E., and Battle, J. M., 1995, „Hydrodynamic design of the humpback whale flipper", *Journal of morphology*, Vol. 225 (1), pp. 51-60.

[2] van Nierop, E. A., Alben, S., and Brenner, M. P., 2008, "How bumps on whale flippers delay stall: an aerodynamic model", *Physical review letters,* Vol. 100 (5), p. 54502

[3] Miklosovic, D. S., Murray, M. M., Howle, L. E., and Fish, F. E., 2004, "Leading-edge tubercles delay stall on humpback whale (Megaptera novaeangliae) flippers.", *Physics of Fluids,* Vol. 16 (5), pp. L39-L42.

[4] Pedro, C., and Kobayashi, M., 2008, "Numerical Study of Stall Delay on Humpback Whale Flippers.", *46th AIAA Aerospace Sciences Meeting and Exhibit*, Reno, Nevada

[5] Custodio, D., 2007, "The Effect of Humpback Whale-like Protuberances on Hydrofoil Performance." *Master thesis, Worcester Polytechnic Institute.*

[6] Cai, C., Zuo, Z. G., Liu, S. H., Wu, Y. L., and Wang, F. B., 2013, "Numerical evaluations of the effect of leading-edge protuberances on the static and dynamic stall characteristics of an airfoil.", *IOP Conf. Ser.: Mater. Sci. Eng*., Vol. 52 (5), p. 52006.

[7] Johari, H., 2007, "Effects of Leading-Edge Protuberances on Airfoil Performance", *AIAA Journal*, Vol. 45 (11), pp. 2634-2642

[8] Hansen, K. L., Kelso, R. M., and Dally, B. B., 2011, "Performance Variations of Leading-Edge Tubercles for Distinct Airfoil Profiles.", *AIAA Journal*, Vol. 49 (1), pp. 185-194.

[9] Pfleiderer, C., and Petermann, H., 2005, *Strömungsmaschinen*, 7. Edition, Berlin, Springer.

[10] Riegels, F. W., 1961, *Aerofoil Selections. Results From Wind-Tunnel Investigations,* London, Butterworth & Co

[11] Schwarze, R., 2013, *CFD-Modellierung*, Berlin, Springer

[12] Dropkin, A., Custodio, D., Henoch, C. W., and Johari, H., 2012, "Computation of Flow Field Around an Airfoil with Leading-Edge Protuberances", *Journal of Aircraft*, Vol. 49 (5), pp. 1345-1355

Conference on Modelling Fluid Flow (CMFF'22)
The 18th International Conference on Fluid Flow Technologies
Budapest, Hungary, August 30-September 2, 2022

Stability analysis of a streaky boundary layer generated by Miniature Vortex Generators

András SZABÓ[1], Péter Tamás NAGY[2], Maarten VANIERSCHOT[3] György PAÁL[2],

[1] Corresponding Author. Department of Hydrodynamic Systems, Faculty of Mechanical Engineering, Budapest University of Technology and Economics. Bertalan Lajos u. 4 - 6, H-1111 Budapest, Hungary. E-mail: aszabo@hds.bme.hu
[2] Department of Hydrodynamic Systems, Faculty of Mechanical Engineering, Budapest University of Technology and Economics.
[3] Group T Leuven Campus, Department of Mechanical Engineering, KU Leuven.

ABSTRACT

Delaying laminar-turbulent transition is an attractive method to reduce friction drag on streamlined bodies. In the case of natural transition, in which turbulence is triggered by the growth of two-dimensional Tollmien-Schlichting (TS) instabilities, this growth of the TS instabilities can be attenuated by introducing steady streamwise streaks into the boundary layer. These streamwise streaks are generated by streamwise vortices, which rearrange the flow via the lift-up mechanism. Such streamwise vortices can be induced by so-called Miniature Vortex Generators (MVGs). Although recently considerable attention has been devoted to the investigation of MVGs, and multiple studies investigated MVGs with different parameters, there is still no large-scale parameter study available in the literature. This study aims at (partially) fulfilling this knowledge gap. The methodology of Martín & Paredes (Theor. Comput. Fluid Dyn. 31, 505–517 (2017)) is followed in the calculations. First, the economic solution of the governing equations is discussed. Then, the streak amplitude, the growth factors of the TS-waves and shear-layer instabilities, which potentially lead to premature breakdown of the streaks are analysed in detail.

Keywords: Boundary layer, flow stability, Boundary Region Equation, Parabolized Stability Equations, Miniature Vortex Generators

NOMENCLATURE

Subscripts and Superscripts
Abbrevations

$\mathbf{U} = (U, V, W)$	$[-]$	base flow velocity
P	$[-]$	base flow pressure
$\mathbf{u}' = [u', v', w']^T$	$[-]$	perturbation velocity
p'	$[-]$	perturbation pressure
Re	$[-]$	Reynolds number
$\hat{\delta}$	$[m]$	boundary layer scale
$\hat{U}_0$	$[m/s]$	free-stream velocity
$\hat{\nu}$	$[m^2/s]$	kinematic viscosity
$\mathbf{q} = [u, v, w, p]^T$	$[-]$	perturbation shape function

α	$[-]$	streamwise wavenumber
ω	$[-]$	angular frequency
F	$[-]$	nondimensional frequency
$\hat{\Lambda}$	$[mm]$	MVG spanwise periodicity
$\hat{d}$	$[mm]$	MVG pair distance
$\hat{w}$	$[mm]$	MVG width
$\hat{h}$	$[mm]$	MVG height
$\hat{L}$	$[mm]$	MVG length
$\hat{L}_0$	$[mm]$	characteristic length
$\hat{x}_0$	$[mm]$	start of the computational domain
$\hat{x}_{MVG}$	$[mm]$	location of the MVG
$\hat{x}_{st}$	$[mm]$	start of the stability calculation
$\hat{\delta}_{99}$	$[mm]$	boundary layer thickness
A	$[-]$	streak amplitude
Re_δ	$[-]$	boundary layer scale Reynolds number

1. INTRODUCTION

Delaying laminar-turbulent transition over streamlined aerodynamic bodies has been an actively researched field for a long time. There are two main categories of the transition scenario: transition due to boundary layer instability and bypass transition [1]. In the former case, the boundary layer transition occurs due to the exponential amplification of small-amplitude disturbances, which can be appropriately described by linear theory. After the disturbance amplitude reaches a certain threshold, nonlinear effects set in; this is the secondary instability phase, which covers a much smaller spatial extension of the linear instability [2]. Several instability mechanisms exist; in the case of an incompressible two-dimensional boundary layer with small-to-none surface curvature, the dominant instability mechanism is the two-dimensional Tollmien-Schlichting (TS) wave. This is a well-understood, classical instability mechanism. The dampening of the TS

$\hat{\square}$ dimensional quantities
$\tilde{\square}$ variables with boundary layer scaling

MVG	Miniature Vortex Generator
BRE	Boundary Region Equations
PSE	Parabolized Stability Equations
fGMRES	flexible Generalized Minimal Residual Method

waves is the main interest of our research. The previously described instability-amplification scenario is only valid in the case of low background disturbance, i. e. turbulence intensity. In the case of high-level free-stream turbulence, instead of the slow, linear disturbance amplification, fast, nonlinear transition can occur whose mechanism can be manifold and partly poorly understood and which is termed bypass transition. However, in the first stage of the investigation of boundary-layer modification techniques to achieve drag reduction by transition-delay, always a low external disturbance level is assumed.

Several control techniques exist to modify the flow so that transition is postponed downstream. A promising method to attenuate the TS waves is the introduction of periodically varying slow-fast regions, so-called streamwise streaks into the boundary layer. It was shown both in numerical [3] and laboratory experiments [4] that with properly generated streaks, TS waves can be dampened. The physical mechanism of the TS wave attenuation is also clear: the spanwise shear generated by the streaks in the boundary layer is responsible for decreasing the disturbance energy growth [3]. Generally, the higher the streak amplitude, the higher this stabilization [3]. However, a too high streak amplitude is not desirable since then streaks become themselves unstable to inviscid secondary sinuous instabilities, which can result in an early breakdown to turbulence.

Streaks in a boundary layer can be generated in several ways. A promising passive technique was reported by Shahinfar et al.[5]: using winglet-type miniature vortex generators (MVGs), strong streaks can be generated; therefore, effective stabilization of the boundary layer can be achieved while the streaks remain stable. Following experimental studies [6, 7, 8, 9, 10] report additional information regarding the MVGs, such as: how changing a single parameter of the MVGs independently affect the boundary layer; using a second MVG row the streaks that decay downstream can be reinforced; the instability growth in the near-field of the MVGs, and also further downstream; the effect of the pressure gradient. Furthermore, the stabilization of the TS waves [9] and oblique disturbances [11] were also observed experimentally in a streaky boundary layer introduced by MVGs. In most of these studies, triangular MVGs were used, except for the investigations of Sattarzadeh et al. [9] and Sattarzadeh and Fransson [12], who examined rectangular MVGs. Interestingly, in some cases, rectangular MVGs were able to produce stronger streaks than triangular ones. Furthermore, the stronger streaks remained stable. Therefore, it can be concluded that the previous experimental studies have well established that MVGs are able to successfully generate a streaky boundary layer in which the growth of the TS waves is attenuated.

The numerical investigation of streaky boundary layers has received much less attention. Bagheri and Hanifi [13] used nonlinear Parabolized Stability Equations (PSE) to investigate the optimal spacing of the streaks to suppress TS waves. Later, Siconolfi et al. [14] used direct numerical simulation to calculate the flow around an MVG and BiGlobal stability analysis to calculate the instability modes. They obtained a reasonable agreement with the experiments. They identified several instability modes in the downstream vicinity of the MVGs, which cause local disturbance growth that might result in a premature transition to turbulence. Siconolfi et al. [15] substituted the effect of MVGs with streamwise vortices and showed that vortices placed outside the boundary layer can be much more effective for streak generation than vortices inside the boundary layer, therefore such vortices might lead to better transition delay. However, the practical generation of such vortices remains an open question.

Parallel to these numerical studies, Martín and Paredes [16] proposed a computationally effective numerical method to assess the stability of streaky boundary layers. They calculated the evolution of streaks with Boundary Region Equations (BRE), which are the extensions of the boundary layer equations: the boundary layer scaling is applied in both the wall-normal and spanwise direction. The evolution of the disturbances in the streaky boundary layer is calculated with linear PSE, which accounts for both non-local and non-parallel effects. The initial disturbances are calculated using BiGlobal stability equations. They modeled the effect of the vortex generators with Rankine vortices that have a fixed maximum amplitude, and obtained similar results to the ones of Siconolfi et al. [15, 14], verifying the validity of their approach. Later, Martín and Paredes [17] examined optimal streaks disturbances with limited maximum amplitude. They found the spanwise wavenumber and the maximum amplitude of the boundary layer streaks both have a significant influence not only on the attenuation of the TS waves but also on the sinuous instability modes. Furthermore, they predicted the transition location using the e^N method.

The above discussion illustrates that there are several topics that need to be addressed before the MVGs can be applied to commercial use. The present paper reports some initial results of our research to investigate MVGs from several different aspects. We discuss the efficient numerical implementation of the model equations used by Martín and

Paredes [16]. Then, we examine the stability of triangular and rectangular MVGs and compare the differences.

2. THEORETICAL FRAMEWORK

We investigate an incompressible zero pressure gradient flat-plate boundary layer. The nondimensional forms of the governing equations are used. Let x, y and z be the streamwise, wall-normal and spanwise coordinates respectively. Small-amplitude perturbations are considered around an equilibrium base flow. Let $\mathbf{U} = [U, V, W]^T$ and P denote the base flow velocity and pressure, and $\mathbf{u}' = [u', v', w']^T$ and p' the velocity and pressure of the small-amplitude perturbations. Then, the governing equations of the base flow are

$$\frac{\partial \mathbf{U}}{\partial t} + (\mathbf{U}\cdot\nabla)\mathbf{U} = -\nabla P + \frac{1}{\mathrm{Re}}\Delta\mathbf{U}, \tag{1}$$

$$\nabla\cdot\mathbf{U} = 0. \tag{2}$$

Furthermore, the linearised Navier-Stokes equations that describe the perturbations are

$$\frac{\partial \mathbf{u}'}{\partial t} + (\mathbf{U}\cdot\nabla)\mathbf{u}' + (\mathbf{u}'\cdot\nabla)\mathbf{U} = -\nabla p' + \frac{1}{\mathrm{Re}}\Delta\mathbf{u}', \tag{3}$$

$$\nabla\cdot\mathbf{u}' = 0. \tag{4}$$

Equations (1-4) are nondimensionalised with the free-stream velocity $\hat{U}_0$ and boundary layer length scale $\hat{\delta}_0 = \sqrt{\hat{L}_0\hat{\nu}/\hat{U}_0}$, where $\hat{\nu}$ is the kinematic viscosity, $\hat{L}_0$ is distinguished streamwise location (defined later) measured from the leading edge; dimensional variables are denoted with $\hat{\square}$. $\mathrm{Re} = \hat{\delta}_0\hat{U}_0/\hat{\nu}$ is the Reynolds number. The nondimensional pressure is $P = \hat{P}/(\hat{\rho}\hat{U}_0^2)$.

Eqs. (1-2) need to be used to describe the stationary equilibrium flow field near the MVG, since there the flow rapidly varies in all three spatial dimensions. However, after some distance downstream of the MVG, the flow-field obeys the boundary layer scaling: the flow varies slowly in the streamwise direction, while it varies more rapidly in the wall-normal and spanwise directions. Furthermore, the spanwise and wall-normal velocities can be assumed to be smaller than the streamwise velocity. Therefore, Eqs. (1-2) can be simplified by using a different nondimensionalization for the different variables. Introducing $\varepsilon = 1/\sqrt{\hat{L}_0\hat{U}_0/\hat{\nu}}$, $[\tilde{X}, \tilde{Y}, \tilde{Z}]^T = [\hat{x}/\hat{L}_0, \hat{y}\varepsilon/\hat{L}_0, \hat{z}\varepsilon/\hat{L}_0]^T$, $[\tilde{U}, \tilde{V}, \tilde{W}]^T = [\hat{U}/\hat{U}_0, \hat{V}\varepsilon\hat{U}_0, \hat{W}\varepsilon/\hat{U}_0]^T$ and $\tilde{P} = \hat{P}\varepsilon^2/(\hat{\rho}\hat{U}_0^2)$, we get

$$\tilde{U}\frac{\partial\tilde{U}}{\partial\tilde{X}} + \tilde{V}\frac{\partial\tilde{U}}{\partial\tilde{Y}} + \tilde{W}\frac{\partial\tilde{U}}{\partial\tilde{Z}} = \frac{\partial^2\tilde{U}}{\partial\tilde{Y}^2} + \frac{\partial^2\tilde{U}}{\partial\tilde{Z}^2}, \tag{5}$$

$$\tilde{U}\frac{\partial\tilde{V}}{\partial\tilde{X}} + \tilde{V}\frac{\partial\tilde{V}}{\partial\tilde{Y}} + \tilde{W}\frac{\partial\tilde{V}}{\partial\tilde{Z}} = -\frac{\partial\tilde{P}}{\partial\tilde{Y}} + \frac{\partial^2\tilde{V}}{\partial\tilde{Y}^2} + \frac{\partial^2\tilde{V}}{\partial\tilde{Z}^2}, \tag{6}$$

$$\tilde{U}\frac{\partial\tilde{W}}{\partial\tilde{X}} + \tilde{V}\frac{\partial\tilde{W}}{\partial\tilde{Y}} + \tilde{W}\frac{\partial\tilde{W}}{\partial\tilde{Z}} = -\frac{\partial\tilde{P}}{\partial\tilde{Z}} + \frac{\partial^2\tilde{W}}{\partial\tilde{Y}^2} + \frac{\partial^2\tilde{W}}{\partial\tilde{Z}^2}, \tag{7}$$

$$\frac{\partial\tilde{U}}{\partial\tilde{X}} + \frac{\partial\tilde{V}}{\partial\tilde{Y}} + \frac{\partial\tilde{W}}{\partial\tilde{Z}} = 0. \tag{8}$$

Eqs. (5-8) are called boundary region equations (BRE). These are essentially the extension of the boundary layer equations and are well known and were previously used for several different flow problems as discussed in [16]. These equations are parabolic, and with suitable initial- and boundary conditions well-posed. Thus, they can be marched downstream without any step size restriction. Note that the wall-normal and spanwise scalings are the same as in Eqs. (3-4) but the streamwise length scale is longer; furthermore, the wall-normal and spanwise velocities are magnified. Essentially, the appropriate stretching and scaling of the independent and dependent variables make the governing equations Reynolds number independent.

Eqs. (3-4) can be also simplified in multiple ways. When studying the convective instabilities in a boundary layer, it is reasonable to assume that the base-flow is locally parallel, i.e. the streamwise variation of the base flow is neglected ($\mathbf{U} = \mathbf{U}(y, z)$). This allows examination of the boundary layer as a series of parallel flows. Then, perturbations can be sought in the form

$$(u', v', w', p')(x, y, z, t) = (u, v, w, p)(y, z)e^{\mathrm{i}(\alpha x - \omega t)} + \text{c.c.} \tag{9}$$

In the equation above, (u, v, w, p) are the disturbance shape functions, ω is the angular frequency, α is the wavenumber, and c.c. means complex conjugate. In general, both α and ω can be complex quantities. In the case of a spatially developing flow such as a boundary layer, spatial stability analysis is appropriate, which means that ω is real, while α is complex. Therefore, the disturbance wave is assumed to be time-periodic which is periodic and exponentially growing or decaying in space. Substituting the above ansatz to Eqs. (3-4), we get

$$(\alpha^2\mathbf{A}_2 + \alpha\mathbf{A}_1 + \mathbf{A}_0)\mathbf{q} = 0, \tag{10}$$

where $\mathbf{q} = (u, v, w, p)$ and the coefficient matrices can be found in [14]. The above problem is a so-called BiGlobal spatial stability problem. Eq. (10) is a polynomial eigenvalue problem, which can be linearised (transformed to a generalised eigenvalue problem) and solved in a straightforward manner.

In the simplification of Eqs. (3-4), we can also assume that the base flow is not strictly parallel but it varies slowly in the streamwise direction. This way, the derived stability equations are still reasonably simple but they preserve more accuracy than Eq. (9). This requires us to seek the disturbances in the form

$$(u', v', w', p')(x, y, z, t) = (u, v, w, p)(x, y, z) e^{\mathrm{i}\left(\int_{x_0}^{x} \alpha(\xi)\mathrm{d}\xi - \omega t\right)} + \text{c.c.} \quad (11)$$

This form decomposes the perturbation into a slowly varying shape function and an exponential variation; furthermore, the streamwise variation of the streamwise wavenumber is also allowed. Substituting this into Eqs. (3-4), and neglecting small terms yields

$$\mathbf{A}\mathbf{q} + \mathbf{B}\frac{\partial \mathbf{q}}{\partial y} + \mathbf{C}\frac{\partial^2 \mathbf{q}}{\partial y^2} + \mathbf{D}\frac{\partial \mathbf{q}}{\partial z} + \mathbf{E}\frac{\partial^2 \mathbf{q}}{\partial z^2} + \mathbf{F}\frac{\partial \mathbf{q}}{\partial x} = 0. \quad (12)$$

where the coefficient matrices can be found in [18]. Eq. (12) is called the parabolized stability equations (PSE), and has been widely used to model flow stability phenomena [19]. There are two important things that must be addressed regarding the PSE. First, the splitting of the perturbation into a shape function and exponentially varying part (Eq. (11)) is ambiguous. The splitting can be defined in different ways [19]. Here, the most common method is utilised; namely, all the exponential growth of the shape-function is absorbed into α by enforcing

$$\int\int \mathbf{q}\frac{\partial \mathbf{q}}{\partial x}\mathrm{d}y\mathrm{d}z = 0 \quad (13)$$

in each marching step. Furthermore, Eq. (12) are ill-posed, because the equations are only partially parabolized but not fully parabolic. This means that there might be solutions that are traveling upstream, opposite to the marching direction, which can cause numerical instabilities. As a partial remedy, we employ the stabilization method proposed by Andersson et al. [20].

2.1. Solution of the full problem

The theoretical framework outlined in the previous section allows us to study the stability characteristics of MVGs rather efficiently. First, Eqs. (1-2) are solved as a stationary problem to obtain the flow field near the MVG. This is carried out using the commercial CFD software Fluent - details of these calculations are reported in a different CMFF22 conference paper [21]. This region is denoted by the brown box in Fig. 1. Then, BRE (Eqs. 5-8) are solved to calculate the evolution of the streaky boundary layer. This region is marked with the blue box in Fig. 1. The BRE are solved starting upstream of the downstream boundary of the 3D CFD calculation: this way the no-stress boundary condition used in the outlet of the CFD calculation does not contaminate the solution. This location is denoted with x_{st}, as this is where the stability calculation also begins. Furthermore, all equations were made nondimensional using the boundary layer length scale at this location; therefore, $\hat{L}_0 = \hat{x}_{st}$. PSE is solved after the base-flow is obtained with BRE. The initial condition for the PSE is determined by solving the BiGlobal stability problem (Eq. (10)).

The following boundary conditions were used in the problem solution. For the CFD calculation near the MVG, the inlet boundary condition is the Blasius velocity profile corresponding to the streamwise location on a theoretical flat plate. In the free-stream, a constant streamwise velocity was prescribed. In the spanwise direction, periodicity was assumed, and a no-slip boundary condition was prescribed on the bottom wall. The boundary conditions are the same for the BRE. For both the BiGlobal stability equations and PSE, periodicity was assumed in the spanwise direction, and disturbances are enforced to vanish in both the free-stream and also on the wall.

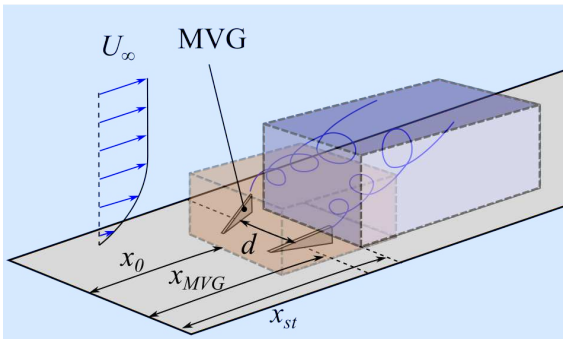

Figure 1. Sketch of the flow configuration

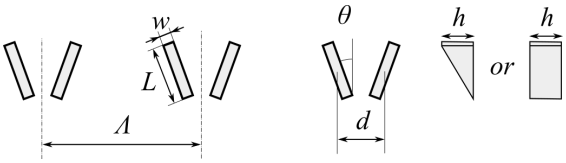

Figure 2. Parameters of the vortex generators

2.2. Parameters of the investigated configuration

The key parameters of the investigated MVG are displayed in Fig. 2 and their numerical values can be found in Table 1; these are the same as in the case investigated in [14]. The key difference in this study is that (i) not only triangular but also rectangular MVGs are considered, and (ii) the streamwise location of the MVG is varied. The different locations of the start of the computational domain, the location of the MVG, and the start of the stability calculation can be found in Table 2. These locations correspond to a flat plate with a leading edge at $x = 0$. Therefore, this also defines the boundary condition for the CFD calcula-

tion near the MVG, which then determined the initial condition of the BRE. The free-stream velocity and kinematic viscosity in this study were $\hat{U}_0 = 7.7$ m/s and $\hat{\nu} = 1.4607 \cdot 10^{-5}$ m^2/s, respectively.

Table 1. Parameters of the MVGs

$\hat{\Lambda}$ (mm)	$\hat{d}$ (mm)	$\hat{h}$ (mm)	$\hat{w}$ (mm)	$\hat{L}$ (mm)	Θ (°)
13	3.25	1.3	0.3	3.25	15

Table 2. Location of the MVGs

$\hat{x}_0$ (mm)	$\hat{x}_{MVG}$ (mm)	$\hat{x}_{st}$ (mm)	$\hat{\delta}_{99}(x_0)$ (mm)
36.95	45.95	58.95	1.3
147.80	156.79	169.79	2.6
230.93	239.93	252.93	3.25

3. NUMERICAL TECHNIQUES

The weak form of the BRE, BiGlobal stability equations and PSE are solved using the open-source finite element software FreeFem [22]. Meshes consisting of 12000 – 15000 triangles were used in the present study which were generated using the mesh generator software BAMG that is integrated with FreeFem. The equations were discretised using $\mathcal{P}_2$ elements for the velocity fields and $\mathcal{P}_1$ elements for the pressure, which together are often referred to as the classical Taylor-Hood discretization method. The parallel version of FreeFem was used: the computational domain was decomposed into multiple parts, and each part is assigned to a single process, which allows using effective distributed-memory algorithms.

The PETSc and SLEPc packages were used to solve the linear/nonlinear equations and the polynomial eigenvalue problem, respectively. The BRE marching procedure requires a solution of a nonlinear problem in each spatial step, which was carried out using an implementation of the Newton method in PETSc. The BiGlobal polynomial eigenvalue problem was transformed using the companion-matrix method [23] in combination with a shift-invert spectral transformation which allows the calculation of the eigenvalues near a prescribed target. The eigenvalues of the transformed system were calculated using the Krylov-Schur method. Finally, the PSE, which is also nonlinear due to the constraint of Eq. (13), was solved using a straightforward fixed-point iteration [19].

The BRE, BiGlobal and PSE equations all require the solution of linear systems of equations. Generally, this is carried out by calculating the LU factorization of the system matrix. This was also the main method utilised in the present study using the external library MUMPS. However, the PETSc library is primarily designed to solve sparse linear systems using iterative methods; this enables us to use a more efficient solution technique to solve the BRE and PSE problems, which require the repeated solution of linear equations in each marching step. The PETSc library always solves preconditioned linear systems with iterative methods:

$$\mathbf{Ax} = \mathbf{b} \rightarrow \mathbf{AP}^{-1}\mathbf{y} = \mathbf{b},\ \mathbf{y} = \mathbf{Px}. \tag{14}$$

Here, $\mathbf{P}$ is the preconditioner matrix. In the case of a direct solver, the preconditioner should be $\mathbf{P} = \mathbf{A}$, and in each marching step, the system matrix, the preconditioner, and its inverse are all calculated repeatedly during the iteration. However, it is possible that the preconditioner is not updated after the first iteration:

$$\mathbf{A}_0\mathbf{A}_0^{-1}\mathbf{y}_0 = \mathbf{b}_0, \tag{15}$$

$$\mathbf{A}_1\mathbf{A}_0^{-1}\mathbf{y}_1 = \mathbf{b}_1. \tag{16}$$

Then, in the second iteration, the system is only approximately solved by the preconditioner. However, as the new system matrix $\mathbf{A}_1\mathbf{A}_0^{-1}$ is relatively close to the identity matrix, it can be solved using iterative methods. This can speed up the calculation significantly, since calculating an LU factorization is computationally demanding even for moderate systems as in the present study. Calculating the LU factorization only once and then using the flexible-GMRES (fGMRES) method (which is readily available in PETSc) for the rest of the iterations in each marching step, we managed to achieve significant computational speedup, which is reported in the next section.

4. RESULTS

4.1. Computational time

Here, we report the computational time for the simulation of the sinuous instability mode in a boundary layer perturbed by idealised Rankine vortices. Such a configuration mimics the effect of the MVGs and was previously studied in the literature [15, 16]. The presented case corresponds to the configuration *E1* studied by [16], which was also used to validate our codes. All the present calculations were carried out on a machine with an AMD Ryzen 9 3900X processor. FreeFem version 4.10 was compiled and run on a virtual machine with Ubuntu 18.04 mounted using Oracle Virtualbox under Windows.

Fig. 3 displays the computational time for solving the BRE equations. Two regions with different scaling can be identified: using 2-4 cores, the computational time decreases fast with increasing the number of cores; then, increasing the number of cores further the scaling falls off. This can be attributed to the fact that the problem size is relatively small. Interestingly, when using 4-10 cores, using an odd number of processes seems advantageous since with even cores the computational time reduction is lower. Comparing LU factorization and fGMRES, the iterative solver outperforms the direct solution procedure significantly: the computational time is reduced by approximately a factor of 0.5 using the iterative solver.

Fig. 4 is the same as Fig. 3 but for the PSE equa-

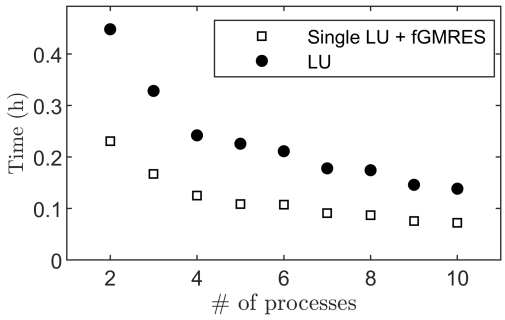

Figure 3. Comparison of the different techniques to solve the linear system of equations, BRE equations

tions. Similar trends can be observed as in the case of BRE, except that the computational time is reduced only by a factor of ≈ 0.4 with the use of the iterative method. This is likely because the solution of the linear system of equations takes up a smaller portion of the PSE calculation. Nevertheless, the computational time decrease is quite significant. Note that the solution of the PSE equations takes significantly more time due to two reasons: (i) here, the equations are complex, and (ii) PSE need to be solved for several frequencies to obtain a complete stability map. Therefore, the decrease of computational time can be considered significant.

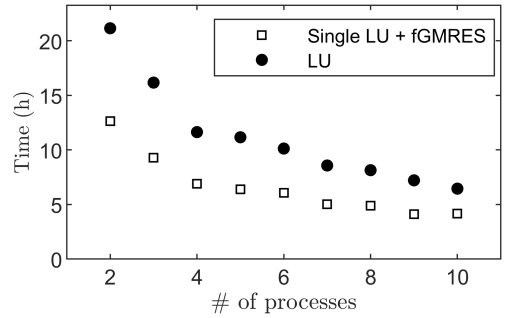

Figure 4. Comparison of the different techniques to solve the linear system of equations, PSE equations

4.2. Stability characteristics of the MVGs

First, results for the streak amplitude generated by the MVGs are reported. The streak amplitude is measured using the formula proposed by Shahinfar et al. [7]:

$$A(x) = \frac{1}{\hat{U}_0} \int_{-0.5}^{0.5} \int_{0}^{\eta^*} \left| \hat{U}(x,\eta,\zeta) - \hat{U}^z(x,\eta) \right| \mathrm{d}\eta \mathrm{d}\zeta, \tag{17}$$

where $\eta = \hat{y}/\hat{\delta}(\hat{x})$, $\zeta = \hat{z}/\hat{\Lambda}$, and U^z is the spanwise average of the streamwise velocity. η^* is a sufficiently high location so that the the free-stream is undisturbed, i.e., the integrand of Eq. 17 vanishes. The streak amplitude is displayed in Figs. 5 and 6 as a function of the nondimensional streamwise coordinate Re_δ in the case of triangular and rectangular MVGs with different positions along the flat plate. It is apparent from the comparison that rectangular MVGs generate stronger vortices than triangular ones for the same MVG height and streamwise position. It can be also deduced that moving the MVG upstream results in the generation of a stronger streak. For $\hat{\delta}_{99} = 2.6$ and 3.25 mm the variation of the amplitude has the same structure: a fast initial increase followed by a slow decay. However, for $\hat{\delta}_{99} = 1.3$ mm the amplitude variation has an oscillatory character, and these streaks are much stronger and more persistent. This is because the increased relative height results in a stronger amplitude and also because vortices close to the edge of the boundary layer are the most effective for generating streaks [15, 16]. However, these latter MVGs with strong streaks are susceptible to secondary sinuous inviscid instabilities; therefore, they are omitted in the following discussion.

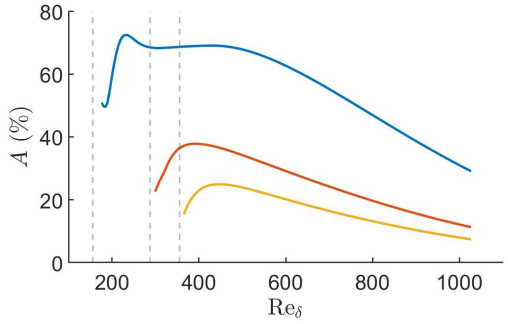

Figure 5. Integral streak amplitude in the case of triangular MVGs. The grey vertical dashed line denotes the location of the MVG. The blue, red and yellow lines correspond to $\hat{\delta}_{99} = 1.3, 2.6$ and 3.25 mm, respectively.

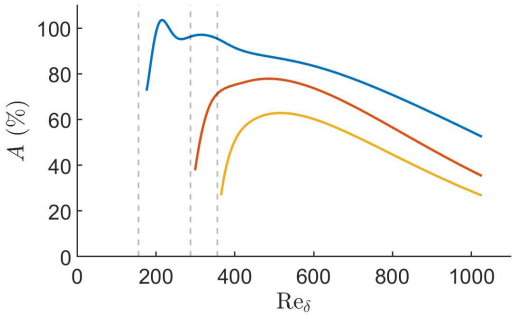

Figure 6. Integral streak amplitude in the case of rectangular MVGs. The grey vertical dashed line denotes the location of the MVG. The blue, red and yellow lines correspond to $\hat{\delta}_{99} = 1.3, 2.6$ and 3.25 mm, respectively.

Fig. 7 shows the neutral stability curves of the different instability modes for a triangular MVG with height $\hat{\delta}_{99} = 3.25$ mm, where $F = \hat{\omega}\hat{\nu}/\hat{U}_0^2 \cdot 10^6$ is the nondimensional frequency parameter. The unstable region is denoted by the shaded grey area. There are two main instability regions: the near field of the MVG ($\mathrm{Re}_\delta < 400 - 500$), where multiple instability modes exist, and the downstream region $\mathrm{Re}_\delta > 500$), where the neutral curve of the TS waves can be observed. In the case of the unstable upstream region, only the modes that form the border of the unstable region are displayed. These results are in agreement with the findings of [14] who studied a configuration is very similar to this ($\hat{\delta}_{99} = 3.12$ mm). However, the shape of the unstable region near the MVG is slightly different between the two cases. This is likely because here, PSE was used, which includes non-local and non-parallel effects, while in [14] Bi-Global stability analysis was used, which assumes a locally parallel flow and is, therefore, less accurate. In Fig. 8, the same neutral curves are displayed but the same MVG is moved further upstream so that $\hat{\delta}_{99} = 2.6$ mm. A stronger stabilization of the TS waves is observed: the unstable region is shifted upstream and also toward lower frequencies. Interestingly, the boundary of the unstable region near the MVG did not move much. However, as the MVG is moved upstream, the spatial extent of this unstable region is much larger; therefore, it is more likely that this MVG advances transition.

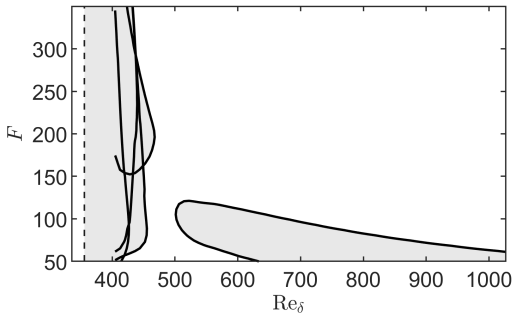

Figure 7. Neutral stability curves of the unstable eigenmodes in the streaky boundary layer. The unstable region is denoted with the shaded grey area. Triangular MVG, $\hat{\delta}_{99} = 3.25$ mm.

In the case of all rectangular MVGs investigated in this study, we found that although strong streaks are generated, and TS waves are completely suppressed, secondary sinuous modes are unstable in the region that has a large spatial extent (not shown). Therefore, the presently investigated rectangular MVG configurations likely advance transition. This finding is different than the observations of [12] and can be explained by the fact that our MVGs are larger compared to the boundary layer height than in the cited reference. These observations point out that the streak amplitude alone is not a good measure of the instability characteristic and further studies are required to assess the interaction of the MVGs with the boundary layer.

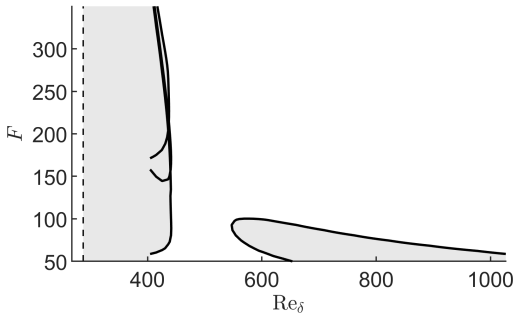

Figure 8. Neutral stability curves of the unstable eigenmodes in the streaky boundary layer. The unstable region is denoted with the shaded grey area. Triangular MVG, $\hat{\delta}_{99} = 2.6$ mm.

Finally, we note that the tracking of the individual modes was problematic in the near-field of the MVGs, especially in the case of rectangular MVGs. The reason for this is that PSE is able to track only a single eigenmode; see [24] for discussion. Therefore, for the near-wake region of the MVG, BiGlobal stability analysis might be a better tool as it can identify multiple modes in the eigenvalue spectrum.

5. CONCLUSIONS

In this paper, a short review of the research on MVGs is presented. Based on suitable approximations for the different flow regions, model equations that allow the economic solution of the problem are presented. Effective numerical solution of the equations is discussed, including an iterative method that reduces the computational cost significantly. Then, the stability of a few MVG geometries is analyzed, including rectangular MVGs, which were not considered in previous numerical studies. The results indicate that different MVG geometries can generate streaks that have remarkably different stability characteristics. Therefore, future studies should investigate the differences between different MVG geometries.

ACKNOWLEDGEMENTS

The authors would like to thank Pierre Jolivet for the help with the parallel capabilities of FreeFem and also for suggesting reusing the LU factorization as a preconditioner for iterative methods.

The work has been performed within the framework of the NKFI project K124939. The generous support of the CELSA foundation is acknowledged.

REFERENCES

[1] Kachanov, Y. S., 1994, "Physical Mechanisms of Laminar-Boundary-Layer Transition", *An-*

nual Review of Fluid Mechanics, Vol. 26, pp. 411–482.

[2] Herbert, T., 1988, "Secondary Instability of Boundary Layers", *Annual Review of Fluid Mechanics*, Vol. 20, pp. 487–526.

[3] Cossu, C., and Brandt, L., 2004, "On Tollmien-Schlichting-like waves in streaky boundary layers", *European Journal of Mechanics - B/Fluids*, Vol. 23, pp. 815–833.

[4] Fransson, J. H. M., Talamelli, A., Brandt, L., and Cossu, C., 2006, "Delaying Transition to Turbulence by a Passive Mechanism", *Physical Review Letters*, Vol. 96, p. 064501.

[5] Shahinfar, S., Sattarzadeh, S. S., Fransson, J. H. M., and Talamelli, A., 2012, "Revival of Classical Vortex Generators Now for Transition Delay", *Phys Rev Lett*, Vol. 109, p. 74501.

[6] Fransson, J. H. M., and Talamelli, A., 2012, "On the generation of steady streamwise streaks in flat-plate boundary layers", *Journal of Fluid Mechanics*, Vol. 698, pp. 211–234.

[7] Shahinfar, S., Fransson, J. H. M., Sattarzadeh, S. S., and Talamelli, A., 2013, "Scaling of streamwise boundary layer streaks and their ability to reduce skin-friction drag", *Journal of Fluid Mechanics*, Vol. 733, pp. 1–32.

[8] Sattarzadeh, S. S., Fransson, J. H. M., Talamelli, A., and Fallenius, B. E. G., 2014, "Consecutive turbulence transition delay with reinforced passive control", *Physical Review E*, Vol. 89, p. 061001.

[9] Sattarzadeh, S. S., and Fransson, J. H. M., 2014, "Experimental investigation on the steady and unsteady disturbances in a flat plate boundary layer", *Physics of Fluids*, Vol. 26, p. 124103.

[10] Downs, R. S., Fallenius, B. E. G., Fransson, J. H. M., and Mårtensson, H., 2017, "Miniature Vortex Generators for Flow Control in Falkner–Skan Boundary Layers", *AIAA Journal*, Vol. 55, pp. 352–364.

[11] Shahinfar, S., Sattarzadeh, S. S., and Fransson, J. H. M., 2014, "Passive boundary layer control of oblique disturbances by finite-amplitude streaks", *Journal of Fluid Mechanics*, Vol. 749, pp. 1–36.

[12] Sattarzadeh, S. S., and Fransson, J. H. M., 2015, "On the scaling of streamwise streaks and their efficiency to attenuate Tollmien-Schlichting waves", *Experiments in Fluids*, Vol. 56, p. 58.

[13] Bagheri, S., and Hanifi, A., 2007, "The stabilizing effect of streaks on Tollmien-Schlichting and oblique waves: A parametric study", *Physics of Fluids*, Vol. 19, p. 78103.

[14] Siconolfi, L., Camarri, S., and Fransson, J. H. M., 2015, "Stability analysis of boundary layers controlled by miniature vortex generators", *Journal of Fluid Mechanics*, Vol. 784, pp. 596–618.

[15] Siconolfi, L., Camarri, S., and Fransson, J. H., 2014, "Boundary layer stabilization using free-stream vortices", *Journal of Fluid Mechanics*, Vol. 764, pp. R21–R212.

[16] Martín, J. A., and Paredes, P., 2017, "Three-dimensional instability analysis of boundary layers perturbed by streamwise vortices", *Theoretical and Computational Fluid Dynamics*, Vol. 31, pp. 505–517.

[17] Martín, J. A., and Paredes, P., 2021, "Transition Prediction in Incompressible Boundary Layer with Finite-Amplitude Streaks", *Energies 2021, Vol 14, Page 2147*, Vol. 14, p. 2147.

[18] Paredes, P., 2014, "Advances in global instability computations: from incompressible to hypersonic flow", Ph.D. thesis, Universidad Politécnica de Madrid.

[19] Herbert, T., 1997, "Parabolized Stability Equations", *Annual Review of Fluid Mechanics*, Vol. 29, pp. 245–283.

[20] Andersson, P., Henningson, D. S., and Hanifi, A., 1998, "On a Stabilization Procedure for the Parabolic Stability Equations", *Journal of Engineering Mathematics*, Vol. 33 (3), pp. 311–332.

[21] Maarten, V., Péter Tamás, N., András, S., and Paál, G., 2022, "Direct Numerical Simulation of the Wake Flow of a Miniature Vortex Generator and its Interaction with a Laminar Boundary Layer", *to appear in: Proceedings of Conference on Modelling Fluid Flow (CMFF'22).*

[22] Hecht, F., 2012, "New development in freefem++", *Journal of Numerical Mathematics*, Vol. 20 (3-4), pp. 251–266.

[23] Bridges, T. J., and Morris, P. J., 1984, "Differential eigenvalue problems in which the parameter appears nonlinearly", *Journal of Computational Physics*, Vol. 55, pp. 437–460.

[24] Towne, A., Rigas, G., and Colonius, T., 2019, "A critical assessment of the parabolized stability equations", *Theoretical and Computational Fluid Dynamics 2019 33:3*, Vol. 33, pp. 359–382.

Conference on Modelling Fluid Flow (CMFF'22)
The 18th International Conference on Fluid Flow Technologies
Budapest, Hungary, August 30-September 2, 2022

A NOVEL MODEL FOR GLAZE ICE ACCRETION

Róbert-Zoltán SZÁSZ[1], Stefan IVANELL[2] and Johan REVSTEDT[3],

[1] Corresponding Author. Department of Energy Sciences, Lund University, PO.Box 118, SE-22100 Lund, Sweden. Tel.: +46 46 222 0480, E-mail: robert-zoltan.szasz@energy.lth.se
[2] Department of Earth Sciences, Uppsala University, Sweden, E-mail: stefan.ivanell@geo.uu.se
[3] Department of Energy Sciences, Lund University, Sweden, E-mail: johan.revstedt@energy.lth.se

ABSTRACT

This paper introduces a novel model to predict ice accretion in glaze ice conditions due to super-cooled water droplets. Glaze icing is controlled by a large number of interacting physical phenomena. The purpose of the suggested model was to offer a faster alternative to explicitly modelling these phenomena. The paper presents the suggested model and investigates the sensitivity of the predictions on the model parameters for three experimental cases in the literature. The results indicate a qualitatively correct behaviour. Quantitatively, the model over-predicts the amount of accreted ice, the error being significantly larger in severe icing conditions. The errors are caused partly by the choice of faster numerical approaches and by the lack of possibility to account for detaching ice from the surface.

Keywords: CFD, glaze ice, ice accretion, LPT

NOMENCLATURE

A	$[m^2]$	area
dV_A	$[m^3]$	added ice volume
dV_T	$[m^3]$	ice volume to add
M	$[kg]$	mass
C	$[K/m]$	solution coefficient
LWC	$[kg/m^3]$	liquid water content
MVD	$[m]$	mean volumetric diameter
R	$[m]$	droplet radius
T	$[K]$	temperature
c_1	$[-]$	collision efficiency
c_2	$[-]$	sticking efficiency
c_3	$[-]$	accretion efficiency
e	$[-]$	impact elasticity coefficient
ft	$[s]$	freezing time
r	$[m]$	radius
t	$[s]$	time
$\underline{dx}$	$[m]$	displacement vector
$\underline{u}$	$[m/s]$	velocity
$\underline{x}$	$[m]$	position vector
α	$[^o]$	angle of attack
γ	$[m^2/s]$	thermal diffusivity
λ	$[1/m]$	solution coefficient
ω	$[-]$	under-relaxation factor
ϕ	$[kg/m^3]$	mass concentration of the particles
θ	$[K]$	temperature difference

Subscripts and Superscripts

N	normal
T	tangential
c	critical
e	exterior
i	initial
n	solution term index
rel	relative
k	iteration

1. INTRODUCTION

Wind power technology, as one of the tools to replace fossil fuels, gained a strong popularity during the past decades. Due to the rapid increase of the number and size of installed power plants, there are more and more wind turbines installed in less favourable areas, such as areas with cold climate conditions. It is estimated that about a quarter of the global installed wind energy capacity is located in areas prone to the risk of icing [1]. In some countries the share of wind turbines located in cold climate areas is significantly higher, e.g. in Sweden more than 80% of the installed capacity in 2020 was located in the most northerly quarter of the country [2].

Although cold climate areas have the advantage of generally lower population density (leading to better acceptance) and larger amount of extractable kinetic energy (for the same wind speed, due to the higher density), ice accretion imposes significant challenges for the manufacturers and for the wind turbine owners. The ice layer changes the aerodynamic shape of the blade, resulting in non-optimal profiles and a decrease of the extracted energy. Furthermore, the extra mass of the ice represents an extra load on the solid structures and may imbalance the

rotor causing vibrations which lead to earlier fatigue and, in extreme cases, mechanical failures. There is a safety hazard as well, ice chunks may detach from the blades and may travel relatively large distances. These chunks represent a danger for the persons or objects located in the turbines' neighbourhood. The current trend of increasing wind turbine sizes increases also the areas affected by ice throw.

The above-described challenges triggered research campaigns focusing on many aspects of ice accretion, like predicting weather conditions leading to ice accretion, investigating the accretion process itself, development of ice detection and de-icing devices, just to name a few research areas. A rather detailed overview of the related research is presented in [3].

The characteristics of the accreted ice depend on the prevailing meteorological conditions. Commonly, icing conditions are divided in two categories. In low temperature (usually below 10^oC) conditions, the water droplets are well below freezing temperature but are still in the liquid state. These supercooled droplets impacting on a surface freeze instantaneously upon contact, and begin to accrete forming rime ice, which is usually opaque due to the air trapped between the frozen droplets. For slightly higher temperatures, but still below freezing, (usually between 5 and 0^oC) the supercooled droplets do not freeze instantaneously upon contacting the surface. Instead, a water film is formed which may run along the surfaces before freezing, leading to the formation of a more compact, so-called glaze-ice. Of course, in practical situations a combination of rime and glaze conditions might occur as well.

The first studies of the impact of icing on airfoils date back to 1930's and originated in the aerospace community [4, 5]. Over the past two decades various authors presented more specific studies on the accretion on wind turbine blades. Makkonen [6, 7] was among the first ones to characterise different kind of icing events and to create models for it. Based on thermodynamic considerations the following model was proposed to predict the rate of ice accretion:

$$\frac{dM}{dt} = c_1 c_2 c_3 \phi \underline{u} A \tag{1}$$

where M is the mass of the ice, t the time, ϕ the mass concentration of particles, $\underline{u}$ the velocity of the particles relative to the object, A the cross sectional area of the object. c_1, c_2 and c_3 are correction factors having values between zero and one and account for the collision efficiency, sticking efficiency and accretion efficiency, respectively. For further details about the model the reader is referred e.g. to [7]. Eq. 1 is still the most widely used ice prediction model, often combined with other methods.

Usually, there is a scale separation between the flow field surrounding the blades and the rate of ice accretion on the blades. As a consequence, a common approach is to compute the ice accretion and the flow around the ice accreted airfoils in separate stages. For the flow computations a common approach is to use simplified methods to reduce the computational efforts. For example, a potential flow solver is used in LEWICE (although there is a possibility to import flow fields from other solvers) [8], whereas the panel method is used in TURBICE (see e.g. [9]). Recently, thanks to the increase in computational power and to the need to account for 3D effects, it is more and more common to solve the full set of Navier-Stokes equations (see e.g. [10, 11, 12]). Droplet transport is commonly modelled either in an Eulerian (e.g. [12]) or Lagrangian (e.g. [13, 14, 10]) framework.

In the case of rime ice conditions, since all droplets hitting the surface freeze instantaneously, there is no need for heat transfer computations. The amount of droplets hitting the surface is determined explicitly or specified via the collection efficiency, depending if a lagrangian or eulerian model is used for droplet transport. To model glaze ice, the most common approach is to compute 1D heat transfer problems based on the so-called Stefan's problem formulated for aeronautical applications by Messinger in 1953 and further improved by Myers in 2001 (see e.g. [10]). In [15] beside the heat transfer, the evolution of the water film formed on the blade surface is accounted as well.

Here, we propose an alternative approach to model glaze ice formation. Instead of accounting for all the interacting physical phenomena occurring during glaze ice formation (wall film formation, its evolution along the surface, heat transfer, etc.) we propose an extension of an already existing rime ice model.

Although its grounding in physics is limited, the suggested lower order model has the advantage of significantly lower complexity, leading to faster computing times. Beside presenting the model, the goal of the paper is to investigate the performance of the suggested model to predict light and severe glaze ice conditions.

2. METHODS

The aim of this work has been to provide a modelling approach which had to be integrated in a model chain where a large number of ice accretion cases had to be computed. For this reason the methods chosen herein are characterised by relatively high computational performance at the expense of somewhat limited accuracy.

The scale separation of the flow time scales and the time scales associated to the growth of the ice layer facilitates the use of staged computations: one determines the flow around the airfoil and then the amount of accreted ice. Nevertheless, in the case of severe icing conditions the ice structures formed on the surfaces may significantly change the flow topology. In order to account for such changes, a common approach is to divide the time interval of the

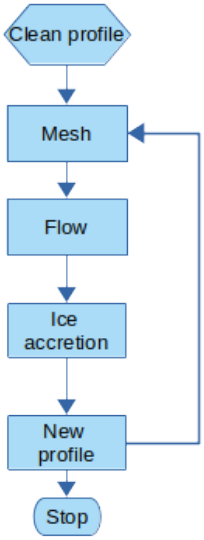

Figure 1. Steps of the multi-staged approach

entire icing event in sub-intervals. During each sub-interval the geometry is considered constant. Before the next time interval is computed, the surface (and the mesh used for the flow computations) is updated to account for the ice accreted during the previous interval. Such a multi-step approach is used e.g. in [10]. A sensitivity study to physical and modelling parameters affecting airfoil icing using such an approach is shown in [12].

Here, we use also such a multi-staged approach, the main steps being shown in Figure 1. The entire icing event will be computed in N_{st} steps. The number of steps is determined by the balance of desired accuracy and available computing time. Since the flow and the airfoil shape is assumed to not change during a step, a too low number of steps will result in decreased accuracy, especially in heavy icing conditions. At the other extreme, dividing the icing event into too many sub-intervals leads to very small changes in the airfoil shape, and therefore results in sub-optimal use of the computing resources.

The ice accretion simulations are performed using the open-source toolbox OpenFOAM [16] in combination with an in-house tool to adjust the airfoil surface based on the amount of ice accreted.

The computations start with the clean airfoil as input. In order to reduce the time needed for the computations only two-dimensional domains are considered. The mesh is generated in two stages. First the snappyHexMesh utility (included in OpenFOAM) is used to generate an unstructured 3D mesh around the airfoil. Next, the 2D mesh is obtained by extruding one of the sides of the 3D mesh.

For the purpose of improving the computational efficiency, the flow and ice accretion computations are separated. It is assumed that during a sub-stage the shape of the airfoil, and by this the flow, is not changing significantly. For this reason, the statistically stationary two-dimensional flow field is simulated first using the SST k-ω RANS model [17]. Thereafter, the ice accretion is determined by Lagrangian Particle Tracking (LPT) based on the steady flow field. The number of injected parcels and the injected droplets' diameter is determined to match the desired LWC. In the LPT computations only the particle drag force and the turbulent dispersion is accounted for. The turbulent dispersion is done with a stochastic model (a.k.a random walk).

Each parcel of Lagrangian particles that impacts the aerofoil surface is registered. Depending if rime- or glaze-ice conditions are computed, the droplet impacting the surface is considered to freeze immediately or is allowed to travel along the surface. The details of the glaze ice model are given in Section 3.

Once the amount and distribution of accreted ice is determined, the airfoil surface is updated using an in-house tool. Before updating the surface, two pre-processing stages are carried out.

First, the ice distribution is smoothed over the airfoil surface. This step is motivated by the fact, that even if the length of the LPT computations is long enough to achieve a statistically converged ice distribution, depending on the mesh resolution used to discretize the airfoil, there might be small cells with no ice accreted, leading to physically irregular shape of the ice accreted surface. This smoothing step is carried out by transferring the information of accreted ice in a mass-conservative manner from the cell centers to the mesh vortices and back. The effect of smoothing can be increased by increasing the number of smoothing loops.

The second pre-processing of the accreted ice mass aims to increase performance. Since the time scale of the flow and the ice accretion differ substantially, with the icing time scale being much longer, one can increase the computational efficiency by scaling the amount of accreted ice everywhere by a factor f, leading to a shortening of the time covered by the LPT computations with the same factor, f. The scaling is limited by the requirement of having statistically representative amount of ice accreted on the airfoil. Our previous investigations show that it is possible to decrease the time scale of ice accretion by a factor 1000, i.e., one second explicitly computed ice accretion can be scaled to predict accretion after 1000 s.

The new shape of the airfoil is determined by an iterative approach using an in-house tool. The tool reads in the surface mesh used in OpenFOAM to discretize the airfoil geometry and the amount of ice accreted on each mesh cell face. Based on the accreted ice mass and a user-provided density (which can be adjusted to account e.g. for trapped air) one can determine the added volume for each cell face and, by integrating it over all cells, the total ice volume to be added to the airfoil, dV_T. Based on the added volume, the face area and the face normal direction, one can compute an initial guess for the average dis-

placement vector at each node of the surface mesh, $\underline{dx}$, as the average of the displacement vectors needed for the surrounding cells. Based on the average displacement, the first approximation of the ice-accreted mesh shape can be obtained by $\underline{x}^1 = \underline{x}^0 + \omega * \underline{dx}$, where exponents 0 and 1 denote the old and new values, respectively, and ω is an under-relaxation factor (set to 0.8 in the present calculations). Based on the estimated positions of the surface nodes, the actually added ice volume, dV_A, can be determined. Since this volume usually differs from the target added volume, the positions of the surface mesh nodes are corrected iteratively using Equation 2, the stopping criterion being $|(dV_T - dV_A^k)/dV_T| < 10^{-10}$.

$$\underline{x}^{k+1} = \underline{x}^k + \omega * \underline{dx} * (dV_T - dV_A^k)/dV_T \tag{2}$$

Once the new airfoil shape is determined a new mesh is generated and the entire process is iterated until the total length of the icing event is covered.

3. GLAZE ICE MODEL

3.1. Goal

As mentioned earlier, in order to accurately model glaze ice conditions, one needs to use a multitude of interacting models to describe the impact of the droplets, the formation of the water film and the heat transfer between the air, the water film and the solid surfaces. The large number of required models renders the Computational Fluid Dynamics (CFD) computations heavy both directly, by increasing the computational time needed to evaluate the models, and indirectly due to slower convergence as a result of the large number of degrees of freedom. Furthermore, even if the individual models can be validated for certain conditions, when a large number of models are interacting the accuracy of the predictions may suffer.

Our goal was to develop a simpler and more efficient model to account for glaze conditions. The increased efficiency was planned to be achieved by reducing the number of physical phenomena explicitly accounted for which inherently leads to a reduced number of model parameters. As a drawback, the model is expected to be less general, requiring validation to adjust the model parameters.

3.2. Model description

The glaze model is an extension of the rime-ice model initially implemented in an in-house solver [13, 14] and later implemented in OpenFOAM as well. The main idea of the model is to not freeze instantaneously the parcels upon impact (as it is the case for rime ice), but let the droplets slide along the surface for a specified freezing time, ft. During this freezing period only the positions of the droplets are updated, the freezing conditions are not re-evaluated. Although this is a rather crude approximation, it is much more efficient than using e.g. a wall film model and heat transfer calculations.

Two options have been implemented for the time being: prescribed freezing time and a first order approximation.

3.2.1. Prescribed freezing time

This is the simplest model and, as the name suggests, requires that the user specifies the time delay, ft, until the droplets (modelling the wall film) freeze. Although very simplistic, this model adds very little computational effort, thus it is affordable to evaluate cases where rime-ice conditions can be evaluated. Although the accuracy is limited, one can easily carry out sensitivity studies and/or validation computations.

During validation computations, it was found that simply imposing a time delay is not sufficient to model glaze ice conditions, since the impacting droplets are deflecting from the surface. In reality the droplets more often attach to the wall due to surface tension effects. To account for this, an additional model parameter has been introduced, e, which can be used to adjust the elasticity of the impact, the normal component of the parcel velocity after impact being computed as $\underline{u}_\mathrm{N} = e \cdot \underline{u}_\mathrm{T}$, $\underline{u}_\mathrm{T}$ being the tangential component. Thus, the normal component can be zeroed by setting $e = 0$. Nevertheless, cancelling the normal component entirely is not physical either because, upon impact, the droplets are located in regions of the boundary layer with very low relative velocity and even long time delays lead to very small displacements of the parcels along the surface. In reality the droplets and the wall film have a non-zero thickness and experience larger relative velocities.

3.2.2. First order approximation

To avoid the need to directly impose the freezing time, a second possibility has been implemented. This approach is based on the heat transfer in a spherical droplet with uniform properties, initial temperature of T_i in a surrounding with the exterior temperature of T_e.

The governing equation in radial direction is:

$$\frac{1}{r^2}\frac{\partial}{\partial r}\left(r^2\frac{\partial \theta}{\partial r}\right) = \frac{1}{\gamma}\frac{\partial \theta}{\partial t} \tag{3}$$

where $\theta(r,t) = T - T_e$. The solution of Eq.3 is of the form:

$$\theta(r,t) = \sum_{n=1}^{\infty} \frac{C_n}{r} sin(\lambda_n r) exp(-\gamma \lambda_n^2 t) \tag{4}$$

The coefficients are given by:

$$C_n = -\frac{T_i}{\lambda_n}(-1)^n \tag{5}$$

and

$$\lambda_n = \frac{n\pi}{R} \tag{6}$$

R being the radius of the spherical droplet.

The idea of the first order approximation is that the A_n coefficients of the solution series in Equation 4 are decreasing with increasing n, in fact the first term is dominating in most cases. Thus, neglecting the terms for $n > 1$, from Equation 4 one can compute the time needed to freeze the droplet as:

$$ft = -\frac{1}{\lambda_1^2 \alpha} ln\left(\frac{\theta_c r_c \lambda_1}{\theta_i sin(\lambda_1 r_c)}\right) \quad (7)$$

$\theta_c = T_f - T_e$ is the critical temperature difference for freezing, r_c is the smallest radius we require to freeze (assuming that the front propagates from the exterior), $r_c = 0.1R$ should be sufficient for most cases.

4. RESULTS

Due to the inherent difficulties in carrying out ice accretion experiments, there is relatively little experimental data available in the literature reporting ice accretion results in well controlled conditions. We chose to apply the glaze ice model on three sets of data, Cases 1 and 3 from Hochart et al. [18] and Run 308 from Wright et al. [19].

4.1. Comparison to the data from Hochart et al. [18]

4.1.1. Case set up

In Hochart et al [18] ice accretion on a NACA 63415 airfoil is investigated in glaze and rime ice conditions. Cases 1 and 3 from [18] correspond to mild and severe glaze ice conditions, respectively. The details of the experimental conditions as well as the amount of accreted ice measured in the experiments are summarised in Table 1.

Table 1. Summary of the experimental cases [18]

Parameter	Case 1	Case 3
LWC $[g/m^3]$	0.37	0.48
MVD $[\mu m]$	27.6	27.6
T_e $[^oC]$	-1.4	-1.4
$\underline{u}_{\text{rel}}$ $[m/s]$	19.9	56.0
t [min]	14.8	24.8
α $[^o]$	6	6
average accreted ice $[g]$	48	354
standard deviation $[g]$	0.25	4.5

The parameter choices and the resulting amount of accreted ice for the computed cases are shown in Table 2. The predictions for Case 1 used 12 loops and a scaling factor of $f = 1000$ to predict the amount of accreted ice. Thus, each iteration in the loop computed the ice accretion for 0.074 s physical time and the airfoil surface was adjusted by assuming that the same trend is valid for 74 s. Since Case 3 involves more severe icing, the number of loops was increased to 25 (each iteration corresponds to 0.062 s), the scaling factor being the same as in Case 1.

A general observation is that the computations are consistently over-predicting the amount of accreted ice, the error being significantly larger for the case with severe icing condition. Furthermore, the predicted amount of accreted ice does not change significantly with changes in the model parameters.

Table 2. Summary of the computed cases

Case	Case in [18]	ft [s]	e [-]	Accreted ice mass [g]	Error [%]
C1T00	1	0.0	0.0	59.52	24.0
C1T01	1	0.1	0.0	59.40	23.7
C1T10	1	1.0	0.0	59.48	23.9
C1T01E05	1	0.1	0.5	59.32	23.6
C3T00	3	0.0	0.0	559.07	57.9
C3T01E05	3	0.1	0.5	563.05	59.1
C3T01E08	3	0.1	0.8	558.55	57.8

4.1.2. Hochart Case 1

Figure 2 shows the isocolors of the average static pressure at the end of the ice accretion event (14.8 minutes) for Case 1. For visualisation purposes, the instantaneous snapshots of the lagrangian parcel field at the last calculated timestep is shown as well. Note, that the lagrangian field is uniformly down-sampled to improve visibility. Figure 2a shows the results when the model was set up to mimic rime ice conditions (by setting $ft = 0$), whereas Figure 2b displays the results for $ft = 0.1$ s and $e = 0.5$. One can observe the smoother ice shape in the leading edge region. Also the higher density of the parcels impacted on the surface stretches to a larger downstream distance in the glaze ice case compared to rime ice conditions.

The influence of the imposed freezing time is illustrated in Figure 3. The figure shows the contour of the clean airfoil (black) together with ice accreted airfoils by setting the model parameter for the freezing time to 0 s (blue, modelling rime ice conditions), 0.1 s (red) and 1 s (green). As a comparison, the timescale based on the relative velocity and the chord length is 0.01 s. The leading and trailing edge regions are enlarged for better visibility. One can observe that even allowing a relatively long freezing time, the shape of the ice does not change significantly. The reason is that the second model parameter, e, controlling the elasticity of the droplet collision with the surface was set to zero. As a consequence, the impacting droplet parcels were trapped in the low velocity region in the proximity of the wall, leading to very small displacements even for long freezing times.

The influence of the parameter controlling the elasticity of the impact is shown in Figure 4, where the clean airfoil (black) is compared to ice accreted airfoils with the same freezing time (0.1 s) but having $e = 0$ (red, no rebounce) and $e = 0.5$ (orange,

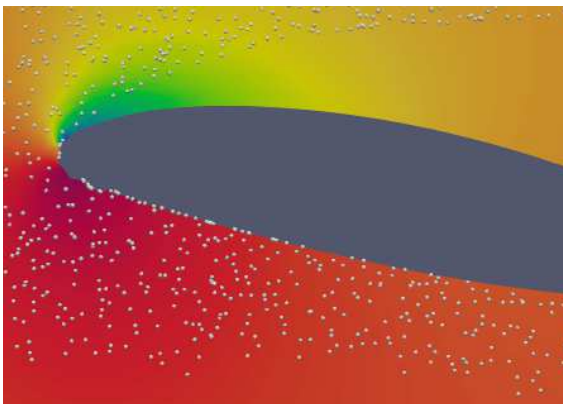

(a) ft=0

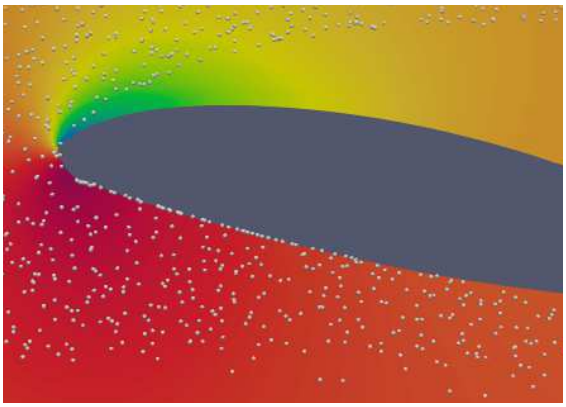

(b) ft=0.1, e=0.5

Figure 2. Illustration of the flow field for Case 1, (a) rime ice model and (b) glaze ice model

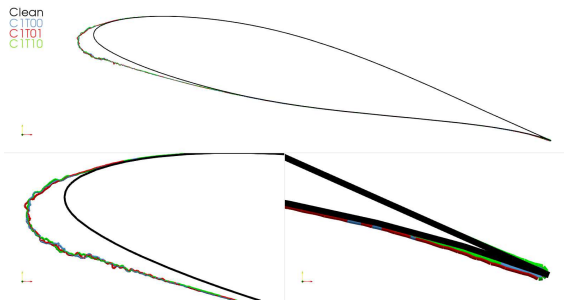

Figure 3. Comparison of the clean and ice accreted airfoil contours for different values of the freezing time. Case 1.

partially elastic collision). One can observe that adjusting the elasticity parameter leads only to minor changes in the accreted ice shape. The quantitative changes are also minor, the error decreases only with 0.1% (see table 2).

4.1.3. Hochart Case 3

Case 3 corresponds to extreme icing conditions and was chosen in order to 'stress-test' the model, to emphasise limitations and clarify targets to be improved in the future.

Figure 5 shows the isocolors of static pressure

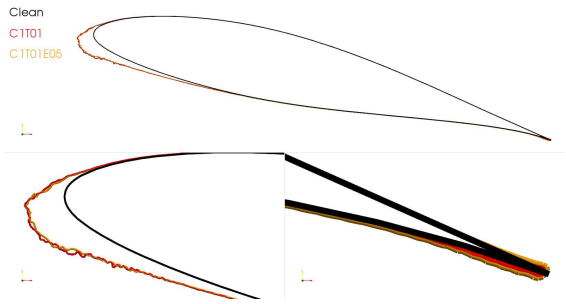

Figure 4. Comparison of the clean and ice accreted airfoil contours for different values of the elasticity parameter. Case 1.

and the droplet parcel field for Case 3 with three different settings of the model parameters. Figure 5a shows rime ice conditions (ft=0), the other two subfigures illustrate glaze ice conditions with different settings of the elasticity parameter.

Unfortunately, all three computations resulted in significant over-prediction of the amount of accreted ice and in the formation of excessively large hornlike structures which are not likely to occur in reality. The closest resemblance to the experimentally observed shapes reported in [18] is found for ft=0.1 s, e=0.5 (Figure 5b): both the tendency to form a shape with two bumps on the suction side and to collect ice in the trailing edge region are captured qualitatively, however, the accreted ice does not have the smooth shape on the pressure side like in the experiments.

4.2. Comparison to the data from Wright et al. [19]

4.2.1. Case set up

Among the multitude of cases reported in [19] the case called Run 308 was chosen since it is a glaze ice case in relatively severe icing conditions. The main parameters describing the icing event are listed in Table 3.

Table 3. Summary of the experimental case [19]

LWC $[g/m^3]$	1.0
MVD $[\mu m]$	20.0
T_e $[K]$	262.04
$\underline{u}_{\text{rel}}$ $[m/s]$	102.8
t [min]	3.85
Airfoil	NACA 0012
α $[^o]$	4

4.2.2. Sample results

Three parameters have been evaluated for this case.

The influence of smoothing of the accreted ice amount is visualised in Figure 6a. Three cases are shown with 1 (red), 10 (green) and 200 (blue) smoothing iterations. As it was expected, smoothing decreases the irregularity of the resulting ice surface. Furthermore, the amount of accreted ice changes as

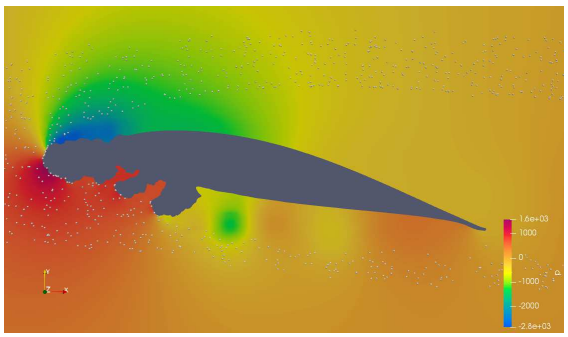

(a) ft=0

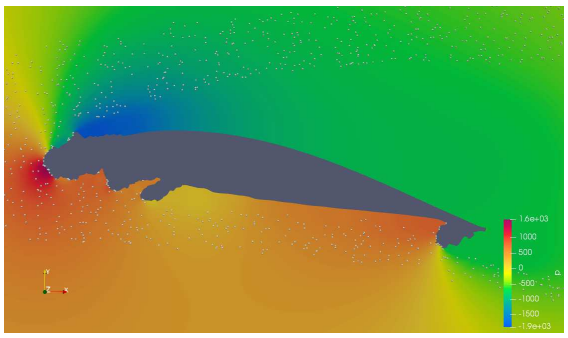

(b) ft=0.1, e=0.5

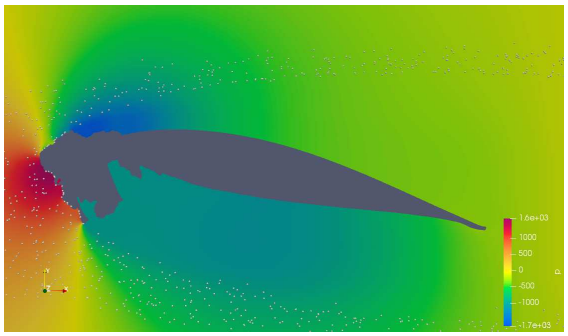

(c) ft=0.1, e=0.8

Figure 5. Illustration of the flow field for Case 3 for three different parameter combinations

well, especially on the pressure side. The reason is that due to smoothing there are smaller irregularities in this region and fewer droplets are collected.

The influence of freezing time is shown in Figure 6b. The rime ice case (ft=0, blue) is compared to glaze model cases with ft=0.1 s and ft=0.2 s. The main impact of the freezing time in this set-up is the reduction of the amount of accreted ice. This is expected since the droplets do not freeze instantaneously. It was expected to see the limit of accreted ice further downstream for glaze conditions. Nevertheless, such effect cannot be observed, probably due to the shape of the accreted ice in the leading edge region.

Finally, the influence of the elasticity parameter, e, is shown in Figure 6c. As it can be seen, with the decrease of e fewer droplets accrete on the surface, the $e = 0.9$ case being very close to the results obtained in rime ice conditions.

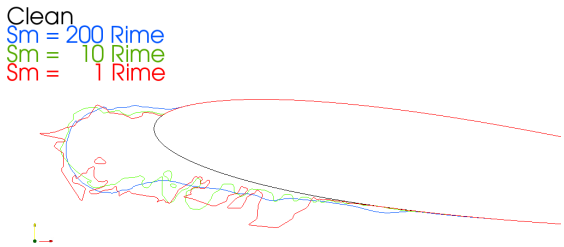

(a) Smoothing

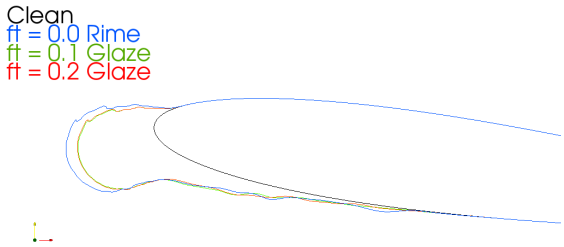

(b) ft

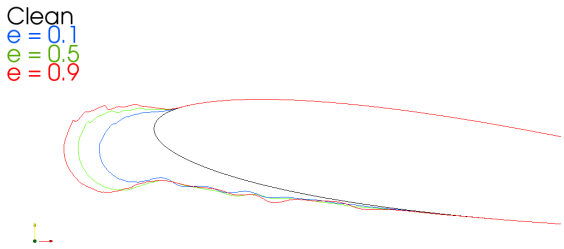

(c) e

Figure 6. Influence of the model parameters on the accreted ice shape.

5. SUMMARY

This work has been a first attempt to implement a fast ice accretion model applicable for glaze ice conditions. Considering the fact that the amount of physical models is significantly reduced we deem that the accuracy of the model is reasonable for mild icing conditions. For severe icing conditions; however, the error in the predicted ice mass increases significantly and unexpected ice shapes are formed, thus further model improvements are needed.

Both the overprediction of the amount of ice and the shape of the ice structures indicate that one significant deficiency of the model is that it does not account for ice loss due to shedding. In reality, ice horns might break due to the aerodynamic forces acting on them. Thus, an important improvement of the model would be to account for ice loss, that feature being important both for rime and glaze ice conditions. We expect that by allowing ice loss both the amount of accreted ice and it's shape would be closer to the experimentally observed ones. By removing the protruding ice horns, fewer droplet parcels would

be captured in the leading edge region and more parcels are expected to deposit further downstream on the pressure side, as it was observed in the experiments.

The model parameters have been adjusted in an ad-hoc manner so far. However, when more experimental data will be available, we expect that the model parameters could be more systematically validated and correlations between icing conditions and the model parameters can be found.

ACKNOWLEDGEMENTS

Financial support for this work was provided by the Swedish Energy Agency, project no. 47053-1. The computational resources were provided by the Swedish National Infrastructure for Computing (SNIC), partially funded by the Swedish Research Council through grant agreement no. 2018-05973 and by LUNARC.

REFERENCES

[1] Stoyanov, D. B., and Nixon, J. D., 2020, "Alternative Operational Strategies for Wind Turbines in Cold Climates", *Renewable Energy*, Vol. 145, pp. 2694–2706.

[2] Badman, D., and Tengblad, Y., 2021, "Roadmap 2040Wind Power: Combating Climate Change and Improving Competitiveness", *Tech. rep.*, Swedish Wind Energy Association.

[3] Laakso, T., Baring-Gould, I., Durstewitz, M., Horbaty, R., Lacroix, A., Peltola, E., Ronsten, G., Tallhaug, L., and Wallenius, T., 2010, "State-of-the-art of wind energy in cold climates".

[4] Jones, R., and Williams, D., 1936, "The Effect of Surface Roughness of the Characteristics of the Airfoils NACA 0012 and RAF 34", *Tech. Rep. Report No.1708*, British ARC.

[5] Gulick, B., 1938, "Effect of Simulated Iced Formation on the Aerodynamic Characteristics of an Airfoil", *Tech. Rep. R.N. NACA- Wr.L-292*, NACA.

[6] Makkonen, L., 1985, "Heat transfer and icing of a rough cylinder", *Cold Regions Science and Technology*, Vol. 10, pp. 105–116.

[7] Makkonen, L., 2000, "Models for the growth of rime, glaze, icicles and wet snow on structures", *Philosophical Transactions of the Royal Society A: Mathematical, Physical and Engineering Sciences*, Vol. 358 (1776), pp. 2913–2939.

[8] Wright, W., 2008, "User ' s Manual for LEWICE Version 3 . 2", *Tech. Rep. NASA/CR–2008-214255*, NASA.

[9] Homola, M. C., Virk, M. S., Wallenius, T., Nicklasson, P. J., and Sundsbø, P. A., 2010, "Effect of atmospheric temperature and droplet size variation on ice accretion of wind turbine blades", *Journal of Wind Engineering and Industrial Aerodynamics*, Vol. 98 (12), pp. 724–729.

[10] Gori, G., Zocca, M., Garabelli, M., Guardone, A., and Quaranta, G., 2015, "PoliMIce: A simulation framework for three-dimensional ice accretion", *Applied Mathematics and Computation*, Vol. 267, pp. 96–107.

[11] Jin, J. Y., and Virk, M. S., 2019, "Study of ice accretion and icing effects on aerodynamic characteristics of DU96 wind turbine blade profile", *Cold Regions Science and Technology*, Vol. 160 (September 2018), pp. 119–127.

[12] Prince Raj, L., Yee, K., and Myong, R., 2020, "Sensitivity of ice accretion and aerodynamic performance degradation to critical physical and modeling parameters affecting airfoil icing", *Aerospace Science and Technology*, Vol. 98, p. 105659.

[13] Szasz, R., and Fuchs, L., 2012, "Numerical modeling of ice accretion on a wing section", J. Vad (ed.), *Proceedings of the Conference on Modelling Fluid Flow*, pp. 292–298.

[14] Szasz, R.-Z., Ronnfors, M., and Revstedt, J., 2016, "Influence of ice accretion on the noise generated by an airfoil section", *International Journal of Heat and Fluid Flow*, Vol. 62, pp. 83–92.

[15] Son, C., and Kim, T., 2020, "Development of an icing simulation code for rotating wind turbines", *Journal of Wind Engineering and Industrial Aerodynamics*, Vol. 203 (June), p. 104239.

[16] "OpenFOAM, https://www.openfoam.org".

[17] Menter, F., 1994, "Two-Equation Eddy-Viscosity Turbulence Models for Engineering Applications", *AIAA Journal*, Vol. 32, pp. 1598–1605.

[18] Hochart, C., Fortin, G., Perron, J., and Ilinca, A., 2008, "Wind turbine performance under icing conditions", *Wind Energy*, Vol. 11 (4), pp. 319–333.

[19] Wright, W. B., and Rutkowski, A., 1999, "Validation Results for LEWICE 2.0", *Tech. rep.*, Lewis Research Center.

Conference on Modelling Fluid Flow (CMFF'22)
The 18th International Conference on Fluid Flow Technologies
Budapest, Hungary, August 30 -September 2, 2022

EFFECTS OF STOKES NUMBER ON PARTICLE DEPOSITION IN PARTICLE-LADEN TURBULENT PIPE FLOWS

Bisrat WOLDE[1], Lee MORTIMER[2], Michael FAIRWEATHER[3]

[1] Corresponding Author. School of Chemical and Process Engineering, Faculty of Engineering and Physical Sciences, University of Leeds. Leeds LS2 9JT, United Kingdom. E-mail: pmbw@leeds.ac.uk
[2] School of Chemical and Process Engineering, Faculty of Engineering and Physical Sciences, University of Leeds. Leeds LS2 9JT, United Kingdom. E-mail: l.f.mortimer@leeds.ac.uk
[3] School of Chemical and Process Engineering, Faculty of Engineering and Physical Sciences, University of Leeds. Leeds LS2 9JT, United Kingdom. E-mail: m.fairweather@leeds.ac.uk

ABSTRACT

The ability to predict particle dispersion, interaction and deposition in pipes is of value in improving the transport and process efficiency of high concentration particulate flows. In this work, the settling and deposition behaviour of suspensions of dense particles in a cylindrical pipe has been studied using direct numerical simulation coupled with Lagrangian particle tracking, with the influence of Stokes number on deposition examined. Fully developed particle-laden pipe flows are first driven to a steady state with shear Reynolds number, $Re_\tau = 720$, and particle Stokes numbers, $St^+ = 5.55$ and 16.78, with the constant pressure gradient forcing term subsequently decreased until the onset of particle deposition. From the analysis performed, it can be concluded that particle deposition is sensitive to Stokes number. Particle dispersion function and mean displacement values are demonstrated to decrease considerably faster with time at the higher Stokes number. Particle migration towards the lower wall regions of the pipe also shows the formation of a bed for such particles, whilst over the same time period only dune-like structures are produced at the lower Stokes number. An analysis of the particle dynamics, carried out by examining probability density functions of particle velocities and positions, confirms these findings.

Keywords: Particle flows, DNS, LPT, Stokes number, particle deposition.

NOMENCLATURE

d_p^*	[-]	Particle diameter
D	[m]	Pipe inner diameter
$D_{y(t)}^*$	[-]	Dispersion function
$\underline{f_i}$	[-]	Flow forcing term
Fr	[-]	Froude number
g	[ms^{-2}]	Acceleration due to gravity
$\underline{\hat{g}}$	[-]	Unit vector in gravity direction
L	[m]	Characteristic length scale
N_p	[-]	Number of particles
p^*	[-]	Pressure in bulk units
r	[m]	Radial coordinate
R	[m]	Pipe radius
Re_b, Re_τ	[-]	Bulk and shear Reynolds number
St	[-]	Stokes number
Δt^*	[-]	Particle timestep
$\underline{u}^*$	[-]	Mean velocity in bulk units
$\underline{u}_p^*, \underline{u}_f^*$	[-]	Particle and fluid velocity vector
$\underline{u}_s^*$	[-]	Slip velocity
$\underline{u}_\tau$	[ms^{-1}]	Shear velocity
U_b	[ms^{-1}]	Bulk mean velocity
$\underline{x}_p^*$	[-]	Particle position vector
$y_{i(t)}^*$	[-]	Particle vertical position
$y_{m(t)}^*$	[-]	Particle vertical mean position
z	[m]	Axial position
θ	[-]	Azimuthal coordinate
μ	[Pa. s]	Dynamic viscosity
ν	[m$^2 s^{-1}$]	Kinematic viscosity
ρ	[kgm^{-3}]	Fluid density
ρ_f, ρ_s	[kgm^{-3}]	Density of fluid and solid phase
ρ_p^*	[-]	Particle-fluid density ratio
$\underline{\underline{\tau}}$	[Pa]	Fluid Stress tensor
ϕ	[-]	Volume fraction
$\underline{\omega}_f^*$	[-]	Vorticity of fluid

Abbreviations and Acronyms

CFD	Computational fluid dynamics
DNS	Direct numerical simulation
LPT	Lagrangian particle tracking/tracker
PDF	Probability density function
SEM	Spectral element method
x, y, z	Cartesian coordinates
*	Non-dimensional units

1. INTRODUCTION

Accurate simulation of multiphase turbulent flows is of fundamental importance in many industrial and scientific research applications. Additionally, the generation of understanding through accurate modelling of turbulent multiphase flows is valuable across numerous industries such as chemical engineering, agriculture and nuclear waste processing [1].

Very few direct numerical simulation (DNS) studies have been performed in the past to investigate turbulent pipe flows at moderately high Reynolds numbers ($\boldsymbol{Re_b}$ = 11,700), and even fewer with a particulate phase present. In the past, multiphase DNS investigations have used mainly one-way coupling between the particles and the fluid, and at low Reynolds numbers [2]. There is a noticeable absence of four-way coupled DNS-based work, particularly in cylindrical geometries. Further, no previous modelling studies have considered the onset of particle deposition in such flows. As computational power increases it is now possible to perform such fully coupled simulations. The effects of particles on the fluid and interparticle collisions in turbulent pipe flows at moderately high Reynolds numbers are therefore being investigated here, with the emphasis placed on the analysis of results to determine particle dispersion and particle deposition out of the flow to form solid beds.

In this work a predictive methodology was developed based on DNS coupled with Lagrangian particle tracking (LPT) to study the details of particle deposition at two different particle Stokes numbers, $St^+ = 5.55$ and 16.78. An openly available computational fluid dynamic (CFD) solver, Nek5000, has been utilised as the basis for the work reported [3]. The solver is based on the spectral element method (SEM) with a high order residual technique. It is favourable for its high spectral accuracy, parallel process scaling and low numerical dispersion and dissipation [4]. The DNS code has been further extended with a four-way coupled LPT code to allow for high fidelity simulation of depositing particle-laden pipe flows.

2. METHODOLOGY

2.1. Single-Phase Flow Simulations

To solve the descriptive CFD equations, the DNS solver Nek5000 was used, as developed by Fischer et al. [3]. This solver is based on the spectral element method, an efficiently parallelisable, high-order weighted residual technique with excellent accuracy, and low numerical dispersion and dissipation. The Navier-Stokes equations are solved in non-dimensional form. In this work, all simulations were performed under the assumption that the fluid was Newtonian. The system studied was a pressure-driven incompressible flow in a long straight pipe with circular cross-section and an internal diameter, D. The time-dependent non-dimensional Navier-Stokes equations are given as:

$$\underline{\nabla}.\underline{u}^* = 0 \tag{1}$$

$$\frac{\partial \underline{u}^*}{\partial t^*} + \left(\underline{u}^*.\underline{\nabla}\right)\underline{u}^* = -\underline{\nabla}p^* + \frac{1}{Re_b}\,\underline{\nabla}\cdot\underline{\underline{\tau}}^* + \underline{f_i} \tag{2}$$

Here, $\underline{u}^*\left(\underline{x}^*, t^*\right)$ is the fluid velocity vector, non-dimensionalised using the bulk velocity, U_b, with the position vector, $\underline{x}^*$, and time, t^*, non-dimensionalised as $\underline{x}^* = \underline{x}/D$ and $t^* = tU_b/D$, respectively. Also, p^* is the non-dimensionalised pressure term for high-velocity flow, $p^* = p/\rho U_b^2$. The bulk Reynolds number, Re_b, is defined as $Re_b = U_b D/\nu$, where ν is the fluid kinematic viscosity. $\underline{\underline{\tau}}^*$ is the non-dimensionalised fluid stress tensor, $\underline{\underline{\tau}}^* = \underline{\underline{\nabla u^*}} + \underline{\underline{\nabla u^{*T}}}$, and $\underline{f_i}$ is a forcing term representing the driving pressure gradient and the two-way interaction between the fluid and the particles.

Eqs. (1) and (2) are solved numerically using the spectral element method along with appropriate boundary conditions. In three-dimensional space, these equations are discretised as grid points by the Lagrange-Galerkin approximation method. Nth-order Lagrange polynomial interpolants on Gauss-Lobatto-Legendre points are implemented as a basis for velocity space and Lagrangian interpolants of order N-2 on Gauss-Legendre quadrature points are employed for pressure space. Resolution of the Kolmogorov length scale was confirmed.

Table 1. Fluid phase mesh parameters.

Re_b	Re_τ	Elements	Grid Points
3975	277	36,576	18,726,912
11700	720	36,576	18,726,912

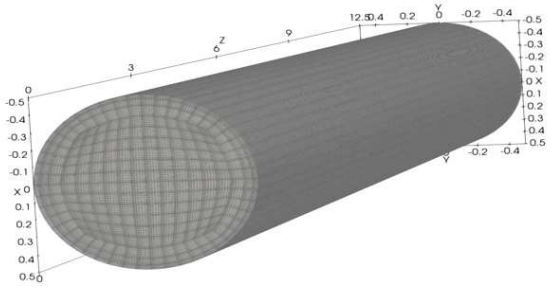

Figure 1. Computational mesh topology with Gauss-Lobatto-Legendre quadrature points (N = 7) for simulations at $Re_\tau = 277$ and $Re_\tau = 720$.

The computational domain consisted of a circular pipe of diameter, D, and length, $L = 12.5D$, partitioned into 36,576 spectral elements. Within the macro-elements the velocity field was represented by high-order tensor-product Gauss-Lobatto-Legendre

polynomial expansions of order N. The flow in the streamwise direction was forced by a constant pressure gradient. The shear Reynolds numbers based on the shear stress velocity considered below were $Re_\tau \approx 277$ and $Re_\tau \approx 720$. For both simulations, the same mesh topology and number of spectral elements was used. Gauss-Lobatto-Legendre quadrature points (N = 7) were used to distribute the vertices in each element [5]. The total number of elements and grid points used are given in Table 1 while Figure 1 illustrates the mesh topology implemented in all simulations.

2.2. Lagrangian Particle Tracking

The LPT solves a force-balance equation for each particle in the system, represented as an impenetrable computational sphere, under the assumption of point particles. The particle equations of motion for all forces considered in the multiphase flows are given below. In this research, a modified Maxey and Riley [6] equation was used. The non-dimensional form of the equations of motion for spherical particles, as implemented in the code, are:

$$\underline{u}_p^* = \frac{\partial \underline{x}_p^*}{\partial t^*} \tag{3}$$

$$\frac{\partial \underline{u}_p^*}{\partial t^*} = \frac{1}{M_{VM}} \left[\begin{array}{l} \dfrac{3C_D\left|\underline{u}_s^*\right|}{4d_p^*\,\rho_p^*}\underline{u}_s^* + \dfrac{1}{Fr}\left(1-\dfrac{1}{\rho_p^*}\right)\underline{\hat{g}} + \\ \dfrac{3C_L}{4\rho_p^*}(\underline{u}_s^* \times \underline{\omega}_f^*) + \dfrac{D'\underline{u}_f^*}{2\rho_p^*\,Dt^*} + \dfrac{D\underline{u}_f^*}{\rho_p^*\,Dt^*} \end{array} \right] \tag{4}$$

In Eqs. (3) and (4), $\underline{u}_p^*$ is the particle velocity vector, $\underline{x}_p^*$ the particle position vector, C_D the drag coefficient, and $\underline{u}_s^*$ the slip velocity given as $\underline{u}_f^* - \underline{u}_p^*$, where $\underline{u}_f^*$ and $\underline{u}_p^*$ are the fluid and particle velocity vectors, respectively. Also, d_p^* is the particle diameter, ρ_p^* the density ratio, Fr is the Froude number, which is defined as $Fr = u_b^2/gD$, where g is gravitational acceleration and $\underline{\hat{g}}$ is a unit vector in the direction of gravitational attraction, $\underline{\omega}_f^*$ is the vorticity of fluid which is given by $\underline{\omega}_f^* = \underline{\nabla} \times \underline{u}_f^*$, and the full equation is divided by $M_{VM} = (1 + 1/2\rho_p^*)$ to account for the virtual mass force. The particle bulk Stokes number is given as $St_b = d_p^{2^*}\rho_p^* Re_b/18$, and the shear Stokes number as $St^+ = d_p^{2^*}\rho_p^* Re_\tau^2/18$. A detailed explanation of these forces is provided by Mortimer et al. [7].

The drag force occurs due to movement through a resistive fluid phase and is a dominant force in the fluid-particle flow [8], while the lift force arises due to shear across the particle. Saffman [9] studied the strength and direction of the lift force for low particle Reynolds number and later Dandy and Dwyer [10] extended it to high particle Reynolds numbers. The virtual mass and pressure gradient forces were based on the fluid acceleration and local pressure gradient, respectively [11]. A gravitational force is also applied in the vertical direction in all simulations. To account for two-way momentum coupling, for a given computational cell, the mean forces applied to each particle during the timestep are also distributed to the local fluid cell. Particle collisions are also taken into account and assumed to be elastic and obey the hard-sphere conditions when calculating rebound positions and velocities.

The Lagrangian particle tracker was developed to model large quantities of dispersed solids and runs concurrently with Nek5000. A fourth-order Runge-Kutta method was implemented to solve the particle equation of motion for each particle at every time-step. To initialise the computations, the particles were injected at a random position within the fully developed fluid flow domain and assigned the fluid velocity at that location. Particles collisions with the pipe wall were considered to be elastic. Periodic boundary conditions were applied at the extents of the streamwise direction and no-slip conditions for the wall at $r^* = 0.5$. Statistical data was gathered for the fully-coupled simulations after a few particle response times ($t^* = 20$) to allow time for the injected phase to adjust to the surrounding fluid.

2.3. Particle Deposition

Rice [12] investigated the settling and deposition behaviour of suspensions of dense particles in closed cylindrical pipes using ultrasonic methods, with the onset of particle deposition and resuspension from beds studied. In the experiments performed, a range of parameters were considered, though pipe diameter was not. Two ways of evaluating the critical deposition velocity were proposed, i.e. the velocity at which particles first start to deposit out in a flow. Both particles depositing as the flow rate was decreased, and in contrast when the particles were resuspended from the pipe floor as the flow rate was increased, were considered, arguing that these approaches were equivalent and represented different ways to obtain the same deposition velocity.

In the present study, depositing pipe flows were performed with the DNS and LPT codes at two different Stokes numbers, $St^+ = 5.55$ and 16.78. A fully developed particle-laden turbulent pipe flow at $Re_\tau = 720$ was first run, with the flow rate subsequently decreased regularly until particle deposition occurred. To achieve this, the pressure gradient along the pipe was lowered by two per cent every 2000 timesteps ($t^* = 2$). The dispersion function and mean displacement of the particles were also monitored, with the dispersion function, $D^*_{y(t)}$, defined as:

$$D^*_{y(t)} = \left(\sum_{i=1}^{N_p} \frac{(y^*_{i(t)} - y^*_{m(t)})^2}{N_p} \right)^{1/2} \tag{5}$$

Here, $y^*_{i(t)}$ is the particle displacement in the vertical direction, $y^*_{m(t)}$ the mean vertical particle position, sampled across the entire domain, and N_p the total number of particles [13]. Table 2 shows the configuration of the depositing pipe flows. In both cases, the same concentration, particle diameter and number of particles were used. It should be noted that the maximum value of ϕ found in regions outside the deposition zone considered below was 2.5×10^{-3}.

Table 2. Particle phase parameters.

Parameter	Shear Reynolds number, $Re_\tau = 720$	
	$St^+ \cong 5.55$	$St^+ \cong 16.78$
Particle diameter, d_p^*	0.005	0.005
Axial length	12.5D	12.5D
Number of particles, N_p	105k	105k
Bulk Stokes number, St_b	0.125	0.379
Density ratio, ρ_p^*	7.71	23.3
Volume fraction, ϕ	0.0007	0.0007
Particle timestep, Δt^*	0.001	0.001

3. RESULTS AND DISCUSSION

3.1. Single-Phase Flow Validation

Single-phase simulations were performed at shear Reynolds numbers of $Re_\tau = 277$ and $Re_\tau = 720$ in order to validate the DNS approach being used. In each simulation, statistical data were gathered for analysis. The simulation results were compared with various DNS and experimental datasets available in the literature at, or approximately equal to, the Reynolds numbers of the simulations performed. For each simulation the mean velocity profiles, and the root mean square of the velocity fluctuations and shear stress, were compared. Only literature data with incompressible and Newtonian fluid flows was used for validation and, where possible, multiple experiments and DNS datasets were compared with the current simulations.

Figure 2 shows the axial mean velocity profile of the present predictions at a shear Reynolds number $Re_\tau = 720$, and compares this with the DNS results of El Khoury [14] at $Re_\tau = 720$ and Singh et al. [15] at $Re_\tau \approx 640$. The present work agrees with the results of El Khoury [14] but slightly deviates when contrasted with Singh et al. [15], likely due to the difference in Reynolds number. The results are additionally compared with the den Toonder et al. [2] experimental dataset at $Re_\tau \approx 630$. These results correlate well with the present work given the difference in Reynolds number.

Figure 3 displays the axial, z^*_{rms}, radial, r^*_{rms}, azimuthal, θ^*_{rms}, normal stress profiles, and the Reynolds shear stress, $< u_z\, u_r >^*$, at $Re_\tau = 720$ showing good agreement with El Khoury [14], Singh et al. [15], and den Toonder et al [2]. On the pipe centreline, all the simulations and experimental data are in good agreement with the inner scaled profiles of the present DNS. Overall, comparison of the normal and shear stresses, as a function of $0.5 - r^*$, gives confidence in the present continuous phase predictions. Similar agreement with literature data was also found for the $Re_\tau = 277$ case considered.

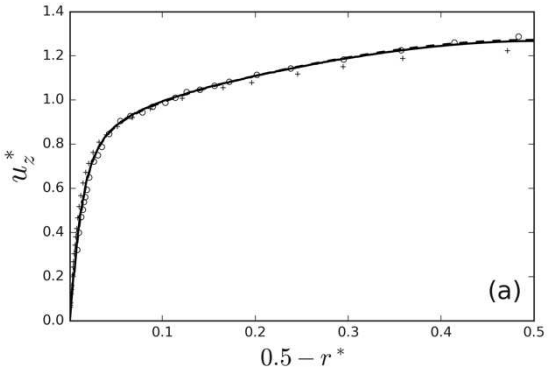

Figure 2. Mean axial velocity u_z^* : — present DNS at $Re_\tau = 720$; − − El Khoury (2013) DNS at $Re_\tau = 720$; + Singh et al. (2018) DNS at $Re_\tau \approx 640$; ○ den Toonder et al. (1997) experiments at $Re_\tau \approx 630$.

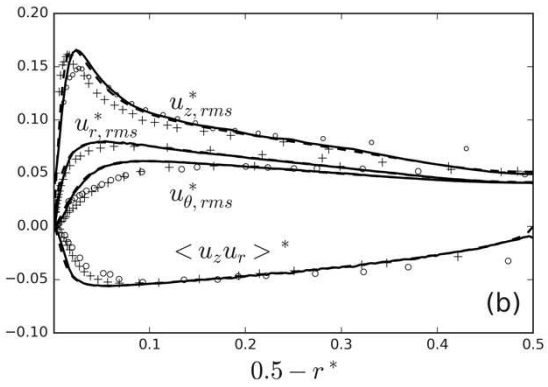

Figure 3. Axial, z^*_{rms}, radial, r^*_{rms}, and azimuthal, θ^*_{rms}, normal stresses and Reynolds shear stress, $< u_z\, u_r >^*$: — present DNS at $Re_\tau = 720$; − − El Khoury (2013) DNS at $Re_\tau = 720$; + Singh et al. (2018) DNS at $Re_\tau \approx 640$; ○ den Toonder et al. (1997) experiments at $Re_\tau \approx 630$.

3.2. Multi-Phase Flow Validation

To validate the coupled DNS and LPT solver, a separate simulation was performed, again at $Re_\tau = 277$, and compared directly with the DNS results of Vreman [16] who considered the dispersion glass-beads. In the present work, the particles were injected at random locations within the computational domain, taking the fluid velocity at their location at the start of the particle simulation. 29,400 particles were injected having a diameter of 60 μm. To best represent the parameters used in the validation case considered,

only drag and gravitational forces were used when calculating the particle trajectories, with the impact of lift considered negligible. The gravitational force was also applied in the mean flow direction, in line with [16]. The only difference was that in the present simulation a much larger number of numerical grid nodes were used. One-way and four-way coupled simulations with the same particle size and number were performed, with mean and fluctuating velocity profiles analysed.

The particle mean velocity profile and stresses are compared with the results of Vreman [16] in Figure 4. Clearly the present one-way coupled simulations are significantly different from those using four-way coupling, with the latter required to simulate the impact of particles on the continuous flow field. There is reasonable agreement with the four-way DNS predictions of Vreman [16], although some differences do occur, this likely being due to significantly increased numerical resolution used in the present work (18.7M nodes as opposed to 607k).

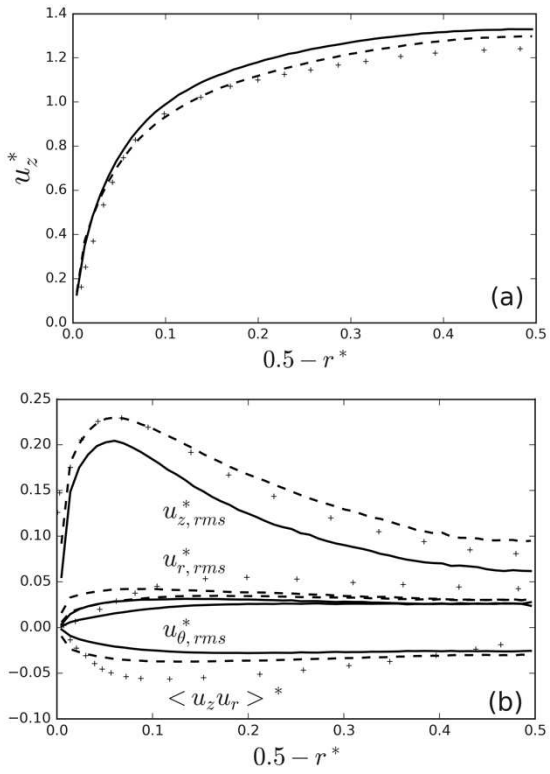

Figure 4. (a) Mean axial velocity and (b) normal and shear stresses at $Re_\tau = 277$: — present DNS one-way coupled; --- present DNS four-way coupled; + Vreman (2007) DNS four-way coupled.

3.3. Particle Deposition

The fully developed $Re_\tau = 720$ flow was used to simulate one- and four-way coupled flows at two different particle Stokes numbers of $St^+ = 5.55$ and 16.78. In both cases, the same particle volume fraction was used; 7×10^{-4}. To initialise the simulations, 105k particles were randomly injected throughout the computational domain and assigned the local interpolated fluid velocity. 50 μm particles with a density ratio (with the fluid) of 7.71 for $St^+ \cong 5.55$ and 23.3 for $St^+ \cong 16.78$ were employed.

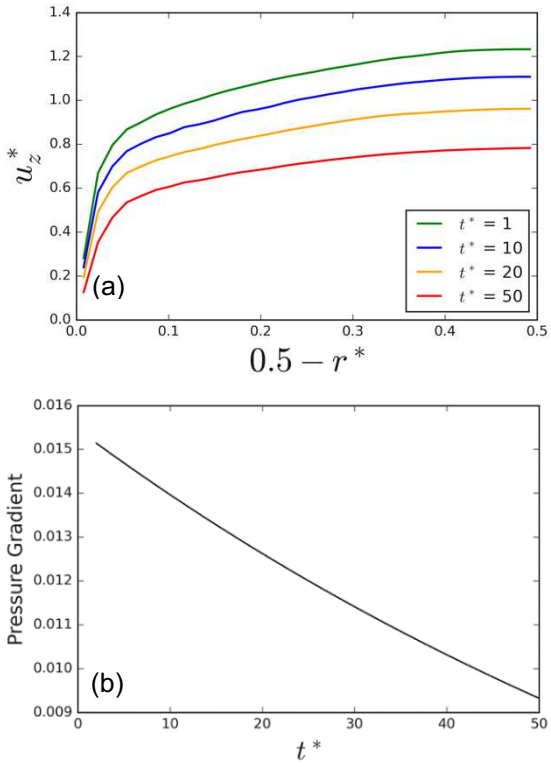

Figure 5. (a) Mean axial velocity at different t^* and (b) prescribed pressure gradient.

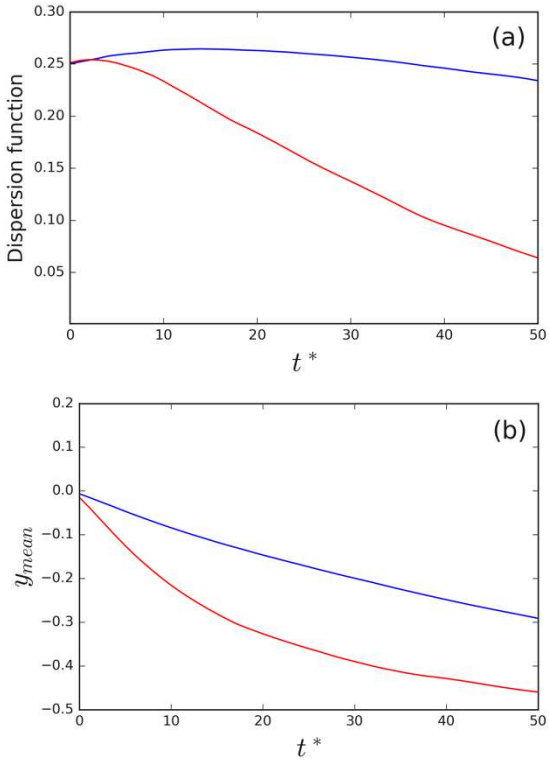

Figure 6. (a) Dispersion function in vertical direction and (b) mean vertical position of particles: blue St^+=5.55; red St^+=16.78.

Figure 5 shows the mean streamwise velocity profile and the non-dimensionalised pressure gradient reduction with time, with the latter used to drive the reduction in mass flow through the pipe in order to encourage particle deposition.

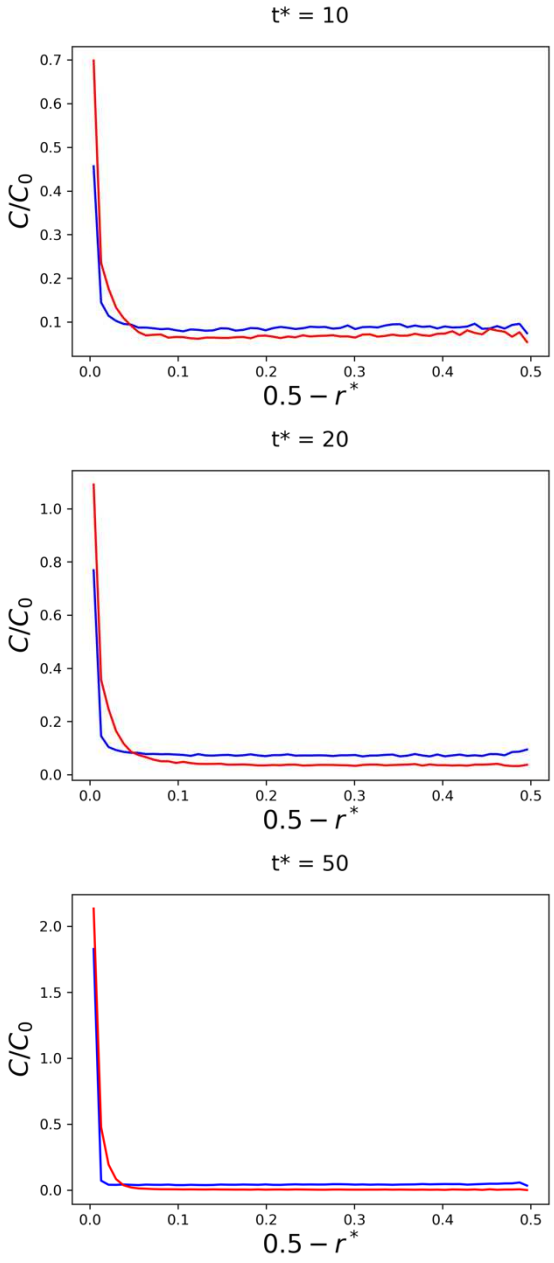

Figure 7. Mean particle concentration of $St^+ = 5.55$ (blue) and $St^+ = 16.78$ (red) particles with time, normalised by initial concentration.

Figure 6 shows the dispersion function, defined in Eq. (5), and the mean vertical position of the particles with time. At the high Stokes number, $St^+ = 16.78$, the particle dispersion and their mean vertical position decrease considerably faster with time than for the lower Stokes number case. This is due to the increased gravitational force causing the particles to accelerate in the negative vertical direction at an increased rate. For the same sized particles of $St^+ \cong 5.55$, the rate of migration towards the lower half of the pipe is much slower when compared to the $St^+ \cong 16.78$ case.

Figure 7 shows mean particle concentration profiles in the vertical direction for both particles cases at various points in time, with the concentration normalised by the initially injected concentration, C_0. The particles are seen to migrate towards the wall region and to ultimately deposit on the bottom of the pipe, with the near-wall concentration of the $St^+ = 16.78$ particles higher than for the lower Stokes number case. This can be seen more clearly in Figs. 8 and 9, which plot the positions of particles close to the wall ($0.49 \leq r^* \leq 0.5$) in the lower half of the pipe with time. Initially, the particles are relatively evenly distributed within the domain, but with increasing time migration to the lower regions of the pipe occurs and for the high Stokes number case by $t^* = 50$ a particle bed appears to have formed. In contrast, for the lower Stokes number case a bed is not formed, although the majority of the particles have migrated towards the bottom of the pipe and formed dune-like structures. These observations are in-line with the calculated dispersion function and mean particle position values given in Fig. 6, where from approximately $t^* = 5$ the higher Stokes number particles start to deviate from the lower Stokes number case, and as time increases particle deposition proceeds at a significantly higher rate.

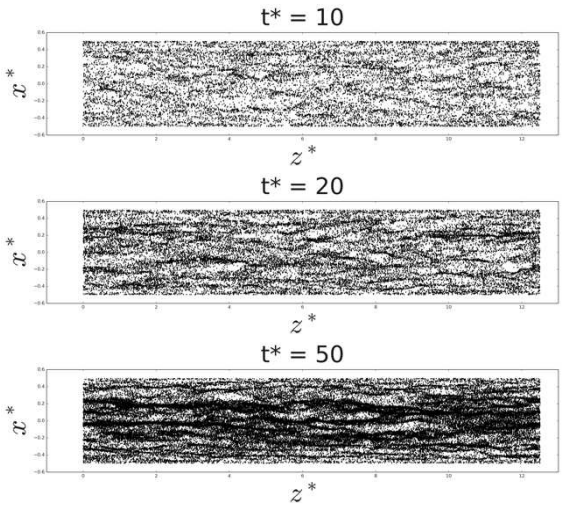

Figure 8. Instantaneous plots of particle position in the near-wall region of the lower half of the pipe for $St^+ \cong 5.55$.

To further examine the local behaviour of the particles, probability density function information on particle properties was also gathered. Figure 10 first shows PDFs for both Stokes number particles for the particle velocity in the vertical direction which illustrates a larger spread of negative vertical velocities for the low Stokes particles. There also exists a slight skew towards negative velocities in both

cases due to the influence of gravity. Secondly, PDFs of the particles' streamwise velocity are given, where for the low Stokes number particles two regimes are observed, with some particles possessing low speeds (those trapped in the wall region) or higher speeds (those in the bulk of the flow). The high Stokes number particles do not exhibit this behaviour, with the majority of particles existing at low velocities due to their proximity to the lower wall of the pipe, underlining the importance of flow and particle interactions within the wall-region such as particle preferential concentration in low speed streaks (seen in Figs. 8 and 9), and particle interaction with near-wall turbulence structures which, through sweep and ejection events, modulate the particle flux towards the wall. PDFs of the slip velocity are also given in Fig. 10 which tend to increase as the Stokes number increases, as would be expected for the more inertial particles. Lastly, PDFs of the vertical position of the particles is considered, with the high Stokes particles occupying much greater negative positions, in line with previous observations.

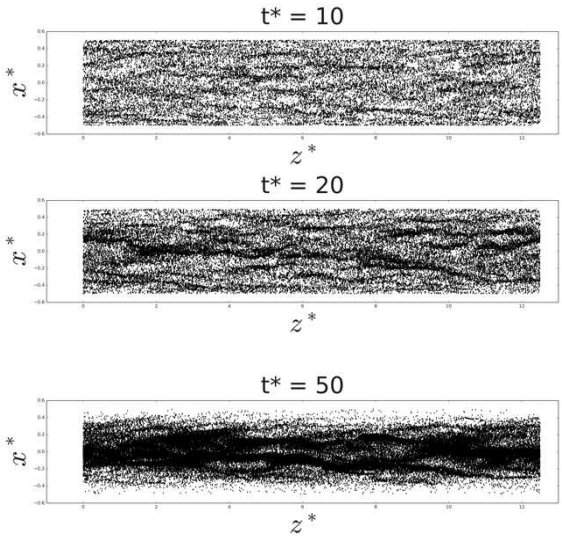

Figure 9. Instantaneous plots of particle position in the near-wall region of the lower half of the pipe for $St^+ \cong 16.78$.

4. CONCLUSIONS

This study has considered the effect of particle Stokes number on particle deposition within a wall-bounded turbulent flow. Direct numerical simulations have been carried out, coupled with Lagrangian particle tracking, for fully developed turbulent pipe flows, with mean velocity, and normal and shear stress, profiles within single-phase flows in agreement with other simulation results in the literature and experimental datasets. A similar validation for particle-laden flows has also been performed, again with good agreement with alternative simulations found.

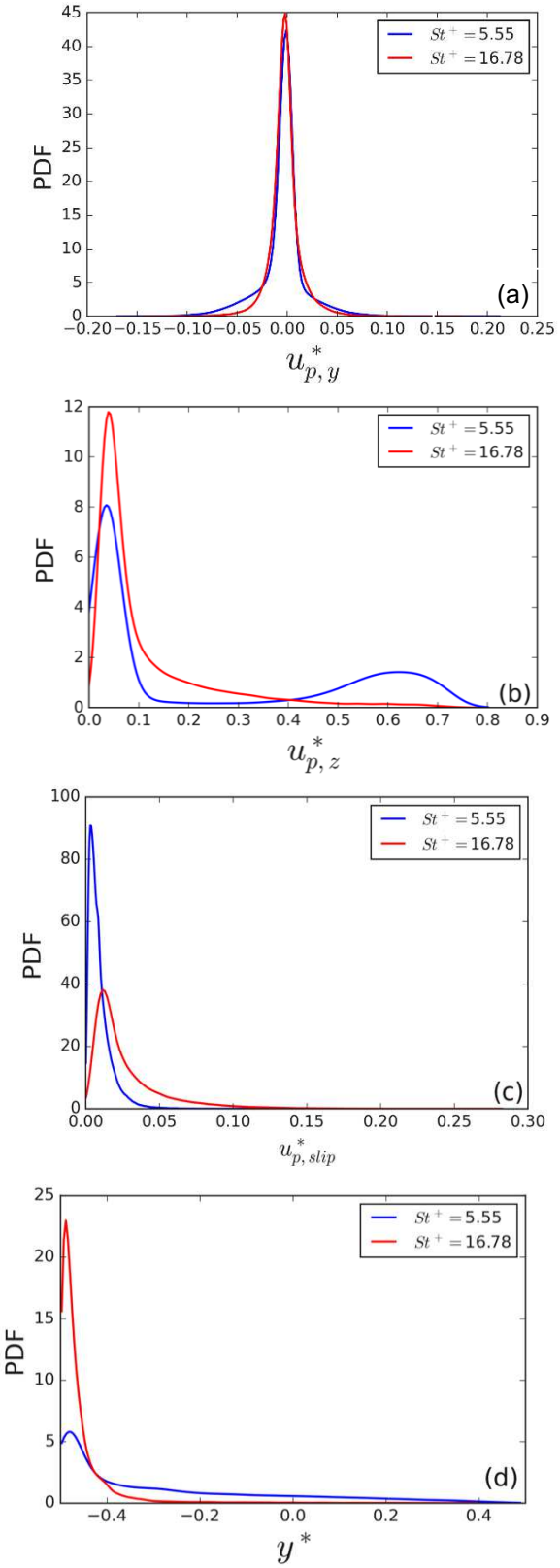

Figure 10. Probability density functions for $St^+ \cong 5.55$ and 16.78 particles at t^*=50: (a) vertical velocity; (b) streamwise velocity; (c) slip velocity; (d) vertical position.

A fully developed $Re_\tau = 720$ pipe flow has been used to perform four-way coupled simulations to

predict particle deposition. These were performed at two different particles Stokes numbers, $St^+ \cong 5.55$ and 16.78. The pressure gradient along the pipe was lowered with time and the gravitational force was applied in the vertical direction. The conveying flow rate then decreased allowing particle deposition to occur.

From the analysis performed, it can be concluded that particle deposition is very sensitive to Stokes number. The determined particle dispersion function and particle mean displacement have been demonstrated to decrease considerably faster with time at higher Stokes numbers due to the increased gravitational force acting on the particles. Particle concentrations demonstrate particle migration towards the lower wall regions and ultimately to deposition on the bottom of the pipe, with a particle bed forming for the higher Stokes number case. In contrast, at lower Stokes number, a bed is not formed, although the majority of the particles do form dune-like structures on the base of the pipe. Lastly, an analysis of the particle dynamics, carried out by examining probability density functions of particle velocities and positions, confirms the above findings.

Further work will examine a wider range of particle Stokes numbers and compare particle deposition velocities derived from the simulations with those obtained experimentally from both particle deposition and resuspension approaches to determining this parameter.

ACKNOWLEDGEMENTS

The authors are grateful for funding from the UK Engineering and Physical Sciences Research Council and the University of Leeds through the TRANSCEND (Transformative Science and Engineering for Nuclear Decommissioning) project (EP/S01019X/1).

REFERENCES

[1] Guha, D., Ramachandran, P. A., Dudukovic, M. P., 2007, "Flow field of suspended solids in a stirred tank reactor by Lagrangian tracking." *Chemical Engineering Science*, Vol. 62, pp. 6143-6154.

[2] den Toonder, J. M. J., Hulsen, M. A., Kuiken, G. D. C., Nieuwstadt, F. T. M., 1996, "Drag reduction by polymer additives in a turbulent pipe flow: Numerical and laboratory experiments." *Journal of Fluid Mechanics*, Vol. 337, pp. 1193-231.

[3] Fischer, P. F., Lottes, J. W., Kerkemeier, S. G., 2008, Nek5000, see http://nek5000.mcs.anl.gov (accessed 12th November 2021).

[4] Patera, A.T., 1984, "A spectral element method for fluid dynamics: Laminar flow in a channel expansion." *Journal of Computational Physics*, Vol. 54, pp. 468-488.

[5] Maday, Y., Patera, A. T., 1989, "Spectral element methods for the incompressible Navier-Stokes equations." In: *State-of-the-Art Surveys on Computational Mechanics*, pp. 71-143.

[6] Maxey, M. R., Riley, J. J., 1983, "Equation of motion for a small rigid sphere in a nonuniform flow." *Physics of Fluids*, Vol. 26, pp. 883-889.

[7] Mortimer, L. F., Njobuenwu, D. O., Fairweather, M., 2019, "Near-wall dynamics of inertial particles in dilute turbulent channel flows." *Physics of Fluids*, Vol. 31, 063302.

[8] Schiller, L., 1934, "Neue quantitative versuche zur turbulenzentstehung." *ZAMM-Journal of Applied Mathematics and Mechanics*, Vol. 14, pp. 36-42.

[9] Saffman, P., 1965, "The lift on a small sphere in a slow shear flow." *Journal of Fluid Mechanics*, Vol. 22, pp. 385-400.

[10] Dandy, D. S., Dwyer, H.A., 1990, "A sphere in shear flow at finite Reynolds number: Effect of shear on particle lift, drag, and heat transfer." *Journal of Fluid Mechanics*, Vol. 216, pp. 381-410.

[11] Stokes, G. G., 1851, "On the effect of the internal friction of fluids on the motion of pendulums." *Transaction of the Cambridge Philosophical Society*, Vol. 9, pp. 8-106.

[12] Rice, H. P., 2013, "Transport and deposition behaviour of model slurries in closed pipe flow." *PhD Thesis, University of Leeds*.

[13] Fairweather, M., Yao, J., 2009, "Mechanisms of particle dispersion in a turbulent, square duct flow." *AIChE Journal*, Vol. 55, pp.1667-1679.

[14] El Khoury, G. S., 2013, "Direct numerical simulation of turbulent pipe flow at moderately high Reynolds numbers." *Flow Turbulence and Combustion*, Vol. 91, pp. 475-495.

[15] Singh, J., Rudman, M., Blackburn, H.M., 2018, "Reynolds number effects in pipe flow turbulence of generalized Newtonian fluids." *Physical Review Fluids*, Vol. 3, 094607.

[16] Vreman, A. W., 2007, "Turbulence characteristics of particle-laden pipe flow." *Journal of Fluid Mechanics*, Vol. 584, pp. 235-279.

Conference on Modelling Fluid Flow (CMFF'22)
The 18th International Conference on Fluid Flow Technologies
Budapest, Hungary, August 30 -September 2, 2022

ARTIFICIAL INTELLIGENT ENHANCED VIRTUAL BLADE MODEL

Gábor ZIPSZER[1], Szilárd VARRÓ[2], Bence DARÁZS[3], Mátyás GYÖNGYÖSI[4], Ákos HORVÁTH[5]

[1] Corresponding Author. eCon Engineering Kft., 4th floor, Kondorosi út 3., H-1116 Budapest, Hungary. Tel.: +36-1-279-0320, E-mail: gabor.zipszer@econengineering.com
[2] Infominero Kft. E-mail: szilard.varro@hiflylabs.com
[3] eCon Engineering Kft. E-mail: bence.darazs@econengineering.com
[4] eCon Engineering Kft. E-mail: matyas.gyongyosi@econengineering.com
[5] eCon Engineering Kft. E-mail: akos.horvath@econengineering.com

ABSTRACT

The Consortium of eCon Engineering Kft. and Infominero Kft. is developing a Virtual Blade Model (VBM) enhanced by Artificial Intelligence (AI) driven three-dimensional (3D) aerodynamic corrections to be applied in airframe-propeller interaction simulations.

The aim of the paper is to demonstrate the novel concept of improving conventional VBM capabilities regardless of propeller blade geometry or operating conditions.

A conventional VBM based on blade element theory was implemented in ANSYS Fluent via User Defined Function (UDF) carrying out the derivation of spanwise aerodynamic load distributions of the propeller blade using inviscid 2D profile data. This conventional VBM was enhanced by applying 3D aerodynamic corrections determined by a stand-alone AI algorithm linked with the Fluent UDF via Python scripts. The required training data for the AI model was derived from explicit 3D propeller blade Computational Fluid Dynamics (CFD) simulations.

The AI enhanced 3D corrected VBM (3D-VBM) shows improvements in overall propeller thrust and torque predictions compared to the baseline VBM (2D-VBM) using only two-dimensional (2D) airfoil data. Furthermore, the radial distribution of blade loading, hence the velocity and pressure profiles behind the propeller plane are in better agreement with the averaged explicit solution when the 3D-VBM is used.

Keywords: artificial intelligence, AI, virtual blade model, VBM, 3D-VBM

NOMENCLATURE

A_{cell}	$[m^2]$	cell area
B	[-]	number of blades
C	$[m]$	chord length
F	$[N]$	force
$\underline{F}$	$[N]$	force vector
$F_{Glauert}$	[-]	Prandtl-Glauert tip loss factor
L	[-]	Huber loss function
$\underline{S_U}$	$[N/m^3]$	volumetric momentum source term
T	$[K]$	temperature
V	$[m/s]$	flight speed
V_{cell}	$[m^3]$	cell volume
c	[-]	force coefficient
f	$[N/m]$	force distribution
n	$[rpm]$	propeller speed of rotation
p	$[Pa]$	pressure
r	$[m]$	radius
r_{rel}	[-]	relative radius
δr	[m]	elemental radius
v	$[m/s]$	absolute velocity magnitude
w	$[m/s]$	relative velocity magnitude
θ	$[deg]$	blade pitch angle
$\delta\Psi$	$[deg]$	elemental azimuth angle
α	$[deg]$	angle of attack
β	$[deg]$	blade element angle
γ	$[deg]$	blade twist
ξ	[-]	AI model function
ρ	$[kg/m^3]$	air density
φ	$[deg]$	relative velocity angle
ω	$[rad/s]$	speed of rotation

Subscripts and Superscripts

hub	propeller hub or spinner
l, d	lift, drag
n, i	n-th or i-th in a sequence
prop	propeller
s	static
tan	tangential
tot	total
a, n, t, r	VBM cylindrical axes: axial or normal, tangential and radial
x, y, z	global cartesian axes: x, y and z
'	corrected

1. INTRODUCTION

The necessity to analyse propeller blade aerodynamics was born with the initial attempts of powered flight. It is known that the Wright Brothers designed the propeller blades for propelling the famous Wright Flyer based on profile data set they gathered from the extensive test campaign conducted within their own wind tunnel [1].

As the science of aerodynamics and its application on aircraft development progressed, the methods for propeller performance analysis developed as well providing better understanding of propeller induced flow-field and its possible effects on flight performance and control.

Nowadays, when aircraft developers need to achieve a wide variety of technical criteria and continuous performance gain is demanded by the market, there is an increasing need to account for propeller induced flow effects even in the case of small and medium size aircraft. Being aware of the propeller induced flow field from the beginning of the design process could save significant time and cost later in the optimisation and prototyping stages. Also, it can ensure improved product performance which is sought for by many aircraft developers.

Using CFD models including explicit propeller blades comes with high costs, therefore it is unaffordable during the initial stages of product development or for detailed design optimisation [2].

The Virtual Blade Model (VBM) with the industrialised Artificial Intelligence (AI) driven 3D correction method (designated as 3D-VBM) developed by the Consortium of eCon Engineering Kft. and Infominero Kft. offers a cost-effective alternative for substituting explicit blade analyses with a 3D corrected VBM providing improved prediction capabilities compared to conventional VBM techniques.

In the following chapters the developed VBM model and the 3D correction method along with the utilised AI model will be discussed, followed by the assessment of the results derived by the explicit blade CFD, conventional and 3D-VBM models.

2. CONVENTIONAL VIRTUAL BLADE MODEL

In the past few years many papers were published discussing different methods of substituting the resource-demanding explicit modelling of propellers or helicopter rotors. The thesis of Bicsák [2] and the work of Stajuda et. al. [3] provide a summary of the papers on the topic.

The simpler methods are based on the axial or the generalised momentum theory, where the propeller is represented by a disc imparting momentum to the flow through it [4] – this disc can be called as the actuator disc and the modelling technique as the Actuator Disc Model (ADM). ADM assumes averaged and constant momentum sources over the disc area.

More detailed methods use blade element theory to derive the momentum source terms based on local flow properties, the geometrical properties of the modelled propeller blade and the lift and drag coefficients of the actual airfoil section. This model can be called as Virtual Blade Model where the source terms are derived for each computational cell or node over the entire VBM sub-domain [5].

Some VBM assumes constant propeller loading around the azimuth at a given radii and apply the same radial blade load distribution over the whole VBM domain. While an enhanced VBM calculates the azimuthal load variation as well, hence providing a better approximation of the propeller or rotor load distribution and the induced flow-field.

It must be noted that in many papers the ADM and VBM acronyms and naming conventions are mixed regardless of the theory actually applied. In this paper ADM refers to the models using axial or generalised momentum theory, while VBM refers to the models applying blade element theory.

Usually, ADM and VBM models are designed to be used in steady-state CFD problems assuming that the time-averaged transient flow induced by the passing blades of a propeller or rotor eventually results in a steady-state flow-field, which can be modelled by a steady-state ADM or VBM. There are VBM and Actuator Line Model (ALM) methods which are designed to be used in unsteady CFD problems [6, 7]. The 2D-VBM and 3D-VBM presented in this paper are valid only for steady-state problems.

2.1. Applied 2D-VBM

The baseline 2D-VBM was implemented as a UDF within ANSYS Fluent finite volume CFD solver using blade element theory and the required aerodynamic and geometric parameters of the simulated propeller and its blades in the process of source term calculation.

The VBM domain built up from hexahedral elements with one-cell thickness. The VBM domain resolution – the number of cells in radial and azimuthal direction – can be adjusted, but must be evenly distributed azimuthally. The applied resolution provided smooth variable distributions behind the disc with a low cell count. The volume mesh around the VBM domain and the interfaces can be any type supported by Fluent.

In order to account for both radial and azimuthal variation of the flow field and to enable source term derivation for each cell accordingly we followed the method described by Wahono [5] to set up the core of the VBM UDF excluding the special treatment required for helicopter rotors and any of the built-in iterative routines. Blade pitch and propeller rpm changes can be carried out manually while calculated thrust and torque can be monitored within Fluent Graphical User Interface (GUI) along with many other parameters used by the VBM algorithm. As

User Defined Memory is allocated for each VBM parameter, those can be accessed during or after the simulations for monitoring or post-processing as required.

As a first step the local flow-field is solved by Fluent and the magnitude of fluid velocity components (v_x, v_y, v_z) are extracted for each cell within the VBM domain. As the VBM domain can be positioned and oriented freely in 3D space, the magnitudes of global velocity components are transformed to the VBM local cylindrical coordinate-system, resulting in axial (v_a), tangential (v_t) and radial (v_r) component magnitudes. This can be done as the positioning and orientation of the VBM domain are known.

The UDF was developed to allow any number of VBM domains to be used within the same Fluent simulation. Each of them can be freely positioned and oriented, the only restriction is that none of the VBM domains can intersect each other or non-fluid regions.

The geometric properties of the propeller and the blades with the operating parameters are defined in a single text file for each VBM domain. These parameters are the followings: speed of rotation (n), number of blades (B), hub and propeller radii (r_{hub}, r_{prop}), blade pitch angle (θ), the distribution of blade chord (C) and twist (γ). Also, the two-dimensional lift (c_l) and drag (c_d) coefficients of dedicated blade sections are stored in input files as a function of radii and local Mach or Reynolds number. c_l and c_d values at specific radii are derived by linear interpolation based on actual blade element radii, Angle of Attack (AoA or α) and Mach number or Reynolds number as specified by the User.

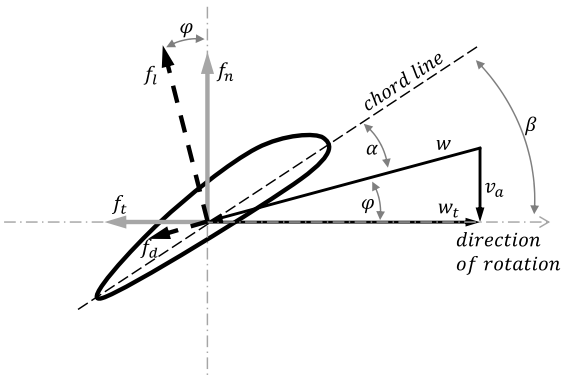

Figure 1. Velocity triangle of a blade element

A typical velocity triangle is depicted in Figure 1. As it is shown in Eqs. (1) to (3) the relative sectional velocity magnitude (w) and its angle relative to the direction of rotation (φ) can be derived from the magnitude of axial and tangential components of the local flow velocity (v_a, v_t,), the propeller speed of rotation (n) and the radii of the actual blade element – which in our case is equal to the distance of the cell centroid (r) measured from the VBM axis.

$$w_t = \omega r + v_t = 2\pi\frac{n}{60}r + v_t \tag{1}$$

$$w = \sqrt{{w_t}^2 + {v_a}^2} \tag{2}$$

$$\varphi = \tan^{-1}\frac{v_a}{w_t} \tag{3}$$

Since the flow-field velocity components are determined from the CFD solution, there is no need to account for any propeller induced velocity components during the calculation process. This induced effect will be implicitly accounted for as the iterative CFD solution progresses.

From the angle φ derived in Eq. (3) and the geometrical properties (θ and γ) the actual AoA (α) for the blade element can be calculated by Eq. (4) following by the calculation of sectional normal and tangential forces for unit span acting on the blade element as given in Eqs. (5) to (6) using the interpolated sectional 2D lift (c_l) and drag (c_d) coefficients. Note, that the effect of radial flow is neglected in the applied model. The compressibility effect or the effect of Reynolds number can be accounted for by using the proper interpolation scheme during the derivation of c_l and c_d.

$$\alpha = \beta - \varphi = \theta + \gamma - \varphi \tag{4}$$

$$f_n = \frac{\rho}{2}w^2 C(c_\mathrm{l}\cos\varphi - c_\mathrm{d}\sin\varphi) \tag{5}$$

$$f_t = \frac{\rho}{2}w^2 C(c_\mathrm{l}\sin\varphi + c_\mathrm{d}\cos\varphi) \tag{6}$$

The calculation described above needs to be carried out for each cell within the VBM domain, using the cell-centroid to determine sectional radii.

Before we can derive the actual source terms for each cell, we need to calculate the magnitudes of the averaged force components induced by the rotating blades at each cell. Based on the work of Wahono [5] we can use the ratio of the mid-cell arc length ($r\,\delta\Psi$) and the distance travelled by the blade element over one revolution ($2\pi r$). Using this arc-length ratio, we can calculate the force magnitudes acting on the fluid volume of a given cell as it is given by Eq. (7) which can be simplified by the expression of cell area in Eq. (8), leading to Eq. (9). This reduction can be utilised for the tangential force component in Eq. (10) as well. Eqs. (9) to (10) were utilised in the VBM UDF.

$$F_n = B \cdot f_n \cdot dr \cdot \frac{r\delta\Psi}{2\pi r} \tag{7}$$

$$A_{cell} = dr \cdot r\,\delta\Psi \tag{8}$$

$$F_n = \frac{B}{2\pi} \cdot f_n \cdot \frac{A_{cell}}{r} \tag{9}$$

$$F_t = \frac{B}{2\pi} \cdot f_t \cdot \frac{A_{cell}}{r} \quad (10)$$

Knowing F_n, F_t and assuming that $F_r = 0$ in the VBM domain cylindrical system allows us to transfer the blade element force components into the absolute cartesian frame of reference ($\underline{F} = [F_x, F_y, F_z]$). As a final step dividing the blade element force vector ($\underline{F}$) by the cell volume (V_{cell}) we can derive the volumetric momentum source term ($\underline{S_U}$) for each cell within the VBM domain, as it is shown in Eq. (11).

$$\underline{S_U} = \frac{1}{V_{cell}} \times \underline{F} \quad (11)$$

2.2. Corrections for Tip-loss

Real flows around rotating propeller blades or rotors are actually complex 3D flows. On the other hand, the implemented 2D-VBM uses 2D profile data. Most of the VBMs, and other analytical methods like Blade Element Momentum theory (BEM) are facing with this problem. Many correction methods have been studied and applied – some with limited, some with greater success [2-6] and [8].

Probably the most common correction method was derived by Prandtl which is assessed in details by Ramdin [8]. Prandtl's method was derived using vortex theory. Fundamentally it is a correction to account for the fact that propellers and rotors have a finite number of blades – correcting the assumption of infinite number of blades applied in ADM and VBM methods. Finite number of finite-span blades forcing the bounding vortex to change rapidly near blade tip, hence reducing lift generation down to zero at the end of the blade [2, 4, 8]. Prandtl derived a correction factor which is the function of the radial position, the blade radii and the distance between two helical wake sheets. The applied 2D-VBM model described in this paper can utilise the Prandtl-Glauert tip loss factor ($F_{Glauert}$) specified in Eq. (12) and the corrected c_l' value from Eq. (13) as it is given in [8].

$$F_{Glauert} = \frac{2}{\pi} \cos^{-1}\left[e^{-\frac{B}{2}\frac{r_{prop}-r}{r_{prop}}\frac{1}{\sin\varphi}}\right] \quad (12)$$

$$c_l' = F_{Glauert}\, c_l \quad (13)$$

In Eq. (13) c_l' is the corrected lift coefficient. We can apply the Prandtl-Glauert correction factor directly to the lift coefficient as there is a linear relationship between the circulation strength and the resultant lift.

3. 3D-VBM

As it can be seen in the previous chapters, all of the ADM, VBM or BEM methods are built on the assumption of infinite number of blades with infinite span, also not accounting for secondary radial flows, however these are clearly non-physical assumptions [8]. Several correction methods exist, like the Prandtl-Glauter tip loss factor which was implemented in our baseline 2D-VBM, but none of these corrections are capable to account for all phenomena which forms the complex 3D flow pattern around rotating blades. Furthermore, most corrections are valid only for a limited geometric and operational parameter range.

The main objective of the consortium working on the KFI-112 tender project was to develop a novel method to account for as many aerodynamic effects as possible regardless of blade geometries or operating conditions.

After the evaluation of fundamentally different concepts, the utilisation of the emerging field of AI was selected as the pillar of the new methodology.

3.1 Process flow

The basic concept is that a trained AI model can predict the behaviour of complex 3D flow phenomena and its effects on the parameters of interest.

In our case it means that using 2D airfoil data – such as c_l and c_d which could be derived from simple inviscid calculations – the AI can predict spanwise force distributions of rotating blades matching explicit 3D CFD results. If the explicit 3D CFD model is validated, we can assume that the AI predicted distributions will closely resemble real case.

The Fluent embedded 3D-VBM process consists of the following five steps:

1. Derivation of local flow parameters (CFD, Fluent)
2. Derivation of AI input dataset (VBM)
3. Derivation of 3D corrected dataset (AI)
4. Derivation of momentum source terms from the 3D corrected dataset (VBM)
5. Update flow field (CFD, Fluent)

The focus was to develop an AI training process required for the 3D-VBM applicable for a given propeller under variable flight conditions – the geometric parameters are kept constant, leaving only the operating parameters to vary. The goal was to make this process applicable for any type of propeller or rotor.

3.2. Generation of the Training Dataset

To train the AI model we need to provide the input dataset and the training dataset which is the desired output for a given input dataset.

The input dataset consists of general operating parameters (flight speed, speed of rotation, blade pitch etc.), propeller performance metrics (overall thrust, torque etc.) and the radial distribution of key parameters (helical Mach number, uncorrected

normal and tangential force etc.). This input dataset is generated by the baseline 2D-VBM using 2D inviscid airfoil data.

The training dataset was the spanwise distributions of normal and tangential forces derived by explicit 3D CFD analyses of the given propeller at different operating conditions. As we considered the explicit 3D CFD results as the reference its validity does not affect the AI training processes and derived corrections, hence it is capable to demonstrate the 3D-VBM method. The discussion of the explicit CFD model is out of the scope of this paper.

3.1. The Artificial Intelligence Model

For the AI model both the input and training data sets were structured into classical tabular (matrix) format.

The input features from the 2D-VBM and the target 3D CFD variables are multidimensional because they are treated as distributions rather than single points. In order to predict a distribution or certain points of a distribution the usage of specific data structures or models are necessary.

Based on practical consideration for the later engineering models, only a sample of points are needed from these distributions as features and as target variables. In the AI models the spanwise distributions were split into discrete points (radial sections). Predictions and the correction model were applied exclusively to these points. The mentioned split means that specific model families should be used which could handle multi response variables, however, these models would be too rigid, because they assume a fixed input/output data structure.

In order to preserve flexibility a work-around was applied combining distribution-like values as section-dependent parameters with other fixed parameters. With this method the correctional model was built successfully as defined in Eq. (14):

$$\xi(x_{i,1}, x_{i,2}, \dots, x_{i,n-1}(s), x_{i,n}(s)) = y_i(s) \tag{14}$$

where, "ξ" represents the AI model, the "$x_{i,n}$" the n-th feature i-th observation, "$x(s)$" and "$y(s)$" are distributional independent and dependent variables, where parameter "s" denotes the section.

Simpler models were tried out first such as linear regression with feature engineering, tree-based methods (e.g., random forest, boosted decision trees), and also explorative analysis and visualisation methods so that we could treat non-linear effects.

The problem could not be modelled precisely and we could not deduct any useful insights with these simpler approaches; presumably because all of the applied variables were of importance in the evaluation of the outcome in such a non-trivial way which these models were not able to unveil adequately.

Finally, the application of a neural network model was decided, which turned out to serve us with trustworthy predictions using a relatively small set of data. Throughout the creation of the neural network, we aspired to create the simplest and smallest architecture to avoid over-fitting.

The final neural network was a simple multi-layer, feedforward network. The hyper-parameter tuning was made using grid-search, the optimised hyper-parameters were the number of neurons, number of layers, activation function, drop-out ratio and other regularisation parameters.

For the activation function a rectified linear unit was used. The most stable and accurate model was a two-layer structure with 200-200 fully-connected dense neurons. By further increase the number of neurons or the number of layers, the model accuracy was not improved and over-fitting became more significant. To overcome the over-fitting phenomenon, several regularisation techniques were tried out, but none of them seemed efficient without decreasing accuracy. By choosing an optimal loss function the model stabilised after all. The Huber loss function as it defined in Eq. (15) was used, known from robust regression models.

$$L = \begin{cases} \frac{1}{2}\|\xi - y\|_2^2 & if \ \ \|\xi - y\|_1 \leq \delta \\ \|\xi - y\|_1 - \frac{1}{2} & \text{otherwise} \end{cases} \tag{15}$$

For training and testing purposes there were 214 independent observations in total. By varying the distributional section parameters – 20 sections used – we got 4280 partly interdependent observations. The data was split into training and testing parts, based on a unique identifier of the independent observations.

Usage of 60% percent of the data set was sufficient for training, but with larger training size the accuracy and the generalisation capability improved significantly. A test dataset was used only after the training and hyper-parameter optimization phase. During the training and optimization procedure a 4-fold cross-validation technique was applied for monitoring the model stability and performance.

The mean absolute percentage error was 15.45% on average in cross-validation with standard deviation of 0.98 and was 14.2% on the test set.

4. RESULT ASSESSMENT

In the following sections the results derived by the different models will be compared. The reference model is the explicit 3D CFD data which is designated as "Exp.". The baseline 2D-VBM data is designated as "2D" while the tip-loss corrected 2D-

VBM data applying the Prandtl-Glauert correction is designated as "2Dcor". Here the 2D refers to the fact that inviscid 2D airfoil data is used. The data derived using the 3D-VBM model is designated as "3D" referring to the applied AI predicted 3D aerodynamic corrections.

For a better comparison both the Exp. and the VBM model domains were built-up having a constant diameter tube along the rotational axis ranging from the inlet up to the outlet functioning as an infinite constant hub. For each case free-slip wall condition was applied on the surface of this hub.

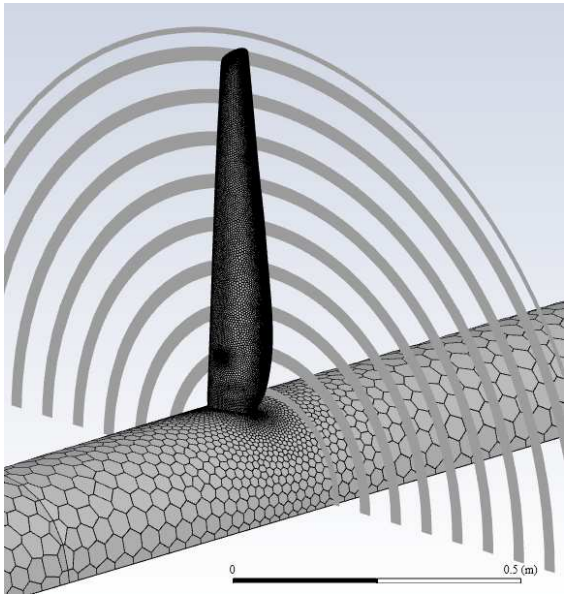

Figure 2. Explicit blade

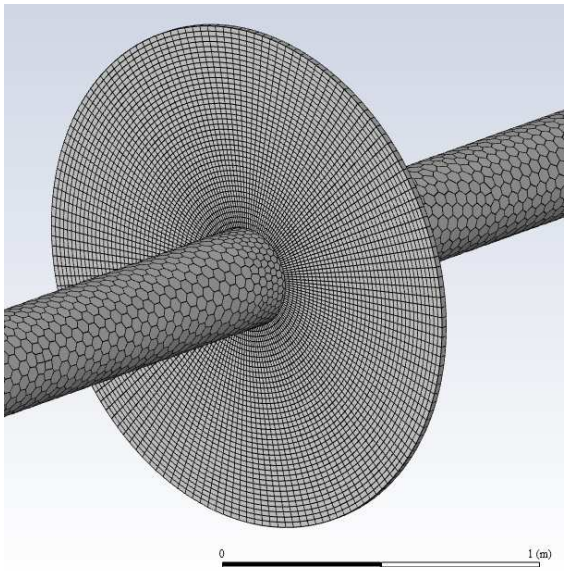

Figure 3. VBM disc

Both the Exp. and VBM CFD domain were built in Fluent Mesher applying poly-hexcore volume mesh with similar volume mesh resolution ensuring better comparability of flow quantities behind the blade and VBM disc. The surface mesh of the explicit blade is depicted in Figure 2 highlighting some of the iso-clip surfaces at 0.1 meter behind the propeller plane used for flow-field evaluation. Figure 3 depicts the structured mesh of the VBM disc and the poly surface mesh of the hub.

The same Fluent solver settings were applied for each model, using the coupled scheme with 2nd order spatial discretization of momentum and pressure, and 1st order upwind for the equations of the applied k-ω SST turbulence model. For the VBM models constant air density was used, while in the explicit 3D CFD model air density was derived using the ideal-gas state equation.

The study was carried out using the CAD model derived by 3D optical scanning technique of an existing propeller blade. The propeller has two blades with a radius of 0.81 meter. The geometric properties and the aerofoil sections were derived from the CAD model. Lift and drag coefficients – which were the basis of all VBM simulations – were derived using XFoil v6.99 (Copyright 2000 Mark Drela and Harold Yougen) assuming inviscid flow, but accounting for the possible variation of local Mach number.

Two different cases are assessed in this paper. The operating conditions for these cases are summarised in Table 1. For each case constant air density were assumed.

Table 1. Operating conditions

Case	*V [m/s]*	*n [rpm]*	*θ [deg]*
Case#1	20	3117	20.0
Case#2	48	2275	39.9

The resulted propeller thrust and torque values for each model are summarized in Table 2 and Table 3 for Case#1 and Case#2, respectively.

Table 2. Case#1 Propeller thrust and torque

Case#1	Thrust [*N*]	Torque [*Nm*]
Exp.	896	98
2D	1189	117
2Dcor.	1068	103
3D	892	96

Table 3. Case#2 Propeller thrust and torque

Case#2	Thrust [*N*]	Torque [*Nm*]
Exp.	1065	275
2D	1753	436
2Dcor.	1188	280
3D	1064	278

As it can be seen from Table 2 and Table 3 both 2D and 2Dcor. show significant deviation from the reference values, while the 3D-VBM propeller thrust and torque agrees very well with the explicit CFD solution. It should be noted that the reference explicit CFD model differs from the one used to generate the AI model training dataset showing the robustness of the 3D correction process.

4.1. Blade load distributions

The spanwise normal force distribution (f_n) was derived from the explicit solutions and compared with the VBM calculated distributions.

It can be concluded from Figure 4 and Figure 5 that the spanwise normal force distributions predicted by the 3D-VBM are in much better agreement with the Exp. results compared to the 2D-VBM and show better agreement than the 2Dcor results, although the 2Dcor. distributions show improved match than the uncorrected 2D-VBM, as it was expected. Similar trends were observed for the tangential force distributions as well.

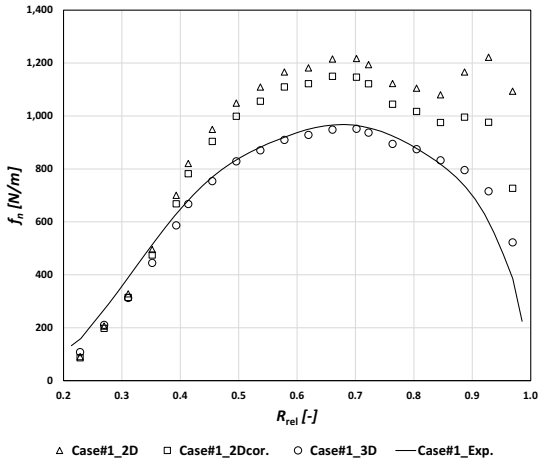

Figure 4. Normal force distributions for Case#1

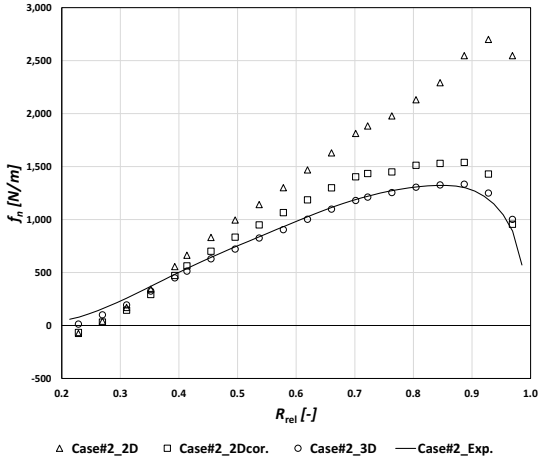

Figure 5. Normal force distributions for Case#2

4.2. Flow-field comparison

An important aspect of comparing different VBM techniques and their accuracy is the flow field assessment downstream the VBM disc and the explicit propeller. Ultimately the purpose of the VBM techniques is the capability to model the propeller induced flow field.

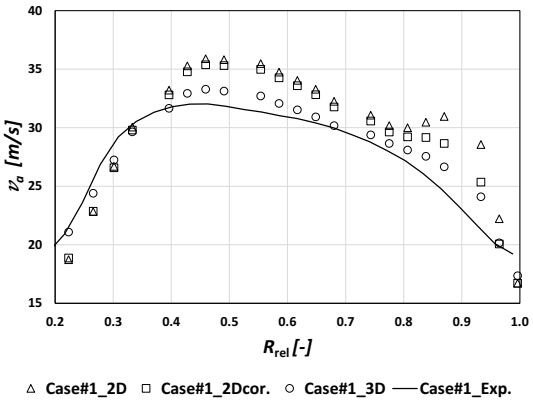

Figure 6. Axial velocity distribution for Case#1

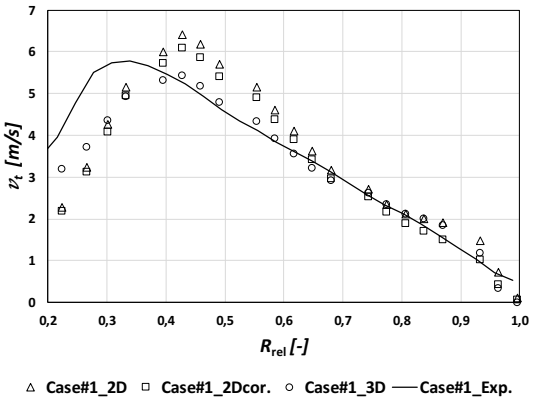

Figure 7. Tangential velocity distribution for Case#1

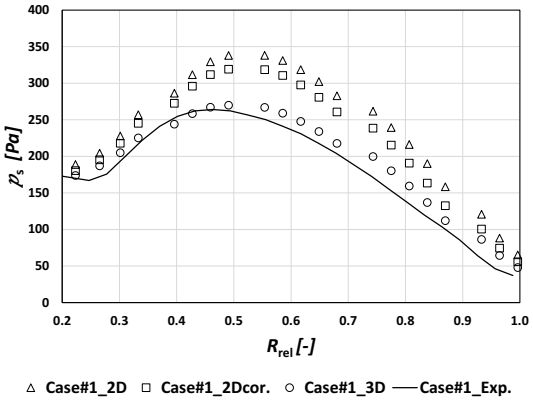

Figure 8. Relative static pressure distribution for Case#1

For this comparison we defined sampling points along a line positioned 0.1 meter behind the VBM disc, where the axial and tangential velocity components and relative static pressure values of the flow were sampled. In order to make it comparable with the VBM results, for the explicit model circumferential surface strips normal to the rotational axis were used, as depicted in Figure 2, to derive the area-averaged values of the investigated parameters. The axial and tangential velocity and relative static pressure distributions are depicted in Figure (6) to (9).

For all depicted distributions the best match with Exp. results were achieved using the 3D-VBM. 2D-VBM shows significant deviations. The 2Dcor. model using the Prandtl-Glauert correction improves the baseline 2D-VBM performance, but still, it is surpassed by the 3D-VBM.

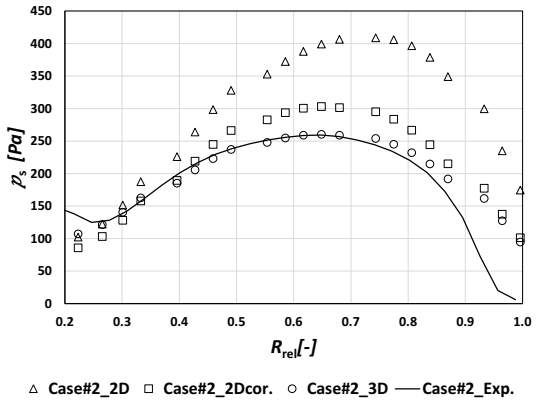

Figure 9. Relative static pressure distribution for Case#2

5. CONCLUSIONS

A new, novel approach for Virtual Blade Model correction was discussed and its superiority over conventional VBM techniques was demonstrated for an existing two bladed general aviation propeller at two operating conditions. It was shown that the propeller performance prediction, spanwise load and flow-field parameter distributions of the explicit CFD model can be matched with improved accuracy by the utilisation of the in-house developed 3D-VBM.

Our aim is to extend the capabilities of the 3D-VBM technique for operating conditions with high rotor inflow angles making the 3D-VBM applicable for the aerodynamic assessment of drones and aircraft with multiple rotors.

ACKNOWLEDGEMENTS

This work has been supported by the Hungarian Government through the NKFI Fund under contract No. 2018-1.2.2-KFI-2018-00057.

REFERENCES

[1] Crouch, Tom D., 2021, "Wright brothers". Encyclopedia Britannica, https://www.britannica.com/biography/Wright-brothers. Accessed 24 January 2022.

[2] Bicsák, Gy, 2017, “Cost Efficient Solutions for Small Aircraft Development Processes Using Numerical Modelling Tools”, *Dissertation Budapest University of Technology and Economics Faculty of Transportation Engineering and Vehicle Engineering Department of Aeronautics, Naval Architecture and Railway Vehicles*, Budapest, Hungary.

[3] Stajuda, M, 2018, “Modified Virtual Blade Method for Propeller Modelling”, *Mechanics and Mechanical Engineering*, Vol. 22, No. 2 (2018) 603-617.

[4] Smith, R. H., 2015, “Engineering Models of Aircraft Propellers at Incidence”, *Dissertation Aerospace Sciences Research Division, School of Engineering, College of Science and Engineering, University of Glasgow,* Glasgow, United Kingdom

[5] Wahono, S., 2013, “Development of Virtual Blade Model for Modelling Helicopter Rotor Downwash in OpenFOAM”, *Aerospace Division, Defence Science and Technology Organisation, Department of Defence, Australian Government,* DSTO-TR-2931

[6] L Wang, Q., Jiang, Z. and Zhang Q., 2014, “Regionalized Actuator Disk Model Designed by Optimisation Method for Propeller Slipstream Computation”, *Engineering Application of Computational Fluid Mechanics*, Vol. 8, pp. 127-139.

[7] Wimshurst, A. and Willden, R., “Validation of an Actuator Line Method for Tidal Turbine Rotors”, Proc. *Department of Engineering Science*, *University of Oxford*, Oxford, United Kingdom.

[8] Ramdin, S. F., 2017, “Prandtl tip loss factor assessed”, *Dissertation Faculty of Aerospace Engineering, Delft University of Technology*, Delft, Netherlands

Conference on Modelling Fluid Flow (CMFF'22)
The 18th International Conference on Fluid Flow Technologies
Budapest, Hungary, August 30 -September 2, 2022

CFD ASSESSMENT OF AN ULTRALIGHT AIRCRAFT INCLUDING IN-FLIGHT TEST DATA COMPARISON

Gábor ZIPSZER[1], Bence DARÁZS[2], Ákos HORVÁTH[2], Dávid TOMA[2], Dániel LAKI[2], Mátyás GYÖNGYÖSI[2], Jenő Miklós SUDA[3], Márton KOREN[3], Balázs FARKAS[3]

[1] Corresponding Author. eCon Engineering Kft., H-1116 Budapest, Kondorosi út 3. 4th floor; e-mail: gabor.zipszer@econengineering.com
[2] eCon Engineering Kft., H-1116 Budapest, Kondorosi út 3. 4th floor, +36-1-279-0320
[3] Department of Fluid Mechanics, Faculty of Mechanical Engineering, Budapest University of Technology and Economics (BME), H-1111 Budapest, Bertalan Lajos utca 4-6. Hungary

ABSTRACT

In summer 2021, an in-flight test campaign was performed on an ultralight aircraft mapping the pressure distribution over its surfaces and surrounding. The measurement system was developed and calibrated at the Department of Fluid Mechanics of BME (BME-ARA) is described in more detail. The measured data served as the reference for the evaluation of the aircraft CFD simulations.

The CFD model considers the entire external geometry of the aircraft accounting for the effect of propeller induced flow field by utilising the 3D corrected Virtual Blade Model specified in Zipszer et al. [1]. The modelling and results are discussed and compared with the in-flight test data.

A derivation of the baseline model was made incorporating a detailed engine bay. The water and oil cooler units were modelled as porous zones with properties derived based on explicit CFD simulations. The assessment of the flow field within the engine bay and the effect of accounting for propeller induced flow is discussed.

Keywords: 3D-VBM, aircraft simulation, CFD, engine bay, in-flight measurement

NOMENCLATURE

AoA	[°]	angle of attack
EAS	[*km/h*]	equivalent air speed
K_0	[-]	compensation factor
$K_{0,H}$	[-]	high compensation factor
$K_{0,L}$	[-]	low compensation factor
TAS	[*km/h*]	true air speed
VBM	[-]	virtual blade model
p_{dyn}	[*Pa*]	measured dynamic pressure
p_M	[*Pa*]	measured static pressure
$p_{M,comp}$	[*Pa*]	compensated static pressure
p_R	[*Pa*]	true static pressure
p_s	[*Pa*]	relative static pressure
p_t	[*Pa*]	relative total pressure
y^+	[-]	dimensionless wall distance

1. INTRODUCTION

Enhancing internal Computation Fluid Dynamics (CFD) toolset is vital to meet the emerging needs and expectations of the general aviation industry. Currently, our focus is at the propeller driven small- and mid-sized aircrafts, to develop methods being capable to account for the propeller induced flow field with higher accuracy [1] and to apply it in steady-state calculations and in multi-objective optimisation tasks. The latter one usually requires fast, robust and accurate simulation methods enabling to perform dozens or even hundreds of simulations within a reasonable time.

Despite the aircraft's engine type – piston-engine or turboprop – the goal is identical: ensure adequate cooling of the engine bay under all circumstances and obtain low overall drag. To fulfil both at the same time, optimised cowls and coolant intake ducts are necessary. Depending on the aircraft design – tractor or pusher configuration, wing- or fuselage mounted engine(s) – the propeller could have a significant effect on cooling; thus, considering it in the models seems to be crucial.

The number of published studies on aircraft engine bay flow field and cooling analyses is limited, but started to increase recently. Balland et al. [2] performed 3D CFD studies in the nacelle core compartment of an aircraft gas turbine engine and compared the results with real engine data. Since 2013 many papers have been published related to the European project called ESPOSA [3]. Many of them focus on thermal analysis of the I-23 aircraft's engine bay, in which the piston-engine was replaced by a

TP100 turboprop engine [4–7]. Stalewski et al. [4] interpret CFD models using virtual blade model (VBM) based on blade element theory (probably without correction of 3D effects), together with parametric shape optimisation method of the engine intake duct and the cowl. Under the same ESPOSA project Buonomo et al. [8] presented the CFD thermal analyses of EM-11 ORKA aircraft's engine nacelle, both considering external and internal flows, but in a separated manner. Olejnik et al. [9] describes detailed CFD analyses of OSA aircraft in pusher configuration both modelling external and internal engine bay flows in the same model utilising an actuator disc with constant pressure jump as substitution of the propeller.

Multiple goals were set for the current research:

1. Validation of the applied CFD method on an aircraft at gliding conditions by comparing results with in-flight test data;
2. Validation of the in-house developed 3D corrected Virtual Blade Model (3D-VBM) [1] in the CFD model of the same aircraft by comparing results with in-flight test data;
3. Assessment of the propeller wash effect on engine bay flow rates and to derive a simplified engine bay model.

To achieve these goals in-flight data acquisition system (Chapter 2), engine bay CFD model (Chapter 3.1) and external aero CFD model of the entire aircraft with 3D-VBM implemented (Chapter 3.3) were developed.

The utilised aircraft was a motor-glider with piston-engine, tractor configuration, called Altus Concept (HA-XDK). It is depicted in Figure 1.

Figure 1. "Altus Concept" motor-glider aircraft

2. IN-FLIGHT MEASUREMENT SYSTEM

The simplified schematic of the data acquisition system (DAQ) is presented in Figure 2. The pressure signal is transmitted via PTFE pneumatic lines from the probes to the transducers. The pressure signals are converted to electric signals by Honeywell analogue pressure transducers. The data acquisition is performed by the National Instruments device controlled by a laptop where the acquired data was stored. The measurements were carried out on 16 channels.

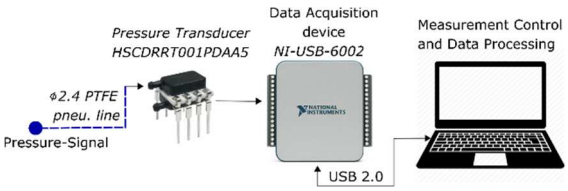

Figure 2. Schematic of the DAQ

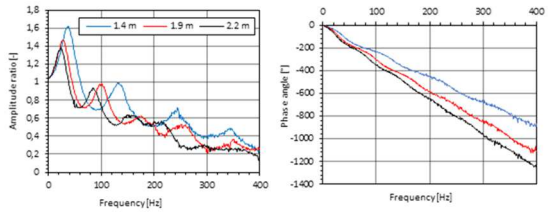

Figure 3. Frequency response curves of the DAQ

The frequency resolution of the DAQ was initially expected to be within the range defined by the blade passing frequency (BPF). The DAQ can acquire data at 6.25 *kS/s* rate, which is adequate within the frequency range of 0-3 *kHz*. A part of the measurement chain was investigated separately to validate if the required frequency resolution was achieved. In order to define the system's frequency response, the pressure tap was placed into an acoustic enclosure. It was excited by a continuous pressure signal provided by a wide frequency range speaker with monotone increased frequency in time [10]. The obtained signal from the transducer was compared to the undisturbed pressure signal which was provided by a precision Endevco 8507C-1 type pressure sensor with 55 *kHz* cut-off frequency. The resulted frequency response curves are plotted in Figure 3 in the case of three different pneumatic line lengths. The lengths of the line sections were defined based on the 3D CAD model of the airframe before the installation of the system on the aircraft. It can be observed that adequate readings can be performed up to 350 *Hz* if the 1.4 *m* long PTFE lines are used.

2.1 Pressure probes

Within the measurement campaign, three different types of pressure probes were used. The reference dynamic and static pressures were measured by a KIMO-TPL-06-800 type Pitot-static probe. During the measurements, the probe was positioned 1 *m* upfront the wing leading edge using a composite boom to provide pressure readings outside the disturbed flow-field by the airframe. The position of the probe was confirmed by preliminary CFD computations.

The total pressure distribution around the airframe was measured by Evolution-Vectoflow Kiel

probes. The probes are manufactured by 3D metal printing and provide an accurate reading within the range of ±60° AoA, which was confirmed by wind tunnel measurements.

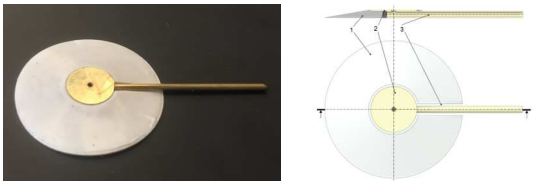

Figure 4. Isolated static pressure probe

The surface static pressure distribution on the airframe was measured by coin type isolated static pressure probes (ISPP) [11] because the airframe itself could not be modified for the purpose of the measurements. It practically meant that the pressure taps could not be mounted flush to the skin of the airframe. Therefore, pressure taps had to be developed which could be mounted to the surface by adhesive. The ISPP can be seen in Figure 4. The tap is built up of three major parts: the moulded silicon fairing (No.1 in Figure 4 b.), the copper disc with the pressure tap orifice (No.2 in Figure 4 b.), and a Ø1.0x Ø1.5 *mm* copper tube (No.3 in Figure 4 b.). The copper tube and the disc are soldered together and are connected to the fairing by an instant adhesive system. The overall height of the pressure tap assembly is ~1.74 *mm*, the outer diameter of the fairing is 30 *mm*, and the diameter of the copper disc is 10 *mm*.

As a result, these ISPP's can be used on almost any surface of the airframe, i.e. they can be easily attached or removed. Although it's practical benefits, this pressure tap needs to be calibrated. Since the pressure tap sticks out from the surface, the measured pressure (p_M) is expected to be lower than the true pressure (p_R) above the surface of the skin of the airplane [12]. The deviation or error caused by the pressure tap was assessed experimentally. The investigated pressure taps were mounted on a flat plate as it can be seen in Figure 5 a. The test setup can be seen in Figure 5 b. as it was installed in the wind tunnel of the Theodore von Kármán Wind Tunnel Laboratory at BME [13]. The horizontally aligned flat plate in Figure 5 b is mounted between two endplates to keep the airflow parallel as the AoA changes. The width of the flat plate is 1 *m* and the length is 0.66 *m* and was equipped with 20 flush mounted pressure tap orifices placed evenly along the longitudinal and lateral midlines. The pressure tap was positioned in the middle of the flat plate and the p_M results were compared to the pressure measured on the empty plate (p_R). The tests were carried out at wind velocities varied between 15–45 *m/s* and AoA's varied from –20° to +10° where positive means leading edge down. The test results are presented in Figure 6. At positive AoA's, the difference between p_R and p_M is low as the isolated pressure tap does not protrude from the thickened boundary layer. At negative AoA's, the difference increases significantly and reaches up to 14% of the dynamic pressure.

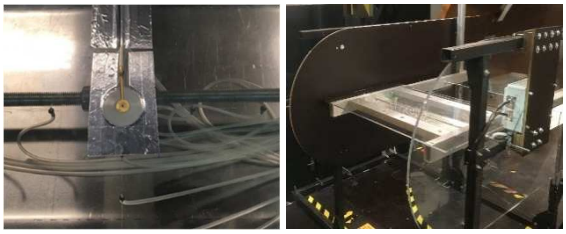

Figure 5. ISPP mounted on the test device

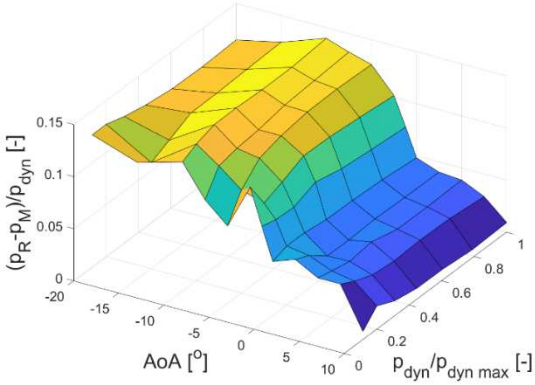

Figure 6. Telative difference between p_M and p_R in the function of the measured p_{dyn} and the AoA

Based on the experimental results the measured pressures can be compensated by using Eq. (1) to reduce the discrepancy between the measured and real pressure.

$$p_{M,comp} = p_M + K_0 p_{dyn} \quad (1)$$

Beside the region presented in Figure 7 the difference between the measured and real pressure (*error*) in function of p_{dyn} and p_M is not monotone, i.e. more than one $error$ value can be assigned to a given pair of p_{dyn} and p_M. Therefore, the definition of the compensation coefficient (K_0) requires further consideration to be taken into account.

In case p_M and p_{dyn} fall in the region presented Figure 7 the measured static pressures (p_M) can be compensated directly with the measured $error$ values.

If the pressure tap is installed into an area where the flow is separated, the results do not have to be compensated since the *error* in this case is expected to be small. The occurrence of flow separation can be confirmed by flow visualisation, e.g. by applying wool tufts.

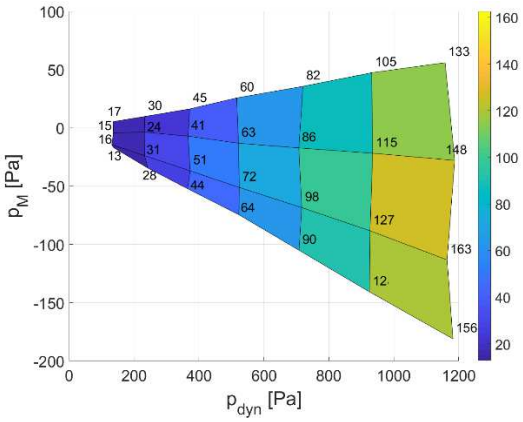

Figure 7. Difference between p_M and p_R (*error*) in the function of p_{dyn} and p_M in the region where direct compensation can be applied

In areas of not fully developed separation or within the bordering region between separated and non-separated regions the K_0=0.05 constant can be applied.

If the given pressure tap is installed into a place, which fell out from the regions described above, then two correction coefficients, $K_{0,H}$=0.1064 and $K_{0,L}$=0.0613 can be applied. In this case, one of the two compensated pressures ($p_{M,comp}$) will fall within the ±30 *Pa* range of the real pressure (p_R). However, based on the only two measured properties, p_{dyn} and p_M, it can be not determined which compensated pressure is the valid one.

If no compensation is applied, the maximum *error* can reach up to 120 *Pa* within the investigated range.

3. CFD MODELS

The CFD modelling approach consisted of two steps:

1. Building and simulating the engine bay internal flow with a portion of the external flow only, together with propeller wash effect using a VBM. The main goal was to determine flow rates through engine cowl openings at different flight conditions.
2. Building and simulating the external aero model of the full aircraft using 3D-VBM with derived engine bay inlet/outlet flow rates.

For both models Ansys Fluent v2020R2 finite volume code was used applying Reynolds-averaged Navier Stokes method in steady-state time frame, together with k-ω SST turbulence model. The solver applied was the pressure based pseudo-transient coupled solver of Fluent, in all cases with second order scheme for pressure and momentum, and first order upwind scheme for turbulence equations.

The working medium was always air at constant density and viscosity at 15°*C*, with operation pressure of 101325 *Pa* (Sea level ISA condition).

3.1 Engine bay model

The engine bay CFD model is depicted in Figure 8. It is a rectangular domain with the aircraft positioned at its second half on the centreline. The aircraft tail and wings' outer sections were outside this domain, as they have negligible influence on flow inside the engine bay. The model is based on the 3D CAD model of the aircraft and parts inside the engine bays. The intakes and exits are depicted in Figure 8 by green and red surfaces, respectively. The CAD model was cleaned in Ansys SpaceClaim. Very small, tight gaps were resolved to decrease cell count and increase mesh quality, but the smallest modelled feature is still in the range of few millimetres. The propeller was substituted using a 1626 *mm* diameter and one-cell thick (20 *mm*) VBM disc constructed from structured hexahedral elements.

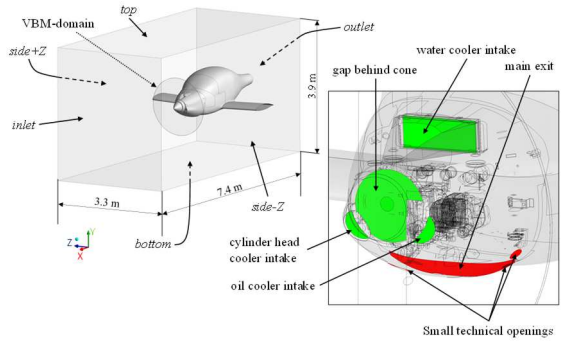

Figure 8. Engine bay CFD model overview

The water and oil coolers were substituted with equivalent porous media, which parameters were determined in separate pre-studies. For that purpose, representative section of each cooler was isolated and simulated to obtain pressure loss characteristics, and the viscous and inertial resistance parameters. It was assumed that these parameters are 1000 times larger in transverse than in streamwise direction.

Usually, for such complex CAD models the fault tolerant meshing workflow (wrapping) is adequate and straightforward to apply, but it could trim features of interest, therefore, the so-called watertight meshing workflow was used instead. The surface mesh minimum and maximum cell sizes were 0.8 *mm* and 200 *mm*, respectively. The volume mesh was poly-hexcore type with 3 boundary layers at walls, both at internal and external surfaces. This resolution at EAS 122 *km/h* flight speed results in y^+≈8 at engine bay internal surfaces, y^+≈60 at engine cowl outer surface, and y^+≈200 at wings and fuselage. The resulting final mesh consisted of 51.7 million nodes and 15.4 million cells. The surface mesh on engine bay internals and the volume mesh in a cross-section view are shown in Figure 9 and Figure 10, respectively.

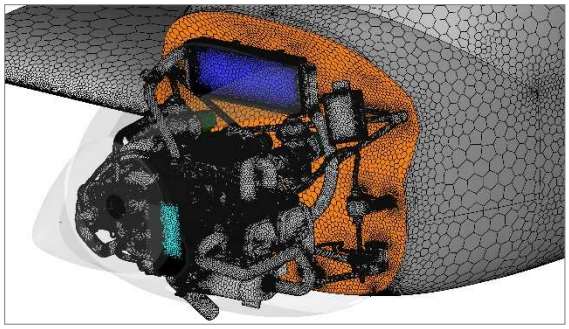

Figure 9. Engine bay surface mesh

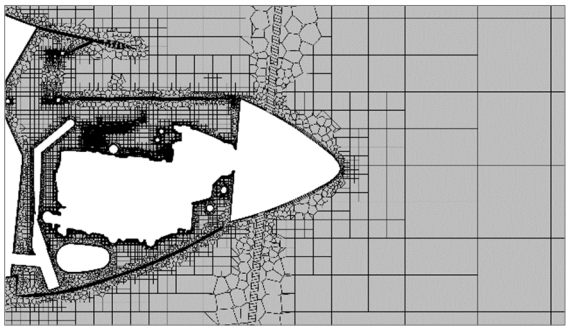

Figure 10. Engine bay volume mesh

The following boundary conditions were applied:

- *inlet*, *side-Z, side+Z, top* and *bottom* surfaces: velocity inlet with x- and y-component according to AoA and flight speed. The turbulent intensity and viscosity ratio were set to 1% and 1, respectively.
- *outlet* surface: pressure outlet with 0 *Pa* average gauge pressure;
- *engine intake filters* (left and right): mass flow rate outlet boundary condition with 0.03762 *kg/s*, each, independently of flight speed;
- *exhaust gas pipe*: mass flow inlet with 0.080232 *kg/s* (fuel + air mass flow rate);
- all physical walls were defined as hydraulically smooth *wall* with no slip boundary condition.

The VBM applied in these simulations was the 2D-VBM specified in Zipszer et al. [1], since at the time of these simulations the 3D correction method was not finalised yet. However, the 2D-VBM was considered sufficient for our purposes since the engine cowl openings are located at lower diameters where 3D effect expected to be less influential. VBM inputs were given as specified in [1].

In total 12 cases were simulated: cruise, take-off and gliding conditions, each at 4 different flight speeds ranging from EAS 94.7 *km/h* to 169.6 *km/h*. The AoA ranged from ≈0° to ≈8.5°, accordingly. The difference between cruise and take-off conditions was the propeller blade pitch with a difference of 3.8°. In glide the VBM was switched off.

The simulations ran until convergence of residuals and monitored flow rates (usually around 50 iterations), and afterwards for additional 500 iterations with *steady statistics* option switched on to obtain iteration-averaged flow field and quantities. Stronger oscillations were observed at higher AoA, particularly in water cooler inlet flow rate.

3.2 Engine bay results

During postprocessing the focus was on the engine bay openings' mass flow rates. In Figure 11 the calculated mass flow rates through the intakes (water cooler, oil cooler, cylinder head cooler and gap behind cone) are depicted in function of AoA for the three flight conditions. As it can be seen, at take-off and cruise conditions the mass flow rates are very similar. In gliding they are a bit different, particularly through the gap behind the cone.

At low AoA (<2°) the water cooler's flow rate is the largest, but decreases fast with increasing AoA, and it becomes ≈0 *kg/s* at AoA≈8°. This is in line with experience: on hot days climbing can be limited due to coolant temperature rise. The running propeller increases the flow rate by 12-18%, but at high AoA it can barely compensate the losses.

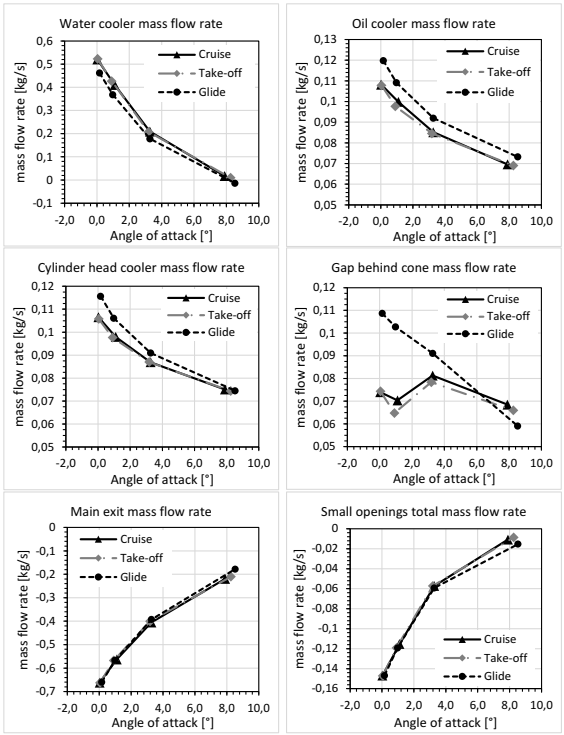

Figure 11. Engine bay openings' mass flow rates

The oil cooler and cylinder head cooler intake ducts' mass flow rates are very similar, particularly at glide condition (±2%). Both are much less sensitive to AoA, and interestingly the propeller wash decreases their flow rate by 6-10%.

The mass flow rate through the gap behind the propeller cone in glide is similar to that of the oil- or cylinder head cooler, but in cruise and take-off it is more like a constant value of 0.073 *kg/s* and 0.07 *kg/s*, respectively.

The hot air can exit the engine bay either through its main exit face or through any of the small technical openings (ring face around exhaust pipe and two technical holes). One can observe that 82-95% of the total flow exits through the main exit, with larger portions at higher AoA. The propeller wash barely affects this ratio.

In order to be able to run fuselage shape optimisation studies later on accounting for engine bay flow, it seems necessary to use some simplified methods to model the engine bay intake/exit flows. For that purpose, the area averaged total pressures were derived at intake surfaces, as well as at the main exit. The intakes' mass flow rates independently of flight condition in function of the calculated total pressure differences (intake-exit) are shown in Figure 12 for the water-, oil- and cylinder head cooler intakes. As can be noted the fitted 2nd order polynomial trendlines agree well with the explicit results, at least in the range of our current interest. The oil- and cylinder head coolers follow very similar trends, as expected from their nearly symmetric arrangement and size. The trendline of the water cooler also fits nicely at both low and high total pressure differences.

In conclusion, the method to define mass flow rates through intakes based on the total pressure differences using the determined characteristics seems reasonable. In our full external aero model described in the next chapter the inlet and outlet flow rates were defined explicitly as the operating conditions were applied.

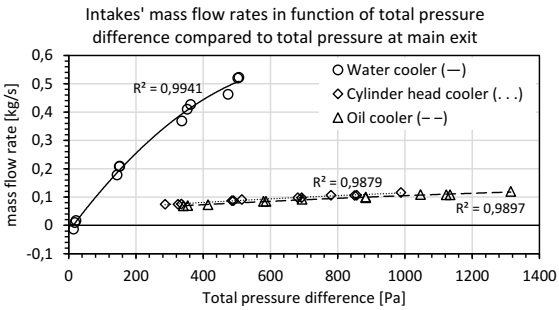

Figure 12. Engine bay intakes' mass flow rates in function of total pressure difference

3.3 Full external aero model

The CFD domain used for the external flow simulations is depicted in Figure 13. It is a cylindrical domain (Ø100 *m*) with a hemisphere *inlet* face at its front. The model is based on the 3D CAD model of the aircraft. In the CFD model the three main air intake ducts (water-, oil- and cylinder head cooler) and the engine bay main exit – shown in Figure 13 – were considered. The propeller was substituted with the same VBM disc domain as in the engine bay model.

The final volume mesh was poly-hexcore type with prism layers at walls. The minimum and maximum hex cell length were 5 *mm* and 1.2 *m*, respectively. The baseline mesh featured 17 prism layers resulting $y^+ \approx 20$ at 47.1 *m/s* free-stream velocity.

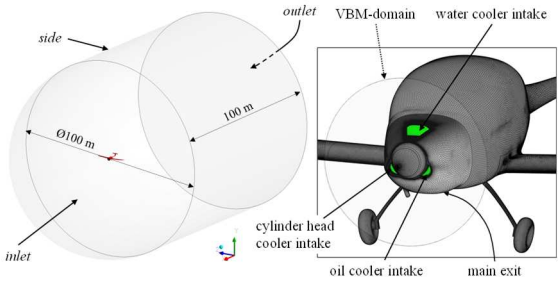

Figure 13. External flow CFD model overview

Mesh dependency study is out of the scope of this paper, however based on the results discussed in section 3.4 we can assume that the applied mesh has sufficient resolution. The mesh of the VBM domain was the same as in the engine bay model. Cross section views of the baseline mesh (36.7 million nodes, 17 million cells) are shown in Figure 14.

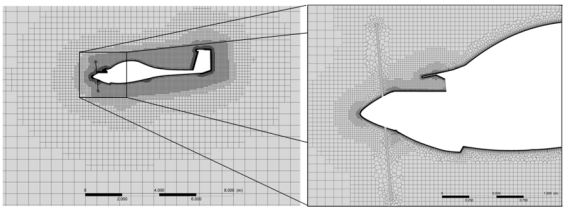

Figure 14. Baseline volume mesh (section views)

The following boundary conditions were applied:

- *inlet* and *side* surfaces: velocity inlet with x- and y-component according to AoA and flight speed. The AoA was tuned in each case to achieve a lift force matching the total weight of the aircraft within 1%. The turbulent intensity and viscosity ratio were set to 1% and 1, respectively.
- *outlet* surface: pressure outlet with 0 *Pa* average gauge pressure;
- water-, oil- and cylinder head cooler intakes and main exit outlet: mass flow outlets and inlet with specified mass flow rates;
- all physical walls were defined as hydraulically smooth *wall* with no slip boundary condition.

The applied VBM model details are specified in Zipszer et al. [1]. The same inputs were used for the 2D- and 3D-VBM; identical to the 2D-VBM inputs used in the engine bay simulations.

3.4 External aero result assessment

The simulated cases were stabilised glide with non-operating engine (VT) and stabilised level flight with cruise blade pitch settings (CR); each at four

flight speeds. The results and test data derived for cruise and take-off blade settings showed very similar trends, therefore only cruise (CR) will be discussed further.

In the CFD model monitor points were defined based on the physical location of the pressure probes. Five monitor points will be discussed, these are depicted in Figure 15. M1 and M5 are static pressure probes on the motor cowling surface. $M1_B$ is a total pressure probe near the cowling. SZT1 and $SZT1_A1$ are static and total pressure probes, respectively, located near to the rear side of the wing-fuselage transition where significant pressure fluctuations were expected to occur. Both total pressure probes were positioned ≈20 *mm* from the airframe surface.

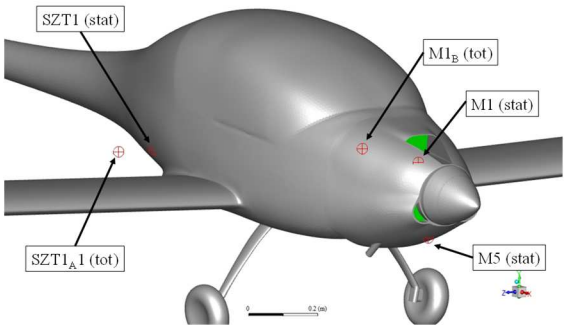

Figure 15. Location of pressure probes

The variation of static and total pressures (p_s, p_t) relative to ambient static pressure will be shown using corrected measurement data. Note, that differences between actual and target flight speeds were insignificant.

In Figure 16 the variation of p_s is depicted for probe M1. For both VT and CR flight conditions a good match between CFD and test data can be observed. Also, the effect of the propeller is clearly visible. The maximum (max.) deviation between CFD and measured values is 23 *Pa* while the average (av.) is 11.3 *Pa* representing 11.2% and 5.5% deviation from the av. measured values, respectively.

From Figure 17 one can conclude that the variation of p_t at $SZT1_A1$ probe shows a similarly good match between measurement and CFD with av. 49.3 *Pa* (5.1%) and max. 124 *Pa* (12.8%) deviation. The propeller down wash effect is clearly visible here as well. For VT case at the lowest flight-speed a significant drop in pressure can be seen which is well captured by the CFD simulation.

In Figure 18 the variation of p_s is depicted at probes M1 and SZT1 for the cruise case. As it was expected the fluctuation of measured pressure at probe SZT1 is significantly higher compared to M1. The visualised error-bars show the standard deviation of the measured dataset: av. std. was 56.7 *Pa* and 99.6 *Pa* for M1 and SZT1, respectively. For SZT1 the max. difference of p_s from measurement is 66.3 *Pa* (24.9%) the av. is 26.6 *Pa* (10.0%). Note that the predicted accuracy of the measurement system is ±30 *Pa*.

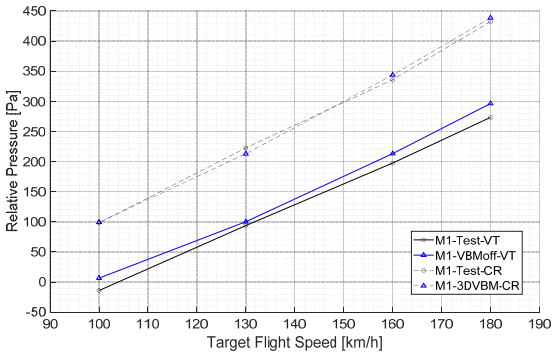

Figure 16. Variation of p_s at probe M1 for condition VT and CR

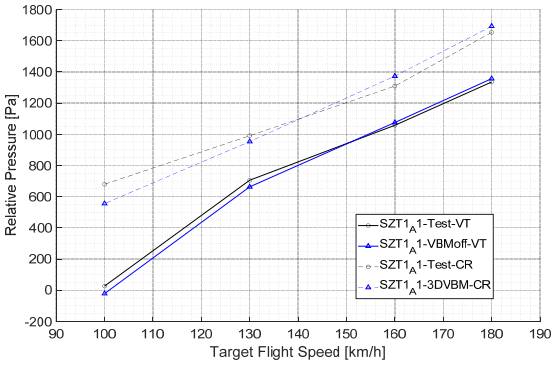

Figure 17. Variation of p_t at probe $SZT1_A1$ for condition VT and CR

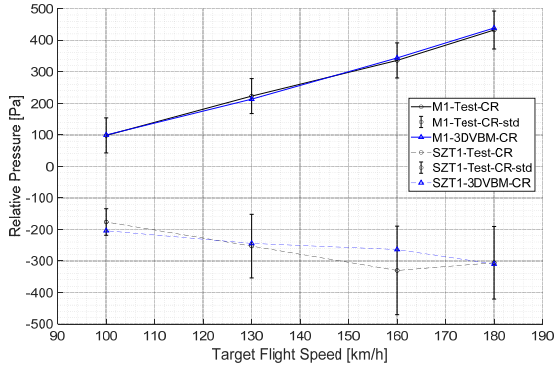

Figure 18. Variation of p_s at probe M1 and SZT1 at condition CR

It can be seen from Figure 19 that 3D-VBM improves the match with measurement compared to the 2D-VBM for M1 at cruise by reducing av. deviation from 14.7 *Pa* (5.4%) to 6.3 *Pa* (2.3%). However, this cannot be said for all probe positions; at many of them switching between 2D- and 3D-VBM resulted in no significant change.

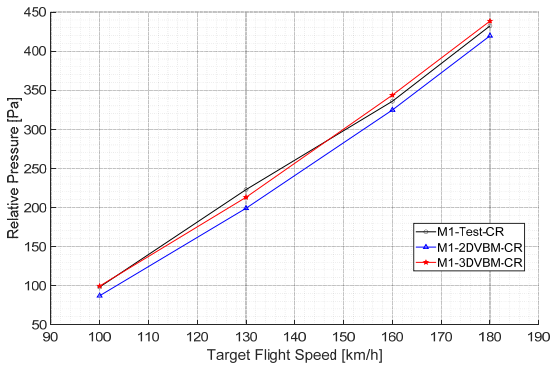

Figure 19. Variation of p_s at probe M1 for conditions CR with 2D- and 3D-VBM

4. SUMMARY

A comprehensive study was carried out concerning the engine bay and the external aerodynamic assessment of a real motor-glider aircraft with the utilisation of 3D corrected VBM.

Engine bay intake and exit flow rates at different conditions were determined using a detailed CFD model. The water cooler intake's sensitivity to AoA was explored, and a simplified model based on pressure differences was proposed.

By comparing flight test data with CFD results the validity of the applied modelling approach was demonstrated. The effect of propeller downwash was clearly visible even further downstream from the propeller which proves the importance to account for propeller wake effects. Both 2D- and 3D-VBM results showed a good match with test data. 3D-VBM offers some improvements for the investigated cases; however, its superiority over 2D-VBM is not conclusive.

ACKNOWLEDGEMENTS

This work has been supported by the Hungarian Government through the NKFI Fund under contract No. 2018-1.2.2-KFI-2018-00057.

REFERENCES

[1] Zipszer, G., Varró, Sz., Darázs, B., Gyöngyösi, M., Horváth, Á., 2022, "Artificial Intelligent enhanced Virtual Blade Model", *Proc. CMFF'22 Conference, Budapest,* in-print

[2] Balland, M., Verseux, O. and Esteve, M.-J., 2005, "AERO thermal computations with experimental comparison applied to aircraft engine nacelle compartment", *Proc. ASME Turbo Expo 2005: Power for Land, Sea, and Air,* Reno-Tahoe, NV, Vol 3, pp.1217-1225.

[3] ESPOSA, 2012, "Efficient systems and propulsion for small aircraft" available at: http://www.esposa-project.eu/

[4] Stalewski, W., Zółtak, J., 2014, "The preliminary design of the air-intake system and the nacelle in the small aircraft- engine integration process", *Aircraft Engineering and Aerospace Technology,* Vol.86, No.3, pp.250-258.

[5] Łapka, P., Seredyński, M., Furmański, P., Dziubiński, A., Banaszek, J., 2014, "Simplified thermo-fluid model of engine cowling in small airplane", *Aircraft Engineering and Aerospace Technology,* Vol.86, No.3, pp.242-249.

[6] Łapka, P., Bakker, M., Furmański, P., H. van Tongeren, 2018, "Comparison of 1D and 3D thermal models of the nacelle ventilation system in a small airplane", *Aircraft Engineering and Aerospace Technology,* Vol.90, No.1, pp.114-125

[7] Guła, P., Ulma, D., Zurek, K., Zurawski, R., 2019, "Challenges of turboprop engine installation on small aircraft", *Aircraft Engineering and Aerospace Technology,* Vol.91, No.7, pp.938-948

[8] Buonomo, G., Musto, M., Bianco, N., Rotondo, G., Pezzella, G., Mingione, G., 2013, „Aerothermal Analysis of an Aircraft Nacelle in the Framework of a Fully Coupled Approach", *Italian Association of Aeronautics and Astronautics XXII Conference, Napoli, 9-12 September 2013.*

[9] Olejnik, A., Dziubiński, A., Kiszkowiak, L., 2021, "CFD Simulation of engine nacelle cooling on pusher configuration aircraft", *Aircraft Engineering and Aerospace Technology,* Vol.93, No.9, pp.1421-1429

[10] Jackson, A. C., Vinegar, A.,1979, "A technique for measuring frequency response of pressure, volume, and flow transducers." *J Appl Physiol Respir Environ Exerc Physiol,* 47(2), pp.462-467.

[11] Pelley, D. L., Morris, D., Richards, P., 2012, "Aerodynamic force deduction on yacht sails using pressure and shape measurements in real time", *4th High Performance Yacht Design Conference 2012,* HPYD 2012. pp.28-37.

[12] Mackay, M., 1990, "Static pressure measurement with surface-mounted disc probes", *Experiments in Fluids,* 9(1-2), pp.105-107.

[13] Balczó, M., Goricsán, I., Lajos, T., Régert, T., & Sebestyén, P., 2006, "Prediction of wind load acting on telecommunication masts", IABSE Symposium, Budapest, January 2006, Report Vol.92(25).

Conference on Modelling Fluid Flow (CMFF'22)
The 18th International Conference on Fluid Flow Technologies
Budapest, Hungary, August 30 -September 2, 2022

THE INVESTIGATION OF COUNTER-ROTATING TURBOMACHINERY BROADBAND NOISE SOURCES AS A FUNCTION OF ROTATIONAL SPEED

Ádám ROMASZ[1], Kristóf TOKAJI[2], Csaba HORVÁTH[3]

[1] Department of Fluid Mechanics, Faculty of Mechanical Engineering, Budapest University of Technology and Economics. Bertalan Lajos u. 4 – 6, H-1111 Budapest, Hungary. E-mail: romasz.adi99@gmail.com
[2] Department of Fluid Mechanics, Faculty of Mechanical Engineering, Budapest University of Technology and Economics. Bertalan Lajos u. 4 – 6, H-1111 Budapest, Hungary. E-mail: tokaji.kristof@gpk.bme.hu
[3] Department of Fluid Mechanics, Faculty of Mechanical Engineering, Budapest University of Technology and Economics. Bertalan Lajos u. 4 – 6, H-1111 Budapest, Hungary. E-mail: horvath.csaba@gpk.bme.hu

ABSTRACT

Counter-rotating turbomachinery often appear in modern aerospace applications. Along with their numerous advantageous properties they are also known to produce high amounts of noise. The emitted noise consists of tonal and broadband noise components, which can be studied utilizing beamforming technology. In order to analyse them more efficiently and reach a better understanding of the noise generation mechanisms, these noise components must be separated. The Double Filtering Method allows one to separate these two noise source categories, making it possible to examine broadband noise components without any interference from tonal noise components. In this paper a series of studies are carried out on various parameters that influence the effectiveness of the Double Filtering Method. The investigation then goes on to apply the method, investigating the effects of changing rotational speed on the broadband noise sources of counter-rotating open rotors, presenting the various categories of broadband noise sources and their occurrence on the beamforming maps and in the spectra. Four major categories are looked at as a function of rotational speed: two different blade angles (simulating take-off and approach conditions), and two different installations (uninstalled and installed with a pylon).

Keywords: beamforming, broadband noise sources, counter-rotating turbomachinery, signal processing

NOMENCLATURE

f	$\left[\frac{1}{min}\right]$	rotational speed
f_{NRNS}	[Hz]	frequency of the NRNS
L_{tot}	[s]	total loss
N	[-]	number of subsegments in a NRNS filtering segment
T_e	[s]	length of a Single filtered segment
T_{NRNS}	[s]	length of a subsegment

Subscripts and Superscripts

ideal	ideal value
max	maximal value
NRNS	non-rotational noise source

1. INTRODUCTION

Counter-Rotating Open Rotors (CROR) are made up of two unducted rotors. Their main advantage over single rotor turbomachinery is lower fuel consumption [1]. However, there are still many obstacles to overcome. Such as its high noise emission, which has been the subject of numerous investigations [2-10]. A sketch of a CROR test rig can be seen in Figure 1. The test rig consists of two rotors (two trapezoids) that are mounted on the hub. The flow is going from left to right, as the flow first interacts with a pylon before reaching the rotors. The pylon can optionally be removed, as marked by the dashed line. Downstream of the rotors, the rest of the test rig is sufficiently far away in order to not influence the flow around the rotors.

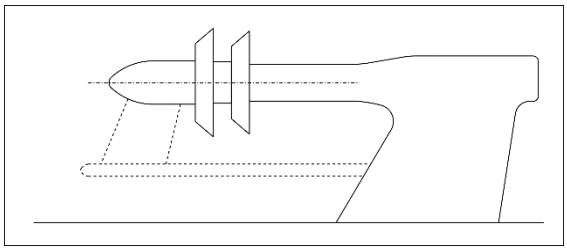

Figure 1. Sketch of a CROR test rig

CROR noise sources can be categorised in many ways [11-13]. This paper focuses on the broadband noise sources, which can be divided into four main groups [14]: Blade root noise sources, Trailing edge

noise sources, Leading edge noise sources, and Blade tip noise sources.

Another aspect of grouping is whether the noise source is located on the suction or pressure side. If it appears on a blade moving towards the observer, it is on the pressure side. If the blade moves away from the observer, the noise source is on the suction side. In our case, the forward blade row shows the pressure side above the shaft, and the suction side below it. The situation is exactly the opposite on the aft blade row, the suction side is visible above the shaft and the pressure side is visible below.

Blade root noise sources are located near the base of the blades on the aft rotor, both on the pressure and suction side. They are created by the interaction between the boundary layer on the shaft and the blade roots. An example of this is shown in Figure 2., marked with a square.

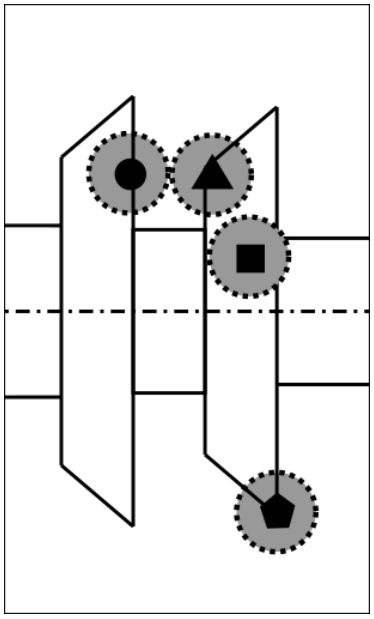

Figure 2. CROR noise sources

Trailing edge noise sources appear dominantly on the pressure side of the forward rotor. This noise source is more pronounced at higher frequencies. The typical region where these noise sources predominantly appear is shown in Figure 2., marked with a circle.

Leading edge noise sources are most significant on the aft blade row and can be seen near the leading edge on both the pressure and suction sides. The typical region where these noise sources predominantly appear is shown in Figure 2., marked with a triangle.

Blade tip noise sources can be seen on the pressure side of the aft rotor. The typical region where these noise sources predominantly appear is shown in Figure 2., marked with a pentagon.

The measurements discussed in this paper have been carried out in the NASA Glenn Research Center 9×15 ft Low-Speed Wind Tunnel, on a F31/A31 historic baseline CROR [15]. The forward rotor has 12 blades with a diameter of 0.652 m, while the aft rotor has 10 blades with a diameter of 0.63 m. The Mach number of the flow has been 0.2, and the angle of attack has been set to 0˚.

Table 1. Uninstalled, approach cases

Case number	Forward rotational speed $\left(\frac{1}{min}\right)$	Aft rotational speed $\left(\frac{1}{min}\right)$	Temp. [˚C]
U-A-5716	5716	5716	28.3
U-A-6463	6463	6463	28.5
U-A-7405	7405	7405	28.9
U-A-7653	7653	7653	29.1

Table 2. Uninstalled, take-off cases

Case number	Forward rotational speed $\left(\frac{1}{min}\right)$	Aft rotational speed $\left(\frac{1}{min}\right)$	Temp. [˚C]
U-T-4725	4725	4724	28.1
U-T-5390	5390	5390	28.4
U-T-5680	5680	5680	28.6
U-T-6211	6211	6212	28.7
U-T-6453	6453	6453	28.8
U-T-6590	6590	6590	28.9

Two different configurations have been investigated: Take-off ((T) blade angles: 40.1˚ for the forward, 40.8˚ for the aft rotor) and Approach ((A) blade angles: 33.5˚ for the forward, 35.7˚ for the aft rotor). Both configurations have been tested uninstalled (U) and installed with a pylon (P), which are support structures the engines (such as a CROR) are mounted on. Tables 1 to 4 contain the various investigated cases and the corresponding rotational speed values. Though the data presented in this paper is from an earlier investigation, this is the first investigation that presents a beamforming comparison of the broadband noise sources of all the test cases presented herein (Tables 1-4) as a function of rotational speed.

Table 3. Installed, approach cases

Case number	Forward rotational speed $\left(\frac{1}{min}\right)$	Aft rotational speed $\left(\frac{1}{min}\right)$	Temp. [˚C]
P-A-5754	5754	5754	32.3
P-A-6503	6503	6503	32.5
P-A-6967	6967	6966	32.7
P-A-7451	7451	7451	32.7
P-A-7700	7700	7700	32.9

Table 4. Installed, take-off cases

Case number	Forward rotational speed $\left(\frac{1}{min}\right)$	Aft rotational speed $\left(\frac{1}{min}\right)$	Temp. [°C]
P-T-4764	4764	4764	33.1
P-T-5430	5430	5430	33.1
P-T-5723	5723	5724	33.2
P-T-6258	6258	6258	33.3
P-T-6501	6501	6501	33.3

2. BEAMFORMING AND DOUBLE FILTERING

2.1 Phased array microphone system and beamforming

During the investigations, an OptiNAV Array48 phased array microphone system has been used, which contains 48 microphones [16]. Signals have been recorded at a sample rate of 96 kHz.

The method used to process the data measured with the phased array microphone system is called beamforming. The specific beamforming method chosen for this investigation has been Delay-and-sum beamforming, which has been found to provide a good signal-to-noise ratio with little loss of information. The data has been processed in the frequency domain [17]. This method is based on compensating the signals recorded by each microphone for every investigated point. This compensation is such that if a noise source exists in that investigated point, the compensated signals will be approximately the same for each microphone. Conversely, if there is no noise source at the investigated point, the compensated signals will be different. After compensating the signals, they are averaged for every investigated point. If a noise source exists in the investigated point, this value - called beamforming level - will be large. The output beamforming level is displayed on the beamforming maps (Figures 1 to 4).

2.2 Double filtering

Broadband noise sources typically have a smaller amplitude than tonal noise sources, which makes them difficult to study. This is especially difficult in the case of CROR, as the tonal noise components dominate many of the frequency bins, as seen in Figure 3, thus hiding the broadband noise components on the beamforming maps. In order to be able to investigate these noise sources, they must be separated from tonal noise sources.

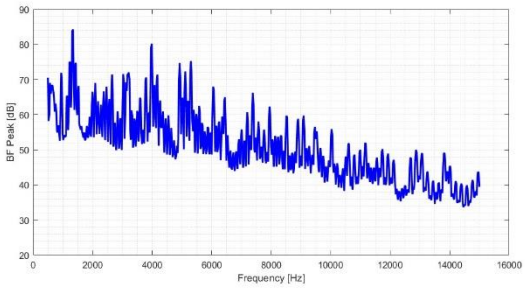

Figure 3. Typical CROR spectrum of the BF Peak value

The Double filtering method builds on a signal processing method developed by Sree and Stephens [18]. This signal processing method removes tonal components related to the rotational speed of a CROR, which are referred to herein as Rotational Noise Sources (RNS) [14]. The resulting signal is referred to herein as a Single filtered signal.

There are also other tonal noise components, which are not related to the rotational speed, called Non-Rotational Noise Sources (NRNS) [14]. In this investigation, a deer whistle, used to verify beamforming maps, is such a noise source. We can filter these noise sources out using a method developed by Tokaji et al. [19] called Double filtering. The resulting signal is called a Double filtered signal.

In carrying out Double filtering, first the signal must be split into segments. In filtering out the RNS components, these segments must be one revolution long [18]. Then, neighbouring segments must be subtracted from one another. This filters out the RNS components, as they repeat in each segment, due to their lengths being one revolution long. Finally, the resulting signal must be divided by $\sqrt{2}$, so that the resulting broadband signal has the same properties as the broadband components in the original signal [18-20].

The principle behind filtering out the NRNS component is similar to that of filtering out the RNS component. All Single filtered segments must be split into new, shorter segments, as seen in Figure 4.

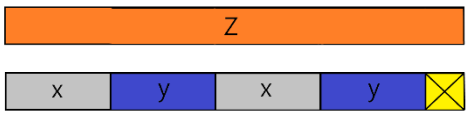

Figure 4. Splitting the signal into segments

While the choice of segment length is straightforward in the case of Single filtering, here

there are multiple options. The NRNS filtering segment length is based on the period time corresponding to the frequency of the NRNS. This is referred to herein as a subsegment [14]. Theoretically, this is the shortest applicable segment length in this case. However, the use of one subsegment long NRNS filtering segments is not recommended, because it is too short, which leads to a lot of information loss and inadequately filtered signals. It can also be stated that the length of the NRNS filtering segments must be shorter than half the length of a Single filtered segment. This is necessary in order to have at least two segments, which can be subtracted. The length of an NRNS filtering segment must be a multiple of the length of a subsegment.

3. PARAMETERS OF NRNS FILTERING, SEGMENT LENGTH

We have seen in the previous section that there are several options when it comes to choosing the NRNS filtering segment's length. First, the frequency of the NRNS (f_{NRNS}) must be determined. This varies slightly between the investigated cases, but it is approximately 3200 [Hz] in this study. Using f_{NRNS}, one can define the length of a subsegment (T_{NRNS}), as given in Eq. (1).

$$T_{NRNS} = \frac{1}{f_{NRNS}} \tag{1}$$

The length of a Single filtered segment (T_e) can be calculated using the rotational speed of the given case (f) as seen in Eq. (2).

$$T_e = \frac{60}{f} \tag{2}$$

Another important parameter of NRNS filtering is N, which is equal to the number of subsegments a NRNS filtering segment consists of. N must be an integer between 1 and N_{max}, which can be calculated as shown in Eq. (3), where [.] refers to the integer function.

$$N_{max} = \left[\frac{T_e}{2T_{NRNS}}\right] \tag{3}$$

The length of the NRNS filtered signal is shorter than the length of the original signal. This is the results of two major factors: segment fragments and a loss of an entire NRNS filtering segment in each Single filtered segment, due to the subtraction in the Double filtering method.

An example for a segment fragment can be seen in Figure 4., represented by the yellow rectangle. The Single filtered segment lengths (Z) are not multiples of the NRNS filtered segment lengths (x and y); hence such fragments are always present. These are lost during the filtering process.

The sum of these two types of losses is called the total loss (L_{tot}), which is related to the value of N. Our investigations have shown that the N corresponding to the maximum total loss ($N(L_{tot,max})$) is between 65% and 77% of the value of N_{max} for the investigated cases. It has been found that Double filtering yields the best results if the chosen N is lower than the one corresponding to the maximum of total loss for that given case.

It has also been stated in the previous chapter, that the use of too few subsegments (meaning N is small) leads to an inadequately filtered signal. During the investigation, every possible Double filtered signal (using all valid N values from 1 to N_{max}, as shown in Eq. 3) have been created for the CROR cases to study this phenomenon. In the investigated cases, $N = 7$ has been found to be the smallest N with which the Double filtered signal has been considered acceptable. Hence it has been chosen as the lower limit for the ideal value of N for these cases.

Combining these findings, the range containing the ideal value of N for the investigated cases is shown in Eq. (4).

$$7 \leq N < N(L_{tot,max}) \tag{4}$$

A trend showing that the ideal value for N is half of N_{max} has also been observed, which is true for most cases. If N_{max} is even, the formula seen in Eq. (5) has been used. If N_{max} is odd, the formula seen in Eq. (6) has been used.

$$N_{ideal} = \frac{(N_{max})}{2} \tag{5}$$

$$N_{ideal} = \frac{(N_{max} \mp 1)}{2} \tag{6}$$

The ideal and the maximum Double filtering segment length for each investigated case can be seen in Table 5. Unmarked cases are the ones for which the ideal value for N is half of N_{max}. Cases marked with yellow are the ones, for which N from Eq. (5) or (6) does not fit in the range defined in Eq. (4). Cases marked with red are the ones, which do not fit the trend at all. As this trend fits the investigated cases well, it can be used as a starting value for future studies and applications of the Double filtering method to other similar test cases.

Table 5. Ideal and maximum N values

Case number	N_{ideal}	N_{max}
U-A-5716	7	16
U-A-6463	7	14
U-A-7405	8	13
U-A-7653	8	12
P-T-4764	10	19
P-T-5430	8	17
P-T-5723	8	16
P-T-6258	7	15
P-T-6501	7	14
U-T-4725	10	19
U-T-5390	8	17
U-T-5680	8	16
U-T-6211	7	15
U-T-6453	7	14
U-T-6590	8	14
P-A-5754	8	16
P-A-6503	7	14
P-A-6967	7	13
P-A-7451	8	12
P-A-7700	8	12

4. INVESTIGATING AND COMPARING THE DOUBLE FILTERED SIGNALS AS A FUNCTION OF ROTATIONAL SPEED

Using the ideal Double filtered segment length shown in Table 5, Double filtered signals have been created for each investigated case. This has made it possible to examine the broadband noise sources with the help of beamforming maps and spectra, comparing the various test cases described in Tables 1-4.

The location of each noise source on the CROR examined during the investigation can be observed on the beamforming maps (Figures 9 to 17). These maps present the highest beamforming levels in a given frequency band and the 5 [dB] dynamic range below it, with the corresponding colour scale in the lower right corner of the figures. The upper left corner of the beamforming map shows the frequency band for that figure. The magnitude of the peak is located in the upper right corner. This value is called beamforming level

The Double filtered spectra for the uninstalled approach, the uninstalled take-off, the installed approach, and the installed take-off cases are shown in Figures 5-8, respectively. Comparing these spectra helps to identify differences between cases with varying rotational speeds, narrowing down the frequency bands of interest. In chapters 4.1 to 4.3, some of these frequency bands are investigated.

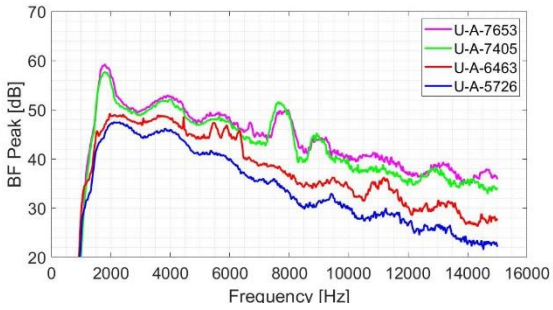

Figure 5. Uninstalled, approach broadband spectra

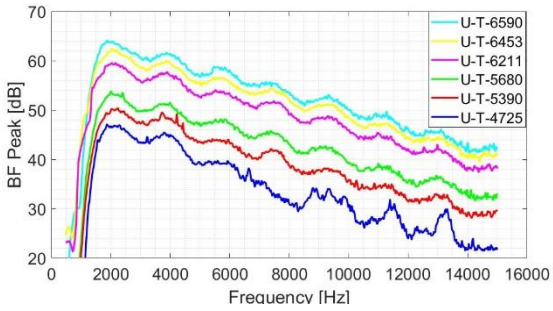

Figure 6. Uninstalled, take-off broadband spectra

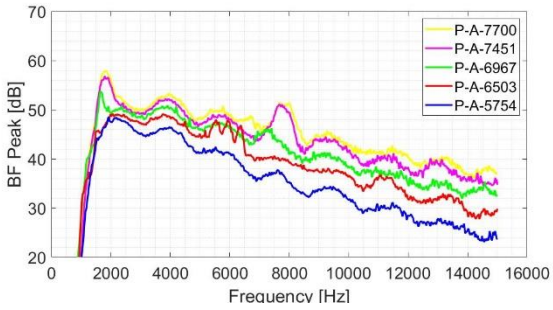

Figure 7. Installed, approach broadband spectra

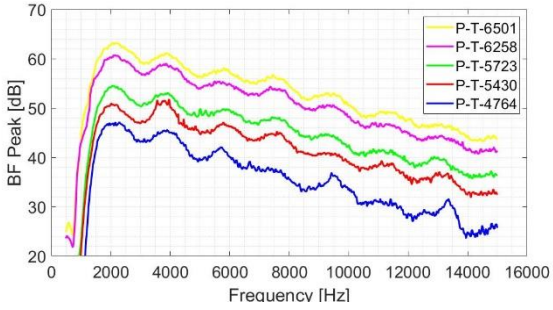

Figure 8. Installed, take-off broadband spectra

4.1 Comparison of approach cases with varied rotational speeds

For take-off mode cases, the shape of the Double filtered spectra have been found to be similar for the installed and uninstalled cases. It can also be seen

that cases with higher rotational speeds have larger beamforming peak levels across the entire frequency domain, as seen in Figures 5 and 7. On the other hand, approach mode cases differ greatly in some frequency bands.

First, a series of three peaks can be seen between 5500 Hz and 6500 Hz, for case numbers U-A-6463 and P-A-6503. These peaks are caused by Trailing edge noise sources, which are rarely found below 7000 Hz for the other cases in this study, and Blade tip noise sources while other cases have Blade root noise sources as their dominant noise source. This can be seen in Figure 9, for the uninstalled case.

Figure 9. Trailing edge and Blade tip noise source, case number U-A-6463

Second, a large increase in the magnitude of the beamforming levels can be observed between 7000 Hz and 8500 Hz, peaking around 7700 Hz for cases with higher rotational speeds (U-A-7405, U-A-7653 and P-A-7451, P-A-7700). The dominant noise sources have been Blade tip noise sources for every case in this frequency band in installed cases, but cases with lower rotational speeds have not produced an increase like this. In the uninstalled cases, case numbers U-A-5726 and U-A-6463 have Blade root noise sources and Trailing edge noise sources as their dominant ones, while the increase in magnitude for case numbers U-A-7405 and U-A-7653 has been caused by Blade tip noise sources, similarly to the installed cases. An example for this can be seen in Figure 10, for case number P-A-7700.

Figure 10. Blade tip noise source, case number U-A-7700

4.2 Trailing edge noise sources

Trailing edge noise sources appear most commonly on the forward rotor, on the pressure side. They dominate higher frequency bands. Investigations have shown that the pylon affects these noise sources.

Figure 11. Trailing edge noise source, uninstalled mode, case number U-T-6453

For uninstalled cases – both take-off and approach – Trailing edge noise sources have appeared above 7500 Hz and become more dominant at higher frequencies, as seen in Figure 11. However, for installed cases, Trailing edge noise sources have only started to appear above 10 kHz, for both take-off and approach settings. An example for a Trailing edge noise source can be seen in Figure 12.

Figure 12. Trailing edge noise source, installed mode, case number P-T-6501

4.3 The effect of a pylon and rotational speed on Blade tip noise sources

Blade tip noise sources appear on the pressure side of the aft rotor. They are greatly affected by both a presence of a pylon and the rotational speed.

Investigations have shown that Blade tip noise sources are more dominant in installed cases. In Figures 13 and 14, an installed and uninstalled case with similar rotating speeds can be seen. While in the installed case, the Blade tip noise source is clearly the dominant one, in the uninstalled case, a Blade root noise source can be seen.

Figure 13. Blade root noise source in the uninstalled case, case number U-T-4725

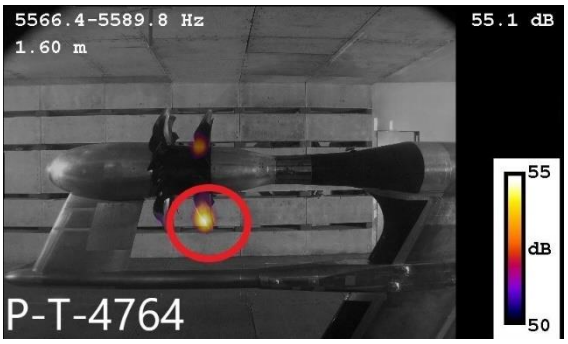

Figure 14. Blade tip noise source in the installed case, case number P-T-4764

The other main factor affecting Blade tip noise sources is the rotational speed, which can be best studied using the uninstalled cases. Investigations have shown that Blade tip noise sources become more dominant as the rotational speed increases. Figures 15 to 17 show uninstalled, take-off cases with various rotational speeds for the same frequency band. While for case number U-T-4725, the Blade root noise source is clearly the dominant source, in case number U-T-5680, we can see a Blade tip noise source appear. As we increase the rotational speed even further, the Blade tip noise sources become more and more dominant, as seen in Figure 17.

Figure 15. Investigating the effect of rotational speed on Blade tip noise, case number U-T-4725

Figure 16. Investigating the effect of rotational speed on Blade tip noise, case number U-T-5680

Figure 17. Investigating the effect of rotational speed on Blade tip noise, case number U-T-6590

5. CONCLUSIONS

In this study, the parameters of Double filtering have been investigated, focusing on ideal segment length. A subsegment and the value of N, which shows how many subsegments a NRNS filtering segment consist of, have been defined. For the investigated cases, a lower limit of 7 has been chosen for the value of N, because below this, Double filtering segments are too short, leading to inadequately filtered signals. An upper limit has been chosen as well, with the help of total loss, which shows how much shorter the Double filtered signal is, as compared to the original signal. The upper limit has a value for N which corresponds to the maximum total loss for each given case. Another trend worth mentioning is that the ideal value for N has half the value of the maximum N, which has been true for 18 of the 20 investigated cases.

Using the ideal segment length, Double filtered signals have been created for every case. The spectra of the take-off cases have been similarly shaped, cases with higher rotational speeds have larger beamforming peak levels across the entire frequency domain. On the other hand, the spectra of approach cases have shown two main differences between cases with different rotational speeds. These have been consistent for both installed and uninstalled cases.

When comparing Trailing edge noise sources in the take-off and approach cases, we have reached the

conclusion that in the installed case, these type of noise sources appear from 10 kHz. In the uninstalled cases, they can be seen from 7500 Hz

Blade tip noise sources have been affected by two main factors: rotational speed and the presence of the pylon. Investigations have shown that Blade tip noise is more dominant in installed cases. Higher rotational speeds result in more dominant Blade tip noise sources as well, best demonstrated by the uninstalled, take-off cases.

ACKNOWLEDGEMENTS

The research reported in this paper and carried out at BME has been supported by the Hungarian NRDI Centre under contract No. K 129023, by the NRDI Fund (TKP2020 NC, Grant No. BME-NCS) based on the charter of bolster issued by the NRDI Office under the auspices of the Ministry for Innovation and Technology, and is part of project no. BME-NVA-02, implemented with the support provided by the Ministry of Innovation and Technology of Hungary from the NRDI Fund, financed under the TKP2021 funding scheme.

REFERENCES

[1] Bowles, M. D., 2010, ""Apollo" of Aeroacoustics: NASA's Aircraft Energy Efficiency Program 1973-1987," NASA Headquarters, Washington, D.C., USA, 113-140

[2] Woodward, R. P., 1987, "Noise of a Model High Speed Counterrotation Propeller at Simulated Takeoff/Approach Conditions (F7/A7)," NASA TM-100206, https://doi.org/10.2514/6.1987-2657

[3] Blandeau, V. P., Joseph, P. F., 2010, "Broadband Noise Due to Rotor-Wake/Rotor Interaction in Contra-Rotating Open Rotors", AIAA Journal, Vol. 48, No. 11, https://doi.org/10.2514/1.J050566

[4] Smith, D. A., A. Filippone, and N. Bojdo., 2020, "Noise reduction of a Counter Rotating Open Rotor through a locked blade row." Aerospace Science and Technology, Vol. 98 No. 105637., https://doi.org/10.1016/j.ast.2019.105637

[5] Yu, L., Wu, H., Antoni, J., & Jiang, W., 2019, "Extraction and imaging of aerodynamically generated sound field of rotor blades in the wind tunnel test", Mechanical Systems and Signal Processing, Vol. 116, pp. 1017-1028., https://doi.org/10.1016/j.ymssp.2018.07.042

[6] Fenyvesi, B., Kriegseis, J. and Horváth, Cs., 2019, "Application of a Combined Method for the Investigation of Turbomachinery Noise Sources: Beamforming and Proper Orthogonal Decomposition", 25th AIAA/CEAS Aeroacoustics Conference, AIAA 2019-2637, Delft, The Netherlands, https://arc.aiaa.org/doi/10.2514/6.2019-2637

[7] Funke, S., Kim, L. and Siller, H. A., 2011, "Microphone-Array Measurements of a Model Scale Contra-Rotating Open Rotor in a Reverberant Open Wind-Tunnel", 17th AIAA/CEAS Aeroacoustics Conference, Portland, OR, USA, AIAA 2011-2766, https://doi.org/10.2514/6.2011-2766

[8] Van Zante, D. E., Gazzaniga, J. A., Elliott, D. M., et al., 2011, "An Open Rotor Test Case: F31/A31 Historical Baseline Blade Set", 20th International Symposium on Airbreathing Engines, Gothenburg, Sweden, ISABE 2011-1310,

[9] Ricouard, J., Julliard, E., Omais, M., Regnier, V., Parry, A., Baralon, S., 2010, "Installation effects on contra-rotating open rotor noise", 16th AIAA/CEAS aeroacoustics conference, pp. 3795., https://doi.org/10.2514/6.2010-3795

[10] Elliott, D., 2011, "Initial investigation of the acoustics of a counter rotating open rotor model with historical baseline blades in a low-speed wind tunnel", 17th AIAA/CEAS Aeroacoustics Conference (32nd AIAA Aeroacoustics Conference), pp. 2760., https://doi.org/10.2514/6.2011-2760

[11] Fenyvesi, B., Tokaji, K., Horváth, Cs., 2019, "Investigation pf a Pylons Effect on the Character of Counter-Rotating Open Rotor Noise Using Beamforming Technology", Acta Acustica United With Acustica, Vol. 105, https://doi.org/10.3813/AAA.919287

[12] Horváth, Cs., Envia, E. and Podboy, G. G., 2014, "Limitations of Phased Array Beamforming in Open Rotor Noise Source Imaging", AIAA Journal, Vol. 52, No. 8, https://doi.org/10.2514/1.J052952

[13] Horváth, Cs., 2015, "Beamforming Investigation of Dominant Counter-Rotating Open Rotor Tonal and Broadband Noise Sources", AIAA Journal, Vol. 53, No. 6, https://doi.org/10.2514/1.J053465

[14] Tokaji, K., Horváth, Cs., 2021, "Effect of a pylon on the broadband noise sources of counter-rotating turbomachinery", International Journal of Aeroacoustics, Vol: 20 No. 8, pp. 979-1002 https://doi.org/10.1177/1475472X211055178

[15] Van Zante, D. E., 2013, "The NASA Environmentally Responsible Aviation Project", 51st AIAA Aerospace Sciences Meeting, https://doi.org/10.2514/6.2013-415

[16] Optinav Inc., Array 48, 2017, https://www.optinav.info/Array48

[17] Mueller, T. J., 2002, “Aeroacoustic Measurements.” Springer Verlag, Berlin, Germany, http://dx.doi.org/10.1017/S0022112003238398

[18] Sree D. and Stephens D. B., 2016, “Improved separation of tone and broadband noise components from open rotor acoustic data.” Aerospace, Vol. 3, No. 3, https://doi.org/10.3390/aerospace3030029

[19] Tokaji, K., Soós Bálint, Horváth, Cs., 2020, “Beamforming method for extracting the broadband noise sources of counter-rotating open rotors”, AIAA Journal, Vol. 58, No 7, https://doi.org/10.2514/1.J058934

[20] Sree, D., “A novel signal processing technique for separating tonal and broadband noise components from counter-rotating open-rotor acoustic data”, International Journal of Aeroacoustics, Vol. 12, No. 1-2, 2013, pp. 169-188., https://doi.org/10.1260/1475-472X.12.1-2.169

Conference on Modelling Fluid Flow (CMFF'22)
The 18th International Conference on Fluid Flow Technologies
Budapest, Hungary, August 30 -September 2, 2022

FLUID DYNAMICS IN A COUNTERCURRENT BUBBLE COLUMN: EXPERIMENTS AND SIMULATIONS

Péter KOVÁTS[1*], Katharina ZÄHRINGER[1], Haris KHAN[2], Roland RZEHAK[2], and Dominique THÉVENIN[1]

[1] Laboratory of Fluid Dynamics and Technical Flows, Otto-von-Guericke-Universität Magdeburg. Universitätsplatz 2, D-39106 Magdeburg, Germany. Tel.: +49 391 - 67 58654, Fax: +49 391 - 67 52840
*E-mail: peter.kovats@ovgu.de
[2] Helmholtz-Zentrum Dresden – Rossendorf, Institute of Fluid Dynamics, Bautzner Landstrasse 400, D-01328 Dresden, Germany

ABSTRACT

Flows in bubble columns are used in many applications in diverse branches of engineering. Moreover, they provide a simple configuration to study fundamental aspects of multiphase flows. Additional co- or countercurrent liquid flow is often used to adjust the residence-time of the bubbles, which is particularly important when mass-transfer occurs. The present contribution reports the initial stage of a joint experimental and numerical effort to understand such flows and to provide models that allow to predict them. To this end, experiments are carried out in a laboratory-scale bubble column and compared with corresponding simulations based on the Euler-Euler framework.

Keywords: bubble column reactor, dispersed two-phase flow, countercurrent flow, shadow imaging, PIV, CFD, Euler-Euler simulation

NOMENCLATURE

a	[mm]	major semi-axis
b	[mm]	minor semi-axis
d_b	[mm]	mean bubble size
d_h	[m]	hydraulic diameter
ESD	[mm]	equivalent sphere diameter
Q_g	[l/h]	gas volume flow rate
Q_l	[l/min]	liquid volume flow rate
v_b	[m/s]	bubble velocity
V_b	[m^3]	volume of the bubble spheroid
v_l	[m/s]	liquid velocity
v_y	[m/s]	vertical liquid velocity
α_G	[-]	gas fraction
μ	[$Pa·s$]	liquid dynamic viscosity
ρ	[kg/m^3]	liquid density
Re	[-]	Reynolds number

1. INTRODUCTION

Bubble column reactors are simple multiphase contactors, where a gas phase is dispersed in a continuous liquid phase. Since they have no moving parts, the operation and maintenance of these reactors is simple. Bubble columns are widely used in chemical, biochemical and petrochemical industries. However e.g. in water and wastewater treatment, countercurrent flow of liquid and gas is applied to increase residence time and gas holdup as well as to enhance mixing and mass transfer.

Besides expensive experiments, multiphase CFD simulation is a smart tool in process engineering to study new reactor designs and scale them up from laboratory to industrial scale [1]. However, to reach industrial scales, the Euler-Euler framework has to be applied for multiphase flow, which heavily relies on modelling unresolved small-scale phenomena (e.g. [2-4] and references therein). Therefore, such simulations have to be validated with experimental data [5].

For these reasons, experiments are carried out in a laboratory-scale bubble column under counter-current flow conditions. For the same setup, Euler-Euler multiphase CFD simulations are performed using a set of closure relations that was extensively validated for co-current flow in pipes and bubble columns in previous works [6, 7]. A monodisperse approximation in the simulations is made feasible by generating bubble swarms of almost uniform size with seven small nozzles in the experiments so that the complexity of modelling bubble breakup and coalescence can be avoided. By comparing the simulation results with the experimental measurements, the validity of the closure models can be established also for counter-current flows. This is a prerequisite for later planned joint investigations of mass transfer phenomena.

Two experiments were performed for several flow conditions with different measurement set-ups. The first investigates properties of the dispersed gas phase such as bubble diameter and bubble velocities by shadow imaging. The second characterizes the

flow of the continuous liquid phase. These data can then be evaluated further to derive correlations for modelling of such two-phase flows. Another objective of these experimental measurements is to provide experimental data for the validation of numerical models. Some preliminary CFD simulation results are also presented in this paper.

2. EXPERIMENTAL SET-UP

To characterize the gas and liquid flow in the bubble column, two different optical measurement methods have been applied, see e.g. [8, 9]. First, the characteristics of the bubbles, such as bubble diameter, velocity, shape or position were measured with shadow imaging. This technique is based on shadow particle recognition combined with Particle Tracking Velocimetry (PTV) to measure the velocity of the bubbles as described in detail in [9]. Then, for the liquid phase, Particle Image Velocimetry (PIV) was used to examine the surrounding hydrodynamics.

Bubble column reactor

A laboratory-scale bubble column with a square cross section of 0.1 x 0.1 m^2 was employed for both experiments (Figure 1). The bubble column was made from acrylic glass and it was especially designed for optical measurements. It consist of 6 main parts: two 0.5 m long inlet (Figure 1, a 1) and outlet (Figure 1, a 2) sections, the water inlet on top (Figure 1, a 3) through four 1" pipes, a 2 m tall acrylic pipe on top of the column with an inner diameter of 0.04 m for gas ventilation (Figure 1, a 4), the 1 m long effective measurement section (Figure 1, a 5) and an interchangeable gas distributor (Figure 1, a 6). In this gas distributor, seven nozzles were mounted in-line, with 12.5 mm equal spacing. The interchangeable design allows the use of different nozzle materials and diameters. In the present study, stainless steel nozzles were applied, with an inner diameter of 0.18 mm. The nozzles were separately connected to seven magnetic valves (Type 6712, Bürkert), which were supplied by a mass flow controller (F-201CV, Bronkhorst) and the pressurized air pipeline.

In order to avoid pulsations induced by a pump, the countercurrent water flow was driven by gravity from an upper water reservoir situated about 4 m above the bottom water reservoir (Figure 1, a 7). This set-up allows a maximum water flow rate of Q_l=55.5 l/min, which corresponds to a Reynolds-number of Re=9000 inside the bubble column. The Reynolds number is defined as $Re=(\rho \cdot v_l \cdot d_h)/\mu$, where ρ is the liquid density, v_l is the liquid velocity, d_h is the hydraulic diameter of the column and μ is the dynamic viscosity of the liquid. The top reservoir was filled with de-ionised water. All the measurements were made at atmospheric pressure and room temperature (20°C). The experimental flow conditions are summarized in Table 1. Shadow imaging measurements were carried out at 2, 6 and 10 l/h air flow rates, while PIV measurements were performed just at 6 and 10 l/h gas flow rates.

Table 1. Experimental conditions.

	Re	Q_g [l/h]	Q_l [l/min]
1	100	2; 6; 10	0.6
2	500	2; 6; 10	3.1
3	1800	2; 6; 10	11.1
4	5000	2; 6; 10	30.8
5	9000	2; 6; 10	55.5

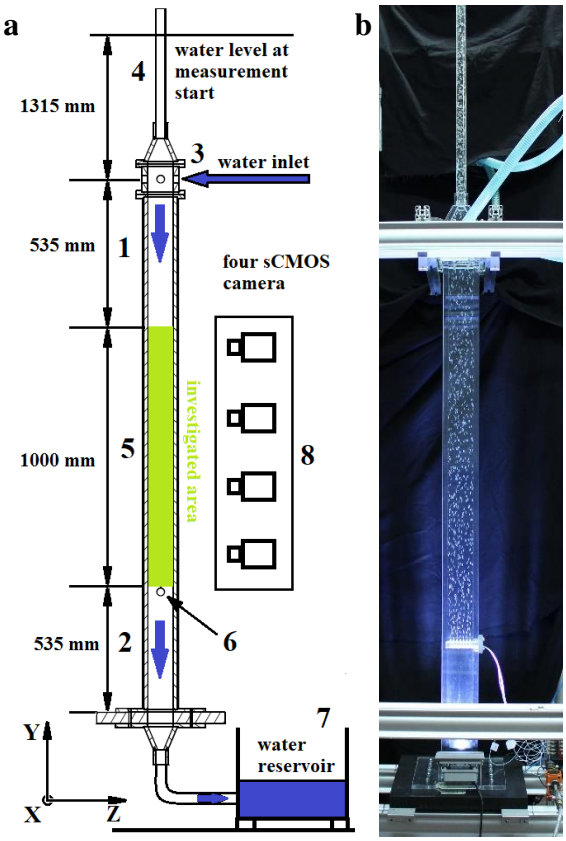

Figure 1. Experimental set-up (a) and photograph of the bubble column (b).

Shadow imaging set-up

For the shadow imaging measurements, four Imager sCMOS cameras (LaVision, (Figure 1, a 8)) were applied with a 2560 x 2160 pixels resolution and 80 Hz frame rate. The cameras were equipped with Nikon AF Nikkor 50 mm lenses. They were focused on the centre of the investigated column volume and the bubbles were, due to the depth of field, identified in a 33 mm thick region. To illuminate the measurement area and generate bubble shadows, 8 high-power COB LEDs (Luminus CXM-32) with an overall nominal power of 1120W were used. Because of the high illumination intensity and for the sake of a homogenous background illumination, the light was

diffused on white drawing paper. 3x1000 images were acquired with a frame rate of 80 Hz at each investigated condition. The experimental images were recorded and processed with the software DaVis (LaVision). Further post-processing steps were made in Matlab.

PIV set-up

For the PIV measurements, the same camera set-up was used as before for the shadow imaging, but in this set-up the cameras were equipped with band-pass filters (590 nm, 50 nm FWHM) to record only the fluorescence signal of the Rhodamin B doped polymethyl methacrylate (PMMA) seeding particles (mean diameter: 1-20 μm). These particles were excited by a double-pulse Nd:YAG laser (Quantel Evergreen) at 532nm. The laser beam was divided into two beams with a 50-50% mirror and these two beams were then expanded by two light sheet optics placed above each other, to illuminate the whole 1 m measurement section. The geometrical positions were calibrated with a 3D calibration target over the whole measurement section for both measurement methods. Overall, 4000 experimental images were acquired with 5 Hz in double frame mode for each investigated condition. The delay time between the two frames was 11 ms. From the recorded double-frame images, flow fields were calculated in DaVis. For the vector calculation, a cross-correlation (multi-pass, decreasing size) PIV algorithm was used with an interrogation window size from 64x64 pixels to 32x32 pixels, with 50% overlap. To remove false vectors and refine the vector field, especially in the vicinity and shadows of the bubbles, a median filter was applied.

3. SIMULATION SET-UP

Multiphase CFD simulations of the experiments are performed by applying the Euler-Euler framework with a set of closure relations that was extensively validated in previous works for various different geometries, including pipes, columns, and stirred tanks (e.g. [6, 7] and references therein). Concerning momentum transfer between the phases, closure comprises drag, shear-lift, wall-lift, virtual mass and turbulent dispersion forces, with models listed in Table 2. Turbulence in the liquid phase is described by a k-ω SST model (Menter [10]) with additional source terms for the bubble induced turbulence (Ma et al. [11]). In accordance with the experiments, a monodisperse approximation for the bubble size prescribing the experimentally determined mean value is suitable. The simulations are run in the open-source code OpenFOAM v8 with an add-on developed at HZDR [12].

Table 2. Summary of bubble force correlations.

force	**reference**
drag	Ishii [13]
shear lift	Tomiyama et al. [14]
wall lift	Hosokawa et al. [15]
turbulent dispersion	Burns et al. [16]
virtual mass	constant coefficient $C_{VM} = ½$

The computational domain consists of the 1 m long effective measurement section (Figure 1, a 5) together with the two 0.5 m long inlet (Figure 1, a 1) and outlet (Figure 1, a 2) sections, i.e. it is a 2 m high cuboid 0.1 x 0.1 m^2 cross section. On the side walls a no-slip condition is imposed for the liquid phase and a free-slip condition on the gas phase. Each nozzle is modelled by an individual patch through which the gas enters with a uniform velocity profile such that the total experimental flow rate is split evenly between the 7 nozzles. At the bottom of the column, a uniform flow with an outflow rate corresponding to the experiment is prescribed. At the top of the column the pressure is fixed. Since the area of observation extends only 1 m upwards from the nozzles, the effect of the imposed conditions at the column bottom and top can be expected to be small.

4. RESULTS

Shadowgraphy

The three series of 1000 acquired images were processed in DaVis to collect the parameters of each recognized bubble, like bubble major and minor axis, and velocity. The further data processing has been done in Matlab. First of all, from the major and minor axes of the bubbles the Equivalent Sphere Diameter (*ESD*) was calculated:

$$ESD = \sqrt[3]{\frac{3V_B}{4\pi}} \cdot 2\,, \qquad (1)$$

$$V_B = \frac{4}{3}\pi a^2 b, \qquad (2)$$

where V_B is the volume of the spheroid, a is the major semi-axis, and b is the minor semi- axis. For the further data evaluation, these bubble diameters were used. In the next step, the investigated domain (100x33x1000 mm^3) was divided into 5x5 mm^2 cells in which mean bubble diameters and velocities were calculated over all 3000 images. From these data, global mean parameters were calculated for each investigated condition, which are represented in Table 3. The results show that with increasing gas volume flow, the bubble size is increasing, as well as with an increasing countercurrent liquid flow. In contrast, the bubble velocity is decreasing with an increasing bubble size and it evidently decreases with an increasing countercurrent liquid

flow. Also a slight growth can be found in bubble velocities with increasing gas flow rate.

Table 3. Global mean results of bubble diameters and velocities.

Q_g [l/h]	Q_l[l/min]	*ESD* [mm]	v_b [m/s]
2	0.6	3.28	0.295
2	3.1	3.34	0.289
2	11.1	3.37	0.275
2	30.8	3.43	0.237
2	55.5	3.48	0.191
6	0.6	3.36	0.299
6	3.1	3.43	0.292
6	11.1	3.46	0.28
6	30.8	3.51	0.246
6	55.5	3.58	0.198
10	0.6	3.39	0.301
10	3.1	3.46	0.294
10	11.1	3.5	0.28
10	30.8	3.54	0.249
10	55.5	3.57	0.204

When investigating the bubble size distributions (Figure 2 and Figure 3), no significant differences can be recognized neither with increasing countercurrent liquid flow, nor increasing gas flow rate. However slightly smaller bubbles are observed at the lowest countercurrent liquid flow and at the lowest gas flow rate.

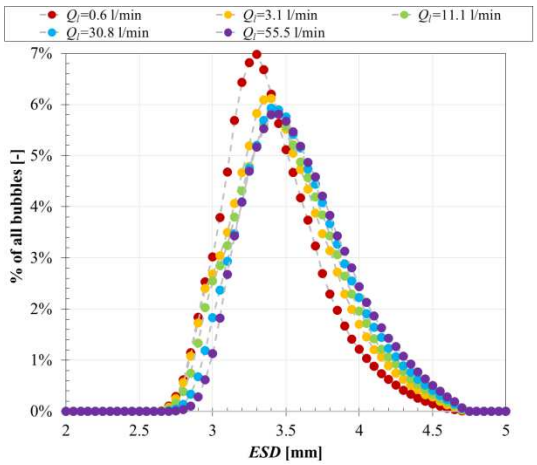

Figure 2. Bubble *ESD* distributions at different countercurrent liquid flow rates for Q_g=10 l/h air volume flow rate.

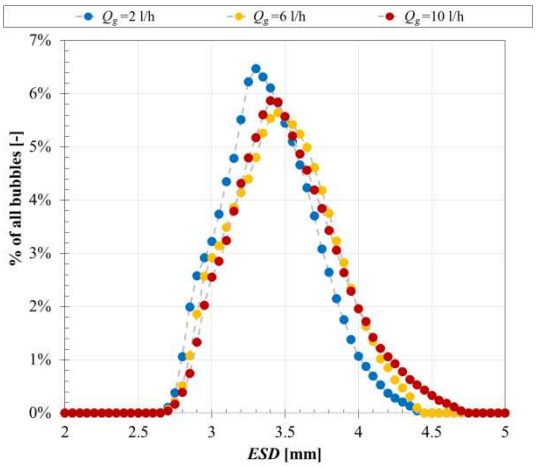

Figure 3. Bubble *ESD* distributions at different air volume flow rates for Q_l=11.1 l/min countercurrent liquid flow rate.

In contrast, considerable mean velocity changes of the bubbles at different countercurrent flow rates can be observed in the velocity distributions in Figure 4. With increasing countercurrent liquid flow, the bubble velocity distributions show similar aspects, but the peaks of the distributions are shifted towards lower velocities. Additionally, with an increasing gas flow rate, the position of the peaks of the bubble velocity distributions remains the same, but the distribution profiles become wider (Figure 5).

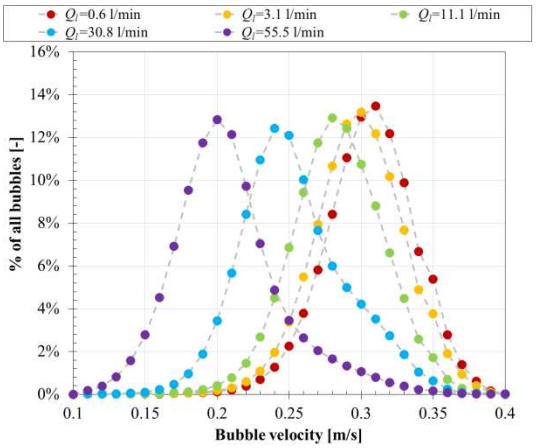

Figure 4. Bubble velocity distributions at different countercurrent liquid flow rates for Q_g=10 l/h air volume flow rate.

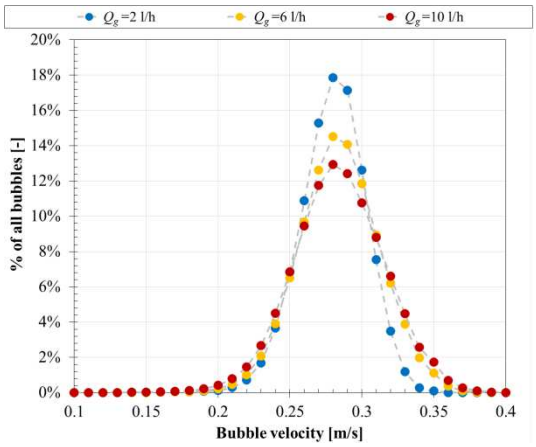

Figure 5. Bubble velocity distributions at different air volume flow rates for Q_l=11.1 l/min countercurrent liquid flow rate.

Liquid dynamics

After combining the results of all four measurement windows (obtained simultaneously with the four cameras) a full view of the liquid flow field within the column can be obtained (Figure 6).

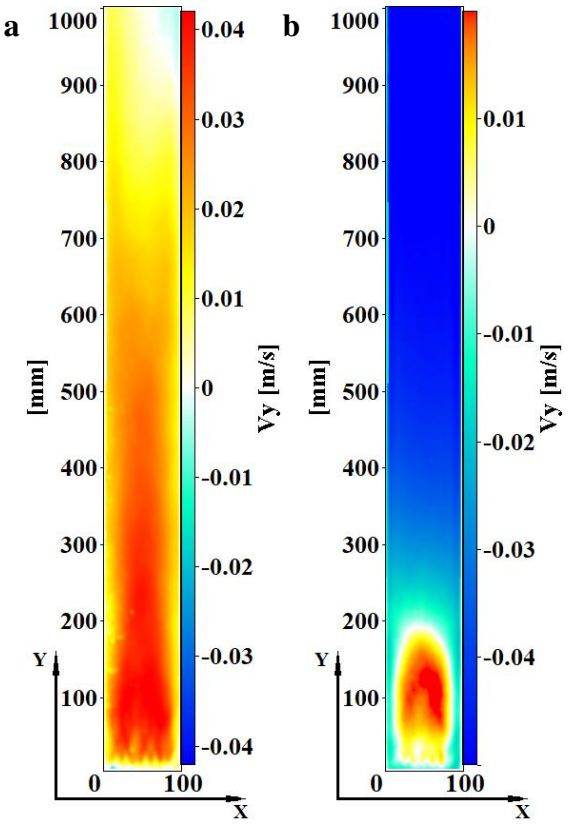

Figure 6. Mean vertical liquid velocity fields obtained from measurements with Q_g=10 l/h air flow rate for Q_l=0.6 l/min (a) and 30.8 l/min (b) countercurrent liquid flow. (Please mind the different colour scales: warm colours represent positive, cold colours negative flow directions).

As expected, the mean images show an almost symmetric vertical velocity field in the bubble column, where the rising bubbles generate an ascending flow in the centre of the column. This ascending flow is slowed down (Figure 6, a) and is stopped (Figure 6, b) by the countercurrent liquid flow. This phenomenon can be followed more clearly on the vertical velocity profiles, which are obtained in the centre of the bubble column (between 45 and 55 mm) for each investigated case (Figure 7 and Figure 8).

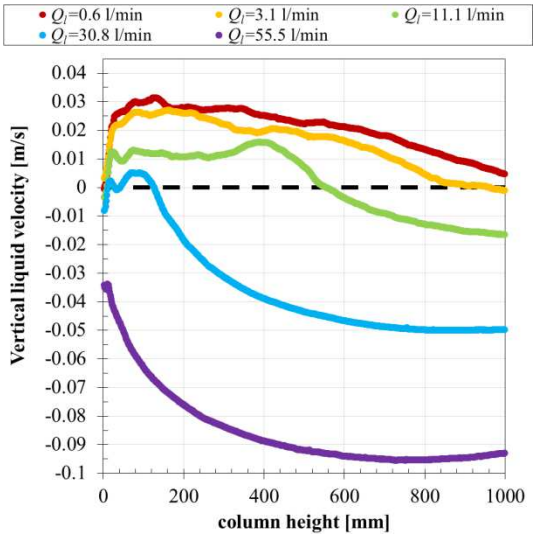

Figure 7. Vertical profiles of the mean vertical liquid velocity in the centre of the bubble column for all investigated countercurrent liquid flows at Q_g=6 l/h air flow rate.

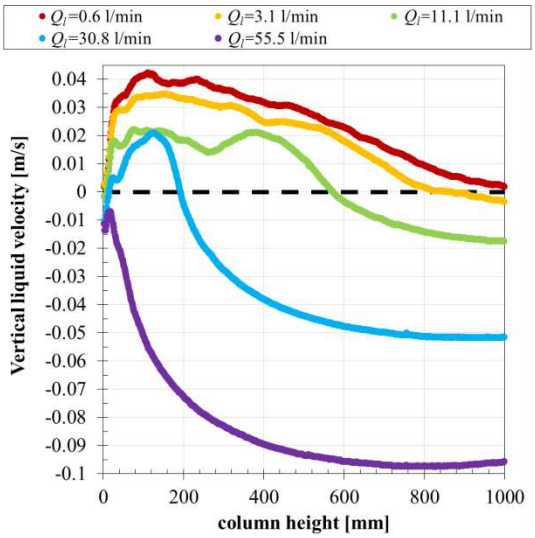

Figure 8. Vertical profiles of the mean vertical liquid velocity in the centre of the bubble column for all investigated countercurrent liquid flows at Q_g=10 l/h air flow rate.

At both investigated gas volume flow rates, 6 and 10 l/h, the vertical profiles show similar trends

at the same countercurrent liquid flow rate. However, due to the slightly larger bubbles and higher bubble velocities, higher vertical velocities are measured at higher gas volume flow rate (Figure 8). At the two lowest liquid flow rates, 0.6 and 3.1 l/min, the bubble generated ascending flow dominates the flow in the bubble column. Starting from the inlet nozzles up to around 100 mm the vertical liquid velocity increases and then it continuously decreases to the end of the investigated domain at 1000 mm. At 11.1 l/min countercurrent liquid flow the vertical velocity increases close to the inlet nozzles, but then it stagnates at around 400 mm. From this height, the vertical liquid velocity suddenly decreases and the flow changes its direction around 580 mm above the nozzles due to the higher countercurrent liquid flow. This point, where the direction of the flow changes, is shifted towards the nozzles with higher countercurrent liquid flow rates. The trend of the vertical velocity profiles at the highest countercurrent liquid flow rates, 30.8 and 55.5 l/min, are nearly the same from 400 mm upwards at both investigated gas flow rates. Below 400 mm, the influence of the different gas flow rates can be observed. As a result of the higher gas flow rate, higher vertical liquid velocities are obtained in this region.

If the measured bubble velocities and vertical liquid velocities are plotted together in one plot, it becomes obvious, that the liquid flow follows the same trend as the bubble velocities. As well as the liquid velocity, also the bubble velocity decreases continuously from 100 mm along the column height at lower countercurrent liquid flows (Figure 9). In these cases, the liquid flow is dominated by the bubbles. Similarly, at higher countercurrent liquid flows (Figure 10) the liquid velocity profiles follow the bubble velocity profiles. Here, the influence of the bubbles on the liquid flow is reduced with the increasing countercurrent liquid flow.

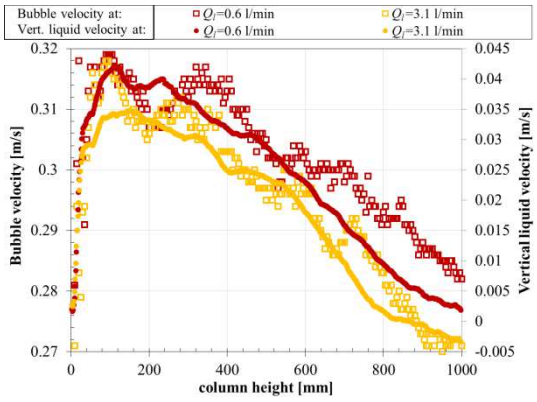

Figure 9. Vertical profiles of the mean vertical bubble velocity and the mean vertical liquid velocity in the centre of the bubble column for Q_l=0.6 and 3.1 l/min countercurrent liquid flows at Q_g=10 l/h air flow rate.

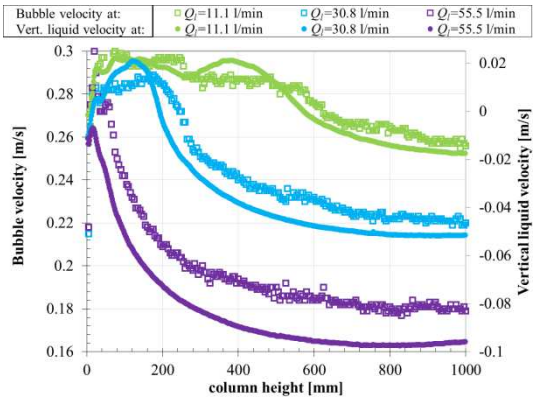

Figure 10. Vertical profiles of the mean vertical bubble velocity and the mean vertical liquid velocity in the centre of the bubble column for Q_l=11.1, 30.8 and 55.5 l/min countercurrent liquid flows at Q_g=10 l/h air flow rate.

From these results it is evident, that with increasing countercurrent flow the bubble velocity decreases, therefore the bubble residence time in the column increases, which is beneficial for mass transfer. From another point of view, in two-phase flows with mass transfer, besides a high residence time also a good mixing is demanded, which enhances mass transfer. Analysing the horizontal liquid velocities in the bubble column (Figure 11), it is noticeable that at the highest countercurrent liquid flow rates at 30.8 and 55.5 l/min, where the bubble residence time is the highest, horizontal velocity fluctuations can be found just in the first 1-200 mm above the inlet nozzles.

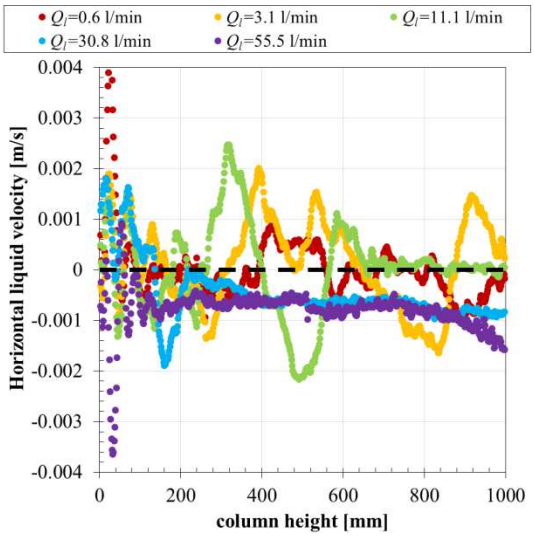

Figure 11. Vertical profiles of the mean horizontal liquid velocity in the centre of the bubble column for all investigated countercurrent liquid flows at Q_g=10 l/h air flow rate.

At lower countercurrent liquid flow rates, where the bubbles have larger effect on the liquid flow in the bubble column, much higher horizontal liquid velocities are measured. Supposedly the best mass transfer rate could be achieved at 11.1 l/min countercurrent liquid flow, where the bubble velocity is noticeably lower than in the cases with 0.6 and 3.1 l/min and remarkably horizontal liquid velocity fluctuations are measured.

Simulation results

For comparison between simulation and experiment, profiles are extracted at the upper edge of the observation region 1 m above the nozzles along the line in which these are arranged (x-direction). Since the flow is unsteady, the simulation data are averaged over a period of time, which has been determined to be sufficiently long to reproduce the expected mirror symmetry in the profiles to a good approximation. In addition, to match the experimental setup, the calculated values are averaged in the horizontal direction perpendicular to the line of the nozzles (y-direction) over a region corresponding to the depth-of-field of the camera used in the measurements.

An exemplary comparison between calculated and measured gas fraction profiles is shown in Figure 12 with the experimental conditions indicated in the caption. The experimental gas fraction here has been determined from the measured bubble trajectories by counting the frequency of occurrence of a bubble centre in cells of a 5 mm^3 grid and multiplying by the bubble volume.

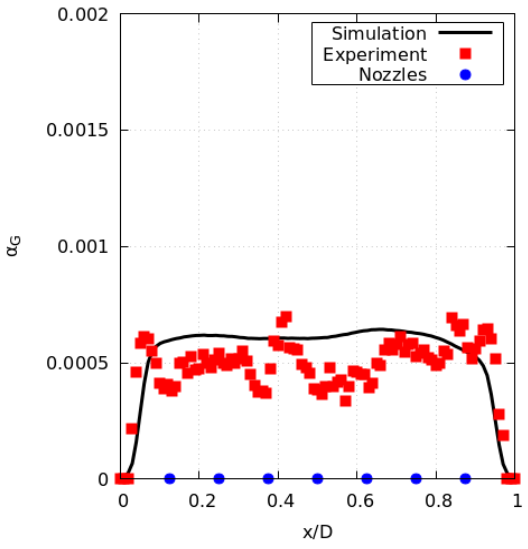

Figure 12. Comparison of calculated (line) and measured (symbols) gas fraction profiles for Q_l=0.6 m/s and Q_g=2 l/h. Bubbles had a mean size of d_b =3.8 mm.

As can be seen from the figure, the overall agreement between simulation and experiment is quite good. The average value in the central part of the column is slightly overpredicted by the simulations, but the drop near the column walls is captured very well. Some amount of fluctuations is visible in the measurements, which is likely due to unavoidable differences between the 7 nozzles resulting in somewhat uneven injection of gas. Such differences are of course absent in the simulations.

The result from the simulations for the liquid and gas velocities for the same flow conditions is shown in Figure 13. For this condition, the liquid flow was not measured so that a direct comparison to the experiment is not possible yet. A more comprehensive comparison for further observables and varied experimental conditions will be pursued in the near future.

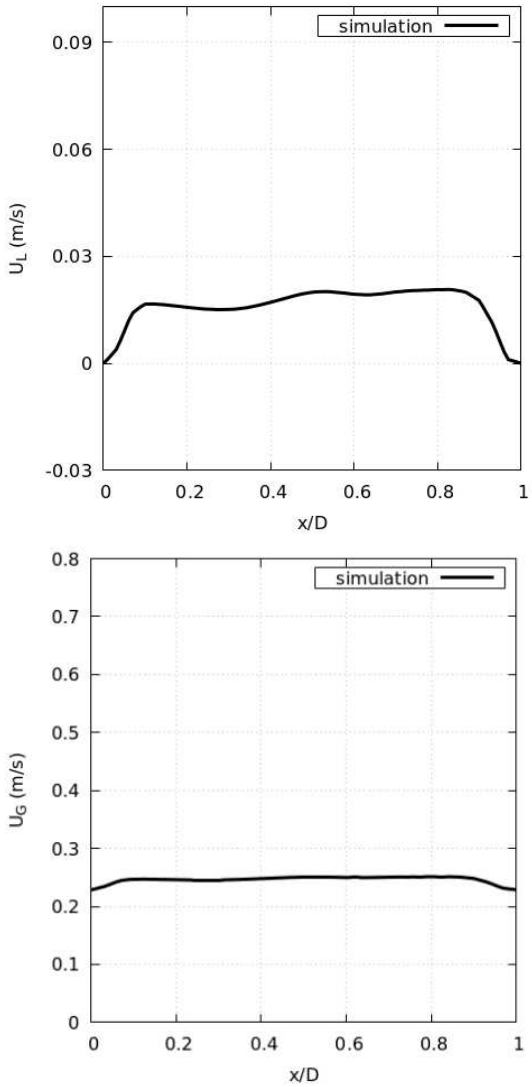

Figure 13. Simulated profiles for the liquid (top) and gas (bottom) velocities at Q_l=0.6 m/s and Q_g=2 l/h respectively.

5. CONCLUSIONS

In this paper two optical measurement techniques for characterizing the fluid dynamics of a countercurrent laboratory-scale bubble column reactor have been used. Shadow imaging combined with PTV was applied to obtain bubble parameters like bubble major and minor axis, and velocity, while the PIV technique was employed to characterize the liquid flow.

The analysis of the gathered bubble diameters has shown that no significant differences exist in the bubble size neither with increasing countercurrent liquid flow, nor with increasing gas flow rate. In contrast, as it was expected, the mean bubble velocity decreases continuously with increasing countercurrent liquid flow.

With the help of PIV, the flow field in the bubble reactor was investigated at different gas and countercurrent liquid flow rates. Combining the images of the four cameras, a full description of the hydrodynamics in the whole column was obtained. It has been found that at lower countercurrent liquid flows the flow is driven by the bubbles, while at higher countercurrent flow rates the ascending liquid flow, generated by the bubbles, is slowed down or close to the inlet nozzles even stopped. This phenomenon could considerably influence the mass transfer in the bubble column. For this reason, also mass transfer measurements are planned for the future in the bubble column.

Euler-Euler simulations according to the experimental setup were run using previously established closure models. A preliminary comparison between simulation results and measured data suggest, that these models are also applicable to the present case. This remains to be verified by a more detailed and comprehensive analysis which is still in progress.

ACKNOWLEDGEMENTS

Authors would like to thank the German Research Foundation (DFG) for the financial support under Grant No ZA 527/3-1 and RZ 11/3-1. We would also like to acknowledge the experimental support of our students Steffen Erichson and Maximilian Mahler. The workshop of LSS supported the set-up of the bubble column and measurement arrangement.

REFERENCES

[1] Joshi JB, Nandakumar K (2015), Computational Modeling of Multiphase Reactors. Annual Review of Chemical and Biomolecular Engineering 6:347-378

[2] Guo K, Wang T, Liu Y, Wang J (2017), CFD-PBM simulations of a bubble column with different liquid properties. Chem Eng J 329:116-127

[3] Besagni G, Guédon GR, Inzoli F (2018), Computational fluid-dynamic modeling of the mono-dispersed homogeneous flow regime in bubble columns. Nucl Eng Des 331:222-237

[4] Braga Vieira C, Litrico G, Askari E, Lemieux G, Proulx P (2018), Hydrodynamics of Bubble Columns: Turbulence and Population Balance Model. ChemEngineering 2:12

[5] Rzehak R, Krauss M, Kovats P, Zahringer K (2017), Fluid dynamics in a bubble column: New experiments and simulations. Int J Multiphase Flow 89:299-312

[6] Rzehak R, Ziegenhein T, Kriebitzsch S, Krepper E, Lucas D (2017), Unified modeling of bubbly flows in pipes, bubble columns, and airlift columns. Chem Eng Sci 157:147-158

[7] Shi P, Rzehak R (2018), Bubbly flow in stirred tanks: Euler-Euler/RANS modeling. Chem Eng Sci 190:419-435

[8] Kováts P, Thévenin D, Zähringer K (2018), Characterizing fluid dynamics in a bubble column aimed for the determination of reactive mass transfer. Heat Mass Transfer 54:453-461

[9] Kováts P (2021), Detailed experimental study of mass transfer and liquid flow in a bubble column with optical measurement techniques, Laboratory of Fluid Dynamics and Technical Flows.

[10] Menter FR (2009), Review of the shear-stress transport turbulence model experience from an industrial perspective. International Journal of Computational Fluid Dynamics 23:305-316

[11] Ma T, Santarelli C, Ziegenhein T, Lucas D, Fröhlich J (2017), Direct numerical simulation–based Reynolds-averaged closure for bubble-induced turbulence. Physical Review Fluids 2,

[12] Schlegel F, Draw M, Evdokimov I, et al. (2021), HZDR Multiphase Addon for OpenFOAM.

[13] Ishii MZ, N. (1979), Drag coefficient and relative velocity in bubbly, droplet or particulate flows. AlChE J 25:843-855

[14] Tomiyama A, Tamai H, Zun I, Hosokawa S (2002), Transverse migration of single bubbles in simple shear flows. Chem Eng Sci 57:1849-1858

[15] Hosokawa S, Tomiyama A, Misaki S, Hamada T (2002), Lateral Migration of Single Bubbles Due to the Presence of Wall.855-860

[16] Burns AD, Frank T, Hamill I, Shi JM, The Favre Averaged Drag Model for Turbulent Dispersion in Eulerian Multi-Phase Flows. In: 5th International Conference on Multiphase Flow, Yokohama, Japan, (2004).

Conference on Modelling Fluid Flow (CMFF'22)
The 18th International Conference on Fluid Flow Technologies
Budapest, Hungary, August 30-September 2, 2022

Dynamics of high-speed drop impact on deep liquid pool

Hui WANG[1], Shuo LIU[2], Annie-Claude BAYEUL-LAINÉ[3], Olivier COUTIER-DELGOSHA[4]

[1] Corresponding Author. Univ. Lille, CNRS, ONERA, Arts et Metiers Institute of Technology, Centrale Lille, UMR 9014 - LMFL - Laboratoire de Mécanique des Fluides de Lille - Kampé de Fériet, F-59000 Lille, France. Tel.: +33 06 08 10 25 28, E-mail: hui.wang@ensam.eu
[2] Univ. Lille, CNRS, ONERA, Arts et Metiers Institute of Technology, Centrale Lille, UMR 9014 - LMFL - Laboratoire de Mécanique des Fluides de Lille - Kampé de Fériet, F-59000 Lille, France. E-mail: shuo.liu@ensam.eu
[3] Univ. Lille, CNRS, ONERA, Arts et Metiers Institute of Technology, Centrale Lille, UMR 9014 - LMFL - Laboratoire de Mécanique des Fluides de Lille - Kampé de Fériet, F-59000 Lille, France. E-mail: annie-claude.bayeul-laine@ensam.eu
[4] Univ. Lille, CNRS, ONERA, Arts et Metiers Institute of Technology, Centrale Lille, UMR 9014 - LMFL - Laboratoire de Mécanique des Fluides de Lille - Kampé de Fériet, F-59000 Lille, France. E-mail: olivier.coutier-delgosha@ensam.eu

ABSTRACT

In this work, high-speed drop impact onto deep volume of the same liquid is numerically studied in 3D using Direct Numerical Simulation (DNS). The numerical results are compared with the previous experimental works by Murphy et al. [1]. Most of the distinctive features during the impact, including the evolution of the crown and cavity, the ligaments emanating from the rim of the crown, the formation of the bubble canopy, the central spiral jet that pierces through the bottom of the cavity and the subsequent broad upward jet, are correctly reproduced. The trajectory of the upper rim of the crown as well as the depth and width of the subsurface cavity are tracked during the simulation. Very reliable quantitative agreements between numerical and experimental data are obtained with respect to the time evolution of the crown rim and cavity dimensions. The simulation shows very good qualitative and quantitative agreement against the available experimental data, which enables the further investigation of the internal mechanisms of drop impact in the future.

Keywords: bubble canopy, crown and cavity, Direct Numerical Simulation, high-speed drop impact, splashing

NOMENCLATURE

H	$[m]$	computational pool depth
L	$[m]$	computational size of domain
P	$[Pa]$	pressure field
d	$[m]$	drop diameter
f	$[-]$	volume fraction
u_0	$[m/s]$	initial impacting speed
$\underline{U}$	$[m/s]$	velocity field
$\underline{\underline{D}}$	$[-]$	deformation tensor
$\underline{a}$	$[m/s^2]$	body force
$\underline{g}$	$[m/s^2]$	gravity
$\underline{n}$	$[-]$	unit vector normal to the interface
δ	$[m]$	initial gap between drop and pool
κ	$[m^{-1}]$	curvature
μ	$[Pa \cdot s]$	dynamic viscosity
ρ	$[kg/m^3]$	density
σ	$[N/m]$	surface tension coefficient

Subscripts and Superscripts

h, v	horizontal and vertical direction
w, a	water phase, air phase

1. INTRODUCTION

The process of drop impact is widely observed in nature and involves many fascinating physical phenomena, but challenging for further studying due to the increased complexity of multi-scale flows and interfacial dynamics [2]. Knowing from daily shower, natural rainfall, soil erosion [3, 4], industrial spray injecting&cooling [5, 6] and agriculture irrigation [7], drop impact exists ubiquitously in our life. Scientific research on uncovering the internal mechanisms of drop impact thus shows huge potential in facilitating the technical applications in various areas where this process is involved.

Since the path-breaking works started more than a century ago [8], various studies of drop impact have been initiated afterwards. Different scenarios of drop impact regarding to liquid [9, 10] or solid target [11, 12], shallow [13, 14] or deep pool [15, 16], miscible [17] or immiscible [18] liquids have been discussed. For drop impact on deep pool, three dimensionless parameters are usually used to describe the splashing, namely Reynolds number $Re = \rho u_0 d/\mu$, Weber number $We = \rho u_0^2 d/\sigma$ and Froude number

$Fr = u_0^2/gd$, where ρ is liquid density, u_0 is initial impacting speed, d is drop diameter, $\underline{g}$ is gravity, μ and σ are viscosity and surface tension. In order to uncover the underlying flow physics, multiple aspects of drop impact such as the behaviour of initial liquid sheet [16, 19, 20, 21], air bubble entrainment [22, 23], evolution of crown and cavity [14, 24, 25], as well as the formation of secondary droplets [1, 26] have been broadly investigated.

In the most recent works, attention has been especially focused on the first stages of impact, where the liquid sheet is ejected from the neck and the entrapped air layer under the droplet is ruptured, resulting in the splashing of very fine spray [19, 27] and the generation of secondary bubbles [28, 22, 23], but the mechanisms are still not well elucidated. Additionally, the non-axisymmetric behaviors of vortex shedding and the observed ejecta behaviour from bottom visualizations in cases of impacts on thin films [29] show that these phenomena break the axisymmetry at fine scale, and may be related to three-dimensional mechanisms. This clearly poses a new challenge to numerical studies, which mostly assume axisymmetry [21, 30]

As for later stages of the impact, qualitatively different regimes of phenomenon have been categorized [31, 32, 33, 34] at relatively small range of Re and We numbers, depending on various impacting conditions. For the most energetic regime of drop impact with higher impacting speed and larger drop diameter, the interfical dynamics can be significantly modified. As schemed by Engel [15], after the first stage of splashing, the liquid sheet expands radially and forms a thin-walled 'crown' above the surface of the target pool. Next, the rim of the crown rises to a maximum position and then closes up into a "bubble canopy" followed by a central liquid jet, trapping a volume of air inside. In this process, ligaments emanate from the rim of crown and eject a great number of fine droplets to the air upwards and outwards. Such tiny airborne droplets may raise potential health issues to the public under certain circumstances [1].

Numerical approaches have been employed to the analysis of drop impact since decades. Both axisymmetric [35, 14, 36, 32, 30] and three dimensional [37, 38, 39] simulations can be found in literature, using mostly DNS approaches. For three-dimension calculations, whose primary objective is to capture the non-axisymmetric mechanisms involved in the splashing. Efforts are focused on dynamic refinement techniques [40, 41], in order to resolve the multiple interfaces resulting from the splashing, while ensuring a reasonable grid size. In the latter study, the authors show that a minimum cell size of about 50 to 100 μm is sufficient to capture most of the features of the splash. However, that conclusion was drawn for Weber numbers around 250, so it may not directly apply to the configuration investigated in the present study.

In this work, we perform three-dimensional direct numerical simulation (DNS) of high-speed drop impact on deep liquid pool. The paper is organized as follows: the numerical approaches are described in Section 2, the flow configurations and numerical parameters are explained in Section 3, the numerical results are demonstrated and discussed in Section 4 and the paper is summarized in Section 5.

2. NUMERICAL APPROACHES

2.1. Governing equations

The drop impact of gas-liquid system is considered as incompressible flows, and it solves a system of the mass balance equation Eq. (1), the momentum balance equation Eq. (2) and the advection of one-fluid formulation Eq. (3), called hereafter the color function.

$$\nabla \cdot \underline{U} = 0 \tag{1}$$

$$\rho\left(\frac{\partial \underline{U}}{\partial t} + (\underline{U}\cdot\nabla)\underline{U}\right) = -\nabla P + \nabla\cdot(\mu\underline{\underline{D}}) + \rho\underline{a} + \sigma\kappa\delta_s\underline{n} \tag{2}$$

$$\frac{\partial f}{\partial t} + \nabla\cdot(f\underline{U}) = 0 \tag{3}$$

Where $\underline{U}$ the velocity field, ρ the density, P the pressure, μ the viscosity, $\underline{\underline{D}}$ the deformation tensor, $\underline{a}$ the body force along the impacting direction. The last term in Eq. (2) is the surface tension force, with κ the curvature of the interface, σ the surface tension coefficient which is taken as constant in the present study, and $\underline{n}$ the unit vector normal to the interface. This term is zero everywhere but at the liquid/gas interface, as controlled by the Dirac function δ_s. The volume fraction f is transported by color function in Eq. (3).

2.2. Numerical solver

We use the open source Basilisk framework [42] to simulate the process of drop impact. The momentum-conserving volume-of-fluid (MCVOF) numerical scheme, introduced by Fuster & Popinet [43], is employed here to simulate the problem of two-phase flow. The color function (Eq. (3)) is solved based on a volume fraction advection scheme proposed in [44], which exhibits the complete mass conservation and makes it ideal for highly energetic free-surface flows. The interface then can be represented using Piecewise Linear Interface Capturing (PLIC) VOF method [45]. For Eq. (2), the Crank–Nicholson discretization of the viscous terms is second order accurate in time and unconditionally stable, while the convective terms are computed using the Bell-Colella-Glaz (BCG) second order unsplit upwind scheme [46], which is stable for CFL numbers smaller than one. The surface tension is

calculated using the continuum surface force (CSF) model described in [47].

The tree-based structure [48] of the spatial discretization is applied to adaptively follow the smallest structures of flow, thus concentrating the computational effort on the area where it is most needed. Starting from a root cell so called "parent"cell at level 0, eight "children" cells will be generated in 3D at level 1 (four "children" in 2D). With the maximum level of refinement n, the finest resolution will be 2^n in each dimension, and various level of local refinement can be presented in the spatial domain at the same time.

Basilisk employs the Adaptive Mesh Refinement (AMR) [49] to adaptively refine/coarsen the grids based on the wavelet-estimated numerical error of the local dynamics, which makes it especially appropriate for the present application where multiple interfaces and numerous droplets and bubbles are expected. The resolution will be adapted every time step according to the estimated discretization error of the spatially-discretized fields (volume fraction, velocity, curvature..). The grid will be refined as long as the wavelet-estimated error exceeds the given threshold, which eventually leads to a multi-level spatial resolution from minimum level L_{min} to maximum level L_{max} over the domain.

The great superiority of parallel capacity and computational efficiency of Basilisk code are discussed in [50]. The capabilities of Basilisk solver have been extensively validated on various problems for multi-phase complex flows here [42].

3. NUMERICAL PARAMETERS

In this work, we reproduce one specific case of high-speed drop impact that was discussed in [1] as a control case for the study of raindrop impact onto oil slick. We use the artificial seawater here for both the drop and pool, since the properties of the liquids are almost the same. The surrounding gas is air. The density and viscosity ratios between seawater and air are $\rho_w/\rho_a = 1018$ and $\mu_w/\mu_a = 180$. The drop is defined as an oblate ellipsoid with horizontal and vertical diameters $d_h = 0.0043m$ and $d_v = 0.0038m$ respectively, which leads to an average diameter $d \approx 0.004m$. The terminal speed of the drop before impact is $u_0 = 7.2m/s$.

As shown in Figure 1, the drop is initialized above the free surface of the liquid pool and the computational domain is a cubic with a side length $L = 16d$. The initial undisturbed surface of pool is located in the middle of the vertical direction, thus the depth of the pool is $H = 8d$, which ensures enough space for the growth of crown and cavity as well as avoids any wall effects from boundaries. The initial gap between drop and pool is $\delta = 0.1d$, allowing the observation of air sheet entrainment near the contact line. The free outflow boundary conditions are imposed on the top of the domain, while the symmetry boundary conditions are applied by default for other boundaries.

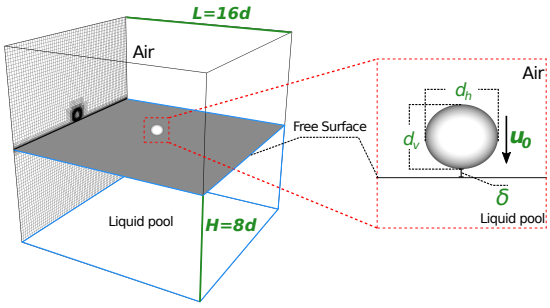

Figure 1. Initial numerical configurations of three-dimensional simulation. The left panel shows the overall computational domain and the initial mesh refinement at a plane cross the center of drop. The right panel shows a zoomed-in view near the drop

At the initial time, it is expected to refine the mesh with a higher level in the vicinity of the drop and free surface as shown in Fig.1, and the mesh is coarser gradually away from the interface. This will give a promising geometric description of the drop and free surface at the beginning and lower the RAM requirement for initialization. Once the simulation starts, the mesh will be redistributed adaptively based on the AMR algorithm using the volume fraction field with tolerance $fErr = 7e-4$ and the velocity field with tolerance $uErr = 1e-1$ as adaption criteria .

We have carried out extensive tests to explore the effects of the minimum spatial resolution in comparison with experimental data. One finds that the dynamics of the early-time liquid sheet and the entrapped air bubble affects significantly the subsequent formation of the thin-walled crown and its closure at high Re and We numbers. Our preliminary study have shown that a grid resolution of at least 1024 cells per diameter is necessary to capture the correct regime of early splashing for the present work. This will need to apply a maximum level of refinement at $L_{max} = 14$, which corresponds to an equivalent uniform grid of more than 4.3 trillion $[(2^{14})^3]$ cells.

Based on the physical characteristics during the impact, we have divided the simulation into two consecutive stages, namely the early-time splashing stage when $t \leqslant 2ms$ (***S1***) and the later crown stage when $t > 2ms$ (***S2***). At stage ***S1***, very thin liquid sheet is ejected and interacts strongly with the surface of the drop&pool, and numerous very fine droplets and bubbles are formed, thus the primary objective would be to capture the flow dynamics near the contact region in finer scale. Figure 2 shows the mesh refinement strategy applied at initial stage. A higher maximum level $L_{max} = 14$ $(3.9\mu m)$ is used in the vicinity of the free surface to resolve the dy-

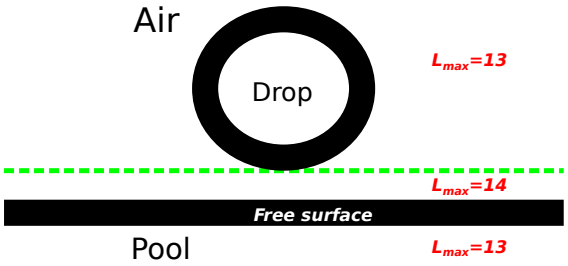

Figure 2. Mesh refinement strategy at stage *S*1. The region close to the free surface of the pool is calculated at higher maximum refinement (L_{max} = 14) for capturing the early-time dynamics of the very thin liquid sheet

namics of the liquid sheet in smaller scale, while L_{max} = 13 (7.8μm) is used for the rest of the domain to capture the statistics of droplets and bubbles. At stage ***S*2**, the crown has been developed and the rim of the crown is thickened due to the effect of surface tension. The secondary droplets shed from the top of the crown at this stage are generally in larger scales, comparing with the one from the initial stage. Therefore, we restart the simulation at $t = 2ms$ using the saved "dump" file from the initial stage with L_{max} = 12 (15.6μm) over the whole computational domain, which allows to capture the main physical dynamics of the crown and cavity till the end of the simulation ($t = 48ms$). This mesh refinement strategy ensures that the simulation is doable in a full three-dimensional configuration and can be accomplished in a "reasonable" time, in considering the available computational resources. The numerical results presented in section 4 were performed on 1024 cores for 33.5 days, which consumes more than 8.21×10^5 CPU-hours totally, using the computational resources on Advanced Research Computing (ARC) at Virginia Tech.

4. RESULTS

4.1. Phenomenology

Figure 3 shows the global evolution of high-energy drop impact during the 48ms after contact. The side-view of numerical results (bottom) are compared with experimental holograms (top) in time series. The time point of the contact is defined as t = 0. At t=-1ms, the drop is initialised above the surface of pool. Once the simulation starts, the drop will fall downwards to hit the pool driven by the combination of initial impacting speed and gravitational force. Directly after the impact (t=1ms), a cylindrical wave is generated around a flat-bottomed disk-like cavity due to the violent penetration of drop liquid. At this time, most of the drop liquid is concentrated on the bottom of the cavity and the submergence of the drop/pool interface can be approximated as half of the initial drop impacting velocity [51]. Next, the drop keeps expanding and spreads into a thin layer of

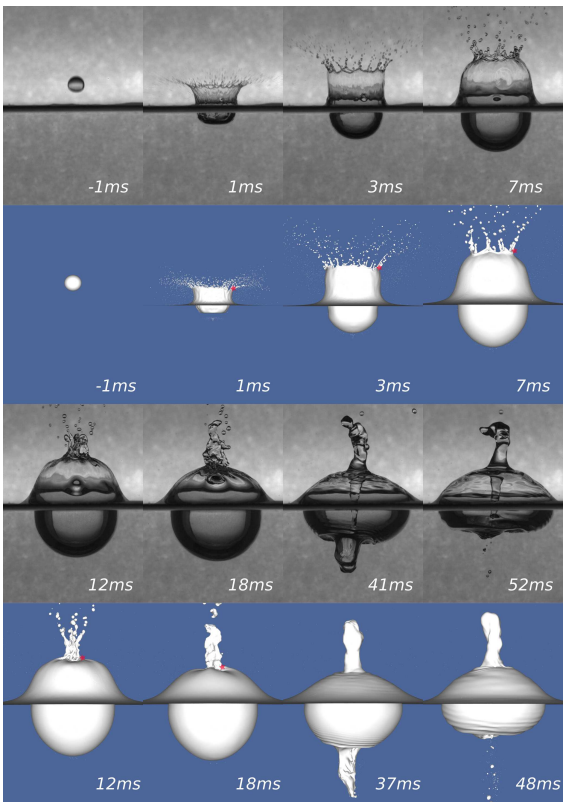

Figure 3. Qualitative comparisons between experimental and numerical results for high-speed drop impact. The red stars indicate the tracked positions of the crown rim

liquid that is distributed along the interior surface of the cavity, stretching the cavity into a typical hemispherical shape (t=3ms). By t=7ms, the orientation of the rim of ligament transitions from almost horizontal to vertical and the top of the crown starts to bend towards the center. At around t=12ms, the crown eventually closes up, trapping a volume of air inside. After the closure of the crown rim, a central spiral jet is then ejected vertically from the merging point and the downward moving jet eventually pierces the cavity bottom at t=37ms, which will result in the formation of a broad upward jet evidenced at t=48ms.

The qualitative comparison shows that our simulation reproduces all the distinctive features observed in the experiments. The correct prediction of the morphologic behavior of the air-water interface, the transition of ligaments orientation, and the exact time where the upper rim of the crown necks in and the central spiral jet pierces the cavity bottom are especially convincing. A general good agreement to the experiments is obtained.

4.2. Kinematics

For further validating our numerical strategy, the kinematic behaviors of the crown and cavity are extracted from numerical and experimental results.

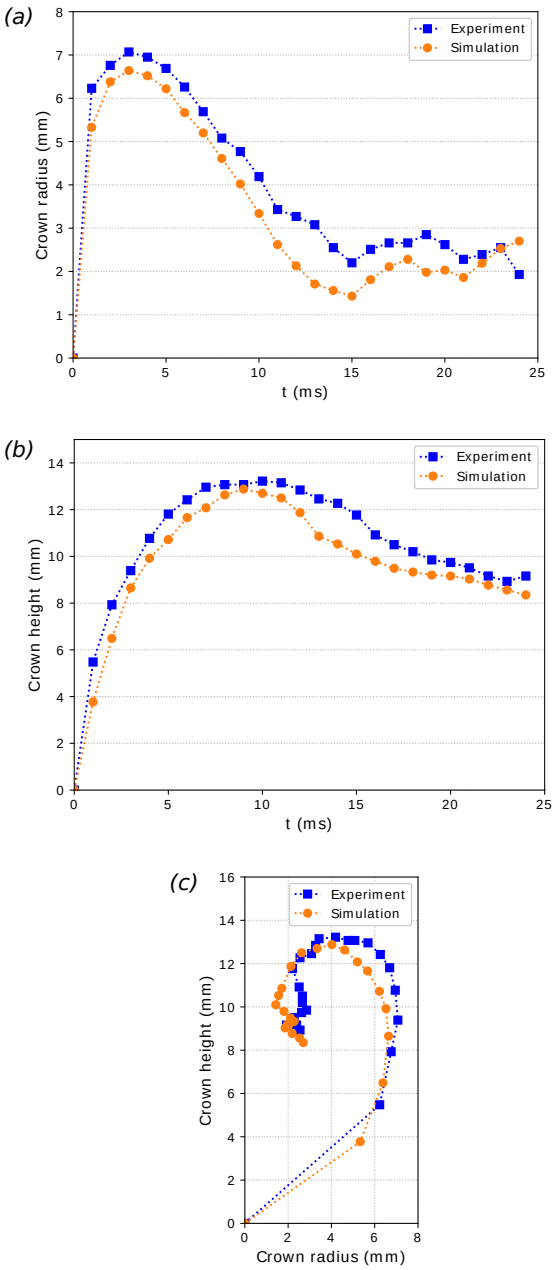

Figure 4. Analysis of the kinematic behaviours of the rim of the crown with time. The definition of the positions of the crown rim are marked as red stars in Fig. 3. (a) Radius of crown rim, (b) Height of crown rim and (c) Trajectory of crown rim

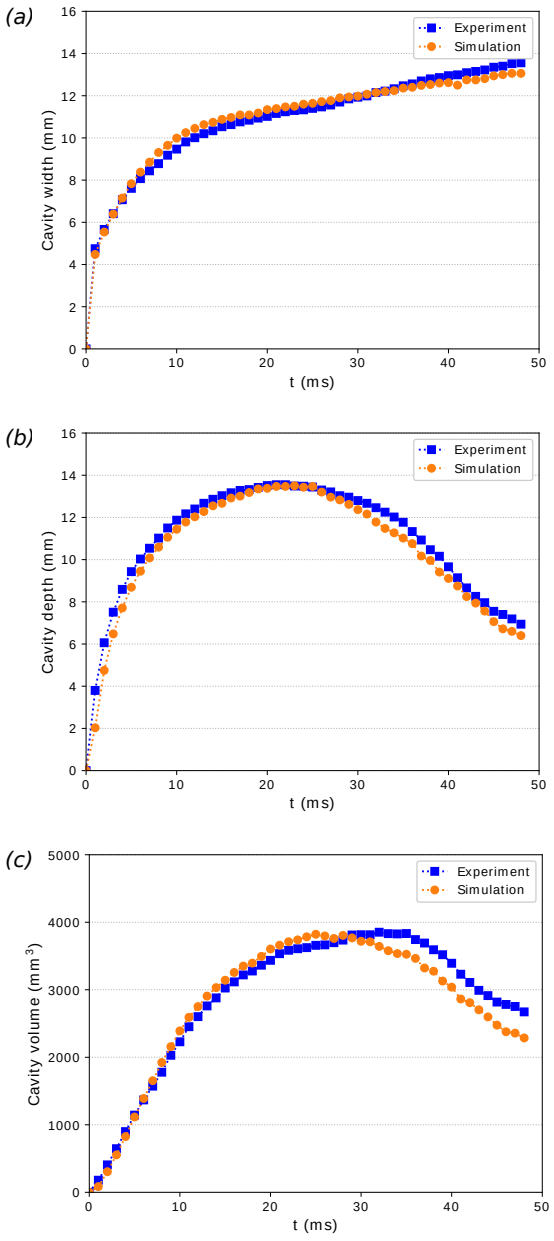

Figure 5. Analysis of the kinematic behaviours of the subsurface cavity with time. (a) Width of cavity, (b) Depth of cavity and (c) Volume of cavity

Figure 4 tracks the positions of the rim of the crown with time. The variation of the radius and height of the crown rim are shown in Fig. 4 (a) and (b), and the trajectory of the crown rim is then plotted in Fig. 4 (c). Below the initial free surface, the dimensions of the radially expanding cavity are also characterized by its width and depth in Figure 5 (a) and (b). The volume of the cavity thus is calculated as half of an ellipsoid in Fig. 5 (c).

Fig. 4 and 5 confirms this conclusion: both the trajectory of the edges of the upper rim and the dimensions of the subsurface cavity are also found in very good quantitative agreement with the experimental measurements.

5. SUMMARY

We present numerical investigation of the high-speed drop impact on deep liquid pool using direct numerical simulation. The full three-dimensional simulations are performed based on the Basilisk framework using volume of fluid and adaptive mesh refinement techniques. The simulations have been conducted in the exact same configuration described

in [1], for the purpose of a detailed comparison with available experimental data. It shows that our simulation successfully reproduced all the distinctive features observed in the experiments. We also found very good quantitative agreements between numerical and experimental results with respect to the trajectory of the crown rim, the cavity dimensions as well as the time point where the dome closes up and the central spiral jet pierces the cavity bottom. The rather good validation confirms the feasibility of the numerical scheme, which also enables to prepare in a future work an in-depth analysis of the internal physical mechanisms that is hard to be observed in the experiments.

ACKNOWLEDGEMENTS

This work has been supported by the scholarship from China Scholarship Council (CSC) under the Grant CSC NO. 201908320462.

REFERENCES

[1] Murphy, D. W., Li, C., d'Albignac, V., Morra, D., and Katz, J., 2015, "Splash behaviour and oily marine aerosol production by raindrops impacting oil slicks", *Journal of Fluid Mechanics*, Vol. 780, pp. 536–577.

[2] Deegan, R., Brunet, P., and Eggers, J., 2007, "Complexities of splashing", *Nonlinearity*, Vol. 21 (1), p. C1.

[3] Ekern, P. C., 1951, "Raindrop impact as the force initiating soil erosion", *Soil Science Society of America Journal*, Vol. 15 (C), pp. 7–10.

[4] Joung, Y. S., and Buie, C. R., 2015, "Aerosol generation by raindrop impact on soil", *Nature communications*, Vol. 6 (1), pp. 1–9.

[5] Kim, J., You, S., and Choi, S. U., 2004, "Evaporative spray cooling of plain and microporous coated surfaces", *International Journal of Heat and Mass Transfer*, Vol. 47 (14-16), pp. 3307–3315.

[6] Srikar, R., Gambaryan-Roisman, T., Steffes, C., Stephan, P., Tropea, C., and Yarin, A., 2009, "Nanofiber coating of surfaces for intensification of drop or spray impact cooling", *International Journal of Heat and Mass Transfer*, Vol. 52 (25-26), pp. 5814–5826.

[7] Yan, H., Bai, G., He, J., and Li, Y., 2010, "Model of droplet dynamics and evaporation for sprinkler irrigation", *Biosystems engineering*, Vol. 106 (4), pp. 440–447.

[8] Worthington, A. M., 1883, "On impact with a liquid surface", *Proceedings of the Royal Society of London*, Vol. 34 (220-223), pp. 217–230.

[9] Mukherjee, S., and Abraham, J., 2007, "Crown behavior in drop impact on wet walls", *Physics of fluids*, Vol. 19 (5), p. 052103.

[10] Guo, Y., Lian, Y., and Sussman, M., 2016, "Investigation of drop impact on dry and wet surfaces with consideration of surrounding air", *Physics of Fluids*, Vol. 28 (7), p. 073303.

[11] Josserand, C., and Thoroddsen, S. T., 2016, "Drop impact on a solid surface", *Annual review of fluid mechanics*, Vol. 48, pp. 365–391.

[12] Jian, Z., Josserand, C., Popinet, S., Ray, P., and Zaleski, S., 2018, "Two mechanisms of droplet splashing on a solid substrate", *Journal of Fluid Mechanics*, Vol. 835, pp. 1065–1086.

[13] Ferreira, A. G., and Singer, M. J., 1985, "Energy dissipation for water drop impact into shallow pools", *Soil Science Society of America Journal*, Vol. 49 (6), pp. 1537–1542.

[14] Berberović, E., van Hinsberg, N. P., Jakirlić, S., Roisman, I. V., and Tropea, C., 2009, "Drop impact onto a liquid layer of finite thickness: Dynamics of the cavity evolution", *Physical Review E*, Vol. 79 (3), p. 036306.

[15] Engel, O. G., 1966, "Crater depth in fluid impacts", *Journal of Applied Physics*, Vol. 37 (4), pp. 1798–1808.

[16] Thoroddsen, S., 2002, "The ejecta sheet generated by the impact of a drop", *Journal of Fluid Mechanics*, Vol. 451, pp. 373–381.

[17] Walker, T. W., Logia, A. N., and Fuller, G. G., 2015, "Multiphase flow of miscible liquids: jets and drops", *Experiments in Fluids*, Vol. 56 (5), pp. 1–14.

[18] Lhuissier, H., Sun, C., Prosperetti, A., and Lohse, D., 2013, "Drop fragmentation at impact onto a bath of an immiscible liquid", *Physical review letters*, Vol. 110 (26), p. 264503.

[19] Thoroddsen, S. T., Thoraval, M.-J., Takehara, K., and Etoh, T., 2011, "Droplet splashing by a slingshot mechanism", *Physical review letters*, Vol. 106 (3), p. 034501.

[20] Zhang, L., Toole, J., Fezzaa, K., and Deegan, R., 2012, "Evolution of the ejecta sheet from the impact of a drop with a deep pool", *Journal of Fluid Mechanics*, Vol. 690, pp. 5–15.

[21] Thoraval, M.-J., Takehara, K., Etoh, T. G., Popinet, S., Ray, P., Josserand, C., Zaleski, S., and Thoroddsen, S. T., 2012, "von Kármán vortex street within an impacting drop", *Physical review letters*, Vol. 108 (26), p. 264506.

[22] Thoroddsen, S., Etoh, T., and Takehara, K., 2003, "Air entrapment under an impacting drop", *Journal of Fluid Mechanics*, Vol. 478, pp. 125–134.

[23] Thoraval, M.-J., Takehara, K., Etoh, T., and Thoroddsen, S. T., 2013, "Drop impact entrapment of bubble rings", *Journal of Fluid Mechanics*, Vol. 724, pp. 234–258.

[24] Bisighini, A., Cossali, G. E., Tropea, C., and Roisman, I. V., 2010, "Crater evolution after the impact of a drop onto a semi-infinite liquid target", *Physical Review E*, Vol. 82 (3), p. 036319.

[25] Michon, G. J., Josserand, C., and Séon, T., 2017, "Jet dynamics post drop impact on a deep pool", *Physrevfluids*, Vol. 2 (2).

[26] Liu, X., 2018, "Experimental study of drop impact on deep-water surface in the presence of wind", *Journal of Physical Oceanography*, Vol. 48 (2), pp. 329–341.

[27] Zhang, L., Toole, J., Fezzaa, K., and Deegan, R., 2012, "Splashing from drop impact into a deep pool: multiplicity of jets and the failure of conventional scaling", *Journal of fluid mechanics*, Vol. 703, pp. 402–413.

[28] Pumphrey, H. C., and Elmore, P. A., 1990, "The entrainment of bubbles by drop impacts", *Journal of Fluid Mechanics*, Vol. 220, pp. 539–567.

[29] Li, E. Q., M.-J., T., Marston, J. O., and Thoroddsen, S. T., 2018, "Early azimuthal instability during drop impact", *Journal of Fluid Mechanics*, Vol. 848, pp. 821–835.

[30] Agbaglah, G., Thoraval, M.-J., Thoroddsen, S. T., Zhang, L. V., Fezzaa, K., and Deegan, R. D., 2015, "Drop impact into a deep pool: vortex shedding and jet formation", *J Fluid Mech*, Vol. 764, p. R1.

[31] Rein, M., 1996, "The transitional regime between coalescing and splashing drops", *Journal of Fluid Mechanics*, Vol. 306, pp. 145–165.

[32] Ray, B., Biswas, G., and Sharma, A., 2015, "Regimes during liquid drop impact on a liquid pool", *Journal of Fluid Mechanics*, Vol. 768, pp. 492–523.

[33] Gielen, M. V., Sleutel, P., Benschop, J., Riepen, M., Voronina, V., Visser, C. W., Lohse, D., Snoeijer, J. H., Versluis, M., and Gelderblom, H., 2017, "Oblique drop impact onto a deep liquid pool", *Physical review fluids*, Vol. 2 (8), p. 083602.

[34] Wu, Z., Hao, J., Lu, J., Xu, L., Hu, G., and Floryan, J. M., 2020, "Small droplet bouncing on a deep pool", *Physics of Fluids*.

[35] Morton, D., Rudman, M., and Jong-Leng, L., 2000, "An investigation of the flow regimes resulting from splashing drops", *Physics of Fluids*, Vol. 12 (4), pp. 747–763.

[36] Ervik, Å., Hellesø, S. M., Munkejord, S. T., and Müller, B., 2014, "Experimental and computational studies of water drops falling through model oil with surfactant and subjected to an electric field", *2014 IEEE 18th International Conference on Dielectric Liquids (ICDL)*, IEEE, pp. 1–6.

[37] Rieber, M., and Frohn, A., 1999, "A numerical study on the mechanism of splashing", *International Journal of Heat and Fluid Flow*, Vol. 20 (5), pp. 455–461.

[38] Brambilla, P., and Guardone, A., 2013, "Automatic tracking of corona propagation in three-dimensional simulations of non-normal drop impact on a liquid film", *Computing*, Vol. 95 (5), pp. 415–424.

[39] Shin, S., Chergui, J., and Juric, D., 2017, "A solver for massively parallel direct numerical simulation of three-dimensional multiphase flows", *Journal of Mechanical Science and Technology*, Vol. 31 (4), pp. 1739–1751.

[40] Nikolopoulos, N., Theodorakakos, A., and Bergeles, G., 2007, "Three-dimensional numerical investigation of a droplet impinging normally onto a wall film", *Journal of computational physics*, Vol. 225 (1), pp. 322–341.

[41] Brambilla, P., and Guardone, A., 2015, "Assessment of dynamic adaptive grids in volume-of-fluid simulations of oblique drop impacts onto liquid films", *Journal of Computational and Applied Mathematics*, Vol. 281, pp. 277–283.

[42] Popinet, S., and collaborators, 2013–2022, "Basilisk", `http://basilisk.fr`.

[43] Fuster, D., and Popinet, S., 2018, "An all-Mach method for the simulation of bubble dynamics problems in the presence of surface tension", *Journal of Computational Physics*, Vol. 374, pp. 752–768.

[44] Weymouth, G. D., and Yue, D. K.-P., 2010, "Conservative volume-of-fluid method for free-surface simulations on cartesian-grids", *Journal of Computational Physics*, Vol. 229 (8), pp. 2853–2865.

[45] Rudman, M., 1998, "A volume-tracking method for incompressible multifluid flows with large density variations", *International Journal for numerical methods in fluids*, Vol. 28 (2), pp. 357–378.

[46] Bell, J. B., Colella, P., and Glaz, H. M., 1989, "A second-order projection method for the incompressible Navier-Stokes equations", *Journal of computational physics*, Vol. 85 (2), pp. 257–283.

[47] Brackbill, J. U., Kothe, D. B., and Zemach, C., 1992, "A continuum method for modeling surface tension", *Journal of computational physics*, Vol. 100 (2), pp. 335–354.

[48] Popinet, S., 2015, "A quadtree-adaptive multigrid solver for the Serre–Green–Naghdi equations", *Journal of Computational Physics*, Vol. 302, pp. 336–358.

[49] Van Hooft, J. A., Popinet, S., Van Heerwaarden, C. C., Van der Linden, S. J., de Roode, S. R., and Van de Wiel, B. J., 2018, "Towards adaptive grids for atmospheric boundary-layer simulations", *Boundary-layer meteorology*, Vol. 167 (3), pp. 421–443.

[50] Wu, S., Zhang, J., Xiao, Q., and Ni, M.-J., 2021, "Comparison of two interfacial flow solvers: Specific case of a single droplet impacting onto a deep pool", *Computers & Mathematics with Applications*, Vol. 81, pp. 664–678.

[51] Fedorchenko, A. I., and Wang, A.-B., 2004, "On some common features of drop impact on liquid surfaces", *Physics of Fluids*, Vol. 16 (5), pp. 1349–1365.

Conference on Modelling Fluid Flow (CMFF'22)
The 18th International Conference on Fluid Flow Technologies
Budapest, Hungary, August 30 -September 2, 2022

FLOW AROUND BUBBLES: 4D MEASUREMENT CONCEPT WITH HIGH-SPEED TOMOGRAPHIC SYSTEM

C. Müller[1*], Y. Chang[1,2], P. Kováts[1], D. Thévenin[1], K. Zähringer[1]

[1] Laboratory of Fluid Dynamics and Technical Flows, Otto-von-Guericke-Universität Magdeburg. Universitätsplatz 2, D-39106 Magdeburg, Germany. Tel.: +49 391 - 67 58654, Fax: +49 391 - 67 52840
[2] State Key Laboratory of Multiphase Flow in Power Engineering, Xi'an Jiaotong University, Xi'an 710049, China
*E-mail: conrad.mueller@ovgu.de

ABSTRACT

The motion and form of single bubbles are investigated usually with 2D optical measurement methods, like shadow imaging or Particle Image Velocimetry (PIV) [1-3]. With improving optical measurement techniques and image processing it becomes possible to investigate single bubbles or bubble groups in a 3D volume with tomographic measurement techniques.

In the present study, small bubble groups and the liquid flow around them are investigated in a stagnant liquid with 4D shadow imaging and 4D particle tracking. Applying four high-speed cameras and LED volume illumination, images of the bubbles and tracer particles are recorded simultaneously. During image processing, bubbles and particles are treated separately. The bubbles are reconstructed with the help of a tomographic sizing algorithm and the centre of mass of the reconstructed 4D objects is tracked, what results in 4D bubble trajectories. From these measurements not only the 3D bubble path and bubble velocity, but also the bubble size, shape and its deformation can be obtained.

Additionally, the segmented tracer particles are used to calculate the instantaneous 3D liquid flow field around the bubble groups with the Shake-the-box algorithm, which is a 4D particle tracking velocimetry method.

This kind of experiments delivers data for the modelling of bubble dynamics in gas-liquid contactors, as e.g. bubble columns, and can be a good validation base for 3D CFD simulations with single bubbles and interactions between multiple bubbles in a bubble swarm.

Keywords: PTV, Shadow imaging, Shake-the-box, Tomographic sizing, Trajectories, Two-phase flow

1. INTRODUCTION

Investigations on single bubbles in two-phase flows, their motion, interactions with each other and with the surrounding liquid is important for the deeper understanding of mass transfer in these systems. Especially for the scale-up process of bubble columns these data are important. Also the validation of numerical simulations demand experimental data with high spatial and temporal resolution. Comparable measurements, e.g. by Hassan et. al., Liu et al. or Yoshimoto et al. [4-6], have been carried out for single bubbles, nevertheless for only the bubble motion, only the liquid flow field or in low temporal resolution.

Recently modern three-dimensional measuring techniques are highly improving in terms of spatial and temporal resolution and optical accessibility. The range of different measurement methods to characterize a flow field and their processing ranges from tomographic PIV, over PTV to high resolution time-resolved PTV, using modern processing algorithms like Shake-the-Box (STB) [7]. This enables tomographic high-speed measurement systems with PTV to increase the spatial resolution, because the algorithm can handle higher particle concentrations than common PTV algorithms. For the postprocessing the Fine Scale Reconstruction (FSR) algorithm introduced by Schneiders et al. 2018 [8] is used. All those measurement systems have been compared and their capabilities tested e.g. by Sellappan et. al. 2020 [9] for single phase jet flows. Even combinations of flow velocity measurements using high-speed PIV or tomographic PIV with shadow imaging were performed by Lee and Park 2022 [10] or She et al. 2021 [11]. All these methods are only applicable for low gas contents otherwise single bubbles cannot be recognized nor be reconstructed. Neither can the flow be measured, due to illumination purposes.

In order to investigate the bubble motion of multiple bubbles in a bubble swarm together with the flow field around the bubbles, in this study high-speed shadow imaging is used. By segmenting the bubble shadows from those of tracer particles in the surrounding water, the bubble motion, size and shape can be tracked and reconstructed. The tracer particle

field is then used to calculate the flow field in the investigated volume.

The results from such measurements can be used as validation for bubble interaction simulations such as performed by Zhang et al. [12,13].

NOMENCLATURE

d_{eq}	[mm]	bubble equivalent diameter
Q	[-]	Q-criterion
t	[ms]	time (step)
v_B	[m/s]	bubble velocity
v_L	[m/s]	liquid velocity

2. EXPERIMENTAL SETUP

For the tomographic setup a decagonal acrylic glass tank with a gas inlet in the centre of the bottom was filled with de-ionised water. Four Phantom VEO L640 high-speed cameras (2560x1600 pixels) were set along a horizontal line in an arc-like configuration around the tank, so all camera lenses (Tokina 100 mm) were parallel and equidistant to one face of the tank as shown in Figure 1.

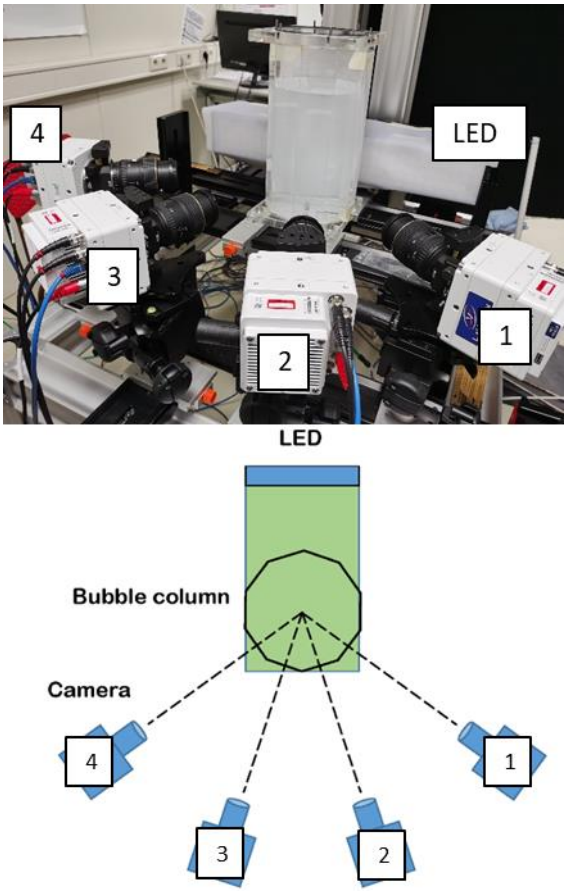

Figure 1. Experimental setup of the four horizontally aligned cameras and the decagonal acrylic glass bubble column with background illumination (top); camera configuration (bottom).

In order to fulfil the Scheimpflug condition all camera's focal planes were aligned with a calibration plate (LaVision 058-5), which was put in the centre of the tank. For the background illumination a triggered blue LED Flashlight 300 (LaVision) and a diffusor were used. For each measurement 5000 images were taken as time-resolved single frames simultaneously with all four cameras at a constant recording frequency of 1 kHz. White Vestosint particles with a mean diameter of 40 µm were used as tracer particles for the liquid phase. The particle concentration was calculated to be 0.0066 ppp (particle per pixel). The images are recorded and mainly processed with DaVis 10.2 (LaVision).

2.1. Calibration

Geometrical calibration, which is a crucial step for the quality of the tomographic reconstruction, has been performed in a two-step procedure: initial geometrical calibration followed by correction with disparity of triangulated particles. For the initial geometrical calibration, a 3D calibration plate (LaVision 058-5) was set first in the centre of the tank and then at two additional positions 5 mm before and 5 mm behind the centre plane. The final calibration reached a fit error of 0.004 pixel with a scale factor of 39.25 pixel/mm for a 1964x2703 pixels dewarped image. The angle between the cameras furthest away from each other (1-4) was 99.53°. The following self-calibration results in an average disparity of 0.03 voxel with a maximum of 0.06 voxel. The final reconstructed volume of 50x68x20 mm³ results in 1963x2702x785 voxels.

For the bubble reconstruction, this original calibration was also scaled down from 39.25 pixel/mm to 25, 12.5 and 6.25 pixel/mm, in order to test the minimization of computing time and final file size (see section 3.2 and 3.3). The influence of the different resolutions on the bubble reconstruction and the trajectories was tested as shown later.

2.2. Flow Conditions

The gas inlet stainless steel capillary had a diameter of 0.13 mm, producing small bubbles, and 1 mm, producing bigger bubbles. Air was introduced by a syringe pump. The investigated rising bubbles can be classified into 5 groups. Single bubbles of different sizes, small bubbles being almost perfectly round with an average diameter of 1 mm, medium bubbles with a diameter of 4 mm and oblate spheroid shape and large bubbles with an instable surface and shape like a jellyfish, which is oscillating. In addition, bubble swarms were measured, with 6-12 medium sized bubbles and one case with very large bubbles with a complex and varying shape. The bubble swarms were produced with manual short and fast pumps (~10 mL) of the syringe without capillary. In both swarms, bubble collisions took place. The gas volume fraction in the measuring volume was always lower than 0.5%.

3. POSTPROCESSING

Most postprocessing procedures are evaluated by the help of DaVis 10.2 from LaVision. The general processing steps and their results are shown in the flow chart in Figure 2.

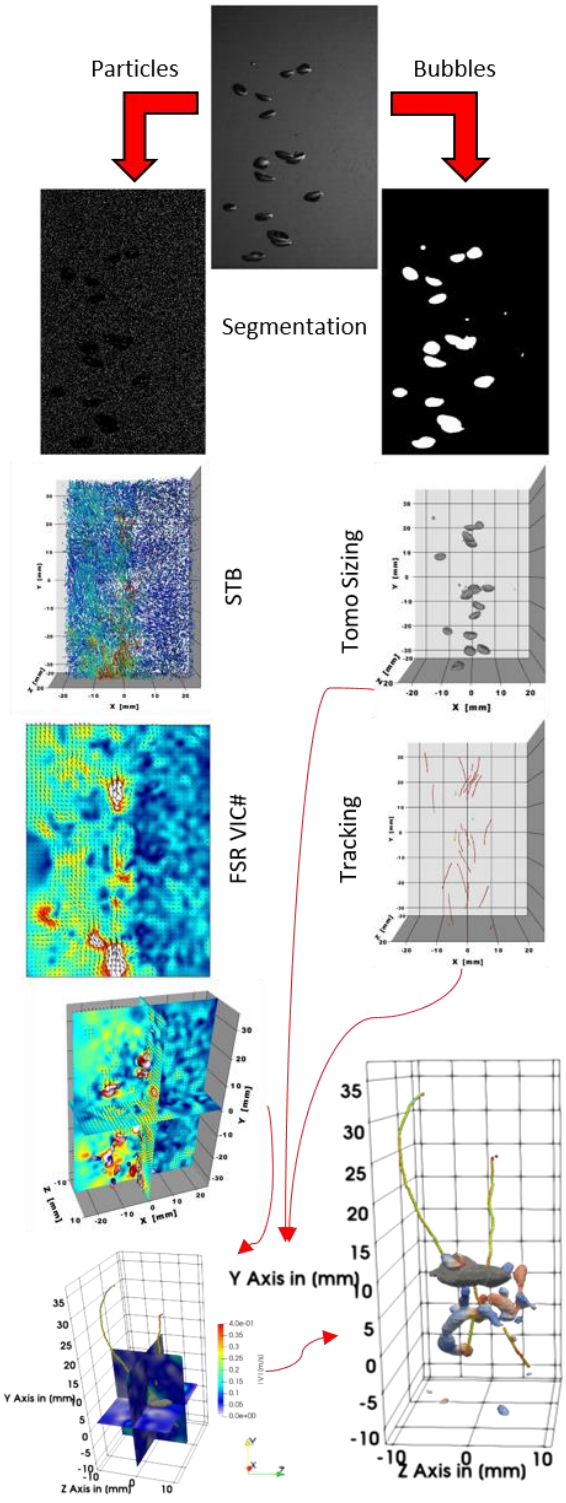

Figure 2. Data postprocessing workflow of the time-resolved shadow imaging measurements.

In the first processing step the tracer particles were separated from the bubble shadows with a segmentation filter and were then treated separately. In the case of bubble swarms with strong differences between large and small bubbles, the small and large bubbles were additionally separated from each other.

For the liquid phase the singled-out particles were reconstructed in 3D and their trajectories were created using the Shake-The-Box algorithm (STB) implemented in DaVis 10.2, which allowed a triangulation error of 1.5 voxel and went for 4 iterations over the inner and outer loop. Particle positions were shaken by 0.1 voxel and have been removed, if being closer than 1 voxel to each other or had a weaker intensity than 0.1 of the average intensity. A minimum required track length of 4 time steps was set with a maximum allowed absolute change in particle shift of 1 voxel and a relative change of 20%. In the next step a time-resolved three-dimensional reconstruction of the flow field was calculated with DaVis 10.2 from the obtained particle trajectories using a fine scale reconstruction (FSR) based on the vector in cell algorithm (VIC#) [14].

For the gas phase, the bubbles were reconstructed using the three-dimensional Tomographic Sizing algorithm implemented in DaVis 10.2. The bubble diameter was calculated from the reconstructed volume of each segment. Segmentation and tracking were then used to determine the centre of gravity of the bubbles and reconstruct the trajectories and bubble rising paths. Velocity, acceleration as well as the bubble equivalent diameter for each time step can then be obtained for all three coordinate directions.

The 3D reconstructions of the bubbles and the volumetric flow field from the FSR VIC+ were then merged with the bubble trajectories in ParaView 5.10. The vorticity and the Q-criterion were also calculated from the flow field.

3.1. Fine Scale Reconstruction VIC#

Since the FSR interpolates the space between the particle trajectories with time-resolved velocity data, the link between the number of trajectories, (thus the found and reconstructed particles from the STB,) and the quality of the FSR is obvious. From 35,000 reconstructed particles in the STB results a particle concentration of 0.0066 ppp. This particle concentration is on the low end of recommended values [15]. As shown in Figure 3 the coarser grids of 24 voxel to 12 voxel show a good agreement of the general vortex structures around the bubbles, but the finest grid of 6 voxel, and so 8 times more vectors than the 12 voxel grid, shows a lot of numerical noise because too much vectors were interpolated between the trajectories, even though the large vortex structures stay in place. In order to use such a fine grid, a higher particle concentration close to 0.125 ppp is recommended. However, higher particle concentrations are only achievable in small volumes

avoiding the effect of particles in front and behind the actually measured volume. Particles outside the investigated volume decrease the overall illumination intensity (background-particle intensity ratio) and also blur the recognized particles. Both issues lead to a more inaccurate and worse particle reconstruction.

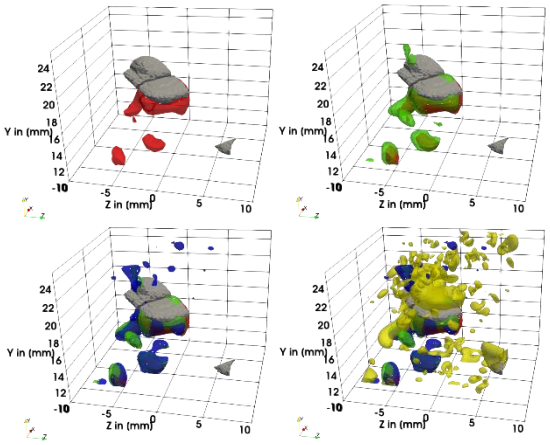

Figure 3. Comparison of vortex structures around two touching bubbles for different grid sizes of Fine Scale Reconstruction VIC#, from top left to bottom right: 24 (red), 16 (green), 12 (blue), 6 (yellow) voxel grid; bubbles in grey.

3.2. Effect of the resolution

The initial resolution of 39.25 pixel/mm was a considerable problem for the reconstruction of the bubbles, due to the large amount of computing power, which requires a very fast CPU and a strong GPU. For loading final images of the reconstruction even a humongous working memory (RAM) is necessary. In order to reduce the computing costs, the resolution of the reconstructions was reduced by downscaling the calibration to 25, 12.5 and 6.25 pixel/mm. The images in Figure 4 show a small, medium and a big bubble as 2D projections of the 3D reconstruction for the different resolutions. It is obvious, that the bigger the bubble, the less the resolution effects the overall reconstructed volume. Nevertheless, for small spherical bubbles the difference of calculated equivalent diameter between low and high resolution is less affected than for big, irregular bubbles. But, it only differs in a negligible range of maximum 0.6%. For later images and calculations, only the lowest resolution of 6.25 pixel/mm was applied for representing the bubbles and the trajectories to minimize computing time. It has to be noted, that even for very high resolutions, the surface of especially the big bubbles cannot be reconstructed quantitatively, due to reflections, glare points and shadows of waves on the bubbles surfaces.

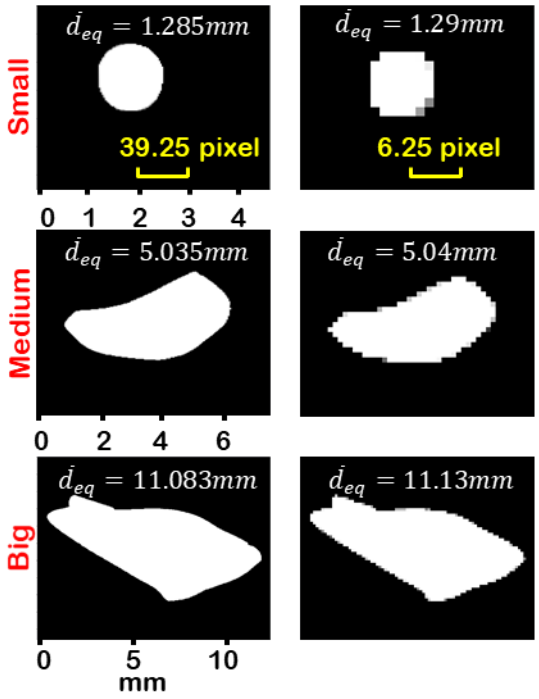

Figure 4. Comparison of original resolution for the 3D-reconstruction of small, medium and big bubbles.

3.3. Computing costs

Measurements performed with high resolution often come under premises of very high computing costs. In the following tables, the computing time on an Intel Core I9-9940X, 14 cores@4.4 GHz with 64 GB RAM and the final file size of an exported DAT-file and the DaVis intern VC7-file are listed for different resolutions of the Tomographic Sizing Reconstruction of bubbles (Table 1) and the Fine Scale Reconstruction of a STB flow field (Table 2). The finest resolution (6 voxel grid) of the FSR VIC# was calculated on the CPU and GPU (NVIDIA Quadro P400, 2 GB). The computing steps of the STB, the calculation of the trajectories and other image processing steps are relatively fast compared to the Tomographic Sizing Reconstruction of the bubbles and the FSR VIC# and are therefore not taken into account.

The final file sizes are especially a problem when trying to merge the different data types together. Humongous DAT-Files (ASCII) are not easy to handle since they overflow most of common editors, like MatLab, NotePad++ or PilotEdit. But even the calculation of the trajectories from reconstructed bubbles becomes a challenge, because the high resolution images have to be reloaded for the calculation, requiring very high RAM, which is the reason why only low resolution reconstructions (Figure 4) were used for the calculation of the trajectories as shown in section 4.

Table 1: Computing time of 250 time steps/images for the 3D bubble reconstruction, file size (.dat/.vc7) of one time step

Resolution	Time	File Size	Reconstructed Volume
6.25 pixel/mm	5 min	592/75 MB	314 x 439 x 189 voxels
12.5 pixel/mm	32 min	4.7/0.59 GB	626 x 879 x 376 voxels
25 pixel/mm	3.6 h	(36.8)/4.6 GB	1251 x 1751 x 751 voxels
39.25 pixel/mm	11.5 h	(46.3)/5.8 GB	1964 x 2749 x 1179 voxels

Table 2: Computing time of 250 time steps/images for the Fine Scale Reconstrucion VIC#, file size (.dat/.vc7) of one time step.

Grid resolution	Time	File Size	Reconstructed Volume
24 voxel	6 h	55/10 MB	82x113x33 vectors
16 voxel	20 h	185/28 MB	123x169x50 vectors
12 voxel	36 h	324/76 MB	164x226x66 vectors
6 voxel	412 h (+GPU)	2.7/0.6 GB	328x451x131 vectors

4. RESULTS

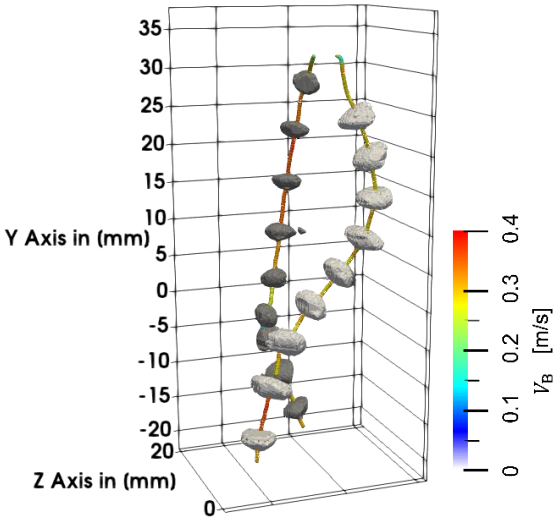

Figure 5. Trajectories of two bubbles (dark and light grey) bouncing on each other in a bubble swarm; Trajectories show the local velocity of the bubbles; time step between the depicted bubbles Δt = 20 ms.

Figure 5 shows the trajectories of two colliding bubbles. Due to the reconstruction method, the trajectories of each individual bubble end, as soon as the bubbles are so close to each other that their shadow image is merging in the processing. Therefore, the resulting trajectory for these time steps was calculated by the mass centre of both bubbles, even though they are not merging in reality. However, the trajectories before and after the collision visualize the bubble velocities of each bubble and the energy conversion between the bubbles after the collision very precisely. The smaller and slower bubble (dark grey) is oscillating after the collision and becomes then faster than the bigger bubble (light grey), which was faster before the collision.

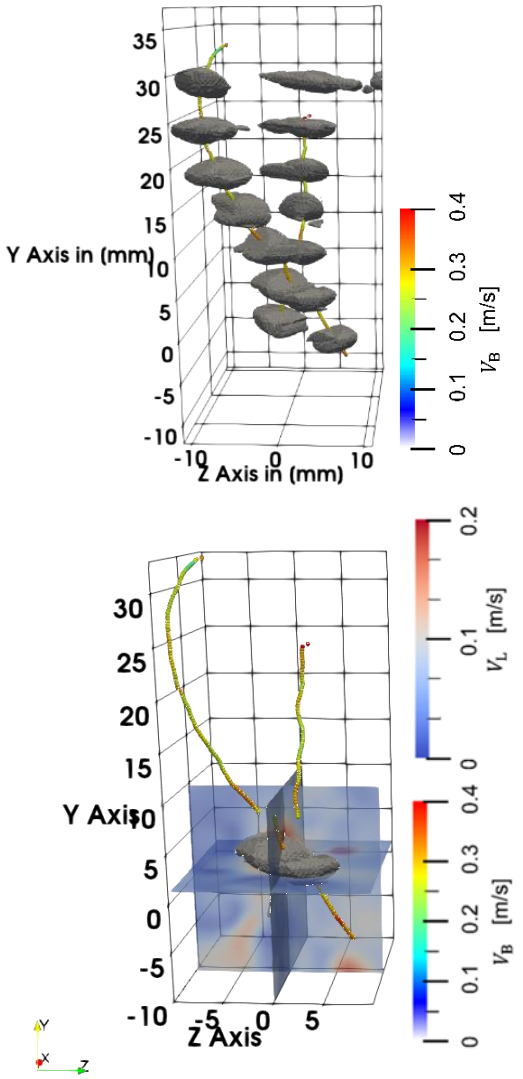

Figure 6. Top: Trajectories of two bubbles (grey) bouncing on each other in a bubble swarm; Trajectories show the local velocity of the bubbles, time step between the depicted bubbles Δt = 20 ms; Bottom: planes show the local liquid velocity field at the moment of collision t = 20 ms.

Figure 6 shows the combination of the trajectories and reconstructed bubbles (top), so the bubble motion, and the volumetric flow field around the bubbles (bottom).

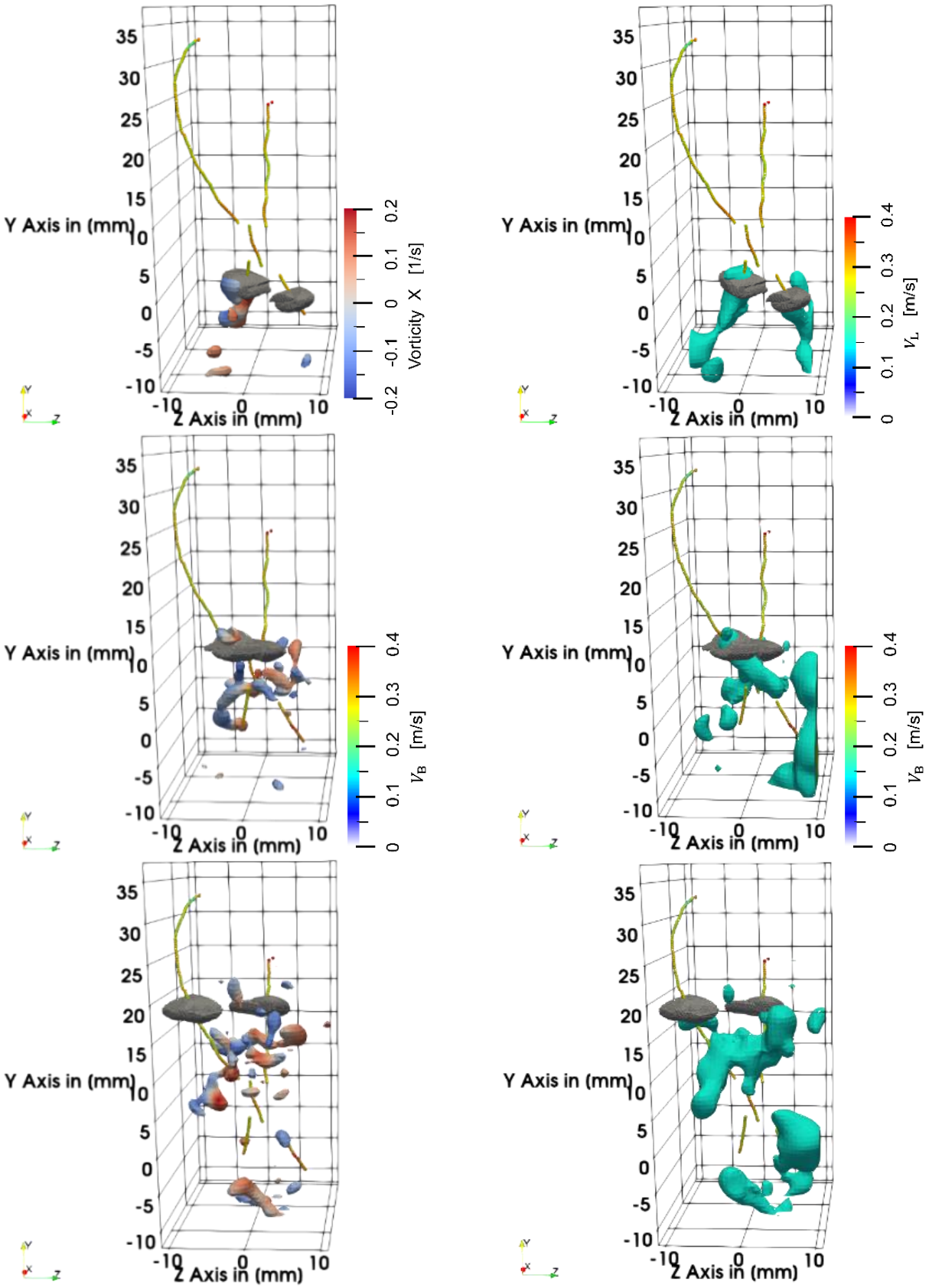

Figure 7. Two bubbles (grey) colliding, trajectories show the average bubble velocity; left column: isosurface of Q-criterion = 0.0035…0.03 coloured with vorticity in x-direction; right column: isosurface of velocity v_L = 0.15 m/s, time step $\Delta t = 40ms$.

Because it is difficult to visualize lots of different three dimensional and time-resolved data in one image, in Figure 7 three time steps of the collision of Figure 6 are shown on different images. The isosurface of the Q-criterion (Q = 0.0035…0.03), visualizes the vortex occurrence coloured with the vorticity in x-direction (left column), and an isosurface of constant velocity (v_L = 0.15 m/s) visualizes the main flow direction (right column).

The following Figure 8 shows the bubble swarm as isosurface (grey) after 100 ms. The bubble's trajectories visualise the bubble velocity and the planes (YX and YZ) show the liquid flow field around the bubbles as vector field (3000 vectors equidistant over boundaries).

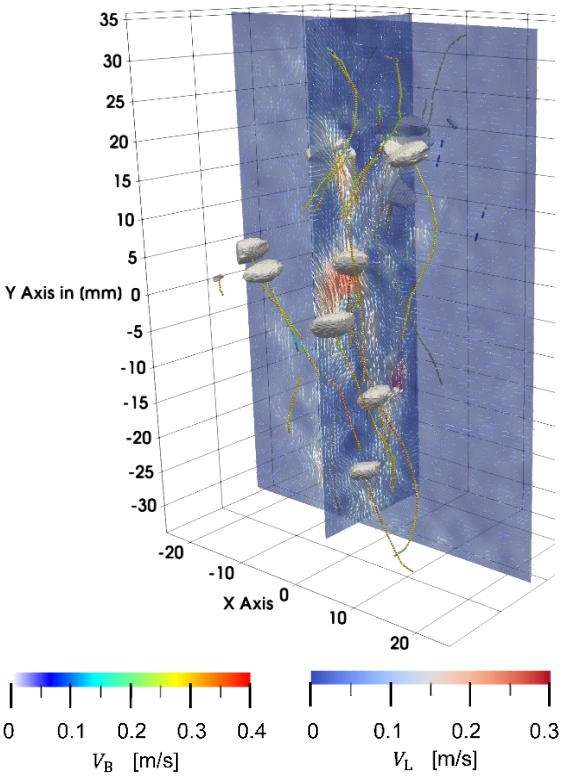

Figure 8. Bubble swarm at time step t = 100 ms (grey) with trajectories (bubble velocity) and liquid velocity vector field in YX and YZ plane.

In both figures (Figure 7 and 8), the flow field around the bubbles shows a physical behaviour. The bubble velocities, the flow field and vortex structures are in a good agreement. However, the local resolution close to the bubble surface needs further improvement, because vectors for the liquid phase are interpolated into the bubbles. Therefore, a higher particle density and an improved postprocessing are mandatory. The reconstructed bubbles should be used as masking functions, creating a physical phase boundary. This would enable a more realistic flow field reconstruction close to the bubbles and a good visualization of streamlines.

5. CONCLUSION

The goal of this work was to evaluate an experimental set-up for the simultaneous characterization of the flow field around bubbles in a bubble swarm and the bubble's shape, size and trajectories. Therefore, a high-speed tomographic shadowgraphy system with four cameras and a triggered LED volume illumination was implemented. Thanks to the STB algorithm high resolution flow fields around each bubble could be reconstructed, even though a higher particle concentration of 0.125 ppp is preferable, but was not feasible in our case, due to the relatively big column volume.

The overall camera setup delivers good results under the assumption that the flow around a bubble is symmetrical, since all cameras are set on one side of the bubble column. A setup with 6 cameras or more around the tank could deliver more precise data, since tracer particles cannot disappear behind bubbles and bubbles in a swarm are not overlapping each other so much in the camera views.

In the future the reconstructed bubbles from the tomographic sizing process should be used as geometric mask and be implemented into the Fine Scale Reconstruction process after the STB reconstruction. This mask can then assure a better reconstruction of the flow field around the bubbles and a detailed analysis of the streamlines. This bubble surface could be set as a wall function with parameters of the bubble motion and its velocity, which would further improve the physics of the reconstruction model, since liquid is being displaced by the bubbles and does not flow through it. The interaction between bubbles in a bubble swarm, the behaviour when bubbles collide, and the influence of the bubbles wake can then be measured in very high resolution as shown in Figure 8.

The reconstruction of the bubble surface stays a complicated task, due to light reflections and glare points. Especially the surface of big bubbles often shows waves, indents and other inconsistent structures messing with the segmentation process. The method is certainly not applicable to realistic bubble column gas fractions, but can help to understand single bubble behaviour, evaluate models and numerical simulations. The afore presented measurements are only a first step to this end and many experience will be necessary to allow for the acquisition of spatially and temporally resolved reliable data sets.

REFERENCES

[1] Aoyama, S.; Hayashi, K.; Hosokawa S.; Tomiyama, A.; 2018; "Shapes of single bubbles in infinite stagnant liquids contaminated with surfactant" *Exp Therm Fluid Sci* 96:460-469 doi: 10.1016/j.expthermflusci.2018.03.015

[2] Filella, A.; Ern, P.; Roig, V; 2015; "Oscillatory motion and wake of a bubble rising in a thin-gap cell"; *Journal of Fluid Mechanics; 778*, 60-88; doi:10.1017/jfm.2015.355

[3] Mikaelian, D.; Larcy, A.; Dhaeck, S.; Haut, B.; 2013; "A new experimental method to analyse the dynamics and the morphology of bubbles in liquids: Application to single ellipsoidal bubbles"; *Chemical Engineering Science,* 100, 529-538; http://dx.doi.org/10.1016/j.ces.2013.04.013

[4] Hassan, Y. A.; Oritz-Villafuerte, J.; Schmidl, W. D.; 2000; "Three-dimensional measurements of single bubble dynamics in a small diameter pipe using stereoscopic particle image velocimetry"; *International Journal of Multiphase Flow* 27 817-842

[5] Liu, Z.; Zheng, Y.; 2006; "PIV study of bubble rising behaviour"; *Powder Technology* 168 10-20; doi:10.1016/j.powtec.2006.05.020

[6] Yoshimoto, K.; Saito, T.; 2010; "3-dimensional liquid motion around a zigzagging ascent bubble measured using tomographic Stereo PIV"; *15th Int Symp on Applications of Laser Techniques to Fluid Mechanics*

[7] Schanz, D.; Gesemann, S.; Schröder, A.; 2016; "Shake-The-Box: Lagrangian particle tracking at high particle image densities"; *Experiments in Fluids*. 57; doi: 10.1007/s00348-016-2157-1.

[8] Schneiders, J.; Scarano, F.; 2016; "Dense velocity reconstruction from tomographic PTV with material derivatives" *Experiments in Fluids*: *experimental methods and their applications to fluid flow*, 57, [139]. https://doi.org/10.1007/s00348-016-2225-6

[9] Sellappan, P.; Alvi, F. S.; Cattafesta, L. N.; 2020, "Lagrangian and Eulerian measurements in high-speed jets using Multi-Pulse Shake-The-Box and fine scale reconstruction (VIC#)" *Experiments in Fluids* 61:157; https://doi.org/10.1007/s00348-020-02993-9

[10] Lee, J.; Park, H.; 2022; "Flow induced by the single-bubble chain depending on the bubble release frequency"; *Physics of Fluids 34, 033312 (2022);* https://doi.org/10.1063/5.0083281

[11] She, W.; Gao, Q.; Zuo, Z.; Liao, X.; Zhao, L.; Zhang, L.; Nie, D.; Shao, X.; 2021; "Experimental study on a zigzagging bubble using tomographic particle image velocimetry with shadow image reconstruction"; *Physics of Fluids 33, 083313(2021);* doi:10.1063/5.0057198

[12] Zhang, J.; Ni, M.; Magnaudet, J.; 2021; "Three-dimensional dynamics of a pair of deformable bubbles rising initially in line. Part 1. Moderately inertial regimes"; *Journal of Fluid Mechanics, Cambridge University Press (CUP);* 320, pp.A16. 10.1017/jfm.2021.429. hal-03382547; https://doi.org/10.1017/jfm.2021.429

[13] Zhang, J.; Ni, M.; Magnaudet, J.; 2021; "Three-dimensional dynamics of a pair of deformable bubbles rising initially in line. Part 2. Highly inertial regimes"; *Journal of Fluid Mechanics, Cambridge University Press (CUP);* https://arxiv.org/abs/2201.09336v1

[14] Jeon, Y. J.; Müller, M., Michaelis, D.; Wieneke, B.; 2019; "Data assimilation-based flow field reconstruction from particle tracks over multiple time steps"; *13th International Symposium on Particle Image Velocimetry – ISPIV 2019*

[15] Raffel, M.; Willert, C. E.; Scarana, F.; Kähler, C. J.; Wereley, S. T.; Kompenhans J.; "Particle Image Velocimetry, A Practical Guide" Third Edition; Springer-Verlag Berlin Heidelberg; ISBN 978-3-319-+9962-0; https://doi.org/10.1007/978-3-319-68852-7

Conference on Modelling Fluid Flow (CMFF'22)
The 18th International Conference on Fluid Flow Technologies
Budapest, Hungary, August 30-September 2, 2022

Direct Numerical Simulation of Shallow Water Breaking Waves Generated by Wave Plate

Shuo LIU[1], Hui WANG[2], Annie-Claude BAYEUL-LAINÉ[3], Olivier COUTIER-DELGOSHA[4]

[1] Corresponding Author. Univ. Lille, CNRS, ONERA, Arts et Métiers Institute of Technology, Centrale Lille, UMR 9014 – LMFL – Laboratoire de Mécanique des Fluides de Lille – Kampé de Fériet, F-59000, Lille, France. Tel.: +33 784 539 404, E-mail: shuo.liu@ensam.eu
[2] Univ. Lille, CNRS, ONERA, Arts et Métiers Institute of Technology, Centrale Lille, UMR 9014 – LMFL – Laboratoire de Mécanique des Fluides de Lille – Kampé de Fériet, F-59000, Lille, France. E-mail: hui.wang@ensam.eu
[3] Univ. Lille, CNRS, ONERA, Arts et Métiers Institute of Technology, Centrale Lille, UMR 9014 – LMFL – Laboratoire de Mécanique des Fluides de Lille – Kampé de Fériet, F-59000, Lille, France. E-mail: annie-claude.bayeul-laine@ensam.eu
[4] Univ. Lille, CNRS, ONERA, Arts et Métiers Institute of Technology, Centrale Lille, UMR 9014 – LMFL – Laboratoire de Mécanique des Fluides de Lille – Kampé de Fériet, F-59000, Lille, France. E-mail: olivier.coutier-delgosha@ensam.eu

ABSTRACT

We present a two-dimensional direct numerical simulation of breaking waves in shallow water generated by a wave plate. The open-source Basilisk solver is used to solve the incompressible, variable-density, two-phase Navier-Stokes equations with surface tension. The air-water interface is advected using a momentum-conservative Volume-of-Fluid (MCVOF) scheme. The surface tension is treated with a balanced-force technique. An Adaptive Mesh Refinement (AMR) scheme is employed for computational efficiency, concentrating computational resources on significant solution regions. By reconstructing the piston-type wave plate numerically, we realize a high-fidelity simulation of experimental waves under the wide-ranging motions of the wave plate. The relationship between varying maximum wave plate speeds and the associated maximum wave heights before breaking is investigated. The onset of wave breaking is determined as a function of the ratio of wave height to water depth to distinguish between non-breaking waves, spilling breakers, and plunging breakers. A typical plunging breaking wave with a large ratio of wave height to water depth is initialized to identify the wave breaking and air entrainment processes. We obtain a good collapse of the simulated free-surface evolution and velocity fields with respect to the experiment. The shape and size of the air entrapped at impact by the plunging jet match closely the experimental observations during wave breaking. The time-evolving energy budget and the bubble characteristics under breaking waves are further discussed based on the numerical results.

Keywords: air entrainment, direct numerical simulation, two-phase flow, wave breaking

NOMENCLATURE

E	$[J]$	energy
H	$[m]$	maximum wave height before breaking
S	$[m]$	wavemaker stroke length
ϵ	$[J/s]$	viscous dissipation rate
σ	$[N/m]$	surface tension coefficient
A	$[m^2]$	area of ingested bubbles
c	$[-]$	volume fraction
d	$[m]$	still water depth
f	$[s^-1]$	wavemaker frequency
L	$[m]$	numerical domain size
l	$[-]$	maximum level of refinement
$N(t)$	$[-]$	number of bubbles
p	$[Pa]$	pressure field
t_{im}	$[s]$	the time of jet impact
V_{max}	$[m/s]$	maximum wave plate velocity
$\underline{\underline{D}}$	$[-]$	deformation tensor
$\underline{f_\sigma}$	$[N/m^3]$	surface tension force per unit volume
$\underline{u}$	$[m/s]$	fluid velocity
μ	$[Pa\ s]$	dynamic viscosity
ρ	$[kg/m^3]$	fluid density

Subscripts and Superscripts

k, p, m, d	kinetic, potential, mechanical, and dissipative energy
x, z	streamwise, vertical direction
1, 2	phase 1, water; phase 2, air

1. INTRODUCTION

Wave breaking has sparked a lot of research interests due to its importance in upper ocean dynamics and air-sea interactions. The experimental investigations of breaking waves by Duncan [1] and Melville [2] have initiated the exploration of the physics governing their instability, breaking onset, and strength.

Progress has been made in several areas, including prediction of geometric properties, breaking onset, energy dissipation, and air entrainment mechanisms in breaking waves. The turbulence directly associated with breaking is dominant in mixing processes beneath the free surface, making it crucial for heat, mass, and momentum transfer [3]. However, splashing, turbulence, and air entrainment make theoretical modeling challenging once the wave breaks. In addition, field measurements using various detection methods have difficulty in quantifying wave breaking due to the strongly nonlinear intermittent breaking process and environmental influences [4]. Controlled laboratory experiments and numerical modelling enable the isolation and analysis of the effects of wave breaking on a variety of fundamental air-sea interfacial properties, measuring the scaling relationships between surface wave fields and the kinematics and dynamics of breaking waves [5, 6]. Measurements of breaking waves generated by wave plate can provide general entrainment processes visualized by high speed imaging and the temporal evolution of turbulence quantified using particle image velocimetry (PIV), but there are also many technical challenges in measuring the temporo-spatial evolution and resolving both the large and small structures simultaneously during wave breaking. Therefore, direct numerical simulation (DNS) has becomes a feasible method for solving complex breaking processes across a wide range of scales, allowing researchers to gain a better understanding of the physical role of entrained air bubbles in basic processes such as wave energy dissipation. The numerical methodology followed in this investigation involves the simulation of incompressible flow of two immiscible fluids. The Navier-Stokes equations are solved numerically on sufficiently fine grids to retain the effects of viscosity and surface tension, allowing the physical properties of breaking waves to be accurately captured.

2. NUMERICAL SCHEME

2.1. Basilisk Solver

We solve the gas-liquid two-phase incompressible Navier-Stokes equations with variable density and surface tension using the Basilisk library. The Basilisk package is an open-source program for the solution of a wide variety of partial differential equation systems on regular adaptive Cartesian meshes. The incompressible, variable density Navier-Stokes equations with surface tension can be written as:

$$\rho(\partial_t \boldsymbol{u} + (\boldsymbol{u}\cdot\nabla)\boldsymbol{u}) = -\nabla p + \nabla\cdot(2\mu\boldsymbol{D}) + \boldsymbol{f}_\sigma \tag{1}$$

$$\partial_t \rho + \nabla\cdot(\rho\boldsymbol{u}) = 0 \tag{2}$$

$$\nabla\cdot\boldsymbol{u} = 0 \tag{3}$$

With $\boldsymbol{u} = (u, v, w)$ the fluid velocity, $\rho \equiv \rho(x,t)$ the fluid density, p the pressure, $\mu \equiv \mu(x,t)$ the dynamic viscosity, D the deformation tensor defined as $D_{ij} \equiv (\partial_i u_j + \partial_j u_i)/2$, and f_σ the surface tension force per unit volume.

The liquid-gas interface is tracked by the momentum-conserving volume-of-fluid (MCVOF) advection scheme [7] combined with quad/octree adaptive mesh refinement (AMR) method, while the corresponding volume fraction field is solved by a piecewise-linear geometrical scheme [8] together with a balanced-force continuous-surface-force model for the surface tension. The generic time loop is used for the implementation of numerical scheme and the timestep is limited by the CFL condition. The momentum equation is projected using the Bell-Colella-Glaz advection scheme [9], and the viscous terms are solved implicitly. Gravity is taken into account using the "reduced gravity approach" [10].

2.2. Momentum-Conserving VOF Method

The VOF method was originally developed by Hirt & Nichols (1981) [11] and modified by Kothe *et al.* (1991) [12], and further coupled with momentum conservation by Fuster & Popinet (2018) [7], with the advantage of allowing variable spatial resolution and sharp representation along the interface, while limiting the appearance of spurious numerical parasitic currents caused by momentum leakage between the dense and light phases [13]. A function $c(x,t)$, defined as the volume fraction of a particular fluid in each cell of the computational mesh, assuming a value from 0 to 1 for each phase, is used to reconstruct the interface of the two-phase flow. The density and viscosity can thus be calculated using arithmetic means as follows:

$$\rho(c) = c\rho_1 + (1-c)\rho_2 \tag{4}$$

$$\mu(c) = c\mu_1 + (1-c)\mu_2 \tag{5}$$

with ρ_1, ρ_2, and μ_1, μ_2 the density and viscosity of the first and second fluids, respectively.

The advection equation for the density can be substituted with an equivalent advection equation for the volume fraction:

$$\partial_t c + \nabla\cdot(c\boldsymbol{u}) = 0 \tag{6}$$

The piecewise linear interface construction (PLIC) approach is applied. The interface normal is computed by the Mixed-Youngs-Centered (MYC) method [14] and the position of the interface in the cell is determined using the method of Scardovelli & Zaleski (2000) [15].

Momentum conserving scheme in the advective momentum fluxes near the interface has proven to be essential to reduce the numerical momentum transfer through the interface, especially for large density difference between the two phases. The total fluxes on

each face are obtained by adding the diffusive flux due to the viscous term, which are computed by a semi-implicit Crank-Nicholson scheme. The Bell-Collela-Glaz (BCG) second-order upwind scheme is used to reconstruct the liquid and gas momentum per unit volume to be advected in the cell.

2.3. Balanced-Force Surface Tension

Surface tension can be important in capturing the main cavity at impact and wave hydrodynamics during the post-breaking process. Surface tension is treated with the method of Brackbill *et al*. (1992) [16] and the balanced-force technique [17] as further developed by Popinet (2009, 2018) [18, 19]. To solve the inconsistency at low interface resolution, a generalized version of the height-function (HF) curvature estimation is used, resulting in accurate and efficient surface-tension-driven flow solutions.

3. PROBLEM DESCRIPTION AND MODEL VALIDATION

3.1. Problem Description

A series of breaking wave experiments have been conducted at Johns Hopkins University in a $6m$ long, $0.3m$ wide, and $0.6m$ high wave flume with the aim to study the dispersion of oil spills by breaking waves [20, 21]. The breaking waves are initialized by driving a piston-type wavemaker over a uniform water depth $d = 0.25m$. A single wave breaking event is generated by a single push of the wavemaker, with a trajectory $x(t)$ and associated wave plate velocity $v(t)$ determined by the following functions:

$$x(t) = \frac{S}{2}(1 - \cos(2\pi f t)), 0 \leq t \leq \frac{1}{2f} \tag{7}$$

$$v(t) = S\pi f \sin(2\pi f t), 0 \leq t \leq \frac{1}{2f} \tag{8}$$

where S is the wavemaker stroke length, f is the frequency, and t is the time.

On the basis of the laboratory experiments, two-dimensional simulations of breaking waves have been performed using the Basilisk solver. A plunging breaking wave with $S = 0.5334m$ and $f = 0.75Hz$ is chosen for detailed study, with a maximum wave plate velocity of $V_{\max} = S\pi f = 1.26m/s$. A parametric study is carried out to relate the wave characteristics to the initial conditions by varying the stroke S and frequency f. We define x as the streamwise direction, and z as the vertical direction, positive upward and measured from the still water level. (see Figure 1).

A constant depth of water for the interface $\eta(x, z)_{(t=0)} = d$, with d the still water depth, is used as the initial condition in a square box of size $L = 6m$. The wave propagates from left to right in the x direction. Based on direct numerical simulations of water-air mixture resulting from the entrainment of bubbles due to breaking, we intend to investigate the mechanisms of breaking waves in terms of free-surface profiles, time-evolving energy budget and bubble characteristics.

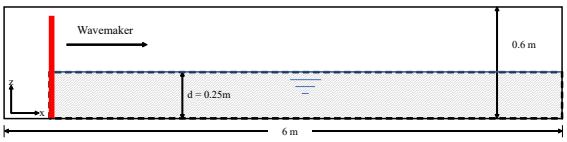

Figure 1. Sketch of laboratory breaking wave experiment and numerical domain.

3.2. Parameter Space

The density and viscosity ratios of the two phases are those of air and water in the experiments, which are $1.29/1018.3$ and $17.9e-6/1.01e-3$, respectively. The Reynolds number in the breaking waves generated by the wave plate can be defined by $Re = \rho V_{\max} S/\mu$, with ρ the density of water, $V_{\max}$ the maximum wave plate velocity, and S the stroke length [22]. The surface tension can be expressed by the Weber number $We = \rho V_{\max}^2 S/\sigma$, with σ the constant surface tension coefficient between water and air. The numerical resolution is given by $\Delta = L/2^l$, where l is the maximum level of refinement in the AMR scheme. The maximum level of refinement depends on the smallest particle size that needs to be resolved in the breaking waves. A maximum level of refinement of 15 is applied in this study, which corresponds to an equivalent conventional grid of 1 billion ($(2^{15})^2$) and a minimum mesh size of $122\mu m$. The grid is adaptively refined/coarsened as the wave propagates, resulting in a total number of grids ranging from 1 million to 10 million. The surface tension scheme is time-explicit, so the maximum timestep is the oscillation period of the smallest capillary wave. For the maximum level of refinement $l = 15$, the corresponding maximum timestep should not be larger than $6.4e-5$. To ensure numerical stability, we require the CFL number to be varied in accordance with the various stages of wave breaking evolution, generally decreasing from 0.5 to 0.3. The refinement criterion is based on the wavelet-estimated discretization error in terms of velocity, vorticity or VOF fields [23]. The refinement criteria on the VOF tracers and the velocity field components are used for adaptive refinement to capture the water-air interface and moving wave plate. The refinement algorithm is invoked at every timestep to determine whether to refine based on the criteria of wavelet estimated error $u_{\text{err}} = 1e-3$ for velocity field and $f_{\text{err}} = 1e-6$ for volume fraction field.

For a plunging breaking wave with $S = 0.5334m$ and $f = 0.75Hz$, due to the limitation of computational resources, combined with the decreasing effects of Reynolds number on the evolution of wave breaking, we choose $Re = 1 \times 10^5$. This value of Reynolds number corresponds to a maximum wave

plate velocity of $0.51m/s$ and a water depth of $0.08m$, which is 5-6 order of magnitude smaller than the actual value. We expect that Reynolds-number effects should not fundamentally alter the basic nature of the scaling we have derived [24]. The effect of surface tension on the formation of the main cavity is analyzed using the physical value of the surface tension coefficient between water and air $\sigma = 0.0728kg/s^2$, which leads to $We = 12000$.

3.3. Breaking Waves Validation

3.3.1. Breaking waves profiles

Three high-speed cameras with a frame rate of 500 frames per second are used in the experiments to visualize the development of wave breaking and the subsequent breakup processes. The horizontal centers of the fields of view, 103×103, 75×75, and $75\times75cm^2$, are located at $x = 1.66$, 2.43, and $3.07m$ for cameras 1, 2, and 3, respectively. The vertical center of all cameras are adjusted to the initial free surface. We compare numerical results of interface evolution over time for a plunging breaker generated by a motion of wave plate with $S = 0.5334m$ and $f = 0.75$ to the experimental snapshots taken with the high-speed cameras. Comparisons of the free surface profile between the simulation results and the snapshots taken during the experiments are shown in Figure 2.

Camera 1, located upstream of the wave direction, close to the side of the wave plate, is primarily responsible for recording the development of the plunging jet, the jet impact and air entrainment, and the generation of the first splash-up. As shown in Fig. 2(a) and Fig. 2(b), comparisons of the free surface evolution at $t = 0.6s$ and $0.7s$ show a great agreement between the present simulations and the experimental results from Camera 1. With the steepening of the wave slope and the curling of the wave crest, A plunging jet can be observed at $t = 0.6s$, with a tendency to project downward to the water surface. At $t = 0.7s$ the plunging jet impacts onto the rising wave front, forming the main cavity by entrapping a tube of air. During this process, the evolution of the free surface, including the development of the wave crest, the curvature of the overturning wave crest, the precise size of the main cavity, and the height and position of the first splash-up, can be accurately predicted by our numerical simulation.

The subsequent development of the initial wave crest and the first splash-up are recorded by Camera 2. From $t = 0.9s$ to $1.0s$, because of the propagation of the perturbations and capillaries at the main free surface prior to the impact of the first splash-up, the free surface beneath the ligaments and droplets of the first splash-up has already been disturbed (c). Following that, the first splash-up dives and connects to the free surface (d). The initial wave crest weakens, the main cavity expands and ruptures, generating a large number of small bubbles that then float to the vicinity of the free surface due to buoyancy. During

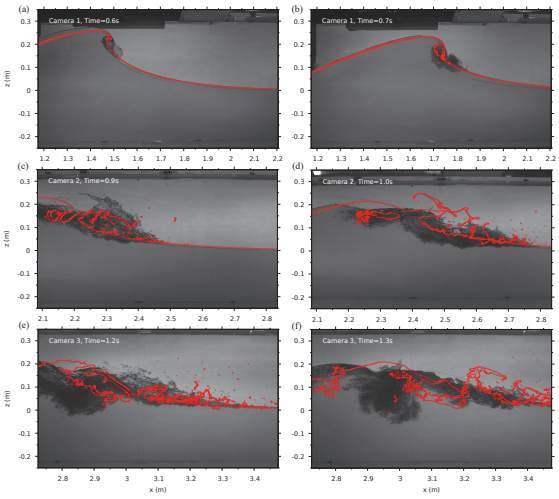

Figure 2. Comparison of free surface profile between laboratory images and numerical results

this process, more abundant water droplets and ligaments are observed in the experiment compared to our numerical results, as indicated by the black region in the experimental snapshots. The explanation for this is that our grid scale is fine enough to capture the formation of water droplets, air bubbles, and ligaments, but these phenomena can not be fully acquired using the present 2D numerical simulation.

Some differences are observed in the simulated free surface evolution compared to the snapshots taken by Camera 3. In comparison to the experimental observations, we find similar phenomena in the occurrence and rising of the second splash-up, as well as the decaying wave crest (e), but the exact development of the second splash-up and the rising wave front are not reproduced by our numerical simulation. It appears to be a phase shift in the distribution of the bubble cloud region (f), but similar bubble cloud size and penetration depth under the water can be obtained. These discrepancies can be explained by the fact that a slight perturbation at the wave front eventually leads to the development of drastically different breaking processes, and this chaotic behavior of breaking waves has been investigated across several runs with the same laboratory setup, demonstrating a non-repeatable breaking process particularly in the post-breaking region [25].

To sum up briefly, a good agreement is obtained in terms of wave shape and maximum wave height before breaking, and the simulated size of the main cavity entrapped by the plunging jet is almost the same compared to the experiment. Some differences can be seen in the location after wave breaking. The generation of water droplets, air bubbles, and ligaments is inaccurate, the profiles of the wave front and the distribution of bubble cloud region can not be well reproduced. This can be explained by the lack of bubbles and droplets generation due to the absence of 3D effects, and the chaotic behavior of

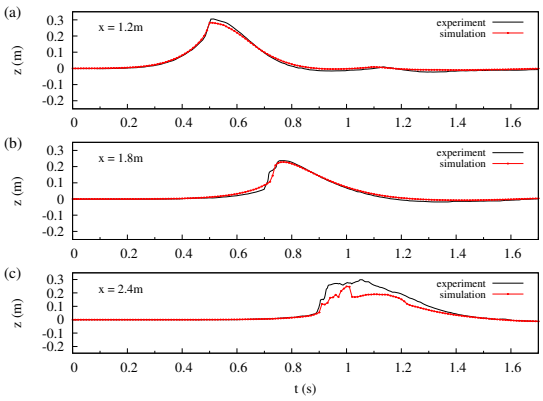

Figure 3. Comparison of surface elevations over time at $x = 1.2m$ (a), $1.8m$ (b), and $2.4m$ (c)

breaking waves in the post-breaking region.

3.3.2. Surface elevation over time

Figure 3. shows the simulated free-surface profiles over time recorded at three positions ($x = 1.2m$, $1.8m$, and $2.4m$) corresponding to the pre-breaking, breaking, and post-breaking regions, respectively, with a comparison to the experimental high-speed imaging results.

The free-surface profile at the first position ($x = 1.2m$) remains smoothly curved, which corresponds to the pre-breaking stage with a smooth free-surface, without the formation of vertical interface and the generation of bubbles and droplets (a). The numerical simulation accurately reproduces the evolution of the free surface, including the development of the rising and falling wave profile, with only a slight underestimation ($0.02m$, 6.7% error) at the peak of the wave profile at $t = 0.5s$.

The second position is located at $x = 1.8m$, within the wave breaking region, near the main cavity entrapped by the plunging jet. We notice that in the experiment, the free-surface appears an immediate rise after jet impact at around $t = 0.7s$, indicating the penetration of the plunging jet into the wave front and the formation of the main cavity. Fig. 3(b) shows that our numerical simulation can closely capture the phenomena during wave breaking. The only discrepancy can be attributed to the lack of the production of small splashes when the plunging jet penetrates into the wave front due to the absence of 3D effects.

The wave propagates to the third position and develops into turbulence, forming a large amount of droplets and bubbles. There are apparent fluctuations of the free-surface between $t = 0.9s$ and $1.4s$, showing the strongly turbulent phenomena during this period. Fig. 3(c) shows an overall underestimation in the elevation of the free surface from $t = 0.9s$ to $1.4s$ by our numerical simulation. This is most likely due to the fact that the free surface elevation is measured differently in the experiment than in the numerical simulation. The value of the free surface elevation in the experiment is the maximum elevation between the wave profile, the splashing bubbles and droplets, as the free surface elevation is recorded from the black region in the experimental snapshots. However, in the numerical simulation, the free surface elevation is primarily determined by the wave profile rather than the splashing droplets scattered above the water surface.

In general, the temporal evolution of the free-surface profile can be precisely reproduced by our simulation compared to the experimental measurements at each location. Despite the limitations of 2D simulation in producing droplets and ligaments in the spanwise direction, the ability of our model to capture wave hydrodynamics, including accurate reproduction of wave height, wave speed, and wave breaking processes, can be demonstrated through the above comparisons.

4. DISCUSSIONS

4.1. Relationship between Wave Height and Maximum Wave Plate Speed

We develop relationships to connect the maximum wave height before breaking H with the maximum wave plate speed used for generating our waves, which is $V_{\max} = A\pi f$ in this study. We restrict consideration to air-water systems close to standard temperature and pressure, so a constant surface tension coefficient is used here. The relationship between H and $V_{\max}$ has been investigated by conducting various cases with different $V_{\max}$. The influence of Reynolds number on the resulting wave height has also been examined by using distinct values of $Re = 10^5$ and $Re = 6 \times 10^5$.

Figure 4. illustrates the relationship between H and $V_{\max}$ normalized by water depth d and shallow water wave speed, $(gd)^{1/2}$, respectively. Experimental measurements performed by Li (2017) [20] are also plotted in this figure. It can be seen that the data collapses onto a single line. As $V_{\max}$ increases, the regular wave begins to break, and the breaking type changes from spilling to plunging. Compared to the experimental data, our numerical results underestimate the wave height, and the differences between them increase with $V_{\max}$. The assumption that the flow becomes independent of the Reynolds number for sufficiently large values of Re can be validated from here. The transitions between regular and breaking waves, spilling and plunging breakers take place at around $H/d = 0.65$ and $H/d = 0.80$, respectively. This is very close to the measurement done by Li (2017), which showed a critical value of $H/d = 0.8$ for spilling and plunging breakers.

A linear correlation between the maximum wave height before breaking H and the maximum wave plate speed $V_{\max}$ has been revealed, showing that the wave height becomes higher as the maximum wave speed increases. The approximate transitions are represented by two critical values. The resulting wave heights between two regimes with distinct Re values are quite consistent, indicating that the evolution

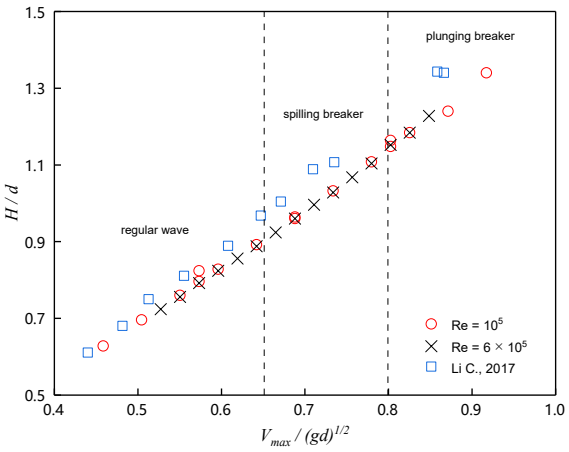

Figure 4. Relationship between maximum wave height before breaking H and maximum wave plate speed $V_{\max}$

of the wave profiles over time is independent on the Reynolds number.

4.2. Energy Budget

We present an energy budget after the jet impact and analyze the energy decay and viscous dissipation due to breaking. The time histories of the kinetic E_{k}, potential E_{p} and total mechanical energy E_{m} are shown in Figure 5. The total mechanical energy of the wave is calculated as the sum of the kinetic and potential components $E_{\mathrm{m}} = E_{\mathrm{k}} + E_{\mathrm{p}}$. The Data are non-dimensionalized using initial values related to the jet impact time t_{im}.

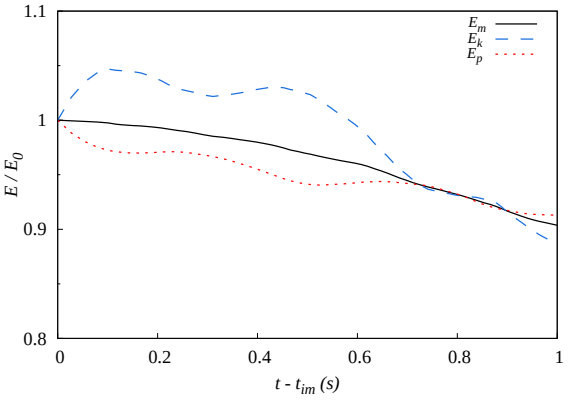

Figure 5. Time histories of the kinetic E_{k}, potential E_{p} and total mechanical energy E_{m}

Starting from the initial impact of the plunging jet, there are two visible energy transfers between kinetic and potential energies, leading to two apparent splash-up productions. As wave breaking develops, the wave crest diminishes, the plunging jet strikes the free surface and penetrates into the water, E_{k} rapidly increases and E_{p} begins to decline, until the first and second splash-ups occur at $t - t_{\mathrm{im}} = 0.1s$ and $t - t_{\mathrm{im}} = 0.45s$, respectively. When the splash-up starts to rise, E_{k}, which has reached its maximum, begins to decline and transfers to potential energy. The total energy decays gradually with a continuously increasing decay rate during this breaking phase. In the later stage of breaking waves, notably after $t - t_{\mathrm{im}} = 0.65s$, the wave becomes more turbulent, and the total mechanical energy exhibits a greater decay due to the substantial air-water mixtures and vortical structures.

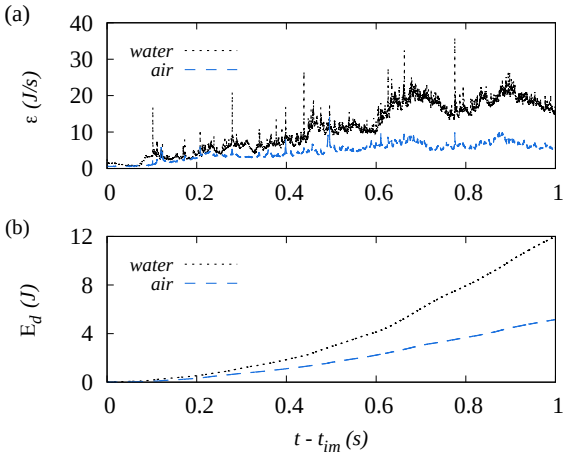

Figure 6. Time histories of the viscous dissipation rate ϵ (a) and corresponding dissipation E_{d} (b)

Figure 6. depicts the time histories of the viscous dissipation rate ϵ and the corresponding dissipation E_{d}. Since we compute breaking waves in a 2D simulation, we consider the width in the spanwise direction as a unit. The dissipation rates in both water and air are markedly intermittent and their fluctuations are strongly synchronized in time. We note that the occurrence of maximum dissipation rate fluctuations is closely related to the exchange time of energy transfer, i.e. the moments when E_{k} and E_{p} reach their extreme values. As breaking process develops, the dissipation rate in water increases greatly, while the dissipation rate in air remains stable (a). Splash-up productions generally occur at a period when the viscous dissipation gradient in water grows dramatically, the viscous dissipation in water continues to increase and no significant decrease in the dissipation rate is observed until $t - t_{\mathrm{im}} = 1s$. Most of the dissipation is caused by air in the early stage after breaking, and then water-induced dissipation dominates the energy dissipation due to the increasing dissipation rate in water (b).

4.3. Air Entrainment

Wave breaking injects a large amount of air into the water by the entrainment of bubbles, which is distinguished by a wide distribution of bubble sizes. The 2D numerical studies in the wave breaking literature may not able to investigate the accurate bubble size distributions, but the evolution of their formation and breakup processes can generally be captured on a fine grid scale through the DNS in this study. Figure 7. shows the time histories of the number of bubbles

$N(t)$ and the total area of bubbles ingested into the water normalized by the main cavity size A/A_0.

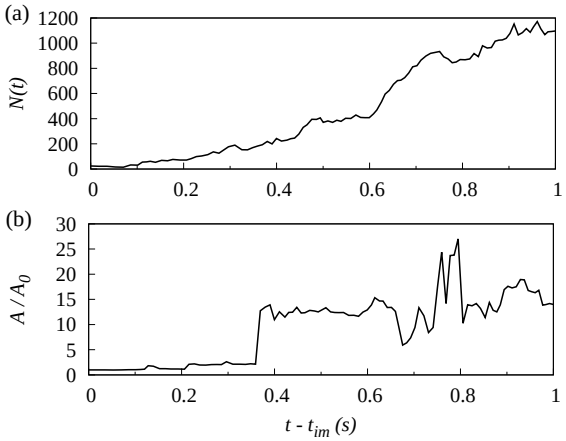

Figure 7. Time histories of the number of bubbles $N(t)$ (a) and the total area of bubbles normalized by the main cavity size A/A_0 (b)

The first bubble can be identified at the moment when the plunging jet impact on the wave front t_{im}, which is also referred to as the main cavity initially ingested in the breaking process. Subsequently, the first splash-up develops and penetrates into the water, with the main cavity being squeezed and distorted, generating a large number of small bubbles. During this period, the total number of bubbles $N(t)$ begins to increase, but the total ingested area of bubbles has no significant increase. Then the total ingested bubbles spikes to a higher size at around $t - t_{\text{im}} = 0.37s$, this abrupt increase is associated with the behavior of the first splash-up impacting on and connecting to the free surface. A similar phenomenon occurs for the second splash-up at $t - t_{\text{im}} = 0.67s$. It shows that the bubble size enclosed by the first and second splash-up is more than ten times larger than that of the main cavity. We also observe a transient collapse in the total ingested area of bubbles due to the intermittent rupture and reconnection of the ligaments on the top face of the splash-ups (b). As shown in Fig. 7(a), there is a roughly constant production rate at $0.1s$ that lasts until $0.6s$, and then the number of bubbles increases rapidly, which is related to the breakup of the main cavity due to turbulence around the cavity. It's worth noting that the temporal development of the number of bubbles shows a high similarity to the viscous dissipation rate during the breaking process, implying a possible link between the number of bubbles and the energy dissipation rate.

5. SUMMARY

We have presented 2D direct numerical simulations of breaking waves in shallow water generated by the wave plate using Basilisk to solve the two-phase Navier-Stokes equations with surface tension. High-fidelity modeling of experimental waves has been achieved by reconstructing the piston-type wave plate numerically to provide precise information on the hydrodynamics and energetics of the breakers as well as statistics on bubble productions. For the relationship between the changing maximum wave plate speed and the associated maximum wave height before breaking, we have investigated the onset of wave breaking in terms of the ratio of wave height to water depth, and determined critical values for the transitions between non-breaking wave, spilling breaker, and plunging breaker. For a typical plunging breaking wave with a large ratio of wave height to water depth, We obtain a good collapse of the free-surface profiles and entrapped air characteristics with respect to the experiment, showing the ability to resolve wave hydrodynamics and breaking processes over a large scale separation. We present a time-evolving energy budget to analyze the energy transfer and decay due to breaking, showing an intermittent and growing viscous dissipation rate induced by air-water mixture and vortical structures in the post-breaking stage. The corresponding relationship between bubble statistics and breaking processes has also been investigated, revealing a strong correlation between the number of bubbles and the energy dissipation rate.

ACKNOWLEDGEMENTS

This work has been supported by the scholarship from China Scholarship Council (CSC) under the Grant No. 201906090270. Computations were performed using computational resources on Advanced Research Computing (ARC) at Virginia Tech.

REFERENCES

[1] Duncan, J., 1981, "An experimental investigation of breaking waves produced by a towed hydrofoil", *Proceedings of the Royal Society of London A Mathematical and Physical Sciences*, Vol. 377 (1770), pp. 331–348.

[2] Melville, W., 1982, "The instability and breaking of deep-water waves", *Journal of Fluid Mechanics*, Vol. 115, pp. 165–185.

[3] Banner, M., and Peregrine, D., 1993, "Wave breaking in deep water", *Annual Review of Fluid Mechanics*, Vol. 25 (1), pp. 373–397.

[4] Melville, W. K., 1996, "The role of surface-wave breaking in air-sea interaction", *Annual review of fluid mechanics*, Vol. 28 (1), pp. 279–321.

[5] Perlin, M., Choi, W., and Tian, Z., 2013, "Breaking waves in deep and intermediate waters", *Annual review of fluid mechanics*, Vol. 45, pp. 115–145.

[6] Derakhti, M., Kirby, J. T., Banner, M. L., Grilli, S. T., and Thomson, J., 2020, "A unified breaking onset criterion for surface gravity water waves in arbitrary depth", *Journal of*

Geophysical Research: Oceans, Vol. 125 (7), p. e2019JC015886.

[7] Fuster, D., and Popinet, S., 2018, "An all-Mach method for the simulation of bubble dynamics problems in the presence of surface tension", *Journal of Computational Physics*, Vol. 374, pp. 752–768.

[8] Scardovelli, R., and Zaleski, S., 1999, "Direct numerical simulation of free-surface and interfacial flow", *Annual review of fluid mechanics*, Vol. 31 (1), pp. 567–603.

[9] Bell, J. B., Colella, P., and Glaz, H. M., 1989, "A second-order projection method for the incompressible Navier-Stokes equations", *Journal of computational physics*, Vol. 85 (2), pp. 257–283.

[10] Wroniszewski, P. A., Verschaeve, J. C., and Pedersen, G. K., 2014, "Benchmarking of Navier–Stokes codes for free surface simulations by means of a solitary wave", *Coastal Engineering*, Vol. 91, pp. 1–17.

[11] Hirt, C. W., and Nichols, B. D., 1981, "Volume of fluid (VOF) method for the dynamics of free boundaries", *Journal of computational physics*, Vol. 39 (1), pp. 201–225.

[12] Kothe, D. B., Mjolsness, R. C., and Torrey, M. D., 1991, *RIPPLE: A computer program for incompressible flows with free surfaces*, Available to DOE and DOE contractors from OSTI.

[13] Zhang, B., Popinet, S., and Ling, Y., 2020, "Modeling and detailed numerical simulation of the primary breakup of a gasoline surrogate jet under non-evaporative operating conditions", *International Journal of Multiphase Flow*, Vol. 130, p. 103362.

[14] Aulisa, E., Manservisi, S., Scardovelli, R., and Zaleski, S., 2007, "Interface reconstruction with least-squares fit and split advection in three-dimensional Cartesian geometry", *Journal of Computational Physics*, Vol. 225 (2), pp. 2301–2319.

[15] Scardovelli, R., and Zaleski, S., 2000, "Analytical relations connecting linear interfaces and volume fractions in rectangular grids", *Journal of Computational Physics*, Vol. 164 (1), pp. 228–237.

[16] Brackbill, J. U., Kothe, D. B., and Zemach, C., 1992, "A continuum method for modeling surface tension", *Journal of computational physics*, Vol. 100 (2), pp. 335–354.

[17] Francois, M. M., Cummins, S. J., Dendy, E. D., Kothe, D. B., Sicilian, J. M., and Williams, M. W., 2006, "A balanced-force algorithm for continuous and sharp interfacial surface tension models within a volume tracking framework", *Journal of Computational Physics*, Vol. 213 (1), pp. 141–173.

[18] Popinet, S., 2009, "An accurate adaptive solver for surface-tension-driven interfacial flows", *Journal of Computational Physics*, Vol. 228 (16), pp. 5838–5866.

[19] Popinet, S., 2018, "Numerical models of surface tension", *Annual Review of Fluid Mechanics*, Vol. 50, pp. 49–75.

[20] Li, C., 2017, "Dispersion of Oil Spills by Breaking Waves", Ph.D. thesis, Johns Hopkins University.

[21] Afshar-Mohajer, N., Li, C., Rule, A. M., Katz, J., and Koehler, K., 2018, "A laboratory study of particulate and gaseous emissions from crude oil and crude oil-dispersant contaminated seawater due to breaking waves", *Atmospheric Environment*, Vol. 179, pp. 177–186.

[22] Sumer, B. M., Jensen, P. M., Sørensen, L. B., Fredsøe, J., Liu, P. L.-F., and Carstensen, S., 2010, "Coherent structures in wave boundary layers. Part 2. Solitary motion", *Journal of fluid mechanics*, Vol. 646, pp. 207–231.

[23] Van Hooft, J. A., Popinet, S., Van Heerwaarden, C. C., Van der Linden, S. J., de Roode, S. R., and Van de Wiel, B. J., 2018, "Towards adaptive grids for atmospheric boundary-layer simulations", *Boundary-layer meteorology*, Vol. 167 (3), pp. 421–443.

[24] Mostert, W., and Deike, L., 2020, "Inertial energy dissipation in shallow-water breaking waves", *Journal of Fluid Mechanics*, Vol. 890.

[25] Wei, Z., Li, C., Dalrymple, R. A., Derakhti, M., and Katz, J., 2018, "Chaos in breaking waves", *Coastal Engineering*, Vol. 140, pp. 272–291.

Conference on Modelling Fluid Flow (CMFF'22)
The 18th International Conference on Fluid Flow Technologies
Budapest, Hungary, August 30-September 2, 2022

FISH INJURY ASSESSMENT OF A HYDROPOWER FACILITY BYPASS

Dennis POWALLA[1], Rishav SAHA[2], Stefan HOERNER[2], Dominique THÉVENIN[2]

[1] Corresponding Author: Laboratory of Fluid Dynamics and Technical Flows, University "Otto von Guericke" of Magdeburg, Universitätsplatz 2, Magdeburg, 39106, Germany, E-mail: dennis.powalla@ovgu.de
[2] Laboratory of Fluid Dynamics and Technical Flows, University "Otto von Guericke" of Magdeburg, Universitätsplatz 2, Magdeburg, 39106, Germany

ABSTRACT

The Las Rives hydropower plant is located on the Ariège river in France. A fish ladder and bypass system was installed in the facility in order to ensure river continuity. The downstream fish pass is located after a rack in front of the intake channel of the power plant. It later connects through a free-stream jet to the tailwater. Objective of this work is to investigate the injury risk for the fish passing the device, caused by possible impacts when penetrating the water surface or hitting the river bed. The study is based on a custom numerical framework combining fluid dynamics with particle-based fish surrogates. In a first step the free stream bypass is modelled with Computational Fluid Dynamics (CFD). The water jet is simulated as an Eulerian multiphase flow, which is described by the Volume of Fluid method (VOF). After establishing a suitable fluid dynamical model of the bypass installation, particles are injected at the bypass inlet while coupling CFD with the Discrete Element Method (DEM). The particles act as fish surrogates in the model. The DEM is a Lagrangian method that allows for tracking contacts between particles and with the wall. Based on the information gained from the unsteady simulations and a multitude of particle tracks, a statistical evaluation of the data regarding fish compatibility is possible. The work presented here is ongoing and provides a first base for further investigations of the site. In a parallel experiment live-fish and passive sensor probes were injected in the bypass by research partners from France and Estonia. The sensors allow for a recording of acceleration and pressure data during the passage. Future work will compare this experimental data and the data gained by the simulations to validate the numerical methodology.

Keywords: Computational fluid dynamics (CFD), Ecohydraulics, Eulerian Multiphase, Hydropower, Reynolds-Averaged Navier-Stokes (RANS), Volume of Fluid (VOF)

NOMENCLATURE

CFD	[]	Computational Fluid Dynamics
CFL	[]	Courant number
DEM	[]	Discrete Element Method
LES	[]	Large-Eddy Simula- tions
RANS	[]	Reynolds-Averaged Navier-Stokes
SIMPLE	[]	Semi-implicit Method for Pressure Linked Equations
SST	[]	Shear stress transport
VOF	[]	Volume of Fluid
k	$[m^2/s^2]$	Turbulent kinetic energy
y^+	$[-]$	Dimensionless wall distance
ω	$[1/s]$	Specific rate of dissipation

1. INTRODUCTION

River continuity is an important aspect of the ecology of water bodies, since it is a requirement for reproduction and migration of a large part of aquatic fauna. Anthropogenic barriers often strongly impact the surrounding ecosystems, in particular for devices that block the natural river continuity. This is typically the case for run-of-river power plants, where a dam interrupts fish passage in both directions, compromising the sustainability of fish populations [1]. In Europe, run-of-river power plant operators have to conform to the European Water framework directive, which states the requirements related to their ecological impact [2]. To enable fish the passage of those obstructions, the current state of the art consists of fish ladders or lifts, which offer alternative paths for fish and reconnect the upper and lower parts of the river otherwise separated by the dam.

It is mandatory to provide information about the mortality and injury risk potential on migrating fish passing either the power plant itself or the upstream and downstream fish passage installations. Especially passing the power plant leads to a higher risk of injury/mortality by collision with the turbine structure or, if a certain threshold of turbine head is exceeded, through barotrauma as shown by Trumbo et

al., 2014 [3] or Bevelhimer et al., 2017 [4]. Up to now these assessments are mostly gained using live fish tests. Giesecke et al. 2014 [5] considers life fish tests to be morally questionable, time-consuming, complex and costly, and in most cases only valid for the specific installation and operating point tested. Considering the limitations and uncertainties of this approach, as well as the very stressful and harmful experience imposed on the animals, an urgent need for the development of alternative prediction models for their replacement can be stated. Already introduced alternative prediction models are so called blade strike models, which can be either of physical or empirical nature. Common physical models are introduced by von Raben ([6]), Monten ([7]) and Turnpenny ([8]) which are based on the same principle and differ in the degree of complexity of the underlying assumptions for the probability of collision between fish and turbine blade. Empirical models such as Larinier and Travade 2002 [9], or Ebel 2008 [10] use statistical evaluation methods by combining observed mortality rates and technical parameters. The physical model have in common that the fish's "behaviour" is simplified as a passive buoyant neutral object carried with the flow, whereas the emperical models require extensive live fish. To address these simplifications and reduce live animal tests further improvements should be developed.

The development of such alternative prediction models is also the aim of the RETERO-project (www.retero.org). This project strives for a reduction of live fish testing for the assessment of any hydropower facility and other descent corridors in installations. This is done by reducing (and in the longer term fully replacing) animal probands by complementary methods such as passive probes, partly-autonomous sensors and numerical simulations. The numerical work presented here employs a combination of Computational Fluid Dynamics (CFD) and Discrete Element Method (DEM) - overlaid by fish behaviour models. CFD-DEM coupling means, that the hydraulic conditions of a given installation are simulated by CFD, while the trajectory of particles seeded in the flow are solved by a DEM solver. A coupling algorithm describes the interaction between fluid and solid particles. Each particle is described individually and acts in the application at hand as a fish surrogate. The DEM solver allows for a tracking of the contact interactions of particles with their environment, more specifically the inter-particle contacts and contacts between particles (i.e., fish) and wall boundaries. For the risk assessment model at hand interactions between particles are of no importance and the focus is laid on wall interactions, as they describe blade strike events in hydraulic installations and in pumps or turbines. Adding to the CFD-DEM model a complex fish behaviour model is the next logical step to improve prediction accuracy. The collision prediction capabilities of the CFD-DEM simulations are combined with rules of conduct for individual particles derived from data obtained by ethohydraulic experiments on live fish. It is obvious, that an important role in the development of such a prediction tool is the validation with experimental data from laboratory or field tests.

Data from field tests exist for the Las Rives hydropower plant. In this study it serves as an example of those anthropogenic barriers mentioned above. The plant is located on the Ariège river in France. To increase the performance of the site a dam was built to elevate the water intake. Therefore, a fish ladder for upstream migration and a bypass system for downstream migration were installed in the facility to maintain river continuity. The upstream fish passage is located at the upstream end of the dam and the downstream fish bypass is located after a rack in front of the intake channel of the power plant. The downstream fish bypass later connects to the tailwater by a free-stream jet. The objective of the original experiments was to investigate the injury risk for the fish in a downstream passage of the facility, caused by impacts during water surface penetration or by hitting the river bed. In France, the only currently available criterion for such a water jet bypass system has been proposed by Odeh and Orvis, 1998 [11]; it states that a minimum water depth of one quarter of the fall height – with a minimum value of about 1 m – has to be maintained. This expression omits other important parameters like the jet velocity at the impact point, which depends on the initial flow velocity at the outlet of the bypass, and the flow rate, which determines the thickness and the penetration depth of the jet.

The goal of this work is to develop a numerical model of the downstream fish passage. This model will form the basis for further investigations, where the numerical data will be compared to passive sensor probes and live-fish tests.

2. METHOD AND MATERIAL

2.1. Numerical model of the Las Rives installation

The dimensions chosen for the numerical model are based on the technical drawings of the Las Rives site. To keep acceptable computing times, only the important part of the installation is considered, i.e., the channel and the pool region. The channel is 4 m in length and 1 m wide, with a slope of 4°. The ground profile of the river is provided by measurements carried out on site. In the simulation setup, the pool/river basin has dimensions of 10 m × 10 m × 6 m [length, width, height]. The vertical drop from the channel outlet to the river ground is approx. 3.6 m and the entire numerical domain is shown in Figure 2.

The downstream fish bypass at the Las Rives hydropower plant site, which connects the intake channel to the tailwater by a free-stream jet is shown in Figure 1.

Figure 1. The water jet leaving the downstream fish passage into the underlying river at the Las-Rives-Site

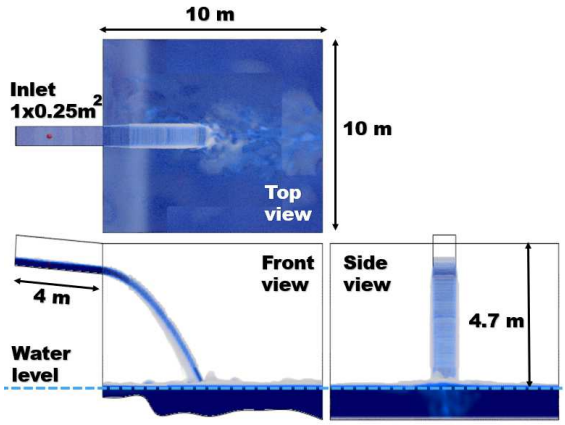

Figure 2. Technical sketch of the numerical domain.

2.2. Numerical set up

The numerical simulations were built with use of the Star-CCM+ software package, while the two-phase flow was described by an Eulerian multiphase model using the Volume of Fluid (VOF) method [12]. The VOF method is a simple multiphase flow model able to resolve the interface between the phases of the mixture by adding a volume fraction transport equation. For two phases only one volume transport fraction is calculated. It is assumed, that no interface interaction occurs and therefore all phases share the same velocity, pressure, and temperature fields. A segregated SIMPLE (Semi-implicit Method for Pressure Linked Equations) solver was chosen. The incompressible form of the Reynolds-Averaged Navier-Stokes (RANS) equations were deployed to capture the highly turbulent, fluctuating flow with reasonable computational costs. More sophisticated, but also much more expensive methods, like Large-Eddy Simulations (LES), were not considered, since many operating points of the device shall be investigated in future work. Based on preliminary studies, the two-equation $k-\omega$-SST (shear stress transport) approach introduced by Menter was chosen for turbulence modeling [13], where k is the turbulent kinetic energy and ω is the specific rate of dissipation. The quality of this model has been demonstrated in many applications, but it may still underpredict anisotropy effects, and as a consequence the flow field [14]. The boundary layer is treated in an adaptive wall model depending on the y^+ criteria. y^+ is the non-dimensional wall distance. Overall, the numerical model described in Table 1 appears as a good trade-off between numerical robustness, computational costs, and resulting accuracy. Simulations were run in parallel on 25 nodes (16 core- Haswell), corresponding to 400 CPUs on the high-performance Linux cluster Sofia of the University of Magdeburg, progressing at a rate of approx. 0.12 CPU hours per simulated second of physical time. One CFD simulation requires approximately 960 CPU-hours in total to reach a quasi steady state, which corresponds to 2.4 hours.

Table 1. Overview of numerical set up.

Solver physics	3d, implicit unsteady, incompressible, turbulent,Eulerian -multiphase, segr. flow
Solver algorithm	SIMPLE
Temporal discretization	
Accuracy	first order
Time step	$1 \cdot 10^{-3}$ s
Spatial discretization	
mesh type	core: trimmed cells, near-wall region: orthogonal prism cells
core cell size:	0.1 m
refinement cell size:	0.05 m
finest cell size:	0.04 m
Total amount of cells	$\approx$ 2.4 million
CFL (target)	< 0.5
Turbulence model	(Menter) $k-\omega$ SST
Wall treatment model	adaptive
Multiphase model	Volume of fluid (VOF)
Convergence criteria	
Residuals determined by	RMS
X-Momentum equations	residual target= 0.005
Y-Momentum equations	residual target= 0.005
Z-Momentum equations	residual target= 0.005

2.2.1. Boundary condition

The inlet of the numerical domain is implemented as velocity inlet condition. The velocity of the bypass is given by experimental data; velocity and flow direction are specified. Inlet volume flux as well as the fluxes of momentum and energy are subsequently calculated. The pressure condition at the inlet is set to zero gradient. To model the interactions with the environment (atmosphere and domain outlet), a pressure outlet boundary condition is set. This boundary

pressure can be considered as the static pressure of the environment (here, static pressure of air and water) into which the fluid enters. The boundary face velocity is extrapolated from the inner domain and the static pressure. The water height level of the underlying river is controlled by setting the pressure at the pressure outlet boundaries to the hydrostatic pressure, which is calculated by the predefined depth of water. The components of the volume fractions at the pressure outlet boundaries are also set in accordance to the depth of the water. This definition sets the boundaries equal to an indefinite extended basin with constant water level. However, this assumption isn't fully in accordance with the real river flow direction, which runs *perpendicular* to the inlet chamber. However, the effects regarding the interest of the study, a fish injury risk assessment, were considerd to be negligible. An overview of the boundary conditions can be seen in Figure 3.

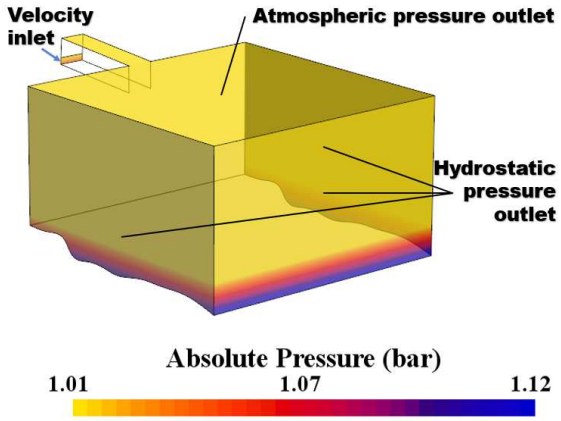

Figure 3. Sketch of the numerical domain and its boundary conditions. The inflow direction is displayed by the blue arrow at the channel inlet.

2.2.2. Meshing

The discretization of the core domain is achieved by a hexahedral mesh, whereas the near-wall region is generally meshed with a moderately refined boundary layer according to the upper limit range of the adaptive y^+-based near-wall treatment ($30 < y^+ < 100$). The centroid of the near-wall cell lies in the log-layer of the boundary layer. A full resolved boundary layer was considered to be to computational costly and not necessary for the study at hand. Using the VOF model comes with certain stability requirements for the spatial and temporal discretisation. One of those best-practice guidelines from the software provider relates to the Courant-Friedrich-Lewy number (CFL). The CFL number is a non dimensional number to evaluate the spatial and temporal resolution of a CFD simulation. It relates the time scale for the flow through a mesh cell to the time step size. A value smaller than one means that the flow 'remains' in one cell in between two timesteps, which is a convergence criteria for explizit formulated numerical schemes. An increase of the value over one will lead to inaccuracies and instabilities in this case. For simulations applying the VOF-model, the CFL number should be less than 0.5 following the code documentation of the software used in this study.

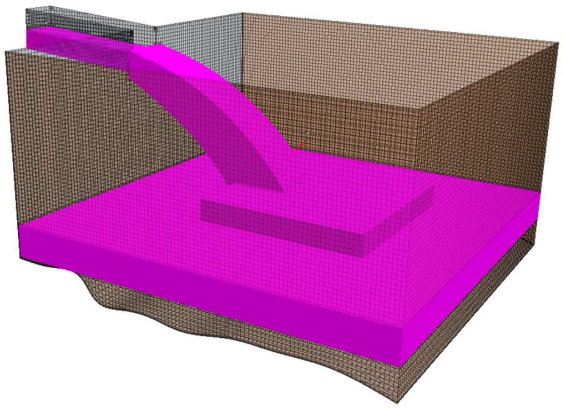

Figure 4. The area of mesh refinement in the simulation domain is highlighted in pink

To follow the computational requirements, a refinement area is defined (see figure 4). It contains the water jet and its impact on the water surface, down to the river bed. This can be seen even more clearly in figure 5. The time step is set to $1 \cdot 10^{-3}$ s, ensuring stability.

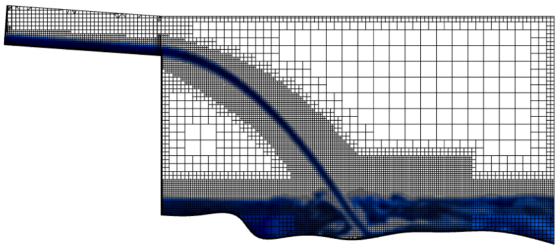

Figure 5. Cross-section through the middle of the domain, showing mesh size and two-level refinement areas. The first is located at the air/water boundary while the second, even finer refinement is placed at the location of the jet/river bed interaction

2.2.3. Grid independence study

To ensure grid independency, a mesh size study was performed. The refinement in this study only takes place in the area, which contains the water jet and the area around the place where the jet hits the bottom. This is chosen, for the aim of the study is to show the impact of objects hitting the water surface and the river bottom through the jet. The refinement has been carried out in three levels. The first

level is coarse with a cell size of 0.1 m, the second refinement level has a cell size of 0.05 m and the third/finest refinement level has a cell size of 0.04 m. The three refinement levels are compared on a velocity sample placed in the middle region of the jet stream. The placement of the velocity sample is shown in Figure 6 in a top and side view.

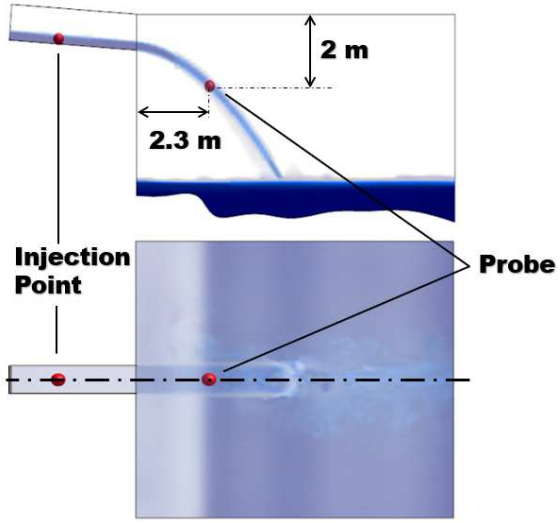

Figure 6. Probe and injection point location for grid independence study in water jet stream

The comparison of the refinement levels is shown in Figure 7 . Here, the averaged velocity at the sample point is plotted against the number of cells in the simulation area. The averaging of the velocity takes place over a period of 5 s of physical time and after the simulation has reached a quasi static state (after around 15 s of physical time). Considering the computational cost and the grid independency the cell size of the fine (1.6M cells) refinement level is decided to be sufficient enough for the present work.

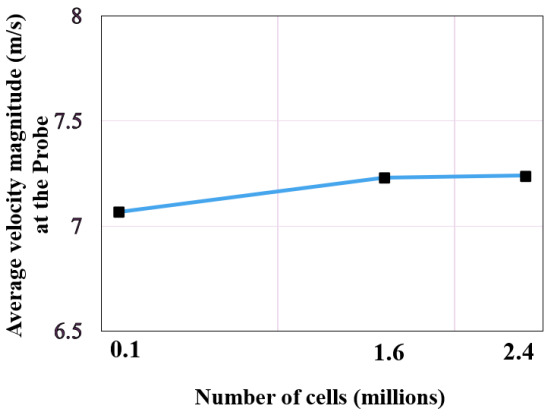

Figure 7. Grid independence study by average velocity magnitude at sample point over number of cells for three different refinement levels.

2.2.4. Domain size independence study

In addition to the grid independence study, a domain size independence study has also been conducted. The topology of the river bottom is only known for a quite limited area. The piercing of the the water surface by the jet and the subsequent hitting of the river bed results in a complex two-phase flow with entrained air. This flow is dominated by the air entrainment effects and the redirection of the jet at the river bed. The main direction of flow is in the x-direction which convects these disturbances in this direction. Due to the short distance to the outlet, the flow remains chaotic with back flow regions at the boundary of the domain in the initial configuration. The simulation domain boundary was iteratively extended (in x-direction) to investigate the influence of the domain size.

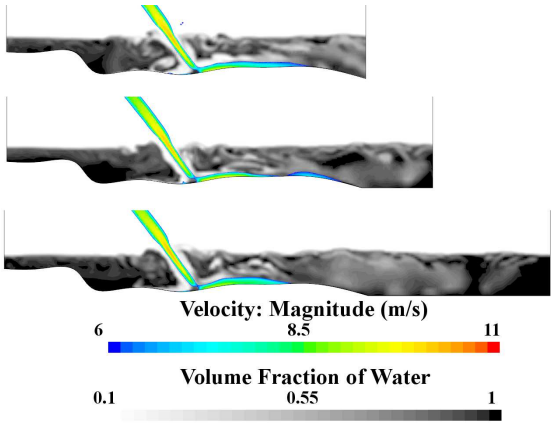

Figure 8. Domain size independence study of three different configurations showing the cross-sections in x-direction with velocity field of the liquid phase, from jet injection to its impact on the pool ground. Additionally the gray-scaled area shows the local volume fraction of the water

Figure 8 shows the influence of the extension of the simulation domain. The velocity field of the jet (colored) and volume fraction of water (black and white) are depicted. The first two variants still feature a strong mixing of air and water up to the boundary limits. The widest simulation domain shows a homogeneous flow field and the outlet flow consists entirely of water. This allows for a stable simulation. In consequence the last setting is chosen for further investigations.

2.3. Active particles as fish surrogate in CFD-DEM

The overall goal in this study is the investigation of injury and mortality risk of fish in the bypass by an extension of the established CFD model with a coupled DEM method using active and passive particles.

The particles are described in a Lagrangian framework, which means that each path of an in-

jected particle is tracked when travelling through the domain. The continuous phase is described in an Eulerian framework and the combination of both leads to an Eulerian-Lagrangian multiphase flow. The deployed Eulerian-Lagrangian multiphase model calculates the trajectory of each particle and the momentum equations for the fluid flow – taking all interactions between the dispersed phase and the continuous phase into account. Different coupling levels are possible, in which only flow to particle information transfer is considered (one-way-coupling), or additionally the feedback of the particle onto the flow (two-way-coupling). Choosing the DEM model as a Lagrangian representation of the particle adds two more coupling levels, when taking into account particle-particle and/or particle-wall interaction. For this project the particle-wall interactions is of highest interest because it corresponds to fish (i.e., particle) – blade (i.e., wall) interactions. The DEM model enables the recording of contact forces for impacts, which can be used for prediction models regarding fish mortality and injury risk. Besides using generic, passive particles as fish surrogates a novel approach with active particles, first introduced in [15] will be deployed as well. The intention of the novel approach is an active motion of the particles according to a fish-like behavior, based on ethohydraulic observations. The method adds an additional body force to the particle equation of motion, with which the velocity and orientation of the particle can be controlled. Here, different rules of conduct for the particle can be defined and combined to mimic real fish's behavior. Such rules of conduct can be for instance: to follow the instantaneous main flow, the willingness to move downstream/upstream, or to swim close to the wall or to the ground. A detailed description of the method can be found in Powalla et al. 2021 [15].

In figure 9 an example (see [16] for details) of the active particle approach is shown. In this example, two rules of conduct are acting on the particles. One is the willingness to migrate downstream the power plant. The other is to follow the main flow. They are both linked by a weighting function, which controls the impact of each rule of conduct. Their combination results in a final orientation of the particle and can be combined with individual weights for each particle.

3. RESULTS

In the application at hand, specific challenges in the numerical model are found in the region where the water jet enters the river and subsequently, when the jet hits the river bed. Here, the propagation of strong waves caused by the impact of the jet on the surface has to be captured. Even more complex is to capture the air entrainment effects. Figure 10 shows the water phase for the entire domain. It can be seen how the water mixes up with the air when piercing the water surface. It is also visible that surface waves travel toward the domain boundaries, which causes further challenges for stability and accuracy.

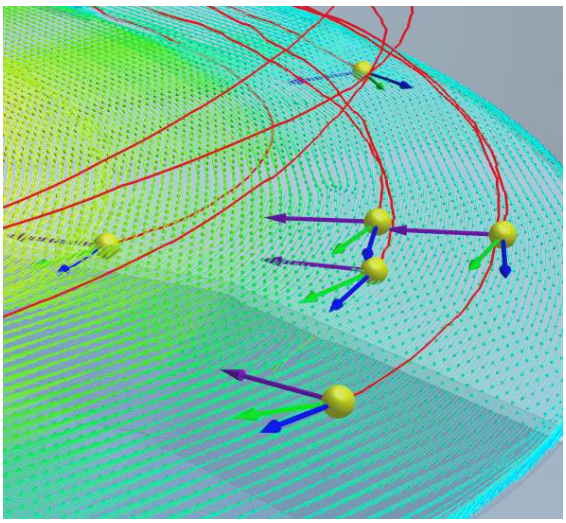

Figure 9. Example showing the active particle method. Two rules of conduct guide the particles (yellow): follow the stream (blue vector), and willingness to migrate downstream (purple vector). The combination of both results in the final orientation (green vector).

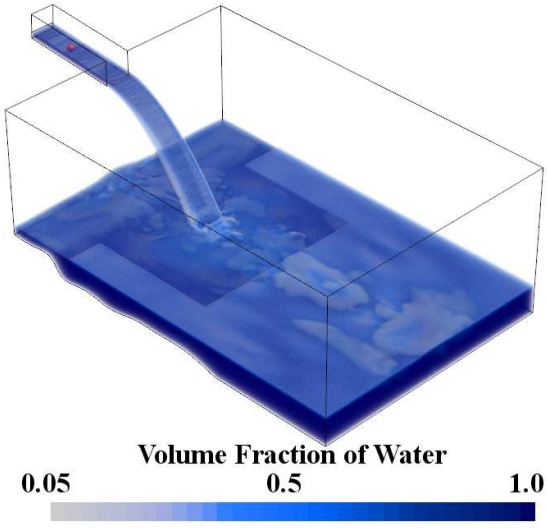

Figure 10. 3D Simulation of the water jet displaying the liquid phase (defined by volume fraction of water > 0.5)

As discussed in the meshing section, the VOF method requires a certain temporal and spatial resolution. An indication for that can be seen by the CFL number. Figure 12 shows the CFL number for the water phase. It can be seen, that it ranges for the main jet stream in between 0 to 2. This is above the best-practice limit of 0.5, due to locally large velocities (see for comparison figure 11). However, the spatial resolution of the simulation is found to be sufficient in most areas.

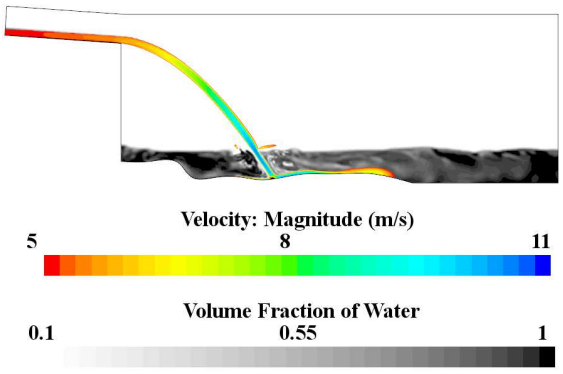

Figure 11. Cross-section with velocity field of the liquid phase, from jet injection to its impact on the pool ground. Additionally the gray-scaled area shows the local volume fraction of the water.

The transport of the air and water mixture by the jet into the pool is highlighted in figure 11. The figure clearly shows the highly turbulent and complex fluid structure not only caused by the multiphase mixture but also by the impact of the jet onto the river bed. It also shows the acceleration of the flow from leaving the top channel to the bottom of the pool. Here, the flow accelerates from its initial value of 5 m/s up to about 11 m/s.

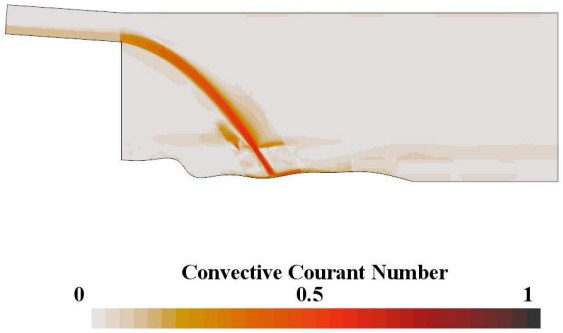

Figure 12. CFL number of the liquid phase in the central cross-section, shown together with mesh refinement.

In figure 13 a first simulation involving particles is shown. The particles are injected at the level of the inlet channel and are transported by the jet into the underlying water basin where they finally hit the ground. The aforementioned method allows to extract the acceleration and contact data of each particle which will be used ultimately to quantify risk injury for fish in such a bypass system.

4. CONCLUSION AND OUTLOOK

In this ongoing work the numerical model of a water jet from a bypass facility for downstream fish passage has been presented. This model describes both hydrodynamic features and fish behavior. The piercing of the water surface by the jet and the subsequent hitting onto the river bed results in a complex two-phase flow, which leads to a numerical challenging task. In this work a grid independence study and a domain study has been conducted to ensure numerical stable conditions for the upcoming tasks. The assessment of the injury risk for fish passing the bypass structure. It has to be mentioned that in the current setting the flow velocity of the underlying river is not yet considered and the influence has to be discussed and addressed in the future

In the next steps, this model will be used to quantify injury and mortality risk of fish in the downstream passage of the bypass, using the formerly introduced procedure combining CFD/DEM with active fish behavior [15]. The particles will be tracked during their path through the domain and the data will be validated with use of experimental measurements gained by passive probes [17] and live fish tests.

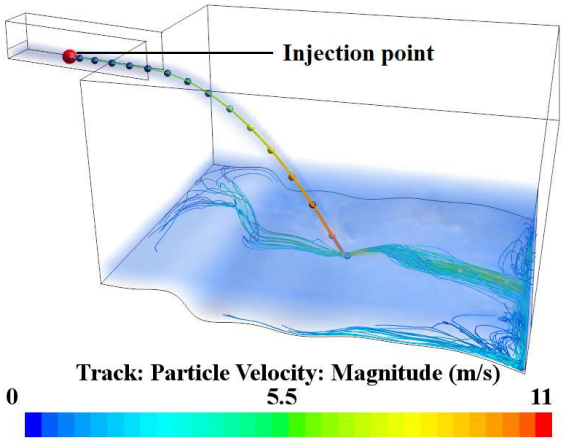

Figure 13. First simulation with particle injection. The injection is at the channel inlet (red spheres) and the particles are then colored according to their instantaneous velocity.

ACKNOWLEDGEMENTS

The authors are grateful for the support of Sylvie Tomanova and Dominique Courret from the Office français de la biodiversité (OFB) in sharing data and insights of the Las Rives site necessary for the realization of the study at hand.

REFERENCES

[1] Silva, A. T., Lucas, M. C., Castro-Santos, T., Katopodis, C., Baumgartner, L. J., Thiem, J. D., Aarestrup, K., Pompeu, P. S., O'Brien, G. C., Braun, D. C., Burnett, N. J., Zhu, D. Z., Fjeldstad, H.-P., Forseth, T., Rajaratnam, N., Williams, J. G., and Cooke, S. J., 2018, "The Future of Fish Passage Science, Engineering, and

Practice", *Fish and Fisheries*, Vol. 19 (2), pp. 340–362.

[2] EP, 2000, "Directive 2000/60/EC of the European Parliament and of the Council of 23 October 2000 Establishing a Framework for Community Action in the Field of Water Policy", .

[3] Trumbo, B. A., Ahmann, M. L., Renholds, J. F., Brown, R. S., Colotelo, A. H., and Deng, Z. D., 2014, "Improving Hydroturbine Pressures to Enhance Salmon Passage Survival and Recovery", *Reviews in Fish Biology and Fisheries*, Vol. 24 (3), pp. 955–965.

[4] Bevelhimer, M. S., Pracheil, B. M., Fortner, A. M., and Deck, K. L., 2017, "An Overview of Experimental Efforts to Understand the Mechanisms of Fish Injury and Mortality Caused by Hydropower Turbine Blade Strike", *Technical Report, US Dpt of Energy*.

[5] Giesecke, J., Heimerl, S., and Mosonyi, E., 2014, *Wasserkraftanlagen: Planung, Bau und Betrieb*, Springer Vieweg, Berlin, 6., aktualisierte und erw. aufl edn., ISBN 978-3-642-53870-4.

[6] von Raben, K., 1957, "Zur Frage der Beschädigung von Fischen durch Turbinen", *Die Wasserwirtschaft*, Vol. 4, pp. 97–100.

[7] Montén, E., 1985, *Fish and turbines: fish injuries during passage through power station turbines*, Vattenfall.

[8] Turnpenny, A., Clough, S., Hanson, K., Ramsay, R., and McEwan, D., 2000, "Risk assessment for fish passage through small, low-head turbines", *Final Report, Energy Technical Support Unit, Harwell, UK*.

[9] Larinier, M., and Travade, F., 2002, "Downstream migration: problems and facilities", *Bulletin Français de la Pêche et de la Pisciculture*, pp. 181–207.

[10] Ebel, G., 2008, *Turbinenbedingte Schädigung des Aals (Anguilla anguilla) : Schädigungsraten an europäischen Wasserkraftanlagenstandorten und Möglichkeiten der Prognose*, Ebel, Büro für Gewässerökologie und Fischereibiologie, ISBN 9783000254451.

[11] Odeh, M., and Orvis, C., 1998, *Downstream fish passage design considerations and developments at hydroelectric projects in the northeast USA*, Fishing News Books.

[12] Hirt, C. W., and Nichols, B. D., 1981, "Volume of fluid (VOF) method for the dynamics of free boundaries", *Journal of Computational Physics*, Vol. 39 (1), pp. 201–225.

[13] Menter, F. R., 1994, "Two-equation eddy-viscosity turbulence models for engineering applications", *AIAA journal*, Vol. 32 (8), pp. 1598–1605.

[14] Wallin, S., and Johannsen, A. V., 2000, "An explicit algebraic Reynolds stress model for incompressible and compressible turbulent flows", *Journal of Fluid Mechanics*, Vol. 403, p. 89–132.

[15] Powalla, D., Hoerner, S., Cleynen, O., and Thévenin, D., 2022, "A Numerical Approach for Active Fish Behaviour Modelling with a View Toward Hydropower Plant Assessment", *Renewable Energy, (in press)*.

[16] Powalla, D., Hoerner, S., Cleynen, O., Müller, N., Stamm, J., and Thévenin, D., 2021, "A Computational Fluid Dynamics Model for a Water Vortex Power Plant as Platform for Etho- and Ecohydraulic Research", *Energies*, Vol. 14 (3), p. 639.

[17] Tuhtan, J., Fuentes, J., Angerer, T., and Schletterer, M., 2018, "Monitoring upstream passage through a bypass pipe and drop at the fish lift Runserau: Comparing dynamic pressure measurements on live fish with passive electronic fish surrogates", *12th International Symposium on Ecohydraulics Aug19 Aug24,2018, Tokyo, JAPAN*.

Conference on Modelling Fluid Flow (CMFF'22)
The 18th International Conference on Fluid Flow Technologies
Budapest, Hungary, August 30 - September 2, 2022

INDUSTRY 4.0 PERSPECTIVES OF AXIAL AND RADIAL FANS IN SMART INDUSTRIAL VENTILATION: CONCEPTUAL CASE STUDIES

Dominik TÓTH[1], János VAD[2]

[1] Department of Fluid Mechanics, Faculty of Mechanical Engineering, Budapest University of Technology and Economics. Bertalan Lajos u. 4 – 6, H-1111 Budapest, Hungary. Tel.: +36 30 268 3347, E-mail: toth.dominik0@gmail.com
[2] Corresponding Author. Department of Fluid Mechanics, Faculty of Mechanical Engineering, Budapest University of Technology and Economics. E-mail: vad.janos@gpk.bme.hu

ABSTRACT

Industry 4.0 envisages new functions in industrial air technology. The paper presents novel overall concepts for smart industrial ventilation, for which smart features are adopted to axial and radial flow fans. The applicability of the resultant smart fans is illustrated in two conceptual case studies. Commercial fan units were selected as candidates for the smart fans. These fan units, incorporating optional metering devices, were developed on the initiative of the manufacturers at the authors' Department. Thanks to their customized hardware, the selected fan units represent a transition in the evolution from common fans to smart fans with the following potential: comprehensive monitoring and control of gas parameters, aerodynamic performance, and noise; a priori high, controlled efficiency; a priori high, monitored resistance to harsh operating conditions; condition monitoring for the fan. Instrumentation is in the focus. Therefore, a multifunctional metering device included in the fan unit is discussed, giving a potential for measurement of flow rate, air temperature, and static pressure, even for harsh conditions. Concepts for further instrumentation built in the compact fan unit for condition monitoring, as well as sensors located inevitably out of the fan unit, are systematically discussed, together with the features of smart data processing.

Keywords:
axial flow fans, Industry 4.0, industrial air technology, industrial ventilation, radial flow fans, smart fan, smart ventilation

NOMENCLATURE

Latin letters

A	$[m^2]$	cross-section
a	$[m/s]$	speed of sound in gas
D	$[m]$	diameter of fan duct or blade tip
d	$[m]$	hub diameter of axial fan rotor
K	[-]	flowmeter calibration factor
L_W	[dB]	overall fan sound power level
ΔL_{Woct}	[dB]	relative sound power level, octave
N	[-]	blade count for fan rotor
n	$[1/s]$	fan rotor speed
P_{eff}	$[W]$	effective performance
P_{in}	$[W]$	fan drive input electric power
p	$[Pa]$	static pressure
p_a	$[Pa]$	measured annulus mean pressure
p_d	$[Pa]$	dynamic pressure
p_t	$[Pa]$	total pressure
Δp_t	$[Pa]$	total pressure rise
q_V	$[m^3/s]$	gas volume flow rate
Re	[-]	flowmeter Reynolds number
R	[-]	specific gas constant
T	$[K]$	gas temperature
T_b	$[K]$	bearing temperature
u_{tip}	$[m/s]$	rotor tip circumferential speed
v	$[m/s]$	local mean flow velocity
v_v	$[m/s]$	vibration velocity

Greek letters

η	[-]	fan efficiency based on P_{in}
η_D	[-]	efficiency of the fan drive
η_t	[-]	fan total efficiency
κ	[-]	specific heat ratio
ν	$[m^2/s]$	gas kinematic viscosity
ρ	$[kg/m^3]$	gas density

Subscripts and Superscripts

a	flowmeter annulus
P	fan pressure side
S	fan suction side

1. INTRODUCTION AND OBJECTIVES

The Industry 4.0 concept has a significant effect on the industrial processes. Energy efficiency, and reliable operation became the governing principles. The effect of Industry 4.0 is the continuous improvement of the automation into "smart

factories". This necessitates the development of smart process systems [1-2]. A smart system is capable to operate without human intervention, with the aid of a computer-assisted control system and high-level sensor implementation [3]. This automated system is able to operate with high effectiveness, and is designed to avoid any failures or shutdowns. In order to assure this, the system has to be provided with an effective maintenance procedure, supported by condition monitoring [4-5]. Referring to advanced Operation & Maintenance strategies, condition monitoring is a complex predictive maintenance method, which is capable to prognosticate and diagnose a machine malfunction. This greatly reduces the maintenance time, because the planning of maintenance can be started before the work process has to be stopped. Nowadays, the condition monitoring systems operate on the basis of advanced signal processing techniques and Artificial Intelligence, thus improving the speed and reliability of decision-making [6].

As suggested by the 327/2011/EU Fan Regulation [7], fans are operated in industrial air technical and ventilation systems in such a great volume that their impact on the global economy is significant. Consequently, Industry 4.0-driven smart factories are also envisaged to incorporate systems of industrial air technology and ventilation, served by fans, in a significant portion. In line with the Industry 4.0 concept, in a smart factory equipped with industrial air technology and ventilation, "smart ventilation" systems are presumed to operate, incorporating "smart fans". This would envisage that the concepts of "smart ventilation" and "smart fan" are incorporated in the Industry 4.0 perspective, and are well-established in industrial ventilation and air technology. Nevertheless, a literature survey reveals that the concept of "smart ventilation" is nowadays mainly restricted to ventilation in residential buildings [8-9]. Furthermore, a "smart fan" is usually regarded as a room ceiling fan [10-11], or a simple home cooling fan [12-13]. The "smartness" of the aforementioned fans is often confined to features of advanced and remote personal control supervised by the user. Although the name of the SmartFAN European project may suggest a focus of smart ventilation, the project regarded the material development of the fan impeller for applications of various kind [14]. The above overview reflects that the "smart ventilation" and "smart fan" concepts are less elaborated for Industry 4.0 applications incorporating processes related to industrial air technology and ventilation.

The objective of the present paper is to provide a supplementary and comprehensive overview on the potential of smart industrial ventilation from the Industry 4.0 perspectives. To this end, novel concepts are presented for the extension of the smart ventilation and smart fan features to industrial air technology and ventilation, in accordance with the Industry 4.0 perspective. The new features of these concepts are outlined, in comparison with the traditional characteristics of systems in industry-related ventilation and air technical systems, embedding classic fans. The concept of a smart fan is feasible only with the development of an eligible system of instrumentation. This sensor system has to be able to assure the effectiveness of fan operation and the avoidance of any failures or shutdowns. Accordingly, the instrumentation to be associated with a smart fan is discussed herein. To the best knowledge of the authors, this paper is the first one providing a comprehensive discussion and synthesis on the aforementioned novel items in the present form.

2. ILLUSTRATIVE EXEMPLARY CASE STUDIES

2.1 Initial remarks

In this paper, the smart fan features are illustrated via two substantially different, representative industrial examples. One of them is a gas engine power plant, in which the delivered combustion air is utilized as input chemical component into the combustion process, i.e. it is non-recirculating. The other one is an air technical separator used for classification of multitudes of solid particles, e.g. municipal waste being processed. Here, the air serves as auxiliary medium in addition to the mass flow of the solid phase under classification, and is recirculated in the technology. These two examples are representative also in terms of the two substantially different types of the fans applied. The combustion air supply system for the gas engine power plant is typically served by *axial flow fans* in parallel connection. This is in accordance with the need for a volume flow rate of combustion air being large relative to the fan driving power, driven through system elements of relatively low pressure drop. The air technical separator is typically operated using a *radial flow fan*. Here, the flow rate is low relative to the driving power, and is converted into a concentrated, high-velocity air jet produced by a nozzle. This fact, together with the dust content of the air necessitating rough filtration casing relatively high pressure drop, results in a need of relatively high total pressure rise. Therefore, the two examples represent the possible smart application of axial as well as radial fans, being mostly widespread in industries.

The discussion on the fans is organized within the examples in the paper in an evolutionary approach. As detailed in the following, such approach means that the fans applied at various states of system development are discussed as units corresponding to the following phases of evolution: *common* fan units, without any special features $\rightarrow$ fans with selectively improved, *favourable* hardware

features → fans exhibiting *eminent* features when operated as smart fans in a smart system.

A) *Common fan units* with traditional geometry and hardware, used in conventional air technical systems, are outlined first in Sections 2 2. and 2.3.

B) Options of further development of the traditional geometry and hardware within the fan units is then discussed, in correspondence to case-specific application demands, resulting in improved, *favourable fan features*. Three examples of such favourable features are as follows.

a) *A priori* high fan efficiency, by fulfilment of minimum criterion on energy efficiency.

b) In-built tool for flow rate measurement exploitable in process control.

c) *A priori* high resistance against harsh operational conditions, i.e. improved robustness, via less inclination of sensitivity to dust load.

In Section 3, commercial fan units will be selected herein with *favourable features*, as potential candidates for further development into a "smart fan" status.

C) Concepts for enhancement of the aforementioned favourable fan features to *eminent fan features* are finally outlined, via application of the smart fan concept to the candidate fans. In order to achieve *eminent fan features*, being embedded in the Industry 4.0 perspective, the previously given three examples evolve as well as interact with each other as follows.

a) Continuous monitoring and possible maximization of the fan efficiency, being *a priori* high, as contribution to rationalization of energy management for the smart factory, and providing time series of empirical data for fan condition monitoring.

b) In-built toolkit for multipurpose, comprehensive monitoring of air state variables, air technical properties, and fan input power; thus forming a basis for efficiency monitoring and advanced air technical process control in the smart factory. This necessitates instrumentation for fluid mechanics and input power.

c) Continuous fan condition monitoring e.g. on the effects of dust load, for monitoring and maintaining the resistance against harsh conditions, being *a priori* high, aiding the improvement of effectiveness of maintenance of the fan via occasional cleaning. On this basis, the periodic and relatively long, mandatorily prescribed maintenance periods can be exchanged for short, occasional, demand-based cleaning actions in a smart factory.

The implementation of the smart fan concept in point C) is organized into the following groups. 1) What "smart" hardware tools can be incorporated in an integrated, compact smart fan unit itself? 2) What "smart" hardware tools are to be installed within the system inevitably out of the fan unit? 3) What "smart" software, i.e. information technology and the incorporated theoretical as well as legislative considerations, are to supervise the aforementioned hardware in a smart ventilation system?

2.2 Gas engine power plant

The gas engine is a reciprocating engine, which transforms the chemical energy of the gaseous fuel to kinetic energy. The engines of such kind usually operate with natural gas as fuel, but there are increasing number of examples for which the fuel is biogas [15]. This power plant provides energy by cogeneration [16]. This means that not only the electrical power delivered by the driven generator is made available for use but the heat power contained by the exhaust gas and by the coolant, which would originally be wasted, may be utilized in the factory as well.

The aim of the ventilation system is supplying the gas engine with combustion air. Multiple air technical subsystems are operated in parallel connection for this purpose. Each subsystem is served by an individual fan. The structural scheme of a single air technical subsystem is shown symbolically (not to scale) in **Figure 1**, based on [16]. The fan sucks the ambient air via a rain protection grille and a segmented air duct equipped with a silencer and a preheater – the latter is for winter operation. The air is delivered into the gas engine compartment via a louvre equipped with a servomotor.

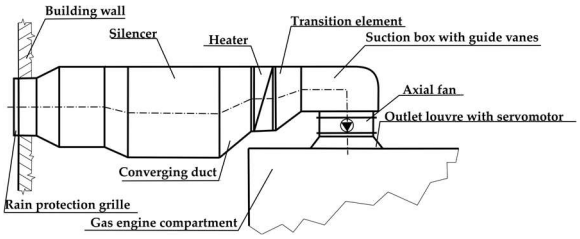

Figure 1. Structural scheme of the combustion air supply system of a gas engine power plant

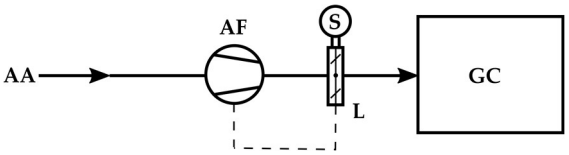

Figure 2. Operational scheme for the combustion air supply system of a gas engine power plant: a traditional layout. Notation: AA: atmospheric air, AF: axial fan, GC: gas engine compartment, L: louvre, S: servomotor.

The operational scheme of a conventional system corresponding to point A) in Subsection 2.1, incorporating a *common* fan unit, is presented in **Figure 2.** The features of the *common* fan unit, being in contrast with items a)-c) in point B) in Subsection 2.1, are as follows. a) Provided that the fan was installed prior to the date of effect of the EU Fan Regulation [7], no minimum energy efficiency

requirement is set for the fan. b) Neither the fan unit itself nor the connecting system contains any flow metering devices. The flow rate-measuring as well as -controlling feature is completely missing. The louvre is fully closed when the fan is switched off. After switching on, the fan gradually reaches its full rotational speed. When the normal speed of operation is reached, the louvre is opened fully by the servomotor, following the command given by the system automatics. This action is indicated with a dashed line in Fig. 2. In this layout, the individual fan operation cannot be matched with the connecting system in terms of flow rate and efficiency demands, and changing conditions (e.g. external wind effect, or temporary lack of the gas-tightness of compartment due to door opening). c) The working condition of the fan is not monitored. The system is in lack of automatic detection of any malfunction of the fan, increasing the risk of non-forecasted failure.

2.3 Air technical separator

The air technical separator, used e.g. in processing of shredded municipal waste, is capable for separating the multitude of solid particles into various fractions, according to their difference in the ratio of mass to the aerodynamic drag [17]. This ratio is relatively large e.g. for pieces of pressed plastic bags, characterized by three-dimensional (3D) shape – hereinafter termed "heavy" fraction –, and is relatively small e.g. for pieces of sheets of plastic foil, modelled as two-dimensional (2D) in shape – hereinafter termed "light" fraction. One aim of the separator is to separate the selectively collected and shredded plastic waste into heavy – 3D – as well as light – 2D – fractions. The operation of the separator is illustrated in the structural scheme in **Figure 3**, as well as in the operational scheme in **Figure 4**. During operation, the waste is loaded onto a conveyor, which delivers it to the rotating separator drum. From below the feeding conveyor, a high-velocity air jet is blown, through a nozzle, to the upper surface of the separator drum, and is attached to the upper part of the drum via the Coanda effect. The heavy fraction is falling through the air jet, since the vertically downward motion due to the weight force dominates over the jetwise motion due to the aerodynamic drag. The heavy fraction falls to a conveyor at the bottom, and is removed (label "Heavy" in Fig. 3). The light fraction travels together with the jet, and is delivered to the other side of the drum, into the settling chamber. Here, the light fraction is settled onto a conveyor belt, and is removed from the chamber (label "Light" in Fig. 3). The injector effect due to the suction phenomenon caused by the air jet generates inward leakage flow from the surroundings via the air gaps on the casing of the separator, e.g. at the conveyor ends. This inward air leakage, indicated as AL in Fig. 4, is useful in terms of preventing the dusty air from being released to the surroundings. The air corresponding to the sum of jet flow and the inward air leakage is sucked from the settling chamber, and is recirculated to the suction port of the fan. The dominant portion of the airflow available on the pressure port of the fan is diverted by an adjustable diverting valve toward the nozzle, forming the air jet. The rest of the air is sent through a filter, and is then exhausted to the surroundings, as replacement of the inward air leakage.

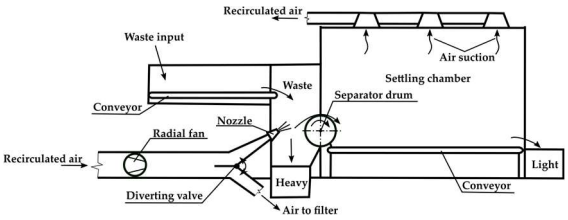

Figure 3. Structural scheme for the air handling system in an air technical separator

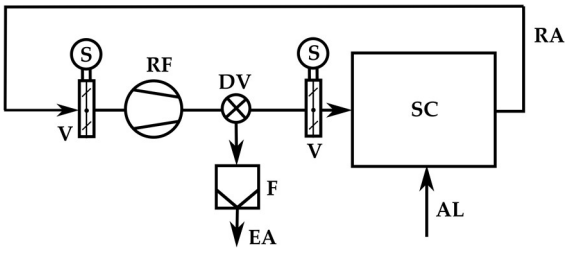

Figure 4. Operational scheme for the air handling system in an air technical separator: a traditional layout. Notation: AL: air leakage, DV: diverting valve, EA: exhaust air, F: air filter, RA: recirculated air, RF: radial fan, S: servomotor, SC: settling chamber, V: valve.

In the traditional system, the air motion is assured by a *common* radial fan with backward-curved impeller blades, corresponding to point A) in Subsection 2.1. In the case of this *common* fan unit, no special treatment has been done for fulfilment of the expectations which have been detailed in items a)-c) in point B) in Subsection 2.1. More specifically: a) No minimum energy efficiency requirement is set for the fan. b) Neither the fan unit itself nor the connecting system contains any flow metering device. c) No special treatment has been done against the optional dust load of the fan, originating from the contaminated air recirculated from the settling chamber. No condition monitoring is applied on the fan on the possible consequences of dust load, such as rotor imbalance, or performance degradation due to blade contamination.

In the traditional system, three controlling devices operate, on the basis of the details in [17]. One throttling valve, optionally operated with a servomotor, is located at the suction port of the fan, providing a general flow control on the air technical system via throttling. The diverting valve distributes the air into two directions at a ratio presumed empirically to be suitable: toward the nozzle, and toward the filter. The flow toward the nozzle can be

adjusted using an additional valve, optionally operated using a servomotor. This controlling system is more complex than the one in Subsection 2.2. It is to be emphasized that the throttling method used for flow control causes additional losses in the system. Furthermore, the traditional system has no sensors implemented, neither for flow control nor for fan condition monitoring purposes.

3. POTENTIAL CANDIDATES FOR FURTHER DEVELOPMENT INTO A SMART FAN STATUS

As further development of the examples in Subsections 2.2 and 2.3 incorporating *common* fan units, being in line with point B) in Subsection 2.1, commercially available fans and their optional accessories are discussed herein, in possession of *favourable fan features*, thus being potential candidates for further development into a smart fan status. Specifying these commercial products herein is not to be considered as commercialism; i.e. the commercial products taken below as examples are not to be regarded as exhaustively preferred and sole candidates for the smart fan solutions outlined herein. However, they demonstrate the industrial and commercial feasibility and cost-effectiveness of the smart fan concept discussed herein, with details being well-known for the present authors, because the authors' Department played a key role in their research and development.

3.1 Axial flow fan

In relationship with the case study on the gas engine power plant, one possible candidate of *favourable fan features* to be further developed into a smart industrial axial fan status is a member of the VHA ducted fan family [18] manufactured by Hungaro-Ventilátor Kft. (Hungaro-Ventilátor Ltd.). This fan family and its accessories have been developed by the firm in collaboration with the authors' Department. Further details on the fan family are given in [19-20]. This fan family provides examples for the *favourable* features as fulfilment of criteria in examples a) and b) within point B) in Subsection 2.1 as follows.

a) Thanks to its careful aerodynamic design carried out at the Department, the fan family meets the prescribed efficiency criterion fixed in the Fan Regulation [7]. Such efficiency requirement is fulfilled even by applying an easy-to-manufacture geometry, i.e. circular-arc plate blading, providing cost-effectiveness, and thus, competitiveness on the market.

b) The members of the fan family can be equipped with a commercially available in-line volume flow rate metering device, developed for the company by the Department, being fixed upstream of the axial fan with minimum space requirement, and thus, being integrated into the compact axial fan unit itself. Therefore, a compact fan-and-measurement unit can be made available, providing flow rate data for process control, and also enabling a potential for smart features which are detailed later in this paper.

Hungaro-Ventilátor Kft. equips its axial fans with the compact in-duct inlet metering device upon demand by the customers. The front axial view and the longitudinal section of the metering device are outlined in **Figures 5 and 6**. From operational point of view, this instrument acts like a giant Pitot-static (Prandtl-) probe, conf. [21]. Accordingly, the volume flow rate is deduced from measuring a single mean velocity measured by the flowmeter, being representative for the rotor annulus (i.e. the annular region embedding the rotor blades), and multiplying it by the annulus area. The flanged flowmeter is to be coaxially attached directly to the upstream flange of the fan casing. The upstream installation of the flowmeter is to exclude the flow irregularities caused by the fan from the measurement (e.g. swirling outflow, wake of the hub incorporating the driving motor). The central part of the device is the nose. The steady nose acts practically as the protrusion of the rotating hub of the impeller, being identical in diameter, and having only a small gap in between. The rear wall of the nose is closed. Therefore, the nose embeds a stagnant flow zone, and therefore, enables the measurement of inlet total pressure p_t by means of a Pitot probe immersed radially into the nose from outside. The flanged outer part, labelled as duct extension in the figures, is actually an upstream elongation of the fan casing. It supports the nose coaxially with use of radially aligned flat plates, acting also as inlet guide vanes against accidental inlet flow distortions. Inside the nose, wall pressure taps are executed and connected by an internal round piping. By such means, the averaged pressure over the outer surface of the nose – wetted by the annular flow – is tapped, and is led out of the flowmeter using a pressure transducer pipe. The internal surface of the duct extension, exposed to the annular flow, is also equipped with wall taps, connected by an external round piping. The pressure provided by the internal and external round pipes is averaged via a T-connector, thus providing a spatially averaged annulus mean pressure p_a, being an approximation of the mean static pressure valid for the annular flow.

The flowmeter has thoroughly been designed by the Department for fulfilment of demands of compactness, robustness, operational safety, and simple, easy-to-manufacture flowmeter geometry, thus guaranteeing cost-effective production and market competitiveness. Thanks to the large extension of the stagnant fluid region inside the nose, p_t can be measured in a robust and accurate manner, i.e. insensitively to accidental inlet flow distortions. The internal Pitot probe can be manufactured with relatively large internal diameter. This fact, together with the large "stagnation tap" represented by the

nose itself, guarantees that the measurement of p_t can be carried out also in contaminated (e.g. dusty) flow with moderate risk of clogging. The relatively large number of wall taps located over the circumference of both the nose and the duct extension guarantees a robust and accurate determination of p_a, even for inlet ducts with increased flow distortions – e.g. an elbow or throttle located close upstream –, and even for harsh operating conditions such as gas flow laden with solid contaminants. In addition, the flowmeter acts as a flow straightener from the perspective of arrangement of inflow to the rotor blades, being anyway of increased non-uniformity due to the upstream flow distortions. The measurement experiences of the company justify the robustness of this flowmeter technology. By the aforementioned means, this flowmeter technology is competitive with other techniques available commercially for inbuilt flow rate measurements for fans, e.g. [22-23].

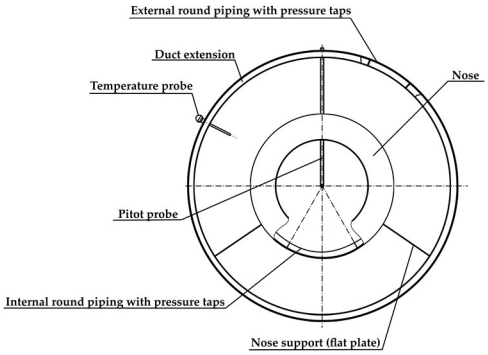

Figure 5. Compact inlet metering device for ducted axial fan units: front axial view

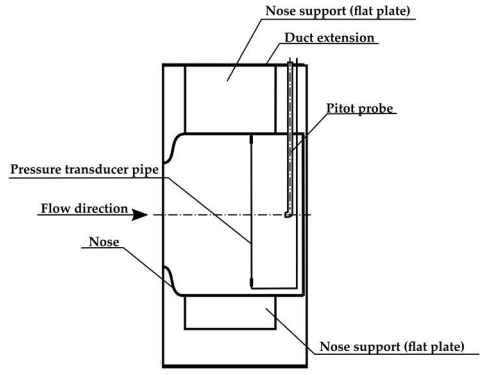

Figure 6. Compact inlet metering device for ducted axial fan units: longitudinal section

With use of the measurement-based p_t and p_a pressure data, provided by the flowmeter as a giant Pitot-static probe, the flow rate is calculated as follows. Taking the idealistic assumption that p_a represents the mean static pressure in the annulus, the dynamic pressure p_d is derived as follows.

$$p_d = p_t - p_a \tag{1}$$

The mean velocity in the annulus is calculated using the following equation:

$$v_a = \sqrt{\left(\frac{2 \cdot p_d}{\rho}\right)} \tag{2}$$

The need for accuracy of the measurement, being influenced by the knowledge of the gas density ρ, is dependent on the demand by the customer. For a brief estimation of the flow rate, the standard air technological air density of $\rho = 1.20\ kg/m^3$ can be used in Eq. (2). In more demanding applications, ρ is to be determined from measurements, as discussed in Subsections 4.1 and 4.2.

The annulus cross-section is obtained as follows:

$$A_a = \frac{(D^2 - d^2)}{4} \cdot \pi \tag{3}$$

In the idealistic approach described above, the volume rate would be obtained as product of the mean velocity and the annulus cross-section. In order to consider the realistic effects, the idealistically obtained volume flow rate is to be multiplied by a calibration factor K:

$$q_V = K \cdot A_a \cdot \sqrt{\left(\frac{2 \cdot p_d}{\rho}\right)} \tag{4}$$

In order to obtain K, the flowmeters are factory-calibrated, with use of standardized fan facilities [21], over Reynolds number intervals representing the operational range for the fans. The calibration diagrams are case-specific for given types of flowmeter-fan assemblies. The Reynolds number is calculated using the mean velocity in Eq. (2) as follows:

$$Re = \frac{v_a \cdot D}{\nu} \tag{5}$$

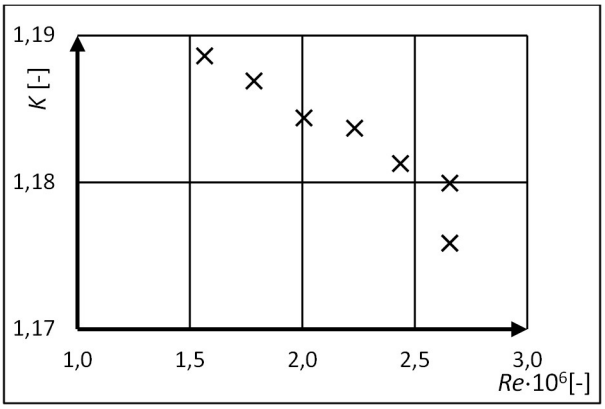

Figure 7. Calibration diagram for the compact inlet metering device: an example

Figure 7 shows an example for the calibration diagram $K(Re)$ for an operational range being representative for a given fan application. The figure indicates that the relative variance of K, with respect to the mean value, is significantly below the ± 2 % maximum allowable uncertainty of standardized [21]

fan flow rate measurements. Therefore, the developed flowmeter can suitably be applied with a practically constant calibration factor, thus aiding a straightforward evaluation method.

3.2 Radial flow fan

In connection with the case study on the air technical separator, one possible fan exhibiting *favourable features*, and thus being a candidate to be further developed into a smart industrial radial fan status, is a member of the new LDL radial fan family [24]. The manufacturer is Szellőző Művek Kft. (Ventilation Works Ltd.). This fan family has been designed, developed and experimentally tested by the authors' Department for the company. A detailed description is given on the fan family in [25], and therefore, only a brief summary is given here. This fan family provides examples for the *favourable* features as follows, in fulfilment of criteria in examples a) and c) within point B) in Subsection 2.1.

A classic air technical separator system is equipped with a traditional fan with backward-leaned, curved – i.e. cambered plate – impeller blades. However, in the separator case study presented herein, the inbuilt radial fan delivers air with apparent dust load. The traditionally curved sheet metal blades exhibit an increased inclination to be contaminated. In order to moderate blade contamination due to the dust load, the backward-leaned rotor blades have been designed as straight, planar sheet metal blades, instead of the traditional curved blade geometry. Despite the simplified blade geometry, the fitting and assembly of the inlet cone, the rotor, and the scroll casing has been developed by such means that a reasonably high efficiency has been reached, fulfilling the Fan Regulation [7].

The straight blade design enables an increased resistance against abrasion and cake formation – „self-cleaning" geometry –, whereas the entire machine exhibits a reasonably high efficiency. On this basis, the criteria in examples of both c) and a) within point B) in Subsection 2.1 are fulfilled.

4. OPTIONS FOR SMART FAN FEATURES

In what follows, details a)-c) within point C) in Subsection 2.1 are discussed, via the examples of the axial and radial fan units presented in Subsections 3.1 and 3.2. Namely, it will be examined how the *features* of these fan units, being *a priori favourable*, can be further developed to *eminent fan features* via the application of the smart fan concept to these candidate fans, in the Industry 4.0 perspective. In accordance with items a)-c) within point C) in Subsection 2.1, the present section is organized into the following topics: efficiency monitoring and control; instrumentation for fluid mechanics and input power; condition monitoring. As written at the end of Subsection 2.1, these topics are discussed in terms of 1) hardware built compactly in the fan unit; 2) hardware installed in the system out of the fan unit; 3) software, involving theoretical as well as legislative and reference considerations – such as regulation, standards, graphs of standardized certification measurements on fans and driving motors –, and solutions in information technology.

4.1 Efficiency monitoring and control

The effective aerodynamic performance P_{eff} of the fan is obtained as product of volume flow rate q_{V} and total pressure rise Δp_{t}:

$$P_{\mathrm{eff}} = q_{\mathrm{v}} \cdot \Delta p_{\mathrm{t}} \tag{6}$$

In the case of the ducted fans playing role in the two exemplary case studies, the total pressure rise Δp_{t} is obtained as the difference between the total pressures valid for the fan pressure and suction sides:

$$\Delta p_{\mathrm{t}} = p_{\mathrm{tP}} - p_{\mathrm{tS}} \tag{7}$$

At either on the pressure side or on the suction side, the total pressure is obtained as follows:

$$p_{\mathrm{t}} = p + \rho \cdot \frac{v^2}{2} \tag{8}$$

The air density is obtained from the ideal gas equation:

$$\rho = \frac{p}{R \cdot T} \tag{9}$$

In accordance with the Fan Regulation [6], the input power P_{in} to be considered herein for efficiency calculation is the input electrical power to the fan driving motor. On this basis, the fan efficiency η is obtained using the following formula:

$$\eta = \frac{P_{\mathrm{eff}}}{P_{\mathrm{in}}} \tag{10}$$

For continuous monitoring of fan efficiency on the basis of Eqs. (6) to (10), the following quantities are to be measured. The discussion follows the sequence of the equations, with additional comments as appropriate.

Eq. (6): q_{V} is to be measured. If the possible measurement location is restricted to the vicinity of the fan, a section upstream of the fan is recommended, in order to avoid the flow irregularities caused by the fan on the measurement.

Eq. (7): p_{tS} and p_{tP} are to be determined. One possibility is the direct measurement of the local total pressure p_{t}.

Eq. (8): Another possibility is obtainment of the total pressure as sum of locally measured static pressure p and locally calculated dynamic pressure. The latter can be obtained from the measured q_{V} with knowledge of the local cross-sectional area (obtaining v) and the density ρ. In the duct in the vicinity of the fan, usually only the upstream static pressure p_{S} can be measured correctly, because of the

irregularities caused by the fan on the downstream flow field.

Eq. (9): For determination of the density ρ, the temperature T is to be measured at a location where the local static pressure p is known. Since the assumption of incompressibility is a reasonable approximation in the case of fans [26], the density determined by such means can be taken as a single representative value for fan operation.

Eq. (10): The electric power P_{in} input to the driving motor is to be measured.

The above described workflow, resulting in the *data package for efficiency monitoring and control*, is summarized as follows, in the sequence of Eqs. (6) to (10).

- Measurement-based quantities: q_V, p_t and/or p at both the S and P locations, T at one location where p is obtained from measurement, P_{in}.
- Derived quantities: Δp_t, P_{eff}, ρ, η.

The continuous monitoring of the elements of the *data package for efficiency monitoring and control* offers the following benefits for Industry 4.0 functions in smart ventilation.

- P_{in} serves as input data to the overall energy management of the smart factory, in terms of energy consumption as well as loading of the subsystem supplying electric energy to the fan driving motor; e.g. monitoring of electric current input to the motor in relationship of the electrical fuse.
- η indicates the rationality of energy use in fan operation, and provides input data to system control for a possible, smart improvement of energy efficiency for system operation. The evaluation of measurement-based η is to be carried out on the following, *multilevel basis*. a) As a first phase in judgment of η, it is to be compared with the efficiency criterion dictated by the Fan Regulation [7] for the best efficiency point of the fan. b) As a second phase in evaluation of η, it is to be compared with data of the $\eta(q_V)$ fan efficiency curve known from the standardized certification measurements [21] to be provided by the fan manufacturer/vendor company, for given operating conditions of ρ and n. c) As a third phase, the system operator must have the complete smart air technical system – equipped with all components and instrumentation – to carry out *reference "self-measurements"*, over the entire controllable operational range, *prior to* the actual industrial utilization of the system. Such *self-measurements* provide associated reference data packages on q_V, Δp_t, and η over the entire controllable operating range. These reference data are to be compared with time series of such data obtained later, during system operation, for condition monitoring purposes. On the above multilevel basis, the possibility for modification of the actual operational point of the fan for improvement of the energy efficiency and/or moderation of energy consumption of the system, by means of appropriate control, can be overviewed. For smart control of the electric input power and the efficiency, throttle-based control elements, such as the ones outlined in Fig. 4, tend to be partly or fully replaced with speed control of the fan, whenever possible, for more energy-efficient operation.
- q_V, p_t and/or p at the S and P locations, and T are characteristics not only for the fan but also for the connected system. As such, they can be used in development of advanced flow control, thus enabling a flexible fitting of the fan to the connected system, in accordance with the user demand.
- A two-level comparison can be carried out as follows. a) With knowledge of q_V, the actual operation point can be identified on the fan characteristic curve $\Delta p_t(q_V)$ and on the efficiency curve $\eta(q_V)$ originated from the standardized certification measurements [21] provided by the fan manufacturer/vendor. On this basis, certified reference measurement data are to be made available for both Δp_t and η. The actual measurement-based Δp_t and η quantities are to be compared to the aforementioned certified reference data. b) Another type of referencing is made possible on the basis of the aforementioned *reference self-measurements*. A deterioration of the actually measured Δp_t and/or η quantities relative to the reference data indicates fan degradation. Therefore, the dataset of q_V, Δp_t and η can be utilized in fan condition monitoring, discussed in Subsection 4.3.

It is to be generally emphasized that in comparison of the actual measurement-based quantities with references – such as [7], or certified [21] $\Delta p_t(q_V)$ and $\eta(q_V)$ data –, the uncertainty of the actual measurements as well as of the experimental references, the tolerance grades [27] stated for the fan, and the related allowable variance in the quantities, are to be considered.

For conversion of the $\Delta p_t(q_V)$ and $\eta(q_V)$ graphs to the actual operating conditions via the fan similarity laws [26], ρ and n is to be known. Since n is generally not expected to be measured herein, additional information is necessary on the fan drive for determination of the rotor speed n. For example, for fans driven directly by asynchronous electric motors, the $P_{in}(n)$ characteristic curve of the motor, being made available by the motor manufacturer via certification measurements, serves as basis for determination of n with knowledge of P_{in} measured.

4.2 Instrumentation for fluid mechanics and input electric power

The fluid mechanics instrumentation for smart ventilation features outlined above is illustrated via the exemplary case studies in Subsections 2.2 and

2.3. Referring to Fig. 1, a smart axial fan serving for the gas engine air supply system is equipped with speed control. The louvre is fully open when the fan operates. The compact inlet metering device detailed in Subsection 3.1 enables measurements upstream of the fan. Referring to Fig. 1, the integration of the metering device and the fan into a compact fan unit makes possible the installation of the fan unit in the confined vertical space between the suction box and the ceiling of the gas engine compartment. This appears to be the sole adequate solution for q_V measurements in this particular system. The robust metering device can operate well despite the flow distortion caused by the suction box located close upstream of the meter. As already indicated in Fig. 5, the meter, serving originally for measuring q_V, can be supplemented with a temperature probe, following the guidelines in [21] for temperature measurements as a first approach. By such means, the compact inlet metering device can be further developed into a multifunctional meter providing the following data, conf. the comments in Subsection 4.1: p_{tS}, T, q_V, and p_S – the latter is calculated from Eq. (8) with consideration of ρ (Eq. 9) and the inlet dynamic pressure based on the mean inlet velocity obtained from q_V. All of the locally measured pressures discussed herein are taken relative to a fixed reference (gauge) pressure in the system, e.g. ambient atmospheric pressure.

For obtaining Δp_t, p_{tP} or p_P is also to be determined; the two latter are related via Eq. (8). Due to flow irregularities caused by the fan on the downstream flow field, and due to the presence of the outlet louvre, the pressure close downstream of the fan cannot be measured appropriately. Therefore, it is inevitable to install a p_P sensor farther away from the fan, i.e. in the nearly motionless air field in the gas engine compartment. Neglecting the loss of the fully open outlet louvre, the measured p_P value is considered to be valid as ambient static pressure in the jet close downstream of the fan. With knowledge of q_V and the fan outlet cross-section, the obtained mean outlet velocity makes possible the calculation of p_{tP} via Eq. (8).

Referring to Fig. 3 for the smart radial fan serving for the air technical separator, the direct application of the above described compact multifunctional inlet metering device – customized to the axial fan rotor annulus – is irrelevant. Instead, traditional methods are to be used farther away upstream and downstream of the fan for determining q_V, p_t, and/or p at both the S and P locations, and T at one location of static pressure measurement. The apparent dust load in the transported air is to be considered in design of the instrumentation. The standard [21] serves with guidelines regarding the location, installation and execution of these measurements. One possibility is the following installation of measurements, in analogy to the gas engine air supply measurements discussed above. a) Measurement of p_{tS} or p_S, T, and fan q_V in the straight duct of recirculated air near the suction port of the fan. b) Measurement of p_P close downstream of the fan, after a straightener inserted in the pressure-side duct. c) Measurement of flow rate from the diverting valve toward the filter, for calculation the flow rate in the nozzle.

In order to measure P_{in}, the electric motor driving of the given fan is to be equipped with an input electric power measuring method. For this purpose, [21] recommends the two Watt-meter measuring method provided that the fan is driven by a three-phase electric motor.

4.3. Fluid mechanics-based condition monitoring

As was described in Subsection 4.1, the measurement-based actual q_V, Δp_t and η data are to be compared with reference data on a *multilevel basis*. This comparison serves for fluid mechanics-based fan condition monitoring. The discrepancy detected in such comparison, and / or the temporal trend of deterioration recognized in the time series of Δp_t and / or η at a fixed q_V indicates a degradation of the fan, e.g. due to abrasion, or to contamination caused by the dust load. Condition monitoring and recognition of degradation for industrial turbomachinery such as compressors, gas turbines and gas turbine systems is established in the literature [28-30]. This methodology is to be adapted to industrial fans with appropriate modifications. Since the present literature lacks in directly available guidelines for trend analysis and monitoring the degradation in fans, the adaption of the available knowledge [28-30] to fans is subject of future research.

The fluid mechanics-based condition monitoring methodology can be supplemented with further features, thus establishing an extended toolkit for condition monitoring of smart fans. These features, discussed in the following section, are as follows:

- Noise monitoring and control
- Vibration monitoring
- Bearing temperature monitoring

5. EXTENDED TOOLKIT FOR CONDITION MONITORING

5.1 Noise monitoring and control

Incorporating an extended dataset on various types of industrial fans, guideline [31] can serve as an experimental reference database for noise monitoring of fans. Based on the work by Regenscheit (discussed in [26]), as well as presenting measurement data, guideline [31] provides semi-empirical formulae for estimation of the L_W level of sound power – in both A-weighted and linear form upon need – emitted by the normally operated fan into the outlet duct. Correlations for estimation of

level of sound power radiated toward the inlet duct, or emitted at a free outlet, are also available in [31]. The necessary Δp_t and q_V data inputs to these formulae are available from the *data package for efficiency monitoring and control* discussed in Subsection 4.1. Further necessary data inputs are the rotor tip circumferential speed u_{tip}; the speed of sound a; and the total efficiency η_t of the fan in itself, i.e. disregarding the losses of the fan drive. u_{tip} can be calculated with knowledge of the rotor speed n determined as discussed at the end of Subsection 4.1 a can be determined with use of the measured temperature T as follows: $a = (\kappa \cdot R \cdot T)^{0,5}$. η_t is to be calculated using Eq. (11), i.e. the rotor shaft input power is to be considered instead of P_{in}. The η_D efficiency of the fan drive, representing the ratio between the rotor shaft input power and P_{in}, can be determined e.g. using the $\eta_D(n)$ characteristic curve of the driving motor, being made available by the motor manufacturer via certification measurements, conf. the end of Subsection 4.1.

$$\eta_t = \frac{\eta}{\eta_D} \qquad (11)$$

Guideline [31] provides empirical formulae also for the spectral distribution of fan noise, in the form of ΔL_{Woct} relative sound power level in octave bands, as function of u_{tip}. According to [31], such spectral distribution is to be corrected for consideration of rotational noise, by adding an empirical value to ΔL_{Woct} for the octave band containing the blade passing frequency $N \cdot n$. By such means, [31] potentially represents a theoretical relationship between the noise and vibration monitoring methodologies – the latter is discussed in Subsection 5.2 –, since the peaks at $N \cdot n$ and at its overtones may appear also in the spectral distribution of vibration, via rotor-stator interaction effects. Furthermore, since guideline [31] establishes correlations between the aerodynamic power loss and the fan noise, it also represents a theoretical relationship between the monitoring/control packages of efficiency and noise.

By means of a single microphone / multiple microphones installed appropriately in the vicinity of the fan, representative sound pressure data can be acquired on the actual operation of the fan. Such sound pressure data may *implicitly indicate* the sound power emitted by the fan, and can thus be utilized for noise-based fan condition monitoring purposes. In this paper, when system measurement data on L_W and ΔL_{Woct} are referred to, they are to be considered as locally measured sound pressure data representing *implicitly* the aforementioned quantities. Such acoustic measurements can incorporate both overall sound pressure levels and the spectral distributions of noise. Following the methodology outlined for η in Subsection 4.1, the evaluation of such acoustic measurements can be carried out on a *multilevel basis*, in comparison with the following reference data. In this comparison, the uncertainty of the actual measurements as well as of the experimental references, reported e.g in [31], are to be considered. a) L_W and ΔL_{Woct} data based on [31]. b) L_W and ΔL_{Woct} data provided by the fan manufacturer/vendor company on the basis of standardized factory measurements. c) Acoustic *reference self-measurements* on the system over the entire controllable operational range.

Taking [31] as basis for comparison, reference data of L_W and ΔL_{Woct} are to be obtained using operational and geometrical data of the fan in point. The actually measured acoustic data are to be exposed to Fast Fourier Transformation (FFT) and to be represented in logarithmic scaling. The relevant frequency range is to be determined from the dimensionless Strouhal number range specified in [31] for the octave-band spectrum of the given fan type, using n as parameter. In order to make the measurement-based sound pressure spectrum comparable with the reference ΔL_{Woct} distribution derived from [31], octave-band averaging is to be carried out on the measured dataset. Significant discrepancies between the spectral trends of measured and reference ΔL_{Woct} data are to be suspected as signatures of extraordinary fan operation, e.g. extreme throttling, or fan degradation. Narrowband signatures of detected noise, peaking out of the octave-band averaged spectrum, such as the rotational noise at the blade passing frequency $N \cdot n$, are to be monitored and interpreted in a distinct manner, with special attention. FFT on algorithmically selected shorter-term time series of acoustic data provides a means for discovery of extraordinary fan phenomena, such as vibration of a loose internal machine element, e.g. a piece of plate guide vane, generating occasional noise.

Temporally evolving discrepancies in the trends between the actually measured acoustic data and the aforementioned a)-c) references can be considered as precursors of deterioration of fan conditions. Microphone installation, data acquisition and processing, establishment of correlations between various types of fan degradation and their acoustic signatures, and incorporation of acoustics-based recognition of fan degradation in smart ventilation, are subjects of further research.

It is to be emphasized that the actual air technical system and its environment may have a significant impact on the acoustic measurements. From this point of view, the on-site *reference self-measurements* – incorporating the acoustic features of the system and the site – are of especial importance in evaluation of the noise measured during the actual utilization of the system. As an approximation for considering the acoustic features of the system connected to the fan, guidelines [32-33] can be considered.

In order to moderate / avoid the acoustic impact of the connected ductwork on the observation of fan noise, noise monitoring can be carried out via

sections of acoustically transparent duct [34] developed at the Department. The application of acoustically transparent ducts to industrial ventilation systems, and evaluation of fan noise data for condition monitoring purposes is a topic of future research.

The continuous monitoring of noise serves as basis also for the moderation of noise via an appropriate flow control of the system. However, attention is drawn that the primary aim of system control is fulfilment of the functionality of the air technical system, i.e. realization of the necessary q_V at favourable operating conditions, e.g. moderate aerodynamic loss. The Regenscheit fornula in [31] provides a theoretical basis for noise reduction via reducing both the aerodynamic power loss of the fan and u_{tip}, i.e. via appropriately tuning q_V, Δp_t, η_t and n by system control. Such noise control can be considered as an important action in fulfilment of Environmental, Health, and Safety (EHS) measures serving for the personnel and the environment of the smart factory.

For modern ventilation systems, a recent trend is to exchange the classic metal ductwork with textile air duct elements [35], as far as the particular industrial application allows for that. Textile elements are available for straight duct sections, perforated air distributors, elbows, T-junctions, and throttles. Compared to classic ductwork, among others, the following benefits of textile air duct elements represent possible competitive advantages in a smart ventilation system. Silent textile ductwork, i.e. reduced impact on noise generation, thus making possible a more effective noise monitoring and control. Energy-efficient air transport and distribution. Quick and easy processes of removal, cleaning in washing machine, and re-installation of the textile duct elements, as part of the demand-based, effective, smart maintenance actions.

5.2 Vibration monitoring

The aforementioned tools for condition monitoring can effectively be supplemented with the means of vibration monitoring. Periodically executed non-continuous monitoring [36] of vibration is a well-established technique in diagnostics of rotating machinery. In the case of a smart fan, continuous monitoring of vibration and the associated trend analysis [36] can be a means for early recognition of risk of malfunction.

Every rotating machine has a normal level of vibration. If this level increases, it forecasts a sort of malfunction, leading to damage [36]. The increased level of vibration could originate from mechanical issues – e.g. bearing degradation, shaft imbalance, rotor imbalance due to abrasion or contaminant deposit, or resonance –, and from aerodynamic phenomena, e.g. extraordinary operational states incorporating extreme throttling, rotating stall, or surge.

The vibration can be characterized using its displacement, velocity v_v, or acceleration. The type of vibration sensors is to be selected on the basis of the layout of the fan. In the exemplary case study of Subsection 3.1, the axial fan is directly driven by the electric motor, i.e. the fan impeller is attached to the shaft of the motor. Furthermore, the motor is equipped with roll-bearings. For such kind of bearings, the recommended [37] sensor type is the accelerometer. Modern sensors of this kind operate with an integrator, which can convert the vibration acceleration to velocity v_v or displacement upon need. Signal processing techniques such as FFT are available for precise diagnosis. The placement of the vibration transducers is recommended by the standard [36]. In principle, three sensors are to be placed to each bearing house, for the axial, horizontal, and vertical directions of vibration. Reasonable compromises are to be made in installation of the sensors upon the accessibility of the bearing houses [36] e.g. in the case of electric motors with embedded bearings.

In order to realize a methodology fitting the best to the one outlined for η in Subsection 4.1, the evaluation of vibration measurements can be carried out on a *multilevel basis*, in comparison with the following reference data, considering the experimental uncertainties. a) Displacement or v_V data based e.g. on [36], specifying empirical threshold values for vibration displacement or velocity root-mean-square (RMS), for which unlimited long-term operation is allowable; short-term operation is allowable; and vibration causes damage. b) Upon availability, factory-measured v_V data provided by the fan manufacturer/vendor company. c) Vibration *reference self-measurements* on the fan over the entire controllable operational range.

In order to retrieve valuable information from the acquired signals about the condition of the machine, signal processing techniques are to be carried out. Firstly, the analogous measurement signal is to be converted into binary digital data for computer processing. For this purpose, an A/D converter is applied. This processor samples the data at regular time intervals [37]. The sampling time interval is usually expressed by its reciprocal value, i.e. the sampling frequency. The required minimum of sampling frequency is defined by the Nyquist-theorem, stating that the sampling frequency needs to be at least twice as much as that of the highest-frequency component of interest in the sampled signal [38]. In the case of an insufficiently high sampling frequency, the converted signal is affected, i.e. aliasing occurs [38]. The obtained digital signal is in the time domain. As such, it provides a means for monitoring how the vibration level varies in time. The standards usually refer to the RMS of the monitored vibration amplitude level [36]. Tracking of the vibration level through the time gives the smart

fan an effective tool to alarm a malfunction well in advance. For improving the diagnostics capability, time-domain tracking is combined with transforming the signal into the frequency domain. The applied method is termed Discrete Fourier Transform (DFT). A less computation-demanding algorithm is FFT [37, 38]. In the frequency domain, the type of malfunction can be diagnosed. The main concept is that various kinds of malfunctions show signatures of changed amplitudes at various frequencies, which makes them distinguishable [37]. The signal is measured in a finite temporal interval, which may cause "leakage", because usually the first and the last sampled data are not the same. In order to avoid such anomaly, the signal is to be provided with a window function. The windowing method makes the first and the last data of the sampled signal zero. By such means, a continuous signal is obtained [37, 38].

The trend analysis in vibration monitoring for smart fans, as well as its relations with the other smart condition monitoring features from a smart data processing point of view, is subject of future research.

5.3 Bearing temperature monitoring

Temperature measurement within the fan driving electric motor is routine even in traditional layouts for overheat protection, and therefore, is not discussed herein. This subsection regards temperature measurements on the bearings, being strategically important elements in rotating machinery. The forthcoming failure of the bearings is probably associated with increased friction, leading to increased heat generation. Therefore, measuring T_b is a sensible means for monitoring the condition of the bearings [39], also influenced by the particular circumstances of lubrication. A preset limit of T_b must not be exceeded in operation. The methodologies of vibration, noise, and bearing temperature monitoring can be linked in a smart manner, in the view that the signatures of upcoming bearing failure probably appear as precursors in each of the noise and vibration spectra as well as in the T_b registrations.

Temperature monitoring is feasible with one sensor per bearing [39]. The default sensor type is the resistance-based temperature probe. For certain motor layouts, thermocouple is an alternative [39]. The probes are to be built inside the bearing houses, near the bearings.

There is no standard or any other generalised legislative reference for judging the measured T_b data in monitoring. This topic, and its relations within the overall toolkit of smart fan monitoring, is subject of further research.

6. AN OVERVIEW OF THE ESTABLISHED SMART FAN CONCEPT

Figure 8 presents a flowchart making a connection between the all-round pool of measured quantities – presented in the uppermost row –, the quantities derived from the measured data – organized into multiple levels below –, and their input into the all-round set of possible smart functions – lowermost row. The figure depicts a rich interaction and multiple data exploitation within the entire set of measured and processed data as well as the smart functions. In addition to the smart functions indicated in the figure, the capabilities of the smart ventilation system also enable advanced features of flow control.

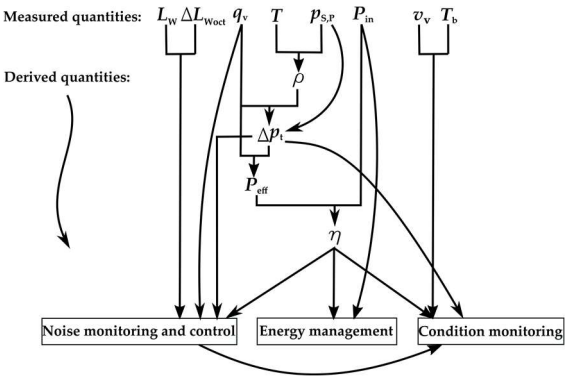

Figure 8. Flowchart between the measured quantities and the all-round set of possible smart

Figures 9 and 10 show the operational schemes for the smart layouts of the systems in the two exemplary case studies, being in accordance with the former discussion. Making a comparison to the operational schemes for the traditional layouts, i.e. comparing Fig. 9 to Fig. 2, and Fig. 10 to Fig. 4, the extensive implementation of sensors in the smart systems is conspicuous. A recent trend is to apply low-cost "Do-It-Yourself" (DIY) sensors, e.g. [40]. DIY pressure, temperature, power, noise, and vibration sensors may provide a cost-effective solution even in the case of multiple instrumentation, whereas they may be sufficiently reliable for detecting the quantities and their temporal trends for control and monitoring purposes in a smart system.

Associated time series of the measured quantities are to be acquired during the normal use of the air technical system, and the set of derived quantities are to be provided. For and control and condition monitoring purposes, these quantities are to be compared to reference data. The former discussion leads to the following generalization of *multilevel basis* for referencing for the various tools of fan condition monitoring, upon availability: a) Legislative, standardized, and guideline references [7, 31, 36]. b) Certified factory measurements on fans and drives. c) *Reference self-measurements*. The differences between the actual and reference data,

and the temporal trend of these differences are to be analysed, and precursors of deterioration of fan conditions are to be recognised. Temporal predictions are to be made for various items of fan degradation, as an aid to demand-based maintenance actions.

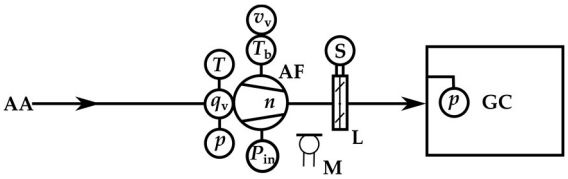

Figure 9. Operational scheme for the combustion air supply system of a gas engine power plant: a smart layout. Notation: i) See the caption of Fig. 2. ii) n: fan speed control. iii) M: microphone for noise monitoring. iv) Symbols in circles: instrumentation for measuring quantities from the Nomenclature.

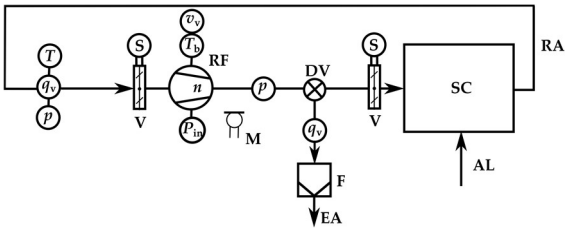

Figure 10. Operational scheme for the air handling system in an air technical separator: a smart layout. Notation: See the captions of Figs. 4 and 9.

A complex and comprehensive evaluation and trend analysis of the entire dataset in Fig. 8, being a subject of data science, provides a plentiful means for multipurpose control and condition monitoring. The expected physical phenomena, the signatures and precursors of which are "hidden" in the data, are supposed to be linked to multiple data in Fig. 8. Such redundancy of information provides a means for efficient discovery and multi-perspective confirmation of the presumed phenomena, and refinements in fan diagnosis – i.e. making distinctions between various deterioration mechanisms –, via analysing the correlations between the time series of various data. Some examples for such redundancy of information in the proposed "smart" dataset are as follows. First, the presumed physical phenomenon in point is specified. Then, followed by a "→" sign, the quantities presumably modified due to the phenomenon are listed, with additional comments in brackets as appropriate.

- Rotor blade abrasion or contaminant deposit → Δp_t, η (at a given q_V, presumably due to modification in blade section lift and/or drag [26]); L_W, ΔL_{Woct} (presumably via modification of aerodynamic power loss [31]); v_v spectrum (via rotor imbalance, presumably at frequencies related to n and its overtones).
- Rotor blade and/or shaft deformation → L_W, ΔL_{Woct}; v_v spectrum.
- Degradation of fan drive (e.g. V-belt drive) → Δp_t, η (presumably via the deterioration of P_{eff}); L_W, ΔL_{Woct}; v_v spectrum.
- Bearing degradation → L_W, ΔL_{Woct}; v_v spectrum; T_b.

The trends outlined above are to be discovered in a synchronized manner, by means of proper algorithms. For improving the effectiveness of the smart system for the future, the system is to learn the experiences gathered in the past on fan condition monitoring, with also incorporating the experiences gained during the resultant, demand-based maintenance actions. The elaboration of complex, concerted smart data processing and smart learning methodology is subject of future research.

As an overview of smart fan features, **Table 1** provides some headwords of a SWOT analysis on the smart fan concept.

Table 1. SWOT analysis of the smart fan concept

Strengths	**Weaknesses**
Condition monitoring	More costly investment
Malfunction prediction	Need for complex knowledge
Energy management	Need for sensors also out of the fan
Cost-effective operation	
Integrated sensors	
Opportunities	**Threats**
Smart flow control	Malfunctions due to system complexity
Smart noise control	Errors in electronics
Smart maintenance	Cybercrime
Smart system learning	

7. CONCLUSIONS AND FUTURE REMARKS

The concept of smart industrial air technology / ventilation has been introduced in this paper, fitting to the Industry 4.0 perspective. The industrial implementation of smart fan concept has been illustrated in an evolutionary approach, in the sequence of common fans → advanced fans → smart fans, via two exemplary conceptual case studies. The "Gas engine power plant" and "Air technical separator" case studies are representative for axial and radial fans, respectively. The paper is summarized as follows.

1) Fan candidates for further development into smart fan status have been introduced in the two case studies, with features of *a priori* high efficiency; robust in-built toolkit with a potential of multipurpose fluid mechanics measurements; and *a priori* high resistance against solid contaminants.

2) Interacting concepts and the related data packages for smart fan features have been introduced as follows: efficiency monitoring and control; fluid mechanics-based condition monitoring; noise

monitoring and control; vibration monitoring; bearing temperature monitoring.

3) As support to noise monitoring and control, the concept of acoustically transparent duct, as well as optional application of textile air duct systems, have been recommended.

4) The extensive instrumentation being necessary for the aforementioned smart fan features have been detailed, and illustrated via operational schemes. The perspective of using DIY sensors in smart fan systems has been outlined.

5) In order to provide references for comparing with the actually measured and derived quantities, a *multilevel basis* has been proposed for referencing for the various tools of fan condition monitoring, upon availability: a) Legislative, standardized, and guideline references. b) Certified factory measurements on fans and drives. c) *Reference self-measurements.*

6) Concepts for complex and comprehensive smart processing and utilization of the gathered data, from a data science perspective, have been outlined.

7) A SWOT analysis has been delivered, in headwords, on the smart fan concept.

8) The following topics are subjects to further research and to gathering practical experience:

- Trend analysis and monitoring the degradation in fans;
- Instrumentation, data acquisition and processing, and trend analysis in acoustics-based condition monitoring of fans, optionally involving acoustically transparent ducts;
- Trend analysis in vibration monitoring for fans;
- Bearing temperature monitoring for fans;
- A complex, comprehensive treatment of all of the above features in smart data processing and smart learning methodology, from a data science perspective; and elaboration of well-designed actions on the air technical system as practical exploitation of the smart fan concept, e.g. demand-based maintenance.

ACKNOWLEDGEMENTS

The authors acknowledge the support by the following organizations and projects. a) Hungarian National Research, Development and Innovation Office, under contract No. NKFI K 129023. b) Hungaro-Ventilátor Kft. c) Szellőző Művek Kft., within the framework of the VEKOP-2.1.7-15-2016-00647 project, supported by the Hungarian Ministry of Finance. d) DAAL-CON Kft., within the framework of the GINOP_PLUSZ-2.1.1-21-2022-00044 project, supported by the Hungarian Ministry of Finance. e) In the topic of air technical separation: 3B Hungária Kft., within the framework of the 2019-1.1.1-PIACI-KFI-2019-00200 project, supported by the Hungarian National Research, Development and Innovation Office.

REFERENCES

[1] Reis, M. S., Gins, G., 2017, „Industrial process monitoring in the Big Data/Industry 4.0 era: from detection, to diagnosis, to prognosis", *Processes*, **5**(35), 16 p.

[2] Trstenjak, M., Cosic, P., 2017, "Process planning in Industry 4.0 environment", *Procedia Manufacturing*, **11**, pp. 1744-1750.

[3] Schütze, A., Helwig, N., Schneider, T., 2018, "Sensors 4.0 – smart sensors and measurement technology enable Industry 4.0", *Journal of Sensors and Sensor Systems,* **7**, pp. 359-371.

[4] Eastway, 2021, "Whitepaper: Condition monitoring of the age of Industry 4.0", *www.eastwaytech.com*

[5] Goyal, D., Chaudhary, A., Dang, R. K., Pabla, B. S., Dhami, S. S., 2018, "Condition monitoring of rotating machines: a review", *World Scientific News: An International Scientific Journal,* **113**, pp. 98-108.

[6] Ali, A., Abdelhadi, A., 2022, „Condition-based monitoring and maintenance: state of the art review", *Applied Sciences,* **2022** ,12(2), 688.

[7] *Commission Regulation* (EU) No 327/2011 of 30 March 2011 implementing Directive 2009/125/EC of the European Parliament and of the Council with regard to ecodesign requirements for fans driven by motors with an electric input power between 125 *W* and 500 k*W.*

[8] Durier, F., Carrier, R., Sherman, M., 2018, "What is smart ventilation?", *Ventilation Information paper* No. 38, Air Infiltration and Ventilation Centre, Sint-Stevens-Woluwe, Belgium, 8 p.

[9] Guyot, G., Sherman, M., Walker, I., Clark, J. D., 2017, "Residental smart ventilation: a review", *Research Report* LBNL-2001056, Lawrence Berkeley National Laboratory, hal-01670527, 92 p.

[10] Coronado, A., 2021, "Best smart ceiling fans that can be controlled by your phone or voice", *https://ideaing.com/ideas/best-smart-ceiling-fans/*

[11] Hunter Industrial Ceiling Fans, 2022, *https://hunterindustrialfan.eu/industrial-products/,* HVLS *Selection Guide* 2022

[12] Mi Smart Standing Fan Pro, *Product description, https://www.mi.com/global/product/mi-smart-standing-fan-pro/*

[13] Smartmi Fan 3, *Product description, https://eu.smartmiglobal.com/pages/standing-fan-3*

[14] SmartFAN *Project-Newsletter* No. 8, 2021, The European Union's Horizon 2020 research

and innovation programme under grant agreement No 760779.

[15] Mustafi, N. N., Raine, R. R., Bansal, P. K., 2006, "The use of biogas in internal combustion engines: a review", *ASME Internal Combustion Engine Division 2006 Spring Technical Conference,* Aachen, Germany, *Paper No.* ICES2006-1306, 10 p.

[16] Vad J., Lukács E., 2020, "*Fluid mechanics measurements*", Akadémiai kiadó, Budapest, Hungary, ISBN: 978 963 454 484 5

[17] Nihot Recycling Technology B.V., *Product overview*, *https://nihot.nl/wp/wp-content/uploads/2021/07/Nihot-Product-Overview-brochure-UK.pdf*

[18] Hungaro-Ventilátor Ltd., 2021, *Product Catalogue*, *https://hungaro-ventilator.hu/*

[19] Vad, J., 2010, „Design and measurement of axial flow flue gas extractor fans of high specific performance and energetically favourable operation", *GÉP*, **61**(11), pp. 15-18. (in Hungarian, with English abstract)

[20] Vad, J., 2011, „Blade sweep applied to axial flow fan rotors of controlled vortex design", *Doctoral Thesis*, Hungarian Academy of Sciences.

[21] *Standard* ISO 5801:2017, Fans. Performance testing using standardised airways.

[22] Rosemount, 2008, Annubar flowmeter series. *Product data sheet* 00813-0100-4809, Rev GA. November 2008.

[23] TROX X-Fans GmbH, 2018, Der intelligente Ventilator „X-Fan System". Volumenstrom-Messeinrichtung VME. In: Abluftventilatoren für industrielle Prozesse. *Product description, Quick Selection Guide 2018. https://www.trox-xfans.de/downloads/0e3c67e196820769/QSG_Druck_2018_low.pdf?type=product_info*

[24] Szellőző Művek Ltd., 2022, *LDL Product Catalogue*, *http://www.szellozomuvek.hu/ldl_product_catalog.pdf*

[25] Ferenczy, P., Balla, E., Benedek, T., Daku, G., Kocsis, B., Kónya, A., Vad, J., 2022, „Development of a radial flow fan family for contaminated gases of relatively high flow rate", *Conference on Modelling Fluid Flow* (CMFF'22), Budapest, Hungary. Paper No.: CMFF22-048.

[26] Carolus, T., 2003, *Ventilatoren*, Teubner Verlag, Wiesbaden, Germany.

[27] *Standard* ISO 13348:2007. Industrial fans – Tolerances, methods of conversion and technical data presentation.

[28] Kurz, R., Brun, K., 2001, „Degradation in gas turbine systems", *Trans ASME, Journal of Engineering for Gas Turbines and Power*, **123** (1), pp. 70-77.

[29] Abdelrhman, A. A., Hee, L. M., Leong, M. S., Al-Obaidi, S., 2014, "Condition monitoring of blade in turbomachinery: a review", *Advances in Mechanical Engineering*, **2014**, Article ID 210717, 10 p.

[30] Zagorowska, M., Spüntrup, F., S., Ditlefsen, A.-M., Imsland, L., Lunde, E., Thornhill, N. F., 2020, "Adaptive detection and prediction of performance degradation in off-shore turbomachinery", *Applied Energy*, **268** (2020) 114934, 17 p.

[31] VDI Richtlinien, 1990, *Guideline* VDI 3731 – Blatt 2, Emissionskennwerte technischer Schallquellen, Ventilatoren.

[32] VDI Richtlinien, 2001, *Guideline* VDI 2081 – Blatt 1, Geräuscherzeugung und Lärmminderung in Raumlufttechnischen Anlagen.

[33] VDI Richtlinien, 2005, *Guideline* VDI 2081 – Blatt 2, Geräuscherzeugung und Lärmminderung in Raumlufttechnischen Anlagen, Beispiele.

[34] Tokaji, K., Horváth, Cs., 2018, „Acoustically transparent duct", *International Journal of Aeroacoustics*, **17**(3), pp. 238-258.

[35] DAAL Group, EXANDAIR textile air ducts for draught-free working environment, *Product description, https://exandair.com/en/*

[36] *Standard* ISO 10816-3:2009(E). Mechanical vibration – Evaluation of machine vibration by measurements on non-rotating parts – Part 3: Industrial machines with nominal power above 15 k*W* and nominal speeds between 120 *r*/*min* and 15 000 *r*/*min* when measured in situ.

[37] Scheffer, C., Girdhar, P., 2004, *Practical machinery vibration analysis and predictive maintenance*, Elsevier.

[38] Norton M. P., Karczub D. G., 2003, *Fundamentals of noise and vibration analysis for engineers*, Second Edition, Cambridge University press.

[39] Mistry, R., Finley, W. R., Hashish, E., Kreitzer, S., 2018, „Rotating machines: the Pros and Cons of monitoring devices", *IEEE Industry Applications Magazine*, **24**(6), pp. 44-55.

[40] Corsini, A., Tortora, C., Feudo, S., Sheard, A. G., Ulluci, G., 2016, "Implementation of an acoustic stall detection system using near-field DIY pressure sensors", *Proc IMechE, Part A – Journal of Power and Energy*, **230**(5), pp. 487-501.

Conference on Modelling Fluid Flow (CMFF'22)
The 18th International Conference on Fluid Flow Technologies
Budapest, Hungary, August 30-September 2, 2022

VALIDATION OF AN IMMERSED BOUNDARY FRAMEWORK FOR URBAN FLOWS

Patricia VANKY[1], Andreas MARK[2], Marie HAEGER-EUGENSSON[3], Joaquim TARRASO[4], Marco ADELFIO[5], Angela SASIC KALAGASIDIS[6], Gaetano SARDINA[7].

[1] Corresponding Author. Department of Mechanics and Maritime Sciences, Division of Fluid Dynamics, Chalmers University of Technology. Hörsalsvägen 7A, SE-412 96 Gothenburg, Sweden. Tel.: +46 73 07 88 617, E-mail: patricia.vanky@chalmers.se
[2] Fraunhofer-Chalmers Research Centre for Industrial Mathematics. Email: andreas.mark@fcc.chalmers.se
[3] Department of Earth Sciences, Gothenburg University and COWI, Gothenburg, Sweden E-mail: mrhr@cowi.com
[4] Department of Architecture and Civil Engineering, Division of Urban Design and Planning, Chalmers University of Technology. E-mail: joaquim.tarraso@chalmers.se
[5] Department of Architecture and Civil Engineering, Division of Urban Design and Planning, Chalmers University of Technology. E-mail: adelfio@chalmers.se
[6] Department of Architecture and Civil Engineering, Division of Building Technology, Chalmers University of Technology. E-mail: angela.sasic@chalmers.se
[7] Department of Mechanics and Maritime Sciences, Division of Fluid Dynamics, Chalmers University of Technology. E-mail: sardina@chalmers.se

ABSTRACT

Urban heat islands, or the phenomena of locally increased temperatures of urban areas compared to their rural surroundings, are becoming increasingly problematic with global warming and the rise of urbanization. Therefore, new areas must be planned considering appropriate ventilation to mitigate these high-temperature regions and cooling strategies, such as green infrastructures, must be considered. Typically, these critical environmental issues are assessed in the final stages of urban planning when further strategic interventions are no longer possible. Here, a numerical framework is tested, that urban planners can use as a future tool to analyze complex fluid dynamics and heat transfer in the early stages of urban planning. The framework solves the RANS equations using an immersed boundary approach to discretize the complex urban topography in a cartesian octree grid. The grid is automatically generated, eliminating the complex pre-processing of urban topographies and making the framework accessible for all users. The results are validated against experimental data from wind tunnel measurements of wind-driven ventilation in street canyons. This work present similarities and differences between experiments and simulations using three different turbulence models. Finally, guidelines will be provided on the choice of minimum grid sizes required to capture the relevant flow structures inside a canyon accurately.

Keywords: Immersed Boundary, Street Canyons, Urban climate, Ventilation

NOMENCLATURE

ν	$[m^2/s]$	kinematic viscosity
ν_t	$[m^2/s]$	kinematic eddy viscosity
ω	$[1/s]$	specific dissipation rate
ρ	$[kg/m^3]$	density
$\tilde{\nu}$	$[m^2/s]$	Spalart-Allmaras solution variable
ε	$[m^2/s^3]$	dissipation rate
$\vec{u}$	$[m/s]$	mean velocity
g	$[\sqrt{s}]$	turbulent time scale
k	$[m^2/s^2]$	turbulent kinetic energy
p	$[Pa]$	mean pressure
t	$[s]$	time
H	$[m]$	reference roof height
U_{ref}	$[m/s]$	reference inlet velocity

1. INTRODUCTION

In urban areas, the local temperatures are higher than in their rural surroundings. This temperature difference is often refereed to as Urban Heat Islands (UHI), and it can be tied to significant physical and mental health issues for residents and visitors of the cities [1]. During summer, when the temperatures are already high, the UHIs increase mortality significantly, especially during heat waves [2, 3]. Nowadays, the World Health Organisation (WHO) classes heat waves as one of the most dangerous natural disasters, with 70,000 dead during the 2003 heat wave in Europe [4]. Furthermore, the Urban Heat Islands also both impact and are impacted by global warming, creating a spiraling effect of heated cities. As the temperature increases in the cities, the usage of energy consuming equipment, such as air

conditioning, rises [5] contributing to global warming and, as a consequence, increasing the temperatures in the cities even further. With global urbanization, the amount of people living in the cities have surpassed majority in the last decade and it is estimated that close to 70% of the world's population will be residing in urban areas by the year 2050 [6]. Given that the majority of people will continue to be negatively affected by the increasing temperatures, it is essential to consider urban heat islands when planning and designing cities so that temperature mitigation is possible.

There have been several studies done on what attributes in urban design can improve thermal comfort and limit the effect the UHIs [7, 8, 9, 10]. Key factors presented in these studies are land use, city density, the presence of urban blue and green spaces and thermal storage in building materials. In particular, the first two key factors are taken into account to increase heat mitigation enhancing ventilation, while the others aim to limit heat storage by introducing cooling materials and natural blue and green areas. However, these design strategies are strongly interconnected, therefore addressing their effects one by one as a possible solution without considering their interactions is too simplistic. On the other hand, the coupling between heat storage, ventilation, and cooling strategies generate a complex system where the global effect of temperature mitigation is hard to predict. Therefore, modern urban design procedures have to be evaluated on their success in improving the thermal climate in practice. Typically, urban comfort is assessed in the final stages of urban planning when further strategic interventions are no longer possible due to the complexity of the assessment. For this reason, there is a need to develop new and accurate numerical methodologies to assess the complex relations between fluid dynamics and heat transfer processes in urban regions so that urban designers can use them in the early stages of the design process.

Previous CFD studies typically consider only one of the factors determining the urban environmental quality, either the wind [11, 12, 13, 14] or the heat [15, 16, 17]. More recent studies [18, 19] show that the interest in these, more complex, combinations of wind and heat phenomena is increasing. However, these numerical simulations are still highly dependent on skilled professionals to generate the complex unstructured mesh needed to simulate all these phenomena. Additionally, in most of these works, the turbulence is modeled using some version of the k-ε turbulence model, without further evaluation of the model or proper comparison to other possible turbulence models.

This paper describes the validation of a user-friendly fluid dynamic numerical solver developed for predicting wind speed and ventilation in urban areas. The framework is based on an immersed boundary methodology which employees an automatically generated Cartesian octree grid, eliminating the complex pre-processing of urban topographies and making the framework accessible for general users with different backgrounds. The simulations using three different turbulence models are validated against wind tunnel data from Allegrini 2018 [20] related to a typical urban topography area.

2. METHODOLOGY

In this paper, the isothermal ventilation of urban street canyons is studied and validated against wind tunnel experiments. The numerical framework is evaluated for three different turbulence models, the one equation model Spalart-Allmaras as well as two equation models realizable k-ε and k-g SST, which is a variant of the well-known k-Ω SST model.

2.1. Flow solver

The inputs to a wind simulation are an xml-file describing the simulation setup and a number of geometry files. In the setup xml-file the simulation domain, inlet conditions, grid refinements, residuals and turbulence model are defined. The input geometries consist of an oriented triangulated surface mesh that is automatically connected to the background grid describing the local topography of the terrain and the buildings.

In this paper we use the steady-state version of the in-house flow solver, IBOFlow® [21] developed at Fraunhofer-Chalmers Reseach Centre. The solver integrates the Reynolds' averaged Navier-Stokes equations,

$$\nabla \cdot \vec{u} = 0, \tag{1}$$

$$\frac{\partial \vec{u}}{\partial t} + \vec{u} \cdot \nabla \vec{u} = -\frac{\nabla p}{\rho} + \nabla \cdot ((\nu + \nu_t)\nabla \vec{u}), \tag{2}$$

along with the turbulent transport equations. The finite volume method is used to discretize all equations on a Cartesian octree grid that is automatically refined around the geometries. The Navier-Stokes equations are solved in a segregated manner, and the SIMPLEC method derived in [22] is used to couple the pressure and the velocity fields. All variables are stored in a co-located arrangement, and the pressure weighted flux interpolation proposed in [23] is used to suppress pressure oscillations. The steady-state solver is based on artificial time stepping and solved until all relative solution residuals are lower than the specified residual. Finally, the mirroring immersed boundary method [24] is employed to model the presence of all geometries, without the need of a body-fitted mesh.

In this paper three different turbulence models are compared, the Spalart-Allmaras, the realizable k-ε and the k-g SST model.

The Spalart-Allmaras model evolves the kinematic turbulent eddy viscosity that is given by $\nu_t = f_{v1}\tilde{\nu}$, where the viscous damping is given by $f_{vt} =$

$\frac{\chi^3}{\chi^3+c_{v1}^3}$, and $\chi = \frac{\tilde{\nu}}{\nu}$. $\tilde{\nu}$ is given by

$$\frac{\partial \tilde{\nu}}{\partial t} + \vec{u}\cdot\nabla\tilde{\nu} = P - D + \frac{1}{\sigma}\left[\nabla\cdot((\nu+\tilde{\nu})\nabla\tilde{\nu}) + c_{b2}|\nabla\tilde{\nu}|^2\right] \tag{3}$$

where P is the production term and D is the destruction term. For complete description see [25]. $\tilde{\nu}$ is set to zero on the geometries with help of the implicit immersed boundary condition.

The realizable k-ε model [26] handles many problems that the standard model has, especially for rotating flows. Let's define S_{ij} as the mean strain and Ω_{ij} as the rotation rate tensor, then the governing equations are

$$\frac{\partial k}{\partial t} + \vec{u}\cdot\nabla k = \nabla\cdot\left(\left(\nu + \frac{\nu_t}{\sigma_k}\right)\nabla k\right) + \nu_t S^2 - \epsilon \tag{4}$$

$$\frac{\partial \epsilon}{\partial t} + \vec{u}\cdot\nabla\epsilon = \nabla\cdot\left(\left(\nu + \frac{\nu_t}{\sigma_k}\right)\nabla\epsilon\right) + C_{1\varepsilon}S - C_{2\varepsilon}\frac{\epsilon^2}{k+\sqrt{\nu\epsilon}} \tag{5}$$

$$\nu_t = C_\mu \frac{k^2}{\epsilon} \tag{6}$$

where $S = \sqrt{2S_{ij}S_{ij}}$, $C_{1\varepsilon} = \max\left(0.43, \frac{\eta}{\eta+5}\right)$ and $\eta = S\frac{k}{\epsilon}$. In the model the eddy viscosity coefficient changes as

$$C_\mu = \frac{1}{A_0 + A_s\frac{kU^*}{\epsilon}} \tag{7}$$

where $U^* = \sqrt{S_{ij}S_{ij} + \Omega_{ij}\Omega_{ij}}$, $A_0 = 4.04$, $A_s = \sqrt{6}\cos\phi$, $\phi = 1/3\arccos\sqrt{6}W$, and $W = \frac{S_{ij}S_{jk}S_{ki}}{\sqrt{(S_{ij}S_{ij})^3}}$.

In the $k-\omega$ SST model the turbulence is modeled by the Menter SST (shear-stress transport) [27, 28] model that is based on the standard $k-\epsilon$ model, and the original (1988) Wilcox $k-\omega$ equation [29],

$$\frac{\partial k}{\partial t} + \vec{u}\cdot\nabla k = P - \beta^*\omega k + \nabla\cdot\left((\nu + \sigma_k\nu_t)\nabla k\right), \tag{8}$$

$$\begin{aligned}\frac{\partial \omega}{\partial t} + \vec{u}\cdot\nabla\omega &= \frac{\gamma}{\nu_t}P - \beta\omega^2 + \nabla\cdot\left((\nu+\sigma_k\nu_t)\nabla\omega\right) \\ &+ 2(1-F_1)\sigma_\omega\frac{1}{\omega}\nabla k\cdot\nabla\omega, \qquad (9)\\ \nu_t &= \frac{a_1 k}{\max(a_1\omega, F_2 S)}. \qquad (10)\end{aligned}$$

The hybrid method switches between $k-\omega$ close to walls ($F_1 = 1$) and $k-\epsilon$ in the free-stream ($F_1 = 0$). The eddy viscosity damping is using the strain rate and the damping factor F_2, which is 1 at walls. Here, the SST model has been adapted to the immersed boundary setting where the variable ω is changed to the turbulence time scale $g^2 = \frac{1}{C_\mu\omega}$, see [30] for more details. So in practice a k-g SST model is used. After the variable change both k and g are set by wall functions at the boundary of the geometries with the immersed boundary method.

2.2. Case Description

The aim is to validate the solver using the Particle Image Velocimetry (PIV) experimental data by Allegrini 2018 [20] where a compilation of wooden blocks of various sizes are placed in a wind tunnel to describe a general urban area. The test domain consists of a 5x5 row configuration of buildings with straight, continuous streets between them forming regular canyons. In front of these buildings, a set of irregularly sized shaped and placed buildings is inserted to create an irregular flow pattern representing that of a typical city. The flat roof height, H, of these buildings is equal, 14 cm. In one of the street canyons between the organized buildings, the air velocity is measured using PIV. Some modifications are made to this set-up to create five different cases to study the flow field, namely case A-E. Case A is the case described before, while the other cases consists in changing the inclination of the roof of the leading building (cases B and C) or changing the width of the leading and trailing (cases D and E) building in the measured canyon.

Here, the case called Case C in [20] will be analyzed for a inlet velocity, U_{ref}, of 1.94 m/s. This case was chosen as it includes a building with a pitched roof leading up to the measured street canyon, adding domain complexity to the otherwise flat roofs and inducing a separation region inside the canyon. The wind tunnel data correspond to a vertical and horizontal velocity plane from Particle Image Velocimetry (PIV) measurements, shown in Figure 1. The vertical plane is located at the center of the canyon and the horizontal plane is set at half of the roof height. A complete simulation of the full wind tunnel chamber is too computationally expensive, therefore the simulations were performed over a portion of the domain consisting of six lines of buildings. A flat region was added at the beginning to develop the flow instead of the irregular buildings in the experiment. Several preliminary tests on the initial geometry and domain streamwise lengths have been performed to achieve a compromise between quality of the results and computational time. Figure 1 shows the final domain configuration with 6x5 rows of buildings, that together with the developing region gives a domain of the size 2.0 x 1.9 x 0.85 m. The PIV-planes are marked in red (horizontal) and green (vertical) in the top panel and as dashed lines in the bottom panel.

The grid of the simulation domain is set up with a uniform base cell size of $0.05 \times 0.05 \times 0.05$ m, which is refined around the near-wall regions of the ground and buildings. The ground and buildings along the sides of the domain are refined two times, whereas the six buildings along the middle column, where the PIV-planes are located, is refined further, up to four additional refinement corresponding to 48 grid points inside the canyon and a total of approximately four million cells in the domain. A grid study to find

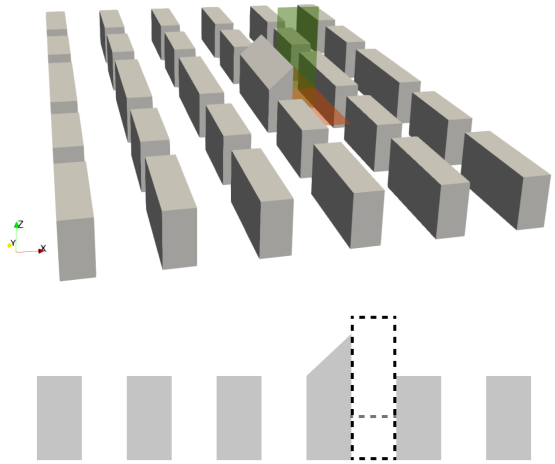

Figure 1. Top: 3D visualization of the domain where the red and green planes shows the horizontal and vertical PIV-planes respectively. Bottom: 2D side view, PIV-planes showed as dashed lines.

the number of refinements to reach numerical convergence of the mean velocity field will be described in the Results section.

Additionally, the framework is evaluated for three turbulence models as previously mentioned and a convergence study is performed by monitoring the order of magnitude of the residuals needed to reach a steady solution.

3. RESULTS

Comparison between the wind tunnel data and the numerical simulations can be done by observing the velocity contours over the PIV-planes as well as the one-dimensional (1D) velocity over the center line of the previously defined planes. In this paper, the contours are only showed for the vertical or horizontal PIV-plane, never both, due to lack of space.

3.1. Grid Study

To accurately evaluate the minimum number of cells to solve the mean flow field inside the canyon, a grid convergence study has been performed. The case under investigation, using the Spalart-Allmaras model and a value of maximum relative residual of 10^{-6}, has been run using three different grids. The three grids employ two, three and four refinements corresponding to 12, 24 and 48 cells along the canyon width. The results are presented in Figures 2 and 3.

Figure 2 shows the contours of the in-plane mean velocity magnitude on the vertical plane for the experimental (a) and the numerical data (b-d) at different resolutions. Comparing the different results, we obtain a fair agreement against the experimental data for the four and three refinements grid as a qualitative impression. On the other hand, the simulation in the most coarse grid shows a large part of the canyon with low velocity magnitude probably induced by numerical dissipation. Moreover, the experimental data show a recirculation region in the lower right corner of the canyon, a feature captured by both the two most refined simulations but not by the two refinement mesh. This would indicate that some important fluid dynamics phenomena might be missed if the mesh is not refined well enough.

To have a quantitative comparison between the different solution field, we plot in Fig. 3 the vertical (top panel) and horizontal (bottom panel) profile of the horizontal mean velocity component. Both profile confirm the qualitative impression obtained by the previous figure that grid convergence is reached by the two most resolved grids using four and three refinements. The coarser grid predicts a lower mean velocity inside the canyon close to the ground to then become similar after the roof level. The bottom panel shows that the velocity in the coarser grid differs at the center of the perpendicular street canyon, with fair agreement to the experimental velocity close to

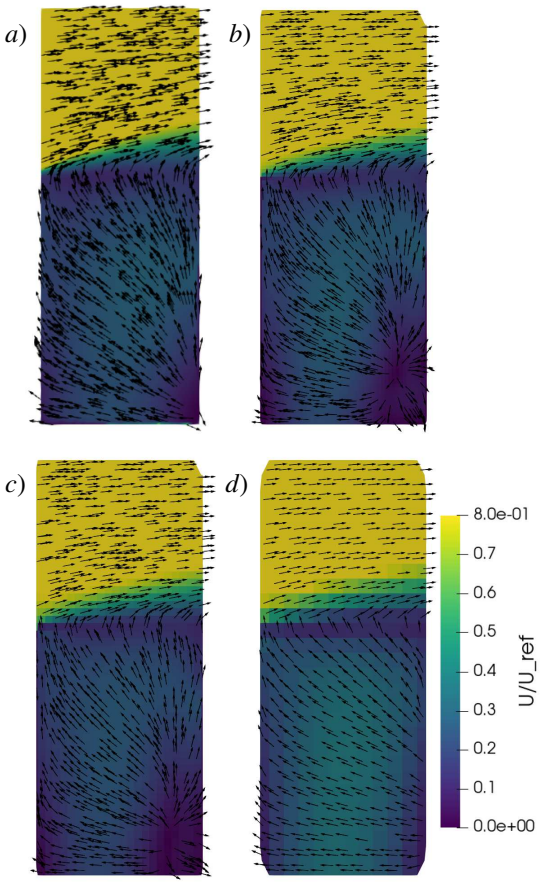

Figure 2. Contour plots and streamlines of the in-plane mean velocity magnitude on the vertical plane. The panels represent the PIV data (a) followed by the results of three simulations with different grid resolution, b) 4 refinements, c) 3 refinements and d) 2 refinements

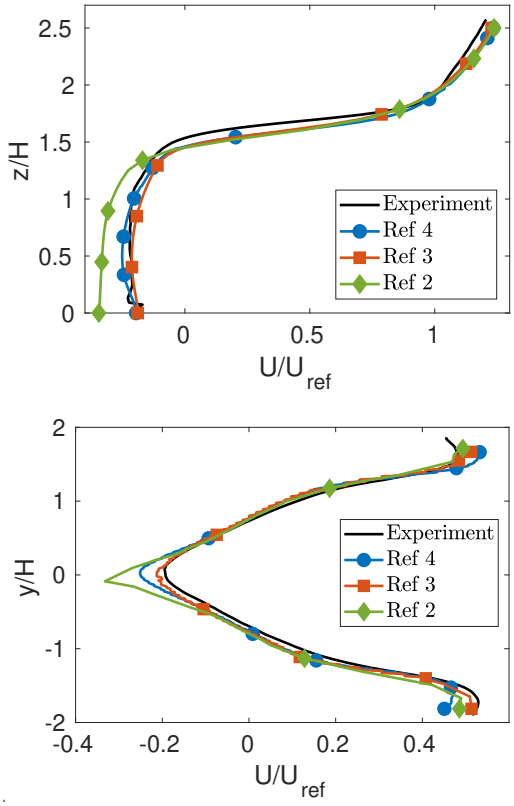

Figure 3. Vertical (top panel) and horizontal profiles (bottom panel) of the horizontal average velocity component at the center of the street canyon for case C. The simulations results with grid refinements (solid lines with symbols) are compared against PIV experimental data (black solid line).

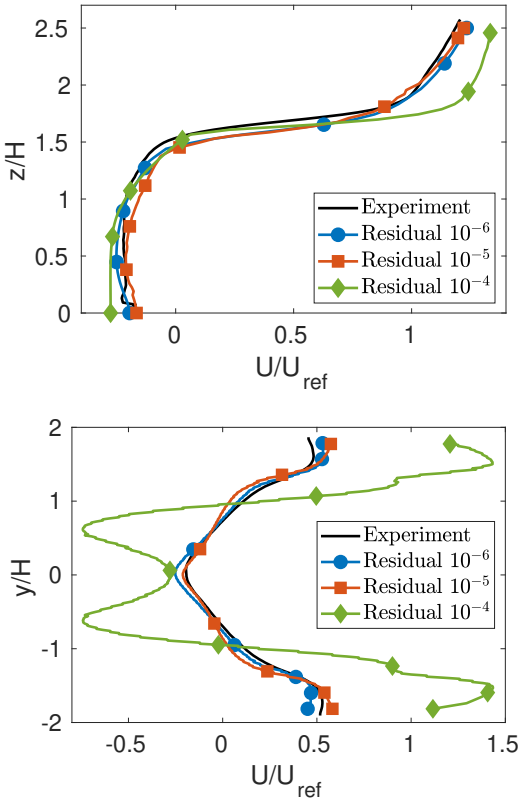

Figure 4. Temporal convergence of vertical 1D velocity for the case C of the experiments. Residual 10^{-4}, 10^{-5} and 10^{-6} compared to experimental velocity

the street canyons parallel to the wind.

To conclude, the grid study shows that 24 cells per canyon are sufficient. A coarser mesh can give a fair results overall, but fails to predict detailed results of the flow field inside the canyon.

3.2. Residual

The temporal convergence has been evaluated by comparing the numerical horizontal mean velocity profiles with residual 10^{-4}, 10^{-5} and 10^{-6} to the experimental velocities in Figures 4 and 5. With both residuals of 10^{-6} and 10^{-5}, the simulated results are good in the entire canyon region and can be considered converged.

The reasons for the mismatches can be seen in Fig. 5 for a residual of 10^{-4}, the recirculation regions in the horizontal velocity plane have started to form but are not yet fully developed. This explains the high velocities that are found in the bottom panel of Fig. 4 and also the large negative velocities around the canyon center that are not seen in the further resolved cases. The flow simply needs additional iterations before it can be considered fully developed and therefore the lower residual is not sufficient. The contours also show that, although the 1D velocities show little variation between residual 10^{-5} and 10^{-6}, the flow does develop slightly to come even closer to the experimental results for the finest convergence. However, a residual of 10^{-5} can indeed be considered sufficiently converged in cases where high computational time is an issue.

3.3. Turbulence models

A sensitivity study of three different turbulence models has been performed for the converged case with four grid refinements and temporal convergence of 10^{-6}. These results are displayed in Figures 6 and 7.

All three of the turbulence models give results fairly representing the experimental data. The one-equation model, Spalart-Allmaras, and two-equation model k-g SST yield very similar results. The realizable k-ε model however yields slightly lower velocities which make a better match in the horizontal velocity but not in the vertical velocity. The vertical velocity at the top of the street canyon (roof level) is linked to the ventilation inside the canyon and is shown in Figure 8 where the k-ε model is noticeably less accurate in predicting the experimental profile than the other two models. The same trend is shared in the other simulation test cases mimicking the experiments in [20] that are not shown in this ma-

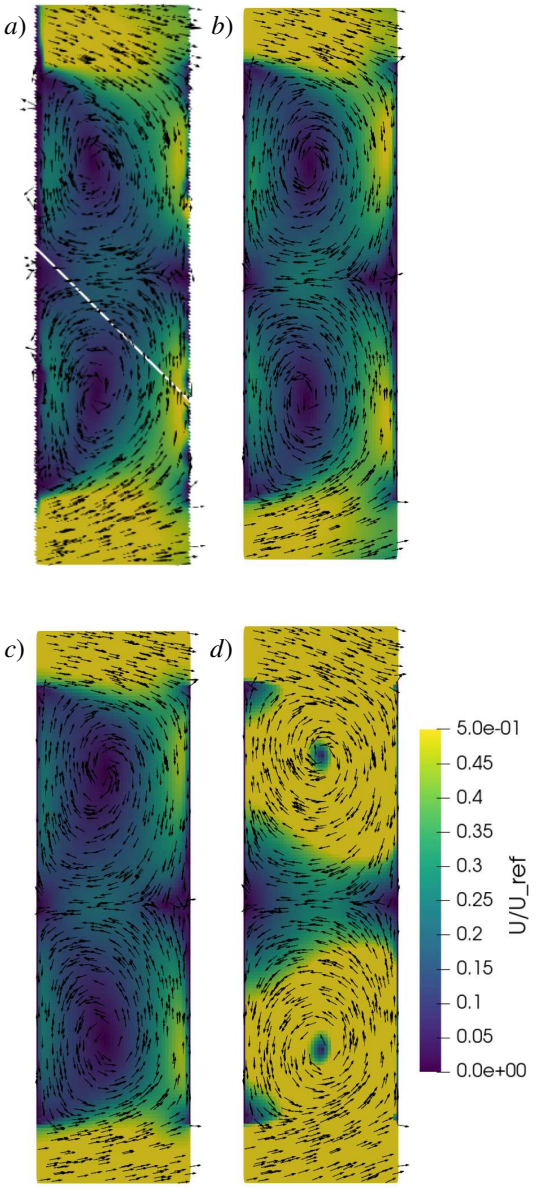

Figure 5. Contour plots and streamlines of the in-plane average velocity magnitude on the horizontal plane for different residuals: a) Reference experimental results, b) residual 10^{-6}, c) residual 10^{-5}, d) residual 10^{-4}.

nuscript: the realizable k-ε model underperforms in comparison to the other two turbulence models.

As previously mentioned, the realizable k-ε model and the k-ε model, in general, is commonly used for environmental and urban simulation today. This could be a good approach for less dense areas where the high Reynolds number approximation would be valid in large parts of the domain. The model could also perform well in street canyons parallel to the wind direction, as another know limitation of the model, separation regions, should likely not be present in these areas. However, in this work, the

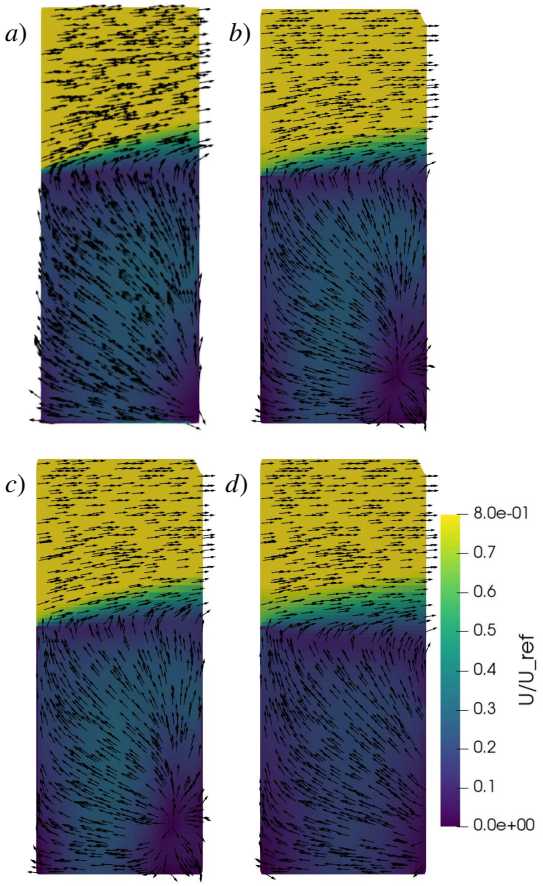

Figure 6. Contour plots and streamlines of the in-plane average velocity magnitude on the vertical plane for different turbulence models: a) Reference experimental results, b) k-G SST model, c) Spalart-Allmaras model, d) realizable k-ε model.

canyon-of-interest is perpendicular to the wind, with a rather deep recirculation area in combination with a relatively dense configuration of buildings. Therefore, depending on the areas of interest the k-ε model could be more or less appropriate, and in this case it was shown to be less optimal.

The other two turbulence models show some discrepancies in velocity in the near-ground area and the free-stream region, however, the overall results are good. The horizontal velocity profile also shows a difference between experiment and simulation in the street canyons parallel to the flow, however in the canyon perpendicular to the flow, the one-dimensional velocities are close to the laboratory-measured results. Since the k-g SST model considers both the issue with near walls where the Reynolds number is low and the overestimation of the shear stress induced by the separation areas in the k-ε model, this model is expected to perform better in the studied configuration case. The Spalart-Allmaras model should in theory not perform well for meshes where the first cell has a $y+ > 1$, however, in these simulations wall functions are used to handle the near-wall velocities which allow for a coarser

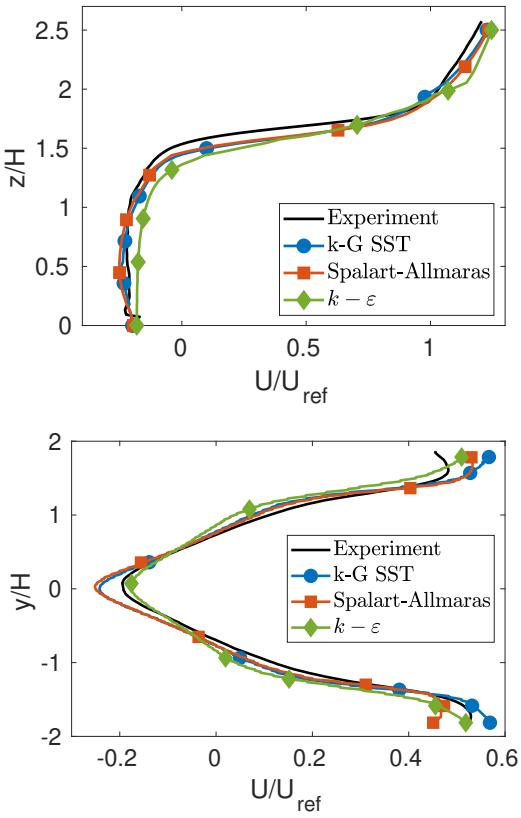

Figure 7. Vertical (top panel) and horizontal profiles (bottom panel) of the horizontal average velocity component at the center of the street canyon for case C. The simulations results with different turbulence models (solid lines with symbols) are compared against PIV experimental data (black solid line).

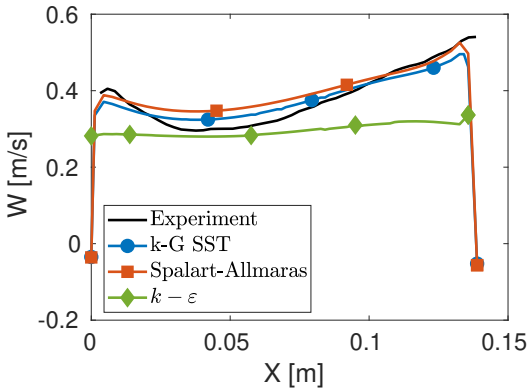

Figure 8. Streamwise profile of the vertical mean velocity components at the top of the street canyon. The simulations results with different turbulence models (solid lines with symbols) are compared against PIV experimental data (black solid line).

mesh. The validation shows that for these simulations, either k-g SST or Spalart-Allmaras would yield desired results. However, in general, the k-g SST model requires more computational resources making it less efficient compared to the Spalart-Allmaras model. Since there is no loss in accuracy, the Spalart-Allmaras model will be used in our future works.

4. CONCLUSION AND OUTLOOK

A series of simulations have been conducted to validate a numerical framework against wind tunnel experiments of wind behavior and ventilation in urban street canyons. The framework has been tested using three turbulence models, realizable k-ε, k-g SST, and Spalart-Allmaras on a domain of aligned block buildings forming an idealized urban area with some added complexity in the form of a pitched roof in front of the investigated street canyon. All three turbulence models give good results; however, the realizable k-ε underperforms compared to the other two. On the other hand, the Spalart-Allmaras model is preferred as it is more computationally efficient than the k-g SST model.

Furthermore, it was found that the center of the street canyon is where it is hardest to estimate the wind velocity. However, it is possible to reach sufficient accuracy with high enough resolution. The necessary resolution has been estimated to be approximately 24 cells inside the canyon. Note that this resolution in the canyons has been evaluated for a small-scale test in a wind tunnel, where the Reynolds number differs from a full-scale city area. Using 24 cells per canyon in a full-scale model, where a narrow street might be approx 6-8 meters wide, implies a cell size of fewer than 0.5 meters which might not be feasible for domains of several square kilometers. This computational aspect will be further investigated in future works. In addition to necessary grid resolution, it has been found that a residual of at least 10^{-5} is needed to reach a temporally converged solution.

In this paper, we have only considered the wind behavior in an isothermal urban area. However, in [20] the same test cases have also been performed considering the impact of heat transfer. Our future developments will focus on implementing and investigating buoyancy effects due to the introduced heat in the wind tunnel cases. Moreover, we plan to introduce heat storage in building materials for façades and the ground, radiative heat transfer, and latent heat effects due to vegetation or blue areas. The final solver will constitute a complete tool for realistic urban area simulations that can be employed and easily used by urban planners for the design and development of future sustainable cities.

ACKNOWLEDGEMENTS

This work was supported by the Swedish Research Council for Sustainable Development Formas under the grants 2019-01169 and 2019-01885. The computations were enabled by resources provided by the Swedish National Infrastructure for Com-

puting (SNIC) at HPC2N partially funded by the Swedish Research Council through grant agreement no. 2018-05973. This work is also part of the Digital Twin Cities Centre supported by Sweden's Innovation Agency Vinnova under Grant No. 2019-00041. Finally, we would like to thank Professor Jan Carmeliet and his team at ETH for allowing the usage of experimental data for simulation validation purposes in this paper.

REFERENCES

[1] Huang, H., Deng, X., Yang, H., Li, S., et al., 2020, "Spatial Evolution of the Effects of Urban Heat Island on Residents' Health", *Tehnički vjesnik*, Vol. 27 (5), pp. 1427–1435.

[2] Smargiassi, A., Goldberg, M. S., Plante, C., Fournier, M., Baudouin, Y., and Kosatsky, T., 2009, "Variation of daily warm season mortality as a function of micro-urban heat islands", *Journal of Epidemiology & Community Health*, Vol. 63 (8), pp. 659–664.

[3] Rydin, Y., Bleahu, A., Davies, M., Dávila, J. D., Friel, S., De Grandis, G., Groce, N., Hallal, P. C., Hamilton, I., Howden-Chapman, P., et al., 2012, "Shaping cities for health: complexity and the planning of urban environments in the 21st century", *The lancet*, Vol. 379 (9831), pp. 2079–2108.

[4] McGregor, G. R., Bessmoulin, P., Ebi, K., and Menne, B., 2015, *Heatwaves and health: guidance on warning-system development.*, WMOP.

[5] Hassid, S., Santamouris, M., Papanikolaou, N., Linardi, A., Klitsikas, N., Georgakis, C., and Assimakopoulos, D., 2000, "The effect of the Athens heat island on air conditioning load", *Energy and Buildings*, Vol. 32 (2), pp. 131–141.

[6] United Nations, Department of Economic and Social Affairs, Population Division, 2018, "World Urbanization Prospects: The 2018 Revision", Online Edition.

[7] Pramanik, S., and Punia, M., 2020, "Land use/land cover change and surface urban heat island intensity: source–sink landscape-based study in Delhi, India", *Environment, Development and Sustainability*, Vol. 22 (8), pp. 7331–7356.

[8] Ramírez-Aguilar, E. A., and Souza, L. C. L., 2019, "Urban form and population density: Influences on Urban Heat Island intensities in Bogotá, Colombia", *Urban Climate*, Vol. 29, p. 100497.

[9] Vos, P. E., Maiheu, B., Vankerkom, J., and Janssen, S., 2013, "Improving local air quality in cities: to tree or not to tree?", *Environmental pollution*, Vol. 183, pp. 113–122.

[10] Alchapar, N. L., Correa, E. N., and Cantón, M. A., 2014, "Classification of building materials used in the urban envelopes according to their capacity for mitigation of the urban heat island in semiarid zones", *Energy and Buildings*, Vol. 69, pp. 22–32.

[11] He, J., and Song, C. C., 1999, "Evaluation of pedestrian winds in urban area by numerical approach", *Journal of Wind Engineering and Industrial Aerodynamics*, Vol. 81 (1-3), pp. 295–309.

[12] Tominaga, Y., Mochida, A., Yoshie, R., Kataoka, H., Nozu, T., Yoshikawa, M., and Shirasawa, T., 2008, "AIJ guidelines for practical applications of CFD to pedestrian wind environment around buildings", *Journal of wind engineering and industrial aerodynamics*, Vol. 96 (10-11), pp. 1749–1761.

[13] Blocken, B., Janssen, W., and van Hooff, T., 2012, "CFD simulation for pedestrian wind comfort and wind safety in urban areas: General decision framework and case study for the Eindhoven University campus", *Environmental Modelling Software*, Vol. 30, pp. 15–34.

[14] Antoniou, N., Montazeri, H., Wigo, H., Neophytou, M. K.-A., Blocken, B., and Sandberg, M., 2017, "CFD and wind-tunnel analysis of outdoor ventilation in a real compact heterogeneous urban area: Evaluation using "air delay"", *Building and Environment*, Vol. 126, pp. 355–372.

[15] Takahashi, K., Yoshida, H., Tanaka, Y., Aotake, N., and Wang, F., 2004, "Measurement of thermal environment in Kyoto city and its prediction by CFD simulation", *Energy and Buildings*, Vol. 36 (8), pp. 771–779, performance Simulation for Better Building Design.

[16] Ashie, Y., and Kono, T., 2011, "Urban-scale CFD analysis in support of a climate-sensitive design for the Tokyo Bay area", *International Journal of Climatology*, Vol. 31 (2), pp. 174–188.

[17] Wang, Y., Berardi, U., and Akbari, H., 2016, "Comparing the effects of urban heat island mitigation strategies for Toronto, Canada", *Energy and Buildings*, Vol. 114, pp. 2–19.

[18] Antoniou, N., Montazeri, H., Neophytou, M., and Blocken, B., 2019, "CFD simulation of urban microclimate: Validation using high-resolution field measurements", *Science of the total environment*, Vol. 695, p. 133743.

[19] Brozovsky, J., Simonsen, A., and Gaitani, N., 2021, "Validation of a CFD model for the evaluation of urban microclimate at high latitudes:

A case study in Trondheim, Norway", *Building and Environment*, Vol. 205, p. 108175.

[20] Allegrini, J., 2018, "A wind tunnel study on three-dimensional buoyant flows in street canyons with different roof shapes and building lengths", *Building and Environment*, Vol. 143, pp. 71–88.

[21] Mark, A., Rundqvist, R., and Edelvik, F., 2011, "Comparison between different immersed boundary conditions for simulation of complex fluid flows", *Fluid dynamics & materials processing*, Vol. 7 (3), pp. 241–258.

[22] Van Doormaal, J., and Raithby, G., 1984, "Enhancements of the SIMPLE method for predicting incompressible fluid flows", *Numerical heat transfer*, Vol. 7 (2), p. 147.

[23] Rhie, C., and Chow, W. L., 1983, "Numerical study of the turbulent flow past an airfoil with trailing edge separation", *AIAA journal*, Vol. 21 (11), p. 1525.

[24] Mark, A., and van Wachem, B. G., 2008, "Derivation and validation of a novel implicit second-order accurate immersed boundary method", *Journal of Computational Physics*, Vol. 227 (13), pp. 6660–6680.

[25] Allmaras, S., Johnson, F., and Spalart, P., 2012, "Modifications and non-linear in the boundary layer. Several validation cases Clarifications for the Implementation of the Spalart-Allmaras in both two and three dimensions were provided, exhibit- Turbulence Model", *Seventh International Conference on Computational Fluid Dynamics (ICCFD7)*.

[26] Shih, T.-H., Liou, W., Shabbir, A., Yang, Z., and Zhu, J., 1995, "A new $k - \epsilon$ eddy viscosity model for high Reynolds number turbulent flows", *Journal of Computational Physics*, Vol. 24 (3), pp. 227–238.

[27] Menter, F. R., 1994, "Two-Equation Eddy-Viscosity Turbulence Models for Engineering Applications", *AIAA Journal*, Vol. 32 (8).

[28] Menter, F. R., Kuntz, M., and Langtry, M. R., 1994, "Ten Years of Industrial Experience with the SST Turbulence Model", *Turbulence, Heat and Mass Transfer*, Vol. 4.

[29] Wilcox, D., 2010, *Turbulence Modeling for CFD*, DCW Industries.

[30] Kalitzin, G., Medic, G., Iaccarino, G., and P.Durbin, 2005, "Near-wall behavior of RANS turbulence models and implications for wall functions", *Journal of Computational Physics*, Vol. 204.

Conference on Modelling Fluid Flow (CMFF'22)
The 18th International Conference on Fluid Flow Technologies
Budapest, Hungary, August 30-September 2, 2022

Can black blood MRI predict hemodynamics in intracranial aneurysms? - An analysis of in-vitro signal intensity and CFD

Jana KORTE[1,3], Laurel MARSH[2,3,4], Mariya PRAVDIVTSEVA[5], Franziska GAIDZIK[2,3], Naomi LARSEN[5], Gábor JANIGA[2,3], Philipp BERG[2,3],

[1] Corresponding Author. Department of Fluid Dynamics and Technical Flows, University of Magdeburg, Universitaetsplatz 2, 39106 Magdeburg, Germany, E-mail: jana.korte@ovgu.de
[2] Department of Fluid Dynamics and Technical Flows, University of Magdeburg, Magdeburg, Germany
[3] Research Campus STIMULATE, University of Magdeburg, Germany
[4] Department of Mechanical Engineering, University of Washington, Seattle, USA
[5] Department of Radiology and Neuroradiology, University Medical Center Schleswig-Holstein (UKSH), Kiel University, Kiel, Germany

ABSTRACT

By visualizing vascular walls of intracranial aneurysms (IA) using black blood magnetic resonance imaging (BB MRI), wall adjacent and luminal hyperintense signal intensity (SI) is found. These SI have been linked to vessel wall inflammation, higher rupture risk, and slow flow. However, the relationship between SI and other hemodynamic features has not been investigated before. Therefore, here computational fluid dynamics (CFD) simulations are carried out to compare the flow behaviour to the SI values. In this study, three patient-specific aneurysm phantoms are undergone BB MRI. Next BB MRI SI were evaluated inside the aneurysm lumen and is then compared to in-silico flow behaviour. The comparison is performed by taking both, the time-averaged (TA) and time-resolved CFD data into account. The overall comparison reveals high dependencies of increasing velocity and kinetic energy (KE) to decreasing SI, which can be explained by the design of BB MRI. BB MRI eliminate the signal of flowing fluid and works best for higher flows. Still, not all BB signal originated from fluid with high average velocities was eliminated, in this case it shows higher oscillatory velocity indices. By analysing regions of vortex formation within the highly-resolved CFD data, a correlation to low SI is found. The comparative investigation of BB and CFD results indicates specific relations between hemodynamics and SI noticeable in velocity, KE and vortex formation. The analysis of BB MRI SI reveals correspondences to hemodynamic parameters for TA values, a strong correlation has to be further proofed.

Keywords: Computational fluid dynamics, Black blood magnetic resonance imaging, Hemodynamics, Intracranial aneurysm

NOMENCLATURE

KE	$[J]$	kinetic energy
OVI	$[-]$	oscillatory velocity index
SI	$[a.u.]$	signal intensity
VEL	$[m/s]$	velocity

Subscripts and Superscripts

BB	black blood
CFD	computational fluid dynamics
IA	intracranial aneurysm
MAD	median absolute deviations
MRI	magnetic resonance imaging
TA	time average
VC	vortex core
VW	vessel wall

1. INTRODUCTION

Intracranial aneurysms (IAs) are a pathology occurring in cerebral arteries, presenting as a dilatation of the vessel [1]. Due to the weak structure of an aneurysm dome, IAs carry the risk of rupture which leads to subarachnoid bleedings. IAs can be treated, but each intervention has complication risk, moreover some IAs do not rupture during the lifetime. However, reliable aneurysm rupture risk assessment is a clinical challenge [2][3]. Many metrics associated with rupture risk can be derived from state-of-the-art CFD methods [4]. Specific hemodynamic parameters characterizing the blood flow are linked to rupture like oscillatory shear index and wall shear stress. Recently, signal enhancement on BB MRI was linked to the aneurysm wall inflammation and higher aneurysm rupture risk [5][6][7]. BB MRI recordings comprise of signal intensity and is designed to suppress the signal of flowing blood [8][9]. Low SI within measurements of IAs has been

related with high velocities. Nevertheless, recent studies show that low or high velocities can lead to low SI [8][10]. Overall the link between SI and aneurysm hemodynamics is of great interest concerning the estimation of rupture risks of IAs. Since this link was poorly investigated up to now, the purpose of this study is to determine relations of the intra-aneurysmal flow field to the BB SI. To explain the variations in SI trends and pseudo enhancement, the SI is compared to specific hemodynamic parameters.

2. MATERIAL AND METHODS

The underlying experiments and simulations are based on previous studies by Gaidzik et al. [10] and Pravdivsteva et al. [8].

2.1. Patient selection

Three IA models are created using 3D rotational angiography (3D RA, Allura XperFD 20/10, Philips, Best, The Netherlands) of three different patients over the age of 50. Each patient-specific IA model has a unique shape, size and location to ensure a diverse basis for the study. Size and shape of each model is shown in Figure 1 and are further described in [10][8].

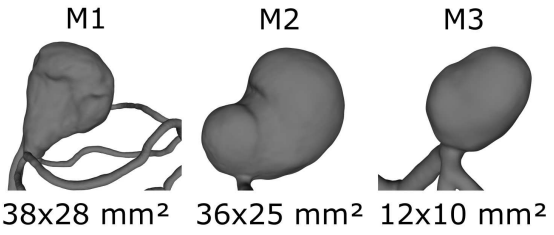

Figure 1. Aneurysm models (M1-3) of three different patients with varying anatomical cross sections (mm²) located at the basilar tip (M1), the carotid terminus (M2) and the middle cerebral artery bifurcation (M3).

2.2. Black blood MRI

Blood flow inside the IA models is analysed via in-vitro experiments of the patient-specific models. The IA geometry models are 3D-printed for this purpose and a blood mimicking fluid is pumped through the vessels with a pulsatile flow. Blood flow is then recorded with BB MRI. Within BB MRI the flowing blood is suppressed and enhancement zones further visualized. If the suppression sequencing is successful, blood is visualized as black (in contrast to this for in-vivo experiments the static tissue is illuminated). These visualizations are digitised to SI values, which are time averaged over one cardiac cycle. Resolution of the BB MRI voxel is 0.7mm³. For further details on the experimental setup the interested reader is referred to [8].

2.3. Hemodynamic simulations

For each model a blood-flow simulation is carried out based on the experimental setup to create a basis for comparison. The detailed setup is given in [10]. Fluid properties are set to equal the experimental parameters with a density of 1114.5 kg/m³ and a dynamic viscosity of 3.72 mPas, respectively. Time dependent pulsatile flow curves, recorded during the experiments, are set as inlet boundary conditions. Two different flow curves are imposed to analyse the impact of a high and low flow field. The mean value of the low flow curves are 160 ml/min (M1), 203 ml/min (M2) and 208 ml/min (M3). For the high flow curves, the mean values are 266 ml/min (M1), 307 ml/min (M2) and 311 ml/min (M3). Outlet boundary conditions are pressure curves, likewise recorded and set equal for high and low inflow conditions. The mesh comprises of polyhedral and prismatic cells with a base size is 0.1 mm and the discretised models comprised of 9.8 (M1), 15.1 (M2) and 8.5 (M3) million elements. The finite-volume solver used for the simulations is StarCCM+ (Siemens Product Lifecycle Management Software Inc., Plato, TX, USA).

2.4. Analysis

To compare the SI data recorded within the BB MRI experiments to the CFD data, relevant hemodynamic parameters are evaluated from the numerical simulations. Accordingly, velocity magnitude as well as velocity components (V_x, V_y, V_z), kinetic energy (KE), and oscillatory velocity index (OVI) are analysed [11][12].

$$KE = \frac{\rho v^2}{2} \tag{1}$$

$$OVI = \frac{1 - \frac{|\int_0^T f v_i dt|}{\int_0^T |f v_i| dt}}{2} \tag{2}$$

The qualitative as well as quantitative evaluation of the raw CFD data is carried out in EnSight v10.2 (ANSYS Inc., Canonsburg, PA, USA). MATLAB R2020b (MathWorks, USA) is used for the analysis of the processed data [13]. For an accurate comparison the BB SI data has to be registered onto the numerical model results. Registration is carried out in Blender 3.1 (Blender Foundation, Amsterdam, NL). Once this SI data is registered, the CFD data, whether time-averaged or resolved, can be mapped, using Ensight, onto the BB voxels to allow for direct comparison.

2.4.1. Time-averaged data analysis

After registration of the SI data onto the hemodynamic simulation parameters, the latter are averaged and mapped onto the registered SI data. Thus, a point-wise comparison of the averaged data is accomplished. Since the mapped, time-averaged (TA)

data still may be slightly misaligned, a voxel-wise comparison is completed as well. For this, the CFD data is spatially discretised and the averaged parameters are calculated for a new, artificial voxelisation. This new voxel size is 2.1mm³, which is three times the size of the BB MRI resolution. The spatially averaged CFD data are then similarly mapped onto the new SI data which is spatially averaged to the same resolution, to analyze the correlation of the data voxel-wise.

Additionally, the mapped SI data is clustered into 10 and 25 regions depending on the value of the SI. Thus, the cluster boundaries feature a regular interval and the dimensions of each cluster differs in size. The cluster-wise averages of the hemodynamic parameters depending on the SI values within each cluster, are then correlated to the cluster-wise SI values.

To define these clusters, the range of SI is divided in equal amounts between the minimum and maximum based on the number of regions. Thus, every cluster has a specific size and discretizing a model into more than 25 clusters would not improve the analysis since clusters become bare or completely void. On top of that, for the highly resolved CFD data, the OVI is calculated. Since this index shows the fluctuation of velocity over time, it is first calculated and then mapped onto the registered BB SI data. Here, a cluster-wise correlation allows for an analysis of the dependency of velocity fluctuations over time onto SI.

2.4.2. Time-resolved data analysis

To further investigate the fluxes of SI observable in the flow fields and possible causes of pseudo-enhancement, the time-resolved CFD data is analysed in detail and then mapped onto the BB SI. This analysis contains the evaluation of each time-step's velocity values. Focusing on the systolic time-step, the inflow jet into the aneurysm is evaluated and the depending velocity parameters are analysed.

Next, the dependencies between vortex formation and BB MRI are analysed. By extracting the vortex core (VC) lines from the high resolved CFD data, the geometric points of the inner vortex is formed. These are given over 20 time-steps within one cardiac cycle. After the vortex core region is located, the BB SI is analysed in this location. The variation of high and low BB SI and the mean and median values are analysed.

3. RESULTS

3.1. Qualitative results

Figure 2 shows the qualitative comparison of the three models. A contour inside each aneurysm model is colored by time-averaged KE (first and third row) and SI (second and forth row). Similar flow patterns are present within M1 and M2 for SI and KE for low and high flow rates, constituting the appearance of higher SI in areas with lower KE (see black arrow heads). This is also noticeable within M3 for the high flow rate (see black arrow heads). KE pattern is similar within M3 for low and high flow rate, but the SI pattern shows a different behaviour between low and high flow. Furthermore, SI is much lower (highest value 830 a.u. lower) within M3 for low flow.

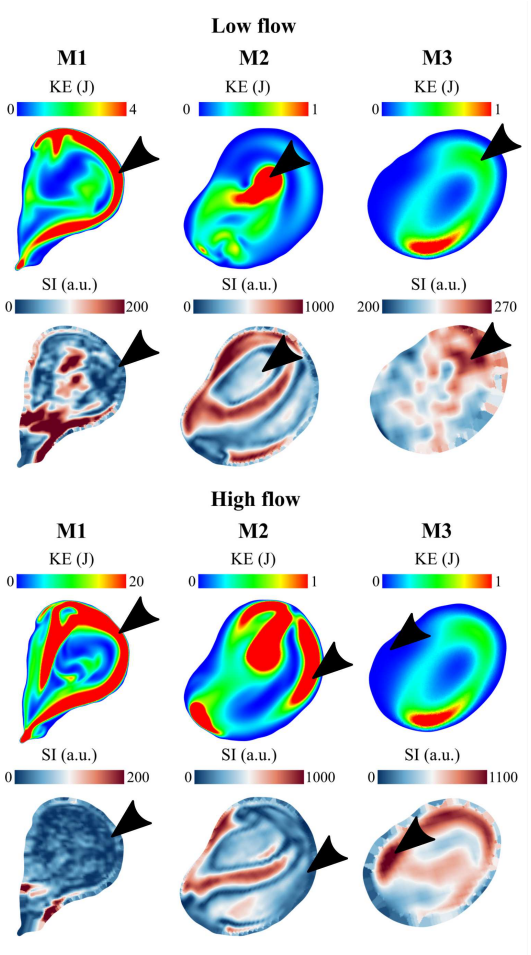

Figure 2. Contour through each aneurysm model (M1-M3) colored with KE (first and third row) and with SI (second and forth row) for the two applied flow rates. Areas with higher KE correlate with areas with lower SI and vice versa (black arrow heads).

3.2. Quantitative results

3.2.1. Time-averaged data

As previously reported, the mean TA velocity correlates to the inverse of the SI when clustering the domain into regions based on equivalent intervals of SI. Comparing the values point-wise and voxel-wise as described in section 2.4 does not give insight into the flow behaviour and its impact on the SI. Nevertheless, the cluster-wise comparison shows similarities between the BB MRI SI and other hemodynamic parameters. In Figure 3 the TA velocity is presented for each of the ten SI clusters. In this Figure as well as in Figure 4 and Figure 5 the SI values are nor-

malized by the highest SI value outside the aneurysm lumen. In the graph on the left, the TA velocity is plotted with all data points while the graph on the right shows the data with outlying velocity removed. Outliers are defined as points with more than three scaled median absolute deviations (MAD). Figure 3 shows the wide range of velocities that can induce low SI for M1. While high velocities are expected in the lower range of SI, a large percentage of the first two clusters show a vast range which includes very low velocity. After removing the outliers, the median shifts most noticeably for the first, second and third clusters. Considering only the velocities falling within three MAD of the median, shows that the last region's median velocity is similar to the results including the outliers. Therefore, further investigation

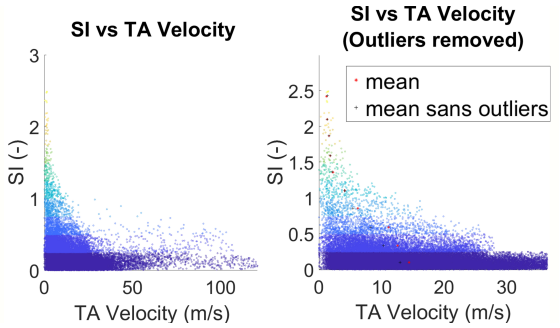

Figure 3. TA velocity (m/s) over the SI clusters (1-10) with (left) and without (right) outliers.

is performed to elucidate the correspondence of this large scale of velocities and SI.

3.2.2. Time-resolved data

Concerning the time-resolved CFD data, the systolic time step is analysed first. Here, the high velocity and the corresponding OVI are taken into account. The high velocity inflow of M1 at systolic state is shown in Figure 4 along with the OVI. In the first row, the velocity inflow jet is presented using only velocity above the 90th (left) and 99th (right) percentile of the overall velocity values. The jet is colored by velocity; the red dots are a subset of the CFD resolution thereby representing the aneurysm. In the second row, the jet is simply colored blue while the aneurysm representative dots are scaled and colored by OVI. The high velocity zone has a consistent direction throughout the cardiac cycle producing a low OVI. However, the fluid surrounding the jet changes direction throughout the cycle.

A high OVI (OVI > 0.2) is typically found in low velocity areas where relatively minor change in direction or particularly in magnitude can lead to an elevation of OVI. In Figure 5 the distribution of the OVI in the aneurysm lumen is presented on the left. In the middle, the aneurysm lumen is presented with blue dots. Using the first quartile of velocity as a limit, velocity in this range exhibits a high OVI over the entire range of SI as shown in Figure 5 in the

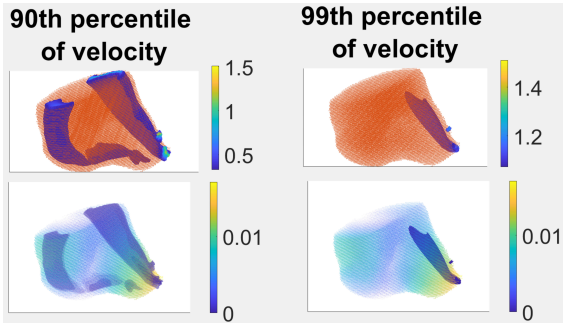

Figure 4. Velocity inflow jet into aneurysm M1 scaled by OVI inside the red colored aneurysm (first row) and the velocity inflow jet colored blue inside the aneurysm scaled with OVI (second row).

middle. However, for the fluid with velocity greater than the mean and OVI greater than 0.2, the SI tends to be in its higher range (see Figure 5 right). The

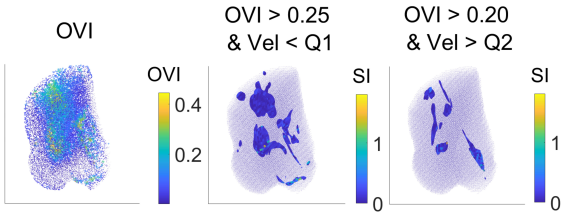

Figure 5. OVI distribution inside the aneurysm (left). Distribution of OVI>0.25 and velocity lower than the first cluster (middle). Distribution of OVI>0.2 and velocity higher than the second cluster (right).

relationship between TA velocity and SI does not hold for time-resolved velocities in most cases even at systole where the largest ranges of velocity would be seen. The M1 high flow case saw the largest velocities of the study. In Figure 6, the velocities of systolic flow are analysed in comparison to the averaged cardiac cycle. Here it is more apparent that a majority of flow, even at median velocities, is suppressed well in the first two regions. However, average velocity does not correlate with SI. A lack of any trend between velocity and SI is noted when the clustering is based on velocity.

Concerning the vortex core analysis, the SI, revealed in the vortex core regions, is analysed for each time-step. No specific curve representing a periodicity of the SI is found over time. Calculating the mean values of the SI of each time-steps reveals very low (<first cluster = 50 a.u.) SI values. In Figure 7 the mean and median as well as maximum and minimum values are shown. The maximum comprises of a high range ($\vec{\Delta}$230 a.u.) over SI, while the mean, median and minimum values range only up to 4 a.u..

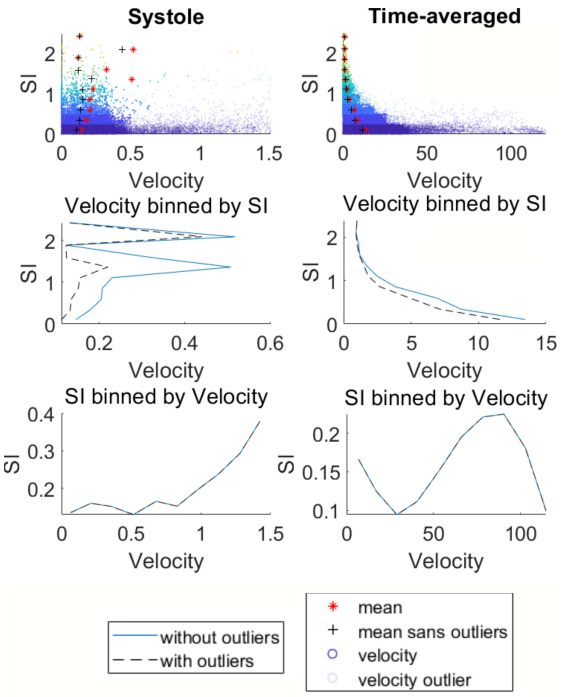

Figure 6. SI plotted over velocity in systolic state (left column) and TA (right column).

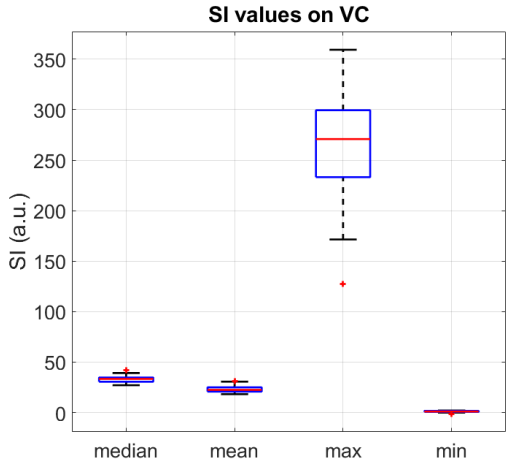

Figure 7. SI values on the VC of aneurysm M1, comprising the median, mean, maximum, and minimum values of SI for each time-step over one cardiac cycle.

4. DISCUSSION

Investigating the dependencies between SI and hemodynamics reveals a visible connection that with increasing kinetic energies the SI decreases. This strengthens the findings by [10] and [8]. A point-wise correlation, whether using highly-resolved or voxelised data, does not provide any clear correlation. For the high resolution data, this could be attributed to the manual registration and lower resolution of BB MRI. The artificial voxelisation provides an averaging effect that can obscure registration errors, but also erases important information like velocity component directions and peaks. Thus, still no direct relationship arose between the hemodynamics and SI, when analysing spatial averages. Dividing the SI data into 10 clusters reveals a correlation to TA velocity. The analysis of the time-resolved data is narrowed down by focusing on systole and diastole along with OVI, a metric summarising the entire cardiac cycle. There is no specific correlation found for the time-resolved data. Since the SI data is inherently time-averaged itself, this may mean that only time-averaged data is able to be infered. Similarly and more surprisingly, time-averaged data may be the only way of determining why enhancement and other artifacts arise in BB MRI. This leads to the assumption that SI data correlates solely to TA hemodynamics. Velocities greater than the first quartile of values is much less likely to have an OVI > 0.2; however, when these velocities, particularly when greater than the mean, experience high OVI, the flow exhibits a higher SI. This indicates that higher average velocities that are not consistently suppressed are yielding a higher SI due to an elevated OVI. This corresponds with Henningson et al., who found out that the signal suppression is more successful when a stronger turbulence appears [14]. A relationship is found for the TA data, but does vary between models. A larger number of models must be analysed to further strengthen the study.

5. CONCLUSION

In this study, three IA models are analysed with BB MRI and CFD to investigate their correlation. Therefore, the correlation between hemodynamic parameters calculated in CFD are linked to SI measured in VW MRI to investigate any possible correspondence. In summary, a qualitative and quantitative relation is clear for TA data. However, point-wise comparison as well as spatial discretization reveals no fertile insights. Especially when analysing the time-resolved CFD data separately, low OVI values paired with high velocities lead to better signal suppression (low SI). Vortex core lines are also correlated with low SI. All in all, a relation is found for BB MRI SI and TA hemodynamic parameters, showing lower velocity values with higher SI values.

ACKNOWLEDGEMENTS

This study was funded by the Federal Ministry of Education and Research within the research campus STIMULATE (grant number13GW0473A). The authors are grateful for the financial and intellectual support by the Research Training Group “Materials4Brain” (GRK2154; P2) and the European Structural and Investment Funds (ZS/2016/08/80646). Further support by the cluster of excellence Precision Medicine in Inflammation PMI 1267 and the faculty of medicine for funding the core facility MOIN CC is acknowledged. Furthermore, the financial sup-

port of the DFG (Deutsche Forschungsgemeinschaft) for Jana Korte within the project SPP2311 “Robust Coupling of Continuum-biomechanical In Silico Models to Establish Active Biological System Models for Later Use in Clinical Applications – Co-design of Modelling, Numerics and Usability” (project number 441884911) is gratefully acknowledged.

REFERENCES

[1] Cebral, J. R., Castro, M. A., Burgess, J. E., Pergolizzi, R. S., Sheridan, M. J., and Putman, C. M., 2005, “Characterization of cerebral aneurysms for assessing risk of rupture by using patient-specific computational hemodynamics models”, *AJNR: American Journal of Neuroradiology*, Vol. 26 (10), pp. 2550–2559.

[2] Kaminogo, M., Yonekura, M., and Shibata, S., 2003, “Incidence and outcome of multiple intracranial aneurysms in a defined population”, *Stroke*, Vol. 34 (1), pp. 16–21.

[3] Winn, H. R., Jane, J. A., Taylor, J., Kaiser, D., and Britz, G. W., 2002, “Prevalence of asymptomatic incidental aneurysms: review of 4568 arteriograms”, *Journal of neurosurgery*, Vol. 96 (1), pp. 43–49.

[4] Qian, Y., Takao, H., Umezu, M., and Murayama, Y., 2011, “Risk analysis of unruptured aneurysms using computational fluid dynamics technology: preliminary results”, *AJNR: American Journal of Neuroradiology*, Vol. 32 (10), pp. 1948–1955.

[5] Larsen, N., Flüh, C., Saalfeld, S., Voß, S., Hille, G., Trick, D., Wodarg, F., Synowitz, M., Jansen, O., and Berg, P., 2020, “Multimodal validation of focal enhancement in intracranial aneurysms as a surrogate marker for aneurysm instability”, *Neuroradiology*, Vol. 62 (12), pp. 1627–1635.

[6] Edjlali, M., Guédon, A., Ben Hassen, W., Boulouis, G., Benzakoun, J., Rodriguez-Régent, C., Trystram, D., Nataf, F., Meder, J.-F., Turski, P., Oppenheim, C., and Naggara, O., 2018, “Circumferential Thick Enhancement at Vessel Wall MRI Has High Specificity for Intracranial Aneurysm Instability”, *Radiology*, Vol. 289 (1), pp. 181–187.

[7] Quan, K., Song, J., Yang, Z., Wang, D., An, Q., Huang, L., Liu, P., Li, P., Tian, Y., Zhou, L., and Zhu, W., 2019, “Validation of wall enhancement as a new imaging biomarker of unruptured cerebral aneurysm”, *Stroke*, Vol. 50 (6), pp. 1570–1573.

[8] Pravdivtseva, M. S., Gaidzik, F., Berg, P., Hoffman, C., Rivera-Rivera, L. A., Medero, R., Bodart, L., Roldan-Alzate, A., Speidel, M. A., Johnson, K. M., Wieben, O., Jansen, O., Hövener, J.-B., and Larsen, N., 2021, “Pseudo-enhancement in intracranial aneurysms on black-blood MRI: Effects of flow rate, spatial resolution, and additional flow suppression”, *Journal of Magnetic Resonance Imaging : JMRI*.

[9] Mandell, D. M., Mossa-Basha, M., Qiao, Y., Hess, C. P., Hui, F., Matouk, C., Johnson, M. H., Daemen, M. J. A. P., Vossough, A., Edjlali, M., Saloner, D., Ansari, S. A., Wasserman, B. A., and Mikulis, D. J., 2017, “Intracranial vessel wall MRI: Principles and expert consensus recommendations of the american society of neuroradiology”, *AJNR: American Journal of Neuroradiology*, Vol. 38 (2), pp. 218–229.

[10] Gaidzik, F., Pravdivtseva, M., Larsen, N., Jansen, O., Hövener, J.-B., and Berg, P., 2021, “Luminal enhancement in intracranial aneurysms: fact or feature?-A quantitative multimodal flow analysis”, *International Journal of Computer Assisted Radiology and Surgery*, Vol. 16 (11), pp. 1999–2008.

[11] Mut, F., Löhner, R., Chien, A., Tateshima, S., Viñuela, F., Putman, C., and Cebral, J., 2011, “Computational hemodynamics framework for the analysis of cerebral aneurysms”, *International Journal for Numerical Methods in Biomedical Engineering*, Vol. 27 (6), pp. 822–839.

[12] Sano, T., Ishida, F., Tsuji, M., Furukawa, K., Shimosaka, S., and Suzuki, H., 2017, “Hemodynamic differences between ruptured and unruptured cerebral aneurysms simultaneously existing in the same location: 2 case reports and proposal of a novel parameter oscillatory velocity index”, *World neurosurgery*, Vol. 98, pp. 868.e5–868.e10.

[13] Korte, J., Marsh, L., Gaidzik, F., Pravdivtseva, M., Larsen, N., and Berg, P., 2021, “Correlation of black blood MRI with image-based blood flow simulations in intracranial aneurysms”, *Current Directions in Biomedical Engineering*, Vol. 7 (2), pp. 895–898.

[14] Henningsson, M., Malik, S., Botnar, R., Castellanos, D., Hussain, T., and Leiner, T., 2022, “Black-blood contrast in cardiovascular MRI”, *Journal of magnetic resonance imaging : JMRI*, Vol. 55 (1), pp. 61–80.

Conference on Modelling Fluid Flow (CMFF'22)
The 18th International Conference on Fluid Flow Technologies
Budapest, Hungary, August 30 -September 2, 2022

STEADY AND UNSTEADY PRESSURE LOSS DUE TO A DESIGN OBSTRUCTION VARIATION WITHIN A SMALL-SCALE CHANNEL

Mirza POPOVAC[1], Helmut KÜHNELT[2]

[1] Corresponding Author. Austrian Institute of Technology, Electric Vehicle Technologies, Center for Low-Emission Transport. Giefinggasse 2, 1210 Vienna, Austria. E-mail: mirza.popovac@ait.ac.at
[2] Austrian Institute of Technology, Electric Vehicle Technologies, Center for Low-Emission Transport. Giefinggasse 2, 1210 Vienna, Austria. E-mail: helmut.kuehnelt@ait.ac.at

ABSTRACT

This paper is presenting the results of the numerical study of a flow through a small-scale channel with varying design obstruction. The goal is to analyse the integral flow properties within a channel with obstruction: the steady state pressure loss across the channel with obstruction, and the unsteady force exerted on the obstruction with respect to the obstruction rate of change. The generalization of the impact was examined through the anticipated exponential fitting function. For a comparative evaluation, the characterisation of the pressure loss was sought in a classical engineering form related to the sudden pipe contraction flow (Borda-Carnot expression). However, in order to account for the differences in the respective flow features, the modification of the original expression is put forward and tested.

Keywords: **Borda-Carnot expression, Channel with flap, CFD, OpenFoam, Overset simulations.**

NOMENCLATURE

A	$[m^2]$	incoming flow surface area
A_c	$[m^2]$	contraction surface area
A_s	$[m^2]$	separation surface area
m	[-]	modification exponent
p	$[m^2/s^2]$	kinematic pressure
v_{in}	$[m/s]$	inlet velocity
ΔP	$[Pa]$	total pressure loss
α	$[^o]$	flap angle
μ	$[Pa.s]$	fluid viscosity
ρ	$[kg/m^3]$	fluid density
τ	$[s]$	flap motion time

1. INTRODUCTION

The system of small-scale channels, with the characteristic length of the millimetres order of magnitude, is typically to be found in different cooling applications (e.g. in batteries or as evaporators). If a protruding obstruction appears within these channels, the pressure distribution will be changed in the entire system, which can cause the change of the flow pattern and the cooling characteristics overall. For example, by changing the pressure difference between the incoming and the outflowing evaporator header, its active area (and hence the temperature distribution within the entire evaporator) can change significantly. In order to investigate the effect of the additional pressure loss within a small-scale channel due to an obstruction, a numerical analysis was performed on a simple plain channel geometry with a flap motion representing the protruding obstruction. Being a niche application, to the best of authors' knowledge, there are no publicly available results on the related topic. However, this problem can be viewed as a flow around the flap valve, the application of which can be found in a number of large-scale engineering problems, ranging from the flows in the HVAC systems [1] to the nuclear vessel flows [2].

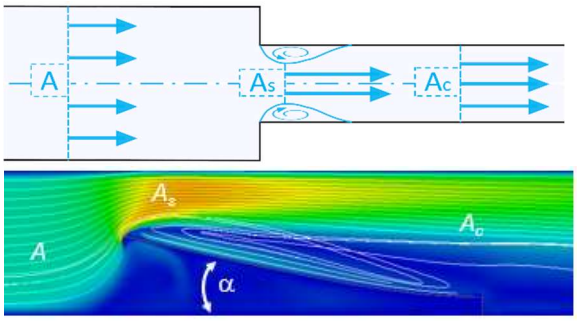

Figure 1. Sketch of a sudden pipe contraction flow (top) and flow over a flap within a channel (bottom)

Depicted in Figure 1 is a resemblance between the flow through a sudden pipe contraction and the flap-channel case: the incoming flow (with the cross-section surface area A) features the reduction of the flow cross-section, and passing the edge of the

contraction the flow separates and causes further reduction of the flow cross-section (vena contracta, A_s), before recovering subsequently to the final contraction flow conditions (having the cross-section surface area A_c). The similarity can be found (in particular with the symmetrical part of the pipe contraction) by looking at the small-scale channel, with a flap under given angle α for modeling the obstruction: at the flap leading edge the flow is being pushed upwards, flowing over the flap surface a separation zone is created, and further downstream the flow recovers its contracted state (eventually developing fully if the channel length permits).

For the sudden pipe contraction flow the empirical correlation of Borda-Carnot is based on a well-established engineering practice to corelate the total pressure loss ΔP to the kinetic energy of the flow defined by the incoming flow velocity v_{in} [3]:

$$\frac{\Delta P}{\rho} = \frac{v_{in}^2}{2}\xi_{BC}$$
$$\xi_{BC} = \left(1-\frac{1}{\sigma}\right)^2\left(\frac{A}{A_c}\right)^2 \qquad (1)$$
$$\sigma = \frac{A_s}{A_c} = (n-1) + n\left(\frac{A_c}{A}\right)^q$$

where ρ is the fluid density, and ξ_{BC} is the Borda-Carnot loss coefficient expressed in terms of the geometrical quantities which are characterizing the sudden pipe contraction, i.e. the incoming flow and the contracted surface areas A and A_c. respectively. In the literature one can find different methods for calculating the smallest surface area at the location of the flow separation A_s [4]. In this work, following the measurements of Weisbach [5], it is expressed in terms of the contraction ratio σ, which is for a sharp-edged contraction approximated as a weighted average between the relative incoming (A/A) and contracted flow area (A_c/A) with $n=0.37$ and $q=3$.

For a flap-channel flow the contracted surface area is related to the flap angle α, following $1-\sin\alpha$ if the flap is fixed to the bottom wall. In the flap-channel case, however, the contraction recovery is not directly limited by the downstream geometry. Therefore, in the original Borda-Carnot framework, Eq.(1), the modification is put forward:

$$\frac{A_c}{A} = (1-\sin\alpha)^m \qquad (2)$$

where the contraction ratio exponent m is introduced to capture the effect of the flow contraction which is not geometrically confined.

Based on the observation that the flow after flap will spread further downstream, given that the expression between the brackets in Eq.(2) is less than unity, also m needs to be less than unity to account for the spreading of the contraction zone. The value adopted for the modification exponent in Eq.(2) is $m=0.5$, although it is expected to feature some dependency on the channel mass flow rate. In this work, however, the focus is only on the plausibility testing, while further fine tuning is yet to be done.

2. SIMULATION SETUP

Resembling a flap valve placed within the straight section of the duct connecting two large reservoirs, the adopted geometry is sketched in Figure 2. The domain consists of a plane channel of *6 mm* height and *65 mm* length. Located at the channel's half-length is *0.1 mm* thick flap, which can rotate around its lower edge shifted *0.15 mm* from the bottom wall. Next to the rotation axis is *0.1 mm* thick block, with *0.15 mm* clearance to the flap (allowing for the "leakage" around the flap valve shaft). The block is reducing the flow under the flap, thus supporting the flow development over the leading edge of the flap. The flow effects in the spanwise direction are neglected.

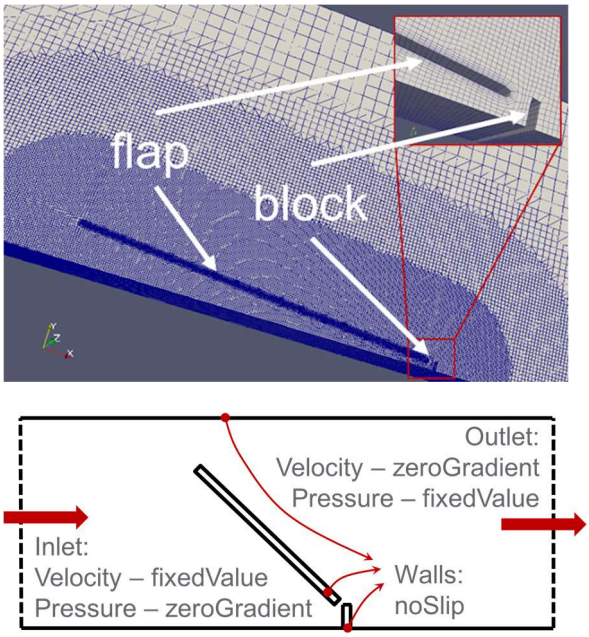

Figure 2. Numerical mesh (top) and boundary conditions (bottom) for the flap-channel case.

The simulations have been performed using open-source CFD library suite *OpenFoam* [6]. The hex-dominant mesh shown in Figure 2 (generated with *snappyHexMesh*) is featuring different levels of cell refinement based on the distance from the flap and boundary layer cells around the flap. This is ensuring sufficient near-wall mesh resolution: y^+ below 1 on the flap, and on other walls below 10. As for the boundary conditions, constant velocity v_{in} was imposed at the inlet, and at the outlet the constant (zero) pressure was specified. All walls are treated as no slip boundaries, and in the spanwise direction symmetry was imposed. The constant fluid

properties of water have been assumed: density $\rho=998.2\ kg/m^3$, and $\mu=1.01\ mPa.s$ for the dynamic viscosity. The steady state simulations have been performed using incompressible isothermal Newtonian fluid flow solver based on SIMPLE pressure-velocity coupling (*simpleFoam*). Since the flow properties are taken constant, instead of the total pressure P the kinematic pressure $p=P/\rho$ was used as the flow variable in solving the momentum and continuity equations (the same way as the kinematic viscosity $\nu=\mu/\rho$ was used instead of μ). This approach was extended for the unsteady simulations, capturing the flap motion using the overset method for overlapping meshes (*overPimpleDyMFoam*). In order to ensure the convergence of the simulation, the time stepping was controlled through the $CFL=1$ stability criterion.

3. FLOW CHARACTERISTICS

The distributions of the velocity magnitude and pressure are shown in Figure 3 for the flow case with the flap angle 10°, representing low flap angles. The obtained results indicate that the low flap angle cases feature the flow effects similar to the sudden pipe contraction flow. Namely, the incoming flow separates at the leading edge of the flap, and after the recirculation bubble on the flap surface, it recovers to its contraction state downstream. This is also mirrored in the pressure distribution, showing a transition from the high-pressure region upstream, over the under-pressure in the separation zone on the flap, finally to the imposed zero value at the outlet.

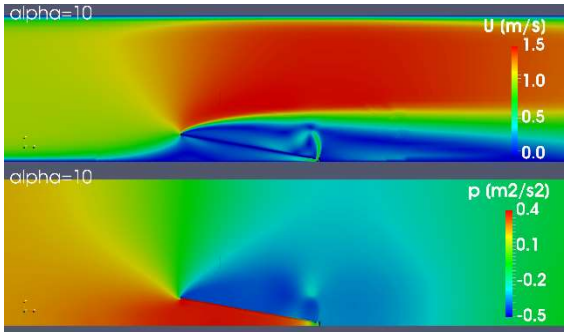

Figure 3. The velocity magnitude (top) and the kinematic pressure (bottom) for the flap-channel case with low flap angle (α=10°).

Completely different is the flow pattern obtained for the high flap angles, as shown in Figure 4 for the flow case with 80° flap angle. Given that a constant velocity was imposed at the inlet, the mass flow rate through the domain is also constant, and therefore most of the flow is squeezed through the gap between the flap edge and at top wall (since the small gap at the bottom wall allows for relatively small mass flow from below). Being ejected from the flap leading edge, the high velocity fluid creates a massive recirculation zone behind the flap leaving the flow pattern without "classical" contraction region (assumed for the Borda-Carnot expression). This behavior is reflected in the pressure distribution, where the high pressure up-stream is sharply divided from the low pressure behind the flap.

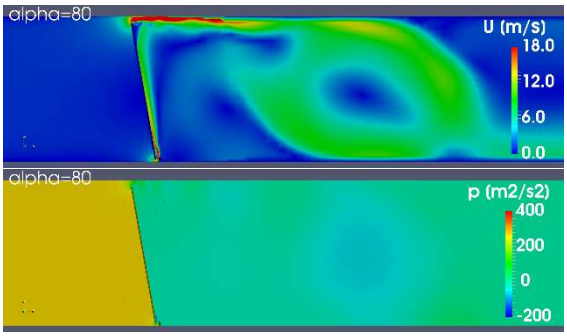

Figure 4. The velocity magnitude (top) and the kinematic pressure (bottom) for the flap-channel case with high flap angle (α=80°).

With the described numerical setup the flap-channel pressure loss characteristics is obtained from the series of simulations, aiming to generalize it through the anticipated exponential fitting function. Regarding the casting of the obtained characteristics into the modified Borda-Carnot pressure loss, the differences in the flow patterns between the low and high flap angle cases are setting low the expectations for this simplified engineering approach.

3.1. Steady state pressure loss

The assessment of the steady state pressure characteristics for a range of inlet velocities was performed through the series of subsequent simulations with different flap angle α. In Figure 5 the kinematic pressure at the flap-channel inlet (corresponding to the pressure loss across the flap-channel, since the outlet pressure is set to zero) is plotted over all investigated flap angles (dots). For the obtained results the anticipated exponential function was fitted (dashed lines), and the coefficient of determination R^2 shows good agreement over the investigated flap angle range for all calculated inlet velocities. As for the modified Borda-Carnot approximation (full lines), there is a good agreement up to approximately 45° flap angle (half of the investigated flap angle range), after which it starts to depart strongly. Looking closer at the agreement range (shown enlarged in Figure 5), one can see that the modified Borda-Carnot expression fits the stimulation predictions within 10% accuracy. Important to note, though, is the agreement departure of the modified Borda-Carnot predictions for different inlet velocity cases. This is an indication that instead of the assumption of a constant value of the modification exponent m, more appropriate seem to be its dependency on the mass flow rate through the channel.

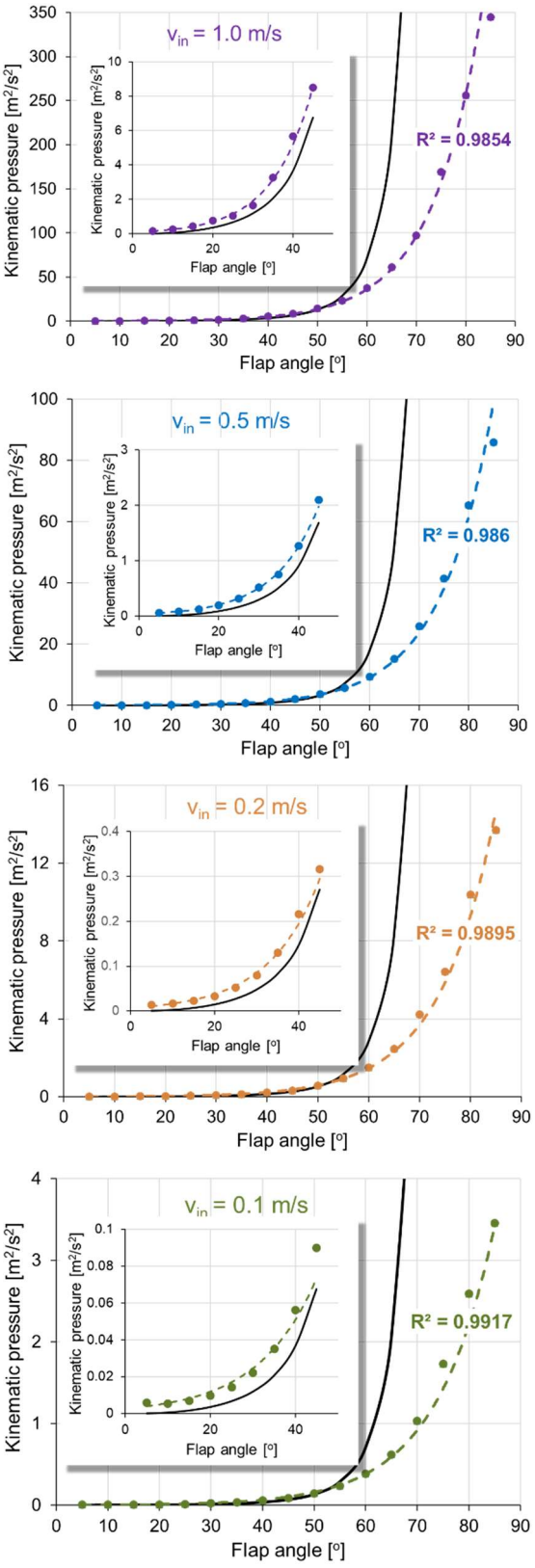

Figure 5. Steady state kinematic pressure (corresponding to the pressure loss across the flap-channel) for different inlet velocities (top to bottom: *v_{in}=1.0, 0.5, 0.2, 0.1*, coloured violet, blue, orange and green respectively): simulations – dots, exponential fit – dashed line, modified Borda-Carnot – full line.

Having adopted the anticipated exponential fit for the obtained curves, the generalization of the calculated pressure loss values ΔP_{calc} is accomplished through the normalization with the squared inlet velocity v_{in}. This is equivalent to the definition of the pressure loss coefficient ξ, which is also sought in the exponential form:

$$\xi = \frac{\Delta P_{calc}/\rho}{v_{in}^2/2} = C_1 e^{\alpha C_2} \qquad (3)$$

where C_1 and C_2 are respectively the base coefficient and the exponent in the anticipated exponential function.

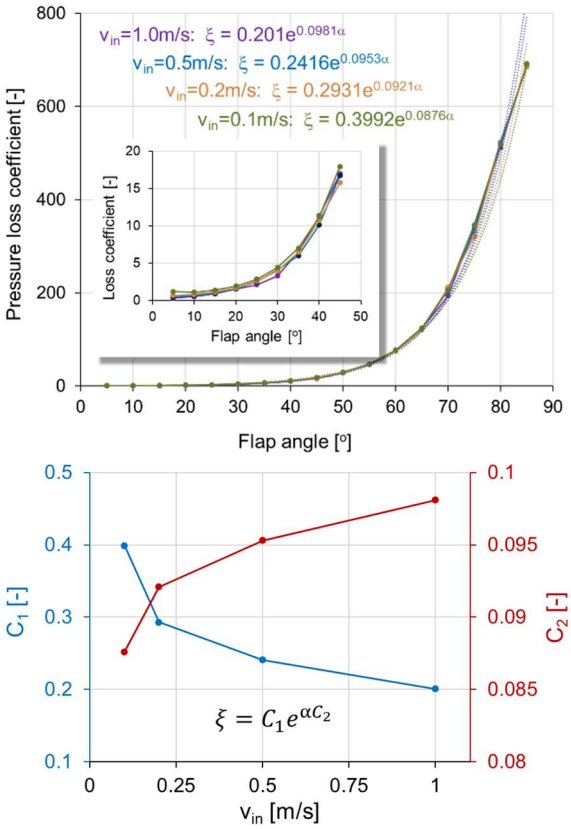

Figure 6. Steady state pressure loss coefficient in the flap-channel for different inlet velocities (top) and the coefficients of the pressure loss exponential fit depending on the inlet velocity (bottom).

As shown in Figure 6 (top), these normalized curves are tending to collapse to a single one for the entire calculated flap angle range. A closer look reveals particularly good agreement for the pressure loss coefficient at the smaller flap angles, while for higher flap angles the deviation is more pronounced. However, from the plot of coefficients as a function of the inlet velocity v_{in} (Figure 6, bottom) one can note that the base coefficient C_1 (blue) has a large spreading over different inlet velocities. The relative standard deviation of C_1 over v_{in} amounting to 30% can be seen as the quantification of the above-

mentioned dependency of m on the inlet velocity. For the exponent C_2 (red), however, this spreading is less pronounced (relative standard deviation less than 5%). As a result, it can be assumed that the exponent of the fitting function for ξ is generally valid for the investigated case.

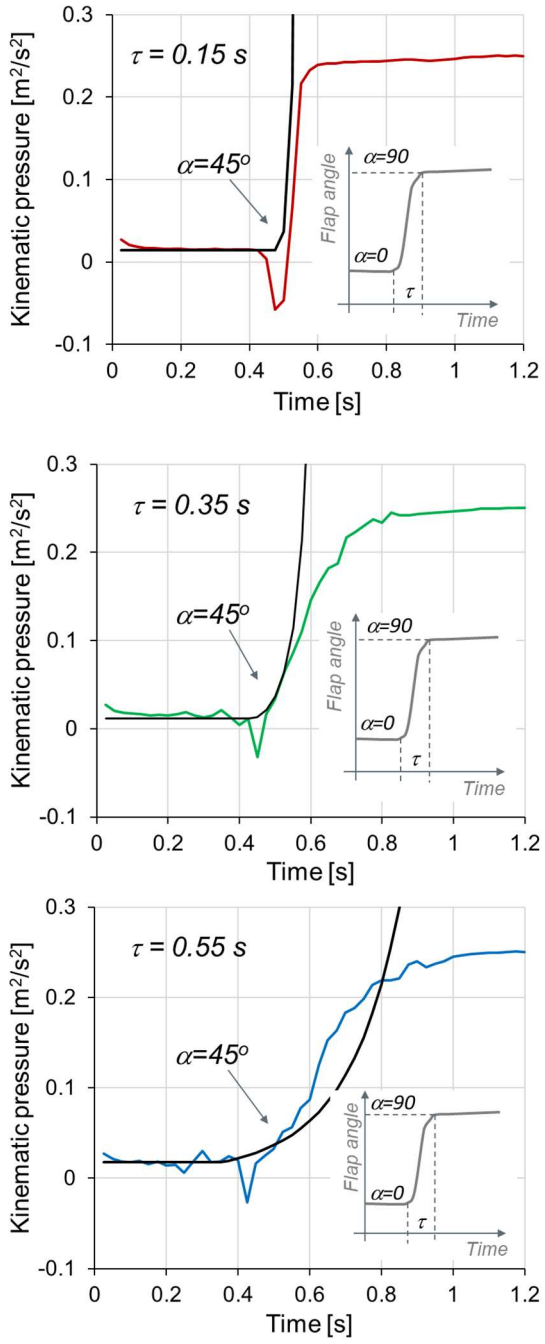

Figure 7. Unsteady kinematic pressure (corresponding to the pressure loss across the flap-channel) with fixed inlet velocity v_{in}=1.0m/s for different flap angular change rate (top to bottom: τ=0.15s, 0.35s, 0.55s, coloured red, green and blue respectively) compared to the modified Borda-Carnot expression (black).

3.2. Unsteady pressure loss

In order to analyze the pressure loss behavior in the flap-channel under unsteady flow conditions, as well as to test the applicability of the proposed Borda-Carnot modification there, the flap-channel simulations have been repeated with the same numerical setup (constant inlet velocity v_{in}=1.0m/s), only for the flap the angular motion was imposed through the predefined sigmoid function:

$$\alpha(t) = \alpha_{end}\frac{1 + erf\left(\frac{t - t_0}{0.25\tau}\right)}{2} \qquad (4)$$

where α_{end}=90° is the end position of the flap, and the error function varies between -1 and 1 within the time interval τ (characteristic increase time) around the specified time instant t_0 (here selected t_0=0.5s).

Since the mass flow rate remains constant in this case (set with v_{in}=1.0m/s), the overall pressure loss increases with the imposed flap motion. Its time evolution is shown in Figure 7 for different characteristic increase times (red, green and blue for τ = 0.15s, 0.35s and 0.55s respectively), and the corresponding forces acting on the flap, normalized with the maximum force occurring at α_{end}=90°, are shown in Figure 8. The comparison with the proposed Borda-Carnot modification (Figure 7, black) indicates qualitatively the same output as in the steady state case: the modified Borda-Carnot predictions follow the magnitude of the pressure loss increase only up to a certain limit (about 45° flap angle), after which they fail completely.

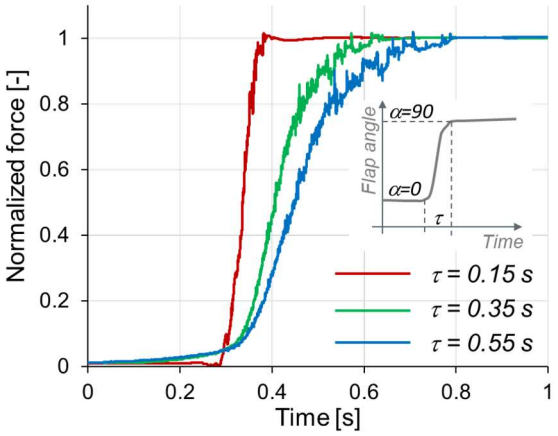

Figure 8. Unsteady normalized force acting on the flap surface in the flap-channel with fixed inlet velocity v_{in}=1.0m/s for different flap increase times (τ=0.15s, 0.35s, 0.55s, coloured red, green and blue respectively).

An interesting feature in these unsteady numerical simulations is observed as the under-pressure peak in the pressure loss temporal evolution at the beginning of the flap angular motion (around t=0.4s). As the flap is forced into its motion, a cavitating under-pressure field is established, before

the pressure starts to rise due to the increased flow resistance from the flap. It is the flap angular change rate (through Eq.(4) determined by τ) that characterizes this under-pressure peak, together with the relaxation time needed for reaching the final pressure loss.

4. CONCLUSIONS

This work presented the analysis of the pressure loss within a small-scale channel with protruding obstruction, here modelled through the motion of a flap within the channel. Furthermore, an attempt was made to generalize the pressure loss characterization through the exponential function. Finally, the applicability of the Borda-Carnot empirical expression for the pressure loss within pipes with sudden contraction, was tested for this flap-channel flow case.

It has been observed that the exponential function describes well the variation of the static flap-channel pressure loss for different channel mass flow rates, in particular for the lower flap angles. However, while in the exponential fit it can be assumed that the exponent features universal validity for the investigated case, the base coefficient has a large spreading over different inlet velocities. In addition to the steady-state characteristics, for the unsteady flap-channel flow one can identify the under-pressure peak as a consequence of the imposed flap angular motion. Its intensity depends on the flap angular change rate, influencing thus the pressure relaxation time.

In the view of similarity between the flap-channel case and the flow through the sudden pipe contraction, the modification of the original Borda-Carnot expression was introduced to account for the recovery of the contracted flow which is not directly limited by the geometry. The obtained results suggest a dependency of the modification exponent m on the channel mass flow rate. Nevertheless, as a proof of concept, with a constant value for m, acceptable pressure loss predictions are obtained for low flap angles (corresponding to small protruding obstructions), although. For high flap angles (big protruding obstructions) the characterization of the flow contraction loses its validity, as the massive recirculation zone is created behind the flap, and the pressure loss predictions fail completely.

ACKNOWLEDGEMENTS

The presented work has been financially supported through the EU Programme Horizon 2020, Project SELFIE (Grant Agreement number: 824290).

REFERENCES

[1] Lukács E. and Vad J. (2021), "Flow topology and loss analysis of a square-to-square sudden expansion relevant to HVAC systems: A case study", *Journal of Building Engineering*, Vol. 41, https://doi.org/10.1016/j.jobe.2021.102802.

[2] Belliard M., (2018), "Numerical modeling of an in-vessel flow limiter using an immersed boundary approach", *Nuclear Engineering and Design*, Vol. 330, pp. 437-449, https://doi.org/10.1016/j.nucengdes.2018.01.027.

[3] Batchelor, G. K. (1967), *An Introduction to Fluid Dynamics*, Cambridge University Press, ISBN 978-0-521-66396-0.

[4] Dayev Zh. A. and Kairakbaev A. K. (2019), "Modeling of coefficient of contraction of differential pressure flowmeters", *Flow Measurement and Instrumentation*, Vol. 66, pp. 128-131, https://doi.org/10.1016/j.flowmeasinst.2019.02.009.

[5] Oertel H., Prandtl L., Böhle M. and Mayes K. (2004), *Prandtl's Essentials of Fluid Mechanics*, Springer, ISBN 978-0-387-40437-0.

[6] OpenCFD (2019), *OpenFOAM: The Open Source CFD Toolbox - User Guide v1906*, OpenCFD Limited. Reading UK.

eConference on Modelling Fluid Flow (CMFF'22)
The 18th International Conference on Fluid Flow Technologies
Budapest, Hungary, August 30 -September 2, 2022

TRANSIENT 3D CFD SIMULATION OF A PELTON TURBINE – A STATE-OF-THE-ART APPROACH FOR PELTON DEVELOPMENT AND OPTIMISATION

Lukas SANDMAIER[1], Helmut BENIGNI[2], Peter MEUSBURGER[3]

[1] Corresponding Author. Institute of Hydraulic Fluid Machinery, Graz University of Technology. Kopernikusgasse 24/4, 8010 Graz, Austria. Tel.: +43 316 873 8074, E-mail: lukas.sandmaier@tugraz.at
[2] Institute of Hydraulic Fluid Machinery, Graz University of Technology. E-mail: helmut.benigni@tugraz.at
[3] Institute of Hydraulic Fluid Machinery, Graz University of Technology. E-mail: peter.meusburger@tugraz.at

ABSTRACT

The complexity of the flow structure in Pelton turbines makes it challenging to gain a detailed insight into the local flow processes. However, CFD methods offer vast potential for developing and optimising Pelton turbines due to these complex flow conditions. In a comprehensive examination, a six-nozzle prototype Pelton turbine with 19 buckets has been investigated using 3D CFD simulations. First, the steady simulations of the manifold and the unsteady runner simulation have been performed with a mesh-based, commercial CFD code, whereby a two-equation turbulence model and the homogeneous two-phase model were used. Then, to limit the simulation time and the computational cost, symmetry was applied in the runner simulation, and also a sophisticated meshing strategy. Subsequently, the simulation results are analysed. The examination of the manifold provided a detailed insight into the occurrence of losses and local flow conditions, especially upstream the nozzle, which allows for a better understanding of the jet shape. Furthermore, the results of the runner simulation were analysed with special regard to the jet-bucket interaction from start to end of the impingement cycle of a particular bucket. Finally, the enhancement potential could be derived from the summary.

Keywords: Computational fluid dynamics, Hydropower, Numerical modelling, Pelton turbine

NOMENCLATURE

A	$[m^2]$	cross-section (of the jet)
B	$[mm]$	bucket width
D	$[mm]$	pitch diameter
Fr		Froud number
H	$[m]$	head
H_v	[m]	head loss
Q	$[m^3/s]$	flowrate
T	$[Nm]$	torque
T_{ref}	$[Nm]$	torque on the reference bucket
T_{th}	$[Nm]$	theoretical torque of a bucket
We		Weber number
c_{ax}	$[m/s]$	axial velocity
c_{circ}	$[m/s]$	circumferential velocity
c_{th}		theoretical velocity
d_0	$[mm]$	jet diameter
g	$[m^2/s]$	gravitational acceleration
k	$[m^2/s]$	turbulent kinetic energy
n	[rpm]	rotational speed
p_{atm}	[Pa]	atmospheric pressure
p_{ref}	[Pa]	reference pressure
p_{rel}	[Pa]	relative pressure
z		number of buckets
Δ_t	$[s]$	simulation time step
ε		turbulent eddy dissipation
η		efficiency
ρ	$[kg/m^3]$	density (of water)
σ	$[kg/s^2]$	surface tension
ω	[1/s]	angular velocity
ω		turbulent eddy frequency

Subscripts and Superscripts

inlet	inlet
n	nominal
total	total
–	arithmetic mean

1. INTRODUCTION

The application of computational fluid dynamics (CFD) has a long history in investigating, designing, and optimising hydraulic fluid machinery. This is especially true for Francis and Kaplan turbines, which can largely be transferred to a steady-state problem. Success and experience with the simulation of flow in Kaplan and Francis turbines subsequently

led to the technique and know-how also being applied to components of Pelton turbines [1].

Due to the entirely different operating principle of Pelton turbines, the transfer of know-how took place in various stages. The research started with the components that are easier to simulate, namely the distributor and the nozzle, which have a primarily single-phased flow. The flow in the distributor, including the nozzles, was investigated in a single-phase flow setup in the early days of numerical simulations in Pelton hydraulics in [2]. Conclusions were made about possible losses and disturbing influences on the formation of the jet. Downstream of the nozzles, the flow is two-phased, which had to be considered in the modelling. Muggli and Zhang [3] carried out a two-phase flow simulation of the jet formation, based on a planar numerical grid using rotational periodicity, and compared the results with experimental data. However, the situation turns out to be much more complex when investigating the Pelton runner. As of the working principle, significantly more complex flow phenomena occurred than is the case with Kaplan or Francis turbines. For example, the transient behaviour has to be considered when simulating the jet-bucket interaction and the bucket flow. In addition, high gradients of pressure, velocity and the two phases to be considered, water and air, further complicate numerical investigations. Splash water and droplets in the turbine housing cause ventilation losses due to interaction with the runner and the jets, which can hardly be tracked by the grid-based numerical simulations. In the early stage, CFD simulations of the jet-bucket interaction were carried out using the impingement of a stationary bucket, as shown in [4]. With the increasing performance of modern computers and data storage, the complexity of the numerical investigations carried out on Pelton turbines also progressed. This is increasingly evident in numerical experiments including the entire flow path of the Pelton turbine, as shown in [5].

Progress in this area enables an increasing understanding of the flow processes. It also reduces the dependence on model tests in the development process, even if these cannot be entirely dispensed. As a result, numerical simulation of Pelton turbines is no longer only used for theoretical analysis. On the contrary, it has already taken the path to a development and optimisation tool, not only for the distributor and the nozzles but also the turbine runner, as Židonis has shown in [6].

Many published studies on numerical investigations of Pelton turbines use a single-nozzle turbine model, e.g. as in [6–8]. However, suppose the aim is to investigate the overall performance of multi-nozzle Pelton turbines. In that case, it is sometimes crucial to consider all nozzles in the simulation setup. Only in this way can the bucket emptying be assessed, and possible jet interference be detected, which considerably influences the overall operating behaviour.

When using a Eulerian CFD code, the number of necessary grid cells respectively nodes may increase considerably, and so does the simulation time. This detail is especially significant when combining the number of nozzles and the number of buckets of a given turbine does not allow for symmetry effects in the circumferential direction. The Pelton turbine investigated in the present paper represents such a case, with a six-nozzle turbine and a runner with 19 buckets.

As alternative to a Eulerian CFD code, Lagrangian CFD codes, such as Smoothed Particle Hydrodynamics (SPH) or Fast Lagrangian Solver (FLS), are used to analyse Pelton turbines. An overview of the application of SPH in Pelton turbines is given in [9].

2. NUMERICAL SIMULATION

This study's numerical modelling and simulation were based on the commercial code Ansys CFX, Release 20.1. This code is widely used in hydraulic fluid machinery, as it has provided good results in the simulation of Pelton turbines in terms of accuracy. Still, it is associated with long simulation durations and correspondingly high numerical costs [10].

The numerical study of the given Pelton turbine was split into two distinct parts. In the first part, an analysis of the Pelton distributor was conducted, whereby the hydraulic losses and the jet shape were of interest. Therefore, the calculations were performed in a single- and two-phase setup.

In a second step, the behaviour of the runner was investigated. Regarding the runner simulation, the focus was laid both on the overall performance in the form of the hydraulic efficiency as well as the generated torque and the evaluation of the jet-bucket interaction. The latter was based on the pressure distribution analysis on the runner surface and the flow situation between jet and bucket. Unlike in various publications [11–13], the numerical investigation did not cover a series of different operating points regarding a variation of the head H or the flowrate Q. In this case, rather a numerically stable and most efficient procedure for the simulation of Pelton turbine runners should be developed. This procedure should enable the modelling of a wide range of turbines, regardless of the number of nozzles or buckets, and finally, it should allow for a numerically based, relative performance comparison of different runner geometries based on an identical load case.

2.1. Prototype Turbine Model

The study was based on the geometric model of a vertical six-nozzle turbine in prototype scale. The design of the distributor and the runner represent the result of a design optimisation process. As a result,

the final distributor geometry incorporates changes of the general layout and the design of the bifurcations compared to the baseline design, as it is shown in Figure 1. The design of the Pelton runner was slightly modified in its main dimensions throughout the study, leading to three different runner geometries. Subject to changes were e.g. the length, width, depth of the bucket. Also, minor changes were applied to specific geometric details.

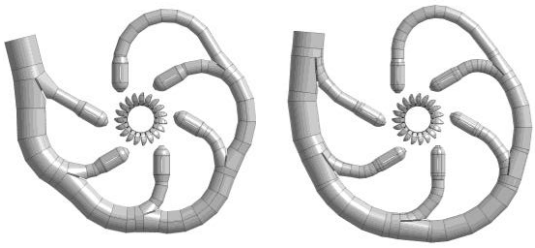

Figure 1. Tubine design, baseline (left) vs. final (right)

The nominal operating point of the turbine was given with a head H_n of 382 m and a flowrate Q_n of 5.5 m^3/s, both reached at a nozzle opening of 75%. The rotational speed n was given with 600 rpm.

Table 1. Main dimensions of the turbine

D	1310.00 mm
B	375.25 mm
d_0	115.00 mm
D/B	3.50
z	19

The critical dimensions of the turbine are provided in Table 1, whereby D indicates the pitch diameter of the runner, B the inner width of the buckets, d_0 the jet diameter and z the number of buckets. The ratio D/B gives a number, which is widely used to characterise Pelton turbines.

2.2. Numerical Modelling of the Distributor

The modelling of turbulence in the steady-state simulations of the distributor was realised with the k-ω SST model with automatic wall function.

The high-resolution scheme in ANSYS CFX was used to model the advection terms. In addition, relaxation factors for gradient dependent advection terms were set to enhance numerical stability.

For modelling of the two-phase flow, there are two reasonable options, the inhomogeneous model and the homogeneous model. The first mentioned uses a set of conservation equations for each fluid with specific terms, which model the coupling of the different phases [14]. The higher complexity of this model with its higher number of equations results in a better performance compared to the homogeneous model [15]. On the other hand, the complexity causes an increased computational effort to solve the equations. The homogeneous model assumes that both fluids share the same flow field. Therefore, only one set of conservation equations needs to be solved with an additional equation, which determines the concentration of each fluid in the gird cells. Thus, a less demanding numerical scheme is necessary than with the inhomogeneous model. However, the homogeneous model was preferred over the more accurate inhomogeneous model due to higher numerical costs. The selected model also provided a good trade-off between the duration of the simulations and the numerical stability.

Surface tension σ and gravity were not considered in the modelling since the flow in Pelton turbines is determined by high Froude numbers Fr and Weber numbers We. Hence, influence of both is considerably weak on the flow in the distributor and the jet [5].

The timestep Δ_t was set to $5 \cdot 10^{-5}\,s$, which provided a good balance between convergence speed and numerical stability. Additionally, double precision was selected to enhance the stability further.

The geometric model of the distributor was extended by two components. A cylinder of the length of five times the inlet diameter was added to the inlet of the distributor. Furthermore, another component was added at the outlets of the nozzles. These volumes correspond to the space in which the jets are formed. Only minor geometric simplifications were made to simplify the numerical modelling.

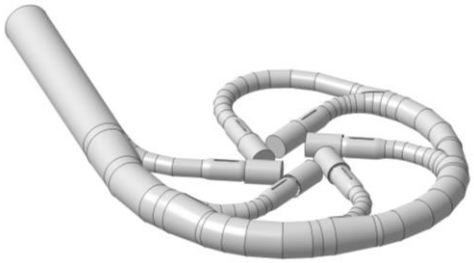

Figure 2. Geometry of the distributor simulation domain

The geometry shown in Fig. 2 represents the basis for the spacial discretisation. The final mesh was composed of several blocks of structured and unstructured meshes. Components including rather complex geometry elements, e.g. bifurcations, were meshed with tetrahedral and pyramidal elements. The same mesh topology was used for the leading and the trailing edge of the support ribs in the nozzles and the area of the needle tip. The other elements of the geometry were discretised with structured meshes containing primarily prismatic and hexagonal elements. Along all solid walls, thin layers of prismatic elements were placed.

Fig. 3 shows the mesh of the distributor model. In regions of particular interest or with high gradients in relevant flow variables, such as the nozzle exit and the area where the phase boundary of the jet was to be expected, the grid was refined (see Fig. 4). Between the mesh components of the distributor and the nozzles general interfaces were placed. The remaining connections between structured and unstructured mesh topologies had a direct mesh connection.

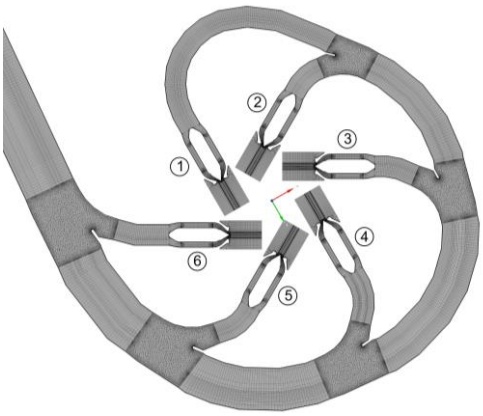

Figure 3. Distributor mesh in the symmetry plane

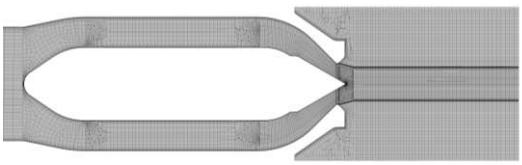

Figure 4. Mesh of the nozzle and jet area

The mesh of the entire simulation domain had about 8.67 million nodes and 14.57 million elements in total. Additional mesh characteristics are summarised in Table 2.

Table 2. Distributor mesh quality characteristics

	min.	max.	ave.
Min. Face Angle	11.3°	90.0°	57.8°
Max. Face Angle	60.0°	157.3°	97.2°
Aspect Ratio	1	351	24.1
Y Plus	-	-	41.1

Regarding the boundary conditions, all solid walls of the model were treated as smooth, no-slip walls, without any specific surface roughness defined. The boundary surfaces of the jet domains were modelled as opening boundaries with the relative pressure p_{rel} set to zero, while the reference pressure p_{ref} is equal to the atmospheric pressure p_{atm}. At the inlet a total pressure $p_{\mathrm{tot,inlet}}$ was imposed, which corresponds to the given hydraulic head of the turbine.

In order to accelerate the simulation and to increase the numerical stability results of single-phase simulations of the distributor were used to initialise the flow field. At the start of the simulation, the jet domains were fully filled with air.

2.3. Numerical Modelling of the Runner

In recent publications [10] the *k-ω* SST model was used for turbulence modelling in Pelton runner simulations. Perrig showed in his thesis [15], that the *k-ω* SST model outperforms the *k-ε* model in terms of accuracy. Similar behaviour was summarised in [16]. However, due to significantly, less stable numerical behaviour in runner simulations compared to the distributor simulations, the *k-ε* turbulence model was applied for the runner simulations. The lack of accuracy of the chosen model is seen as a minor problem, since the overall degree of model simplifications is relatively high. Moreover, a relative comparison of different runner geometries, based on identical numerical settings, was not impaired by this.

In analogy to the distributor simulation the high resolution scheme was used to model the advection terms. The same relaxation factors as in the study of the distributor were applied. The Second Order Backward Euler scheme was selected for the time discretisation of the transient terms.

Analogous to the numerical modelling of the distributor, the homogenous model was used to model the two-phase flow in the runner. Concerning surface tension and gravity, the same assumption as in the numerical setup of the distributor were made.

The definition of the transient time step Δ_t is linked to a discrete angle of runner rotation. The size of the angle-step has been proven as crucial for some factors. A small step provides more stability to the numerical scheme, which leads also to a faster convergence behaviour and a lower overall computation time. Both effects have been observed in several simulations. Moreover, the size of the timestep influences the simulation results concerning the torque. The best simulation behaviour was found with a timestep Δ_t of approximately $4.63 \cdot 10^{-5}$ s, which corresponds to one sixth of a degree runner rotation. In the solver settings double precision was selected to further increase the numerical stability of the simulation.

The runner simulation was based on the geometric model given in Fig. 5. The simulation domain is composed of three main components: the runner, the casing and the nozzles. The former is defined as the rotating domain while the casing and the nozzles remain stationary. The runner is further split into two subdomains, which are indicated by different shadings in Fig. 5. Subsequently, these subdomains serve differently in the analysis of the runner performance. The medium grey shaded runner component is later used to analyse the performance, while the dark grey component represents some sort of a dummy.

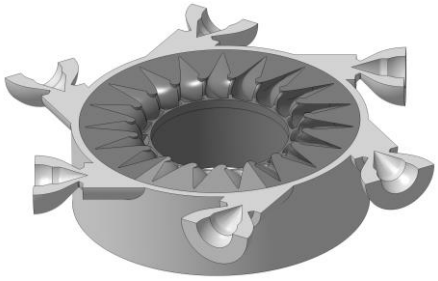

Figure 5. Geometric model of the runner simulation domains

To simplify the model, the distributor as well as the real turbine housing were not considered for the simulation. Moreover, the symmetric layout of Pelton turbines was utalised to further reduce the compexity of the geometric model. This is a common strategy, which is seen in various publications, e.g. [8, 11, 14]. A non-idealised jet configuration was used. Thus, the last section of the nozzle, the nozzlehead, was included in the model to account for the effects of the fluid acceleration and the friction in the spear valve on the jet formation. The nozzle opening was set to 75%, what corresponds to the opening in the nominal operation point of the prototype turbine.

The numerical mesh of the geometry in Fig. 5 is composed of components with structured and unstructured meshes (see Fig. 6). The nozzles and the casing are represented by a structured mesh of prismatic elements. The two subdomains of the runner, with its complex geometry were split into two blocks. The first block contains the buckets and was therefore meshed with an unstructured, tetrahedral mesh. The second block of prismatic mesh elements adds up with the first one to complete the rotating runner subdomain. In areas with strictly aligned flow, such as in the nozzle and jet area, the mesh cells are primarily oriented according to the main flow direction. Grid refinements were placed in strategic areas, as shown for the distributor mesh. Near the walls of the runner as well as the nozzle layers of prismatic elements were placed.

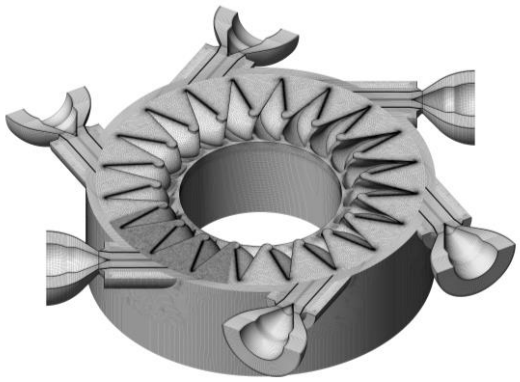

Figure 6. Numerical mesh of casing and nozzles

The subdomains of the runner were meshed with two different approaches. The one, which incorporates only three consecutive buckets (medium grey shading in Fig. 5), was meshed with a comparably high mesh density. The mesh of the other runner subdomain is rather coarse. This approach allows to use the entire symmetric runner half to be taken into account and yet limits the size of the numerical grid to a manageable number of nodes and elements. For both subdomains, refinements were placed along the leading edge, the trailing edge as well as the cutout edge and its adjoining surfaces. A detailed view of the refined mesh of the buckets is given in Fig. 7.

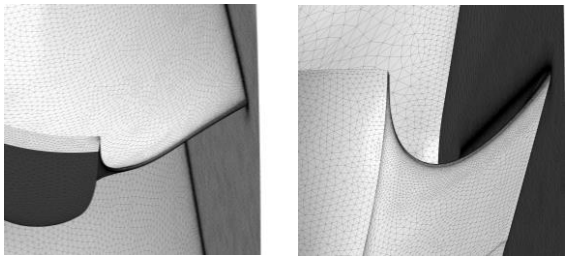

Figure 7. Detail view of the mesh refinements in the cutout region of the bucket

The statistics of the mesh components of the runner simulation are given in Table 3. Quality characteristics of the runner simulation mesh are given in Table 4.

Table 3. Mesh statistics of the casing and the runner subdomains (in millions)

	Nodes	Elements
Nozzle, Casing	2.604	2.352
Runner fine	4.530	17.101
Runner coarse	5.597	16.511
Total	12.732	35.965

Table 4. Runner mesh quality characteristics

	min.	max.	ave.
Min. Face Angle	10.4°	90.0°	47.9°
Max. Face Angle	60.0°	153.2°	92.5°
Aspect Ratio	1	226	6.3
Y Plus	-	-	53.1

Regarding the boundary conditions, the solid walls of the nozzle and the runner were treated in the same way as those of the distributor, which were modelled as no-slip walls, without any surface roughness defended. A symmetry condition was applied to the symmetry plane of the turbine model. The remaining boundary surfaces were treated with an opening boundary condition since the turbine housing was not considered. The relative pressure p_{rel} is set to zero, while the reference pressure p_{ref} was defined with the atmospheric pressure p_{atm}.

Each nozzle has an inlet surface, which is perpendicular to the corresponding nozzle axis. On these a mass flow rate Q_{inlet} normal to the boundary was imposed. The link between the sliding meshes of the rotating runner and the stationary casing was treated with a transient rotor stator interface.

At the start of the first simulation a result of a distributor simulation with corresponding nozzle opening was used to initialise the stationary domain. The rotating domain was fully filled with air at the start of a simulation run. Subsequent simulations were then initialised with results of previous transient turbine simulations.

3. RESULTS

3.1 Results of the Distributor Analysis

The simulation of various Pelton distributor geometries in this study showed, that the applied changes to the geometry have led to a reduction of the hydraulic loss in the distributor and improved the flow situation upstream the nozzles. The latter is important for a good jet quality, which is indicated by a circular cross section and a homogeneous velocity profile of the jet.

A direct correlation between the jet shape and quantitative flow characteristics is difficult to determine. To overcome this, a swirl number SN was introduced in order to quantify the intensity of secondary flow. The definition of the SN is given in Eq. (1) whereby c_{circ} and c_{ax} are the velocities in circumferential and the axial direction respectively on a given plane of the cross section A.

$$SN = \frac{1}{A} \cdot \int_A \sqrt{\frac{c_{\text{circ}}^2}{c_{\text{ax}}^2}} \cdot \mathrm{d}A \qquad (1)$$

For each nozzle the velocities are referred to the corresponding nozzle axis (positive in jet direction). In the optimisation process of the distributor design, the SN was later used as an additional indicator for an improvement or a deterioration of the jet shape. If the SN decreases, an improvement of the jet shape can be expected, as smaller values indicate a lower intensity of the secondary flows, which primarily act negatively on the jet shape.

Fig. 8 shows the cross section of jet number 4 on a plane about 4.25 jet diameters downstream the nozzle outlet, which was the jet with the most disturbed jet shape of all. The jet velocity, which is related to the theoretical velocity c_{th}, is plotted on the cross sections in a range of 0.75 to 1. The boundary of the cross section is determined by a water volume fraction of 50%. c_{th} is given in Eq. (2).

$$c_{\text{th}} = \sqrt{2 \cdot g \cdot H_{\text{n}}} \qquad (2)$$

The left plot corresponds to the baseline geometry of the distributor, the right plot to the new design. The swirl numbers, which are evaluated at the nozzle inlet, are 0.12 and 0.036 respectively, which is equivalent to a reduction of about 70%.

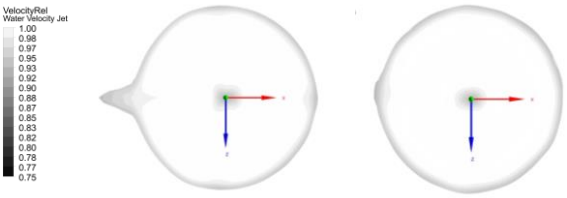

Figure 8. Jet corsssection, baseline (left) vs. new design (right)

The hydraulic losses H_v in the distributor are determined as a hydraulic head loss from the inlet to the outlet of the corresponding nozzles. H_v is given in Eq. 3 whereby $\bar{p}_{tot,Inlet}$ and $\bar{p}_{tot,Nozzle}$ represent mass flow averaged total pressure values at the inlet and a plane, which was placed 30 mm upstream the corresponding nozzle mouthpiece.

$$H_v = \frac{\bar{p}_{tot,inlet} - \bar{p}_{tot,nozzle}}{\rho \cdot g} \qquad (3)$$

These were lowered by roughly 16% compared to the baseline design. A comparison of the head losses, which are related to the nominal head H_n, are given in Fig. 9. The largest share of the losses was caused by the nozzle, while the distributor contributed less than 20% to the head loss.

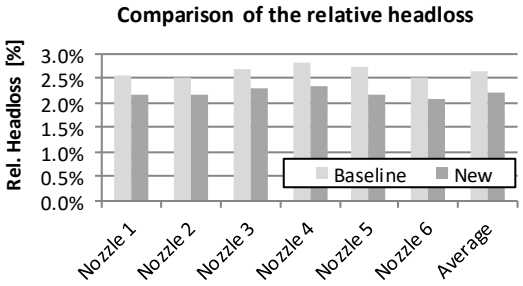

Figure 9. Comparison of the relative headloss

3.2 Results of the Runner Simulation

The results of the three runner simulations, based on different runner geometries, are analysed with a special procedure. For the analysis of the turbine performance in general, a reference bucket was defined. The reference bucket corresponds to the second bucket of the light grey shaded and comparably fine meshed runner domain in Fig. 5. Additionally, to the refence bucket, the leading and the successive bucket are considered to analyse possible, negative interactions on the runner outside surface.

To calculate the runner torque, a "bucket load cycle" was defined. One load cycle corresponds to what a single bucket experiences during 360 timesteps or 60 ° of runner rotation, since the angular spacing between the nozzles in the case of the present six-nozzle turbine equals 60 °. In this period every bucket is once impinged by a jet. The arithmetic average of the torque $\bar{T}_{\mathrm{ref}}$ over 360 timesteps or 60 ° of runner rotation, which is acting on the reference bucket, was finally used to calculate the runner torque. Additionally, $\bar{T}_{\mathrm{ref}}$ was used as an indicator for the state of convergence of the simulation. A constant level of $\bar{T}_{\mathrm{ref}}$ indicates a steady-state operation as well as a sufficiently converged solution. The total torque T of the entire turbine runner corresponds to Eq. (4).

$$T = 2 \cdot \bar{T}_{\mathrm{ref}} \cdot z \tag{4}$$

The efficiency η is calculated from $\bar{T}_{\mathrm{ref}}$ and the corresponding hydraulic head H at the inlets as well as the total imposed flowrate Q at the inlets. The efficiency is given in Eq. (5), whereby ω represents the angular velocity of the turbine, ρ the density and g the gravitational acceleration.

$$\eta = \frac{z \cdot \bar{T}_{\mathrm{ref}} \cdot \omega}{Q \cdot H \cdot \rho \cdot g} \tag{5}$$

The simulation of the baseline runner design in this study has shown an efficiency of 91.65%. The periodic curve of the generated torque, normalised by $\bar{T}_{\mathrm{th}}$ for the inside, the outside and the total torque is shown in Fig. 10. The splitting of the bucket surface into an interior and an exterior surface is depicted in the upper left-hand corner of Fig. 10. The dark grey shaded surface indicates the interior, the light grey one the exterior surface. $\bar{T}_{\mathrm{th}}$ represents a theoretical torque of a bucket based on the simulated head and the flow rate in the nominal operating point with an efficiency of 100%. $\bar{T}_{\mathrm{th}}$ is given in Eq. (6).

$$\bar{T}_{\mathrm{th}} = \frac{Q_n \cdot H \cdot g \cdot \rho}{19} \tag{6}$$

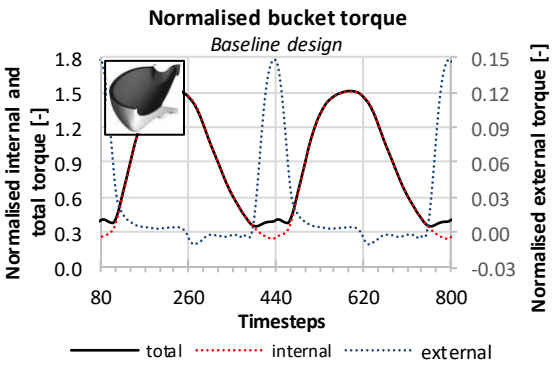

Figure 10. Normalised torque (baseline design)

The torque of the primarily impinged interior surface and the exterior bucket surface add up to the torque contribution of the reference bucket. The external curve in Fig. 10 indicates the start of the load cycle with its sharp rise after roughly 390 timesteps. A low-pressure zone on the exterior surface causes the growth of the torque in this phase (see Fig. 11, left side). Perrig reported in his thesis the existence of such an external torque and explained it with the Coanda Effect [15].

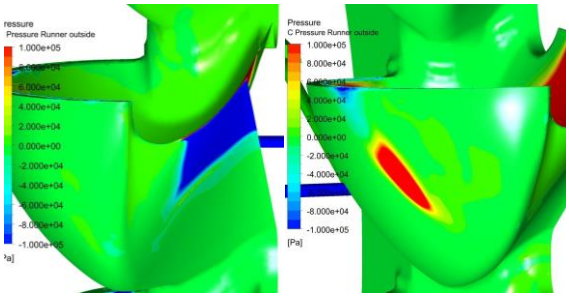

Figure 11. Pressure distribution on the runner exterior surface (baseline design)

However, due to non-appropriate trailing edge angles, the same curve shows a loss following timestep 610. The impingement of the external bucket surface is caused by water, which is exiting the leading bucket. A zone of increased pressure on the exterior surface indicates the source of the loss (see Fig. 11, right side).

The bucket or the runner geometry design was modified to overcome adverse effects in an iterative process, as seen in the baseline geometry. Changes to the bucket width, the trailing edge angles, as well as the splitter and the cutout design have improved the efficiency compared to the baseline runner design. As a result, an efficiency of 91.95% was reached.

Another set of geometry parameters of the Pelton bucket was changed consecutively in a second approach. As a result, the bucket width was slightly increased compared to the first design iteration process, and a modification of the bucket depth was realised. In addition, the positioning of the bucket on the pitch circle diameter was changed towards a smaller bucket position angle. Finally, the leading edge (splitter) and the cutout edge were further altered compared to the first design update. In the end, the numerically calculated efficiency was increased to a level of 92.30% by those measures.

Fig. 11 shows the normalised torque of the second design update. Additionally, the total torque of the baseline design and the design update 1 is overlaid (dashed, green and orange curve respectively).

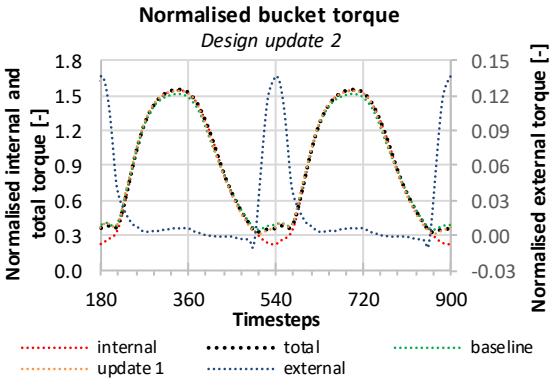

Figure 12. Normalised torque (design update 2 vs. baseline and design update 1)

In addition to the change of the bucket position angle, the increase of the bucket width and the bucket depth significantly contributed to a remarkable rise in the magnitude of the internal torque compared to the baseline and a small rise compared to the design update 1. On the other hand, the magnitude of the external torque in its maximum decreased compared to the baseline, which is most likely due to the changed bucket position. However, the external torque load cycle average is still higher because of the modified trailing edge angles.

5. CONCLUSION

While the simulation of the Pelton distributor for optimisation is quite common these days, the numerical investigation of the Pelton runner raises more questions.

As presented in this paper, the numerical approach to simulate Pelton runners, primarily of multi-nozzle turbines, should give a direction for an efficient way to analyse their hydraulic behaviour. By focusing on a single reference bucket, especially the numerical grid of the runner domain reduces to a manageable size. Furthermore, with a smaller mesh but still preserving the advantage of a high spatial discretisation in the selected regions, the computational costs and the required simulation time can be reduced significantly. Thus, numerical simulation has come one step closer to possible utilisation for the design and optimisation of Pelton runners.

Within the approach presented, three different Pelton runner designs were analysed with a consistent numerical setup, resulting in efficiencies of 91.65%, 91.95% and 92.30% for the baseline design and two design updates, respectively.

Nevertheless, the calculated efficiencies are partly subject to strong model assumptions and simplifications, such as the non-consideration of the turbine housing, the missing impact of the distributor, and the flow modelling. Therefore, it is essential to point out that the efficiencies given in this paper should not be confused with experimentally determined efficiencies.

In various publications, see e.g. [5, 6, 11], discrepancies between numerically simulated and experimentally measured efficiencies of Pelton turbines were reported. Whereby over- and underprediction have been shown, primarily depending on the numerical modelling, including mesh density, and physical modelling. Based on this knowledge, the reported efficiency enhancement of 0.65% points between the baseline design and the design update 2 is primarily regarded as an indicator for the actual improvement rather than an absolute value for the efficiency enhancement. Verification of the simulation results still has to be done based on a model test.

REFERENCES

[1] H. Keck and M. Sick, "Thirty years of numerical flow simulation in hydraulic turbomachines," *Acta Mech*, vol. 201, 1-4, pp. 211–229, 2008, doi: 10.1007/s00707-008-0060-4.

[2] M. Sick, M. Schindler, P. Drtina, C. Schärer, and H. Keck, "Numerical and experimental analysis of Pelton turbine flow," *XX IAHR Symposium, Charlotte*, 2000.

[3] F. A. Muggli, J. Zhang, C. Schärer, and L. Geppert, "Numerical and experimental analysis of Pelton turbine flow," *XX IAHR Symposium, Charlotte*, 2000.

[4] B. Zoppé, C. Pellone, T. Maitre, and P. Leroy, "Flow analysis inside a Pelton turbine bucket," *Journal of Turbomachinery*, vol. 128, no. 3, pp. 500–511, 2006, doi: 10.1115/1.2184350.

[5] C. Zeng *et al.*, "Hydraulic performance prediction of a prototype four-nozzle Pelton turbine by entire flow path simulation," *Renewable Energy*, vol. 125, pp. 270–282, 2018, doi: 10.1016/j.renene.2018.02.075.

[6] A. Židonis, "Optimisation and efficiency improvement of Pelton hydro turbine using computational fluid dynamics and Experimental Testing," PHD Thesis, Department of Engineering, Faculty of Science and Technology, Lancaster University, Lancaster, UK, 2015.

[7] A. Rossetti, G. Pavesi, G. Cavazzini, A. Santolin, and G. Ardizzon, "Influence of the bucket geometry on the Pelton performance," *Proceedings of the Institution of Mechanical Engineers, Part A: Journal of Power and Energy*, vol. 228, no. 1, pp. 33–45, 2014, doi: 10.1177/0957650913506589.

[8] A. Perrig, F. Avellan, J.-L. Kueny, M. Farhat, and E. Parkinson, "Flow in a Pelton turbine bucket: Numerical and experimental investigations," *Journal of Fluids*

Engineering, vol. 128, no. 2, pp. 350–358, 2006, doi: 10.1115/1.2170120.
[9] M. Rentschler, J. C. Marongiu, M. Neuhauser, and E. Parkinson, "Overview of SPH-ALE applications for hydraulic turbines in ANDRITZ Hydro," *J Hydrodyn*, vol. 30, no. 1, pp. 114–121, 2018, doi: 10.1007/s42241-018-0012-y.
[10] S. Bhattarai, P. Vichare, K. Dahal, A. Al Makky, and A. G. Olabi, "Novel trends in modelling techniques of Pelton Turbine bucket for increased renewable energy production," *Renewable and Sustainable Energy Reviews*, vol. 112, pp. 87–101, 2019, doi: 10.1016/j.rser.2019.05.045.
[11] D. Jošt, P. Mežnar, and A. Lipej, "Numerical prediction of Pelton turbine efficiency," *IOP Conf. Ser.: Earth Environ. Sci.*, vol. 12, p. 12080, 2010, doi: 10.1088/1755-1315/12/1/012080.
[12] Y. Xiao, Z. Wang, J. Zhang, C. Zeng, and Z. Yan, "Numerical and experimental analysis of the hydraulic performance of a prototype Pelton turbine," *Proceedings of the Institution of Mechanical Engineers, Part A: Journal of Power and Energy*, vol. 228, no. 1, pp. 46–55, 2014, doi: 10.1177/0957650913506711.
[13] C. Zeng, Y. Xiao, Z. Wang, J. Zhang, and Y. Luo, "Numerical analysis of a Pelton bucket free surface sheet flow and dynamic performance affected by operating head," *Proceedings of the Institution of Mechanical Engineers, Part A: Journal of Power and Energy*, vol. 231, no. 3, pp. 182–196, 2017, doi: 10.1177/0957650916689507.
[14] A. Santolin, G. Cavazzini, G. Ardizzon, and G. Pavesi, "Numerical investigation of the interaction between jet and bucket in a Pelton turbine," *Proceedings of the Institution of Mechanical Engineers, Part A: Journal of Power and Energy*, vol. 223, no. 6, pp. 721–728, 2009, doi: 10.1243/09576509JPE824.
[15] A. Perrig, "Hydrodynamics of the free suface flow in Pelton turbine buckets," Doctoral Thesis, EPFL, Lausanne, 2007.
[16] S. Chitrakar, B. W. Solemslie, H. P. Neopane, and O. G. Dahlhaug, "Review on numerical techniques applied in impulse hydro turbines," *Renewable Energy*, vol. 159, pp. 843–859, 2020, doi: 10.1016/j.renene.2020.06.058.

Conference on Modelling Fluid Flow (CMFF'22)
The 18th International Conference on Fluid Flow Technologies
Budapest, Hungary, August 30 -September 2, 2022

DEVELOPMENT OF A RADIAL FLOW FAN FAMILY FOR CONTAMINATED GASES OF RELATIVELY HIGH FLOW RATE

Péter Ferenczy[1], Esztella Balla[2], Tamás Benedek[2], Gábor Daku[2], Bálint Kocsis[2], Antal Kónya[1], János Vad[3]

[1] Szellőző Művek Kft. Építész utca 8-12., H-1116 Budapest, Hungary. Tel.: +36 1 204 5972. E-mail: ferenczypeter1@gmail.com
[2] Department of Fluid Mechanics, Faculty of Mechanical Engineering, Budapest University of Technology and Economics.
[3] Corresponding Author. Department of Fluid Mechanics, Faculty of Mechanical Engineering, Budapest University of Technology and Economics. Bertalan Lajos u. 4 – 6, H-1111 Budapest, Hungary. Tel.: +36 1 463 4072, E-mail: vad.janos@gpk.bme.hu

ABSTRACT

The paper outlines the development of a new radial fan family for performing relatively high flow rate for gases laden with solid impurities in technological processes. The paper presents the conceptual preliminary design of the fan family, based on theoretical considerations and empirical guidelines from the literature. The target point of fan design, representing the actual demands by customers on the fan market, was identified on the Cordier diagram. The results of preliminary design have iteratively been refined with involvement of Computational Fluid Dynamics (CFD), the details of which are discussed in the paper, with special regard to flow features being characteristic for this special fan family. The challenging design assignment of finding an aerodynamic compromise between a) the blade geometry customized to the contaminated gas and high specific flow rate, and b) a sufficiently high fan efficiency being in accordance with legislative measures, was successfully solved. A test sample fan was manufactured, and was tested via global measurements. Representative details of the measurements of the fan characteristic and efficiency curves are presented and evaluated in the paper. The potential Industry 4.0 features of the members of the new fan family, being treated as candidates of smart fans operated in smart air technical systems in smart factories, are outlined in the paper.

Keywords:

high specific flow rate, gas with solid contaminants, industrial air technology, radial fan, smart fan

NOMENCLATURE

Latin symbols

A	$[m^2]$	flow cross-section
AR	[-]	aspect ratio of rotor blading
B	$[m]$	fan rotor width (axial extension)
c	$[m/s]$	absolute velocity
D	$[m]$	fan rotor diameter
D_{ref}	$[m]$	reference diameter
N	[-]	rotor blade count
n	$[1/s]$	rotor speed
n_{ref}	$[1/s]$	reference speed
P	$[W]$	useful aerodynamic performance
P_M	$[W]$	shaft input power
Δp_t	$[Pa]$	total pressure rise
q_v	$[m^3/s]$	volume flow rate
u	$[m/s]$	circumferential velocity
u_t	$[m/s]$	rotor tip circumferential velocity
v_{ref}	$[m/s]$	reference velocity
t	$[C°]$	gas temperature

Greek symbols

δ	[-]	diameter factor
η	[-]	fan total efficiency
ρ	$[kg/m^3]$	gas density
σ	[-]	speed factor
Φ	[-]	flow coefficient
Ψ	[-]	total pressure coefficient

Subscripts and superscripts

*	blade-passage-averaged data
1	rotor inlet
2	rotor outlet
A	axial flow fan
D	design point
IS	isentropic (ideal, inviscid)
max	maximum
R	radial flow fan
t	rotor blade tip
u	tangential component

1. INTRODUCTION AND OBJECTIVES

The layout of fans is basically customized to demands being specific to the particular industrial applications. Fans applied in industrial air technology and ventilation often serve for fulfilling tasks for which the fluid being transported contains particles of solid contaminants, e.g. dust [1]. The particle-laden flow is usually associated with increased pressure loss in the elements of the air technical system connected to the fan. Furthermore, the system usually incorporates a dust separation equipment, e.g. [2], representing a relatively high pressure loss. In order to cover the demand of relatively high fan pressure rise winning over the aforementioned sources of pronounced pressure drop, the usual type of fan applied for particle-laden gas flows is a *radial flow fan*, e.g. [3].

If the introduction of the solid particles into the fan cannot be avoided for technological reasons, the particles represent a risk of abrasion and deposit formation on the rotor blades and on their surroundings, such as the front and back walls of the rotor. Such risk potentially leads to rotor imbalance as well as deterioration of fan performance and life cycle. As a first-hand guideline for minimizing such unfavourable effects, the flow deflection inside the fan rotor is to be limited. By such means, the inclination of the particles to leave the curved flow paths and to attach on the solid surfaces can be moderated. Radial fan rotors with backward-leaned blades tends to exhibit a moderate flow deflection in comparison to forward-leaned blades. Therefore, *radial fans with rotors of backward-leaned blades*, e.g. [4], tend to be the most widespread in transportation of dusty gas flows, forming the focus of the present paper.

In order to further improve the resistance of the fan against dust load, it is to be emphasized that it is mainly the rotor blades that are exposed to strong effects of abrasion and deposition. Therefore, an appropriate design of rotor blade layout provides a potential for improvement of dust resistance. One principal option to keep mostly away the granular material from the blade surfaces can be carried out by intentional realization of flow separation zones in the vicinity of the blades. A classic example for such layout is when straight, radially aligned blades, e.g. [5-7], are applied in transportation of dusty gas, exhibiting massive flow separation regions within the blade passages. However, flow separation is detrimental from the perspective of the energy efficiency of the fan. Attention is to be drawn to the fact that nowadays' industrial fans are to correspond to the minimum efficiency requirements established in the 327/2011/EU Fan Regulation [8]. Considering only rotors with backward-leaned blades from this point onwards, one possibility for moderating the dust-sensitivity of the blades is to moderate their camber, i.e. to moderate their concavity. By such means, the inclination of the dust to be deposited over the concave blade sections tends to be reduced. Straight, i.e. uncambered backward-leaned blades, e.g. [6], provide a sort of "self-cleaning" geometry, i.e. the developing deposit layer can migrate along the blade chord, and can thus be evacuated from time to time out of the blade passages. However, applying straight blades, instead of curved blades [4, 9-10] of advanced aerodynamic design, tends to be associated with separation of the blade boundary layer, thus deteriorating the efficiency.

Szellőző Művek Kft., termed from this point onwards as Company in the paper, has been engaged in developing a new radial fan family for handling dusty gases with an increased resistance against dust load. This operational requirement has been coupled with demands and orders by industrial customers prescribing a relatively high volume flow rate, as will be illustrated with quantitative data taken from industrial examples. As detailed in the next section, the demand of increased specific flow rate tends to result in preliminary blade design in an increase of the relative outlet width of the rotor, B_2/D_2. Furthermore, in order to adapt the rotor inlet geometry to the increased specific flow rate, a moderation of rotor outer-to-inner diameter ratio D_2/D_1 is to be carried out in preliminary design, resulting in a moderation of the relative blade height $(D_2-D_1)/D_2$ as well. The aforementioned trends suggest that the *aspect ratio* of rotor blading, $AR = [(D_2-D_1)/2]/B_2$ tends to be remarkably reduced. Such moderated AR represents that the outward flow deflection and pressure rise within the rotor, associated with adverse streamwise pressure gradients, is to be realized within a confined space, thus increasing the risk of flow separation over both the front wall of the rotor and along the rotor blades. In order to act against adverse pressure gradients in fluids engineering equipments, e.g. [11], and thus, controlling boundary layer separation for loss reduction, easily adaptable passive flow control techniques, e.g. [12-13], are beneficial.

In order to simultaneously fulfil the aforementioned demands by the industrial customers, being so far uncovered by commercially available products of the Company, the paper presents the outline of developing a new fan family. The new fan product family, termed as LDL fan family, has been developed by the Company in collaboration with the Department of Fluid Mechanics (DFM), Faculty of Mechanical Engineering, Budapest University of Technology and Economics. The multilevel, iterative product development process incorporated preliminary design considerations, Computational Fluid Dynamics (CFD), and prototype testing via global measurements at the premises of the firm. The paper is structured in accordance with these methodological steps. The following work phases were carried out by DFM: preliminary design; design refinements incorporating the evaluation of CFD

results; participation in the experimental tests; evaluation of measurement results.

In lack of any allowances of going into details of long-term and costly basic research, the presented project was dedicated to a robust, cost-effective, and time-effective fulfilment of prescribed practical demands, thus having a new and competitive fan family made available on the market in a relatively short timespan. In this view, the development process demonstrates a *new combination* of *already known*, well-established *methods* in fan design and analysis. From scientific point of view, the objectives of the product development process outlined herein are as follows. These objectives represent the fluids engineering challenges and engineering compromises in simultaneous fulfilment of the following demands, being often contradictory to each other.

- Development of fan rotor blade geometry with backward-leaned, straight plate blades, for increased resistance against dust load, as required by the industrial customers.
- Development of a fan family with increased specific flow rate, i.e. increased design flow coefficient Φ_D, enabling a relatively high volume flow rate even at moderate rotor outlet diameter D_2 and/or rotor speed n, according to the specific industrial demands. By means of limiting D_2, the increase of Φ_D serves for a moderation of space demand and weight of the fan. Furthermore, the limitation of D_2 and/or n results in a reduction of rotor tip circumferential velocity u_t. This is beneficial from the viewpoint of moderating rotordynamic load, and gives also a potential for fan noise reduction, as suggested e.g. by the guideline [14].
- In accordance with the demand of increased Φ_D, development of an aerodynamically effective rotor blade geometry with relatively low *AR*.
- An increased risk of flow separation is foreseen over the blades as well as on the rotor front wall, due to the straight plate blading and relatively low *AR*. Despite such negative tendencies, a reasonably high total efficiency η is to be achieved, in order to guarantee the energy-efficient operation of the fan, and to fulfil the legislative demand manifested in the Fan Regulation [8].
- In solving the contradictory demands outlined above, the *a priori* available passive flow control technology, offered by the unavoidably developing incoming gas jet between the suction cone and the rotor inlet, is to be systematically and purposefully exploited.

The product development process outlined herein resulted in the LDL fan family that has been made available yet on the market. The public technical data presented in the paper are restricted for confidentiality reasons.

2. INDUSTRIAL DEMANDS, AND PRELIMINARY DESIGN CONSIDERATIONS

In what follows, preliminary design considerations are outlined for the radial fan blade layout performing a relatively high volume flow rate, i.e.. high specific flow rate, manifested in a relatively high Φ_D value. For this purpose, axial and radial flow rotors are compared to each other in this section, in a general and comprehensive manner, pointing to the substantial operational differences between the two rotor types. Then, the concept of the radial flow rotor is further developed for obtaining an increased specific flow rate.

As shown in **Figure 1**, comparable axial and radial flow rotors are considered. They are comparable in terms of having identical rotor tip diameters D_t and being driven at identical speed n. Therefore, the rotor tip circumferential velocity u_t is identical. Furthermore, the absorbed power, i.e. the mechanical power input P_M to the rotor shaft, is also taken to be equal. The approximation of identical total efficiencies $\eta = P/P_M$ implies the equality of the useful aerodynamic performance $P = \Delta p_t \cdot q_V$. Representative points in the flow field at rotor inlet (1) and outlet (2) are indicated with cross-symbols in the figure.

For the present comparison, swirl-free inlet to the rotors is assumed. The Euler equation for turbomachines [5, 13, 15-16] reads that the isentropic total pressure rise through the rotor is $\Delta p_{t\,IS} = \rho \cdot u_2 \cdot c_{u2}$. Taking blade-passage-averaged data at the rotor outlet, indicated below with superscript *, Fig. 1 illustrates that the rotor outlet mean circumferential velocity is higher for the radial flow rotor than that for the axial rotor: $u_{2R}^* > u_{2A}^*$; since $u_{2R}^* \equiv u_t$, but $u_{2A}^* < u_t$, taken as an intermediate value between the hub and tip radii of the annulus for the axial rotor. Furthermore, the radial flow rotor blading is capable for performing an increased flow deflection in tangential direction in comparison to the axial flow blading, since the trailing edges of its blades are more inclined toward the circumferential direction (i.e. the trailing edges make a smaller angle with the $\underline{u}$ vector). Considering blade-passage-averaged data again, this yields $c_{u2R}^* > c_{u2A}^*$. Based on the above discussed two inequalities, the Euler equation reads $\Delta p_{t\,IS\,R} > \Delta p_{t\,IS\,A}$. Taking the approximation of equal hydraulic efficiencies for the two rotors, expressing the ratio of $\Delta p_t / \Delta p_{t\,IS}$, the above discussion reflects that *the radial flow rotor tends to perform a higher total pressure rise than the comparable axial rotor:* $\Delta p_{t\,R} > \Delta p_{t\,A}$.

Considering identical useful aerodynamic performances $P = \Delta p_t \cdot q_V$, the condition $\Delta p_{t\,R} > \Delta p_{t\,A}$ implies $q_{V\,R} < q_{V\,A}$, i.e. *the radial flow rotor tends to perform a lower flow rate than the comparable axial rotor*. As Fig. 1 suggests, the particular rotor geometries are adapted to such diverse flow rate-generating capabilities. The entire annulus cross-

section of the axial fan is available for flowing through the blade passages at both inlet and outlet. Contrarily, the inlet cross-section A_{1R} of the radial fan is limited by D_1., and, by such means, $A_{1R} < A_{1A}$. In order to moderate the flow velocity for moderation of the fluid mechanics loss, such limitation of the inlet cross-section is associated with a moderation of the flow rate as well. The outlet cross-section of the radial rotor, determined by the B_2 as well as by the fixed D_2 values, accommodates the design flow rate, in order to ensure an appropriately limited outlet velocity for loss moderation.

The trends discussed above, expressed in the form of equalities and inequalities, are summarized in **Table 1.**

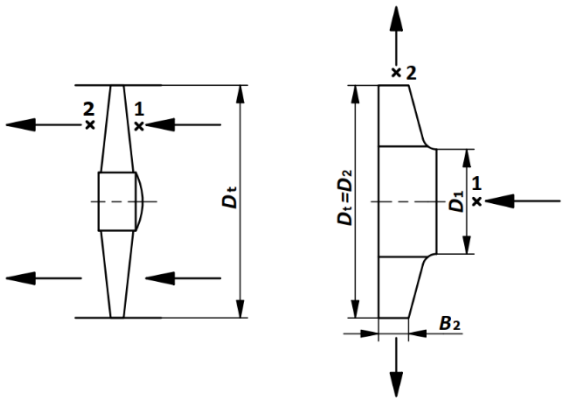

Figure 1. A sketch on comparable axial and radial flow rotors

Table 1. Trends for the comparable axial and radial flow rotors

Axial		**Radial**
D_{2A}	=	D_{2R}
n_A	=	n_R
P_A	=	P_R
u_{2A}*	<	u_{2R}*
c_{u2A}*	<	c_{u2R}*
$\Delta p_{t\,A}$	<	$\Delta p_{t\,R}$
A_{1A}	>	A_{1R}
$q_{v\,A}$	>	$q_{v\,R}$

Table 2. Representative data of market demand survey

q_v [m^3/h]	Δp_t [Pa]	t [$C°$]
$7{,}0\cdot10^3$	400	80
$1{,}0\cdot10^4$	500	35
$2{,}9\cdot10^4$	1000	50
$7{,}5\cdot10^4$	1000	60
$1{,}0\cdot10^5$	1000	170
$1{,}2\cdot10^5$	1600	20
$1{,}5\cdot10^5$	1000	50

As detailed later in this section, the demand by the industrial customers necessitated the increase of the Φ_D value for the radial fan. In order to increase the flow rate delivered by the comparable radial rotor, B_2 is to be increased for increasing the rotor outlet cross-section. This means that the relative outlet width of the rotor B_2/D_2 is to be increased in design. Furthermore, in order to adapt the rotor inlet cross-section to the increased flow rate, D_1 is to be increased, causing a moderation of the relative blade height $(D_2\text{-}D_1)/D_2$. Therefore, for an increased Φ_D, the rotor blades become smaller in height and larger in width, i.e. $AR = [(D_2\text{-}D_1)/2]/B_2$ tends to be reduced. The reduction of AR poses the following challenges: a) The outward flow deflection from the axial inlet toward the radial outlet is to be carried out within an axially extended but radially confined space, thus increasing the risk of boundary layer separation over the rotor front wall. b) Flow turning realized by the rotor blades in tangential direction is to be carried out along radially confined blades, increasing the risk of boundary layer separation along the blades. A purposeful and careful fan design, described in the paper, is to treat the aforementioned challenges.

Table 2 gives an overview of examples for operational data out of a market demand survey, representing demands by potential customers towards the Company. These demands were uncovered by already existing fans of the Company, thus initiating the development of the new fan family presented herein. Therefore, the new fan family aims at extending the operational ranges coverable by the products manufactured by the Company, with a reasonable overlap with the ranges covered by the already existing machines. The datasets are arranged in the sequence of increasing flow rate. They span over more orders of magnitude of flow rate, suggesting the relevance of developing an entire new fan family. Based on the table, a design target was to extend the available product range by a fan family performing up to the order of magnitude of $q_v = 1{,}5\cdot10^5\ m^3/h$, whereas keeping the total pressure rise within the range of Δp_t = 1000-6000 Pa. Further desirable targets were the following. a) Reduced noise and vibration by possibly moderating the rotor tip speed, by means of setting the specific flow rate to an appropriately large Φ_D value. b) Increased resistance against gases laden by dusty or fibrous solid components. To this end, the rotor was instructed by the Company to be designed with backward-leaned straight, i.e. uncambered, plate blades. c) Meeting the efficiency criteria set in the Fan Regulation [8]. Realizing a fairly high efficiency is a design challenge especially in the case of the aforementioned straight rotor blades, in the view that the risk of flow separation is *a priori* increased in the low-AR blades as discussed above. Based on the formulae in [8], a minimum efficiency target of 64 % to 68 % is dictated in the electric input power range

of 10 k*W* to 500 k*W*. Exceeding this efficiency range, achieving at least 70 % maximum efficiency was set as design target, i.e. $\eta_{max} \geq 0{,}70$.

The data in Table 2 enable a classic preliminary design approach [5, 15-16] on the basis of the well-known diameter factor δ and speed factor σ, being in direct relationship with design values of flow coefficient Φ and total pressure coefficient Ψ.

With consideration of gas content as well as pressure and temperature data in Table 2, representative values of ρ can be obtained. Considering each Δp_t data in Table 2 as a fictitious dynamic pressure related to a fictitious reference velocity v_{ref}, such reference velocity can be calculated for each case in Table 2. Considering each qv data in Table 2 as volume flow rate of a fictitious pipe flow at a velocity of v_{ref} through a fictitious circular pipe cross-section $D_{ref}^2 \cdot \pi/4$, the fictitious reference diameter D_{ref} can be calculated for each case. A reference speed n_{ref} can also be obtained for each case, viewing v_{ref} as a fictitious circumferential velocity of solid body rotation at n_{ref} at a fictitious radius of $D_{ref}/2$, i.e. $v_{ref} = D_{ref} \cdot \pi \cdot n_{ref}$.

The ratio between the true rotor outlet diameter and the reference diameter is the diameter factor δ. The ratio between the true rotor speed and the reference speed is the speed factor σ.

$$\delta = D_2 / D_{ref} \quad (1)$$

$$\sigma = n / n_{ref} \quad (2)$$

Once relevant empirical data are obtained for δ and σ, the D_2 and n characteristics being necessary for realizing the operational data in Table 2 can therefore be calculated for each case of specific market demand. The Cordier diagram [5, 15, 17] presents empirical [δ, σ] data couples for fans realizing reasonably high efficiency. According to the long-term experiences gathered at DFM in industrial fan design, the following approximate ranges and correlations are valid for δ and σ for high-efficiency radial fans with backward-leaned blades:

$$2 \leq \delta \leq 4 \quad (3)$$

$$\sigma = 1 / \delta \quad (4)$$

A direct relationship exists between the [δ, σ] and [Φ, Ψ] data couples enabling high-efficiency operation. Considering the definitions of the flow and total pressure coefficients,

$$\Phi = q\text{v} / [(D_2^2 \cdot \pi/4) \cdot u_t] \quad (5)$$

$$\Psi = \Delta p_t / (\rho \cdot u_t^2/2) \quad (6)$$

and substituting $u_t = D_2 \cdot \pi \cdot n$, the following relationships can be obtained [5, 15]:

$$\delta = \Psi^{0,25} \cdot \Phi^{-0,5} \quad (7)$$

$$\sigma = \Phi^{0,5} \cdot \Psi^{-0,75} \quad (8)$$

By taking Eqs. (3) to (8) into account, the following approximate ranges and values of dimensionless operational coefficients are characteristic for high-efficiency radial fans with backward-leaned blades: $\Phi = 0{,}06 \ldots 0{,}25$; $\Psi = 1{,}0$.

Intermediate calculations were carried out for the cases in Table 2, in order to establish preliminary design values of [δ, σ] as well as [Φ, Ψ] for the new fan family. During these calculations, the following requirement were taken into consideration. a) The obtained D_2 values are to fit to the Rénard series of usual rotor diameters [18-19]. b) The necessary rotor speed n is to be realizable by usually available means, i.e. either by direct drive using an asynchronous electric motor, or by using a direct-driven asynchronous motor equipped with a frequency converter, or by using a V-belt indirect drive. Such intermediate calculations resulted in the following compromise in the preliminary design phase: $\delta_D = 2{,}36$; $\sigma_D = 0{,}42$; $\Phi_D = 0{,}18$; $\Psi_D = 1{,}0$. **Figure 2** illustrates the Cordier diagram, e.g. [5, 7, 15, 17], and position of the design [δ, σ] data couple of the new fan family in the diagram. Representative zones for various types of turbomachines – not necessarily covering the entire range of validity in the figure – are indicated with grey regions. As the diagram reflects, the new fan family is characterised by relatively small δ_D as well as by relatively large σ_D values. It is located at the boundary of the radial fan range, forming a sort of transition towards the group of mixed-flow fans, usually characterized by higher Φ_D and lower Ψ_D than radial machines. Indeed, the diameter factor $\delta_D = 2{,}36$ is in the vicinity of the lower threshold of the usual radial fan range of $2 \leq \delta \leq 4$, corresponding to a relatively high flow coefficient $\Phi_D = 0{,}18$ within the usual range of $\Phi = 0{,}06 \ldots 0{,}25$; thus corresponding to the industrial demand of increased specific flow rate, as discussed previously in the paper.

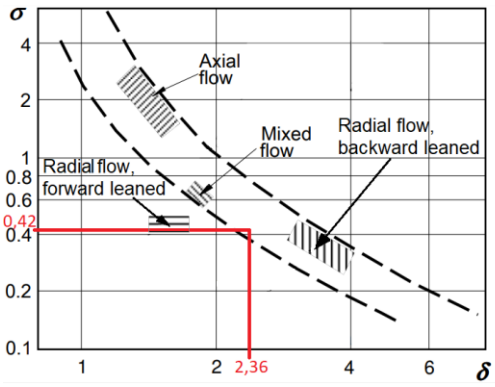

Figure 2. Cordier diagram, reproduced from [7], indicating the design point of the new fan family

3. FAN DESIGN AND DEVELOPMENT

The preliminary design of each component of the new fan family – i.e. suction and pressure ducts, inlet cone, rotor with front and back walls enclosing the blades, and scroll casing – was carried out in line with the recommendations originating from the classic literature [5, 15-16], considering the basic fluid mechanics principles and turbomachinery laws documented in references [13, 20]. The design guidelines and drawings of the already existing LDH fan family of the Company, proven to be successful on the market, were taken as a reference and starting point. Examples for the literature-based preliminary design guidelines are as follows – considering that publication of quantitative data is restricted, due to confidentiality reasons.

N = 12 rotor blades have been designed, in accordance with the guidelines formulated by Bommes in [15]. Although such blade count appears to be relatively high for rotors with backward-leaned blades, the relatively high blade solidity associated with the high blade count tends to exhibit the advantage of moderating the flow separation within the blade passages; thus improving the efficiency.

In the rotating frame of reference of the rotor, the angle of rotor-inlet flow with respect to the circumferential direction has been determined with consideration of the displacement effect caused by the blades. Relative to this inflow direction, the inlet metal angle of the rotor blades was increased by empirical means for improving the dust-resistance of the blading, following the recommendation in Reference [15] after Bommes.

According to the guidelines for designing high-efficiency radial fans in [5, 15], the diameter ratio D_2/D_1 was set between 1,3 and 2; taking into account that higher design flow coefficient Φ_D tends to reduce the diameter ratio, as was qualitatively explained in Sections 1 and 2.

The blade outlet metal angle – relative to the circumferential direction – and the chord length of the blades, being results of the prescribed inlet metal angle and the D_2/D_1 ratio for the backward-leaned straight blades, have been in accordance with the recommendations by Bommes and Eck [5, 15].

In order to assess the appropriateness of the preliminarily designed fan geometry, and to realize sensitivity studies on setting the geometrical parameters, CFD computations were carried out. The simulations were elaborated in ANSYS Fluent® software environment, using the frozen rotor model, e.g. [3-4], in order to rationalize the cost of CFD, in terms of both computational time and utilization of computational capacity, for the multiple CFD runs applied. The applicability of the frozen rotor approach has been confirmed via making a comparison with a moving-mesh model in a representative scenario. A fair agreement has been experienced between the results obtained using the frozen rotor model and the moving-mesh model.

The effect of turbulent phenomena was taken into account using the SST k-ω model, commonly used in the simulation of rotating machines, e.g. [3, 7]. The accuracy of this turbulence model is increased by improving the spatial resolution of the boundary layer along the walls. Therefore, special care was taken in keeping the first near-wall cells sufficiently small over the critical solid surfaces, such as the rotor blades, the rotor front wall, and the rotor back wall. Hexahedron elements were used for the mesh, enabling a fair spatial resolution using a relatively low number of cells. Nearly 15 million cells were used in the overall model, judged to be adequate, as grid dependence studies revealed. The CFD models were validated to global measurement data on the commercially available LDH fan family, for which the applied CFD methodology has been adopted in representative validation scenarios.

In what follows, a few representative CFD scenarios and results are discussed qualitatively in exemplary case studies. The geometries presented in the CFD results represent intermediate phases of the development, i.e. they differ from the finalized geometry, due to confidentiality reasons.

Applying uncambered, i.e. straight rotor blades, as well as having a reduced AR for the rotor blading, represent simultaneous challenges from the design perspective of moderating flow separation within the rotor, in order to achieve a reasonably high efficiency, conf. [8]. Therefore, the primary goal of the CFD campaign was to identify separated flow regions, and to elaborate remedial strategies against them. The effect of straight blades is discussed first. The originally blunt leading and trailing edges of the plate (sheet metal) blades were appropriately profiled, as a compulsory practice in moderation of separation from the blades. In accordance with the literature, e.g. [5], the CFD studies confirmed the development of separation zones on the suction side of the blades, due to the straight blade geometry. The blockage effect due to these flow separation zones causes a non-uniform, jet-like rotor exit flow, resulting in the increase of rotor exit loss, approximated as loss of a Borda-Carnot type sudden expansion [11, 13] from the jet-like rotor exit flow cross-sections to the scroll casing. The CFD runs justified that increasing the blade solidity caused a suppression of the interblade flow separation, and thus led to efficiency improvement, predominantly by reducing the Borda-Carnot type loss. By such means, the appropriateness of the preliminarily set blade count of N = 12 has been confirmed. Reducing the blade count relative to this design value would result in a deterioration of the efficiency, as CFD sensitivity studies pointed out. In addition to choosing the adequate blade count, a suitable fine-adjustment of the blade angle was carried out. On this basis, flow separation from the blade surfaces has significantly been reduced. **Figure 3** shows an example for the radial velocity distribution within the

rotor, for a representative intermediate development phase of the fan. The CFD example is related to D_t = 1,60 *m*; n = 950 1/*min*; u_t = 79,6 *m*/*s*; design flow rate. In the figure, zones of negative radial velocity are indicators of reverse flow within the regions of flow separation. One of such reverse flow zones is labelled in the figure for illustration. As the figure suggests, flow separation from the blades is an *inevitable* consequence of applying straight blades; however, the CFD-aided careful design process resulted in a significant suppression of such separation.

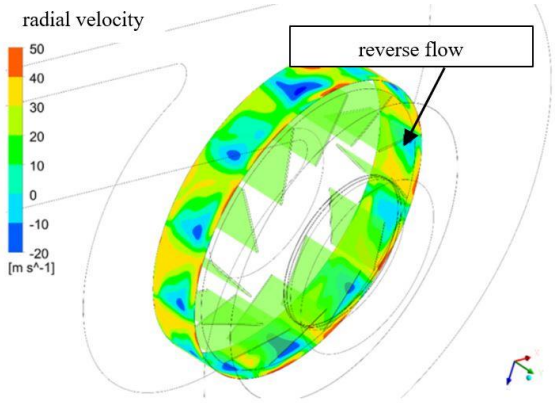

Figure 3. CFD representation of radial velocity within the rotor: an example.

During preliminary design, the geometry of the suction cone, as well as the geometry of the front wall of the rotor was prescribed following the guidelines in the literature [5, 15-16]. The preliminary design incorporated selection and harmonization of rounding radii applied to the suction cone and to the rotor inlet section. Even by setting such suction cone and front wall geometry, considered as favourable by empirical means, the CFD analyses revealed a separation zone over the conical front wall of the rotor, due to the relatively low blade *AR*, corresponding to a drastic outward flow deflection within the front region of the rotor. A high-loss zone was also recognized during the CFD campaign in the zone close downstream of the fitting between the suction cone and the rotor, for certan geometrical varieties. Another consequence of increased rotor width is the non-uniformity of velocity inlet to the blading, as indicated by the CFD studies. As remedial strategy against all of the aforementioned adverse effects, the concept of passive boundar layer control was selected, utilizing the *a priori* and inevitably occurring leakage flow between the suction cone and the rotor front wall. Such leakage flow develops from the high-pressure zone of rotor outlet toward the gap between the suction cone and the rotor front wall, within the scroll casing, and therefore, is primarily the adverse manifestation of volumetric loss. However, such leakage flow, appearing in the form of a concentrated high-momentum jet incoming at the periphery of the rotor inlet, may be exploited for energizing the boundary layer, thus moderating the extension of flow separation, and promoting flow reattachment [13]. The efficiency-increasing benefit of such boundary layer control may significantly dominate over the efficiency-reducing effect of volumetric loss.

According to the above, the geometry and size of the gap between the suction cone and the front wall of the rotor was treated with special care. In preliminary design of the gap geometry, the empirical correlations available in the literature [5] between the available maximum fan efficiency and the gap-to-D_2 size ratio were considered. After preliminary design, the geometrical arrangement and size of the gap were refined via CFD-aided campaigns. **Figures 4 and 5** provide two CFD examples for tested intermediate geometries of gap layouts during the development process. The conditions of investigation are as written for Fig. 3. Fig. 4 is an example in which the suction cone outlet and the rotor inlet are coaxial cylindrical surfaces, and a radial gap is set in between them. The figure indicates a boundary layer separation zone over the introductory section of the divergent part of the rotor front wall. Such separation zone extends also into the blading. The above suggest that the incoming leakage flow was unable to significantly contributing to remediating such separation phenomenon. Fig. 5 presents another example for the CFD-aided gap design, in an intermediate development phase. Here, the rotor suction cone represents a convergent-divergent cross-section, and the gap between the suction cone and the rotor front wall has been shifted to the outlet of the divergent section of the suction cone, fitting to the nearly conical front wall of the rotor. In this case, the incoming sloped leakage flow tends to eliminate fully the flow separation over the suction cone; the separating region is confined to the front part of the rotor blading.

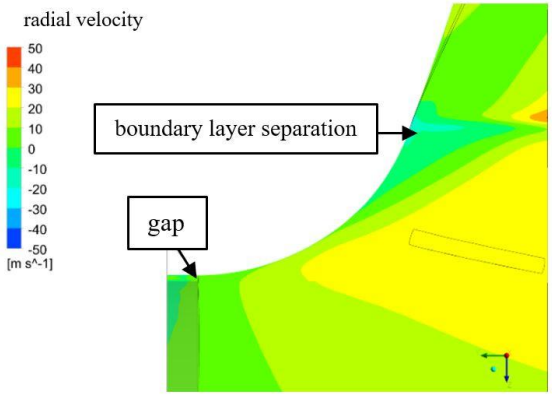

Figure 4. An example for a CFD test on a radial gap between the suction cone and the rotor front wall. Part of the meridional section. Radial velocity distribution.

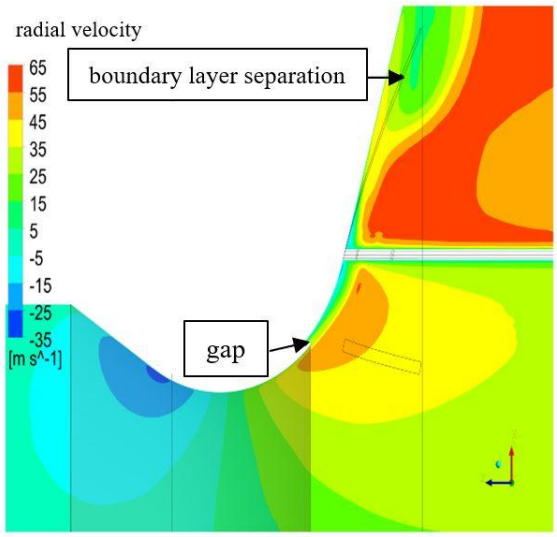

Figure 5. An example for a CFD test on a modified inlet and gap geometry. Part of the meridional section. Radial velocity distribution.

The CFD-aided design of the gap was a challenge in realizing a compromise between the following trends. a) The gap is to be reasonably small for enabling a sufficiently high volumetric efficiency. b) The gap is not be too small, in order to avoid the necessity for excessive strictness of manufacturing tolerances, and to guarantee an easy assembly process. c) The gap is to be sufficiently large, and the geometrical arrangement of the gap (i.e. gap direction) is to be chosen adequately, in order to maintain an appropriate incoming leakage flow for refreshing the boundary layer. Determining a suitable gap size and geometry, and finalizing the rounding radii applied to the suction cone and to the rotor inlet section, were subject to CFD campaigns. The edges of the suction cone and the rotor inlet, made of sheet metal, were also treated appropriately, in order to further moderate flow separation.

4. MANUFACTURING AND TESTING OF A REPRESENTATIVE FAN

Based on the design process outlined above, a representative test sample of the new LDL fan family was manufactured. The test sample, corresponding to the fan of type identifier of LDL-k63, has the following characteristics: D_2 = 630 *mm*, nominal rotor speed n = 1470 1/*min*, direct-driven by an 11 k*W* 4-pole asynchronous electric motor. The photograph of the fan is shown in **Figure 6**.

The aim of manufacturing the test fan was to experimentally justify the success of the design process, to examine the aerodynamic characteristics of the fan via global measurements, and, on this basis, to establish an initial empirical basis for characteristic and efficiency curves to be incorporated in the commercial documentation of the new fan family. For the global measurements, a test facility was realized at the premises of the Company, with consideration of the guidelines documented in standard [21]. The test rig selected by the Company is a type "C" [21] ducted-inlet, free-outlet configuration. In accordance with [8], such facility is primarily assigned to determining the static pressure rise as well as static efficiency. In addition, with knowledge of the gas density, volume flow rate, and cross-section of the pressure-side port of the fan, the outlet dynamic pressure can be approximated, and thus, estimation can be given to the total pressure rise Δp_t and total efficiency η , as presented in this paper. The flow rate was measured in the inlet duct using a throughflow orifice plate, with consideration of standards [22-23]. The following relative errors were estimated conservatively as representative mean values over the actual measurement ranges for the quantities playing role in the experiments. These errors meet the instructions for the maximum allowable uncertainties in [21]. Barometric pressure: ± 0,2 %. Absolute temperatures: ± 0,2 %. Electric input power to the driving motor: ± 2,0 %. Static pressure upstream of the orifice plate, relative to atmospheric; pressure difference on the orifice plate; depression upstream of the fan, relative to the atmospheric pressure: max. ± 0,2 %. Pressure rise: ± 0,4 %. Volume flow rate: ± 1,5 %. Rotor speed: ± 0,2 %. Carrying out an error propagation analysis with consideration of the guidelines in [21-23], taking the „root-mean-square" propagation concept for the relative errors into account (examples e.g. in [21-22]), the following absolute uncertainties have been estimated for the dimensionless global characteristics presented in the paper. These absolute uncertainties are valid at 95 % confidence level for the operational range of $\Phi = 0{,}1 \ldots 0{,}18$ fulfilling the design criterion of $\eta \geq 0.70$. Absolute errors: for Φ: ± 0,003; for Ψ: ± 0,01; for η: ± 0,03.

Figure 6. Photograph of the LDL test fan

Figures 7 and 8 present the measurement-based dimensionless characteristic and efficiency curves. In the figures, 4th order polinomials have been fitted to the data points, by means of the least-squares method.

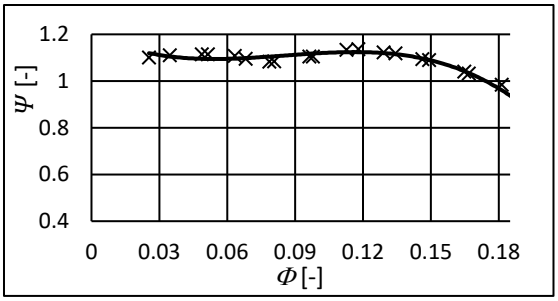

Figure 7. Measurement-based dimensionless $\Psi(\Phi)$ characteristic curve

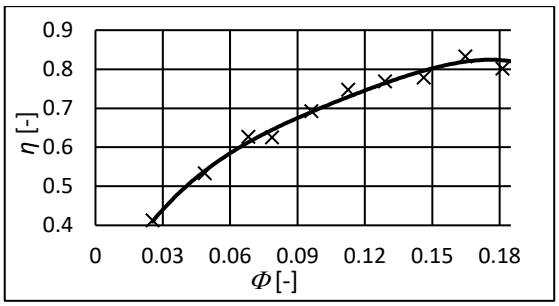

Figure 8. Measurement-based dimensionless $\eta(\Phi)$ efficiency curve

The curves presented in this paper indicate an upper limit of the measurements at $\Phi = 0{,}18$. Such limitation is predominantly due to the throttling effect of the orifice plate, in absence of a booster fan. Since an especial interest is to apply these fans at increased specific flow rates, the measurement methodology was necessary to be extended toward higher Φ values, as will be discussed in a future paper. The characteristic and efficiency curves justify the appropriateness of the design method, from the following perspectives. At the design flow rate of $\Phi_D = 0{,}18$, the fan fairly well realizes the designed total pressure rise of $\Psi_D = 1{,}0$. The maximum of the efficiency curve is related to the design point at $\Phi_D = 0{,}18$, indicating that the design process was successful also in terms of energy efficiency, i.e. the design point is also regarded as the best efficiency point. The obtained maximum efficiency is significantly higher than the set minimum design target of $\eta_{max} \geq 0{,}70$. The operational range of $0.12 \leq \Phi \leq 0.18$ exhibits Ψ values continuously decreasing with Φ, ensuring stable operation. In this range, the efficiency values are fairly above $\eta = 0{,}70$, thus guaranteeing energy-efficient operation, and meeting the Fan Regulation [8] with a reassuring safety reserve.

Standard [24] specifies tolerance grades, to be guaranteed by the fan manufacturer for its products, with regard to assigned nominal values of the volume flow rate, pressure rise, efficiency, and absorbed power. **Table 3** gives an overview of the tolerance grades, according to [24]. The tolerance is negative for the efficiency, and is positive for the absorbed power; meaning that an efficiency deterioration and power input increase is accepted – provided that the fan also meets the tolerances specified for the volume flow rate and pressure rise. If sheet material is applied in fan manufacturing, with surface protection, the standard *a priori* assigns the expectable tolerance grade of AN4 to the products. In the case of sheet material with special surface protection enabling increased geometrical accuracy – e.g. hot dip galvanizing –, the tolerance grade AN3 is also achievable [24]. Since the Company manufactures its fans from sheet metal parts, the tolerance grade AN4 is routine, or the stricter tolerance grade AN3 may also be ambitioned in the case of the new LDL fan family. This fits also to the fact that the standard [24] assigns the tolerance grades AN4 and AN3 to e.g. industrial fans operated in process engineering under harsh (abrasive or corrosive) circumstances.

If the measurements carried out on the test sample fan are to be used for generation of the commercial documentation of the LDL fan family, using the fan scaling laws [5, 15-16], the following considerations are to be made when determining the reportable tolerance grades. a) Measurement errors, as reported above. b) Reynolds number effects, affecting the accuracy of scaling laws. c) Manufacturing tolerances. Considering the reported measurement errors, the Reynolds number effects, and the manufacturing tolerances being usual in the practice of the Company, the AN4 tolerance grade is feasible as routine for the LDL family. For special requirements, necessitating more strict manufacturing tolerances, the AN3 grade is also achievable, upon demand by the customer. It is noted herein that the strategy of the Company is striving to satisfy the customers' needs by allowing for only positive tolerances for the volume flow rate and pressure, i.e. overestimating the nominal duty point in an optimistic approach, within the specified ranges in the tolerance grade under consideration.

Table 3. Tolerance grades and tolerance boundaries, in accordance with standard [24]

Quantity	Tolerance grade			
	AN1	AN2	AN3	AN4
Flow rate	±1 %	±2,5 %	±5 %	±10%
Pressure rise	±1 %	±2,5 %	±5 %	±10%
Efficiency	-1%	-2%	-5%	-12%
Power	+2%	+3%	+8%	+16%

In future applications of the fans manufactured by the Company, the Industry 4.0 perspectives may gather an increased importance, in the view that smart factories may incorporate smart industrial air technology and smart ventilation. Such systems are

to be served by smart fans. Among others, as described in [25], the smart features of a fan incorporate smart condition monitoring, self-diagnostics and intelligent maintenance against contamination and erosion, e.g. via vibration and acoustics measurements. As outlined in [25], members of the new LDL fan family can be regarded as candidates for implementing such smart features, being in accordance with the vision by the Company. The importance of smart condition monitoring for the LDL family, coupled with smart operation and maintenance, is emphasized by the fact that the solid contaminants may cause erosion or deposit on the fan components, and such negative effects can be monitored e.g. via on-line vibration diagnostics.

5. SUMMARY

Szellőző Művek Kft., in collaboration with the Department of Fluid Mechanics, Faculty of Mechanical Engineering, Budapest University of Technology and Economics, have developed a new radial flow fan family for increased specific flow rate for transporting gases laden with solid contaminants. The new fan family, labelled as LDL fans, is equipped with backward-leaned straight plate blades, for increased resistance against blade erosion or deposit formation. The relatively large specific flow rate prescribed in the design process necessitated the development of a rotor with moderate outlet-to-inlet diameter ratio, and moderate aspect ratio. The preliminary design of the fan family was carried out on the basis of literature recommendations. The design challenges posed by the simultaneous risk of separation zones over the blade suction sides and over the front wall of the rotor necessitated the application of CFD-aided careful iterative refinement of the fan geometry, in order to moderate the separation regions. As a remedial strategy against flow separation, a passive flow control method was elaborated by purposefully exploiting the incoming leakage flow in the gap between the suction cone and the rotor inlet for energizing the boundary layers in the critical flow regions. A test sample was manufactured and tested via global measurements. The experiments revealed the appropriateness of the design method, in terms of achieving the target design point, and enabling a fairly high efficiency, being in accordance with the Fan Regulation [8]. Experimental testing, together with manufacturing considerations, enables the accordance of the new LDL fan family to the AN4 or even AN3 tolerance grades [24]. Corresponding to the vision by the Company, the new fan family is a potential candidate for adapting smart fan features, e.g. intelligent condition monitoring and maintenance, against blade erosion or contaminant deposit, in line with the Industry 4.0 perspective [25]. Thanks to the relatively simple – but purposefully designed – geometry, the LDL fans can be manufactured in a relatively cost-effective and quick manner. This fact, together with the fairly good aerodynamic properties, and resistance against solid contaminants, increases the competitiveness of the fan family on the market.

ACKNOWLEDGEMENTS

The authors acknowledge the support by the following organizations and projects. Hungarian National Research, Development and Innovation Centre, under contract No. NKFI K 129023. VEKOP-2.1.7-15-2016-00647 project, supported by the Hungarian Ministry of Finance. The National Talent Programme of the Ministry of Human Capacites, Hungary (NFTO-21-B-0279). The role of Fluid-Lab.Hu Kft. is acknowledged in delivering the CFD data.

REFERENCES

[1] Thakur, P., 2019, *Advanced mine ventilation – Respirable coal dust, combustible gas and mine fire control.* Woodhead Publishing, Duxford, United Kingdom.

[2] U.S. Chemical Safety and Hazard Investigation Board, 2015, US Ink/Sun Chemical Corporation: Ink dust explosion and flash fires in East Rutherford, New Jersey. *Case Study* No. 2013-01-I-NJ. 40 p.

[3] Ghenaiet, A., 2021, Study of particle dynamics and erosion in a centrifugal fan. *Proc. 14th European Conference on Turbomachinery Fluid Dynamics & Thermodynamics ETC14*, April 12-16, 2021; Gdansk, Poland (virtual conference). Paper ID: ETC2021-495. 12 p.

[4] Aldi, N., Casari, N., Pinelli, M., Suman, A., Vulpio, A., Saccenti, P., Beretta, R., Fortini, A., Merlin, M., 2019, Erosion behavior on a large-sized centrifugal fan. *Proc. 13th European Conference on Turbomachinery Fluid Dynamics & Thermodynamics ETC13*, April 8-12, 2019; Lausanne, Switzerland. Paper ID: ETC2019-389. 13 p.

[5] Gruber J. and co-authors, 1978, *Ventilátorok* (*Fans*)(in Hungarian). Műszaki Könyvkiadó, Budapest, Hungary.

[6] The RSES HVACR Training Authority, 2009, Fans and blowers Part I. *Service Application Manual*, SAM Chapter 630-132, Section 11B. 11 p.

[7] Vad, J., Horváth, Cs., Kovács, J. G., 2014, Aerodynamic and aero-acoustic improvement of electric motor cooling equipment. *Proc. Institution of Mechanical Engineers – Part A: Journal of Power and Energy*, **228** (3), pp. 300-316.

[8] *Commission Regulation (EU) No 327/2011* of 30 March 2011 implementing Directive

2009/125/EC of the European Parliament and of the Council with regard to ecodesign requirements for fans driven by motors with an electric input power between 125 *W* and 500 k*W*. Official Journal of the European Union, pp. L90/8-L90/21.

[9] Biedermann, T. M., Moutamassik, Y., Kameier, F., 2022, Assessment of the impeller/volute relationship of centrifugal fans from an aerodynamic and aeroacoustic perspective. *ASME Paper* GT2022-79389.

[10] Vulpio, A., Oliani, S., Suman, A., Zanin, N., Saccenti, P., 2022, A mechanistic model for the predictive maintenance of heavy-duty centrifugal fans operating with dust-laden flows. *ASME Paper* GT2022-82862.

[11] Lukács, E., Vad, J., 2021, Flow topology and loss analysis of a square-to-square sudden expansion relevant to HVAC systems: A case study. *Journal of Building Engineering*, **41**, Paper: 102802, 13 p.

[12] Lukács, E., Vad, J., 2022, A passive loss reduction method of square-to-square sudden expansions. *Energy & Buildings*, **266**, Paper: 112113, 13 p.

[13] Lajos, T., 2015, *Az Áramlástan alapjai* (*Fundamentals of Fluid Mechanics*)(in Hungarian), Vareg Hungary Kft., Budapest, Hungary.

[14] VDI Richtlinien, 1990, *Guideline* VDI 3731 – Blatt 2, Emissionskennwerte technischer Schallquellen, Ventilatoren.

[15] Carolus, T., 2003, *Ventilatoren*, Teubner Verlag, Wiesbaden, Germany.

[16] Osborne, W. C., 1966, *Fans*. Pergamon Press, London, UK.

[17] Wang, J., 2021, Design for high efficiency of low-pressure axial fans: use of blade sweep and vortex distribution. *Ph.D. Thesis*, University of Twente, The Netherlands.

[18] Daly, B. B., 1992, *Woods Practical Guide to Fan Engineering*. Fläkt Woods Ltd. Sixth impression.

[19] Cory, W. T. W., 2005, *Fans & Ventilation – A practical guide*. Elsevier, New York, US.

[20] Fűzy, O., 1991, *Áramlástechnikai gépek és rendszerek* (*Fluid machinery and flow systems*)(in Hungarian). Tankönyvkiadó, Budapest, Hungary.

[21] *International Standard* ISO 5801:2017. Fans - Performance testing using standardized airways.

[22] *International Standard* ISO 5167-1:2003. Measurement of fluid flow by means of pressure differential devices inserted in circular cross-section conduits running full – Part 1: General principles and requirements.

[23] *International Standard* ISO 5167-2:2003. Measurement of fluid flow by means of pressure differential devices inserted in circular cross-section conduits running full – Part 2: Orifice plates.

[24] *International Standard* ISO 13348:2007. Industrial fans – Tolerances, methods of conversion and technical data presentation..

[25] Tóth, D., Vad, J., 2022, Industry 4.0 perspectives of axial and radial fans in smart industrial ventilation: conceptual case studies. *Proc. Conference on Modelling Fluid Flow (CMFF'22)*, 30 August to 02 September 2022, Budapest, Hungary. Paper No.: CMFF22-040.

Conference on Modelling Fluid Flow (CMFF'22)
The 18th International Conference on Fluid Flow Technologies
Budapest, Hungary, August 30 -September 2, 2022

NUMERICAL STUDY ON THE SOLID-LIQUID RESIDENCE TIME DISTRIBUTION IN A COUNTER-CURRENT SCREW EXTRACTOR

Annemarie LEHR[1], Gábor JANIGA[2], Andreas SEIDEL-MORGENSTERN[3], Dominique THÉVENIN[4]

[1] Department of Fluid Mechanics and Technical Flows, Faculty of Process and Systems Engineering, Otto von Guericke University Magdeburg, Universitätsplatz 2, 39106 Magdeburg, Tel.: +493916758109, E-mail: annemarie.lehr@ovgu.de
[2] Department of Fluid Mechanics and Technical Flows, Faculty of Process and Systems Engineering, Otto von Guericke University Magdeburg, E-mail: janiga@ovgu.de
[3] Max Planck Institute for Dynamics of Complex Technical Systems, E-mail: seidel-morgenstern@mpi-magdeburg.mpg.de
[4] Department of Fluid Mechanics and Technical Flows, Faculty of Process and Systems Engineering, Otto von Guericke University Magdeburg, E-mail: thevenin@ovgu.de

ABSTRACT

The efficiency of extraction processes highly depends on the contact times and areas between the solvent and the valuable substance. In this study a solid-liquid screw extraction process of artemisinin from *Artemisia Annua* leaves has been investigated in a continuously working counter-current screw extractor with computational fluid dynamics (CFD). Artemisinin is increasingly used as efficient anti-malaria drug. Experimental data have been used for validation.

Mass transfer processes have been first neglected to decrease the complexity of the three-phase flow simulation. The soaked leaves have been represented by a rotating geometry with constant volume equal to the experimentally observed volume of the leaves. This enabled a simplified model by solving only a two-phase flow of liquid solvent and air. A Eulerian-based Volume of Fluid (VoF) model has been implemented to capture the free surface.

After four screw rotations a quasi-steady counter-current flow has been reached. Contact times have been observed by measuring the solvent residence time distribution (RTD) using the species transport method. A very good agreement between CFD and experiments could be found. Consequently, the contact area between leaves and solvent can be determined accurately by CFD, providing important information regarding the mass transfer behaviour during the extraction process.

Keywords: computational fluid dynamics (CFD), extraction, residence time distribution

NOMENCLATURE

D_o	[m]	outer screw diameter
D_i	[m]	inner screw diameter
L	[m]	length
N	[-]	theoretical number of steps
V	[m^3]	volume
$\dot{m}$	[kg/s]	mass flow
n	[rpm]	screw rotation rate
s	[-]	storage factor
t	[min]	time
w	[m]	width
π	[-]	pi
ρ	[kg/m^3]	density
σ	[min]	standard deviation
σ^2	[min^2]	variance
τ	[min]	residence time

Subscripts and Superscripts

API	active pharmaceutical ingredients
CFD	computational fluid dynamics
CFL	convective courant number
CM	compartment model
E, R	extract, raffinate
EC	extraction cake
Exp	experimental
L, S	leaves, solvent
PD	perforated disc
SL	soaked leaves
RTD	residence time distribution
VoF	Volume of Fluid
t	total
x, y, z	axial (along the extractor), transversal, spanwise (coordinate)
–	temporal mean

1. INTRODUCTION

Gaining natural products by implementing solid-liquid extraction is used since centuries to obtain ingredients for perfumes or pharmaceutically active oils and waxes. Extracts of plant material contain lead compounds for nutraceutical or pharmaceutical applications. Nevertheless, the content of active ingredient in the feed material (e.g., leaves, flowers, branches) is usually only between 0.3 – 3 % [1]. This leads to an increasing interest in optimising the extraction efficiency of active ingredients.

In this work a continuous counter-current extraction process in a horizontal screw extractor has been implemented to obtain the active pharmaceutical ingredient (API) artemisinin from *Artemisia Annua* leaves. Derivatives of artemisinin (e.g., artesunate) are well known as standard treatment against malaria, which is still the most deadly infectious disease worldwide [2,3].

The continuous counter-current process implemented here provides advantages compared to the generally used batch extraction. Fresh solvent and feed material are continuously fed into the device without dead times while loading or unloading the apparatus. The counter-current flow enables high contacting times and surfaces leading to higher extraction yields compared to batch processes.

The modular screw design allows high flexibility but leads also to challenges, in particular regarding the optimal screw configuration for specific process requirements [4]. In order to reduce experimental efforts Computational Fluid Dynamics (CFD) can be used for a fast optimisation since screw geometry and rotating speed, diameter and length of the extruder can be adapted easily in CFD. Nevertheless, the numerical complexity of the described extraction process with a gas, a liquid and a solid phase is very high. A transient 3D model is required [5].

The performance of continuous counter-current solid-liquid extraction processes is rarely published [6]. A representation with CFD simulations could not be found by the authors. More generally, solid-liquid extraction processes have been represented by transient 3D CFD models e.g., for the investigation of hydrodynamics of a tea bag during tea infusion [7]. Turgut et al. (2020) [8] presents a solid-liquid extraction of trans-resveratrol from grape cane powder in a semi-continuous pressurized water column under steady-state conditions regarding heat and momentum transfer. A three-phase flow extraction is reported by He and Zhang (2012) [9] who used a cyclone with turbulent air flow to perform liquid extraction from solid particles. A more similar configuration to the recent work is published by Shokrian et al. (2019) [10] who described a three phase flow in a horizontal rotating drum with a screw conveyor used for olive oil extraction. They represented the olive seeds as particulate solids. A 3D CFD model is represented by Wang et al. [11] to represent a two-phase solid-liquid extraction of wax-containing brown coal in randomly packed beds and observe the particle size distribution. Further the CFD simulation of continuous two-phase protein extraction in a fluidized bed ion exchange system is reported by Dadashi et al. (2014) [12]. Several publications in the field of fluidized beds represent three-phase solid-liquid-gas flows in counter-current operation mode [13,14]. The usage of full 3D models for counter-current flows have been reported mainly for two-phase flows [15–17].

This work will introduce a model for representing a three-phase screw extraction process in counter-current mode by using a transient 3D model. To simplify this first model, mass transport processes between the phases have been neglected. For a later optimisation the contact times between liquid and solid phase are essential. They will be determined by quantifying their residence time distribution in the extractor. The species model is used in CFD since it solves only one additional transport equation, enabling short computational times. The aim is to improve our understanding of the process, ultimately increasing extraction efficiency of artemisinin.

2. MATHEMATICAL MODEL

The mean residence time and variance can be determined from the residence time distribution (RTD), which is a function of the length of the observed extruder. For measuring the RTD in a device, the stimulus response technique with pulse or stepwise input of a tracer is typically used. The tracer concentration is measured by an appropriate device at the outlet of the extruder. This leads to concentration curves named $E(t)$ and $F(t)$ curves, also known as normalised residence time distribution function and cumulative exit age distribution function, respectively. Both functions can be transformed into each other following Eq. (1) and (2) [18].

$$F(t) = \int_0^t E(t)dt \tag{1}$$

or conversely

$$E(t) = \frac{dF(t)}{dt} \tag{2}$$

The mean residence time $\bar{\tau}$ and the variance σ^2 can be derived from $E(t)$ according to Eq. (3) and (4).

$$\bar{\tau} = \int_0^\infty t \cdot E(t)dt \tag{3}$$

$$\sigma^2 = \int_0^\infty (t-\tau)^2 \cdot E(t)dt \qquad (4)$$

The standard deviation σ of the RTD curve can be derived by the square root of the variance σ^2.

For characterizing the extruder, the theoretical number of steps N is of high importance. It can be derived from the mean residence time $\bar{\tau}$ and the variance σ^2 following Eq. (5).

$$N = \left(\frac{\bar{\tau}^2}{\sigma^2}\right) \qquad (5)$$

3. EXPERIMENTAL SETUP AND VALIDATION DATA

The counter-current extraction process is performed in a screw extractor with a total length L of 0.320 m. The dried *Artemisia Annua* leaves are introduced into the extractor at the left side of the horizontal extruder and are conveyed by the screw towards a perforated disc. There, an extraction cake forms due to the increasing pressure induced by the screw rotation. This cake prevents a solvent leakage at the raffinate outlet. Consequently, the introduced solvent flows in counter-current direction to the leaves resulting in high contact times and contact surfaces between both phases. This leads to a high extraction efficiency, resulting in high amounts of the active substance artemisinin in the extract (Figure 1).

To validate the results of the numerical model and consequently its applicability, experiments have been performed. The operating conditions and procedure for reaching a continuous process are summarised here briefly in the interest of space. They will be described in a dedicated publication.

The active substance artemisinin has a low polarity and, hence, a poor solubility in water [19]. Consequently, organic solvents like hexane or toluene should be used for high extraction efficiencies since they provide high solubility values [20,21]. Considering that the performed CFD simulations neglects mass transfer processes between the phases, water has been used as solvent to simplify the experiments.

For measuring the residence time of the solvent, a 10 % concentrated sodium chloride - water solution has been implemented after reaching a quasi-steady state, which took visually 30 minutes. The conductivity of the extract has been measured every minute, repeating three times each experiment.

The extraction cake at the perforated disc does not significantly influence the extraction efficiency of the process; the substance artemisinin has already been almost completely extracted at this location.

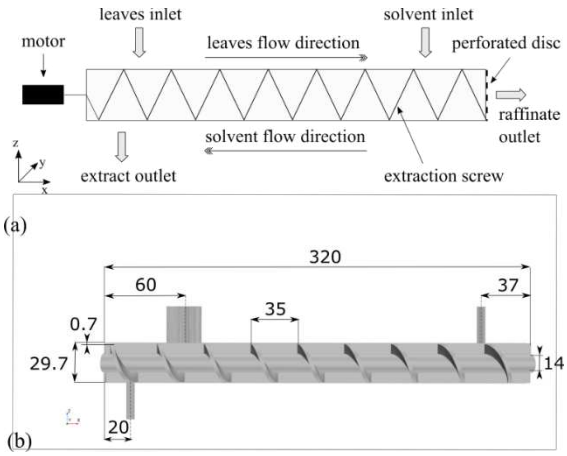

Figure 1. Counter-current screw extraction process (a) schematically and (b) with important dimensions (in mm) along a vertical cut-plane.

Nevertheless, the stability of the extraction cake is very important for reaching a quasi-steady state. Consequently, the width of the extraction cake is constant for all possible steady-state operations.

This work focusses on one continuous steady state operating point in the experimentally defined operating window. To capture possible deviations three repetitions of this operating point have been performed. The operating conditions and the averaged residence times of leaves and solvent measured in the experimental setup are listed in Table 1.

Table 1. Operating conditions and output parameters for the observed steady state.

Input		Value	Unit
mass flow			
leaves	$\dot{m}_L$	$1.05 \cdot 10^{-3}$	kg/min
solvent	$\dot{m}_S$	$2.08 \cdot 10^{-2}$	kg/min
screw rotation rate	n	2.2	rpm
Output			
residence time			
perforated disc	$\bar{\tau}_{SL,PD}$	15.45	min
extraction cake	$\bar{\tau}_{SL,EC}$	9.74	min
solvent	$\bar{\tau}_S$	4.87	min
width			
extraction cake	w_{EC}	$5 \cdot 10^{-3}$	m
density			
soaked leaves	ρ_{SL}	922	kg/m³

The averaged residence time of leaves $\bar{\tau}_{SL,PD}$ describes the final outcome at the perforated disc. Previous measurements at several sampling points inside the extruder showed that the constant axial velocity of leaves in the extruder decreases significantly at the perforated disc due to the compression process. Since the extraction cake does not play a significant role for the extraction efficiency the residence time of leaves in front of the

extraction cake $\bar{\tau}_{SL,EC}$ is of higher interest and has been used in this work for further estimations.

The dry *Artemisia Annua* leaves absorb solvent during their transport towards the perforated disc. This absorbed solvent can be called internal extract. To consider this internal extract in the mass flow balance a storage factor *s* was measured. This storage factor describes how much mass of solvent is absorbed by 1 g of dry leaves in equilibrium state. For the used solvent (water) this value has been determined as 4.34 by observing several batch mixtures until equilibrium state. The theoretical extract mass flow $\dot{m}_E$ and raffinate mass flow $\dot{m}_R$ can be calculated using Eq. (6) and (7).

$$\dot{m}_E = \dot{m}_S - (\dot{m}_L \cdot s) \tag{6}$$

$$\dot{m}_R = (\dot{m}_L + \dot{m}_S) - \dot{m}_E \tag{7}$$

The experimental observations provide important information for setting up the numerical model in order to measure the RTD and the solid-liquid contact areas.

4. NUMERICAL MODEL

The flow investigation was performed with the commercial CFD software package StarCCM+ (Simcenter STAR-CCM+ 2021.3 Build 16.06.008). The dimensions of the computational geometry correspond exactly to the experimental setup (Figure 1). According to a previously performed mesh-independence study a block-structured mesh has been generated with a total number of 1,020,570 finite-volume cells. With this resolution numerical diffusion caused by the mesh can be reduced leading to an accurate representation of the solvent flow behaviour. The screw rotation has been realised by separating the domain into a rotating and a stationary one. Since the rotation is very slow (2.2 rpm) the flow can be assumed as laminar. A Eulerian-based Volume of Fluid (VoF) model has been used to resolve sharply the gas/liquid interface. Initially this free surface is located in the *x*-*y* plane at $z = 0$ (Figure 2 (a)). To stabilize the free surface and reduce the costs for this multiphase simulation the solvent inlet has been rotated by 90° around the *x*-axis, to ensure that liquid solvent directly enters the initially implemented liquid phase. The boundary conditions resulting from the described setup and the simulation mesh are shown in Figure 2.

As the extraction cake does not play an important role for the extraction efficiency it has been neglected in this work. Consequently, the soaked leaves do not enter or exit the process in CFD. They remain at their fixed (steady-state) position and are represented by an additional rotating geometry distributed along the screw and turning with it in a solid movement. Companion experiments showed

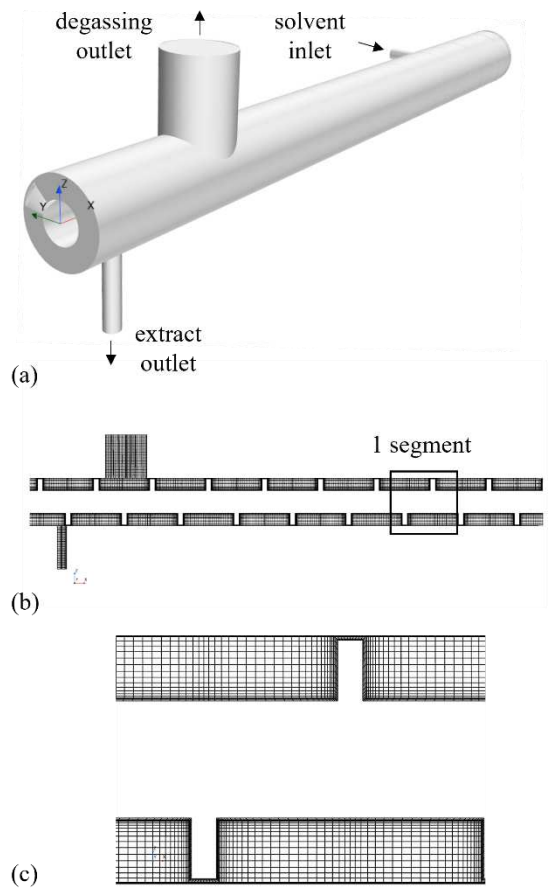

Figure 2. (a) 3D geometry for CFD simulation with boundary conditions, (b) 3D grid on a vertical plane with a block-structured mesh, (c) detailed grid for one segment showing gaps between screw and wall.

that the distribution of the soaked leaves during their transport from inlet to raffinate outlet stays nearly constant during the process at steady-state. Visually, the solid phase can be clearly separated from the solvent phase in the transparent extractor. The inlet mass flow rate of solvent has been set to the calculated extract mass flow rate according to Eq. (6), including the loss of solvent during the extraction process due to the absorption by the leaves.

A constant position of the solid-phase distribution in the extruder has been implemented. The total volume of the soaked leaves $V_{SL,t}$ in the extruder is composed of the distributed volume of soaked leaves in all segments V_{SL} and the volume of the extraction cake V_{EC}. It can be calculated according to Eqs. (8) to (10) by using the observed output parameters in Table 1 and the calculated raffinate mass flow according to Eq. (7). The inner and outer screw diameter D_i and D_o can be taken from Fig. 1 (b).

$$V_{SL,t} = V_{SL} + V_{EC} \quad (8)$$

$$V_{SL} = \frac{\dot{m}_R \cdot \bar{\tau}_{SL,EC}}{\rho_{SL}} \quad (9)$$

$$V_{EC} = \frac{\pi}{4} \cdot (D_o - D_i)^2 \cdot w_{EC} \quad (10)$$

Since the solid phase is fixed in space and rotates with the screw, a transient measurement of the solid phase RTD in CFD is not possible; consequently, only a rough theoretical assumption is proposed. According to Eq. (9) the residence time depends on the volume of soaked leaves inside the extruder. By setting the experimental and numerical solid volumes equal, the resulting residence times become also comparable since all dimensions, material properties and operating parameters are the same.

For validation procedure the experimental solvent volume has been calculated by using the solvent residence time and the extract mass flow rate (Table 1 and Eq. (6)). The solvent density ρ_S equals the liquid phase density in Table 2.

$$V_S = \frac{\dot{m}_E \cdot \bar{\tau}_S}{\rho_S} \quad (11)$$

The implementation of an adaptive time step model using a convective mean CFL number ensures the stability of the simulation and an accurate representation of the free liquid surface. Table 2 summarises the used physical models and parameters.

For analysing the residence time distribution of the solvent at the extract outlet, the species method has been used which is involved in StarCCM+ as the passive scalar model. First, the flow has been solved until reaching steady state. This is observed visually after 4 or 5 rotations of the screw. Starting from this time, each rotation delivers similar outflows of solvent and velocities. To investigate this point in more detail, both quasi-steady state conditions (obtained after 4, or 5 rotations of the screw) have been considered in the analysis. The flow field at quasi-steady state is then frozen and the tracer species has been initialised, tracking only convection processes. A constant time step of 0.1 s has been implemented for this post-processing step, allowing short calculation times. Finally, an additional transport equation is solved in the domain for the tracer species.

Table 2. Physical models and parameters.

Description	Settings
Discretization scheme: momentum	2nd order
Under-relaxation factor	
Velocity	0.4
Pressure	0.2
Discretization scheme: volume fraction	2nd order
Under-relaxation factor	
Volume fraction	0.2
Temporal discretization	1st order
Adaptive time step criteria	
Convective mean CFL number	1
Minimum time step (s)	1E-4
Maximum time step (s)	0.01
Inner iterations	10
Boundary conditions	
Solvent inlet	Mass flow inlet
Extract outlet	Split outlet
Degassing outlet	Pressure outlet
Operating pressure (Pa)	101325.0
Mass flow solvent (kg/s)	$2.71 \cdot 10^{-4}$
Gravity in vertical direction (z)	-9.81
Liquid phase (water)	
Density (kg/m³)	997.56
Viscosity (Pa·s)	$8.89 \cdot 10^{-4}$
Gas phase (air)	
Density (kg/m³)	1.18
Viscosity (Pa·s)	$1.86 \cdot 10^{-5}$

5. RESULTS

5.1. Validation of phase distribution

The solvent residence time depends on its volumetric flow rate and on the free volume in the extruder, which is influenced by the fixed solid phase volume in the model employed here. To ensure the compatibility of this assumption one segment has been observed and compared with experiments.

The volume of the soaked leaves and the solvent in the numerical model have been calculated theoretically according to Eq. (8) and (11) by using the experimentally measured residence time, respectively.

Table 3 shows a good agreement of the resulting width of soaked leaves in one segment estimated from the experimental image in

Figure 3 (CFD: $1.67 \cdot 10^{-2}$ m, Exp: 1.6 - 1.7· 10^{-2} m).

Table 3. Results from the soaked leaves volume for experiments and CFD.

Parameter		Exp	CFD	error (%)
total volume (10^{-5} m³)	$V_{SL,t}$	6.02	6.13	1.8
width in segment (10^{-2} m)	w_{SL}	1.6 - 1.7	1.67	-

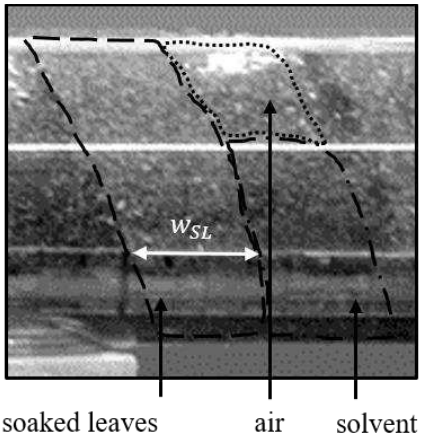

Figure 3. Experimental phase distribution in one segment.

Experimental observations of the water surface can only be estimated roughly. It is hindered by soaked leaves sticking to the inner wall of the extractor. Figure 4 shows a comparison of the calculated total solvent volume in experiments with ± 5 % range and the determined CFD solvent volume after each screw turn. After reaching the quasi-steady state at four screw turns the solvent volume fits into the experimental volume range. Further screw turns show similar values ensuring the quasi-steady state.

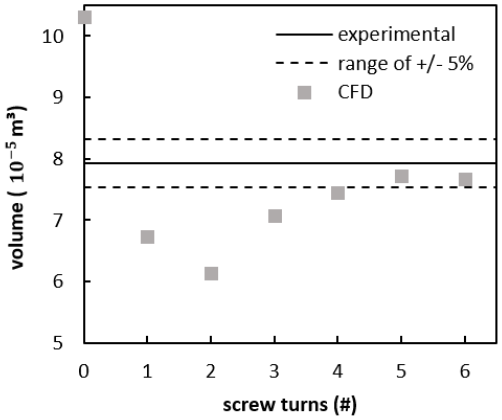

Figure 4: Comparison of total solvent volume between experiments with ± 5% range and CFD data after each screw turn.

Consequently, the phase distribution appears to be represented sufficiently well by the numerical simulation.

5.2. Residence Time Distribution of solvent phase

The residence time distribution (RTD) of the solvent phase in CFD has been measured by using the species method for two quasi-steady state conditions (after 4 or 5 full rotations of the screw). The resulting RTD curves are shown in Figure 5 and compared with the experimentally measured RTD curves, involving three identical runs. Although all three repetitions have identical operating conditions, minor deviations are found in the results. These can occur due to minute changes in local particle distributions, particle-particle interactions, or small variations in the screw rotation speed.

Comparing the numerical RTD curves with the experimental RTD data, a good agreement can be observed. Nevertheless, there are still deviations between numerical and experimental results. Both numerical curves increase faster and show a higher maximum than the experimental curve (Exp: 0.22 1/min, CFD: 0.275 1/min).

Analysing the mean residence time and its standard deviation for both steady-state conditions, the obtained agreement is still found to be quite good (Table 4). The experimental mean residence time of 4.87 min is higher than both numerically calculated residence times (4 turns: 4.08 min, 5 turns: 3.70 min). However, considering additionally the standard deviation, the numerical results fit into the experimentally measured range. The deviations between the numerical residence times (± 10 %) result from the performed quasi-steady state with unsteady solver. Consequently, the liquid velocity profile differs slightly for each screw rotation influencing the species movement.

Furthermore, the calculated theoretical number of steps N results in a value of three for both experiments and CFD. This indicates a good representation of the RTD behaviour by our CFD model.

Table 4. Results of numerical RTD study and comparison to deviations observed when repeating the experiments.

Operation	$\bar{\tau}$ (min)	σ (min)	N (-)
Exp	4.87	± 2.96	3
CFD			
4 turns	4.08	± 2.28	3
5 turns	3.70	± 2.03	3

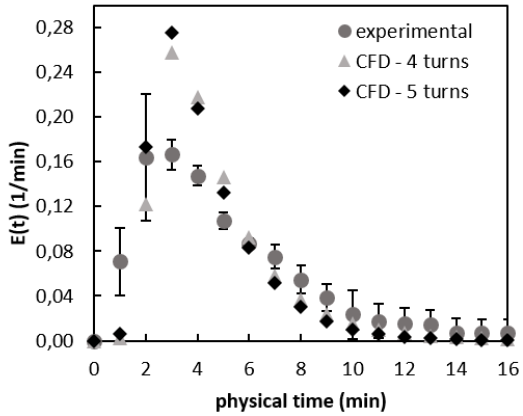

Figure 5: Results from the solvent RTD study by comparing the deviations observed when repeating three experimental runs with two quasi-steady states of the CFD simulation (after 4 and 5 screw turns).

5.3. Contact area

The contact area between the solid leaves and the liquid solvent influences the reaction kinetics since mass transfer processes take place at this location. In the described model the leaves are not represented as single particles and consequently the exact mass transfer areas cannot be determined. Nevertheless, it has already been shown that the CFD simulation can capture the phase distribution in the extruder. This allows an approximation of the contact surfaces by using the Eulerian particle phase. Figure 6 represents the determined contact areas in the screw extruder starting from the extract outlet (segment one) for 4 and 5 turns of screw rotation (the two quasi-steady states considered previously).

The contact areas for both observations are very similar, showing again that quasi-steady state has been reached. At the extract outlet no leaves are present, which results in a zero-contact area. With increasing length of the extruder, the contact area increases and stabilizes at a value of approx. $3.5\ 10^{-4}$ m² in the middle segments 3 - 7. The largest contact area appears in the segment 9 that is located between the inlet of solvent and the extraction cake. At this position fresh solvent is introduced in the extractor and is pushed by the screw towards the extraction cake. Consequently, higher water surfaces arise and contact areas between leaves and solvent increase.

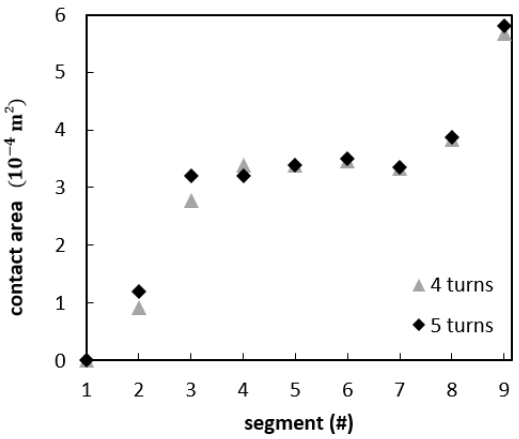

Figure 6. Contact area between leaves and solvent for two quasi-steady states in CFD for all segments starting from the extract outlet (segment 1).

6. CONCLUSIONS

In this study the residence time distribution of a liquid solvent has been analysed in a counter-current screw extractor by using 3D CFD simulations. According to companion experiments the soaked leaves phase is equally distributed between inlet and outlet. Consequently, the theoretically estimated leaves volume was implemented as a constant rotating geometry. This allowed short calculation times due to a reduced model, a two-phase flow of liquid and gas phase that has been solved with the Volume of Fluid (VoF) approach. Since the solvent residence time depends on the free volume in the extractor an optical validation of the model assumptions has been first performed in one screw segment, showing a good agreement. The comparisons of the RTD confirm the good estimation of the residence time by using the described model. The two selected quasi-steady states deliver residence times of 4.08 min (4 screw turns) and 3.70 min (5 screw turns), fitting into the range of the experimental measurements when considering repeatability. The CFD number of steps is equal to that of the experiments, demonstrating a good representation of the counter-current process. The resulting contact areas of leaves and solvent in the segments are an important information for mass transfer interactions during the actual extraction process.

In future studies these contact areas shall help to parametrize compartment models (CM), in order to consider mass transfer interactions with acceptable computational times. This combined CFD/CM model shall ultimately be used to optimise the extraction process and increase the extraction efficiency of artemisinin from *Artemisia Annua* leaves.

ACKNOWLEGDEMENT

The authors gratefully acknowledge the support given by the International Max Planck Research School for Advanced Methods in Process and Systems Engineering (IMPRS ProEng).

REFERENCES

[1] Bart, H.-J., Pilz, S., 2011, *Industrial Scale Natural Products Extraction*, Wiley-VCH, Weinheim.

[2] World malaria report 2021, Geneva: World Health Organization, 2021, Licence: CC BY-NC-SA 3.0 IGO.

[3] Gilmore, K., Kopetzki, D., Lee, J.W., Horváth, Z., McQuade, D.T., Seidel-Morgenstern, A., Seeberger, P.H., 2014, "Continuous synthesis of artemisinin-derived medicines", *Chemical communications*, Vol. 50, pp. 12652–12655.

[4] Eitzlmayr, A., Matić, J., Khinast, J., 2017, "Analysis of flow and mixing in screw elements of corotating twin-screw extruders via SPH", *AIChE J*, Vol. 63, pp. 2451–2463.

[5] Kovacevic, A., Rane, S., Stosic, N., 2016, "Computational fluid dynamics in rotary positive displacement screw machines", *16th International Symposium in Transport Phenomena and Dynamics of Rotating Machinery,* HAL archives-ouvertes.fr.

[6] Ferreira, M.C., Gonçalves, D., Bessa, L.C., Rodrigues, C.E., Meirelles, A.J., Batista, E.A., 2022, "Soybean oil extraction with ethanol from multiple-batch assays to reproduce a continuous, countercurrent, and multistage equipment", *Chemical Engineering and Processing - Process Intensification*, Vol. 170, 108659.

[7] Dhekne, P.P., Patwardhan, A.W., 2021, "CFD model for transient flow fields around teabag during tea infusion", *Food and Bioproducts Proceedings*, Vol. 130, pp. 79–91.

[8] Turgut, S.S., Feyissa, A.H., Baltacioglu, C., Kucukoner, E., Karacabey, E., 2020, "Extraction simulation of porous media by CFD: Recovery of trans-resveratrol from grape cane by pressurized low polarity water system", *Chemical Engineering and Processing - Process Intensification,* Vol. 148, 107779

[9] He, A., Zhang, N., 2012, "CFD for cyclone optimization for liquid extraction from solid particles in turbulent air flows", *ASME International Mechanical Engineering Congress and Exposition, Proceedings (IMECE),* Vol. 7, pp. 183–187.

[10] Shokrian, A., Mobli, H., Akbarnia, A., Jafari, A., Mousazade, H., Zhu, B., 2019, "A study on the three-phase separator machine (tricanter) for olive oil extraction", *Journal of Theoretical and Applied Mechanics*, Vol. 49, pp. 233–240.

[11] Wang, Y., Herdegen, V., Repke, J.-U., 2016, "Numerical study of different particle size distribution for modeling of solid-liquid extraction in randomly packed beds", *Separation and Purification Technology*, Vol. 171, pp. 131–143.

[12] Dadashi, A., Zhu, J., Zhang, C., 2014, "CFD modelling of continuous protein extraction process using liquid-solid circulating fluidized beds", *The Canadian Journal of Chemical Engineering*, Vol. 92, pp. 1911–1919.

[13] Bednarz, A., Weber, B., Jupke, A., 2017, "Development of a CFD model for the simulation of a novel multiphase counter-current loop reactor", *Chemical Engineering Science,* Vol. 161, pp. 350–359.

[14] Gillani, S.S.J., Ullah, A., Zaman, M., Chugtai, I.R., Inayat, M.H., 2017, "Counter-current three-phase fluidization in a turbulent contact absorber: A CFD simulation", *Particuology*, Vol. 35, pp. 51–67.

[15] Chen, K., Bachmann, P., Bück, A., Jacob, M., Tsotsas, E., 2019, "CFD simulation of particle residence time distribution in industrial scale horizontal fluidized bed", *Powder Technology*, Vol. 345, pp. 129–139.

[16] Tan, H., Wen, N., Ding, Z., 2021, "Computational fluid dynamics simulation of multi-phase flow characteristics in an industrial-scale randomly packed tower", *Asia-Pac J Chem Eng*, Vol. 16, e2708.

[17] Yang, L., Liu, F., Song, Z., Liu, K., Saito, K., 2018, "3D Numerical Study of Multiphase Counter-Current Flow within a Packed Bed for Post Combustion Carbon Dioxide Capture", *Energies*, Vol. 11, 1441.

[18] Levenspiel, O., 1999*, Chemical Reaction Engineering. 3rd edition*, John Wiley & Sons.

[19] Haynes, R.K., Fugmann, B., Stetter, J., Rieckmann, K., Heilmann, H.D., Chan, H.W., Cheung, M.K., Lam, W.L., Wong, H.N., Croft, S.L., Vivas, L., Rattray, L., Stewart, L., Peters,

W., Robinson, B.L., Edstein, M.D., Kotecka, B., Kyle, D.E., Beckermann, B., Gerisch, M. Radtke, M., Schmuck, G., Steinke, W., Wollborn, U., Schmeer, K., Römer, A., 2006, "Artemisone - A highly active antimalarial drug of the artemisinin class", *Angewandte Chemie International Edition*, Vol. 45, pp. 2082-2088.

[20] Lapkin, A.A., Plucinski, P.K., Cutler, M., 2006, "Comparative assessment of technologies for extraction of artemisinin", *Journal of natural products*, Vol. 69, pp. 1653–1664.

[21] Liu, Y., lü, H., Pang, F., 2009, "Solubility of Artemisinin in Seven Different Pure Solvents from (283.15 to 323.15) K", *Journal of Chemical & Engineering Data*, Vol. 54, pp. 762–764.

Conference on Modelling Fluid Flow (CMFF'22)
The 18th International Conference on Fluid Flow Technologies
Budapest, Hungary, August 30-September 2, 2022

Performance Investigation of a Savonius Wind Turbine with Unconventional Blade Designs Inspired by Sand Eels

Islam HASHEM*[12], Emeel KERIKOUS[12], Stefan HOERNER[1], Dominique THÉVENIN[1]

[1] Laboratory of Fluid Dynamics and Technical Flows, Otto von Guericke University Magdeburg, 39106 Magdeburg, Germany.
[2] Mechanical Power Engineering Department, Faculty of Engineering-Mattaria, Helwan University, 11718 Cairo, Egypt. *Corresponding Author. E-mail: islam.hashem@ovgu.de

ABSTRACT

Wind turbines allow us to harness the power of the wind and turn it into mechanical energy. When the wind blows, the rotor blades spin, capturing available energy from the wind. Out of many kinds of wind turbines, efforts have been made here to improve the performance of Savonius turbines. The main drawback of such a turbine is its low efficiency. In the present study, a Savonius rotor with unconventional blade designs inspired biologically by sand eels has been proposed; aiming to improve its performance in terms of the output power coefficient (C_P). Sand eels are small elongated sea fish and can frequently be found in shallow water. Two main geometrical parameters have been considered and normalized by the blade diameter (d); the maximum camber (f_{max}) and the maximum camber location ($X_{f_{max}}$); whereas the maximum thickness (t_{max}) is kept as 20% of the maximum camber value to resemble the shape of a sand eel. A total of 54 blade designs have been evaluated using 2D numerical simulations to determine the aerodynamic behaviour of the new bio-inspired design. By comparison between th erotor with semi-circular arc blades and that with sand eel-like blades ($f_{max}/d = 0.4$ and $X_{f_{max}}/d = 0.8$), a noticeable improvement in the performance (up to 8.3% at $\lambda = 0.8$) can be obtained in this manner.

Keywords: Bio-inspiration, CFD, performance, sand eels, Savonius rotor

NOMENCLATURE

C_P	$[-]$	Power coefficient
C_Q	$[-]$	Torque coefficient
f_{max}	$[m]$	Maximum camber
t_{max}	$[m]$	Maximum thickness
$X_{f_{max}}$	$[m]$	Maximum camber location
θ	$[^\circ]$	Azimuth angle
λ	$[-]$	Tip speed ratio
Ω	$[1/s]$	Angular speed

1. INTRODUCTION

Due to the global energy crisis, research and development activities in the field of renewable energy, particularly wind energy, have increased significantly in many nations in recent years. Wind turbines are well-known devices for harvesting available energy from the wind and transform it into mechanical energy. Wind turbines are mainly classified into horizontal axis wind turbines (HAWTs) and vertical axis wind turbines (VAWTs). Horizontal axis wind turbines (HAWTs) are currently the most common type of wind turbines used for power generation. However, the performance of these turbines is limited due to the need for orientation mechanism (yaw), high installation cost, and the need for high-speed wind. Therefore, vertical axis wind turbines (VAWTs) have recently gained importance as a suitable alternative for energy production in residential and isolated places with low-speed wind. Vertical axis wind turbines (VAWTs) are divided into two basic types, Darrieus-type and Savonius-type rotors (Figure 1). The Darrieus-type VAWT was patented by the French engineer J. M. Darrieus in 1931 [1]. In principle, it consists of two curved blades with airfoil cross-section profile that generate aerodynamic lift, when the wind passes over its surface, as shown in Figure 1(a). The Savonius-type VAWT was invented by J. Savonius in 1929 [2]. The Savonius turbine is mainly a drag-driven VAWT and consists in its original design of two semi-circular buckets attached to a rotating shaft in opposing directions, as shown in Figure 1(b). Savonius wind turbines are commonly used owing to the simple design of its blades. Moreover, they are characterized by capability of self-starting, ability to capture wind from any direction, low manufacturing and maintenance costs, robustness and low cut-in speed. However, Savonius wind turbines have poor efficiency (less than 25%) compared to other types of wind turbines. Therefore, many researchers have tried to modify blade design and geometical parameters of the Savonius rotors,

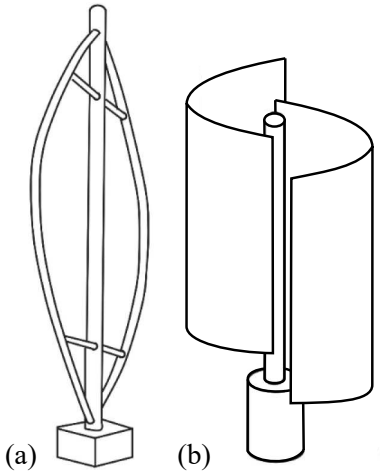

Figure 1. A schematic of vertical axis wind turbines (VAWTs): (a) Darrieus-type and (b) Savonius-type

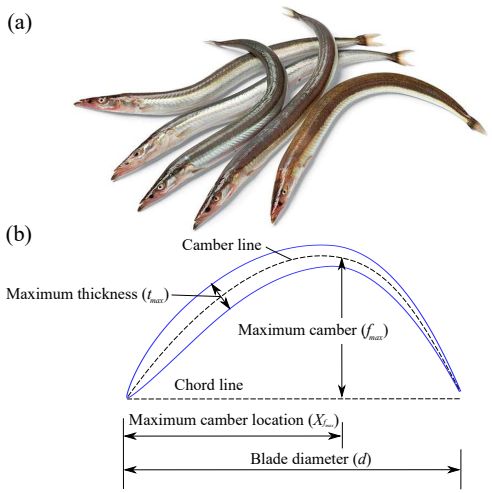

Figure 2. Analogy between sand eels (a) and bio-inspired blades (b) suggested for a Savonius rotor

aiming to increase its efficiency. Some important works from the literature about unconventional blade designs to improve the performance of Savonius rotors are reported in Table 1.

2. PURPOSE OF THE PRESENT STUDY

Sand eels, also known as sand lances, are small, slender eel-like fish that grow to be approximately 9 inches long and often live in vast shoals. An analogy between sand eels and bio-inspired blades suggested for Savonius wind turbines is shown in Figure 2. However, while keeping the general geometrical ratios analog to a sand-eel shape (Figure 2(a)) the particular geometry, such as curvature should be adjusted for improved aerodynamics. For this purpose, two main geometrical parameters of the sand-eel inspired blade (Figure 2(b)) have been considered and normalized by the blade diameter (d); the maximum camber (f_{max}) and the maximum camber location ($X_{f_{max}}$); whereas the maximum thickness (t_{max}) is kept as 20% of the maximum camber value to remain in geometric ratios of a sand eel. In this way, a total of 54 sand eel-like blades have been generated and investigated as Savonius wind turbine to increase the turbine performance, as depicted in Figure 3. This is the focus of the present study.

3. METHODOLOGY

Savonius rotors typically consist of two semi-circular arc blades, namely advancing blade (Blade A) and returning blade (Blade R). Figure 4 shows the geometrical parameters of a standard Savonius rotor as described by Hayashi et al. [12] in their experiment. D is the rotor diameter, H is the rotor height, S is the rotor overlap, d is the blade diameter and a is the shaft diameter. The azimuth angle (θ) is 0 when the chord line is parallel to the wind direction U_0. The length along the circular arc (l) is calculated as $\pi/2$. The coordinate s is defined along the circular arc so that s/l is 0 and 1 at leading edge and trailing edge, respectively. The specifications of the tested rotor and its main dimensions are listed in Table 2.

By referring to the notations of Figure 4, the tip speed ratio (λ) is defined as:

$$\lambda = \frac{\Omega D}{2U_0} \tag{1}$$

The mechanical torque Q and the mechanical power P output from the Savonius rotor can be defined in non-dimensional forms as:

$$C_Q = \frac{4Q}{\rho D^2 H U_0^2} \tag{2}$$

and

$$C_P = \frac{2P}{\rho D H U_0^3} \tag{3}$$

where C_Q and C_P are the torque power coefficient and power coefficient of the Savonius rotor, respectively. The corresponding values of C_Q and C_P at each tip speed ratio (λ) are used to characterize the global performance of the turbine.

In the present study, the geometry is treated in two dimensions since the blade section is simply extruded along the rotor height. However the 2D approach will neglect any 3D effects, such as those from presence of the end plates. The computational grids are generated with the trimmed cell mesher. The mesh consists of two grid components, namely, background and rotor meshes, in addition to the wake refinement that is embedded in the background mesh (see Figure 5). An overset mesh approach was applied in-between the background and the rotor meshes. The domain size is $-10D \times 30D$ in x-direction and $10D$ wide in y-direction to avoid any confinement effects. Figure 5(d) shows a typical mesh around the blade with 18 prism layers next to

Table 1. A review of unconventional blade designs from literature about Savonius rotors

Design	Description	Gain
Dual splitters [3]	Dual splitters are introduced to the concave side of a Savonius rotor through two approaches; top splitter fixed or bottom splitter fixed	A blade with top splitter positioned at 105° succeeded in improving the performance of the Savonius rotor by 7.3%
Koi fish-like blade [4]	Metamodeling-based optimization is applied to optimize the overlap ratio and gap ratio of a Savonius rotor with two blades inspired by a couple of swimming Koi fish	A Savonius rotor consists of two Koi fish-like blades with overlap and gap ratios of 0.2085 and 0.0057 exhibited about 17.6% increase in output power coefficient
V-shaped rotor [5]	A Savonius rotor of aspect ratio of 0.7 was developed by varying length and arc radius of 90° V-edges of the V-shaped blade profile	About 19.3% increase in the maximum power coefficient of a Savonius rotor having V-edge length and arc radius of 0.43 and 0.56 times the reference length, respectively
Thick blade [6]	An optimization process including 12 geometrical parameters was executed to obtain a thick (non-constant thickness) blade profile	A relative increase of 12% in output power coefficient has been reported at λ=1.1
Different concave and convex sides [7]	An optimization procedure was adopted to independently modify the convex and concave surface shapes of a classical Savonius rotor blade	The power coefficient was increased by about 4.41% through Particle Swarm Optimization (PSO) applied to optimize the concave and convex sides
Multiple quarter blades [8]	A new configuration comprises multiple quarter blades added to the traditional configuration of a Savonius rotor	An improvement in power coefficient ranging between 8.89% and 13.69% for different inlet velocities has been obtained by using multiple quarter blades
Combined blades [9]	A combination was made between semi-circular arc-shaped blade and concave elliptical-shaped blade to enhance the performance of a reference Savonius rotor.	An increase up to 11% in output power coefficient can be achieved through the application of combined blades
Airfoil-shaped blade [10]	A Savonius rotor comprises innovative airfoil-shaped blades was developed by modifying Goettingen 462 and NACA 0012 airfoils, resulting in SR3345 and SR5050 airfoils, respectively	The SR3345 achieved a slight increase in C_P at λ<0.5, while the SR5050 rotor showed an enhancement in performance at λ>0.9. However, both rotors exhibited lower C_P-values than that of the conventional rotor at 0.5<λ<1.0
Myring Equation-based blade [11]	A novel blade shape was designed according to Myring Equation with the aim of increasing the power coefficient of the conventional Savonius rotor	A Savonius rotor with a blade fullness of 1 resulted in 10.98% better performance than a conventional Savonius rotor

the wall. The averaged y^+ is kept less than unity to capture accurately the viscous boundary layer. A mesh independence test is carried out at the design tip speed ratio ($\lambda = 0.8$). The mesh density increased gradually from coarse to fine by a refinement ratio of about 1.3. Following three mesh refinements, a difference of less than 1% is obtained. The total number of cells employed is about 200k. The simulation requires about 24h to complete 20 revolutions on two parallel nodes of the HPC-Cluster at "Otto von Guericke" University Magdeburg.

The commercial software Simcenter STAR-CCM+ 2021.3 is used for the solution of the unsteady Reynolds-averaged Navier-Stokes (URANS) equations. The $k-\omega$ Shear-Stress-Transport (SST) turbulence model by Menter [13] was applied. This

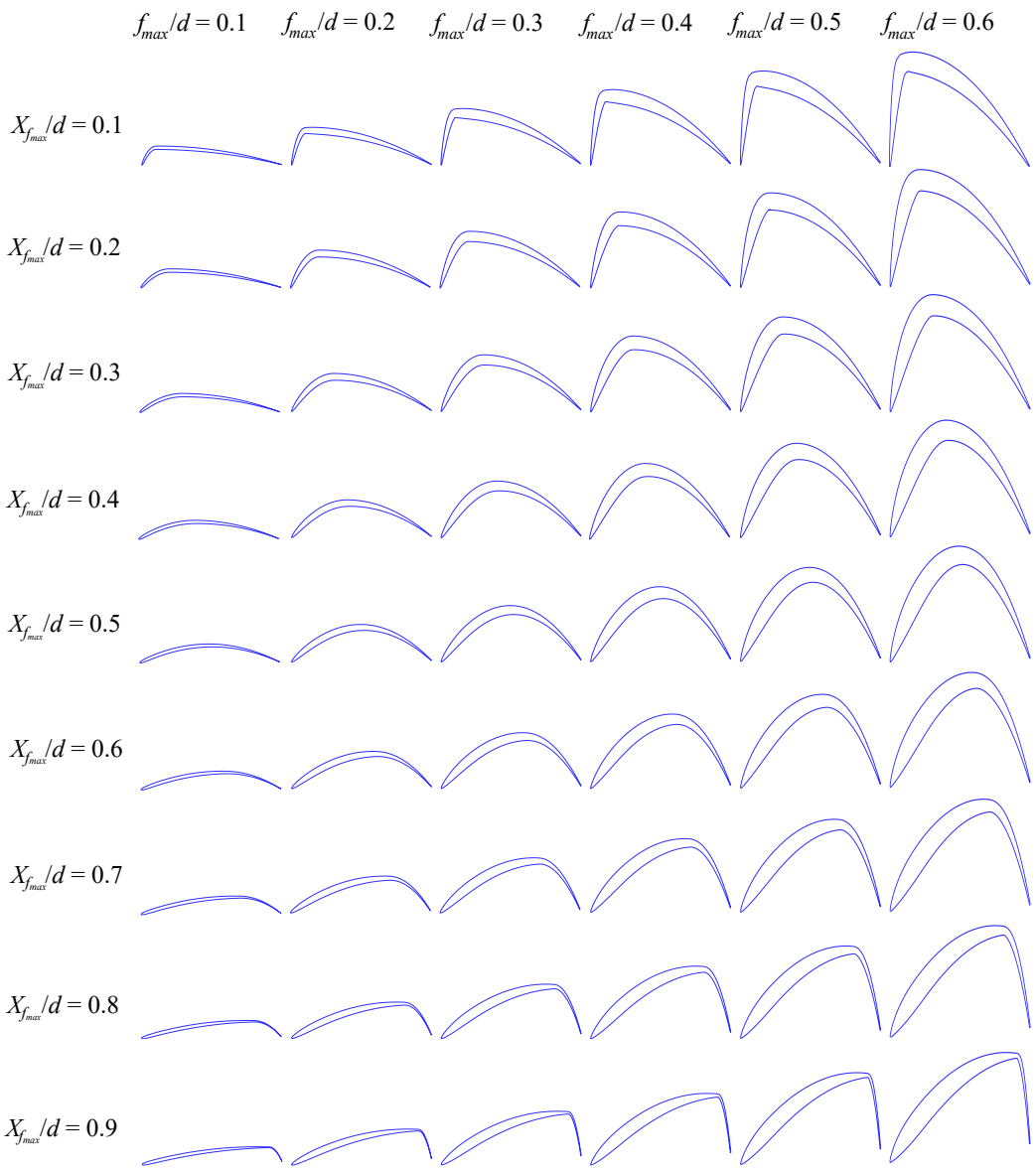

Figure 3. Various models of sand eel-like blades with different values of maximum camber (f_{max}) and maximum camber location ($X_{f_{max}}$) at t_{max} = 20% f_{max}

Table 2. Specifications of the Savonius rotor with semi-circular arc blades [12]

Parameter	Value
Rotor diamater D	0.33 m
Rotor height H	0.23 m
Rotor overlap C	0.066 m
Blade diamater d	0.184 m
Shaft diamater a	0.015 m

model delivers efficient predictions for flows involving strong adverse pressure gradients. Double-precision accuracy of floating point numbers and second-order discretization in space and time is applied. The governing equations are solved using a segregated flow solver. Three different timestep sizes corresponding to azimuth angles of 2°, 1° and 0.5° were investigated. According to the results of a time-independent analysis, a timestep size of 0.5° is found necessary for the present numerical simulations.

The number of revolutions plays a critical role in obtaining a converged solution for numerical simulations of turbomachinery. To maintain reasonable computational time, each numerical simulation was allowed to run for 20 revolutions to ensure that the average torque coefficient (C_Q) shows periodicity in time. After 20 revolutions (t = 4.32 s), the average

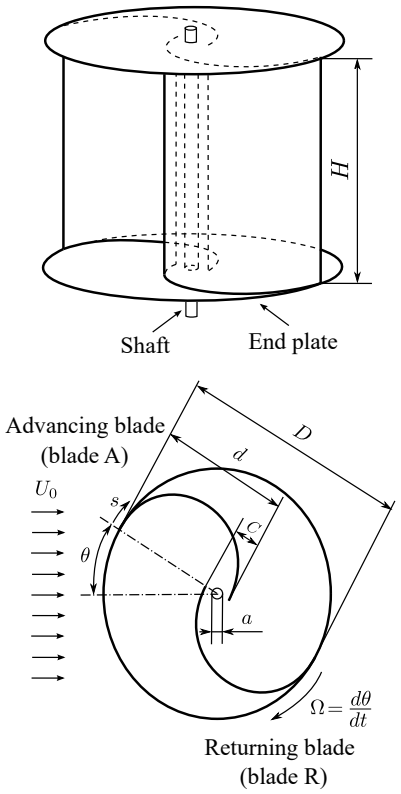

Figure 4. Geometry of the standard Savonius rotor

torque coefficient (C_Q) does not show any significant changes over time (variations below 0.003). The average torque coefficient (C_Q) has always been calculated by time-averaging the values over the last five revolutions.

4. RESULTS AND DISCUSSION

The full numerical procedure has been validated with published numerical results [14] and experimental measurements [12] based on a standard Savonius rotor. The present numerical results match very well with numerical results of Mohamed et al. (2011), both using the $k-\omega$ SST turbulence model (see Figure 6). However, there is a significant deviation compared to the experimental measurements that can be attributed to the 2D assumption. It is worth mentioning that the presence of endplates in the experiment conducted by Hayashi et al. [12] is not taken into account in the present study.

As can be noticed from Figure 6(b), the maximum deviation between the present numerical 2D results and experimental measurements for C_P is about 37.30%. A comparable deviation has been reported by Mohamed et al. [14] and Hosseini Imeni et al. [15] as 36.45% and 25.44%, respectively; all these studies involve 2D numerical simulations with the $k-\omega$ SST model. In other words, the $k-\omega$ SST model usually overpredicts the performance of Savonius rotors when the problem is modeled as two-dimensional or planar. To support this statement, the maximum deviation between the numerical results and experimental measurements is reduced to be only 12.22% when a 3D numerical simulation is carried out, as reported by Elmekawy et al. [16].

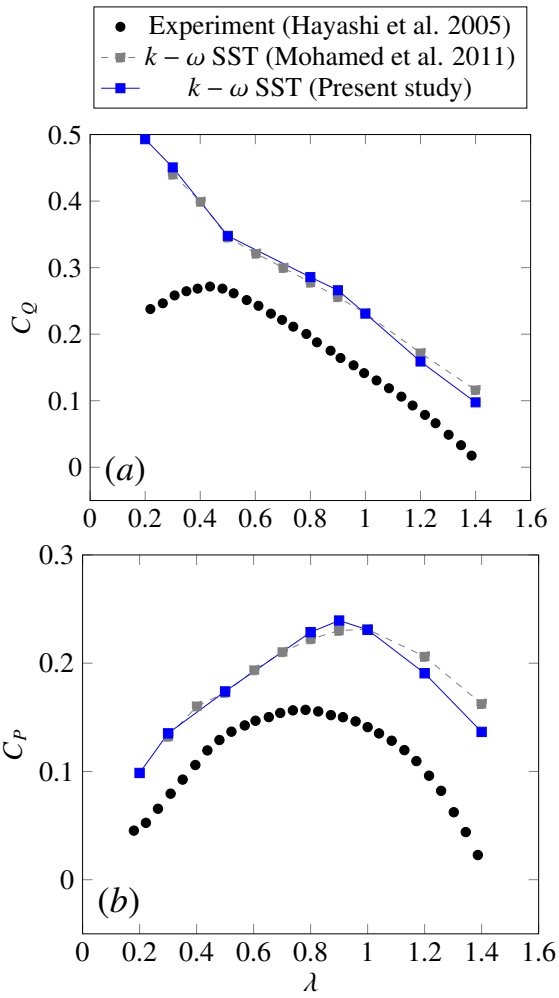

Figure 6. A comparison of the predicted (a) torque coefficient (C_Q) and (b) power coefficient (C_P) to published numerical results [14] and experimental measurements [12]

Before starting the parametric study, two different arrangements of sand eel-like blades were examined at the design tip speed ratio ($\lambda = 0.8$), one when the fish head is facing outward and the other when the fish head is facing inward with respect to the rotor axis. This preliminary study showed that the output power coefficient (C_P) is higher when the fish head is facing inward compared to the other arrangement. Therefore, only one arrangement (fish head facing inward) is considered in the parametric study (see Figure 5).

Figure 7 represents a scatter plot for the calculated power coefficient (C_P) of sand eel-like blades with different maximum camber (f_{max}/d) and maximum camber location ($X_{f_{max}}/d$) values at $\lambda = 0.8$. The highest performance could be achieved with

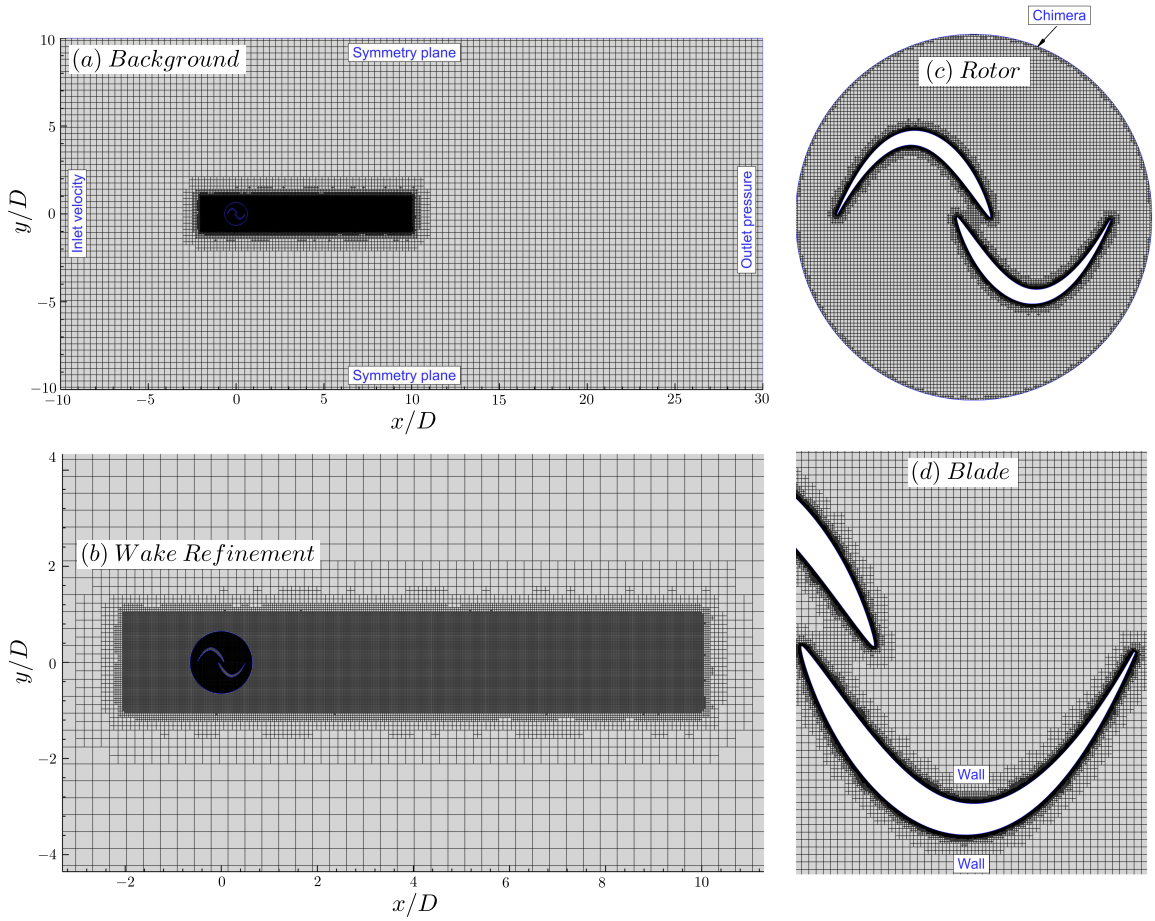

Figure 5. Computational mesh for a Savonius rotor with sand eel-like blades: background (a), wake refinement (b), rotor (c) and blade (d). The boundary conditions are described by the blue-coloured text

high cambered sand-eel like blades, particularly at camber locations ($X_{f_{max}}/d$) of 0.5 and 0.8. On the other hand, sand eel-like blades with low camber and camber location values deliver the worst performance for the Savonius wind turbine. From the simulations, the output power coefficient (C_P) has been calculated for 54 sand eel-like blades. In this manner, the best and the worst blade designs could thus easily be distinguished for $\lambda = 0.8$. Therefore, the best blade design corresponds to $f_{max}/d = 0.4$ and $X_{f_{max}}/d = 0.8$ with $C_P = 0.2486$ whereas a blade design with $f_{max}/d = 0.1$ and $X_{f_{max}}/d = 0.1$ exhibited the lowest power coefficient ($C_P = 0.0581$), as presented in Figure 7. For the best-performing sand eel-like blade ($f_{max}/d = 0.4$ and $X_{f_{max}}/d = 0.8$), this gain leads to an improvement in turbine performance of about 8.3% at the design tip speed ratio ($\lambda = 0.8$), compared to a Savonius wind turbine with semi-circular arc blades.

Figure 8 shows the streamlines around the standard Savonius wind turbine with semi-circular arc blades (a) and that with the best-performing sand eel-like blades (b) at $\lambda = 0.8$. For both rotors, a separation vortex can be observed on the convex side located near the leading edge (fish head) of the advancing blade (blade A). However, the separation vortex is less intensive for the sand eel-like blade. It can be noticed that the stagnation point on the surface of the returning blade (blade R) of the sand eel-like blade is shifted to occur near the trailing edge (fish tail) whereas it occurs nearly at middle of the semi-circular arc blade. The flow through the gap between the blades is more pronounced in case of the Savonius rotor with sand eel-like blade compared to the standard rotor.

The pressure distributions at $\lambda = 0.8$ are shown in Figure 9. The deep differences in the pressure distributions between the two rotors due to different blade designs are obvious. The sand eel profile experiences considerably higher pressure on the concave surface of the advancing blade (blade A) compared to the semi-circular arc. Moreover, the pressure is relatively lower on the convex side of the sand eel-like blade than for the semi-circular blade. The larger pressure difference between both sides of the sand eel-like blades produces a higher force, explaining the better performance.

5. CONCLUSIONS

The present study investigated the performance of a Savonius wind turbine with unconventional

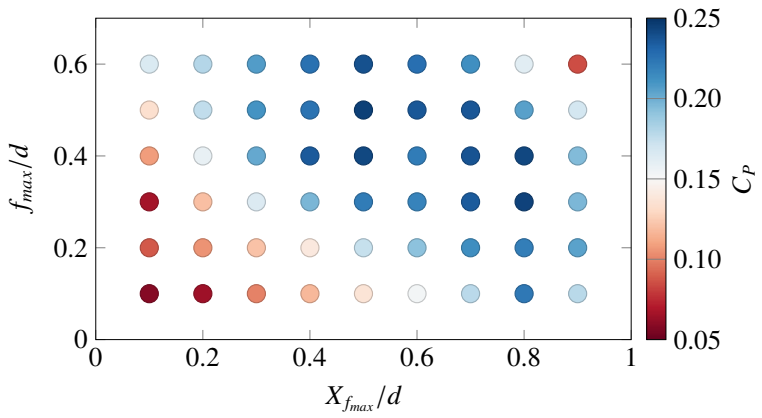

Figure 7. Scatter plot for different maximum camber (f_{max}/d) and maximum camber location ($X_{f_{max}}/d$) values colored by power coefficient (C_P) of the Savonius rotor with sand eel-like blades at λ = 0.8

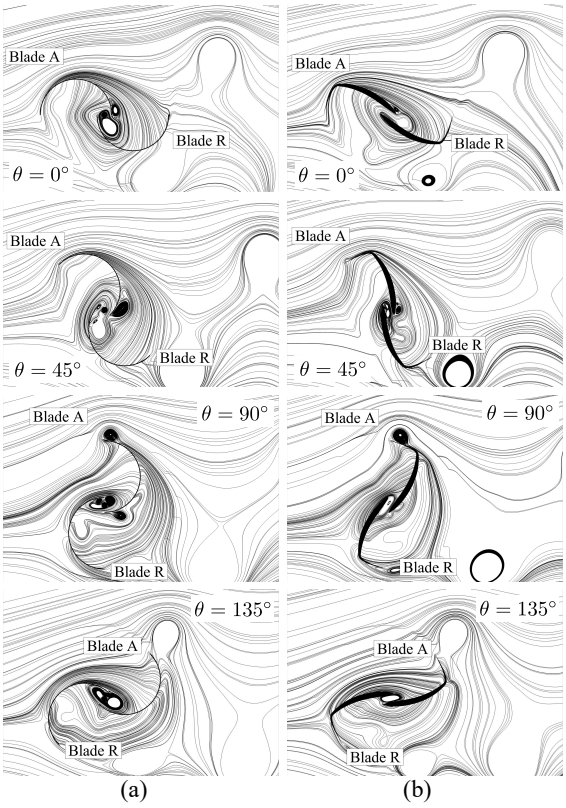

Figure 8. Streamlines around Savonius rotor with semi-circular arc blades (a) and that with the best-performing sand eel-like blades (b) at λ = 0.8

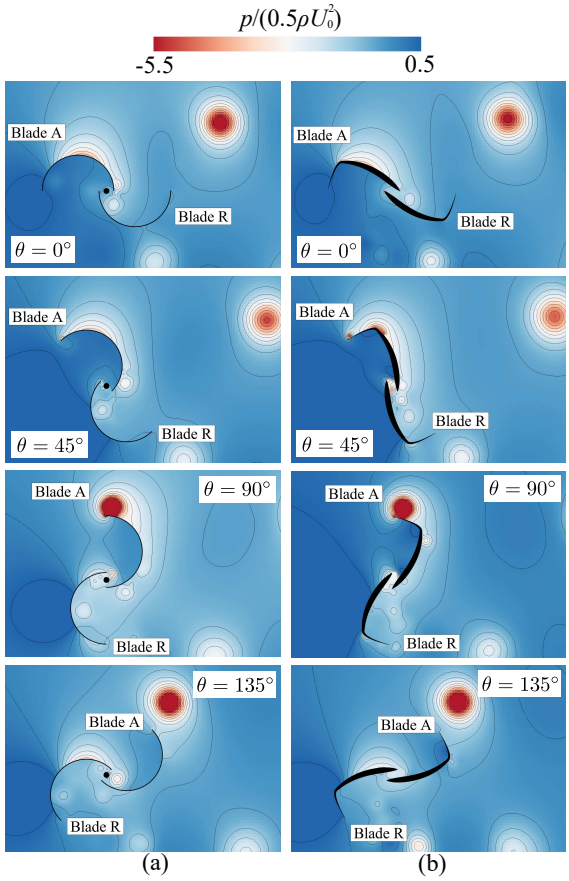

Figure 9. Pressure distributions of Savonius rotor with semi-circular arc blades (a) and that with the best-performing sand eel-like blades (b) at λ = 0.8

blade designs inspired biologically by sand eels. A total of 54 sand eel-like blades are obtained by changing the camber and camber location of bio-inspired blades that fitted into a Savonius rotor. The new bio-inspired blade designs were evaluated by means of 2D numerical simulations to assess the performance in terms of output power coefficient (C_P). The parametric study identifies a better Savonius rotor than the standard one with semi-circular blades, leading to an improvement in performance by 8.3% at the design tip speed ratio (λ = 0.8). Analyzing the flow field around both Savonius rotors explains this superior performance.

In this study, the best-performing bio-inspired blade has been obtained manually out of 54 designs.

It might not be the optimal one. Accordingly, the next step could involve a systematic optimization procedure to reach the optimal sand eel-like blade. Furthermore, in the present parametric study, the sand eel-like blades were evaluated only at the design tip speed ratio ($\lambda = 0.8$). However, the new blade should also be tested at off-design conditions (several λ-values) to check how the gain changes through the full operating range.

ACKNOWLEDGEMENTS

The first author would like to thank Prof. Dr.-Ing. habil. Gábor Janiga for his continued support.

REFERENCES

[1] Marie, D. G. J., 1931, "Turbine having its rotating shaft transverse to the flow of the current", US Patent 1,835,018.

[2] Johannes, S. S., 1929, "Rotor adapted to be driven by wind or flowing water", US Patent 1,697,574.

[3] Patel, V., and Patel, R., 2021, "Free energy-extraction using Savonius hydrokinetic rotor with dual splitters", *Materials Today: Proceedings*, Vol. 45, pp. 5354–5361.

[4] Hashem, I., and Zhu, B., 2021, "Metamodeling-based parametric optimization of a bio-inspired Savonius-type hydrokinetic turbine", *Renewable Energy*, Vol. 180, pp. 560–576.

[5] Shashikumar, C., Honnasiddaiah, R., Hindasageri, V., and Madav, V., 2021, "Experimental and numerical investigation of novel V-shaped rotor for hydropower utilization", *Ocean Engineering*, Vol. 224, p. 108689.

[6] Kerikous, E., and Thévenin, D., 2019, "Optimal shape of thick blades for a hydraulic Savonius turbine", *Renewable energy*, Vol. 134, pp. 629–638.

[7] Tian, W., Mao, Z., Zhang, B., and Li, Y., 2018, "Shape optimization of a Savonius wind rotor with different convex and concave sides", *Renewable energy*, Vol. 117, pp. 287–299.

[8] Sharma, S., and Sharma, R. K., 2016, "Performance improvement of Savonius rotor using multiple quarter blades–A CFD investigation", *Energy Conversion and Management*, Vol. 127, pp. 43–54.

[9] Sanusi, A., Soeparman, S., Wahyudi, S., and Yuliati, L., 2016, "Experimental study of combined blade savonius wind turbine", *International Journal of Renewable Energy Research (IJRER)*, Vol. 6 (2), pp. 614–619.

[10] Tartuferi, M., D'Alessandro, V., Montelpare, S., and Ricci, R., 2015, "Enhancement of Savonius wind rotor aerodynamic performance: a computational study of new blade shapes and curtain systems", *Energy*, Vol. 79, pp. 371–384.

[11] Tian, W., Song, B., VanZwieten, J. H., and Pyakurel, P., 2015, "Computational fluid dynamics prediction of a modified Savonius wind turbine with novel blade shapes", *Energies*, Vol. 8 (8), pp. 7915–7929.

[12] Hayashi, T., Li, Y., and Hara, Y., 2005, "Wind tunnel tests on a different phase three-stage Savonius rotor", *JSME International Journal Series B Fluids and Thermal Engineering*, Vol. 48 (1), pp. 9–16.

[13] Menter, F. R., 1994, "Two-equation eddy-viscosity turbulence models for engineering applications", *AIAA journal*, Vol. 32 (8), pp. 1598–1605.

[14] Mohamed, M., Janiga, G., Pap, E., and Thévenin, D., 2011, "Optimal blade shape of a modified Savonius turbine using an obstacle shielding the returning blade", *Energy Conversion and Management*, Vol. 52 (1), pp. 236–242.

[15] Hosseini Imeni, S. Z., Kaabinejadian, A., Ami Ahmadi, H., and Moghimi, M., 2022, "Optimal design and sensitivity analysis of airfoil-shaped rotor blade for Savonius wind turbine by using response surface methodology", *Wind Engineering*, p. 0309524X211072868.

[16] Elmekawy, A. M. N., Saeed, H. A. H., and Kassab, S. Z., 2021, "Performance enhancement of Savonius wind turbine by blade shape and twisted angle modifications", *Proceedings of the Institution of Mechanical Engineers, Part A: Journal of Power and Energy*, Vol. 235 (6), pp. 1487–1500.

Conference on Modelling Fluid Flow (CMFF'22)
The 18th International Conference on Fluid Flow Technologies
Budapest, Hungary, August 30 -September 2, 2022

CALCULATING PARTICLE RESIDENCE TIMES IN VESSEL GEOMETRIES WITH ANEURYSM

Dániel GYÜRKI[1], István SZIKORA[2], György PAÁL[3]

[1] Corresponding Author. Department of Hydrodynamic Systems, Faculty of Mechanical Engineering, Budapest University of Technology and Economics. Műegyetem rkp. 3, H-1111 Budapest, Hungary. Tel.: +36 1 463 1680, E-mail: dgyurki@hds.bme.hu
[2] Department of Neurointerventions, National Institute of Clinical Neurosciences, E-mail: h13424szi@ella.hu
[3] Department of Hydrodynamic Systems, Faculty of Mechanical Engineering, Budapest University of Technology and Economics. E-mail: paal@hds.bme.hu

ABSTRACT

Numerous studies focus on the formation and rupture of intracranial aneurysms which are saccular deformation of blood vessel walls on the brain arteries. Computational fluid dynamics (CFD) is often used in these studies. Our research concentrates on particle paths calculated from the results of CFD simulations of such malformations.

First, the flow field was obtained using lattice-Boltzmann simulations. A generalized inlet velocity signal was used, while at the outlets the flow rates were given. Paths of massless, passive particles were calculated, based on the flow field using a fourth order Runge-Kutta method. For each particle the reached outlet and the particle residence time (PRT) were recorded. The heart cycle was divided into 10 points evenly in time, and the particles were started at these time instances, hence obtaining 10 sets of outlets and PRTs for the particles.

The paths are strongly dependent on the flow velocity. Therefore, the instabilities, namely the fluctuating velocity arising during the decelerating phase strongly alter the paths of the particles through a stretching and folding action, resulting in filamentary fractal-like patterns. Our results show in the case of four geometries that the starting time of the particles during the heart cycle plays an important role.

Keywords: aneurysm, particle path, residence time

NOMENCLATURE

$\underline{r}$	$[m]$	position vector of particle
$\underline{v}$	$[m/s]$	velocity vector
t	$[s]$	time

Subscripts and Superscripts

0	at the start of the integration

1. INTRODUCTION

The main roles of blood vessels are to deliver nutrient- and oxygen-rich blood to the organs, and transfer the deoxygenated blood from the tissues back to the heart. The arterial system, which stems at the heart, is subjected to high blood pressures, therefore the arterial walls are prone to different malformations.

The two main malformations are stenosis and aneurysm. In case of the former, the lumen of the artery is narrowed down because of plaque formation in the inner wall of the vessels. The latter is the local dilatation of the arterial wall. Intracranial aneurysms (IA) are saccular, berry-like malformations on the wall of brain arteries, mainly found on the Circle of Willis.

IAs are usually asymptomatic but they carry a huge risk on the patient. If an aneurysm ruptures, it causes subarachnoid hemorrhage (SAH), which can result in the patient remaining dependent (~33%) or even cause death in half of the cases [1].

Different methods are available to prevent rupture when an aneurysm is found. Clipping the sac of the aneurysm is the oldest technique, the drawback is that this is an open skull surgery and not all aneurysms can be treated this way. During coiling, the sac is filled with a thin wire, therefore the blood coagulates there. The latest method is the use of braided devices called flow diverters (FD) which act as a hydrodynamic resistance between the parent vessel and the sac, and help the coagulation of the blood [2].

Because of the importance of the disease and the high number of affected people, much research concentrate on either the forming or the rupture of IAs, since these are unanswered questions to this day. Computational fluid dynamics (CFD) is a widely used tool of the studies in investigating the blood flow in vessel wall malformations.

Hemodynamic quantities derived from these simulations are correlated with the initiation location or the ruptured state of aneurysms [3]. However, numerous other parameters are used beside the hemodynamic factors, for example there are researchers who concentrate on simulating particle paths or concentrations in the geometries.

Reza et al. [4] computed and correlated six widely used residence time measures, stating that the appropriate one should be chosen according to the application. Rayz et al. [5] investigated Eulerian advection in IAs modelling the thrombus deposition, while Meschi et al. [6] even calculated drug delivery patterns in diseased arteries. Leemans et al. [7] compared particle residence times (PRT) of Lagrangian particles with aneurysm morphology and the ruptured state, and found that morphology plays an important role on PRT, while the correlation with the ruptured state is not significant.

In most cases, the flow through the arteries of the brain is considered laminar in CFD studies, since the Reynolds number does not exceed the 1000 region. However, some researchers found, that instabilities may arise during some parts of the cardiac cycle. For example, Valen-Sendstad et al. [8] express that in detailed CFD simulations, high frequency instabilities occurred in the carotid siphon right after the systolic peak, during the deceleration of the flow. Khan et al. [9] found a similar phenomenon in the simulation of flows in aneurysm geometries.

Závodszky et al. [10] showed that particles placed inside the flow of an aneurysm display a chaotic nature as fractal-like patterns emerged of the particles. Similar phenomenon was observed in the carotid bifurcation in 2D by Silva et al. [11]. However, as it was discussed earlier, flows in vessel wall malformations may initiate a transitional flow during the decelerating phase. Instabilities, which are considered as oscillations of the velocity, may have an enormous effect on PRT. Suh et al. [12] taken this effect into account during an abdominal aneurysm simulation by dividing the heart cycle to 10 points and calculated a mean PRT by averaging the PRTs of particles released at each point. This takes into account the release time, but does not show the effect of the decelerating phase of the heart cycle.

During our research, we investigated the particle paths with different particle release time points to qualitatively show the effect of the flow instabilities arising from the deceleration of the flow.

2. METHODS

2.1. Geometry preparation

The first step of the study is to obtain real aneurysm geometries and prepare them for the simulation.

Our medical partner provides digital subtraction angiography (DSA) images of patients with IAs found on one or more of their brain arteries. The resolution of the images was 0.22 mm. The DSA images are segmented using 3DSlicer [13], then additional smoothing was applied using MeshLab (version 1.3.2) [14]. The 3D geometries were evaluated based on our previous experience and consultations with neurointerventionalists.

Following the segmentation and smoothing, openings of the geometries are extended in order to limit the effects of the imposed boundary conditions. Last, the geometry was box-cut in a way that the inlet plane is parallel with the XY plane of the box. These procedures were made with an in-house script written in Python.

2.2. Flow simulation

Lattice-Boltzmann method (LBM) was used during the flow simulations. This method originates in the lattice gas automaton, and is used to solve numerically a fluid flow problem. But unlike the commercial methods, which usually solve the discretised Navier-Stokes equations, like the finite volume method, LBM calculates the collision and streaming of fictive particles. Macroscopic quantities, like pressure or velocity can be calculated based on the probability density function of these particles. This way the Navier-Stokes equations are solved on a mesoscopic scale. One of the greatest advantage of the LBM is its potential of parallelisation, therefore the application of high performance computers is possible, which means that the computational time can be reduced greatly compared to regular fluid flow simulations.

The LBM requires a rectangular domain discretised into a uniform grid, hence the box cut mentioned in the previous subsection. The preparation of the grid is named voxelisation, and was performed using an in-house Python script.

During voxelisation, each voxel is assigned either the Unused or the Fluid value. Unused voxels are outside the geometry and no equation is calculated in them. The fluid domain is formed from Fluid voxels, that is where the equations of the flow simulation are calculated. The Fluid voxels can be further assigned as boundary conditions, like wall, inlet or outlets.

The only parameter of the voxel domain is the voxel size. Too large voxel size results in inaccurate results, while too small voxel size increases computational cost unreasonably. In our study, the voxel size was around 0.06 *mm* in each case, resulting in around 5 million Fluid voxels.

At the inlet boundary, parabolic velocity profile was prescribed. The maximum of the parabola is controlled throughout the time by a 1 *s* long generic signal from the literature. This signal can be seen in Figure 1. The Reynolds number at the inlet is set to be 250, calculated from the average of the parabola at the maximum value of the signal and the diameter of the inlet vessel.

The outlet with the smallest area is defined as a pressure outlet in order to avoid overdefining the simulation. The other outlets are set as velocity outlets with parabolic velocity profiles. Their velocities are calculated based on the Murray's law [15], which splits the volumetric flow rate based on the areas of the outlets. Bounce back scheme is prescribed at the wall of the fluid geometry.

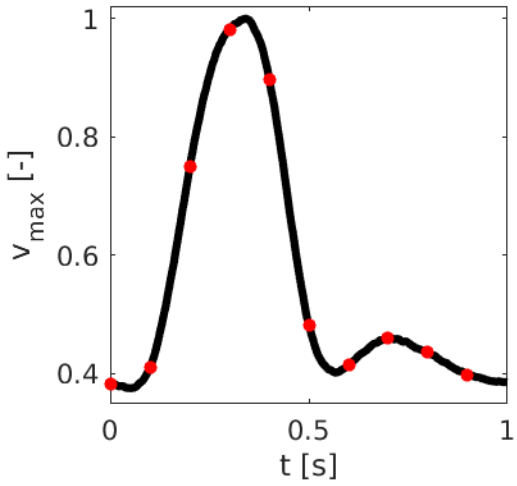

Figure 1. Signal controlling the velocity of the inlet

The time step of the simulation is determined according to a stability criterion of the LBM. At each simulation it was around 1.5×10^{-5} *s*, while the velocity field was saved at every 0.01 *s*, resulting in 100 flow fields. The simulations were made using an in-house code based on Palabos [16].

2.3. Particle tracing

After obtaining the flow field through the time, the last step is to acquire the paths of particles. The particles are considered as massless and passive, therefore they instantaneously pick up the velocity of a given point in the flow field (see Eq. (1)), and do not have an effect on the flow itself. To acquire the position of such particles at a given time, one has to integrate the velocity field in time, from a given initial position and time, see Eq. (2).

$$\dot{\underline{r}}(t) = \frac{d\underline{r}(t)}{dt} = \underline{v}\left(\underline{r}(t), t\right) \tag{1}$$

$$\underline{r}(t) = \int_{t_0}^{t} \underline{v}\left(\underline{r}(t'), t'\right) dt' + \underline{r}(t_0) \tag{2}$$

The paths are calculated using a fourth order Runge-Kutta method written in C++. The time step of the integration is set to 10^{-4} *s*. Choosing too small integration step may result in an unreasonably slow computation, while too large integration step could be inaccurate. The integration is done until 10 heart cycles in order to let enough time for the particles to leave the domain. The PRT (the time for the particle to leave the domain) and the outlets are recorded for every particle.

The paths of 1 million particles are calculated for every case. These particles are started from a plane near the inlet. For each aneurysm geometry, 10 different integrations were made, starting from different time instances. The length of the heart cycle was divided into 10 points, which are marked with red dots in Fig. 1. These 10 time points are the starting times of the path calculation resulting in a qualitative temporal investigation.

Four intracranial aneurysm geometries were investigated in this study. The procedure described previously was carried out for each geometry, the results for one geometry are 10 set of PRT and outlet for the 1 million particles.

Contour plots were made in order to investigate the effect of the release time of the particles. The points of the starting plane are coloured according to the outlet number of the particle started from that given point.

3. RESULTS

Figure 2 shows the results for the first case. The geometry can be seen at the top of the figure. The red plane at the bottom of the geometry is the starting plane of the particles. The aneurysm sac is coloured blue, and the outlets are coloured differently. Fig. 2 also contains the starting points coloured according to the outlet colour of the geometry for the 10 different starting times ordered in a 5 by 2 grid.

As it is seen, there are remarkable differences between the contour plots. Usually, it takes the particles 0.5-0.7 seconds to leave the domain in this smaller geometry. Therefore, if the particles are released at the start of the heart cycle, most of them have already left the aneurysm, or even the domain when the systolic peak (maximum velocity) takes place. That is the reason why there are simple, well-defined regions on that subfigure. However, if the particles are released later in the heart cycle, more of them are yet to reach the aneurysm at the systolic peak and when the decelerating phase starts. As a result of this, the subfigures corresponding to the 0.3 and 0.4 *s* starting time show complex, filamentary structures, similarly to Závodszky et al. [10].

This great dependence on the initial position and the resulting filamentary structure are signs of chaotic advection of the particles. There is a strong connection between the instabilities arising at the decelerating phase of the heart cycle and the chaotic nature of the particle paths, as Eq. (2) suggests.

The signal used in this study (Fig. 1) varies less after the decelerating phase, therefore the structures appearing in the subsequent subfigures are less complicated, and similar to each other. Therefore, one can assume, that the flow stabilises after the deceleration phase.

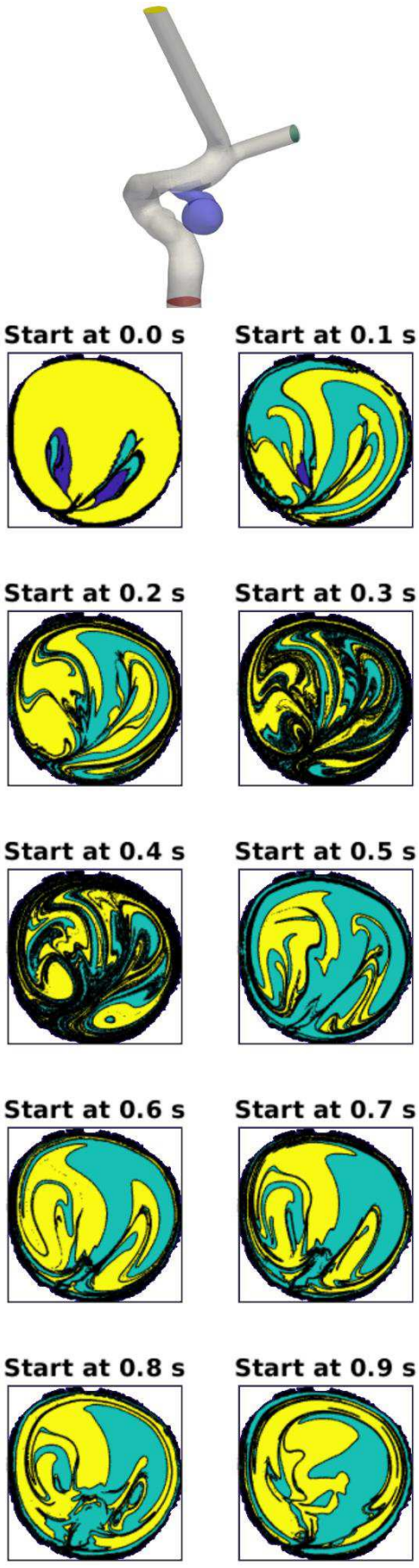

Figure 2. The geometry and the inlet coloured according to the outlets for the first aneurysm

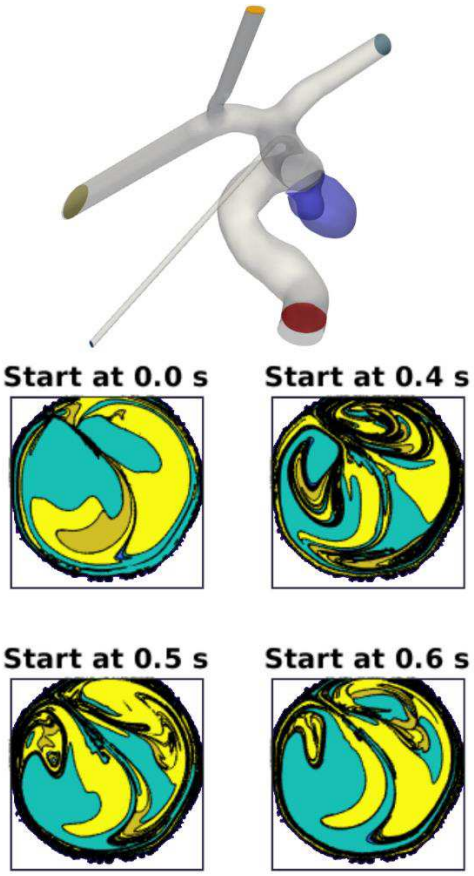

Figure 3. The geometry and the inlet coloured according to the outlets for the second aneurysm

Only four starting times are shown for the rest of the aneurysm geometries in order to concentrate on the greatest differences. Figure 3 shows the results for the second geometry. This geometry has 4 outlets and slightly more bends, and generally it takes a little longer time for the particles to reach the aneurysm, or leave the domain. Therefore, the 0.4, 0.5 and 0.6 *s* cases are shown, beside the 0.0 *s* case. The red plane at the bottom is the plane of the starting points, and the subfigures are coloured according to the colours on the geometry.

Similarly to the previous geometry, the particles released at the start of the heart cycle show a simple structure, only few folded patterns appear, the different regions are well-defined. In contrast with this, the other subfigures display the complex filamentary structures, mainly at the top part of the starting plane. Presumably, the slight bends stabilise the flow, therefore the magnitude of the instabilities may be limited, affecting the paths of the particles less. It was also found by checking the paths, that the filamentary part of the inlet is the place, from where the particle paths travel close to the aneurysm sac, which swirls the flow field, hence the complexity of the patterns.

The results of other starting times, which are not shown in the figure, are similar to the first aneurysm, they show less folded, filamentary structure.

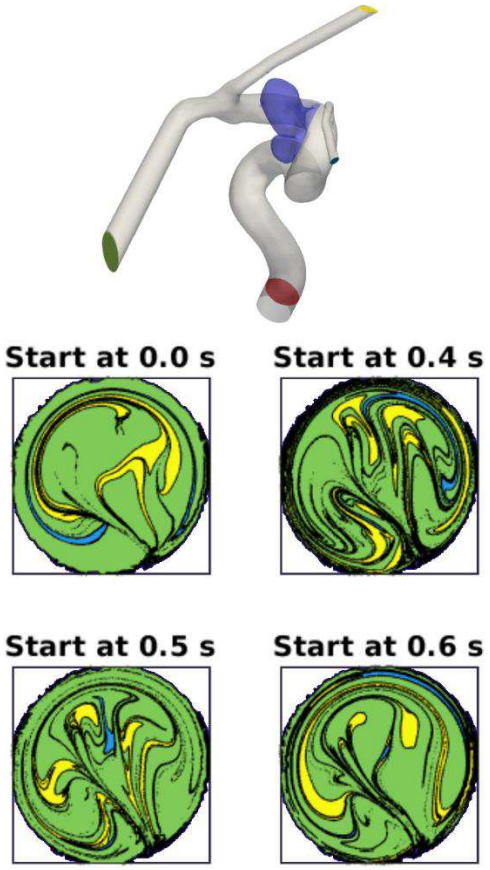

Figure 4. The geometry and the inlet coloured according to the outlets for the third aneurysm

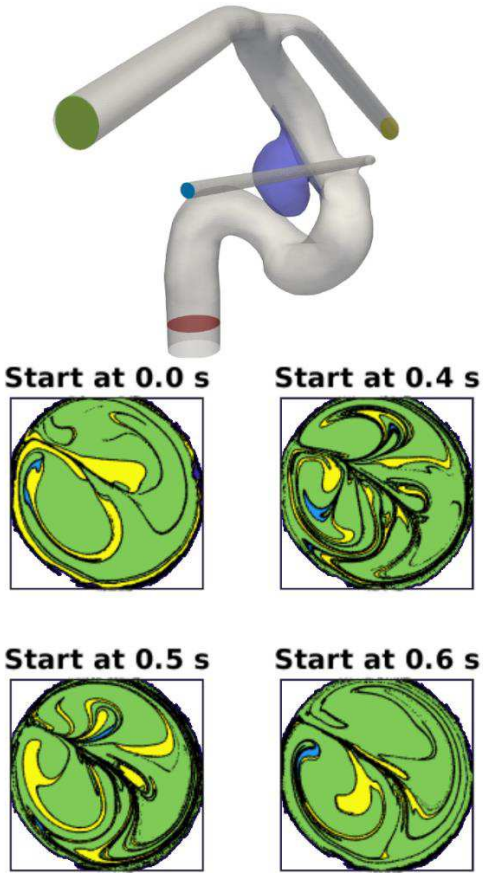

Figure 5. The geometry and the inlet coloured according to the outlets for the fourth aneurysm

The results of the third aneurysm can be seen in Figure 4. Again, only the most different three starting time instances are shown, beside the start of the cycle. This geometry has three outlets and is the most bendy of the four. The bending may be the reason why the results of the case started at the beginning of the heart cycle show little filamentary structure. The secondary flows originating from the bends fold the paths of the particles already. However, it is clearly shown in the subfigures of Fig. 4, that the particles released in the decelerating phase of the heart cycle display a more complex structure, similarly to the previous cases.

They are not shown in Fig. 4, but the results of the last three points of the heart cycle are almost identical, the small deceleration after diastolic peak of the inlet curve creates so small scale instabilities, or none at all, that the paths are not affected by them.

Figure 5 shows the last aneurysm geometry and part of the results. Similar conclusions can be drawn based on this figure to the previous cases. The first subfigure displays a slight folded structure, for example because of the bends or the wide neck of the aneurysm. The rest of the subfigures show the previously mentioned complex structures. Similarly to the third case, the not shown results of the last three points are almost the same. The instabilities arising in this flow may be limited.

Altogether, all four results are similar. The instabilities during the deceleration phase of the heart cycle have an enormous effect on the particle paths, resulting in a folded, fractal-like structure. After the deceleration, the flow is stabilised and so are the paths, as indicated by the less complex structures. The increase of the complexity and foldedness of the displayed structure should be quantified and correlated with morphological factors.

4. CONCLUSIONS

This study focused on following particle paths inside intracranial aneurysms. These particles can model the real particles or molecules, which can be the part of physiological processes, like blood coagulation or drug adsorption. However, as the paths depend greatly on the local velocity, the arising instabilities of a decelerating flow alter them greatly.

Transient lattice-Boltzmann simulations were performed to obtain the flow field in case of four patient-specific 3D IA geometries. Based on the velocity fields, the paths of 1 million particles started near from the inlet are calculated. The heart cycle was divided to 10 points, and the path calculation was repeated starting at each point. Particle residence times and reached outlets were recorded.

All of the four geometries display similar tendency, particles released closer to the decelerating

phase show more complex, fractal-like structure based on the reached outlet. This is the result of the stretching and folding action of the arising instabilities. These results show, that the release time instance should be taken into consideration during particle tracing in pulsatile flows.

ACKNOWLEDGEMENTS

This research was supported by the National Brain Research Program under the Contract Number 2017-1.2.1-NAP-2017-00002, and by the National Research, Development, and Innovation Fund of Hungary under Grant TKP2021-EGA-02. The conference participation was supported by the Végh Gábor Neurointervention Fundation.

REFERENCES

[1] van Gijn, J, and Rinkel, G.J., 2001, "Subarachnoid haemorrhage: diagnosis, causes and management", *Brain*, Vol. 124(2), pp. 249-278.

[2] Fiorella, D., Lylyk, P., Szikora, I., Kelly, M.E., Albuquerque, F.C., McDougall, C.G., and Nelson, P.K., 2008, "Curative cerebrovascular reconstruction with the pipeline embolization device: the emergence of definitive endovascular therapy for intracranial aneurysms", *J Neurointerv Surg*, Vol. 1(1), pp. 56-65.

[3] Qian, Y., Takao, H., Umezu, M., and Murayama, Y., 2011, "Risk Analysis of Unruptured Aneurysms Using Computational Fluid Dynamics Technology: Preliminary Results", *AJNR Am J Neuroradiol*, Vol. 32(10), pp. 1948-1955.

[4] Reza, M.M.S., and Arzani, A., 2019, "A critical comparison of different residence time measures in aneurysms", *J Biomech*, Vol. 88, pp. 122-129.

[5] Rayz, V.L., Boussel, L., Ge, L., Leach, J.R., Martin, A.J., Lawton, M.T., McCulloch, C., and Saloner, D., 2010, "Flow residence time and regions of intraluminal thrombus deposition in intracranial anuerysms", *Ann Biomed Eng*, Vol. 38(10), pp. 3058-3069.

[6] Meschi, S.S., Farghadan, A., and Arzani, A., 2021, "Flow topology and targeted drug delivery in cardiovascular disease", *J Biomech*, Vol 119, pp. 110307.

[7] Leemans, E.L., Cornelissen, B.M.W., Rosalini, G., Verbaan, D., Schneiders, J.J., van den Berg, J.J., Vandertop, W.P., van Bavel, E.T., Slump, C.H., Majoie, C.B.L.M., and Marquering, H.A., 2019, "Impact of Intracranial Aneurysm Morphology and Rupture Status on the Particle Residence Time", *J Neuroimaging*, Vol. 29(4), pp. 487-492.

[8] Valen-Sendstad, K., Piccinelli, M., and Steinman, D.A., 2014, "High-resolution computational fluid dynamics detects flow instabilities in the carotid siphon: Implications for aneurysm initiation and rupture?", *J Biomech*, Vol. 47(12), pp. 3210-3216.

[9] Khan, M.O., Chnafa, C., Gallo, D., Molinari, F., Morbiducci, U., Steinman, D.A., and Valen-Sendstad, K., 2017, "On the quantification and visualization of transient periodic instabilities in pulsatile flows", *J Biomech*, Vol. 52, pp. 179-182.

[10] Závodszky, G., Károlyi, G., and Paál, G., 2017, "Emerging fractal patterns in a real 3D cerebral aneurysm", *J Theor Biol*, Vol. 368, pp. 95-101.

[11] Silva, I.M., Schelin, A.B., Viana, R.L., and Caldas, I. L., 2020, "Transport of blood particles: Chaotic advection even in a healthy scenario", *Chaos*, Vol. 30(9), pp. 093135.

[12] Suh, G., Les, A.S., Tenforde, A.S., Shadden, S.C., Spilker, R.L., Yeung, J.J., Cheng, C.P., Herfkens, R.J., Dalman, R.L., and Taylor, C.A., 2011, "Quantification of Particle Residence Time in Abdominal Aortic Aneurysms Using Magnetic Resonance Imaging and Computational Fluid Dynamics", *Ann Biomed Eng*, Vol. 39(2), pp. 864-883.

[13] Fedorov, A., Beichel, R., Kalpathy-Cramer, J., Finet, J., Fillion-Robin, J.C., Pujol, S., Bauer, C., Jennings, D., Fennessy, F.M., Sonka, M., Buatti, J., Aylward, S.R., Miller, J.V., Pieper, S., and Kikinis, R., 2012, "3D Slicer as an Image Computing Platform for the Quantitative Imaging Network", *Magn Reson Imaging*, Vol. 30(9), pp. 1323-1341.

[14] Cignoni, P., Callieri, M., Corsini, M., Dellepiane, M., Ganovelli, F., Ranzuglia, G., 2008, "MeshLab: an Open-Source Mesh Processing Tool", *Sixth Eurographics Italian Chapter Conference*, Salerno, Italy, pp. 129-136.

[15] Chnafa, C., Brina, O., Pereira, V.M., and Steinman, D.A., 2018, "Better Than Nothing: A Rational Approach for Minimizing the Impact of Outflow Strategy on Cerebrovascular Simulations.", *AJNR Am J Neuroradiol*, Vol. 39(2), pp. 337-343.

[16] Latt, J., Malaspinas, O., Kontaxakis, D., Parmigiani, A., Lagrava, D., Brogi, F., Belgacem, M.B., Thorimbert, Y., Leclaire, S., Li, S., Marson, F., Lemus, J., Kotsalos, C., Conradin, R., Coreixas, C., Petkantchin, R., Raynaud, F., Beny, J., and Chopard, B., 2021, "Palabos: Parallel Lattice Boltzmann Solver", *Comput Math,* Vol. 81, pp. 334-350.

Conference on Modelling Fluid Flow (CMFF'22)
The 18th International Conference on Fluid Flow Technologies
Budapest, Hungary, August 30-September 2, 2022

COMPARISON OF OPENFOAM TURBULENCE MODELS FOR NUMERICAL SIMULATION OF THERMALLY-DRIVEN WINDS

Jose I. ROJAS[1], Santiago ARIAS[2], Rathan B. ATHOTA[2], Adeline MONTLAUR[2]

[1] Corresponding Author. Dept. of Physics - Division of Aerospace Eng., Universitat Politècnica de Catalunya. c/ Esteve Terradas 7, 08860, Castelldefels, Spain. Tel.: +34 93 413 4130, Fax: +34 93 413 7007, E-mail: josep.ignasi.rojas@upc.edu
[2] Dept. of Physics - Division of Aerospace Eng., Universitat Politècnica de Catalunya. E-mails: santiago.arias@upc.edu, rathan.babu.athota@upc.edu, adeline.de.montlaur@upc.edu

ABSTRACT

Commercial computational fluid dynamics (CFD) codes have often been used for simulation of atmospheric boundary layer (ABL) flows. The present work explores the potential of the open-source CFD software OpenFOAM for simulating thermally-driven winds, by comparing several turbulence models. Indeed, in ABL and other large-scale flows, turbulence is critical to the mixing process of momentum and buoyancy, and simulations with commercial CFD codes have usually been done with Reynolds-Averaged Navier-Stokes (RANS) turbulence modelling.

In this work, the formation of thermally-driven winds is studied in an idealised mountain-valley system, with realistic values of parameters such as the slope angle, the diurnal temperature cycle, etc. Performances of various OpenFOAM RANS turbulence models (k–ε, re-normalisation group (RNG) k–ε, k–ω shear stress transport (SST)) are compared. A preliminary study of LES using Smagorinsky closure is also contemplated. Velocity contours, velocity and temperature profiles, the shapes of vortexes/convective cells, and the computational times are presented for all the studied turbulence models, to help identify the most suitable one for simulation of thermally-driven winds.

Keywords: computational fluid dynamics (CFD), OpenFOAM, slope winds, thermally-driven winds, turbulence models

NOMENCLATURE

C_k	[−]	Kolmogorov constant
C_μ	[−]	turbulence viscosity ct.
D	[s^{-1}]	strain rate tensor
H_{ref}	[m]	reference height
N	[s^{-1}]	Brunt-Väisälä frequency
Pr	[−]	Prandtl number
T	[K]	temperature
T_E	[s]	Earth diurnal period
U_{ref}	[ms^{-1}]	reference velocity
W	[m]	valley width
c_p	[$Jkg^{-1}K^{-1}$]	specific heat at ct. pressure
h	[$Wm^{-2}K^{-1}$]	convective heat transfer coef.
k	[m^2s^{-2}]	turbulence kinetic energy
p	[Pa]	static pressure
p_{rgh}	[Pa]	dynamic pressure
p_T	[Pa]	total pressure
q_k	[Kms^{-1}]	kinematic heat flux
t	[s]	time
u^*	[ms^{-1}]	friction velocity
z_0	[m]	roughness length scale
U	[ms^{-1}]	flow velocity
$\vec{g}$	[ms^{-2}]	gravity acceleration vector
$\vec{r}$	[ms^{-1}]	position vector
α	[°]	slope angle
α_{ef}	[m^2s^{-1}]	effective thermal diffusivity
β	[K^{-1}]	volumen expansion coef.
κ	[−]	Von Kármán ct.
μ	[$kgm^{-1}s^{-1}$]	dynamic viscosity
ν	[m^2s^{-1}]	molecular kinematic viscosity
ν_{ef}	[m^2s^{-1}]	effective kinematic viscosity
ω	[s^{-1}]	turb. specific dissipation rate
ρ	[kgm^{-3}]	density
θ_*	[K]	potential temperature
ε	[m^2s^{-3}]	turbulence dissipation rate

Subscripts and Superscripts

0	sea level
x, z	along-slope, slope-normal coordinates
max	maximum
t	turbulent
X, Y, Z	width, depth and height coordinates
∞	free stream or far field

1. INTRODUCTION

Commercial computational fluid dynamics (CFD) codes have frequently been used for simulating atmospheric boundary layer (ABL) flows,

e.g., for wind energy applications. However, to increase the ability to create individualised solutions, and in a context of sometimes limited scientific funding, availability of open-source CFD software such as OpenFOAM is very attractive, especially as it has proven to be very useful for simulating ABL flows [1]. This is why, in this work, the potential of OpenFOAM for simulating a type of ABL flows (*i.e.*, thermally-driven winds) is explored, by studying several OpenFOAM turbulence models for simulating such flows. Indeed, in ABL and other large-scale flows, turbulence is critical to the mixing process of momentum and buoyancy [2]. In this regard, simulations of ABL flows with commercial CFD codes have been usually done with Reynolds-Averaged Navier-Stokes (RANS) turbulence modelling, applying the standard k–ε model [1, 3], the realisable k–ε model [4], or other modified k–ε models [1, 5]. The standard k–ε model has also been used in similar studies conducted with OpenFOAM [6].

Other possible RANS turbulence models are the k–ω shear stress transport (SST) model and the k–kl–ω turbulence model [7, 8, 9, 10, 11]. The latter is an extension of the k–ω SST model that includes laminar-turbulent transition prediction [12]. Numerical simulations have also been done considering the solution of the RANS, LES model, and 2-layer turbulence model [13], or have incorporated LES in the calculation, using a DES approach to solve the flow near walls (DES incorporates buoyancy, stratification, developed turbulence and complex topography) [14]. DES is a suitable option for making the most of the advantages of LES for modelling turbulent ABL flows, without the high computational cost associated with using LES in complex geometries or topographies [15]. Similarly, Favre-averaged Navier-Stokes eqs. have also been used to predict turbulent flows. To close this system of eqs., transport eqs. are used for turbulence kinetic energy (TKE) and its dissipation rate [16]. Finally, implementing non-linear k–ε turbulence models is also under consideration, as this could lead to better performance of the numerical model [1], particularly for prediction of TKE.

As per, OpenFOAM standard k–ε model RANS turbulence was used to simulate the wind flow over Mount Saint Helens, USA [17], over the Giza Plateau in Egypt [18], and convective winds in the Aburra open valley, Medellín, Colombia [19]. OpenFOAM was also used to study non-buoyant wind flows over complex terrains using RANS turbulence models with wall functions, to make accurate predictions of wind power production [20]. Finally, an OpenFOAM solver was developed using LES to simulate buoyant flows within the Boussinesq approach, focusing on flow interaction with wind turbines [21].

In this work, the diurnal cycle for thermally-driven winds is studied in an idealised mountain-valley system with realistic values of several parameters such as the slope angle, diurnal temperature profile, etc. The performance of various OpenFOAM RANS turbulence models (k–ε, re-normalisation group (RNG) k–ε, k–ω SST [7, 8, 9, 10, 11]) is compared. A preliminary study of LES with Smagorinsky closure [22, 23] is also presented on the same mesh used as for RANS simulations.

2. METHODOLOGY

The numerical method used in this work (including the governing eqs. based on the Boussinesq approach, main hypotheses, solver, boundary conditions (BC) and initial conditions (IC), etc., except from the turbulence models that will be tested herein) is described in-depth in [24, 25]. The mountain-valley geometry studied in this work (shown in Figure 1) is also the same as used in our previous research [24]. A proper mesh validation for the k–ε turbulence model can be found in [24]. While our numerical results were not validated against empirical field measurements, they were validated against large-eddy simulation (LES) results by Axelsen and van Dop [2, 26], who had validated their LES results against experimental measurements. Note that it is very difficult to find research in the literature reporting wind speed measurements in mountain-valley systems with configurations coincident with the simple geometry that we are using for our simulations, and data from non-similar geometries cannot obviously be used for validation purposes.

The most suitable settings for simulating thermally-driven flows identified in [24] are: 1) slip wall BC on the domain top surface; 2) uniform field temperature and pressure as IC; 3) fluid domain height of 2600 m; and 4) valley width W = 458 m (W does not affect significantly the thermally-driven wind convective cell, if W > 458 m [24]). Finally, the roughness length value used in this work is z_0 = 0.03 m, as in [27], and the slope angle is $\alpha = 20°$.

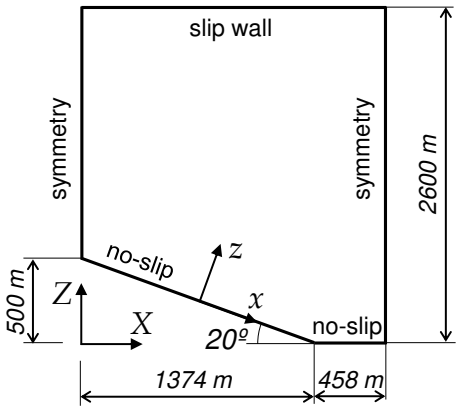

Figure 1. Studied mountain-valley geometry

2.1. Model - governing equations

If the flow field is assumed as a continuum, the mass, momentum, and energy conservation eqs. (Navier-Stokes eqs.) can be used to describe

the flow behaviour. Slope winds are due to natural convection, and the ABL formation is driven by temperature gradients. Thus, the energy and momentum conservation eqs. are coupled and, unless information from the energy equation goes into the momentum equation, the ABL growth cannot be solved. This can be overcome by using the Boussinesq approach. Here, if heat transfer is non-negligible, then the flow properties usually depend on temperature, and, if changes in density ρ are not significant, ρ can be considered constant in the unsteady and convection terms, while it is not so in the body force term of the Navier-Stokes eqs.

In this work, the Boussinesq approach is used [28, 29] with the following assumptions: the air is a Newtonian, dry, perfect gas at rest [27], ; radiation effects are negligible, as well as Coriolis effects, since the focus is on relatively small scales and local mechanisms in the near-ground-surface region [27, 28, 30]; the geostrophic wind velocity is zero; the diffusion is predominant in the direction normal to the slope, compared to along the slope; and the Brunt-Väisälä frequency N, a measure of the atmospheric stratification, is constant, as in [28, 29]. Applying the Boussinesq approach and the previous assumptions to the Navier-Stokes eqs.:

$$\nabla \cdot \vec{U} = 0 \tag{1}$$

$$\frac{\partial \vec{U}}{\partial t} + \nabla \cdot (\vec{U}\vec{U}) - \nabla \cdot (2\nu_{ef} D(\vec{U})) = = -\frac{1}{\rho_0}(\nabla p - \rho \vec{g}) \tag{2}$$

$$\frac{\partial T}{\partial t} + \nabla \cdot \left(\frac{\rho}{\rho_0}\vec{U}T\right) - \nabla \cdot \alpha_{eff} \nabla T = 0 \tag{3}$$

where $\vec{U}$ is the velocity vector, ν_{ef} the effective kinematic viscosity (sum of molecular kinematic viscosity ν and turbulent kinematic viscosity ν_t), $D(\vec{U}) = \frac{1}{2}\left(\nabla\vec{U} + (\nabla\vec{U})^T\right)$ the strain rate tensor, p the static pressure, T the temperature, ρ_0 the reference density at the reference temperature T_0, and α_{ef} the effective thermal diffusivity. In turn, ρ (updated in the temperature governing equation using the Boussinesq approach) and α_{ef} can be computed as follows:

$$\rho = \rho_0(1 - \beta(T - T_0)) \tag{4}$$

$$\beta = -\frac{1}{\rho}\left(\frac{\partial \rho}{\partial T}\right) \tag{5}$$

$$\alpha_{ef} = \frac{\nu}{Pr} + \frac{\nu_t}{Pr_t} \tag{6}$$

where $\beta = 3.5 \times 10^{-3}$ K^{-1} is the volume expansion coefficient (treated as constant), $\nu = 1.455 \times 10^{-5}$ m^2/s, $T_0 = 288.15$ K, and the laminar and turbulent Prandtl numbers $Pr = 0.7$ and $Pr_t = 0.9$.

Among the OpenFOAM solvers for heat transfer analysis that seem applicable for our research, *buoyantBoussinesqPimpleFoam* was chosen, which uses Navier-Stokes eqs. with Boussinesq approach. The simulations were performed using an Euler implicit time scheme, with time step 0.1 s, limiting the maximum value of the Courant number to ≈0.5.

2.2. Boundary conditions

As seen in Figure 1, no-slip wall is imposed as BC on the slope and valley, symmetry BC on both sides of the computational domain, and slip wall BC on its top. More details can be found in [24, 25]. While our previous work studied the formation of thermally-driven flows by imposing steady altitude-dependent temperature on the slope [24], the current work aims at studying the generation of such winds under time-dependent temperature (but constant with altitude) applied on the slope. To reproduce the diurnal cycle, the periodic temperature profile $T(t) = 288.15 - 10 \sin(2\pi t/T_E)$ [K], where $T_E = 86\,400$ s, is set on the slope.

2.3. Turbulence models

The objective of this study is to simulate the diurnal cycle of thermally-driven winds using RANS eqs., which are the application of the Reynolds decomposition, consisting of expressing the solution variables as they appear in the instantaneous Navier-Stokes eqs. as the sum of a mean and a fluctuating component. To that end, k–ε, RNG k–ε, and k–ω SST models are considered. To determine k and ε, formulas typically used for inlet BC are considered [31]:

$$k(z) = \frac{u^{*2}}{\sqrt{C_\mu}} \text{ and } \varepsilon(z) = \frac{u^{*3}}{\kappa(z + z_0)} \tag{7}$$

where the turbulence viscosity constant $C_\mu = 0.09$ [32], the Von Kármán constant $\kappa = 0.41$, and the friction velocity u^* is given by:

$$u^* = \kappa \frac{U_{ref}}{ln\left(\frac{H_{ref}+z_0}{z_0}\right)} \tag{8}$$

Given that our BC do not include any inlet, the values of these parameters are only imposed as IC of the simulation and in the slope and valley wall functions. Thus, constant values are considered, taking as reference the value at $H_{ref} = 50$ m, where a reference velocity $U_{ref} \approx 1$ m s^{-1} is expected.

For k–ω SST, the turbulence specific dissipation rate is calculated as $\omega = \varepsilon/(C_\mu k)$. The obtained values of k, ε, and ω can be found in Table 1. Note that an analysis of the effect of these parameters is not included in this work, but this is of interest and will thus be considered in future research.

Table 1. Turbulence models and associated parameters (all RANS models use $k = 0.0102$ m^2 s^{-2})

Models	Parameters
RANS k–ε	$\varepsilon = 8.24 \times 10^{-6}$ m^2 s^{-3}
RANS RNG k–ε	$\varepsilon = 8.24 \times 10^{-6}$ m^2 s^{-3}
RANS k–ω SST	$\omega = 0.009$ s^{-1}
LES	$C_k = 0.094$
	$C_e = 1.048$

A preliminary study of LES is also presented. LES distinguishes between the large eddies in the flow, which are mainly determined by the geometry of the problem under study, and the smaller eddies that tend to be more universal. A filter is applied so that scales smaller than the filter size are removed from the variables, and their effect on the resolved scales is modelled by means of a turbulence model. Here, the Smagorinsky closure scheme [22, 23] is used, where:

$$\nu_t = C_k \Delta k^{0.5} \tag{9}$$

where C_k is the Kolmogorov constant and k is given by the solution of a quadratic eq. In this work, OpenFOAM default model coefficients are used (see Table 1). This study is made on the same mesh as the RANS study. It only aims at validating the applicability of the LES model to this problem, since a refined mesh would need to be adapted for the LES case, and the time step should be carefully chosen to properly solve the LES scales of the flow.

All simulations were run on 16 cores (of 8 GB of DDR4-2666 ECC RAM each) of a Dual AMD EPYC™ 7001 Series Processors. Table 2 shows the computational time needed to run 24 h of simulation time (864 000 time steps). Contrary to what is usual, LES shows shorter simulation time than the RANS models. The reason is that this is a preliminary study made on the same computational mesh as that for the RANS models. A finer mesh would be needed for LES, and possibly a smaller time step, which would lead to much higher computational time.

Table 2. Computational time (in days) to obtain 24 h of simulation time

Models	Time [days]
RANS k–ε	17.98
RANS RNG k–ε	13.30
RANS k–ω SST	18.63
LES	4.85

Between RANS models, RNG k–ε is the fastest one, k–ε and k–ω SST being ≈35% computationally more expensive. Note that for RANS models, at constant Δt, for 1000 s of simulation, computational time goes from ≈1 h in the katabatic phase (low velocity in the whole domain), to ≈15 h in the anabatic phase where, as seen in Section 3, flow velocity is higher and vortices appear. Future studies will include the possibility of considering adaptive time step.

3. RESULTS

Results were obtained for 2 diurnal cycles in all cases. Figure 2 shows the diurnal cycle of the maximum along-slope velocity measured at mid-slope for the different turbulence models. Though the time-dependent temperature profile shows symmetric range values (from −10 K at 6 h to +10 K at 18 h, with respect to the field initial temperature), it can be seen that the maximum speeds for katabatic flow (at 6 h) are much lower than for anabatic flow (at 18 h), as reported also in [33, 34, 35]. The diurnal timing of the speed peaks is consistent with the typical profiles of mountain breezes [36]. Finally, the values obtained for maximum velocity at mid-slope are very similar for all RANS models, though RNG k–ε shows more oscillations (especially in the anabatic phase), and the amplitude of the values obtained with LES is wider and with highly oscillating component in the anabatic phase.

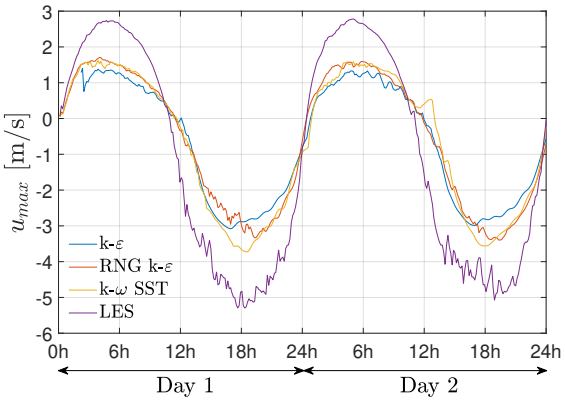

Figure 2. Diurnal cycle of maximum along-slope velocity u_{max} (at mid-slope) for the tested turbulence models

Figures 3 and 4 show velocity magnitude U corresponding to katabatic and anabatic configurations, respectively. In the katabatic case (Fig. 3), downslope velocity is observed, with very similar paterns for k–ε and RNG k–ε models. Contours obtained with k–ω SST model show higher vorticity in the top part of the domain, and LES ones lots of small vortices. While convective cells can hardly be perceived in the katabatic case, convective cells are clearly visible in the anabatic one (Fig. 4). In this case, as already seen in Fig. 2, the obtained velocities are significantly higher, and the choice of turbulence model does have some influence on the convective cell/vortex obtained: the cells from the k–ε and k–ω SST models are very similar, while the cell from the RNG k–ε model is a bit different, and LES shows lots of secondary cells, suggesting the need for a deeper study of the mesh and time step effects, to validate the choice of this turbulence model. Also note that though velocity contours seem to indicate that the domain height is affecting the results obtained from the anabatic simulations, a complete domain-height independence study [24], made in steady conditions, validated the choice of this height. It was further confirmed by performing a 24h-cycle simulation, with the k–ε model, using a height of 3250 m. In the area of interest, i.e. within 20 m above the slope ground, a maximum error of 1.5% was found when using H_D = 2600 m instead of 3250 m. It is also worth noting the increased difficulties in modelling the anabatic flow. This might be due to the fact that

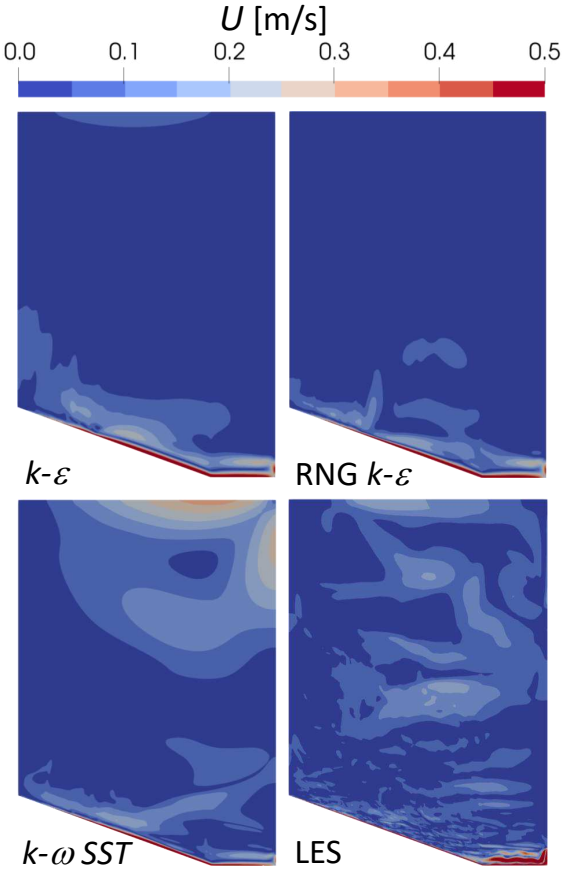

Figure 3. Katabatic flow (6 h, day2): velocity U for the tested turbulence models

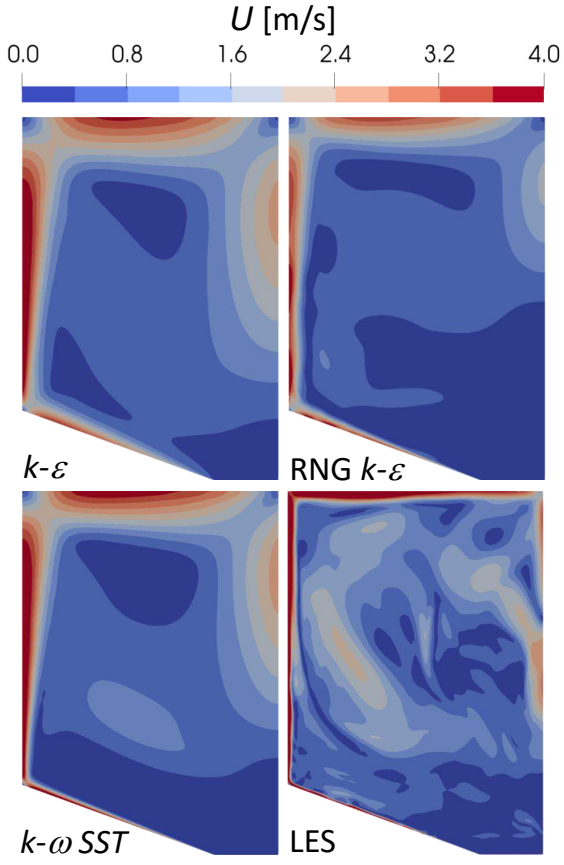

Figure 4. Anabatic flow (18 h, day2): velocity U for the tested turbulence models

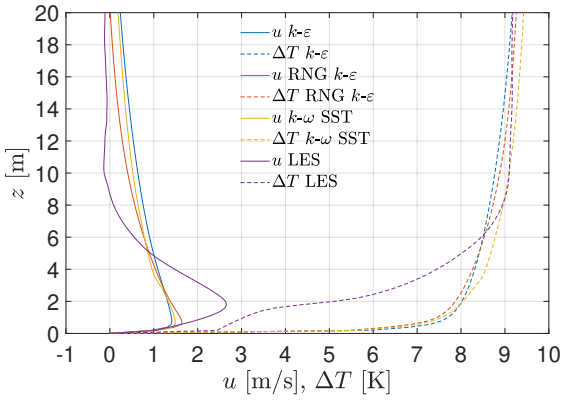

Figure 5. Katabatic flow: along-slope velocity u and ΔT profiles at 6 h (day2) for the tested turbulence models

anabatic flows are associated with absolute static instability inducing convective motions above a heated surface, as has been widely observed in the literature [28].

Figures 5 and 6 show the along-slope velocity and temperature profiles as a function of the slope-normal distance (z), at mid-slope, for the katabatic and anabatic cases (6 h and 18 h, day2), respectively.

Along-slope velocity profiles are expected to exhibit logarithmic behaviour, as for an ideal ABL [7]. In both cases, the flow velocity peak obtained with LES is clearly of higher magnitude and is observed at higher z than the peaks obtained with the RANS models. It can also be observed that the results obtained with RANS models both for velocity and temperature are very similar in the katabatic case, while in the anabatic case they show more discrepancies, especially in the results obtained with k–ω SST, which show a smoother temperature profile close to the ground, leading to a higher value of the along-slope flow velocity. As for the k–ε anabatic results, the temperature profile is the one showing a faster decrease in the near-ground area, but then, above ≈15 m, temperature decreases slower than with any other RANS method. This leads to the lowest absolute peak value of velocity (below 3 m/s vs above 3.5m/s for the other methods), but then the absolute velocity value decreases slower than with the other RANS methods.

Figure 7 shows the along-slope velocity u at mid-slope, at different slope-normal distances, for the four tested turbulence models. This representation can be useful when thinking of wind energy applications, in order to get an estimation of the magnitude of the thermally-driven wind speed for different heights. For instance, all results show that,

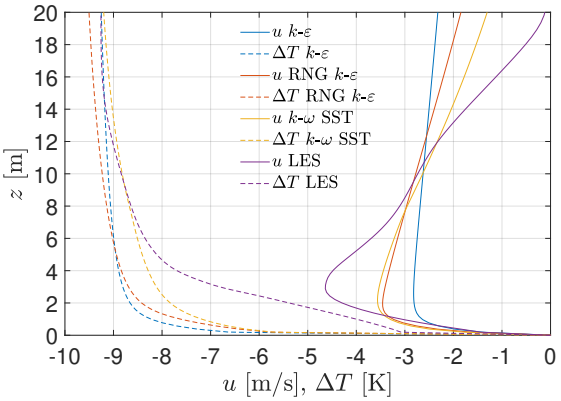

Figure 6. Anabatic flow: along-slope velocity u and ΔT profiles at 18 h (day2) for the tested turbulence models

for z between 5 and 10 m, katabatic velocities remain extremely low (≈1 m/s). Wind energy generation could only be envisaged in the current configuration (no synoptic wind considered, slope angle of 20°, diurnal temperature difference between the slope and the air of 20 K, etc.) during the anabatic phase (velocities around 2 or 3 m/s) with small wind turbines. As for the differences observed in the results obtained with the four tested turbulence models, again, LES (Fig. 7d) and (to a less extent) RNG k–ε (Fig. 7b) results show more oscillations in the velocity profile, while k–ε (Fig. 7a) and k–ω SST (Fig. 7c) show similar, smoother profiles. Again, k–ω SST leads to higher (in absolute terms) values of the along-slope flow velocity, especially at low slope-normal distance (z = 2.5 and z = 5 m). The decrease of velocity with z is very fast with LES (u remains close to 0 all the time for z > 20 m), and quite fast also with RNG k–ε and k–ω SST models. With the k–ε model, the shape of the velocity profile at 40 m is similar to the one at lower values of z, given that, as also observed in Fig. 6, the decrease of velocity with z is much slower.

4. CONCLUSIONS

This work reports a preliminary comparison of turbulent models used with OpenFOAM for studying the diurnal cycle of thermally-driven winds in mountain-valley systems. Our results suggest that k–ε and k–ω SST models are the most promising models, with a small advantage to k–ω SST for the near wall simulation, as it gives a smoother temperature transition away from the slope (especially in the anabatic phase), leading to more realistic vertical profiles of along-slope flow velocity. As for k–ε, it leads to a much slower decrease of velocity when going away from the ground. LES model was able to simulate this type of winds but complementary simulations using finer mesh are needed to confirm its suitability. In next steps, the results obtained for these idealised mountain-valley systems with RANS

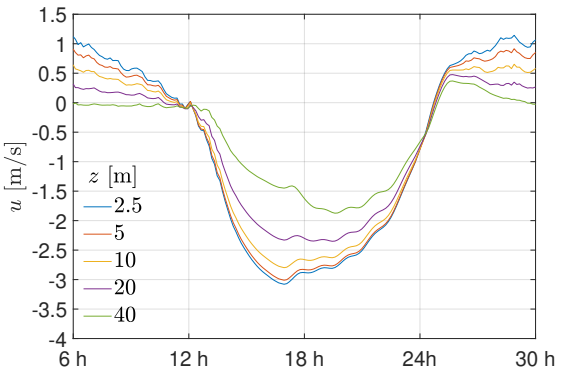

(a) k-ε

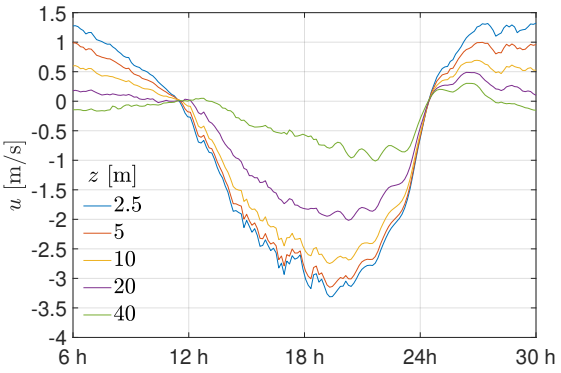

(b) RNG k-ε

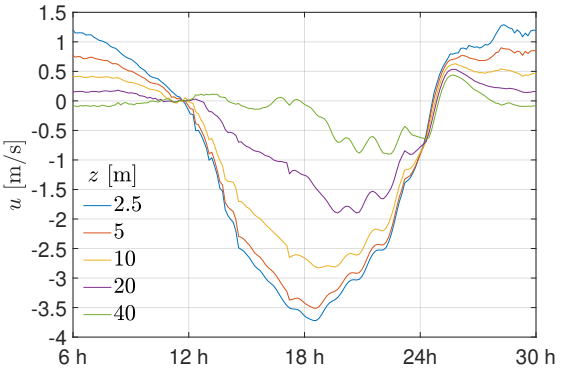

(c) k-ω SST

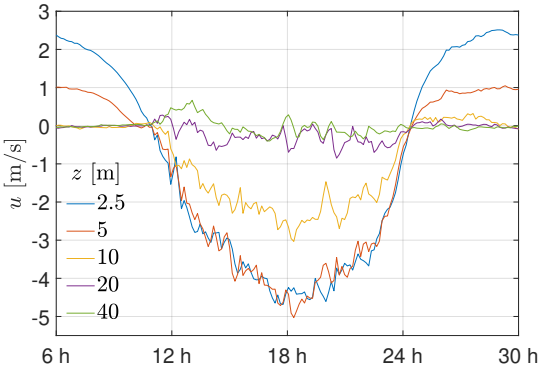

(d) LES

Figure 7. Along-slope velocity u at mid-slope, at different slope-normal distances, for the tested turbulence models

and LES models will be validated against direct numerical simulations (DNS), as well as against results from suitable experimental campaigns reported in the literature [37, 38, 36].

ACKNOWLEDGEMENTS

This work is supported by the project PID2019-105162RB-I00 funded by MCIN/AEI/10.13039/501100011033 and by the project 2017 SGR 1278 from the AGAUR *Generalitat de Catalunya*.

REFERENCES

[1] Balogh, M. G., Parente, A., and Benocci, C., 2012, "RANS simulation of ABL flow over complex terrains applying an enhanced k-epsilon model and wall function formulation: Implementation and comparison for Fluent and OpenFOAM", *J Wind Eng Ind Aerodyn*, Vol. 104–106, pp. 360–368.

[2] Axelsen, S. L., and van Dop, H., 2009, "Large-eddy simulation of katabatic winds. Part 2: Sensitivity study and comparison with analytical models", *Acta Geo*, Vol. 57, pp. 837–856.

[3] Alinot, C., and Masson, C., 2005, "k-epsilon model for the atmospheric boundary layer under various thermal stratifications", *J Sol Energy Eng ASME*, Vol. 127, pp. 438–443.

[4] An, K., Fung, J. C. H., and Yim, S. H. L., 2013, "Sensitivity of inflow boundary conditions on downstream wind and turbulence profiles through building obstacles using a CFD approach", *J Wind Eng Ind Aerodyn*, Vol. 115, pp. 137–149.

[5] Batt, R., Gant, S. E., Lacome, J.-M., and Truchot, B., 2016, "Modelling of stably-stratified atmospheric boundary layers with commercial CFD software for use in risk assessment", *Proc 15th Int Symp Loss Prev Saf Promot, Chem Eng Trans*, Freiburg, Germany, pp. 61–66.

[6] Franke, J., Sturm, M., and Kalmbach, C., 2012, "Validation of OpenFOAM 1.6.x with the German VDI guideline for obstacle resolving micro-scale models", *J Wind Eng Ind Aerodyn*, Vol. 104–106, pp. 350–359.

[7] Bautista, M. C., 2015, "Turbulence Modelling of the Atmospheric Boundary Layer over Complex Topography", Ph.D. thesis, Université de Québec, École de Technologie Supérieure.

[8] Hu, P., Li, Y., Cai, C. S., Liao, H., and Xu, G. J., 2013, "Numerical simulation of the neutral equilibrium atmospheric boundary layer using the SST k–ω turbulence model", *Wind Struct*, Vol. 17, pp. 87–105.

[9] Yang, Y., Xie, Z., and Gu, M., 2017, "Consistent inflow boundary conditions for modelling the neutral equilibrium atmospheric boundary layer for the SST k–ω model", *Wind Struct*, pp. 465–480.

[10] Hamisu, M. T., Jamil, M. M., Umar, U. S., and Sa'ad, A., 2019, "Numerical study of flow in asymmetric 2D plane diffusers with different inlet channel lengths", *CFD Lett*, Vol. 11, pp. 1–21.

[11] Michalcová, V., Lausová, L., Skotnicová, I., and Pospísil, S., 2017, "Computational simulations of the thermally stratified atmospheric boundary layer above hills", *Procedia Eng*, Vol. 190, pp. 134–139.

[12] Samala, B. P. R., 2016, "Active Flow Control of Boundary Layer Separation on Airfoils Using Fluidic Oscillators", Ph.D. thesis, Universitat Politècnica de Catalunya, Dept. of Physics.

[13] Bhuiyan, A. A., Karim, R. M., Hart, J. T., Rahman, M. M., and Naser, J., 2016, "Experimental and numerical investigation of coherent structure dynamics on mass transfer in a separated cavity flow", *Exp Therm Fluid Sci*, Vol. 76, pp. 146–162.

[14] Flores, F., Garreaud, R., and Muñoz, R. C., 2014, "OpenFOAM applied to the CFD simulation of turbulent buoyant atmospheric flows and pollutant dispersion inside large open pit mines under intense insolation", *Comput Fluids*, Vol. 90, pp. 72–87.

[15] Flores, F., Garreaud, R., and Muñoz, R. C., 2013, "CFD simulations of turbulent buoyant atmospheric flows over complex geometry: solver development in OpenFOAM", *Comput Fluids*, Vol. 82, pp. 1–13.

[16] Pereira, F. S., Grinstein, F. F., Israel, D. M., Rauenzahn, R., and Girimaji, S. S., 2021, "Modeling and simulation of transitional Taylor-Green vortex flow with partially averaged Navier-Stokes equations", *Phys Rev Fluids*, Vol. 6, p. 054611.

[17] Garcia, M., and Boulanger, P., 2006, "Low altitude wind simulation over Mount Saint Helens using NASA SRTM digital terrain model", *Proc 3rd Int Symp 3D Data Proces, Visualiz, Trans*, Univ North Carolina, Chapel Hill, USA.

[18] Hussein, A. S., and El-Shishiny, H., 2009, "Influences of wind flow over heritage sites: a case study of the wind environment over the Giza Plateau in Egypt", *Environ Modell Software*, Vol. 24, pp. 389–410.

[19] Garcia, M., and al., 2008, "CFD analysis of the effect on buoyancy due to terrain temperature based on an integrated DEM and Landsat infrared imagery", *Ing Cienc*, Vol. 4, pp. 65–84.

[20] Pedruelo, X., 2009, "Modelling of wind flow over complex terrain using OpenFOAM", Ph.D. thesis, Dept Technol Built Environ, University of Gavle.

[21] Churchfield, M., 2010, "A description of the OpenFOAM solver buoyantboussinesqpisofoam", *Tech. rep.*, National Renewable Energy Laboratory, National Wind Technology Center.

[22] Majander, P., and Siikonen, T., 2002, "Evaluation of Smagorinsky-based subgrid-scale models in a finite-volume computation", *Int J Numer Methods Fluids*, Vol. 40, pp. 735–744.

[23] Cao, S., Wang, T., Ge, Y., and Tamura, Y., 2012, "Numerical study on turbulent boundary layers over two-dimensional hills - Effects of surface roughness and slope", *J Wind Eng Ind Aerodyn*, Vol. 104, pp. 342–349.

[24] Athota, R. B., Rojas, J. I., Arias, S., and Montlaur, A., 2022, "Simulations of thermal wind formation in idealised mountain-valley systems using OpenFOAM", Available at SSRN: `https://ssrn.com/abstract=4086430` or `https://dx.doi.org/10.2139/ssrn.4086430`.

[25] Athota, R. B., Rojas, J. I., and Montlaur, A., 2021, "OpenFOAM computational fluid dynamics simulations of thermal wind generation in mountain/valley configurations", *14*$^{\text{eff}}$ *WCCM & ECCOMAS Congress*.

[26] Axelsen, S. L., and van Dop, H., 2009, "Large-eddy simulation of katabatic winds. Part 1: Comparison with observations", *Acta Geophys*, Vol. 57, pp. 803–836.

[27] Brun, C., Blein, S., and Chollet, J., 2017, "Large-eddy simulation of a katabatic jet along a convexly curved slope. Part I: Statistical results", *J Atmos Sci*, Vol. 74, pp. 4047–4073.

[28] Fedorovich, E., and Shapiro, A., 2009, "Structure of numerically simulated katabatic and anabatic flows along steep slopes", *Acta Geo*, Vol. 57, pp. 981–1010.

[29] Shapiro, A., Burkholder, B., and Fedorovich, E., 2012, "Analytical and numerical investigation of two-dimensional katabatic flow resulting from local surface cooling", *Boundary-Layer Meteorol*, Vol. 145, pp. 249–272.

[30] Giometto, M. G., Katul, G. G., Fang, J., and Parlange, M. B., 2017, "Direct numerical simulation of turbulent slope flows up to Grashof number $Gr = 2.1 \times 10^{11}$", *J Fluid Mech*, Vol. 829, pp. 589–620.

[31] Richards, P., and Hoxey, R., 1993, "Appropriate boundary conditions for computational wind engineering models using the k—e turbulence model", *J Wind Eng Ind Aerodyn*, Vol. 47, p. 145–153.

[32] Richards, P. J., and Norris, S. E., 2011, "Appropriate boundary conditions for computational wind engineering models revisited", *J Wind Eng Ind Aerodyn*, Vol. 99, pp. 257–266.

[33] Svensson, G., Holtslag, A. A. M., Kumar, V., Mauritsen, T., Steeneveld, G. J., Angevine, W. M., Bazile, E., Beljaars, A., de Bruijn, E. I. F., Cheng, A., Conangla, L., Cuxart, J., Ek, M., Falk, M. J., Freedman, F., Kitagawa, H., Larson, V. E., Lock, A., Mailhot, J., Masson, V., Park, S., Pleim, J., Söderberg, S., Weng, W., and Zampieri, M., 2011, "Evaluation of the diurnal cycle in the atmospheric boundary layer over land as represented by a variety of single-column models: The second GABLS experiment", *Boundary-Layer Meteorol*, Vol. 140, pp. 177–206.

[34] Giovannini, L., Laiti, L. Serafin, S., and Zardi, D., 2017, "he thermally driven diurnal wind system of the Adige Valley in the Italian Alps", *Q J R Meteorol Soc*, Vol. 143, pp. 2389–2402.

[35] Barcons, J., Avila, M., and Folch, A., 2019, "Diurnal cycle RANS simulations applied to wind resource assessment", *Wind Energy*, Vol. 22, pp. 269–282.

[36] Román-Gascón, C., Yagüe, C., Arrillaga, J. A., Lothon, M., Pardyjak, E. R., Lohou, F., Inclán, R. M., Sastre, M., Maqueda, G., Derrien, S., Meyerfeld, Y., Hang, C., Campargue-Rodríguez, P., and Turki, I., 2019, "Comparing mountain breezes and their impacts on CO_2 mixing ratios at three contrasting areas", *Atmos Res*, Vol. 221, pp. 111–126.

[37] Charrondière, C., Brun, C., Sicart, J., Cohard, J., Biron, R., and Blein, S., 2020, "Buoyancy effects in the turbulence kinetic energy budget and Reynolds stress budget for a katabatic jet over a steep Alpine slope", *Boundary-Layer Meteorol*, Vol. 177, pp. 97–122.

[38] Charrondière, C., Brun, C., Cohard, J., Sicart, J., Obligado, M., Biron, R., Coulaud, C., and Guyard, H., 2022, "Katabatic winds over steep slopes: Overview of a field experiment designed to investigate slope-normal velocity and near-surface turbulence", *Boundary-Layer Meteorol*, Vol. 182, pp. 29–54.

Conference on Modelling Fluid Flow (CMFF'22)
The 18th International Conference on Fluid Flow Technologies
Budapest, Hungary, August 30-September 2, 2022

NUMERICAL MODELLING OF ICE DEPOSITION IN A LYOPHILIZER CONDENSER

Blaž KAMENIK[1], Matjaž HRIBERŠEK[2], Matej ZADRAVEC[3]

[1] Chair for Power, Process and Environmental Engineering, Faculty of Mechanical Engineering, University of Maribor. E-mail: blaz.kamenik@um.si
[2] Chair for Power, Process and Environmental Engineering, Faculty of Mechanical Engineering, University of Maribor. E-mail: matjaz.hribersek@um.si
[3] Corresponding Author. Chair for Power, Process and Environmental Engineering, Faculty of Mechanical Engineering, University of Maribor.Smetanova ulica 17, 2000 Maribor, Slovenia. Tel: +386 (2) 220 7783, E-mail: matej.zadravec@um.si

ABSTRACT

Freeze drying is a form of drying in which the product is dried at low temperatures and low pressure. In order not to damage the vacuum pump that maintains the set system pressure, the water vapour is directed to the condenser where it is removed by the process of deposition (phase change from vapour to solid). Current research focuses on numerical modelling of ice deposition in a condenser. The process is modelled as a volumetric sink of water vapour in the first cell adjacent to the cooled wall. The ice deposition model was developed in Ansys Fluent using user-defined functions (UDF-s). The advantage of such an approach is that the modelling boundary of the lyophilization process is moved from the drying chamber, where most of the current simulation domain ends with a pressure boundary condition, to the condenser, in the outlet pipe leading to the vacuum pump. This eliminates the need to define boundary conditions in the connecting pipe between the drying chamber and the condenser, which is usually the boundary of the modelling domain in the current numerical models. To validate the developed numerical model, an experiment was performed on a laboratory device to determine the kinetics of ice sublimation using an ice tray.

Keywords: Computational fluid dynamics, Freeze-drying, Ice deposition, Lyophilization, Mathematical modeling

NOMENCLATURE

E	$[J/kg]$	energy
S_h	$[W/(m^3)]$	energy source
S_m	$[kg/(m^3 s)]$	mass source
T	$[K]$	temperature
U	$[m/s]$	velocity in x direction
V	$[m/s]$	velocity in y direction
W	$[m/s]$	velocity in z direction
p	$[Pa]$	pressure
t	$[s]$	time
$\underline{F}$	$[kg/(m^2 s^2)]$	external body forces
$\underline{g}$	$[m/s^2]$	gravitational acceleration
$\underline{u}$	$[m/s]$	velocity vector
ρ	$[kg/m^3]$	density

1. INTRODUCTION

Freeze drying is a form of drying in which water is removed from a frozen product by a sublimation process at low pressure. The product is usually found in pharmacies (active pharmaceutical ingredients - API) in vials or other glass packaging. In the food industry, the product trays are loaded directly onto temperature-controlled shelves inside the drying chamber. After the freezing phase, the process of ice sublimation (release of water vapor) begins when the system pressure drops and heat is supplied from the shelves. The water vapor then flows through the connecting pipe to the condenser, where ice deposition (freezing of water vapor) takes place on the cold walls. In this case, it is a phase transition, where the gas passes directly to the solid phase without passing through the liquid phase. The rest of the moisture, which is not removed, travels together with the inert gas through the outlet or the pipe connected to the vacuum pump. Experimental determination of drying kinetics is often very time-consuming because of the problems of transferring cycles between devices of different sizes, or it is not feasible because of the consumption of an expensive product. Much effort is put into numerical modelling of the time-dependent drying process inside the vial, with models of varying complexity. Various geometric approximations for vials are used, ranging from 0D models [1] to 1D models [2] to 2D axisymmetric vial models [3, 4]. Due to rarefied gas flow conditions, the focus is on developing models to describe the heat transfer to the vial, i.e., to determine the K_v values [5, 6]. The design of the connecting pipe between the drying chamber and the condenser has a significant impact on the process, as choked flow can occur. This happens when the mass flow of water vapor through the

connecting pipe is very high and the velocity of the water vapor reaches the speed of sound. In this case, the pressure in the chamber begins to rise, resulting in an increased heat supply to the product and increasing the possibility of product collapse. This is avoided by using more conservative drying cycles, which increase the drying time. Because of the tendency to optimize drying with more aggressive drying cycles, it is necessary to know the conditions under which choked flow occurs and the effect of system geometry on the process. All these effects are difficult to evaluate experimentally (or are time consuming for all possible cycles), so numerical simulations are increasingly used to study the phenomenon. Due to the low system pressures typical of freeze-drying processes, a fluid slip can occur on the solid walls due to incomplete momentum accommodation of the gas molecules, and a temperature jump can occur. This raises the question of the validity of the continuum modeling approach on which the computational fluid dynamics (CFD) codes used to solve 3D flows are based. However, at lower degrees of rarefaction, it is possible to model fluid flows with continuum-based transport equations (Navier-Stokes equations) if the boundary conditions at the solid walls are adjusted accordingly [7]. Examples of such an approach are the numerical models that study the effects of the geometry and position of the valves [8], the deposition of ice on the cold surfaces of the condenser [9], and the choked flow [10]. [11], which give us additional insight into the hydrodynamic conditions within the system.

In the work of Patel et al. [10], which presents a model for predicting and studying the conditions under which choked flow occurs, the boundary of the modeling is the condenser inlet, without modeling the process of ice deposition on the cold walls of the condenser, which would fully describe the process numerically, which is the case addressed in this work.

2. NUMERICAL MODEL

In the present work, the focus is on modeling the ice deposition process on the cold walls of the condenser. The commercial software ANSYS Fluent was used to simulate the gas flow within the system, with which additional volume sinks were programmed via user-defined functions (parts of the programmed C code, UDF).

2.1. Governing equations and numerical model

The governing equations solved by the ANSYS Fluent software, in which the ice deposition model was added over user defined program functions, describe the fundamental physical laws in fluids. The equation for the conservation of mass (continuity equation) is as follows [12]:

$$\frac{\partial \rho}{\partial t} + \nabla \cdot (\rho \underline{u}) = S_m, \tag{1}$$

where S_m represents the mass source. Momentum conservation is in following form [12]:

$$\frac{\partial (\rho \underline{u})}{\partial t} + \nabla \cdot (\rho \underline{u}\underline{u}) = -\nabla p + \nabla \cdot (\tau) + \rho \underline{g} + \underline{F}, \tag{2}$$

where $\underline{F}$ represents external body forces. In software package ANSYS Fluent, the energy conservation law is considered in following form [12]:

$$\frac{\partial (\rho E)}{\partial t} + \nabla \cdot (\underline{u}(\rho E + p)) = \nabla \cdot \left(k \nabla T - \sum_i h_i \underline{J_i} + (\tau_{eff} \cdot \underline{u}) \right) + S_h, \tag{3}$$

where E is the total energy, k is the thermal conductivity, and $\underline{J_i}$ represents component diffusion in multi-component flow of i components. The first term on the right side of the equation stands for the energy transfer by conduction, the second for the diffusion of the components in multi-component flow and the third for the viscous dissipation. The term S_h represents the energy source (e.g., energy source from chemical reactions or other volumetric sources). Total energy E is calculated as

$$E = h - p/\rho + u^2/2 \tag{4}$$

where h is the sensible enthalpy. To calculate the density of a multi-component compressible gas, an ideal gas model is used that calculates the density according to the following equation

$$\rho = \frac{p_{op} + p}{RT \sum_i \frac{Y_i}{M_{w,i}}}, \tag{5}$$

where p is assumed to be the local relative pressure, p_{op} operating pressure, Y_i mass fraction of the i-th component, and $M_{w,i}$ molar mass of the i-th component. Due to the low system pressures, the model also uses the Maxwell model of fluid slip on the wall.

2.2. Model of ice deposition

In the literature, we do not find many examples of modeling ice deposition on cold condenser walls. Examples of this type of modeling is work of Petitti et all [9] and Sarjas's master's thesis [13], in which ice deposition is described by first-order kinetics.

$$j = k \rho \epsilon_v A, \tag{6}$$

where j is the mass flow density of desublimated water vapor [kg/s], A is the wall surface area, k is the reaction rate constant [m/s], ρ the gas density, and ϵ_v the mass fraction of water vapor. In both cases described in this work, it is also assumed that the condenser is appropriately sized and that the temperature of the cooled walls of the condenser remains constant during the deposition. In this case, the deposition rate depends only on the density, the mass fraction of the water vapor, and the empirical constant k. In the following, we present a mechanistic model of ice deposition that allows us to avoid using an empirical model.

The process of ice deposition is modeled as uni-

lateral diffusion of water vapor in the normal direction to the cold walls of the condenser in the following form [14]:

$$\underline{J_v} = \frac{C_v}{C_v + C_i}\underline{J_v} - D_{v,i}\nabla C_v. \tag{7}$$

where the $\underline{J_v}$ represents the molar desublimation flux, ∇C_v the concentration gradient, C_v the water vapor concentration, C_i the inert gas concentration, and $D_{v,i}$ the diffusivity of the binary mixture of water vapor and inert gas. In the direction z, perpendicular to the surface of the cold wall of the condenser (local), the molar flux of the water vapor is [14]:

$$J_v = \frac{C_v}{C_v + C_i}J_v - D_{v,i}\frac{dC_v}{dz}. \tag{8}$$

Concentrations are replaced by partial pressures using the ideal gas equation

$$p_v = C_v RT, \tag{9}$$

and the equation for the molar flow with partial pressures is as follows

$$J_v = \frac{p_v}{p_v + p_i}J_v - \frac{D_{v,i}}{RT}\frac{dp_v}{dz}. \tag{10}$$

The diffusivity of water vapour in a binary mixture is calculated according to the theory of diffusion in gases at low densities [14] as:

$$D_{v,i} = 0.01883\frac{\sqrt{T^3\left(\frac{1}{M_v} + \frac{1}{M_i}\right)}}{(p_i + p_v)\sigma_{vi}^2\Omega_D}. \tag{11}$$

Here Ω_D is the integral of the collision energy of the molecules in T gas temperature. The Lennard-Jones parameters for a binary mixture are

$$\sigma_{vi} = \frac{\sigma_v + \sigma_i}{2}, \qquad \epsilon_{vi} = \sqrt{\epsilon_v \epsilon_i}. \tag{12}$$

Here the collision diameter for water vapor is σ_v = 3.737 Å and for inert gas σ_i = 3.771 Å. If we substitute the equation (11) into the equation (10), we obtain

$$p_i J_v = -0.01883\frac{\sqrt{T\left(\frac{1}{M_v} + \frac{1}{M_i}\right)}}{R\sigma_{vi}^2\Omega_D}\frac{dp_v}{dz}. \tag{13}$$

To obtain the molar current, an integration from the center of the cell ($p_{v,g}$) to the cold wall of the condenser is necessary ($p_{v,i} = p_v^\star$),

$$J_v\int_0^h dz = -0.01883\frac{\sqrt{T\left(\frac{1}{M_v} + \frac{1}{M_i}\right)}}{p_i R\sigma_{vi}^2\Omega_D}\int_{p_{v,g}}^{p_{v,i}} dp_v, \tag{14}$$

where the water vapor pressure just above the ice (saturation pressure) $p_{v,i}$ is calculated from Clausius-Clapeyron relation

$$p_{v,i} = \exp\left(28.8912 - \frac{6139.6}{T_i}\right) \tag{15}$$

Where T_i is the temperature of the cold wall of the condenser. The final expression to calculate the molar flow is as follows

$$J_v = -0.01883\frac{\sqrt{T\left(\frac{1}{M_v} + \frac{1}{M_i}\right)}}{p_i R\sigma_{vi}^2\Omega_D}\frac{p_{v,i} - p_{v,g}}{h}. \tag{16}$$

The water vapor sink due to the deposition process S_m, which takes place on the cold walls of the condenser, is modeled as a volume sink in the following form

$$S_m = J_v M_{H_2O}\frac{\delta A}{\delta V}, \tag{17}$$

where δA is the cell face area of the cold wall and δV is the volume of the first cell near the interface, J_v is the molar flux in the direction from the center of the first cell near the wall (where the water vapor is present) to the center of the wall surface (condenser wall). The equation in this form, with units $kg/(m^3 s)$, represents the mass of water vapor removed per unit time from the cell near the wall by the process of desublimation. At the interface where the water vapor freezes, there is a loss of momentum, which in this case is considered in the equation of conservation of momentum as a sink in the following form for all three directions

$$F_U = US_m, F_V = VS_m, F_W = WS_m, \tag{18}$$

here U, V, W stand for the velocities in the x, y, and z directions. The deposition process removes heat from the gas region, which is modeled as an additional sink in the energy conservation equation S_h

$$S_h = S_m h_v = \int_{T_g}^{T_i} c_{p,v} dT, \tag{19}$$

where h_v is the sensitive enthalpy of water vapor.

2.2.1. Material properties

The following material properties were used for the calculation. For water vapor, the following values are used: Molar mass 18.015 kg/kmol, characteristic length σ = 2.605 Å, energy parameter ϵ/k_b = 572.5 K, energy accommodation coefficient α_c = 0.48, tangential accommodation coefficient α_t = 0.91 and specific heat $c_{p,v}$ = 1859 J/(kgK). For inert gas (nitrogen) the following values are used: Molar mass 28.0134 kg/kmol, characteristic length σ = 3.798 Å, energy parameter ϵ/k_b = 71 K, energy accommodation coefficient α_c = 0.45, tangential accommodation coefficient α_t = 0.91 and specific heat $c_{p,v}$ = 1006 J/(kgK). For viscosity, in both cases, the power relation $\mu = \mu_{ref}(T/T_{ref})^n$ (power law) is used with the values for water $\mu_0 = 8.9e-06\ Pa\cdot s$,$T_{ref}$ = 273 K in n = 1 [15], and for nitrogen $\mu_0 = 1.66e-05\ Pa\cdot$ s, T_{ref} = 273 K in n = 0.74 [15].

2.3. Geometry and boundary conditions

The geometry of the system under consideration is shown in Figure 1. The overall geometry of the system is modeled such that the modeling boundary is the condenser outlet tube (through which in-

ert gas and remaining water vapor are discharged). The model consists of a drying chamber (height 0.21 m, width 0.34 m and depth 0.39 m) where a pipe is placed through which inert gas is fed into the chamber to maintain the set pressure in the chamber, two shelves with dimensions $0.3x0.3$ m (the trays are at the bottom and upper shelf), a condenser with a diameter of 0.2 m (in which ice is deposited), a connecting duct between the chamber and a condenser with a diameter of 0.072 m, and a valve located in a connecting duct.

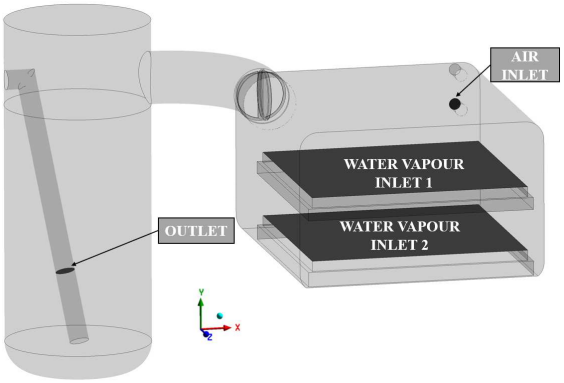

Figure 1. Geometry of the freeze dryer and the main elements of the numerical model (main surfaces where the boundary conditions are specified).

An estimated value at the outlet was prescribed for the operating pressure, namely 1.5 Pa (gauge pressure 0 Pa with reference/operating pressure of 1.5 Pa). On the surfaces of the shelf, a temperature of $-8\ ^oC$ was prescribed, corresponding to the experimental temperature of the shelf walls in the selected interval, on the surface where ice is deposited $-60\ ^oC$, the other surfaces being adiabatic. On the surfaces " water vapor inlet 1 and 2 ", which represent the sublimation fronts, the prescribed mass flow of water vapor was $1.2 \cdot 10^{-5}$ kg/s, where the UDF function calculates the temperature of the gas from the pressure over the sublimation surface (pressure in the first cell centers of the inlets) using the Clausius-Clapeyron relationship, and on the surface air inlet $1.7 \cdot 10^{-7}$ kg/s at temperature $20\ ^oC$ to account for the air intake due to system leakage. The sinks described in section 2.2 are prescribed in the first numerical cells located adjacent to the surface wall shown in Figure 2.

2.3.1. Numerical methods

The calculation is performed using the SIMPLE algorithm and the PRESTO! for the pressure discretization, with a second-order upwind scheme for density, momentum, component mass, and energy. Since the simulated material is a gas consisting of two components (H_2O vapour and N_2), a species transport model was used. Different laws were used to calculate the properties of the mixture. The law

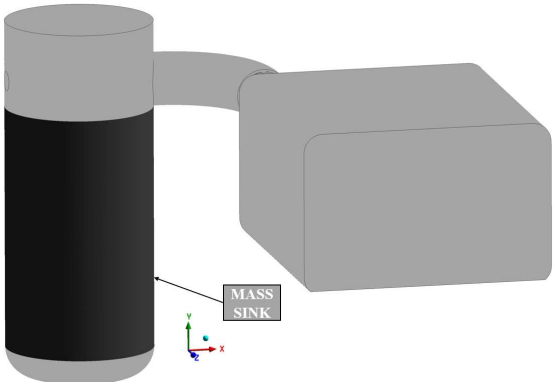

Figure 2. Surface where the process of deposition of the ice takes place (perscribed mass sinks).

of mixture was used for the specific heat, the law of ideal gas mixture was used for the thermal conductivity and viscosity, and kinetic theory was used to calculate the diffusivity between the components.

Three computational grid densities were considered and validated, leading to the final grid with 1.5 million polyhedral elements for performing the CFD computations. The convergence criterion was set at RMS of 10^{-6} for continuity, momentum and energy equations.

3. CONDENSER PRESSURE MEASUREMENT

To determine the relationship between chamber pressure and condenser pressure, experiments were conducted using a laboratory-scale LIO-2000 FLT freeze dryer manufactured by Kambic. The freeze dryer has two temperature-regulated shelves (from -40 to $+40^oC$), with a distance between the shelves of 71.5 mm, each with a shelf area of about 0.09 m^2 (width and length of 300 mm), and the minimum achievable pressure in the drying chamber is 1 Pa. The drying chamber is connected to the condenser by a connecting duct, where the butterfly valve is installed. The condenser has a cylindrical shape and a capacity of 5 kg of ice.

3.1. Experimental Protocol

Since the objective of the experiment was to determine the ratio between chamber and condenser pressures, water runs were performed. Two steel trays (width and length of 300 mm) were filled with distilled water and placed on the shelves. The freezing step lasted 6 hours at a shelf temperature of -35^oC, then the temperature of the shelf was lowered to -40^oC and the chamber pressure was reduced to the minimum achievable pressure (about 1.5 Pa). Then the temperature of the shelf was increased to increase the mass flow rate of the sublimate. In this way, the chamber pressure began to increase as the flow through the duct was in choked flow regime (the water vapour reaches the speed of sound and cannot be accelerated further). To determine the chamber pres-

sure, the temperatures of the ice were also measured, from which the Clausius-Clapeyron relationship was used to calculate the pressure over the ice. In the condenser the pressure was measured with the capatice manometer. Temperatures were measured using type T thermocouples that were 0.5 mm thick. Data were collected using the National Instrument NI cDAQ-9174 system.

4. RESULTS

Figure 3 shows the streamlines of water vapor. We see that the velocity of the water vapor increases as the fluid moves through the valve opening and the connecting duct (the velocity at the exit of the duct reaches 1 Mach), which is followed by a decrease as the fluid enters the condenser. As the water vapor enters the condenser, it flows to the opposite wall where some of the vapor is diverted upward and some downward (to the bottom of the condenser). The water vapor is then removed on the walls where the sink is prescribed. The remaining water vapor and the inert gas exit through the outlet pipe.

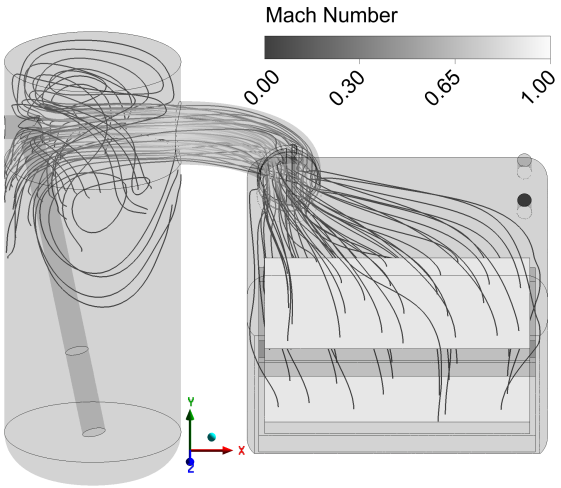

Figure 3. Streamlines of the water vapor from the inlet planes (sublimation surfaces) through the system.

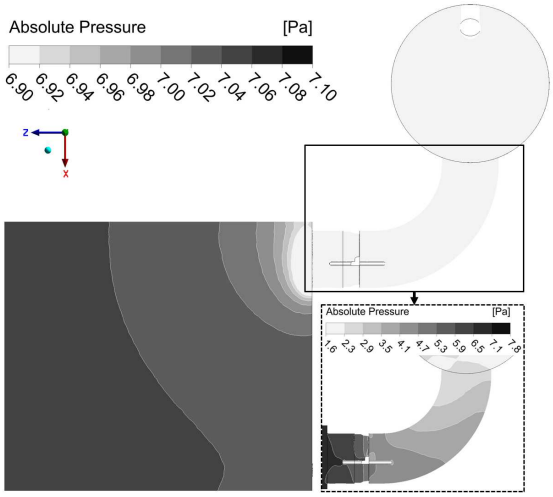

Figure 4. Pressure field in the sublimation chamber, the connecting channel and at the top of the condenser (above the mass sink).

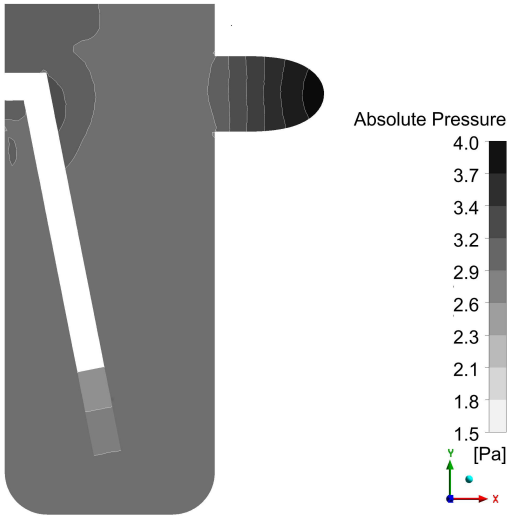

Figure 5. Pressure field in the condenser and the outlet pipe.

Figures 4 and 5 show the pressure field along the cross-sectional planes. The highest pressure occurs inside the chamber, where the water vapor inlets (sublimation fronts) and the pipe through which the inert gas is supplied are located. The pressure inside the chamber is uniform due to the choked flow regime. The pressure decreases through the connecting pipe towards the condenser. Inside the condenser, an almost uniform pressure is again observed, followed by a pressure drop in the outlet pipe.

Figures 6 and 7 show the velocity fields inside the system. As we can see, the water vapor velocities inside the chamber are relatively low, followed by a significant increase in velocity through the entrance to the connecting duct due to the reduction in cross-sectional area through which the fluid can move. As the fluid passes through the connecting valve, an asymmetric pattern is observed as the velocity in one opening formed by the valve is slightly higher than the other. The velocity downstream of the valve drops slightly, followed by a velocity increase toward the condenser where the fluid reaches the speed of sound (1 Mach). The fluid is then accelerated towards the opposite side of the condenser, where the outlet from the connecting duct is directed, in the condenser the velocity of the fluid is then reduced.

As can be seen in the Figure 8, which shows the deposition rate, the deposition rate is highest on the side opposite the inlet, or where the connecting duct is aligned (the water vapor entering the condenser moves in the direction dictated by the connecting

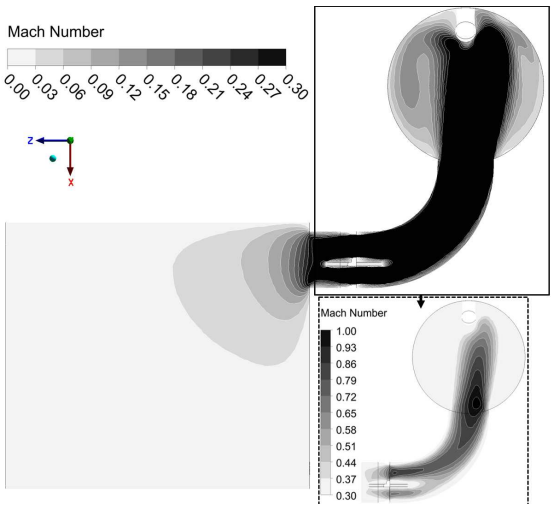

Figure 6. Velocity magnitude in the sublimation chamber, the connecting channel and at the top of the condenser (above the mass sink).

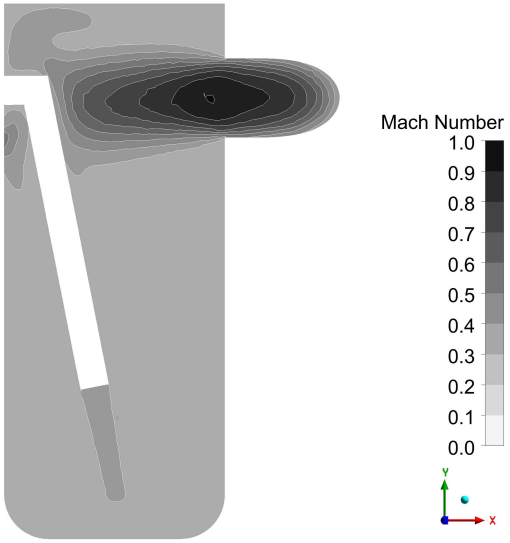

Figure 7. Velocity magnitude field in the condenser and the outlet pipe.

duct). The remaining water vapor deposits around the circumference, and toward the bottom of the condenser the deposition rate decreases.

The reason for the lower deposition rate is the lower concentration of water vapor, as you can see in the Figure 9, which shows the molar fraction of water vapor. This is highest at the inlet, where it is 0.97, and then decreases toward the bottom of the condenser to a value of about 0.2, which is due to the removal of water vapor by the process of deposition of ice.

4.1. Comparison with the experiment

The system pressure in the chamber predicted by the numerical model is 7.06 Pa and 2.26 Pa for

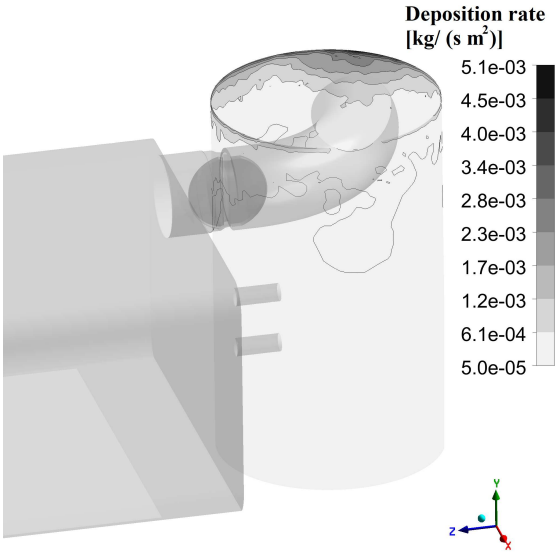

Figure 8. Deposition rates obtained with the numerical modelling.

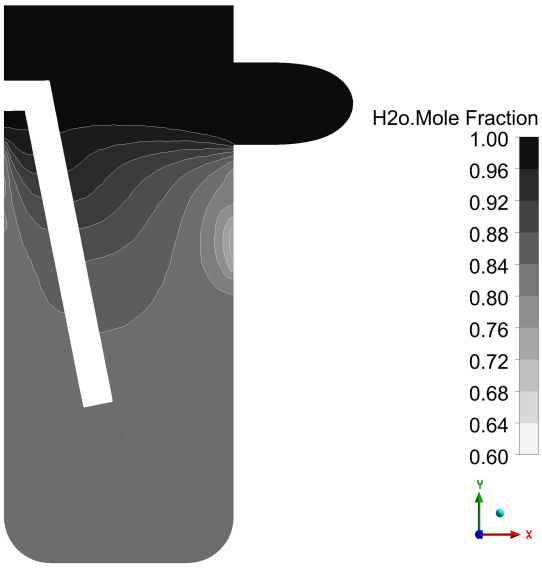

Figure 9. Molar fraction of water vapour in the condenser.

the pressure inside the condenser, which agrees well with the experiment where the average pressure in the chamber was 7.36 Pa and inside the condenser was 1.71 Pa. The results of the numerical model also allow us to determine the efficiency of the condenser η. This is calculated according to the following equation

$$\eta = \frac{\dot{m}_{in,H_2O} - \dot{m}_{out,H_2O}}{\dot{m}_{in,H_2O}} \tag{20}$$

In this case, the efficiency of the condenser is 98.6 %, indicating good efficiency in extracting water vapor from the system.

5. CONCLUSION

The paper presents a mechanistic model of ice deposition on cold walls of a condenser. The results of the numerical model show good qualitative agreement with experimental results, with the deposition rate being highest on the opposite side of the condenser inlet. The predicted ratio between chamber and condenser pressures measured in experiment and the numerical results show good agreement. The model will be used in the future to predict the phenomenon of choked flow, since this phenomenon is unacceptable due to the possibility of collapse of the product structure (excessive heat input into the product). In the future, modeled solid walls and a model of latent heat release during ice deposition will be added to the numerical model. Further experimental measurements will be performed to determine the mass flow rate of the sublimate and to measure the pressure ratios for further operating conditions.

ACKNOWLEDGEMENTS

The authors wish to thank the Slovenian Research Agency (ARRS) for the financial support in the framework of the Programme P2-0196 Research in Power, Process and Environmental Engineering.

REFERENCES

[1] Pikal, M., Roy, M., and Shah, S., 1984, "Mass and Heat Transfer in Vial Freeze-Drying of Pharmaceuticals: Role of the Vial", *Journal of Pharmaceutical Sciences*, Vol. 73 (9), pp. 1224–1237, URL https://www.sciencedirect.com/science/article/pii/S0022354915463026.

[2] Ravnik, J., Golobič, I., Sitar, A., Avanzo, M., Irman, Š., Kočevar, K., Cegnar, M., Zadravec, M., Ramšak, M., and Hriberšek, M., 2018, "Lyophilization model of mannitol water solution in a laboratory scale lyophilizer", *Journal of Drug Delivery Science and Technology*, Vol. 45, pp. 28–38, URL https://www.scopus.com/inward/record.uri?eid=2-s2.0-85042844902&doi=10.1016%2Fj.jddst.2018.02.015&partnerID=40&md5=728a4811f46bac7bb4fd6b210738001c.

[3] Zhai, S., Su, H., Taylor, R., and Slater, N. K., 2005, "Pure ice sublimation within vials in a laboratory lyophiliser; comparison of theory with experiment", *Chemical Engineering Science*, Vol. 60 (4), pp. 1167–1176.

[4] Ramšak, M., Ravnik, J., Zadravec, M., Hriberšek, M., and Iljaž, J., 2017, "Freeze-drying modeling of vial using BEM", *Engineering Analysis with Boundary Elements*, Vol. 77, pp. 145 – 156, URL http://www.sciencedirect.com/science/article/pii/S0955799716304301.

[5] Brülls, M., and Rasmuson, A., 2002, "Heat transfer in vial lyophilization", *International Journal of Pharmaceutics*, Vol. 246 (1), pp. 1 – 16, URL http://www.sciencedirect.com/science/article/pii/S0378517302003538.

[6] Scutellà, B., Passot, S., Bourlés, E., Fonseca, F., and Tréléa, I. C., 2017, "How Vial Geometry Variability Influences Heat Transfer and Product Temperature During Freeze-Drying", *Journal of Pharmaceutical Sciences*, Vol. 106 (3), pp. 770–778.

[7] Zhu, T., Moussa, E. M., Witting, M., Zhou, D., Sinha, K., Hirth, M., Gastens, M., Shang, S., Nere, N., Somashekar, S. C., Alexeenko, A., and Jameel, F., 2018, "Predictive models of lyophilization process for development, scale-up/tech transfer and manufacturing", *European Journal of Pharmaceutics and Biopharmaceutics*, Vol. 128 (January), pp. 363–378.

[8] Marchisio, D. L., Galan, M., and Barresi, A. A., 2018, "Use of computational fluid dynamics for improving freeze-dryers design and process understanding. Part 2: Condenser duct and valve modelling", *European Journal of Pharmaceutics and Biopharmaceutics*, Vol. 129 (January), pp. 45–57, URL https://doi.org/10.1016/j.ejpb.2018.05.003.

[9] Petitti, M., Barresi, A. A., and Marchisio, D. L., 2013, "CFD modelling of condensers for freeze-drying processes", *Sadhana - Academy Proceedings in Engineering Sciences*, Vol. 38 (6), pp. 1219–1239.

[10] Patel, S. M., Chaudhuri, S., and Pikal, M. J., 2010, "Choked flow and importance of Mach I in freeze-drying process design", *Chemical Engineering Science*, Vol. 65 (21), pp. 5716–5727, URL http://dx.doi.org/10.1016/j.ces.2010.07.024.

[11] Ganguly, A., Alexeenko, A. A., Schultz, S. G., and Kim, S. G., 2013, "Freeze-drying simulation framework coupling product attributes and equipment capability: Toward accelerating process by equipment modifications", *European Journal of Pharmaceutics and Biopharmaceutics*, Vol. 85 (2), pp. 223–235, URL http://dx.doi.org/10.1016/j.ejpb.2013.05.013.

[12] Inc., A., 2016, *ANSYS ® Academic Research, Release 17.2, Help System, Solver Theory, Multiphase Flow Theory*, ISBN 978-3-527-34306-5.

[13] Sarjaš, A., 2019, "Razvoj in numerična analiza kondenzatorja v procesu zamrzovalnega sušenja", Master's thesis, Univerza

v Mariboru, Fakulteta za strojništvo, URL https://dk.um.si/IzpisGradiva.php?lang=slv&id=74822.

[14] RB Bird, WE Stewart, E. L., 2007, *Transport phenomena*, Wiley.

[15] Ganguly, A., and Alexeenko, A. A., 2012, "Modeling and measurements of water-vapor flow and icing at low pressures with application to pharmaceutical freeze-drying", *International Journal of Heat and Mass Transfer*, Vol. 55 (21-22), pp. 5503–5513, URL http://dx.doi.org/10.1016/j.ijheatmasstransfer.2012.05.021.

Conference on Modelling Fluid Flow (CMFF'22)
The 18th International Conference on Fluid Flow Technologies
Budapest, Hungary, August 30 -September 2, 2022

ONE-DIMENSIONAL MODELLING OF THE ARTERY NETWORK USING THE METHOD OF CHARACTERISTICS WITH A LUMPED HEART

Richárd WÉBER[1], Dániel GYÜRKI[2], György PAÁL[3]

[1] Corresponding Author. Department of Hydrodynamic Systems, Faculty of Mechanical Engineering, Budapest University of Technology and Economics. Bertalan Lajos u. 4 – 6, H-1111 Budapest, Hungary. Tel.: +36 1 463 3484, E-mail: rweber@hds.bme.hu
[2] E-mail: dgyurki@hds.bme.hu
[3] E-mail: paal@hds.bme.hu

ABSTRACT

Since circulatory diseases are leading causes of death in high-income countries, and such disorders often originate from hemodynamic effects, arterial network modelling, which can support diagnostics or medical treatment, is relevant. Human blood circulation can be described using a one-dimensional (1D), distributed parameter model for the arterial network, and lumped models for the heart and peripheral effects. An extended method of characteristics is applied here to solve the momentum and mass conservation equations and the Poynting-Thomson model mimicking the material properties of arterial walls. The heart and the peripheral lumped models are solved with a general zero-dimensional (0D) linear solver handling the boundary conditions, i.e. characteristic equations from the 1D model. The 0D heart model consists of the left chamber and left atrium with mitral and aortic valves. While a capacitance-varying compliance element represents the elastance of the heart, the valves are modelled as check valves with diodes and resistances. A three-element Windkessel model is applied to approximate the effect of the different organs (e.g. kidney, spleen, liver) and peripheries. The model parameters are based on the literature suggestions and by validating the output data from the literature to obtain physiologically relevant results.

artery modelling, lumped heart, method of characteristics, one-dimensional

NOMENCLATURE

D	$[m]$	diameter
E	$[Pa]$	elastic modulus
p	$[Pa]$	static pressure
t	$[s]$	time
u	$[m/s]$	axial velocity
x	$[m]$	spatial coordinate
δ	$[m]$	wall thickness
ε	$[-]$	radial strain
η	$[Pas]$	viscoelastic damping factor
ν	$[m^2/s]$	kinematic viscosity
ρ	$[kg/m^3]$	density

Subscripts and Superscripts

0	nominal values
L	left characteristic point
R	right characteristic point
P	new characteristic point

1. INTRODUCTION

In understanding cardiovascular diseases in modern medicine, numerical simulation of blood flows is relevant. There are two directions of these simulations. Three-dimensional blood flow simulations concentrate on local flow structures in the vessels; many of these are in vessel wall anomalies, like aneurysms or stenoses. The advantage of these simulations is to understand better the small details of the flow and the effects of the malformation. The other direction is a low-dimensional modelling of the whole arterial system. These simulations can model the effect of local illnesses for the entire system or can create boundary conditions for the 3D simulations.

During the last decades, several journal papers were published by our research group on the modelling of the arterial system in one dimension, see, e.g. [1]. This research aims at continuing this low-level modelling approach and extend the modelled cardiovascular system with detailed peripherals, especially the heart. The new model creates more opportunities to analyse circulatory system diseases, such as heart malfunctions or organ failures.

2. MATHEMATICAL MODELLING

2.1. Method of characteristics

The traditional equations (mass balance and momentum) of fluid dynamics are solved, that is, the conservation of mass and momentum. Besides, the arterial wall is considered viscoelastic, described with a Poynting-Thomson model. Overall, Eq. (1) shows the modified mass balance equations.

$$2\frac{\partial \varepsilon}{\partial t} + 2u\frac{\partial \varepsilon}{\partial x} + (2\varepsilon + 1)\frac{\partial u}{\partial t} = 0 \tag{1}$$

The momentum equation is Eq. (2), assuming laminar flow and a circular cross section.

$$\frac{\partial u}{\partial t} + u\frac{\partial u}{\partial x} + \frac{1}{\rho}\frac{\partial p}{\partial x} + \frac{32\nu}{D^2}u = 0\,. \tag{2}$$

The equation of the Poynting-Thomson model can be found in Eqs. (3) to (5).

$$\frac{pD_0}{2\delta_0}(2\varepsilon + 1) = E_1\varepsilon_1 \tag{3}$$

$$\frac{pD_0}{2\delta_0}(2\varepsilon + 1) = E_2\varepsilon_2 + \eta_2\frac{d\varepsilon_2}{dt} \tag{4}$$

$$\varepsilon = \varepsilon_1 + \varepsilon_2 \tag{5}$$

While the "1" notation stands for the linear element of the Poynting-Thomson, the "2" indicates the viscoelastic property. The partial differential equations (PDE) are traditionally solved by the finite volume method in fluid mechanics, or nowadays, the finite element method is also applied. However, during this research, the method of characteristics has been used that transforms the PDEs to ordinary differential equations (ODE) along the characteristic lines. The ODE system can be transformed to algebraic equations with the explicit Euler technique, see Eqs. (6) and (7). The detailed description of the transformation can be found in [1].

$$v_P - v_L + \frac{1}{\rho a_L}(p_P - p_L) = -\Delta t J_L \tag{6}$$

$$v_P - v_R - \frac{1}{\rho a_R}(p_P - p_R) = -\Delta t J_R \tag{7}$$

The J_L and J_R are the source terms containing the geodetic height differences, the laminar pressure loss, and the viscoelastic vessel wall effect. The two unknown variables are at the P level, since every quantity is known at the L and R time level. For notations, see Fig. 1. The time step Δt is predefined by the characteristic lines, depending on the vessel's exact geometry (mainly the length) and the number of inner calculation points. Since a real arterial system contains numerous vessels, the common time step is the minimum amongst all the inner time steps.

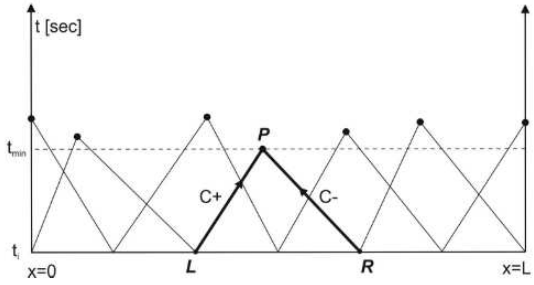

Figure 1. The method of characteristic [1].

Boundary conditions must be defined at each end of an edge, as there is only one characteristic line, and additional information is required from the surrounding of the vessel. For the inner nodes in the arterial system, see Fig. 3 white points, the continuity equation is solved. The peripherals and the heart are handled with lumped, zero-dimensional models.

2.2. Lumped Solver

As there are different models required to mimic the behaviour of different organs, such as the heart or the peripherals, a general lumped or zero-dimensional (0D) solver is relevant. Table 1 shows the type of elements a 0D model might include. All the components are linear, and either an algebraic equation or an ODE must be solved. The ODEs are transformed to algebraic ones using the explicit Euler formula.

Table 1. Elements of the 0D model with their continuous equation and parameter

Type	Parameter	Equation
Resistor	R	$\Delta p = Rq$
Capacitor	C	$q = C\frac{d\Delta p}{dt}$
Elastance	E_{min}, E_{max}	$q = \frac{d\left(\frac{\Delta p}{E(t)}\right)}{dt}$
Inductor	L	$\Delta p = L\frac{dq}{dt}$
Diode	R	$\Delta p = Rq$ and $q > 0$
Battery	V	$\Delta p = V$
Node	-	$\sum_{in} q_i - \sum_{out} q_i = 0$
Ground	-	$p = 0$

A speciality is the elastance for modelling the effect of the heart contraction. The elastance is the function of time, and it describes the pressure-volume relationship of the left chamber. It is general, as it is valid for every healthy adult regardless its age, weight or living habits [2]. Fig. 2 depicts the shape

as a function of time. There are only two parameters: the peak E_{max} and the minimum E_{min} [3].

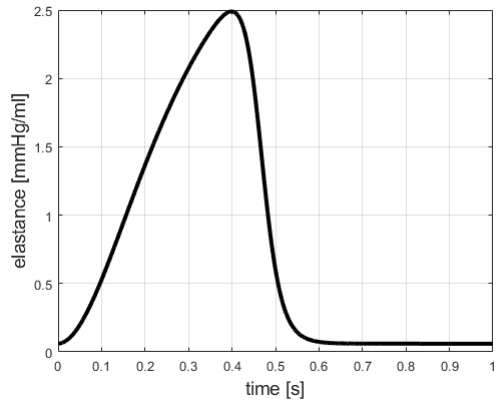

Figure 2. The time history of the elastance.

Although the elastance seems mathematically convenient: continuous, smooth and also differentiable multiple times, numerical instabilities occur during the solution of its equation (see Tab. 1). The appearance of the dE(t)/dt over E(t) lies behind this issue as the minimum value of E(t) is low, while the derivative can be high, especially at the beginning of the cycle. The matrix of the linear equation system would have a high conditional number, making it numerically unstable. One possible solution is to eliminate this term by introducing a new variable, that is $y=\Delta p/E$, as in [3].

The process of the combined 1D-0D solver is briefly the following. First, every inner point and inner boundaries are calculated in the 1D model, also the time step is determined. Second, the neighbouring characteristic equations from the 1D are added to the corresponding 0D equations and are solved together with 0D elements in one step.

3. MODEL BUILDING

3.1. Topology

The topology of the arterial system is based on the system presented in [4]. Beside the main arterial vessels, the brain is introduced in detail, see Fig. 3 top side. The circle of Willis is considered with most of the neighbouring arteries. Moreover, the spine and the arteries of the organs around the spine are also part of the model. The heart and the peripherals are built using 0D models according to [4,5], see Fig. 4.

The standard, three-element Windkessel model is applied for mimicking the peripheral effects of the arterial system. Although the structure of the heart is more complex, the mitral and aortic valves are modelled with an ideal diode and a resistance in series. While the diode serves the role of the check valve effect, i.e. it does not allow any backflow, the resistor causes the pressure loss at the valve. The two inductors mimic the inertia of the fluid. The left atrium pressure is prescribed by a battery or "voltage" component. In low-dimensional modelling, it is an acceptable approximation to keep the left atrium pressure constant. The elastance, i.e. a capacitor with variable parameters, is responsible for mimicking the contraction effect of the heart. Interestingly, it is the same function in time for all patients regardless of their age, weight or race.

3.2. Parameter Identification

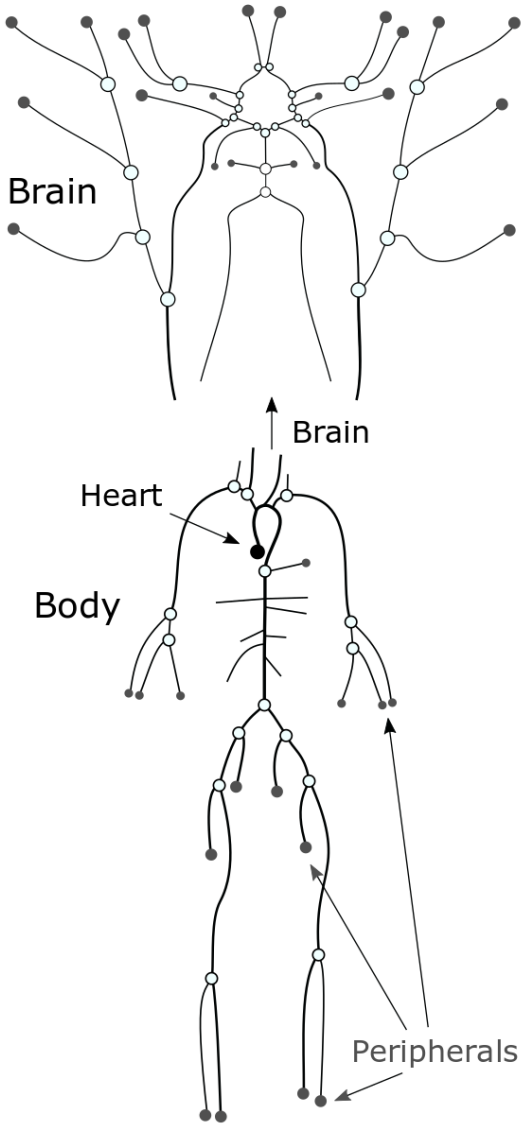

Figure 3. Main body and brain arteries. [4]

The biggest challenge in building a proper model for describing the arterial system is not the topology but determining the countless parameters. Each artery has five geometrical (length, proximal and distal diameter, proximal and distal thickness), three material wall parameters (two elasticities, damping factor), and the number of inner division points in the nine parameters. Moreover, the peripherals are modelled with a three-element Windkessel model; there are three independent parameters. Finally, the

heart is built using two resistors, one capacitor, one elastance and two inductors; overall, it means seven independent parameters. There are 99 arteries and 44 peripherals, meaning the number of all parameters is 99*9+44*3+7=1030. The question is how to choose these to have physiologically relevant outputs?

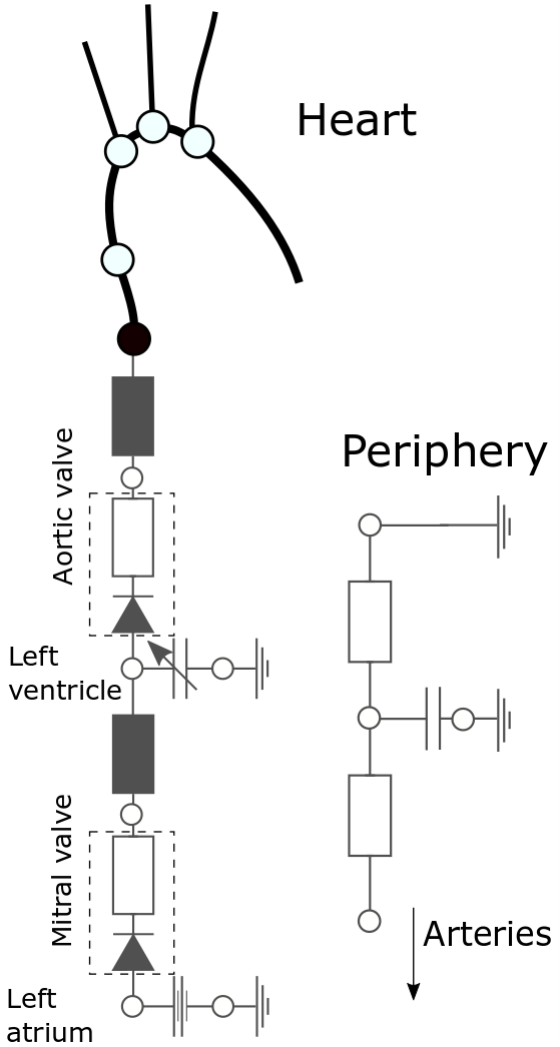

Figure 4. Lumped models: heart and three-element Windkessel at peripherals.

With the help of imaging tools (e.g. CT or MRI), physicians can measure the geometrical parameters with high accuracy. The data found in [4] are used in the current research. Since the literature barely contains information about the wall thickness, it is set to 10% of the diameter for all vessels. The value of the elasticities is critical, as it determines the wave propagation speed (Eq. (8)), thus the pulse wave velocity (PWV) also.

$$a_0 = \sqrt{\frac{E_1 \delta_0}{\rho D_0}} \tag{8}$$

[6] presented a study recently about the measured PWV values from the literature as a function of the nominal (or lumen) diameter. A fitted approximation was used to keep the physiologically proper PWV values (see Fig. 5). The equation mathematically is a power-law function, which was also proposed in [6]. On the one hand, from the Eq. (8) and the definition of the pulse wave velocity, one elasticity value can be calculated; on the other hand, the elasticity parallel to the damping E_2 is set to 1.8 times of E_1 according to previous studies [1].

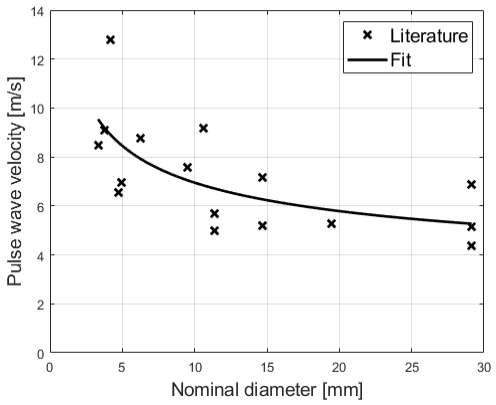

Figure 5. Pulse wave velocity as a function of lumen diameter in the literature from [6] and a fitted power-law function.

The number of division points along a vessel can be determined by manually tuning and checking the average time step values in each vessel. The primary purpose is to accurately approximate the governing fluid dynamical equations, but a secondary goal is to obtain a uniform time step distribution. The lowest value determines the common time step of the model; thus, an exceptionally low time step might inhibit the computational efficiency. The time step is influenced primarily by the length of the artery, the number of division points and the PWV. Since the PWV is typically in the range of 5 to 9 *m/s*, see Fig. 5, it can be assumed to be equal for all vessels at this point. Overall, the proportion of the division points and the length should be uniform, and the sum of the division points is decreased until the approximation error is negligible.

Determining the parameters of the lumped models, such as the heart or the peripherals, is critical and challenging. None of the parameters can be directly measured or estimated. The only suitable method here is tuning the parameters to have a physiologically proper output, e.g. aortic pressure or cardiac output. The exact values for this research is coming from [4] for the peripherals, while the heart parameters are from [2].

4. RESULTS

One of the most crucial hemodynamic quantities in low-dimensional fluid mechanical modelling is the volume flow rate of the heart in time. Fig. 6 depicts the results from the simulation and the literature [6]. The first peak indicates the heart contracting and releasing blood from the left

ventricle. After the peak, it decreases back to zero, but as the signal from the literature suggests, it might undershoot, causing a reverse flow rate or backflow. The simulation cannot catch such details as it is built using perfectly operating diodes (or check valves).

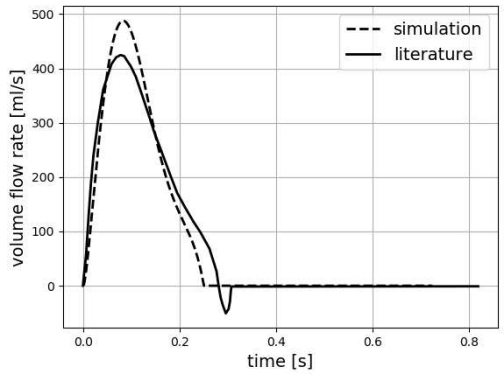

Figure 6. Volume flow rate of the heart from the literature [6] and the simulation over time.

Another relevant and diagnostically important physiological output is the aortic pressure; see Fig. 7 for the results from the simulation and the literature. Although the overall shape is similar and the amplitude is in the same range, the distal and proximal values are not well approximated by the simulation.

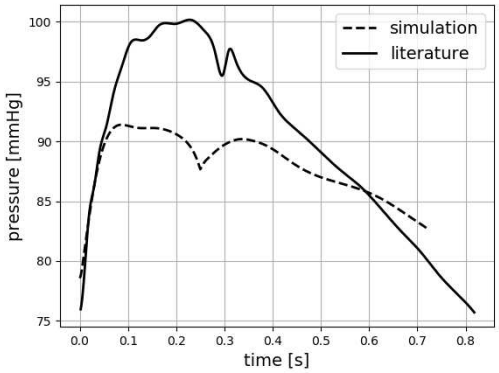

Figure 7. Aortic pressure in time from the literature [6] and the simulation over time.

Similar observations can be drawn based on Fig. 8, which indicates the femoral pressure. The general nature of the signals is identical; however, the diastolic and systolic values differ. Fig. 9 depicts the velocity from the exact location. Slightly more significant differences appear as the simulation constantly underestimates the velocity.

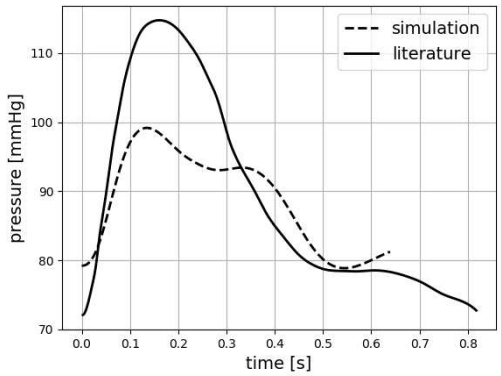

Figure 8. Femoral pressure in time from the literature [6] and the simulation over time.

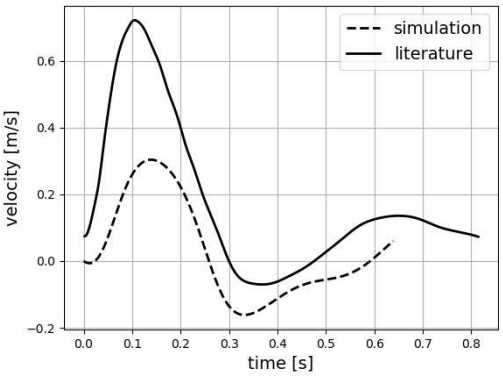

Figure 9. Femoral velocity in time from the literature [6] and the simulation over time.

5. DISCUSSION

The prediction of the proposed model for the pressure and volume flow rates is qualitatively accurate. However, to increase the precision of the model, some additional parameter calibration is inevitable. Even though the model is low-dimensional with low computational time, it contains more than one thousand independent parameters; thus, the question is how to decrease their number. Recently [7] proposed a grouping based on the location of the arteries, then assigned the same multiplier factor to each parameter within the group. The question is whether this (or any other) grouping technique reduces the size of the search space, i.e. it might decrease the accessibility of the optimal solution.

The flow rate of the heart gives an excellent approximation to the literature data; however, catching the reverse flow is not possible with the current model due to the ideal check valves. One possible solution is introducing a hysteresis to the diodes modelling the heart valves. Again, how to choose the parameters correctly to achieve the physiologically relevant solution emerges. The direct

measurement of this phenomenon is not possible, and also, the literature lacks modelling such features.

Considering the femoral outputs, the exact location of the signals is a question. The femoral artery is one of the longest vessels in the human body; it can be over 400 mm. The location of the literature data and the simulation may differ, causing some additional discrepancy. Further analysis should find the exact location of such data or designate points which position is precisely prescribed.

The combined, general 1D-0D solver is the most valuable result of this research, as it creates numerous opportunities. Still, the model can be extended with additional 0D elements of the cardiovascular system. Recently [8] introduced a 0D model to describe the cardiopulmonary circulation. Moreover, a lumped model was proposed in [9] for modelling the venous system. Such parts of the circulatory system can be easily added to our model as the 1D-0D solver in general.

6. SUMMARY

This research introduced a 1D-0D modelling approach for the arterial system, the heart and the peripherals. The main arterial branches are resolved in 1D, and the governing fluid mechanical equations are solved using the method of characteristics. The material of the vessels is considered viscoelastic and described with the Poynting-Thomson model. The heart and the peripherals are handled with 0D models. The critical point is to set the model parameters correctly, which are set based on the data from the scientific literature.

The overall quality of the simulation data is acceptable, as it gives a satisfactory approximation of literature results, even without additional calibration of the parameters. Further investigation is necessary in the direction of input parameter calibration, which carries significant uncertainties (e.g. peripheral resistances, elasticities or heart parameters). Moreover, the model extensions are available, as the combined 1D-0D solver is general, and any model topology can be accurately solved. Pulmonary, venous or coronary circulation elements can be added in further research.

ACKNOWLEDGEMENTS

Project no. NKFI-K129277 (“Evaluation of cerebrovascular events in patients with occlusive carotid artery disorders based on morphological and hemodynamic features”) has been implemented with the support provided by the Ministry of Innovation and Technology of Hungary from the National Research, Development and Innovation Fund.

The project was also funded by the National Research, Development, and Innovation Fund of Hungary under Grant TKP2021-EGA-02.

REFERENCES

[1] Bárdossy, G., Halász G. 2013, „A " backward" calculation method for the estimation of central aortic pressure wave in a 1D arterial model network”, *Computers and Fluids*, Vol. 73, pp. 134-144

[2] Ferreira, A., Chen S., Simaan M., et al., 2005, „A nonlinear state-space model of a combined cardiovascular system and a rotary pump”, *CDC-ECC '05*, Vol. 1, pp. 897-902

[3] Gul R., Shahzadi S., 2019, „Beat-to-beat sensitivity analysis of human systemic circulation coupled with the left ventricle model of the heart: A simulation-based study”, *European Physical Journal Plus*, Vol. 134., pp.1-23

[4] Reymond, P., Merenda, F., Perren, F., et al., 2009, “Validation of a one-dimensional model of the systemic arterial tree”, *American Journal of Physiology - Heart and Circulatory Physiology*, Vol. 297, pp. 208-222

[5] Kim, H., Vignon-Clementel, I., Coogan J., et al., 2010, „Patient-specific modeling of blood flow and pressure in human coronary arteries”, *Annals of Biomedical Engineering*, Vol. 38, pp. 3195-3209

[6] Charlton, P., Harana, J., Vennin, S., et al., 2019, “Modeling arterial pulse waves in healthy aging: a database for in silico evaluation of hemodynamics and pulse wave indexes”, *American Journal of Physiology - Heart and Circulatory Physiology*, Vol. 317, pp. H1062-H1085

[7] Jones, G., Parr, J., Nithiarasu, P., et al. 2021, “A physiologically realistic virtual patient database for the study of arterial haemodynamics”, *International Journal for Numerical Methods in Biomedical Engineering*, Vol. 37, pp. 1-28

[8] Li, B., Wang, H., Li G., et al. 2020, “A patient-specific modelling method of blood circulatory system for the numerical simulation of enhanced external counterpulsation”, *Journal of Biomechanics*, Vol. 111, pp. 1-12

[9] Zhang, H., Fujiwara, N., Kobayashi, M., et al. 2016, „Development of a Numerical Method for Patient-Specific Cerebral Circulation Using 1D–0D Simulation of the Entire Cardiovascular System with SPECT Data”, *Annals of Biomedical Engineering*, Vol. 44, pp. 2351-2363

Conference on Modelling Fluid Flow (CMFF'22)
The 18th International Conference on Fluid Flow Technologies
Budapest, Hungary, August 30-September 2, 2022

Resolving sub-kolmogorov bubble dynamics in turbulent flows: Formulation of a multiscale numerical framework

Niklas HIDMAN[1], Henrik STRÖM[2], Srdjan SASIC[3], Gaetano SARDINA[4]

[1] Corresponding Author. Chalmers University of Technology, Department of Mechanics and Maritime Sciences-Division of Fluid Dynamics, Gothenburg, Sweden. E-mail: niklas.hidman@chalmers.se
[2] Chalmers University of Technology, Department of Mechanics and Maritime Sciences-Division of Fluid Dynamics, Gothenburg, Sweden. E-mail: henrik.strom@chalmers.se
[3] Chalmers University of Technology, Department of Mechanics and Maritime Sciences-Division of Fluid Dynamics, Gothenburg, Sweden. E-mail: srdjan@chalmers.se
[4] Chalmers University of Technology, Department of Mechanics and Maritime Sciences-Division of Fluid Dynamics, Gothenburg, Sweden. E-mail: sardina@chalmers.se

ABSTRACT

Bubbly flows are important in a range of industrial and natural processes. Still, accurately predicting the flow dynamics at industrial scales is an immense challenge, mainly because of the multiscale nature of processes occurring at bubble (micro/millimetre) scales interacting with processes at industrial scales (meters). In this work, a multiscale numerical framework is formulated that couples a macro- and a microscale fluid dynamics solver to study such interactions. The former solver predicts the turbulent liquid phase, and the latter captures the bubble dynamics in response to the turbulent fluctuations. The framework handles arbitrary gas/liquid density ratios and uses a Moving Reference Frame method that follows fast-rising bubbles due to high-density ratios and gravitational forces. The framework predicts realistic bubble dynamics, considering the turbulent liquid fluctuations that modify the bubble shapes and alter their motion. Several simulation cases are performed with different surface tensions and show bubble dynamic processes that are even faster than the Kolmogorov times. The numerical framework can be used with any general DNS technique that handles two-phase flows to treat droplets, bubbles or particles in laminar and turbulent flows.

Keywords: Bubbles, DNS, Moving reference frame, Multiphase flows, Multiscale method, Turbulence

NOMENCLATURE

C_D	$[-]$	drag force coefficient
D	$[m]$	bubble diameter
Eo	$[-]$	Eötvös number
Ga	$[-]$	Galilei number
K_P	$[s^{-2}]$	proportional coefficient
Re	$[-]$	Reynolds number
S	$[s^{-1}]$	strain rate tensor
T_D	$[s]$	derivative coefficient
T_I	$[s]$	integral coefficient
U	$[m/s]$	linearised velocity field
v	$[m/s]$	bubble velocity
a	$[m/s^2]$	acceleration
c	$[-]$	volume fraction field
e	$[m]$	error value
f	$[m/s^2]$	random forcing
g	$[m/s^2]$	gravitational acceleration
p	$[Pa]$	pressure field
t	$[s]$	time
u	$[m/s]$	velocity field
x	$[m]$	spatial coordinate
$\hat{n}$	$[-]$	interface normal
β	$[-]$	density ratio
χ	$[-]$	bubble aspect ratio
δ	$[-]$	Kronecker delta
ϵ	$[-]$	Levi-Civita symbol
η	$[m]$	Kolmogorov length scale
κ	$[m^{-1}]$	curvature
λ	$[m]$	Taylor length scale
μ	$[Pa\ s]$	dynamic viscosity
ν	$[m^2/s]$	kinematic viscosity
ω	$[s^{-1}]$	vorticity
ϕ	$[^\circ]$	bubble orientation angle
ρ	$[kg/m^3]$	density
σ	$[N/m]$	surface tension
τ	$[s]$	time scale
ε	$[m^2/s^3]$	dissipation rate

Subscripts and Superscripts

b	bubble
e	external flow
g	gas
l	liquid

mrf	moving reference frame
r	ratio
i, j, k	spatial indices
(1)	linear field
$*$	non-dimensional
0	initial value
$\wedge$	relative to the MRF

1. INTRODUCTION

Bubbly flows are important in various industrial and natural processes such as chemical reactors, nuclear reactors, heat exchangers and atmosphere-ocean exchanges. This type of multiphase flow is characterised by good heat and mass transfer properties without the need for mechanical mixing and therefore require lower operating and maintenance costs [1]. To understand and design such systems, it is crucial to predict the dynamics of bubbles and how the bubbles affect the liquid phase. However, those dynamics are not yet fully understood, and reliable models for the dynamics are still needed [2].

The main challenges of modelling multiphase flows are their multiscale nature, where phenomena occurring at the smallest scales of the order of a bubble diameter (micro-/millimetres) affect the macroscales of the order of the entire system (meters) and vice versa [3]. Because of this large range of interacting scales, even the most advanced experimental or numerical methods cannot capture all relevant dynamics in industrial systems.

Currently, standard modelling methods for multiphase flows are based on a bottom-up hierarchical strategy [4]. This strategy aims to parameterise the relevant physical phenomena starting from the small to the large scales of the system using different techniques.

At the smallest scales, the dynamics and deformation of every single bubble can be resolved on an Eulerian grid (bubble-resolved DNS) [5, 6, 7]. However, this microscopic approach requires a grid size much smaller than the bubble diameter and involves a high computational cost. Furthermore, it is only feasible to simulate computational domains of the order of several bubble diameters because of the high cost. Nevertheless, using the microscopic approach, makes it possible to formulate models for small-scale bubble phenomena such as interfacial force coefficients, breakup and coalescence criteria, bubble shape and deformation characteristics. In the bottom-up modelling strategy, these models are then used in larger-scale (macroscopic) simulation methods such as the Eulerian–Lagrangian (EL) or Eulerian–Eulerian (EE) frameworks that consequently do not resolve the smallest scales.

Although the bottom-up hierarchical modelling strategy accounts for the effects of small-scale phenomena on the larger scales, it does not consider the multiscale coupling present in multiphase flows. For example, small-scale dynamics such as the bubble deformation and motion are, in reality, influenced by, and interact with, unsteady intermittent turbulent fluctuations in the liquid phase that originate at larger scales.

To understand and model the influence of the large-scale turbulent fluctuations on the small scale bubble dynamics, there is still a need to develop numerical frameworks where the bubbles are exposed to realistic turbulent fluctuations. At the same time, the framework must still be able to fully resolve the bubble dynamics occurring at scales smaller than their diameter.

In this paper, a multiscale numerical framework is formulated that captures the small-scale bubble dynamics in response to an external turbulent flow. Specifically, the multiscale framework predicts the large-scale characteristics of turbulence and impose a more realistic flow around a bubble whose size is comparable to or smaller than the Kolmogorov length scale $\eta = (\nu^3/\varepsilon)^{1/4}$, where ν is the liquid kinematic viscosity, and ε is the turbulent kinetic energy dissipation rate. The microscale bubble dynamics is resolved using a Volume of Fluid (VOF) solver with an unsteady external flow field sampled from a Lagrangian bubble trajectory. The Lagrangian bubble is tracked in a macroscopic pseudospectral solver that simulates homogeneous isotropic turbulence. This framework is an extension of the multiscale approach by [8] to bubbles with arbitrary density ratios between the phases and where the turbulent signal from the macroscale simulation is sampled following a Lagrangian bubble rather than a passive tracer. Additionally, the computational speed of the methodology is increased by at least two orders of magnitude by using additional body forces proportional to the rate of change of the turbulent external flow field. Therefore, the approach in this work does not require any computationally expensive sub-iterations between time steps.

To account for the relative velocity between the phases, induced by the density difference and the gravitational force, the reference frame is changed in the microscopic solver to one moving with the bubble. The moving reference frame (MRF) is non-inertial and consequently introduces an additional term in the Navier–Stokes equations proportional to the bubble acceleration [9]. To follow the motion of the bubble, the MRF acceleration is determined using a Proportional Integral Derivative (PID)-controller based on the bubble displacement from its initial MRF position (P and I parts) and the bubble velocity relative to the MRF (D part).

The PID-controlled MRF approach is a combination of the MRF methods used by [10, 11] that updated the velocity of the MRF using the particle volume-averaged velocity, [12] that updated the velocity of the MRF based on the bubble displacement from its initial position and the approach used by [13] that kept the bubble in its initial position by applying a PID-controlled artificial body force. By determining the MRF acceleration using a PID-controller, the

MRF accelerates smoothly and potential numerical drifts of the bubble are minimised while still allowing the bubble to move freely.

The paper starts with an outline of the numerical framework and then provides a few simulation results of a rising bubble in homogeneous isotropic turbulence to show the capabilities of the framework.

2. NUMERICAL METHODOLOGY

The multiscale framework consists of two coupled fluid dynamics solvers. A macroscopic Eulerian-Lagrangian solver generates a homogeneous isotropic turbulent flow and samples the undisturbed liquid velocity and gradients along a Lagrangian rising bubble trajectory. The sampled turbulent signals are used to impose a fluctuating velocity field in the microscopic framework. This approach makes it possible to study the microscopic bubble dynamics in response to the macroscopic turbulent fluctuations. A detailed description and validation of the multiscale framework can be found in [3].

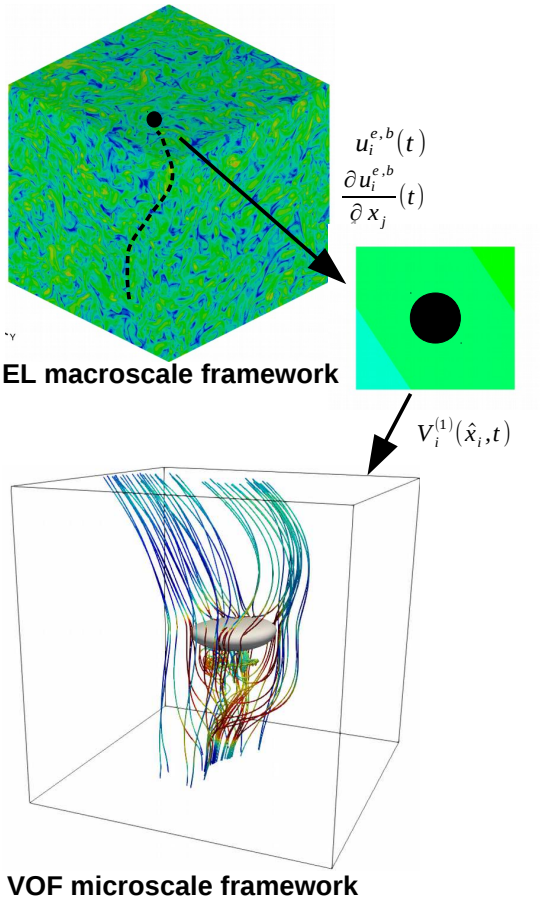

Figure 1. Illustration of the multiscale framework. Turbulent liquid fluctuations are sampled following a spherical Lagrangian bubble in the macroscale simulation. Based on these signals, a linearised unsteady flow field is imposed on the microscale simulation. The contour levels represents the liquid vorticity magnitude.

2.1. Macroscale Eulerian-Lagrangian (EL) solver

A pseudo-spectral solver is used to simulate the external homogeneous isotropic turbulent liquid flow. At low bubble volume fractions, the flow satisfies the incompressible Navier-Stokes equations according to

$$\frac{\partial u_i^{\mathrm{e}}}{\partial x_i^{\mathrm{e}}} = 0\,, \tag{1}$$

$$\frac{Du_i^{\mathrm{e}}}{Dt} = \frac{\partial u_i^{\mathrm{e}}}{\partial t} + u_j^{\mathrm{e}}\frac{\partial u_i^{\mathrm{e}}}{\partial x_j^{\mathrm{e}}} = -\frac{1}{\rho_{\mathrm{l}}}\frac{\partial p^{\mathrm{e}}}{\partial x_i^{\mathrm{e}}} + \nu\frac{\partial^2 u_i^{\mathrm{e}}}{\partial x_j^{\mathrm{e}}\partial x_j^{\mathrm{e}}} + f_i \tag{2}$$

where t and x_i^{e} are the time and space coordinates, u_i^{e} and p^{e} are the liquid velocity and pressure, ρ_{l} is the liquid density, and f_i is a random forcing that maintains the turbulent velocity at a statistically steady state. The Eqs. (1)-(2) are solved in the Fourier space using a fast Fourier transform.

The bubble evolution is tracked in a Lagrangian reference frame with the following forces included: drag, buoyancy, gravity, added mass, pressure gradient and lift. The bubble motion is computed by

$$\frac{dx_i^{\mathrm{b}}}{dt} = v_i^{\mathrm{b}}, \tag{3}$$

$$\frac{dv_i^{\mathrm{b}}}{dt} = \beta\frac{Du_i^{\mathrm{e}}}{Dt} + \frac{u_i^{\mathrm{e}} - v_i^{\mathrm{b}}}{\tau_{\mathrm{b}}}f(Re_{\mathrm{b}}) + (1-\beta)g\delta_{i3} + \\ - \epsilon_{ijk}(v_j^{\mathrm{b}} - u_j^{\mathrm{e}})\omega_k, \tag{4}$$

where x_i^{b} is the position of the bubble, v_i^{b} is the bubble velocity, $\beta = 3\rho_{\mathrm{l}}/(\rho_{\mathrm{l}} + 2\rho_{\mathrm{g}})$ is the density ratio and ρ_{g} is the bubble density, $\tau_{\mathrm{b}} = D^2/8\nu\beta$ is the bubble relaxation time and D is the diameter of the bubble, g is the gravitational acceleration, δ is the Kronecker delta and ϵ is the Levi-Civita symbol, ω is the liquid vorticity at the position of the bubble. $f(Re_{\mathrm{b}})$ is the nonlinear correction for the drag depending on the bubble Reynolds number $Re_{\mathrm{b}} = |u_i - v_i^{\mathrm{b}}|D/\nu$ according to [14, 15]

$$f(Re_{\mathrm{b}}) = 1 + \frac{Re_{\mathrm{b}}}{8 + \frac{1}{2}\left(Re_{\mathrm{b}} + 3.315\sqrt{Re_{\mathrm{b}}}\right)}. \tag{5}$$

The added mass and the lift coefficients is assumed equal to 0.5. More numerical details regarding the macroscale EL solver can be found in [16, 17].

2.2. Microscale Volume of Fluid (VOF) solver

Here, a brief outline of the microscale numerical framework is given. For more details and validation please refer to [3].

The problem of a single bubble rising due to buoyancy in a liquid is entirely defined by four dimensionless parameters [6]: the Galilei number $Ga = \rho_{\mathrm{l}}\sqrt{gD}D/\mu_{\mathrm{l}}$ that is the ratios of buoyancy to viscous forces, the Eötvös number $Eo = \rho_{\mathrm{l}}gD^2/\sigma$ that is the ratios of buoyancy to surface tension

forces, the density ratio $\rho_r = \rho_l/\rho_g$ and the dynamic viscosity ratio $\mu_r = \mu_l/\mu_g$. The symbols l and g denote the liquid and the gas phases, D is the spherical equivalent bubble diameter, σ is the surface tension, and $\rho_r = 1000$ and $\mu_r = 100$ are used that approximately represents a water-air system. All variables in the microscopic solver are made non-dimensional using D, g, ρ_l and μ_l: $x_i^* = x_i/D$, $u_i^* = u_i/\sqrt{gD}$, $t^* = t/\sqrt{D/g}$, $\rho^* = \rho/\rho_l$, $\mu^* = \mu/\mu_l$, $p^* = p/(\rho_l g D)$, $g_i^* = g_i/g$ and $\kappa^* = \kappa D$.

To keep the bubble position fixed in the computational domain, a change of reference frame is made:

$$\hat{x}_i^* = x_i^* - x_{\mathrm{mrf},i}^* \,, \tag{6}$$

$$\hat{u}_i^* = u_i^* - u_{\mathrm{mrf},i}^* \,, \tag{7}$$

$$\hat{t}^* = t^* \tag{8}$$

where $\hat{x}_i^*$ is the non-dimensional position relative to the MRF and $\hat{u}_i^*$ is the fluid velocity relative to the MRF, $x_{\mathrm{mrf},i}^*$ and $u_{\mathrm{mrf},i}^*$ represents the absolute (lab) position and velocity of the MRF itself. For brevity, the asterisks are omitted in the remainder of this paper.

The motion of the MRF should follow that of the bubble to keep the bubble at its initial position relative to the MRF. Since the bubble motion is unknown a-priori a PID-controller is used that continuously update the acceleration of the MRF based on the error value $e_i(t) = \hat{x}_i^{\mathrm{b}}(t) - \hat{x}_i^{0,\mathrm{b}}$, that represent the distance between the bubble centre of mass and the initial bubble position in the MRF, and the velocity of the bubble relative to the MRF $\dfrac{de_i}{dt}$. The acceleration and velocity of the MRF are determined as

$$a_{\mathrm{mrf},i}(t) = K_{P,i}\left(e_i + \frac{1}{T_{I,i}}\int_0^t e_i(t')dt' + T_{D,i}\frac{de_i}{dt}\right), \tag{9}$$

$$u_{\mathrm{mrf},i}(t) = u_{\mathrm{mrf},i}^0 + \int_0^t a_{\mathrm{mrf},i}(t')dt' \,, \tag{10}$$

where $u_{\mathrm{mrf},i}^0$ is the initial velocity of the MRF and $K_{\mathrm{P},i}$, $T_{\mathrm{I},i}$ and $T_{\mathrm{D},i}$ are the i^{th} component of the proportional, integral and derivative coefficients, respectively. Using the heuristic and systematic Ziegler-Nichols tuning method [18, 19], the obtained parameters are ($K_{\mathrm{P},i} = 330$, $T_{\mathrm{I},i} = 0.2$ and $T_{\mathrm{D},i} = 0.13$) that produce stable regulations and minor bubble displacements $e_i(t)$ for all our simulations.

An unsteady velocity field is imposed, in the microscopic solver, that is obtained by sampling the external undisturbed turbulent liquid velocity and gradient tensor at the Lagrangian bubble position $x_i^{\mathrm{b}}(t)$ in the macroscopic solver. Assuming the bubble to be smaller than or comparable with the Kolmogorov length scale, the liquid velocity field surrounding the bubble can be approximated as linear [20]. With a first-order Taylor's expansion, this flow field is defined as:

$$U_i^{(1)}(\hat{x}_i, t) = u_i^{\mathrm{e,b}}(t) + \frac{\partial u_i^{\mathrm{e,b}}}{\partial \hat{x}_j}(t)(\hat{x}_j - \hat{x}_j^{\mathrm{b}}) \,, \tag{11}$$

where $u_i^{\mathrm{e,b}}(t)$ is the absolute velocity and $\dfrac{\partial u_i^{\mathrm{e,b}}}{\partial \hat{x}_i}(t)$ is the gradients of the undisturbed liquid velocity field at $x_i^{\mathrm{b}}(t)$ extracted from the macroscale simulations. $\hat{x}_j^{\mathrm{b}}$ is the position of the bubble in the MRF.

The linearised field $U_i^{(1)}(\hat{x}_i, t)$ is imposed on the microscopic solver by continuously updating the boundary conditions $\hat{u}_{\mathrm{BC},i}(\hat{x}_j, t) = U_i^{(1)}(\hat{x}_j, t) - u_{\mathrm{mrf},i}(t)$ and by correspondingly accelerate the microscopic flow field according to

$$a_{U,i}^{(1)}(\hat{x}_i, t) = \frac{d}{dt}(u_i^{\mathrm{e,b}}) + \frac{d}{dt}\left(\frac{\partial u_i^{\mathrm{e,b}}}{\partial \hat{x}_j}\right)(\hat{x}_j - \hat{x}_j^{\mathrm{b}}) \,. \tag{12}$$

The Volume of Fluid (VOF) numerical approach is used to solve the microscopic two-phase flow problem [21]. The governing equations in the MRF are the non-dimensional incompressible Navier-Stokes equations and the advection of the volume fraction field c:

$$\frac{\partial \hat{u}_i}{\partial \hat{x}_i} = 0 \,, \tag{13}$$

$$\rho\left(\frac{\partial \hat{u}_i}{\partial \hat{t}} + \hat{u}_j\frac{\partial \hat{u}_i}{\partial \hat{x}_j}\right) = \rho\left(g_i - a_{\mathrm{mrf},i} + a_{U,i}^{(1)}\right) + \\ -\frac{\partial p}{\partial \hat{x}_i} + \frac{1}{Ga}\frac{\partial}{\partial \hat{x}_j}\left(\mu\left(\frac{\partial \hat{u}_i}{\partial \hat{x}_j} + \frac{\partial \hat{u}_j}{\partial \hat{x}_i}\right)\right) + \frac{\hat{\kappa}\delta_S \hat{n}_i}{Eo} \,, \tag{14}$$

$$\frac{\partial c}{\partial \hat{t}} + \frac{\partial c\hat{u}_i}{\partial \hat{x}_i} = 0 \,, \tag{15}$$

where δ_S is the Dirac distribution function, κ and n_i are the interface curvature and the normal vector. The extra acceleration terms in Eq. 14 represents the acceleration due to the motion of the MRF and the unsteady external velocity field given by the macroscale framework. The VOF method is a one-fluid formulation where the fluid density ρ and viscosity μ varies according to

$$\rho(c) = c\rho_l + (1-c)\rho_g \,, \tag{16}$$

$$\mu(c) = \left(\frac{c}{\mu_l} + \frac{1-c}{\mu_g}\right)^{-1} \,, \tag{17}$$

where a harmonic mean is used to for the viscosity since that is generally more accurate for gas-liquid interfaces with a continuous shear stress [22]. The governing equations are solved with the open-source code Basilisk on a tree-structured Cartesian grid with an efficient adaptive grid refinement technique [23, 24].

2.3. Case setup

The multiscale framework is used to simulate a rising bubble in a turbulent liquid flow. With the macroscale pseudo-spectral solver, homogeneous isotropic turbulence is simulated at the Taylor Reynolds number $Re_\lambda = u_{\mathrm{rms}}\lambda/\nu = 180$. Here, u_{rms} is the root mean square of the velocity fluctuations and $\lambda = \sqrt{\varepsilon/15\nu u_{\mathrm{rms}}}$ is the Taylor length scale. The computational domain is cubical with the side length $2\pi^3$

and a spatial resolution of 256^3 grid points. Periodic boundary conditions are used in all three directions. With water as the liquid and assuming a turbulent dissipation rate of 1.5 10^{-5} m^2/s^3, the Kolmogorov length scale becomes 0.5 *mm*, the spherical bubble diameter is 0.76 *mm* and the time scale is 0.26 *s*. In non-dimensional form, the Kolmogorov length scale is 0.015 and the Kolmogorov time becomes 0.35.

In the microscopic framework the parameter $Ga = 65$ is used that corresponds to the 0.76 *mm* air bubble in water. To study the effects of different bubble deformations the cases $Eo = (10, 30, 50, 120)$ are simulated that corresponds to the air bubble but with a reduced surface tension. A cubic computational domain of $(10D)^3$ is specified where the bubble is kept in the centre by the PID-controlled MRF technique and an unsteady external velocity field is imposed based on the signal from the macroscopic simulation according to Eq. 11. The adaptive grid refinement technique in Basilisk is used to obtain sufficient grid refinement in regions containing the interface and with relatively high values of the second gradient of the velocity field. The maximum grid resolution corresponds to more than 50 cells/D.

3. SIMULATION RESULTS

A snapshot from the microscopic simulation case with $Ga = 65$ and $Eo = 50$ is shown in Figure 2. Here, the bubble is kept in the centre of the computational domain by the PID-controlled MRF technique and the external fluctuating liquid velocity field predicted by the macroscopic solver is imposed as described in Section 2.2. The contours represent the velocity magnitude relative to the MRF made non-dimensional by the characteristic velocity scale $\sqrt{gD}$. Throughout the simulation, the orientation angle ϕ is computed, defined as the angle between the bubble minor axis a and the vertical y-axis, and the bubble aspect ratio $\chi = b/a$ defined as the ratio of the major, b, to minor bubble axes. ϕ and χ are computed using the approach by [25] where χ is defined as the ratio of the larger to the smaller eigenvalues, $\chi \approx (I_{\max}/I_{\min})^{1/2}$, of the second moment of inertia tensor

$$I_{ij} = \frac{1}{m^{\mathrm{b}}} \int_{\Omega^{\mathrm{b}}} (\hat{x}_i - \hat{x}_i^{\mathrm{b}})(\hat{x}_j - \hat{x}_j^{\mathrm{b}}) \rho_{\mathrm{g}} d\hat{V}\,, \tag{18}$$

where Ω^b is the bubble volume.

Figure 3 shows how the χ, ϕ and instantaneous bubble drag force coefficient C_{D} vary in the microscopic simulations. All simulations are stopped at $t/\tau_\eta = 4$ and the same unsteady external velocity field signal is imposed on all cases.

The top panel shows the modulus of the imposed velocity field strain rate tensor $|S^{\mathrm{e}}_{ij}| = \sqrt{S^{\mathrm{e}}_{ij} S^{\mathrm{e}}_{ij}}$, ($S^{\mathrm{e}}_{ij}$ is the symmetric part of the imposed velocity gradient $\partial u_i^{\mathrm{e,b}}/\partial \hat{x}_j$ obtained at the bubble position in the macroscopic simulation). This quantity gives a representation of a typical turbulent signal for the gradients with large localised peaks. The second panel of Fig. 3 shows how the bubble aspect ratio χ vary in response to the imposed fluctuating velocity field and due to unsteady small-scale bubble dynamics such as shape and trajectory oscillations. The case $Eo = 10$ corresponds to the case with the highest relative surface tension force and results in a $\chi \in [3.0, 3.2]$ during the simulation. This case show a correlation between the imposed strain rate $|S^{\mathrm{e}}_{ij}|$ and χ with a Pearson's correlation coefficient of 0.5 in the interval $t/\tau_\eta = [0.5, 4]$. The cases $Eo = 30$ and $Eo = 50$ are, however, not well correlated with $|S^{\mathrm{e}}_{ij}|$ and show fluctuations of χ that are characterised by time scales smaller than the Kolmogorov time scale. At $Eo = 30$, χ is overall larger than for $Eo = 10$ and fluctuate roughly between $[3, 4]$. However, at $Eo = 50$, χ decreases and fluctuates around $[2, 3]$. That χ is the lowest for the highest Eo-number can be explained by the definition of χ and the change of characteristic bubble shapes with reduced surface tension illustrated in Figure 4. Here, the bubble shape for $Eo = 50$ is close to a spherical cap that have a lower aspect ratio than the oblate spheroid shape at $Eo = 10$. At $Eo = 120$, the surface tension is too low to keep the bubble intact and a peripheral breakup occur. Because of the breakup, no quantitative data are presented for the $Eo = 120$ case.

The third panel of Fig. 3 shows the orientation angle ϕ and clearly indicate that the different Eo-numbers result in different oscillating behaviors. The fastest oscillations, in the case $Eo = 30$, are around an order of magnitude faster than the Kolmogorov time scale τ_η and are more related to the capillary time scale [26] $\tau_\sigma = \sqrt{\rho_{\mathrm{l}} D^3/\sigma} \approx 0.2\tau_\eta$ indicating that bubble shape oscillations significantly influence the bubble motion for this case.

The bottom panel of Fig. 3 shows the instantaneous bubble drag force coefficient that fluctuates at around $C_{\mathrm{D}} \approx 2$ for the case $Eo = 10$ but increase to $C_{\mathrm{D}} \approx 3$ for the $Eo = 30$ and $Eo = 50$ cases. This 50% drag coefficient increase is related to the change of bubble shapes at different Eo-numbers. Fig. 4 shows the characteristic shapes of the bubbles during the simulations. At $Eo = 10$, the bubble is approximately an oblate spheroid with a lower C_D than the cases $Eo = 30$ and $Eo = 50$ that are closer to a spherical cap shape.

That C_{D} oscillate in the case $Eo = 30$ can be explained by the aforementioned bubble shape oscillations and the bubble trajectory in the absolute, or lab, reference frame shown in Figure 5. Although the bubble shape and trajectory at $Eo = 30$ is similar to $Eo = 50$, the former case has the oscillating shape and a spiralling trajectory (seen as oscillations of the trajectory in Fig. 5) that cause the instantaneous C_{D} to vary. Since the time-averaged C_{D} is similar for both $Eo = 30$ and $Eo = 50$, the overall trajectories for both cases become similar. In the case $Eo = 10$, the C_{D} is lower and therefore this bubble travels further in the y-direction.

By performing a time lagged cross correlation

between the $|S^{e}_{ij}|(t)$ and $C_D(t)$ a peak Pearson's correlation coefficient is obtained when C_D lags about $t/\tau_\eta \approx 0.2$, or, in the capillary time scale $t/\tau_\sigma = O(1)$, for all cases (the $C_D(t)$ signal is shifted back $t/\tau_\eta \approx 0.2$). At this time lag, the correlation coefficient is about 0.3 for $Eo = 10$, 0.2 for $Eo = 30$ and 0.15 for $Eo = 50$. These values indicate the C_D is correlated with the imposed fluctuating strain rates but with a response time of $t/\tau_\sigma = O(1)$ implying that capillary effects are governing the response dynamics.

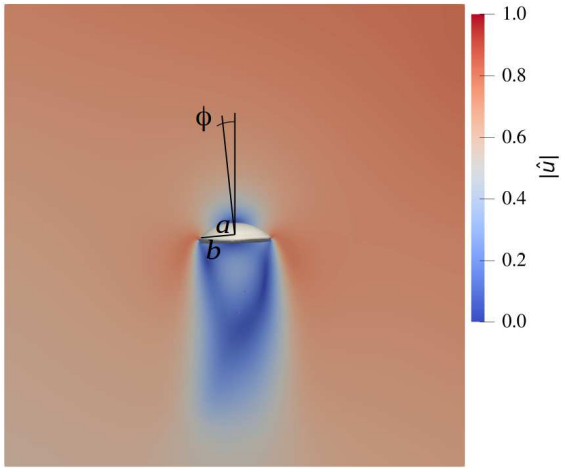

Figure 2. Snapshot of the velocity magnitude relative to the MRF, normalised with the characteristic velocity scale $\sqrt{gD}$, in the simulation case $Ga = 65, Eo = 50$. The angle between the bubble minor axis a and the vertical y-axis is defined as the orientation angle ϕ. The ratio of the major b and minor a semi-axes is the bubble aspect ratio $\chi = b/a$.

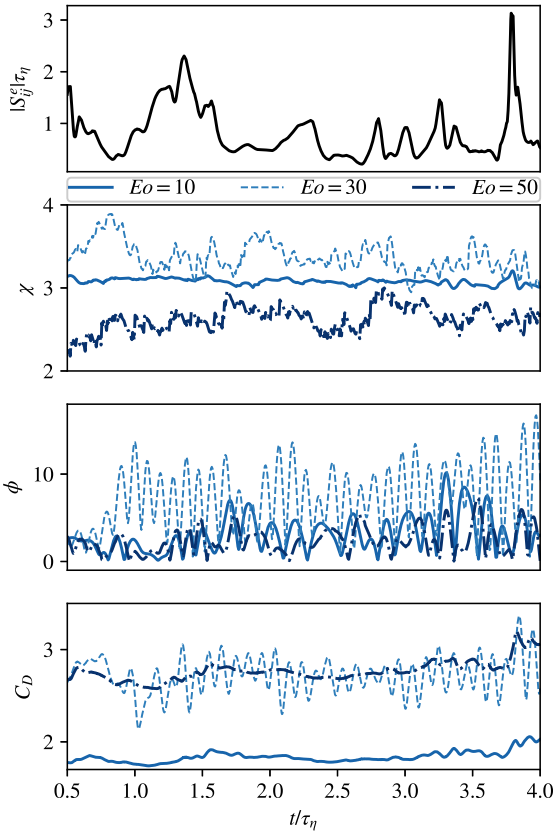

Figure 3. Evolution of the modulus of the external velocity field strain rate (top panel), the bubble aspect ratio (second panel), the bubble orientation angle (third panel) and the instantaneous bubble drag force coefficient (bottom panel). The modulus of the strain rate is the same for all simulation cases while the evolution of the other bubble properties (in the three bottom panels) change with the Eo number. The legend above the second panel applies to all three bottom panels.

4. CONCLUSIONS

In this paper, a multiscale numerical framework is formulated that handles bubbles or droplets with diameters comparable to, or smaller than, the Kolmogorov length scale and with arbitrary density ratios to the carrier phase. A PID-controlled moving reference frame technique is used to follow the motion of bubbles or droplets with high relative velocities to the carrier phase due to gravitational forces. The fluctuating external velocity field is efficiently imposed on the bubble microscale solver by adding body forces proportional to the time derivatives of the linearised external velocity field. This imposition method improves the efficiency of the algorithm by at least two orders of magnitudes compared with the framework suggested by [8].

The multiscale numerical framework resolves the effects of both large-scale turbulent fluctuations and small-scale phenomena such as bubble induced flow disturbances and capillary effects. The simulations capture bubble dynamics that are at least an order of magnitude faster than the Kolmogorov time scale. In particular, the results show significant changes in the small-scale bubble dynamics by varying the surface tension. The relative importance of the surface tension also influence how several bubble properties correlate with the imposed external strain rate. These results illustrate the ability of the proposed multiscale framework to resolve and study both the bubble deformations induced by turbulent fluctuations and the small-scale bubble dynamics associated with capillary effects.

The numerical framework is presented in a general way so that it can be used with any DNS technique for two-phase flows (VOF, level-set, lattice-Boltzmann, diffuse interface approach). In future works, the multiscale framework can be further improved by running the two solvers in parallel. Then, the turbulent fluctuations from the macroscale simulation can be computed along the bubble trajectory given by the microscale simulation. This extension would provide a complete two-way coup-

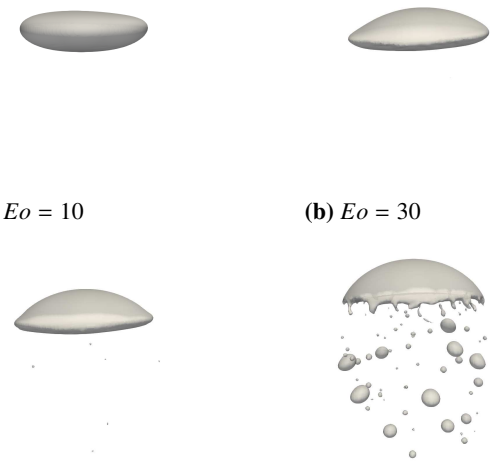

(a) $Eo = 10$ **(b)** $Eo = 30$

(c) $Eo = 50$ **(d)** $Eo = 120$

Figure 4. Characteristic bubble shapes in cases where a bubble rise in homogeneous isotropic turbulence. The same simulation setup and turbulent field is used in all cases but an increasing Eo number is specified that reduce the relative importance of the surface tension force. At increasing Eo-number, the bubble is more deformed and, at $Eo = 120$, a peripheral breakup occurs.

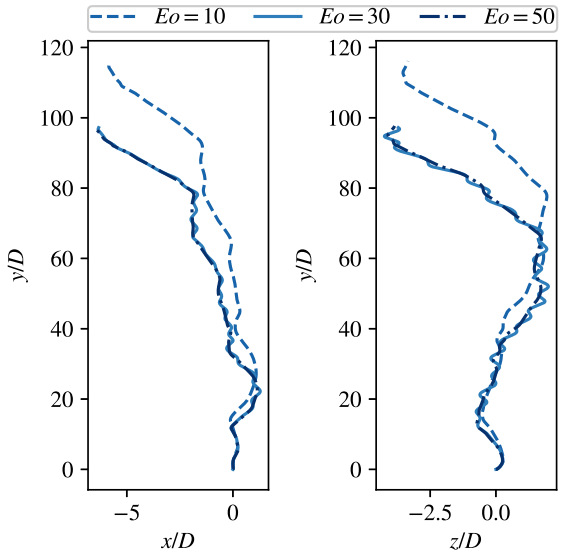

Figure 5. Bubble trajectories in an absolute, or lab, reference frame predicted by the microscale simulation in the x/y-plane (left panel) and the z/y-plane (right panel). The same turbulent fluctuations are imposed on all simulations but the different Eo-numbers results in different small-scale bubble dynamics that influence the trajectory.

ling between the small-scale bubble dynamics and the large-scale turbulent field.

ACKNOWLEDGEMENTS

We acknowledge support from the Swedish Research Council (Vetenskapsrådet), grant VR 2017-05031. The computations were performed using resources provided by the Swedish National Infrastructure for Computing (SNIC) at NSC partially funded by the Swedish Research Council through grant agreement no. 2018-05973.

REFERENCES

[1] Mudde, R. F., 2005, "Gravity-driven bubbly flows", *Annu Rev Fluid Mech*, Vol. 37, pp. 393–423.

[2] Magnaudet, J., and Eames, I., 2000, "The motion of high-Reynolds-number bubbles in inhomogeneous flows", *Annual Review of Fluid Mechanics*, Vol. 32 (1), pp. 659–708.

[3] Hidman, N., Ström, H., Sasic, S., and Sardina, G., 2022, "A multiscale methodology for small-scale bubble dynamics in turbulence", *International Journal of Multiphase Flow*, p. 103976.

[4] van der Hoef, M. A., van Sint Annaland, M., Deen, N., and Kuipers, J., 2008, "Numerical simulation of dense gas-solid fluidized beds: a multiscale modeling strategy", *Annual Review of Fluid Mechanics*, Vol. 40, pp. 47–70.

[5] Bunner, B., and Tryggvason, G., 1999, "Direct numerical simulations of three-dimensional bubbly flows", *Physics of Fluids*, Vol. 11 (8), pp. 1967–1969.

[6] Tripathi, M. K., Sahu, K. C., and Govindarajan, R., 2014, "Why a falling drop does not in general behave like a rising bubble", *Scientific Reports*, Vol. 4, p. 4771.

[7] Cano-Lozano, J. C., Martinez-Bazan, C., Magnaudet, J., and Tchoufag, J., 2016, "Paths and wakes of deformable nearly spheroidal rising bubbles close to the transition to path instability", *Physical Review Fluids*, Vol. 1 (5), p. 053604.

[8] Milan, F., Biferale, L., Sbragaglia, M., and Toschi, F., 2020, "Sub-Kolmogorov droplet dynamics in isotropic turbulence using a multiscale lattice Boltzmann scheme", *Journal of Computational Science*, Vol. 45, p. 101178.

[9] Maxey, M. R., and Riley, J. J., 1983, "Equation of motion for a small rigid sphere in a nonuniform flow", *The Physics of Fluids*, Vol. 26 (4), pp. 883–889.

[10] Lörstad, D., and Fuchs, L., 2004, "High-order surface tension VOF-model for 3D bubble

flows with high density ratio", *Journal of Computational Physics*, Vol. 200 (1), pp. 153–176.

[11] Lörstad, D., Francois, M., Shyy, W., and Fuchs, L., 2004, "Assessment of volume of fluid and immersed boundary methods for droplet computations", *International Journal for Numerical Methods in Fluids*, Vol. 46 (2), pp. 109–125.

[12] Rusche, H., 2002, "Computational fluid dynamics of dispersed two-phase flows at high phase fractions", Ph.D. thesis, University of London.

[13] Fan, Y., Fang, J., and Bolotnov, I., 2021, "Complex bubble deformation and break-up dynamics studies using interface capturing approach", *Experimental and Computational Multiphase Flow*, Vol. 3 (3), pp. 139–151.

[14] Mei, R., and Klausner, J. F., 1992, "Unsteady force on a spherical bubble at finite Reynolds number with small fluctuations in the free-stream velocity", *Physics of Fluids A: Fluid Dynamics*, Vol. 4 (1), pp. 63–70.

[15] Spandan, V., Ostilla-Mónico, R., Verzicco, R., and Lohse, D., 2016, "Drag reduction in numerical two-phase Taylor–Couette turbulence using an Euler–Lagrange approach", *Journal of Fluid Mechanics*, Vol. 798, pp. 411–435.

[16] Sardina, G., Picano, F., Brandt, L., and Caballero, R., 2015, "Continuous growth of droplet size variance due to condensation in turbulent clouds", *Physical Review Letters*, Vol. 115 (18), p. 184501.

[17] Sardina, G., Jareteg, K., Ström, H., and Sasic, S., 2019, "Assessing the ability of the Eulerian-Eulerian and the Eulerian-Lagrangian frameworks to capture meso-scale dynamics in bubbly flows", *Chemical Engineering Science*, Vol. 201, pp. 58–73.

[18] Ziegler, J. G., Nichols, N. B., et al., 1942, "Optimum settings for automatic controllers", *trans ASME*, Vol. 64, p. 11.

[19] McCormack, A. S., and Godfrey, K. R., 1998, "Rule-based autotuning based on frequency domain identification", *IEEE transactions on control systems technology*, Vol. 6 (1), pp. 43–61.

[20] Pope, S. B., 2001, *Turbulent flows*, IOP Publishing.

[21] Benson, D. J., 2002, "Volume of fluid interface reconstruction methods for multi-material problems", *Applied Mechanics Reviews*, Vol. 55 (2), pp. 151–165.

[22] Tryggvason, G., Scardovelli, R., and Zaleski, S., 2011, *Direct numerical simulations of gas–liquid multiphase flows*, Cambridge University Press.

[23] Popinet, S., 2015, "A quadtree-adaptive multigrid solver for the Serre–Green–Naghdi equations", *Journal of Computational Physics*, Vol. 302, pp. 336–358.

[24] URL `http://basilisk.fr`.

[25] Bunner, B., and Tryggvason, G., 2003, "Effect of bubble deformation on the properties of bubbly flows", *Journal of Fluid Mechanics*, Vol. 495, p. 77.

[26] Popinet, S., 2018, "Numerical models of surface tension", *Annual Review of Fluid Mechanics*, Vol. 50, pp. 49–75.

Conference on Modelling Fluid Flow (CMFF'22)
The 18th International Conference on Fluid Flow Technologies
Budapest, Hungary, August 30-September 2, 2022

Use of High-Order Curved Elements for Direct and Large Eddy Simulation of Flow over Rough Surfaces

Kenan Cengiz*, Sebastian Kurth, Lars Wein, and Joerg R. Seume

Leibniz Universität Hannover, Institute of Turbomachinery and Fluid Dynamics. An der Universität 1, DE-30823 Garbsen
* E-mail: cengiz@tfd.uni-hannover.de

ABSTRACT

In the present study, the curved element capabilities of a high-order solver are scrutinized. The devised approach not only suggests a plausible way to adopt a body-fitted grid approach as an alternative to immersed boundary method (IBM), but also enables performing LES instead of DNS without under-resolving the roughness. The method is first tested using various polynomial degrees. Then, it is validated against reference DNS-IBM results from a rough channel flow setup having various Reynolds numbers corresponding to the entire roughness range. The results confirm the validity of the new approach.

Keywords: curved elements, DNS, high-order discretization, ILES, roughness

NOMENCLATURE

ESx	[−]	effective slope
Sa	[m]	mean roughness height
SSk	[−]	skewness
$S_{z,5\times5}$	[m]	mean maximum roughness height of 5×5 tiles
ks	[m]	equivalent sand-grain roughness
k	[m]	taken as $S_{z,5\times5}$
u_τ	[m/s]	friction velocity
Re_τ	[−]	friction velocity Reynolds number, $(u_\tau\delta)/\nu$
ν	[m^2/s]	kinematic viscosity
δ	[m]	channel half height
p	[−]	polynomial degree of the flow solver
Q	[−]	polynomial degree of the mesh export
SP, DP	[−]	single precision, double precision

Subscripts and Superscripts

+	dimensionless quantity in wall units (u_τ, ν_w)
eff.	effective resolution with respect to the solution points in an element

1. INTRODUCTION

The Direct Numerical Simulation (DNS) of the flow over rough surfaces has been a hot topic amongst the fluid research community, because understanding the influence thereof on the flow can be significant in industrial applications. For instance, deciding when to replace turbomachinery blades to retain the roughness-related performance degradation at acceptable levels requires a reliable prediction of the influence. At this point, DNS provides a good amount of information for building, and tuning roughness models in Reynolds-averaged Navier-Stokes (RANS) approaches. The current trend to perform such a DNS persists in the immersed-boundary method (IBM) for a reason. In fact, IBM is definitely superior to the classical body-fitted grid approach, making it effortless to cover realistic rough surfaces with perfect mesh quality. However, one is often restricted to DNS because the resolution of the roughness becomes essential in addition to the resolution of the flow, particularly in the range from hydraulically smooth to transitionally rough regimes. On top of that, there can be a need for an over-resolved DNS to fully represent the roughness sufficiently, resulting in fairly high computational costs for such low Reynolds numbers [1].

The IBM approach is adopted in many investigations of roughness [2, 3, 4, 5]. They are mainly based on rigorous simulations in channel flows to scrutinize the effects of different roughness characteristics such that useful roughness correlations and models can be deduced for use in RANS of industrial applications. Simulating roughness on real applications, such as turbomachinery blades, is a relatively new research area. Only recently have the computationally demanding resources required become fairly affordable. Such resources are not only needed for adequate resolution of the flow, but also for resolution of the roughness elements over the blade. In a recent study, Hammer *et al.* [6] experimented with two approaches to incorporating the roughness effect into the flow over a T106A cascade in their LES sim-

ulations: 1) adding a source term to the governing equations to serve as a roughness model, 2) applying the "boundary data immersion method", akin to IBM, to an as-cast surface on the same blade. The latter case requires that they go up to a DNS-level resolution on the rough surface, so that the effect of smaller roughness elements are not missed. The former approach, on the other hand, despite being cost-effective, proved to be a mere approximation to the impact of roughness.

In the present study, the possibility to curve the high-order elements is exploited for high-fidelity flow simulation over rough surfaces. To the authors' knowledge, this is a rather novel approach. The closest study we could find is by Garai *et al.* [7]. They used a space-time discontinuous Galerkin spectral-element method applied on artificial roughness, which is generated as sinusoidal displacement of the surface using a linear-elasticity analogy [8]. On the other hand, real roughness is considered in the present work. A discontinuous Galerkin scheme based on flux reconstruction (FR) is used, wherein the mesh is fitted to the roughness using arbitrary inverse-distance weighted smoothing [9]. As the first study of its kind, a filtered roughness is considered only, whereby fitting the polynomial-based element faces on the rough surface should not be troublesome.

2. SIMULATION SETUP

2.1. Methodology and the Numerical Solver

A high-order solver called PyFR (version 1.12.2) is utilized [10]. The numerical scheme is based on flux reconstruction with the DG correction function, where polynomial degrees up to $p = 4$ for mixed elements are possible. A detailed description of the solver is given in [10].

A plain channel flow with periodic conditions in streamwise (x) and spanwise (y) directions are considered. The flow is driven by a constant body force in the x-direction, ensuring a certain u_τ on the wall. In fact, such an arrangement is a substantially efficient way to investigate the effect of roughness on the boundary layers. The compressible Navier-Stokes equations for an ideal gas with constant viscosity are solved. No turbulence model is in question, leading to either a DNS or an Implicit Large Eddy Simulation (ILES) depending on the resolution and the polynomial degree. The Mach number is kept below 0.2 for all cases.

On the element interfaces, a Rusanov Riemann solver is applied. A Local Discontinuous Galerkin Scheme (LDG) scheme, with the upwind and penalty parameters of $\beta = 0.5$ and $\tau = 0.1$, is used for the viscous fluxes. The time marching is based on the explicit RK45[2R+] scheme with proportional-integral (PI) adaptive time-step controlling. The Gauss-Legendre flux and solution point sets are used. Unless stated otherwise, anti-aliasing through approximate L^2 projection of flux in the volume and on the face is activated. This is indeed considered necessary because aliasing-driven instabilities can become severe in the case of highly curved elements. Another reason is the spurious transfer of energy from the unresolved modes to the resolved ones, which can be even higher in under-resolved configurations (such as ILES) without using anti-aliasing.

In the present investigation, not only the flow solver's support for curving elements, but also the support of the mesh generation software is vital. In other words, if the mesh generation software lacks the support of high-order elements, the flux points placed on the face of the resulting linear element would not improve the representation of the rough surface at all.

2.2. The Rough Surface and the Mesh Parameters

Since validation of the proposed method is targeted initially, the IBM-DNS results by Thakkar *et al.* [1] over the surface "s8" are considered, where a wide range of roughness heights (as well as Reynolds numbers) are covered. The surface was extracted from measurements of a grit-blasted surface. Irrelevantly high wave numbers on the surface were filtered out using a low-pass filter [2]. In order to keep Re_τ high enough while lowering roughness levels (from $k^+ = 30$ to 3.75), the roughness patch was first scaled down by 2, 4 and 8, then tiled accordingly (as in Table 1). The same conditions are adopted for the validation, except that the computational domain is a half channel with a symmetry condition on the mid-plane.

For a computational domain with flat boundaries, elevating the order of the linear elements would be as simple as adding planar nodes on the faces and in the volume. Nevertheless, adding planar nodes on the faces would not be a good representation of curved geometries. Hence, the face nodes must be placed on the boundary defined by the given geometry. The resulting high-order mesh must also be smoothed because the curved boundary may result in inverted elements, especially in the tightly packed boundary layer regions. With this, the curving of the elements is handled during the export of the mesh using Pointwise [9]. This involves three stages:

1. Elevate the linear elements to high-order elements by adding new interior and face nodes. Fictional linear sub-elements are formed in the process.

2. Perturb the nodes using a perturbation field based on inverse distance weighted smoothing

3. Improve the mesh quality by applying an optimization-based smoothing on the linear sub-elements. The resulting sets of linear sub-elements form the high-order elements of high quality.

Polynomial degrees up to $Q = 4$ are possible in the mesh export process. In order to adequately fit the perceived surface (i.e. the resulting mesh boundary) to the original surface (i.e. the geometry model), a mesh export with $Q \geq 2$ as well as simulations with $p \geq 2$ is desired. The selection of high Q values during the mesh export may initially sound plausible to ensure a good representation of the original surface. However, the mesh export process can easily get troublesome because of convergence difficulties during the smoothing phase. Since the original surface in question is filtered, $Q = 2$ is found to be sufficient.

A qualitative comparison of the surfaces provided by $Q = 1$ and $Q = 2$ is shown in Figure 1. Clearly, the $Q = 2$ mesh better represents the original CAD geometry. Note that the visualization tool uses the uniform nodes provided by the mesh and utilizes Lagrange polynomials to interpolate. From the perspective of the flow solver, however, there is no guarantee for the surface flux points to be located on the original geometry because the point sets used by the mesh generation tool and the flow solver are different. After reading the uniformly distributed points given by the mesh generator, the flow solver creates its own points (Gauss-Legendre) on the projected surface based on the provided points.

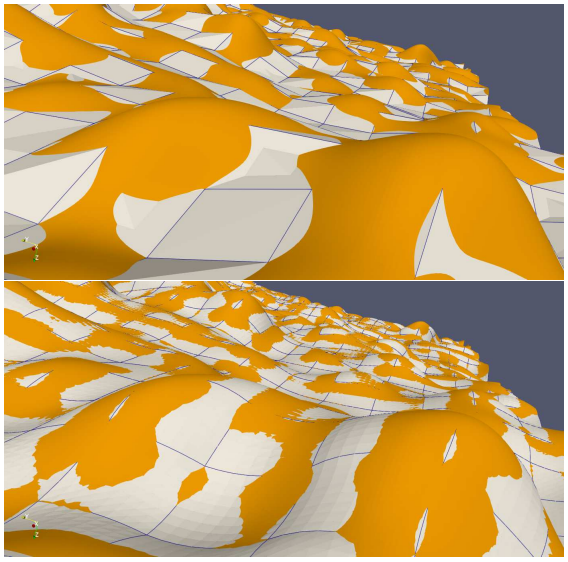

Figure 1. A view from the wall boundary. top: $Q = 1$ (with $p = 1$); bottom: $Q = 2$ (with $p = 4$). The orange surface is the original CAD geometry. The gray surface represents how the surface is interpreted by the flow solver.

Table 1 gives details about the simulations as well as the mesh. The same mesh is used for all simulations, but with different p. The mesh consists of $48 \times 24 \times 22$ elements in streamwise, spanwise, and wall-normal directions, respectively. The height of the first element is taken to be $z^+ \approx 1.76$ for $\mathrm{Re}_\tau = 180$, corresponding to $z^+ \approx 7.04$ for the $\mathrm{Re}_\tau = 720$ case. Therefore, the first Gauss-Legendre solution point (denoted as $z^+_{\mathrm{eff.}}$) falls well below $z^+ = 1$ for all simulations. The computational boundaries and the wall surface mesh can be seen in Figure 3, where the curvature of the wall boundary can also be observed clearly. The view direction of the snapshot is the streamwise ($+x$) direction; the left boundary is in the $+y$ direction; and the top boundary is the channel mid-plane ($z = \delta$), on which the symmetry condition is enforced. All lateral boundaries are subject to periodic conditions in the respective directions.

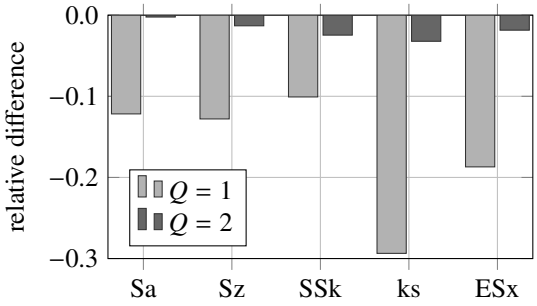

Figure 2. Comparing differences of roughness parameters calculated for the roughness represented by the higher order mesh ($Q = 2$) and a linear mesh ($Q = 1$) relative to the roughness parameter of the input surface.

The down-scaled patches (Simulations 1–3 in Table 1) may require higher polynomial degrees ($Q > 2$) for the same mesh because the topology can feature multiple extrema in one direction in one element. Therefore, $Q = 3$ is chosen for the surfaces with lower roughness (Simulations 1–2).

For an accurate simulation, adequate representation of the roughness by the mesh is crucial. For the evaluation of accuracy, some roughness parameters are used. The mean roughness height Sa, the maximum roughness height Sz, the skewness SSk, and the effective slope ESx in main flow direction are calculated according to DIN EN ISO 25178-2 [11]. The equivalent sand-grain roughness ks is calculated with the ks-correlation of Sigal and Danberg (1990) [12] using the shape and density parameter by Dirling (1973) [13]. Figure 2 shows the relative differences of these roughness parameters calculated for the representation by the higher order mesh ($Q = 2$) and a linear mesh ($Q = 1$) in comparison to the roughness parameters of the original surface geometry. It can be seen that the representation of the roughness by the linear mesh decreases all roughness parameters. The highest relative difference is found for the equivalent sand-grain roughness (-0.29). The representation of the roughness by a higher-order mesh significantly improves the fidelity. The highest difference, once again found for the equivalent sand-grain roughness, is reduced to -0.03. All in all, the higher-order mesh provides a satisfactory representation of the original surface topology.

Table 1. The conducted simulations over the surface s8. Number of elements ($N_x \times N_y \times N_z$) is $48 \times 24 \times 22$ for all of the simulations. No anti-aliasing is used for 4c.

simulation #	k^+	Re_τ	tiles	Δx^+, Δy^+	$\Delta x^+_{\mathrm{eff.}}$, $\Delta y^+_{\mathrm{eff.}}$	$z^+_{\mathrm{eff.}}$	Q	p	precision
1	3.75	180	8×8	21.2	5.3	0.13	3	3	SP
2	7.5	180	4×4	21.2	5.3	0.13	3	3	SP
3	15	180	2×2	21.2	5.3	0.13	2	3	SP
4a	30	180	1×1	21.2	4.2	0.08	2	4	DP
4b	30	180	1×1	21.2	7.1	0.20	2	2	SP
4c	30	180	1×1	21.2	5.3	0.13	2	3	SP
4d	30	180	1×1	21.2	5.3	0.13	2	3	SP
4e	30	180	1×1	21.2	5.3	0.13	1	3	SP
5	60	360	1×1	42.3	10.6	0.25	2	3	SP
6	90	540	1×1	63.5	12.7	0.25	2	4	SP
7	120	720	1×1	84.6	17.0	0.34	2	4	SP

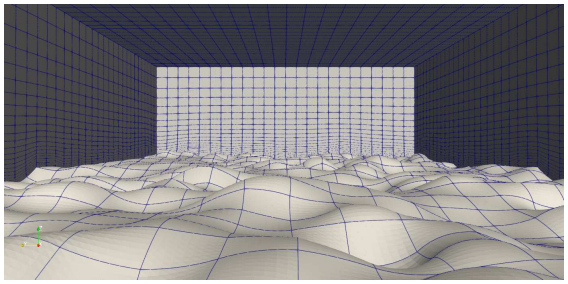

Figure 3. The computational domain and the surface mesh ($Q = 2$).

3. RESULTS

A set of simulations are conducted in the channel to investigate several numerical effects as well as the effect of Reynolds number. Table 1 lists the simulations with their roughness height, Reynolds number, and the resolutions they provide. The effective resolutions give an idea about the resolving power of the high-order method based on the number of freedom degrees in the element. Moreover, z^+_{eff} takes the approximate location of the first solution point over the surface. It can be deduced that the high Reynolds number cases ($Re_\tau = 360, 540, 720$) correspond to an ILES, whereas the lower Re_τ cases are of DNS resolution.

The simulations start from stillness, where the flow is driven by the constant body force that ensures the nominal Re_τ values. After an initial transient phase of at least $60\delta/u_\tau$, the flow statistics are collected for around $80\delta/u_\tau$. This is found to be sufficient according to Figure 4, where the sampling error is estimated based on the mean-square error (MSE) of the sample mean $\overline{g}$,

$$\mathrm{MSE}\,(\overline{g}) = \frac{\mathrm{Var}_N(g)}{N} \qquad (1)$$

according to [14]. Here, $\mathrm{Var}_N(g) = \frac{1}{N}\sum_{i=0}^{N-1}(g_i - \overline{g})^2$ is the biased estimate of the population variance. It is observed that the estimated sampling error agrees with the nominal Re_τ value, which is imposed as a body force. The reason the nominal value cannot be precisely reached may be uncertainties relating to the force integration, the compressibility, and the sampling error altogether.

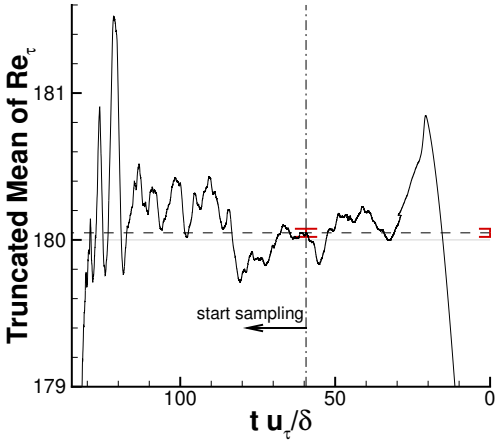

Figure 4. Truncated mean of effective Re_τ calculated from the force on the wall for Sim. 4d (Tab. 1). *Dashed:* the mean; *Gray:* the nominal value $Re_\tau = 180$; *Red:* error bar for the mean

Before presenting results from the entire range of roughness, some validation tests on $\mathrm{Re}_\tau = 180$ are conducted (simulations 4a–e in Table 1). The results are gathered in Figure 5. Firstly, the highest resolution is considered (Simulation 4a). It achieves a DNS resolution with $240 \times 120 \times 110$ degrees of freedom in streamwise, spanwise, and normal directions, respectively (cf. [1]). At the same time, DP is used, as commonly required by a proper DNS. Compared to Simulation 4d, using of $p = 4$ and DP together does

not improve the mean velocity profile discernibly, although the turbulence quantities get closer to the reference IBM-DNS. It should be noted that the quantities deviate from the reference towards the channel mid-plane because the half-channel simplification is adopted, unlike in the reference setup. The lowest possible polynomial approximation ($p = 2$), which can sufficiently imitate the surface topology ($Q = 2$) as shown in Figure 2, is also considered (Sim. 4b). Once again, while the mean velocity profile is of acceptable accuracy, there is a clear overprediction in the turbulence kinetic energy. Another interesting test is the effect of anti-aliasing (Sim. 4c). Even though the simulation does not crash due to the aliasing-related instabilities, the accuracy is impaired. Thus, anti-aliasing is used for all of the simulations. Lastly, the effect of low-order surface approximation is tested (Sim. 4e). A linear approximation to the roughness ($Q = 1$), as seen in Figure 1 degrades the velocity profile prediction and the prediction of the turbulent quantities. On the other hand, a higher degree of approximation to the surface improves the results considerably.

The streamwise mean velocity profiles for the entire range of roughness are shown in Figure 6. There is a good agreement with the reference DNS for all cases. Particularly for the highest Reynolds number ($\mathrm{Re}_\tau = 720$), the simulation falls into an ILES. Even so, the impact of the roughness (i.e. roughness function ΔU^+) seems to be predicted accurately. The mean velocity profile prediction over the tiled surface also agrees with the reference DNS. It should be noted that a refinement of the grid was found to be necessary for the reference IBM-DNS [1] to be able to resolve the roughness. For instance, they had to use almost 59 million cells for the 2×2 tiled surface (Sim. 3), whereas around 1.6 million degrees of freedom were used in the present approach.

Figure 7 is a snapshot showing the isosurface of Q-criterion coloured by the velocity magnitude for the case with the highest Reynolds number. It illustrates how flow structures smaller than the mesh element can be captured without sacrificing the curvature of the boundary. For the same simulation, the resolved turbulence on a spanwise plane can be viewed in Figure 8.

4. CONCLUSION AND OUTLOOK

A novel approach to predicting the impact of roughness on the boundary layer is investigated. The method proved to be competitive amongst other approaches such as IBM. It not only yields high accuracy, but also allows LES without sacrificing the topological features of the rough surface. Above all, efficient simulation of slightly rough surfaces, ranging from hydraulically smooth to the transitionally rough regime ($0 < k_s^+ < 70$), is made possible. In this roughness range, other methods like the IBM can fall into over-resolved DNS when the roughness topology is desired to be preserved. In contrast, in the present method, LES-level resolutions are shown to be adequate to resolve the surface sufficiently.

In an ongoing investigation, the method is being applied to a low-pressure turbine (LPT) cascade

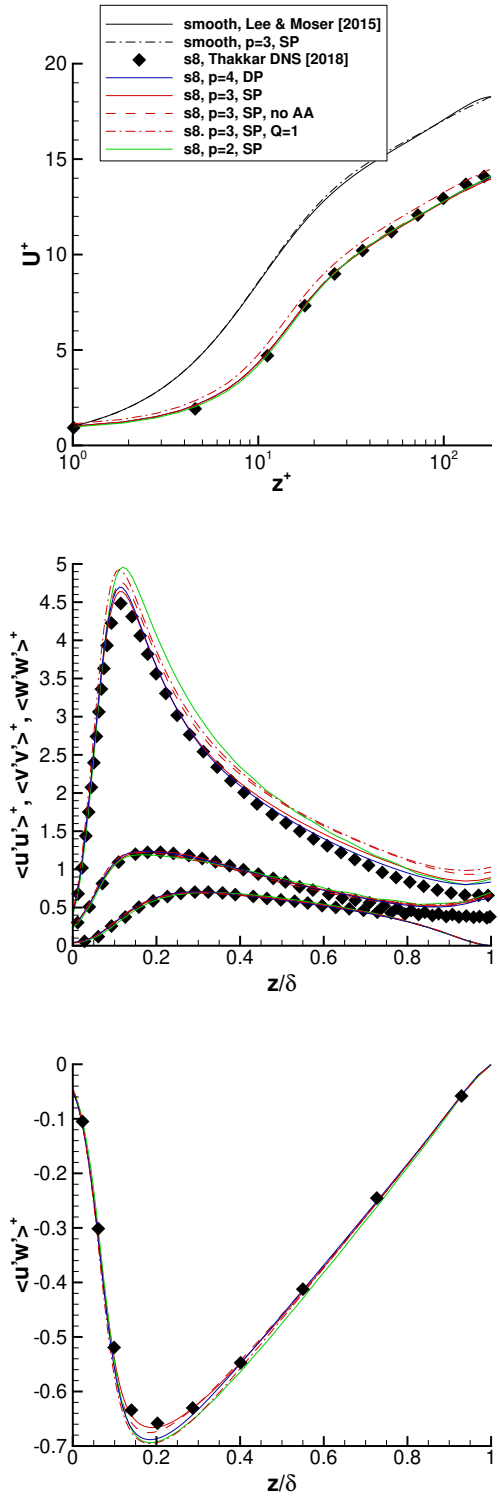

Figure 5. Mean velocity profiles (top) and turbulence variances (middle,bottom) in wall units for $\mathrm{Re}_\tau = 180$. Black symbols represent IBM-DNS by Thakkar *et al.* [1]

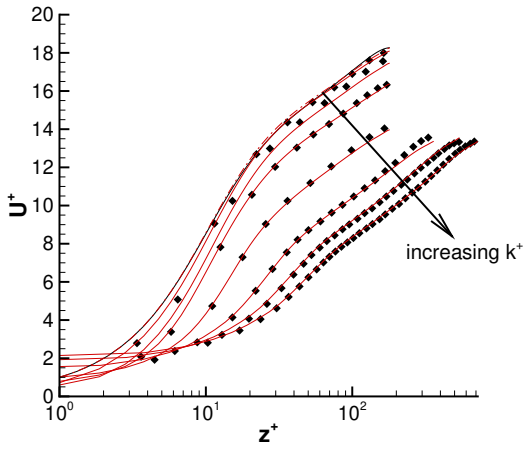

Figure 6. Mean velocity profiles in wall units. Black points represent DNS by Thakkar *et al.* [1]; red solid lines are current results, 1, 2, 3, 4d, 5, 6, 7; dashdotted line is the current smooth reference; black solid line is the smooth reference DNS with $Re_\tau \approx 180$ [15]

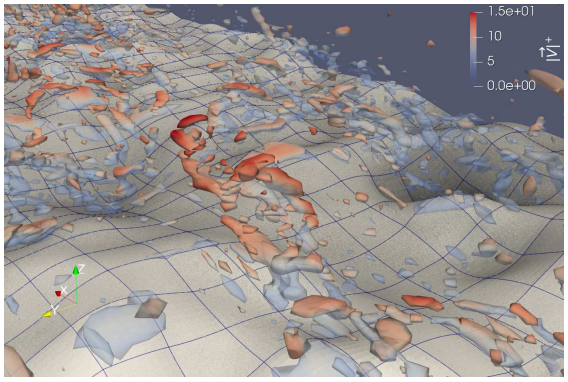

Figure 7. Isosurface of Q-criterion for $Re_\tau = 720$ (Sim. 7) coloured by the velocity magnitude in wall units. The surface mesh is also shown.

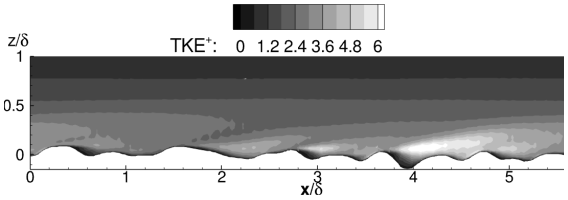

Figure 8. Turbulent kinetic energy for $Re_\tau = 720$ (Sim. 7) in wall units, taken from the mid-span plane.

with and without a roughness patch on the suction side of the profile. The preliminary runs show that the efficiency of this method enables scale-resolving simulation of a rough turbine cascade blade in only six days, using 4 V100 GPU cards, including the collection of first and second-order statistics of turbulence. The outcomes will be used in future work to investigate the influence of roughness on the aerodynamic performance of compressor and turbine cascades. Based on this, available roughness models for industrial applications will be assessed.

ACKNOWLEDGEMENTS

The work was partially supported by the North-German Supercomputing Alliance (HLRN) and partially by the cluster system team at the Leibniz University of Hannover (LUIS), Germany.

REFERENCES

[1] Thakkar, M., Busse, A., and Sandham, N. D., 2018, "Direct numerical simulation of turbulent channel flow over a surrogate for Nikuradse-type roughness", *Journal of Fluid Mechanics*, Vol. 837, p. R1.

[2] Busse, A., Lützner, M., and Sandham, N. D., 2015, "Direct numerical simulation of turbulent flow over a rough surface based on a surface scan", *Computers & Fluids*, Vol. 116, pp. 129–147.

[3] Thakkar, M., Busse, A., and Sandham, N., 2017, "Surface correlations of hydrodynamic drag for transitionally rough engineering surfaces", *Journal of Turbulence*, Vol. 18 (2), pp. 138–169.

[4] Hartung, K., Gilge, P., and Herbst, F., 2018, "Towards Immersed Boundary Methods For Complex Roughness Structures In Scale-Resolving Simulations", pp. 359–365.

[5] Kurth, S., Cengiz, K., Wein, L., and Seume, J. R., 2021, "From Measurement To Simulation - A Review Of Aerodynamic Investigations Of Real Rough Surfaces By DNS", *Proceedings of Global Power and Propulsion Society*, Vol. GPPS Xi'an21.

[6] Hammer, F., Sandham, N. D., and Sandberg, R. D., 2018, "Large Eddy Simulations of a Low-Pressure Turbine: Roughness Modeling and the Effects on Boundary Layer Transition and Losses", Vol. Volume 2B: Turbomachinery of *Turbo Expo: Power for Land, Sea, and Air*.

[7] Garai, A., Diosady, L. T., Murman, S. M., and Madavan, N. K., 2018, "Scale-Resolving Simulations of Low-Pressure Turbine Cascades With Wall Roughness Using a Spectral-Element Method", Vol. Volume 2C: Turbomachinery of *Turbo Expo: Power for Land, Sea, and Air*.

[8] Diosady, L. T., and Murman, S. M., 2018, "A linear-elasticity solver for higher-order space-time mesh deformation", *2018 AIAA Aerospace Sciences Meeting*, p. 0919.

[9] Karman, S. L., Erwin, J. T., Glasby, R. S., and Stefanski, D., 2016, "High-order mesh curving using WCN mesh optimization", *46th AIAA Fluid Dynamics Conference*, p. 3178.

[10] Witherden, F., Farrington, A., and Vincent, P., 2014, "PyFR: An open source framework for solving advection–diffusion type problems on streaming architectures using the flux reconstruction approach", *Computer Physics Communications*, Vol. 185 (11), pp. 3028–3040.

[11] DIN EN ISO 25178-2, 2012, "Geometrische Produktspezifikation (GPS) - Oberflächenbeschaffenheit: Flächenhaft - Teil 2: Begriffe und Oberflächen-Kenngrößen (ISO 25178-2:2012), Deutsche Fassung EN ISO 25178-2:2012", *Beuth Verlag*.

[12] Sigal, A., and Danberg, J. E., 1990, "New correlation of roughness density effect on the turbulent boundary layer", *AIAA journal*, Vol. 28 (3), pp. 554–556.

[13] Dirling, R., 1973, "A method for computing roughwall heat transfer rates on reentry nosetips", *8th Thermophysics Conference*, p. 763.

[14] Bergmann, M., Morsbach, C., Ashcroft, G., and Kügeler, E., 2021, "Statistical Error Estimation Methods for Engineering-Relevant Quantities From Scale-Resolving Simulations", *Journal of Turbomachinery*, Vol. 144 (3), 031005.

[15] Lee, M., and Moser, R. D., 2015, "Direct numerical simulation of turbulent channel flow up to $Re_\tau \approx 5200$", *Journal of Fluid Mechanics*, Vol. 774, p. 395–415.

Conference on Modelling Fluid Flow (CMFF'22)
The 18th International Conference on Fluid Flow Technologies
Budapest, Hungary, August 30 -September 2, 2022

DEVELOPMENT OF SEWAGE PUMPS WITH NUMERICAL AND EXPERIMENTAL SUPPORT

David BECK[1], Yvonne HOLZBAUER[2], Paul Uwe THAMSEN[3]

[1] Corresponding Author. Chair of Fluid System Dynamics, Faculty of Mechanical Engineering and Transport Systems, Technische Universität Berlin. Straße des 17. Juni 135, 10623 Berlin, Germany. Tel.: +49 314 21037, E-Mail: david.beck@tu-berlin.de
[2] Chair of Fluid System Dynamics, Faculty of Mechanical Engineering and Transport Systems, Technische Universität Berlin.
[3] Chair of Fluid System Dynamics, Faculty of Mechanical Engineering and Transport Systems, Technische Universität Berlin.

ABSTRACT

Especially in the field of wastewater pumps, the design of radial impellers focuses not only on maximum efficiency but also on functionality in terms of susceptibility to clogging by fibrous media.

In general, the efficiency of wastewater impellers is significantly lower than that of clear water impellers. These wastewater impellers are designed with a low number of blades to ensure that fibrous media can be pumped.

This paper describes the methodology of an optimisation for a wastewater impeller. The optimisation is carried out on a semi-open two-channel impeller as an example. Therefore, a new impeller is designed for a given volute casing.

Based on a basic design for given boundary conditions, the impeller is verified by means of numerical simulation. The manufactured impeller is then tested on the test rig to verify the simulation. With regard to the optical investigations, the clogging behaviour of the impeller is specifically improved over three different modifications in order to finally present an impeller with good efficiency and a low clogging tendency.

Keywords: Wastewater impeller, CFD, optical measurement, test rig

NOMENCLATURE

D_{LTF}	[-]	degree of long-time functional performance
H	[m]	head
m	[g]	mass
n	[1/s]	number of revolutions
n_q	[-]	specific speed
Q	[m³/h]	flow
β_1	[°]	blade inlet angle
η	[-]	efficiency

Subscripts and Superscripts

BEP	best efficiency point
CLE	connected leading edges
CW	clear water
fps	frames per second
FWT	freshwater tank
L25	low contamination
L50	medium contamination
L100	high contamination
PLA	polyactid acid
SST	shear stress transport
w	wet wipes
WWT	wastewater tank

1. INTRODUCTION

Wastewater pumps face increased operational problems due to clogging, for example clogging within the impeller or the volute casing, according to increased contamination of solids in wastewater. This represents the main reason for downtime, wear and manual labour in wastewater plants [1,2]. These solids, which are mainly responsible for pump clogging, are often tear-resistant fibrous materials, for example wet wipes. Figure 1 shows the components of a pump blockage, where tear-resistant fibrous materials are the main component for the pump blockage, which were found in [3].

Figure 1. Constituents of pump blockage [3]

In contrast to freshwater pumps, impellers with a low number of blades or special impeller shapes are

deliberately used in wastewater pumps to handle solids in wastewater as efficiently as possible. Typical impellers for wastewater conveyance are closed and semi-open multi-channel impellers, closed and semi-open single-channel impellers as well as special forms such as the vortex impeller [4].

Up to now, pumps have been evaluated according to DIN EN ISO 9906 only with regard to their clear water values. There is no general criterion for pumping wastewater containing solids about the susceptibility to clogging [5].

Compared to the described classical approach, the functional performance test has already been introduced in [6], which tests both the efficiency and the clogging susceptibility of pumps.

In this paper, the methodology of an optimisation for a wastewater impeller is described. As an example, a semi-open two-channel impeller is designed. By means of simulation and functional performance tests on the test rig, a hydraulic system is to be developed which, in addition to good efficiency, should have a low susceptibility to clogging. A classification of the susceptibility to clogging for the semi-open two-channel impeller is carried out using the evaluation criteria of the long-time functional performance test.

2. MATERIALS AND METHODS

2.1 Basic Design

The new impeller is designed as a semi-open two-channel impeller. In contrast to closed impellers, which have both a hub and a shroud, semi-open impellers do not have a rotating shroud. For this impeller, the shroud is installed stationary in the housing, which creates a small gap between the impeller and the volute casing. This gap shall assist the discharge of added fibrous materials.

The impeller should be designed as a radial impeller and be within a range for the specific speed of $n_q = 30...50$, which is typical for radial wastewater impellers [7]. The specific speed is calculated according to [8] as follows:

$$n_q = n \frac{\sqrt{Q}}{H^{3/4}} \qquad (1)$$

The design point for this impeller is given in normalised form, as the main focus in this paper is on the methodology of optimisation. The design point is continuously given for the flow with $Q_{design} = 1.0$, analogously the head results in $H_{design} = 1.0$.

One requirement of the impeller is the maximum variability for changing the leading edge geometry of the blades. Previous investigations have shown that impellers with classic leading edges often tend to increased clogging in two-channel impellers. The aim for this impeller is to be able to incorporate a 3D-printed geometry to connect the leading edges of the impeller, so called connected leading edges (CLE), with maximum variability for the basic impeller. The classic impeller with two leading edges and a possible design of CLE are shown schematically in Figure 2.

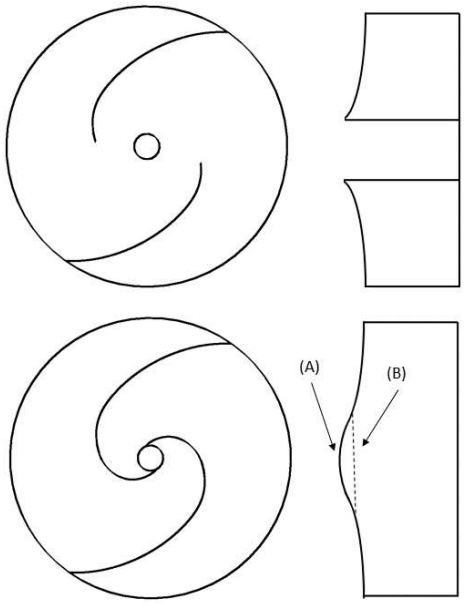

Figure 2. Meridional section and plan view for the semi-open two-channel impeller with two leading edges (top) and for the CLE (bottom)

The upper part of Figure 2 shows a classic approach for a semi-open two-channel impeller. The lower part of the figure shows two variants of a possible meridional contour for CLE: (A) shows a convex shape, which is intended to follow the course of the blade widths of the original blades. (B) shows a meridional contour for CLE that is flat and parallel to the suction side of the pump.

For the basic design of the impeller, the shape of two leading edges is chosen according to the upper part of Figure 2. The impeller is designed for the maximum specific speed according to the said range with an specific speed of $n_{q,design} = 50$, since a shift of the best efficiency point (BEP) due to the CLE in the direction of smaller flows is expected. This shift of the best efficiency point towards smaller flows is caused, among other things, by the fact that the effective area of the impeller suction side due to a decreasing inlet diameter as well as the blade inlet angle β_1 are reduced. Accordingly, a steeper characteristic curve is to be expected for the impeller with CLE compared to the impeller with two leading edges [4].

The impeller is designed for a given wastewater volute. Previous investigations of this volute casing have shown that it is particularly resistant to clogging. This is necessary in order to evaluate the impeller in terms of susceptibility to clogging. Clogging in the volute casing has a negative influence on the general susceptibility of the

hydraulic and thus on the measurement result, because it is only possible to measure the total amount of wet wipes within the pump after the end of the test.

The spiral contour of the volute casing is circular. The built-in stationary shroud is used for all measurements.

The theoretical throttle curve is calculated for the impeller according to [8]. However, this is only a reference and is verified by the subsequent simulation and the measurement results of the tests.

2.2 Numerical Simulation

The impeller with two leading edges is simulated before manufacturing to evaluate the design.

For the numerical simulation, the software ANSYS CFX is used. For the impeller, a structured mesh is used. The volute is meshed as an unstructured mesh. The setup including the mesh is shown in Figure 3. Details on the mesh qualities are shown in Table 1.

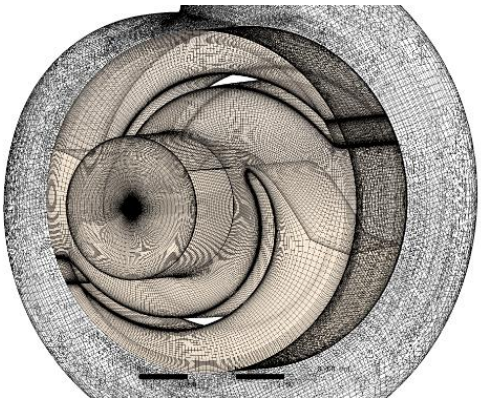

Figure 3. Mesh used for simulation

Table 1. Mesh statistics

Part	Elements
Impeller	827772
Volute	864356

The simulation is calculated in a stationary manner in order to shorten the calculation time. The shear stress transport model (SST) is chosen as the turbulence model in order to generate good resolution and convergence both in near-wall areas and free streams [9].

Some simplifications are applied for the simulation: The impeller, which is designed as a semi-open two-channel impeller, is simulated without the sidewall gap, as primarily the simulation is used for estimating the general design. The same applies to the gap between the impeller and the stationary shroud, as the size of the gap has an influence on the discharge of the wet wipes, which must be determined experimentally. Likewise, disk friction losses are not represented in their entirety by the setup.

Accordingly, the focus of the simulation is on verifying the basic geometry of the impeller. It can be assumed that the simulated results are better than the manufactured impeller due to the neglected losses. This applies in particular to the efficiencies at higher volume flows, as the hydraulic losses for higher volume flows have greater influence.

Ten operating points are simulated. Of these, the design point as well as three operating points to smaller flows compared to the design point and six points to higher flows compared to the design point are simulated.

Since the impeller is a semi-open two-channel impeller simulated without a gap, the shroud is assumed to be a counter-rotating wall. In addition, the shaft-hub connection of the hub is assumed to be a free-slip wall, as this does not exist in the prototype, so that the described CLE can be installed.

2.3 Impeller Prototyping

The basic impeller with two leading edges is made of cast iron, the only design change compared to the simulation is the shaft-hub connection. The impeller is manufactured in such a way that a 3D-printed attachment can be placed on the central shaft screw to connect the leading edges.

The impeller manufactured from cast iron is shown in Figure 4.

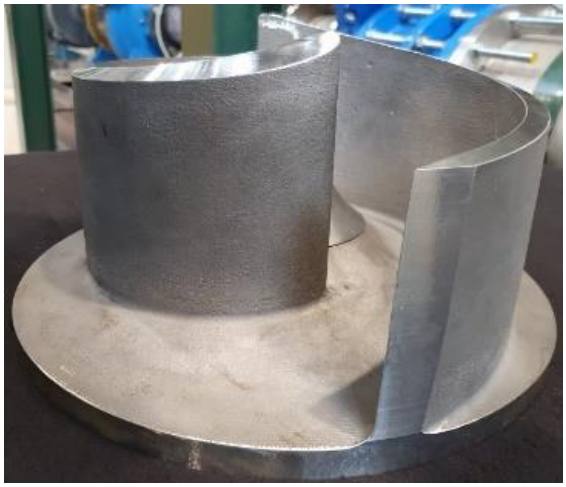

Figure 4. Modification 0 – manufactured impeller

The attachments are made from the plastic polyactic acid (PLA) using a 3D printer, as this manufacturing is relatively inexpensive and fast concerning design changes. In addition, previous tests have shown, that PLA exhibits sufficient strength, when used with artificial wastewater.

2.4 Test Procedure

The test rig for functional performance of the Chair of Fluid System Dynamics at the Technische Universität Berlin has two tanks, the wastewater tank (WWT) and the freshwater tank (FWT), each with a volume of 4 m³.

Two different clogging tests can be carried out on the test rig using tear-resistant wet wipes - the functional performance test and the long-time functional performance test. The test rig has pinch valves, which make it possible to switch between the different tests and shut off the pump. In addition, a filter is installed in the FWT, which is decoupled from the system and removes all residual fibres in the test rig. The results of this paper are generated with the long-time functional performance test. Tear-resistant wet wipes according to the contamination classes in Table 2 are used for the tests.

Table 2. Contamination classes

Contamination Class	Wipes / m³
Clear water (CW)	0
Low contamination (L25)	25
Medium contamination (L50)	50
High contamination (L100)	100

Figure 5 shows the wet wipes used for the experiment. These have the dimension of 22x30 cm and a surface weight of 60 g/m².

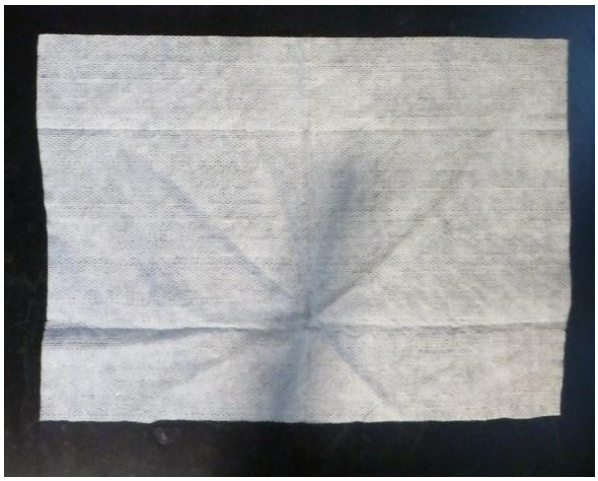

Figure 5. Wet wipes used for tests

Generally, for both tests, the pumps are tested at their BEP, as well as at 80% of the BEP in partial load and at 120% of the BEP in overload. A total of nine measurements per impeller are thus carried out on the test bench.

Long-time functional performance test:

The long-time functional performance test describes the 60-minute pumping of the artificial wastewater in a loop from the WWT to the WWT, shown in Figure 6. In the process, the measured values of the head, the flow and the electrical power are recorded every second. The efficiency is determined using these data. After the test, the pump is shut off, opened and the remaining wet wipes are documented and removed. From this, the degree of long-time functional performance (D_{LTF}) is determined according to equation 2*:*

$$D_{LTF} = \frac{1}{2}\frac{\eta_{test,0-60min}[-]}{\eta_{CW,OP}[-]} + \frac{1}{2}\frac{m_{W,total}[g] - m_{W,pump}[g]}{m_{W,total}[g]} \quad (2)$$

Here, the first part of the D_{LTF} represents the ratio of the averaged efficiency over the 60-minute measurement period to the clear water efficiency at the corresponding operating point. The second term of the D_{LTF} represents the ratio of the difference between the total amount of wipes supplied and the wipes remaining in the pump to the total amount of wipes supplied.

A D_{LTF} of 0 indicates that the impeller is completely clogged and conveying is no longer possible, while a value of 1 describes clog-free operation. Based on the tests already carried out, a D_{LTF} of at least 0.7 is required for the prototype, as it has been shown that impellers above a value of 0.7 exhibit good clogging behaviour and can handle the added fibrous material well.

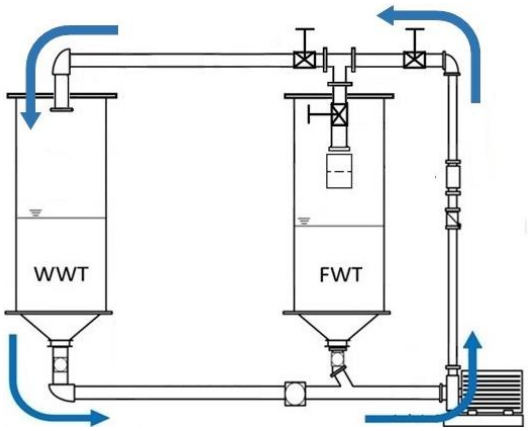

Figure 6. Long-time functional test cycle

2.5 Optical Access

The test rig has an optical access on the suction side, which is similar to the optical access presented in [10]. By means of an endoscope, an LED light ring and a high-speed camera, it is possible to get closer insights at the impeller inlet during operation. Figure 7 shows the installed access.

As an additional measurement method, this approach provides an opportunity to describe the interaction between the flow and the wet wipes during operation and to make targeted changes to the geometry from the results. For these tests, the camera records at 1000 fps over a period of 20 seconds with a resolution of 768 x 768 pixels. The test cycle is analogous to the long-time functional performance test, but the contamination class is different. For these tests, ten wet wipes per m³ of water are used, as it has been shown that with this quantity, initial clogging behaviour can be easily seen, while there

are not too many wipes to impair the optimal measurement.

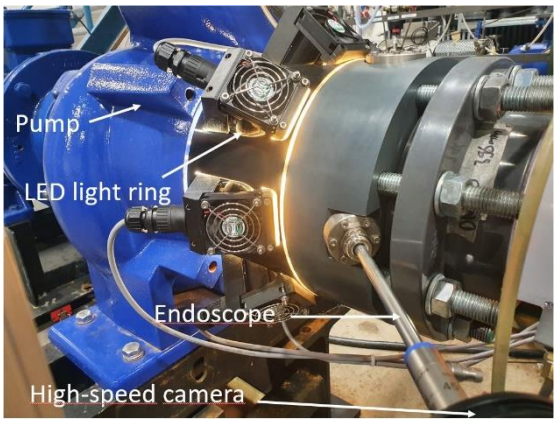

Figure 7. Test setup for optical access

The endoscope has a diameter of 10 mm and a viewing direction of 45°. Due to the resulting installation position, this angle ensures that the wipes do not clog on the endoscope and thus a uniform supply of the wipes into the inlet of the pump is possible. The field of view is 88°. The LED light ring consists of eight individual LEDs, which provide a luminous flux of 5595 lumen each.

3. RESULTS AND DISCUSSION

3.1 Results - Simulation

The simulation results in relation to the theoretical design curve is shown in Figure 8. For the simulation results, only the throttle curves are compared with each other, as an efficiency estimate was not carried out.

The results of the simulation show the same trend of the design characteristic. The simulated throttle curve shows a slightly higher level and is superior to all calculated operating points of the design throttle curve. This is due, among other things, to the simplifications of the simulation described above. This can also be said about the efficiency, for which a value of $\eta_{BEP,CFD} = 79.5$ % is achieved in the simulation. However, it can be seen that the BEP of the hydraulic with $Q_{BEP,CFD} = 1.2$ is slightly larger than the design point.

Overall, this comparison shows that the design is well represented by the simulation with regard to its design characteristic. Due to the simplified assumptions, the efficiency reaches a higher value in the simulation than is to be expected in the measurement. Especially not all hydraulic losses are taken into account by the simplifications. Since these increase with higher flows, a shift of the optimal efficiency is to be expected with smaller flows. Likewise, a reduced efficiency at the BEP of the manufactured impeller can be assumed.

3.2 Results – Modification 0

Figure 8 additionally shows the measurement of the characteristic curves of the impeller with two leading edges on the test bench in relation to the simulation results as well as the design throttle curve.

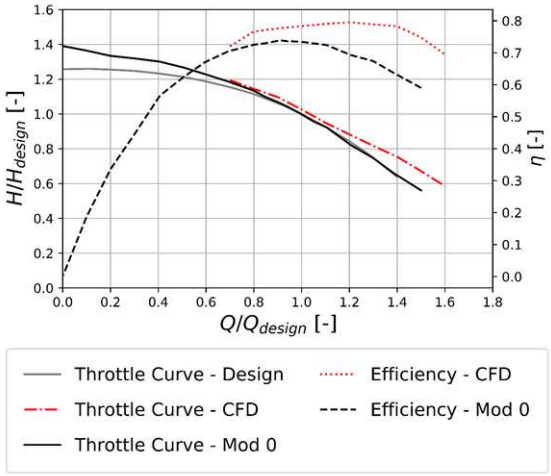

Figure 8. Modification 0 – characteristic curves

The measured characteristic curves show the same trend of the simulation around the design point. Especially in the direction of smaller flows of the design point, the simulated and the measured throttle curves show an almost identical trend.

For strong partial load and overload, the measured throttle curve deviates from the design throttle curve. However, the design throttle curve only represents a trend and is mainly to be assumed for the range of best efficiency.

The maximum efficiency of the measured impeller is around 5% lower than the best efficiency value of the simulation. The BEP of the impeller is thus at a flow of $Q_{BEP,0} = 0.9$ with a efficiency value of $\eta_{BEP,0} = 73{,}9\%$. This deviation is again due to the simplified assumptions of the simulation. This BEP results in a specific speed of $n_{q,0} = 48$, which, taking into account the boundary conditions for the specific speed, provides a good starting point for the further process of inserting a printed part for CLE.

To get an impression of the susceptibility to clogging of the basic impeller, the long-time functional performance test with medium contamination (L50) is carried out for the impeller in Modification 0.

The impeller clogs with a result of $D_{LTF,0} = 0.32$. The amount of wet wipes removed from the impeller at the end of the test corresponds to 72% of the amount of wet wipes supplied. The clogging has accumulated at the leading edges during the test and has grown from there. The clogging inside the impeller after the end of the long-time functional performance test can be seen in Figure 9.

Figure 9. Modification 0 – clogging after long-time functional test (BEP, L50)

This impeller geometry is not able to discharge the wet wipes. Due to the high susceptibility to clogging, no further tests of the impeller are carried out.

3.3 Results – Optimization

Modification 1: For the first modification, a printed part for the CLE with a strongly convex shape in the meridional section as shown in Figure 2, example (A), is used, which follows the width progression of the two blades. The characteristic curves of modification 1 compared to modification 0 are shown in Figure 10.

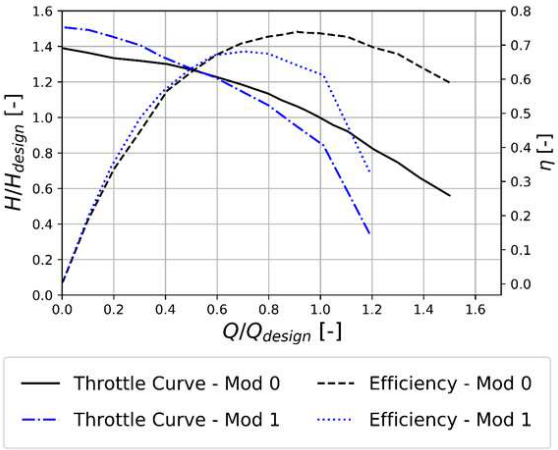

Figure 10. Modification 1 – characteristic curves

The characteristic curves of Modification 1 show that the BEP shifts towards smaller flows due to the CLE. The optimum efficiency of $\eta_{BEP,1} = 68.1$ % is achieved for a flow of $Q_{BEP,1} = 0.7$. The resulting specific speed is $n_{q,1} = 37$ and is therefore within the specified limits.

The long-time functional performance test with low contamination (L25) at the BEP shows a poor clogging result with a $D_{LTF,1} = 0.19$, which is insufficient. Overall, 91% of 310g of supplied wet wipes are absorbed. A conveying of the wipes does not seem possible due to this result of the long-time functional performance test.

The result of the long-time functional test suggests that conveying of the wet wipes cannot take place with high numbers of wet wipes arriving in the impeller at the same time, which clogs the impeller. In addition, the convex shape of the CLE extends very far forward into the inlet that the wipes cannot be discharged via the gap between the impeller and the volute casing as soon as the clogging has reached a certain degree.

In Figure 11 on the left-hand side, it is shown, that the accumulation of the wet wipes extent into the suction pipe. As soon as the wipes are lying on the CLE and are not conveyed, the clogging grows in the direction of the suction pipe. In this case, self-cleansing of the impeller can no longer be expected.

The optical measurement shows the extent to which the wet wipes interact with the impeller. The investigation has shown, that single wet wipes lay loose on the printed part for the CLE, but are conveyed within a few revolutions. A screenshot from the optical investigation is shown in Figure 11 on the right-hand side.

Figure 11. Modification 1 – clogging after long-time functional test (BEP, L25) (left) and optical investigations (right)

The impeller has suitable free-flushing characteristics for the arrival of single wet wipes, as the investigation has shown. Nevertheless, it can be said that the impeller is no longer able to flush off the wet wipes for higher incoming concentrations of wet wipes.

Modification 2: The second modification has a printed part for the CLE that is plane and parallel to the inlet of the pump, according to shape (B) in Figure 2. This is intended to prevent the flow from decreasing due to throttling on the suction side in the inlet pipe because of wet wipes, as can be seen for Modification 1.

While looking at the characteristic curves in Figure 12, the maximum efficiency of $\eta_{BEP,2} = 69.1$ % is reached at a flow of $Q_{BEP,2} = 0.7$. As a result, the impeller achieves a specific speed of $n_{q,2} = 35$. The throttle curve of Modification 2 shows a similar behaviour to Modification 1.

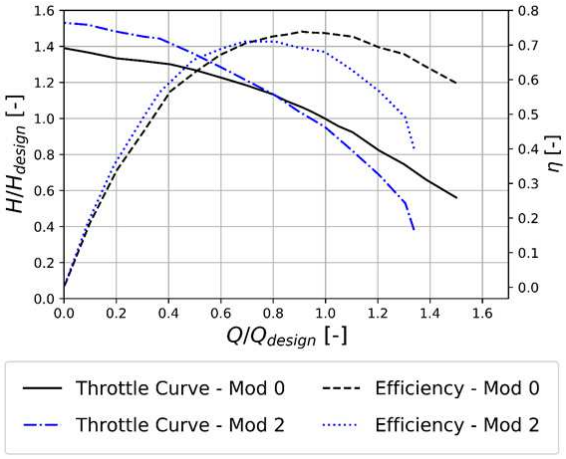

Figure 12. Modification 2 – characteristic curves

The long-time functional performance test for the Modification 2 results in a $D_{LTF,2} = 0.43$ for the BEP with low contamination (L25). In total, 64% of 309g of supplied wet wipes are absorbed, which shows a significant improvement in clogging compared to Modification 1.

The clogging inside the impeller after the end of the long-time functional performance test can be seen in Figure 13 on the left-hand side.

Contrary to Modification 1, the wipes do not grow into the suction pipe and do not throttle the incoming flow. The impeller appears to have a degree of saturation, which, once reached, cannot accommodate any further wipes. This is particularly evident from the fact that a significantly lower proportion of wet wipes are absorbed compared with Modification 1.

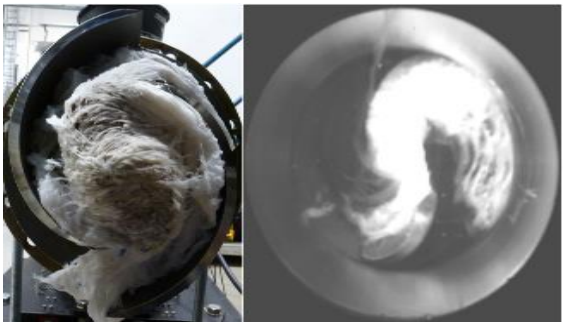

Figure 13. Modification 2 - clogging after long-time functional test (BEP, L25) (left) and optical investigations (right)

By means of optical observations, it can be seen in Figure 13 on the right-hand side, that the wet wipes, which are sucked in centrally, also hit the centre of the CLE analogously to Modification 1, where they accumulate. In addition, the clogging on the CLE increases between the beginning of the test and the end of the test, which could be detected through the optical investigations. The geometry of the impeller is not able to discharge the wet wipes. Likewise, the wet wipes cannot be loosened by the impact of further incoming wet wipes. Accordingly, this flat contour is also not optimal for conveying wet wipes and tends to clog, even if the clogging result is improved compared to Modification 1.

Altogether, the modification is not able to convey wet wipes even in small concentrations, even if this modification shows a minor saturation of wet wipes and therefore has a higher D_{LTF}.

Modification 3: Another printed part is manufactured for the third modification, which combines the good conveying characteristics of Modification 1 with the advantages of the axial length of Modification 2 concerning the maximum amount of wet wipes absorbed.

The third modification shows a significantly smaller convex shape compared to Modification 1 to reduce the axial length and maintain the conveyance characteristics. Analogous to the first two modifications, Figure 14 shows the characteristic curves of Modification 3.

Modification 3 has its BEP as well as the other two modifications at $Q_{BEP,3} = 0.7$. The best efficiency for this modification is $\eta_{BEP,3}$ 64.5 %. This modification results in a specific speed of $n_{q,3} = 37$.

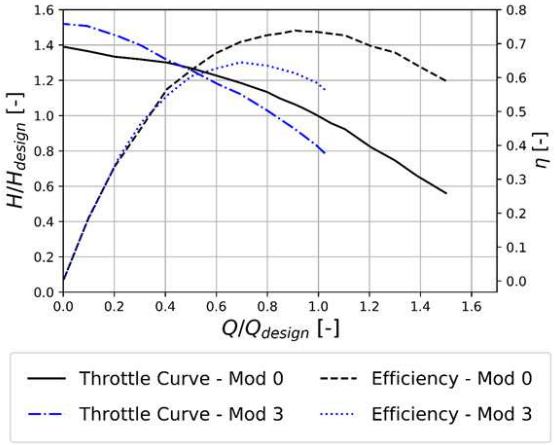

Figure 14. Modification 3 – characteristic curves

A long-time functional performance test with low contamination (L25) is also carried out for this modification. The impeller achieved a $D_{LTF,3} = 0.98$. At the end of the measurement, the impeller had not absorbed any wet wipes from the 299g supplied. The missing 2% of the D_{LTF} also can be attributed concerning eq. (2) to slight hydraulic dips during the test, which occur due to brief blockages within the test caused by the wet wipes. However, the impeller manages to continuously discharge the wet wipes.

The impeller manages to convey the wet wipes into the channels continuously over the measurement period for this type of CLE.

Table 3 shows the results for the long-time functional performance tests for all nine measurement setups:

Table 3. Measurement results: D_{LTF} for Modification 3 for three operating points

Q / Q_{BEP}	L25	L50	L100
0.8	0.97	0.99	0.94
1.0	0.98	0.91	0.94
1.2	0.74	0.90	0.74

No further modification is necessary, as the impeller exceeds the required degree of long-time functional performance of 0.7 for all measurement points and thereby has the best clogging behaviour of all modifications.

3.4 Comparison of Results

Overall, the optimisation shows a considerable improvement in the D_{LTF} and thus the susceptibility to clogging, as can be seen in Figure 15.

Modification 0 shows a poor clogging result for the medium contamination with two leading edges. By using the CLE, the first modification also achieves an insufficient result in the long-time functional performance test. This is improved by targeted changes to the geometry through the detection of the weak points by means of optical tests as well as the long-time functional test.

The second modification still shows a high susceptibility to clogging with wet wipes, even though the D_{LTF} is improved a lot.

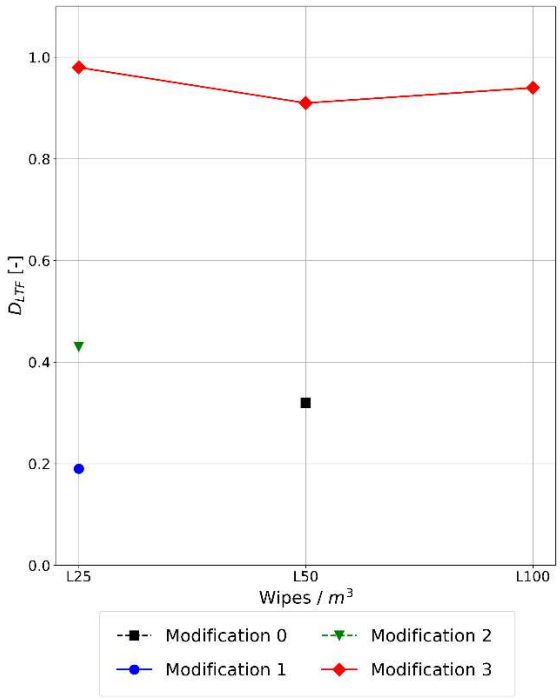

Figure 15. Overview over D_{LTF} for tested modifications for $Q / Q_{BEP} = 1.0$

Through renewed optimisation based on the findings of the optical tests and the test results of both previous modifications, a modification is tested, that delivers a clog-free result for the low contamination. Likewise, the required D_{LTF} of over 0.7 will be achieved for all contaminations, both in the BEP, in partial load and in overload.

4. CONCLUSION

The use of simulations for a calculated wastewater impeller in combination with a test rig to test the susceptibility to clogging has shown that impellers for wastewater pumps can be designed and optimised according to specific criteria. The use of optical access is particularly noteworthy, to specifically address the interaction between the wet wipes and the impeller and for making specific design changes.

REFERENCES

[1] Von Sperling, Marcos, 2007, "Wastewater Characteristics, Treatment and Disposal", *ASME J Turbomachinery*, Vol. 1 London, IWA Publishing.

[2] Gerlach, S., and Thamsen, P.U., 2007, "Cleaning sequence counters clogging – a quantitative Assessment under real operation conditions of a wastewater pump", Proc. *ASME 2017 Fluids Engineering Division Summer Meeting*, July 31 – August 3, Waikoloa, Hawai'i, USA.

[3] Mitchell, R.-L., 2019, "Causes, effects and solutions of operational problems in wastewater systems due to nonwoven wet wipes", *Mensch und Buch* Verlag, Berlin

[4] Gülich, J., 2008, "Centrifugal Pumps", *Springer*, Vol. 3, Berlin

[5] DIN EN ISO 9906:2013-03, 2013, "Kreiselpumpen – Hydraulische Abnahmeprüfungen – Klassen 1, 2 und 3"

[6] Pöhler, M., 2020, "Experimentelle Entwicklung eines standardisierten Abnahmeverfahrens für Abwasserpumpen", *Mensch und Buch* Verlag, Berlin.

[7] Surek,D., 2014, "Pumpen für Abwasser- und Kläranlagen: Auslegung und Praxisbeispiele", Springer, Wiesbaden.

[8] Pfleiderer, C. And Petermann, H., 2006, "Strömungsmaschinen" *Springer*, Auflage 7, Berlin Heidelberg New York.

[9] Versteeg, H.K. and Malalasekera, W., 2007, "An Introduction to Computational Fluid Dynamics", *Pearson Education Limited*, Secon edition, Essex, England.

[10] Steffen, M. And Thamsen, P.U., 2021, "Visualisation of interactions between impeller and textile in a wastewater pump", Proc. AS*ME 2021 Fluids Engineering Division Summer meeting,* August 10-12, Virtual, Online.

Conference on Modelling Fluid Flow (CMFF'22)
The 18th International Conference on Fluid Flow Technologies
Budapest, Hungary, August 30 -September 2, 2022

BOUNDARY CONDITION OPTIONS FOR CAROTID BIFURCATION ANALYSIS USING DOPPLER VELOCITY MEASUREMENTS

Márton Bence NÉMETH[1], Benjamin CSIPPA[2], Zsuzsanna MIHÁLY[3], György PAÁL[2], Péter SÓTONYI[3]

[1] Corresponding Author. Department of Hydrodynamic Systems, Budapest University of Technology and Economics. Műegyetem rkp. 3., H-1111 Budapest, Hungary, E-mail: mnemeth@hds.bme.hu
[2] Department of Hydrodynamic Systems, Faculty of Mechanical Engineering, Budapest University of Technology and Economics. Műegyetem rkp. 3., 1111 Budapest, Hungary
[3] Department of Vascular and Endovascular Surgery, Semmelweis University Budapest, Városmajor Str. 68, 1122 Budapest, Hungary

ABSTRACT

The common carotid artery (CCA) is a major blood vessel in the neck that bifurcates into the internal (ICA) and external carotid arteries (ECA) where a stenosis (narrowing of the vessel) can occur. Three-dimensional computational fluid dynamics (CFD) analysis of this bifurcation is a standard practice, although it is challenging to prescribe patient specific boundary conditions to approach patient-specific flow conditions. Our aim was to analyze the effect of different boundary conditions to find the most accurate flow conditions that fit the available measured data best.

We conducted CFD simulations on a carotid bifurcation geometry with an ICA stenosis. Six boundary condition groups were analyzed using patient-specific Doppler velocity measurement data at the inlet and both outlets. Three methods were implemented with defined inlet flow rate and either 0 Pa pressure (Basic), Windkessel model, or given flow division (Murray-law) at the outlets. For the other three methods we defined flow rates at two boundaries and a 0 Pa pressure at the third one.

When all the velocity measurements are available, defining two boundary flow rates shows the closest results to the patient-specific data. However, a problem arises from the difficulty of the Doppler measurements on ICA and ECA, which makes the velocity amplitudes to appear higher than expected. Therefore, cross-sectional corrections were implemented to fit the outlet and inlet flow rates while keeping the measured velocity histories.

Our results show that the Murray and Basic methods, while easily available, might exclude carotid-specific flow conditions since downstream flow resistances are not considered. We conclude that a Windkessel-method could produce the most accurate results without forcing outflow conditions. However, usually unavailable pressure and velocity measurements are necessary for its application.

Keywords: Doppler velocity measurements, Carotid bifurcation, Boundary condition

NOMENCLATURE

A	$[m^2]$	cross-sectional area
C	$[Pa\ s/m3]$	capacity
D	$[m]$	diameter
K	[-]	area ratio
R_d	$[Pa\ s/m3]$	distal resistance
R_p	$[Pa\ s/m3]$	proximal resistance
Q	$[ml/s]$	volume flow rate
t	$[s]$	time
v	$[m/s]$	velocity

Subscripts and Superscripts

CCA	at the common carotid branch
ECA	at the external carotid branch
ICA	at the internal carotid branch
avg	spatial mean
norm	normalized value
*	corrected geometry
−	temporal mean

1. INTRODUCTION

Cardiovascular diseases are the leading causes of death in western countries [1] and therefore thoroughly researched in literature. One of the most common types of such diseases is the so-called stenosis, a narrowing of the vessel, which can lead to stroke by occlusion (blocking) of arteries, which supply the brain. Since bifurcations and junctions are more prone to stenosis [2], the carotid bifurcation is a high-risk area, causing it to be the subject of many investigations to identify the effects of vessel

occlusion [3-5]. A common carotid artery can be found on both sides of the neck. It bifurcates into the internal carotid artery (ICA), and the external carotid artery (ECA). The ICA supplies the brain with blood without backflow during the entire heart cycle, therefore its resistance is low. Meanwhile, the ECA is a peripheral artery with higher resistance.

A standard method in research is to investigate the carotid bifurcation with three-dimensional numerical simulations [6-8]. To accomplish this, patient-specific geometry is necessary, which is usually acquired by segmenting computed tomography angiography (CTA) or magnetic resonance angiography (MRA) images. The segmentation method, however, has the inherent problem of subjectivity. This often appears as over-segmentation, which can cause inaccuracies in the geometry and simulation results [9, 10].

Well-defined boundary conditions are also necessary to achieve patient-specific flow conditions. Many methods are used in the literature to solve this problem [11-13], but a general solution has not been found. The difficulty of this task arises from the fact that, in most cases, patient-specific measurement data are not available, limiting the potential boundary conditions. Usually, non-invasive techniques, such as Doppler velocity measurements are used to gain patient-specific data; however, this is also limited because of the difficulty of the ECA and ICA measurements [14].

We investigate the applicability of six selected boundary conditions based on their effect on basic flow conditions. Furthermore, we attempt to offer simple methods to utilize the available measurement data to improve the simulation geometry.

2. METHODS

2.1 Clinical data, geometry

A patient specific geometry was chosen from a series of CTA and Doppler measurements are given by the Dept. of Vascular and Endovascular Surgery of Semmelweis University and the necessary data were anonymised before the described process. The CTA contains the left Common Carotid Artery (CCA) and its bifurcation, and a 68.5 % stenosis is detected on the Internal Carotid Artery (ICA). The degree of stenosis was calculated with the North American Symptomatic Endarterectomy Trial criteria [15]. The CTA image segmentation was completed using itk-SNAP, focusing only on the major arteries: CCA, ECA, ICA. The Vascular Modeling Toolkit (VMTK) was used for surface smoothing and generating the necessary extensions at the inlet and outlets, including the different cross-sectional transitions described in the geometry boundary correction section.

Doppler velocity measurements were performed for the CCA, ICA, and ECA. From the measurement images of the velocity distribution (Figure 1) the enveloping curve was selected using the image recognition tools of MATLAB. The gained curve is the maximum velocity at the location of the measurement. The maximum velocity waveforms were averaged over multiple heart cycles, to gain a patient-specific velocity waveform for a single (0.85 sec) heart cycle (Figure 2). Doppler images of the respective arterial sections are also created during the measurement, which was used to correct the segmented arterial diameters.

2.2 Geometry boundary correction

CTA image-based segmentation is a subjective method of arterial geometry reproduction since the low resolution of CTA images can lead to uncertainty in the morphological parameters of the artery. This uncertainty generally takes the form of over-segmentation, thus resulting in larger artery diameters [9].

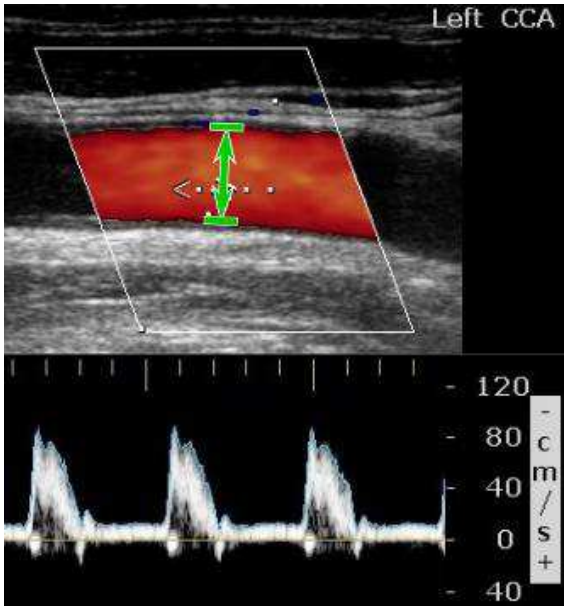

Figure 1. Measured diameter on the Doppler image (top), and Doppler velocity measurement on the CCA (bottom)

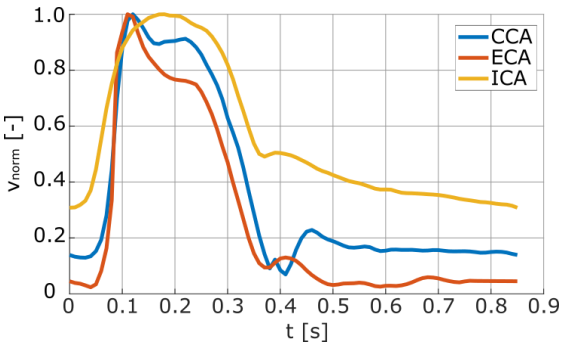

Figure 2. Normalized velocity waveforms of the CCA, ECA and ICA calculated from the Doppler velocity measurements

Two types of geometry modifications were implemented to correct these inaccuracies using patient-specific Doppler measurements.

The CCA cross-section, obtained from CTA images were modified using the Doppler measurement (DCor) images (Fig 1). These images only contain a small section of the arterial geometry, but it is shown in higher resolution than in the CTA. Therefore, in some instances, when an artery can be reliably scanned with the Doppler method, we assumed that its image can be used to measure the diameter of the artery with higher accuracy. We implemented this method to the chosen geometry to approximate the CCA diameter better, correcting the over-segmented (Raw) 42.7 mm^2 cross-section to 28.0 mm^2 (Figure 3).

The second geometry modification (QCor) was implemented to achieve a similar correction of the ECA and ICA sections. Since the ECA and ICA branches of the bifurcation are not straight and the change in cross-section is not negligible, Doppler images cannot be used to determine an accurate diameter. However, calculating the flow rate from the velocity shows the necessity of the cross-sectional correction since continuity is not fulfilled. The area ratio *K* is the ratio between the ECA and ICA outlet areas. We assumed that the segmentation overestimation at the outlet boundaries is proportional to the cross-sectional area. Therefore, the area ratio *K* is constant, and it is possible to rescale the geometry utilizing the flow continuity. The area ratio *K* of the outlets in the examined geometry is

$$K = \frac{A_{ECA}}{A_{ICA}} = \frac{A_{ECA}{}^*}{A_{ICA}{}^*} = 0.595 \qquad (1)$$

where A_{ECA} and A_{ICA} are the cross-sectional areas of the ECA and ICA at the location of the Doppler measurements, respectively before the area correction, while A_{ECA}* and A_{ICA}* are the corrected cross-sectional areas. The cross-sectional areas were calculated using the time averaged flow continuity:

$$\bar{Q}_{CCA} = \bar{Q}_{ECA} + \bar{Q}_{ICA} \qquad (2)$$

where $\bar{Q}$ is the time-averaged volumetric flow rate. Implementing the *K* area ratio, the new areas can be calculated as

$$A_{ICA}{}^* = \frac{A_{CCA}\bar{v}_{avg,CCA}}{K\bar{v}_{ECA} + \bar{v}_{avg,ICA}} \qquad (3)$$

where $\bar{v}_{avg}$ is the time and cross-sectional average of the velocities in the respective cross sections.

$$A_{ECA}{}^* = KA_{ICA}{}^* \qquad (4)$$

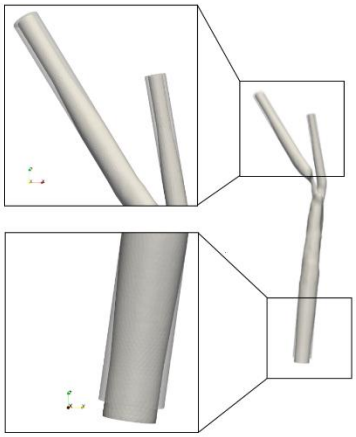

Figure 3. Alteration of the bifurcation geometry produced by the DCor correction (left) and the QCor correction (right)

2.3 Boundary conditions

Six boundary condition groups with different measurement data requirements were analyzed during our investigation (Table 1). First, we chose two commonly used methods, where only the CCA velocity data are necessary to define the inlet condition as time-varying volumetric flow rate. Outlet boundary conditions were defined without any additional measurement data necessary. In one case, constant 0 Pascal pressure was defined at the outlets (Basic) with the option to allow backflow [11]. In the other case, a constant ratio of flow division was calculated using the Murray-law (Mur) described by [16]. This flow division method relies on the ratio between the outlet cross-section area and the flow rate of the outlets:

$$\frac{Q_1}{Q_2} = \left(\frac{D_1}{D_2}\right)^3 \qquad (5)$$

Therefore, the volume flow ratio had to be recalculated for the geometries where the outlet dimensions were modified.

Three other boundary condition groups were defined utilizing the available outlet velocity measurements. Using the known ECA or ICA velocities, we defined two boundaries as time-varying volume flow, while constant 0 Pa pressure was used at the third one, similar to the Basic method. This created three possible arrangements with at least one outlet having a boundary where the patient-specific flow condition is forced at the given branch (C+E, C+I, E+I).

Last, a three-element Windkessel method (WK3) was implemented at the outlets, with a given volume flow at the inlet. This zero-dimensional model of the downstream system contains a proximal resistance, a distal resistance and a capacity. Aside from velocity measurements, pressure measurements are needed to calculate the patient-specific values of

these constants. Since pressure measurements were unavailable, approximative values were chosen based on [12, 17, 18] to describe the Windkessel-model.

All the boundary condition groups were analyzed for the Raw, DCor, and QCor modified geometries.

Table 1. Inlet and outlet boundary condition definitions

Nr.	Name	Inlet	Outlet
1	Basic	CCA waveform	ECA: Opening ICA: Opening
2	Mur	CCA waveform	Flow rate division
3	C+I	CCA waveform	ECA: Opening ICA: Waveform
4	C+E	CCA waveform	ECA: Waveform ICA: Opening
5	E+I	Opening	ECA: Waveform ICA: Waveform
6	WK3	CCA waveform	3-Element Windkessel-model

2.4 Simulations

In order to gain the volume flow rate values at the inlet and outlets, computational fluid dynamics simulations were carried out. At the carotid bifurcation only low velocities are present, therefore the transient laminar solver of ANSYS CFX was applied for the numerical calculations. As the initial condition of the transient simulations, stationary fluid and zero Pa pressure was defined throughout the volume. To eliminate the effect of the initial condition, three heart cycles were simulated, and only the third cycle was analyzed. To enable transient flow structure generation, the 0.85 sec heart cycles were divided into 5000 times steps, based on the findings of Khan et al. [19].

Triangular surface meshes with 1 million elements were generated for each modified geometry and implemented as rigid walls for the numerical calculations. The effects of the non-Newtonian properties of blood on the flow conditions are considered negligible, therefore we implemented a Newtonian fluid with a density of 1055 kg/m^3 and dynamic viscosity of 0.0034 Pas.

In total, 18 setups were simulated for all the possible geometry and boundary group combinations in the present case study.

3. RESULTS

Simulation results of the volume inflow and outflow rate were examined at the third heart cycle. These results were analyzed in four groups based on the similarities in the boundary condition setup.

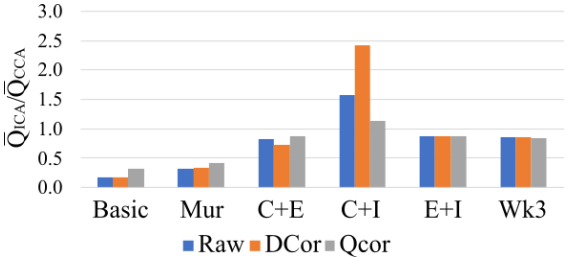

Figure 4. The effect of geometry corrections on volume flow ratio at the different boundary condition groups

Table 2. Main effects of the geometry corrections on the volume flow rate

Nr.	Name	DCor	QCor
1	Basic	Downscaled inlet flow rate	Flow division change
2	Mur	Downscaled inlet flow rate	Flow division change
3	C+I	Downscaled inlet flow rate	Downscaled Q_{ICA}
4	C+E	Downscaled inlet flow rate	Downscaled Q_{ECA}
5	E+I	-	Downscaled Q_{ECA} & Q_{ICA}
6	WK3	Downscaled inlet flow rate	-

3.1 Basic and Murray-law boundary condition groups

Basic and Murray-law simulations resulted in similar volume flow rate waveforms (Figure 5), following the defined Q_{CCA} characteristics. In the Murray-law case, this characteristic is prescribed, while the Basic case produced these results without a forced flow at the boundaries, although the ratio between ICA and ECA differed.

The CCA geometry correction (DCor) resulted in the downscaling of the volume flows since only the Q_{CCA} was decreased via the A_{CCA} reduction (Table 2).

After the second geometry correction (QCor), the volume flow division of the Murray-law was recalculated, producing a more negligible difference between the outlet flow rates, consequently increasing the Q_{ECA} ratio form 0.34 zo 0.42. The QCor simulation of the Basic case showed a similar ratio increase from 0.18 to 0.31, as shown in Figure 4.

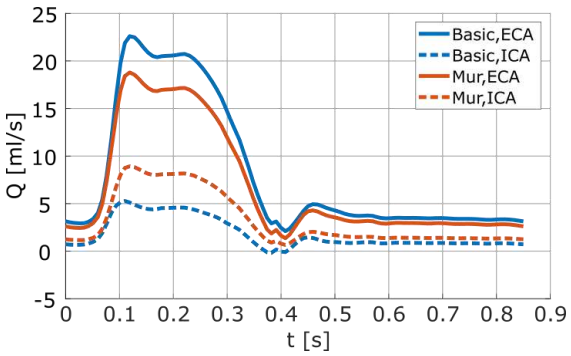

Figure 5. Waveforms of the outlet flow rates between the Basic and Mur boundary condition groups before the geometry corrections

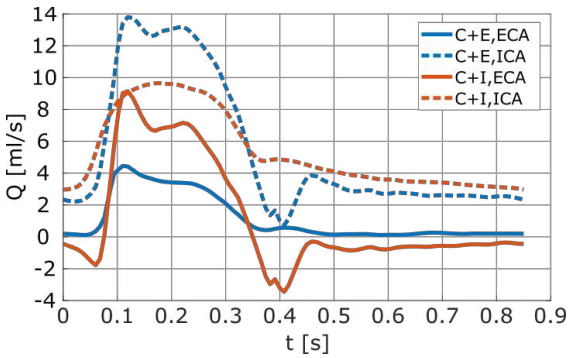

Figure 6. Waveforms of the outlet flow rates between the C+E and C+I boundary condition groups after the QCor geometry correction

3.2 C+E and C+I boundary condition groups

Boundary condition groups where the inlet flow rate and one outlet flow rate are given, produce a flow rate at the other outlet that can be calculated using a continuity equation. Therefore, the geometry correction alters the results only because the flow velocity is the known parameter instead of the volume flow rate.

Ideally, these two boundary condition groups should have the same results since practically all the flow rates are known. However, a clear difference is observable (Figure 6). This difference is the result of a non-simultaneous measurement of the Doppler velocities. In both cases, the volume flow ratio is higher than 0.5, and it stays true after both geometry corrections. This means that $Q_{ICA} > Q_{ECA}$, which could result in a significant velocity increase at the ICA stenosis. In contrast with the previous simulations, the flow rate ratio changes after the first geometry correction, especially at the C+I case from 2.41 to 1.13. The second QCor correction has the opposite effect to the flow division resulting in a similar ratio at the C+E as in the Raw case (0.82 and 0.87) and a lower ratio at C+I (1.58 and 1.13) (Fig. 4).

In the case of the C+I boundary condition group, a flow rate ratio of >1 is observable, which is the equivalent of backflow at the ECA. The Doppler measurements show no such flow condition, however, there are other stenosis cases where backflow is the valid solution.

3.3 E+I boundary condition group

The E+I boundary condition group has a similar setup to the C+E and C+I cases, but the inlet is the 0 Pa boundary instead of one of the outlets. Defining both outlets result in a constant flow rate ratio when the DCor or QCor geometry corrections are applied (Fig. 4). However, the inlet velocity increases with the first correction because of the decreased inlet cross-section. The QCor correction decreases the outlet flow rates and, therefore, the inlet flow rate to a similar average value that was defined in the other boundary conditions based on the CCA Doppler measurements (Figure 7). The average Q_{CCA} is only 1.6 % lower than what can be calculated with the measured velocity and the DCor corrected A_{CCA}, the maximum flow rate differs by 4.8 ml/s and the minimum flow rate differs by 1.8 ml/s. Meanwhile, the flow rate ratio is only 0.96 % lower than in C+I and 28.7 % higher than in C+E in the QCor cases.

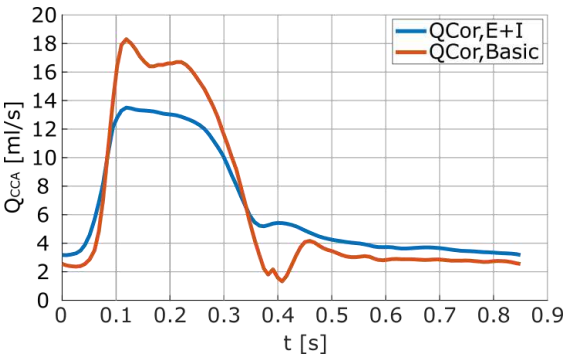

Figure 7. Q_{CCA} waveforms between E+I and Basic boundary condition groups

3.4 Windkessel-method

To calculate the parameters of a three-element Windkessel model, velocity and pressure measurements are necessary. Pressure measurements were not available in our case; therefore, their values were chosen based on the range of values used in the literature (Table 3).

Simulations with the Windkessel model provide a similar flow rate ratio as the E+I option (Fig. 4), with Q_{ICA} being the higher volume flow at the outlets and Q_{ECA} showing temporary backflow. Furthermore, neither the flow rate ratio nor the inflow is sensitive to the Cor and QCor geometry corrections.

Table 3. Approximated values of the 3-element Windkessel parameters

	ECA	ICA
Rp [Pa s/m^3]	10^9	10^8
Rd [Pa s/m^3]	10^{10}	10^9
C [m^3/Pa]	10^{-11}	10^{-10}

4. DISCUSSION

It is essential to define the boundary conditions correctly because they can significantly affect the flow conditions. At the carotid bifurcation, multiple such boundary condition options are used in the literature [11-13]. While the used boundary conditions are primarily chosen based on the available measured data, some variations can still be accessible. Such variation can be the correction of the inlet or outlet geometries utilizing Doppler imaging to decrease over or under segmentation. In this paper, we investigated the capabilities of 6 different boundary condition groups and the effect of applying two geometry corrections.

At the Murray and Basic methods, the volume flow results are determined by the geometry of the modelled arterial section. This can be seen in their similar waveforms and the effect of the geometry corrections on the flow ratio. While the Murray-law method applies the relation of the cross-sectional diameter and the volume flow rate [16], it does not consider that the resistances of downstream arteries greatly influence the flow conditions at the carotid bifurcation. In our case, these two boundary condition groups underestimated the volume flow at the ICA section compared to the later simulations where the Doppler velocity measurements were applied at the ICA outlet.

The second set of boundary conditions was introduced with C+E, C+I, and E+I, where the volume flow was defined at two boundaries. In these simulations, the flow rate ratio shows that Q_{ICA} is higher than Q_{ECA}. This is the expected flow division since ICA supplies blood to the brain, therefore its demand is expected to be higher [20, 21]. This volume flow ratio is further validated in our case with the Doppler velocity measurements, which show the same effect. Although these three solutions have similar flow divisions, significant differences were observed in the amplitudes and waveforms of the volume flow rate cycle. These differences could be the result of the Doppler measurements not being simultaneous. If the properties of the heart cycle change between the measurements, then the calculated volume flow rates will not fulfil the continuity.

Another problem with the defined outlet is that the Doppler measurements are challenging to perform at the ICA and ECA [14]. For example, if a velocity cycle is measured close to the stenosis, the maximum velocities will appear higher, causing any defined flow rate in that branch to be invalid. Therefore, these solutions are highly dependent on the accuracy of the measurements. However, if well-executed measurements are available, a patient-specific solution can be achieved by directly forcing the downstream physics at the outlets. While such forced boundary conditions are usually avoided in computational practice, these methods can allow flow conditions that do not develop with the more conventional Basic or Murray-law methods. For example, backflow is possible from the outlets, which can occur in highly stenotic cases [22].

The Windkessel boundary condition applies the physical properties of the downstream arteries, but without forced outlet conditions. With certain values of the WK3 parameters, a backflow condition can also be achieved. The downside of this model is the additional measurements necessary to apply a patient-specific flow condition [17]. This method could provide the most accurate results, but it is rarely accessible for the lack of pressure and velocity data.

The inlet and outlet geometry corrections were implemented based on the idea that a more accurate geometry can be produced from the segmented geometry using the Doppler measurements with novel methods. The results of the corrections are dependent on the used boundary conditions, but in most cases, significant rescaling or flow division change is observable. Since DCor applies the CCA diameter measured from the Doppler image, and QCor applies the outlet diameters based on the measured outlet velocities, the resulting geometry is closer to the actual geometry of the patient. Therefore, the resulting volume flows are a better approximation of patient-specific flow conditions.

The problems with these corrections are similar to the issues of the complex boundary conditions. Namely, it requires additional measurements to calculate the new geometry parameters, and the applicability of these measurements is dependent on their accuracy. In cases where CCA Doppler images are available, a simpler alternative could be to use the DCor method to test the quality of the segmentation. If a significant correction is necessary, it is worth considering resegmentation or additional measurements and application of the QCor method.

It is also essential to note that our investigation only focused on the volume flow results of the simulations. Changes in velocities and wall shear stress could have relevant impacts even at low volume flow changes.

5. SUMMARY

We investigated a single carotid bifurcation with stenosis at the ICA branch, intending to analyze the differences between boundary condition types. To accomplish this, six boundary condition groups were chosen. Furthermore, two geometry correction methods were established utilizing data from Doppler measurements.

We found that boundary conditions without patient-specific outlets are not sufficient at the carotid bifurcation, because they do not consider the resistances of downstream arteries. Other boundary condition setups were implemented with defined velocity waveforms at the outlets to resolve this problem. Although forced flow physics at the outlets is unconventional in practice, these simulations showed closer results to patient-specific conditions. One of the important effects of these setups is the possibility of backflow from an outlet. A three-element Windkessel model was also examined and showed that it produces similar patient-specific conditions without forcing flow physics on the outlets. The drawback of the complex boundary conditions is the additional measurements required and the necessary accuracy of these measurements.

Aside from the boundary conditions, two methods were created to correct the segmented geometry based on the Doppler images and measured velocities. We found that these corrections can significantly affect the amplitude and waveform of the resulting flow rates. The first geometry correction can offer a simple way to test the geometry using the CCA cross-sectional diameter, since the magnitude of the correction is dependent on the inaccuracies of the segmentation. The second correction further improves the geometry in cases where Doppler velocity measurements are available at the outlets without the need of resegmentation.

ACKNOWLEDGEMENTS

This study was supported by the National Research, Development and Innovation Office. under Grant number NKFIH-K 129277 and the Research, Development and Innovation Fund of Hungary under Grant TKP2021-EGA-02.

REFERENCES

[1] C. J. Murray and A. D. Lopez, “Alternative projections of mortality and disability by cause 1990–2020: Global Burden of Disease Study,” *The Lancet*, vol. 349, no. 9064, pp. 1498–1504, May 1997, doi: 10.1016/S0140-6736(96)07492-2.

[2] R. Ross, “The Pathogenesis of Atherosclerosis — An Update,” *New England Journal of Medicine*, vol. 314, no. 8, pp. 488–500, Feb. 1986, doi: 10.1056/NEJM198602203140806.

[3] J. C. Grotta, “Carotid Stenosis,” *New England Journal of Medicine*, vol. 369, no. 12, pp. 1143–1150, Sep. 2013, doi: 10.1056/NEJMcp1214999.

[4] D. Liu, C. Du, W. Shao, and G. Ma, “Diagnostic role of carotid intima-media thickness for coronary artery disease: A meta-analysis,” *BioMed Research International*, vol. 2020. Hindawi Limited, 2020. doi: 10.1155/2020/9879463.

[5] A. M. McKinney *et al.*, “Carotid bifurcation calcium and correlation with percent stenosis of the internal carotid artery on CT angiography,” *Neuroradiology*, vol. 47, no. 1, pp. 1–9, Jan. 2005, doi: 10.1007/s00234-004-1301-4.

[6] S. E. Lee, S. W. Lee, P. F. Fischer, H. S. Bassiouny, and F. Loth, “Direct numerical simulation of transitional flow in a stenosed carotid bifurcation,” *Journal of Biomechanics*, vol. 41, no. 11, pp. 2551–2561, Aug. 2008, doi: 10.1016/j.jbiomech.2008.03.038.

[7] D. Azar *et al.*, “Geometric determinants of local hemodynamics in severe carotid artery stenosis,” *Computers in Biology and Medicine*, vol. 114, Nov. 2019, doi: 10.1016/j.compbiomed.2019.103436.

[8] D. Gallo, D. A. Steinman, P. B. Bijari, and U. Morbiducci, “Helical flow in carotid bifurcation as surrogate marker of exposure to disturbed shear,” *Journal of Biomechanics*, vol. 45, no. 14, pp. 2398–2404, Sep. 2012, doi: 10.1016/j.jbiomech.2012.07.007.

[9] P. Berg *et al.*, “Multiple Aneurysms AnaTomy CHallenge 2018 (MATCH): Phase I: Segmentation,” *Cardiovascular Engineering and Technology*, vol. 9, no. 4, pp. 565–581, Dec. 2018, doi: 10.1007/s13239-018-00376-0.

[10] B. Csippa *et al.*, “Comparison of manual versus semi-automatic segmentations of the stenotic carotid artery bifurcation,” *Applied Sciences (Switzerland)*, vol. 11, no. 17, Sep. 2021, doi: 10.3390/app11178192.

[11] C. J. Lee, N. Uemiya, S. Ishihara, Y. Zhang, and Y. Qian, “A comparison of estimation methods for computational fluid dynamics outflow boundary conditions using patient-specific carotid artery,” *Proceedings of the Institution of Mechanical Engineers, Part H: Journal of Engineering in Medicine*, vol. 227, no. 6, pp. 663–671, Jun. 2013, doi: 10.1177/0954411913479540.

[12] U. Morbiducci *et al.*, “Quantitative analysis of bulk flow in image-based hemodynamic models of the carotid bifurcation: The influence of outflow conditions as test case,” *Annals of Biomedical Engineering*, vol. 38, no. 12, pp. 3688–3705, Dec. 2010, doi: 10.1007/s10439-010-0102-7.

[13] M. Malvè *et al.*, “Impedance-based outflow boundary conditions for human carotid haemodynamics,” *Computer Methods in Biomechanics and Biomedical Engineering*, vol. 17, no. 11, pp. 1248–1260, 2014, doi: 10.1080/10255842.2012.744396.

[14] W. Lee, “General principles of carotid Doppler ultrasonography,”

Ultrasonography, vol. 33, no. 1, pp. 11–17, Dec. 2013, doi: 10.14366/usg.13018.

[15] A. Saxena, E. Y. K. Ng, and S. T. Lim, "Imaging modalities to diagnose carotid artery stenosis: Progress and prospect," *BioMedical Engineering Online*, vol. 18, no. 1. BioMed Central Ltd., May 28, 2019. doi: 10.1186/s12938-019-0685-7.

[16] C. Chnafa, O. Brina, V. M. Pereira, and D. A. Steinman, "Better Than Nothing: A Rational Approach for Minimizing the Impact of Outflow Strategy on Cerebrovascular Simulations," *American Journal of Neuroradiology*, vol. 39, no. 2, pp. 337–343, Feb. 2018, doi: 10.3174/ajnr.A5484.

[17] I. E. Vignon-Clementel, C. A. Figueroa, K. E. Jansen, and C. A. Taylor, "Outflow boundary conditions for 3D simulations of non-periodic blood flow and pressure fields in deformable arteries," *Computer Methods in Biomechanics and Biomedical Engineering*, vol. 13, no. 5, pp. 625–640, Jan. 2010, doi: 10.1080/10255840903413565.

[18] U. Morbiducci *et al.*, "Outflow conditions for image-based hemodynamic models of the carotid bifurcation: Implications for indicators of abnormal flow," *Journal of Biomechanical Engineering*, vol. 132, no. 9, Sep. 2010, doi: 10.1115/1.4001886.

[19] M. O. Khan, K. Valen-Sendstad, and D. A. Steinman, "Narrowing the expertise gap for predicting intracranial aneurysm hemodynamics: Impact of solver numerics versus mesh and time-step resolution," *American Journal of Neuroradiology*, vol. 36, no. 7, pp. 1310–1316, Jul. 2015, doi: 10.3174/ajnr.A4263.

[20] J. Kochanowicz *et al.*, "Normal reference values of ratios of blood flow velocities in internal carotid artery to those in common carotid artery using Doppler sonography," *Journal of Clinical Ultrasound*, vol. 37, no. 4, pp. 208–211, May 2009, doi: 10.1002/jcu.20502.

[21] M. Schöning, J. Walter, and P. Scheel, "Estimation of cerebral blood flow through color duplex sonography of the carotid and vertebral arteries in healthy adults.," *Stroke*, vol. 25, no. 1, pp. 17–22, Jan. 1994, doi: 10.1161/01.STR.25.1.17.

[22] J. Wang, C. Zheng, B. Hou, A. Huang, X. Zhang, and B. Du, "Four collateral circulation pathways were observed after common carotid artery occlusion," *BMC Neurology*, vol. 19, no. 1, Aug. 2019, doi: 10.1186/S12883-019-1425-0.

Conference on Modelling Fluid Flow (CMFF'22)
The 18th International Conference on Fluid Flow Technologies
Budapest, Hungary, August 30 -September 2, 2022

INSIGHTS INTO THE FLOW SITUATION OF A MULTI-STAGE CENTRIFUGAL PUMP

Helmut BENIGNI[1], Stefan HÖLLER[2], Bernhard LECHNER[3], Jürgen KONRAD[3], Helmut JABERG[1,2]

[1] Corresponding Author. Institute of Hydraulic Fluidmachinery, Graz University of Technology. Kopernikusgasse 24/IV, A-8010 Graz, Austria. Tel.: +43 316 873 7578, Fax: +43 316 873 107578, E-mail: helmut.benigni@tugraz.at
[2] Prof. Dr. Jaberg und Partner GmbH, Kerscheckstrasse 41, 8076 Vasoldsberg, Austria
[3] Dickow Pumpen GmbH & Co. KG, Siemensstraße 22, 84478 Waldkraiburg, Germany

ABSTRACT

The present paper analyses a multi-stage ring-section pump concerning head, efficiency, cavitation and optimisation potential and comparison with existing test bench results and systematic optimisation. The investigation was carried out within the scope of several stages. An extracted fluid volume with many details is necessary to enable the highest possible accuracy of the simulations. The runner side spaces, radii at impeller and diffuser blades, and narrow gaps were not considered to obtain a computational grid with the highest possible quality (mostly block-structured grid). The impeller and diffuser were rebuilt and meshed using reverse engineering. Thus, the blade surfaces of the impeller and guide vanes could be extracted and used in a blade model tool for turbomachinery to modify the blade accordingly during the optimisation run. Vortex structures and dissipation were analysed within the transient calculations of the initial situation. The multi-stage centrifugal pump optimisation was mainly done in a simplified model to minimise the calculation effort. Impeller, inflow area and volute were optimised manually. Automated optimisation was realised for the guide vane and refeed channel. A multi-objective optimisation method based on an evolutionary algorithms was applied to a previously generated meta-model. An efficiency breakdown of the optimised two-stage pump geometry and a comparison with the original geometry were made as well. As a result of the optimisation, the efficiency is mainly increased in the entire operating range; in the single-stage variant by approx. 10%, and in the two-stage variant by approx. 7%! Hence the geometric specifications of the pump connection dimensions (retrofit) are adhered to, and the characteristic stability based on the CFD simulations is improved.

Keywords:
CFD, Multi-stage pump, Comparison of measurement and simulation

NOMENCLATURE

A	[m²]	Area
D	[m]	Diameter
g	[m/s²]	Gravity
Q	[m³/s]	Flow rate
H	[m]	Pump head
T	[Nm]	Torque
n	[rpm]	Rotational speed
NPSH	[m]	Net pressure suction head
n_q	[rpm]	Specific speed
p	[Pa]	Pressure
ρ	[kg/m³]	Density
φ	[-]	Flow coefficient
η	[-]	Efficiency
ψ	[-]	Pressure number

Subscripts and Superscripts, Abbreviations

BEP	Best efficiency point
SIC	Silicium carbide
GV	Guide vane
Histo	Histogram
IT	Intake (Suction side)
L	Loss
OT	Outtake (Pressure side)
RU	Runner
vap	Vapour
i	incipient
in	Inlet
hydr.	hydraulic
out	Outlet
stat	static
tot	total

1. INTRODUCTION

The HZ-type is a single- or multi-stage between bearings ring section centrifugal pump with shaft seal realised with radial split casing design.

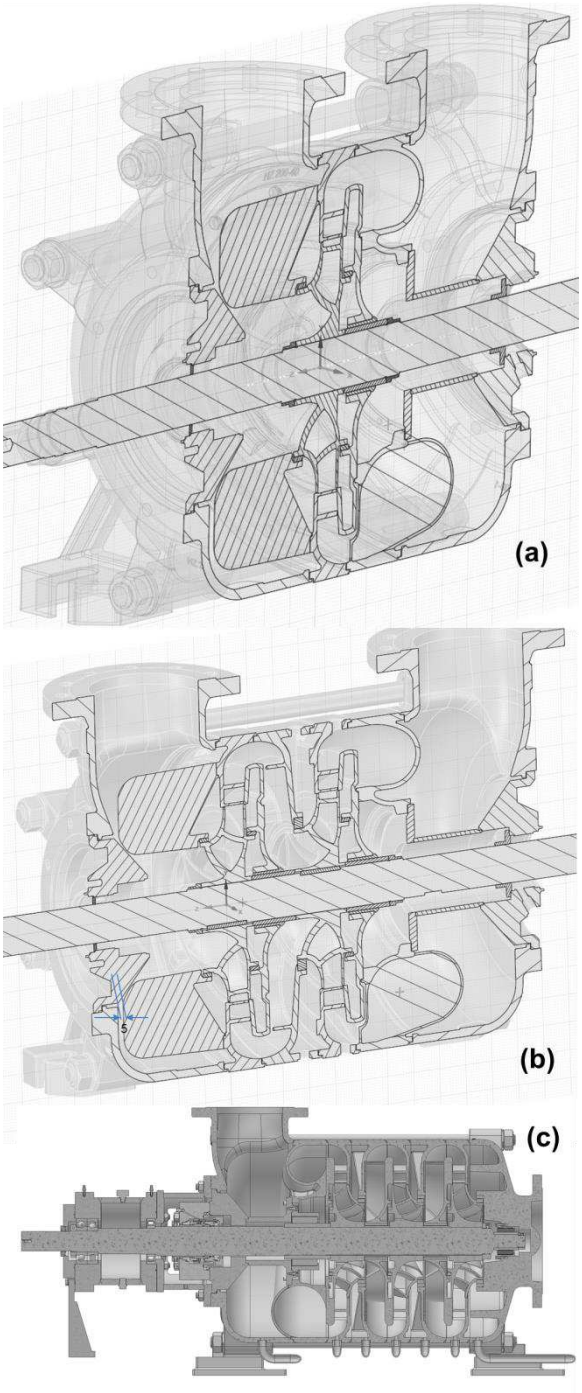

Figure 1. Single, double and multi stage arrangement

To achieve low NPSH values, the suction stand is designed as an inlet spiral or in axial direction. The suction side impeller is developed with an enlarged inlet cross-section (see Figure 1(a) for single, Figure 1(b) for double-stage and Figure 1(c) for multistage arrangement).

This series is applied in the industrial and municipal water supply, for the handling of condensates, boiler feed water, fuels, and other applications such as pressure boosting systems, boiler feed water, or condensate production.

The axial thrust compensation takes place through relief boreholes and throttle gaps. Suction, discharge and stage casings, as well as diffusers, are fitted with interchangeable wear rings as a standard.

The impellers are centred inside the diffusers. The diffusers are designed as fixed guide vane blade diffuser channels converting a part of the generated kinetic energy in the impeller into static pressure. The return vanes on the backside of the diffuser feed the pumped liquid to the impeller eye of the following stage. The closed impellers are hydraulically balanced through wear rings and balance holes in the impeller hubs. The pump is offered with axial and radial inlet. The bearings can be realised with roller bearings or slide bearings with oil lubrication (see example in Figure 1 (c), to be used on an oil platform in the North Sea..

2. NUMERICAL SIMULATION

2.1. Basics

The pump presented in this paper is designed for a stage-specific speed of n_q=36 rpm as a multi-stage pump. The specific speed n_q of the pump stage is calculated with Eq. (1) with the delivery head per stage.

$$n_q = n \cdot \frac{\sqrt{\frac{Q_{BEP}}{Q_{REF}}}}{\left(\frac{H_{BEP}}{H_{REF}}\right)^{0.75}} = 1480\ rpm \cdot \frac{\sqrt{\frac{0.13\ m^3/s}{1 m^3/s}}}{\left(\frac{35.6\ m}{1 m}\right)^{0.75}} = 35.9\ rpm \qquad (1)$$

Table 1. Nominal data of the pump

Speed	n	1480	rpm
Head	H_{BEP}	35.6	m
Discharge	Q_{BEP}	0.125	m³/s
Specific speed	$n_{q\_SingleStage}$	35.9	rpm
Efficiency	eta_{BEP}	0.73	%
Nominal Diameter	D_{out}	0.35	m
Pressure Number	$\psi_{BEP,Dout}$	0.978	-
Flow coefficient	$\varphi_{BEP,Dout}$	0.050	-

Similar to the applicable standard for turbine refurbishment [1], this paper follows the same procedure and first recalculates the existing initial geometry verified on the test rig and determines the potential for optimisation. For this purpose, the numerical calculation is compared with the test rig results using different models and considerable effort. Based on this initial situation, the optimisation is then carried out according to Figure 2. Based on a literature study [2]-[5] and a 1D

design on several streamlines, the first 3D model of the new hydraulic design was built utilising Ansys BladeGen®. A manual optimisation was performed for the impeller, the intake region, and the spiral area. For the elements of the guide vane (diffuser) and the return channel, an automated optimisation variant was applied.

2.2. Numerical models

An extracted fluid volume with many details is necessary to enable the highest possible accuracy of the simulations. The runner side spaces, radii at the impeller and diffuser blades (= guide vane), as well as narrow gaps were not taken into account to obtain a computational grid with the highest possible quality (most of the grid is block-structured). In addition, the extension on the inlet side and the outlet side was done by a straight pipe section with 10xD (D = 0.2 m) = 2 m each.

The impeller was rebuilt and meshed using "reverse engineering". Balancing holes were not included in the model.

Two models were generated and analysed before optimisation started. The single-stage model consists of 1 runner and 2 guide vanes (each as a 360° circular segment). The double-stage model consists of an additional return part with 8 blades after the guide vane and a second runner and second diffusor. Each model also includes a suction side and a spiral and outtake section with a full 360-degree model. Like the pressure side, this mesh was generated with ICEM®. In between, two stages are realised (see Figure 2).

The rotor now consists of 7 out of 7 passages for the impeller domain. The guide vane domain consists of 10 passages. The periodic boundaries of the impeller and diffusor domains have 1-to-1 interfaces, and Turbogrid® generates the mesh.

Table 2 itemises all important models with their overall mesh sizes. The HJCL mode of Turbogrid® follows an automated block topology depending on the blade metal angle, including full periodicity. In addition, it employs an algebraic, semi-isogeometric surface mesh generation procedure.

The commercial CFD code Ansys CFX V17.1 helped to solve the Navier-Stokes equations. These Navier-Stokes equations describe the fluid motion in all three dimensions and are applied for Reynolds averaged Navier-Stokes (RANS) formulation. RANS uses equations where – with the help of a Reynolds decomposition – the instantaneous variables are decomposed into mean and fluctuating values, whereas these variables are time-averaged.

For the stationary and single-phase CFD simulations, the frozen-rotor approach was used to model the transition from stationary calculation areas (suction area, guide vane) to the rotating calculation area (impeller) and vice versa. Five different positions impeller positions ("clocking") were analysed. In addition, the so-called mixing-plane interface model (stage) was also used. In this case, a circumferentially averaged velocity field is transmitted between the computational regions. Experience has shown that the stage interface provides more accurate results but is rather unstable, especially under unfavourable flow conditions.

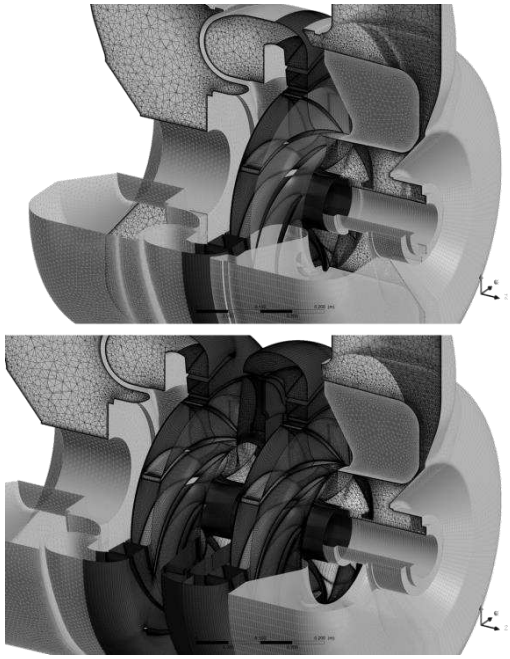

Figure 2. Models for CFD calculation, top - single-stage, bottom: double stage arrangement

At the inlet to the intake pipe, the mass flow and the inflow direction (free from swirl) are specified. At the outlet from the outlet pipe a constant static pressure was defined. The delivery head of the pump thus adjusts itself depending on the selected flow rate (mass flow) in the course of the CFD simulation.

Table 2. Model, mesh sizes in million

Standard model		Single stage		Double stage	
Domain	*# blades, info*	**Nodes**	**Elements**	**Nodes**	**Elements**
Intake		1.71	3.06	1.25	2.19
Runner1	*7/7*	2.20	2.08	2.20	2.08
Diffuser1	*10/10*	2.98	2.80	2.98	2.80
Rueck1	*8/8*			3.05	2.92
Runner2	*7/7*			2.20	2.08
Diffuser2	*10/10*	1.49	3.48	2.98	2.80
PressureEnd				1.49	3.48
All Domains		**8.38**	**11.42**	**15.95**	**17.96**

Optimisation model		fine		medium	
Domain	*# blades, info*	**nodes**	**elements**	**nodes**	**elements**
Intake	*"suction casing+ inlet pipe"*	0.60	0.56	0.39	0.36
Runner	*1/7*	0.38	0.74	0.18	0.32
Diffuser	*2/10*	0.03	0.06	0.14	0.30
PressureEnd	*"spiral+pressure pipe"*	0.32	0.30	0.20	0.18
All Domains		**1.55**	**2.19**	**0.91**	**1.17**

The SST model developed by Menter [6] was applied to stationary calculations as the turbulence model. Based on an Eddy-viscosity concept, this two-equation approach is commonly used for hydraulic turbomachinery combining the 2-

equations-turbulence-models k-ε- and k-ω. The transient analyses were carried out with the SAS-SST turbulence model by Menter. Although, using the SST turbulence model for transient simulations (URANS) could be an option. However, experience has shown that its application does not always provide satisfying results, even if the grid and time step resolution would be adequate. Hence, preference was given to the scale resolving turbulence model SAS-SST. The concept of the SAS turbulence model rests on the introduction of the Von Karman length scale into the turbulence scale equation [7]. The model dynamically adjusts to resolved vortex structures in the URANS (Unsteady Reynolds Averaged Navier Stokes) method, resulting in a LES-like (Large Eddy Simulation) behaviour in unsteady regions of the flow field. For the investigations and the transient simulations presented in this paper, the choice fell on the Shear-Stress-Transport turbulence model for Scale Adaptive Simulations (SST-SAS), combined with the Curvature Correction (CC) model developed by Smirnov and Menter and a production limiter model according to Kato-Launder.

2.3. Post-processing

The key figures mentioned in the following are of interest for evaluating hydraulic performance. In general, the net head is the difference between the total pressure at the outlet and the total pressure at the inlet. According to the standard ISO 9906 [8], the net head represents the difference between the inlet's and the outlet's static pressure. The mean kinetic energy head difference is added to the head (geodetic head difference neglected, see Eq. 2). The pressure was measured on the test rig on 4 pressure measuring taps displaced by 90° of each other, the locations being 2D away from the flange (Figure 3). Therefore, the post-processing of the CFD results was carried out similarly (Eq. 3).

$$H = \frac{1}{\rho g}\left[\left(\frac{1}{4}\sum_{i=1}^{4} p_i + \frac{\rho}{2}\left(\frac{Q}{A}\right)^2\right)\Big|_{Outlet} - \left(\frac{1}{4}\sum_{i=1}^{4} p_i + \frac{\rho}{2}\left(\frac{Q}{A}\right)^2\right)\Big|_{Inlet}\right] \quad (2)$$

$$H = \frac{1}{\rho g}\left[\frac{1}{A_{Outlet}}\left(\int p_{stat}\cdot dA\right)|_{Outlet} - \frac{1}{A_{Inlet}}\left(\int p_{stat}\cdot dA\right)|_{Inlet}\right] + \frac{\left(\frac{Q_{Outlet}}{A_{Outlet}}\right)^2 - \left(\frac{Q_{Inlet}}{A_{Inlet}}\right)^2}{2g} \quad (3)$$

The NPSH evaluation was carried out employing histogram analysis, which requires only a single phase calculation. This method was cross-checked several times [9,10]. The pressure $p_{Histogram}$ is the value when the pressure at a certain blade surface percentage exhibits pressure lower than the $p_{Histogram}$. The idea is that a single value for the minimum pressure is not real but happens in a numerical simulation. This pressure allows for the conventional calculation of the NPSH value within a single-phase calculation without a cavitation model. The area percentage representative for the pump type under investigation has to be known. However, this percentage changes from one pump type to the other. To determine the corresponding data is only possible by comparing a sufficiently large number of experimental and numerical results for different pump types. Reducing the area percentage results in a shift of the calculated NPSH value towards $NPSH_i$, by increasing it towards $NPSH_3$. Index 3 means a 3% drop of the delivery head per stage [8].

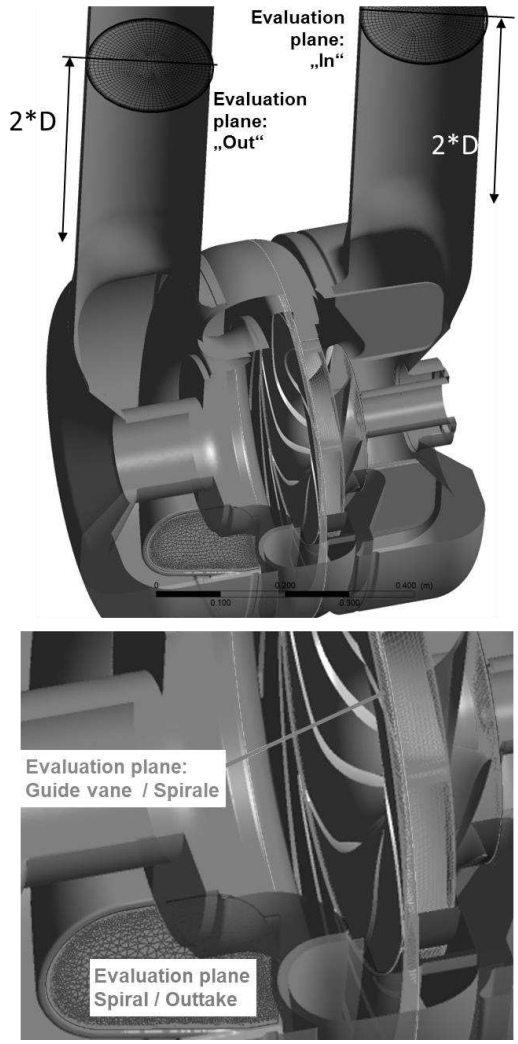

Figure 3. Evaluation planes CFD model

The efficiency is the benefit versus the expenditure and is described with Eq. 5. To analyse each component separately, a head loss analysis (see Eq. 6) was performed to calculate a cumulative distribution of the total unit. In this case, the total pressure difference between the inlet and outlet of each component was set in comparison to the net head. For the runner, the shaft power was also considered and added to the losses (Eq. 8).

$$NPSH = \frac{p_{tot,s} - p_v}{\rho \cdot g} = \frac{p_{tot,s} - p_{Histo}}{\rho \cdot g} \quad (4)$$

$$\eta_{hydr} = \frac{P_{hydr}}{P_{mech}} = \frac{\rho \cdot g \cdot Q \cdot H}{T_{Runner} \cdot \omega} = \frac{\rho \cdot g \cdot Q \cdot H}{(T_{Ru-Blades} + T_{Ru-Hub} + T_{Ru-Shroud}) \cdot \frac{2 \cdot \pi \cdot n}{60}} \quad (5)$$

$$\eta_{hydr} = \frac{H_{Pump}}{H_{Pump} + \sum H_{Loss}} = \frac{H_{Pump}}{H_{Pump} + H_{L-IT} + H_{L-Ru} + H_{L-GV} + \cdots + H_{L-OT}} \quad (6)$$

$$H = {}_{L-IT} = \frac{p_{Tot@Inlet} - p_{Tot@Inlet-Runner}}{\rho \cdot g} \quad (7)$$

$$H_{L-Ru} = \frac{p_{Tot@Inlet-Ru} - p_{Tot@Ru-GV}}{\rho \cdot g} + \frac{T_{Ru} \cdot \omega}{\rho \cdot g \cdot Q} \quad (8)$$

$$H_{L-GV} = \frac{p_{Tot@Runner-Guidevane} - p_{Tot@Guidevane-Spiral}}{\rho \cdot g} \quad (9)$$

$$H_{L-Spiral} = \frac{p_{Tot@Guidevane-Spiral} - p_{Tot@Out}}{\rho \cdot g} \quad (10)$$

3. RESULTS OF EXISTING HYDRAULIC DESIGN

For comparison purposes concerning the measured data of the existing pump, the CFD simulations were calculated with different models for the rotor-stator interface. Figure 4 shows the result of the steady-state calculation with the frozen rotor and the stage interface. In addition, a transient calculation was also evaluated and compared with the existing measurement data. Finally, the data for the experimental test was extrapolated to full load.

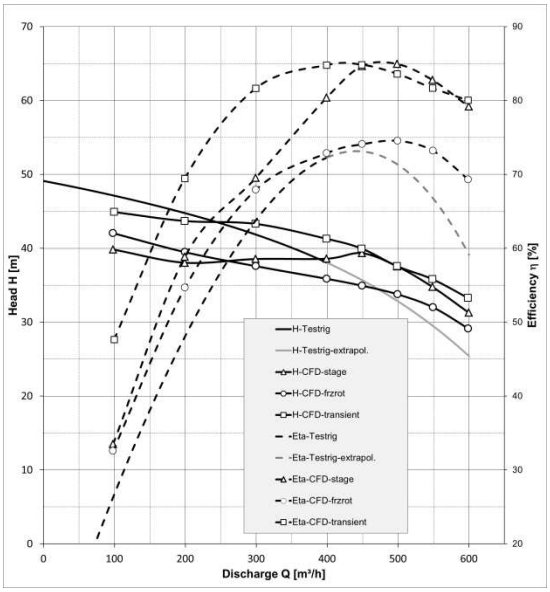

Figure 4. Single-stage, CFD vs test rig

The optimum position in the transient calculation is quite good in terms of discharge. The difference in efficiency is mainly due to the use of hydraulically smooth walls and the non-modelled impeller side spaces, leakage losses, and bearing losses

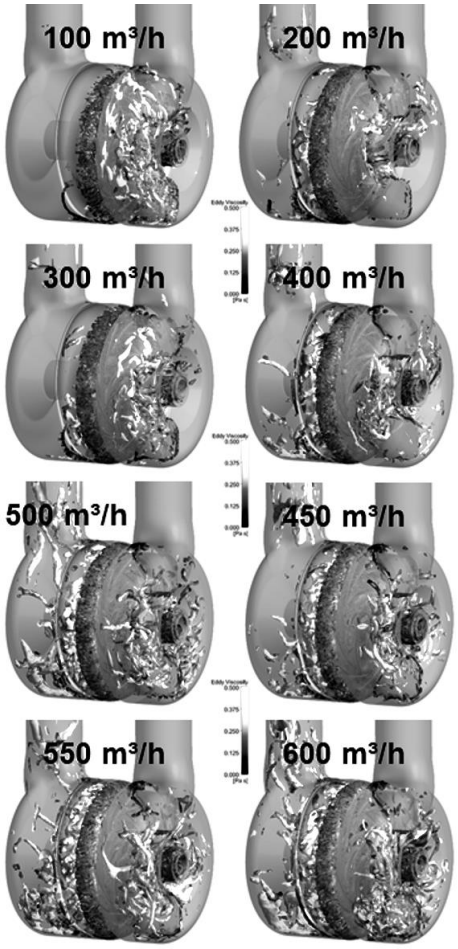

Figure 5. Q-criterion, single-stage, original geometry

At this point, Figure 5 shows an analysis of the existing vortex structures and their dissipation with the help of the Q-criterion shows a high dissipation rate in the suction area at the lowest flow rates and in the pressure area at the highest flow rates. The area of the guide vane, on the other hand, is filled with vortex structures whose intensity, however, is significantly lower. Figure 6 shows the efficiency splitting for the 2-stage case. This cumulative efficiency plot shows the individual components with their losses. One clearly sees the losses increasing from the optimum point in both directions to part and overload. In addition, the measurement result from the measurement of the 2-stage case from the test rig is shown, with the optimum points slightly shifted to overload for the measurement. The result of the cavitation measurement now indicates a somewhat different behaviour than that of the numerical simulation. The measured values are clearly below those of the numerical simulation, whereby the distance to full

load, the dimensioning variable, becomes visibly smaller and is equalised at 600m³/h in any case.

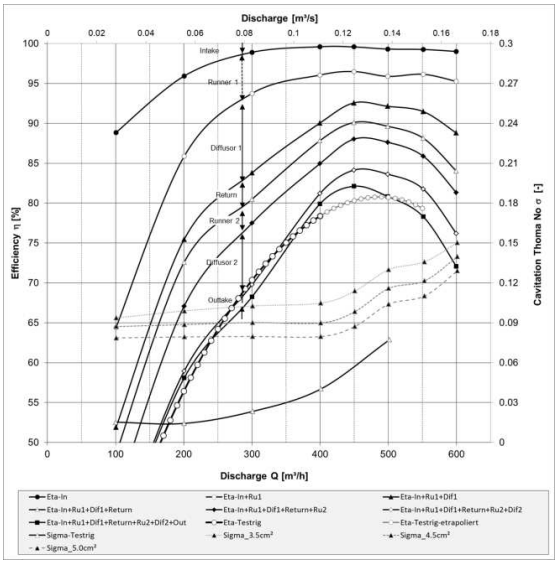

Figure 6. Double-stage, efficiency splitting

4. MODIFICATIONS

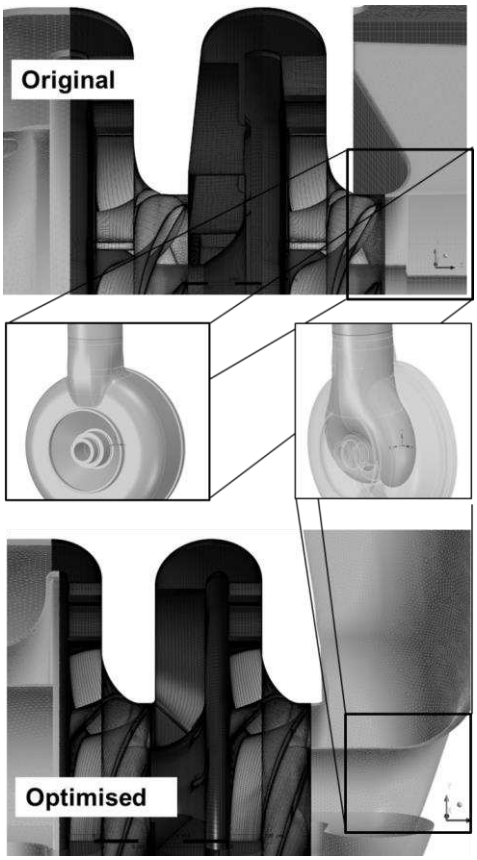

Figure 7. Modifications, top original, bottom optimised.

The optimisation of the suction area (Figure 7) also affects the improvement of the head curve stability. Still, a possible reduction in efficiency must also be taken into account. The spiral outlet was left at the lowest point for self-priming. Now 10 planar guide vanes and 8 curved return vanes are used, which are the result of the parametric optimisation model for the meridian and the shape of the blades. This model has about 50 geometric degrees of freedom. The outer diameter of the stage dramatically influences the head and efficiency at all the operating points studied (300, 400 and 500 m³/h), and it proves the more significant, the better.

The diameter of the trailing edge of the return vanes has a major influence on the head and efficiency of the downstream impeller. Here, it proves the smaller, the better. The length of the stage is not so decisive.

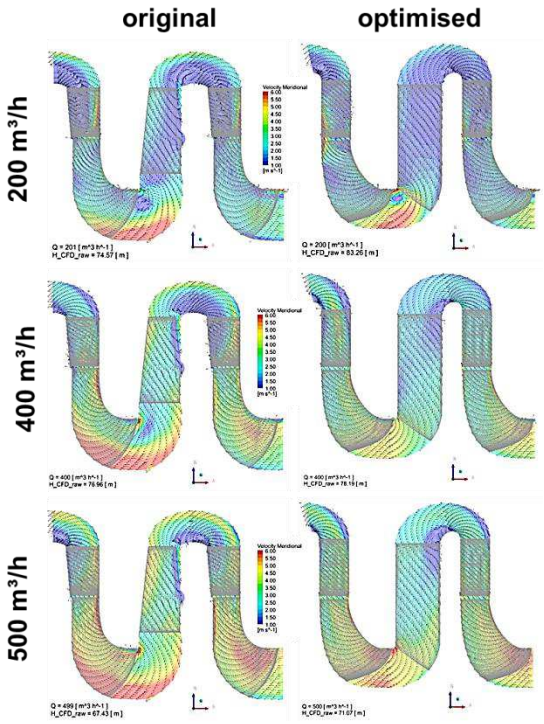

Figure 8 Modification of the guide vane

The velocity distribution in the meridian section at different operating points (at Q = 200 m³/h – top Q = 400 m³/h – centre; Q = 500 m³/h – bottom for the original geometry (left) and the optimised pump geometry (right) is illustrated in Figure 8, in which a reduction of areas with high velocities is present.

The distribution of the meridional component of the velocity (c_m – Figure 9) and the circumferential component (c_u – Figure 10) at Q = 450 m³/h are analysed at different positions in the pump for the original geometry (grey) and the optimised pump geometry (black).

Even a slight change in the shape of the blade (variation of the exit angle by +- 2°) can significantly change the shape of the characteristic curve and the position of the efficiency optimum with otherwise unchanged geometry (Figure 11).

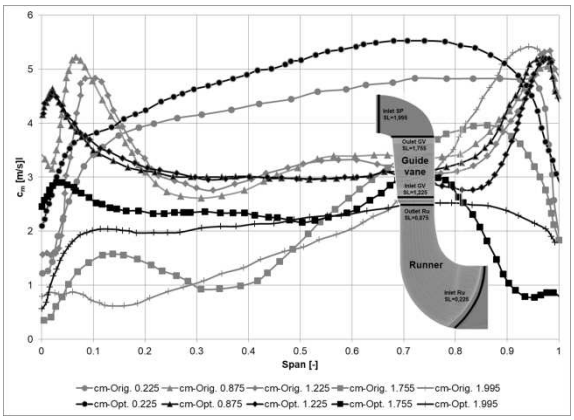

Figure 9. Meridional velocity at different locations

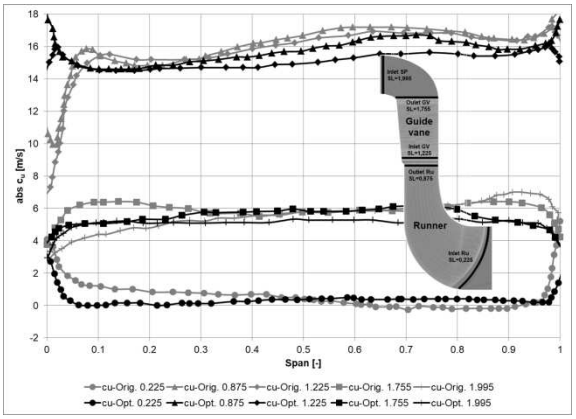

Figure 10. Circumferential velocity at different locations

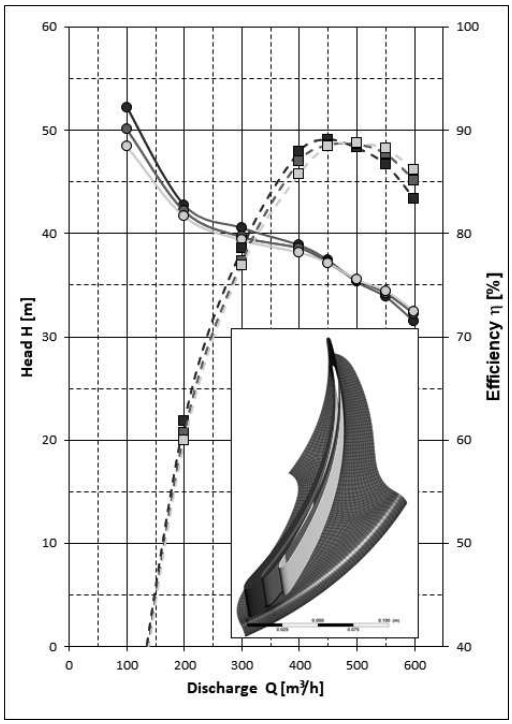

Figure 11 Modification of the guide vane

5. RESULTS OF THE OPTIMISED HYDRAULIC DESIGN

Comparing the initial geometry with the optimised variant in terms of efficiency shows each component's advantageousness and interaction. In the desired optimum of the pump at Q=450 m³/h, the efficiency could be increased by $\Delta\eta$=7%. Figure 12 shows the efficiency breakdown of the optimised pump geometry (1-stage) and a comparison with the original geometry (grey lines). An improvement of the flow situation (loss minimisation) can be observed in all components; most of the efficiency increase is due to the optimised guide vane. However, at 500 m³/h, there are already approx. 4% points of losses in the outtake! There may be further potential here.

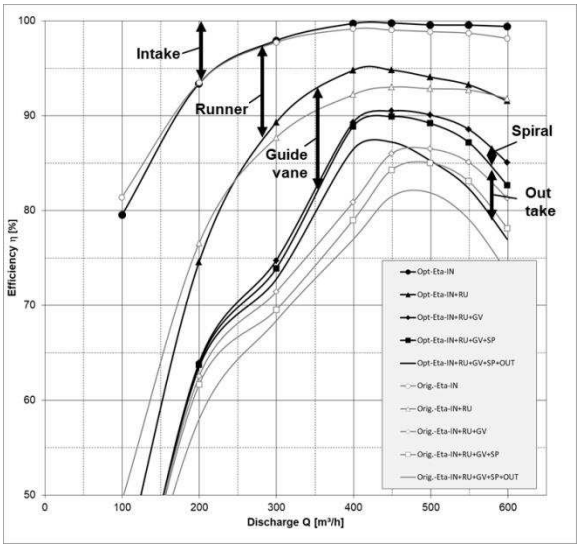

Figure 12. Single-stage, efficiency splitting, optimised versus original geometry

Figure 13 shows the comparison of the pump head curve determined through CFD simulation in the full model for the original pump geometry (black with circles) and the final optimisation variant (black with diamonds). The CFD simulation also shows a slight head curve bend (full load bend) of the final optimisation variant for the 2-stage version; original geometry also shows this behaviour. At 400 m³/h, the head could be increased by 4 m; the efficiency in the entire operating range between 300 m³/h and 600 m³/h by approximately 7 %. Like the transient calculation of the single-stage original geometry, the final transient calculation is above the steady-state results. The improvement of the cavitation behaviour is shown in the lower part of Figure 13. The increase after overload could be pushed to even higher flow rates. Finally, Figure 14 shows the flow situation at the pump-eye. For this purpose, $NPSH_{required}$ was plotted on the impeller walls to avoid falling below the vapour pressure.

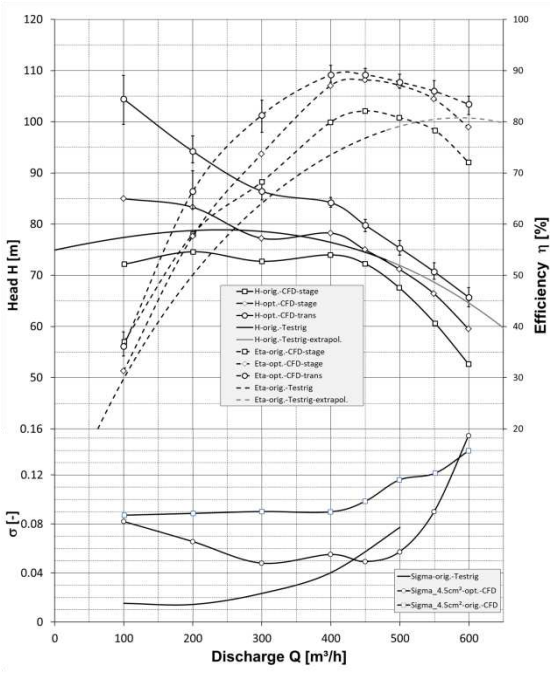

Figure 13. 2-stage optimised versus original geometry

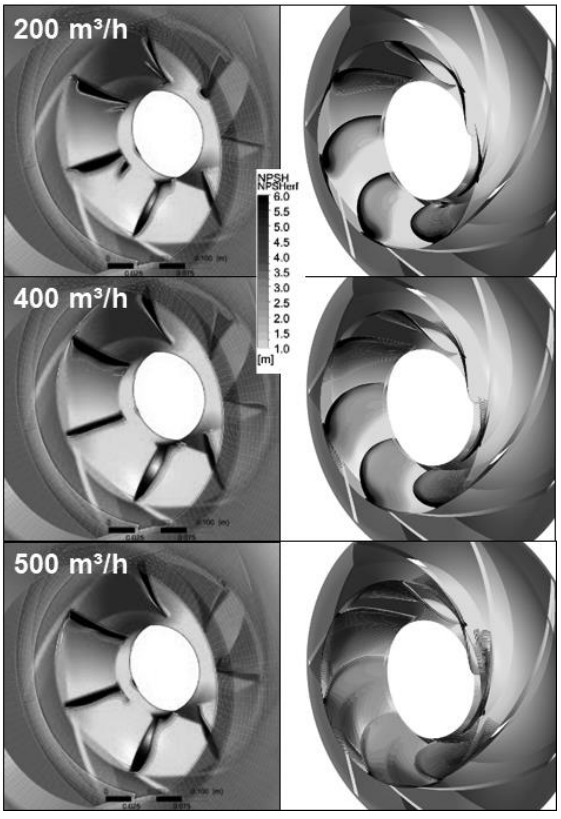

Figure 14. Runner inlet at different discharges, cavitation behaviour

The dark zones mean that 6 m of NPSH are necessary to prevent falling below the vapour pressure. Again, clearly pronounced zones can be found on the left side of the original geometry. In contrast, on the right side of the optimised variant, these are, if at all, significantly smaller.

6. CONCLUSION

For a pump series built in single- and multiple-stage design, a corresponding optimisation potential could be determined based on an extensive recalculation of the actual status. The individual components could be successively improved through a hybrid approach consisting of manual and automated optimisation. Thus, the efficiency in the entire operating range could be significantly increased. In the single-stage variant at Q = 400 m³/h by approx. 10% (!), two-stage in the entire operating range between 300 m³/h and 600 m³/h by approx. 7%! It was also possible to improve the characteristic stability based on the CFD simulations and increase the delivery head. Geometry specifications concerning retrofit could all be met.

REFERENCES

[1] International Electrotechnical Commission, IEC 62256:2017, Hydraulic turbines, storage pumps and pump-turbines – Rehabilitation and performance improvement.

[2] Stepanoff, A. J., 1959, Radial- und Axialpumpen, Springer.

[3] Guelich, J. F., 2004, Kreiselpumpen, Springer.

[4] Pfleiderer, C., Petermann, H., 2005, "Strömungs-maschinen", 7th Edition, ISBN 3-540-22173-5, Springer.

[5] Karassik, I, Messina, J. P., Cooper, P., Heald, C.C., 2001, "Pump Handbook", 3rd Edition, ISBN 0-07-0304032-3, McGraw-Hill.

[6] Menter, F. R., 1994, "Two-equation eddy-viscosity turbulence models for engineering applications", *AIAA Journal*, Vol. 32, pp.1598–1605.

[7] Menter, F. R., Egorov, Y., 2005, "A Scale-Adaptive Simulation Model Using Two-Equation Models", *AIAA Journal*., pp. 271–283

[8] International Standard ISO 9906:2012, Rotodynamic pumps – Hydraulic performance acceptance tests – Grades 1, 2 and 3.

[9] Gehrer, A., Benigni, H., Penninger, G., 2004, "Dimensioning and Simulation of Process Pumps," *Karlsruhe Pump Users Technical Forum*, Karlsruhe, Germany.

[10] Benigni, H., Jaberg, H., Yeung, H., Salisbury, T., Berry, O., 2012, „Numerical Simulation of Low Specific Speed API Pumps in Part-Load Operation and Comparison with Test Rig Results", In: Journal of fluids engineering 134 (2012) 2, pp. 024501-024501.

Conference on Modelling Fluid Flow (CMFF'22)
The 18th International Conference on Fluid Flow Technologies
Budapest, Hungary, August 30-September 2, 2022

MECHANISTIC TURBULENCE: TARGETED ENERGY TRANSFER IN A MULTI-DEGREE-OF-FREEDOM NONLINEAR OSCILLATOR

Bendegúz D. BAK[1], Róbert ROCHLITZ[2], Tamás KALMÁR-NAGY[3], Gergely KRISTÓF[4]

[1] Corresponding Author. Department of Fluid Mechanics, Faculty of Mechanical Engineering, Budapest University of Technology and Economics. Bertalan Lajos u. 4 - 6, H-1111 Budapest, Hungary. E-mail: bak.bendeguz@gpk.bme.hu
[2] Department of Fluid Mechanics, Faculty of Mechanical Engineering, Budapest University of Technology and Economics. E-mail: rochlitz.robert.z@gmail.com
[3] Department of Fluid Mechanics, Faculty of Mechanical Engineering, Budapest University of Technology and Economics. E-mail: kalmar.nagy.tamas@gpk.bme.hu
[4] Department of Fluid Mechanics, Faculty of Mechanical Engineering, Budapest University of Technology and Economics. E-mail: kristof.gergely@gpk.bme.hu

ABSTRACT

We study the energy transfer process in a binary tree structured mechanical oscillator that has strongly nonlinear dissipative elements. The masses and spring stiffnesses of the system are tuned to closely match the eigenfrequencies of the oscillator with the eddy frequencies deduced from the characteristic eddy lengths of a turbulent flow. These eddy lengths were obtained from actual measurements of airflow passing through an urban street canyon model carried out in the large wind tunnel of the Theodore von Kármán Wind Tunnel Laboratory. We demonstrate that the model exhibits an energy cascade and compare its features with those of the classical turbulent energy cascade for different types of excitations. We show how the energy is distributed across the different scales of the system. The primary mechanism behind the observed energy transfer is analyzed for different excitation types. We compute wavelet transforms and visualize them on the so-called frequency-energy plot of the system to show the underlying dynamics. The results demonstrate evidence of irreversible energy transfer from the linear part towards the nonlinear dissipative parts of the system through nonlinear beats and fundamental targeted energy transfer.

Keywords: energy cascade, nonlinear dynamics, turbulent flow

NOMENCLATURE

A	[-]	amplitude
E	[-]	total energy
K	[-]	level stiffness
L	[m]	eddy length
M	[-]	level mass
Q	[-]	quality function
a	[-]	parameter for setting the initial energy
c	[-]	damping coefficient
d	[-]	common ratio of geometric series
k	[-]	element stiffness
m	[-]	element mass
n	[-]	number of levels
x	[-]	position
δ	[-]	Kronecker delta
κ	[-]	wavenumber
Ω	[$1/s$]	eddy frequency
ω	[-]	frequency
ρ	[$1/m^3$]	density

Subscripts and Superscripts

i	index of element
j	index of level
$\bar{}$	temporal average
$\hat{}$	spectrum with respect to wavenumber

1. INTRODUCTION

In many engineering applications, there are processes involving energy transfer between a range of different scales. Nowadays an important aspect of this is targeted energy transfer (TET). Kerschen et al. [1] showed that by attaching a nonlinear energy sink (NES) to a linear system, a major portion of the induced energy can be dissipated leading to irreversible targeted energy transfer from the primary system towards the nonlinear dissipative element. The study of the dynamics of systems involving one or multiple NESs has generated tremendous amount of papers. E.g., Gendelman [2] extended the existing methods to systems with non-polynomial nonlinearity, that were originally developed to analyse cubic TET in systems with cubic nonlinearity. Viguié et

al. [3] used passive nonlinear TET to stabilize drill strings, reducing the torsional vibrations arising during operation. Motato et al. [4] showed that the use of NESs in automotive drivelines resulted in redistribution of vibrational energy. In a recent paper Chen et al. [5] demonstrated that parallel-coupled NESs are more efficient at dissipating medium shocks than parallel NESs and perform no worse than a single degree of freedom NES in the whole force range examined.

Targeted energy transfer also arises in turbulent flows. According to Richardson [6], the larger vortical structures that represent the large scales of turbulent flow break up into smaller ones due to their instability, transferring their kinetic energy to smaller and smaller scales, until viscous processes take over. A mathematical description of the energy spectrum of these turbulent scales was given by Kolmogorov [7] for 3D homogenous isotropic turbulence, which characterizes Richardson's energy cascade. In this description, the total energy E is given by

$$E = \int \hat{E}(\kappa) \mathrm{d}\kappa, \tag{1}$$

where $\kappa \sim 1/L$ is the wavenumber associated to the turbulent scale L, $\hat{E}(\kappa)$ is the energy content associated with the scales that have wavenumber κ.

In recent years there have been efforts to reproduce the Kolmogorov spectrum using a mechanistic model of turbulence, consisting of linear oscillators. Kalmár-Nagy and Bak [8] showed that for a well chosen power law describing the stiffnesses of the system, the $\hat{E}(\kappa) \propto \kappa^{-5/3}$ inertial range of the spectrum can be qualitatively obtained from the model.

In this paper a new nonlinear variant of the mechanistic model of Kalmár-Nagy and Bak [8, 9] is studied. The difference between the structure of this nonlinear model variant and the original model is that the dissipative elements are nonlinear energy sinks and they are not attached to a motionless wall. After introducing the chosen parameters of the model and the tools of the analysis in Section 2, the dynamics of the system is analyzed in Section 3 for different types of initial conditions. In Section 4 conclusions are drawn.

2. MECHANISTIC TURBULENCE

2.1. Description of the model

In this paper, a mechanistic model of turbulence is used, which is a $n = 6$ level binary tree of masses connected by springs and dampers as shown in Figure 1. The mass in the top level is connected to a stationary ceiling, and the masses in the bottom level are connected to the previous level by springs with cubic nonlinearity and linear dampers. In general, an element i of level j is connected to the element $\lfloor i/2 \rfloor$ of level $j-1$, and the elements $2i, 2i+1$ of level $j+1$.

The model parameters are considered to be the same across the elements of a level, thus each level j can be characterized with the mass m_j of its elements,

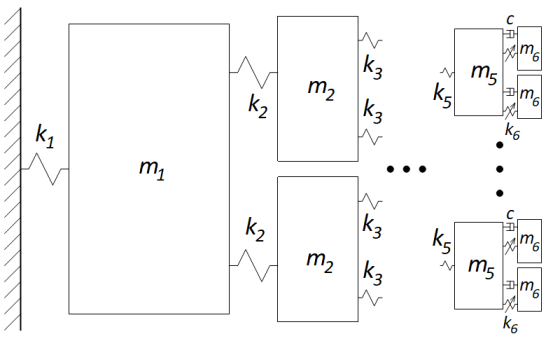

Figure 1. Binary tree of spring connected masses

the stiffness k_j of its springs, and with the damping c in the case of the last level. The equations describing the motion of the i^{th} mass in the j^{th} level:

$$\begin{aligned}
&m_j\ddot{x}_i + k_j x_i + k_{j+1}(x_i - x_{2i}) + \\
&\quad + k_{j+1}(x_i - x_{2i+1}) = 0, \quad \text{if } j = 1, \\
&m_j\ddot{x}_i + k_j(x_i - x_{\lfloor i/2 \rfloor}) + k_{j+1}(x_i - x_{2i}) + \\
&\quad + k_{j+1}(x_i - x_{2i+1}) = 0, \quad \text{if } j \in \{2, 3, 4\}, \\
&m_j\ddot{x}_i + c(\dot{x}_i - \dot{x}_{2i}) + c(\dot{x}_i - \dot{x}_{2i+1}) + \\
&\quad + k_j(x_i - x_{\lfloor i/2 \rfloor}) + k_{j+1}(x_i - x_{2i})^3 + \\
&\quad + k_{j+1}(x_i - x_{2i+1})^3 = 0, \quad \text{if } j = 5, \\
&m_j\ddot{x}_i + c(\dot{x}_i - \dot{x}_{\lfloor i/2 \rfloor}) + k_j(x_i - x_{\lfloor i/2 \rfloor})^3 = 0, \\
&\qquad\qquad \text{if } j = 6
\end{aligned} \tag{2}$$

Throughout this work, Eq. (2) is solved using Wolfram Mathem- atica's built-in numerical differential equation solver (NDSolve). The desired accuracy was set to 8 significant digits. The NDSolve function automatically determines the best numerical scheme for the problem and uses adaptive step size to obtain the required accuracy.

An important quantity is the energy of a given level j that is defined to be the kinetic energy of the masses of the level, and half of the potential energy of the springs connecting to these masses:

$$\begin{aligned}
E_j(t) = &\tfrac{1}{2} m_j \textstyle\sum_{i=2^{j-1}}^{2^j-1} \dot{x}_i(t) + \\
&+ \tfrac{(1+\delta_{1,j})}{4(1+\delta_{n,j})} k_j \textstyle\sum_{i=2^{j-1}}^{2^j-1} \left(x_i(t) - x_{\lfloor i/2 \rfloor}\right)^2 + \\
&+ \tfrac{1}{4(1+\delta_{n-1,j})} k_{j+1} \textstyle\sum_{i=2^j}^{2^{j+1}-1} \left(x_i(t) - x_{\lfloor i/2 \rfloor}\right)^2, \\
&\qquad\qquad \text{for } j \in \{1, \ldots, 6\},
\end{aligned} \tag{3}$$

where δ is the Kronecker delta ($\delta_{i,j} = 1$, if $i = j$ and $\delta_{i,j} = 0$ otherwise). With these, the total energy of the system is

$$E(t) = \sum_{j=1}^{6} E_j(t). \tag{4}$$

The temporal average energy of a level for a time

window $t \in [t_1, t_2]$ is

$$\bar{E}_j = \frac{1}{t_2 - t_1} \int_{t_1}^{t_2} E_j(t) dt \tag{5}$$

A temporal energy spectrum of the system can be interpreted as the level energies scaled by the total energy of the system, i.e.

$$\hat{E}_j(\kappa_j) = \bar{E}_j / \bar{E}, \tag{6}$$

where $\kappa_j = 1/m_j$ is the mass wavenumber. This energy spectrum shows the contribution of each scale m_j to the total energy of the system.

2.2. Model parameters

The masses and the spring stiffnesses were set based on eddy lengths and frequencies of a turbulent flow. These were obtained from measurements of an airflow passing through an urban street canyon model, that was performed in the large wind tunnel of the Theodore von Kármán Wind Tunnel Laboratory. This experiment provided several eddy lengths and frequencies, from which six were selected such that they represent different scales, these are shown in Table 1.

The masses of the elements were directly calculated from the eddy lengths as

$$m_j = \rho L_j^3. \tag{7}$$

The choice of parameter ρ is arbitrary, but in order to obtain masses with the same order of magnitude as in previous works [8, 9], the value of $\rho = 1000\ 1/m^3$ was chosen. Note that due to the model parameters being dimensionless, the unit of ρ was changed to preserve dimensional homogeneity in Eq. (7).

The light damping was prescribed to ensure that the system exhibits strongly nonlinear dynamics, the damping coefficient values were set to

$$c = 0.001. \tag{8}$$

It was found that for significantly higher or lower damping, it is difficult to obtain targeted energy transfer. As examining TET in the system was the goal of the paper, c was chosen such that the oscillator could exhibit this behaviour.

Table 1. Turbulent flow measurements

j	Eddy length, L_j [m]	Eddy frequency, Ω_j [1/s]
1	0.14637	23.208
2	0.12775	53.222
3	0.08710	68.074
4	0.07789	39.060
5	0.03418	84.279
6	0.01502	170.663

The spring stiffnesses were set such that the eigenvalues of the purely linear variant of the model approximately match the eddy frequencies listed in Table 1. In the linear model variant the nonlinear springs are simply replaced by linear springs. In order to obtain the correct spring stiffnesses, one more simplification was employed to reduce computational burden: the binary tree was replaced by a chain of M_j masses connected by linear springs with stiffness K_j, where $M_j = 2^{j-1} m_j$ and $K_j = 2^{j-1} k_j$. This reduced model shown in Figure 2 made the search for the spring stiffness parameters computationally affordable, while it also "preserved" the eigenvalues of the linear binary tree structured oscillator. This means that every eigenvalue of the reduced chain oscillator is an eigenvalue of the binary tree structured oscillator, while obviously the binary tree structured oscillator has additional eigenvalues.

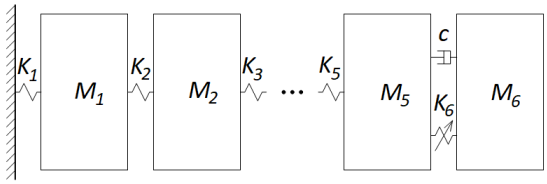

Figure 2. Chain of spring connected masses

The K_j stiffnesses were optimised by searching for the minimum of the quality function

$$Q = \sum_{j=1}^{6} \left| \Omega_j - \Im(\lambda_j) \right| \tag{9}$$

using a simple genetic algorithm, where λ_j are the eigenvalues of the model and $\Im(.)$ denotes the imaginary part function.

The resulting model parameters are shown in Table 2.

Table 2. Model parameters obtained from the turbulence measurements

j	m_j	k_j
1	3.13586	5303.1
2	2.08489	1391.54
3	0.660776	1190.65
4	0.472547	510.463
5	0.0399316	80.9006
6	0.00338852	98.6928

2.3. Frequency-energy plot

A very powerful tool of analysing these nonlinear systems is the frequency-energy plot (FEP). As a nonlinear system has no normal modes or eigenvalues, nonlinear normal modes (NNM) are defined as a time-periodic oscillation of a non-dissipative nonlinear dynamical system [10]. Thus the FEP shows the energy dependence of the frequency corresponding to the NNMs. This plot can be produced by assum-

ing periodic oscillations as

$$x_i(t) = A_i \cos(\omega t). \tag{10}$$

By substituting this expression into Eq. (2), and solving for A_i at $t = 0$, the $A_i(\omega)$ amplitude-frequency functions can be obtained. From these, the total energy-frequency function can be determined from Eqs. (3) to (4). This was done for both the nonlinear binary tree model and the nonlinear reduced model (see Figs. 1 to 2), that are compared in Figure 3. This demonstrates that the dynamics of the reduced model is similar indeed, but its FEP shows that the NNMs of the reduced chain oscillator have a higher energy content for a given frequency in general.

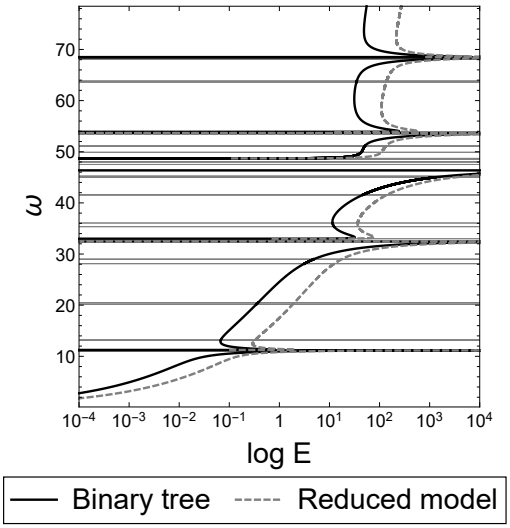

Figure 3. FEPs of the binary tree structured and the chain oscillator

3. SIMULATION RESULTS

The system was investigated with impulsive excitations exclusively, meaning that no forcing was applied. In every examined case, the system was started from equilibrium, i.e.

$$x_i(0) = 0 \quad \forall i \in \{1, \ldots, 63\}. \tag{11}$$

Three types of initial velocities were investigated, the first is nonzero initial conditions in the first five levels. In this case, the initial kinetic energy of different levels follows a geometric sequence, it is equal for elements in the same level, and is zero for the bottom level:

$$\begin{aligned} &\dot{x}_i(0) = \sqrt{\tfrac{ad^j}{m_j}}, \quad i \in \left\{2^{j-1}, \ldots, 2^j - 1\right\}, \\ &\quad j \in \{1, \ldots, 5\}, \\ &\dot{x}_i(0) = 0, \quad i \in \left\{2^{j-1}, \ldots, 2^j - 1\right\}, j = 6, \end{aligned} \tag{12}$$

where the parameter a was used to set the initial total energy of the system. The next type is nonzero initial conditions in a single $j \in \{2, 3, 4\}$ level of the tree, where the initial velocities of the masses in level j follow a geometric sequence:

$$\begin{aligned} &\dot{x}_i(0) = ad^i, \quad i \in \left\{2^{j-1}, \ldots, 2^j - 1\right\}, \\ &\dot{x}_i(0) = 0, \quad i \notin \left\{2^{j-1}, \ldots, 2^j - 1\right\}. \end{aligned} \tag{13}$$

Finally, in the last type the first level was started with an initial velocity of 1, and the elements of the second level with initial velocities of ±1:

$$\begin{aligned} &\dot{x}_1(0) = 1, \\ &\dot{x}_2(0) = \pm 1, \\ &\dot{x}_3(0) = \pm 1. \end{aligned} \tag{14}$$

3.1. Nonzero initial conditions in the first five levels

The system was launched from the initial conditions Eq. (12) for several $E(0)$ initial energy levels and d common ratios. At $t = 1000$, the ratio of the total energy and the initial energy were calculated, the contour plot of this ratio is shown in Figure 4 for the different $E(0)$ and d values. This shows that the behaviour of the system is very sensitive to the initial energy level, as well as the initial energy distribution among the levels of the binary tree.

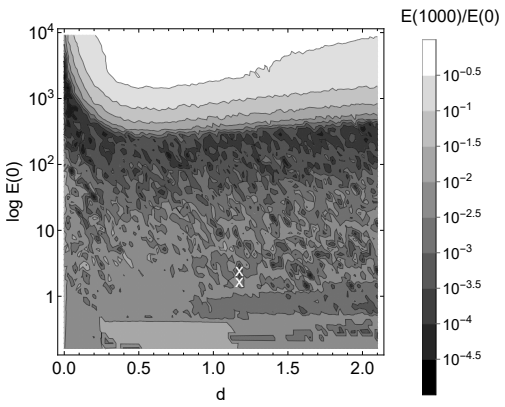

Figure 4. Fraction of the remaining energy as a function of $E(0)$ and d, with initial conditions given in Eq. (12). White x's denote the points used as initial conditions in Eq. (15)

Next the system was examined for two particular sets of initial conditions that are marked by white crosses in Fig. 4. These were chosen such that they are close to each other, but have a significantly different portion of their initial energy remaining at $t = 1000$. In both cases, $d = 1.175$, and the initial energies are:

$$\begin{aligned} E_{(1)}(0) &= 1.728 \\ E_{(2)}(0) &= 2.488 \end{aligned} \tag{15}$$

The fraction of the total energy of the system in the two cases is shown in Figure 5, demonstrating that even for two very similar initial conditions the behaviour of the system is drastically different.

The fraction of the total energy stored in the last level was calculated for the two cases, these are

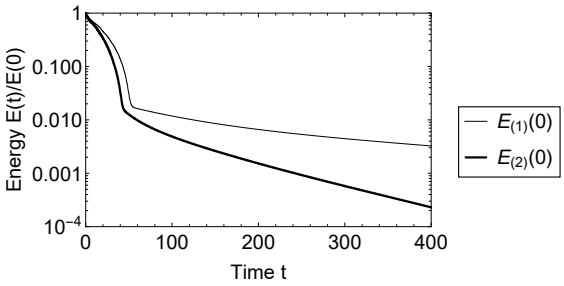

Figure 5. Fraction of the total energy as a function of time, with $d = 1.175$ and initial energy levels from Eq. (15), and initial conditions given in Eq. (12)

shown in Figures 6 and 7. The figures show that for both initial conditions there is a TET, but this occurs around $t = 80$ for $E(0) = E_{(1)}(0)$, in contrast for $t = 100$ for $E(0) = E_2(0)$, and the peak of the energy transfer is also higher for the lower initial energy.

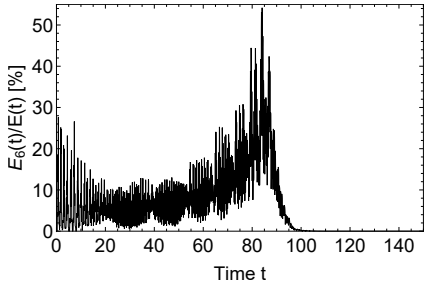

Figure 6. Fraction of the energy stored in the last level as a function of time, $d = 1.175$, $E(0) = E_{(1)}(0)$, with initial conditions given in Eq. (12)

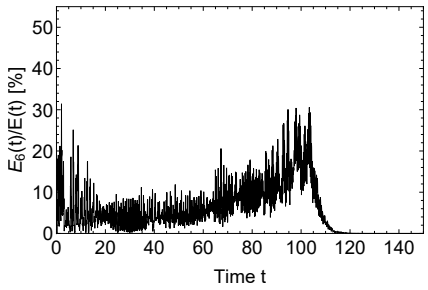

Figure 7. Fraction of the energy stored in the last level as a function of time, $d = 1.175$, $E(0) = E_{(2)}(0)$, with initial conditions given in Eq. (12)

Figures 8 and 9 show the wavelet transform of x_{32}, which shows the frequency of the vibration as the function of its energy content, superimposed onto the FEP for the two initial conditions. In the case of $E(0) = E_{(1)}(0)$, the system follows a backbone curve of the FEP very closely, which indicates that fundamental targeted energy transfer takes place in this case. In case of the higher initial energy level the system does not excite a single NNM, which indicates that the main mechanism of energy transfer is nonlinear beating that allows a more efficient dissipation.

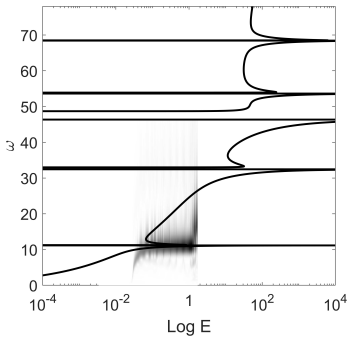

Figure 8. Wavelet transform of x_{32}, with $d = 1.175$, $E(0) = E_{(1)}(0)$, with initial conditions given in Eq. (12)

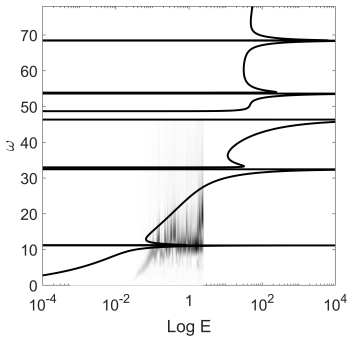

Figure 9. Wavelet transform of x_{32}, with $d = 1.175$, $E(0) = E_{(2)}(0)$, with initial conditions given in Eq. (12)

The temporal average of the energy of the levels was calculated with $t_1 = 0, t_2 = 200$ (see Eq. (5)) and the energy spectra are shown in Figure 10. The main difference between the two results is the energy stored in the last level, which is much lower for the higher initial energy, suggesting that the energy of this level is more efficiently dissipated. Though these spectra do not resemble the Kolmogorov spectrum, their overall trend is qualitatively similar.

3.2. Nonzero initial conditions in a single level

In this case the system was simulated with initial velocities given in Eq. (13) for different $E(0)$ initial energies and d common ratios. Figures 11 to 13 show the fraction of the remaining energy as function of d and $E(0)$ for levels $j \in \{2, 3, 4\}$. Comparing these to Fig. 4, it can be concluded that the behaviour of the system is more sensitive to the distribution of energy among the levels than it is to the distribution among

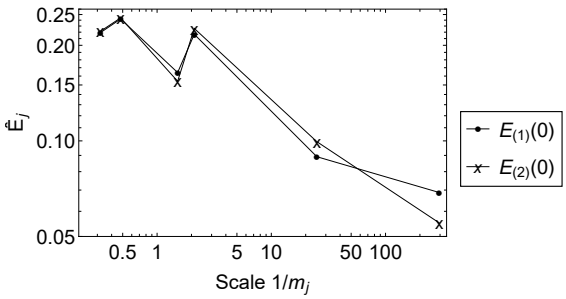

Figure 10. Energy spectrum of the system, with $d = 1.175$ and initial energy levels from Eq. (15), and initial conditions given in Eq. (12)

the masses of the same level. In these cases, the energy dissipation is much more affected by the initial energy.

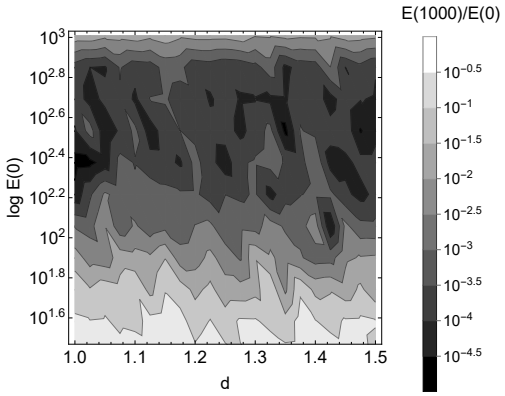

Figure 11. Fraction of the remaining energy as a function of $E(0)$ and d, with initial conditions given in Eq. (13) for level $j = 2$

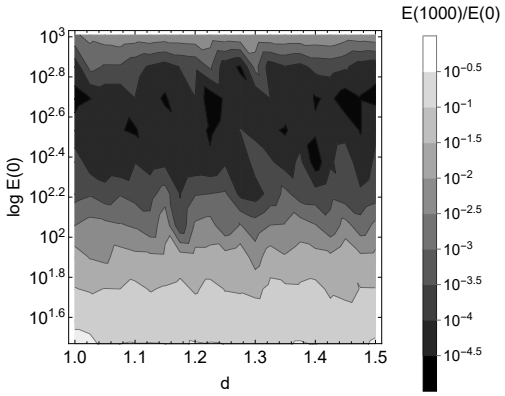

Figure 12. Fraction of the remaining energy as a function of $E(0)$ and d, with initial conditions given in Eq. (13) for level $j = 3$

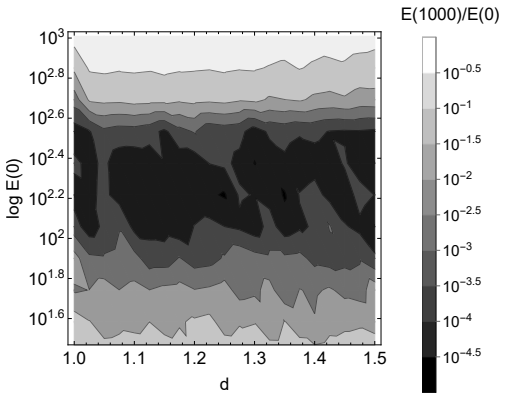

Figure 13. Fraction of the remaining energy as a function of $E(0)$ and d, with initial conditions given in Eq. (13) for level $j = 4$

3.3. Nonzero initial conditions in the first two levels

Finally, the system was examined for the third type of initial conditions specified by Eq. (14). Depending on the sign of $\dot{x}_2(0)$ and $\dot{x}_3(0)$, the system behaves very differently. As the binary tree model is symmetric, there are only 3 cases to be considered:

- $\dot{x}_2(0) = \dot{x}_3(0) = 1$, this will be denoted with $+++$,
- $\dot{x}_2(0) = 1$, $\dot{x}_3(0) = -1$, this will be denoted with $++-$,
- $\dot{x}_2(0) = \dot{x}_3(0) = -1$, this will be denoted with $+--$.

Figure 14 shows the total energy of the system over time for the three set of initial conditions. The total energy dissipation is the highest in the case of $+++$, and the lowest for $+--$.

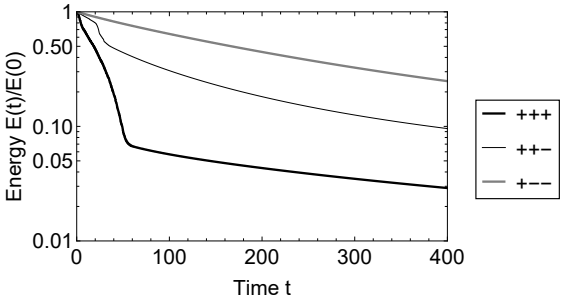

Figure 14. Fraction of the total energy as a function of time, with initial conditions given in Eq. (14

It is clear from Figures 15 to 21 that the energy fraction of the last level is overall the highest for $+++$, and again it is the lowest for $+--$, in which case the peak energy fraction is lower than for the $+++$ and $++-$ initial conditions by a factor of 100.

As there is only significant TET for + + +, it is expected that this initial condition would cause the highest dissipation. Indeed, as there is virtually no energy in the last level for + − −, the behaviour of the system is close to linear.

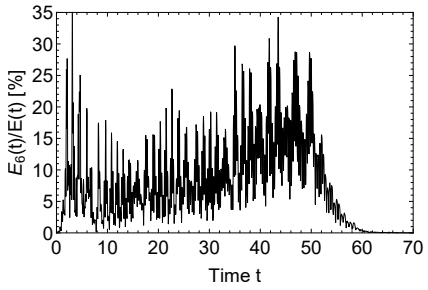

Figure 15. Fraction of the energy stored in the last level as a function of time, with initial conditions given in Eq. (14) and + + +

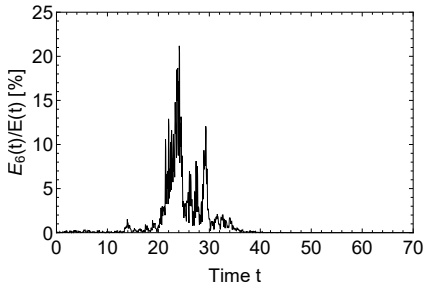

Figure 16. Fraction of the energy stored in the last level as a function of time, with initial conditions given in Eq. (14) and + + −

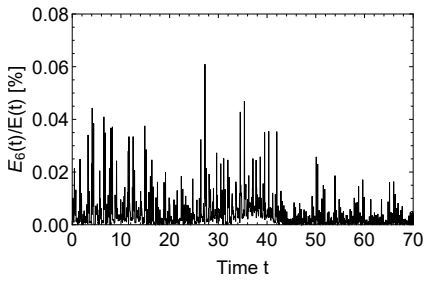

Figure 17. Fraction of the energy stored in the last level as a function of time, with initial conditions given in Eq. (14) and + − −

At last, the wavelet transform of x_{32} is computed for the examined cases, shown in Figures 18 to 20. For the + + + initial condition, the system follows one of the backbone curves, whereas in the other two cases the system remains below the curves throughout the simulation.

Figure 21 shows the energy spectrum of the system in the three cases. The energy stored in the last level was significantly lower for the + + − and + − − initial conditions than for the + + + initial condition. This demonstrates that if the energy of the last level is less, the dissipation is reduced.

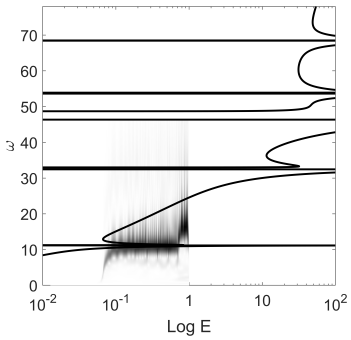

Figure 18. Wavelet transform of x_{32} for initial conditions in Eq. (14) and + + +

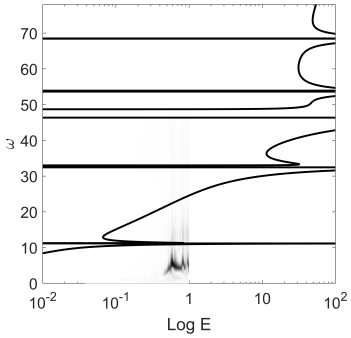

Figure 19. Wavelet transform of x_{32} for initial conditions in Eq. (14) and + + −

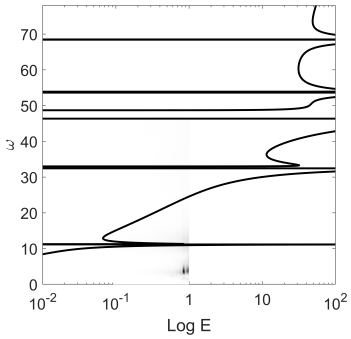

Figure 20. Wavelet transform of x_{32} for initial conditions in Eq. (14) and + − −

4. SUMMARY

The mechanistic model of turbulence was introduced as a binary tree of spring connected masses. The parameters of this model were derived from turbulence measurement data using a reduced model. FEPs were created for the two models to demonstrate their similar behavior. It was found that the reduced model predicts somewhat higher energies for a given frequency of the NNM.

The system was simulated for three types of ini-

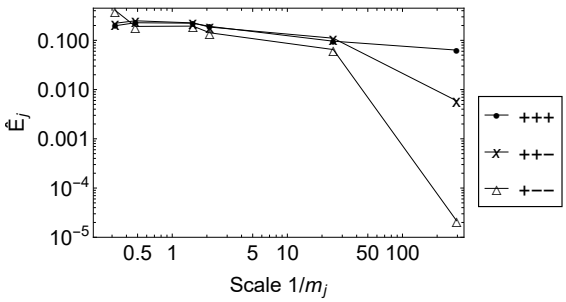

Figure 21. Energy spectrum of the system for initial conditions in Eq. (14)

tial conditions distinguished by the elements with nonzero initial velocities. With nonzero initial velocity in the first 5 levels, the behaviour of the system was found to be very sensitive to both the initial energy and the energy distribution among the levels. It was demonstrated that even a small change in the initial energy content can lead to drastically different dynamical response.

With nonzero initial velocities in a single level, the dynamics of the system were still sensitive to the initial energy, but the energy distribution within the level has little effect on the dissipation of the system.

A case where the only nonzero initial velocities were prescribed for the first two levels was also examined. It was shown that for this initial energy, the dissipation was much more substantial when the three elements started in the same phase in contrast to one or two elements starting in opposite phase to the element of the first level.

The energy spectra of the investigated cases do not resemble the Kolmogorov spectrum, but we also did not expect this from a 6-level system. For now, the purpose of this paper was to present numerical experiments with different initial conditions to give an overview about the dynamics of the system. In future work we intend to investigate the system with much more levels to incorporate a broad scale of masses that will result in a more detailed energy spectrum.

ACKNOWLEDGMENTS

The research reported in this paper and carried out at the Budapest University of Technology and Economics has been supported by the National Research Development and Innovation Fund (TKP2020 National Challenges Subprogram, Grant No. BME-NCS) based on the charter of bolster issued by the National Research Development and Innovation Office under the auspices of the Ministry for Innovation and Technology.

The research reported in this paper is part of project no. BME-NVA-02, implemented with the support provided by the Ministry of Innovation and Technology of Hungary from the National Research, Development and Innovation Fund, financed under the TKP2021 funding scheme.

This work has been supported by the Hungarian National Research, Development and Innovation Fund under contract NKFI K 137726.

REFERENCES

[1] Kerschen, G., Kowtko, J. J., and Mcfarland, D. M. e. a., 2006, "Theoretical and Experimental Study of Multimodal Targeted Energy Transfer in a System of Coupled Oscillators", *Nonlinear Dynamics*, Vol. 47, pp. 285–309.

[2] Gendelman, O. V., 2008, "Targeted energy transfer in systems with non-polynomial nonlinearity", *Journal of Sound and Vibration*, Vol. 315, pp. 732–745.

[3] Viguié, R., Kerschen, G., Golinval, J.-C., McFarland, D. M., Bergman, L. A., F., V. A., and Wouw, N. v. d., 2009, "Using passive nonlinear targeted energy transfer to stabilize drill-string systems", *Mechanical Systems and Signal Processing*, Vol. 23, pp. 148–169.

[4] Motato, E., Haris, A., Theodossiades, S., Mohammadpour, M., Rahnejat, H., Kally, P., Vakakis, A. F., McFarland, D. M., and Bergman, L. A., 2017, "Targeted energy transfer and modal energy redistribution in automotive drivetrains", *Nonlinear Dynamics*, Vol. 87, pp. 169–190.

[5] Chen, J., Zhang, W., Liu, J., and Hu, W., 2021, "Vibration absorption of parallel-coupled nonlinear energy sink under shock and harmonic excitations", *Applied Mathematics and Mechanics (English Edition)*, Vol. 42 (8), pp. 1135–1154.

[6] Richardson, L. F., 1922, *Weather prediction by numerical process*, Cambridge, University Press.

[7] Kolmogorov, A. N., 1941, "The local structure of turbulence in incompressible viscous fluid for very large Reynolds numbers", *Dokl Akad Nauk SSSR*, Vol. 30, pp. 301–305.

[8] Kalmár-Nagy, T., and Bak, B. D., 2019, "An intriguing analogy of Kolmogorov's scaling law in hierarchical mass-spring-damper model", *Nonlinear Dynamics*, Vol. 95.

[9] Bak, B. D., and Kalmár-Nagy, T., 2019, "Energy Cascade in a Nonlinear Mechanistic Model of Turbulence", *Technische Mechanik*, Vol. 39, pp. 64–71.

[10] Vakakis, A. F., Gendelman, O. V., Bergman, L. A., McFarland, D. M., Kerschen, G., and Lee, Y. S., 2008, *Nonlinear Targeted Energy Transfer in Mechanical and Structural Systems*, Springer.

Conference on Modelling Fluid Flow (CMFF'22)
The 18th International Conference on Fluid Flow Technologies
Budapest, Hungary, August 30 -September 2, 2022

HEAT TRANSFER AND FLUID FLOW ANALYSIS FOR ELECTROOSMOTIC FLOW OF CARREAU FLUID THROUGH A WAVY MICROCHANNEL CONSIDERING STERIC EFFECT

Sumit Kumar MEHTA[1], Sukumar PATI[2], László BARANYI[3]

[1]Department of Mechanical Engineering, National Institute of Technology Silchar, Silchar, India-788010, E-mail: sumit090391@gmail.com
[2] Corresponding Author: Department of Mechanical Engineering, National Institute of Technology Silchar, Silchar, India-788010, E-mail: sukumar@mech.nits.ac.in
[3] Department of Fluid and Heat Engineering, Institute of Energy Engineering and Chemical Machinery, University of Miskolc, 3515, Miskolc-Egyetemváros, Hungary. E-mail: laszlo.baranyi@uni-miskolc.hu

ABSTRACT

We investigate the heat transfer and flow characteristics for an electroosmotic flow of Carreau fluid through a wavy microchannel, considering the finite size of ions i.e., steric effect. The flow of electrolytic liquid is considered steady, two-dimensional and incompressible. The modified Poisson-Boltzmann equation, Laplace equation, continuity equation, momentum equation, and energy equation are solved numerically using a finite element method-based solver. The computed flow and temperature fields are validated by comparison with published results. The flow and temperature fields and average Nusselt number are computed by varying the steric factor, Weissenberg number and Brinkman number in the following ranges: $0 \leq \upsilon \leq 0.3$, $0.01 \leq Wi \leq 1$, $10^{-5} \leq Br \leq 10^{-3}$. We found the locations of the local maxima and minima of Nusselt number at the convex and concave surfaces of the channel for a lower Brinkman number ($=10^{-5}$). In contrast, the corresponding locations are swapped at higher Brinkman number ($=10^{-3}$). The value of average Nusselt number increases with the increase in Weissenberg number and decreases with the steric factor for the smaller Brinkman number ($=10^{-5}$). Whereas, it decreases with Wi for non-zero values the of steric factor with higher Brinkman number ($=10^{-3}$).

Keywords: Electroosmosis; heat transfer; steric effect; viscous heating, wavy microchannel.

NOMENCLATURE

Br	[-]	Brinkman number
E^*_{ref}	[V/m]	Reference external electric field
G	[-]	Joule heating parameter
H	[m]	Inlet half height of microchannel
Nu	[-]	Nusselt number
$\overline{Nu}$	[-]	Average Nusselt number
q	[W/m^2]	Heat flux
$\mathbf{u}$	[-]	Dimensionless velocity vector
Wi	[-]	Weissenberg number
υ	[-]	Steric factor

1. INTRODUCTION

In recent times, analysis of transport phenomena in microfluidic channels has received serious attention due to its wide range of engineering applications, such as biomedical and pharmaceutical industries. For microfluidic transport of electrolyte, flow actuated by an external electrical forcing also known as electroosmotic flow (EOF) is one of the suitable flow actuation mechanism widely used due to better flow control and simplicity of the system [1-8]. Further, the micro-level heat exchanging systems using EOF is getting significant attention because of its applications in electronics cooling [9].

Using wavy surfaces, the fluid-solid interfacial area for heat transfer can be enhanced and accordingly channel with wavy walls wall is one of the effective methods for heat transfer enhancement [10-15]. Cho et al. [16] investigated the heat transfer characteristics for the combined electroosmotic and pressure-driven flow through a complex wavy microchannel considering the Joule heating effect. They found that the value of maxima of Nusselt number increases with the increase in the amplitude of the complex wavy wall.

For several microfluidic applications, fluid is non-Newtonian in nature [3]. Researchers have developed and employed several models, namely, power-law model [17], Carreau model [3], Casson

model [18], moldflow second-order model [19] to describe the constitutive behaviour of non-Newtonian fluids. Moghadam [20] investigated the heat transfer characteristics for electrokinetic-driven flow of non-Newtonian power-law fluid through a circular microtube and found that the trend of fully developed Nusselt number is either increasing or decreasing with the increase in flow behaviour index and the length scale ratio. Noreen et al. [21] studied the heat transfer characteristics for electroosmotic flow of Carreau fluid through a wavy microchannel and reported that the increase in Weissenberg number increases the Nusselt number.

The classical Poisson-Boltzmann model over-predicts the ionic concentration in electric double-layer (EDL) by neglecting the effect of finite ion size. However, the effect of ions size cannot be ignored for the higher surface charge density. Accordingly, several researchers have used the modified Poisson-Boltzmann equation duly incorporating the effect of finite size of ions by introducing steric factor to find the EDL potential [22, 23]. Dey et al. [24] investigated the effect of finite size of ions on the heat transfer characteristics for combined electroosmotic and pressure-driven flow through the microchannel. They reported that the point charge assumption overestimates the Nusselt number.

This brief literature survey reveals that no work has been reported investigating the effect of finite size of ions on the heat transfer characteristics for flow of Carreau fluid in a wavy microchannel, which is the main focus of the present work.

2. THEORETICAL FORMULATION

We consider an electroosmotic flow of Carreau fluid through a wavy microchannel with inlet half-height, $2H$, as shown in Fig. 1. Both walls of the channel at the inlet and outlet are planar having an axial length of $5H$ each and in the intermediate part having an axial length of $20H$, the walls are wavy, the sinusoidal profiles of which are taken as [3, 8, 16]:

$$S^*_{Top}\left(x^*\right) = 2H + 0.3H\sin\left(\pi\left(x^* - 5H\right)/H\right) \quad (1)$$

$$S^*_{Bottom}\left(x^*\right) = 0.3H\sin\left(\pi\left(x^* - 5H\right)/H\right). \quad (2)$$

The amplitude of the wavy walls is taken as 0.3 times of the inlet half-height [3, 8, 16], such that the curvature effect on the ionic distribution can be neglected as the radius of curvature ($\left(H_w/4\right)^2/A = 5.2H \gg H$) is large compared to the inlet half-height [3], where, $H_w\left(=5H\right)$ is the wavelength. The planar walls are insulated, while the wavy walls are imposed with constant heat flux q. It is assumed that flow of electrolytic liquid is steady, two-dimensional and incompressible. The temperature-independent thermo-physical properties are taken into consideration. Moreover, the ionic distribution is static as the ionic Peclet number is smaller than unity. The governing equations (modified Poisson-Boltzmann equation, Laplace equation, continuity equation, momentum equation and energy equation) in dimensionless form relevant to the present work are as follows [3, 21]:

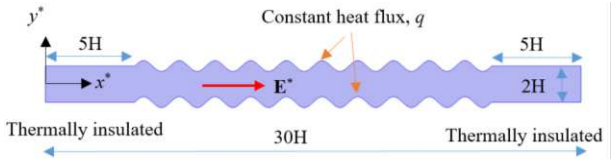

Figure 1. Physical domain.

$$\nabla^2\psi = \kappa^2\frac{\sinh\left(\psi\right)}{1+4\upsilon\sinh^2\left(\psi/2\right)}, \quad (3)$$

$$\nabla^2\varphi = 0, \quad (4)$$

$$\nabla\cdot\mathbf{u} = 0, \quad (5)$$

$$Re\left(\mathbf{u}\cdot\nabla\right)\mathbf{u} = -\nabla P + \left(\nabla\cdot\boldsymbol{\tau}\right) + \left[\kappa^2\frac{\sinh\left(\psi\right)}{1+4\upsilon\sinh^2\left(\psi/2\right)}\right]\nabla\left(\psi/\Lambda + \varphi\right) \quad (6)$$

$$Pe\left(\mathbf{u}\cdot\nabla\theta\right) = \nabla^2\theta + Br\phi + G. \quad (7)$$

Here ψ and φ are the dimensionless induced and external potential fields normalized by the scale $\psi^*_{ref}\left(=k_BT/ze\right)$ and $\varphi^*_{ref}\left(=\Delta V\times H/30H\right)$, respectively; $\mathbf{u}\equiv\left(u,v\right)$ is the dimensionless velocity vector normalized by the Helmholtz-Smoluchowski velocity $u^*_{HS}\left(=-\psi^*_{ref}E^*_{ref}\varepsilon/\mu_o\right)$; $\nabla\equiv\left(\mathrm{x},\mathrm{y}\right)$ is normalized by H; pressure P is normalised by $\mu_o u^*_{HS}/H$; $\boldsymbol{\tau} = \boldsymbol{\tau}^*\left(\mu_o u^*_{HS}/H\right)^{-1}$ is the dimensionless deviatoric stress tensor, where $\boldsymbol{\tau}^* = \mu\left(\dot{\gamma}^*\right)\left[\left(\nabla\mathbf{u}^*\right)+\left(\nabla\mathbf{u}^*\right)^T\right]$; $\dot{\gamma}^* = \sqrt{(1/2)(\mathbf{S}:\mathbf{S})}$ is the second invariant of the rate of deformation tensor and $\mathbf{S} = \left[\left(\nabla\mathbf{u}^*\right)+\left(\nabla\mathbf{u}^*\right)^T\right]$ is the strain rate tensor. The apparent viscosity for Carreau fluid can be written as [3]: $\mu\left(\dot{\gamma}^*\right) = \mu_\infty + \left(\mu_o-\mu_\infty\right)\left(1+\left(\lambda\dot{\gamma}^*\right)\right)^{((n-1)/2)}$, where μ_∞, μ_o, λ, and n are the infinity and zero shear rate viscosity, relaxation time parameter, and flow behaviour index, respectively. Moreover, the dimensionless temperature is expressed as $\theta = \left(T-T_{in}\right)/\left(qH/k\right)$.

Here, $\phi = \left[\frac{\partial u}{\partial x}\left(\tau_{xx}-\tau_{yy}\right)+\left(\frac{\partial u}{\partial y}+\frac{\partial v}{\partial x}\right)\tau_{xy}\right]$ is the viscous dissipation parameter; $\tau_{xx} = 2\left(\bar{\mu}_\infty+\left(1-\bar{\mu}_\infty\right)\left(1+\left(\mathrm{Wi}\,\dot{\gamma}\right)\right)^{((n-1)/2)}\right)\frac{\partial u}{\partial x}$; $\tau_{xy} = \left(\bar{\mu}_\infty+\left(1-\bar{\mu}_\infty\right)\left(1+\left(\mathrm{Wi}\,\dot{\gamma}\right)\right)^{((n-1)/2)}\right)\left(\frac{\partial u}{\partial y}+\frac{\partial v}{\partial x}\right)$ and $\tau_{yy} = 2\left(\bar{\mu}_\infty+\left(1-\bar{\mu}_\infty\right)\left(1+\left(\mathrm{Wi}\,\dot{\gamma}\right)\right)^{((n-1)/2)}\right)\left(\frac{\partial v}{\partial y}\right)$ are the components of stresses, where $\dot{\gamma} = \sqrt{2\left(\frac{\partial u}{\partial x}\right)^2+\left(\frac{\partial u}{\partial y}+\frac{\partial v}{\partial x}\right)^2+2\left(\frac{\partial v}{\partial y}\right)^2}$ [21]. Here, $\bar{\mu}_\infty$ is

defined as $\bar{\mu}_\infty = \mu_\infty / \mu_o$ the value of which is taken as 0.0616 [3]. Here, υ, $\kappa (= H/\lambda_D)$ and $Re \left(= \rho u_{HS}^* H / \mu_o\right)$ are the steric factor, Debye parameter, Reynolds number, respectively; $Wi = \left(\lambda u_{HS}^* / H\right)$, $\Lambda \left(= \varphi_{ref}^* / \psi_{ref}^*\right)$, and $Pe \left(= \rho c_p H u_{HS}^* / k\right)$ are the Weissenberg number, ratio of reference applied to EDL potential, thermal Peclet number, respectively; $Br \left(= \mu_o \left(u_{HS}^* / H\right)^2 H / q\right)$, and $G \left(= \sigma \left(E_{ref}^*\right)^2 H / q\right)$ are the Brinkman number, and Joule heating parameter, respectively. Note that $\lambda_D \left(= \left(2 n_o z^2 e^2 / \varepsilon k_B T\right)^{-0.5}\right)$, ΔV, ρ, c_p, k, ε, $E_{ref}^* \left(= \Delta V / 30 H\right)$, n_o, T and σ are the Debye length, applied external potential difference, density, specific heat capacity, thermal conductivity, electrical permittivity of the liquid, reference external electric field, bulk ionic concentration, reference absolute temperature, and electrical conductivity of the liquid, respectively.

The boundary conditions employed are follows:

At inlet:

$$\mathbf{n} \cdot (\nabla \psi) = 0, \ \varphi = 30, \ P = P_{atm}, \ \theta = 0. \tag{8a}$$

At wavy walls:

$$\psi = \zeta = 4, \ \mathbf{n} \cdot (\nabla \varphi) = 0, \ \mathbf{u} = 0, \ \partial\theta / \partial n = 1. \tag{8b}$$

At planar walls:

$$\psi = 4, \ \mathbf{n} \cdot (\nabla \varphi) = 0, \ \mathbf{u} = 0, \ \partial\theta / \partial n = 0 \quad . \tag{8c}$$

At outlet:

$$\mathbf{n} \cdot (\nabla \psi) = 0, \ \varphi = 0, \ P = P_{atm}, \ \partial\theta / \partial x = 0. \tag{8d}$$

Here $\mathbf{n}$ is the unit vector normal to wavy wall.

The heat transfer rate is presented in terms of local Nusselt number (Nu) as [1, 7]:

$$Nu = 1 / (\theta_{wall} - \theta_{mean}) \tag{9}$$

Here $\theta_{mean} \left(= \int_{y_1}^{y_2} u \theta \, \mathrm{d}y \Big/ \int_{y_1}^{y_2} u \, \mathrm{d}y \right)$ is the bulk mean temperature of the fluid [7].

The average Nusselt number $\left(\overline{Nu}\right)$ is calculated as [11, 12, 14]:

$$\overline{Nu} = 0.5 \left[\left(\int_{x=5}^{x=25} Nu \, \mathrm{d}S \Big/ \int_{x=5}^{x=25} \mathrm{d}S \right)_{Top} + \left(\int_{x=5}^{x=25} Nu \, \mathrm{d}S \Big/ \int_{x=5}^{x=25} \mathrm{d}S \right)_{Bottom} \right] \tag{10}$$

Here S is the normalised axial length of the wavy walls.

3. NUMERICAL METHODOLOGY AND MODEL BENCHMARKING

We employ a finite element method based numerical solver to obtain the flow and temperature fields. The computational domain is divided into large number of small sub-domains in non-uniform manner with denser mesh near the walls. The mesh used for the present computational investigation is presented in Fig. 2. Using Galerkin weighted method, the governing equations are first discretised and then the resulting equations are solved iteratively until the pre-defined residual value of 10^{-6} is reached. An exhaustive grid independence test was performed by calculating the average Nusselt number as depicted in Table 1; the relative difference of the value for the mesh system with 130144 elements and the next level finer mesh was less than 1%. Accordingly, the mesh with 130144 elements was used for all the simulations.

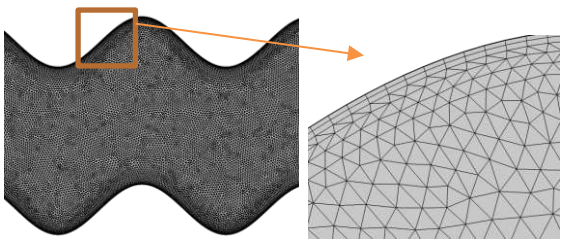

Figure 2. Grid distribution in wavy microchannel.

Table 1. Grid independence test at different mesh system (M) calculating average Nuselt number when υ =0.3, n=0.4, Wi=1, Br=10^{-3} and κ=30.

Mesh type	Number of elements	Average Nusselt number	Percentage error w r t M4
M1	20206	3.5294	24.586
M2	51869	3.0219	6.671
M3	130144	2.8376	0.166
M4	218108	2.8329	0

We validate the solver by comparing the electroosmotic flow velocity profile with the results of Zhao et al. [5] for parallel plate channel shown in Fig. 3(a) for n=1, κ=10, υ=0 and ζ=1. The second validation is presented in Fig. 3(b) by comparing the dimensionless wall temperature for EOF in a plane microchannel with the results of Horiuchi and Dutta [25]. For this validation, the values of different parameters considered are as follows: Pe=100, κ=100, Br=0, n=1 and υ=0. The comparisons show a good agreement of the present result with the published works [5, 25].

4. RESULTS AND DISCUSSION

We analyse the heat transfer and flow characteristics for an ionic size dependent electroosmotic flow of Carreau fluid through a wavy microchannel. The results are presented in terms of flow and temperature fields, local Nusselt number (Nu) and average Nusselt number ($\overline{Nu}$) by varying the steric factor (υ), Weissenberg number (Wi) and Brinkman number (Br) in the range of $0 \leq \upsilon \leq 0.3$, $0.01 \leq Wi \leq 1$, [3, 21, 26], and $10^{-5} \leq Br \leq 10^{-3}$, respectively [1, 5]. The value of n and Re is kept fixed at 0.4 and 0.001, respectively [3, 26].

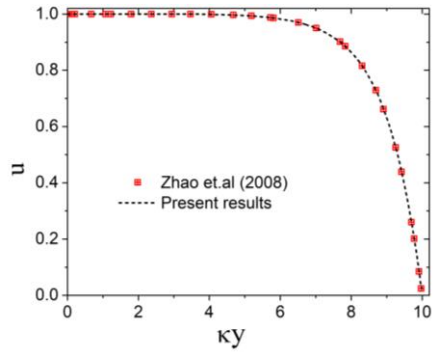

(a)

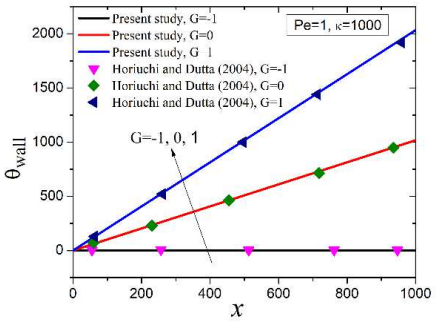

(b)

Figure 3. (a) Comparison of dimensionless electroosmotic flow velocity in a parallel plate channel κ=10, υ=0 and ζ=1 at the limiting case, n=1, (b) Comparison of non-dimensional wall temperature for EOF through a plane microchannel for different G values with the results of Horiuchi and Dutta [25] for Pe=100, κ=100, Br=0, n=1 and υ=0.

Figure 4 shows the transverse variation of dimensionless flow velocity at x=10.5 for different values of Wi and υ. It is observed that the increase in υ from 0 to 0.3 decreases the flow velocity due to the increase in flow resistance caused by the electrostatic pull inside the EDL by the finite size of ions [3]. It is also seen that the decrement is higher near the walls as the flow resistance is only within the EDL. Furthermore, the flow velocity at any transverse location increases as Wi increases which is attributed to the decreases in apparent viscosity of the fluid.

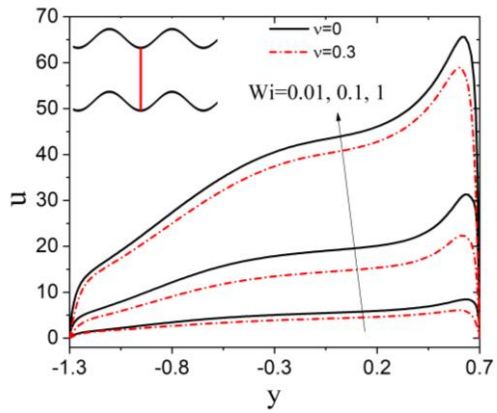

Figure 4. Variation of transverse dimensionless velocity profile at x=10.5 for different values of steric factor and Wi.

The streamlines and dimensionless flow velocity contours at different Wi are presented in Fig. 5 at υ=0.3. It is observed that the streamlines near the wall follow the profile of the wavy walls and accordingly they become a wavy. Further, the minima and maxima of velocity exist near the concave and convex surfaces due to the smaller and higher electric field intensity, respectively. Moreover, the flow velocity is enhanced with Wi due to the decrease in the apparent viscosity of the fluid.

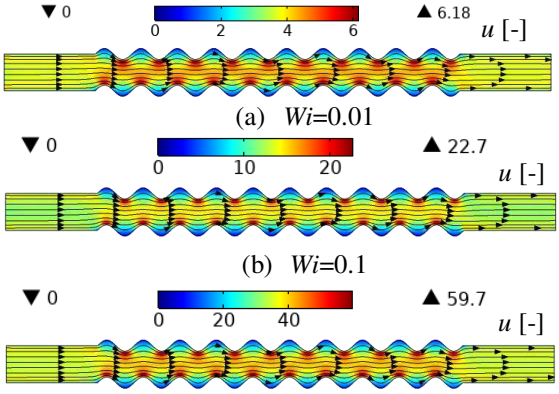

(c) Wi=1

Figure 5. Streamlines and dimensionless flow velocity contours at different Wi for υ =0.3, n=0.4 and κ=30.

Figures 6(a) and (b) show the contours of dimensionless isotherms at different Wi and Br for υ=0 and 0.3, respectively. It is seen that the increase in Wi from 0.01 to 1 decreases the temperature in the domain due to the increase in convective heat transfer (see Fig. 4). Further, the decrease in convection strength with the increase in steric factor from 0 to 0.3 (see Fig. 4) increases the isotherms values for υ=0.3 compared to υ=0. It is also noted that the increase in Br augments the temperature of fluid due to the increase in viscous dissipation effect. The increment is significantly higher for the higher Wi (=1) values, which is attributed to the higher velocity gradient (see Fig. 4).

Figure 7(a) and (b) shows the variation of local Nusselt number (Nu) at the top wall for different υ values with Br=10^{-5} and 10^{-3} at Wi=1. It is observed that the locations of the local maxima and minima of Nu are at the convex and concave surfaces, respectively due to higher and smaller velocity gradient for the smaller Br (=10^{-5}). In contrast, these minima and maxima locations are shifted to convex and concave surface, respectively at Br =10^{-3}. It is attributed to the higher velocity near the convex surface causing very high viscous dissipation effect at higher Br. Furthermore, the increase in υ decreases the value of Nu for Br=10^{-5} and the trend is opposite for Br =10^{-3}. These observations can be explained as follows. For smaller Br (=10^{-5}) values the significant increase in wall temperature compared to the core temperature (see Fig. 6) due to the decrease in flow velocity (see Fig. 4) increases the difference of (θ_{wall}

- θ_{mean}) with υ. Whereas, for higher Br (=10^{-3}), the decrease in velocity gradient with υ (see Fig. 4) near the walls significantly reduces the viscous heating and augments the heat transfer rate with υ.

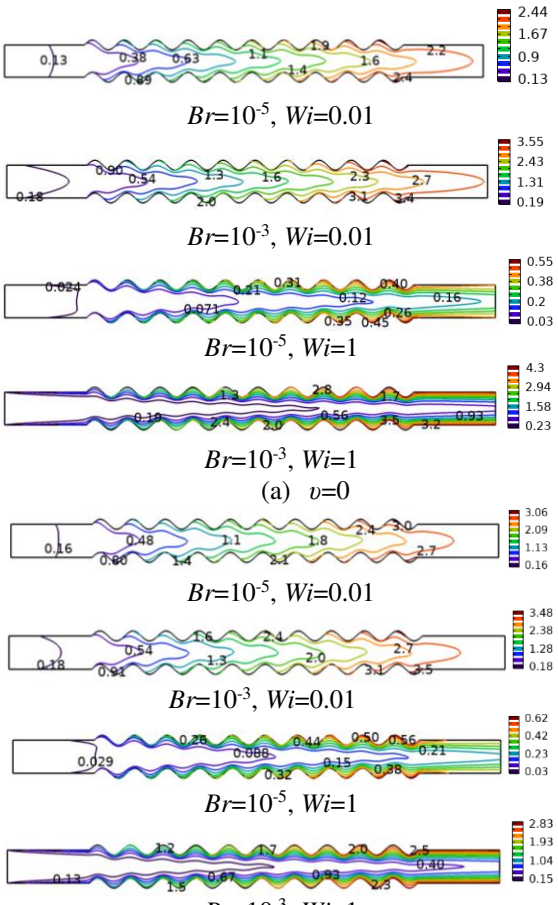

Figure 6. Contours of dimensionless isotherms for different Br and Wi values at (a) υ=0 and (b) υ=0.3, when ζ=4, κ=30, Pe=5, n=0.4 and G=1. The colour legends represent the dimensionless temperature, θ.

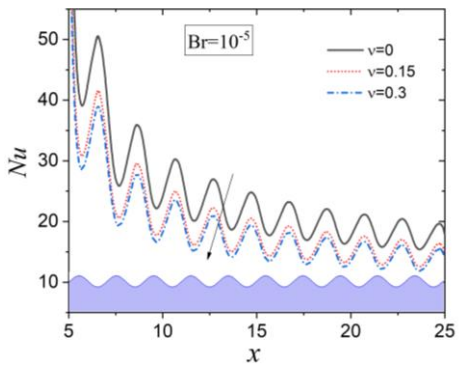

(a)

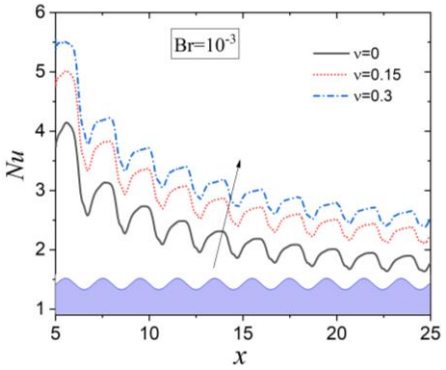

(b)

Figure 7. Variation of local Nusselt number at different υ values for (a) Br=10^{-5} and (b) Br=10^{-3} when ζ=4, κ=30, Pe=5, n=0.4 and G=1.

The variation of average Nusselt number ($\overline{Nu}$) with Wi for different υ values is shown in Fig. 8(a) and (b) for Br=10^{-5} and 10^{-3}, respectively. It is

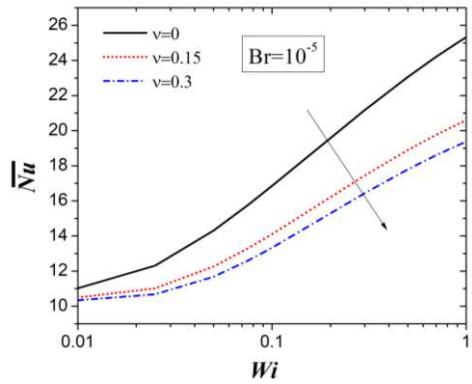

(a)

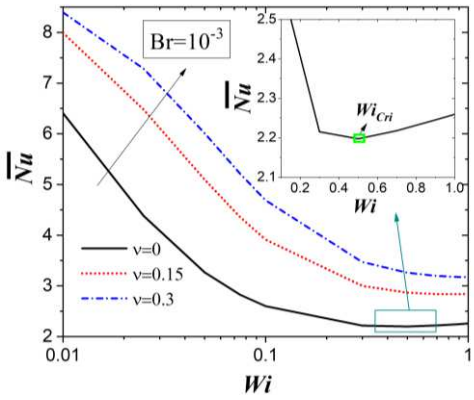

(b)

Figure 8. Variation of average Nusselt number with Wi at different υ values for (a) Br=10^{-5} and (b) Br=10^{-3} when ζ=4, κ=30, Pe=5, n=0.4 and G=1.

observed that the value of $\overline{Nu}$ increases with Wi for Br =10^{-5}. It is attributed to fact that the increase in flow velocity with Wi (see Fig. 4) significantly reduces the wall temperature compared to the bulk temperature and the decrease in (θ_{wall} - θ_{mean}) with Wi increases the value of $\overline{Nu}$. Also, it is seen in Fig. 8(a) that $\overline{Nu}$ decreases with υ for smaller (Br =10^{-5})

which can be explained from the variation of local Nusselt number with υ. The value of $\overline{Nu}$ decreases with Wi for υ=0.15 and 0.3, and it follows the increasing-decreasing trend with Wi for the point charge case (υ=0), and a critical Wi (Wi_{Cri}) is found for Br=10^{-3}. The decrease in $\overline{Nu}$ with Wi is attributed to the augmentation in viscous heating (see Fig. 4), which decreases the heat transfer rate. Whereas, for higher Wi values (>Wi_{Cri}), the enhanced convective strength decreases the core region temperature and hence the value of (θ_{wall} - θ_{mean}). Furthermore, it is seen in Fig. 8(b) that the value of $\overline{Nu}$ increases with υ which can be explained from the variation of local Nusselt number. The values of the decrease and increase in $\overline{Nu}$ are obtained as 23.49% and 40.51% for change in υ from 0 to 0.3 for Br=10^{-5} and 10^{-3}, respectively, when Wi=1.

5. CONCLUSIONS

In the present study we investigate the heat transfer and flow characteristics for an ionic size dependent electroosmotic flow of non-Newtonian Carreau fluid through a wavy microchannel. The results are presented in terms of flow and temperature fields, local Nusselt number (Nu) and average Nusselt number ($\overline{Nu}$) by varying the steric factor (υ), Weissenberg number (Wi) and Brinkman number (Br) in the following range: 0≤ υ ≤0.3, 0.01≤Wi ≤1, [3, 21, 26], and 10^{-5}≤ Br ≤10^{-3}. The important findings are summarised as follows:

- The flow velocity increases with Wi and decreases with υ.
- The locations of the local maxima and minima of Nusselt number are at the convex and concave surfaces for smaller Br (=10^{-5}). In contrast, the locations are swapped at higher Br (=10^{-3}).
- The value of $\overline{Nu}$ increases with Wi and decreases with υ for smaller Br (=10^{-5}) values. Whereas the value of $\overline{Nu}$ decreases with Wi for υ=0.15 and 0.3, and it follows the increasing-decreasing trend with Wi for point charge case (υ=0), and a critical Wi is found for higher Br (=10^{-3}). Moreover, $\overline{Nu}$ increases with υ for higher Br (=10^{-3}).
- The values of the decrease and increase in $\overline{Nu}$ are obtained as 23.49% and 40.51% for the change in υ from 0 to 0.3 for Br=10^{-5} and Br=10^{-3}, respectively, when Wi=1.

REFERENCES

[1] Pabi, S., Mehta, S.K., and Pati S., 2021, "Analysis of thermal transport and entropy generation characteristics for electroosmotic flow through a hydrophobic microchannel considering viscoelectric effect", *Int Commun Heat Mass Transf*, Vol. 127, p. 105519.

[2] Vasista, K.N., Mehta, S.K., Pati, S., and Sarkar, S., 2021, "Electroosmotic flow of viscoelastic fluid through a microchannel with slip-dependent zeta potential", *Phys Fluids*, Vol. 33, p. 123110.

[3] Mehta, S.K., Pati, S., and Mondal, P.K., 2021, "Numerical study of the vortex-induced electroosmotic mixing of non-Newtonian biofluids in a nonuniformly charged wavy microchannel: Effect of finite ion size". *Electrophoresis*, Vol. 42, pp. 2498-2510.

[4] Sujith T., Mehta, S.K., and Pati, S., 2021, "Effect of non-uniform heating on electroosmotic flow through microchannel", *Recent Advances in Mechanical Engineering. In: Pandey KM, Misra RD, Patowari PK, Dixit US, editors. Springer Singapore*; pp. 499–508. https://doi.org/10.1007/978-981-15-7711-6_50

[5] Zhao, C., Zhao, E., Masliyah, J.H., and Yang, C., 2008, "Analysis of electroosmotic flow of power-law fluids in a slit microchannel", *J. Colloid Interface Sci.* Vol. 326, pp. 503–510.

[6] Mondal, B., Mehta, S.K., Pati, S., and Patowari, P.K., 2021, "Numerical analysis of electroosmotic mixing in a heterogeneous charged micromixer with obstacles" *Chem Eng Process - Process Intensif*. Vol. 168, p. 108585.

[7] Banerjee, D., Mehta, S.K., Pati, S., and Biswas, P., 2021, "Analytical solution to heat transfer for mixed electroosmotic and pressure-driven flow through a microchannel with slip-dependent zeta potential", Int *J Heat Mass Transf*. Vol. 181, p. 121989.

[8] Vasista, K.N., Mehta, S.K., and Pati, S., 2021, "Numerical assessment of hydrodynamic and mixing characteristics for mixed electroosmotic and pressure-driven flow through a wavy microchannel with patchwise surface heterogeneity", *Proc Inst Mech Eng Part E J Process Mech Eng*. https://doi.org/10.1177/09544089211051640

[9] Eng, P.F., Nithiarasu, P., Arnold, A.K., Igic, P., and Guy, O. J.,2007, "Electro-osmotic flow based cooling system for microprocessors", *International Conference on Thermal, Mechanical and Multi-Physics Simulation Experiments in Microelectronics and Micro-Systems. EuroSime 2007*, pp. 1-5, https://doi.org/10.1109/ESIME.2007.360041

[10] Mehta, S.K., and Pati, S., 2019, "Analysis of thermo-hydraulic performance and entropy generation characteristics for laminar flow through triangular corrugated channel*", J Therm Anal Calorim.* Vol. 136, pp. 49–62.

[11] Mehta, S.K., and Pati, S., 2021, "Thermo-hydraulic and entropy generation analysis for magnetohydrodynamic pressure driven flow of

nanofluid through an asymmetric wavy channel", *Int J Numer Methods Heat Fluid Flow*. Vol. 31, pp. 1190–213.

[12] Mehta, S.K., Pati, S., Ahmed S, Bhattacharyya, P., and Bordoloi, J.J., 2021, "Analysis of thermo-hydraulic and entropy generation characteristics for flow through ribbed-wavy channel", *Int J Numer Methods Heat Fluid Flow*. Vol. 32 No. 5, pp. 1618-1642.

[13] Pati, S., Mehta, S.K., and Borah, A., 2017, "Numerical investigation of thermo-hydraulic transport characteristics in wavy channels: Comparison between raccoon and serpentine channels", *Int Commun Heat Mass Transf*. Vol. 88, pp. 171–176.

[14] Mehta, S.K., Pati, S., and Baranyi, L., 2022, "Effect of amplitude of walls on thermal and hydrodynamic characteristics of laminar flow through an asymmetric wavy channel", *Case Stud Therm Eng*. Vol. 31, p. 101796.

[15] Mehta, S.K., and Pati, S., 2020, "Numerical study of thermo-hydraulic characteristics for forced convective flow through wavy channel at different Prandtl numbers", *J Therm Anal Calorim*. Vol. 141, pp. 2429–2451.

[16] Cho, C.C., Chen, C.L., and Chen, C.K., 2012, "Characteristics of combined electroosmotic flow and pressure-driven flow in microchannels with complex-wavy surfaces", *Int J Therm Sci.* Vol. 61, pp. 94–105.

[17] Babaie, A., Sadeghi, A., and Saidi, M.H., 2011, "Combined electroosmotically and pressure driven flow of power-law fluids in a slit microchannel", *J Nonnewton Fluid Mech*. Vol. 166, pp. 792–798.

[18] Bag, N., and Bhattacharyya, S., 2018, "Electroosmotic flow of a non-Newtonian fluid in a microchannel with heterogeneous surface potential", *J Nonnewton Fluid Mech*. Vol. 259, pp. 48–60.

[19] Koh, Y.H., Ong, N.S., Chen, X.Y., Lam, Y.C., and Chai, J.C., 2004, "Effect of temperature and inlet velocity on the flow of a nonnewtonian fluid", *Int Commun Heat Mass Transf*. Vol. 31, pp. 1005–1013.

[20] Moghadam, A.J., 2013, "Electrokinetic-driven flow and heat transfer of a non-Newtonian fluid in a circular microchannel". *J Heat Transfer*. Vol. 135, p. 021705.

[21] Noreen, S, Waheed S., Hussanan, A., and Lu, D., 2019, "Analytical solution for heat transfer in electroosmotic flow of a Carreau fluid in a wavy microchannel", *Appl Sci.*, Vol. 9(20), p. 4359.

[22] Liu, Y., and Jian, Y., 2019, "The effects of finite ionic sizes and wall slip on entropy generation in electroosmotic flows in a soft nanochannel". *J Heat Transfer*. Vol. 141. p. 102401.

[23] Fadaei, P., Niazmand, H., and Raoufi, M.A., 2022, "Influence of finite size of ions on thermal transport of a simultaneous electrokinetic-pressure driven flow of power-law fluids in a slit microchannel", *Colloids Surfaces A Physicochem Eng Asp.* Vol. 634, p. 127857.

[24] Dey, R., Ghonge, T., and Chakraborty, S., 2013, "Steric-effect-induced alteration of thermal transport phenomenon for mixed electroosmotic and pressure driven flows through narrow confinements", *Int J Heat Mass Transf*. Vol. 56, pp. 251–262.

[25] Horiuchi, K., and Dutta, P., 2004, "Joule heating effects in electroosmotically driven microchannel flows" *Int J Heat Mass Transf*. Vol. 47, pp. 3085–3095.

[26] Hayat, T., Saleem, N., and Ali, N., 2010, "Effect of induced magnetic field on peristaltic transport of a Carreau fluid", *Commun Nonlinear Sci Numer Simul.*, Vol. 15, pp. 2407–2423.

Conference on Modelling Fluid Flow (CMFF'22)
The 18th International Conference on Fluid Flow Technologies
Budapest, Hungary, August 30 -September 2, 2022

DESIGN RECOMMENDATIONS FOR WASTEWATER PUMPING STATIONS – RESULTS FROM MODEL TESTS

Tim NITZSCHE[1], Julija PETER[2], Sebastian HAUEISEN[3], Paul Uwe THAMSEN[4]

[1] Corresponding Author. Chair of Fluid System Dynamics, Faculty of Mechanical Engineering and Transport Systems, Technische Universität Berlin. Straße des 17. Juni 135, 10623 Berlin, Germany. E-mail: tim.nitzsche@tu-berlin.de
[2] Chair of Fluid System Dynamics, Faculty of Mechanical Engineering and Transport Systems, Technische Universität Berlin. Straße des 17. Juni 135, 10623 Berlin, Germany. E-mail: julija.peter@tu-berlin.de
[3] Chair of Fluid System Dynamics, Faculty of Mechanical Engineering and Transport Systems, Technische Universität Berlin. Straße des 17. Juni 135, 10623 Berlin, Germany. E-mail: sebastian.haueisen@tu-berlin.de
[4] Chair of Fluid System Dynamics, Faculty of Mechanical Engineering and Transport Systems, Technische Universität Berlin. Straße des 17. Juni 135, 10623 Berlin, Germany. E-mail: paul-uwe.thamsen@tu-berlin.de

ABSTRACT

Pumping stations are essential components in wastewater systems. At these nodes, wastewater from the sewer network is collected and conveyed, for example to the downstream wastewater treatment plant. Due to this key position in the wastewater system, the trouble-free operation of these pumping stations is of utmost importance.

Since wastewater is generally a very inhomogeneous media, which carries a variety of solids (sand, gravel, wet wipes, etc.), these interfering substances result in a variety of negative effects on the operation of wastewater systems. The main challenges in designing pumping stations result from: air entrance, sedimentation, swimming layers and clogging of pumps.

The presented paper deals with recommendations for designing pumping stations regarding sedimentation based on investigations in downscaled models and their transfer to original systems. The studies focus on geometrical design criteria: the overall shape of the pit, the inlet, the sloped walls, the sump, etc.

physical model, pumping station, sedimentation, sump, wastewater,

NOMENCLATURE

A	$[m^2]$	area
D	$[m]$	characteristic length (e.g. diameter)
F	$[kgm/s^2]$	force
Fr	[-]	Froude Number
g	$[m/s^2]$	gravitational acceleration
L	$[m]$	Lenght
M	[-]	Scale
Q	$[m^3/s]$	flow rate
Re	[-]	Reynolds number
T	$[s]$	time
v	$[m/s]$	velocity
We	[-]	Weber number
ν	$[m^2/s]$	kinematic viscosity
ρ	$[kg/m^3]$	density
σ	$[N/m]$	surface tension

Subscripts and Superscripts

O	original
M	model

1. INTRODUCTION

Industrial and municipal wastewater is collected in the sewage system and conveyed further to the treatment plants. Pumping stations are an integral part of these complex systems.

To prevent wastewater overflow and the associated environmental pollution, disruptions must be prevented along the entire transport chain.

A variety of challenges such as sedimentation, air entrainment [1] and swimming layers [2] may occur in wastewater pumping stations. These compromise the safe and reliable operation and thus result in increased maintenance costs. The susceptibility to these issues may be influenced by a suitable design of the entire pumping station (shape of the pit, inlet, wall geometry, etc.) as well as the choice of the used pumps.

1.1. Wastewater Pumping Stations

Wastewater pumping stations differ in size and design. The location and the type of machines influence the design parameters of pumping stations. For example, the requirements for pumping stations

in rural areas differ from those in urban areas in terms of the composition of wastewater and its capacity. Two types of machines are commonly used in pumping stations: dry-installed pumps are housed in an additional machine room as shown in Fig. 1a), whereas wet-installed pumps are embedded in the suction chamber as shown in Fig.1b) and are surrounded by wastewater. Dry-installed designs may result in higher construction costs, however, the pumps are easier to access when required [3].

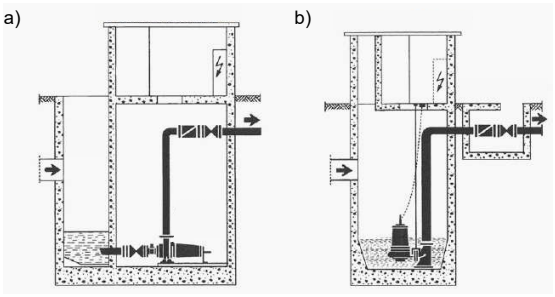

Figure 1. Sectional view of a suction chamber with a) dry-installed, b) wet-installed pumps after [3]

Even though wastewater pumps are essential components in the design and operation of wastewater pumping stations, the following investigations focus on structural investigations, especially the suction chambers of the pumping stations. The interaction between pump and wastewater is restricted to pump positions and volumetric flows. For a more detailed interaction, reference can be made to the following studies [1, 4]

This paper aims to present research approaches for designing wet pit pumping stations regarding sedimentation based on investigations in downscaled models and their transfer to original systems. The studies focus on geometrical design criteria: the overall shape of the pit, the inlet, the sloped walls and flushing routines.

More detailed studies on the problem of air entrainment were presented in [1].

1.2. Physical Model Studies

Detailed, preliminary investigations are necessary for the design of complex hydrodynamic systems to guarantee the desired functionality in the subsequent operation. A physical model investigation is a tool for analysing the correlations of design parameters. This tool enables the validation of cost-intensive issues in advance and verification of potential modifications. In the field of wastewater pumping systems, model investigations are useful for non-standard designs. These can be prototypes for novel designs or modifications for existing structures due to changed operation conditions.

2. METHOD

2.1. Dimensioning

To be able to carry out meaningful model investigations of scaled, hydraulic structures, compliance with relevant similarity laws is of utmost importance.

The geometric similarity between the model and the original must be maintained, which means that dimensions between the two investigated systems must be in a defined relationship to each other [5].

$$M = \frac{L_M}{L_O} = const. \tag{1}$$

Furthermore, the dynamic similarity must be ensured, which brings forces acting on the respective fluid of the model and the original into a defined relationship. For the design of hydraulic models with open surfaces, the Froude number Fr, which is a ratio of inertial force to gravitational force, can be used [5, 6].

$$Fr = \frac{v}{\sqrt{g \cdot D}} \tag{2}$$

To ensure Froude similarity between the model and the original, the respective Froude numbers must be identical [5, 6].

$$\frac{Fr_M}{Fr_G} = 1 \tag{3}$$

When designing the model, further attention must be paid to selecting a design range in which viscous and surface tension effects are negligible. These effects can be estimated using the Reynolds number Re and Weber number We. The Reynolds number takes inertial and frictional forces into account [7].

$$Re = \frac{v \cdot D}{\upsilon} \tag{4}$$

The Weber number accounts for inertial forces and surface tension forces.

$$We = \frac{v^2 \cdot D \cdot \rho}{\sigma} \tag{5}$$

According to [7, 8], the Reynolds number is recommended to be at least above $Re > 3 \times 10^4$. The Weber number We should be higher than $We > 120$. For both values, an additional safety factor of 2 is advised.

By maintaining dynamic similarity in two geometrically similar systems, the kinematic similarity is also achieved, which puts velocities and accelerations in the two systems in proportion.

If the Froude similarity adheres, various scaling rules can be applied when scaling the geometry linearly, which are listed in Table 1.

Table 1. Froude similarity scaling rules [6]

Parameter	Conversion
Lengths	$L_O/L_M = M$
Areas	$A_O/A_M = M^2$
Velocities	$v_O/v_M = M^{1/2}$
Times	$T_O/T_M = M^{1/2}$
Flow rates	$Q_O/Q_M = M^{5/2}$
Forces	$F_O/F_M = M^3$

2.2. Sediments

Wastewater is very diverse in its composition. In mixed sewer systems, not only water but suspended particles as well as dissolved components can be found [9]. For investigations in sedimentation of wastewater in suction chambers, it is necessary to reflect a spectrum of sedimentable particles in the wastewater.

Depending on the type and size of the particles expected to be introduced in the original, appropriate plastic particles with selected characteristics are used. For the investigation described in this paper, the following particles were selected.

Table 2. Overview of Particle Properties

Colour	Density
red	1090 kg/m^3
black	1690 kg/m^3

The red particles were chosen to represent light, fine particles. They are only slightly heavier than water and are easily activated by the flow. The black particles represent much heavier particles such as sand or stone. Fig. 2 shows the exemplary distribution of the particles used.

Figure 2. Exemplary particle distribution around a suction pipe inlet

In comparisons of actual conditions in the original structures and modelled conditions, deposits of sedimentation could be reproduced very well with the help of synthetic particles.

2.3. model tests on large pumping stations

The models test rigs were developed as a representation of existing suction chambers, which included both dry-installed and wet-installed pumps. Furthermore, systems with basins in rectangular, round and oval shapes were simulated. After reproducing the flow conditions, optimization approaches were formulated and implemented.

A rectangular model that is shown in Fig. 3 was selected to show exemplary results and recommendations for this case.

Figure 3. Test rig with the rectangular suction chamber

For the evaluation of the individual tests, schematic diagrams were created, which show the test setup and document the sediment deposits according to their colour marking as shown in Fig. 4. Pumps 1 to 6 are labelled as P1 to P6. Similarly, inlets 1 and 2 are marked as I1 and I2 and the flush pipe as F1.

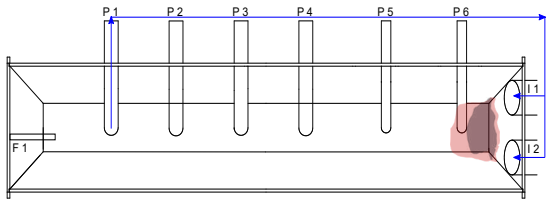

Figure 4. Schematic illustrated model test rig

All parts of the chamber and the suction pipes are made from transparent PMMA parts. This setup allows sedimentation to be viewed throughout the entire suction chamber. Table 3 gives an overview of the main model dimensions. The test rig was built as a closed system, so outgoing flow is equal to the incoming flow.

Table 3. Model Dimension

Parameter	Value
Scale	1:6.3
Length	3.8 *m*
Width	0.8 *m*
Volume	3.5 m^3
Number of Pumps	4 to 6
flow rate (model)	3.7-14.7 m^3/h
flow rate (original)	360-1440 m^3/h

3. RESULTS

3.1. angle of sloped walls

Wastewater contains various solids of different densities. To avoid deposits on the walls and to transport the solids to the suction pipes or pump inlets, the walls of the sump are designed at a defined angle. The sloping angles of 45° to 60° recommended in the literature [7] were proven in preliminary studies by the Chair of Fluid System Dynamics. In these, the sloping angle was determined for various solids that may be present in the wastewater. The investigated solids (stones, plastic, gauze bandage, paper tissue, gravel and sand) were positioned on a coated plate, which was angled until the component slid. Fig. 5 shows the sloping angles for different solids combined with various coatings. It could be shown, that an angle of 45 ° is usually sufficient to realize a sliding of sediments. However, the influence of the flow was not taken into account here.

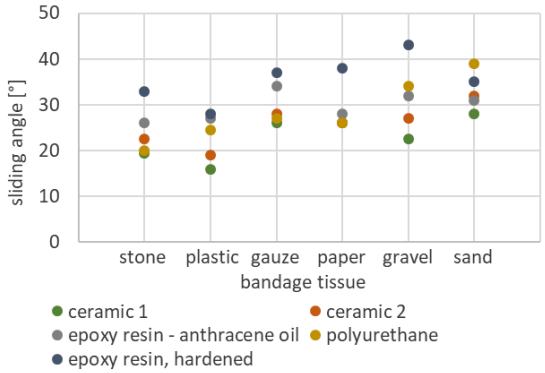

Figure 5. Test results for minimum sloping angles

Investigations of modelled suction chambers have often shown a shortfall of the recommended minimum angle. Increased sedimentation deposits occurred on these walls as shown in Fig. 6. Sedimentation on walls is significantly reduced by using angles of 45° to 60°.

Figure 6. Sedimentation deposits on sloped walls

3.2. design on basin bottom

The ability of suction pipes or wet-installed pumps to remove deposited sediments within a radius is limited. As an optimisation approach, intake manifolds can be installed to increase the operating radius. Furthermore, special attention must be paid to the surrounding sloped wall geometry and other built-in structures in the suction chamber. Requirements to avoid sedimentation are among other things the reduction of bottom surfaces, providing sloped walls with an angle of at least 45° as mentioned in 3.1. or an increase of the local velocity to transport particles to the operation areas of the suction pipes.

One significant obstacle of the presented model test is the marginal average velocity in the suction chamber combined with slope angles less than 45° and extended bottom surfaces. As a result, a high amount of sedimentation accumulates immediately under the inlets I1 and I2 as shown in Fig. 7. In the shown case pump number 6 was running and directly connected to the inlet. Incoming particles accumulated outside the operating radius of the suction pipe and could not be removed.

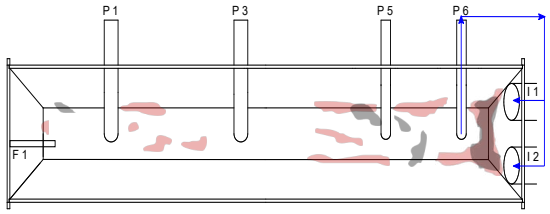

Figure 7. Particle distribution with initial suction chamber setup

Fig. 8 shows how to handle this amount of sedimentation with several combined modifications to the suction pipe design and built-in structures. In this context, the increase of the sloping wall angles up to 60° reduced the surfaces with low angles to minimize the areas of sedimentation. On the other hand, the decrease in bottom clearance increases the local velocity to move sedimentations. Filling up the edges with curved structures reduced the areas of sedimentation once again. Finally, the use of a weir prevents the particles from being scattered in the suction chamber and ensures that the deposits are collected under the suction pipe of pump 6.

The effect of this combined modification is a significantly reduced amount of sedimentation under the inlets with a focus directly under the suction pipe of a sewer pump.

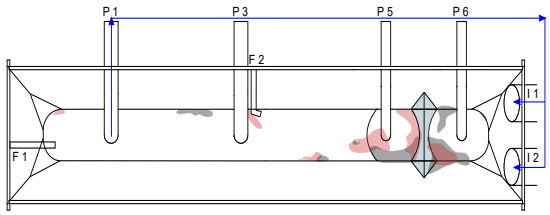

Figure 8. Suction chamber with combined design approaches

3.3. inlets direction and position

The direction and position of the inlet strongly influence the location of sedimentation areas on the bottom of the pit. In rectangular sumps, the inflow is usually carried out on the short side orthogonal to the wall. The height of the inlet combined with the water level strongly influences the movement of the sediments. While at high levels the particles deposit mostly near the inlet (Fig. 7), at lower levels a greater circulation of the flow at the bottom exists and thus a better distribution of solids is observed.

Fig. 9 shows the water level dependency that was observed in the tests. In both tests, pump 1 is used with a flow rate of 14.7 m^3/h. In Fig. 9a, the water level is 0.96 m, more than 0.5 m above the inlets. In Fig. 9b, the water level is at a height of 0.1 m, just below the inlets.

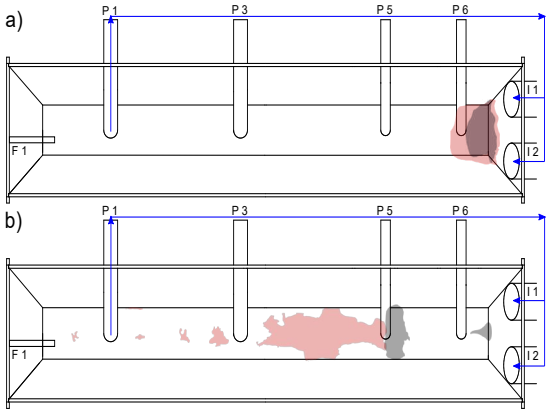

Figure 9. Particle distribution depending on a) high b) low water level

A round or oval-shaped pit offers further possibilities for the inlet design, for example, a tangential inlet offers advantages regarding sedimentation as well as reduced air entrainment and swimming layers [1, 10]. With a suitably designed wall geometry, sediments are guided reliably into the center of the pit and thus to pump sumps due to the pressure distribution in curved structures. (Fig. 10).

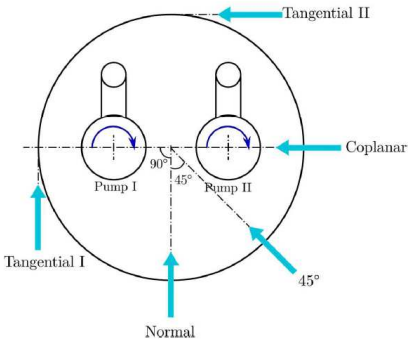

Figure 10. Variations in inlet designs in round wet pits [1]

When designing the inlet necessary minimum levels must be considered regarding air intake. This depends on the machines used as well as the inlet volume flow and the distance between the inlet pipe and the water level.

3.4. Flushing

As part of the design process, some compromises may have to be made due to the constraints of the structure. The reasons can be diverse. If sedimentation areas are not preventable the implementation of flushing can be suitable to remove accumulated sedimentations.

A flushing sequence can include some of the steps:

- stop normal operation,
- close valves to stop the incoming flow,
- adjust sewage level to a low value,

- operate a flushing pipe for a certain time,
- reduce the water level to the absolute minimum,
- open valves for incoming flow and
- start normal operation.

Flushing pipes are installed in the suction chamber and operate with one of the sewage pumps. The open diameter of the flushing pipe should provide a free jet with high velocity. Influencing test factors for flushing sequences were the position of the flushing pipe, velocity and angle of the water jet, duration of the flushing operation and water level in the suction chamber, whereas the position of the flushing pipe is especially important.

In this model test velocities up to 6 m/s were successfully investigated. Also, the combination of several flushing pipes in one suction chamber to increase the flushing effect was examined.

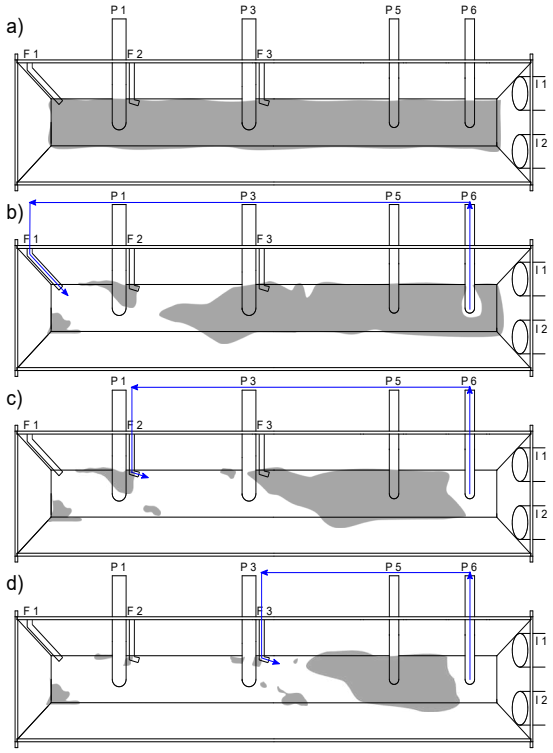

Figure 11. Removing sedimentation of the suction chamber with a flushing sequence

In the model test, shown in figure Fig. 11, a worst-case scenario was examined. The entire suction chamber bottom was covered with particles of high density. During the flush sequence flushing pipes 1 to 3 operate in sequence one at a time as illustrated in Fig. 11a)-d). Each pipe was running for 4 minutes. The result of the flush sequence was accumulated sedimentation around the low-level wastewater pumps. The flush pipes 2 and 3 increase the scope of the flushing jet and reduce the wake space between suction pipes.

5. SUMMARY

With the help of model tests, investigations can be carried out on suction chambers with dry-installed as well as wet-installed pumps. These investigations are particularly suitable for existing structures with challenging framework conditions. With this method, design investigations can be carried out on the following design parameters, among others:

- inlets
- sloped walls
- built-in structures
- suction nozzles
- flushing sequences
- air entrainment

Overall, model tests improve the operation of the suction chamber and pump stations significantly and result in a much better operation.

REFERENCES

[1] Ackl, R. A., 2018, “Enhancing the Design of the Wet Pit Pumping Stations Based on Experimental and Numerical Investigations”, *Dissertation Technische Universität Berlin, Fakultät V Verkehrs- und Maschiensysteme*

[2] Mitchell, R. L., 2019, “Causes, Effects and Solutions of Operational Problems in Wastewater Systems Due to Nonwoven Wet Wipes”, *Dissertation Technische Universität Berlin, Fakultät V Verkehrs- und Maschiensysteme*

[3] Surek, D., 2014, *Pumpen für Abwasser- und Kläranlagen*, Springer Fachmedien Wiesbaden

[4] Pöhler, M., 2020, “Experimentelle Entwicklung eines standardisierten Abnahmeverfahrens für Abwasserpumpen”, *Dissertation Technische Universität Berlin, Fakultät V Verkehrs- und Maschiensysteme*

[5] Surek, D., Stempin, S., 2017, *Technische Strömungsmechanik*, Springer Fachmedien Wiesbaden

[6] Strobl, T., Zunic, F., 2006, *Wasserbau*, Springer Berlin Heidelberg

[7] ANSI/HI 9.8-2018, 2013, “American National Standard for Rotodynamic Pumps for Pump Intake Design”

[8] Heller, V., 2011, “Scale Effects in physical hydraulic engineering models”, *Journal of Hydraulic Research,* Vol. 49, No. 3, pp. 293-306

[9] Quevauviller, P., Van Der Becken, A., Thomas, O., 2007, *Wastewater Quality Monitoring and Treatment*, New York: Wiley

[10] Ackl, R. A., Swienty, A., Lykholt-Ustrup, F., Thamsen P. U., 2015, “Avoiding Sedimentation and Air Entrainment in Pump Sump for Wet Pit Pumping Stations”, *Proceedings of the ASME-*

JSME-KSME Joint Fluids Engineering Conference

Conference on Modelling Fluid Flow (CMFF'22)
The 18th International Conference on Fluid Flow Technologies
Budapest, Hungary, August 30 -September 2, 2022

INITIATION OF BIFURCATION ANEURYSMS: A PILOT STUDY

Péter FRIEDRICH[1], Benjamin CSIPPA[2], György PAÁL[3], István SZIKORA

[1] Corresponding Author. Department of Hydrodynamic Systems, Faculty of Mechanical Engineering, Budapest University of Technology and Economics. Műegyetem rkp 3., H-1111 Budapest, Hungary. Tel.: +36 1 463 1680, E-mail: Friedrich.peti@gmail.com
[2] Department of Hydrodynamic Systems, Faculty of Mechanical Engineering, Budapest University of Technology and Economics. E-mail: bcsippa@hds.bme.hu
[3] Department of Hydrodynamic Systems, Faculty of Mechanical Engineering, Budapest University of Technology and Economics. E-mail: gypaal@hds.bme.hu
4 Department of Neurointerventions, National Institute of Mental Health, Neurology and Neurosurgery. E-mail: h13424szi@ella.hu

ABSTRACT

Intracranial aneurysms are saccular lesions forming on the vessel wall of brain arteries. The most common type is the bifurcation aneurysm located at the sites of arterial junctions. The exact cause of the disease is not yet understood as it involves a complex cascade of physical and biochemical processes. According to the current hypothesis the hemodynamic fluid forces due to wall-shear stresses initiate a biochemical process in the innermost layer of the vessel, the endothelium. In this study our objective was to analyse the flow field near the vessel wall before the aneurysm inception. Five bifurcation aneurysms and five control cases were selected for numerical comparison. The aneurysms were removed virtually by an objective interpolation method to reconstruct the vessel shape before the emergence of the aneurysm. For each geometry a time-varying inlet velocity-profile with outlet flow rates according to Murray's law were set case-specifically. Velocity vectors were decomposed to axial and secondary - radial and circumferential - components and evaluated throughout a centreline originating from one outlet to the accompanying outlet of the bifurcation. Inherently, secondary flow features emerge at a vessel bifurcation in all cases. However, in the cases of aneurysmal geometries, elevated secondary flow activities were found.

Keywords: Aneurysm, Bifurcation, CFD, Digital reconstruction, IA-initiation, Murray's law

NOMENCLATURE

$\underline{Fr}$	[-]	frenet unit vector
$\underline{r}$	[-]	vector
p	[-]	arbitrary point in plane
r_c	[-]	centreline point in plane
$\underline{v}$	[m/s]	absolute velocity vector

Subscripts and Superscripts

n, b, t	normal, binormal, tangent components of the Frenet system
ax	axial velocity
sec	secondary velocity
rad	radial component
circ	circumferential velocity
x, y, z	axes
$-$	temporal mean

1. INTRODUCTION

Aneurysms are a dangerous medical condition on the arteries of the human body. They come in two distinct shapes. The first one is barrel like called fusiform and usually form on the aorta, the other ones are the saccular berry-shaped aneurysms. They mostly manifest themselves on arteries inside the brain, either on the side of an artery or at a junction of arteries, called bifurcations as it can be seen on Figure 1 in pink. Regardless of the form of the aneurysm their danger lies in the fact that they do not carry specific symptoms and can be lethal. The most common way for an aneurysm to cause problem is a rapture. A rupture can occur due to weakened walls Ruptures can also be caused by external factors such as getting the head hit. Risk of aneurysm formation increases with age, but high blood pressure and genetics also play a role. [1]

Modern medical techniques allow the treatment of aneurysm with minimally invasive methods. The affected area is reached through the arteries by a micro catheter. A flow diverter stent is placed at the opening of the aneurysm to stabilize the vessel wall and to restrict blood flow in to the aneurysm sack, causing the blood inside the sack to coagulate.

The exact cause and pathophysiology of the disease is not yet understood as it involves complex physical and biomechanical processes. According to the current hypothesis in hemodynamics the Wall

Shear Stress (WSS) caused by fluid forces on the inner layer of the vessel, the endothelium, initiate a biomechanical process resulting in the formation of an aneurysm. It is accepted that the wall shear stress field is highly sensitive to the small alterations of the surface of the 3D model. This model is made by a non-medical professional in a subjective way, thus resulting in a less robust surface. WSS is also dependent on the way of smoothing of the surface. It is accepted that the velocity field is more robust and is less dependent on small surface alternations than WSS [2][3].

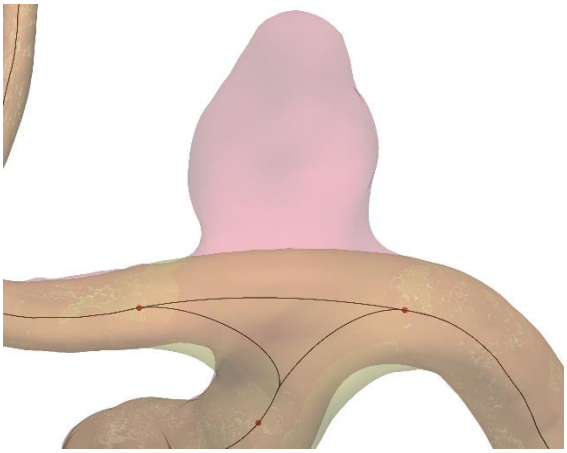

Figure 1. Bifurcation aneurysm, interpolated centrelines can be seen in black, the clipping points in red, and the reconstructed model in yellow. This is a worst-case scenario; the thickening of the bifurcation section is a rare occurrence.

In this paper the secondary velocity field is studied on 4 geometries with bifurcation aneurysms in the pre-disease state using digital reconstruction. There are also 4 control cases without aneurysms to compare the velocity fields at the bifurcation.

2. METHOD

2.1 Digital Reconstruction

Three cases out of the total 8 were provided in the form of DSA images under the National Brain Research Program of Hungary. The rest were obtained as surface models from the Aneurysk [4] database. The DSA images were captured with a GE Innova device, with the resolution of 0.22 mm.

DSA imaging is a medical imaging method using a contrast agent to show the arteries on the image. The above-mentioned cases were segmented using the program called Slicer 4.10.2, which uses a marching cubes algorithm to compute the surface, and applies a smoothing to the surface, as the algorithm generates a rough surface.

Subsequently, follows the digital reconstruction to remove the aneurysm and restoration of the parent vessel to the pre-disease state. The procedure was performed with the algorithms of Morphman [5][6], an open-source program based on the Vascular Modelling Tool Kit. The removal can be done using the bifurcation manipulation component. It was designed for the changing of angles between the outflow arteries, but by setting the angle change to zero degrees it can be used to remove a bifurcation aneurysm. The algorithm follows the same steps as those previously used in VMTK. First, computation of the centrelines and the Voronoi diagram of the model is performed. The diagram contains the radius of the maximum inscribed sphere to every point of the centreline. It is used to represent the surface around the centreline. In the next step the domain of interest is defined, either by coordinates or by using a 3D view of the model and selecting two relevant outlets of the bifurcation. Using this data, an algorithm finds the diverging points of the centrelines at the bifurcation region and cuts all 5 of the centrelines. One is going between the outlets, two from the inlet to the outlets, and two from the outlets into the aneurysm. Further back from the diverging points also marks the planes where in-between the section of the Voronoi diagram will be removed [7]. These points are called clipping points. The next step involves the interpolation of the centrelines and the Voronoi diagram, both are done by objective interpolation algorithms. In this step Morphman differs from the VMTK method optionally. In VMTK, first the centrelines are interpolated from the inlet to the outflow sides, just these two. Then the Voronoi diagram gets interpolated from the three clipping points towards each other, but only between the inlet and the outlets, and not between the two outlets across the bifurcation. In Morphman by setting the “bifurcation” option to true, it also computes an interpolated centreline between the two outlets across the bifurcation and uses up this line when interpolating the Voronoi diagram. The clipping points and the interpolated centrelines can be seen in Fig. 1. The effects of this method will be shown in the next step, surface generation. Using the interpolated Voronoi diagram, the surface of the geometry can be computed by the inscribed sphere radii. If using VMTK the bifurcation will have a notch on top of the bifurcation, because only the centrelines going from the inlet to the outlets were used for the interpolation. With Morphman, enabling the above-mentioned option, the reconstructed surface does not have this notch, and is more representative of the pre disease state of the bifurcation [8]. The last step is smoothing the surface before output.

The reconstructed models underwent additional modifications to prepare them for simulation. First the inlet and outlet profiles were extended by 8 diameters and adapted to a circular shape. This is done to ensure properly developed flow through profiles at the investigated regions [3].

2.2 Simulation

The following section will cover the Computational Fluid Dynamic (CFD) simulation, from meshing, through boundary conditions to running settings. Everything related to the above was carried out using ANSYS components. For meshing Mesher was used, and the simulations were run in CFX.

The surfaces were open at the boundaries after the reconstruction and needed to be closed. This was done using Space Claim. The cross-sectional areas of the inlets and outlets were also measured in this step for computing the boundary conditions.

The numerical mesh for the simulations were done with the same parameters. The tetrahedron cells were chosen. Ten inflation layers were used adjacent to the vessel wall with a growth factor of 1.1. The target value for skewness was set to 0.8. These resulted in meshes with around 5 million elements in size.

Transient simulations were run, with adaptive timesteps and a Courant number of 0.8. Three heartbeat cycles were simulated, each 0.8 seconds long. Only the data of the third cycle were exported for post-processing to eliminate the effect of numerical transients. The arterial walls were assumed to be rigid, and blood to be a Newtonian fluid. The last assumption may cause error, but the error of not perfect rheology is much smaller compared to one caused by the subjectivity in the segmentation process. Table 1 contains all the simulation settings.

Patient-specific boundary conditions were set to each geometry. The inlet was a velocity inlet. The velocity was calculated according to scaling law that was experimentally obtained using the area of the inlet [9]. The calculated velocity was a cross-sectional average. The heart cycle waveform that can be seen in Figure 2 [10]. was imposed on the inlet with a parabolic velocity profile. The used heart cycle profile was 0.8 seconds long.

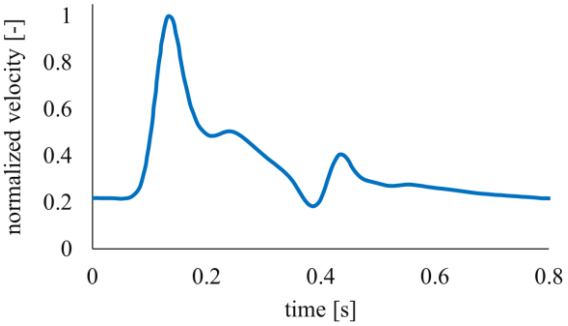

Figure 2. The normalized velocity waveform used as input for the heart-rate cycle.

Mass flow outlets were set as outlet boundary conditions according to Murray's law, except for the smallest one, which was an opening with 0Pa. Aneutools was used for computing the mass flow percentage on each outlet [11]. It was originally developed for the Internal Carotid Artery (ICA), but it was used even when the bifurcation was higher up than the ICA bifurcation, as there is no accepted method of setting boundary conditions for that section. This also means, that in these cases the whole ICA section was simulated as well.

Table 1. Parameters of the simulations

ID	Mean inlet velocity [m/s]	Reynolds-number [-]	Inlet area [mm^2]
C0035	0.2548	417.48	21.90
C0064	0.1770	233.36	14.19
C0066_c	0.1670	218.80	13.52
C0086	0.1858	252.28	15.04
C0066	0.1670	218.80	13.52
NAP191230C	0.2145	317.17	17.84
NAP200812C	0.2426	386.06	20.66
NAP200909C	0.2790	482.58	24.40

For post processing the results were exported in a format that can be used in ParaView.

2.3 Post-processing

The post-processing was done by in-house built Python scripts. In the centre of the post processing is the Frenet system, thus, having a clear understanding of these orthogonal coordinate systems is essential.

Each geometry has centrelines defined. In each point of the centreline an orthogonal coordinate system can be defined. In case of a Frenet system each of the three axes point in a specific direction. The Frenet tangent vector $\underline{Fr_t}$ is parallel to the tangent of the centreline at that point. The Frenet normal vector $\underline{Fr_n}$ is perpendicular to the Frenet tangent vector, and points towards the centre of the tangent circle of the centreline. The third axis is the Frenet binormal vector $\underline{Fr_b}$ and is perpendicular to the other two axes. All of them are unit vectors. The geometry can be sliced with a plane defined by the frenet normal and binormal vectors, creating a cross section of the artery perpendicular to the centreline. All further calculations were done in these slices along the centreline at each point.

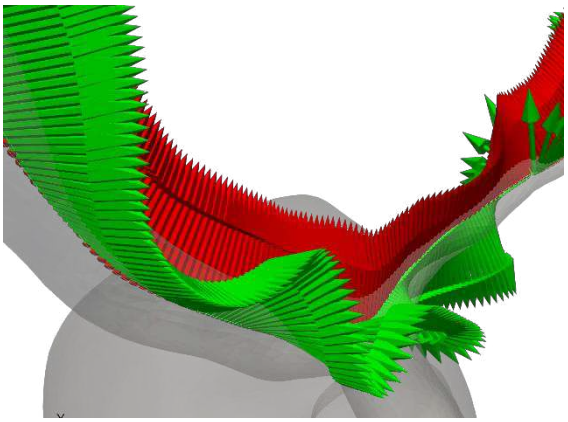

Figure 3. Effect of Frenet smoothing, green non smoothed, red smoothed

Centrelines for post-processing were calculated and smoothed with a distance of 0.15 mm between the points. An optimal smoothing factor and iterations must be used to compute a smooth, but true centreline, smoothing factor was set to 1.2 and the number of iterations to 100 [12]. Centreline smoothing helps smooth out the sudden orientation changes of the frenet systems, but it is not perfect. In this study for bifurcation aneurysms the slicing of the geometry went between the two outlets of the bifurcation. For the calculations, the Frenet systems needed to have slow orientation change along the length of the centreline. To achieve this a properly smoothed temporary centreline was computed, with the same number of points as the previous one, and then the Frenet systems were interpolated to the points of that centreline. This resulted in a Frenet system with the same orientation along the centreline as can be seen on Fig. 3.

Using the Frenet systems the velocity field in a slice can be decomposed to an axial and a secondary component. The axial component can be calculated using the Frenet tangent unit vector as seen in Eq. (1). Then by using Eq. (2) the secondary velocity vector is calculated by subtracting $\underline{v}_{ax}$ from the velocity vector $\underline{v}$.

$$\underline{v}_{ax} = (\underline{v} \cdot \underline{Fr}_t) \cdot \underline{Fr}_t \tag{1}$$

$$\underline{v}_{sec} = \underline{v} - \underline{v}_{ax} \tag{2}$$

The secondary flow can be further separated into radial and circumferential components by switching to a local polar coordinate system around the centreline point r_c in the slice. In order to decompose the secondary velocity to these components, first a radial unit vector was defined by Eq. (3) between the centreline and an arbitrary point p in the slice. Thus, the radial velocity $\underline{v}_{rad}$ can be calculated as seen in Eq. (4). The circumferential velocity $\underline{v}_{cir}$ is calculated by subtracting the radial component from the secondary velocity see in Eq. (5) [13].

$$\underline{r}_{rad} = \frac{p - r_c}{|p - r_c|} \tag{3}$$

$$\underline{v}_{rad} = (\underline{v}_{sec} \cdot \underline{r}_{rad}) \cdot \underline{r}_{rad} \tag{4}$$

$$\underline{v}_{cir} = \underline{v}_{sec} - \underline{v}_{rad} \tag{5}$$

The slices were transformed in such way, that the slices are parallel with the global X-Y plane, with the Frenet normal matching to the X axis, and the origins of the local and global systems matching. This way the slices could be divided into an inner side (IS) (inner bend) and an outer side (OS) (outer bend). The various velocity components were averaged on these half slices. Python scripts were written to perform these calculations for every slice in all the timesteps. Thus, reducing the data, and enabling the examination of the results in both space and time.

3. RESULTS

In this section visualization techniques of the data will be explained, along with the findings, based on the comparisons of the cases with the control cases.

In order to represent the velocity fields in both space and time a 3D waterfall diagram would be needed which is hard to understand. Instead, a spatio-temporal contour plot was chosen, as it allows the representation of the velocity magnitudes in a 2D form. All 4 velocity components were plotted, with the inner and outer sides separately. Along with the velocity various centreline attributes were plotted as well. These include the Inscribed Sphere Radius (ISR), torsion κ and curvature τ. With these additional data the velocity plots can be examined together with the geometry. As an example, a rise in axial velocity results in a drop in ISR. On the vertical axes of the velocity plots is time, and on the X axis is the length along the centreline. On the velocity plots both the systolic maximum velocity point and diastolic velocity minimum point of the heart cycle can be seen as horizontal lines. The systolic maximum is at 0.15 s and the diastolic minimum is at 0.4 s. The area of the aneurysm ostium (the inlet of the sack) is marked on the plots with a yellow shading. For the control cases the shaded area marks the site of the bifurcation.

After examining all 8 cases, a difference emerged between the normal and control cases. In the following section this will be shown and explained on two characteristic examples. C0064 was chosen as the control case, and C0066 as the one with an aneurysm, both came from the Aneurysk database. As the difference occurs on the outer side between the radial and circumferential components only these are shown here.

The plots for C0064 can be seen on Fig. 4. Both secondary velocity components show elevated values only at the site of the bifurcation. Their values

are similar, and span a similar area in both space and time. Also, the bifurcation can be clearly seen on the ISR plot, as at the bifurcation it increases.

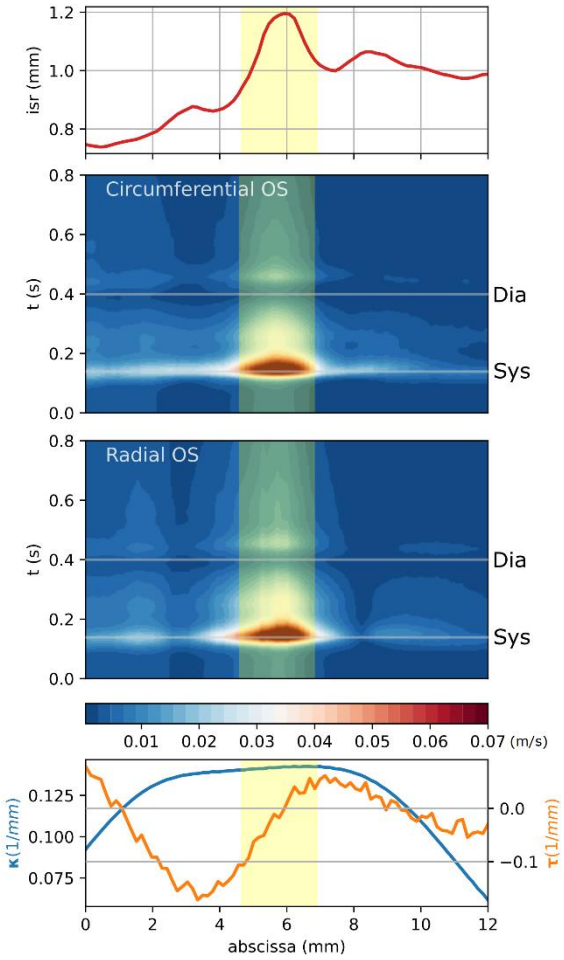

Figure 4. Plots for case C0064. Top: inscribed sphere radius along the centreline. Middle: spatio-temporal contour plots for the circumferential and radial velocity components. Bottom: curvature (blue line) and torsion (orange line) characteristics along the centreline. Yellow shading: bifurcation site

The plots for C0066 can be seen in Fig. 5. here we see a stark difference between the plots of the radial and circumferential components on the outer side. The radial velocity has an elevated zone at diastole at the site of the aneurysm, but its extent is small in both space and time, also the velocity values are not as high compared to the rest of the diagram. Looking at the circumferential diagram it is the opposite. The velocity component reaches higher values, and this elevated zone extends longer, covering a bigger area, and all of the area of the aneurysm opening. It also extends more in time, nearly till the diastolic point. Thus, creating a strong circumferential wash at the site of the aneurysm for a non-marginal part of a heart cycle. Similar plots were observed with the other reconstructed cases too.

Also, in this case the effect of the smaller artery after the bifurcation can be seen on the secondary component diagrams. The accelerating axial flow calms down the secondary components quicker than on the other side, where the diameter is larger.

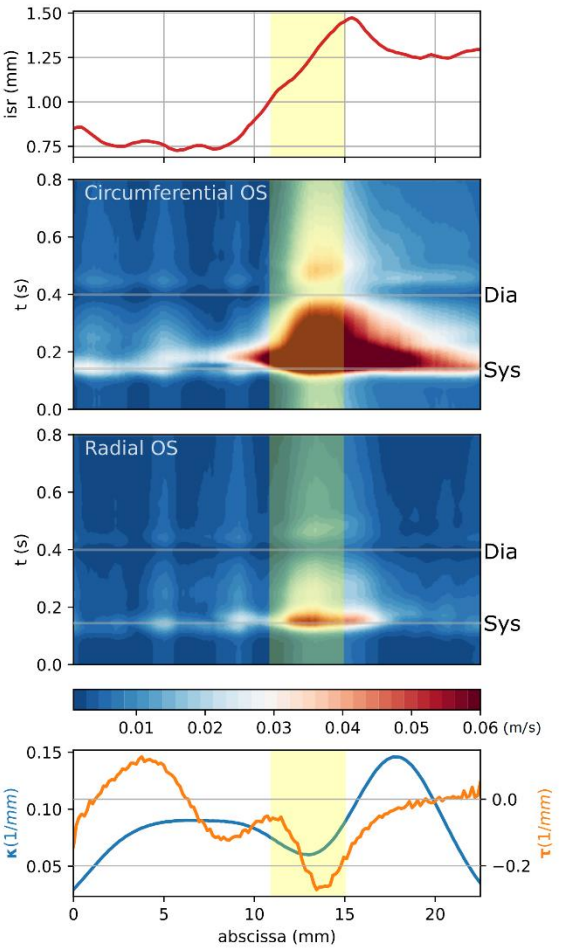

Figure 5. Plots for case C0066. Explanations are the same as in Figure 4. except for the yellow shading, here it marks the site of the aneurysm

4 CONCLUSIONS

This paper focused on the secondary flow characteristics at the site of bifurcation aneurysms. It is believed that elevated secondary flows play a key role in the formation of aneurysms, but it is a complicated biomechanical process, and it has not been fully understood yet.

Four geometries were reconstructed to their pre disease state using an objective interpolation-based method. Transient CFD simulations were run on these four cases along with four control cases. The secondary velocity field was decomposed into radial and circumferential components in a way to allow studying the results in both space and time.

After comparing the results, the secondary components differ on the outer side at the bifurcation between the control and reconstructed cases. On the control cases the radial and circumferential velocities

were comparable in strength. and the elevated velocity zone was comparable in space and time and was concentrated at the diastole time. In the case of the reconstructed geometries, the radial velocity strength was less than the circumferential component. Also, the elevated velocity zone of the circumferential component was more spread in space, but also time. This is in line with the hypothesis that the secondary flow of the blood plays a role in the formation of the aneurysm. Based on these eight cases there are definitive characteristic differences between the control and reconstructed cases, so more cases will be examined to confirm the findings of this paper.

ACKNOWLEDGEMENTS

The conference participation was supported by the Végh Gábor Neurointervention Fundation and by the Hungarian Brain Research Program under the Contract Number 2017-1.2.1-NAP2017-00002.

REFERENCES

[1] D. M. Sforza, C. M. Putman, and J. R. Cebral, "Hemodynamics of Cerebral Aneurysms," *Annual Review of Fluid Mechanics*, 2009, doi: 10.1146/annurev.fluid.40.111406.102126.

[2] B. Csippa, G. Závodszky, G. Paál, and I. Szikora, "A new hypothesis on the role of vessel topology in cerebral aneurysm initiation," *Computers in Biology and Medicine*, vol. 103, no. June, pp. 244–251, 2018, doi: 10.1016/j.compbiomed.2018.10.018.

[3] Á. Ugron and G. Paál, "On the boundary conditions of cerebral aneurysm simulations," *Periodica Polytechnica Mechanical Engineering*, vol. 58, no. 1, pp. 37–45, 2014, doi: 10.3311/PPme.7392.

[4] Aneurisk-Team, "{AneuriskWeb project website}, http://ecm2.mathcs.emory.edu/aneuriskweb." 2012. [Online]. Available: http://ecm2.mathcs.emory.edu/aneuriskweb

[5] A. W. Bergersen, H. A. Kjeldsberg, and K. Valen-Sendstad, "A framework for automated and objective modification of tubular structures: Application to the internal carotid artery," *International Journal for Numerical Methods in Biomedical Engineering*, vol. 36, no. 5, pp. 1–18, 2020, doi: 10.1002/cnm.3330.

[6] H. Kjeldsberg, A. Bergersen, and K. Valen-Sendstad, "morphMan: Automated manipulation of vascular geometries," *Journal of Open Source Software*, vol. 4, no. 35, p. 1065, 2019, doi: 10.21105/joss.01065.

[7] M. D. Ford, Y. Hoi, M. Piccinelli, L. Antiga, and D. A. Steinman, "An objective approach to digital removal of saccular aneurysms: Technique and applications," *British Journal of Radiology*, vol. 82, no. SPEC. ISSUE 1, pp. 55–61, 2009, doi: 10.1259/bjr/67593727.

[8] A. W. Bergersen, C. Chnafa, D. Gallo, M. Piccinelli, D. A. Steinman, and K. Valen-Sendstad, "Automated and objective removal of bifurcation aneurysms: Incremental improvements, and validation against healthy controls," *Journal of Biomechanics*, vol. 96, p. 109342, 2019, doi: 10.1016/j.jbiomech.2019.109342.

[9] J. R. Cebral, M. A. Castro, C. M. Putman, and N. Alperin, "Flow-area relationship in internal carotid and vertebral arteries," *Physiological Measurement*, vol. 29, no. 5, pp. 585–594, 2008, doi: 10.1088/0967-3334/29/5/005.

[10] H. G. Morales, I. Larrabide, A. J. Geers, M. L. Aguilar, and A. F. Frangi, "Newtonian and non-Newtonian blood flow in coiled cerebral aneurysms," *Journal of Biomechanics*, vol. 46, no. 13, pp. 2158–2164, 2013, doi: 10.1016/j.jbiomech.2013.06.034.

[11] C. Chnafa, O. Brina, V. M. Pereira, and D. A. Steinman, "Better Than Nothing: A Rational Approach for Minimizing the Impact of Outflow Strategy on Cerebrovascular Simulations," *American Journal of Neuroradiology*, vol. 39, no. 2, pp. 337–343, 2018, doi: 10.3174/ajnr.A5484.

[12] H. A. Kjeldsberg, A. W. Bergersen, and K. Valen-Sendstad, "Automated landmarking of bends in vascular structures: a comparative study with application to the internal carotid artery," *BioMedical Engineering Online*, vol. 20, no. 1, pp. 1–17, 2021, doi: 10.1186/s12938-021-00957-6.

[13] B. Csippa, L. Sándor, and G. Paál, "Decomposition of velocity field along a centerline curve using frenet-frames: Application to arterial blood flow simulations," *Periodica Polytechnica Mechanical Engineering*, vol. 65, no. 4, pp. 374–384, 2021, doi: 10.3311/PPME.18517.

Conference on Modelling Fluid Flow (CMFF'22)
The 18th International Conference on Fluid Flow Technologies
Budapest, Hungary, August 30 -September 2, 2022

OPTIMIZATION OF THE PRESSURE INCREASE OF AN ADAPTED PITOT PUMP FOR THE SEPARATION OF OIL-WATER MIXTURES

Jessica KÖPPLIN[1], Dominique THÉVENIN[2]

[1] Corresponding Author. Laboratory of Fluid Dynamics and Technical Flows, Otto von Guericke University Magdeburg, Universitaetsplatz 2 39106 Magdeburg, Germany. Tel.: +49 391 67-52539. Fax: +49 391 67-42840, E-mail: jessica.koepplin@ovgu.de
[2] Laboratory of Fluid Dynamics and Technical Flows, Otto von Guericke University Magdeburg. E-mail: thevenin@ovgu.de

ABSTRACT

A Pitot-tube jet-pump for separating and transporting liquids of different densities is in use in our group for cleaning oil-contaminated water. Previous simulations and experimental validation tests showed that a separation efficiency over 99% can be achieved. The separation efficiency has been experimentally confirmed for various oils, such as sunflower oil, rapeseed oil, diesel fuel, heating oil, and motor oil.

This high separation efficiency is essential; however, a sufficient pressure increase is also necessary to transport the purified water afterwards. But measures providing additional head should not induce back-mixing and decrease of the separation efficiency. A new version of the impeller with cut-off blades has been developed. The position and geometry of the blades must be optimized to increase pressure while keeping excellent separation efficiency. Experiments have been carried out for various impellers; their effect on separation efficiency and pressure head are investigated.

First success has already been obtained with a very simple design. Adapting further the blade shape, even better results are expected.

experiments, liquid-liquid separation, Pitot-tube jet-pump, radial pump

NOMENCLATURE

Latin letters

FS	[-]	flow-split
g	[m s^{-2}]	gravitational acceleration
H_{HPO}	[m]	pressure head
$\dot{m}_{inlet}$	[kg s^{-1}]	inlet mass flow rate
n	[s^{-1}]	rotational speed
p	[Pa]	static pressure

Greek letters

α	[-]	oil concentration
ρ	[kg m^{-3}]	mixture density
η	[-]	separation efficiency

Subscripts and Superscripts

CF	Coriolis mass flowmeter
HPO	high-pressure outlet
inlet	flow properties at inlet
LPO	low-pressure outlet
Sep	separation
OiW	oil in water
ppm	parts per million
rpm	revolutions per minute
PTJ	Pitot-tube jet-pump

1. MOTIVATION/BACKGROUND

Environmental efforts due to water pollution are becoming increasingly relevant for society. Disasters are becoming more frequent and oil is a growing threat to oceans and rivers [1].
In 2010 more than 800 million litres of crude oil spilled into the Gulf of Mexico caused by the *'Deepwater Horizon'* disaster. There have also been plenty of examples of oil spills in past years. E.g., the accident off Mauritius in 2020, when a tanker sank off the coast and 1,000 tons of crude oil spilled. In Norilsk (Siberia) an industrial accident occurred in which 21,000 tons of diesel oil spilled into the surrounding rivers. It was attempted to build barriers around the contaminated areas, but this takes too much time and oil was also detected behind those barriers. Alternatives, like the use of chemicals and controlled burning might have worst effects on the ecosystem than the oil itself [2,3].

Even in Germany there is a need for an innovative technical solution, to remediate water after illegal oil disposal in lakes, truck accidents polluting the surrounding rivers with their fuels, or most recently the disastrous floods in parts of Germany; oil tanks from basements that leaked, and

spilled fuel from vehicles contaminated surface water and groundwater.

No existing solution is fast, scalable, and robust enough to meet all these challenges. Our approach relies on a novel Pitot-tube Jet-Pump (PTJ) to separate multiphase mixtures based on the prevailing centrifugal forces, and transport afterward the separated, pure phases. Thanks to the simultaneous separation and pumping, high separation rates can be achieved and the purified water can be returned to the sea/watershed in the shortest possible time.

2. ADAPTED PITOT-TUBE JET-PUMP

The modified PTJ pump is an innovative solution for integrating oil-water separation and transport of the two separated phases. It has been developed at the *Laboratory of Fluid Dynamics and Technical Flows* in Magdeburg within the last years, in cooperation with an industrial partner [4–7].

The standard PTJ pump is an unconventional, single-stage radial pump. It is generally used for strongly increasing the pressure head and consists of three main elements: The rotor, the impeller and the stationary Pitot tube. Figure 1 shows a PTJ pump. Rotating components are marked in yellow, while the stationary components are red or grey. The fluid enters the casing through an impeller. It rotates in the rotor with almost the same speed as the rotor walls. The Pitot tube (red in Fig. 1) extends in radial direction from the rotation axis almost up to the inner wall of the rotor (used as a centrifuge). At this point, the liquid reaches its highest velocity and enters the Pitot tube [4].

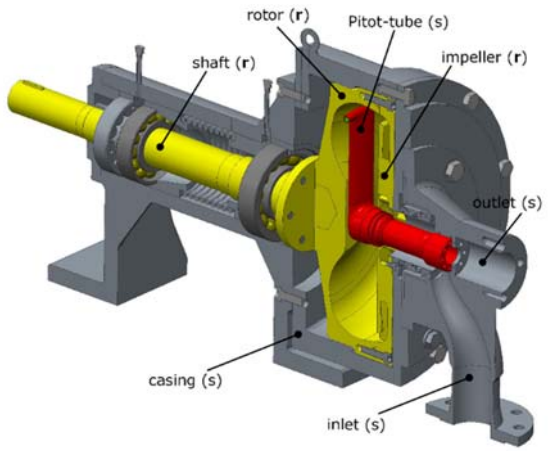

Figure 1. Standard Pitot-tube jet-pump [5].

Both, the name and principle of the whole system are based on the concept of Henri Pitot. Typically, a Pitot tube consists of a spindle-shaped metal body which is aligned in the flow direction and has a drilling on top of the Pitot tube. The drilling is connected to the surroundings. Ideally, the fluid flows parallel into the drilling. If the Pitot tube would be closed at the other end, the fluid in the tube would come to a complete standstill, allowing the measurement of total pressure. However, in a PTJ pump, the Pitot tube is not a (closed) measuring probe but an open diffuser. It is therefore connected to the high-pressure outlet and is typically constructed with a constant cross-sectional extension, though better designs are possible. Within the Pitot tube, the high kinetic energy of the fluid inside the rotor is converted into useable pressure energy. In that sense, the Pitot tube takes the same role as a volute casing in a classical centrifugal pump. The PTJ pump is widely used, in particular as a cleaning system in the food industry, for paper production and petrochemicals, but also for high-pressure water injection in gas turbines [6]. The main advantages of the PTJ pump are on one hand its simple and robust design and on the other hand the operating point, which is at low specific speeds. This means that very high pressures can be achieved at low mass flows.

Figure 2 shows a PTJ pump modified for separating fluid-fluid mixtures. As in the standard PTJ pump also the modified Pitot tube is stationary while the rotor rotates around the pitot tube. There is now an inlet and two separate outlets. The entering liquid, for instance an oil-in-water (OiW) emulsion, again experiences centrifugal forces within the rotor, working as a centrifuge. The heavier phase (water) is pressed toward the rotor walls, while the lighter phase (oil) gathers in the core close to the rotation axis. Hence, the water exits through the Pitot tube and experiences there a pressure increase before exiting through the high-pressure outlet (HPO), while the oil leaves the rotor through the low-pressure outlet (LPO).

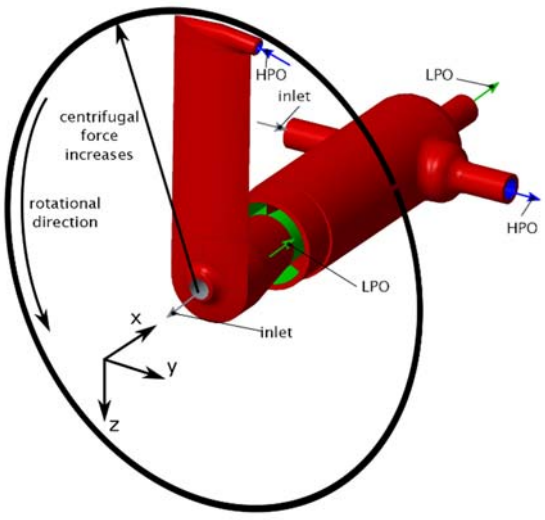

Figure 2. Modified Pitot-tube for separating liquids of different densities [5].

The central objective of the separation system is to obtain water with a high purity at the HPO. Four parameters define the operating conditions:

- rotational speed n
- inlet mass flow rate $\dot{m}_{inlet}$
- oil concentration α_{inlet}
- flow-split FS.

The rotational speed n and the inlet mass flow rate $\dot{m}_{inlet}$ are standard quantities for any turbomachine. The flow-split FS is specific to the PTJ pump and describes the ratio between the mass flow-rate at the outlets and at the inlet

$$FS = \frac{\dot{m}_{LPO}}{\dot{m}_{inlet}} = 1 - \frac{\dot{m}_{HPO}}{\dot{m}_{inlet}} \quad (1)$$

This non-dimensional quantity varies between 0 (all of the entering fluid leaves through the HPO) and 1 or 100% (all of the entering fluid leaves through the LPO). The value of FS is controlled during operation by a throttle valve.

Two parameters measure the resulting efficiency of the PTJ pump. The first parameter is the separation efficiency:

$$\eta_{Sep} = 1 - \frac{\alpha_{HPO}}{\alpha_{inlet}} \quad (2)$$

The separation efficiency is the ratio between the oil concentration at the HPO α_{HPO} and the oil concentration at the inlet α_{inlet}. If $\eta_{Sep} = 1$, pure water is found at the HPO. If $\eta_{Sep} = 0$, the oil content at the HPO is equal to the initial oil content at the inlet, and no separation occurs.

The second parameter is the pressure head at HPO, a standard quantity for turbomachines:

$$H_{HPO} = \frac{p_{HPO} - p_{inlet}}{\rho_{HPO} \cdot g} + \frac{v_{HPO}^2 - v_{inlet}^2}{2g} \quad (3)$$

It is possible to achieve a high separation efficiency η_{Sep} of the pumped water at HPO using the PTJ pump, as demonstrated by preliminary experiments. The corresponding experimental procedure is explained in the next section.

3. EXPERIMENTAL SETUP

The schematic setup is shown in Figure 3. The central component of the setup is the separation pump, shown with concentric yellow/blue circles. The water and oil for the experiments are stored in separate tanks. A pipe system connects the tanks to the rest of the system. The fine-adjustment valves are used to control the appropriate mass flows so that the oil content of the mixture can be set. The mass flows, as well as the temperatures and densities of oil and water, are measured at the Coriolis mass flowmeters (CF). The measured values are displayed directly on the CF, but also displayed and stored in the connected *Diadem* software. Check valves between the CF and the T-piece prevent communicating tubes which, amplified by the buoyancy of the oil, cause undesired mixing of the liquids during standstill. Before the mixture flows into the centrifuge, the reference pressure is measured.

Inside the centrifuge, the mixture is separated and due to the PTJ structure, the separated fluids flow from two separate outlets. The water is forced to the outer edge of the centrifuge due to centrifugal forces, where it is then removed at the head of the Pitot tube and pumped out of the centrifuge. A pressure gauge and a Coriolis gauge are attached to the HPO; thus, the pressure difference and the achieved pressure build-up can be determined. Mass flow, density and temperature are measured again via the CF. Based on the mass balance of density at the oil inlet, water inlet and at the high-pressure outlet, the residual oil concentration at the HPO can be determined. The oil flows out of the low-pressure outlet; the pressure is also measured there and the pressure build-up is calculated. However, no significant pressure build-up is expected at the low-pressure outlet, close to the rotation axis. Valves for fine adjustment of the mass flow can be found at both the HPO and the LPO. This allows to control the ratio of the mass flow rate between the two outlets, FS. These valves and adjustment possibilities are very important in order to adjust the operating parameters and to determine its influence on the objectives.

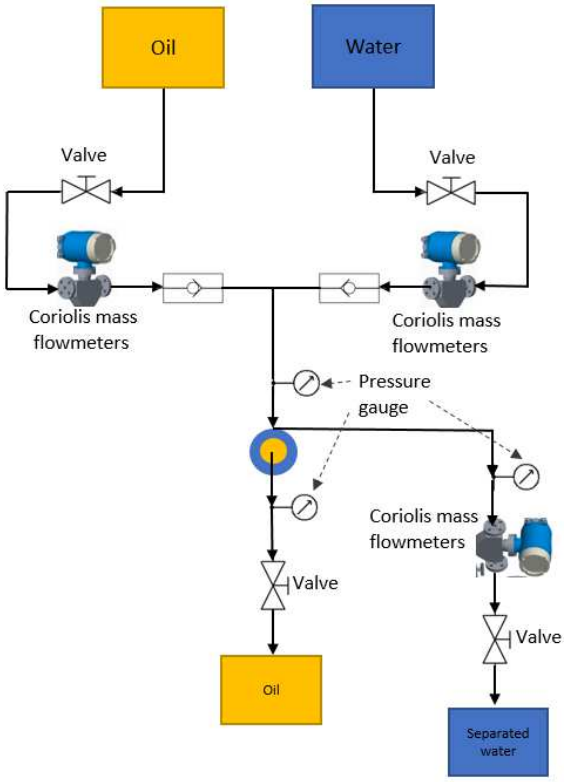

Figure 3. Schematic setup of the pilot plant

Figure 4 shows a section of the Pitot-Tube Jet-pump test rig during operation at the laboratory. The transparent rotor rotates while the pitot tube is

stationary. It can be clearly seen here that an interface is formed during operation; the two immiscible fluids are reliably separated in the rotor. The operating point in the figure was set so that a separation efficiency above 99% at the high-pressure outlet (HPO) was achieved.

The *Diadem* software is used for data storage and evaluation of the recorded measurement data from the pressure and CF gauges. Not only could a separation efficiency of over 0.99 be detected here, but the collection tanks also show a clear separation of the water from the oil. Figure 5 shows the two collection tanks during operation. The left tank collects the purified water (high-pressure outlet), while the right tank collects the oil from the low-pressure outlet (LPO).

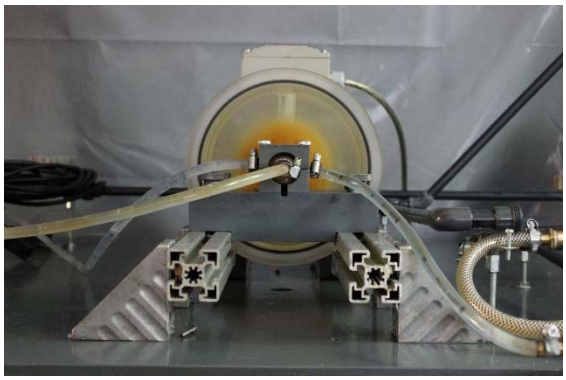

Figure 4. Centrifuge during operation

Figure 5. Containers after separating oil and water

4. EXPERIMENTAL RESULTS

For an efficient operation the separation efficiency and the pressure head need to be maximized simultaneously. These two parameters quantify the main objectives of the PTJ pump, as explained in Section 2. The next experiments investigate the influence of various operating parameters on the objectives. The purpose of these tests is to increase the pressure head while keeping the separation efficiency at a high level. This pressure build-up is necessary to allow the separation pump to function as a pump and not only as a simple separator – like a centrifuge.

The first correlation to be analyzed is the effect of the mass flow on the pressure head and the separation quality (Figs. 6 and 7). With an increasing mass flow at the inlet a decrease in pressure head and separation quality can be seen. The drop in head H_{HPO} with increasing mass flow $\dot{m}_{inlet}$ corresponds to a typical pump characteristic. The decreasing separation efficiency η_{Sep} with increasing mass flow $\dot{m}_{inlet}$ is easily explained by the decreased residence time within the rotor. A lower residence time means less time for the separation processes and thus a higher residual oil concentration at the HPO.

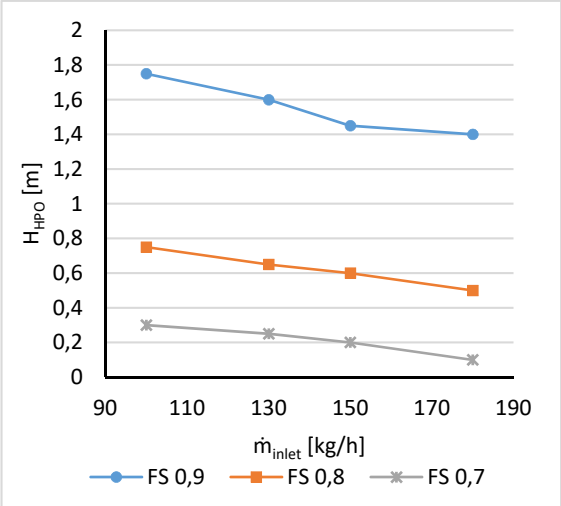

Figure 6. Pressure head H_{HPO} as a function of the mass flow $\dot{m}_{inlet}$

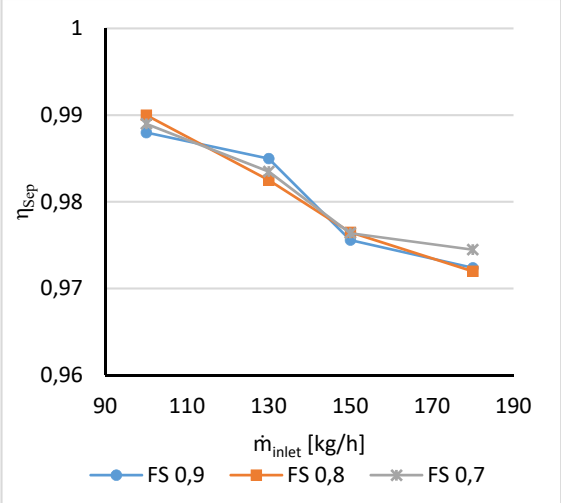

Figure 7. Separation efficiency η_{Sep} as a function of the entering mass flow $\dot{m}_{inlet}$

As already implied in the previous diagram it can be seen that the head H_{HPO} increases with an increasing speed n. This happens due to the higher kinetic energy of the fluid at higher tangential speeds

and it corresponds to the typical behavior of centrifugal pumps according to the affinity laws (Fig. 8).

However, as the rotation speed n increases, the separation efficiency η_{Sep} decreases (Fig. 9). This behavior is explained due to the higher shear forces and the resulting smaller droplet size, leading to lower sedimentation velocities and hindering separation.

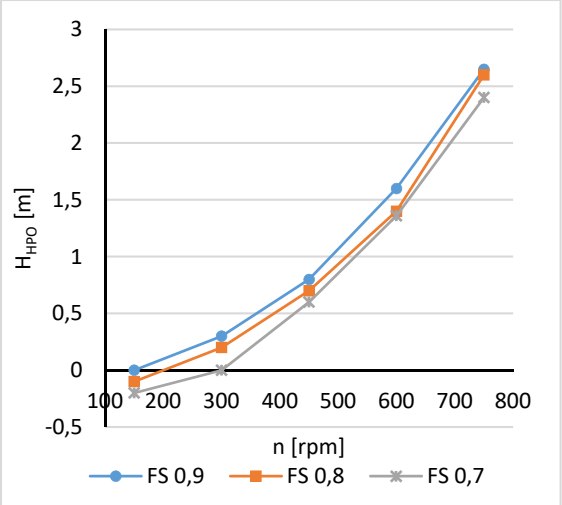

Figure 8. Pressure head H_{HPO} as a function of the rotational speed n

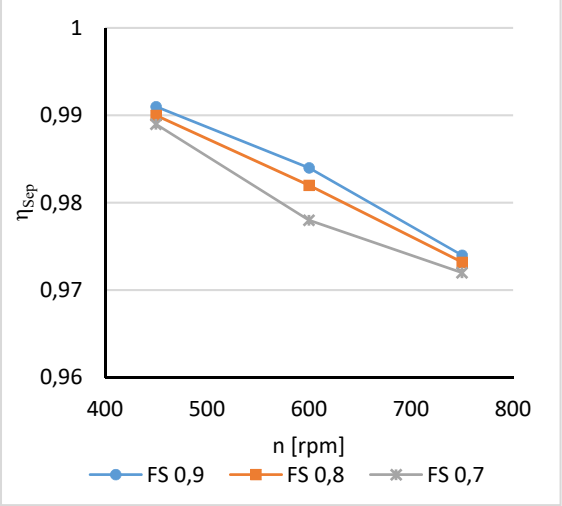

Figure 9. Separation efficiency η_{Sep} as a function of the rotational speed n

The operating parameter *oil concentration at inlet* α_{inlet} does not directly affect the objectives. The head H_{HPO} is not influenced by an increasing oil fraction as long as the mass flow $\dot{m}_{inlet}$ remains constant. The separation quality η_{Sep} is only affected if the oil concentration at the inlet α_{inlet} exceeds a certain value. If the oil core in the centrifuge becomes too large, the oil is discharged at the high-pressure outlet, which leads to an increasing oil concentration at the outlet, and to a decreasing separation quality η_{Sep}. However, if the oil content remains below a certain threshold, then there is no influence on the separation quality.

Previous studies have shown that a positive correlation exists between the flow-split FS and the separation efficiency η_{Sep}. As can be seen in Figure 10, separation efficiencies over 0.9 can only be achieved for a flow-split above 0.6. This correlation is relevant, since the negative effects of mass flow, oil concentration, or rotational speed can often be compensated by a higher flow split. This allows the separation efficiency to remain above 0.99 while the rotational speed is increased in order to achieve an increase in pressure head.

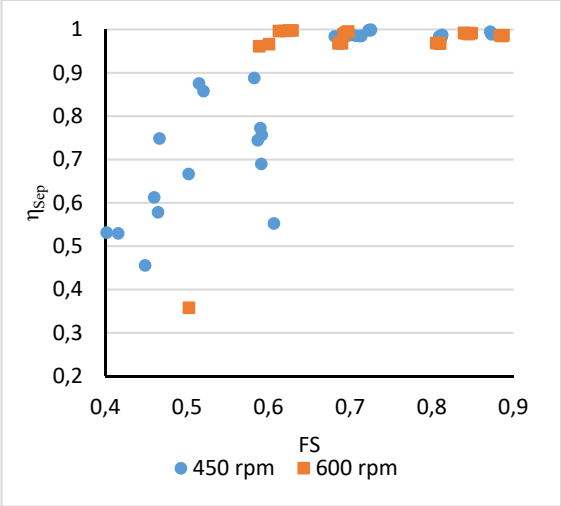

Figure 10. Separation efficiency η_{Sep} as a function of the flow-split FS

5. GEOMETRY OPTIMIZATION

In order to be able to use and operate the pump effectively, it is important to optimize the pressure head as well as the separation quality. In the tests performed so far, the influence of the boundary conditions on the separation pump have been determined and adjusted so that the separation quality is maximized.

Although an increase in pressure can be achieved by varying the operating parameters, this also has a significant effect on the separation efficiency. Furthermore, the pressure head alone is not sufficient to guarantee an efficient operation. Therefore, the geometry of the cover plate will be modified in the next steps. The blade geometry must be optimized to increase the pressure head without affecting the separation efficiency.

Figure 11 shows the reference model of the cover plate, without any blades. The preliminary tests were performed with this geometry.

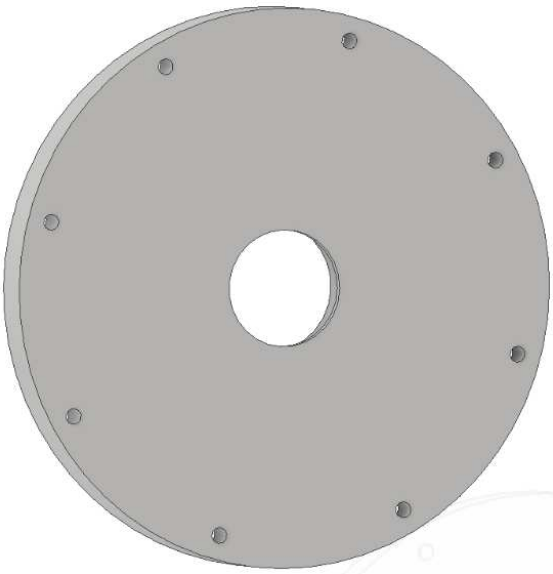

Figure 11: V0 Reference geometry

By using this geometry, a maximum pressure head of 2.5 m was achieved. The separation efficiency is constant at 0.99 (the measurement uncertainty of our system). This represents the initial situation. The pressure head is now to be maximized while maintaining the separation efficiency.

As a first variant, a cover plate was constructed in which four blades were attached. During operation, the blades rotate both in the oil and in the water phase. Figure 12 shows this blade geometry.

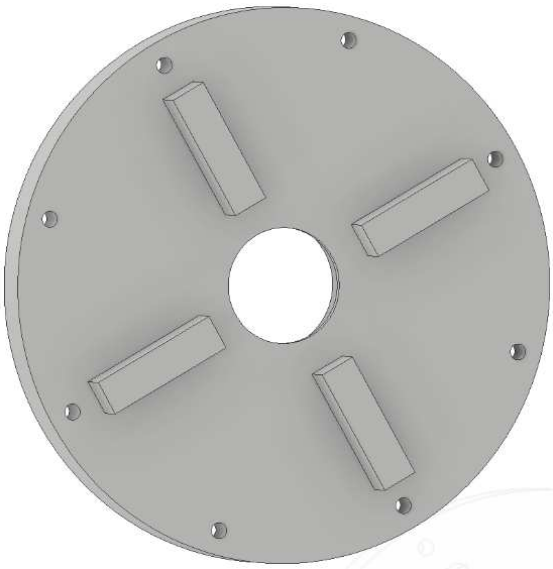

Figure 12: V01 Geometry

Although an increase of the pressure head to 4.2 m was achieved with V01, the separation efficiency decreased to 0.93. Hence, this geometry is not suitable. Due to the blades rotating in both phases, a strong back-mixing of the two phases is observed.

The next geometry variation is shown in Fig. 13.

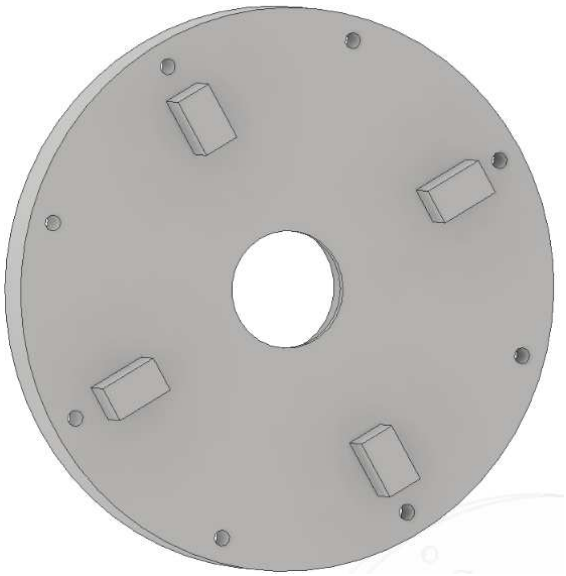

Figure 13: V02 Geometry

For the second variant, a blade cover was designed in which the blades have been shortened and rotate only in the water phase, so that back-mixing can be minimized.

With V02, the pressure head increases to 11.2 m while the separation efficiency stayed stable over 0.99 (the limit of our measurement system).

6. CONCLUSION

In this paper, optimal operating conditions of the Pitot-tube Jet-Pump have been discussed. The influence of these operating points on the objectives was determined. By varying the operating conditions, a separation efficiency above 0.99 could be achieved (this value being limited by the accuracy of the measurement system). The intention is to increase the pressure at HPO while maintaining optimal separation efficiency.

The increase in pressure is to be achieved by changes in the operating parameters and by constructive modifications.

It has been shown that these measures are successful. With a simple geometry involving shortened blades, attached to the cover plate of the centrifuge, a head of 11.2 m could be achieved, compared to only 2.5 m without any blade. Together with this massive increase of almost 350% in pressure head, the separation efficiency still remains stable at over 0.99.

In the next steps, the blade geometry will be optimized again.

ACKNOWLEDGEMENT

This Project was funded by the German Federal Ministry for Research (BMBF) as ZIM project (ZF4063102KO8).

REFERENCES

[1] M. Ebrahimi, M. Aden, B. Schnabel, F. Liebermann, P. Czermak, Membranverfahren zur Aufbereitung von Abwässern, die mit Kohlenwasserstoffen belastet sind, unter Integration eines online Monitoring System, F&S Filtrieren und Separieren (2014).

[2] C. Hu, C. Herz, R.L. Hartman, Microfluidic dispersion of mineral oil-seawater multiphase flows in the presence of dialkyl sulfonates, polysorbates, and glycols, Green Processing and Synthesis 2 (2013).

[3] E.B. Kujawinski, M.C. Kido Soule, D.L. Valentine, A.K. Boysen, K. Longnecker, M.C. Redmond, Fate of dispersants associated with the deepwater horizon oil spill, Environmental science & technology 45 (2011) 1298–1306.

[4] J. Meyer, Optimierung einer Pitot-Pumpe und deren Adaption zur Öl-Wasser-Trennung, Dissertation, Magdeburg, 2018.

[5] J. von Deylen, J. Köpplin, D. Thevenin, Development and Validation of a Design Tool for an Improved Pitot-Tube Jet-Pump Allowing Continuous Fluid-Fluid Separation, Journal of Fluids Engineering (2021).

[6] J. Meyer, L. Daróczy, D. Thévenin, Shape optimization of the pick-up tube in a Pitot-tube jet-pump, Journal of Fluids Engineering 2017 021103/1-11.

[7] J. Meyer, D. Thévenin, Using centrifugal forces in a Pitot-tube jet-pump for cleaning and pumping oil-water mixtures in a continuous loop: an experimental study of separation efficiency, 9th International Conference on Multiphase Flow, Firenze, Italy, 2016.

Conference on Modelling Fluid Flow (CMFF'22)
The 18th International Conference on Fluid Flow Technologies
Budapest, Hungary, August 30-September 2, 2022

Aeroservoelasticity Investigation with Panel Method

Ábel OLGYAY[1], Béla TAKARICS[2], Bence KÖRÖSPARTI[3], János LELKES[4], Csaba HORVÁTH[5], Bálint VANEK[6]

[1] Corresponding Author. Development Engineer, Institute Computer Science and Control. Kende u. 13 - 17, H-1111 Budapest, Hungary. Tel.: +36 1 279 6000, Fax: +36 1 466 7503, E-mail: abel.olgyay@sztaki.hu
[2] Institute Computer Science and Control. E-mail: takarics@sztaki.hu
[3] Institute Computer Science and Control. E-mail: korosparti.bence.balazs@sztaki.hu
[4] Department of Fluid Mechanics, Faculty of Mechanical Engineering, Budapest University of Technology and Economics. E-mail: lelkes.janos@gpk.bme.hu
[5] Department of Fluid Mechanics, Faculty of Mechanical Engineering, Budapest University of Technology and Economics. E-mail: horvath@ara.bme.hu
[6] Institute Computer Science and Control. E-mail: vanek@sztaki.hu

ABSTRACT

When designing a new technological device that is affected by aerodynamic forces, it is almost common practice to model it with 3D CFD methods to study the design and to decide in which direction further developments should be taken. An elastic wing aircraft is considered to be a particularly complex model in which the number of parameters to be tested is too large to consider calculations that take tens or even hundreds of hours per simulation for each factor. In the industry, "high fidelity" Finite Volume Method simulations have become the general practice. Instead we use a so called panel method, where modelling the entire flow field is not necessary, only the surface mesh of the investigated body has to be generated. With this method the computational demand decreases drastically, but we know that there's no such thing as a free lunch. In addition to reducing the calculation time, we need to put the accuracy of the results on the other arm of the balance. The panel method solves only one Laplace equation for the full velocity potential, therefore it cannot model the additional drag due to the viscous medium.

Keywords: Aeroservoelastic Trim, CFD, Elastic wing, Panel Method

NOMENCLATURE

δ_e	[deg]	Elevator deflection
η	$[-]$	Modal coordinates
Φ	$[-]$	Mode shape matrix
ρ	$[\frac{kg}{m^3}]$	Density of the fluid
a_i	[deg]	Aileron deflection
C	$[-]$	Modal damping
C_L	$[Pa]$	Total pressure
C_M	$[m/s]$	Absolute velocity vector
$F_{aero,i}$	$[N]$	Aero force
K	$[-]$	Modal stiffness
L	$[N]$	Lift force
M	$[-]$	Modal mass
M_y	$[Nm]$	Pitching moment
MAC	$[m]$	Mean Aerodynamic Chord (MAC)
S	$[m^2]$	Surface of the wings
T	$[-]$	Transformation matrix
u	$[m]$	Displacement
V	$[\frac{m}{s}]$	Free velocity
M_i	$[Nm]$	Aerodynamic moment

Subscripts and Superscripts

L, D	lift, drag
PS, SS	pressure side, suction side
ref	reference
x, y, z	roll axis, pitch axis, yaw axis

1. INTRODUCTION

The basis of the flight control is a relatively easy task to do if there is only one criteria towards the aircraft: make it fly. But when the originally neglected effects are taken into consideration (such as wind gusts, flutter, drag minimization with aileron deflections), things get more and more complex. In this section a brief overview will be given of the Flipased (Flight Phase Adaptive Aero-Servo-Elastic Aircraft Design Methods) project's aerodynamical development, where an entire investigation model was created for the previously manufactured Flexop UAV. The model was written in Matlab, where the Panukl simulations were controlled with a windows batch file.

2. TRIM CONDITION

The concept of trim condition has to be taken under scrutiny. In this investigation the rate of rota-

tion was neglected, this way a trimmed out aircraft will maintain the set altitude without any rotation around any axes. According to Newton's first law, it leads to the conclusion that the aeroplane will continue in steady rectilinear flight only if the resultant force acting on it is zero, and the resultant moment acting about the center of gravity is also zero. In equations it can be written as:

$$\sum_{i=1}^{3} \mathbf{F}_i = 0, \quad (1)$$

$$\sum_{i=1}^{3} \mathbf{M}_i = 0, \quad (2)$$

where

- The coordinate axes: $i = \{1, 2, 3\} = \{x, y, z\}$
- The acting forces according to the coordinate axes: $\mathbf{F}_i$
- The acting momentums according to the coordinate axes: $\mathbf{M}_i$

It can be written in a dimensionless form. Two dimensionless quantities have to be defined. The lift coefficient and the pitching moment coefficient. (The other two moments around the other two axes are irrelevant in this case due to the symmetrical aircraft geometry, and since the free stream velocity is parallel to the travelling direction.) The describing equations can be seen in equations (3)-(4).

$$C_L = \frac{L}{\frac{1}{2}\rho V^2 S_{ref}} \quad (3)$$

$$C_M = \frac{M_y}{\frac{1}{2}\rho V^2 S_{ref} \cdot MAC} \quad (4)$$

There are important variables in these equations, which have to be described:

- Density of the fluid: $\rho \left[\frac{kg}{m^3}\right]$ (parameter in Panukl).
- Free stream velocity: $V \left[\frac{m}{s}\right]$ (parameter in Panukl).
- Reference area (area of the wings): $S_{ref} \left[m^2\right]$ (calculated by Panukl).
- Mean Aerodynamic Cord length: $MAC\,[m]$ (calculated by Panukl.)
- Lift force: $L\,[N]$ (acts in the z coordinate direction).
- Pitching moment: $M_y\,[Nm]$ (acts in the y coordinate axis).

To maintain steady rectilinear flight, the lift force and the gravitational force have to be equal, and the pitching moment has to be zero, which means the pitching moment coefficient also has to be zero. The next section is about finding the trim condition in Panukl.

2.1. Finding the trim condition in Panukl

The simulation result, which should be investigated, have to be in trim condition. For this, a modelling method has to be derived. Two variables were taken into consideration when the modelling of the trim condition was derived: the angle of attack and the elevator deflection. Angle of attack (AoA) has the greatest influence in the generated lift force and the elevator flaps are designed directly for pitching moment modification. Two sweeps have been run in Panukl and two variables have been investigated:

Variable sweep

- Angle of attack sweep $(0 - 10\,[°])$
- Elevator deflection sweep $(0 - 10\,[°])$

Investigated variables

- Lift coefficient: $C_L\,[°]$
- Pitching moment coefficient: $C_M\,[°]$

When the angle of attack was varied, the elevator deflection was kept at zero and vice versa. The two investigated parameters are plotted below. In Figure 1 the results of the AoA sweep, and in Figure 2 the results of the elevator deflection's results can be seen.

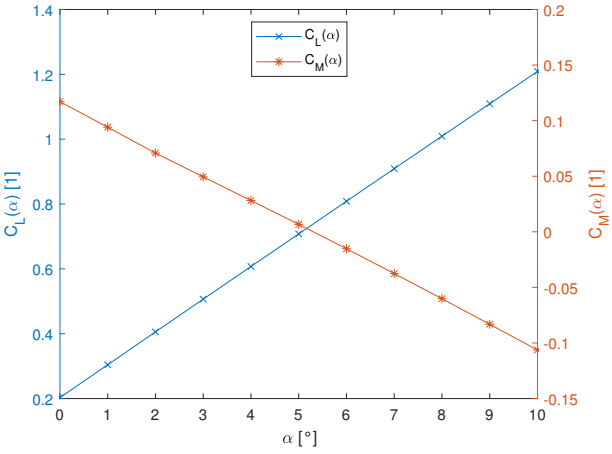

Figure 1. Result of the Angle of attack sweep in Panukl

With a very good approximation, it can be said that the lift coefficient and the pitching moment coefficient are also linear. This property can be seen in the results of the elevator deflection sweep as well.

In the investigated range of angle of attack and elevator deflection, these functions have to be approximately linear. The result of the simulations meets the expectations. Panukl can provide simulation results, which corresponds to those described in the literature [1]. Thus a linear function should be

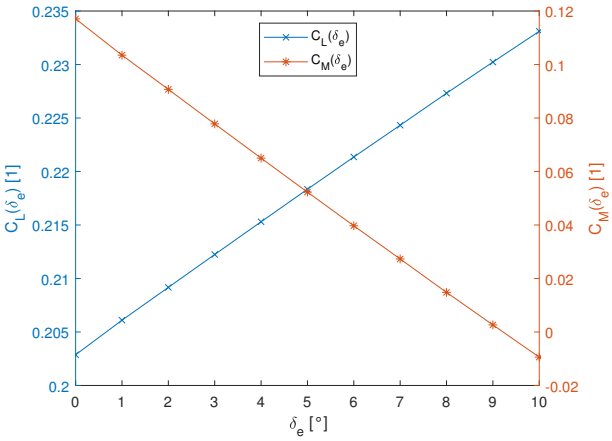

Figure 2. Result of the elevator deflection sweep in Panukl

written in the following form:

$$C_L(\alpha,\delta_e) = C_{L,0} + C_{L,\alpha}\cdot\alpha + C_{L,\delta_e}\cdot\delta_e \quad (5)$$

$$C_M(\alpha,\delta_e) = C_{M,0} + C_{M,\alpha}\cdot\alpha + C_{M,\delta_e}\cdot\delta_e \quad (6)$$

In equations (5)-(6) the constant variables are the following:

$$C_{L,0} = C_L(0,0)$$

$$C_{L,\alpha} = \frac{\partial C_L(\alpha,\delta_e)}{\partial\alpha}$$

$$C_{L,\delta_e} = \frac{\partial C_L(\alpha,\delta_e)}{\partial\delta_e}$$

$$C_{M,0} = C_M(0,0)$$

$$C_{M,\alpha} = \frac{\partial C_M(\alpha,\delta_e)}{\partial\alpha}$$

$$C_{M,\delta_e} = \frac{\partial C_M(\alpha,\delta_e)}{\partial\delta_e}$$

Three unknowns require three equations for the coefficients to be sought to be determinable. The set of the simulation parameters can be seen in Table 1.

Table 1. Set of parameters

$(\alpha;\delta_e)$	$C_L(\alpha,\delta_e)$	$C_M(\alpha,\delta_e)$
(0;0)	$C_{L,0}$	$C_{M,0}$
(1;0)	$C_{L,0}+C_{L,\alpha}$	$C_{M,0}+C_{M,\alpha}$
(0;1)	$C_{L,0}+C_{L,\delta_e}$	$C_{M,0}+C_{M,\delta_e}$

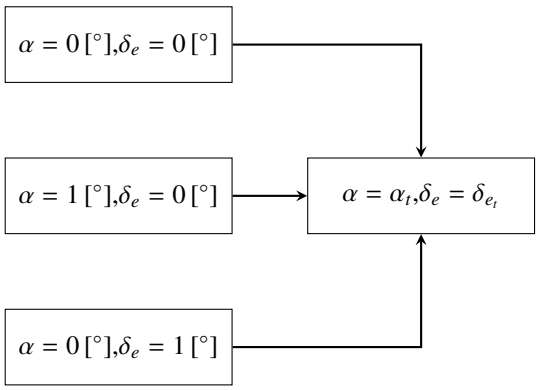

Figure 3. Defining the trim condition

With 3 simulations, the coefficients in the lift and pitching moment functions can be determined, and this way the trim condition can be calculated. As mentioned in section 2, the lift coefficient has to be equal with the non-dimensioning weight of the aircraft and the pitching moment coefficient has to be zero. The AoA and elevator deflection values which correspond to the trim condition are signed with a subscription of "t". All subsequent investigation were performed in trim condition.

2.2. Checking the result

The accuracy of the trim condition modelling can be checked with the help of another run of the simulation using the calculated variables that correspond to the trim condition (α_t, δ_{e_t}). If the investigated coefficients are within an acceptable range of the theoretical value, then the modelling method can be accepted. The results are in Table 2 and Table 3.

Table 2. Simulation parameters

δ_e [°]	8.608
α [°]	-0.270
Ma [1]	0.133

Table 3. Important variables of the simulation

C_l [1]	-1.036e-4
C_m [1]	7.939e-3
C_n [1]	-6.697e-6
C_L [1]	2.088

Two important conclusions can be drawn:

- The pitching moment coefficient is approximately zero, and is close to the other two axis rotation coefficient. The geometry is symmetric to the x-z plane, the side-slip angle was 0°, roll/pitch/yaw rate 0 rad/s, thus these values are caused by numeric error.
- The lift coefficient differs by 0.82% from the theoretical value (0.2105).

With a result like this, it can be said that the modelling method works, and it provides a good approximation for the investigated coefficients.

3. DEFORMATION COMPUTATION

To achieve true trim flight conditions, the elastic deformation of a flexible vehicle may not be ignored, since in this case structural vibration modes

have a larger effect on flight dynamics compared to rigid airframes. To account for this effect, aside from the aerodynamic representation, a structural dynamics model is also required. In this section the methods used in the deformation calculation and their implementation are described.

3.1. Flexible aircraft modeling

To compute the deformation of flexible aircraft, an aerodynamic model, a structural model and an additional method that achieves connection between the two models is used. As previously described, the aerodynamic model computes the aerodynamic load woken on the airframe. A structural representation is created based on the structural properties of the aircraft using the finite element method (FEM). It allows the computation of the deformation due to the aerodynamic load. Since the different models are created using different methods, establishing the connection between them is not a straightforward task. To achieve interconnection of the flexible dynamic system shown in Figure 4., surface spline theory is used, which enables the transformation of aerodynamic forces and moments to the structural model and structural deformation to the aerodynamic model. The result is an iterative process with the undeformed aircraft geometry an structural properties as the input and the deformed geometry as the output.

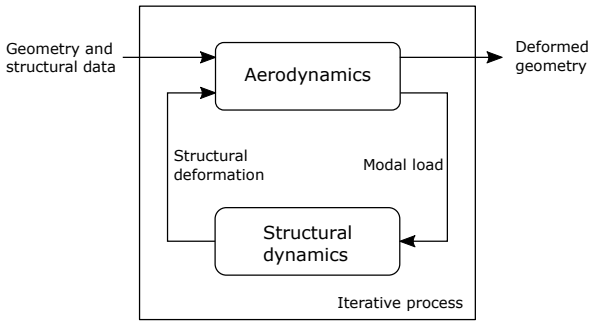

Figure 4. Trim flight deformation calculation process

3.1.1. Structural dynamics model

A brief description of FEM is given here. It is a commonly used modeling tool to perform the analysis of complex structures. Widely employed finite element techniques and procedures are presented in [2] and [3]. Major benefits of this method are its computational efficiency combined with sufficient accuracy of its results.

The linear finite element method separates the geometry into a finite number of beams and nodes with varying structural and geometric properties. The structural model created for the Flipased aircraft has 6 degrees of freedom for each node. The representation can be described in modal coordinates as

$$M\ddot{\eta} + C\dot{\eta} + K\eta = F, \tag{7}$$

where M, C and K represent the modal mass, damping and stiffness matrices respectively, η are the modal coordinates and F is the external excitation expressed in modal coordinates. The matrices are constructed based on the structural properties of the aircraft. The physical displacement u_{struc} of the structural grid expressed in the same coordinate system as the aerodynamic grid can be calculated using the mode shape matrix Φ_{mode} corresponding to the modal coordinates as

$$u_{struc} = \Phi_{mode}\eta. \tag{8}$$

Applying this model allows the computation of the deformed geometry taking the load acting on the aircraft as its input.

3.1.2. Surface spline theory

The surface spline theory is capable of interpolating a given set of deformation using thin plate deformation equations to solve for the unknown deformation at any point on a given surface. This serves as an aid in the transformation of the aerodynamic load to the FEM model and the resulting structural deformation to the aerodynamic grid by adding an in-between step. The spline grid is constructed based on both the structural and aerodynamic grid similarly to the example depicted in Figure 5. The model consists of the structural nodes, each of them complemented by two additional nodes connected to the corresponding central node with a stiff rod. The deformation of the FEM model is transformed as follows: first, all 6 degrees of freedom of the structural grid nodes are transformed purely into heaving motion of the spline grid nodes using the matrix T_{spline}. This allows the structural deformation to be applied on an infinite thin plate and its corresponding equations to be used to interpolate the deformation onto the aerodynamic grid using the matrix T_{plate}. The overall transformation matrix T_{as} used in Equation (10) can be calculated as

$$T_{as} = T_{plate}T_{spline}. \tag{9}$$

$$u_{aero} = T_{as}u_{struc} \tag{10}$$

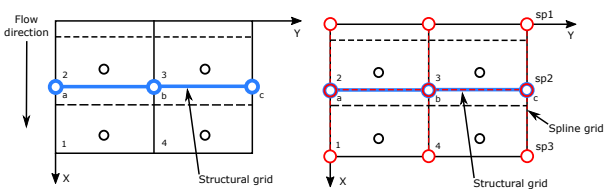

Figure 5. Spline grid

The transformation of the aerodynamic forces and moments require similar steps but in the opposite direction. Firstly, the calculated load components

perpendicular to the thin plate are distributed among the the spline nodes. The resulting load that purely consists of forces is then transformed onto the 6 degrees of freedom of the structural grid. It is important to mention that the effect of the resulting load applied on the structural grid is identical to that of the load applied on the aerodynamic grid. A more detailed description of this process can be found in [4] for which the applied thin plate deformation equations are derived in [5].

3.2. Implementation

The application of the previously described tools begins with the construction of the different models, namely the aerodynamic, the FEM and the spline model. Panukl software is used to model aerodynamics as detailed previously. This representation computes the aerodynamic load acting on the rigid panel model. Pressure coefficients (C_{p_i}) are taken from the results to calculate the aerodynamic force (F_i) and moment (M_i) acting on each panel, as in equation (11) and (12).

$$F_{aero,i} = C_{p_i} \frac{\rho}{2} V^2 S_{panel,i} \tag{11}$$

$$\begin{bmatrix} F_i \\ M_i \end{bmatrix} = \begin{bmatrix} 1 \\ \frac{c_{p,i}}{4} \end{bmatrix} F_{aero,i}, \tag{12}$$

where ρ represents air density, V is the airspeed, $S_{panel.i}$ and $c_{p,i}$ are the panel surface and the panel chord corresponding to the i^{th} panel respectively.

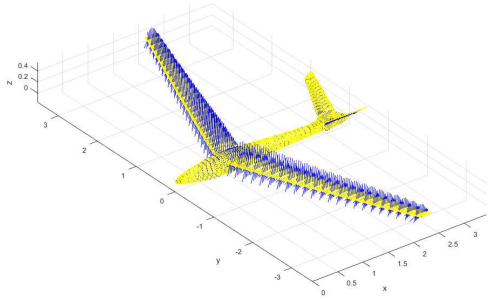

Figure 6. Aerodynamic load calculated from pressure coefficients

These components are applied on the structural grid in the form of modal forces using the surface spline method and the transpose of the mode shape matrix. To convert this load into components that are applicable on the aircraft structure, the spline model has to be built. The spline nodes along the center of every component of the aircraft are geometrically identical to the structural grid points and the outer nodes were created in alignment with these central nodes based on the aerodynamic model.

The presented spline model is able to account for forces in the z direction and moments acting in the x-y plane. To create a system where the 'x' component of the aerodynamic force is taken into consideration, an additional vertical spline grid can be added to the spline model, which includes the moments acting in the x-z plane as well. The complete spline representation is shown in Figure 7. This additional element promotes a more precise solution for the trim deformation calculation.

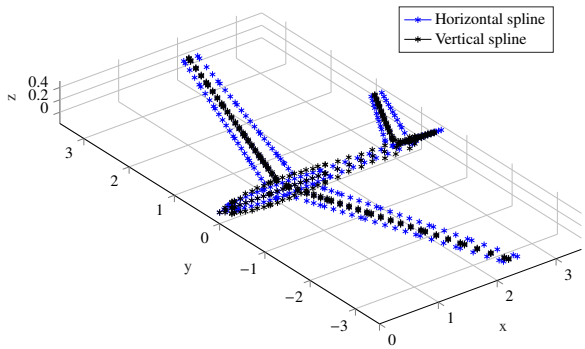

Figure 7. Horizontal and vertical spline

The FEM model is created based on the structural properties of the given airframe. This results in a structural grid for which the dynamic properties are arranged into a state-space model. Here the states are the modal coordinates and their first derivatives. This achieves the solution of Equation (7) with the aerodynamic load expressed in modal coordinates as input and the modal coordinates for the deformed geometry as output.

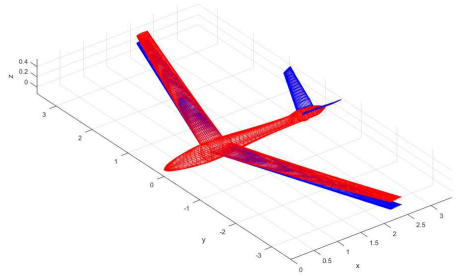

Figure 8. Aerodynamic grid and its deformation

The deformed aerodynamic geometry in Figure 8 will become the input for the next iteration step, where Panukl software takes the leading- and trailing edge coordinates to generate the a new panel model, for which a new set of aerodynamic load will be computed.

4. AEROSERVOELASTIC TRIM CONDITION

All the methods and calculation techniques correspond to a rigid-body aircraft geometry. It is also known that the aerodynamic load deforms the body placed in the flow. This is what happens here as well. The aerodynamic force will bend and twist the aircraft's fuselage, wings, and tails. Due to the change in geometry, the descriptive equations of the aircraft's dynamical behavior will also change. The structural dynamics of the aircraft have been derived by TUM, and the calculations were implemented to Flipased Project by Réka Mocsányi. Only a small description of the derivation was presented earlier. For further information, please refer to [6], [7], [8].

4.1. Finding the aeroservoelastic trim condition

The structural dynamics was implemented into the Matlab model. The geometry deformation was calculated, and the original geometry definition file was rewritten. Nothing was made by hand, everything was handled by a Matlab script. In this way the developed computational method could be implemented in a computational loop. Three simulations are run in every step, in order to calculate the searched trim condition's state variables (α_t, δ_{e_t}), and then another simulation is run with trim conditions. The solution of this simulation is the input of the structural dynamics calculation, the geometry is overwritten based on this, and the loop is moving on to the next step. The calculation loop can be run as long as there is no significant change between two steps of the loop.

First, for research purposes a 10 step long loop was investigated. With the experience of these solutions, a bigger picture can be seen regarding to the importance of these steps. The plots of a few investigated parameters can be seen in Figure 9.

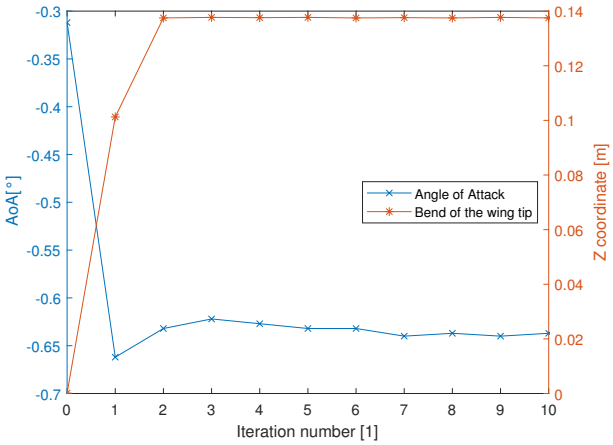

Figure 9. Convergence of some quantities

The 0th iteration number corresponds to the rigid-body simulation. It seems like the elevator deflection converges after just one iteration step, although both the angle of attack and the bending of the wing tip are changing in the further step. With a good approximation 2 iteration steps seem to be enough to reach the converged state, but for a safety reason, for the further calculations 3 iteration steps were set in the modelling method. This converged state is called aeroservoelastic trim condition.

5. RESULTS

5.1. Perturbation around three base values

A simulation investigation has been created, where the perturbation of the aircraft's aileron deflection was investigated. The Flipased UAV has four control surfaces on each wing (symmetrically). Three base angles were chosen $(-2.5\,[°]\,; 0\,[°]\,; 2.5\,[°])$, and the perturbation angle was $\pm 0.5\,[°]$. This way three sets of simulations were created, where every set contained 81 cases $\left(3^4\right)$. One case consisted of a set of aileron deflections, for example $\{a_1; a_2; a_3; a_4\} = \{-2.5; -2.5; -2.5; -2\}$, where a_1 is the closest control surface to the fuselage and a_4 is the farthest. The three sets of simulated base angles resulted in 243 cases. Note that one case means the result of a simulation with aeroservoelastic trim conditions. Thus one result of one case needs 4 simulations in order to attain for the trim simulation, and one rigid body with 3 iterations are calculated in order to find the aeroservoelastic trim condition. Thus the presented exaple results in 3888 simulations.

The simulations were run on an AMD Ryzen™ 4800H. Panukl can use the CPU cores in parallel mode, but the efficiency is poor. If the simulation ran on only one core, the average occupancy during the simulation was nearly 95%. When Panukl used all the 8 physical cores, this value decreased to 25%. This is due to the poorly optimized parallel calculation in the Panukl solver. In most of the time, the CPU waits for some information. One simulation took approximately 1 minute to finish with the tasks. The Matlab script's run time is negligible (close to 1 second). Thus the 3888 simulations took approximately 2.5 days.

The first presented set of aileron deflections were perturbated around $-2.5\,[°]$. The induced drag coefficient was plotted as a function of the wing deflection in Figure 10. Three consecutive values (in the direction of the horizontal axis) belong to the a_4 sweep, where the sweep starts from $-3\,[°]$, the second a_4 value is $-2.5\,[°]$ and the last one is $-2\,[°]$ (from left to right) and every horizontal grid line correspond to a change of one aileron. The grid values can be seen on the bottom of the Figure, where (a_2, a_3) corresponds to the second and third aileron (the smaller the index, the closer it is to the fuselage). One color with a specific marker describes one fixed a_1 value.

In the Figure, it can be seen that the three plots are shifted upwards as the aileron deflection is increased. This means that the first aileron has the biggest effect on the drag force. With a good approx-

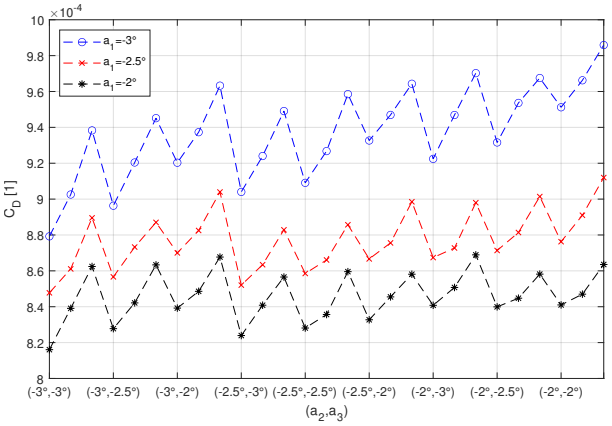

Figure 10. Results of the perturbation (base angle was -2.5 [°])

imation it can be said that the three plotted functions fluctuate around a mean value. There are no peaks or significant increasing/decreasing behavior in the plots.

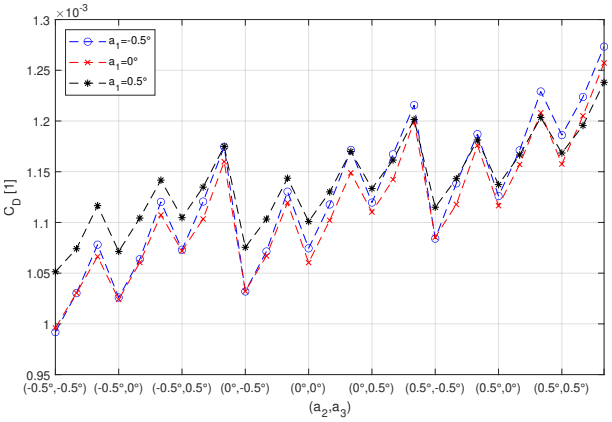

Figure 11. Results of the perturbation (base angle was 0 [°])

In both Figure 11 and 12 a constant increasing behavior can be noticed. This kind of trend is caused by the asymmetric aerofoils on the wings. The higher deflection always starts with a higher drag coefficient value, but the slope of the increasing drag coefficient is smaller than the other curves corresponding to other a_1 value. At the bottom-left corner in Figure 11 the highest value belongs to the $a_1 = 0.5$ [°] case, and the lowest value to the $a_1 = -0.5$ [°] case, but on the top-right corner they swap places. In Figure 12 this effect is more moderate.

5.2. Effect of different flap deflection angles

Closely similar parameters were investigated as in section 5.1, where the perturbation was investigated. In this section, the perturbation was increased to ± 1 [°] and the base value was 0 [°]. The background of the investigation was provided by modern UAV flight control systems. An aircraft's slender wings' structure, as on Flipased UAV, is deformed by

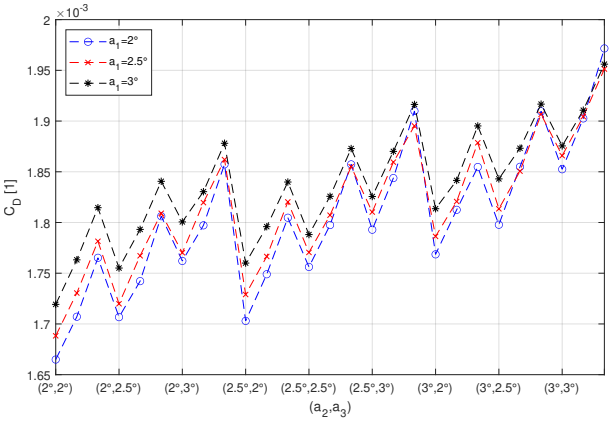

Figure 12. Results of the perturbation (base angle was 2.5 [°])

the acting forces on its body, which can cause permanent damage, even wing breakdown. The main acting force is the lift force (more than one magnitude greater than along the other two axes). With ailerons deflected in different directions, most of the lift force generation can be concentrated near to the fuselage, where the lever of the bending motion is small, and the structure is stronger too.

The results of the simulations can be seen in Figure 13. The plot is similar to Figure 11, but this is what can be expected. On one hand, the values are stretched relative to the ± 0.5 [°] perturbation. The minimal drag is lower, and the highest drag value is greater. A constantly increasing tendency can be noted here too, and the slope of the $a_1 = 1$ [°] set is smaller than the other two, which change together and are close to each other.

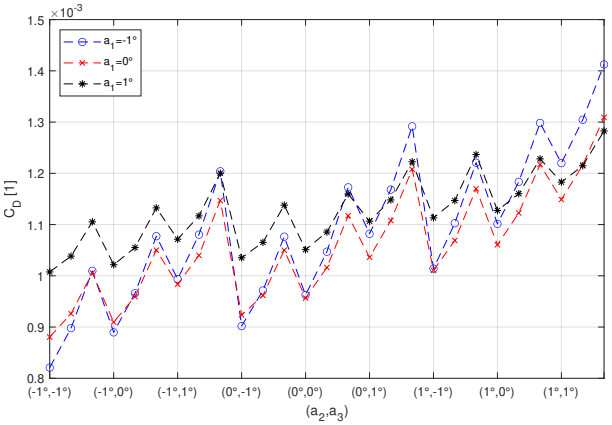

Figure 13. Perturbation with 1 [°]

5.3. Comparing different solutions

Thiemo Kier from Deutsches Zentrum für Luft- und Raumfahrt (DLR) developed a similar investigation tool-chain, where he used his own aerodynamic solver [9], [10] with Nastran [5]. In DLR, a big data was generated, where the aileron deflection and the velocity has been varied. Later on, an optimization algorithm defined the ideal aileron deflections

for each investigated velocity.

The same velocity and aileron deflection were investigated in Panukl also. The results can be seen in Figure 14. These results correspond to the aeroservoelastic trim condition obtained by two different approaches. The induced drag in Newton dimension can be seen in the vertical axis and the velocity on the horizontal axis. The results approach quadratic functions and it can be concluded, that the two different theoretical approaches show a good match.

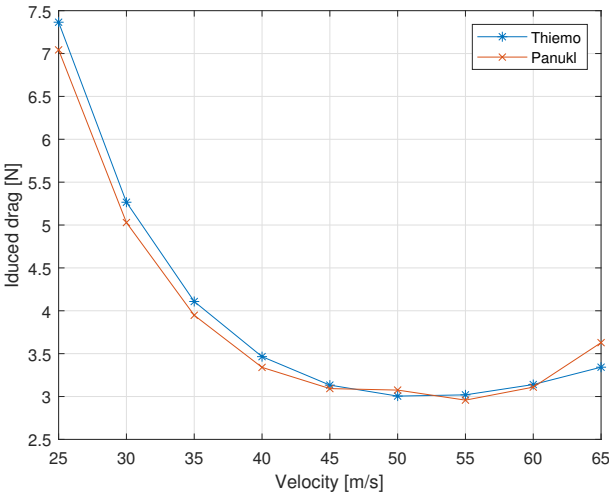

Figure 14. Comparison of the induced drag solutions

6. SUMMARY

A simulation tool-box has been developed and the compared results with different solvers shows good match. In further work, a bigger database will be generated. With the help of these information a control system can be developed, which will take the deformation of the aircraft into consideration, causes lower drag during flight. Lower drag means less burned fuel. With the help of the developed toolchain, a more environmentally friendly flight condition can be set. If the conclusions can be implemented in bigger aircraft, it could lower the CO_2 emission during a flight.

ACKNOWLEDGEMENT

The research leading to these results is part of the FLiPASED project. This project has received funding from the Horizon 2020 research and innovation programme of the European Union under grant agreement No 815058.

The research was supported by the Ministry of Innovation and Technology NRDI Office within the framework of the Autonomous Systems National Laboratory Program.

Supported by the ÚNKP-21-5 New National Excellence Program of the Ministry for Innovation and Technology from the source of the National Research, Development and Innovation Fund.

This paper was supported by the János Bolyai Research Scholarship of the Hungarian Academy of Sciences.

This project has received funding from the European Union's Horizon 2020 research and innovation programme under grant agreement No 815058.

REFERENCES

[1] L. Jenkinson, P. Simpkin, D. Rhodes, Civil Jet Aircraft Design, 1999, American Institute of Aeronautics and Astronautics

[2] Klaus-Jürgen Bathe, Finite Element Procedures, Book, 2014, Klaus-Jürgen Bathe

[3] G.R. Liu, The Finite Element Method: A Practical Course, Book, 2013, Butterworth-Heinemann

[4] A. Kotikalpudi, Robust Flutter Analysis for Aeroservoelastic Systems, University of Minnesota, Twin Cities,2017

[5] William Rodden, MSC/NASTRAN Aeroelastic Analysis User's Guide, Book, 1994, MSC

[6] Wang, Zhicun & Mook, Dean & Gao, David & Hajj, Muhammad R. & Hendricks, Scott & Librescu, Liviu & Preidikman, Sergio. (2004). Three-Dimensional Configurations, Unstable Aeroelastic Responses, and Control by Neural Network Systems Zhicun Wang.

[7] Panda, Chinmaya & S R Pappu, Venkatasubramani. (2009). Aeroelasticity-In General and Flutter Phenomenon. 10.1109/ICETET.2009.23.

[8] T. Luspay, T. Péni and B. Vanek, "Control oriented reduced order modeling of a flexible winged aircraft," 2018 IEEE Aerospace Conference, 2018, pp. 1-9, doi: 10.1109/AERO.2018.8396496.

[9] Thiemo M. Kier, An Integrated Modelling Approach for Flight Dynamics, Manoeuvre- and Gust-Loads Analysis, German Aerospace Center (DLR), 82234 Weßling, Germany

[10] Thiemo M. Kier, Gertjan H. N. Looye, Unifying manoeuvre and gust loads analysis models, German Aerospace Center, Institute of Robotics and Mechatronics, 82234 Wessling, GERMANY

Conference on Modelling Fluid Flow (CMFF'22)
The 18th International Conference on Fluid Flow Technologies
Budapest, Hungary, August 30-September 2, 2022

IDENTIFICATION OF DATA-DRIVEN AERODYNAMIC MODELS FOR REDUCED-ORDER AEROELASTIC SIMULATIONS

János LELKES[1], Dávid András HORVÁTH[2], Tamás KALMÁR-NAGY[3]

[1] Corresponding Author. Department of Fluid Mechanics, Faculty of Mechanical Engineering, Budapest University of Technology and Economics. Bertalan Lajos u. 4 - 6, H-1111 Budapest, Hungary. Tel.: +36 1 463 2464, Fax: +36 1 463 3464, E-mail: lelkes.janos@gpk.bme.hu
[2] Department of Fluid Mechanics, Faculty of Mechanical Engineering, Budapest University of Technology and Economics. E-mail: david_horvath67@yahoo.com
[3] Department of Fluid Mechanics, Faculty of Mechanical Engineering, Budapest University of Technology and Economics. E-mail: kalmar.nagy.tamas@gpk.bme.hu

ABSTRACT

Multiple approaches exist for calculating the time-dependent aerodynamic loads of thin, flexible structures subjected to airflow. For calculating the aerodynamic loads, analytical, semi-empirical, CFD-based, and various reduced-order models exist. These models are usually only applicable for small deformations; in the case of large deformations, calculating aerodynamic loads is computationally costly. In this paper, a data-based identification method to calculate the aerodynamic loads was applied. The most significant advantage of this technique is that it is also accurate for large structure deformations. After the initial data fitting process, the simulations run very quickly. To create the data-based model, we used high-precision validated CFD simulations. The SINDy (Sparse Identification of Nonlinear Dynamics) algorithm was utilized for the model construction. Multiple optimization routines were used to fit the aerodynamic model, e.g., LASSO (Least Absolute Shrinkage and Selection Operator) and STLSQ (Sequentially Thresholded Least Squares). As the result of the paper, we get a data-based aerodynamic model for a single configuration and a compact process, with which the aerodynamic loading of arbitrary moving structures can be calculated in the time domain.

Keywords: Aerodynamics, Aeroelasticity, Nonlinear dynamics, Sparse identification

NOMENCLATURE

NRMS	[1]	normed root mean square error
C_L	[1]	lift coefficient
H_1, A_i	[1]	flutter derivatives
L	[N]	lift force
M	[Nm]	aerodynamic moment
b	[m]	half chord length
c_α	[Ns/rad]	damping of the pitch DoF
c_h	[Ns/m]	damping of the heave DoF
c_i	[SI]	coefficients of the ROM
h	[m]	heave
k	[1]	Reduced frequency
k_α	[N/rad]	stiffness of the pitch DoF
k_h	[N/m]	stiffness of the heave DoF
m	[kg]	mass
q	[1/(s^{2}rad^3)]	stiffness coefficient of the cubic spring
U	[m/s]	wind velocity
α	[rad]	pitch angle
ω	[rad/s]	angular frequency
ω_α	[rad/s]	angular natural frequency of the pitch DoF
ω_h	[rad/s]	angular natural frequency of the heave DoF
ρ	[kg/m^3]	density
ξ_α	[1]	damping factor of the pitch DoF
ξ_h	[1]	damping factor of the heave DoF
I_α	[kgm^2]	moment of inertia

1. INTRODUCTION

Aerodynamic models are essential for designing aircraft, evaluating static and dynamic aeroelastic stability, and developing feedback control laws. Obtaining accurate and efficient aerodynamic models has been a fundamental objective of research efforts in aeronautics over the past century [1]. Closed-form solutions for the attached incompressible unsteady flow problem around a two-dimensional (2D) airfoil exist in both the frequency and time domains [2].

Wagner [3] developed a model for the unsteady lift on a two-dimensional flat plate for arbitrary small-amplitude pitching motion. He computed the effect of idealized planar wake vorticity on the circulation around the plate in response to a step in the

angle of attack analytically. After this, the response to arbitrary motion could be constructed by convolution with this indicial response. Ten years later, Theodorsen [4] derived a complementary model to study the aeroelastic problem of flutter instability in the frequency domain. Wagner's and Theodorsen's theories were derived analytically for an idealized two-dimensional flat plate moving through an inviscid, incompressible fluid. The motion of the flat plate is assumed to be infinitesimal, leaving an idealized planar wake.

The finite state flow model offers state equations for the induced flow field itself [5]. The governing equations of the finite state flow model were derived directly from the potential flow equations (either velocity or acceleration potential). Thus, no intermediate steps were invoked in which restrictions were placed on airfoil motions. The theory is an arbitrary-motion theory from the outset. In contrast to Computational Fluid Dynamics (CFD) and vortex lattice methods, the states represent induced flow expansion fields rather than velocities at discrete nodes. As a result, the states are hierarchical, and the equation coefficients are known in closed form. No numerical fitting of frequency-response or indicial functions is needed to apply the finite state flow model.

The dynamic stall phenomenon and its importance for load calculations and aeroelastic simulations are well known. Different models exist to model the effect of the dynamic stall. For dynamic stall, the physics of the flow separation and stall development differs fundamentally from the stall mechanisms observed for the same airfoil under static (quasi-steady) conditions [6].

The effect of dynamic stall can be defined as a delay in the stall onset: stall occurs at a higher angle of attack than for the static stall case. A strong vortex is formed at the leading edge that separates and is convected along the suction surface of the airfoil. This event begins with a rapid increase in lift and ends with complete flow separation and catastrophic loss of lift as the vortex disturbance is convected past the trailing edge of the airfoil. This behavior can produce hysteresis loops in the force coefficients, producing cyclic pressure loads that are not predicted by conventional lift and drag data obtained at steady angles of attack [1].

The ONERA semi-empirical model [7] describes the unsteady airfoil behavior employing a set of nonlinear differential equations. A first-order linear differential equation describes the inviscid (attached flow) aerodynamic contribution, and a second-order differential equation describes the nonlinear viscous effects associated with the stall.

The Beddoes–Leishman method [8] is a dynamic stall model where the emphasis is on a more accurate and complete physical representation of the overall unsteady aerodynamic problem but still in a form that keeps the complexity of analysis down to minimize computational cost. In this way, it attempts to overcome the limitations of other models where many empirically determined coefficients limit the method's applicability. The Beddoes–Leishman model essentially consists of four subsystems: 1. an attached flow model for the unsteady (linear) aerodynamic forces based on Duhamel superposition, 2. a separated flow model for the nonlinear aerodynamic forces, 3. a dynamic stall onset model, 4. a dynamic stall model for the vortex-induced aerodynamic forces.

The nonlinear, second-order dynamic stall model developed by H. Snel [9, 10] is an example of a modern semi-empirical engineering model used to include dynamic stall effects in aeroelastic response codes for wind turbines. This model uses no airfoil-specific parameters in its modeling equations but still can predict the dynamic stall with the same accuracy as models that require such input. This characteristic makes Snel's dynamic stall model desirable for application in an aeroelastic design code where numerous airfoil profiles need to be evaluated, negating the need for any parameter identification from dynamic wind tunnel tests.

Lelkes and Kalmár-Nagy modeled the aerodynamic forces for large angles of attack as a piecewise linear function, which was able to capture the phenomenon of dynamic stall [11].

First, the applied data-driven system identification method is described in this paper. Then, the identified models are presented for three different reduced frequency values compared with the simulation data. Afterward, the models are applied for a simple 2-DOF aeroelastic model of a flat plate.

2. SPARSE IDENTIFICATION OF NONLINEAR DYNAMICAL SYSTEMS

Traditionally, dynamical systems are modeled by first principles, such as Newton's second law. However, this approach can be time-consuming while requiring expert knowledge, and the resulting models can be too simplistic to capture the real-world dynamics accurately. With the advent of powerful computers and efficient machine learning algorithms, modeling based on real-world measurement data becomes possible.

In this paper, we use the Sparse Identification of Nonlinear Dynamical systems (SINDy) method, introduced by Brunton et al. [12, 13], and later refined in the work of Champion et al. [14]. An overview of the method, as well as the description of the Python package that is used in our paper, is given by Silva et al. [15]. Several alternate versions of this method have been proposed. Kaheman et al. [16] introduced SINDy-PI, which is a parallel version that can be used to identify implicit dynamics while being robust to noise. Kaptanoglu et al. [17] proposed a modification of the SINDy algorithm, which is useful for identifying globally stable models. The SINDy method can also be modified to be applicable to various boundary value problems, as shown by Shea et

al. [18].

An overview of data-driven methods in aerospace engineering is given by Brunton et al. [19]. In the work of Sun et al. and Pohl et al. [20, 21] the SINDy method is used to derive polynomial models for the lift of an airfoil.

Here, a brief introduction to SINDy is given; more information can be found in the articles mentioned above. Our aim is to determine a model for a dynamical system in the following form:

$$\dot{\underline{x}}(t) = \underline{f}\left(\underline{x}, t\right), \tag{1}$$

where $\underline{x}$ is the vector of the state variables, and t is the time variable. We want to determine the function $\underline{f}$. The idea of the SINDy method is that usually, $\underline{f}$ has a sparse representation in the space of the possible functions. Due to this, a sparse regression is used to discover $\underline{f}$. Let us denote

$$\underline{\underline{X}} = \begin{bmatrix} \underline{x}^T(t_1) \\ \vdots \\ \underline{x}^T(t_n) \end{bmatrix}, \tag{2}$$

$$\dot{\underline{\underline{X}}} = \begin{bmatrix} \dot{\underline{x}}^T(t_1) \\ \vdots \\ \dot{\underline{x}}^T(t_n) \end{bmatrix}, \tag{3}$$

where we measure the state vector $\underline{x}$ at $t_1, \ldots, t_n$ time points, and either also measure the derivative of the state vector, or calculate it numerically from $\underline{x}$. The feature library is denoted by $\underline{\underline{\Theta}}\left(\underline{\underline{X}}\right)$, for example, for a polynomial library

$$\underline{\underline{\Theta}}\left(\underline{\underline{X}}\right) = \left[\underline{1} \quad \underline{\underline{X}} \quad \underline{\underline{X}}^{P_2} \cdots\right], \tag{4}$$

where $\underline{\underline{X}}^{P_2}$ denotes the second order polynomials

$$\underline{\underline{X}}^{P_2} = \begin{bmatrix} x_1^2(t_1) & x_1(t_1)x_2(t_1) & \cdots & x_2^2(t_1) & \cdots & x_m^2(t_1) \\ \vdots & \vdots & \ddots & \vdots & \ddots & \vdots \\ x_1^2(t_n) & x_1(t_n)x_2(t_n) & \cdots & x_2^2(t_n) & \cdots & x_m^2(t_n) \end{bmatrix}. \tag{5}$$

We are searching for the vector $\underline{\underline{\Xi}} = \begin{bmatrix} \xi_1 & \cdots & \xi_m \end{bmatrix}$

$$\dot{\underline{\underline{X}}} = \underline{\underline{\Theta}}\left(\underline{\underline{X}}\right)\underline{\underline{\Xi}}. \tag{6}$$

Once this is found, a model can be constructed as follows

$$\dot{\underline{x}} = \underline{f}\left(\underline{x}\right) = \underline{\underline{\Theta}}\left(\underline{x}^T\right)\underline{\underline{\Xi}}. \tag{7}$$

For real-world data, usually $\underline{\underline{X}}$, and $\dot{\underline{\underline{X}}}$ are contaminated with noise, so instead of equation (6) we have

$$\dot{\underline{\underline{X}}} = \underline{\underline{\Theta}}\left(\underline{\underline{X}}\right)\underline{\underline{\Xi}} + \eta\underline{\underline{Z}}, \tag{8}$$

where noise is modeled as a Gaussian distribution with zero mean and η noise magnitude. Numerous objective functions can be used for the sparse regression, we have primarily used the sequentially thresholded least squares (STLSQ), and the least absolute shrinkage and selection operator (LASSO), which are respectively l_2, and l_1 regularized regressions promoting sparsity [12], these will be detailed in the next section.

2.1. SINDy optimizers

The LASSO optimizer is a simple l_1 regularized regression with the following objective function

$$\frac{1}{2n}\left\|\underline{y} - \underline{\underline{X}}\,\underline{w}\right\|_2^2 + \lambda\left\|\underline{w}\right\|_1, \tag{9}$$

where $\underline{y}$ is the training data of the algorithm, $\dot{\underline{\underline{X}}}$ in equation (8), $\underline{\underline{X}}$ is the function library $\underline{\underline{\Theta}}(\underline{\underline{X}})$, $\underline{w}$ is the vector of weights $\underline{\underline{\Xi}}$, and λ is the regularization parameter. The norms are defined the following way

$$\left\|\underline{x}\right\|_1 = \sum_{i=1}^{n} |x_i|, \tag{10}$$

$$\left\|\underline{x}\right\|_2 = \sqrt{\sum_{i=1}^{n} |x_i|^2}, \tag{11}$$

where $\underline{x} = \begin{bmatrix} x_1 & x_2 & \ldots & x_n \end{bmatrix}^T$. The other optimizer that we have used is the STLSQ, which was originally proposed to be used with the SINDy algorithm in [12]. It has the following objective function

$$\frac{1}{2n}\left\|\underline{y} - \underline{\underline{X}}\,\underline{w}\right\|_2^2 + \lambda\left\|\underline{w}\right\|_2^2. \tag{12}$$

It can be observed that this is very similar to the objective function that LASSO uses. The only difference is that STLSQ utilizes an l_2 regularization instead of an l_1. However, there is one more important difference. The algorithm works by finding the optimum weights for the objective function and then masking out every coefficient that is lower than a set threshold. Afterward, it iterates these steps for the non-masked-out coefficients. This iteration procedure is useful to promote sparsity in the learned model.

3. IDENTIFIED MODELS

The CFD simulations that the models have been trained on were obtained by prescribing a sinusoidal oscillation for the angle of attack of the flat plate. The details of the CFD simulations are described in [22, 23].

Data were obtained for three oscillation amplitudes and angles of attack, resulting in 9 different time series of the aerodynamic lift force. Three models were identified, one for each frequency. The frequency was nondimensionalized; the resulting reduced frequency is defined as $k = \frac{\omega b}{U}$, where b is the half chord length, U is the wind velocity, and ω is the angular frequency of the oscillation. Reduced frequency is the dimensionless number used in general for the case of unsteady aerodynamics and aeroelasticity [6]. It is one of the parameters that defines the degree of unsteadiness of the problem. The aerodynamic model equations were created by using the

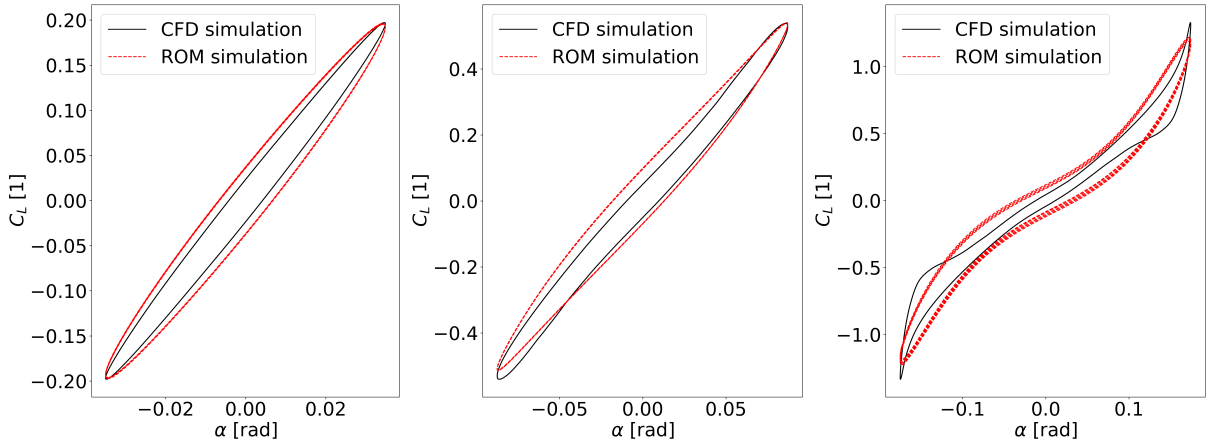

(a) $k = 0.1$, $\alpha_{amp} = 2°$ **(b)** $k = 0.1$, $\alpha_{amp} = 5°$ **(c)** $k = 0.1$, $\alpha_{amp} = 10°$

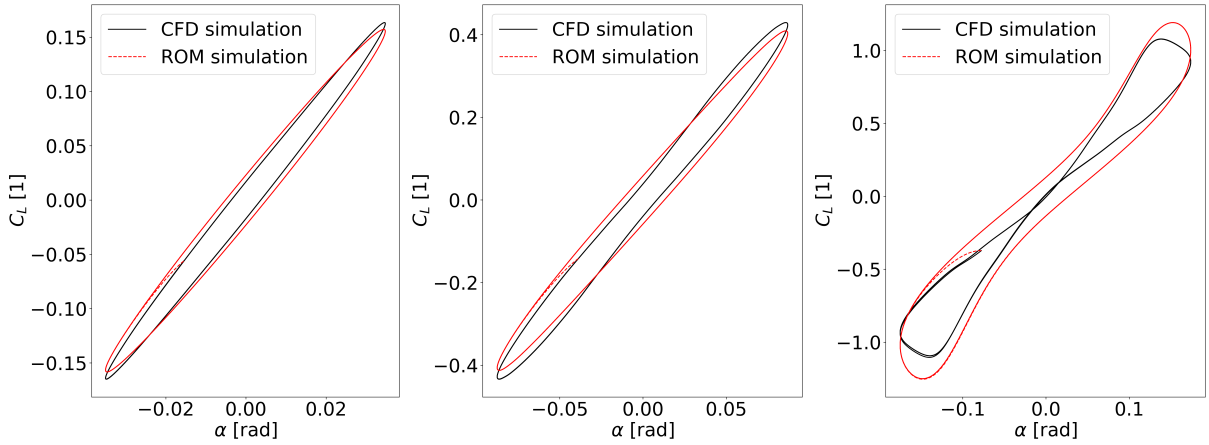

(d) $k = 0.2$, $\alpha_{amp} = 2°$ **(e)** $k = 0.2$, $\alpha_{amp} = 5°$ **(f)** $k = 0.2$, $\alpha_{amp} = 10°$

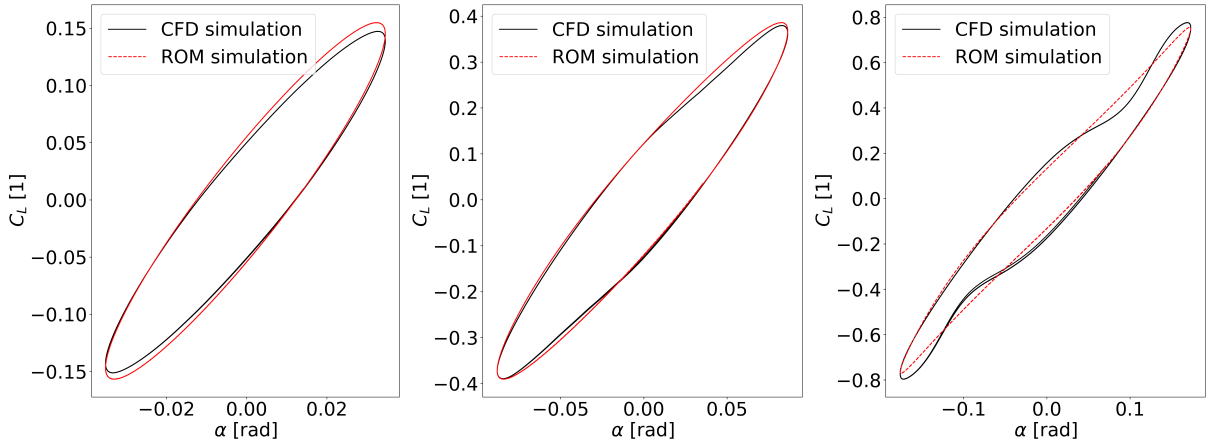

(g) $k = 0.5$, $\alpha_{amp} = 2°$ **(h)** $k = 0.5$, $\alpha_{amp} = 5°$ **(i)** $k = 0.5$, $\alpha_{amp} = 10°$

Figure 1. Comparison of the identified ROM with the CFD simulation for $k \in \{0.1, 0.2, 0.5\}$ and $\alpha_{amp} \in \{2°, 5°, 10°\}$.

Reduced frequency	c_1	c_2	c_3	c_4	c_5	c_6	c_7
$k = 0.1$	0.213	5.42	0	249	0	0	$-1.52 \cdot 10^6$
$k = 0.2$	12.2	0	-2.70	0	0	0.799	0
$k = 0.5$	4.01	6.32	-1.34	0	-56.5	0.463	0

Table 1. The coefficients of the reduced-order model Eq. (13)**.**

state variables α, $\dot{\alpha}$, C_L, where α, $\dot{\alpha}$ are considered as known inputs, which can be measured. The general form of the Reduced-Order Model (ROM) can be written as

$$\begin{aligned}\dot{C}_L(\alpha, \dot{\alpha}, C_L; k) = \quad & c_1(k)\alpha + c_2(k)\dot{\alpha} + c_3(k)C_L \\ & + c_4(k)\alpha^2 + c_5(k)\alpha\dot{\alpha} + \ldots,\end{aligned} \tag{13}$$

where a lexicographic ordering was used for the coefficients $c_i(k)$, which are listed in Table 1. The fitting procedure is relatively fast, and it takes only a couple of seconds with given optimization parameters such as λ in equations (9), (12).

For the reduced frequency $k = 0.1$, $k = 0.2$, $k = 0.5$, the lift coefficients from the CFD simulation and the fitted model as the a function of the angle of attack for oscillation amplitudes $\alpha_{amp} \in \{2°, 5°, 10°\}$ are shown in Figure 1. These reduced frequencies were chosen because they cover the region of possible values during flutter. We determined the Normed Root Mean Squared Error (NRMS) of the aerodynamic models using the formula

$$\mathrm{NRMS}_{C_L} = \frac{1}{C_{Lmax} - C_{Lmin}} \sqrt{\frac{\sum_{i=1}^{N} \left(C_L - \hat{C}_L\right)^2}{N}}, \tag{14}$$

where N is the number of data points, C_L is the CFD simulation data, $\hat{C}_L$, is the predicted value by the ROM simulation, C_{Lmax} is the maximum, while C_{Lmin} is the minimum value of the CFD simulation data. The NRMS for the three models can be found in Table 2. It can be observed that the models provide an excellent fit and can reproduce the nonlinear behavior associated with the high angle of attack and high-frequency oscillations.

Amplitude	$k = 0.1$	$k = 0.2$	$k = 0.5$
2°	2.53%	1.88%	1.66%
5°	2.45%	2.25%	0.94%
10°	3.44%	4.62%	1.61%

Table 2. The NRMS values of the identified aerodynamic models.

4. TEST CASES

In this section, we apply the identified aerodynamic models to a 2-DOF aeroelastic system. In the model, α describes the pitch (positive clockwise), while h is the plunge displacement (positive downward). The mass is m, the moment of inertia around the pitching axis is I_α, the semichord of the wing is b. The spring, and the damping coefficient for the plunge DOF is k_h, c_h, respectively, while these for the pitch are $k_\alpha(\alpha)$, c_α [24].

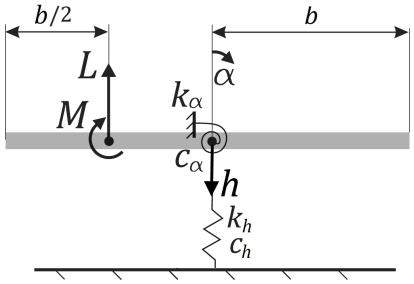

Figure 2. The 2-DOF flat plate

Equations of motion for a simple 2-DOF flat plate (see Figure 2) can be written generally as [25]:

$$m\ddot{h} + c_h\dot{h} + k_h h = -L, \tag{15}$$

$$I_\alpha\ddot{\alpha} + c_\alpha\dot{\alpha} + k_\alpha(\alpha)\alpha = M, \tag{16}$$

where L and M are the aerodynamic lift and moment, respectively. They can be calculated from the pressure distribution on the surface, i.e.

$$L = \int p d\underline{A}, \tag{17}$$

$$M = \int p x d\underline{A}, \tag{18}$$

where p is the pressure distribution, x is the distance from the point where the lift is applied.

The identified models are now applied to predict flutter for similar parameter values as the training data. We used Eq. (16) in combination with the identified models described in the previous sections to simulate flutter. It needs to be noted that the lift in this model also depends on the plunge state, but when training the SINDy models, we did not take this into account. Due to this, we used Theodorsen's lift theory to model the plunge parts of the lifts.

We have also added a cubic spring to the angular DOF to keep the vibrations inside the applicability region of the model and the better approximate reality in the process, i.e., $k_\alpha(\alpha)\alpha = k_{\alpha 1}\alpha + k_{\alpha 3}\alpha^3$. Using the identified models in Section 3, the lift force and the aerodynamic moment can be expressed as

$$L = \frac{1}{2}\rho U^2 b\left(C_L(k) + \frac{2kH_1(k)}{U}\dot{h} + \frac{2k^2 H_4(k)}{b}h\right) \tag{19}$$

$$M = \frac{1}{2}\rho U^2 b^2 \left(\frac{C_L(k)}{4} + \frac{2kA_1(k)}{U}\dot{h} + \frac{2k^2 A_4(k)}{b} h \right) \tag{20}$$

where $H_1(k), H_4(k), A_1(k), A_4(k)$ are the flutter derivatives of the heave motion [4], and $C_L(k)$ is the identified lift coefficient variable from the pitching motion. Substituting (19) and (20) into (15) and (16) we get

$$\ddot{h} + 2\omega_h \xi_h \dot{h} + \omega_h^2 h = \\ = -\frac{\rho U^2 b}{2m}\left(C_L(k) + \frac{2kH_1(k)}{U}\dot{h} + \frac{2k^2 H_4(k)}{b} h \right), \tag{21}$$

$$\ddot{\alpha} + \omega_\alpha \xi_\alpha \dot{\alpha} + \omega_\alpha^2 \alpha + q\alpha^3 = \\ = \frac{\rho U^2 b^2}{2I_\alpha}\left(\frac{C_L(k)}{4} + \frac{2kA_1(k)}{U}\dot{h} + \frac{2k^2 A_2(k)}{b} h \right), \tag{22}$$

where $q = k_{\alpha^3}/I_\alpha$ is the stiffness coefficient of the cubic spring, $\xi_h = \xi_\alpha = \xi$ is the damping factor, and ω_h, ω_α are the angular natural frequencies of the h, and α degrees of freedom. The evolution of the lift coefficient from the pitching motion is

$$\dot{C}_L(k) = \begin{array}{l} c_1(k)\alpha + c_2(k)\dot{\alpha} + c_3(k)C_L \\ +c_4(k)\alpha^2 + c_5(k)\alpha\dot{\alpha} + \ldots, \end{array} \tag{23}$$

with the coefficients listed in Table 1. We solve the model equations (21-23) numerically using the Mathematica software. For the numerical solution, we used the following initial conditions

$$\begin{array}{l} h(0) = 0.1\,\text{m},\ \alpha(0) = 0\,\text{rad},\ C_L(0) = 0, \\ \dot{h}(0) = 0\,\text{m/s},\ \dot{\alpha}(\text{rad}/s) = 0\,\text{m}. \end{array} \tag{24}$$

Figure 3 illustrates the results of the ROM simulation (Eqs. (21-23)) using the parameters from Tables 1 and 3, where $\xi_\alpha = \xi_h = \xi$.

Parameter	$k = 0.1$	$k = 0.5$
ω_h [rad/s]	0.628	3.14
ω_α [rad/s]	0.754	3.267
ξ [1]	0.1	0.1
q [1/(s^{2}rad^3)]	40	10
U [m/s]	1	3

Table 3. Parameters of the ROM

The models determined for $k = 0.1$ and $k = 0.5$ are able to reproduce flutter, as shown in Figure 3. In the case of $k = 0.2$, the simulation showed that divergence occurred, not flutter. From Table 1, it can be observed that in this model, the coefficient of $\dot{\alpha}$ is zero, while for the other two models, it is positive. So in the future, it might be useful to use constrained optimization techniques to prescribe a nonzero value of this coefficient to get more useful models. Although only three models have been fitted, it cannot be certain that this technique will result in better models, so more research is necessary in this direction.

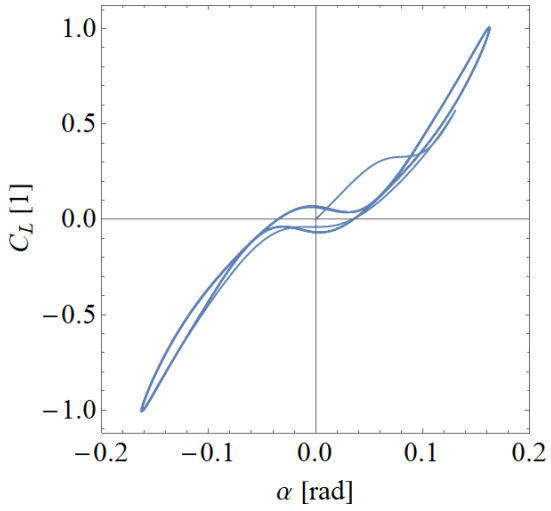

(a) $k = 0.1$

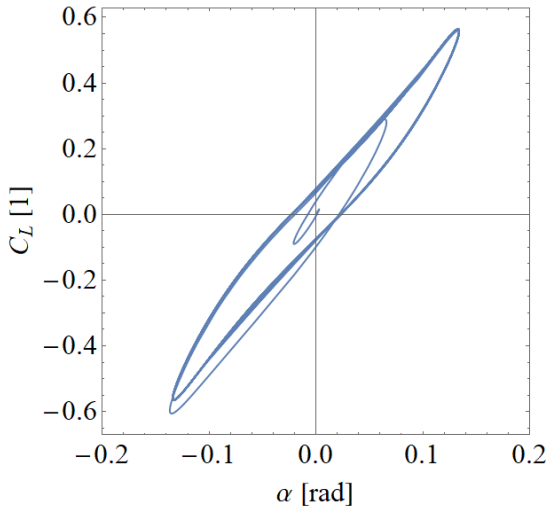

(b) $k = 0.5$

Figure 3. Dynamic lift coefficient for $k = 0.1$, and $k = 0.5$

5. CONCLUSIONS

The significant problem of creating reduced-order models for aerodynamic loads, valid for large amplitude, and frequency oscillations, was studied. The SINDy method was utilized to extract the governing differential equation of the aerodynamic lift coefficient from CFD data of a flat plate with pitching motion. This method resulted in easily interpretable, simple models. It was shown that the identified models for one particular frequency show excellent agreement with the CFD simulation data for varying amplitude oscillations. The test cases showed that some identified models could reproduce the flutter phenomenon. Suggestions to improve the optimization procedure were also given.

ACKNOWLEDGEMENTS

The research reported in this paper and carried out at BME has been supported by the ÚNKP-21-3 New National Excellence Program of the Ministry

for Innovation and Technology from the source of the National Research, Development and Innovation Fund, and the NRDI Funds (TKP2020 NC, Grant No. BME-NCS; NKFI K-21 137726) based on the charter of bolster issued by the NRDI Office under the auspices of the Ministry for Innovation and Technology. The research reported in this paper is part of project no. BME-NVA-02, implemented with the support provided by the Ministry of Innovation and Technology of Hungary from the National Research, Development and Innovation Fund, financed under the TKP2021 funding scheme.

REFERENCES

[1] Holierhoek, J., De Vaal, J., Van Zuijlen, A., and Bijl, H., 2013, "Comparing different dynamic stall models", *Wind Energy*, Vol. 16 (1), pp. 139–158.

[2] Boutet, J., and Dimitriadis, G., 2018, "Unsteady lifting line theory using the wagner function for the aerodynamic and aeroelastic modeling of 3d wings", *Aerospace*, Vol. 5 (3), p. 92.

[3] Wagner, H., 1924, "Über die Entstehung des dynamischen Auftriebes von Tragflügeln", .

[4] Theodorsen, T., 1935, "Report No. 496, general theory of aerodynamic instability and the mechanism of flutter", *Journal of the Franklin Institute*, Vol. 219 (6), p. 766–767.

[5] Peters, D. A., Karunamoorthy, S., and Cao, W.-M., 1995, "Finite state induced flow models. I-Two-dimensional thin airfoil", *Journal of Aircraft*, Vol. 32 (2), pp. 313–322.

[6] Leishman, G. J., 2006, *Principles of helicopter aerodynamics with CD extra*, Cambridge University Press.

[7] Tran, C., and Petot, D., 1980, "Semi-empirical model for the dynamic stall of airfoils in view of the application to the calculation of responses of a helicopter blade in forward flight", *ONERA*.

[8] Leishman, J. G., and Beddoes, T., 1989, "A Semi-Empirical model for dynamic stall", *Journal of the American Helicopter society*, Vol. 34 (3), pp. 3–17.

[9] Snel, H., and Schepers, J., "Joint investigation of dynamic inflow effects and implementation of an engineering method", .

[10] Snel, H., 1997, "Heuristic modelling of dynamic stall characteristics", *EWEC-CONFERENCE-*, Bookshop for Scientific Publications, pp. 429–433.

[11] Lelkes, J., and Kalmár-Nagy, T., 2021, "Analysis of a piecewise linear aeroelastic system with and without tuned vibration absorber", *Nonlinear Dynamics*, Vol. 103 (4), pp. 2997–3018.

[12] Brunton, S. L., Proctor, J. L., and Kutz, J. N., 2016, "Discovering governing equations from data by sparse identification of nonlinear dynamical systems", *Proceedings of the National Academy of Sciences*, Vol. 113 (15), p. 3932–3937.

[13] Brunton, S. L., Proctor, J. L., and Kutz, J. N., 2016, "Sparse Identification of Nonlinear Dynamics with Control (SINDYc)", *IFAC-PapersOnLine*, Vol. 49 (18), p. 710–715.

[14] Champion, K., Zheng, P., Aravkin, A. Y., Brunton, S. L., and Kutz, J. N., 2020, "A Unified Sparse Optimization Framework to Learn Parsimonious Physics-Informed Models From Data", *IEEE Access*, Vol. 8, p. 169259–169271.

[15] Silva, B. D., Champion, K., Quade, M., Loiseau, J.-C., Kutz, J., and Brunton, S., 2020, "PySINDy: A Python package for the sparse identification of nonlinear dynamical systems from data", *Journal of Open Source Software*, Vol. 5 (49), p. 2104.

[16] Kaheman, K., Kutz, J. N., and Brunton, S. L., 2020, "SINDy-PI: a robust algorithm for parallel implicit sparse identification of nonlinear dynamics", *Proceedings of the Royal Society A: Mathematical, Physical and Engineering Sciences*, Vol. 476 (2242), p. 20200279.

[17] Kaptanoglu, A. A., Callaham, J. L., Aravkin, A., Hansen, C. J., and Brunton, S. L., 2021, "Promoting global stability in data-driven models of quadratic nonlinear dynamics", *Physical Review Fluids*, Vol. 6 (9).

[18] Shea, D. E., Brunton, S. L., and Kutz, J. N., 2021, "SINDy-BVP: Sparse identification of nonlinear dynamics for boundary value problems", *Physical Review Research*, Vol. 3 (2).

[19] Brunton, S. L., Kutz, J. N., Manohar, K., Aravkin, A. Y., Morgansen, K., Klemisch, J., Goebel, N., Buttrick, J., Poskin, J., Blom-Schieber, A. W., and et al., 2021, "Data-Driven Aerospace Engineering: Reframing the Industry with Machine Learning", *AIAA Journal*, p. 1–26.

[20] Sun, C., Tian, T., Zhu, X., and Du, Z., 2020, "Sparse identification of nonlinear unsteady aerodynamics of the oscillating airfoil", *Proceedings of the Institution of Mechanical Engineers, Part G: Journal of Aerospace Engineering*, Vol. 235 (7), p. 809–824.

[21] Pohl, J., Semaan, R., and Jones, A. R., 2019, "Dynamic lift measurements on an airfoil with periodic flap motion at high Reynolds number", *AIAA Scitech 2019 Forum*.

[22] Lendvai, B., and Lelkes, J., 2021, “Aeroelasztikus szárnymodell numerikus vizsgálata: Numerical analysis of aeroelastic wing model”, *Nemzetközi Gépészeti Konferencia–OGÉT*, pp. 48–51.

[23] Lelkes, J., and Lendvai, B., 2021, “Torziós csillapító alkalmazása belebegés megszüntetésére: Application of a torsional absorber for flutter suppression”, *Nemzetközi Gépészeti Konferencia–OGÉT*, pp. 44–47.

[24] Lelkes, J., and Kalmár-Nagy, T., 2020, “Analysis of a piecewise linear aeroelastic system with and without tuned vibration absorber”, *Nonlinear Dynamics*.

[25] Dowell, E. H., Curtiss, H. C., Scanlan, R. H., and Sisto, F., 1989, *A modern course in aeroelasticity*, Vol. 3, Springer.

Conference on Modelling Fluid Flow (CMFF'22)
The 18th International Conference on Fluid Flow Technologies
Budapest, Hungary, August 30-September 2, 2022

Classification of Percolation Clusters with Artificial Neural Networks

Kálmán Kustány[1], Gergely Hajgató[2], Bendegúz Dezső Bak[3], Tamás Kalmár-Nagy[4]

[1] Corresponding Author. Department of Fluid Mechanics, Faculty of Mechanical Engineering, Budapest University of Technology and Economics. Bertalan Lajos u. 4 - 6, H-1111 Budapest, Hungary. Tel.: +36 1 463 2464, Fax: +36 1 463 3464, E-mail: kalman.kustany96@edu.bme.hu
[2] Department of Telecommunications and Media Informatics, Faculty of Electrical Engineering and Informatics, Budapest University of Technology and Economics. E-mail: ghajgato@tmit.bme.hu
[3] Department of Fluid Mechanics, Faculty of Mechanical Engineering, Budapest University of Technology and Economics. E-mail: bak@ara.bme.hu
[4] Department of Fluid Mechanics, Faculty of Mechanical Engineering, Budapest University of Technology and Economics.

ABSTRACT

The classification capabilities of artificial neural networks (ANNs) were examined in the study focusing on recognizing 2-dimensional percolating lattices. The performance of a classifier based on a multi-layer perceptron (MLP) was compared to a classifier based on a convolutional neural network (CNN). A large number of lattices were generated with different occupation probabilities from 0 to 1 to form a dataset that was split in three different ways to find out the possible difficulties of the learning.

While the classification recall was above 77% for each ANN in each case, significant differences were seen when the data were imbalanced. In such cases, the CNN-based classifier clearly outperformed the one based on MLP in recognizing the lattices of the underrepresented kind.

When the ANNs were trained on 4397 samples drawn randomly uniform from the full dataset, both of the networks achieved a similar recall being the CNN the better with a recall of ≈ 0.93. Moreover, the CNN-based classifier achieved a higher recall in general in all three cases suggesting its superiority compared to the MLP for recognizing percolating lattices.

Keywords: artificial neural networks, convolutional neural network, machine learning, multilayer perceptron, percolation, supervised learning

1. INTRODUCTION

The development and usability of machine learning (ML) algorithms went through a massive upsurge in the last decades due to the increasing computational capacity and the rapidly growing amount of available data. The main tools can be roughly divided into three large groups: supervised, unsupervised, and reinforcement learning. Supervised techniques fit labeled datasets while unsupervised methods are able to learn useful features in the absence of labels. Reinforcement learning is based on agent-environment interaction which is useful for learning control policies or to learn from such datasets where the loss function cannot be described by an exact mathematical formula.

Artificial neural networks (ANNs) are widely used for classification due to the fact that they are universal function approximators [1]. Owing to this property, ANNs were successfully applied in the field of computer vision, natural language processing, recommendation systems, etc. Besides these, ANNs have also been adapted in science and engineering – such as in this case – for the classification of percolating lattices [2, 3, 4, 5].

Percolation theory is applied in the field of mercury porosimetry (among others) that was investigated by Bak and Kalmár-Nagy in [6]. Mercury porosimetry is applied to specify the pore size distribution of rock samples primarily in the oil industry. During the process, the mercury is forced into the sample with constantly increasing pressure while the volume of the injected mercury is measured vs. the applied pressure, which is the saturation curve. In practice, this curve is assumed to be directly related to the cumulative pore size distribution. On the other hand, the real distribution of the pore size does not coincide with the cumulative pore size distribution because of the "non-accessibility" of the pores at a given pressure. The goal of the study by Bak and Kalmár-Nagy was to determine a more accurate cumulative pore size distribution which was achieved by treating the mercury propagation as a percolation process. Their results showed a good agreement between the experimental saturation curve and those

obtained from their method [6, 7, 8].

Bottiglione et al. [9] used percolation theory and contact mechanics to investigate fluid leakage through seals. They observed that it is not enough to have a partial connection between the sealing surfaces (because of the surface roughness) but a channel has to be also formed from the previously independent chambers to have leakage. This phenomenon can be effectively described by percolation theory.

Zhao et al. [10] studied the conductivity of liquid metal embedded elastomers (LMEEs). These elastomers have attracted interest from researchers due to their low elastic modulus, tunable electrical and/or thermal conductivity, and high flexibility. One impressive feature of LMEEs is that their electrical resistance stays constant when stretched, which means that the resistance is no longer proportional to the length of the conductive material if only a moderate length change occurs. This feature makes LMEEs desirable in real-world applications. During the research, finite element analysis was carried out to examine the electromechanical coupling response of a percolated liquid droplet. After that, they generalized the results to a network of LMEE droplets.

Salt caverns are a promising opportunity to store renewably produced hydrogen underground to reduce CO2 emissions by enhancing the utilization of volatile renewable energy sources. Rock salt is able to reduce the infiltration of hydrogen into the cavern walls due to its low permeability. Nevertheless, the pressure-driven percolation effect may form discrete pathways for the fluid through the walls which cause damage in the cavern. Zill et al. [11] created a model which shows good agreement with the pressure-driven percolation of hydrofracturing experiments.

Based on the researches mentioned above, the advantage of training of neural networks to learn percolation is unambiguous. Here we focus on using two types of neural nets, the multi-layer-perceptron (MLP) and the convolutional neural network (CNN) with approximately the same number of trainable parameters, train them for the classification of percolation lattices, and compare the accuracies of these nets. After that, we investigate the effect on the accuracy of different training datasets.

The outline of this paper is as follows. In Sec. 2 we introduce the basic concept of percolation theory and the algorithm we used to generate the percolating lattices for classification. Sec. 3 contains the general background for those kind of artificial neural networks that were used in this study. After that, we describe the training dataset and the parameters of the neural nets in Sec. 4. Sec. 5 and Sec. 6 contain the results and the conclusion, respectively.

2. PERCOLATION THEORY

Percolation theory and percolation models have been developed for a differing range of applications such as fractal diffusion, the conductivity of semiconductors, or modeling fluid propagation through a porous medium. Percolation theory studies the properties of lattice clusters. The simplest problems in percolation theory are site-percolation and bond-percolation whose schematics can be seen in Fig. 1.

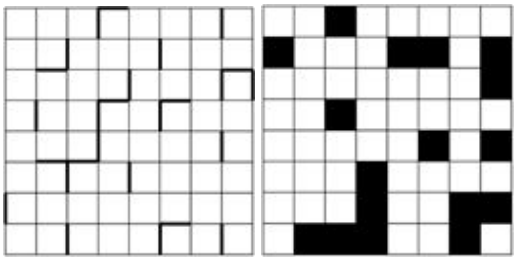

Figure 1. Bond percolation (left) and site percolation (right).

These percolation models deal with lattices in which a site/bond can be occupied with probability p (occupation probability). A group of neighboring occupied sites/bonds is called a cluster. A cluster that connects the top and bottom sides of the lattice is called spanning cluster. The existence of a spanning cluster means that the modeled fluid percolated through the lattice. Fundamental questions in percolation theory is whether a spanning cluster exists and how the existence of spanning clusters is dependent on the occupation probability p. There is a percolation threshold (p_c) which refers to the critical occupation probability. Under this value, the probability that a spanning cluster exists is zero in infinite lattices. On the other hand, for $p > p_c$, the probability that a spanning cluster exists is one. Thus, percolation theory can be thought of as the study of a geometrical phase transition, since at a critical fraction of addition the network of small, disconnected clusters merge into a spanning cluster (visual representation can be seen in Fig. 2).

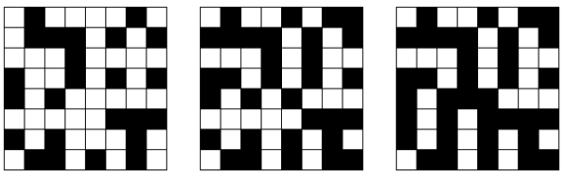

Figure 2. Lattices with different occupation probabilities.

3. ARTIFICIAL NEURAL NETWORKS

Feed-forward artificial neural networks stem from biological neural networks, but the similarities should be examined only from a sufficiently distant view. As it was mentioned before, neural nets are widely used due to their flexibility which ensures the fact that the architecture can be constructed from dif-

ferent types of building blocks. In this research, the multi-layer perceptron and the convolutional layer are used in the network architecture and the theory behind these building blocks is detailed here.

3.1. Multi-layer perceptron

The basic calculation unit of such a network is the perceptron which receives different signals on its input, multiplies each input with a corresponding weight, sums them up, and applies a nonlinear function on the summation. The nonlinear function is called activation function in the machine learning terminology and its output is the output of the perceptron. The weights quantify the importance of the specific input values regarding to the output and the activation function ensures that the summed output of multiple perceptrons can mimick the output of general functions. The schematic of a standalone perceptron is shown in Fig. 3.

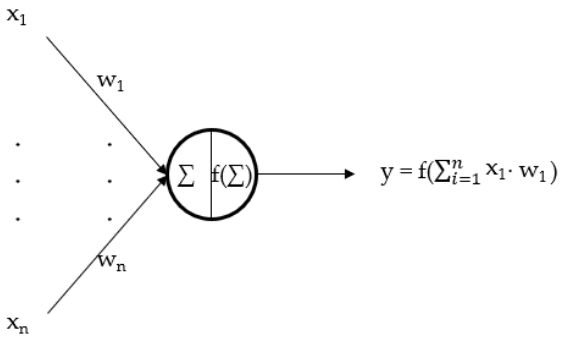

Figure 3. Schematic representation of a perceptron.

In order to enable the higher level feature and pattern recognition with a neural network, the perceptrons are arranged into layers and layers are stacked into a network which is called multi-layer perceptron. Such a network is shown in Fig. 4.

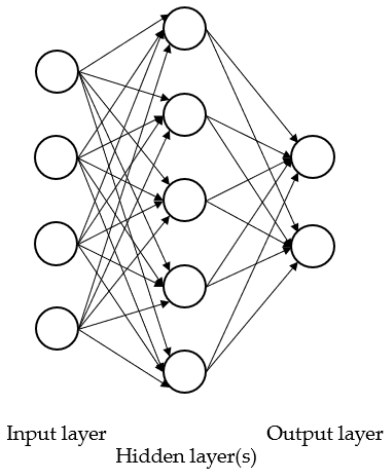

Figure 4. Example of a multi-layer perceptron.

With this arrangement, the network is able to learn abstract features from the data, which is desirable in real-world applications. The first layer of a network is the input layer, thereafter come the so-called hidden layers and at the end of the network is the output layer. If every neuron inside a specific layer is connected to every neuron in the previous layer (in other words: if the output signal of the neurons in the preceding layer is fed to the input of all the neurons in the actual layer), the two layers are densely or fully connected.

To evaluate the accuracy of a neural net, a loss function (or cost function) is needed, which expresses the difference between the ground truth and the output calculated by the network regarding to a specific input. The loss function can be minimized by finding the optimum set of weights for the perceptrons in the ANN. As the ANN builds up from elementary activation functions (like the sigmoid or the tanh function), the contribution of each perceptron to the overall error on the output can be calculated by the backpropagation of the error calculated with the loss function. This process is called training in the machine learning terminology. Since calculating the gradient with respect to the loss is cheap, even traditional gradient seeking methods like gradient descent are suitable for training ANNs.

3.2. Convolutional neural network

Convolutional layers are able to capture the features of the data with less layers compared to MLPs if the relevant features are small compared to the dimensionality of the input which means the size of the input of a layer (or the network). The most obvious example is image recognition where the elementary building blocks like edges are small compared to the full image.

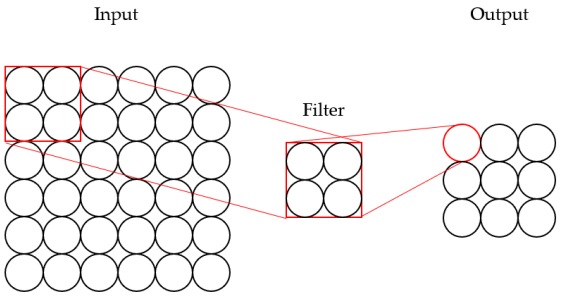

Figure 5. Schematic of the convolutional filter.

The convolutional layer applies a filter on the input where the filter size is smaller than the input size. The output of the layer is the convolution of the filter and the input or in other words it is the element-wise product of the filter and the appropriate parcel of the data where the filter is applied which leads to the reduction of the dimension as seen in Fig. 5.

This structure allows the filters to learn smaller features that are reoccurring in the input regardless on their exact location. This property makes them

ideal for image recognition tasks where topologies built on convolutional neural networks dominate the state-of-the-art in the recent years [12, 13, 14].

4. METHODOLOGY

4.1. Datasets

The dataset for training and evaluating the classifier is based on lattices generated by the Hoshen-Kopelman algorithm [15] . 5000 8-by-8 lattices were generated with different occupation probabilities (from 0 to 1 with stepsize 0.01) and they were labeled according whether they are percolating or not. The duplicates were filtered thereafter in order to avoid biased data that yielded 220996 unique lattices. The filtered dataset is referred to as the full dataset. The distribution of the percolating and the non-percolating lattices in the full dataset are seen in Fig. 6.

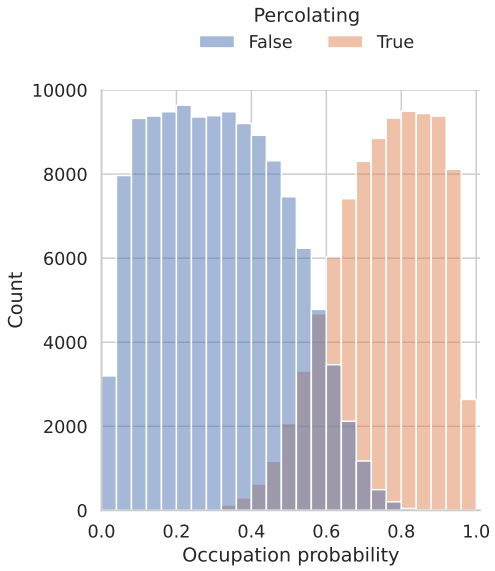

Figure 6. Histogram of the percolating and non-percolating lattices in the full dataset.

For 2D lattices the critical occupation probability is ≈ 0.593. Fig. 6 shows that non-percolating lattices are over-represented where occupation probability is subcritical and percolating lattices are over-represented for supercritical occupation probabilities (the drops for occupation probabilities near 0 and 1 are due to the much smaller number of lattices resulting from the removed duplicates).

The dataset was split to training, validation, and test sets in three different ways to examine the capabilities of the ANNs in case of different data distributions. These cases are referred to as *case A*, *case B*, and *case C*. As the aim of the study was to compare the multi-layer perceptron and the convolutional neural network in terms of prediction accuracy, the number of training samples was kept low compared to the test samples in each of the cases.

In *case A*, training data were selected as the portion of the full dataset with an uniform random distribution. The 1% of the full data were allocated for training and an additional 1% of the data were allocated for validation. The rest of the data were used purely for testing the accuracy of the trained models. *case A* models such cases where samples of all kinds (all occupation probability) are available for training; hence, it is considered as an easy case to learn.

In *case B*, lattices generated by occupation probabilities smaller than 10% and greater than 90% were allocated for training and validation while the rest of the data were allocated for testing. The training-to-validation ratio was 4 : 1. In this case, the model was trained on sparsely and densely occupied lattices only and was tested on almost every kind of lattices thereafter. Thus, it is considered a harder case to learn than *case A*.

Lattices belonging to most of the occupation probabilities were excluded from the training data in *case B*. This difficulty was tried to increase in *case C* by including lattices with such occupation probabilities that yield to an imbalanced training dataset. Training data were selected according to occupation probability between 20% and 45% which yielded a skewed data distribution. The rest of the data were used for testing, the training-to-validation ratio was again 4 : 1.

Both in cases *B* and *C* the validation data were selected according to a uniform random distribution from the data allocated for training and validation. The data distributions are visualized in Fig. 7 with the number of samples indicated in the captions of the histograms.

4.2. Neural network architectures

There are many practical applications that could benefit from a classifier that can decide whether a 2D lattice percolates or not. However, there is no best practice on creating such classifiers; hence, two ANNs built from different kinds of layers were investigated in this study to find out whether CNNs are outperforming MLPs in this task as they do in computer vision problems. In order to do a fair comparison, the architectures were created in such a way that the number of the trainable parameters – that refers to the expression capacity of the ANN – were almost the same for the two networks. Moreover, the activation functions of the artificial neurons were rectified linear units (ReLU) in both networks. The lattices were fed to the classifiers as 2D arrays and the classifiers gave a probability $p \in [0, 1]$ on whether the lattice is percolating in return. The error of the prediction was quantified with the binary cross-entropy during the training and this error was backpropagated to the individual neurons.

The lattices were flattened in the first place in the MLP and the 64 input dimensions were fed to 2 hidden layers. Both layers utilized 4 neurons with ReLU activations and the prediction was given by a

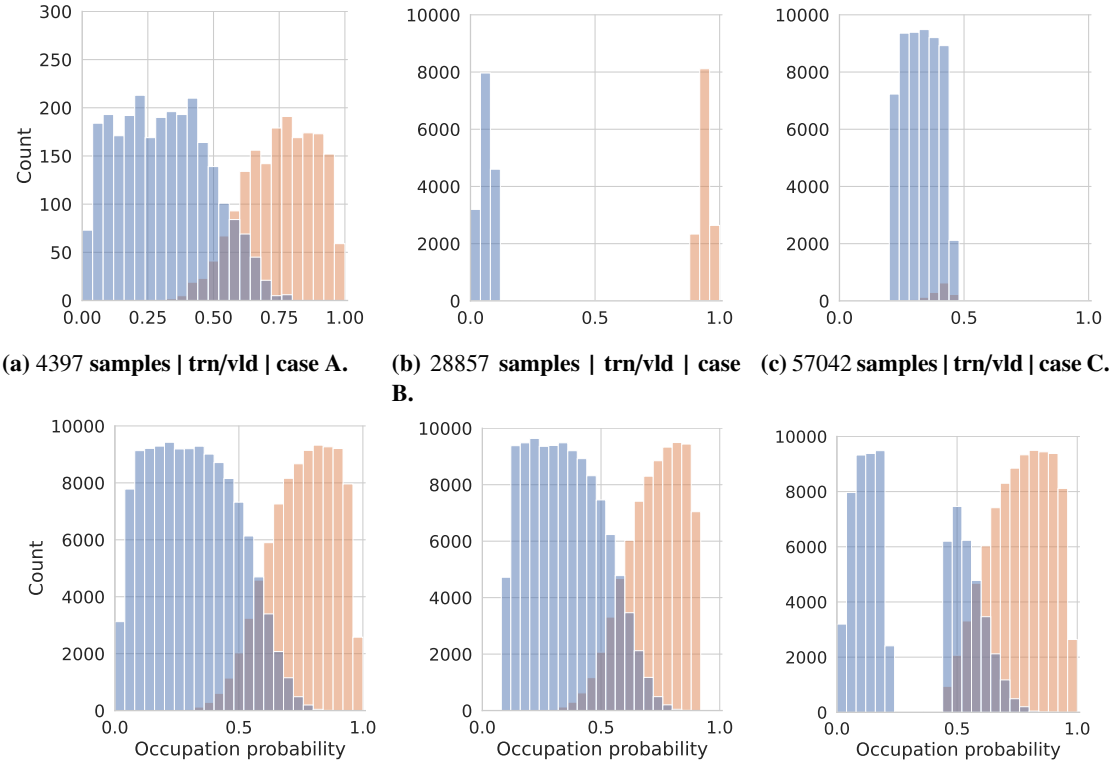

(a) 4397 **samples | trn/vld | case A.** **(b)** 28857 **samples | trn/vld | case B.** **(c)** 57042 **samples | trn/vld | case C.**

(d) 216599 **samples | tst | case A.** **(e)** 192139 **samples | tst | case B.** **(f)** 163954 **samples | tst | case C.**

Figure 7. Histograms of the training/validation data (trn/vld) and the test data (tst) for the different cases.

single neuron activated by the softmax function.

The CNN was able to handle the lattices without transformation by nature; hence, the input was directly fed to the convolution layers. 3 convolution layers were utilized in sequence with 3 filters of size 2x2, and a convolution layer with only 1 filter of the same size as before. The output of the last convolution was flattened yielding a 16 dimensional latent representation of the lattice. This representation was fed to 2 dense layers with 8 and 4 neurons in sequence. The output of the last dense layer was fed to a classifying neuron utilizing the softmax function as its activation as in the case of the MLP.

The number of trainable parameters were 284 and 282 for the MLP and the CNN, respectively. These numbers are so small that no overfitting of the ANNs was suspected; hence, no attempt was taken in order to regularize the weights during the training. The weights were aligned according to the error calculated on the training data and the out-of-sample accuracy of the network was calculated on the validation data. The training was stopped after the validation accuracy did not rose for 30 consecutive epochs while the weights of the classifier were saved when the validation accuracy reached its maximum.

5. RESULTS

The MLP and the CNN were trained multiple times for each cases to examine the effect of random weight initializations. As the loss surface can have many local minima, different weight initializations can lead to different results even if the topology and the other hyperparameters are kept the same.

This disadvantageous behavior could be observed in *case B* and in *C*, but could not be observed in *A*. Hence, the trainings were repeated three times for *case B* and for *case C* for both topologies and the results were averaged over the repetitions.

The trainings were similar regarding the training and validation losses and the accuracies; hence, only a typical learning curve is depicted in Fig. 8. The closeness of the training and the validation curve indicates that omitting the regularization of the trainable parameters was a safe choice for this study.

In order to compare the accuracy of the different architectures in the different cases, the model weights were loaded back after each training and the model performance was evaluated on the test data. The results are visualized as confusion matrices in Fig. 9, while the corresponding data distributions are to be found in Fig. 7.

A good classification accuracy was achieved with both topologies in *case A*. This case was the only one wherein the training and the testing data shared the same distribution. Despite the size of the training data was greatly reduced compared to the other cases, it was not a difficulty for neither of the ANNs to achieve a recall over 90% for percolating and non-percolating lattices.

Case B presented a harder task and this fact is reflected in the recall metrics as well. Both topologies'

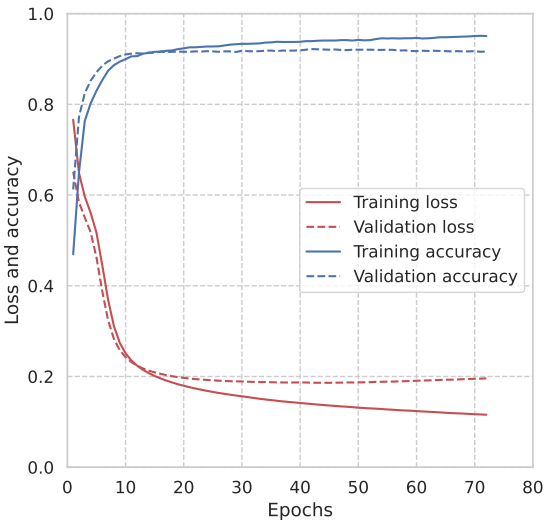

Figure 8. Learning curves of a typical training.

performance degraded in classifying non-percolating lattices but the MLP showed a worse performance than the CNN. However, the MLP performed better in classifying percolating lattices in contrast. Data distribution explains the bias of the recall towards the percolating lattices: these kind of lattices are a bit over-represented in the training and validation dataset compared to the non-percolating ones.

While the recalls provided by the MLP and the CNN were comparable in *B*, the CNN clearly outperforms the MLP in *case C*. The training and validation dataset contained almost twice as much lattices than in *case B* but the data distribution was strongly skewed as depicted in Fig. 7. While the MLP was able to achieve a recall of almost 80% for the underrepresented kind of data (percolating lattices), the CNN achieved a recall of 93.9% for the same lattices.

6. SUMMARY

The capabilities of ANNs were examined in this study on the classification of percolating lattices. The focus was on the comparison of the MLP and the CNN layer types as the latter represents the state-of-the-art for common image recognition tasks.

Two different classifiers were constructed with similar modeling capacity based on the two layer types and a comprehensive dataset was generated including more than 220000 unique 2D lattices with occupation probabilities spanning the range from 0 to 1. Three different test cases were set up to find out the behavior of the classifiers when their training data suffers from different difficulties.

Both the MLP and the CNN performed well when they were trained on a reduced dataset, achieving a recall above 90% for each kind of lattices. Although the CNN recognized non-percolating lattices a slightly better than the MLP, the difference was considered marginal.

The second test case contained a slightly imbalanced dataset but with training samples selected with extreme occupation probabilities that were close either to 0 either to 1. The CNN classifier gave slightly more accurate predictions for the underrepresented type of lattice than the MLP but both of the ANNs showed a degraded accuracy on recognizing that kind of lattice compared to the other.

The third case contained a larger but strongly imbalanced dataset than the second case. The CNN clearly outperformed the MLP in this case by giving a decent (above 90%) recall on both the under- and the overpresented kind of lattices.

The overall high accuracy of the CNN-based classifier and its superiority compared to the classifier based on MLP suggests that CNNs should be considered in the first place for the recognition of percolating lattices. This decision is also supported by the fact that real-world datasets are often imbalanced as is the case e.g. with the recognition of surface cracks in rocks [16]. When the imbalanced data cannot be cured with data augmentation, CNN-based classifiers can still deliver acceptable accuracies according to the findings of the present study.

REFERENCES

[1] Cybenko, G., 1989, “Approximation by superpositions of a sigmoidal function”, *Mathematics of Control, Signals, and Systems*, Vol. 2 (4), pp. 303–314.

[2] Zhang, W., Liu, J., and Wei, T.-C., 2019, “Machine learning of phase transitions in the percolation andXYmodels”, *Physical Review E*, Vol. 99 (3), p. 032142.

[3] Yu, W., and Lyu, P., 2020, “Unsupervised machine learning of phase transition in percolation”, *Physica A: Statistical Mechanics and its Applications*, Vol. 559, p. 125065.

[4] Kamrava, S., Tahmasebi, P., Sahimi, M., and Arbabi, S., 2020, “Phase transitions, percolation, fracture of materials, and deep learning”, *Physical Review E*, Vol. 102 (1), p. 011001.

[5] Bayo, D., Honecker, A., and Römer, R. A., 2021, “Machine learning the 2D percolation model”, `2111.13116`.

[6] Bak, B. D., and Kalmár-Nagy, T., 2017, “Porcolation: An Invasion Percolation Model for Mercury Porosimetry”, *Fluctuation and Noise Letters*, Vol. 16 (01), p. 1750008.

[7] Vizi, M. B., Mizsák, P. Á., and Kalmár-Nagy, T., 2018, “Saturation in Regular, Exotic and Random Pore Networks”, *Fluctuation and Noise Letters*, Vol. 17 (03), p. 1850024.

[8] Bak, B. D., and Kalmár-Nagy, T., 2021, “A Size-Perimeter Discrete Growth Model for Percolation Clusters”, *Complexity*, Vol. 2021, pp. 1–16.

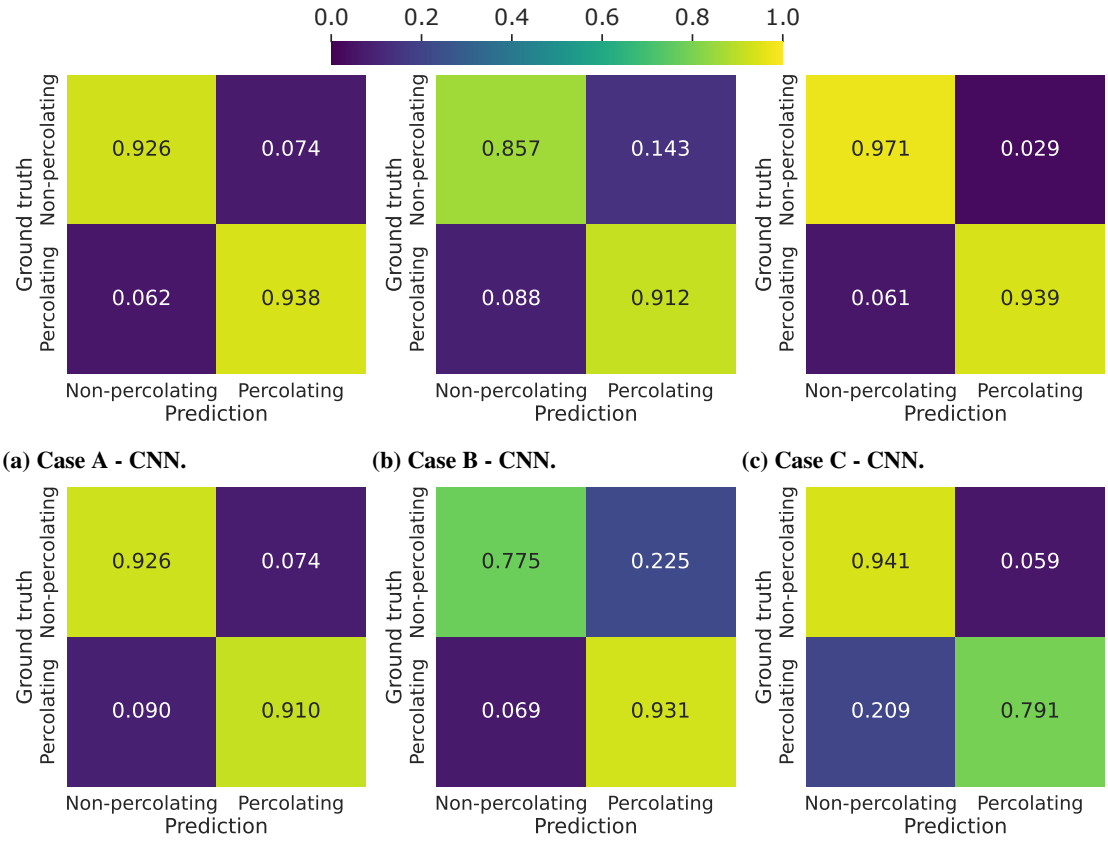

(a) Case A - CNN. **(b) Case B - CNN.** **(c) Case C - CNN.**

(d) Case A - MLP. **(e) Case B - MLP.** **(f) Case C - MLP.**

Figure 9. Accuracies reached on the test data sets. Numbers indicate the recall: the number of predictions related to the number of lattices in the corresponding ground truth category.

[9] Bottiglione, F., Carbone, G., and Mantriota, G., 2009, "Fluid leakage in seals: An approach based on percolation theory", *Tribology International*, Vol. 42 (5), pp. 731–737.

[10] Zhao, Y., Khandagale, P., and Majidi, C., 2021, "Modeling electromechanical coupling of liquid metal embedded elastomers while accounting stochasticity in 3D percolation", *Extreme Mechanics Letters*, Vol. 48, p. 101443.

[11] Zill, F., Lüdeling, C., Kolditz, O., and Nagel, T., 2021, "Hydro-mechanical continuum modelling of fluid percolation through rock salt", *International Journal of Rock Mechanics and Mining Sciences*, Vol. 147, p. 104879.

[12] Krizhevsky, A., Sutskever, I., and Hinton, G. E., 2012, "ImageNet Classification with Deep Convolutional Neural Networks", F. Pereira, C. J. C. Burges, L. Bottou, and K. Q. Weinberger (eds.), *Advances in Neural Information Processing Systems*, Curran Associates, Inc., Vol. 25, pp. 1–9, URL `https://proceedings.neurips.cc/paper/2012/file/c399862d3b9d6b76c8436e924a68c45b-Paper.pdf`.

[13] Szegedy, C., Liu, W., Jia, Y., Sermanet, P., Reed, S., Anguelov, D., Erhan, D., Vanhoucke, V., and Rabinovich, A., 2015, "Going deeper with convolutions", *2015 IEEE Conference on Computer Vision and Pattern Recognition (CVPR)*, IEEE, pp. 1–9.

[14] He, K., Zhang, X., Ren, S., and Sun, J., 2016, "Deep Residual Learning for Image Recognition", *2016 IEEE Conference on Computer Vision and Pattern Recognition (CVPR)*, IEEE, pp. 770–778.

[15] Hoshen, J., and Kopelman, R., 1976, "Percolation and cluster distribution. I. Cluster multiple labeling technique and critical concentration algorithm", *Physical Review B*, Vol. 14 (8), p. 3438.

[16] Alzubaidi, F., Mostaghimi, P., Si, G., Swietojanski, P., and Armstrong, R. T., 2022, "Automated Rock Quality Designation Using Convolutional Neural Networks", *Rock Mechanics and Rock Engineering*.

Conference on Modelling Fluid Flow (CMFF'22)
The 18th International Conference on Fluid Flow Technologies
Budapest, Hungary, August 30-September 2, 2022

A METHODOLOGY FOR THE BLADE SHAPE OPTIMISATION OF A VERTICAL AXIS TIDAL TURBINE UNDER CONSTRAINTS

Karla RUIZ HUSSMANN[1], Pierre-Luc DELAFIN[3], Cyrille BONAMY[3], Yves DELANNOY[3], Dominique THÉVENIN[2], Stefan HOERNER[2]

[1] Corresponding Author. Laboratory of Fluid Dynamics and Technical Flows, Institute of Fluid Dynamics and Thermodynamics, Otto von Guericke University, Magdeburg, Germany and Univ. Grenoble Alpes, CNRS, Grenoble INP, LEGI, 38000 Grenoble, France, E-mail: karla.ruiz@ovgu.de
[2] Laboratory of Fluid Dynamics and Technical Flows, Institute of Fluid Dynamics and Thermodynamics, Otto von Guericke University, Magdeburg, Germany
[3] Univ. Grenoble Alpes, CNRS, Grenoble INP, LEGI, 38000 Grenoble, France

ABSTRACT

Hydrokinetic vertical axis turbines have found use in the field of tidal energy exploitation as they can operate under varying flow directions. Due to the vertical rotation axis, the blades undergo continuous variations of the angles of attack, resulting in alternating forces on the turbine structure. This may lead to structural damage and fatigue failure. By actively and continuously pitching the turbine blades, it is possible to reduce these forces and to improve the power coefficient of the turbine. For this reason the OPTIDE project aims at developing a Darrieus turbine with an active, variable blade pitch. A customized actuator will be embedded in the blades for improved flow characteristics. The aim of this paper is to describe the methodology for the optimisation process needed to find the optimal blade shape, suitable to fit the actuation system at quarter chord with best hydrodynamic properties. The optimisation consists of a computational fluid dynamics (CFD) simulation coupled with a Genetic Algorithm (GA). OPAL++, the optimisation software used in this work, outputs ten design variables, which, together with the constraining points of the actuator, describe the hydrofoil shape. These points are imported into a *Python* script to interpolate the full hydrofoil shape with use of a Bézier spline curve, which is then uploaded into the automatised meshing tool. The subsequent numerical simulation provides the power and thrust coefficients of each individual setup, i.e., the objectives of the optimisation.

Keywords: active variable pitch, blade shape optimisation, CFD, Vertical Axis Tidal Turbine

NOMENCLATURE

D	$[mm]$	Diameter
N	$[-]$	Number of blades
P	$[W]$	Power output
P_∞	$[W]$	Power of the flow
R	$[mm]$	Radius
c	$[mm]$	Chord length
c_p	$[-]$	Power coefficient
v_∞	$[m/s]$	Velocity of the free stream
λ	$[-]$	Tip-speed ratio
ω	$[rad/s]$	Angular velocity
σ	$[-]$	Solidity

1. INTRODUCTION

In 2020 a global energy consumption of 556.63 EJ was recorded, from which only 69.87 EJ were covered by renewable energy [1]. In order to achieve the energy transition from fossil to renewable energy it is necessary to increase the amount of renewable energy installed worldwide. The most implemented renewable energies nowadays are wind, solar and hydropower. Out of these, hydropower is independent of weather-dependent fluctuations and therefore represents a reliable energy source. Conventional hydroelectric power plants usually reach high efficiencies by taking advantage of the potential energy of the water [2]. In order to reach sufficient hydraulic head, these water turbines need support structures such as dams. Apart from being cost-intensive, these dams are not environmentally friendly as they alter natural waterways and therefore affect the local ecosystems. In addition the expansion of conventional hydropower is currently stagnating as most of the potential sites worldwide are already being exploited [3].

However, ocean energy is one branch of hydropower which still shows a large untapped potential. It is projected that by 2030 around 10 GW of ocean energy could be installed worldwide [4], out of which until 2020 only 527 MW have been installed [5]. Ocean energy is divided into tidal, wave,

salinity gradient, and ocean thermal energy conversion (OTEC) out of which the tidal energy has the highest installed capacity [4]. Tidal turbines work similar to wind turbines as they only use the kinetic energy of the flow. Therefore, these kind of turbines do not need significant support or guiding structures and present easier constructions as well as a lower impact on the environment [6].

Similar to wind turbines, tidal turbines can be classified into two categories: vertical-axis turbines (VAT) and horizontal-axis turbines (HAT). In this project the focus will be set on VAT or so-called cross flow turbines, which have their axis perpendicular to the incoming flow (see Fig. 1) [7]. One of the main advantages of these cross-flow turbines is that they are omni-directional, meaning that they operate independently from the direction of the flow [6, 8]. This characteristic makes them extremely suitable for the operation in tidal currents or unsteady flows [6]. Due to the vertical axis it is also possible to position the electrical drive system above the water level, making it easily reachable for maintenance [9, 10, 11]. One of the most important advantages of hydrokinetic turbines with a vertical axis is that they feature a magnitude higher area-based power density in farm installations compared to HAT [12].

Darrieus turbines, feature bad self-starting characteristics as the angle of attack of each blade varies during one rotating cycle of the turbine leading to stall [9]. Due to the occurring stall on the turbine blades, the rotor also experiences complex rotor dynamics, which lead to high structural loads, vibrations and significantly lower efficiencies compared to HAT [6, 13, 11]. This being one of the biggest drawbacks of Darrieus turbines it is necessary to reduce the occurring stall as much as possible.

Different approaches can be found in order to increase the efficiency of Darrieus turbines. One typical approach of the optimisation process is to change typical geometrical design features, such as the hydrofoil shape as well as the solidity of the turbine [2, 14]. The solidity σ of a turbine comprises the number of blades, the cord length and the turbine radius, and is one of the main parameters used to describe the geometry of a VAT [15]. It is defined by the following equation: $\sigma = \frac{Nc}{R}$, where N is the number of blades, c the chord length of one blade and R the rotor radius. *Shiono et al. (2000)* found in an experimental study that the efficiency of Darrieus turbines for tidal power generation increases with decreasing number of blades N. Meanwhile the starting torque increases with a higher amount of blades, while at the same time torque ripple decreases [16]. In general a global tendency to three-bladed turbines is observed as they feature lower manufacturing costs, less drag force induced by the support structure and a lower torque ripple [2, 17, 11].

By optimizing the hydrofoil shape of a VAT it is possible to increase the turbine efficiency and reduce the occurring stall, which might improve the self-starting capacity of the turbine [9]. *Mohamed (2012) and Hashem (2018)* analysed different symmetric and cambered airfoils for a Darrieus wind turbine with constant solidity in order to increase the overall output power coefficient c_p, which is defined by the ratio between the power output of the turbine (P) and the power of the flow crossing the swept-area of the turbine (P_∞). They both found that the S-1046 profile performs best [15, 18]. Another approach is to couple CFD simulations with an evolutionary algorithm in order to find the best suitable hydro- or airfoil shape for the desired application. *Daróczy et al. (2018)* coupled GA with CFD simulations in order to find the best airfoil shape for an H-Darrieus turbine [19]. *Yang and Shu (2012)* optimised the hydrofoil shape of a helical vertical axis turbine and were able to increase the power output to 41.2%, compared to a classical NACA0012 that only reaches 32.9% [7]. Similar optimisations were done by [20, 21].

Besides varying the number of blades and optimizing the hydrofoil shape, pitching the turbine blades during the turning cycles can eliminate blade stall and therefore increase the turbine efficiency and deliver high starting torque [9]. Pitching can be passive, where the blade is allowed to move freely, or active, where the blade is mechanically driven to a specific angle of attack. *Ridho Hantoro et al. (2011)* found that passive pitching of the blades of vertical axis tidal turbines increases the capability of self rotating, while it decreased the potency of stall [22]. Still, the effect of passive pitching is rather arguable [9]. Otherwise, many studies have shown the effectiveness of active blade pitching and the impact of different pitching laws [11, 10, 8, 6]. For instance, CFD simulations by *Hwang et al. (2009)* showed that a cycloidal pitching motion increases the turbine performance by 70%. Further simulations demonstrated, that an individual blade pitching is able to improve the performance by around 25% compared to the cycloidal pitching motion. Unfortunately, validation experiments with the cycloidal motion revealed quite lower performance values than the simulations. This was due to drag forces of the mechanical pitching device, which featured a central actuator on the turbine shaft with rods as a mechanical transmission to the blades [17]. *Liang et al. (2016)* equipped each blade with a servomotor, which allows the individual pitching of each blade [23]. As the drives are positioned outside of the blade structure they are unfavorable to hydrodynamics, leading again to increased drag forces, which reduce the overall turbine performance.

Although further research on the mechanical implementation of active pitching needs to be done, it can clearly be seen, that individual pitching increases the turbine efficiency and is able to decrease stall, vibration and both torque and thrust ripples [11]. For this reason the OPTIDE project aims at developing a H-Darrieus tidal turbine, which integrates the in-

dividual pitching actuator in each blade. Figure 1 shows the current prototype of the OPTIDE turbine. The idea of the project is to explore the effects of an optimised pitch motion law through CFD and experimental research. Besides delivering validation data, flume tank experiments will be performed in order to optimise the pitching law. State-of-the-art instrumentation, providing data describing the turbine performance, will be coupled with an optimisation algorithm in order to achieve an optimal pitching trajectory. As mentioned before, in order to improve flow characteristics the pitching actuator shall be positioned inside each turbine blade. For this reason, the blades are connected to the turbine shaft through two blade support structures (at the top and bottom of the blades). This way it is also possible to have a discontinuous shaft, which does not affect the flow in the cross-section of the turbine.

Figure 1. 3D Model of the Darrieus turbine being developed in the OPTIDE project

As shown by *Abbaszadeh et al. (2019)* only a bandwith of 30 to 40 degrees are necessary for the optimal blade motion law [6]. Therefore, a special limited-angle torque motor is being developed for the OPTIDE turbine, which will be able to satisfy the needed pitching range and the required torque [24]. In order to fit the actuator, with a maximum height of 13 mm and width of 35 mm, it is necessary to determine an optimal blade shape in the design process of the turbine model for flume tests and pitching trajectory optimization. The aim of this paper is to present the methodology to be employed in order to find the most suitable blade shape for the turbine being designed as part of the OPTIDE project. This optimisation setup consists of three parts which will be described in detail in the following.

2. METHODOLOGY

As mentioned before, the solidity is a design parameter that describes the correlation between number of blades N, chord length c and rotor radius R. In literature different equations can be found to describe the solidity σ. For this work, the solidity will be described through equation 1:

$$\sigma = \frac{Nc}{R} \tag{1}$$

The tip-speed ratio λ is another important parameter [25]. It describes the ratio between the tangential velocity, which results from the rotating motion, and the inlet velocity v_∞. λ is defined with the following equation, where the tangential velocity is given by the angular velocity ω multiplied with the turbine radius R:

$$\lambda = \frac{\omega R}{v_\infty} \tag{2}$$

The correct combination of λ and σ are very important in order to find the optimal operating point of a turbine. For high solidities the best turbine efficiency is found at low tip speed ratios [19], while at the same time, lower solidities increase the turbine efficiency. Although higher solidities increase the hydrodynamic loads on the turbine, they are often favored as they improve the self-starting ability of the turbine. As hydrokinetic turbines have, compared to wind turbines, less self-starting problems it is possible to lower the solidity in order to increase the efficiency [2, 10]. Darrieus-turbines in tidal energy applications show their highest efficiency at a solidity σ in between 1 and 1.2 and a tip speed ratio λ in between 2 and 3 [16, 13, 10, 6, 26]. As the OPTIDE turbine will be equipped with a blade-embedded pitching actuator it is possible to run the turbine at higher solidities and therefore at lower tip-speed ratios, while still achieving high efficiencies. Stall and vibrations can be mitigated by blade pitching. By lowering the tip-speed ratio blade-blade interactions and mechanical losses will also be reduced.

The turbine designed for the OPTIDE project has a rotor diameter of 400 mm, a blade height of also 400 mm and will be equipped with three blades (see Fig. 1. In order to achieve a solidity $\sigma = 1.2$ a chord length of about 80 mm would be suitable. Due to the size of the blade-embedded pitching actuator, which is 13 mm high and 35 mm wide, it is not possible to use a standard airfoil shape, such as the S-1046 recommended by [15] and [18]. Figure 2 (a) shows the possible design of the pitching actuator embedded at quarter chord of a S-1046 foil with a chord length of 80 mm. It can clearly be seen that the actuator can

not fit in the hydrofoil. In order to install the motor in the S-1046 blade, it is necessary to increase the chord length up to around 100 mm (see Fig. 2 (b)) leading to a solidity $\sigma = 1.5$. In this case lower tip-speed ratios are required to reduce blade-blade interactions. This makes it even more necessary to employ a successful blade pitch trajectory for stall mitigation. In consequence the optimal hydrofoil shape will be a trade-off of blade thickness and length along with an adapted λ to satisfy all the requirements.

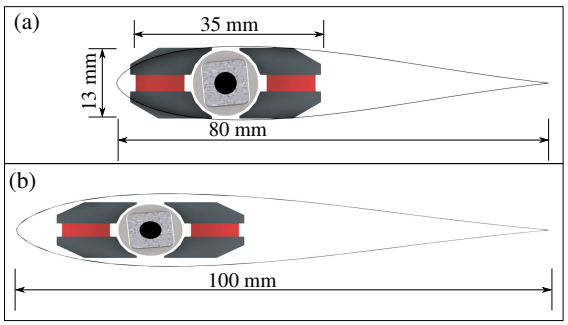

Figure 2. S-1046 hydrofoil with the blade-embedded actuator at the quarter chord for chord length 80 mm (a) and 100 mm (b)

For the given application it is reasonable to perform an optimisation, which allows to test many different hydrofoil shapes by using CFD simulations coupled with evolutionary algorithms. The optimisation consists of three main components: the optimisation software, the numerical simulation and a *Python* script, needed in order to couple the optimiser with the CFD. Figure 3 shows a flowchart describing the optimisation process.

2.1. Optimisation software

A multitude of optimisation methods can be employed in engineering optimisation tasks. Beside analytical solutions of physical models of reduced order, gradient-based methods (e.g. for maximum-power-point-tracking) or evolutionary algorithms (for very complex systems) are mostly used. Gradient-based methods search for the optimum by calculating local gradient information, resulting in an acquired local optimum, which does not always correspond to the global optimum [21, 20]. Genetic Algorithms (GA) on the other hand evaluate the fitness of a population, here a set of different hydrofoils, in order to satisfy a specific fitness function [20]. For this reason GA are more likely to find a global optimum instead of a local optimum [21, 20]. In the framework of this study an in-house genetic algorithm software called OPtimization Algorithm Library++ (short: OPAL++) developed at the Otto von Guericke University Magdeburg [27] will be applied. OPAL++ allows single- as well as multi-objective optimisations and has already successfully been used for many optimisation problems [27, 19, 28, 29].

For this work, a multi-objective optimisation will be performed, with the objectives to maximise the tangential forces and to minimise the normal forces on the blades during one revolution of the Darrieus tidal turbine. This way the power output will be maximised, while the occurring loads shall be kept as low as possible. A minimum of 500 individuals is expected to be analysed during the optimisation process, which will be performed on the cluster at the Laboratoire des Ecoulements Géophysiques et Industriels (LEGI) in Grenoble, France. The hydrofoil shape will be constrained by five points, given by the size of the pitching actuator and the pivot point. OPAL++ will optimise the y-location of eight different points, three at the hydrofoil leading edge, one at the trailing edge and four on the upper and lower hydrofoil surface. Additionally the cord length of the turbine as well as the tip-speed ratio λ will be varied, resulting in ten design parameters. As shown in Fig. 3, the optimisation software, OPAL++, will read the results from the CFD simulation, compare the outcome of the fitness function for the different individuals and create a new set of hydrofoil design parameters, which are derived from the best performing individuals in the previous simulation. These parameters are then read into the *Python* script, as detailed in the next section.

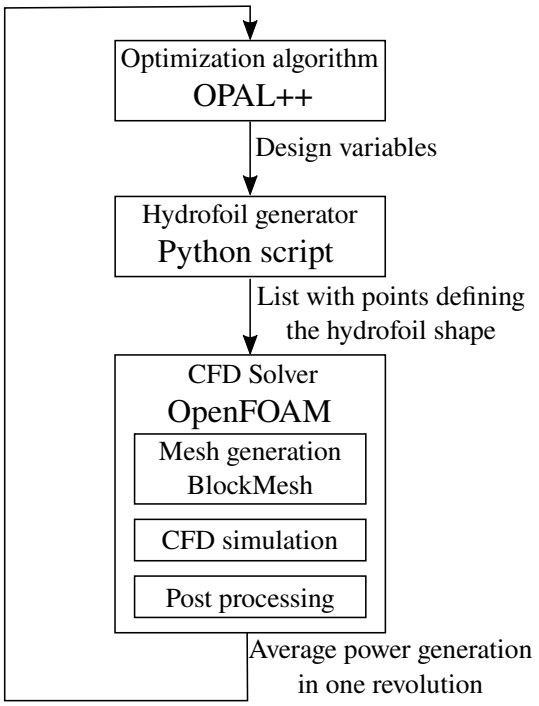

Figure 3. Flowchart of the optimisation

2.2. Hydrofoil shape generation

The optimisation software described above decides on a new set of variables for the hydrofoil shape for the next generation of individuals. The set of variables together with the fixed points, given by the po-

sition and size of the motor, define the rough shape of the hydrofoil. A *Python* script processes the given points in order to create a smooth hydrofoil shape. Here the *scypy* interpolation package is used in order to find the B-spline representation of a 1D-curve [30]. The degree of the B-Spline is automatically chosen by the program.

After the spline generation, lists with x- and y-coordinates needed to define the hydrofoil shape are generated. These lists are then converted in order to match the required format for the meshing utility and are then imported into *BlockMesh* in order to create a mesh, which will be described in the following section. Besides creating the spline out of the variable set defined by OPAL++, the *Python* script also creates a plot of the generated hydrofoil, in order to allow the user to visibly check the created shape.

2.3. Mesh generation and CFD simulation

One of the most important steps in order to achieve good and valid results in a CFD simulation is the design of a mesh with a good quality. The CFD simulations will be performed using *OpenFOAM* v2112. For this reason the *BlockMesh* utility, which is part of *OpenFOAM*, will be used in order to create a multi-block structured mesh of the turbine. The two-dimensional computational domain is divided into six sub-domains (see Fig. 4: an outer stator (in yellow), a rotating ring (in green), the three blades (in red) and an inner stator (in blue). In order to get cells with a good quality and refine each section as necessary each sub-domain will be blocked as shown in Fig. 4

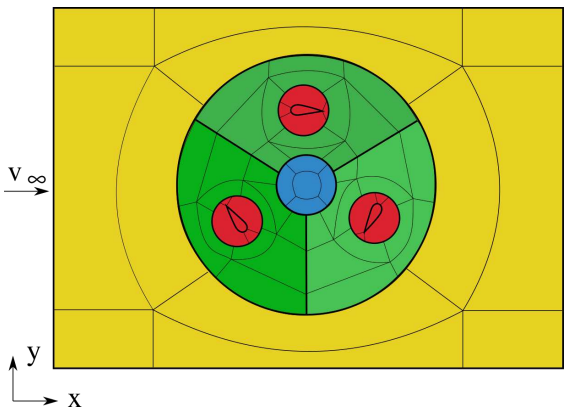

Figure 4. Computational domain and blocking of the mesh. Divided into four subdomains: outer stator (yellow), rotating ring (green), blades (red) and inner stator (blue)

For the first simulation a large outer domain with a length (x-direction) of $45D$ and a width (y-direction) of $60D$ was chosen. The distance between the inlet and the center of the turbine amounts to $15D$. The size of the outer domain will be adapted through a preliminar confinement study, on which the distance from the sides to the center of the turbine will be iteratively reduced.

The sub-domain of the rotating ring is composed by three identical sections with an inner and outer radius of about $2R = 400$ mm and $0.25R = 50$ mm, respectively. One section is meshed and then rotated by 120° and 240° to complete the ring. These sections will then be joined using the *stitchMesh* function of *OpenFOAM*. In the center of the rotating ring sub-domain lies an inner stator, which is meshed using an O-Grid blocking.

The blade sub-domain is located inside each section of the rotating ring. This section of the mesh is highly parametrised in order to adapt correctly to the imported B-spline points from the *Python* script. The grid created with *BlockMesh* is defined in a so-called *blockMeshDict* .txt-file which is automatically edited by the scripts. Each block of the hydrofoil sub-domain is refined to satisfy $y^+ < 1.6$ for a fully resolved boundary layer accordingly to *Maître et al.* [31].

After meshing all the sub-domains, they are subsequently joined using the *mergeMeshes* command in *OpenFOAM*. Between the sliding interfaces of the sub-domains a so-called Arbitrary Mesh interface (AMI) is employed, which maps the flow quantities from one sub-domain onto the adjacent domain with a weighted interpolation function to respect mass conservation. This is necessary due to the rotating motion of the ring sections.

In order to accurately evaluate the averaged performance of the turbine for one revolution, the incompressible Unsteady Reynolds-Averaged Navier-Stokes (URANS) equations will be solved using the open-source software *OpenFOAM*. The $k-\omega\ SST$ (Shear Stress Transport) method is chosen in order to accurately model the turbine. Various studies have found, that this turbulence model is suitable for airfoil and VAT simulations [11, 32]. After the numerical simulations are finished, the *OpenFoam* results are read into a python script using the *FluidFoam package* (https://github.com/fluiddyn/fluidfoam) in order to calculate the tangential and the normal forces [33]. These values are then imported into OPAL++ and analysed, in order to get a new set of hydrofoil design variables for the subsequent generation. This process is iteratively repeated until the optimization converges.

A first simulation has been conducted in order to check that the mesh setup and the simulation parameters are set correctly. 10 revolutions with a step of 1° at a λ of 2 (inlet velocity of 0.8 m/s) were carried out. With the current mesh, consisting of 188.000 cells, the simulation took about 10 hours to calculate. The average power coefficient c_p for the last revolution was equal to 0.347 and the difference in c_p between the last two revolutions was lower than 0.5%. Figure 5 shows the velocity field in the vicinity of the turbine at the last time step (10th revolution).

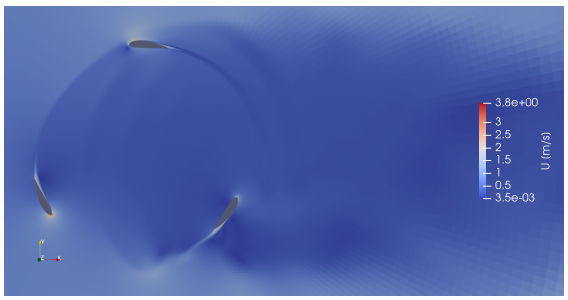

Figure 5. Velocity field in the vicinity of the turbine at the last time step at a TSR=2 and an inlet velocity=0.8 m/s

3. CONCLUSION

In order to implement a blade-embedded pitching actuator in the blade of a H-Darrieus tidal turbine it is necessary to optimise numerically the blade shape. In this paper, the methodology for such an optimisation is presented. A CFD simulation is coupled with an evolutionary algorithm to find the blade shape that presents the highest average performance during one turbine revolution. The shape of the hydrofoil is constrained by the size of the pitching actuator and its position at quarter chord. The OPAL++ software is used to govern the optimization process by generating the individual parameter sets from the variables and analyze of the results of subsequent simulations. The hydrofoil shape is retrieved by a *Python* script, which interpolates the shape with use of a B-Spline from the parameter sets. The interpolated points of the new hydrofoil are directly imported into the *blockMesh* utility for mesh generation. After creating the fully parametrised mesh the numerical simulations are executed in the OpenFOAM framework. Through this method, the optimal blade shape for a H-Darrieus tidal turbine, which should fit an actuator of 13 mm by 35 mm, can be found.

ACKNOWLEDGEMENTS

This work is part of the OPTIDE project and has been supported by the Deutsche Forschungsgemeinschaft (DFG (FKZ: 457325924)) and the labex Tec21 Investissements d'avenir - agreement n°ANR-11-LABX-0030.

REFERENCES

[1] BP, 2021, "Statistical Review of World Energy 2021 / 70th edition", *Tech. rep.*

[2] Balduzzi, F., Melani, P. F., Soraperra, G., Brighenti, A., Battisti, L., and Bianchini, A., 2021, "Some design guidelines to adapt a Darrieus vertical axis turbine for use in hydrokinetic applications", *E3S Web of Conferences*, Vol. 312, p. 08017.

[3] Balmer, M., and Spreng, D., 2008, "Hydroelectric power", *Future Energy*, Elsevier, pp. 193–209.

[4] Irena, 2020, "Innovation Outlook: Ocean energy technologies", *Tech. rep.*, International Renewable Energy Agency.

[5] Irena, 2021, "Renewable Energy Statistics 2021", *Tech. rep.*, The International Renewable Energy Agency.

[6] Abbaszadeh, S., Hoerner, S., Maître, T., and Leidhold, R., 2019, "Experimental investigation of an optimised pitch control for a vertical-axis turbine", *IET Renewable Power Generation*, Vol. 13 (16), pp. 3106–3112.

[7] Yang, B., and Shu, X., 2012, "Hydrofoil optimization and experimental validation in helical vertical axis turbine for power generation from marine current", *Ocean Engineering*, Vol. 42, pp. 35–46.

[8] Branger, H., Paillard, B., Roy, S., Luneau, C., Perrot, E., and Bourras, D., 2018, "Experimental and numerical study on a model of offshore vertical axis wind turbine with pitching blades", *7th Conference on Bluff Body Wakes and Vortex-Induced Vibrations, BBVIV-7*.

[9] Kirke, B., and Lazauskas, L., 2011, "Limitations of fixed pitch Darrieus hydrokinetic turbines and the challenge of variable pitch", *Renewable Energy*, Vol. 36 (3), pp. 893–897.

[10] Chen, B., Su, S., Viola, I. M., and Greated, C. A., 2018, "Numerical investigation of vertical-axis tidal turbines with sinusoidal pitching blades", *Ocean Engineering*, Vol. 155, pp. 75–87.

[11] Delafin, P.-L., Deniset, F., Astolfi, J. A., and Hauville, F., 2021, "Performance Improvement of a Darrieus Tidal Turbine with Active Variable Pitch", *Energies*, Vol. 14 (3), p. 667.

[12] Dabiri, J. O., 2011, "Potential order-of-magnitude enhancement of wind farm power density via counter-rotating vertical-axis wind turbine arrays", *Journal of Renewable and Sustainable Energy*, Vol. 3 (4), p. 043104.

[13] Hoerner, S., Abbaszadeh, S., Cleynen, O., Bonamy, C., Maître, T., and Thévenin, D., 2021, "Passive flow control mechanisms with bioinspired flexible blades in cross-flow tidal turbines", *Experiments in Fluids*, Vol. 62 (5).

[14] Rezaeiha, A., Montazeri, H., and Blocken, B., 2018, "Towards optimal aerodynamic design of vertical axis wind turbines: Impact of solidity and number of blades", *Energy*, Vol. 165, pp. 1129–1148.

[15] Hashem, I., and Mohamed, M., 2018, "Aerodynamic performance enhancements of H-rotor Darrieus wind turbine", *Energy*, Vol. 142, pp. 531–545.

[16] Shiono, M., Suzuki, K., and Kiho, S., 2000, "An experimental study of the characteristics of a Darrieus turbine for tidal power generation", *Electrical Engineering in Japan*, Vol. 132 (3), pp. 38–47.

[17] Hwang, I. S., Lee, Y. H., and Kim, S. J., 2009, "Optimization of cycloidal water turbine and the performance improvement by individual blade control", *Applied Energy*, Vol. 86 (9), pp. 1532–1540.

[18] Mohamed, M., 2012, "Performance investigation of H-rotor Darrieus turbine with new airfoil shapes", *Energy*, Vol. 47 (1), pp. 522–530.

[19] Daróczy, L., Janiga, G., and Thévenin, D., 2018, "Computational fluid dynamics based shape optimization of airfoil geometry for an H-rotor using a genetic algorithm", *Engineering Optimization*, Vol. 50 (9), pp. 1483–1499.

[20] Ouyang, H., Weber, L. J., and Odgaard, A. J., 2006, "Design optimization of a two-dimensional hydrofoil by applying a genetic algorithm", *Engineering Optimization*, Vol. 38 (5), pp. 529–540.

[21] Shahrokhi, A., and Jahangirian, A., 2007, "Airfoil shape parameterization for optimum Navier–Stokes design with genetic algorithm", *Aerospace Science and Technology*, Vol. 11 (6), pp. 443–450.

[22] Hantoro, R., Utama, I. K. A. P., Erwandi, E., and Sulisetyono, A., 2011, "An Experimental Investigation of Passive Variable-Pitch Vertical-Axis Ocean Current Turbine", *Journal of Engineering and Technological Sciences*, Vol. 43 (1), pp. 27–40.

[23] Liang, Y., Zhang, L., Li, E., and Zhang, F., 2016, "Blade pitch control of straight-bladed vertical axis wind turbine", *Journal of Central South University*, Vol. 23 (5), pp. 1106–1114.

[24] Zhao, Z., Hoerner, S., and Leidhold, R., 2021, "Design and Analysis of a blade-embedded limited-angle torque motor for vertical-axis water turbines", *11th International Conference on Power Electronics, Machines and Drives*.

[25] Hoerner, S., Kösters, I., Vignal, L., Cleynen, O., Abbaszadeh, S., Maître, T., and Thévenin, D., 2021, "Cross-Flow Tidal Turbines with Highly Flexible Blades—Experimental Flow Field Investigations at Strong Fluid–Structure Interactions", *Energies*, Vol. 14 (4), p. 797.

[26] Patel, V., Eldho, T., and Prabhu, S., 2017, "Experimental investigations on Darrieus straight blade turbine for tidal current application and parametric optimization for hydro farm arrangement", *International Journal of Marine Energy*, Vol. 17, pp. 110–135.

[27] Daróczy, L., Janiga, G., and Thévenin, D., 2014, "Systematic analysis of the heat exchanger arrangement problem using multi-objective genetic optimization", *Energy*, Vol. 65, pp. 364–373.

[28] Mansour, M., Zähringer, K., Nigam, K. D., Thévenin, D., and Janiga, G., 2020, "Multi-objective optimization of liquid-liquid mixing in helical pipes using Genetic Algorithms coupled with Computational Fluid Dynamics", *Chemical Engineering Journal*, Vol. 391, p. 123570.

[29] Kerikous, E., and Thévenin, D., 2019, "Optimal shape of thick blades for a hydraulic Savonius turbine", *Renewable Energy*, Vol. 134, pp. 629–638.

[30] Virtanen, P., Gommers, R., Oliphant, T. E., Haberland, M., Reddy, T., Cournapeau, D., Burovski, E., Peterson, P., Weckesser, W., Bright, J., van der Walt, S. J., Brett, M., Wilson, J., Millman, K. J., Mayorov, N., Nelson, A. R. J., Jones, E., Kern, R., Larson, E., Carey, C. J., Polat, İ., Feng, Y., Moore, E. W., VanderPlas, J., Laxalde, D., Perktold, J., Cimrman, R., Henriksen, I., Quintero, E. A., Harris, C. R., Archibald, A. M., Ribeiro, A. H., Pedregosa, F., van Mulbregt, P., and SciPy 1.0 Contributors, 2020, "SciPy 1.0: Fundamental Algorithms for Scientific Computing in Python", *Nature Methods*, Vol. 17, pp. 261–272.

[31] Maître, T., Amet, E., and Pellone, C., 2013, "Modeling of the flow in a Darrieus water turbine: Wall grid refinement analysis and comparison with experiments", *Renewable Energy*, Vol. 51, pp. 497–512.

[32] Yang, B., 2001, "A new blade design scheme for reversible axial flow fan & research on the combined cascades", *Doctoral dissertation*.

[33] Bonamy, C., Chauchat, J., Augier, P., Mathieu, A., Clemencot, Q., Chassagne, R., Maurice, G., Gilletta, A., Renaud, M., and Gonçalves, G., 2022, "fluiddyn/fluidfoam: Release v0.2.3", URL `https://doi.org/10.5281/zenodo.6453090`.

Conference on Modelling Fluid Flow (CMFF'22)
The 18th International Conference on Fluid Flow Technologies
Budapest, Hungary, August 30 -September 2, 2022

STUDY OF THE INFLUENCE OF THERMODYNAMIC EFFECTS ON VENTURI CAVITATION FLOW

Xu MENG[1], Le XIANG[2], Kaifu XU[3], Bo LI[4], Huan HAN[5], Shuhong LIU[6], Zhigang ZUO[7]

[1] State Key Laboratory of Hydro Science and Engineering, and Department of Energy and Power Engineering, Tsinghua University. Beijing 100084, China. E-mail: zgbh.mx@163.com
[2] Xi'an Aerospace Propulsion Institute, Xi'an 710100, Shaanxi, China.
[3] Xi'an Aerospace Propulsion Institute, Xi'an 710100, Shaanxi, China.
[4] State Key Laboratory of Hydro Science and Engineering, and Department of Energy and Power Engineering, Tsinghua University, Beijing 100084, China.
[5] College of Robotics, Beijing Union University, Beijing 100020, China
[6] Corresponding Author. State Key Laboratory of Hydro Science and Engineering, and Department of Energy and Power Engineering, Tsinghua University, Beijing 100084, China. E-mail: liushuhong@mail.tsinghua.edu.cn
[7] Corresponding Author. State Key Laboratory of Hydro Science and Engineering, and Department of Energy and Power Engineering, Tsinghua University, Beijing 100084, China. E-mail: zhigang200@mail.tsinghua.edu.cn

ABSTRACT

Research on cavitation flow in thermosensitive conditions is important since the thermodynamic effects are too strong to ignore. Due to the limitation of the measurement technology, and the difficulties of experiments, experimental dynamic results and field results are few. Numerical simulation research is needed to provide more results of thermosensitive conditions and more information on the flow field.

This paper focuses on both the experimental and numerical study of the cavitation flows in a specific Venturi structure with particular emphasis on the dynamic evolution and the thermodynamic effects. A blow-down type water tunnel is built to conduct experiments with water in a wide range of water temperatures and the high-speed photography of the upper side avoids the misjudgement of cavitation break-off caused by the cavity superposition spanwise. For comparison, working conditions same as the experiments are numerically investigated. Good agreements are obtained between the experimental measurements and the numerical results, including the area of cavitation and its frequency. A corrected ZGB cavitation method is used and different turbulence models are compared. k-ε model better simulates the cavitation structure in this research. Results also show that the mean cavitation length/cavitation area decreases when the kappa number increases and the thermodynamic effects parameter increases, which means the thermodynamic effects suppress the cavitation flow and the cavitation-related pressure recovery is reduced. Also, the cavitation is more stable and the collapse and rebound processes of cavity clouds and clusters at the Venturi throat are less violent in larger Σ. Stronger thermodynamic effects are observed at a higher temperature.

Keywords: Cavitation flow; Thermodynamic effects; Venturi

NOMENCLATURE

c_p	[J/(g·K)]	isobaric heat capacity
f	[Hz]	frequency
f_v	[-]	mass fraction
H	[m]	height
L	[kJ/kg]	latent heat
L_{cav}	[m]	length of cavity cloud
P	[Pa]	pressure
P_a	[Pa]	atmosphere
T	[K]	temperature
u	[m/s]	velocity
vf	[m/s]	volume fraction
α_l	[cm^2/s]	liquid thermal diffusivity
κ	[-]	pressure recovery coefficient
λ	[W/(m·K)]	thermal conductivity
ν_l	[m^2/s]	kinematic viscosity
ρ	[kg/m^3]	density
Σ	[-]	thermodynamic parameter
σ	[-]	cavitation number

Subscripts and Superscripts

l	liquid phase
v	vapour phase
in	at the inlet of the Venturi
out	at the outlet of the Venturi
th	at the throat of the Venturi
∞	free-stream
m	mixture

1. INTRODUCTION

A large number of research studies have focused on the cavitation flows in fluid machinery such as turbines and pumps [1,2]. Cavitation flow is formed by the rapid pressure change in the working liquid, which will lead to the formation of small cavities in places where the local pressure is lower than the saturated vapor pressure. Its occurrence sometimes brings negative impacts such as structural vibration, pressure fluctuations, and performance deterioration. Phase change and heat transfer exist when cavitation occurs, which reduces the temperature at the bubble wall and generates a thermal boundary layer around the bubble. The decrease in temperature reduces the saturated vapor pressure of the surrounding liquid, thereby affecting the subsequent growth and collapse of cavitation bubbles and changing the cavitation flow. This process describes the thermodynamic effects of cavitating flow [3,4].

In some special scenes, cryogenic liquids are used as working liquids work and work under thermosensitive conditions. For example, liquid hydrogen and liquid oxygen are fuels of some liquid rockets. When fuels flow through the inducer of the turbine in a liquid rocket engine, cavitation is inevitable. Cavitation may also occur in LNG transportation. The thermodynamic effects are too strong to be ignored for fluids working under thermosensitive conditions [5]. Therefore, the thermodynamic effects of cavitation must be considered in cryogenic applications. However, experimental research on such low-temperature cavitation flow is difficult. Hence it is necessary to carry out numerical simulation research when studying the cavitation flow of working fluids in thermosensitive conditions.

Considering the complexity of flow conditions in hydraulic machinery, some researchers conduct research on the characteristics of cavitation flow in a C-D nozzle (Venturi), which is one of the typical cavitation flows [6-8]. And its different cavitation patterns, including supercavitation, cloud cavitation, and sheet cavitation are produced by changing the cavitation number σ or the pressure recovery number κ if the thermodynamic effects are neglected [9,10].

$$\sigma = \frac{p_{ref} - p_v}{0.5\rho V^2} \tag{1}$$

$$\kappa = \frac{p_1 - p_v}{p_1 - p_2} \tag{2}$$

While for other thermosensitive conditions, parameter of thermdynamic effets

$$\Sigma = \frac{\rho_v^2 L^2}{\rho_l^2 c_{pl} T_\infty \sqrt{\alpha_l}} \tag{3}$$

is defined by Brennen [11] to estimate the thermodynamic effects of cavitation, which depends only on the fluid temperature and the physical properties of the liquid.

Both experimental and numerical research of Venturi cavitation flow on thermosensitive conditions have lasted decades. In terms of the experimental research, Petkovšek et al. [12,13], Zhang et al. [14], and Ge et al. [15] conducted cavitation experiments on a Venturi with hot water. Watanabe et al. [16] analyzed the cavitation length and the cavitation instability in HFE liquid. Ohira et al. [17], Zhu et al. [18] Wei et al. [19], and Chen et al. [20,21] conducted experiments using LN_2. In the above study of typical cavitation flow considering thermodynamic effects, some experimental results are inconsistent with the theory that thermodynamic effects inhibit the development of cavitation, and there is a lack of comprehensive and systematic experimental research, resulting in the unclear influence of thermodynamic effects on the averaged and dynamic characteristics of the cavitation flow.

As for the numerical study, some research works didn't change the cavitation model and the thermodynamic effects of cavitation is considered by solving the energy equation and updating the physical properties of the fluid or calibrating the empirical coefficients [22,23]. The characteristic that the saturated vapor pressure of the working fluid is very sensitive to the temperature change is not considered enough in these cases. And some other research works further correct the saturated vapor pressure expression terms in the cavitation model and use B-factor [5,24] to estimate the temperature drop due to cavitation [25,26]. In such cases, the universality of B-factor still needs to be verified [22]. Last, some researchers corrected the evaporation and condensation source terms in the cavitation model [27,28]. The assumption in such kind of research is closer to the actual process of cavitation development. Among these studies, the correction method based on the ZGB cavitation model has better applicability and higher efficiency than others, which assumes that all the latent heat near the bubble wall is used for the evaporation process. However, due to the lack of systematic experiments, the existing studies mostly use the average characteristics of experiments obtained in the early stage [29] for simulation verification. Therefore, the simulation study of Veturi cavitation flow considering the thermodynamic effects need to be further carried out and compared with the experimental results to verify the effectiveness of the numerical simulation methods.

In short, some results of experimental research contradict each other. Numerical study on the effectiveness of the numerical simulation methods in the dynamic characteristics prediction of cavitation flow needs to be further investigated.

2. EXPERIMENTAL APPARATUS

It is found that when the cavitation number or thermodynamic parameter of the same liquid changes singly, the initial cavitation number when

the flow changes from non-cavitation to visible cavitation is different [30,31]. There is also no obvious change rule or trend. Even if the working fluid has been fully degassed before the experiment, the increase of cavitation nuclei in the liquid cannot be eliminated as experiments proceed. With the development of the experiment, the cavitation nuclei in the liquid increase, and the cavitation is more likely to occur, resulting in the gradual increase of the initial cavitation value. Considering that it is hard to control the influence of nuclei on cavitation flow in a circulating water tunnel, a blowdown-type cavitation tunnel is used in this experiment to reduce the influence of nuclei as much as possible through fully degassing pre-treatment. The blowdown-type cavitation tunnel uses the pressure difference between the two liquid storage tanks to drive the working fluids to flow through the experimental section, so the flow rate is gradually reduced in a single experiment.

The schematic diagram is shown in Fig. 1. The working fluid (degassed water in this paper) is stored in the upstream tank (150 *liters*). Driven by the differential pressure, it will flow along with the turbine flowmeter, honeycomb structure, contraction section, experimental section, expansion section, pneumatic valve, and finally to the downstream tank (30 *liters*). The upstream tank is designed larger to obtain a more stable upstream pressure and the downstream tank keeps open during the experiment, which makes each experiment last more than 30 seconds. Figure 2 shows the pressure change in the tanks during an example condition. As shown in the enlarged view, the pressure difference changed about 3% in 1 *s* and 0.6% in 0.1*s*. Also, the characteristic time scale in our experiments was <0.04 *s*. Therefore, cavitation events in 0.1 *s* were thought to be quasi-steady and we use the averaged values of p_{in}, p_{out}, and T during 0.1 *s* when calculating the κ and Σ. Two tanks are both connected to a vacuum pump and an air compressor to realize independent pressure regulation in the range of 0.03-0.8 *MPa*. Two 3 *kW* heating rods and a PT100 thermal resistance are installed in the upstream tank. Before experiments, the PID control system can be used to adjust and stabilize the temperature (290-360 *K*) of the water in the tank.

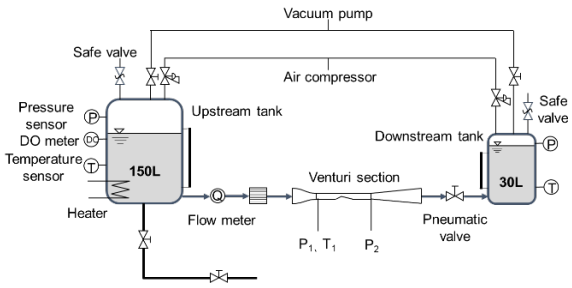

Figure 1. Schematic of the blowdown-type cavitation tunnel

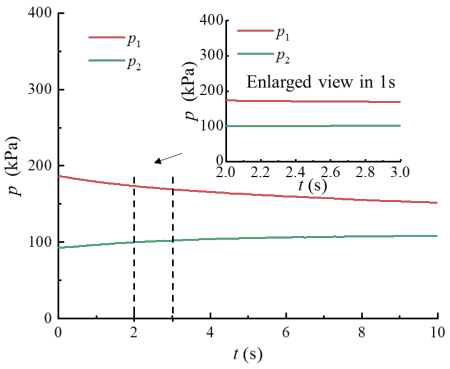

Figure 2. Pressure difference at p_{in}=230 *kpa*, p_{out}=100 *kpa*, and T=292 *K*

The honeycomb section, contraction, and expansion section are used to prevent flow separation and make the inflow of Venturi uniform. The experimental section is a contraction-diffusion Venturi made of plexiglass material. The specific size and structure are shown in Fig. 3. The inlet and outlet are 10×10 *mm* square sections and the throat height H_{th} is 5 *mm*. The constriction angle and divergent angle of the Venturi are 18 ^{o} and 8 ^{o} respectively. A variety of cavitation types can be generated by using this experimental apparatus.

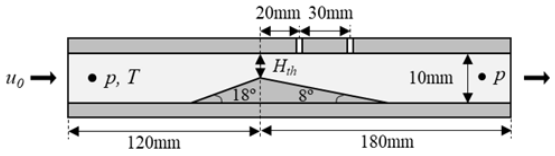

Figure 3. Detailed drawing of the convergent-divergent Venturi section

To capture the detailed characteristics of cavitation flow, the front and upper sides of the experimental section will be photographed by a high-speed camera (Phantom v2012). A specially designed mirror system shown in Fig. 4 enables the cameras to shoot both sides horizontally in front. Then, the high-speed photography of the upper side avoids the misjudgement of cavitation break-off caused by the superposition effect of spanwise cavitation. It is shooting at 10,000 *fps*, with a spatial resolution 1024 ×512 *pixels*, and an exposure time 2 μs.

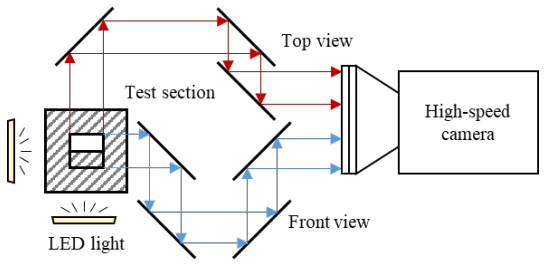

Figure 4. Schematic of the mirror system

The temperature of the incoming flow is measured with a Pt100 sensor with an uncertainty ±0.05 *K*. Pressure sensors are located in the two tanks, and before and after the Venturi section, with a measurement range of 0-1 *MPa* and uncertainty of ±0.025% *FS*. Two additional high-frequency dynamic pressure sensors are positioned respectively 20 *mm* and 50 *mm* downstream of the Venturi throat. They are all synchronous triggered.

3. NUMERICAL METHODS AND SETUP

3.1. Numerical setup

The computation domain is shown in Fig 5. The applied construction and dimensions of the Venturi in the simulations are consistent with that in the experiments. The height H_{in}=H_{out}=10 *mm*, and H_{th}=5 *mm*. Angles of the C-D square nozzle are α_1=18º and α_2=8º respectively. The distance between the inlet and the Venturi throat is $10H_{in}$, which is consistent with the position of the pressure and temperature measuring points at the experimental inlet, and the outlet is appropriately extended, which is $35H_{in}$ from the Venturi throat.

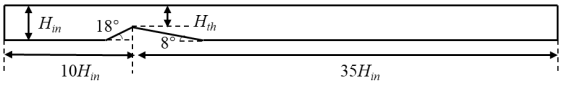

Figure 5. Computation domain

Because the experimental results mainly show the two-dimensional characteristics, it is set as a two-dimensional model with only one layer of the grid in the spanwise direction (the spanwise width is 1mm). water in specific temperature was used as the working fluid at the inlet. Its uniform velocity at the inlet of the upstream channel and constant pressure at the outlet of the downstream channel were chosen as the boundary conditions. To control the κ, the inlet velocity is adjusted to obtain the specific p_{in}. The sidewall of the computation domain is set as the symmetrical boundary condition. And "No-slip" conditions were imposed on all the other stationary walls.

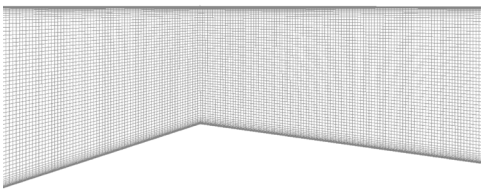

Figure 6. Mesh of C-D square nozzle and its refinement

Structured grid systems were developed by using commercial software ICEM-CFD in this study. The simulations were conducted in ANSYS CFX. Wall function varied with the turbulence model. Schlable wall function is used when the turbulence model is *k-ε,* and RNG *k-ε.* Enhanced wall treatment is used for SST *k-ω.* Because Schlable wall function adds limit to force Standard wall functions to use logarithmic law when y^+ are too small and the same grid is used for all the models. The first boundary grid layer is set located in a viscous sublayer, required by SST *k-ω*. Therefore, local grid refinements to the boundary layers were applied at the walls and the thickness of the first grid is specified as 6×10^{-5} *mm* with a size growth ratio of 1.2. The maximum y^+ on the diverging wall is about 2 in steady simulations. The grid around the Venturi contraction and diffusion is shown in Fig. 6.

In order to resolve the real transient evolution of cavitating flow, the time step needs to be set as 1.25×10^{-6} *s* (which is equivalent to $H_{th}/200U_{th}$). However, to save the computational resources, it is set as 5×10^{-6} *s* when we found the results changed little. The Courant number $C = u\Delta t/\Delta s < 1$ (where u, Δt, and Δs are the characteristic flow velocity, the time step size, and typical cell size, respectively). Second order backorder Euler upwind is chosen as transient scheme. The transient simulation was started from a steady case. Simulation convergence was achieved when the residual error was lower than 10^{-6}, or the variation of the operational parameter inlet pressure p_{in} was below 0.01%.

3.2 Governing equations

Numerical simulations of cavitating flow in this paper are established based on the three-dimensional compressible Navier–Stokes equations. The homogeneous mixture model is chosen. The conservation equations of mass, momentum, and energy are as follows [32]:

Continuity equation

$$\frac{\partial \rho_m}{\partial t}+\frac{\partial\left(\rho_m u_j\right)}{\partial x_j}=0 \tag{4}$$

Momentum equation

$$\frac{\partial}{\partial t}\left(\rho_m u_i\right)+\frac{\partial\left(\rho_m u_i u_j\right)}{\partial x_j}$$

$$=-\frac{\partial p}{\partial x_i}+\nabla \tau_{ij}+S \tag{5}$$

$$\tau_{ij}=\mu_{eff}\left[\left(\frac{\partial u_i}{\partial x_j}+\frac{\partial u_j}{\partial x_i}\right)-\frac{2}{3}\delta_{ij}\frac{\partial u_k}{\partial x_k}\right]$$

Energy equation

$$\frac{\partial\left(\rho_m c_p T\right)}{\partial t}+\frac{\partial}{\partial x_j}\left(\rho_m u_j c_p T\right) \tag{6}$$

$$=\nabla\cdot\left(k_{eff}\nabla T\right)+S_E$$

$S, \mu_{eff}, k_{eff}, S_E$ represent respectively, the source item generated by volume force or user-defined,

effective viscosity, the effective thermal conductivity, the volumetric heat sources, and the volume fraction of the vapor phase.

3.4. Cavitation model

The cavitation model is important in cavitation numerical simulation. At present, the widely used transport equation model is based on the homogeneous mixture model. The mass conversion between two phases is characterized by the evaporation source term $\dot{m}^+$ and the condensation source term $\dot{m}^-$. The volume fraction or mass fraction of two phases in the flow process is obtained by solving the transport equation. The expressions of two typical transport equations are as follows:

$$\begin{aligned} &\frac{\partial\left(\rho_l\alpha_l\right)}{\partial t}+\nabla\cdot\left(\rho_l\alpha_l\vec{u}\right)=\dot{m}^+ +\dot{m}^- \\ &\frac{\partial\rho_m f_v}{\partial t}+\nabla\cdot\left(\rho_m f_v\vec{u}\right)=\dot{m}^+ +\dot{m}^- \end{aligned} \tag{7}$$

Zwart-Gerber-Belamri (ZGB) cavitation model derived from the Rayleigh-Plesset equation [33] is mainly used in numerical simulations. In the derivation process, the temperature change is not considered, and the influence of surface tension and viscosity are both ignored. The expression of transport source term is as follows:

$$\begin{aligned} &p\le p_v\left(T_\infty\right) \\ &\qquad \dot{m}^- = C_{vap}\frac{3\alpha_{nuc}\rho_v\left(1-\alpha_v\right)}{R_B}\sqrt{\frac{2\left(p_v\left(T_\infty\right)-p\right)}{3\rho_l}} \\ &p> p_v\left(T_\infty\right) \\ &\qquad \dot{m}^+ = C_{\mathrm{cond}}\frac{3\alpha_v\rho_v}{R_B}\sqrt{\frac{2}{3}\frac{\left(p-p_v\left(T_\infty\right)\right)}{\rho_l}}, \end{aligned} \tag{8}$$

where α_{nuc} and R_B are the volume fraction of non-condensable gas and the mean radius of bubble separately. C_{vap} and C_{cond} are empirical constant.

Take thermodynamic effects into consideration, a modified model is also applied [28,34,35]:

$$\begin{aligned} &p\le p_v(T) \qquad \dot{m}^- = C_{vap}\frac{3\alpha_{nuc}\rho_v\left(1-\alpha_v\right)}{R_B} \\ &\left(\sqrt{\frac{2}{3}\frac{\left(P_v(T)+P_{\mathrm{turb}}-P\right)}{\rho_l}}-\frac{\rho_l C_{pl}\sqrt{\lambda_l}\left(T_\infty-T\right)}{\rho_v L\sqrt{t}}\right) \\ &p> p_v(T) \qquad \dot{m}^+ = C_{\mathrm{cond}}\frac{3\alpha_v\rho_v}{R_B} \\ &\left(\sqrt{\frac{2}{3}\frac{\left(P_v(T)+P_{\mathrm{turb}}-P\right)}{\rho_l}}-\frac{\rho_l C_{pl}\sqrt{\lambda_l}\left(T_\infty-T\right)}{\rho_v L\sqrt{t}}\right) \end{aligned} \tag{9}$$

3.3. Turbulence model

Several turbulence models are chosen to compare in this paper, such as SST *k-ω*, *k-ε*, and RNG *k-ε*, which are the extensive application of the Reynolds-averaged Navier–Stokes-based models in simulating the cavitating flow.

4. RESULTS AND DISCUSSION

4.1. Image post-processing

There develops an attached cavity cloud at the throat of the Venturi. The mean area or length of such a cavity cloud and its oscillation are important parameters for quantitative analysis. For cloud cavitation, the cavity cloud grows larger and longer at first, then a large part of the cloud breaks off at the position near the throat, and finally, the remaining part grows again. The length and its oscillation frequency can be obtained from image post-processing of high-speed video.

The same image post-processing method in Reference [14] is conducted in the present research to estimate the mean length of attached cavitation $\overline{L}_{cav}$,the mean cavitation area $\overline{A}_{cav}$ and frequency *f*. The first step is choosing a background image that is a non-cavitating condition and using it to normalize the instantaneous image intensity distribution *I* of each frame. Thus calculate the 'grey-level' of $(I\text{-}I_0)/I_0$ for each pixel. All the frames of the video which contain several cavity cloud circles are processed as above, then mean values and standard deviations are determined. Suppose that black (grey-level=0) is totally liquid and white is contrast, $\overline{A}_{cav}$ is integrated. The position of the cavity cloud closure is then located where the standard deviation of the grey level reaches its maximum value. Assume that the mean values and the standard deviations did not change significantly when more than 5000 images were analyzed [7]. The mean cavitation length $\overline{L}_{cav}$ is measured from the Venturi throat to the closure line with an uncertainty of <2%. Frequency *f* is got from the FFT results of the average value of the 10×10 *pixels* region shown in Fig. 7(b).

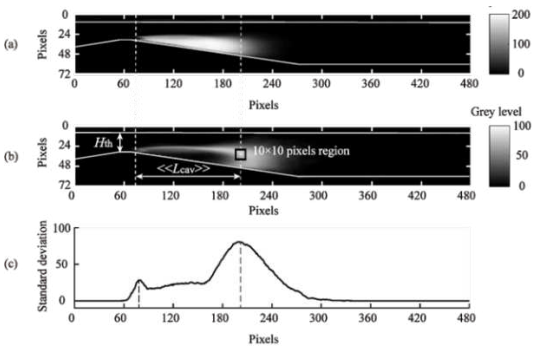

Figure 7. Image post-processing [cited from Reference 14]

4.2. Numerical validation with experiments

The averaged cavitation area of simulation results is calculated by the equation:

$$\overline{A}_{cav}=\frac{1}{W\Delta t}\sum_{t=0}^{\Delta}\left(\sum_{i,j}\alpha_{i,j}(t)V_{i,j}(t)\right), \tag{10}$$

where $a_{i,j}$ and $V_{i,j}$ represent the volume fraction and volume of a grid cell, respectively. W and Δt represent the spanwise width of the computational model and the time length for time averaging, respectively.

As preliminary tests, steady simulations using five mesh systems were carried out to find out the plausible number of grids. Uniform velocity at the inlet u_{th} is 20.02 *m/s* and constant pressure at the outlet of the downstream channel p_{out} is 100 *kPa* here. The results are shown in Fig. 8: $\overline{A}_{cav}$ becomes almost constant when the number of grids is greater than 2.29×10^5. Therefore, the mesh system with a 3.75×10^5 grid is chosen for the following simulation.

Table 1 shows the comparison of averaged cavitation area $\overline{A}_{cav}$ and frequency f between the transient-flow simulations and experimental results. Simulation results with different turbulence models are also compared. It shows that simulation results with SST k-ω model and k-ε model have less than 2% error in $\overline{A}_{cav}$ and k-ε model has only 1.15% error in f with the results of the experiments. It shows that the structure of Venturi cavitation flow is better predicted by the present simulation with the k-ε model. Therefore, it is chosen for further simulations.

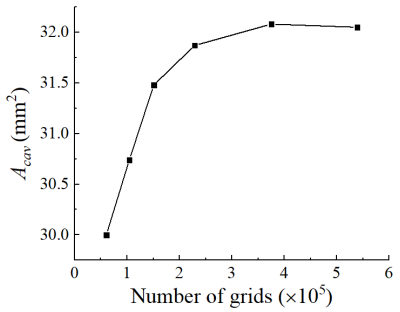

Figure 8. Grid independence test at u_{th}=20.02 *m/s*, p_{out}=100 *kPa*, T=292 *K* (steady simulation)

Table 1. Comparison between simulations and experiments at u_{th}=20.02 *m/s*, p_{out}=100 *kPa*, T=292 *K* (transient simulation)

	$\overline{A}_{cav}$: Experiment	$\overline{A}_{cav}$: Simulation		Error (%)
$\overline{A}_{cav}$ (mm^2)	30.38	SST k-ω	30.87	1.61
		k-ε	30.74	1.18
		RNG k-ε	28.93	4.77
f (Hz)	303.3	SST k-ω	294.0	3.07
		k-ε	299.8	1.15
		RNG k-ε	318.9	5.14

4.3. The cavitating Venturi flow

Set the pressure of the upstream tank to 300 *kPa*, and the downstream tank is open. As mentioned before, cavitation will occur at the throat of the venturi and develop downstream after opening the valve. In one blowdown experiment, with the decrease of the pressure difference, the velocity at the throat decreases, and the type of cavitation undergoes a transition from supercavitation (Fig. 9(a)), to cloud cavitation (Fig. 10), and finally to sheet cavitation (Fig. 9(b)). Supercavitation occurs at the beginning, with the largest flow velocity at the throat and the smallest κ. On this condition, the cavitation is fully developed, and the cavitation area exceeds the visualization window. At last of the experiment, it becomes to sheet cavitation. Under this condition, the length of the attached cavity cloud changes very little, and its shape is relatively stable.

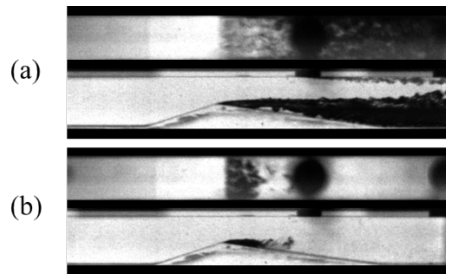

Figure 9. (a) super cavitation κ=1.31;(b) sheet cavitation κ=5.40 (T=292 *K*, Σ=3.43)

As for cloud cavitation, there exists a periodic shedding phenomenon. As shown in Fig. 10, the cavitation can be regarded as two parts of attached cavity cloud and detached cavity clouds/clusters. The length of the attached cavity cloud increases continuously until the fracture occurs near the throat, and then detached cavity clouds/clusters will fall off downstream. Subsequently, the attached cavity cloud regenerates, and its length will grow further as the cavitation develops. While the detached cavity clouds/clusters continue to move downstream and finally collapse.

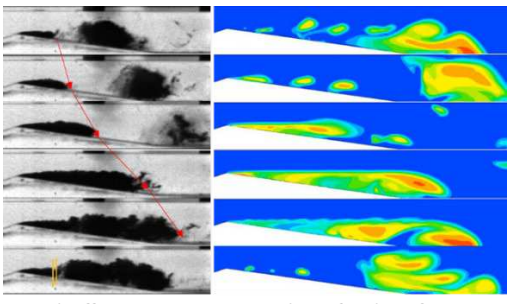

Figure 10. Evolution of cloud cavitation at T=292 *K*, Σ=3.43, κ=1.85 (results of experiment and transient-flow simulation)

4.4. Influence on mean characteristic

According to the definition of Σ, which is used to characterize the degree of the cavitation thermodynamic effects, it is only related to the temperature/physical properties of the working

liquid. Therefore, when experiment conducted at the same temperature, Σ keeps almost the same, while kappa number κ changes. Results in Fig. 11 show the mean area of cavitation (simulation results) and mean length (experimental results) decreases with the increase of κ. Results in Fig. 12 show that they also decrease with the increase of Σ or temperature. At a larger Σ, the cavitation is more stable and the collapse and rebound processes of cavity clouds and clusters at the Venturi throat are less violent in our experiments.

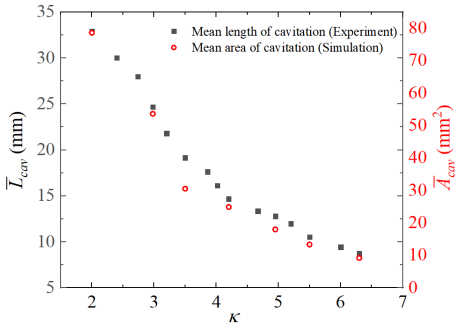

Figure 11. $\overline{L}_{cav}$ of experimental and $\overline{A}_{cav}$ against kappa number κ (T=292 K, Σ=3.43)

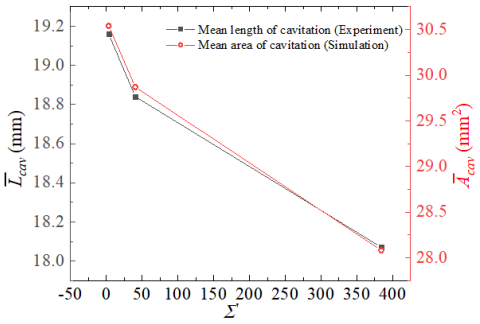

Figure 12. $\overline{L}_{cav}$ and $\overline{A}_{cav}$ against parameter of thermodynamic effect Σ (κ=3.49)

5. CONCLUSIONS

Experimental and numerical research of a specific Venturi structure on the water in a range of 290-360 K are both conducted. A corrected ZGB cavitation method is used and different turbulence models are compared. k-ε model mostly suits such kind of cavitation flow. Both averaged and dynamic results of experimental measurement and numerical results agree well, which means this numerical method can be used in simulations to fill more thermosensitive conditions and obtain more information about flow in the future.

Some conclusions are summarized: 1. Results show that the mean cavitation length of experiments $\overline{L}_{cav}$ and the mean cavitation area of simulations $\overline{A}_{cav}$ have the same trend; 2. $\overline{L}_{cav}$ and $\overline{A}_{cav}$ both decrease as κ increases; 3. They also decrease as Σ increases, which means the thermodynamic effects suppress the cavitation flow and the cavitation-related pressure recovery is reduced.

ACKNOWLEDGEMENTS

This work was partially supported by the National Nature Science Foundation of China (No.52076120 and No.52079066).

REFERENCES

[1] Luo, X. W., Ji, B., & Tsujimoto, Y. (2016). A review of cavitation in hydraulic machinery. Journal of Hydrodynamics, 28(3), 335-358.

[2] Lu, G., Zuo, Z., Sun, Y., Liu, D., Tsujimoto, Y., & Liu, S. (2017). Experimental evidence of cavitation influences on the positive slope on the pump performance curve of a low specific speed model pump-turbine. Renewable Energy, 113, 1539-1550.

[3] Brennen, C. E., Hydrodynamics of pumps; Cambridge University Press, New York, 2011; pp. 114.

[4] Franc, J.P.; Michel, J.M., Fundamentals of cavitation; Springer science & Business media, Berlin, 2006; pp. 10.

[5] Stahl H. A.; Thermodynamic aspects of cavitation in centrifugal pumps, Trans. Am. Soc.Mech. Eng 1956, 78, 1691.

[6] Tomov, P., Khelladi, S., Ravelet, F., Sarraf, C., Bakir, F., & Vertenoeuil, P. (2016). Experimental study of aerated cavitation in a horizontal Venturi nozzle. Experimental Thermal and Fluid Science, 70, 85-95.

[7] Danlos, A., Ravelet, F., Coutier-Delgosha, O., & Bakir, F. Cavitation regime detection through proper orthogonal decomposition: dynamics analysis of the sheet cavity on a grooved convergent–divergent nozzle. International Journal of Heat and Fluid Flow, 2014. 47, 9-20.

[8] Jahangir, S., Hogendoorn, W., & Poelma, C. (2018). Dynamics of partial cavitation in an axisymmetric converging-diverging nozzle. International Journal of Multiphase Flow, 106, 34-45.

[9] Coutier-Delgosha, O., Devillers, J. F., Pichon, T., Vabre, A., Woo, R., & Legoupil, S. (2006). Internal structure and dynamics of sheet cavitation. Physics of fluids, 18(1), 017103.

[10]Callenaere, M., Franc, J. P., Michel, J. M., & Riondet, M. (2001). The cavitation instability induced by the development of a re-entrant jet. Journal of Fluid Mechanics, 444, 223-256.

[11]Brennen, C. (1973). The dynamic behavior and compliance of a stream of cavitating bubbles. Journal of Fluids Engineering, 95(4), 533-541.

[12]Petkovšek M, Dular M. IR measurements of the thermodynamic effects in cavitating flow[J]. International Journal of Heat and Fluid Flow, 2013, 44: 756-763.

[13]Petkovšek M, Dular M. Observing the thermodynamic effects in cavitating flow by IR thermography [J]. Experimental Thermal and Fluid Science, 2017, 88: 450-460.

[14]Zhang H, Zuo Z, Mørch K A, et al. 2019. Thermodynamic effects on Venturi cavitation characteristics. Physics of Fluids [J], 31: 097107.

[15]Ge M, Petkovšek M, Zhang G, et al. Cavitation dynamics and thermodynamic effects at elevated temperatures in a small Venturi channel[J]. International Journal of Heat and Mass Transfer, 2021, 170: 120970.

[16] Watanabe S, Enomoto K, Yamamoto Y, et al. Thermal and dissolved gas effects on cavitation in a 2-D convergent-divergent nozzle flow [C]// Proceedings of the ASME 2014 4th Joint US-European Fluids Engineering Division Summer Meeting Collocated with the ASME 2014 12th International Conference on Nanochannels, Microchannels, and Minichannels, 2014.

[17]Ohira K, Nakayama T, Nagai T 2012. Cavitation flow instability of subcooled liquid nitrogen in converging–diverging nozzles. Cryogenics [J], 52: 35-44.

[18]Zhu J, Xie H, Feng K, et al. 2017. Unsteady cavitation characteristics of liquid nitrogen flows through Venturi tube. International Journal of Heat and Mass Transfer [J], 112: 544-552.

[19]Wei A, Yu L, Gao R, et al. Unsteady cloud cavitation mechanisms of liquid nitrogen in convergent–divergent nozzle[J]. Physics of Fluids, 2021, 33(9): 092116.

[20]Chen T, Chen H, Liang W, et al. Experimental investigation of liquid nitrogen cavitating flows in converging-diverging nozzle with special emphasis on thermal transition[J]. International Journal of Heat and Mass Transfer, 2019, 132: 618-630.

[21]Chen T, Chen H, Liu W, et al. 2019. Unsteady characteristics of liquid nitrogen cavitating flows in different thermal cavitation mode. Applied Thermal Engineering [J], 156: 63-76.

[22]Hosangadi A, Ahuja V. Numerical study of cavitation in cryogenic fluids[J]. Journal of Fluids Engineering, 2005, 127(2): 267-281.

[23]Long X, Liu Q, Ji B, et al. Numerical investigation of two typical cavitation shedding dynamics flow in liquid hydrogen with thermodynamic effects[J]. International Journal of Heat and Mass Transfer, 2017, 109: 879-893.

[24]Stepanoff A J. Cavitation Properties of Liquids[J]. ASME Journal of Engineering for Power, 1964, 86: 195.

[25]Tani N, Tsuda S, Yamanishi N, et al. Development and validation of new cryogenic cavitation model for rocket turbopump inducer[C]//Proceedings of the 7th International Symposium on Cavitation(CAV2009), Michigan, USA, 2009.

[26]Chen T, Wang G, Huang B, et al. Numerical study of thermodynamic effects on liquid nitrogen cavitating flows[J]. Cryogenics, 2015, 70: 21-27.

[27]Zhang Yao, Luo Xianwu, et al. A thermodynamic cavitation model for cavitating flow simulation in a wide range of water temperatures [J]. Chinese Physics Letters, 2010, 27(1):016401.

[28]Sun T, Zong Z, Zou L, et al. Numerical investigation of unsteady sheet/cloud cavitation over a hydrofoil in thermo-sensitive fluid[J]. Journal of Hydrodynamics, Ser. B, 2017, 29(6): 987-999.

[29]Hord J. Cavitation in liquid cryogens. 2: Hydrofoil[R]. National Aeronautics and Space Administration, Lewis Research Center, 1973.

[30]Zhu J, Wang S, Zhang X. Influences of thermal effects on cavitation dynamics in liquid nitrogen through Venturi tube[J]. Physics of Fluids, 2020, 32(1): 012105.

[31]Kikuta K, Yoshida Y, Hashimoto T, et al. Influence of rotational speed on thermodynamic effect in a cavitating inducer [C]// Proceedings of the ASME 2009 Fluids Engineering Division Summer Meeting, 2009.

[32]Christopher Earls Bernnen. Fundamentals of multiphase flow. California Institute of Technology, 2003:19~51.

[33]Zwart P J, Gerber A G, Belamri T. A two-phase flow model for predicting cavitation dynamics [C].// In Fifth International Conference on Multiphase Flow,Yokohama, Japan, 2004.

[34] Zhang S, Li X, Zhu Z. Numerical simulation of cryogenic cavitating flow by an extended transport-based cavitation model with thermal effects[J]. Cryogenics, 2018: 89-104.

[35]Li X J, Shen T J, Li P C, et al. Extended compressible thermal cavitation model for the numerical simulation of cryogenic cavitating flow[J]. International Journal of Hydrogen Energy, 2020, 45:10104-10118.

Conference on Modelling Fluid Flow (CMFF'22)
The 18th International Conference on Fluid Flow Technologies
Budapest, Hungary, August 30-September 2, 2022

Investigations on the Separation of Two Immiscible Liquids in Helical Pipes with Different Conditions and Dimensions

Michael MANSOUR[1;2], Conrad MÜLLER[3], Dominique THÉVENIN[4], Katharina ZÄHRINGER[5]

[1] Corresponding Author. Mechanical Power Engineering Department, Faculty of Engineering - Mataria, Helwan University, 11718 Cairo, Egypt. E-mail: m.botros@m-eng.helwan.edu.eg
[2] Lab. of Fluid Dynamics & Technical Flows, University of Magdeburg "Otto von Guericke", 39106 Magdeburg, Germany. Tel.: +493916758569, Fax: +493916742840, E-mail: michael.mansour@ovgu.de
[3] Lab. of Fluid Dynamics & Technical Flows, University of Magdeburg "Otto von Guericke", 39106 Magdeburg, Germany. E-mail: conrad.mueller@ovgu.de
[4] Lab. of Fluid Dynamics & Technical Flows, University of Magdeburg "Otto von Guericke", 39106 Magdeburg, Germany. E-mail: thevenin@ovgu.de
[5] Lab. of Fluid Dynamics & Technical Flows, University of Magdeburg "Otto von Guericke", 39106 Magdeburg, Germany. E-mail: katharina.zaehringer@ovgu.de

ABSTRACT

The separation of two immiscible liquids in helical pipes was investigated in this study. Assuming perfectly mixed liquids at the pipe inlet, the flow conditions and pipe dimensions have been varied in order to study the separation performance. The two immiscible liquids are water and amine. Three different pipe orientations were compared, i.e., vertical upward, vertical downward, and horizontal flow. A laminar flow is considered, covering the optimal range of Reynolds numbers (around Re = 225-563) for separation. Additionally, the separation behaviour was compared in two different pipe diameters. The Volume Of Fluid (VOF) method was used to model the contact surface between the two immiscible liquids. The separation is quantified using the average mixing coefficient of the two liquids. Companion experiments to validate the results of this numerical study are currently running.

Keywords: CFD, Effect of geometrical parameters, Helical pipes, Immiscible liquids, Liquid-liquid separation and mixing, VOF

NOMENCLATURE

A	$[m^2]$	cross-sectional area
A_f	$[m^2]$	grid face area
D	$[m]$	coil diameter
L	$[m]$	length of coil
M_c	$[-]$	mixing coefficient
P	$[m]$	coil pitch
V	$[m^3]$	volume of computational cell
V_m	$[m^3]$	volume of phase m
X/L	$[-]$	dimensionless axial length
CFL	$[-]$	Courant–Friedrichs–Lewy number
De	$[-]$	Dean number
Re	$[-]$	superficial Reynolds number
d	$[m]$	pipe diameter
f_b	$[N]$	body force
g	$[m/s^2]$	gravitational acceleration
i	$[-]$	unit vector of Cartesian axes
k	$[-]$	number of fluid phases
n	$[-]$	number of turns
p	$[N/m^2]$	pressure
u	$[m/s]$	flow velocity
v	$[m/s]$	average flow velocity
$\overline{V}$	$[m^3]$	Average volume of computational cell
α	$[-]$	volume fraction
α_m	$[-]$	local grid volume fraction of phase m
δ	$[-]$	curvature ratio (d/D)
γ	$[-]$	dimensionless pitch $(P/\pi D)$
μ	$[Pa\ s]$	dynamic viscosity
$\overline{\alpha_\mathrm{m}}$	$[-]$	surface-averaged volume fraction of phase m
ρ	$[kg/m^3]$	density

Subscripts and Superscripts

a, m, w	amine, phase m, water
f	grid face
c	coefficient

1. INTRODUCTION

In helical pipes, a centrifugal force is generated due to the fluid motion in a curved path, creating a secondary flow in the form of counter-rotating vortices (also known as Dean vortices) even for laminar flow conditions [1]. Due to this secondary flow, the performance of helical pipes concerning several processes like mixing, heat transfer, mass transfer,

and residence time distributions is improved when compared to that of straight pipes [2–6]. Helical pipes provide other advantages when used for such processes as they involve no moving parts, need no source of power, and are compact in design. Accordingly, helical pipes need low maintenance and consume low energy. On the other hand, the pressure drop in helical pipes is usually higher compared to a straight pipe of the same length [4].

Multiphase flows of immiscible fluids can be found in important physical and chemical applications, comprising petroleum, food, oil, nuclear, polymer, and pharmaceutical industries [5]. The flow of immiscible fluids can involve gas-liquid or liquid-liquid flows. The complexity of such flows depends strongly on the properties of the phases, their volume fractions, and the flow regime (e.g., disperse, slug, plug, segregated...). Furthermore, the presence of the centrifugal force and the secondary flow in helical pipes add to the complexity when investigating such flows [5].

Numerous studies can be found in the literature for the flow in helical pipes concerning miscible fluids [3, 4, 6–9] as well as immiscible fluids [5, 10–13]. When investigating miscible fluids in helical pipes, researchers consider mainly the overall flow features, the structure of the generated vortices, mixing performance, enhancement of heat/mass transfer, and process intensification in general.

Similarly, different objectives are considered for studies examining immiscible fluids in helical pipes (as in the present work). For instance, the enhancement of mass transfer between two immiscible liquids in a curved pipe was investigated by Gelfgat et al. 2003 [11]. Their results showed that the intensity of Dean vortices does not increase in a monotonous manner when increasing Reynolds number (Re). They found an optimal value of Reynolds number at Re = 50 to enhance mass transfer for the considered pipe dimensions.

The phase distributions and the flow regimes of immiscible liquid-liquid flows in helical and curved pipes were thoroughly studied in the literature. Three main flow regimes were found in the study of Sharma et al. 2011 [14] for a kerosene–water flow through curved return bends, including stratified, plug, and dispersed flow regimes. Though they found no significant effect of the flow orientation (upward, downward, or horizontal) on the flow regimes, this may be due to the small pipe length considered in their study (only a half-coil turn). In the experimental studies of Pietrzak 2014 [15] as well as Ali and Mandal 2019 [10] for oil-water two-phase flows, additional flow regimes were observed, such as dispersed (drops), plugs, stratified, wavy, and annular-dispersed flows. These flow regimes were found different when compared to those of straight pipes, whereas it was shown that the viscosity plays a key role concerning flow regimes [10]. Based on pipe dimension and flow conditions, numerous flow regimes can be obtained for curved pipes, as found in some recent studies [16].

Several applications necessitate separation of fluid phases, including for instance pharmaceutical and oil industries [17], to extract, isolate, purify, reuse, or recover either of the phases. However, the separation of immiscible fluids is not easy once the fluids are in contact. Examples of known separation techniques are distillation [18], chromatography [19], filtration [20], centrifugation [21], and gravity settling [22]. These techniques depend on various forces like centrifugal, buoyant, surface tension, capillary, viscous, and/or gravitational force, as well as combinations of them to separate the phases [23]. Consequently, numerous types of separators can be found in the literature. However, most separators are complex in design, limited to specific applications, or not suited for continuous processes.

The simple and compact design of helical pipes was considered for separation processes in several studies. For instance, Zhang et al. 2006 [12] investigated the separation of oil-water flows in a coiled configuration. It was shown that the separation is normally faster when the water droplet diameter is larger. It was also found that the increase of the flow rate or the reduction of the curvature ratio can improve the separation [12, 24]. However, this is valid only for a restricted flow range due to the continuous change of vortical structure with the flow rate [3, 4, 25, 26]. This was confirmed in gas-liquid separation studies in a helical configuration, where it was revealed that the trend of the separation behaviour changes for different flow rates [13, 23]. For example, three different trends were found in [13] by increasing the fluid velocity, i.e., increasing, decreasing, and increasing again. A similar conclusion was reported in [23], where the increase of the centrifugal force was not always positive concerning separation. This is mainly happening because the flow velocity affects the structure of the Dean vortices, the magnitude of different forces acting on the flow, and the residence time available for separation. Accordingly, there exist optimal conditions (in particular in terms of the Reynolds number) for fluid separation in helical pipes.

Based on the literature, the underlying process is still not fully understood. Additionally, most of the previous studies involve some limitations, i.e., too short pipes, a single pipe orientation, a single measurement location (outlet), and/or a limited range of flow conditions. Therefore, the present work investigates in more detail the separation behaviour, particularly when the fluids are initially perfectly mixed at the inlet, which is common in industrial processes. For example, to improve chemical reactions, catalysts should be highly dispersed and well mixed with the main flow. In our previous study [27], the flow of two immiscible liquids (amine and water) in helical and straight pipes was studied computationally to identify optimal separation conditions. It was shown that the separation is very limited in straight pipes

for different orientations, while a very good separation was obtained in a horizontal helical pipe at an optimal water Reynolds number of about 225. However, a single helical pipe with constant dimensions was considered. Accordingly, in the present paper, we extend these investigations further by considering helical pipes with two different pipe diameters. An implicit, unsteady, and segregated solver was employed. The Volume Of Fluid (VOF) method was used to model the interface between the two immiscible liquids. The separation was quantified using the average mixing coefficient of the two liquids [3, 4]. Companion experiments to validate the results of this numerical study are currently running.

2. NUMERICAL MODELING

2.1. Governing equations

For transient conditions, Cartesian coordinates, an incompressible, Newtonian, and adiabatic flow, the governing equations of the CFD (Computational Fluid Dynamics) model can be written as: Continuity equation:

$$\frac{\partial u_i}{\partial x_i} = 0, \tag{1}$$

Momentum equation:

$$\rho\left(\frac{\partial u_i}{\partial t} + u_j\frac{\partial u_i}{\partial x_j}\right) = -\frac{\partial p}{\partial x_i} + \frac{\partial}{\partial x_j}\left[\mu\left(\frac{\partial u_i}{\partial x_j} + \frac{\partial u_j}{\partial x_i}\right)\right] + \rho g_i + f_\mathrm{b}, \tag{2}$$

where $i = 1, 2, 3$, p is the pressure, u is the velocity, μ is the dynamic viscosity, ρ is the density, g is the gravitational acceleration, and f_b is the body force.

2.2. Volume Of Fluid method

The Volume Of Fluid method (VOF) was used to model the interactions between the two immiscible fluids. The VOF technique was initially established to predict the interface between different fluids. In the VOF formulation, an additional transport equation is solved for the local volume fraction (α) of the liquids, while keeping the benefit of modeling the two fluids by one set of conservation equations (one-fluid formulation). Common velocity, pressure, and temperature fields are assumed. The VOF method was successfully employed in several studies considering immiscible fluids, showing reliable results, e.g., [27–31]. In a flow of k phases (here, $k = 2$), the phase volume fraction of phase m is given by:

$$\alpha_\mathrm{m} = \frac{V_\mathrm{m}}{V} \tag{3}$$

where, V_m is the volume of the phase m in the computational cell, and V is the volume of the cell. In each cell, the summation of the volume fractions of all phases must be one. Accordingly, based on the volume fraction, the existence of different fluids in a computational cell can be distinguished. If a phase m is not existing in a cell, a value of $\alpha_\mathrm{m} = 0$ is expected, while $\alpha_\mathrm{m} = 1$ means that the phase m completely fills the cell. The phase volume fraction between 0 and 1 ($0 < \alpha_\mathrm{m} < 1$) indicates partial presence of the phase m, which also means that the cell contains a local interface between both phases. The scalar transport equation of the volume fraction of phase m (α_m) is given by:

$$\frac{\partial \alpha_\mathrm{m}}{\partial t} + \vec{u}\cdot\frac{\partial \alpha_\mathrm{m}}{\partial x_i} = 0 \tag{4}$$

For the cells containing a local interface, the mixture properties are determined based on the fraction of each phase.

2.3. Mixing and separation quantification

The mixing coefficient (M_c) was used to quantify the separation behaviour in the present work [3,4,27, 28]. The mixing coefficient indicates how well the phases are mixed (or separated) on a specific cross-section. It can be calculated for a phase m over a cross-sectional area of A by:

$$M_{\mathrm{c\,m}} = 1 - \frac{\sum_\mathrm{f} |\alpha_\mathrm{m} - \overline{\alpha_\mathrm{m}}| A_\mathrm{f}}{|\overline{\alpha_\mathrm{m}}| \sum_\mathrm{f} A_\mathrm{f}} \tag{5}$$

with

$$\overline{\alpha_\mathrm{m}} = \frac{1}{A}\int \alpha_\mathrm{m}\, dA \tag{6}$$

where $\overline{\alpha_\mathrm{m}}$ is the surface-averaged volume fraction of phase m over the cross-sectional area A, and A_f is the area of a computational cell face. To obtain the overall mixing value M_c of the two liquids, the mixing coefficient is calculated individually for each liquid, and then an average is calculated. Note that, the separation would be easier if the liquids are only incompletely mixed [12]. Accordingly, a value of $M_\mathrm{c} = 1$ means 100% mixing (i.e., no separation at all), which was assumed always at the inlet, representing the worst-case initial condition for the separation of the liquids.

2.4. Numerical settings

The CFD code STAR-CCM+ was employed to perform the numerical simulations. An implicit, unsteady, and segregated solver was used. The second-order upwind scheme was chosen for calculating the convective fluxes. Further, the first-order upwind scheme was set for temporal discretization. To ensure that the maximum local Courant–Friedrichs–Lewy number (CFL) is always lower than 1, an adaptive time step was utilized, where the CFL number was calculated based on the maximum velocity and the minimum cell size of the whole domain. Accordingly, the time step varies in the approximate range between 2×10^{-4} and 8×10^{-4} s. Ten inner iterations were necessary to ensure convergence of all absolute residuals within each time step. The simulations were stopped after a total physical time of at least 1.4 times the average residence time of the flow in the pipes. For instance, the total physical time computed was 20 and 75 s for the superficial Reynolds number of water $\mathrm{Re_w} = 563$ and $\mathrm{Re_w} = 225$,

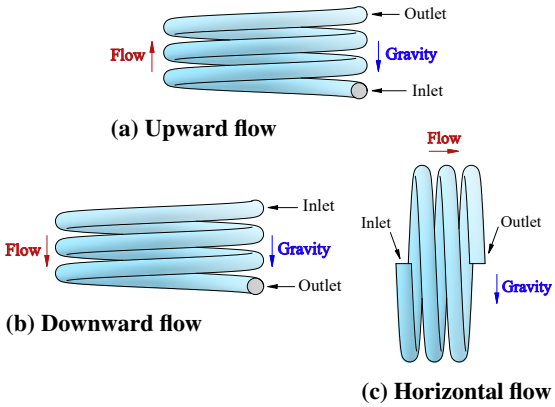

Figure 1. Different orientations considered.

respectively. A no-slip boundary condition was set on the walls. At the inlet of the computational domain, a Hagen-Poiseuille parabolic velocity profile was considered, to avoid the numerical errors coming with the plug-flow (uniform velocity) assumption [3]. Additionally, a perfect mixture was always set at the inlet surface (100% mixing, $M_c = 1$) with a volume fraction of 0.5 for each liquid. This condition corresponds to the theoretical worst case for the separation of the liquids. At the outlet surface, a constant-pressure boundary condition was applied.

2.5. Geometrical settings

As mentioned in the introduction, three different pipe orientations were considered in the investigations: horizontal, vertical upward, and vertical downward, as shown in Figure 1. The dimensions of the basic helical pipe (G1) were selected based on an existing prototype, which was used in several previous experimental and numerical studies [2–4,6,7,26,27]. The geometrical parameters of the different pipes considered in the present study are listed in Table 1. The first geometry (G1) has a pipe diameter of $d = 10$ mm, a coil diameter of $D = 118$ mm, a pitch of $P = 16$ mm, a total number of turns of $n = 3$, and total length of $L = n\sqrt{(\pi D)^2 + P^2} = 1112$ mm. G2 has similar dimensions except that the pipe diameter is $d = 5$ mm.

Table 1. Geometrical parameters of the different helical pipes considered in this study.

Coil	P mm	d mm	D mm	L mm	$\delta = d/D$	$\gamma = P/\pi D$	n
G1	16	10	118	1112	0.084	0.043	3
G2	16	5	118	1112	0.042	0.043	3

2.6. Flow conditions

The liquids considered are water and amine, typically found in the hydroformylation process [27]. The density of water is $\rho_w = 999.79$ kg/m^3, the density of amine is $\rho_a = 791$ kg/m^3, the dynamic viscosity of water is $\mu_w = 8.887 \cdot 10^{-4}$ Pa·s, the dynamic viscosity of amine, $\mu_a = 1.99 \cdot 10^{-3}$ Pa·s. The considered surface tension coefficient between water and amine is set to 0.0285 N/m [27]. Two different Reynolds numbers were studied as given in Table 2, corresponding to the optimal range for separation [27]. Re_w and Re_a are the superficial Reynolds numbers of water and amine, as defined by Equations 7 and 8, respectively, and v is the average velocity of the flow at the inlet surface. At the end, three flow cases with three different values of Dean number ($De = Re\sqrt{\delta}$) are considered as listed in Table 2.

$$Re_w = \frac{\rho_w v d}{\mu_w} \tag{7}$$

$$Re_a = \frac{\rho_a v d}{\mu_a} \tag{8}$$

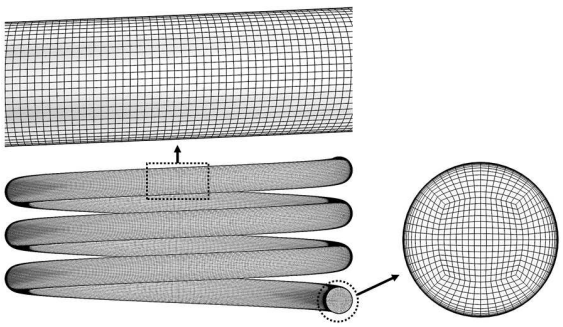

Figure 2. Sample view of the applied hexahedral mesh (G1 with 1.85 million cells).

Table 2. Different flow conditions considered.

Case #	Coil	v (m/s)	Re_a	Re_w	De_a	De_w
1	G1	0.02	79	225	23	65
2	G1	0.05	199	563	58	164
3	G2	0.04	79	225	16	46

3. COMPUTATIONAL MESH

The meshing parameters were selected based on previous studies after performing a mesh-independence test to ensure that mesh-independent results are obtained [27, 32]. Since the coil geometries have different dimensions, scale factors were used to always generate cell elements of the same size as in [27, 32], ensuring a constant resolution in space for all geometries. This leads to hexahedral grids with approximately 1.85 million cells for G1, while G2 has approximately 0.84 million cells. A sample view of a selected mesh is shown in Figure 2.

4. RESULTS AND DISCUSSIONS

4.1. Time averaging

For a specific cross-section, the instantaneous mixing coefficient M_c varies strongly with time due to the various flow regimes generated along the coil. Accordingly, a time-averaged value of M_c was used. When averaging on time intervals lower than 3 s, noticeable variations in the mixing coefficient values are observed; while, when averaging for more than 3.5 s, a stable average could be obtained. For in-

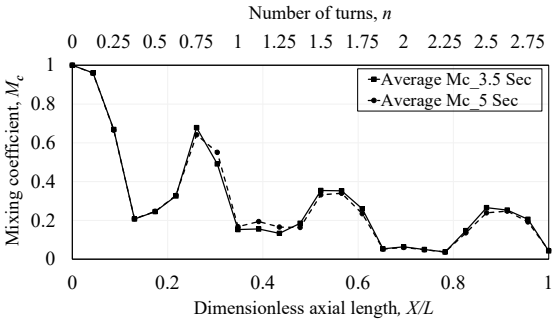

Figure 3. Time-averaged M_c of two different averaging times (3.5 or 5 s) for horizontal flow in G1 at Re_w = 563.

stance, the value of M_c obtained when averaging during 3.5 and 5 s are identical for the horizontal flow in G1 at Re_w = 563. The averaged M_c is shown in Figure 3 against the coil axial length. No significant changes can be seen between the averaged curves of the two time periods, confirming proper time averaging. Accordingly, a time duration of 3.5 s has been kept to calculate the time-averaged mixing coefficient.

4.2. Effect of pipe orientation

Figures 4a, 4b, 4c show the volume fraction of amine for upward, downward, and horizontal flow, respectively, at Re_w = 563 in G1. To track phase separation, the amine phase is represented in Figure 4 by (red) iso-surfaces that show all cells with amine volume fractions between 0.99 and 1 (almost pure amine). The blue color indicates almost pure water, while the green color represents a perfect mixture of the two liquids, as prescribed at the inlet surface.

For the upward flow shown in Figure 4a, a thin water layer separates and accumulates gradually on the lower side of the pipe due to its higher density. However, no significant separation is observed for this pipe orientation. This is also the case for the downward flow shown in Figure 4b, which shows only a minor separation of amine after two coil turns. On the other hand, rapid separation of amine is taking place after only half a turn as demonstrated in Figure 4c for the horizontal pipe orientation. Additionally, the amine phase is accumulating (red color) at the end of each turn, showing significant separation. Note that, the buoyant force changes direction each half-turn, allowing a local accumulation of amine (the lighter phase) before the maximum pressure (at the lowest part of each turn).

Figure 5 shows the minimum, average, and maximum mixing coefficients for different pipe orientations at Re_w = 563 in G1. For the upward flow shown in Figure 5a, the mixing coefficient drops progressively with the accumulation of water phase shown above, yet a very limited separation takes place. Similarly, a poor separation is taking place for the downward flow as shown in Figure 5b. Additionally, large fluctuations of the mixing coefficient occur in

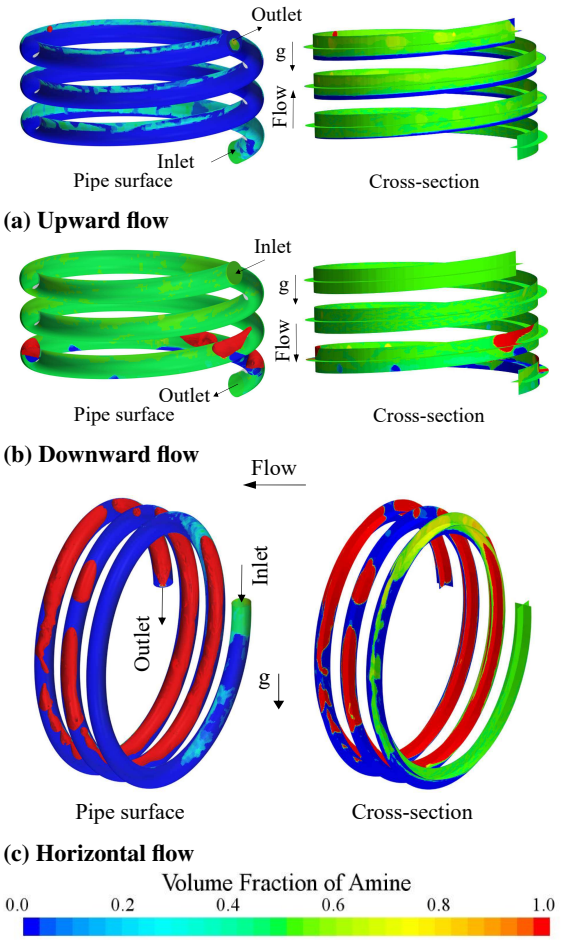

Figure 4. Upward, downward, and horizontal flow in G1 at Re_w =563.

the third coil turn due to the separation of amine droplets and slugs. For the horizontal flow, the average mixing coefficient fluctuates periodically along the pipe length corresponding to local accumulations of amine. Here, the average mixing coefficient is very low (0.04) after about two turns, with very limited changes between minimum, average, and maximum mixing coefficients, demonstrating very good separation.

4.3. Effect of Reynolds number

Figure 6 compares the volume fraction of amine (red represents pure amine) in G1 between Re_w = 225 and Re_w = 563. As shown, a very good separation takes place for both values. Nonetheless, a plug flow regime occurs on the left side of the pipe at Re_w = 225, while an intermittent flow regime is observed at Re_w = 563 on the same side. For the higher value of the Reynolds number, the residence time is lower, leading to a slightly lower separation (smaller accumulation of amine). The corresponding mixing coefficients are shown in Figure 7. Again, the mixing coefficient behaviour is similar for both Reynolds number values. However, it is slightly higher for Re_w = 563, due to the lower residence time.

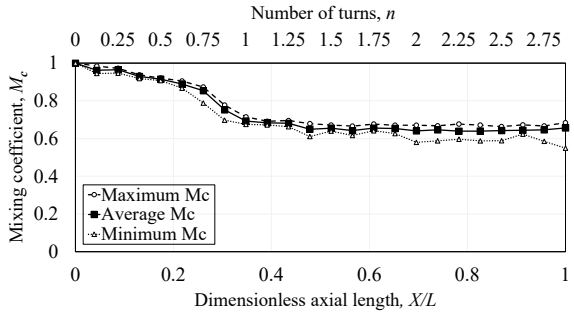

(a) Upward flow

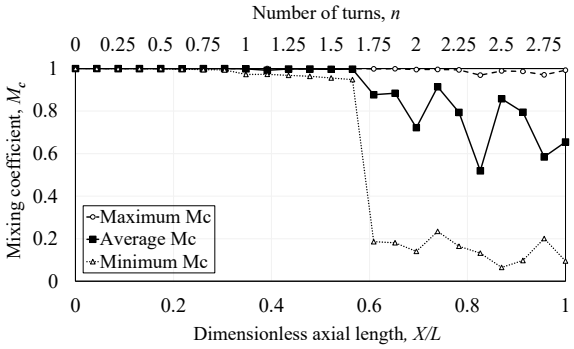

(b) Downward flow

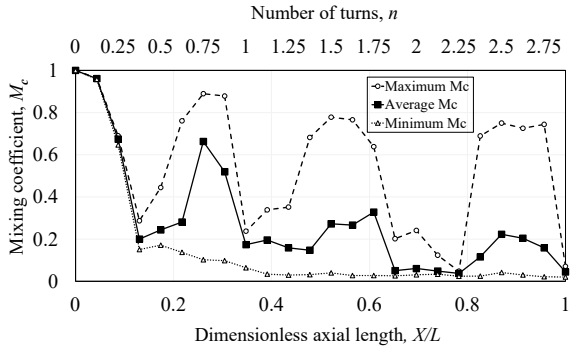

(c) Horizontal flow

Figure 5. Mixing coefficients in G1 at Re_w = 563.

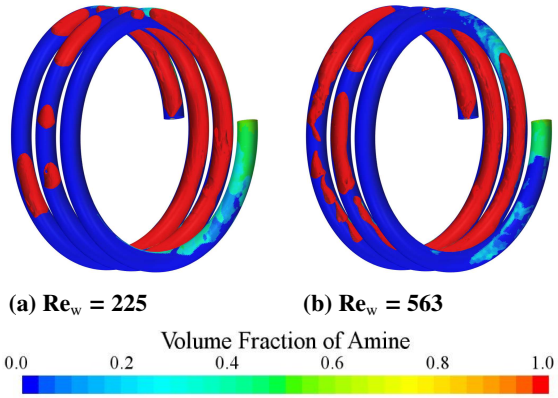

(a) Re_w = 225 **(b) Re_w = 563**

Figure 6. Volume fraction of amine for horizontal flow in G1 at Re_w = 225 and Re_w = 563.

4.4. Effect of pipe diameter

In this section, the influence of varying the pipe diameter is considered comparing G1 with d = 10 mm and G2 with d = 5 mm for the same Reynolds number (Re_w=225); yet the Dean number is different due to the change in the curvature ratio (see again Tables 1 and 2). As shown in Figure 8, the separation is strongly reduced in the lower pipe diameter coil (G2), where a flow regime transition occurs and only a plug flow is observed after approximately two coil turns, leading to a very slow and improper separation. In G2, no accumulation of amine can be observed. This happens mainly due to the increased flow velocity and the strongly reduced residence time as well as the decreased curvature ratio. For the very low curvature ratios, the flow behaviour becomes close to that in a straight pipe, decreasing the separation. This reduced separation is quantified by the mixing coefficients as shown in Figure 9, where the values are much higher when compared to those of G1 shown in Figure 7a. Consequently, it would be recommended to utilize the horizontal orientation with appropriate flow conditions and pipe diameter to ensure efficient separation of immiscible liquids. The investigations will be extended in the future to study the other geometrical parameters as well as fluid properties.

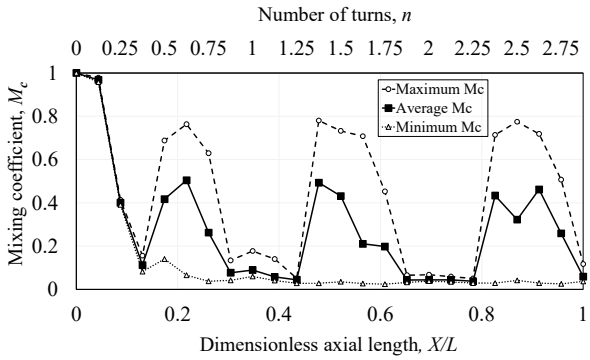

(a) Re_w = 225

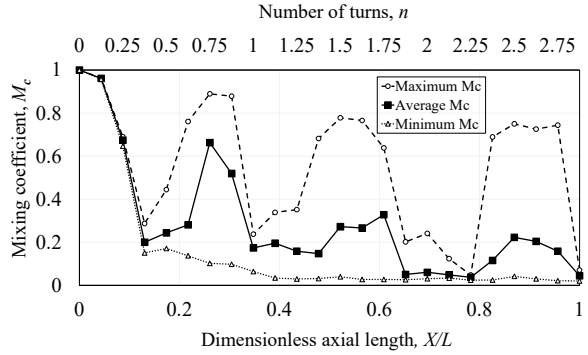

(b) Re_w = 563

Figure 7. Mixing coefficients for horizontal flow in G1 at Re_w = 225 and Re_w = 563.

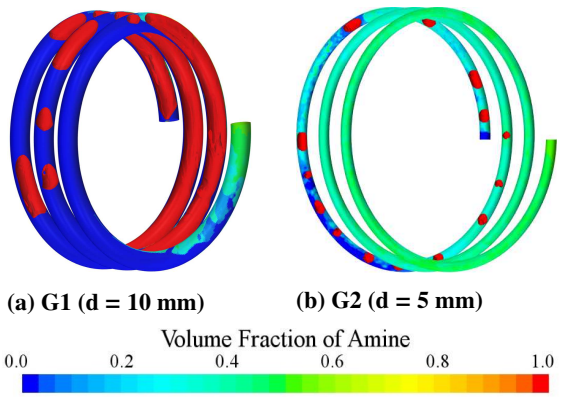

Figure 8. Volume fraction of amine for horizontal flow in G1 and G2 at Re_w = 225.

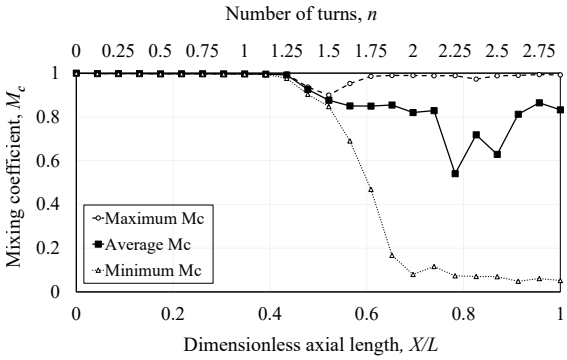

Figure 9. Mixing coefficients for horizontal flow in G2 at Re_w = 225.

5. CONCLUSION

The separation of two immiscible liquids (water and amine) in helical pipes was studied for various conditions. The Volume Of Fluid (VOF) method was used to model the contact surface between the two immiscible liquids. The separation is quantified using the average mixing coefficient of the two liquids. A perfect mixture was assumed at the pipe inlet, representing the worst case for the two liquids two separate. The separation performance was compared for three different pipe orientations, i.e., vertical upward, vertical downward, and horizontal flow. Additionally, two values of Reynolds number and pipe diameters were studied. Only very poor separation is happening in the upward and the downward flow, while the horizontal pipe orientation leads to much better separation. When increasing the Reynolds number from 225 to 563, the residence time decreases, leading to a slightly lower separation. Further, when reducing the pipe diameter from 10 to 5 mm at the same Reynolds number (225), a flow transition occurs, leading to a plug flow in the pipe, which eliminates the accumulation of the lighter phase and reduces the phase separation strongly. Accordingly, it would be generally recommended to employ the horizontal orientation with appropriate flow conditions and coil dimensions to ensure efficient separation of immiscible liquids.

ACKNOWLEDGEMENTS

The authors would like to thank the Deutsche Forschungsgemeinschaft (DFG, German Research Foundation) - TRR 63 “Integrated Chemical Processes in Liquid Multiphase Systems” (subproject B1) - 56091768 (Gefördert durch die Deutsche Forschungsgemeinschaft (DFG) - TRR 63 “Integrierte chemische Prozesse in flüssigen Mehrphasensystemen” (Teilprojekt B1) – 56091768).

REFERENCES

[1] Dean, W. R., 1927, “Note on the motion of fluid in a curved pipe”, *Lond Edinb Dubl Phil Mag*, Vol. 4 (20), pp. 208–223.

[2] Jokiel, M., Wagner, L.-M., Mansour, M., Kaiser, N. M., Zähringer, K., Janiga, G., Nigam, K. D., Thevenin, D., and Sundmacher, K., 2017, “Measurement and simulation of mass transfer and backmixing behavior in a gas-liquid helically coiled tubular reactor”, *Chem Eng Sci*, Vol. 170, pp. 410–421.

[3] Mansour, M., Liu, Z., Janiga, G., Nigam, K. D., Sundmacher, K., Thévenin, D., and Zähringer, K., 2017, “Numerical study of liquid-liquid mixing in helical pipes”, *Chem Eng Sci*, Vol. 172, pp. 250–261.

[4] Mansour, M., Khot, P., Thévenin, D., Nigam, K. D., and Záhringer, K., 2020, “Optimal Reynolds number for liquid-liquid mixing in helical pipes”, *Chem Eng Sci*, Vol. 214, p. 114522.

[5] Mansour, M., Landage, A., Khot, P., Nigam, K. D., Janiga, G., Thévenin, D., and Záhringer, K., 2020, “Numerical study of gas–liquid two–phase flow regimes for upward flow in a helical pipe”, *Ind Eng Chem Res*, Vol. 59 (9), pp. 3873–3886.

[6] Mansour, M., Thévenin, D., Nigam, K. D. P., and Zähringer, K., 2019, “Generally-valid optimal Reynolds and Dean numbers for efficient liquid-liquid mixing in helical pipes”, *Chem Eng Sci*, Vol. 201, pp. 382–385.

[7] Khot, P., Mansour, M., Thévenin, D., Nigam, K. D. P., and Zähringer, K., 2019, “Improving the mixing characteristics of coiled configurations by early flow inversion”, *Chem Eng Res Des*, Vol. 146, pp. 324–335.

[8] Mansour, M., Zähringer, K., Nigam, K. D., Thévenin, D., and Janiga, G., 2020, “Multi-objective optimization of liquid-liquid mixing in helical pipes using Genetic Algorithms coupled with Computational Fluid Dynamics”, *Chem Eng J*, Vol. 391, p. 123570.

[9] Mansour, M., Thévenin, D., and Zähringer, K., 2020, “Numerical study of flow mixing and heat transfer in helical pipes, coiled flow inverters and a novel coiled configuration”, *Chemical Engineering Science*, Vol. 221, p. 115690.

[10] Ali, N., and Mandal, M. M., 2019, "Immiscible liquid-liquid flow in coiled tube", *International Conference on Sustainable and Innovative Solutions for Current Challenges in Engineering & Technology*, Springer, pp. 307–319.

[11] Gelfgat, A. Y., Yarin, A., and Bar-Yoseph, P., 2003, "Dean vortices-induced enhancement of mass transfer through an interface separating two immiscible liquids", *Phys Fluids*, Vol. 15 (2), pp. 330–347.

[12] Zhang, J., Guo, J., Gong, D.-t., Wang, L.-y., Tang, C., and Zheng, Z.-c., 2006, "An investigation on oil/water separation mechanism inside helical pipes", *J Hydrodyn*, Vol. 18 (1), pp. 336–340.

[13] Zhang, Y., Guo, C., Hou, H., and Xue, G., 2014, "Experimental research and numerical simulation on gas-liquid separation performance at high gas void fraction of helically coiled tube separator", *Int J Chem Eng*, Vol. 2014.

[14] Sharma, M., Ravi, P., Ghosh, S., Das, G., and Das, P., 2011, "Studies on low viscous oil–water flow through return bends", *Exp Therm Fluid Sci*, Vol. 35 (3), pp. 455–469.

[15] Pietrzak, M., 2014, "Flow patterns and volume fractions of phases during liquid–liquid two-phase flow in pipe bends", *Exp Therm Fluid Sci*, Vol. 54, pp. 247–258.

[16] Al-Azzawi, M., Mjalli, F. S., Husain, A., and Al-Dahhan, M., 2021, "A review on the hydrodynamics of the liquid–liquid two-phase flow in the microchannels", *Ind Eng Chem Res*, Vol. 60 (14), pp. 5049–5075.

[17] Weiwei, E., Pope, K., and Duan, X., 2020, "Separation dynamics of immiscible liquids", *SN Appl Sci*, Vol. 2 (12), pp. 1–14.

[18] Hartman, R. L., Sahoo, H. R., Yen, B. C., and Jensen, K. F., 2009, "Distillation in microchemical systems using capillary forces and segmented flow", *Lab Chip*, Vol. 9 (13), pp. 1843–1849.

[19] Culbertson, C. T., Jacobson, S. C., and Ramsey, J. M., 2000, "Microchip devices for high-efficiency separations", *Anal Chem*, Vol. 72 (23), pp. 5814–5819.

[20] Juang, D. S., Berry, S. M., Li, C., Lang, J. M., and Beebe, D. J., 2019, "Centrifugation-assisted immiscible fluid filtration for dual-bioanalyte extraction", *Anal Chem*, Vol. 91 (18), pp. 11848–11855.

[21] von Deylen, J., Köpplin, J., and Thévenin, D., 2022, "Development and Validation of a Design Tool for an Improved Pitot-Tube Jet-Pump Allowing Continuous Fluid-Fluid Separation", *J Fluids Eng*, Vol. 144 (7), 071401.

[22] Steinhoff, J., Charlafti, E., Leleu, D., Reinecke, L., Franken, H., Becker, K., Kalem, M., Sixt, M., Braß, M., Borchardt, D., et al., 2021, "Energy and resource savings through innovative and CFD-based design of liquid/liquid gravity separators", *Chem Ing Tech*.

[23] da Mota, F. R., and Pagano, D. J., 2014, "Simulation and experimental study of phase segregation in helical pipes: A new method for flow conditioning", *Flow Meas Instrum*, Vol. 35, pp. 99–108.

[24] Xu, B., Zhang, X., Zhao, L., Jiang, M., Liu, L., and Xia, H., 2020, "Structure design and preliminary experimental investigation on oil-water separation performance of a novel helix separator", *Sep Sci Technol*, pp. 1–12.

[25] Kováts, P., Martins, F. J., Mansour, M., Thévenin, D., and Zähringer, K., 2020, "Tomographic PIV measurements and RANS simulations of secondary flows inside a horizontally positioned helically coiled tube", *Exp Fluids*, Vol. 61 (5), pp. 1–15.

[26] Kováts, P., Velten, C., Mansour, M., Thévenin, D., and Zähringer, K., 2020, "Mixing characterization in different helically coiled configurations by laser-induced fluorescence", *Exp Fluids*, Vol. 61 (9), pp. 1–17.

[27] Mansour, M., Kasetti, S., Thévenin, D., Nigam, K. D., and Zähringer, K., 2021, "Numerical study of the separation of two immiscible liquids in helical and straight pipes", *Chem Eng Process*, p. 108654.

[28] Mansour, M., Parikh, T., Engel, S., Wunderlich, B., and Thévenin, D., 2020, "Numerical investigations of gas-liquid two-phase flow in a pump inducer", *J Fluids Eng*, Vol. 142 (2), pp. 021302–1–021302–12.

[29] Kopparthy, S., Mansour, M., Janiga, G., and Thévenin, D., 2020, "Numerical investigations of turbulent single-phase and two-phase flows in a diffuser", *Int J Multiph Flow*, Vol. 130, p. 103333.

[30] Parikh, T., Mansour, M., and Thévenin, D., 2020, "Investigations on the effect of tip clearance gap and inducer on the transport of air-water two-phase flow by centrifugal pumps", *Chem Eng Sci*, Vol. 218, p. 115554.

[31] Mansour, M., Parikh, T., and Thévenin, D., 2020, "Influence of blade pitch and number of blades of a pump inducer on single and two-phase flow performance", *ASME Turbo Expo 2020: Turbomachinery Technical Conference and Exposition*, American Society of Mechanical Engineers, p. V009T21A010.

[32] Mansour, M., Khot, P., Kováts, P., Thévenin, D., Zähringer, K., and Janiga, G., 2019, "Impact of computational domain discretization and gradient limiters on CFD results concerning liquid mixing in a helical pipe", *Chem Eng J*, Vol. In Press, (2019), p. 123121.

Conference on Modelling Fluid Flow (CMFF'22)
The 18th International Conference on Fluid Flow Technologies
Budapest, Hungary, August 30 – September 2, 2022

BUILDING PATTERNS FAVORABLE FOR AIR QUALITY: A PARAMETER STUDY USING LES

Bálint PAPP [1], Gergely KRISTÓF [2]

[1] Corresponding Author. Department of Fluid Mechanics, Faculty of Mechanical Engineering, Budapest University of Technology and Economics. Bertalan Lajos u. 4 – 6, H-1111 Budapest, Hungary. Phone: +36-1-463-2546, E-mail: papp.balint@gpk.bme.hu
[2] Department of Fluid Mechanics, Faculty of Mechanical Engineering, Budapest University of Technology and Economics. E-mail: kristof.gergely@gpk.bme.hu

ABSTRACT

In this paper, a numerical wind tunnel is demonstrated, constructed in a new GPU-based simulation software, in which statistically converged LES results can be obtained within a couple of hours of computational time – a hundred times faster than using conventional CPU-centered CFD models. Using passive turbulence generators near the inlet, the numerical wind tunnel is capable of producing the mean velocity and turbulence intensity profiles characterizing atmospheric boundary layers. In our previous study, the model results were validated with wind tunnel measurements: good agreement was found in terms of both velocity and concentration distributions. The modification of the geometry, as well as the instantaneous flow visualization, is possible during the simulation, enabling the rapid comparison of numerous design concepts.

In the present study, the characteristic velocity and pollutant distributions of typical urban building arrangements – such as street canyons of uniform and heterogeneous roof height, high-rise buildings, as well as vertically elevated buildings with a significant ground clearance – are presented. The optimum building patterns with superior pollutant removal efficiency can be identified by maximizing the mass Stanton number. Based on the parameter studies covering 28 quasi-periodic building patterns of equal volume, recommendations are given for building arrangements to mitigate pedestrian exposure to traffic-induced air pollutants.

Keywords: atmospheric boundary layer (ABL), Computational Fluid Dynamics (CFD), graphics processing unit (GPU), Large Eddy Simulation (LES), pedestrian exposure, traffic-related air pollution

1. INTRODUCTION

Several studies point out the advantages of Large Eddy Simulation (LES) in microscale dispersion modeling via Computational Fluid Dynamics compared to the Reynolds Averaged Navier-Stokes (RANS) approach [1–3]; however, due to its high computational cost, most investigations focus on a single geometry. The analysis of widely varying geometrical parameters using scale-resolving turbulence models is yet to be carried out.

The most frequently investigated parameter of the urban canopy regarding air quality is the street canyons' height-to-width (*H/W*). However, Da Silva et al. [4] concludes that this aspect ratio in itself is not enough to assess street ventilation, even for uniform building height; and other parameters, such as the porosity of the canopy and the size and placement of openings to the wind, can influence the concentration distribution substantially.

Apart from the uniform street canyon geometry, several studies provide information on more complex building configurations, such as asymmetric street canyons [5], lifted up buildings (with significant ground clearance) [6], and arrays consisting of high-rise buildings of uniform and variable height [7–9].

Recommendations for favorable building shapes are compiled in the recent review paper by Huang et al. [10]; moreover, the impact of several geometrical parameters on pollutant transport is summarized by Kluková et al. [11], both highlighting the favorable effect of building height non-uniformity. A comprehensive literature survey was also carried out by Palusci et al. [12] on the impact of the above-mentioned and additional morphological parameters on urban air quality, such as the roof shape, the plan area density and the frontal area density.

In the present study, the total building volume of the investigated building layouts and the installation raster size – which are important economic and urban planning parameters – are set at constant values, following the approach of Kristóf and Füle [13].

2. METHODOLOGY

In this paper, a numerical wind tunnel (Figure 1) is utilized, based on a real boundary layer wind tunnel of the Institute for Hydromechanics of Karlsruhe Institute for Technology (KIT), which was previously validated [14] and applied for urban dispersion studies [15, 16]. Note that the GPU-based LES model was also found applicable for testing the dynamic wind loads of buildings [17, 18].

The numerical wind tunnel, identically to the original, has a model scale of M = 1:150, and it consists of a 19H long flow preparation section (fetch) and an 11H long test section. The width and height of the numerical wind tunnel are 16H and 5H. The reference length is H = 120 [mm] (thus 18 [m] in full scale), which is equal to the uniform building height of simple H/W = 1 aspect ratio street canyons.

2.1. Building Patterns

The main goal of the present study is to analyze and compare several periodic building patterns (examples are shown in Figure 2) in order to find the optimum geometrical arrangement of a given building volume for the best air quality; hence, the total volume of the building configurations presented in this paper is kept constant.

As a reference case, a series of **uniform street canyons** were investigated. Using six rows of buildings, five H/W = 1 aspect ratio street canyons were constructed perpendicular to the wind direction in the test section of the numerical wind tunnel, containing a $W/2$ wide emission zone at the bottom of the canyons representing the traffic lanes. The laterally oriented street canyons are divided by two streamwise cross streets into two 2H wide section at

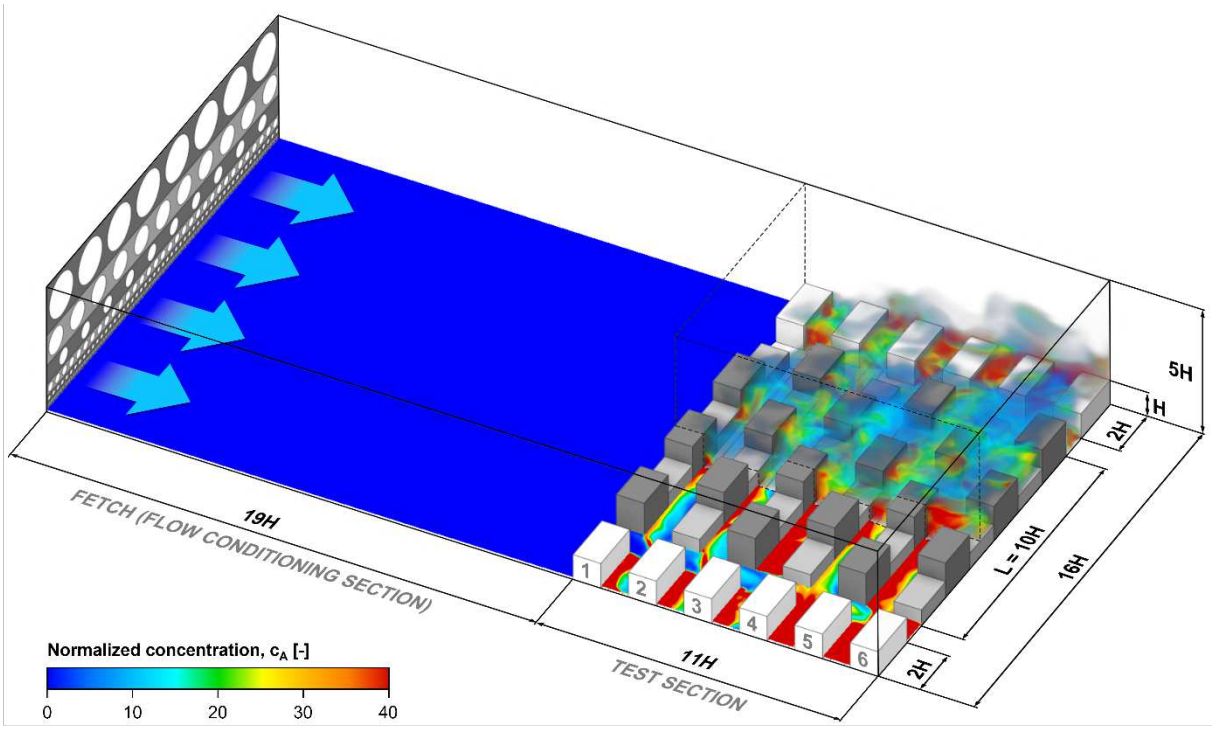

Figure 1. Layout and dimensions of the computational domain relative to the reference building height H = 120 [mm]. The horizontal cut plane shows the instantaneous normalized concentration distribution at pedestrian head height (z/H = 0.0833) for a staggered tower arrangement. Within the volume designated by dashed lines, the 3D dispersion field is displayed.

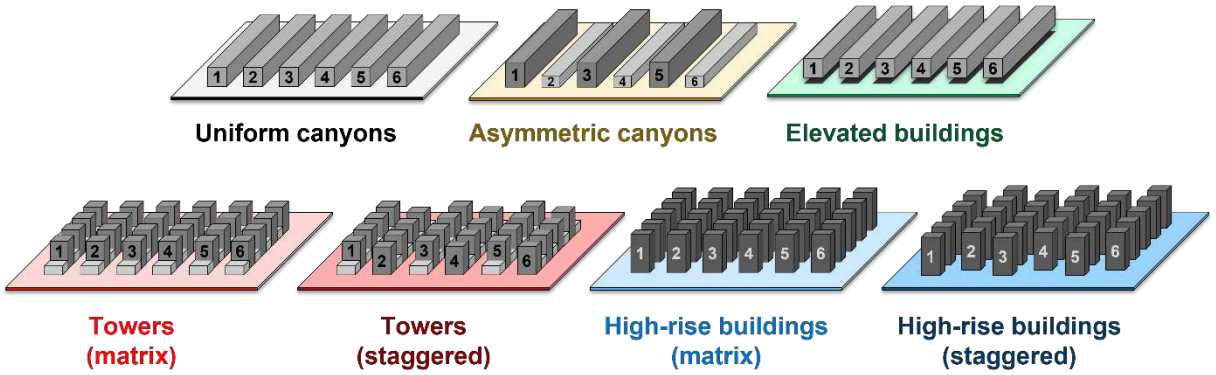

Figure 2. Schematics of the investigated building patterns. Wind direction: from left to right.

the sides and one $L = 10H$ wide section in the middle, as shown in Figure 1. The present investigation focuses on the $L = 10H$ wide central section only.

Asymmetric street canyons can be constructed from the uniform canyons by increasing and decreasing the roof height of consecutive buildings by $\pm\Delta z$. Therefore, each building has a constant roof height along the lateral direction ($H+\Delta z$ or $H-\Delta z$), i.e., the roof height varies only in the streamwise direction, and it is homogeneous in the lateral direction. In these cases, the impact of the roof height heterogeneity ($\Delta z/H$) will be investigated (see Section 3.1 for the results). Note that two simulations were run for each roof height offset: in one, even-numbered buildings were taller, while in the other, the odd-numbered ones. The reason for this is that the flow and dispersion fields are significantly different in the case of finite rows of buildings starting with a short building compared to starting with a tall one. The results for these two arrangements were later averaged to obtain the final ventilation indices.

Towers can be constructed on top of the buildings by dividing the blocks within the $L = 10H$ wide central section laterally and changing the roof height by $\pm\Delta z/H$ of each segment. The width of the towers is $T = L/2N$, in which N is the tower count in a single row ($N = 2, 3, 4, 5$ in this paper). Towers can be placed in the so-called **matrix (aligned) arrangement**, in which there is a full overlap in the streamwise direction between the towers in consecutive streets ($\Delta y/T = 1$), resulting in the roof height varying in the lateral direction only. On the other hand, in the so-called **staggered arrangement**, towers are followed by shorter building sections in the streamwise direction (and vice versa, thus $\Delta y/T = 0$), so the roof height varies in both streamwise and lateral directions (see also Figure 1). For the two tower configurations, the impact of the tower width (T/H, analogous to the impact of the tower count N; see Section 3.2 for the results), and the impact of the tower height ($\Delta z/H$; see Section 3.3) will be analyzed for both matrix and staggered arrangements.

If the roof height offset of the towers is $\Delta z/H = 1$, the resultant geometry consists of fully separated **high-rise buildings**, each of $2H$ height. In these cases, the approach flow can directly access the emission zones at ground level, which is unprecedented in any of the above-mentioned configurations. For these types of building patterns, the impact of the streamwise overlap of the buildings between consecutive rows ($\Delta y/H$) will be studied for both $N = 3$ and 5 towers in a single row (Section 3.4).

Finally, the **uniform buildings** of the reference case can be **vertically elevated**, which also enables the direct transport of pollutants away from the source zones, similar to the high-rise buildings. The impact of the ground clearance (i.e., the gap between the ground and the buildings, $\Delta z/H$) will be investigated (Section 3.5).

2.2. Simulation Setup

For CFD modeling, the GPU-based simulation software ANSYS Discovery Live 2019R3 was used, which was originally developed for mechanical engineering optimization applications. During the transient flow simulations coupled with heat transfer, the continuity, Navier-Stokes and energy equations are solved using the Finite Volume Method (FVM) for discretization. Turbulence is modeled using the standard Smagorinsky subgrid-scale stress model [19] with $C_s = 0.1$.

For resolving the geometries, an equidistant Cartesian mesh is applied, the cell count of which is dependent on the VRAM capacity of the utilized GPU. In the present study, an Nvidia GTX 1080Ti graphics card was employed with 11 GB VRAM, resulting in a total of 9.1 million cells in total. The $H/W = 1$ aspect ratio of the street canyon was chosen as a sweet spot between the number of street canyons and the spatial resolution of each canyon: this way, we have the opportunity to observe five street canyons with the building height and the street width both being resolved by 16 cells, which is sufficiently high for capturing the large-scale eddies governing the dispersion processes using LES [20]. The time step size is adaptively set during the simulation based on the Courant-Friedrichs-Lewy condition [21], with the maximum of the Courant number being kept around $C_{max} = 1.8$, resulting in an average time step size of $5.2 \cdot 10^{-4}$ [s]. Note that a single simulation case required only a couple of hours to cover 20 [s] of physical time (in $M = 1{:}150$ model scale), the last 15 [s] of which was used for time-averaging.

The simulation details and the solution methods of the applied software are given in [18]**.** Note that the latest release at the time of publishing, ANSYS Discovery 2022R1, is capable of performing a fully unstructured FVM similar to the general unstructured FVM in ANSYS Fluent but implemented for GPU HPC.

Atmospheric dispersion processes – both in wind tunnels and in numerical modeling – are notoriously sensitive to the characteristics of the approach flow, i.e., the proper specification of the atmospheric boundary layer (ABL), which in our case is characterized by the below mean velocity and turbulence intensity profiles.

$$u(z) = u_H \cdot (z/H)^{\alpha_u} \tag{1}$$

$$I_u(z) = I_{u,H} \cdot (z/H)^{\alpha_{I,u}} \tag{2}$$

In the above formulas, u [m/s] denotes the streamwise mean velocity, I_u [%] is the turbulence intensity, and z [m] is the vertical coordinate. Moreover, $u_H = 4.64$ [m/s] and $I_{u,H} = 20.98$ [%] are the reference velocity and reference turbulence intensity values taken at roof height $H = 120$ [mm], and $\alpha_u = 0.30$ [–] and $\alpha_{I,u} = -0.36$ [–] are the profile exponents. The characteristic Reynolds number

$Re_H = u_H H/\nu = 37{,}000$ is sufficiently high to assume that the flow and dispersion fields are independent of the Reynolds number [22, 23].

In the present study, an unconventional inlet design (shown in Figure 1 and described in detail in [14]) is employed in order to shorten the length of the flow preparation section. The resultant streamwise mean velocity and turbulence intensity profiles at the beginning of the test section (19H downstream from the inlet) showed good agreement with the wind tunnel profiles (described by coefficients of determination $R^2 = 0.982$ and 0.927), as displayed in Figure 3 below.

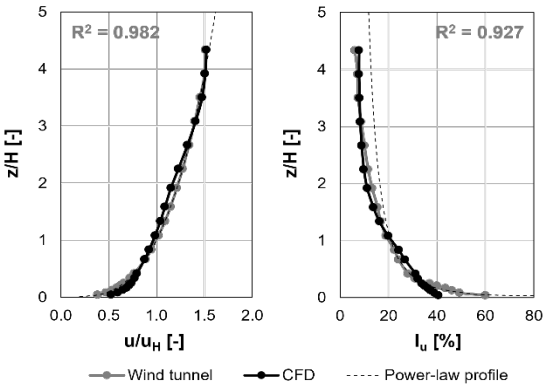

Figure 3. Approach flow profiles: normalized mean velocity and turbulence intensity.

The simulation domain is bounded by symmetry boundary conditions at the lateral sides and at the top. At the solid surfaces, the no-slip condition is maintained. At the downstream boundary 0 [Pa] gauge pressure is assumed.

2.3. Dispersion Modelling Using a Thermal Analogy

In order to simulate the dispersion of traffic-induced air pollutants, a thermal analogy must be applied [14], necessitated by the fact that ANSYS Discovery Live 2019R3 cannot handle user defined scalars (nor can the latest release, ANSYS Discovery 2022R1). The analogy is based on the identical forms of the diffusive and the thermal transport equations of constant property fluids (shown below), supplemented with identical boundary conditions.

$$\frac{dc}{dt} = \nabla \cdot (D \nabla c) \tag{3}$$

$$\frac{dT}{dt} = \nabla \cdot (a \nabla T) \tag{4}$$

In the above equations, c [kg/m^3] denotes the concentration of non-settling, passive pollutants in the air, t [s] is time, T [K] is the absolute temperature, while D and a are the diffusivity and thermal diffusivity coefficients expressed in the same kinematic unit [m^2/s]. The thermal analogy requires the heat conductivity of the fluid to be chosen for the Lewis number to be one ($Le = a/D = 1$); thus, the heat conductivity of air λ [W/(m·K)] in the numerical model is set to

$$\lambda = D \rho c_p \,, \tag{5}$$

where ρ [kg/m^3] is the density, and c_p [J/(kg·K)] is the specific heat of air. Note that in the energy balance both the expansion work and the viscous dissipation need to be neglected.

In conclusion, in the thermal analogy, the temperature field represents the spatial distribution of air pollutants (with 0°C indicating clear air), and the vehicle emissions are taken into account by temporally constant heat sources placed at the traffic areas.

2.4. Ventilation Indices

In the present paper, air quality and the ventilation effectiveness of the different building configurations are assessed using three main properties.

The **normalized velocity** is calculated as

$$u/u_{BL} \,, \tag{6}$$

in which u [m/s] is the streamwise mean velocity and u_{BL} [m/s] is the freestream velocity, i.e., the streamwise mean velocity obtained by spatially averaging at the top of the domain. This approach guarantees that the artificial acceleration of the flow over the urban canopy – caused by the limited domain height and the moderate blockage ratio (20…40%) – are taken into account in the results.

Building patterns of higher roughness, that is, the ones with more heterogeneity in building height, extract more energy from the atmospheric boundary layer. Therefore, some previous investigations employ the friction velocity $u^* = (\tau/\rho)^{0.5}$ for normalization to account for the deceleration of the wind [13]. In contrast to this long-term approach, the present analysis focuses on the local effects, which is also a reasonable and widely used alternative in experimental and computational dispersion studies.

To assess the exposure of pedestrians and residents to traffic-related air pollution, the **normalized concentration** is defined as

$$c_A = \left[\frac{u_{BL} T \cdot \rho c_p}{Q_{heat}/A}\right]_{model} = \left[\frac{u_{BL} c}{Q_{poll}/A}\right]_{real} , \tag{6}$$

in which A [m^2] is the total plan area of the investigated region and Q_{heat} [W] is the source intensity, i.e., the amount of heat introduced to the system through the aforementioned area. Note that if the freestream velocity, the total plan area of a real location and the corresponding pollutant emission intensity Q_{poll} [kg/s] is known, the real pollutant concentration distribution c [kg/m^3] can be realized based on the model results.

Finally, the **mass Stanton number**, i.e., the dimensionless mass transfer coefficient or dilution

coefficient, corresponding to the ventilation efficiency of each building pattern, can be calculated as the reciprocal of the normalized concentration:

$$k_A = \frac{1}{\langle c_A \rangle} \tag{7}$$

Note that the average normalized concentration $\langle c_A \rangle$ in the above formula can be calculated following two slightly different approaches:

1) based on the average concentration **at pedestrian head height** (at z/H = 0.0833 for the present buildings) corresponding to the pedestrian exposure to traffic-related air pollutants, or
2) based on the average concentration **below roof height** ($z < H_{max} = H + \Delta z$) corresponding to the exposure of the residents of the buildings.

3. RESULTS AND DISCUSSION

In the following sections, the impact of five different geometrical parameters will be analyzed. The discussion of the results mainly focuses on the near-ground normalized concentration as the canopy average concentration significantly decreases in all cases compared to the reference case. The detailed numerical quantitative results for all 28 simulation cases can be found in Table A1 in the Appendix.

3.1. The Impact of the Roof Height Heterogeneity in Asymmetric Street Canyons

According to Oke [24], a so-called skimming flow regime develops over densely packed buildings similar to the majority of the building configurations presented in this study. In the case of a series of parallel, H/W = 1 aspect ratio street canyons for perpendicular wind direction, the flow field below roof height is principally governed by the canyon vortex (with a horizontal axis of rotation) at the middle of the 10H long buildings and the vertically rotating corner eddies forming near the intersections (see Figures A1 and A2 in the Appendix).

In asymmetric canyons, the street is bordered by $H \pm \Delta z$ tall buildings, and a more complex vortex structure is formed. The results shown in Figure 4 indicate that smaller (although still substantial) roof height offsets ($\Delta z/H$ = 0.25 and 0.375) cannot mitigate the pedestrian exposure. However, for greater offsets ($\Delta z/H$ = 0.5 and 0.75) resulting in particularly asymmetric street canyons (H_{max}/H_{min} = 3 and 7), the effective aspect ratio of the street canyons formed by every second building increases; hence, the resultant velocity field resembles the wake interference flow regime described by Oke [24]. In these configurations, the large horizontal vortices located between the tall buildings (and above the short ones) become more dominant, and they can effectively transport the traffic-induced air pollutants above roof level, resulting in a concentration decrease of 32% at pedestrian head height.

3.2. The Impact of the Tower Width and Tower Count

A series of simulations with different tower counts were performed with a $\Delta z/H$ = 0.375 roof height offset, resulting in a ratio of the building heights of H_{max}/H_{min} = 2.2. Note that this offset was not able to improve the near-ground air quality for asymmetric street canyons (see the previous section).

It is shown in the upper part of Figure 5 that towers in **matrix (aligned) arrangement** are also unable to improve the near-ground air quality, regardless of the tower count. On the other hand, the air quality of the entire canopy improves by over 30%: the decrease of the average concentration below roof height is the consequence of the wind penetrating the canopy between the towers and letting the pollutants escape from the upper region more efficiently.

In the case of the **staggered tower arrangement**, however, the tower count does matter, as the increased mixing between the towers (illustrated in Figure A2/d in the Appendix) is capable of facilitating an increased wind speed at

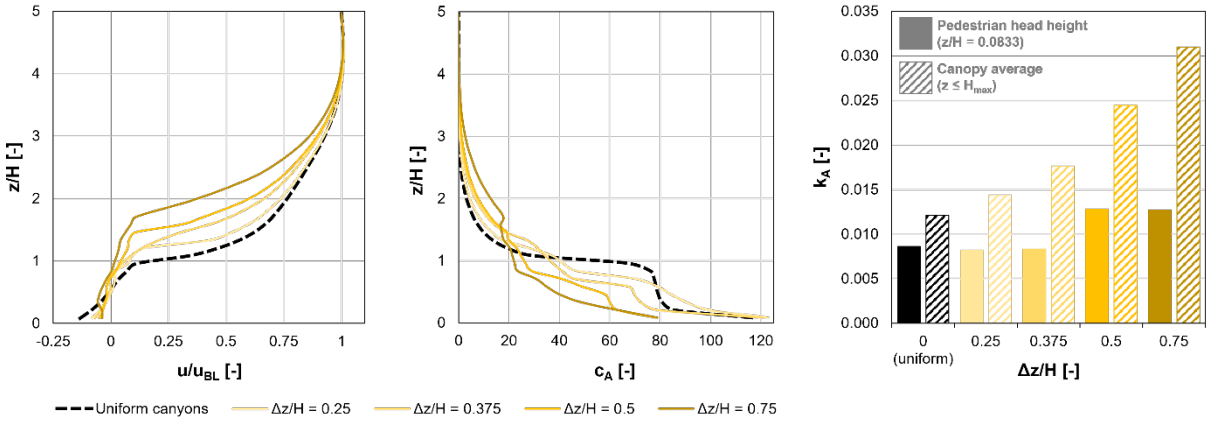

Figure 4. Asymmetric canyons: the impact of the roof height offset ($\pm\Delta z$), compared to the uniform canyons reference case ($\Delta z = 0$). The height difference between the short and tall buildings is actually $2 \cdot \Delta z$. The figure shows the vertical profiles of normalized velocity and concentration as well as the ventilation efficiency.

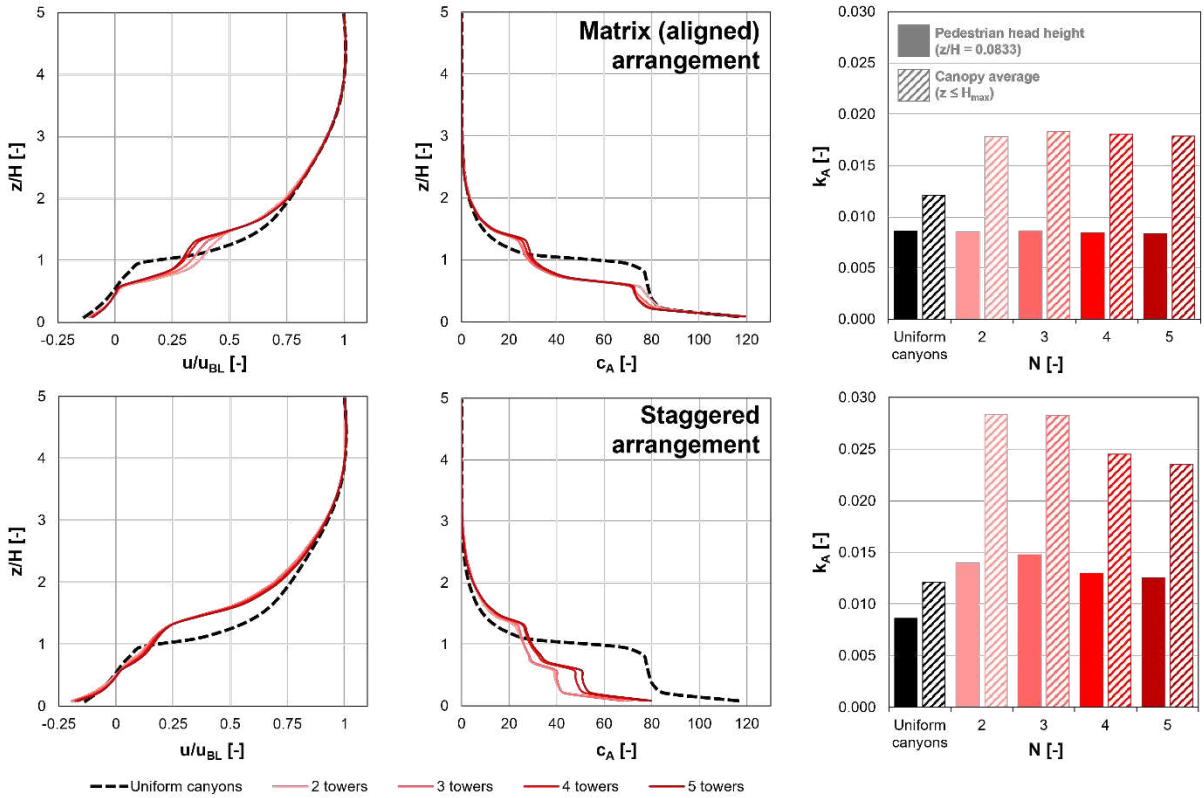

Figure 5. Towers: the impact of the tower count in a single row (N), compared to the uniform canyons reference case. The roof height offset is $\Delta z/H$ = 0.375 for all non-reference cases. The figure shows the vertical profiles of normalized velocity and concentration as well as the ventilation efficiency.

ground level; thus, more efficient pollutant removal is achieved from pedestrian head height. It can be seen in the lower part of Figure 5 that the near ground concentration can be decreased by 38…42% for 2 and 3 towers, while in the presence of 4 and 5 towers, the air quality can be improved by 31…34% compared to the reference case consisting of a series of uniform street canyons. The most favorable three-tower case has a tower width of $T = L/6 = 1.667H$.

3.3. The Impact of the Tower Height

In order to figure out how the air quality depends on the tower height, the superior three-tower setup was further investigated for both the matrix and the staggered arrangement.

Based on the results shown in Figure 6, high rise buildings (corresponding to $\Delta z/H$ = 1) should be clearly separated from the rest of the cases in the **matrix (aligned) arrangement**; as the wind can directly reach the emission zones to sweep away the near-ground pollutants, resulting in a significant decrease of the pedestrian exposure (–42%). In contrast to this configuration, towers placed on top of the base buildings in the matrix arrangement are not able to improve the air quality in the near-ground region, regardless of the tower height.

In contrast, for the **staggered arrangement of** the towers, the pedestrian exposure gradually decreases with the tower height (–32…45% in pedestrian head height); moreover, staggered high-rise buildings (in this case, three in each row) can mitigate the pedestrian exposure to traffic-induced air pollutants by 46%.

3.4. The Impact of the Streamwise Overlap of the High-Rise Buildings

Let us now analyze the effect of the streamwise overlap of the high-rise buildings of the consecutive rows (relative to the tower width: $\Delta y/T$) on air quality in the case of both three and five buildings per row.

It is reinforced by the results shown in Figure 7 that fewer but broader buildings are more favorable for air quality, at least in the first few rows directly subjected to the approach flow, most likely because the wind can penetrate the canopy deeper due to the wider gaps between the buildings.

Shifting the high-rise buildings laterally, starting from the matrix arrangement (full overlap, $\Delta y/T$ = 1) causes more surface to obstruct the wind, which is hence slowed down to a higher degree below roof height, although the mixing is enhanced (see Figure A3 in the Appendix). Depending on the building overlap, however, the mean near-ground concentration decrease is between 42% and 55% for three towers, and between 25% and 32% for five towers, thus the matrix ($\Delta y/T$ = 1), intermediate ($\Delta y/T$ = 0.5) or staggered ($\Delta y/T$ = 0) high-rise buildings are all remarkably efficient solutions for locally mitigating exposure to traffic-related air pollutants compared to a series of uniform street canyons.

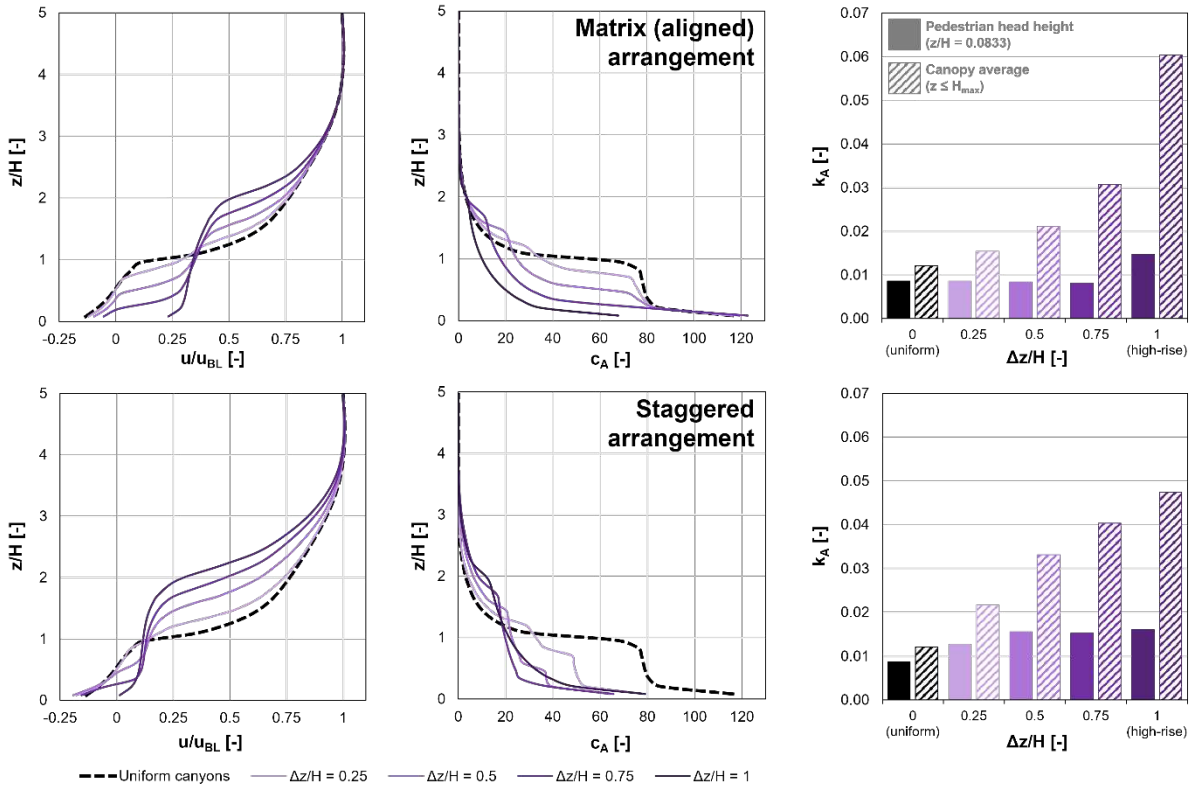

Figure 6. Towers: the impact of the tower height offset ($\pm\Delta z$), compared to the uniform canyons reference case. The height difference between the short and tall buildings is actually $2\cdot\Delta z$. The tower count is $N = 3$ for all non-reference cases. Note that $\Delta z/H = 1$ corresponds to high-rise buildings. The figure shows the vertical profiles of normalized velocity and concentration as well as the ventilation efficiency.

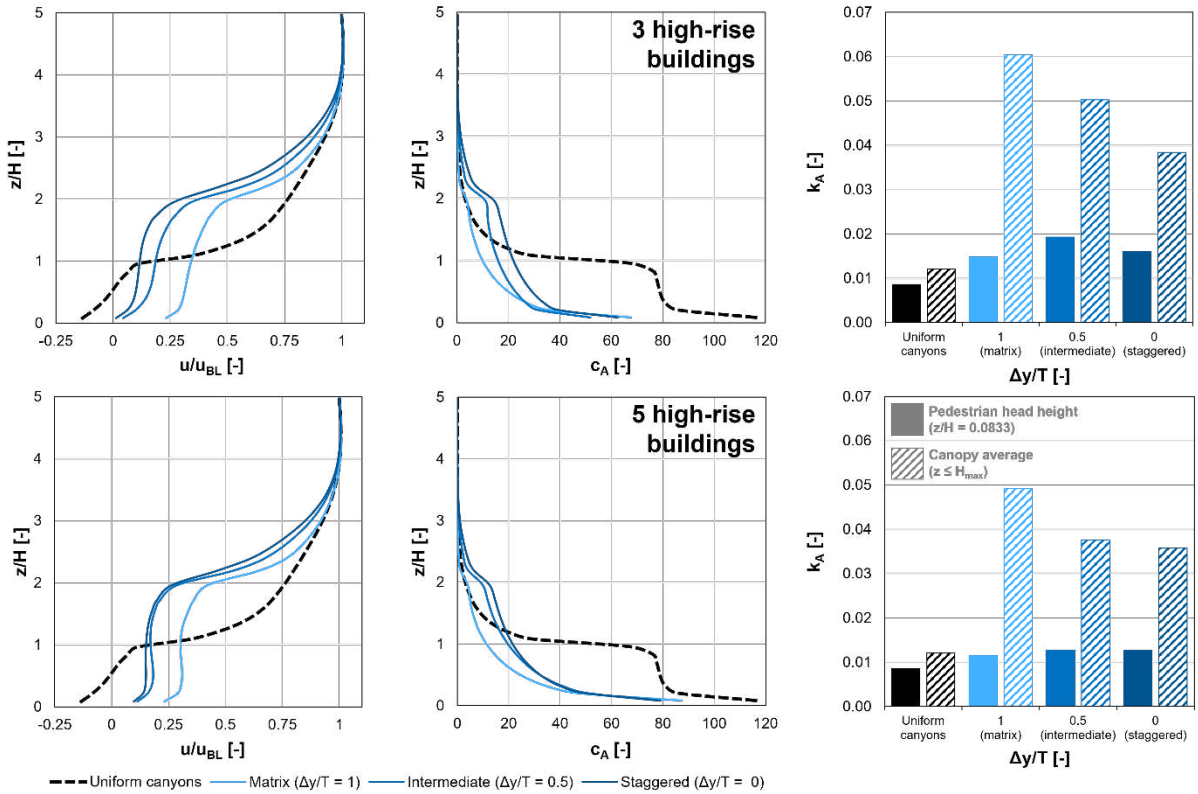

Figure 7. High-rise buildings: the impact of the streamwise overlap of the buildings in consecutive rows (Δy), compared to the uniform canyons reference case. The building height is $2H$ in all non-reference cases. The figure shows the vertical profiles of normalized velocity and concentration as well as the ventilation efficiency.

3.5. The Impact of the Building Elevation

Direct access to the pollutant emission zones can also be achieved by elevating the buildings forming the uniform canyons vertically, that is, by creating a gap at the location of the ground floor.

It is shown in Figure 8 that a ground clearance of $\Delta z/H = 0.1667$ (corresponding to 3 [m] in full scale) is already able to reduce the near-ground concentration by 29%, and if the ground clearance is increased to $\Delta z/H = 0.3333$, the concentration decrease is 60% based on the results of the first five canyons of the city.

Basal openings can cause excessively high near-ground velocities, which is disadvantageous for pedestrian wind comfort. Moreover, as shown in Figures A1 and A2, a stark streamwise near-ground concentration gradient is present as the wind speed decreases and the pollutants accumulate due to the hydraulic resistance of the urban canopy. This implies that the elevation of the buildings could be effective only in the first few canyons that are subjected directly to the wind (e.g., located on the border of the city or next to a larger opening inside).

4. CONCLUSIONS AND OUTLOOK

In this paper, the ventilation characteristics of 28 different periodic building arrangements of equal total volume were analyzed using GPU-based Large Eddy Simulation in ANSYS Discovery Live 2019R3. The pedestrian exposure to traffic-induced air pollutants was characterized by the normalized near-ground pollutant concentration as well as the mass Stanton number, i.e., the dimensionless mass transfer coefficient of the building configurations.

The most important findings are listed below, based on the comparison to a baseline case consisting of a series of $H/W = 1$ aspect ratio parallel street canyons subjected to a perpendicular atmospheric boundary layer approach flow. The results cover six consecutive rows of buildings (thus five streets), and it is acknowledged that the results can differ in the longer run.

a) Asymmetric street canyons are only able to mitigate the pedestrian exposure if the effective street canyon aspect ratio is high enough, i.e., if every second building is rather short ($\Delta z/H > 0.5$).
b) For towers placed on top of shorter continuous buildings in matrix (aligned) arrangement, the near-ground concentration cannot be improved regardless of the tower width or the tower height.
c) For towers in staggered arrangement, the pedestrian exposure decreases with the building height heterogeneity (i.e., the roof height offset).
d) For staggered towers, the near-ground concentration decrease improves proportionally to the roof height offset. The highest decrease was found in the presence of three pieces of $T = 1.667H$ wide towers.
e) High-rise buildings can effectively mitigate pedestrian exposure to traffic-related air pollutants in matrix, intermediate, and staggered arrangements. The near-ground, as well as the canopy average concentration decrease is greater for three wide high-rise buildings ($T = 1.667H$) in a row compared to five slender ones ($T = H$).
f) Vertically elevating the buildings also results in a substantial concentration decrease, which grows with the ground clearance ($\Delta z/H = 0.1667 \ldots 0.3333$).

Note that in cases a) – d), the plan area density of the buildings is kept constant ($\lambda_p = 0.5$). For the high-rise buildings (e), the plan area density is $\lambda_p = 0.25$, and for the elevated buildings (f) $\lambda_p = 0$.

The present study also highlights the importance of screening preliminary design ideas in the conceptual phase of the urban planning process. Following the parameter studies presented in this paper, potentially favorable building patterns were tested in detail via wind tunnel experiments and by CFD simulations in ANSYS Fluent [25], underlining the positive effect of roof height heterogeneity compared to uniform street canyons, as well as supporting the applicability of the presented GPU-based LES method for such investigations.

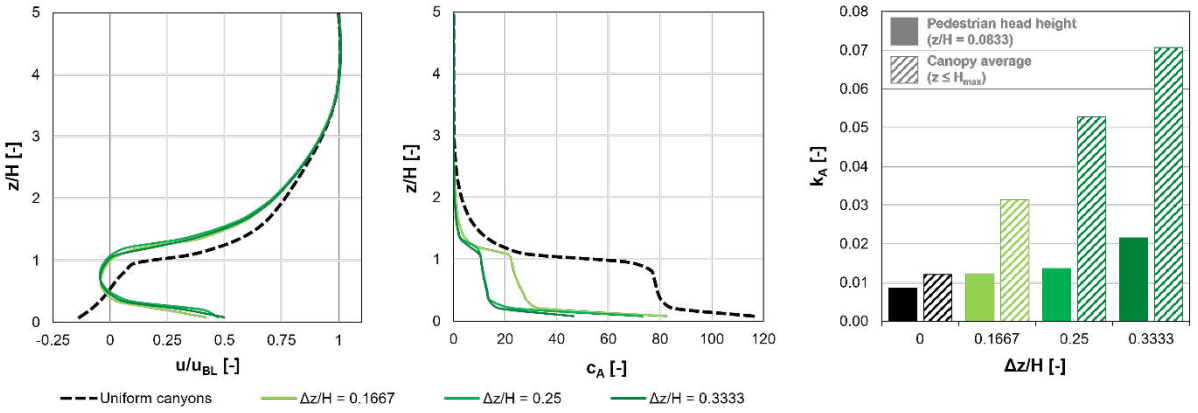

Figure 8. Elevated uniform buildings: the impact of the ground clearance (Δz), compared to the uniform canyons reference case ($\Delta z = 0$). The figure shows the vertical profiles of normalized velocity and concentration as well as the ventilation efficiency.

ACKNOWLEDGEMENTS

This study was funded by grant no. K 124439, NKFIH from the National Research, Development, and Innovation Office, Hungary. The research reported in this paper and carried out at BME has been supported by the NRDI Fund (TKP2020 NC, Grant No. BME-NCS) based on the charter of bolster issued by the NRDI Office under the auspices of the Ministry for Innovation and Technology. The research reported in this paper is part of project no. BME-NVA-02, implemented with the support provided by the Ministry of Innovation and Technology of Hungary from the National Research, Development and Innovation Fund, financed under the TKP2021 funding scheme. Bálint Papp's contribution to this paper was supported by the Gedeon Richter Talent Foundation (registered office: Gyömrői út 19-21, 1103 Budapest, Hungary), established by Gedeon Richter Plc., within the framework of the Gedeon Richter PhD Scholarship. The authors acknowledge the support of CFD.HU Ltd. in providing access to the necessary hardware and software, as well as express their gratitude towards Dipankar Choudhury (Vice President, Research) and Justin Hendrickson (Director of Product Management) of ANSYS, Inc. for providing insight to the simulation methods applied in ANSYS Discovery.

REFERENCES

[1] Tominaga, Y., & Stathopoulos, T. (2013). CFD simulation of near-field pollutant dispersion in the urban environment: A review of current modeling techniques. Atmospheric Environment, 79, 716-730. [DOI]

[2] Tominaga, Y., & Stathopoulos, T. (2016). Ten questions concerning modeling of near-field pollutant dispersion in the built environment. Building and Environment, 105, 390-402. [DOI]

[3] Blocken, B. (2018). LES over RANS in building simulation for outdoor and indoor applications: A foregone conclusion? Building Simulation, 11(5), 821-870). [DOI]

[4] da Silva, F. T., Reis Jr, N. C., Santos, J. M., Goulart, E. V., & de Alvarez, C. E. (2021). The impact of urban block typology on pollutant dispersion. Journal of Wind Engineering and Industrial Aerodynamics, 210, 104524. [DOI]

[5] Li, Z., Zhang, H., Wen, C. Y., Yang, A. S., & Juan, Y. H. (2020). Effects of height-asymmetric street canyon configurations on outdoor air temperature and air quality. Building and Environment, 183, 107195. [DOI]

[6] Du, Y., Mak, C. M., & Li, Y. (2018). Application of a multi-variable optimization method to determine lift-up design for optimum wind comfort. Building and Environment, 131, 242-254. [DOI]

[7] Hang, J., Li, Y., & Sandberg, M. (2011). Experimental and numerical studies of flows through and within high-rise building arrays and their link to ventilation strategy. Journal of Wind Engineering and Industrial Aerodynamics, 99(10), 1036-1055. [DOI]

[8] Hang, J., & Li, Y. (2012). Macroscopic simulations of turbulent flows through high-rise building arrays using a porous turbulence model. Building and Environment, 49, 41-54. [DOI]

[9] Chen, L., Hang, J., Sandberg, M., Claesson, L., Di Sabatino, S., & Wigo, H. (2017). The impacts of building height variations and building packing densities on flow adjustment and city breathability in idealized urban models. Building and Environment, 118, 344-361. [DOI]

[10] Huang, Y., Lei, C., Liu, C. H., Perez, P., Forehead, H., Kong, S., & Zhou, J. L. (2021). A review of strategies for mitigating roadside air pollution in urban street canyons. Environmental Pollution, 280, 116971. [DOI]

[11] Kluková, Z., Nosek, Š., Fuka, V., Jaňour, Z., Chaloupecká, H., & Ďoubalová, J. (2021). The combining effect of the roof shape, roof-height non-uniformity and source position on the pollutant transport between a street canyon and 3D urban array. Journal of Wind Engineering and Industrial Aerodynamics, 208, 104468. [DOI]

[12] Palusci, O., Monti, P., Cecere, C., Montazeri, H., & Blocken, B. (2022). Impact of morphological parameters on urban ventilation in compact cities: The case of the Tuscolano-Don Bosco district in Rome. Science of the Total Environment, 807, 150490. [DOI]

[13] Kristóf, G., & Füle, P. (2017). Optimization of urban building patterns for pollution removal efficiency by assuming periodic dispersion. Journal of Wind Engineering and Industrial Aerodynamics, 162, 85-95. [DOI]

[14] Kristóf, G., & Papp, B. (2018). Application of GPU-based Large Eddy Simulation in urban dispersion studies. Atmosphere, 9(11), 442. [DOI]

[15] Papp, B., Kristóf, G. (2019). Épületmintázatok optimalizálása a levegőminőség javításának érdekében GPU alapú nagyörvény szimulációval. XXVII. Nemzetközi Gépészeti Konferencia (OGÉT 2019) kiadványkötete (ISSN 2068-1267), 400-403.

[16] Szilágyi, M.Á., Papp, B. (2021). Miskolc átszellőzésének vizsgálata GPU-alapú nagyörvény szimulációval: XXVIIII. Nemzetközi Gépészeti Konferencia (OGÉT 2021)

kiadványkötete (ISSN 2668-9685), 80-83. [PDF][Video]
[17] Papp, B., Kristóf, G., Gromke, C. (2020). Épületek szélterhelésének becslése GPU alapú nagyörvény szimulációval numerikus szélcsatornában: XXVIII. Nemzetközi Gépészeti Konferencia (OGÉT 2020) kiadványkötete (ISSN 2668-9685), 161-165. [PDF]
[18] Papp, B., Kristóf, G., & Gromke, C. (2021). Application and assessment of a GPU-based LES method for predicting dynamic wind loads on buildings. Journal of Wind Engineering and Industrial Aerodynamics, 217, 104739. [DOI]
[19] Smagorinsky, J. (1963). General circulation experiments with the primitive equations: I. The basic experiment. Monthly weather review, 91(3), 99-164. [DOI]
[20] Xie, Z., & Castro, I. P. (2006). LES and RANS for turbulent flow over arrays of wall-mounted obstacles. Flow, Turbulence and Combustion, 76(3), 291-312. [DOI]
[21] Courant, R., Friedrichs, K., & Lewy, H. (1967). On the partial difference equations of mathematical physics. IBM journal of Research and Development, 11(2), 215-234. [DOI]
[22] Snyder, W. H. (1981). Guideline for fluid modeling of atmospheric diffusion (Vol. 81, No. 9). Environmental Sciences Research Laboratory, Office of Research and Development, US Environmental Protection Agency. [PDF]
[23] Meroney, R. N. (2004). Wind tunnel and numerical simulation of pollution dispersion: a hybrid approach. Paper for Invited Lecture at the Croucher Advanced Study Institute, Hong Kong University of Science and Technology, 6-10. [PDF]
[24] Oke, T. R. (1988). Street design and urban canopy layer climate. Energy and buildings, 11(1-3), 103-113. [DOI]
[25] Papp, B., Kristóf, G., Istók, B., Koren, M., Balczó, M., & Balogh, M. (2021b). Measurement-driven Large Eddy Simulation of dispersion in street canyons of variable building height. Journal of Wind Engineering and Industrial Aerodynamics, 211, 104495. [DOI]

APPENDIX A1 – TYPICAL FLOW AND DISPERSION FIELDS

In this section, time-averaged velocity and normalized concentration distributions are presented in order to illustrate the flow and dispersion phenomena described in Section 3.

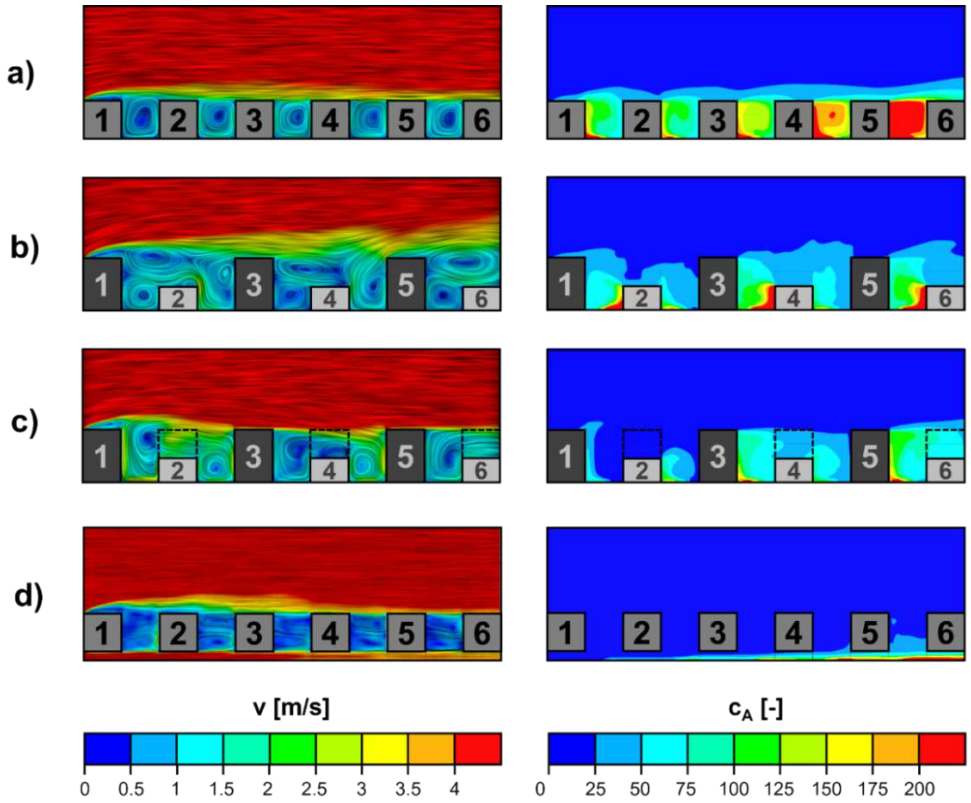

Figure A1. Flow and dispersion fields in the $y/H = 0$ vertical plane for building patterns of equal volume. a) uniform canyons; b) asymmetric canyons, $\Delta z/H = 0.375$; c) towers on top of the buildings in staggered arrangement, $\Delta z/H = 0.375$. d) elevated uniform buildings, $\Delta z/H = 0.25$. Wind direction: from left to right.

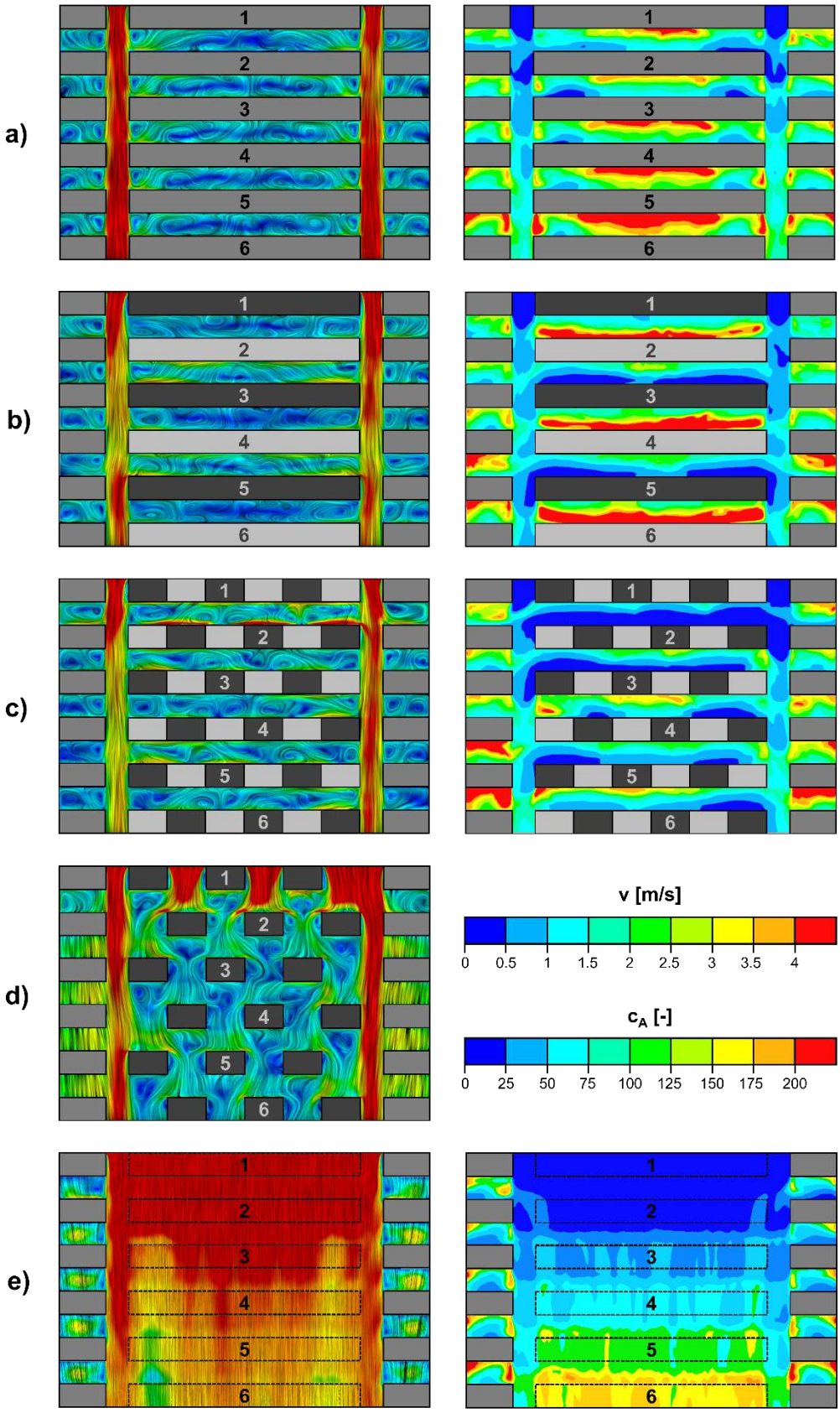

Figure A2. Flow and dispersion fields at pedestrian head height (in the $z/H = 0$ horizontal plane) for building patterns of equal volume. a) uniform canyons; b) asymmetric canyons, $\Delta z/H = 0.375$; c) three towers per row on top of the buildings in staggered arrangement, $\Delta z/H = 0.375$; d) flow field between the staggered towers at $z/H = 1.1875$; e) elevated uniform buildings, $\Delta z/H = 0.25$. Darker grey colors indicate taller buildings. Wind direction: from left to right.

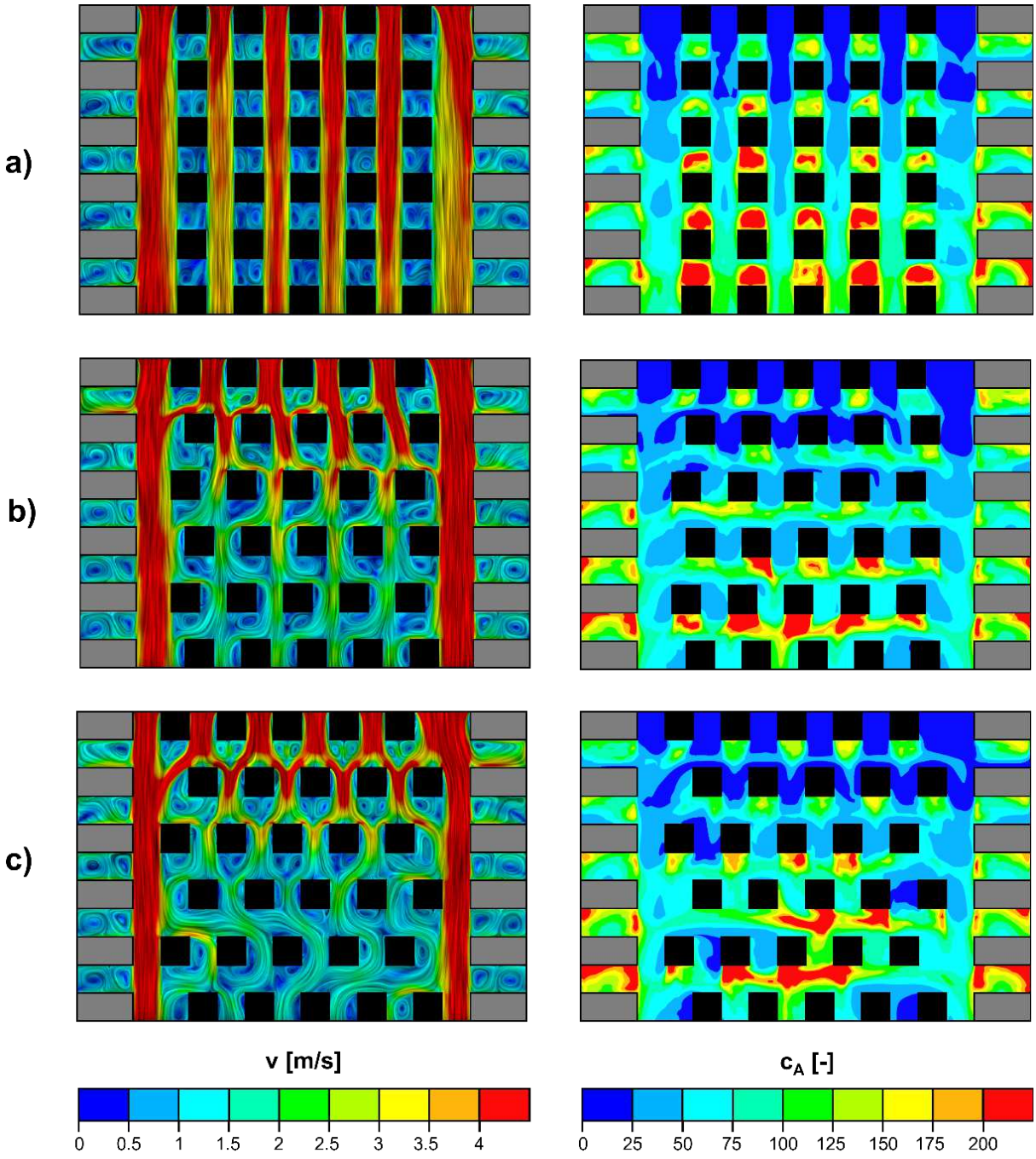

Figure A3. Flow and dispersion fields at pedestrian head height (z/H = 0.0833) for five, 2H tall high-rise buildings per row with different streamwise overlap of the buildings in consecutive rows. a) matrix arrangement, $\Delta y/T$ = 1; b) intermediate arrangement, $\Delta y/T$ = 0.5; c) staggered arrangement, $\Delta y/T$ = 0. Wind direction: from top to bottom.

APPENDIX A2 – QUANTITATIVE RESULTS

Table A1. Summary of the analyzed building arrangements.

ID	Description	Geometrical parameters				Ventilation characteristics			Rank (1…28)
		$\Delta z/H$ [–]	N [–]	T/H [–]	$\Delta y/T$ [–]	$c_{A,ng}$ [–] $c_{A,can}$ [–]	$\Delta c_{A,ng}$ [%] $\Delta c_{A,can}$ [%]	$k_{A,ng}$ [–] $k_{A,can}$ [–]	
1	**Uniform street canyons** *Plan area density: $\lambda_p = 0.5$*	0	N.A.	N.A.	N.A.	116.1 82.6	N.A. N.A.	0.00861 0.01211	19 19
2	**Asymmetric street canyons** *Impact of the roof height heterogeneity* *Plan area density: $\lambda_p = 0.5$*	***0.25***	N.A.	N.A.	N.A.	123.0 69.8	+5.9 –15.4	0.00813 0.01432	28 29
3		***0.375***	N.A.	N.A.	N.A.	120.5 56.8	+3.7 –31.2	0.00830 0.01760	26 27
4		***0.5***	N.A.	N.A.	N.A.	78.3 40.9	–32.6 –50.4	0.01278 0.02442	11 19
5		***0.75***	N.A.	N.A.	N.A.	78.9 32.3	–32.1 –60.8	0.01268 0.03093	13 15
6	**Towers** *Impact of the tower width* ***Matrix (aligned) arrangement*** *Plan area density: $\lambda_p = 0.5$*	0.375	***2***	***2.5***	1	117.5 56.2	+1.2 –31.9	0.00851 0.01779	22 26
7		0.375	***3***	***1.667***	1	116.9 54.7	+0.6 –33.7	0.00856 0.01828	21 23
8		0.375	***4***	***1.25***	1	118.6 55.3	+2.1 –33.0	0.00843 0.01809	23 24
9		0.375	***5***	***1***	1	119.6 56.0	+3.0 –32.1	0.00836 0.01785	25 25
10	**Towers** *Impact of the tower width* ***Staggered arrangement*** *Plan area density: $\lambda_p = 0.5$*	0.375	***2***	***2.5***	0	71.5 35.3	–38.5 –57.3	0.01399 0.02837	8 16
11		0.375	***3***	***1.667***	0	67.7 35.4	–41.7 –57.2	0.01477 0.02827	7 17
12		0.375	***4***	***1.25***	0	77.0 40.8	–33.7 –50.6	0.01299 0.02450	10 18
13		0.375	***5***	***1***	0	79.7 42.5	–31.4 –48.5	0.01255 0.02350	16 20
14	**Towers** *Impact of the tower height* ***Matrix (aligned) arrangement*** *Plan area density: $\lambda_p = 0.5$*	***0.25***	3	1.667	1	116.1 64.7	0.00 –21.6	0.00861 0.01545	20 28
15		***0.5***	3	1.667	1	119.2 47.2	+2.6 –42.9	0.00839 0.02120	24 22
16		***0.75***	3	1.667	1	122.7 20.5	+5.6 –75.1	0.00815 0.04870	27 8
17 [1]		***1***	3	1.667	1	67.7 16.6	–41.7 –79.9	0.01477 0.06040	6 2
18	**Towers** *Impact of the tower height* ***Staggered arrangement*** *Plan area density: $\lambda_p = 0.5$*	***0.25***	3	1.667	0	79.1 46.0	–31.9 –44.3	0.01264 0.02173	15 21
19		***0.5***	3	1.667	0	64.1 30.2	–44.8 –63.5	0.01559 0.03315	4 13
20		***0.75***	3	1.667	0	65.6 24.8	–43.5 –70.0	0.01524 0.04037	5 9
21 [2]		***1***	3	1.667	0	62.4 18.2	–46.2 –78.0	0.01602 0.05496	3 4
22 [1]	**High-rise buildings** *Impact of the streamwise overlap* ***3 buildings*** *Plan area density: $\lambda_p = 0.25$*	1	3	1.667	***1***	67.7 16.6	–41.7 –79.9	0.01477 0.06040	6 2
23		1	3	1.667	***0.5***	51.9 19.9	–55.3 –75.9	0.01927 0.05027	2 6
24 [2]		1	3	1.667	***0***	62.4 26.0	–46.2 –68.5	0.01602 0.03841	3 10
25	**High-rise buildings** *Impact of the streamwise overlap* ***5 buildings*** *Plan area density: $\lambda_p = 0.25$*	1	5	1	***1***	87.3 20.3	–24.8 –75.4	0.01145 0.04918	18 7
26		1	5	1	***0.5***	78.5 26.6	–32.4 –67.8	0.01275 0.03764	12 11
27		1	5	1	***0***	79.1 28.0	–31.9 –66.1	0.01265 0.03574	14 12
28	**Elevated uniform buildings** *Impact of the ground clearance* *Plan area density: $\lambda_p = 0$*	***1.667***	N.A.	N.A.	N.A.	82.4 31.9	–29.0 –61.3	0.01213 0.03133	17 14
29		***0.25***	N.A.	N.A.	N.A.	73.2 19.0	–37.0 –77.0	0.01366 0.05272	9 5
30		***0.3333***	N.A.	N.A.	N.A.	46.4 14.1	–60.1 –82.9	0.02155 0.07071	1 1

[1, 2] The marked cases are identical in terms of geometry and results. They are documented twice for a better understanding of the parameter studies. (Cases 17 and 22 as well as Cases 21 and 24.)

In Table A1 above, the following geometrical parameters and ventilation-related quantities are used:

H	[m]	reference building height
N	[–]	tower count or high-rise building count
T	[m]	tower width (in lateral direction)
Δy	[m]	streamwise overlap of the towers or high-rise buildings in consecutive rows
Δz	[m]	vertical offset of the roofs relative to the reference height H (+/– direction); or vertical offset of the entire building (i.e., ground clearance, + direction only)
λ_p	[–]	plan area density (the ratio of the total plan area of the buildings and the total ground area)
c_A	[–]	normalized concentration (the lower the better)
Δc_A	[%]	change in normalized concentration relative to the reference case (negative changes indicate air quality improvement)
k_A	[–]	mass Stanton number = dimensionless mass transfer coefficient = ventilation coefficient (the higher the better)

Subscripts and Superscripts:

ng	near-ground (average taken at pedestrian head height, $z/H = 0.0833$)
can	canopy average (average taken below roof height, $z \leq H_{max}$)

Conference on Modelling Fluid Flow (CMFF'22)
The 18th International Conference on Fluid Flow Technologies
Budapest, Hungary, August 30 -September 2, 2022

AEROACOUSTIC NOISE REDUCTION OF OPEN PHOTOACOUSTIC CELLS SUPPORTED BY EXPERIMENTS AND SIMULATIONS

Miklós BALOGH[1], Gábor KOSCSÓ[2], Bálint KOCSIS[3], Csaba HORVÁTH[4], Zoltán BOZÓKI[5]

[1] Corresponding Author. Department of Fluid Mechanics, Faculty of Mechanical Engineering, Budapest University of Technology and Economics. Bertalan Lajos u. 4 – 6, H-1111 Budapest, Hungary. Tel.: +36 1 463 1560, E-mail: balogh.miklos@gpk.bme.hu
[2] Department of Fluid Mechanics, Faculty of Mechanical Engineering, Budapest University of Technology and Economics. E-mail: koscso@ara.bme.hu
[3] Department of Fluid Mechanics, Faculty of Mechanical Engineering, Budapest University of Technology and Economics. E-mail: kocsis.balint@gpk.bme.hu
[4] Department of Fluid Mechanics, Faculty of Mechanical Engineering, Budapest University of Technology and Economics. E-mail: horvath.csaba@gpk.bme.hu
[5] University of Szeged, Faculty of Science and Informatics, Department of Optics and Quantum Electronics. E-mail: zbozokiphysx.u-szeged.hu

ABSTRACT

In this study aeroacoustic investigations have been carried out in order to further develop the critical components of a quick responding, open, continuously measured detection cell based photoacoustic (PA) measurement system, in order to reduce the aeroacoustic noise. This is a key aspect to operate the recently developed open PA cell under high velocity throughflow conditions. As compared to other, sampling-based PA systems, the photoacoustic component of the newly developed instrument presented herein is better integrated, significantly reduced in weight and size, and the gas flowrate that can be analysed is several orders of magnitude higher. A good aeroacoustic design is extremely important for an open PA cell, since significant acoustic noise can be generated even at relatively low flow rates, which drastically reduces the signal-to-noise ratio of the concentration measurements. The geometric constraints of the PA measurement system also must be considered. In addition, the structure must be sufficiently rigid so that the interactions between velocity fluctuations and the solid body do not cause mechanical vibrations. The new method has been developed to provide an improved aeroacoustic. Both numerical and experimental investigations have been carried out for the verification of this new method.

Keywords: Computational Aero-Acoustics (CAA), Computational Fluid Dynamics (CFD), Detached Eddy Simulation (DES), noise reduction, OpenFOAM, photoacoustic (PA) measurements

NOMENCLATURE

p_0	[Pa]	reference pressure
T_0	[K]	reference temperature
ρ_0	[kg/m^3]	reference density
ν	[m^2/s]	kinematic viscosity
a	[m/s]	speed of sound
Ma	[-]	Mach number

1. INTRODUCTION

In order to gain a deeper understanding of the operation of the system and to better understand the aeroacoustic noise generation mechanisms in the system (those noise sources which originate from the flow), we need to become acquainted with the basics of photoacoustic spectroscopy and the aeroacoustic problems affecting the system. Photoacoustic spectroscopy is a technique that detects acoustic waves generated from thermal de-excitation of molecules or particles upon absorption of modulated electromagnetic radiation, namely light used to generated by lasers. This technique provides high sensitivity and selectivity, furthermore large dynamic detection range making it suitable for trace gas applications [1,2,3]. Acoustic resonators are used to further increase the sensitivity of the photoacoustic (PA) signals. The modulation frequency of the electromagnetic radiation is matched to an acoustic eigenfrequency of the resonator thus exciting the corresponding acoustic mode. Conventional photoacoustic spectroscopy usually applies closed resonators, where gaseous samples are filled into a sealed resonator, but the sensitivity of measurements from closed resonators is limited [4]. Open resonators eliminate this limited sensitivity and have the additional advantage of

enabling continuous exchange of gas between resonator and environment, which is particularly useful for continuous PA measurement. Experts working on the development of the present system have played a significant role in the research and development of measurement systems with short-response open chambers [5]. One can read more about the theory of photoacoustic measurements in the work of Miklós et al. [6] and in the article of Dumitras et al. [7]. modelled and numerically examined photoacoustic resonators. The numerical examination and modelling of PA cells is discussed e.g. in the paper of Baumann et al. [8], while a shape optimization study is presented by Kost et al. [9]. Until now, the study of the flow and aeroacoustic properties of photoacoustic resonators has not been a primary aspect in the international literature, and therefore personal consultations held with the leading experts in the field of photoacoustics have been key to determining which direction to go.

As compared to other photoacoustic (PA) systems used to date, the photoacoustic component of the instrument developed herein must be better integrated, significantly reduced in size and weight, and be well designed concerning the suppression of aeroacoustic noise sources. As the gas flow rates in earlier applications of the PA method have been several orders of magnitude lower than in the current application, their aerodynamic and resultant aeroacoustic designs have not been suitable, i.e. significant aeroacoustic noise is generated even at relatively low flow rates. The aerodynamic noise at low frequencies is such that it mechanically overdrives the microphone, which thus becomes insensitive at the higher resonance frequency. As a result, such designs cannot be used in the open, continuously measured detection cell based PA measurement system at higher flow rates, and new solutions need to be researched and developed.

Our main goal in this investigation was to solve the problems arising when using PA measurement methods at higher flow rates, namely to reduce the amplitude of aeroacoustics noise at low frequencies, in order to avoid the mechanical overload of the in-built microphones.

For this reason, the available design was investigated experimentally and with numerical simulations, which confirmed our first conjecture that the design should be reviewed and modified. A new cell design is proposed to ensure simultaneously isokinetic sampling and reliable and accurate operation even at high flow rates. The essence of this design is that the gas to be tested flows freely through the streamlined resonator, without significant contraction. The prototype performed better in experimental tests, but it was also limited to a lower flow rate than required. A final optimized version is designed and tested with numerical simulations.

The evaluation showed that the low frequency noise is reduced thanks to the new design, while isokinetic sampling is fulfilled as well.

2. INVESTIGATION OF THE ORIGINAL PA MEASUREMENT SYSTEM

To assess the condition of the original PA measurement system and analyse the original geometry, data was provided by the Department of Optics and Quantum Electronics, University of Szeged. The goal of the investigation was mainly to localize the aeroacoustic noise sources. This was realized by empirical and theoretical methods, and numerical simulations. The examined original open PA cell construction is shown in Figure 1.

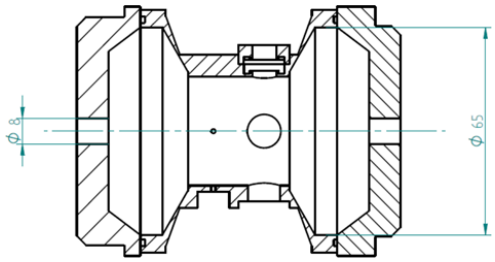

Figure 1. Cross-section of the investigated original PA cell

The following sections will discuss the conclusions drawn as a result of the empirical, theoretical and numerical investigations.

2.1. Empirical and theoretical considerations

The following potential noise sources related to the original cell design were identified based on the vast aerodynamic and aeroacoustic experience of the research team:

- The flow entering the open PA cell through the small inlet cross-section cannot follow the sudden cross-sectional expansion. This results in a free jet. As a result, vortices are generated in the shear layer of the free jet, which create additional noise sources on the exit side of the open PA cell, as the vortices interact with surfaces.
- The medium, acting as a free jet, does not fill the entire volume of the resonator, inducing a secondary flow that appears as a toroidal vortex with a flow velocity. This can cause problems when measuring concentrations, as it significantly increases the residence time.
- Recesses in the resonator wall (microphone neck, laser window) can act as a driven cavity or resonator.

2.2. Preliminary numerical simulations

To support the empirical and theoretical considerations, numerical simulations are performed with a simplified model of the chamber construction under investigation. A block structured mesh was generated in a way to satisfy the requirements of low-Reynolds wall treatment (y+ < 1) results in a fairly high resolution forming 407k cells for a quarter section of the original geometry, assuming tangential periodicity. The geometry was created using proprietary software along with the software Gmsh [10]. The numerical grid (hereinafter referred to as "mesh"), which is the basis of spatial discretization, was constructed with Gmsh as well. Since the problems to be solved are primarily due to microphone overdrive caused by low-frequency noise, we mainly focused on examining the low frequency noise. According to that and considering that the Mach number is fairly low (Ma < 0.05), an incompressible approach to aeroacoustics is applied using aeroacoustic analogies. The numerical simulations were performed in three steps using the OpenFOAM toolbox [11]. In order to model fully developed flow at the inlet, while omitting the need for the approximately one meter long preparatory pipe section (significantly reducing computational costs) a steady state precursor simulation was run, which consisted of an axially periodic domain modelling the long pipe section. The volume flow rate was set to 30 l/min, which corresponds to an average velocity of 10.01 m/s on the inlet side, as earlier measurement experience showed that the aeroacoustic noise was significant at this operation point. During the precursor simulations, the Launder-Sharma k-epsilon turbulence model with a low Reynolds wall function was used, which provides a formalism resolving the laminar sublayer next to the wall. The simulations have been carried out under the ambient conditions corresponding to the planned measurements in the anechoic room. This implies a reference pressure of p_0 = 101325 Pa, a reference temperature of T_0 = 293K, resulting a density of ρ_0 = 1.204 kg m^{-3}, a kinematic viscosity of ν = 1.5e-5 m^2 s^{-1}, and a speed of sound of a = 343 m/s. These reference values were used in all the subsequent simulations.

In the next step, the initial conditions for the time resolved simulations were generated by running a steady state simulation over the entire geometry, using the results of the precursor simulation for the inlet boundary condition.

In the last step, a time resolved simulation was run using the initial and boundary conditions generated by the previous simulations. From the results of the steady state simulations, the time resolved boundary conditions were determined by the Divergence-Free Synthetic Eddy Method [12]. Due to the fine mesh resolution, we utilized a hybrid technique combining the advantages of Large Eddy Simulation and Reynolds averaged models, namely the Spalart-Allmaras DES (Detatched Eddy Simulation) model. In this model, sub-grid turbulence is modelled by the Spalart-Allmaras turbulence model, while in parts of the range where mesh resolution allows, turbulent structures (large vortices) are explicitly simulated. During the simulation, the pressure and the Curle pressure were sampled. The latter is calculated based on the Curle analogy, which is a formal solution to the Lighthill analogy with respect to solid surfaces.

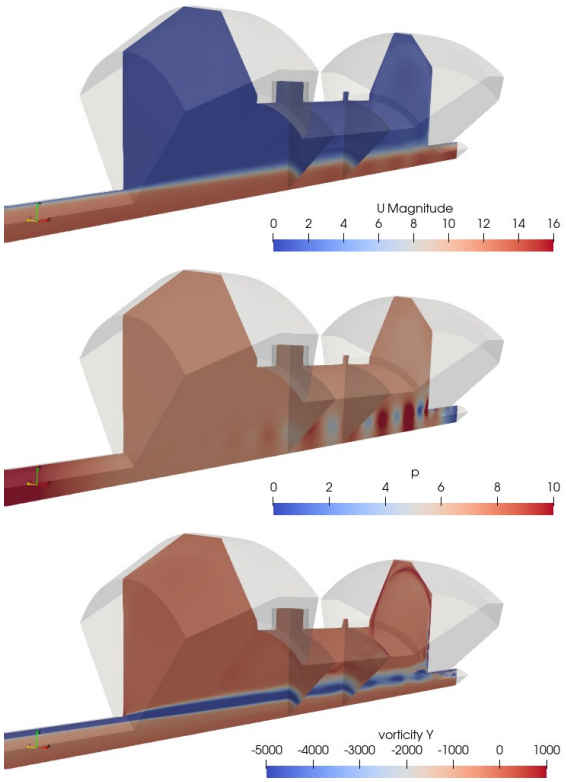

Figure 2. Simulated instantaneous values of velocity magnitude (top), relative pressure (middle), y-component of vorticity (bottom) for the original PA cell.

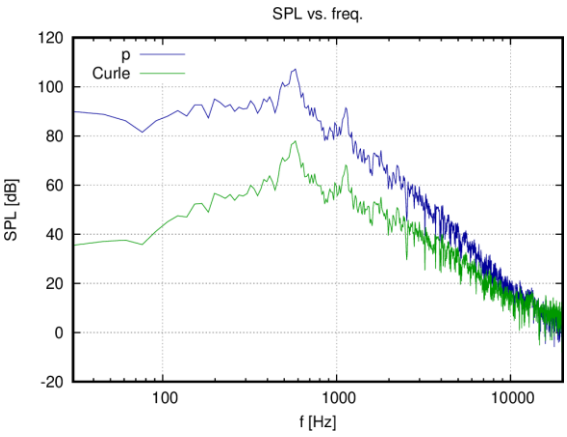

Figure 3. Sound pressure level based on relative pressure and Curle pressure.

Figure 2 shows the vortices generated in the shear layer of the free jet, which impinge on the walls of expansion chamber at the junction of the outlet nozzle. The sound pressure levels calculated from the sampled values of pressure and Curle pressure are shown in Figure 3. The simulations confirmed the conclusions drawn from the empirical considerations that the flow in the PA cell results in a free jet due to the rather sudden cross-sectional changes. The vortices, generated periodically in the shear layer of the free jet and their interactions with the can generates a significant amount of aeroacoustic noise. This makes the given design unacceptable for use as a PA cell, due to the high levels of low frequency noise. This design therefore needs to be further developed.

2.3. Proposal for modified photoacoustic chamber geometry

Studies on the original chamber geometry have shown that sudden changes in cross-sectional area have a negative effect on the aeroacoustic properties of the cell, i.e. they can significantly increase the noise, thus mechanically overdriving the microphone making it impossible to detect the photoacoustic signal. The small inflow cross-section results in a significantly higher velocity at a given volume flow rate, thus a higher Reynolds number, i.e. a more turbulent and at the same time noisier flow. As the goal is to reduce the aeroacoustic noise of the photoacoustic chamber, it is important to introduce the medium into the resonator with the largest possible cross-section and with the least possible change of direction and diameter. In the proposed design shown in Fig. 4, the measuring cell, through which the total amount of gas flows, is optimally connected to the piping in which the concentration of a given substance is to be measured. The microphones and laser are introduced through streamlined supports holding the photoacoustic chamber in the axis of the piping.

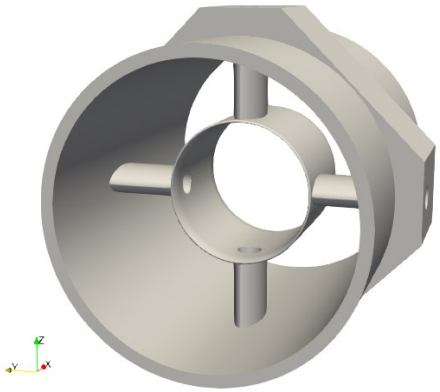

Figure 4. Initially proposed PA chamber design with streamlined resonator and supports (struts).

3. INVESTIGATION OF THE INITIALLY PROPOSED AND IMPROVED OPEN PA CELL GEOMETRIES

3.1. Laboratory measurements

Detailed laboratory measurements were performed in the anechoic room of the Békésy György Acoustic Research Laboratory, the aim of which was to become better familiarized with the acoustic characteristics of the proposed photoacoustic chamber design. Brüel & Kjaer microphone (type 4165) and its electronics (type 2639 preamplifier, type 2636 amplifier) were used during the measurements as reference. The acoustic signals were measured with Knowles SPU0410HR5H-PB MEMS microphones with their dedicated electronics developed by VIDEOTON. The data series are collected with a Lenovo Thinkpad 20C6-00LLHV laptop via the National Instruments NI-9234 dynamic signal acquisition module mounted in an NI cDAQ-9178 chassis.

The measurements were carried out at seven different flow velocities (4, 5.9, 7.5, 8.6, 10.6, 11.9 and 15 m/s) with a sampling frequency of 51.2 kHz. The following conclusions were drawn from the measurements:

- The free jet noise is frequency dependent and does not include contamination from the rpm or blade passing frequency of the air supply system.
- Base noise is particularly common at higher frequencies.
- The generated noise is proportional to the power of 6.27 of the flow velocity, characteristic of predominantly dipole sound generation.
- There is no resonance at 12.5 kHz, which is the eigenfrequency of the PA resonator. The resonance excited by the flow avoids this mode.
- At higher frequencies, the background noise is lower, so it is advisable to keep the frequency of the PA measurements in this range.

3.2. Numerical investigation of the proposed PA cell geometry: geometry and mesh

As a first step in the examination of noise reduction solutions, a numerical investigation of the flow in the proposed prototype was performed.

Based on the CAD files of the prototype, a block-structured approach was used which provided a mesh of very high quality using Gmsh. Thanks to the planes of symmetry of the geometry, only a quarter of the entire PA cell was modelled, which consisted of 620 rectangular blocks. A boundary layer mesh was created which was parametrized

based on the expected magnitudes of the investigated velocities.

3.3. Numerical investigation of the proposed PA cell geometry: simulation

In accordance with the methodology applied in section 2.2, the numerical simulations in phase two were also performed in three steps. In the steady state precursor simulations, the flow was driven by a pressure gradient, which was iteratively tuned as a function of the desired volume flow rate. In this way, it was possible to set volume flow rates equal to those recorded during the measurements, while keeping the numerical costs low. The volume flow rates that were investigated ~ 212 and 848 l/min, which correspond to average velocities of 1 and 4 m/s, respectively.

In the second step, the initial conditions were generated by running steady state simulations as well. In the third and final step, time resolved simulations were run using the initial and boundary conditions generated by the simulations in steps one and two. During the transient simulations, the time step was determined to allow the description of phenomena up to 20 kHz. Due to the high sampling frequency, it was not possible to save and store all the spatial data, and therefore only those that were essential for the evaluation were extracted during the simulations. The simulations were run on 32-thread (16-core) processors. Instantaneous states are shown in Figure 5.

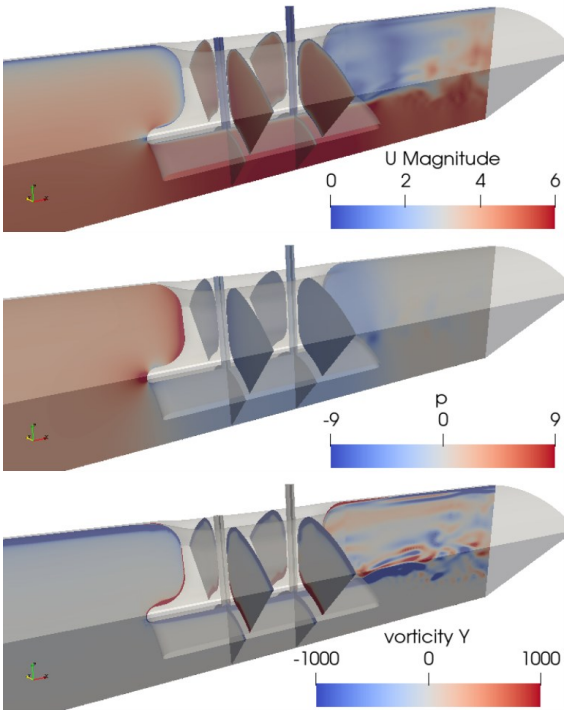

Figure 5. Instantaneous values of velocity magnitude (top), relative pressure (middle), y-component of vorticity (bottom) for the initially proposed PA cell, for a volume flow rate of 848 l/min.

4. ENHANCED DESIGN OF THE PHOTOACOUSTIC CHAMBER GEOMETRY

As it is expected and shown by the previous simulation results, perturbations increase with increasing Reynolds number. While at lower Reynolds numbers the flow shows an orderly picture, at higher values, the disorder due to turbulence is significant, both on the inlet side as well as downstream of the photoacoustic chamber. This turbulent flow is the primary source of noise that makes measurements difficult, and therefore needs to be reduced. A simple means of reducing the Reynolds number is to increase the diameter of the enclosing pipe section. Our experience from the measurements has shown that the generated noise is proportional to the flow velocity raised to the power of 6.27. Therefore, for a given volume flow rate, increasing the diameter will result in a significant reduction of noise.

4.1 A designing method for improving PA cells at higher flow rates

A proper design of the resonator tube and mounting pylons is also key in preventing the noise generation from suppressing the photoacoustic signal.

Geometric constraints important from a photoacoustic point of view must also be taken into account during the design. Such constraints include the cylindrical internal geometry of the resonator tube and the need for introducing/extracting optical and acoustic signals to/from the resonator tube via internal passages in the mounting pylons. In addition, the structure must be sufficiently rigid so that the interactions between flow disturbances (vortices) and the solid body do not cause mechanical vibrations. Table 1 below summarizes the direction in which the various aspects influence the design of the structure.

Table 1. Constraints influencing the design of the photoacoustic chamber

	Photoacoustics	Mechanics	Aeroacoustics
Resonator tube	Regular, cylindrical design	Maximize wall thickness	Minimize sudden change in diameter, minimize wall thickness
Mounting support structures	Minimum required cross-section for optical and acoustic signals	Maximize wall thickness	Minimize relative thickness and streamlined design

The method we have developed results in an aeroacoustically improved design based on the geometrical constraints coming from photoacoustics as well as mechanical considerations. An iterative procedure finds the optimum, which is illustrated in the following steps:

Step 0: Input data (diameter, length and wall thickness of the resonator tube, radius of inlet and outlet edge rounding, diameter and position of optical and acoustic lines along the longitudinal axis of the resonator tube, minimum required wall thickness of the pylons).

Step 1: Based on the given data, the leading edge region of the resonator pipe is designed from a lower and an upper chamber segment using the shape functions of a NACA00XX airfoil.

Step 2: The trailing edge region of the resonator tube is designed similarly to Step 1.

Step 3: The cross section of the pylon (strut) is also designed as a NACAXX00 airfoil with the largest possible chord length, taking into account the shortening caused in step 1 and 2, and the fillet radius of the pylon - resonator tube interference. In this step, the trailing edge is at a fixed location along the longitudinal axis of the resonator tube, the position of the leading edge is changed iteratively, until the maximum relative thickness of the profile reaches a minimum. During the iteration, the minimum distance between the optical and acoustic channels and the envelope curve of the airfoil is equal to the specified minimum wall thickness.

Step 4: Design of the pylon - resonator tube interference. This is the second-order continuous interference (fillet) between the pylon and the resonator tube, where the function describing the transition is defined by a circular arc with the specified fillet radius.

4.2. Numerical investigation of the improved PA design

After performing the shape optimization of the chamber under the current geometric constraints, we carried out simulations according to the simulation methodology described earlier in this chapter. Figure 6 show that the flow disturbance was reduced thanks to the improved design.

A quantitative evaluation of the simulation results was performed using the measurements described at the beginning of this chapter. Since the minimum velocity for which measurements were carried out was 4 m/s, only the corresponding simulation results of ~848 l/min were compared. The Sound Pressure Level (SPL) results of the comparison are illustrated in Figure 7.

Composite SPL were calculated by summing the time series values of the Curle pressure fluctuations and the static pressures, which were used for verification purposes. These results systematically overestimate the measurements by 24 dB. The reason for the discrepancy is that the simulations were carried out for a closed tube section, while the measurements were carried with a free space downstream of the PA cell. Sampling took place in this free space, and therefore a systematic deviation of 24 dB between measurements and simulations is absolutely realistic. The composite results show that shape optimization is effective in reducing the low frequency noise generated by the photoacoustic chamber.

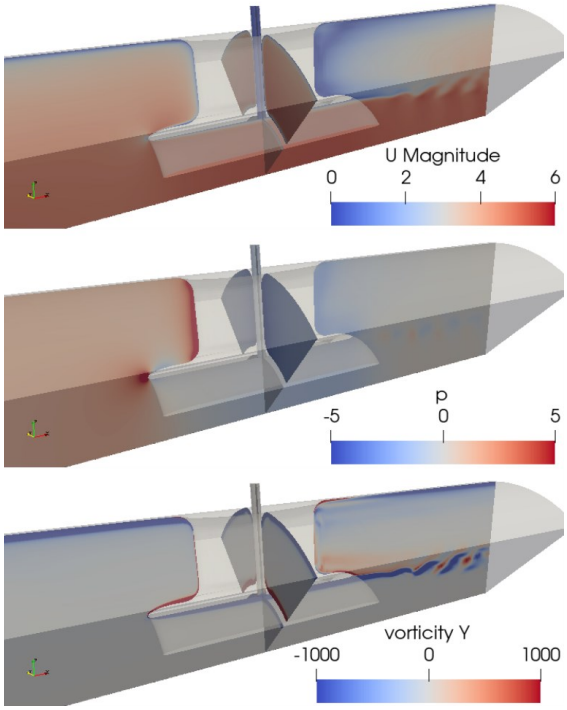

Figure 6. Instantaneous values of velocity magnitude (top), relative pressure (middle), y-component of vorticity (bottom) for the closed PA cell, for a volume flow rate of 848 l/min.

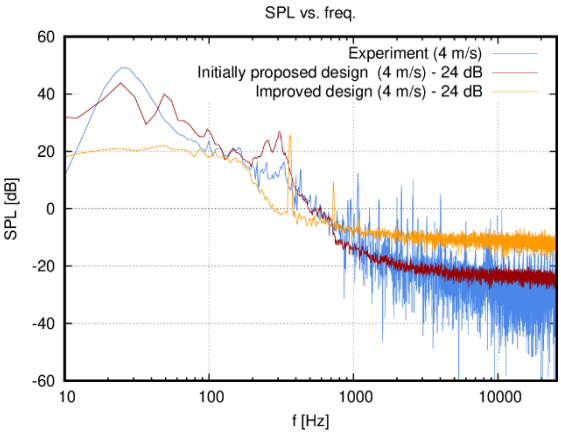

Figure 7. Frequency spectrum of measured and simulated sound pressure levels.

5. NUMERICAL SIMULATIONS TO DETERMINE THE RESIDENCE TIME DISTRIBUTION

One of the main advantages of using an open photoacoustic chamber for isokinetic sampling is that the resonator can be placed in the piping which is transporting the gas to be measured. As a result, the concentration in the gas flowing through the open chamber is the same as that measured in the piping, as it is not necessary to install a deflection or passive/active sampling mechanism. The quality of the isokinetic samples can be determined by investigating the residence time distribution (RTD). For this purpose, numerical simulations with additional passive scalar transport were performed.

The same geometry and mesh used for these calculations as in the former simulations.

For the transient RTD simulations, the time step was chosen so that the Courant number would fall within the appropriate range, which requires it to be kept below 1. Though less stringent than the requirements enforced during the acoustic simulations, even this is a very small time step, and it was not possible to save and store all the spatial data. During the transient flow simulation, passive scalar transport was also activated, taking into account turbulent diffusion, where scalar diffusivity was calculated from turbulent viscosity.

Volume averages were calculated for the inlet and outlet cross-sections of the domain and for the centre plane of the laser beam, which were saved for each time step. The volume average of the scalar passing through the resonator and that of the entire cross-section in the plane of the laser beam was monitored separately. The passive scalar concentration introduced at the inlet varied over time according to a square pulse. The square pulse turned on the scalar source for one tenths of a second from 0.3 seconds to 0.4 seconds. The simulations ran for 4-8 days on 32-thread (16-core) processors, depending on which Reynolds number was being investigated.

Residence Time Distributions (RTD) were evaluated at the inlet, the outlet, and in the plane of the laser beam. The inner cross-section of the resonator, the entire cross-section of the piping and the opening for the laser was monitored separately.

Figure 8. provide information regarding the reference (ideal) residence time distributions (dashed line), along with the outcomes of the simulations (solid lines). Each cross-section is marked with its own colour. The inlet is marked with blue, the inner cross-section of the resonator is denoted with green, the entire cross-section is marked with red, and the outlet cross-section denoted with light blue. Orange indicates the concentration of the scalar mixing into the passage of the microphone within the mounting pylon. Due to the turbulent mixing and the deceleration in the boundary layer, the pulse shapes become more and more adherent to the lognormal distribution away from the inlet. However, in the inner cross-section of the photoacoustic chamber a distribution similar to the source pulse is obtained. This proves that isokinetic sampling is guaranteed with the optimized open chamber design.

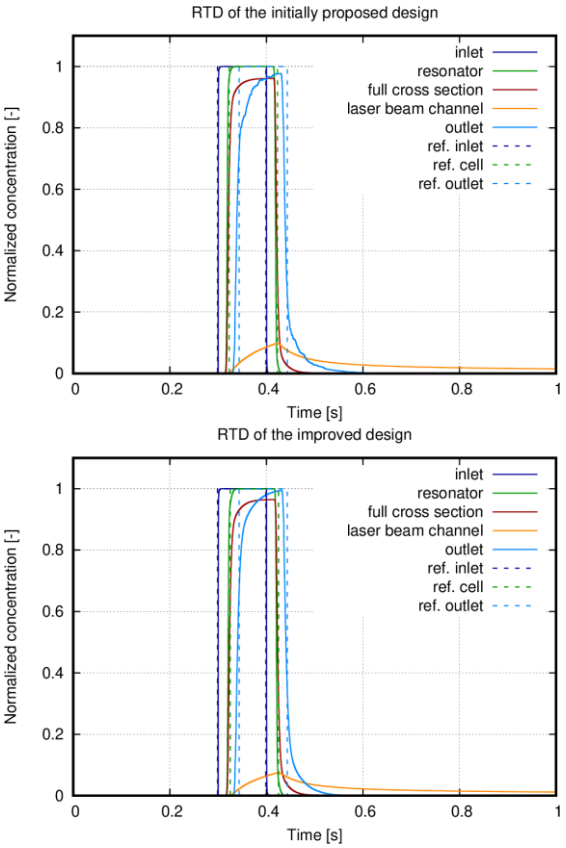

Figure 8. The Residence Time Distribution (RTD) in the investigated cross-sections at a volume flow rate of 848 l/min for the initially proposed PA design (top) and for the improved PA (bottom).

6 CONCLUSIONS

In this study, aeroacoustic investigations had been carried out in order to further develop the critical components of a quick responding, open, continuously measured detection cell based photoacoustic (PA) measurement system, in order to reduce the aeroacoustic noise. The actual design of the measurement system is investigated first. Aerodynamic and aeroacoustic analysis is performed for the existing geometry based on empirical and theoretical considerations along with numerical simulations in order to support the proposition of a quiet geometry. We identified qualitative noise reduction trends and proposed a new design on behalf of the photoacoustic chamber to reduce the aeroacoustic noise and increase the signal-to-noise ratio. These investigations were supplemented with measurements.

During the next phase of the development, we performed aerodynamic and aeroacoustic analysis on the geometry proposed during the initial phase. We

have developed a shape optimization method that takes into account geometric and photoacoustic constraints, based on which the PA design can be further refined. The initially proposed and the further improved PA design was investigated with numerical simulations. The simulation results were compared to the results of the measurements carried out in the acoustic laboratory. A systematic deviation of 24 dB was experienced between the measurements and simulations, but the course of the spectra is very similar. The simulations performed with the improved design resulted in lower sound pressure levels than simulations performed on the initially proposed geometry in the critical low frequency range.

In order to prove the suitability of the new PA design for isokinetic sampling, RTD analysis is performed for each geometry. Based on the results, it can be concluded that both the initially proposed and improved photoacoustic chamber design meets the requirements set for isokinetic sampling, as the peak concentration of the gas flowing through the photoacoustic chamber is nearly equal to the average concentration entering the entire cross-section in the flow normal plane at the location of the laser beam.

ACKNOWLEDGEMENTS

This work has been supported by the Hungarian National Research, Development and Innovation Centre under contract No. K 138176. The research reported in this paper and carried out at BME has been supported by the NRDI Fund (TKP2020 NC: Grant No. BME-NCS and TAK2021: project no. BME-NVA-02) based on the charter of bolster issued by the NRDI Office under the auspices of the Ministry for Innovation and Technology.

REFERENCES

[1] Tavakoli, M., Tavakoli, A., Taheri, M., Saghafifar, H., 2012, „Design, simulation and structural optimization of a longitudinal acoustic resonator for trace gas detection using laser photoacoustic spectroscopy (LPAS)", *Opt. Laser Technol.*, Vol. 42, pp. 828-838

[2] Gong, Z., Chen, K. Chen, Y., Mei, L., Yu, Q., 2019, "Integration of T-type half open photoacoustic cell and fiber-optic acoustic sensor for trace gas detection", *Opt. Express*, Vol. 27, pp. 18222-18231

[3] Gliére, A., Rouxel, J., Parvitte, B., Boutami, S., Zéninari, V., 2013, "A coupled model for the simulation of miniaturized and integrated photoacoustic gas detector", *Int. J. Thermophys.*, Vol. 34, pp. 2119-2135.

[4] El-Busaidya, S. A. S., Baumann, B., Wolff, M., Duggen, L., 2020, „Modelling of open photoacoustic resonators", *Photoacoustics*, Vol. 18, 100161.

[5] Bozóki, Z., Szabó, A., Mohácsi, Á., and Szabó, G., 2010, "A fully opened photoacoustic resonator based system for fast response gas concentration measurements", *Sensors and Actuators B: Chemical*, Vol. 147, pp. 206-212.

[6] Miklós, A., Schäfer, S., and Hess, P., 1999, "Photoacoustic Spectroscopy, Theory", *Encyclopedia Of Spectroscopy And Spectrometry*, pp. 1815-1822.

[7] Dumitras, D.C., Dutu, D.C., Matei, C., Magureanu, A. M., Petrus, M., and Popa, C., 2007, "Laser photoacoustic spectroscopy: principles, instrumentation, and characterization", *Journal of Optoelectronics and Advanced Materials*, Vol. 9(12), pp. 3655 – 3701.

[8] Baumann, B., Kost, B., Wolff, M., and Groninga, H., 2008, "Modeling and Numerical Investigation of Photoacoustic Resonators", *In: Modelling and Simulation*, IntechOpen, pp. 17-38.

[9] Kost, B., Baumann, B., Germer, M., Wolf, M., 2009, "Shape Optimization of Photoacoustic Resonators", *In: Computer Aided Optimum Design in Engineering XI*, Wessex Institute of Technology, pp. 45-54.

[10] Geuzaine, C. and Remacle, J.-F., 2009, "Gmsh: a three-dimensional finite element mesh generator with built-in pre- and post-processing facilities", *International Journal for Numerical Methods in Engineering*, Vol. 79(11), pp. 1309–1331.

[11] Weller, H. G., Tabor, G., Jasak, H., Fureby, C., 1998, "A tensorial approach to computational continuum mechanics using object-oriented techniques", *Computers In Physics*, Vol. 12, No. 6., pp 620–631

[12] Poletto, R., Craft, T., and Revell, A., 2013, "A New Divergence Free Synthetic Eddy Method for the Reproduction of Inlet Flow Conditions for LES". *Flow, Turbulence and Combustion*, Vol. 91, No. 3, pp. 519–539

Conference on Modelling Fluid Flow (CMFF'22)
The 18th International Conference on Fluid Flow Technologies
Budapest, Hungary, August 30-September 2, 2022

1D THERMAL MODELLING OF A WHEEL BEARING TO INVESTIGATE ENERGY LOSSES

Márton KERÉNYI[1], István GORICSÁN[2], Thomas PITOUR[3]

[1] Corresponding Author. Thermo- /Energy Management Development, AUDI HUNGARIA Zrt G/GF-1, Audi Hungária út 1., H-9027 Győr, Hungary. E-mail: marton.kerenyi@audi.hu
[2] Thermo- /Energy Management Development, AUDI HUNGARIA Zrt G/GF-1. E-mail: istvan.goricsan@audi.hu
[3] Energiemanagement, AUDI AG I/EG-31, Auto-Union-Straße AUDI AG 1., 85057 Ingolstadt, Germany. E-mail: thomas.pitour@audi.de

ABSTRACT

This paper presents the 1D thermal multi-mass (TMM) simulation of a wheel bearing in order to estimate how the component temperatures affect the energy loss during the Worldwide Harmonized Light Vehicles Test Cycle (WLTC). The simulation model was developed in *MATLAB/Simulink* on the basis of the conductive and convective heat transfer equations.

The ambient air and bearing components are represented by 7 simplified thermal mass points. The physical quantities necessary to create these points such as area, mass and material of the components were taken from the bearing's 3D computer model. The heat transfer between the individual masses can be determined by setting different values of heat transfer coefficients. In this way it can be observed how much thermal insulation and proper material selection can improve the energy efficiency. The simulation model was created with speed, stability and robustness in mind in order to allow a level of accuracy that meets industrial and scientific expectations.

In order to validate the model, the simulation results were compared to experimental data. A case study with different heat transfer parameters was concluded to quantify the effect of insulation and so, the energy saving potential.

Keywords: 1D simulation, Heat transfer, Insulation, Thermal mass model, Wheel bearing, WLTP driving cycle

NOMENCLATURE

$\dot{Q}$	$[W]$	heat transfer rate
A	$[m^2]$	area
D	$[-]$	relative uncertainty
$FACn$	$[-]$	factor of n observations
FB	$[-]$	fractional bias
HR	$[-]$	hit rate
M_f	$[Nm]$	friction moment
MG	$[-]$	geometric mean
$NMSE$	$[-]$	normalised mean square error
O_i	$[-]$	observation point
P_f	$[W]$	friction power
P_i	$[-]$	prediction point
Q_0	$[kJ]$	initial heat energy
R_th	$[K/W]$	thermal resistance
T	$[K]$	temperature
T_0	$[K]$	initial temperature
V	$[m^3]$	volume
VG	$[-]$	geometric variance
W	$[-]$	absolute uncertainty
c_p	$[kJ/kgK]$	constant pressure specific heat
m	$[kg]$	mass
n	$[1/min]$	rotation speed
α	$[W/m^2K]$	convective heat transfer coefficient
δ	$[m]$	wall thickness
λ	$[W/mK]$	thermal conductivity
ω	$[rad/s]$	angular velocity

1. INTRODUCTION

During normal operation of a road vehicle, unavoidable resistances are being encountered. These resistant forces, such as the aerodynamic drag, gravitational forces due to road gradient, inertial forces during acceleration and rolling resistance all appear in the form of energy loss [1, 2]. The necessity of the reduction of such forces are becoming more significant with the decreasing amount of allowed tank-to-wheel CO_2 emissions and so, fuel consumption imposed by regulations. In the EU, the regulation thresholds are standardised on the basis of driving cycle tests, such as the currently used Worldwide Harmonised Light Vehicles Test Cycle (WLTC). [3]

One of the main causes of wasted energy is friction between mechanical parts that are in physical contact with each other and experience relative displacement. Such can be observed inside the wheel bearing assembly. The power dissipation in the bearing increases with decreasing component temperature which is primarily influenced by the friction heat

and the thermal properties of the materials.[4]

The purpose of this paper is to present a 1D thermal multi-mass (TMM) simulation that can be used to measure the power dissipation of a wheel bearing during a driving cycle. The parts of the bearing and the relevant nearby components are handled as thermal mass points between which heat transfer connection is built using *Fourier's law* for conduction and *Newton's law of cooling* for convection. In the first section, the theoretical considerations behind the model is introduced, then the results of the simulation cycles are compared to the corresponding measurements using statistical metrics as a validation method. In the last section, the different insulation methods are presented and their impact on energy loss due to friction.

2. CONSTRUCTION OF THE MODEL

This section introduces the mathematical and physical methods along which the bearing assembly is modeled as a 1D thermal system.

2.1. Heat generation inside the bearing

The simulation model is based on a double row deep groove ball bearing. Ball bearings are widely used for places where low energy losses due to friction is prioritised. Still, frictional losses cannot be avoided entirely. During operation, relative motion of the inner and outer rings causes the balls to rotate between them. Without radial load on the bearing, the balls' connection with the rings is at a point or along a line. In the presence of radial load, the contact surface transforms into a face as a result of the plastic deformation of the rolling elements caused by stresses according to the Hertzian contact theory [5]. The deformation brings along the increment of the rolling resistance thus more kinetic energy turns into heat. The net effect of friction also appear as a force that creates a counter torque opposing the drive torque.

The other source of the frictional torque is viscous friction. As it is pointed out in Yang and Jeng's work [6], the friction force between the rotating components and the lubricant oil increases with increasing oil viscosity. However, oil viscosity decreases as the temperature goes up [7], proportionally with the speed of the shaft. These relations can be seen in Figure 1 based on measurement data. The exact temperature values in *Kelvin* have been normalised with a constant temperature also measured in *Kelvin*.

With the M_f friction moment at different temperature levels and ω angular velocities, the P_f friction power can be calculated in kW according to Eqn. (1).

$$P_\mathrm{f} = M_\mathrm{f} \cdot \omega \tag{1}$$

2.2. Modeling the heat transfer

The generated heat between the inner and outer rings can dissipate in the form of radiation, conduction and convection [8]. By reason of the relative low

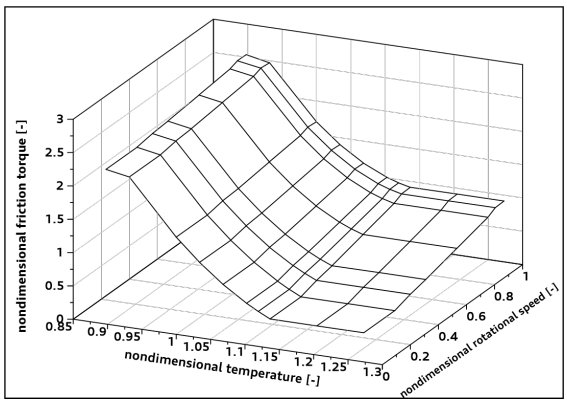

Figure 1. Experimentally determined relation between the friction moment versus temperature and shaft rotation speed

level of operating temperature, propagation through radiation has not been considered in the paper. The heat is transferred to the neighbouring parts like the wheel hub, inner ring and outer ring based upon the ratio of the surfaces that participate in the heat conduction. Because the outer ring has significantly larger connecting surface to the ambient air compared to the other components, convective heat transfer is only modeled between them. The first stage of the heat transfer process is shown in Figure 2.

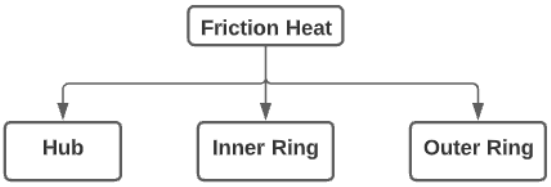

Figure 2. The distribution of friction heat from the source

The friction heat between the rings is transferred to the wheel hub and to both rings via conduction. The balls were considered as parts of the outer ring and in the model they form a single part with their masses combined. A similar method is used by J.Takabi and M. M. Khonsari in their model regarding the mass of the cage and balls [7]. According to our method the cage around the balls was not considered due to the low mass and low heat storage capability. The heat propagation is distributed further in Figure 3.

The inner ring is pressed onto the wheel hub and supported by the shoulder of the driven shaft so there are two surfaces and directions where heat can be transferred. The hub is heated directly by the source of the heat and by the inner ring. The brake disc is supported by an annular surface of the hub through which conduction can take place. The hub is fixed on the driven shaft by a spline connection and by an end plate. Both the net surface of the spline teeth and the annular surface of the plate were considered in

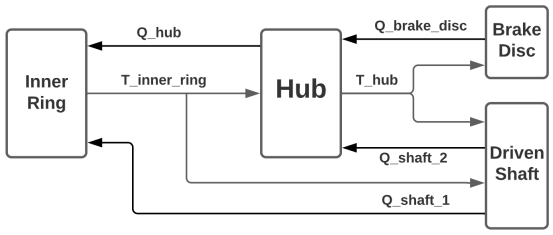

Figure 3. Heat distribution from the inner ring with negative energy feedback

the calculations. It needs to be mentioned that due to the relative large mass of the brake disc and shaft, their initial temperature is modeled so that they remain constant in time, unaffected by the heat transfer process. The negative feedback contains the amount of heat in kJ that the hotter object passes on to the part that it is in connection with. The heat flow at the outer ring is modeled in Figure 4.

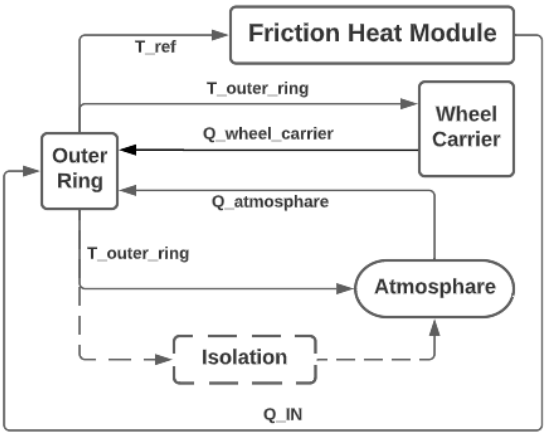

Figure 4. Heat distribution from the outer ring with negative energy feedback

The temperature of the outer ring is the reference signal of the model and in this case, the main parameter that indicates the accuracy of the simulation results relative to the measurement data. The outer ring is only getting heat energy from the source and transfers it directly to the wheel carrier and to the atmosphere through the optional insulation or - if not used - without it. Like in the case of the brake disc and shaft, the temperature of the wheel carrier is also considered time-invariant. The generated amount of friction heat at a given time depends on the temperature of the place where it is being generated. This reference temperature is provided by the signal of the outer ring in a way that it is connected back to the heat generation module at the end of each heat transfer cycle.

The basic nature of a 1D simulation model of a physical object with a complex geometry involves necessary usage of methods by whom the model can provide adequately precise results. In order to avoid dealing with complex geometrical shapes, the parts are represented in the model as nodes with thermal connections between them. These nodes contain the value of heat capacity of the particular component with the product of m mass and c_p specific heat capacity. Additionally, the initial amount of thermal energy is known by multiplying the heat capacity with the starting T_0 temperature, as shown in Eqn. (2). [9]

$$Q_0 = c_\mathrm{p} m T_0 \tag{2}$$

Note that due to the relative small temperature differences the temperature dependence of the specific heat capacity and the heat transfer coefficients have not been taken into account. Heat transfer calculations are solely based on steady-state principles in each simulation cycle.

To guarantee that the accuracy of the heat transfer is not affected by the omission of the geometry, the components are replaced with plain walls with δ thickness calculated from the volume (V) of the part divided by the size of its connecting surface (A). The temperature of a component is interpreted to be at the centre of the wall. To model the connection between the nodes, the transition at the contact area was replaced with thermal resistances (R_th) calculated by the thickness of the equivalent wall and the thermal conductivity (λ) of the materials. This way a similar thermal resistance network can be built like the one in the work of Keiji Mizuta et al. [10]. The calculation of the thermal resistance value of two solid bodies with a shared A connecting surface is according to Eqn. (3).

$$R_\mathrm{th} = \frac{1}{2A}\left(\frac{\delta_1}{\lambda_1} + \frac{\delta_2}{\lambda_2}\right) \tag{3}$$

The resistances (R_{1-8}) at the connecting surfaces are shown in Figure 5.

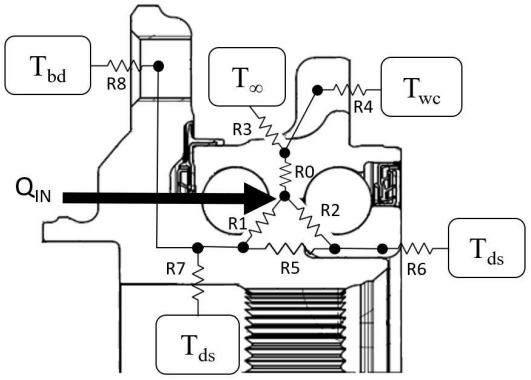

Figure 5. Schematic network of thermal resistances at the connecting surfaces

The abbreviations mean the following:

- Q_IN: friction heat generation [kJ]
- T_∞: atmosphere temperature [K]

- T_{wc}: wheel carrier temperature $[K]$
- T_{ds}: driven shaft temperature $[K]$
- T_{bd}: brake disc temperature $[K]$

The $\dot{Q}$ heat flow rate between two nodes due to their $(T_1 - T_2)$ temperature difference is defined for each time step according to *Fourier's law* for conduction in Eqn. (4) and *Newton's law of cooling* for convection in Eqn. (5).

$$\dot{Q}(t) = \frac{T_1(t) - T_2(t)}{R_{th}} \tag{4}$$

$$\dot{Q}(t) = \alpha A(T_1(t) - T_\infty) \tag{5}$$

Eqn. (4) calculates the conductive heat flow rate between two components with the usage of the R_{th} thermal resistance. In Eqn. (5), the α convective heat transfer coefficient of the fluid can only be defined by experimental measurements since it is not solely determined by the properties of the air but other influencing factors like surface geometry or the nature of the fluid flow. In heat transfer model, natural convection was modeled. The α heat transfer coefficient of the air was set to 20 W/m^2K constant as an estimated value in the case of free convection in gases. [11]

In case of using insulation around the free surface of the outer ring Eqn. (6) is used where T_1 is the surface temperature of the ring and T_∞ is the temperature of the ambient air.

$$\dot{Q}(t) = A \cdot \frac{T_1(t) - T_\infty}{\frac{\delta}{\lambda} + \frac{1}{\alpha}} \tag{6}$$

3. SIMULATION

The goal of the simulation model is to provide a fast, robust and sufficiently accurate method that can be used for estimating the energy losses of the bearing during a driving cycle.

3.1. Applied test cycle

The Worldwide Harmonized Light Vehicles Test Cycle (WLTC) and its associated Test Procedure (WLTP) is an international vehicle legislation and homologation method introduced in 2017 for passenger cars and light trucks [12]. The procedure's aim is to provide a more accurate representation of the real world driving emission and fuel consumption values than its predecessor and to make it possible to compare these values internationally. The simulations and measurements in this study use the WLTC cycle for Class 3b vehicles shown in Figure 6.

The 1800s long cycle contains four sequential ranges in ascending order by the maximum value of the speed in the particular range. The first "Low" region is meant to simulate the real world urban driving scenario while the "Medium", "High" and "Extra High" sections are respectively for the suburban, main road and highway driving scenarios [13]. The test is carried out in laboratory conditions on a chassis dynamometer in a standardised 23°C ambient temperature to ensure the procedure's repeatability.

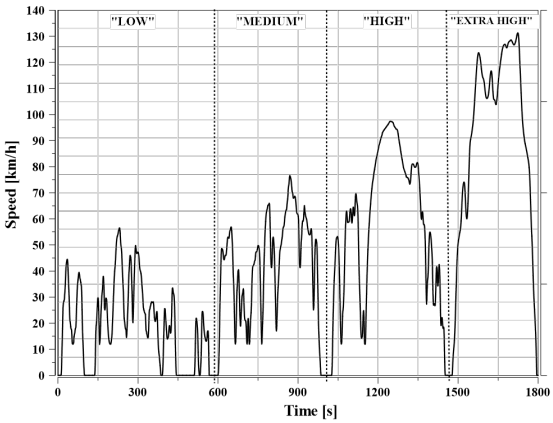

Figure 6. The vehicle speed curve used during the Class 3b WLTC

3.2. Applied validation metrics

The accuracy of the simulation model is evaluated by comparing its results to the measurement data. For that, standardised validation metrics were used which provide quantitative characteristics in addition to the qualitative assessment of the curves. The metrics use the set of prediction points (P_i) of the simulation result and the set of measured observation points (O_i) to define a single value based on which the accuracy can be classified. Both the modeled P_i and observed O_i data sets are normalised.

Many recommendations can be found in the work of Hanna et al. [14, 15] regarding the usage of statistical evaluation metrics for measuring the performance of models. A brief description of the six metrics applied in this paper is introduced in the following.

3.2.1. Hit rate (HR)

The calculation of the Hit rate (q) happens according to Eqs. (7) to (8) where the n number of P_i and O_i data point pairs are assessed whether their deviation falls into a predefined range. The range is limited by the relative uncertainty (D) and the absolute uncertainty (W) of the comparison data. [16]

$$q = \frac{1}{n}\sum_{i=1}^{n} N_i \tag{7}$$

$$N_i = \begin{cases} 1 & : \left|\frac{P_i - O_i}{O_i}\right| \leq D \; or \; |P_i - O_i| \leq W \\ 0 & : else \end{cases} \tag{8}$$

Assuming an ideal model means $q = 1$.

3.2.2. Factor of *n* observations (FACn)

When it comes to measure the effect of infrequent high and low O_i and P_i points, the fraction of predictions within a chosen n number as factor of observations is the most robust measure. It counts those cases when the quotient of the P_i and O_i point pairs are within a band given by a lower and upper limit that are calculated with n. Cases when one or both of O_i and P_i are outside of the W are resulting 0 value according to Eqn. (9). The calculation of the final value of $FACn$ is identical to q in Eqn. (7).

$$N_i = \begin{cases} 1 & : \frac{1}{n} \leq \frac{P_i}{O_i} \leq n \; and \; (O_i, P_i) \leq W \\ 0 & : \; else \end{cases} \tag{9}$$

An ideal model would result $FACn = 1$. [16]

3.2.3. Fractional bias (FB)

With this linear measure over and under predictions can occur due to the fact that it is based on the mean bias. To solve that, false negative (FB_{FN}) and false positive (FB_{FP}) values are used to calculate the final value of FB according to Eqn. (10). The FB indicates only systematic errors.

$$FB = \frac{\sum_i (O_i - P_i)}{0.5 \sum_i (O_i + P_i)} = FB_{FN} - FB_{FP} \tag{10}$$

In case of a perfect model $FB = 0$. [16]

3.2.4. Normalised mean square error (NMSE)

Unlike the FB, the $NMSE$ metric is useful to indicate unsystematic errors. The common drawback of the two is the strong influence by the infrequent peaks of data set points. In Eqn. (11), the symbols with overline indicate the average over all points in the given data set.

$$NMSE = \overline{(O_i - P_i)^2} / \overline{O_i P_i} \tag{11}$$

A perfect model would have $NMSE = 0$. [16]

3.2.5. Geometric variance (VG) and mean bias (MG)

As the previously mentioned FB the MG also measure mean bias and can be used for indicating systematic errors only. The difference is that the MG is using logarithmic scale as shown in Eqn. (12). As Chang and Hanna have mentioned [17], the logarithmic scale used at both metrics helps to provide a more accurate measure when extreme high and low values occur in the data set. Similarly to FB, MG can also be expressed as an under prediction ($MG > 1$) and an over prediction ($MG < 1$). [18]

$$MG = exp(\overline{ln(O_i/P_i)}) \tag{12}$$

Just like the $NMSE$, the VG also can be used for both systematic and random errors according to Eqn. (13).

$$VG = exp(\overline{(ln(O_i/P_i))^2}) \tag{13}$$

For data values of O_i and P_i that are zero the absolute deviation W as lower limit should be used. Both $MG = 1$ and $VG = 1$ if the model is ideally perfect. [16]

4. COMPARISON WITH THE MEASUREMENTS

The prediction of the following parameters have been in focus during the simulations:

- Free surface temperature of the outer ring
- Friction power loss as heat

The temperature curves were normalised by the initial temperature of the simulation in *Kelvin*. The friction power values were normalised by the friction power of a reference bearing in *kW*.

The duration of the simulation is 1800s according to the WLTP with a sampling interval of a constant 0.1s time step. To evaluate the model results relative to the observations, reference signals had to be created. The observation data contains a measurement series of five bearings, each tested two times. As for the temperature parameter, one reference signal was built by calculating the mean of all the the ten temperature measurement data series (*'Temperature_mean_All'*). The average temperature curve of the two test curves of the bearing measurement that best fitted the model result formed the second reference curve (*'Temperature_mean_BestFit'*) for the comparison. Note, that at the start of the simulation the bearing component temperatures are set to the same value as the initial temperature during a preconditioning period. The curves are shown in Figure 7.

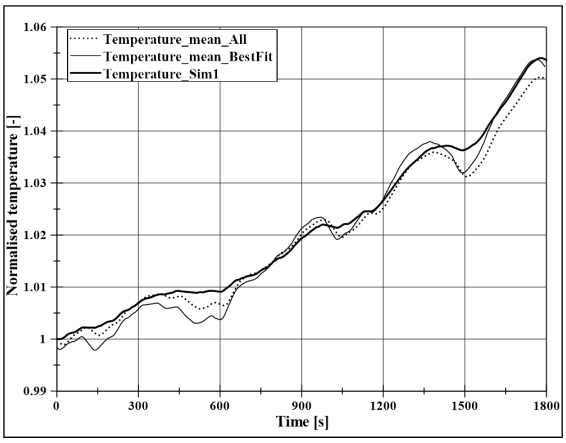

Figure 7. Comparison of the normalised temperature curves

In Figure 8. the HR is presented between the simulated temperature and the two reference signals. The error boundary is defined by the absolute error

$W = 0.006$ and the relative error $D = 0.01$. The acceptance criteria of the matching is set to $q \geq 0.66$. It can be stated based in Fig. 8 that all the points of the best fitting measurement are within the borders and it is almost the same with the mean data of all measurements. Table 1 contains the values of all the metrics used in the validation.

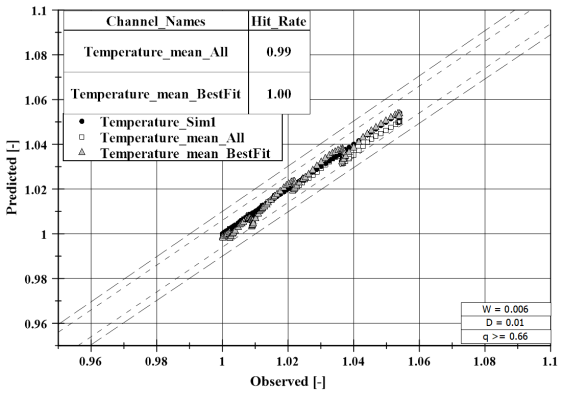

Figure 8. Temperature hit rate

Table 1. Temperature metrics values

Temperature		
Validation metrics (ideal value)	**Value**	
	Temperature mean All	**Temperature mean BestFit**
HR (1)	0.99	1.00
FB (0)	0.0014	0.0161
NMSE (0)	0.0005	0.0006
FACn (1)	0.99	1.00
MG (1)	0.99	0.98
VG (1)	1.00	1.00

It can be summarised that just like *HR*, all the other metrics are close to - or the same as - the ideal value, which means that the simulation approximate the observation quite well. The linearity of the model was checked with $FB \leq 0.15$ condition. For the under and over prediction analysis $0.9 \leq MG \leq 1.1$ was set for the geometric mean and also 10% deviation was allowed in the case of the geometric variance: $VG \leq 1.1$. It can be seen that in the case of $MG \leq 1$ there is a slight over prediction. The band of the $FACn$ is defined with the factor $n = 1.3$. The $NMSE$ metric is upper-limited by 0.2 ($NMSE \leq 0.2$). In Figure 9. the normalised curves are shown. The path of the friction power curve is following the WLTC's vehicle speed profile as it is pointed out in Section 2.1.

In the analysis of the friction power simulation result, the reference curves shown in Figure 10 were produced just like the ones in the case of the temperature. Because of the uncertainty of the friction power measurements the range limits were set wider for the *HR* by setting $W = 0.1$ and $D = 0.25$. The acceptability condition however remained the same

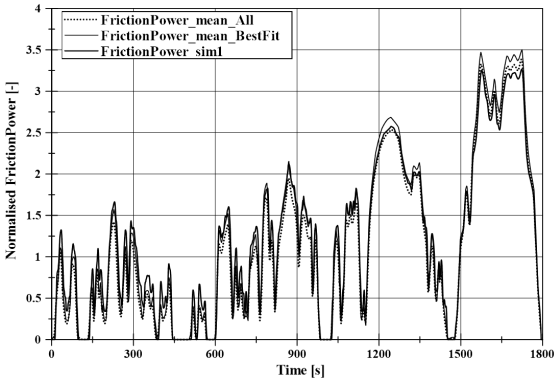

Figure 9. Comparison of the normalised friction power curves

at $q \geq 0.66$. According to the results in Table 2 only 66% of the *'mean_All'* predictions have met the conditions and 71% of the points in the *'mean_BestFit'*. The boundaries of MG, VG and FB were unchanged while the upper limit of $NMSE$ and $FACn$ was modified to 0.25 and 1.5 respectively.

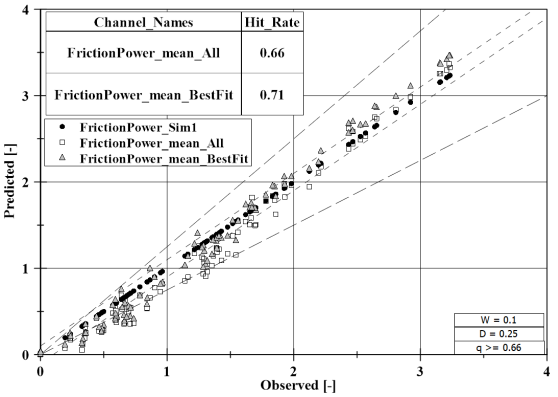

Figure 10. Friction power hit rate

Table 2. Friction Power metrics values

Friction Power		
Validation metrics (ideal value)	**Value**	
	FrictionPower mean All	**FrictionPower mean BestFit**
HR (1)	0.66	0.71
FB (0)	0.1131	0.0988
NMSE (0)	0.0214	0.0139
FACn (1)	0.79	0.84
MG (1)	0.86	0.93
VG (1)	1.19	1.16

5. EFFECT OF INSULATION

As it was mentioned in Section 2.2. the outer ring transfers heat to the wheel carrier and to the surrounding stationary air. On the other end of the assembly, the brake disc receives heat from the wheel hub. The main purpose of the simulation model was

to analyse whether the generated friction heat can be utilised substantively to decrease the rolling resistance of the bearing. As it was discussed in Section 2.1, the more heat is kept inside the bearing the more frictional losses decrease. Of course the amount of closed-in heat is upper limited by the material properties and the resulting shorter maintenance intervals. The use of an additional insulating layer on the outer surface of a part decreases the heat transfer capability. In the model this effect was interpreted in the reduction of the heat transfer coefficient of air. Beside the 23°C WLTC, the simulation was also run with -7°C to see how the colder environment affects the bearing's heat balance. Four different cases of insulation were considered in the tests that are listed here and displayed with numbers in Table 3.

- partial insulation towards the wheel carrier
- partial insulation towards the brake disc (not discussed in this paper)
- partial insulation towards the air
- partial insulation towards all three at the same time

Table 3. Heat transfer parameters for different cases of insulation

	λ **wheel carrier [W/mK]**	λ **brake disc [W/mK]**	α **air [W/m^{2}K]**
Sim 1	170	57	20
Sim 2	50	57	20
Sim 3	0.05	57	20
Sim 4	170	57	10
Sim 5	170	57	5
Sim 6	0.05	0.05	5

In the first scenario (*Sim 1*), there is no insulation on any of the components. In the case of *Sim 2* and *Sim 3* the heat transfer towards the wheel carrier is reduced with insulation in two steps. First, from 170 W/m^2K to 50 then to 0.05. Simulations 4 and 5 are the cases when the outer ring's free surface is isolated from the surrounding air represented by halving the value of α while the other parameters are changed back to their initial values. In the last scenario (*Sim 6*) the insulation is considered to affect the heat flow from the outer ring to the wheel carrier and to the air while on the other side the heat transfer from the hub to the brake disc was also decreased at the same time. The outer ring's surface temperature at each of the six insulation scenarios is displayed in Figure 11. It can be observed that the curves belonging to *Sim 2-3-4-5* are between the two extreme insulation cases when there was no insulation used (*Sim 1*) and when heat flow was blocked the most (*Sim 6*). Discussion of the separate effect of isolating the hub-brake disc connection is not part of this paper.

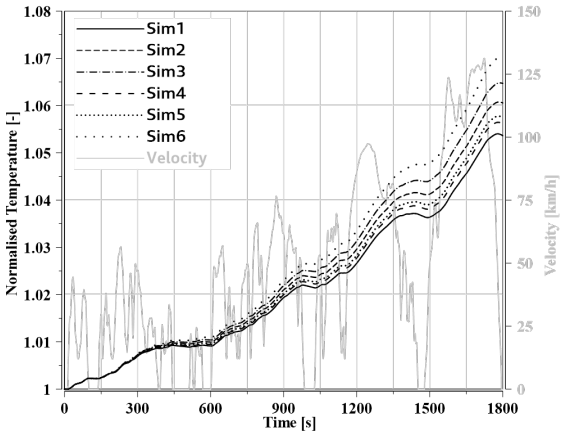

Figure 11. Normalised surface temperatures of the outer ring with different kinds of insulation. (Normalised by the starting temperature value in *Kelvin*)

As it can be observed in Fig. 11.The temperature of the outer ring is higher when more friction heat is retained by using insulation (*Sim 6*). As more heat is kept inside the system, the friction and thus the friction power is decreased. The generated friction heat energy is calculated by integrating the friction power. The effect of the insulation method on friction heat generation compared to *Sim 1* is contained in Table 4. and Table 5. The percentages of Table 4. are interpreted throughout all the WLTC tests, while the data in Table 5. is calculated only when the engine is driving the wheel.

Table 4. Change in friction heat generation with insulation compared to Sim 1. (stops & braking phases included)

	Generated Friction Heat Energy Compared to Sim 1 (stops & braking phases included)	
	WLTC 23°C	**WLTC -7°C**
Sim 2	-2.13 %	-3.08 %
Sim 3	-3.30 %	-4.79 %
Sim 4	-0.79 %	-1.15 %
Sim 5	-1.21 %	-1.75 %
Sim 6	-4.78 %	-6.96 %

Table 5. Change in friction heat generation with insulation compared to Sim 1. (driven by engine)

	Generated Friction Heat Energy Compared to Sim 1 (driven by engine)	
	WLTC 23°C	**WLTC -7°C**
Sim 2	-2.06 %	-3.01 %
Sim 3	-3.21 %	-4.67 %
Sim 4	-0.76 %	-1.11 %
Sim 5	-1.17 %	-1.70 %
Sim 6	-4.62 %	-6.76 %

6. SUMMARY

The aim of the paper was to create a 1D TMM model of a wheel bearing assembly that can be used for estimating the energy losses during a WLTC driving cycle. The 1D model contains the bearing components as thermal mass points and the thermal relations between them are governed by the well-known heat transfer equations.

The simulation results were directly compared to measurement data for validation purposes. The most important parameters were the temperature of the outer ring and the energy losses due to friction. The paper put great emphasis on the statistical evaluation of the model performance regarding its prediction capability and precision. In the following, the relation between insulations and friction heat generation were examined using two driving cycles with different ambient temperatures (23°C and -7°C).

The results of the work showed that with the usage of insulation a significant proportion of otherwise wasted friction heat energy could be utilised to decrease the rolling resistance of a given vehicle.

REFERENCES

[1] Barrand, J., and Bokar, J., 2008, "Reducing tire rolling resistance to save fuel and lower emissions", *SAE International Journal of Passenger Cars-Mechanical Systems*, Vol. 1 (2008-01-0154), pp. 9–17.

[2] Zhou, B., He, L., Zhang, S., Wang, R., Zhang, L., Li, M., Liu, Y., Zhang, S., Wu, Y., and Hao, J., 2022, "Variability of fuel consumption and CO2 emissions of a gasoline passenger car under multiple in-laboratory and on-road testing conditions", *Journal of Environmental Sciences*.

[3] Hooftman, N., Messagie, M., Van Mierlo, J., and Coosemans, T., 2018, "A review of the European passenger car regulations–Real driving emissions vs local air quality", *Renewable and Sustainable Energy Reviews*, Vol. 86, pp. 1–21.

[4] Khonsari, M. M., and Booser, E. R., 2017, *Applied tribology: bearing design and lubrication*, John Wiley & Sons.

[5] Zhaoping, T., and Jianping, S., 2011, "The contact analysis for deep groove ball bearing based on ANSYS", *Procedia Engineering*, Vol. 23, pp. 423–428.

[6] YANG, Y.-K., and JENG, M.-C., 2004, "Analysis of Viscosity Interaction and Heat Transfer on the Dual Conical-Cylindrical Bearing©", *Tribology transactions*, Vol. 47 (1), pp. 77–85.

[7] Takabi, J., and Khonsari, M., 2013, "Experimental testing and thermal analysis of ball bearings", *Tribology international*, Vol. 60, pp. 93–103.

[8] Kovalenko, P., 2021, "Heat Transfer on Wheel-Brake System at Critical Thermal Conditions", Ph.D. thesis, Georgia Institute of Technology.

[9] Flouros, M., 2006, "Correlations for heat generation and outer ring temperature of high speed and highly loaded ball bearings in an aeroengine", *Aerospace Science and Technology*, Vol. 10 (7), pp. 611–617.

[10] Mizuta, K., Inoue, T., Takahashi, Y., Huang, S., Ueda, K., and Omokawa, H., 2003, "Heat transfer characteristics between inner and outer rings of an angular ball bearing", *Heat Transfer—Asian Research: Co-sponsored by the Society of Chemical Engineers of Japan and the Heat Transfer Division of ASME*, Vol. 32 (1), pp. 42–57.

[11] Stephan, P., Kabelac, S., Kind, M., Martin, H., Mewes, D., and Schaber, K., 2010, "B1 Fundamentals of Heat Transfer", *VDI Heat Atlas*, pp. 15–30.

[12] Pavlovic, J., Marotta, A., and Ciuffo, B., 2016, "CO2 emissions and energy demands of vehicles tested under the NEDC and the new WLTP type approval test procedures", *Applied Energy*, Vol. 177, pp. 661–670.

[13] Tutuianu, M., Bonnel, P., Ciuffo, B., Haniu, T., Ichikawa, N., Marotta, A., Pavlovic, J., and Steven, H., 2015, "Development of the World-wide harmonized Light duty Test Cycle (WLTC) and a possible pathway for its introduction in the European legislation", *Transportation research part D: transport and environment*, Vol. 40, pp. 61–75.

[14] Hanna, S. R., Chang, J., and Strimaitis, D., 1993, "Hazardous gas model evaluation with field observations", *Atmospheric Environment Part A General Topics*, Vol. 27 (15), pp. 2265–2285.

[15] Hanna, S. R., 1989, "Confidence limits for air quality model evaluations, as estimated by bootstrap and jackknife resampling methods", *Atmospheric Environment (1967)*, Vol. 23 (6), pp. 1385–1398.

[16] Schatzmann, M., Olesen, H., and Franke, J., 2010, "Model evaluation case studies: approach and results", *COST 732 report*.

[17] Chang, J. C., and Hanna, S. R., 2004, "Air quality model performance evaluation", *Meteorology and Atmospheric Physics*, Vol. 87 (1), pp. 167–196.

[18] Hanna, S. R., and Chang, J. C., 2001, "Use of the Kit Fox field data to analyze dense gas dispersion modeling issues", *Atmospheric Environment*, Vol. 35 (13), pp. 2231–2242.

Conference on Modelling Fluid Flow (CMFF'22)
The 18th International Conference on Fluid Flow Technologies
Budapest, Hungary, August 30 -September 2, 2022

SURFACE LAYER'S SOUND SPEED PROFILES: CLIMATOLOGICAL ANALYSIS AND APPLICATION FOR THE CNOSSOS-EU NOISE MODEL

Tamás WEIDINGER[1], Petra FRITZ[2], Arun GANDHI[2], Abderrahmane MENDYL[2], Ágoston Vilmos TORDAI[2]

[1] Corresponding Author, Department of Meteorology, Institute of Geography and Earth Sciences, Faculty of Sciences, Eötvös Loránd University, Pázmány Péter sétány 1/A, H-1117 Budapest, Hungary. Tel.: +36 1 372 2545, E-mail: weidi@staff.elte.hu
[2] Department of Meteorology, Institute of Geography and Earth Sciences, Faculty of Sciences, Eötvös Loránd University. E-mail: fritzpetra31@gmail.com, arun.elte@gmail.com, mendyl.abderrahmane@gmail.com, tordaiagoston@gmail.com

ABSTRACT

Investigation and regulation of noise pollution and exposure are important environmental tasks, which require micrometeorological knowledge. The harmonised CNOSSOS-EU noise model requires detailed meteorological databases to determine noise propagation between the source and receptor points. For this reason, it is necessary to determine the relative frequencies of sound speed profiles based on wind speed, direction, and stability conditions for different source-receptor directions and for different times of the day (nighttime, daytime, and evening).

Meteorological variables are commonly used in noise modelling (optimally at least 5-year long, hourly dataset); wind speed and direction, temperature, humidity, and atmospheric stability. If the surface turbulence parameters are available, the atmospheric stability can be calculated directly. The noise propagation conditions according to the standardized procedures (stability classes 25 or 2) are calculated based on the SYNOP stations data from Hungarian Meteorological Service (HMS) and the ERA5 meteorological reanalysis database.

Our main goal was to determine the frequency distribution of stability classes for different source-receiver directions with various levels of aggregation using 25 or 2 stability classes. We also estimated the uncertainties of the stability classes favourable (homogeneous) and unfavourable (downward-refraction) in the developed preprocessor.

Keywords: CNOSSOS-EU, noise model, ERA5, meteorological preprocessor, sound speed profiles, stability classes, turbulence

Nomenclature

L_*	$[m]$	Monin-Obukhov length
L_{LT}	$[dB]$	long-term average sound levels
L_H	$[dB]$	homogenous conditions
L_F	$[dB]$	downward-refraction conditions
R_d	$[J/kg\ K]$	specific gas constant for dry air
T_*	$[K]$	temperature scale
T_v	$[K]$	virtual temperature
T_{v0}	$[K]$	reference virtual temperature near the surface
V	$[m/s]$	wind speed
a	$[m/s]$	constant of logarithmic term in the sound speed profile
a_c	$[m/s]$	in virtual temperature profile
a_u	$[m/s]$	in wind speed profile
b	$[1/m]$	constant of the linear term in sound speed profile
b_c	$[1/m]$	in virtual temperature profile
b_u	$[1/m]$	in wind speed profile
c	$[m/s]$	speed of sound in the atmosphere
c_0	$[m/s]$	speed of sound near the surface
c_{ad}	$[m/s]$	adiabatic sound speed
c_{pd}	$[J/kg\ K]$	specific heat capacity for dry air with constant pressure
c_{vd}	$[J/kg\ K]$	specific heat capacity for dry air with constant volume
e	$[Pa]$	water vapour pressure
k	[-]	ratio of c_{pd} and c_{vd}
p	$[Pa]$	pressure
p_f	[-]	probability of occurrence of downward-refraction conditions in the long term (min. 1 year)
q	$[kg/kg]$	specific humidity
u	$[m/s]$	wind speed in source-receptor direction
z	$[m]$	height above the surface
z_0	$[m]$	roughness length
α	[°]	wind direction
β	[°]	position of the source point
γ_d	$[°C/m]$	dry adiabatic temperature gradient $\gamma_d = 0.00976\ °C/m$
φ	[°]	angle between the direction of the sound propagation and the wind
κ	[-]	von Kármán constant

1. INTRODUCTION

Investigation of atmospheric sound propagation is practically important because noise pollution load from transport, industrial production, and also from entertainment and concerts are significant. In sound propagation modelling, there are different types of point, line, and areal sources [1, 2]. We concentrate only on the point sources. Sound levels between 30-90 *dB* are the most common in everyday life, and they are especially bothersome at night. Environmental standards specify the various noise pollution limits in detail. In Hungary, the outdoor sound propagation (MSZ 15036) standard provides a general methodology for noise propagation calculation [3, 4]. „The departmental order 93/2007 (XII. 18.) on the noise emission standards determination" defines the noise limit values for various residential, transport, industrial, and other activities [5]. The average daily noise exposure of industrial buildings during daytime is 56 *dB* and 50 *dB* at nighttime respectively in Hungary. The average noise exposure for traffic sources is 73 *dB* on a daily scale and 65 *dB* at night, respectively. Hospitals, health, and educational institutes are a priority; the optimal noise exposure should be less than 35 *dB*.

Approximately 20% of the European population is subject to long-term excessive noise exposure which is harmful to their health [6]. According to the World Health Organisation (WHO), noise is the second most common environmental cause of health problems, just after the particle matters (PM). Around 30-35% of Budapest's population live in noisy conditions hazardous to their health. The difference between nighttime and daytime noise level is only 4-7 *dB* on average, which means that even at night the noise exposure is significant.

The European Union agreed to harmonise noise propagation modelling and production of noise maps in 2015 [7]. The developed CNOSSOS-EU noise model requires a detailed meteorological database for the calculation of the sound speed profiles between the source and the receptor point [8-10]. The task is to determine the relative frequency of these homogeneous (decreasing or constant with height) and downward-refraction (increasing with height) sound speed profiles in terms of noise exposure. The calculations are provided based on the hourly measurements of temperature, atmospheric stability, wind speed, and direction at different times of the day and source-receiver directions using 5-10 years of time series.

After an overview of the theoretical background of noise propagation, the role of the different atmospheric stability classes is described. Calculation of the Pasquill-Gifford stability classes and the generation of near-surface sound speed profiles are also presented based on the calculation of wind speed and virtual temperature profiles using the Monin-Obukhov similarity theory. Based on the methodology, firstly 25 types of stability and wind speed dependent sound speed profiles were used [8].

The Hungarian meteorological preprocessor developed for the CNOSSOS-EU noise propagation model is also provided. The probability of occurrence of downward-refraction conditions (p_f) is presented based on ten years of hourly SYNOP observations from the György Marczell Main Observatory of the HMS (Budapest, 12843). Three parts of the day are investigated separately: night (22-06 *h* local time), day (06-18 *h*) and evening (18-22 *h*). Differences among years are also analysed. Results obtained from five additional weather stations with a 5-year long time series are also presented. Finally, the comparison of results (p_f) from the measured and the ERA5 reanalysis dataset [11] for Budapest was provided. The ERA5 reanalysis database – together with the meteorological variables – contains the radiation balance components (short- and longwave) and the surface energy budget components, such as momentum, sensible and latent heat fluxes, friction velocity (u_*), temperature scale (T_*), and Monin–Obukhov length (L_*) [12, 13]. The occurrence of downward-refraction conditions (p_f) is calculated based on the meteorological variables and directly from the surface layer turbulence characteristics.

2. SOUND SPEED PROPAGATION

Sound waves are density waves. The equation of propagation velocity (c) in moist air with pressure p, temperature, T and water vapour pressure e is:

$$c_{ad} = \sqrt{k \cdot R_d \cdot T_v}$$

where $k = c_{pd} / c_{vd} = 7/5 = 1.4$ is the ratio of the specific heat capacity for dry air at constant pressure and constant volume, $R_d = 287\, J/kg\, K$. T_v, is the virtual temperature.

$$T_v = T(1 + 0.608 \cdot q)$$

where the specific humidity is the ratio of the water vapour density and the wet air density [13]:

$$q = 0.622 \frac{e}{p - 0.378 \cdot e}$$

If the sound travels from a „more acoustically dense" medium with a lower propagation speed (e.g., a lower temperature) to a „less acoustically dense" medium, it will be diffracted (Figure 1a, b). The propagation speed of the wave increases as it enters the acoustically less dense medium. The direction of sound propagation and the angle of refraction of the sound wave at the boundary of the two media (the angle subtended by the normal of the surface) are also changed. The ratio of the sine of the two angles is equal to the ratio of the speed of sound in the two

media. This is the well-known Snellius-Descartes law, in wave theory [14].

The speed of sound decreases with the height during the daytime and increases at the night (inversion) due to the stratification (Figure 1a, b).

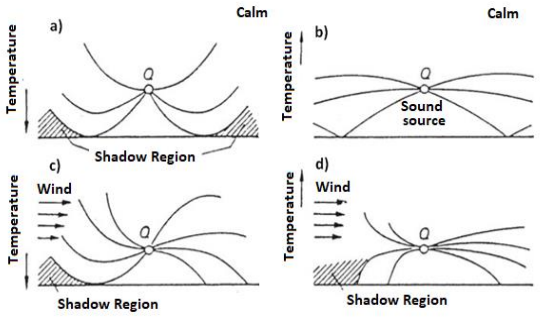

Figure 1: Sound propagation (along curved paths due to diffraction) as a function of temperature stratification during calm periods for unstable (a) and stable (b) stratification, with wind profile modification (c, d) [13].

The noise propagation is modified by the relative wind speed (upwind, crosswind, and downwind depending on the source-receiver position) in the direction of the source-receiver points. Downwind is blowing from the noise source to the receptor point in the direction of the sound propagation and increasing it (Figure 1c, d). Note that the total crosswind (the wind vector perpendicular to the line of the source-receiver points) has no effect on the sound propagation.

Thus, the speed of sound propagation depends on i) the wind speed profile ($u(z)$) and the direction of sound propagation, ii) the angle φ between the point source and the wind flag (Figure 2), as seen from the receptor point in the „centre of the circle", and iii) the temperature changes with height. In a full downwind, the wind blows from the noise source to the receptor point. The angle between the actual wind direction (the wind flag) and the noise source is then $\varphi = 0°$, while $\varphi = 180°$ for upwind and $\varphi = 90°$ or $\varphi = 270°$ for full crosswinds. (In meteorology, the current wind direction is the direction from which the wind blows always on horizontal plane.) The wind develops or strengthens the shadow zone on the upstream side (wind blowing from the receptor point towards the sound source); while on the downstream side, the wind weakens or dissipates the shadow zone, increasing the noise exposure. Note that wind speed always increases with height in the surface layer. For indifferent stratification, we use a logarithmic profile approximation. In the case of unstable stratification, the wind speed increases less than logarithmically with height, while in stable stratification it increases more than logarithmically.

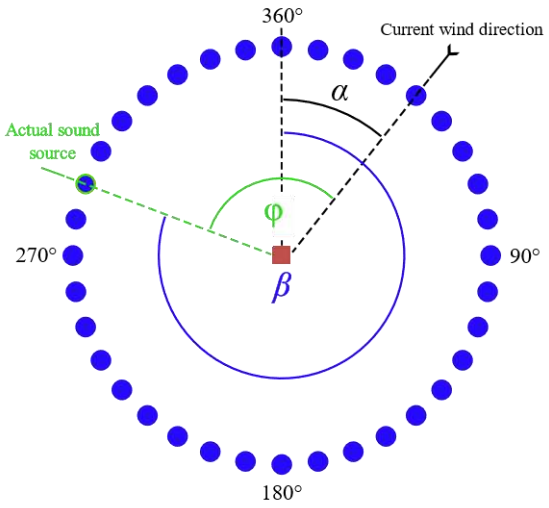

Figure 2: Source-receptor relationships. For a given wind direction (α), the hypothetical noise sources are positioned at every 10 degrees and the angle φ is subtended by the „wind flag" (actual wind direction) as seen from the receptor point. The hypothetical noise sources are indicated by the blue circles and the receptor point by the red rectangle. β corresponds to the position of the actual sound source. Propagation categories (homogeneous or downward-refraction) are given for the 36 hypothetical sources in each hour. This is a typical crosswind situation between the actual sound source (green) and the receiver point (red).

2.1. Sound speed profiles

The variation of the sound speed with height depends on the wind speed and virtual temperature profiles and the angle between the current noise source and the wind direction (Figure 2). Log-linear profile approximations were used for stable and unstable stratifications with different constants, obtained by integrating the simplified universal functions of the Monin-Obukhov similarity theory [12, 16]. The shapes of the commonly used sound speed profiles are in [8, 9, 10, 15]:

$$c(z) = c_{ad}(z) + u(z) = \\ = a \cdot \ln\left(1 + \frac{z}{z_0}\right) + b \cdot z + c_0$$

$$c_{ad}(z) \approx c_0 + \frac{1}{2}\frac{k \cdot R_d}{c_0}\left(T_v(z) - T_{v_0}\right) \approx \\ \approx c_0 + a_c \cdot \ln\left(1 + \frac{z}{z_0}\right) + b_c z$$

$$u(z) = V(z) \cdot \cos\varphi \approx +a_u \cdot \ln\left(1 + \frac{z}{z_0}\right) + b_u z$$

with $a = a_u + a_c$, $b = b_u + b_c$.

The constants in the equations are defined as a function of the atmospheric stability using the

Pasquill-Gifford stability categories [17], following the methodology [8, 9, 10]. We use 5 stability classes based on time of day and cloud cover data (Table 1). There are also more complex methodologies [17], but our purpose is to build up a standard methodology that is simple and easy to use. Daytime hours are defined as the estimated global irradiance from cloud cover above 20 W/m^2.

Table 1: Stability classes, S1 to S5, from unstable to stable.

Stability class	day/night, cloud cover (octas)
S1	day, 0 - 2
S2	day, 3 - 5
S3	day, 6 - 8
S4	night, 5 - 8
S5	night, 0 - 4

The effect of the wind profile on sound propagation depends on the source-receptor line and the angle φ subtended by the wind direction. The crosswind does not affect the sound propagation ($\cos\varphi = 0$). The simplified universal functions used for the calculations [8] were constructed based on [20]. The shape of the logarithmic term:

$$a_u = \frac{u_* \cdot \cos\varphi}{\kappa}$$

The linear term gives the deviation from the logarithmic profile. In the daytime, for unstable stratification ($T_* < 0$, $L_* < 0$, Table 2-5):

$$b_u = \frac{u_* \cdot \cos\varphi}{\kappa} \cdot \frac{1}{L_*}$$

At nighttime, with stable stratification ($T_* > 0$, $L_* > 0$, Table 2–5):

$$b_u = \frac{u_* \cdot \cos\varphi}{\kappa} \cdot \frac{4.7}{L_*}$$

Similar principles are used for the constants of the virtual temperature profile in unstable and stable stratifications:

$$a_c \approx \frac{1}{2}\frac{k \cdot R_d}{c_0} \cdot 0.74\frac{T_*}{\kappa}$$

$$b_c \approx \frac{1}{2}\frac{k \cdot R_d}{c_0} \cdot \left(\frac{T_*}{\kappa}\frac{0.74}{L_*} + \gamma_d\right) \text{ during day}$$

$$b_c \approx \frac{1}{2}\frac{k \cdot R_d}{c_0} \cdot \left(\frac{T_*}{\kappa}\frac{4.7}{L_*} + \gamma_d\right) \text{ during night}$$

Table 2: Wind speed classes W1 to W5 according to wind speeds at 10 m above the ground and estimated friction velocity (u_*).

Wind speed class	$V(z = 10\ m)$	u_*
W1	0 - 1 *m/s*	0.00 *m/s*
W2	1 - 3 *m/s*	+0.13 *m/s*
W3	3 - 6 *m/s*	+0.30 *m/s*
W4	6 - 10 *m/s*	+0.53 *m/s*
W5	>10 *m/s*	+0.87 *m/s*

Table 3: Temperature scale (T_*, $°C$) in different wind speed (W1-W5) and stability classes (S1–S5) classes.

	S1	S2	S3	S4	S5
W1	−0.4	−0.2	0	+0.2	0.3
W2	−0.2	−0.1	0	+0.1	0.2
W3	−0.1	−0.05	0	+0.05	0.1
W4	−0.05	0	0	0	0.05
W5	0	0	0	0	0

Table 4: Values of $1/L_*$ ($1/m$) for different wind speed and stability classes.

	S1	S2	S3	S4	S5
W1	−0.08	−0.05	0	+0.04	+0.06
W2	−0.05	−0.02	0	+0.02	+0.04
W3	−0.02	−0.01	0	+0.01	+0.02
W4	−0.01	0	0	0	+0.01
W5	0	0	0	0	0

Table 5: The effect of the angle between the sound propagation direction and the wind on sound speed profile calculation.

		$u_* \cdot \cos\varphi$
V1= –W5	upwind $V \cdot cos\varphi < -1\ m/s$	–0.87 m/s
V2= –W4		–0.53
V3= –W3		–0.30
V4= –W2		–0.13
V5= ±W1	crosswind	±0.00 m/s
V6= +W2	downwind $V \cdot cos\varphi > 1\ m/s$	+0.13
V7= +W3		+0.30
V8= +W4		+0.53
V9= +W5		+0.87 m/s

2.2. Sound propagation modelling

For us as data providers, it is important to provide the probability of occurrence of downward-refraction (p_f) and homogeneous ($1 - p_f$) conditions for sound propagation, for the calculation of the noise exposure from a given direction to a fixed receptor point (Figure 2).

The variation of sound speed with height by the derivation of the profile equation is:

$$\frac{\partial c}{\partial z} = \frac{a}{z + z_0} + b$$

where the height above the surface is $z = 4\ m$ and the roughness length is $z_0 = 0.1\ m$. We distinguished between favourable cases

(homogeneous conditions) $\frac{\partial c}{\partial z} \leq 0$ and unfavourable cases (downward-refraction) $\frac{\partial c}{\partial z} > 0$ in terms of noise exposure.

The hypothetical noise sources were positioned at 10 degrees around the receptor point (Figure 2) according to the wind directions given in the SYNOP reports. The profile type is provided for each of the 36 cases based on the current a and b values (5-5 classes). The 25 possible classes are given in Tables 6 and 7.

Table 6: Values of a in different classes (a_1, a_5) based on categories of Table 3-5.

Interval	Discrete value (m/s)
$-\infty < a \leq -0.7$	$a_1 = -1.0$
$-0.7 < a \leq -0.2$	$a_2 = -0.4$
$-0.2 < a \leq +0.2$	$a_3 = 0$
$+0.2 < a \leq +0.7$	$a_4 = +0.4$
$+0.7 < a \leq +\infty$	$a_5 = +1.0$

Table 7: Values of b in different classes (b_1, b_5) based on categories of Table 3-5.

Interval	Discrete value ($1/m$)
$-\infty < b \leq -0.08$	$b_1 = -0.12$
$-0.08 < b \leq -0.02$	$b_2 = -0.04$
$-0.02 < b \leq +0.02$	$b_3 = 0$
$+0.02 < b \leq +0.08$	$b_4 = +0.04$
$+0.08 < b \leq +\infty$	$b_5 = +0.12$

The long-term average noise level (L_{LT}) is calculated as the logarithmic sum of the sound pressure levels in decibel (dB) on a logarithmic scale, weighted by the occurrence rate of sound pressure levels between the meteorological conditions L_F, which are „unfavourable" for noise propagation (downward-refraction), and L_H, which are „favourable" for noise propagation (homogeneous cases):

$$L_{LT} = 10 \times \lg\left(p_f \cdot 10^{\frac{L_F}{10}} + \left(1 - p_f\right) \cdot 10^{\frac{L_H}{10}}\right)$$

where p_f is the ratio of the occurrence of downward-refraction conditions during the year, at three time periods of the day in local time (UTC + 1 and UTC + 2 in Central European Winter and Summer Time respectively): 06-18 h (daytime), 18-22 h (evening) and 22-06 h (nighttime), according to our rhythm of life and traffic dynamics.

In the previous standard noise propagation methods, the effect of the near-surface air layer was not taken into account with such detail [3, 4].

3. DATASET

The hourly synoptic datasets of HMS were downloaded from the Meteomanz and Ogimet websites for those years when cloud measurements were available. The amount of cloud cover is given in octaves (0, 1, ..., 8), the eighths of the sky. (Note that, from recent years most stations no longer have cloud detection.)

Hourly observations in Budapest (12843) for the 10-year period of 2009-2018 are analysed. We are also using out the data from five additional synoptic stations for 2014-2018, to get an idea of the differences of p_f, probability of occurrence of downward-refraction conditions within the country. These examined measurement sites are: Siófok, Pécs, Kecskemét, Szeged and Miskolc. The applicability of gridded datasets (here ERA5) is analysed at the closest grid cell to the Pestszentlőrinc, (12843) HMS station for the year-2014.

The quality control of the downloaded SYNOP databases was accomplished by filling in missing data. In cases of short data gaps (up to 6 measurement cycles missing), linear regression was used, while for longer data gaps, the gap-filling was performed based on the data of the previous and the following 1-3 days, leaving a maximum of 3 hours of adjustment time to fit the measured and interpolated data.

4. RESULTS

First of all, we looked at the 10-year data series for Budapest. In ~34% of cases, the daytime – between 06-18 h – was the most unfavourable (downward-refraction) period for noise propagation. In the evening, it is mostly stable between 18-22 *hrs*, and at night, between 22-06 *hrs* ~59% and ~64% respectively. There is a surprisingly high number of indifferent ($a = 0$, $b = 0$) sound velocity profiles, ranging from 15-35% depending on the time of day and receptor point orientation. Based on the results a recommendation can be made to introduce a third quasi-indifferent profile category into the meteorological preprocessor.

Next, we analysed the relative frequencies of the 25 stability categories ($a_1 - a_5$, $b_1 - b_5$). Out of the 25 possible classes, only 10 have an occurrence rate (Figure 3). This is understandable since, e.g., at high wind speeds, highly unstable stratification cannot develop. In this case, stratification is close to indifferent. During the daytime, we are more likely to see homogeneous sound propagation, while during the evening and nighttime, the speed of sound increases with height in most cases (downward-refraction). If we look at the differences between years, e.g., for indifferent cases, ($a = 0$, $b = 0$), the relative standard deviation (% of standard deviation/expected value) is around 5% in all three periods of the day. These are small values. Large

relative standard deviations (>15–20%) are usually found in cases of strong upwind and downwind situations, but the number of cases is small. In weak upwind and downwind situations (with high case rates), the standard deviations are between 10-20%. (These are crosswind situations).

The variation of the sound speed with height ($\partial c/\partial z$) was calculated at $z = 4\,m$ height after consultation with the experts of the Institute for Transport Sciences Non-profit Ltd. (KTI in Hungary). Considering i) the downward-refraction ($100 \cdot p_f$, %), ii) the homogeneous conditions ($(100 \cdot (1-p_f)$, %) and iii) the frequency of indifferent ($a = 0,\ b = 0$) situations which we classify as a subcategory within the homogeneous conditions group in the case of the two-category classification (Figure 4). The highest number of downward-refraction situations (potentially high noise exposure) is found in the northwest/northeast sector. This is understandable because this is the most common wind direction. The highest number of favourable (homogeneous) cases in terms of noise exposure is found on the opposite side. (Our „wind rose" in Figure 4. shows the frequency of cases (in %) depending on the location of the 36 virtual noise sources.) The probability of indifferent cases is high. During daytime hours, the values perpendicular to the main wind direction, together with light crosswind situations, exceed 35%. As expected, the asymmetric distribution of homogeneous and downward-refraction situations is clearly visible. In the evening and nighttime, the difference between the frequencies of each direction is smaller than during the daytime.

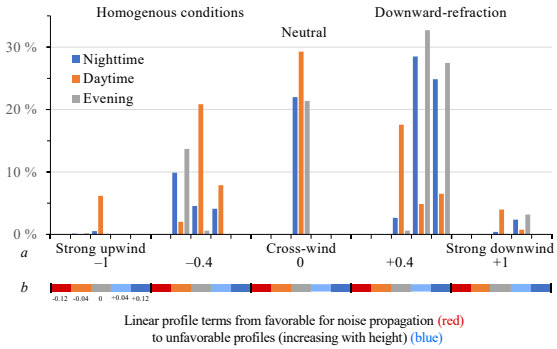

Figure 3: Relative frequency (%) of noise propagation in the 25 stability classes based on the hourly dataset (from 2009 to 2018) for Budapest (12843). Increasing values of *a* (logarithmic term) indicate increased wind speed in the direction of sound propagation while increasing values *b* (linear term) indicate stability (from unstable to stable stratification) and the current wind profile.

The standard deviations of the annual frequencies for each direction are small, between 1-5%, based on the 10-year Budapest data series.

Finally, we examined the differences between the highest and lowest annual relative frequencies (%) in each direction for the homogeneous and downward-refraction situations. The results for daytime hours are presented in Figure 5. The most significant differences are around 15% in the sectors that are perpendicular to the main wind direction. The smallest absolute deviations are in the north and south directions, with values of around 5%.

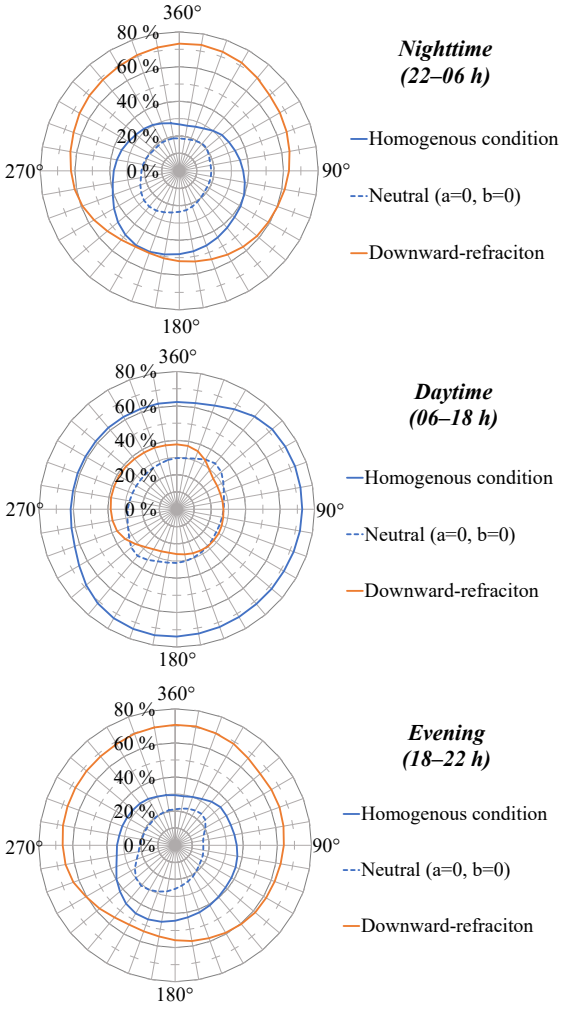

Figure 4: Noise pollution for homogeneous condition, downward-refraction cases, and indifferent stratification (a subcategory of homogenous condition) for nighttime, daytime, and evening in local time (Budapest, 2009-2018).

In addition to the 10-year Budapest dataset, we also analysed the average relative frequencies of probability p_f in all three time periods based on hourly data from 5 other SYNOP stations in Hungary for years between 2014 and 2018 (Figure 6). The difference between p_f values is less than 2% for the two 5-year periods in Budapest for each time period of the day. The variance within the two 5-year periods is less than 1% in the daytime, but not more

than 2% in the other two periods. Thus, it is sufficient to work with 5-year data series.

The results from Budapest and the five rural cities (except Miskolc) provide similar characteristics. The 5-year averages show differences of a few per cent (<5%). However, the evening and night p_f values for Miskolc are significantly higher than those of the other stations, by more than 20%. This is because of many unfavourable cases. The station is located in a valley outside the city. Low wind speeds are the first of the explanatory factors. The average value of wind speed is around 1.5 m/s is nearly half of the average in Hungary (2.5-3.5 m/s). During the daytime, however, there are no major differences compared to other stations.

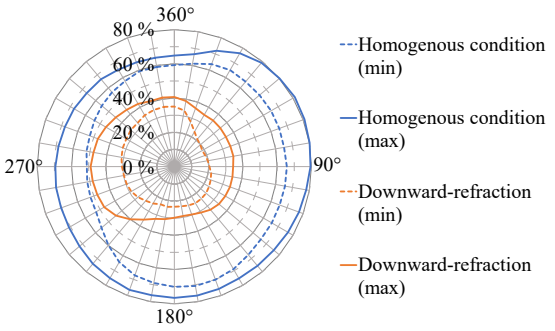

Figure 5: Minimum and maximum annual frequencies (in %) of homogeneous condition and downward-refraction cases for noise pollution for 10 years (2009-2018), based on the hourly data during daytime hours (Budapest).

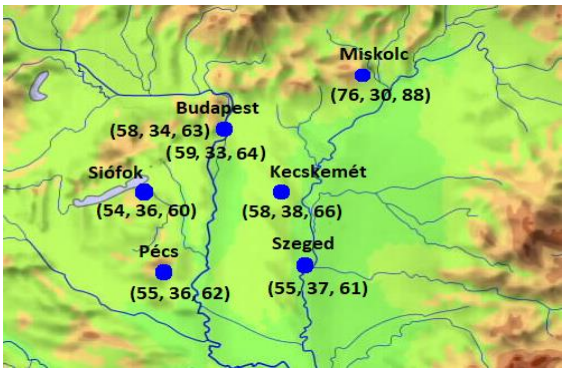

Figure 6: Relative frequencies (p_f, %) of downward-refraction cases for two 5-year periods for Budapest (2009-2013, top) and 2014-2018, bottom) and for five other Hungarian cities (2014-2018). The values in parentheses represent the nighttime, daytime, and evening hours, respectively.

Finally, the applicability of the ERA5 database in noise propagation tasks was analysed. The data of the nearest grid point to the Pestszentlőrinc (12843) station were processed. Our results for the year 2014 are shown in Table 8. Thus, we can compare the probability (p_f) data based on i) directly calculated from the measured data (SYNOP, 12843), ii) the hourly meteorological data (ERA5 MET) and iii) turbulence characteristics (u_*, T_*, L_*) from the ERA5 reanalysis dataset (ERA5 FLUX). Significant differences are found between p_f values calculated using measured and reanalysed meteorological data especially in the evening and in the nighttime, while the daytime values show a surprising similarity. The p_f data calculated from the measured values and ERA turbulence characteristics show a strong agreement at all three times of the day. Differences are below 3%.

Further analysis is required for a more detailed explanation. In any case, it can be concluded that the ERA5 database has „suitable room" for further investigation.

Table 8: Measured and calculated p_f values from the ERA5 database for the Budapest grid point based on hourly data for three time periods in 2014.

Data source	Night	Day	Evening
SYNOP	59%	33%	65%
ERA5 met	48%	35%	51%
ERA5 flux	58%	36%	68%

5. SUMMARY

A meteorological preprocessor was developed for the CNOSSOS-EU noise propagation model to separate homogeneous conditions (favourable) and downward-refraction (unfavourable) noise pollution situations for different times of the day based on the atmospheric stability, temperature and the wind speed and direction data. A virtual noise source was placed around the imaginary receptor point every 10 degrees. Our main conclusions from the investigation of a 10-year dataset for Budapest (12843) are:

- Strong up-winds ($a = -1$) and down-winds ($a = +1$) are most frequent in the main wind directions (NW, SE), while slow winds ($a = \pm 0{,}4$) are generally 30-60 degrees different, while light and crosswinds ($a = 0$) are most frequent in perpendicular to the main wind direction.
- High winds are more frequent during the day.
- The directional distribution of the up- and down-wind cases is almost a mirror image of each other.
- As expected, the most downward-refraction situations for propagation occur in the evening and at night in about 2/3 of the cases, and during the day in about 1/3 of the cases.

Analyses of data from five other Hungarian weather stations, except Miskolc, show the general features. The station at Miskolc is in a valley represented by low wind speed, which does not give

representative results. There were few variations among other stations. There is also moderate variability in the p_f probability values among years.

The ERA5 reanalysis dataset can be successfully used to build a noise propagation meteorological preprocessor. However, significant differences are found between the meteorological reanalysis data and the computations based on the ERA5 derived turbulence parameters. Using i) more stations and ii) grid cells from the ERA5 provides a sensitivity analysis of the preprocessor based on a different set of universal functions, which is also an important goal for the near future.

ACKNOWLEDGEMENTS

The authors would sincerely like to thank Viola Prohászka and Dr. Edina Balogh of the KTI Institute for Transport Sciences Non-profit Ltd. for bringing attention to the topic and their scholarly advice. They would also like to thank Peter Musyimi, who proofread and checked the grammar. This work has been supported partly by the Hungarian National Research, Development, and Innovation Centre under contract No. K-138176.

REFERENCES

[1] Guski, R., Schreckenberg, D., and Schuemer, R., 2017: "WHO Environmental Noise Guidelines for the European Region: A Systematic Review on Environmental Noise and Annoyance", *Int. J. Environ. Res. Public Health,* Vol. 14(12)*,* 1539.

[2] Deepak, J., 2016: "Noise Pollution: A Review", Int. *J Environ. Res. Pub. H.*, Vol. 4(3), pp. 72-77.

[3] Outdoor sound propagation (MSZ 15036), 2002: *Hungarian Standards Institution* (MSZT) (In Hung.)

[4] Krapf, G., and Wetzel, G., 2005: "Adaptation of national noise prediction methods to Directive 2002/49/EC Requirements on Noise Mapping", *Forum Acusticum Conference*, Budapest Hungary, pp. 995-998.

[5] Cserny, A., Tóvári, K., and Domokos, E., 2009: "The experiences of the environmental noise effect examination of industrial and service enterprises", *Acta Univ.* Sapientiae*, Agric. Environ.*, Vol. 1, pp. 151-156.

[6] Environmental noise in Europe — 2020: *EEA Report No 22/2019*. Luxembourg: Publications Office of the European Union, ISBN 978-92-9480-209-5, ISSN 1977-8449

[7] Commission Directive (EU) "2015/996 of 19 May 2015 establishing common noise assessment methods according to Directive 2002/49/EC of the European Parliament and of the Council" (Text with EEA relevance), *Official Journal of the European Union*. L, 168.

[8] Defrance, J., Salomons, E., Noordhoek, I., et al., 2007: "Outdoor Sound Propagation Reference Model Developed in the European Harmonoise Project", *Acta Acustica united with Acustica*, Vol. 93, pp. 213-227.

[9] NMPB2008, 2008: "Methodologic guide, Road noise prediction 2 - Noise propagation computation method including meteorological effects (NMPB2008)", Reference: *0957-2A.*

[10] Environmental NORD2000, 2006: *NORD2000 for road traffic noise prediction. WP4. Weather classes and statistics*. VTT Raimo Eurasto Espoo 7.4., 25 p.

[11] Hersbach, H., Bell, B., Berrisford, P., et al., 2020: "The ERA5 global reanalysis", *Q. J. R. Meteorol. Soc.*, Vol. 146(730), pp. 1999-2049.

[12] Arya, P. S., 2001: *Introduction to Micrometeorology*, 2nd Edition, Elsevier.

[13] Foken, T., 2017: *Micrometeorology*, Second Edition, and Springer Nature.

[14] Garrett S.L., 2020*: Reflection, Transmission, and Refraction. In: Understanding Acoustics*. Graduate Texts in Physics. Springer.

[15] Attenborough, K., 2014: *Sound Propagation in the Atmosphere*, in: Springer Handbook of Acoustics, 117-155.

16] Weidinger, T., Pinto, J. and Horváth, L., 2000: "Effects of uncertainties in universal functions, roughness length, and displacement height on the calculation of surface layer fluxes", *Z. Meteorol*., Vol. 9(3), 139-154.

[17] Mohan, M., and Siddiqui, T.A., 1998: "Analysis of Various Schemes for the Estimation of Atmospheric Stability Classification", *Atmospheric Environ*., Vol. 32(21), pp. 3775-3781.

[18] Holtslag, A.A.M., and Van Ulden, A.P., 1983: "A simple scheme for daytime estimates of the surface fluxes from routine weather data", *J. Appl. Meteorol. Climatol.,* Vol. 22(9), pp. 517-529.

[19] Weidinger, T., Nagy, Z., Baranka, Gy, Mészáros, R., Gyöngyösi, A.Z., 2008: "Determination of Meteorological Preprocessors for Air Quality Models in the New Hungarian Standards", *Hrvat. Meteoroloski Cas.*, Vol. 43, 6 p.

[20] Businger, J.A., Wyngaard, J.C., Izumi, Y., and Bradley, E.F., 1971: "Flux-Profile Relationships in the Atmospheric Surface Layer", *J. Atmos. Sci.*, Vol. 28(2), pp. 181-189.

Conference on Modelling Fluid Flow (CMFF'22)
The 18th International Conference on Fluid Flow Technologies
Budapest, Hungary, August 30-September 2, 2022

PERSPECTIVES ON OPENFOAM NUMERICAL SIMULATIONS OF SLOPE WINDS ON MARS

Jose I. ROJAS[1], Santiago ARIAS[1], Adeline MONTLAUR[1]

[1] Dept. of Physics - Division of Aerospace Eng., Universitat Politècnica de Catalunya, c/ Esteve Terradas 7, 08860 Castelldefels, Spain. Tel.: +34 93 413 4130. Fax: +34 93 413 7007. E-mails: santiago.arias@upc.edu, adeline.de.montlaur@upc.edu
[2] Corresponding author. E-mail: josep.ignasi.rojas@upc.edu

ABSTRACT

Planetary boundary layer phenomena, such as slope winds and nocturnal low-level jets, are frequent on Mars, *e.g.*, whenever diurnal surface temperature variations are significant, and large-scale winds are weak. In particular, thermally-driven winds are very common over sloping regions; they can reach significantly high speeds for steep slopes, and govern near-surface winds in many sites. Simulations of this type of flows on Earth have usually been conducted using commercial computational fluid dynamics software (CFD). In this work, a set-up is described for numerically simulating slope flows on Mars within the framework of the open-source code OpenFOAM CFD. For this purpose, thermally-driven winds are analysed in an idealised 2D Martian mountain-valley system with realistic values of parameters such as the slope angle, temperature difference between the atmosphere and slope, etc. The fluid domain dimensions, and the temperature and pressure initial and boundary conditions used in this work were tested and proven suitable in previous similar investigations for Earth applications. Large-eddy simulations (LES) turbulent model is used here. The results obtained for velocity and temperature profiles are shown both for anabatic (up-slope) and katabatic (down-slope) winds. This study shows the potential of the proposed methodology and the performance of OpenFOAM. Future work aims at facilitating the screening of large numbers of candidate landing sites for future Mars missions, and at estimating the thermally-driven wind speeds for wind resource assessment.

Keywords: computational fluid dynamics (CFD), Mars, OpenFOAM, slope winds, thermally-driven winds

NOMENCLATURE

M	[kg/mol]	Molar mass of Martian air
Pr	[−]	Prandtl number
Pr_t	[−]	turbulent Prandtl number
R'	[J/(kg K)]	specific gas ct.
T	[K]	temperature
T_M	[s]	Martian sol period
c_p	[J/(kg K)]	specific heat at ct. pressure
p	[Pa]	static pressure
t	[s]	time
z_0	[m]	roughness length scale
U	[m/s]	flow velocity
u	[m/s]	along-slope velocity
g	[m/s^2]	gravity acceleration
α	[deg]	slope angle
β	[K^{-1}]	volume expansion coef.
μ	[kg/(m s)]	dynamic viscosity
ν	[m^2/s]	molecular kinematic viscosity

Subscripts and Superscripts

x, z	along-slope, slope-normal coordinates
max	maximum
t	turbulent
X, Y, Z	width, depth, and height coordinates

1. INTRODUCTION

Planetary boundary layer (PBL) phenomena such as slope winds and nocturnal low-level jets (LLJ) are frequent on Mars, *e.g.*, whenever diurnal surface temperature variations are significant and large-scale winds are weak [1]. Particularly, thermally-driven winds are very common over sloping regions, may reach high speeds for steep slopes, and govern near-surface winds in many sites. Most of the Earth's PBL modeling approaches are being applied as well to the Martian PBL, including very high-resolution large-eddy simulations (LES) [2], the same way LES have been used on Earth [3, 4]. In particular, numerical simulations of this type of flows on Earth, framed in the atmospheric boundary layer (ABL), have usually been conducted using commercial computational fluid dynamics (CFD) software. Here, the potential of OpenFOAM for simulating

slope flows on Mars is explored, following previous investigations on OpenFOAM turbulence models and temperature and pressure boundary conditions (BC) and initial conditions (IC) for simulating such flows on Earth [5, 6].

This work aims to facilitate, in the future, the screening of large numbers of candidate landing sites for Mars missions [7], and to estimate the thermally-driven wind speeds for wind resource assessment. Previous investigations report predicted surface wind speeds of 2–10 m/s in the Mars Pathfinder (MPF) rover site [8], 16 m/s in the Mars 2020 Perseverance rover site [9], and 17 m/s in Arsia Mons [1]. Wind gusts of above 30 m/s may occur on Mars [10], and peaks of 14–19 m/s were measured in the Insight and Viking Lander 2 (VL2) sites [11], while slope flow peaks of 10–15 m/s were measured in Aeolis Mons by the Rover Environmental Monitoring Station/Mars Science Laboratory (REMS/MSL) [12], where the Mars-WRF numerical model underpredicted the strength of daytime wind speeds by 2–4 m/s [13]. The wind power density for winds of 20–30 m/s would be 60–203 W/m^2, with the density from NASA's Martian atmospheric model. Hence, the same way that solar energy has potential to become an excellent source to power extended (multi-annual) Mars missions [13], wind energy, though being not optimum for first stages of human settlements on Mars, can become another interesting renewable energy source in the long term or as back-up for solar energy [11].

Slope winds in the area of Gusev Crater and Valles Marineris were simulated in [7]. Haberle et al. [14] developed a model for studying the winds in the Viking Lander 1 (VL1) landing site. VL1 data include a single profile of wind and temperature from 1.5 to 4 km height, and their diurnal variations at 1.6 m above ground level (AGL). The predicted model winds were able to match the wind surface data or wind vertical profiles, but not both simultaneously. The best agreement was obtained using a slope magnitude and/or direction different from the reported values. However, the model was able to reproduce the shape, phase, and sense of rotation of the surface wind hodograph at each site. These simulations included nocturnal LLJ, which may be common on Mars, and a negative feedback between the dust and surface stress.

Martian PBL phenomena were also studied using Prandtl's theory, a 2D mesoscale model, and VL1 data [1]. The model used turbulence and dynamics schemes validated for Earth, while the radiation and surface schemes were modified for Mars. Relevant findings from this work regarding katabatic winds are: 1) *During moderate prevailing large-scale wind:* Nocturnal LLJ are similar to those on Earth, but higher up (at 1 km), due to inertial oscillations after the rapid collapse of thermal turbulence at sunset (and thus LLJ are expected to exist over flat and over sloping regions), with some contribution from slope winds over sloping regions (very common on Mars): slope winds added 15–20% to the LLJ super-geostrophy of 3 m/s in VL1. 2) *During weak, large-scale wind:* Strong, regular drainage flows with strong vertical shear develop at nighttime down Martian slopes, as slopes are colder than the air, with peaks at ≈100 m height. For steep slopes, these winds can reach high speed (*e.g.*, 17 m/s in Arsia Mons). For fixed slope angle and no geostrophic wind, maximum drainage flow speeds are expected at latitude 25–35°. As regards to anabatic winds, the typical afternoon up-slope winds are vertically homogeneous, well-mixed up to 2–3 km (during daytime, the convective PBL grows up to 4–5 km in the late afternoon) and weak (1–4 m/s in magnitude), even over relatively steep, large-scale slopes [1].

The diurnal cycles of surface wind near the MPF rover and the VL1 lander are complex, and a good prediction requires sufficient model resolution to adequately simulate the contributing slope flows in these regions, because, in many Martian sites, near-surface winds are dominated by slope flows of multiple scales. In turn, slope flows dramatically influence the diurnal surface pressure cycle: surface winds from the Fifth-Generation Penn State University/National Center for Atmospheric Research (NCAR) Mesoscale Model adapted to Mars (MMM5) exhibit significant steering and channeling, which are a result of topographical slopes and thermally-induced flows [15].

Compared to investigations on Earth, one of the main challenges of the proposed numerical analysis is the widespread presence of suspended dust on Mars. The dust modifies significantly the radiative properties of the Martian atmosphere [8, 16, 17]. In daytime, the dust absorbs solar radiation, reducing the ground insolation and thus cooling the surface. At nighttime, dust infrared emission keeps the surface warm. Hence, the dust decreases the amplitude of the diurnal temperature variations, without strongly affecting the average surface temperatures. Conversely, dust has a key effect on atmospheric temperature. At sunlit latitudes, even for relatively clear air, the atmosphere at 20 km is 30 K warmer than if it was dust-free. The dust also enhances the horizontal temperature gradients on Mars, and thus the Martian atmospheric circulation [16]. OpenFOAM has been successfully applied for making CFD analyses of turbulent buoyant ABL flows [18, 19] and pollutant dispersion [20, 21, 22]. Therefore, it is expected that OpenFOAM is capable of simulating how suspended dust in the Martian atmosphere affects thermally-driven winds.

As a first step towards complex simulations of thermally-driven winds on Mars, and in order to validate the proposed methodology and the performance of OpenFOAM CFD for these purposes, slope winds are simulated in this work in an idealised 2D Martian mountain-valley system with realistic values of all relevant parameters.

2. NUMERICAL SETUP

To study the generation of thermally-driven winds during Martian diurnal cycles, OpenFOAM free open-source CFD software is used. The details of the methodology used here (such as the governing equations, the solver used, the assumptions made, etc.) is described in-depth in [5, 6], where the same geometry of a 2D 20º slope with valley was used. Among the OpenFOAM solvers for heat transfer analysis applicable for our research, *buoyantBoussinesqPimpleFoam* was chosen, a transient solver for buoyant, turbulent flow of incompressible fluids, which uses Navier-Stokes equations with Boussinesq approximation.

Figure 1 shows the mesh of the studied mountain-valley configuration, with the dimensions of the domain and the applied boundary conditions. A mesh of $254 \times 1 \times 500$ elements has been used, with uniform horizontal size of around 7 m and vertical size increasing from 0.11 m in the first layer on the slope and flat part to 27.6 m near the top area.

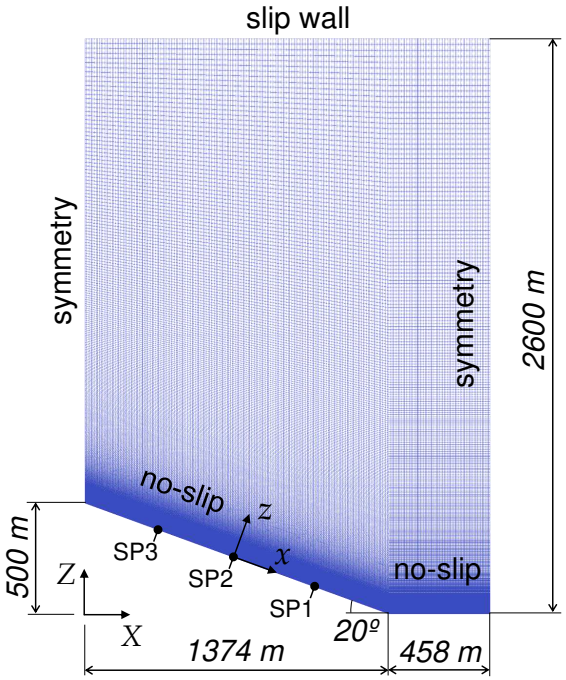

Figure 1. Mountain-valley geometry and mesh

To simulate the change of temperature due to the Martian diurnal cycle, a transient temperature profile was applied as boundary condition on the ground no-slip walls. The whole study considers as time period a sol (solar day on Mars, approximately 24.6 h), and the corresponding hours within a sol (Martian hours, h_M) are represented in all figures. The temperature profile was obtained by applying an analytical fitting to temperatures measured at 2 m on Mars [23]:

$$T(t) = 220.85 + 24.43 \sin(2\pi t/T_M - \pi) \quad [\mathrm{K}] \quad (1)$$

where $T_M = 88\,775$ s, giving an acceptable goodne ss of the fitting ($R^2 = 0.9704$). The temperature measurements and corresponding fitting can be seen in Figure 2. It is important to remark that the hours used in this and the subsequent plots are not terrestrial hours but Martian hours h_M, *i.e.*, the result of dividing a Martian sol in 24 identical time slots. Finally, mean temperatures of the Martian surface air are usually ≈220 K [1, 2, 8]. In his work, the mean temperature obtained in the fitting (220.85 K) is set as initial temperature in the computational field.

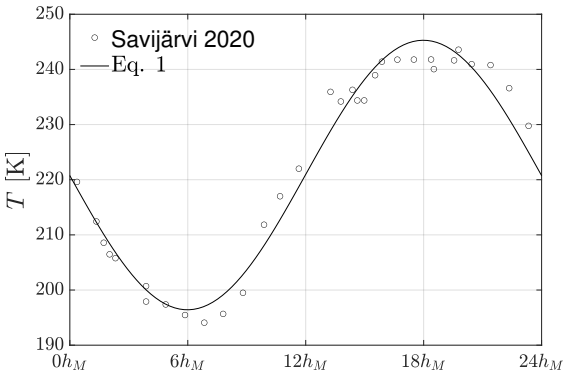

Figure 2. Surface temperature vs time (in Martian hours) for a Martian sol: measurements at 2 m [23] and corresponding analytical fit (Eq. 1)

Apart from correctly adjusting the temperature profile, the thermophysical and transport properties need to be correctly defined in the OpenFOAM setup. The most important simulation parameters are summarised in Table 1.

Table 1. Simulation parameters

Parameter	Value and units
μ	1.422×10^{-5} kg m^{-1} s^{-1}
ν	1.0868×10^{-3} m^2 s^{-1}
Pr	1
Pr_t	3
β	4.762×10^{-3} K^{-1}
R'	192 J kg^{-1} K^{-1}
M	0.0433 kg mol^{-1}
c_p	860 J kg^{-1} K^{-1}
g	3.71 m s^{-2}
p	800 Pa
z_0	0.01 m

LES studies have mostly focused on idealised numerical experiments on Mars PBL, and have produced plausible results with respect to the limited observations available [2]. LES distinguishes between the large eddies in the flow, which are mainly determined by the geometry of the problem under study, and the smaller eddies that tend to be more universal. A filter is applied so that scales smaller than the filter size are removed from the variables, and their effect on the resolved scales is modelled by means of a turbulence model. This is the turbulence model chosen here, with a Smagorinsky closure [3, 24]. Open-

FOAM default model coefficients are used.

The simulation was run for 2 sols on 16 cores (of 8 GB of DDR4-2666 ECC RAM each) of a Dual AMD EPYC™ 7001 Series Processors. The computational time needed to run a Martian sol of simulation time (887 750 time steps) is of around 5.4 days.

3. RESULTS

Figure 3 shows the along-slope flow maximum velocity u_{max} vs time, at different along-slope positions: 25% (SP1), 50% (SP2), and 75% (SP3) from the mountain base. As observed in similar studies on Earth [25], the katabatic flow (positive u_{max}) reaches lower along-slope velocities in absolute terms than the anabatic flow (≈3 vs ≈6 m/s, respectively). The order of magnitude of these values is in line with earlier works in Martian environments [1]. In the katabatic phase, u_{max} is rather constant in the lower part of the slope (SP1 and SP2), but it is ≈34% lower in the upper slope part (SP3), as in [26]. In the anabatic phase, there is a clear increase in flow velocity when going up the slope, with u_{max} at SP3 being twice the one at SP1. During this phase, velocity oscillations with time are also present, while the katabatic phase results are much more regular. Finally, note that the u_{max} value appears to be delayed in time from SP1 to SP3 in the katabatic phase: it occurs before the minimum temperature imposed as BC in the bottom of the slope, and increasingly later as we go up the slope. As for the anabatic case, the maximum value of u_{max} (in absolute value) is harder to identify due to the mentioned oscillations but seems more independent (in time) of the location on the slope.

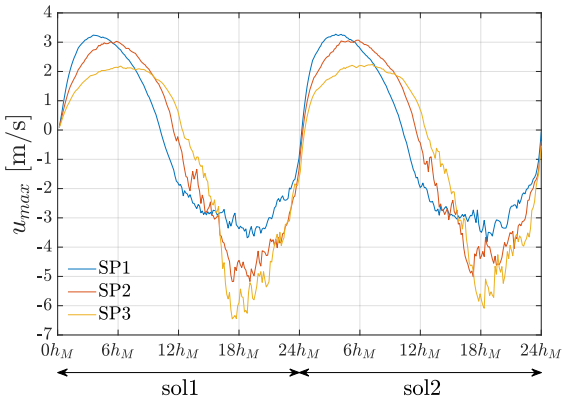

Figure 3. Maximum along-slope velocity u_{max} vs time (in Martian hours) at different positions along the slope

Figures 4 and 5 respectively show the flow velocity magnitude U at 3 h_M (katabatic phase) and at 18 h_M (anabatic phase) of the second sol. In the katabatic phase, a main descending flow is observed on the slope, while the rest of the domain remains rather still, being the obtained flow velocities in general much lower than in the anabatic phase. In Fig. 5, there is a main recirculation vortex confined in the top part of the fluid domain, which should not affect significantly the development of the anabatic flow, as also commented in [27] and studied for similar simulations on Earth in [5, 6]. Future simulations will consider additional computational domain heights H_D to confirm this. Several minor vortexes are also observed, explaining the velocity oscillations observed in Fig. 3.

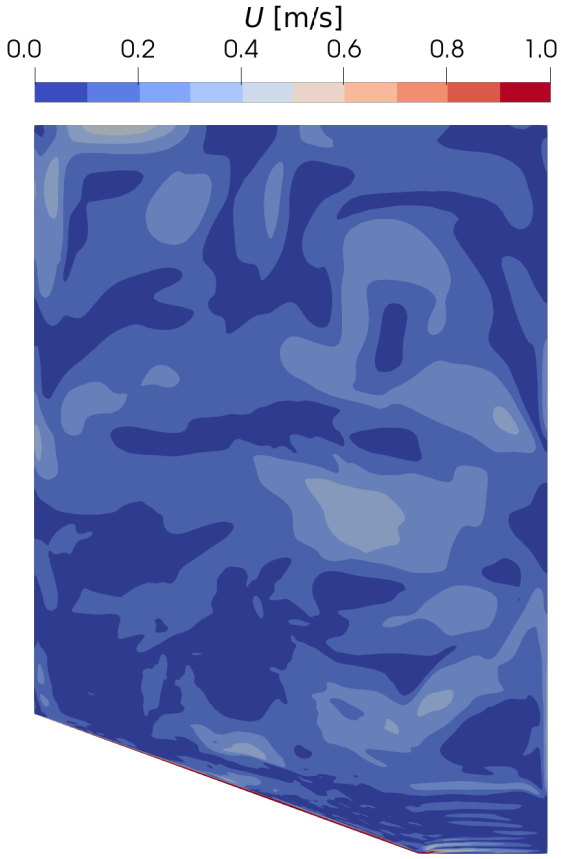

Figure 4. Katabatic: velocity U at 3 h_M for sol2

Figure 6 shows the along-slope flow velocity u vs time, at different slope-normal distances z, at mid-slope. In the katabatic phase, where u is lower, it is also remarkable that u decreases faster with z. This is likely because the temperature difference between the atmosphere and slope ΔT is larger in absolute terms for the anabatic case, as it is shown in Figure 8. Fig. 6 also shows that, for the katabatic case, u_{max} (≈3 m/s) is obtained right above $z = 1$ m, at $z = 5$ m, u is only ≈1 m/s, and for $z > 5$ m, u is close to zero. In the anabatic phase, again, u shows more oscillations, but it is clear that the decrease of u with z is slower than in the katabatic phase, being u virtually identical at $z = 2.5$ and 5 m, for example. This happens though the flow temperature is noticeably different at those z values, as seen in Figure 7, which shows the temperature T vs time, at different slope-normal distances at mid-slope. This figure shows that the time evolution of T is quite similar for all values of z, except, to some extent, for $z = 2.5$ m. Apart

Figure 5. Anabatic: velocity U at 18 h_M for sol2

from the steep decrease of T for z from 0 to 2.5 m, it can also be seen how the original sinusoidal temperature profile (with time), imposed as BC, is lost almost immediately. This behaviour is quite different from the velocity profiles, which do retain a sinusoidal profile.

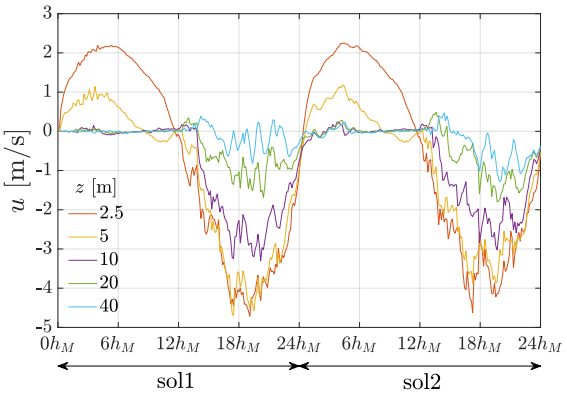

Figure 6. Along-slope velocity u vs time (in Martian hours) at different z-distances at mid-slope

Figures 8 and 9 show the along-slope velocity u and temperature difference ΔT as functions of the slope-normal distance z, at three positions along the slope (SP1, SP2, and SP3), for the katabatic (at 3 h_M)

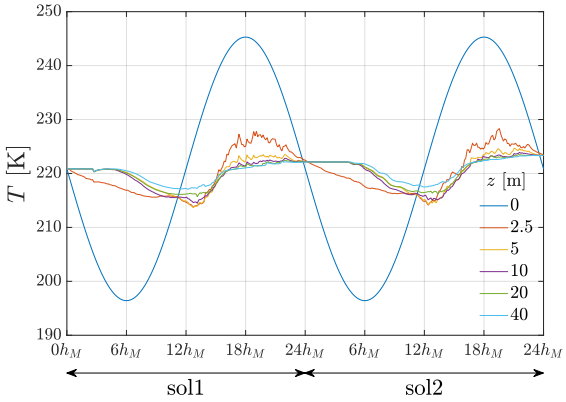

Figure 7. Temperature T vs time (in Martian hours) at different z-distances at mid-slope

and anabatic (at 18 h_M) cases for sol2. For the katabatic case, though all ΔT profiles are quite similar up to $z = 5$ m (showing the already observed steep decrease of T), the steepest ΔT profile at SP3 leads to a quite lower u profile. As also seen in Fig. 3, velocity profiles at SP1 and SP2 are very similar, especially at low values of z. For $z > 5$ m, the profiles of u and ΔT at SP2 and SP3 become very similar, while the profiles at SP1 show significant discrepancies, particularly in ΔT, which might be due to the effect of the flat valley at the bottom of the slope. To be able to ascertain this, future work will study the influence of different valley widths on the results. However, this does not mean that the results presented here-in are not valid, given that the studied geometry may perfectly correspond to real geometries, as valleys with many different widths can be found on Mars. For the anabatic flow, it can be seen that, on the one hand, the temperature decreases more slowly at SP3 than at SP1 and SP2, leading to higher values of u for $z > 2$ m, and the peak position (*i.e.*, the position of u_{max}) rising to higher slope-normal distances. On the other hand, the slope-normal profiles of u and ΔT are very similar at SP1 and SP2.

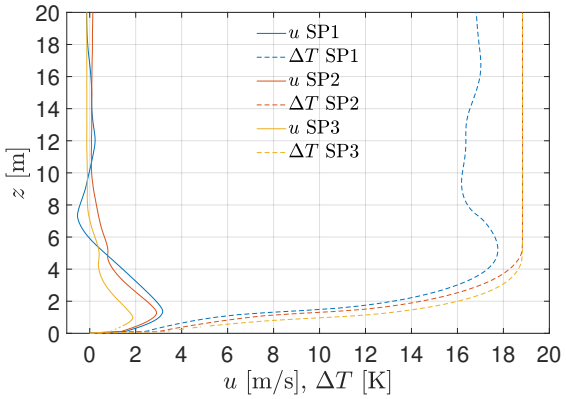

Figure 8. Katabatic: along-slope velocity u and ΔT profiles vs z-distance at 3 h_M for sol2

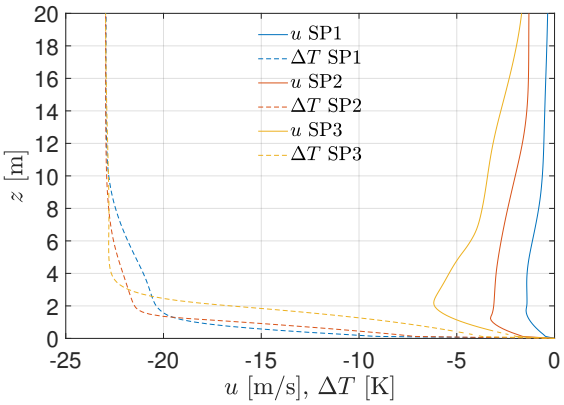

Figure 9. Anabatic: along-slope velocity u and ΔT profiles vs z-distance at 18 h_M for sol2

4. CONCLUSIONS

This work presents a preliminary study of numerical simulations performed with OpenFOAM, which proves its validity for generating slope winds in a Martian environment. The obtained velocity values are in line with previous investigations, showing higher magnitudes of the along-slope velocity in the anabatic case than in the katabatic one. The temperature gradient decreases rapidly from the ground, and thus the most significant along-slope flow velocities are basically observed just below slope-normal distances of 5 and 10 m for the katabatic and anabatic phases, respectively. The position along the slope also shows distinct effects on the flow velocity in the katabatic and anabatic phases.

Future work will compare LES with RANS turbulence models (such as k–ε, very common for simulating ABL flows on Earth [28]), and validate the choice of domain height and mesh size (depending on the chosen turbulence models). In a further step, interaction between geostrophic wind and slope wind may be simulated to study the influence of the geostrophic wind on the total generated wind. Finally, the effect of the Martian dust may be included into the simulations. This, considering realistic Martian geometries, could help assessing the possibility of using wind energy as an additional source to solar energy during long-term Martian missions.

ACKNOWLEDGEMENTS

This work has been supported by the project PID2019-105162RB-I00 funded by MCIN/AEI/10.13039/501100011033 and by the project 2017 SGR 1278 from the AGAUR from *Generalitat de Catalunya*.

REFERENCES

[1] Savijärvi, H. I., and Siili, T., 1993, "The Martian slope winds and the nocturnal PBL jet", *J Atmos Sci*, Vol. 50, pp. 77–88.

[2] Petrosyan, A., Galperin, B., Larsen, S. E., Lewis, S. R., Määttänen, A., Read, P. L., Renno, N., Rogberg, L. P., Savijrvi, H., Siili, T., Spiga, A., Toigo, A., and Vázquez, L., 2011, "The Martian atmospheric boundary layer", *Rev Geophys*, Vol. 49, p. RG3005.

[3] Cao, S., Wang, T., Ge, Y., and Tamura, Y., 2012, "Numerical study on turbulent boundary layers over two-dimensional hills - Effects of surface roughness and slope", *J Wind Eng Ind Aerodyn*, Vol. 104, pp. 342–349.

[4] Bhuiyan, A. A., Karim, R. M., Hart, J. T., Rahman, M. M., and Naser, J., 2016, "Experimental and numerical investigation of coherent structure dynamics on mass transfer in a separated cavity flow", *Exp Therm Fluid Sci*, Vol. 76, pp. 146–162.

[5] Athota, R. B., Rojas, J. I., Arias, S., and Montlaur, A., 2022, "Simulations of thermal wind formation in idealised mountain-valley systems using OpenFOAM", Available at SSRN: `https://ssrn.com/abstract=4086430` or `https://dx.doi.org/10.2139/ssrn.4086430`.

[6] Rojas, J., Arias, S., and Montlaur, A., 2022, "Comparison of OpenFOAM turbulence models for numerical simulation of thermally-driven winds", *Conference on Modelling Fluid Flow (CMFF'22)*, Budapest, Hungary.

[7] Justus, C. G., Duvall, A., and Keller, V. W., 2006, "Validation of Mars Global Reference Atmospheric Model (Mars-GRAM 2001) and planned new features", *Adv Space Res*, Vol. 38, pp. 2633–2638.

[8] Haberle, R. M., Joshi, M. M., Murphy, J. R. Barnes, J. R., Schofield, J. T., Wilson, G., Lopez-Valverde, M., Hollingsworth, J. L., Bridger, A. F. C., and Schaeffer, J., 1999, "General circulation model simulations of the Mars Pathfinder atmospheric structure investigation/meteorology data", *J Geophys Res*, Vol. 104, pp. 8957–8974.

[9] Pla-García, J., Rafkin, S. C. R., Martinez, G. M., Vicente-Retortillo, A., Newman, C. E., Savijärvi, H., de la Torre, M., Rodriguez-Manfredi, J. A., Gómez, F., Molina, A., Viúdez-Moreiras, D., and Harri, A.-M., 2020, "Meteorological predictions for Mars 2020 Perseverance Rover landing site at Jezero Crater", *Space Sci Rev*, Vol. 216, p. 148.

[10] Wilson, C. F., 2003, "Measurement of Wind on the Surface of Mars", Ph.D. thesis, University of Oxford, Linacre College.

[11] Schorbach, V., and Weiland, T., 2022, "Wind as a back-up energy source for mars missions", *Acta Astro*, Vol. 191, pp. 472–478.

[12] Soria-Salinas, A., Zorzano, M. P., Mantas-Nakhai, R., and Martín-Torres, J., 2020, "Wind retrieval from temperature measurements from the Rover Environmental Monitoring Station/Mars Science Laboratory", *Icarus*, Vol. 346, p. 113785.

[13] Newman, C. E., Gomez-Elvira, J., Marin, M., Navarro, S., Torres, J., Richardson, M. I., Battalio, J. M., Guzewich, S. D., Sullivan, R., de la Torre, M., Vasavada, A. R., and Bridges, N. T., 2017, "Winds measured by the Rover Environmental Monitoring Station (REMS) during the Mars Science Laboratory (MSL) rover's Bagnold Dunes Campaign and comparison with numerical modeling using MarsWRF", *Icarus*, Vol. 291, pp. 203–231.

[14] Haberle, R. M., Houben, H. C., Hertenstein, R., and Herdtle, T., 1993, "A boundary-layer model for Mars: Comparison with Viking Lander and entry data", *J Atmos Sci*, Vol. 50, pp. 1544–1559.

[15] Tyler Jr, D., Barnes, J. R., and Haberle, R. M., 2002, "Simulation of surface meteorology at the Pathfinder and VL1 sites using a Mars mesoscale model", *J Geophys Res*, Vol. 107, pp. 2–1–2–16.

[16] Forget, F., 2007, "Water and Climates on Mars", *Lect Astrobiol Vol II, Adv Astrobiol Biogeophys*, Springer-Verlag, Berlin, Heidelberg, pp. 103–122.

[17] Conrath, B. J., Pearl, J. C., Smith, M. D., Maguire, W. C., Christensen, P. R., Dason, S., and Kaelberer, M. S., 2000, "Mars Global Surveyor thermal emission spectrometer (TES) observations: Atmospheric temperatures during aerobraking and science phasing", *J Geophys Res*, Vol. 105, pp. 9509–9519.

[18] Bautista, M. C., 2015, "Turbulence Modelling of the Atmospheric Boundary Layer over Complex Topography", Ph.D. thesis, Université de Québec, École de Technologie Supérieure.

[19] Franke, J., Sturm, M., and Kalmbach, C., 2012, "Validation of OpenFOAM 1.6.x with the German VDI guideline for obstacle resolving micro-scale models", *J Wind Eng Ind Aerodyn*, Vol. 104–106, pp. 350–359.

[20] Flores, F., Garreaud, R., and Muñoz, R. C., 2014, "OpenFOAM applied to the CFD simulation of turbulent buoyant atmospheric flows and pollutant dispersion inside large open pit mines under intense insolation", *Comput Fluids*, Vol. 90, pp. 72–87.

[21] Ejtehadi, O., Mahravan, E., and Sohn, I., 2021, "Investigation of shock and a dust cloud interaction in Eulerian framework using a newly developed OpenFOAM solver", *Int J Multiphase Flow*, Vol. 145, p. 103812.

[22] Islas, A., Rodríguez-Fernández, A., Betegón, C., Martínez-Pañeda, E., and Pandal, A., 2022, "CFD simulations of turbulent dust dispersion in the 20 L vessel using OpenFOAM", *Powder Technol*, Vol. 397, p. 117033.

[23] Savijärvi, H. I., Martinez, G. M., Fischer, E., Renno, N. O., Tamppari, L. K., Zent, A., and Harri, A. M., 2020, "Humidity observations and column simulations for a warm period at the Mars Phoenix lander site: Constraining the adsorptive properties of regolith", *Icarus*, Vol. 343, p. 113688.

[24] Majander, P., and Siikonen, T., 2002, "Evaluation of Smagorinsky-based subgrid-scale models in a finite-volume computation", *Int J Numer Methods Fluids*, Vol. 40, pp. 735–744.

[25] Barcons, J., Avila, M., and Folch, A., 2019, "Diurnal cycle RANS simulations applied to wind resource assessment", *Wind Energy*, Vol. 22, pp. 269–282.

[26] Román-Gascón, C., Yagüe, C., Arrillaga, J. A., Lothon, M., Pardyjak, E. R., Lohou, F., Inclán, R. M., Sastre, M., Maqueda, G., Derrien, S., Meyerfeld, Y., Hang, C., Campargue-Rodríguez, P., and Turki, I., 2019, "Comparing mountain breezes and their impacts on CO_2 mixing ratios at three contrasting areas", *Atmos Res*, Vol. 221, pp. 111–126.

[27] Cintolesi, C., Di Santo, D., Barbano, F., and Di Sabatino, S., 2021, "Anabatic Flow along a Uniformly Heated Slope Studied through Large-Eddy Simulation", *Atmos*, Vol. 12 (7).

[28] Balogh, M. G., Parente, A., and Benocci, C., 2012, "RANS simulation of ABL flow over complex terrains applying an enhanced k-epsilon model and wall function formulation: Implementation and comparison for Fluent and OpenFOAM", *J Wind Eng Ind Aerodyn*, Vol. 104–106, pp. 360–368.

Conference on Modelling Fluid Flow (CMFF'22)
The 18th International Conference on Fluid Flow Technologies
Budapest, Hungary, August 30-September 2, 2022

EXPANSION AND COLLAPSE OF SINGLE CAVITATION BUBBLES RIGHT AT A SOLID BOUNDARY

Christiane LECHNER[1], Max KOCH[2], Werner LAUTERBORN[2], Robert METTIN[2],

[1] Corresponding Author. Institute of Fluid Mechanics and Heat Transfer, TU Wien. Getreidemarkt 9, A-1060 Vienna, Austria. Tel.: +43 1 58801 32211, Fax: +43 1 58801 32298, E-mail: christiane.lechner@tuwien.ac.at
[2] Third Physical Institute, Georg-August University Göttingen. Germany. E-mail: max.koch@phys.uni-goettingen.de, werner.lauterborn@phys.uni-goettingen.de, robert.mettin@phys.uni-goettingen.de

ABSTRACT

We present results from numerical simulations modeling the dynamics of single (laser-generated) cavitation bubbles expanding and collapsing right at a plane solid boundary. The model consists of a bubble filled with a small amount of non-condensable gas in a compressible liquid. The Navier-Stokes equations are discretized with the finite volume method. The volume of fluid method is used to capture the interface between liquid and gas. The model is implemented in the open source software package OpenFOAM.

A millimeter sized bubble in water serves as reference to discuss bubble dynamics. The most intriguing phenomenon that occurs in this configuration is the formation of a fast jet that is directed towards the solid with a speed of the order of 1000 m/s. The jet formation mechanism is explained. Paradoxically, in this setting, jet formation causally is related to the viscosity of the liquid.

Bubble size and liquid viscosity are varied. It is shown that fast jet formation persists for a wide range of liquid viscosities, including e.g. 50 cSt silicone oil. Bubble dynamics and the jet formation mechanism are discussed for values of a bubble Reynolds number, Re_b, ranging from 15 to 50 000, with fast jet formation occurring for $\mathrm{Re}_b \gtrsim 300$.

Keywords: bubble dynamics, cavitation, erosion, finite volume method, jet formation

NOMENCLATURE

B	$[Pa]$	Tait pressure
n_T	$[-]$	Tait exponent
p	$[Pa]$	pressure
t	$[s]$	time
x, y, z	$[\mu m]$	coordinates
$\boldsymbol{U}$	$[m/s]$	velocity
$\mathbb{T}$	$[kg/(ms^2)]$	viscous stress tensor
$\mathcal{R}^{\mathrm{eq}}$	$[\mu m]$	equivalent bubble radius
γ_g	$[--]$	adiabatic exponent, gas
μ	$[kg/(ms)]$	dynamic viscosity
ν	$[m^2/s]$	kinematic viscosity
ρ	$[kg/m^3]$	density
σ	$[kg/s^2]$	surface tension coefficient

Subscripts and Superscripts

init	initial conditions
jet, jf	jet, jet formation
l, g	liquid, gas
max	maximum
∞	ambient conditions

1. INTRODUCTION

Due to their erosive power, cavitation bubbles collapsing close to solid boundaries have been subject to intense investigations for several decades. Mainly two phenomena associated with the collapse of the bubble are considered responsible for the destructive action: a high-speed, axial liquid jet directed towards the solid and the shock waves emitted after the collapse of the resulting torus bubble.

Usually, jets form by involution of the bubble wall and reach a speed of the order of 100 m/s under normal ambient conditions [1, 2, 3, 4], see also [5, Fig. 21]. For bubbles expanding and collapsing in ultimate proximity to the solid, however, very thin axial jets of the order of 1000 m/s are formed, following the violent self-impact of annular liquid inflow at the axis of symmetry [6, 7, 4, 8, 9] and [10].

The mechanism of fast jet formation as well as the explanation of the typical "bell shape" of the bubble during collapse, that is observed in the experiment, see Figure 1, is briefly sketched in Figures 2 – 4 for a millimeter sized bubble in water. Shown are the bubble shape together with the velocity or pressure field at several stages of bubble evolution. During the rapid expansion of the bubble a boundary layer adjacent to the solid forms, as indicated in Fig. 2 (top). This boundary layer causes the outer rim of the bubble to slightly "lift-off" from

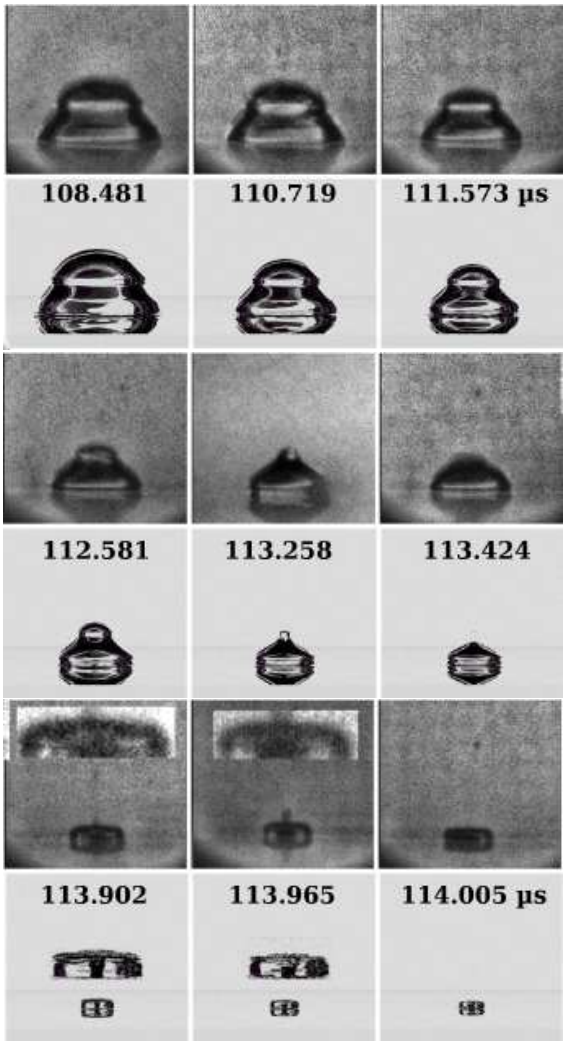

Figure 1. Bubble collapsing right at a plane solid boundary in water, taken from [9, Fig. 16]. Comparison of experimental high-speed photographs (odd rows) and the result of ray-tracing a numerical 3D simulation (even rows). In the last two rows magnifications with enhanced contrast are shown as inserts. Frame width 664.5 μm.

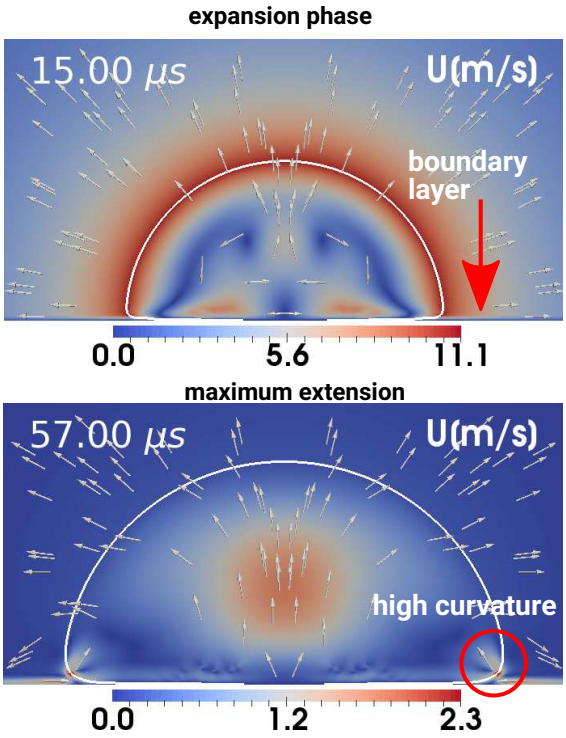

Figure 2. Bubble expanding right at a plane solid boundary in water. Results of an axially symmetric simulation. Shown is a cut through the bubble. The color gives the magnitude of the velocity in m/s. Arrows indicate the direction of the flow. At $t = 57\mu s$ the bubble attains the maximum volume with $\mathcal{R}^{eq}_{max} = 627\mu m$. Frame size 1.6 × 0.8 mm.

the solid surface. At maximum extension the bubble shape is hemi-spherical, except for the region around the outer bubble rim, which exhibits a much larger curvature than the remainder of the bubble, see Fig. 2 (bottom). For bubbles in a low viscosity liquid, such as water, this deviation from hemi-spherical shape might seem marginal. Nevertheless, it is decisive for the fast jet forming in the late collapse phase. The high curvature region at the outer rim collapses faster than the remainder of the bubble leading to an indentation, as shown in Figs 1 and 3.

The indentation sharpens and leads to an annular inflow, that arrives faster at the axis of symmetry, than the spherical cap comes down. As a result, the annular inflow impacts onto itself, momentarily generating a very high pressure. The self-impact leads to the emission of a shock wave and liquid is squeezed into the bubble in form of a very fast, thin jet, see Fig. 4 (middle). The jet ist also seen in the experimental photograph in Fig. 1 in the last but one row. Subsequently, the jet impacts onto the solid with a speed of the order of 1000 m/s, causing a large pressure load on the solid. Finally, the remaining torus bubble collapses, accompanied by the emission of a torus shock wave, see Fig. 4 (bottom).

First photographs of this type of fast jet have been given in [11] for a bubble under reduced ambient pressure, however, no interpretation could be given then. Photographic evidence of the fast jet under normal ambient conditions could only be given recently in [8, 9]. With a combination of experimental photographs and ray-tracing a 3D numerical simulation, see Fig. 1, a lower bound of $732 m/s$ was estimated for the average speed of the fast jet. Recently, [10] presented new experimental evidence for the fast jet, including photographic recordings of the shock wave that is emitted after self-impact of the annular inflow, see Fig. 4. A lower bound of $850 m/s$ for the average jet speed could be inferred from these photographs.

Since the fast annular inflow causally is related to the viscosity of the liquid, it is of interest to quantify the influence of liquid viscosity on the jet formation process. Considering, that in low viscos-

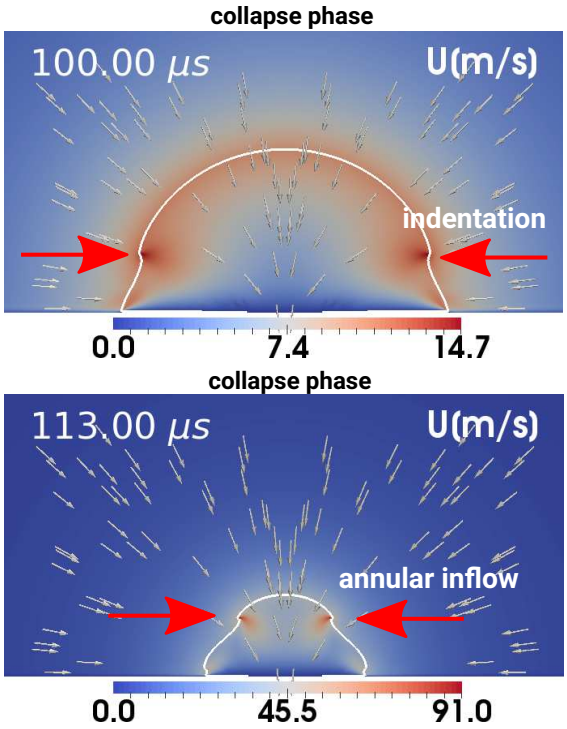

Figure 3. Collapse phase of the bubble in Figure 2. The color gives the magnitude of the velocity in m/s. Frame size 1.6 × 0.8 mm.

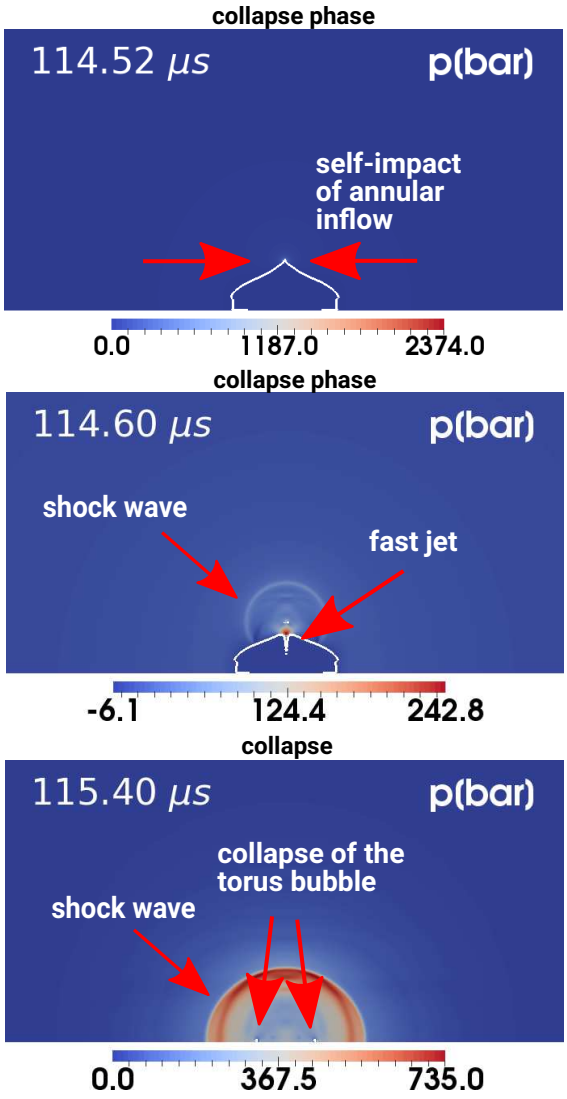

Figure 4. Fast jet formation and final stages of the collapse of the bubble in Figure 2. The color gives the pressure in bar. Frame size 1.6 × 0.8 mm.

ity liquids the bubble shape at maximum extension is hemi-spherical to a very good extent, the equivalent radius of a hemi-sphere,

$$\mathcal{R}^{\rm eq}_{\rm max} := (3V_{\rm max}/(2\pi))^{1/3}, \qquad (1)$$

with $V_{\rm max}$ the maximum volume of the bubble, is taken as a measure of bubble size. Given this, it is natural to define a dimensionless number, a bubble Reynolds number Re_b, from $\mathcal{R}^{\rm eq}_{\rm max}$, the velocity scale $\sqrt{p_\infty/\rho_{l,\infty}}$, and the kinematic viscosity of the liquid, $\nu_l = \mu_l/\rho_{l,\infty}$, as

$$\mathrm{Re}_b = \frac{\mathcal{R}^{\rm eq}_{\rm max}\sqrt{p_\infty/\rho_{l,\infty}}}{\nu_l}, \qquad (2)$$

where p_∞ is the ambient pressure and $\rho_{l,\infty}$ denotes the density of the liquid at ambient conditions.

Bubbles expanding and collapsing right at a solid boundary in liquids with different viscosities have been investigated experimentally by [12] and [13] in different contexts. In [12] the ejection of liquid through a hole in the plate was investigated, whereas the investigations in [13] were in view of laser ablation in liquids. Both works did not investigate the mechanisms of jet formation.

In the following, we vary two parameters, bubble size and viscosity of the liquid, and numerically study the overall dynamics of the bubbles as well as the formation of jets. The bubble shown in Figs 2 – 4 serves as reference for the parameter study. The Reynolds number of the reference bubble with $\mathcal{R}^{\rm eq}_{\rm max} = 627\mu m$ under normal ambient conditions in water evaluates to $\mathrm{Re}_b = 6289$.

We present the bubble model and the numerical implementation in Section 2. Results from the parameter studies are presented in Section 3 and Conclusions are given in Section 4.

2. BUBBLE MODEL AND NUMERICAL IMPLEMENTATION

The bubble model consists of a bubble filled with a small amount of non-condensable gas (air) surrounded by a liquid. The gas is taken to be ideal, undergoing adiabatic changes of state, $p\rho_g^{-\gamma_g} = \text{const}$, with p the pressure, ρ_g the density of the gas and γ_g the ratio of specific heats ($\gamma_g = 1.4$ for air). Phase transition is not considered here. The liquid is modeled as a compressible fluid with the Tait equation of state, $(p + B)\rho_l^{-n_T} = \text{const}$, with ρ_l the density of the liquid, B the Tait pressure and n_T the Tait exponent, taken to be $B = 305MPa, n_T = 7.15$ here. The vapor pressure is small compared to the ambient pressure of

$p_\infty = 101315$ Pa and therefore is neglected. Thermodynamic effects, mass exchange through the bubble wall as well as gravity are neglected. Liquid and gas are considered as viscous fluids. In particular, including the viscosity of the liquid is essential for fast jet formation here. Surface tension is included, but is not essential for the findings presented here.

The equations are formulated for a single fluid with density ρ, pressure p and velocity $\boldsymbol{U}$ satisfying the Navier-Stokes equation (3) and continuity equation (4). In order to distinguish between the two phases liquid and gas, volume fractions α_l and α_g are introduced, with $\alpha_l = 1$ in the liquid phase and $\alpha_l = 0$ in the gas phase and $\alpha_g = 1-\alpha_l$. Since no mass transfer across the interface is considered, the individual phases satisfy the continuity equations (5).

$$\frac{\partial(\rho\,\boldsymbol{U})}{\partial t} + \boldsymbol{\nabla}\cdot(\rho\,\boldsymbol{U}\otimes\boldsymbol{U}) = -\boldsymbol{\nabla}p + \boldsymbol{\nabla}\cdot\mathbb{T} + \boldsymbol{f}_\sigma\,, \quad (3)$$

$$\frac{\partial\rho}{\partial t} + \boldsymbol{\nabla}\cdot(\rho\,\boldsymbol{U}) = 0\,, \quad (4)$$

$$\frac{\partial(\alpha_i\rho_i)}{\partial t} + \boldsymbol{\nabla}\cdot(\alpha_i\rho_i\boldsymbol{U}) = 0\,, \qquad i = l, g\,. \quad (5)$$

$\boldsymbol{\nabla}$ denotes the gradient, $\boldsymbol{\nabla}\cdot$ is the divergence, and $\otimes$ the tensorial product. The density field, ρ, is written as $\rho = \alpha_l\rho_l + \alpha_g\rho_g$. $\mathbb{T}$ is the viscous stress tensor of a Newtonian fluid,

$$\mathbb{T} = \mu\left(\boldsymbol{\nabla}\boldsymbol{U} + (\boldsymbol{\nabla}\boldsymbol{U})^T - \frac{2}{3}(\boldsymbol{\nabla}\cdot\boldsymbol{U})\,\mathbb{I}\right), \quad (6)$$

with $\mu = \alpha_l\mu_l + \alpha_g\mu_g$, where μ_l, μ_g are the dynamic viscosities of liquid and gas, taken to be constant here. Surface tension is included via a force density field $\boldsymbol{f}_\sigma(\boldsymbol{x}, t)$ [see, e.g., 14].

Equations (3)–(5) are discretized with the finite volume method. The numerical implementation is based on the open source software package OpenFOAM [15, 16]. A pressure based two-phase solver is adapted for our purpose [17].

Simulations are performed in axial symmetry. A sketch of the computational domain and the grid structure is given in Figure 5. The grid is Cartesian with a uniform grid spacing of $\Delta x \approx \mathcal{R}^{\mathrm{eq}}_{\mathrm{max}}/627$ in an inner region. Further out, a polar cell ordering is used with the grid spacing increasing progressively in radial direction. The number of cells typically amounts to 140 000 for this series of runs.

Initially, a small hemi-spherical bubble with radius $\mathcal{R}_{\mathrm{init}}$ and high internal pressure $p_{\mathrm{g,init}} \gg p_\infty$ is placed in the still liquid directly at the solid surface. p_∞ denotes the ambient pressure, which is set to $p_\infty = 101315Pa$ in all simulations.

At the solid surface no-slip boundary conditions are imposed for the velocity, $\boldsymbol{U} = 0$, the normal derivative of pressure is set to zero, $\partial_n p = 0$, and the liquid volume fraction α_l is set to 1 at the solid. At the outer boundary approximate non-reflecting boundary conditions are specified for velocity and pressure.

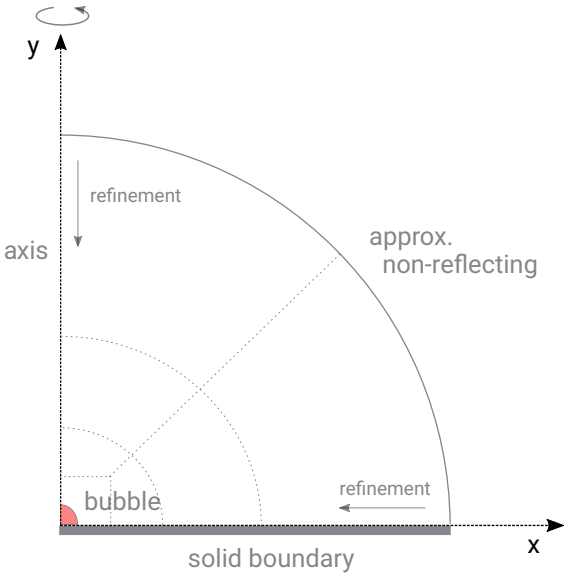

Figure 5. Sketch of the computational domain and the grid structure (not to scale).

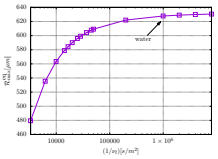

Figure 6. Maximum radius of the bubble as a function of $1/\nu_l$ for series 1. The reference bubble is indicated by an arrow.

3. RESULTS

Bubble dynamics is investigated by means of several series of simulations. Essentially, two parameters are varied, the bubble size and the viscosity of the liquid. In this investigation Re_b varies from 16 to 50 600. Four one-parameter series of simulations are presented.

In **series 1** the liquid viscosity is varied between $\mu_l = 0.125\mu_{H_2O}$ and $\mu_l = 300\mu_{H_2O}$, while initial data $\mathcal{R}_{\mathrm{init}} = 2^{1/2}20\mu m$, $p_{\mathrm{g,init}} = 1.1 \times 10^4 bar$ are kept fixed. The reference bubble is included in this series. The bubble Reynolds numbers lie in the interval $\mathrm{Re}_b \in [16, 50605]$. Figure 6 shows the maximum equivalent radius as a function of $1/\nu_l$. As expected, the maximum radius decreases with increasing viscosity, as the portion of the bubble energy that is dissipated increases.

For **series 2–4** the liquid properties are kept fixed and the maximum radius of the bubble is varied by changing initial data. The three liquids under con-

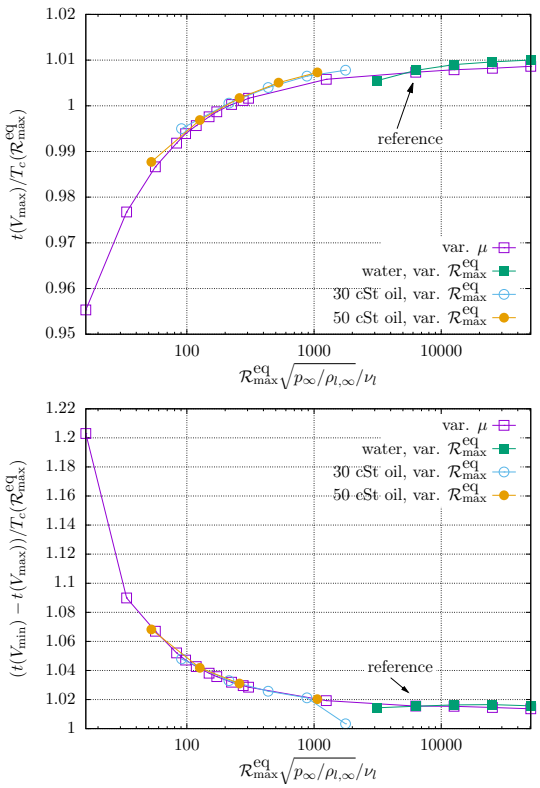

Figure 7. Time from bubble inception to the maximum extension (top) and time from the maximum extension to the first collapse (bottom).

sideration are water and 30 cSt and 50 cSt silicone oils. Material properties of the 30 cSt silicone oil are $\rho_{l,\infty} = 971\,kg/m^3, \mu_l = 0.029\,kg/(ms)$ yielding $\nu_l = 29.9\times10^{-6} m^2/s$ and of the 50 cSt silicone oil $\rho_{l,\infty} = 956\,kg/m^3, \mu_l = 0.0478\,kg/(ms), \nu_l = 50\times10^{-6}\,m^2/s$. For water $\rho_{l,\infty} = 998.2 kg/m^3$ $\mu_l = 0.0001 kg/(ms)$. The reference bubble is included in series 2. Overall, the maximum radii $\mathcal{R}^{eq}_{max}$ vary between 255 μm and 5200 μm. The bubble Reynolds numbers span the range between 52 and 50500.

Figure 7 shows the time from the initial conditions to the maximum extension, $t(V_{max})$, normalized with the Rayleigh collapse time, $T_c(\mathcal{R}^{eq}_{max}) = 0.915\,\mathcal{R}^{eq}_{max}\sqrt{\rho_{l,\infty}/p_\infty}$, of a bubble with radius $\mathcal{R}^{eq}_{max}$ (top). For low viscosity liquids this ratio is close to 1. With increasing viscosity or decreasing bubble size this quantity slightly decreases. The time from maximum extension to the first collapse, on the other hand, considerably decreases with increasing viscosity or decreasing bubble size, as shown in Fig. 7 (bottom). In total, expansion and collapse get more and more asymmetric with increasing viscosity or decreasing bubble size.

Figure 8 shows the bubble shape at maximum extension for selected values of the bubble Reynolds number including the reference bubble with $\mathrm{Re}_b = 6289$. The thickness of the viscous boundary layer during the expansion phase increases with decreasing bubble Reynolds number. As a consequence the dis-

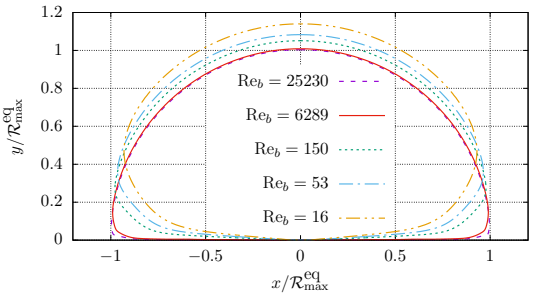

Figure 8. Bubble shapes at maximum extension for different values of Re_b taken from series 1,2 and 4. The solid line represents the reference bubble (water, $\mathcal{R}^{eq}_{max} = 627\mu m$, $\mathrm{Re}_b = 6289$)

tance of the outer rim of the bubble at maximum extension increases with decreasing Re_b. Furthermore, with decreasing Reynolds number bubble expansion along the solid wall is hindered and expansion in the direction orthogonal to the solid is increased. In total, the bubble shape changes from hemi-spherical with a slight "elevation" of the outer bubble rim for very high Reynolds numbers to a shape that resembles more an oblate spheroid for small Reynolds numbers.

Figure 9 shows the bubble shapes during collapse for four liquids from series 1, including the reference bubble. In water with $\mathrm{Re}_b = 6289$ the high curvature region at the outer bubble rim involutes and the bubble shape shows the indentation that has been described in Sec. 1. The indentation ultimately leads to the self impact of the annular inflow and the formation of the fast jet. For $\mathrm{Re}_b = 150$ (second row) the higher curvature region at the outer bubble rim involutes as well. However, here the higher viscosity damps the relative motion and no annular inflow, faster than the surroundings, develops. The bubble surface stays smooth. The timing is such, that a spherical cap with higher curvature on top of the bubble is developing, which collapses faster than the bubble sides. A jet forms at the end of the collapse of the spherical cap by involution of the bubble wall. The speed of the jet for this value of Re_b amounts to approximately 500 m/s.

For even smaller Reynolds numbers $\mathrm{Re}_b = 34$ and 16 (Fig. 9 third and last row), there seem to be three regions during bubble collapse. A region close to the solid, where there is hardly any movement, a middle region around the "belly" of the bubble, which collapses faster and involutes, and a cap which seems to collapse in an approximately spherical manner. These three regions are indicated and separated by sharp edges in the bubble shape, which are more pronounced for the smaller Reynolds number. We note, that these sharp edges are not a numerical artefact, but are seen in the experiment as well, compare e.g. the shape of a collapsing bubble in PAO40 in

[13]. A broad jet with a speed of 110 m/s is formed by involution of the bubble wall for $\mathrm{Re}_b = 34$. There is no jet formation for $\mathrm{Re}_b = 16$.

Figures 10 and 11 show the bubble shape and pressure field around jet formation for the bubbles with $\mathrm{Re}_b = 150$ and $\mathrm{Re}_b = 34$. In Fig. 10 the jet forms at the end of a fast collapsing spherical cap by involution of the bubble wall. A high pressure region forms due to the in-rushing liquid. The magnitude of pressure, however, is several orders of magnitude smaller than after the self-impact of annular inflow in Fig. 4, above. The high pressure region connected to the broad jet in Fig. 11 is one further order of magnitude smaller.

Figure 12 gives the jet speeds for all four series of simulations. For $\mathrm{Re}_b \lesssim 300$ jets are formed by involution of the upper bubble wall, as shown in Fig. 9 in the last three rows and in Figs 10 and 11. Data points of all series of simulations collapse on a single line. For $\mathrm{Re}_b \gtrsim 300$ fast jet formation is observed. Within a series of simulations, the jet speed seems to be roughly independent of Re_b, but differs between the series. We note, however, that the jet speed in the axially symmetric simulations numerically depends on the grid spacing, since jet formation arises from liquid self-impact at the axis, which is a nearly singular phenomenon. Nevertheless, we include these values here, since a trend in variation of the jet speed might be inferred from them.

Figure 13 shows the equivalent radius of the bubble, which is a measure of bubble size, at the moment of jet formation, $\mathcal{R}^{\mathrm{eq}}_{\mathrm{jf}}$. For fast jet formation and the jets forming after the collapse of a spherical cap, the moment of jet formation can be defined by a pressure maximum at the axis. Data concerning the formation of a slow jet, as shown in Fig. 9 (third row) are not included in Fig. 13, since this type of jet formation is not connected to a pressure maximum at the axis.

$\mathcal{R}^{\mathrm{eq}}_{\mathrm{jf}}$ is maximum at $\mathrm{Re}_b \simeq 100$ and decreases for smaller and larger Re_b. The transition from jet formation after the collapse of a spherical cap to jet formation after self-impact of an annular inflow is smooth in the quantity $\mathcal{R}^{\mathrm{eq}}_{\mathrm{jf}}$. Increasing Re_b further, fast jet formation happens later and later in the bubble evolution.

4. CONCLUSION

The dynamics of bubbles expanding and collapsing right at a solid boundary has been investigated numerically for a range of bubble sizes and liquid viscosities.

We find the formation of a fast, thin jet after self-impact from an annular inflow for a wide range of combinations of bubble size and liquid viscosity. In terms of a bubble Reynolds number, Re_b, as defined here, fast jet formation is found for $\mathrm{Re}_b \gtrsim 300$. For larger values of Re_b the formation of the fast jet happens later and later in the bubble evolution, whereas the average jet speed seems to be roughly independ-

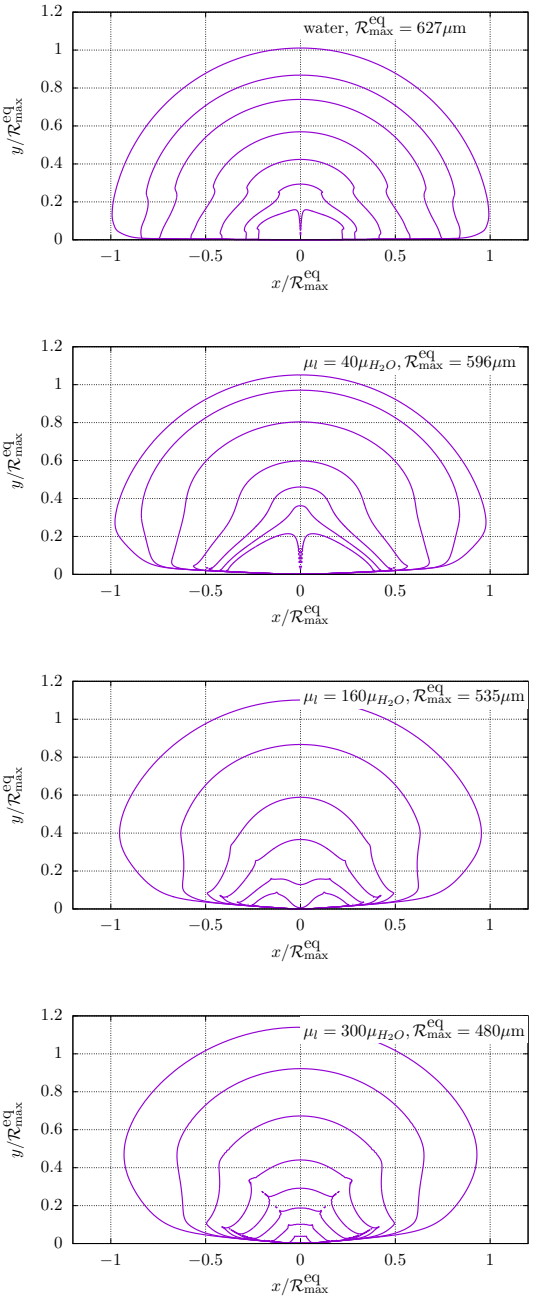

Figure 9. Bubble shape during the collapse phase for four liquids with viscosities $\mu_l = \mu_{H_2O}$ (reference bubble), $\mu_l = 40\mu_{H_2O}$, $\mu_l = 160\mu_{H_2O}$, and $\mu_l = 300\mu_{H_2O}$. The bubble Reynolds numbers are $\mathrm{Re}_b = 6289, 150, 34, 16$. Time proceeds from outer to inner curves.

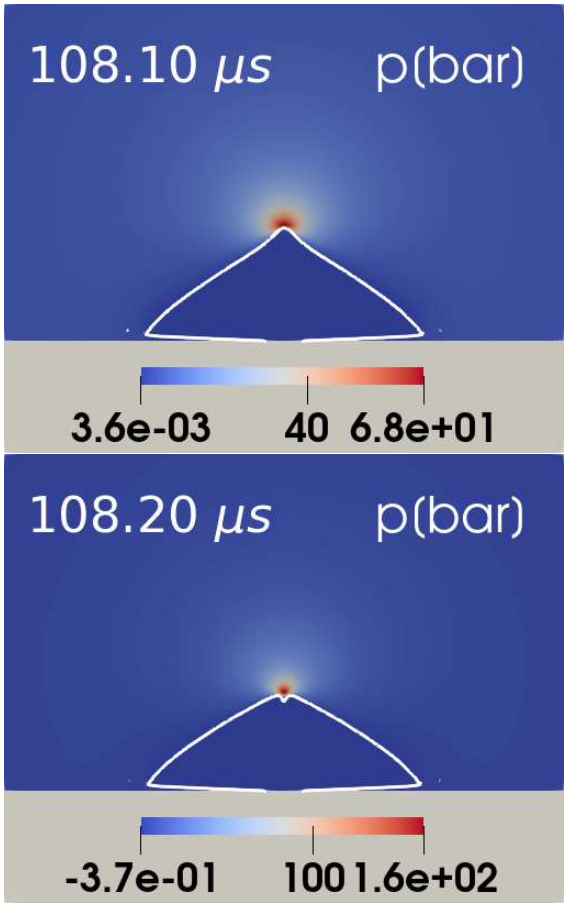

Figure 10. Bubble shape and pressure field in *bar* around jet formation for a bubble with $\mathrm{Re}_b = 150$, as in Fig. 9, second row.

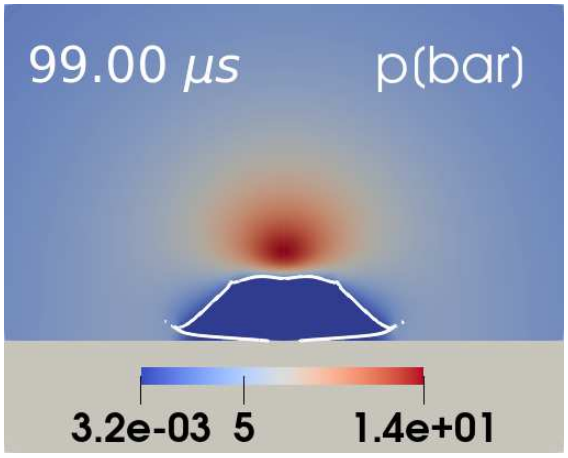

Figure 11. Bubble shape and pressure field in *bar* around jet formation for a bubble with $\mathrm{Re}_b = 34$, as in Fig. 9, third row.

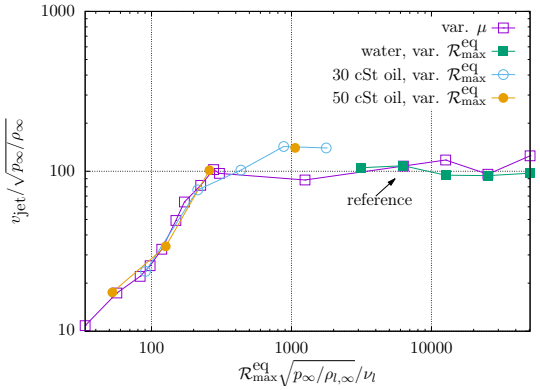

Figure 12. Normalized jet speed as a function of bubble Reynolds number.

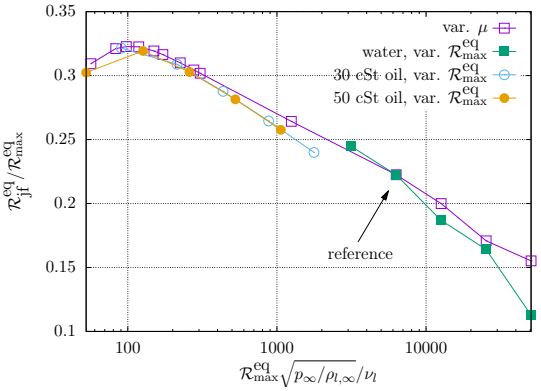

Figure 13. Equivalent radius of the bubble at the moment of jet formation.

ent of Re_b.

For $\mathrm{Re}_b \lesssim 300$ the jet formation mechanism changes and the jet forms by involution of the upper bubble wall. It has been demonstrated for $\mathrm{Re}_b = 150$ that the jet forms after a high curvature spherical cap has collapsed. For $\mathrm{Re}_b = 34$ a "slow", broad jet is formed. The transition between theses types of jet from involution of the bubble wall seems to be gradually. The jet speed continuously decreases with decreasing Re_b. For $\mathrm{Re}_b = 16$ no jet is found, the bubble stays simply connected during the first collapse and beyond.

ACKNOWLEDGMENTS

The work was supported in part by the Austrian Science Fund (FWF) (Grant No. I 5349-N) and the German Science Foundation (DFG) under contracts ME 1645/8-1, ME 1645/8-3 and ME 1645/5-2.

REFERENCES

[1] Philipp, A., and Lauterborn, W., 1998, "Cavitation erosion by single laser-produced bubbles", *J Fluid Mech*, Vol. 361, pp. 75–116.

[2] Brujan, E.-A., Nahen, K., Schmidt, P., and Vogel, A., 2001, "Dynamics of laser-induced cavitation bubbles near elastic boundaries: in-

fluence of the elastic modulus", *J Fluid Mech*, Vol. 433, pp. 283–314.

[3] Supponen, O., Obreschkow, D., Tinguely, M., Kobel, P., Dorsaz, N., and Farhat, M., 2016, "Scaling laws for jets of single cavitation bubbles", *J Fluid Mech*, Vol. 802, pp. 263–293.

[4] Lechner, C., Lauterborn, W., Koch, M., and Mettin, R., 2020, "Jet formation from bubbles near a solid boundary in a compressible liquid: Numerical study of distance dependence", *Phys Rev Fluids*, Vol. 5 (9), p. 093604.

[5] Koch, M., Rosselló, J. M., Lechner, C., Lauterborn, W., and Mettin, R., 2022, "Dynamics of a Laser-Induced Bubble above the Flat Top of a Solid Cylinder—Mushroom-Shaped Bubbles and the Fast Jet", *Fluids*, Vol. 7 (1), p. 2.

[6] Lechner, C., Lauterborn, W., Koch, M., and Mettin, R., 2019, "Fast, thin jets from bubbles expanding and collapsing in extreme vicinity to a solid boundary: A numerical study", *Phys Rev Fluids*, Vol. 4, p. 021601.

[7] Pishchalnikov, Y. A., Behnke-Parks, W. M., Schmidmayer, K., Maeda, K., Colonius, T., Kenny, T. W., and Laser, D. J., 2019, "High-speed video microscopy and numerical modeling of bubble dynamics near a surface of urinary stone", *J Acoust Soc Am*, Vol. 146, pp. 516 – 531.

[8] Koch, M., 2020, "Laser cavitation bubbles at objects: Merging numerical and experimental methods", PhD thesis, Georg-August-Universität Göttingen, Third Physical Institute, http://hdl.handle.net/21.11130/00-1735-0000-0005-1516-B.

[9] Koch, M., Rosselló, J. M., Lechner, C., Lauterborn, W., Eisener, J., and Mettin, R., 2021, "Theory-assisted optical ray tracing to extract cavitation-bubble shapes from experiment", *Exp Fluids*, Vol. 62 (3), p. 60.

[10] Reuter, F., and Ohl, C.-D., 2021, "Supersonic needle-jet generation with single cavitation bubbles", *Appl Phys Letters*, Vol. 118 (13), p. 134103.

[11] Benjamin, T. B., and Ellis, A. T., 1966, "The Collapse of Cavitation Bubbles and the Pressures thereby Produced against Solid Boundaries", *Philos Trans R Soc London, Ser A*, Vol. 260, pp. 221–240.

[12] Gonzalez Avila, S. R., Song, C., and Ohl, C.-D., 2015, "Fast transient microjets induced by hemispherical cavitation bubbles", *J Fluid Mech*, Vol. 767, pp. 31–51.

[13] Hupfeld, T., Laurens, G., Merabia, S., Barcikowski, S., Gökce, B., and Amans, D., 2020, "Dynamics of laser-induced cavitation bubbles at a solid–liquid interface in high viscosity and high capillary number regimes", *J Appl Phys*, Vol. 127 (4), p. 044306.

[14] Tryggvason, G., Brunner, B., Esmaeeli, A., Juric, D., Al-Rawahi, N., Tauber, W., Han, J., Nas, S., and Jan, Y.-J., 2001, "A Front-Tracking Method for the Computations of Multiphase Flow", *J Comput Phys*, Vol. 169, pp. 708–759.

[15] Weller, H. G., Tabor, G., Jasak, H., and Fureby, C., 1998, "A tensorial approach to computational continuum mechanics using object-oriented techniques", *Comput Phys*, Vol. 12 (6), pp. 620–631.

[16] Gschaider, B., Nilsson, H., Rusche, H., Jasak, H., Beaudoin, M., and Skuric, V., 2017, "The foam-extend project", URL `https://sourceforge.net/projects/foam-extend/`.

[17] Koch, M., Lechner, C., Reuter, F., Köhler, K., Mettin, R., and Lauterborn, W., 2016, "Numerical modeling of laser generated cavitation bubbles with the finite volume and volume of fluid method, using OpenFOAM", *Comput Fluids*, Vol. 126, pp. 71–90.

Conference on Modelling Fluid Flow (CMFF'22)
The 18th International Conference on Fluid Flow Technologies
Budapest, Hungary, August 30-September 2, 2022

EFFECTS OF LARGE PARTICLES IN PIPE FLOW AT LOW AND MODERATE REYNOLDS NUMBERS

Johan REVSTEDT[1], Dragana ARLOV[2], Fredrik INNINGS[3]

[1] Corresponding Author. Department of Energy Sciences, Faculty of Engineering, Lund University, P.O. Box 118, SE-22100 Lund, Sweden
Phone.: +46 46 222 4302, E-mail: johan.revstedt@energy.lth.se
[2] Tetra Pak Processing Systems AB. E-mail: dragana.arlov@tetrapak.com
[3] Tetra Pak Processing Systems AB. E-mail: fredrik.innings@tetrapak.com

ABSTRACT

The presence of solid particles in a Newtonian liquid flow will affect the properties of the flow. For small particles these effects are fairly well understood. However, the behaviour of liquids laden with large particles are less well understood and even more so if the carrier liquid is a non-Newtonian fluid. In the present study we consider large particles of spherical shape. By large is here meant particles that are of the same size as the large scale length scales of the flow and larger. We are considering how particles volume fraction affects parameters such as pressure drop and velocity distribution in the pipe flow. The simulations are performed using a finite difference based in-house software and the particles are represented using an virtual boundary method. The size of the spherical particles is about 1/6 of the pipe diameter and the volume fraction is varied between 5 and 20%. The fluid is either Newtonian or shear thinning modelled using a power law expression.

Keywords: non-Newtonian, particles, pipe flow, virtual boundary method

NOMENCLATURE

$\underline{U}$	$[-]$	particle linear velocity
C	$[-]$	a constant
D	$[m]$	pipe diameter
Fr	$[-]$	Froude number
K	$[kg/(ms^{2-n}]$	consistency index
R	$[-]$	pipe radius
Re	$[-]$	Reynolds number
t	$[-]$	time
U_B	$[m/s]$	bulk velocity
V	$[-]$	volume
ψ	$[-]$	distance function
$\underline{u}$	$[-]$	velocity vector
d	$[m]$	particle diameter
f	$[-]$	Darcy friction factor
k	$[-]$	spring coefficient
n	$[-]$	power-law index
p	$[-]$	pressure
r	$[-]$	radial coordinate
x	$[-]$	coordinate
$\underline{v}$	$[-]$	boundary target velocity
$\underline{\underline{S}}$	$[-]$	strain rate tensor
α	$[-]$	shape coefficient
β	$[-]$	shape coefficient
$\dot{\gamma}$	$[-]$	absolute value of strain rate
ε	$[-]$	Levi-Civita symbol
η	$[-]$	damping coefficient
μ	$[-]$	viscosity factor
Φ	$[-]$	source term
ϕ	$[-]$	particle volume fraction
ρ	$[kg/m^3]$	density
τ_w	$[Pa]$	wall shear stress
$\underline{\delta}$	$[-]$	particle overlap
$\underline{\omega}$	$[-]$	particle angular velocity
$\underline{\xi}$	$[-]$	distance vector
$\underline{\mathcal{F}}$	$[-]$	particle force
$\underline{\mathcal{T}}$	$[-]$	particle torque

Subscripts and Superscripts

MR	Metzner-Reed
B	bulk
s	single phase
rel	relative
c	contact
f	fluid
h	hydrodynamic
i, j, k	Cartesian tensor indices
p	particle

INTRODUCTION

Introducing solid particles to a Newtonian liquid flow will alter the properties of the flow compared to a pure the liquid. For small particles these effects are fairly well understood and models, for example for the pressure drop in particle laden pipe flows have been present for a long time. In terms of modelling the effects are often represented in terms of a modified viscosity. This approach to modelling dates back

to the work of Einstein [1, 2] who formulated the viscosity of particle suspension as a function of the volume fraction of particles. Einstein's formulation is, however, only valid for dilute suspensions containing small particles. An extension of this, which is valid for larger volume fractions was proposed by Eilers [3]. Again, Eilers' correlation fits well for small particles which have been confirmed by several studies. Essentially, considering laminar flow, the Darcy friction factor for this type of flow would vary with Reynolds number in a similar way as a flow without particles. Hence, formulating a Reynolds number based on the viscosity from the Eilers formula the curves would collapse on top of each other and the normal Moody chart could be used to predict the pressure drop. This works well for small particles and is also surprisingly accurate for fairly large particles provided the volume fraction is low.

However, liquid flows laden with large particles are less well understood and even less so if the carrier liquid is non-Newtonian. By large is here meant particles that are of the same size as the large scale length scales of the flow and larger. For pipe flows (which is the focus of this study) this would mean particle with hydraulic diameters of about 15 to 20% of the pipe diameter and larger. In such flows several factors influence the flow behaviour. For example, one can find that the pressure drop is not just dependent on particle volume fraction but also on particle shape and size distribution. There are also indications that the presence of particles has a strong influence on the heat transfer in a pipe, either amplifying or attenuating it depending on several parameters.

Although, the influence of larger particles has been less well studied some investigations, both experimental and numerical, can be found in the literature. In a fairly extensive experimental study Matas et al [4] considered particle laden pipe flows with particle volume fractions up to about 35%. They also considered a wide range of particle sizes, particle diameter to pipe diameter (d/D) in the range 0.1 to about 0.003. The focus of their study was how the transition to turbulence is affected by particle content. Two distinct behaviours were observed depending on particle size. For smaller particles the transition was delayed, while for larger particles the transition occurred at a lower Reynolds number that for a single phase flow. Turbulence transition was also studied by Agrawal et al [5]. They considered a particle size ratio d/D of 0.05 and volume fractions up to 24%. Measuring the pressure drop and then considering the Darcy friction factor, they found that even at low volume fractions (about 2%) the friction factor switched from the laminar behaviour, to a turbulent behaviour with friction faction values somewhat higher than for single phase flow, at a lower Reynolds number than for a liquid without particles. Lashgari et al [6] considered numerically a channel flow with particle volume fractions up to 30% with a channel height to particle diameter (H/d) of 10. They found that depending on Reynolds number and volume fraction the flow could be divided into three regimes: laminar like (small Re and volume fraction (ϕ)), turbulent like (large Re and small ϕ) and inertial shear thickening (large ϕ). The turbulent structures of particle laden pipe flows were studied numerically by Wu et al [7]. Also in this studied, a relative particle size of 10 was used and the Reynolds number was fixed to 4900. The results show that the presence of particles attenuated the maximum streamwise fluctuations close to the wall while fluctuations in the radial and tangential directions were increase in the same region and that these effects increased at higher volume fractions. The reason for the increase in radial and tangential fluctuations, according to Wu et al [7], is the small vortices induced by the particles in the region close to the wall. Also, the position of maximum radial fluctuation was shifted slightly towards the wall.

Our focus will be on laminar and moderately turbulent flows considering both Newtonian and non-Newtonian carrier fluids. The overall aim of this study is to further increase the understanding of particle laden flows, in particular pipe flows with large particles.

MATHEMATICAL DESCRIPTION

The momentum equation governing the incompressible flow of a non-Newtonian (shear thinning or shear thickening) fluid can on non-dimensional be written as

$$\frac{\partial u_i}{\partial t} + u_j \frac{\partial u_i}{\partial x_j} = -\frac{\partial p}{\partial x_i} + \mu \left(\frac{\partial^2 u_i}{\partial x_j^2} \right) + \left[\frac{\partial \mu}{\partial x_j} \left(\frac{\partial u_i}{\partial x_j} + \frac{\partial u_j}{\partial x_i} \right) \right] + \Phi_i. \quad (1)$$

The rheology of the fluid is modelled using a power-law expression and the viscosity coefficient in eq. (1) can then be described as

$$\mu = \frac{1}{Re} \dot{\gamma}^{n-1} \quad (2)$$

where n is the power law index and with shear rate, γ, formulated using an isotropic expression, i.e.

$$\dot{\gamma} = \sqrt{S_{ij} S_{ij}} \quad (3)$$

The Reynolds number for a power law fluid in a pipe flow, based on the bulk velocity, U_B, pipe diameter, D and the consistency index of the fluid may be written as

$$Re = \frac{\rho_f U_B^{2-n} D^n}{K} \quad (4)$$

Turbulence modelling

In the present study both laminar and turbulent flows are considered. Turbulence is handled using an implicit large eddy simulation (LES) method. The sub-grid scale stresses are handled using the dissip-

ative nature of the truncation error in the discretisation of the convective terms. Here we use the third order upwind scheme of Kawamura and Kuwahara [8]. This approach has been successfully used in several previous studies, e.g. [9] and, as is shown below works well also in this case.

Virtual boundary method

The source terms Φ_i are introduced to represent solid boundaries, i.e. they replace the boundary conditions on the solid body surface. In this case the sources Φ_i are computed so as to satisfy the local boundary conditions. Hence, the source terms will only be non-zero at the location of the boundary. However, discretising the computational domain will in general lead to that the presence of the boundary must be represented by source terms in positions away from the actual boundary location. This can be achieved in different ways, for example by approximating the Dirac function by a normalised Gaussian distribution [10] or by assuming a certain distribution of the velocity field normal to the boundary [11]. In this work we employ the method developed by Revstedt [9] in which the source term is accumulated over the time steps and iterations within each time step. Hence, the following expression for the contribution to the discretised source terms in the mth iteration is written as:

$$\Delta\overline{\Phi}_i^m = C_1 \frac{v_i - u_i}{\Delta t} e^{-C_2\psi^2} \tag{5}$$

where C_1 and C_2 are positive constants, v_i is the target velocity of the solid surface and ψ is a positive function which should increase rapidly with increasing distance from the solid boundary. Hence, inside the body ψ will be set to zero and far away from the body it will have a large positive value, typically 10^6. Several strategies for setting the ψ-function may be used but here a step function is employed. Finally the magnitude of the source terms in the mth iteration is given by

$$\overline{\Phi}_i^m = \overline{\Phi}_i^{m-1} + \Delta\overline{\Phi}_i^m \tag{6}$$

Numerical method

The incompressible Navier-Stokes equations are discretised on a system of locally refined staggered Cartesian grids (e.g. Fuchs and Zhao [12]). The terms of the momentum and continuity equations are approximated by finite-differences. Basically, one may use finite-differences of any order. Here, we use upwind finite-differences of first- or third-order accuracy. The lower order scheme (first order for the convective terms and second order for the others) implies that the low order terms dominate, leading to a high level of numerical dissipation. Using directly higher order (third and fourth order approximations, respectively), leads to a less robust solver with considerably slower convergence rate. To combine numerical efficiency with higher order accuracy, we introduce the higher order terms as a "single-step" defect correction [13].

The time integration is done by a three level implicit scheme. In each time step, the system of equations is solved iteratively using a Multi-grid solver. Local grid refinements are a part of the multi-grid structure and the boundary conditions are interpolated from the next coarser level using fourth order linear interpolation.The relaxation scheme within the Multi-grid solver comprises of point wise relaxation of the momentum equations coupled with a point wise smoothing of the continuity equation. At the latter step, both the velocity vector and the pressure are corrected so that the residuals of the momentum equations shall not be changed as the continuity equation is satisfied. This approach is equivalent to an approximate diagonalisation of the system of equations [12].

Particle motion and interaction

The linear and angular velocities of each individual particle are governed by the following equations:

$$\frac{dU_i}{dt} = \left(1 - \frac{\rho_f}{\rho_p}\right)\frac{1}{Fr_i^2} - \alpha\frac{\rho_f}{\rho_p}\left(\mathcal{F}_i^{(h)} - \mathcal{F}_i^{(c)}\right) \tag{7}$$

$$\frac{d\omega_i}{dt} = \beta\frac{\rho_f}{\rho_p}\left(\mathcal{T}_i^{(h)} - \mathcal{T}_i^{(c)}\right) \tag{8}$$

where (h) and (c) denotes the hydrodynamic and contact forces, respectively, and α and β are coefficients dependent on the particle shape. For a sphere $\alpha = 6/\pi$ and $\beta = 10\alpha$. The hydrodynamic force is determined by integrating the discretised source term $\overline{\Phi}_i$ from eq. (5) in a volume around the particle.

$$\mathcal{F}_i^{(h)} = \int \overline{\Phi}_i dV. \tag{9}$$

The hydrodynamic torque is calculated in a similar way

$$\mathcal{T}_i^{(h)} = \int \varepsilon_{ijk}\overline{\Phi}_k \xi_j dV. \tag{10}$$

To find the contact forces we use a soft sphere approach similar to the one developed by Costa et al [14]. One can then on non-dimensional form write the force for each particle contact as

$$\mathcal{F}_i^{(c)} = -k\delta_i - \eta u_{i,\mathrm{rel}} \tag{11}$$

Hence, each contact is modelled as a spring and a damper mounted in parallel, with the spring and damping coefficients being evaluated based on the effective particle mass, restitution coefficient and the allowed contact time. The torque generated by a collision is calculated as

$$\mathcal{T}_i^{(c)} = \varepsilon_{ijk}\mathcal{F}_k^{(c)}\xi_j \tag{12}$$

COMPUTATIONAL SET-UP

The computational domain consists of a circular pipe created in a rectangular domain using an virtual boundary method. The length of the pipe is about 6 pipe diameters (D). However, due to how the domain decomposition is done the length to diameter ratio of the pipe may vary somewhat. At the inflow and outflow of the pipe cyclic boundary conditions are used both for the continuous phase and the particles. In the simulations we consider spherical particles of size $d/D = 0.171$. The density ratio is set to unity, i.e. the particles are neutrally buoyant. The computational mesh is Cartesian and structured. Two levels of resolution have been used depending on particle size and flow situation. For the laminar flow the resolution is set to $\Delta x = 0.0625$ which corresponds to about 94 cells over the pipe diameter. For turbulent flow the resolution is $\Delta x = 0.03125$ which corresponds to about 188 cells over the pipe diameter. The temporal resolution in the laminar cases is $\Delta t = 0.01$ and in the turbulent cases $\Delta t = 0.005$. Initially the liquid velocity is set equal to the bulk velocity in the whole pipe. Particles are initially ordered in rows and their velocity is set equal to the liquid velocity. All simulations have been run for 40000 time steps before sampling of data is initiated in order to let the solution develop sufficiently. Sampling was done over an additional 100000 time steps.

Four fluids with different degrees of shear thinning are considered, the power-law index ranging from 0.4 to 1.0. For all fluids flows with Reynolds numbers in the range 250 to 2000 are studied and for $n = 0.4$ and $n = 1.0$ also turbulent flows are considered, i.e. $4000 \leq Re \leq 16000$.

Throughout the study a modified Reynolds number is used

$$Re_{\mathrm{MR}} = \frac{\rho_f U_B^{2-n} D^n}{K\left(\frac{3n+1}{4n}\right)^n 8^{1-n}} \tag{13}$$

This Reynolds number was first presented by Metzner and Reed [15] in order to fit friction factor data for non-Newtonian fluids to the Moody chart.

Code validation

Figure 1 the average velocity and Reynolds normal stresses in a pipe flow at Re=11700 compared to direct numerical simulation (DNS) data from El Khoury et al [16]. As can be seen, our results agree very well with the DNS data indicating that our resolution is sufficient for the turbulent cases considered, event hough the viscous sublayer is not fully resolved in our simulations. Also, our simulation underpredicts the friction losses, in terms of Darcy friction factor, by about 10%.

To further show the capability of the code to predict the resistance in a pipe flow the Darcy friction factor as a function of the Metzner-Reed Reynolds number is depicted in Figure 2 for the range $250 \leq Re_{\mathrm{MR}} \leq 16000$ for the Newtonian fluid. However, the friction factor for a shear-thinning fluid ($n = 0.4$) at $Re_{\mathrm{MR}} = 4000$ is also shown. The solid line in Fig. 2 is the classical $f = 64/Re$ line in the laminar regime. The dashed line is the Haaland equation for a smooth pipe and the dot-dashed line is the extension of the turbulent friction factor by Wilson and Thomas [17] to a power-law fluid with $n = 0.4$. As can be seen, the friction factor is slightly underpredicted in the whole range which is most probably caused by the virtual boundary method introducing a small error in the description of the pipe wall, i.e. the pipe appears slightly larger it should be.

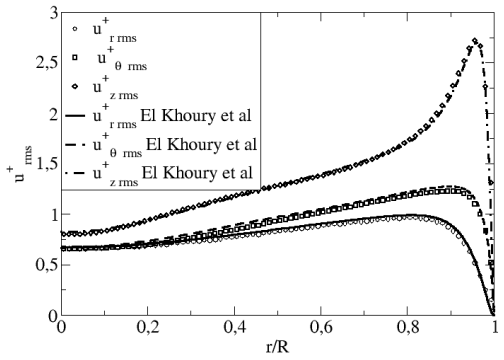

Figure 1. RMS of velocity fluctuations in a pipe flow with Re=11700 compared to DNS data by El Khoury et al [16]

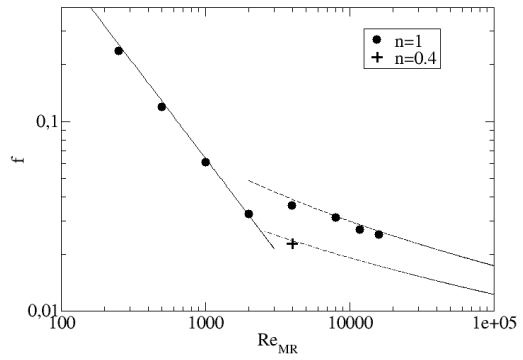

Figure 2. Darcy friction factor without particles

The two grid resolutions used in this study corresponds to 16 or 32 cells over the particle diameter. A previous study on free falling cubical particles [18] shows that 16 cells is sufficient to describe the particle with reasonable accuracy.

RESULTS

Introducing particles to a pipe flow one expects flow resistance to increase, which is indeed the case. Figure 3 depicts the Darcy friction factor ($f = \frac{8\tau_w}{\rho_f U_B^2}$) as a function of the Reynolds number for a New-

tonian fluid. Already at a particle volume fraction $\phi_B = 0.05$ the friction factor is noticeably higher than without particles in a laminar flow. Increasing the volume fraction of particles will further increase the resistance. One may note that in the laminar regime the decrease in friction factor with increasing Reynolds number is still linear in the Moody chart, although with a slope that is dependant on volume fraction. For the turbulent regime the behaviour is somewhat different. For the lowest volume fraction the particles seem to only have a minor influence on the resistance and the friction factor is decreasing with increasing Reynolds number, as it would for a flow without particles. However, increasing the volume fraction to 10 and 20% a different behaviour emerges. Not only is the resistance much higher for a given Reynolds number but the friction factor is now constant or even slightly increasing with Reynolds number. We believe the explanation for this to be that at $\phi_B = 0.05$ the interaction between particles is negligible while for higher volume fractions the particles are more often in contact which strongly increases the resistance. Comparing to the the experimental results of Agrawal et al [5] we find that the friction factors in their collapses nicely on the Hagen-Poiseuille solution in the laminar regime with the proper scaling of the Reynolds number while our results deviates significantly from that. The reason for that is that they use much smaller particles for which effective viscosity models, such as Eilers' model [3], are appropriate, which is not the case for larger particles.

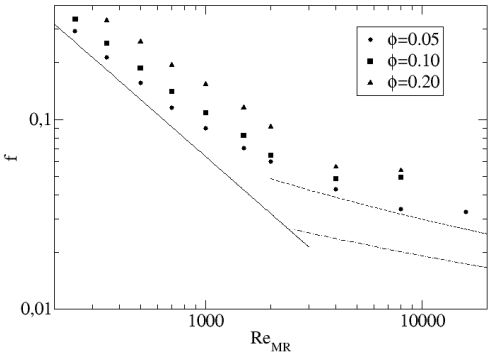

Figure 3. Darcy friction factor as a function of Reynolds number for spherical particles in a fluid with n=1

Comparing the Newtonian results with the resistance of the shear thinning fluid, depicted in Figure 4, the behaviour in the laminar regime is the same in the sense that increasing the volume fraction increases the resistance. Also the behaviour with increasing Reynolds is similar. In the turbulent regime the friction factor falls below the minimum limit for a Newtonian fluid, which would be expected since friction factor is a function of the degree of shear thinning in this range even when using the Metzner & Reed Reynolds number. However, in this case the almost constant friction factor for Re=8000 and beyond appears already at $\phi_B = 0.05$.

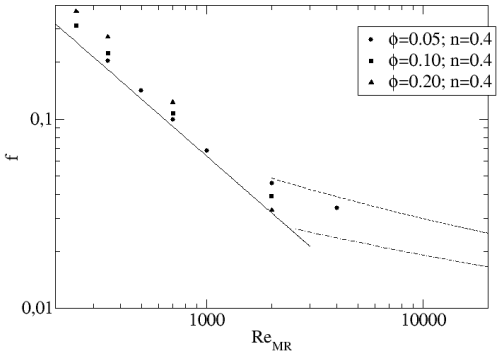

Figure 4. Darcy friction factor as a function of Reynolds number for spherical particles in a fluid with n=0.4

As could be seen from Figs. 3 and 4 there is a difference in friction factor between the Newtonian case and $n = 0.4$. Taking a closer look at how the friction factor varies with degree of shear thinning and Reynolds number, which is shown in Figure 5, one can see that for a low Reynolds number (350) the effect on the friction factor is quite moderate, especially for $\phi = 0.05$ where the value at $n = 0.4$ is about 95% of the Newtonian value. However, the effect of shear thinning seems to get more pronounced with increasing volume fraction and at $\phi = 0.20$ the value at $n = 0.4$ is about 80% of the Newtonian one. The influence of Reynolds number is also very strong leading to a substantial difference in resistance at Re=2000. Comparing the velocity profiles for $n = 0.4$, depicted in Figure 6, one finds for the lowest volume fraction that the maximum velocity decreases as the Reynolds number increases. This also means that the velocity profile in the centre part of the pipe ($r/R \leq 0.5$) gets flatter while the portion of the pipe with a higher velocity gradient gets larger. A interesting observation is that up to $Re = 1000$ the velocity gradient close to the wall is unchanged, meaning that the resistance should be dependant on a constant to the power n divided by Reynolds number in this regime. Increasing the Reynolds number to 2000 results in a change in the velocity distribution such that the shear rate close to the wall increases and one would therefore expect that for this case the friction factor would not fall on the same line in the Moody chart as the lower Reynolds numbers, which is indeed the case considering Fig. 4. It also indicates that the at $Re = 2000$ is, if not fully turbulent, at least in a transition state. Considering instead the case $\phi = 0.20$ the trend is the same concern-

ing the centre line velocity. However, the shapes of the velocity distributions are distinctly different compared to $\phi = 0.05$. For Reynolds number up to 700 one observes to separate behaviours in the inner and outer half of the pipe. In the inner part ($r/R < 0.5$) the velocity profile is fairly flat, much like for lower particle volume fraction, but there is also a plateau in the outer part of the pipe, which is most pronounced at $Re = 700$. Again one observes that $Re = 2000$ differs from the other cases with an almost constant velocity for $r/R < 0.8$. Once more, even though there is a significant Reynolds number effect on the velocity distribution, close to the wall the velocity gradient shows only a minor Reynolds number dependence. This is consistent with what is found in Fig. 4. Further insight in the differences in velocity distribution may be gained by considering the distribution of particle volume fraction along the radius. This is depicted in Figure 7 for $n = 0.4$ at $\phi = 0.05$ and $\phi = 0.2$. For $\phi = 0.05$ at $Re = 1000$ and below the particles are mainly located in the outer part of the pipe with the peak of volume fraction gradually moving towards lower radius with increasing Reynolds number as can be seen in the upper graph of Fig. 7. Again the $Re = 2000$ deviates significantly from this pattern and instead the particles are almost evenly distributed over the pipe radius. Turning the attention to the cases with $\phi = 0.20$ a totally different pattern emerges. Here particles tend to cluster close to the centre line with a secondary peak at about the same position as for the lower volume fraction. However, this situation is drastically altered at $Re = 700$ where most of the particles a located closer to the pipe wall. It is also interesting to note that there is no drastic change at $Re = 2000$ instead the distribution of particle volume is qualitatively similar to the one at $Re = 700$ put shifted to a lower radius.

Turbulent regime

For the turbulent regime $Re > 2000$ it is evident from Fig. 3 that the flow behaves differently. For the Newtonian case a decrease in friction factor is seen going from $Re = 2000$ to $Re = 4000$ for all volume fractions and for $\phi = 0.05$ this decrease continues up to $Re = 8000$. The particle here have only a minor influence on the resistance. However, increasing the volume fraction a significant influence on the resistance from the presence of particles is seen and also that the friction factor stops decreasing already beyond $Re = 4000$. For the shear thinning fluid ($n = 0.4$) a large increase in resistance compared to a flow without particles is seen already at $Re = 4000$. The relative increase in friction factor compared to the case without particles is summarised in Table 1.

From Table 1 it is evident that even a moderate amount of particles will have a substantial influence on the resistance also in a pipe flow. However, the increase is still less than in the laminar regime, where for $\phi = 0.05$ the increase due to particles is about 50% at $Re = 700$ and 100% for $\phi = 0.20$ at

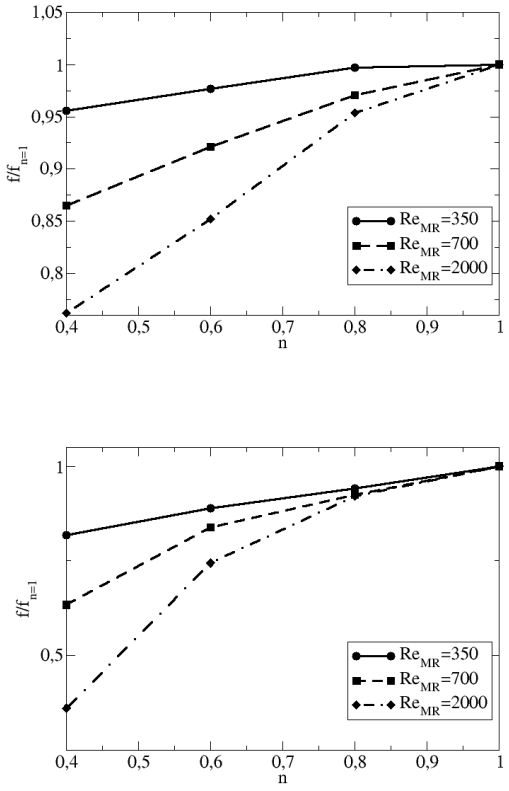

Figure 5. Friction factor normalised with the value for $n = 1$ as a function of as a function of degree of shear thinning for some Reynolds numbers in the laminar regime for $\phi = 0.05$ (upper) and $\phi = 0.20$ (lower)

the same Reynolds number. Furthermore, the influence increases for a shear thinning fluid. Some insight on this matter can be achieved by considering the radial distribution of the particle phase. Figure 8 depicts the local particle volume fraction normalised with the bulk value along the radius for Reynolds numbers 4000 and 8000 for the Newtonian fluid. At $Re = 4000$ the particles tend to be located more towards the centre of the pipe but with a tendency for increased volume fraction close to the wall as the overall volume fraction is increased. This will of course influence the flow close to the wall and in turn also the resistance. At $Re = 8000$ the effect is less pronounced and the distribution of the pipe more even especially for $\phi = 0.02$ and still there is a tendency for the particles to locate themselves closer to the wall with increasing ϕ

SUMMARY

Simulations of pipe flow containing relatively large particles have been performed for both laminar and turbulent flow. It can be concluded that the presence of particles will increase the flow resistance for both shear thinning and Newtonian fluids. The level

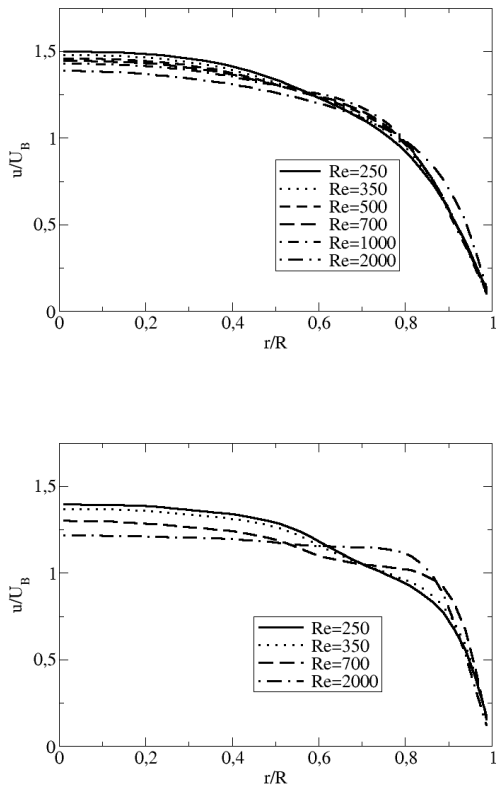

Figure 6. Velocity distribution along the pipe radius at $n = 0.4$ for some Reynolds numbers in the laminar regime for $\phi = 0.05$ (upper) and $\phi = 0.20$ (lower)

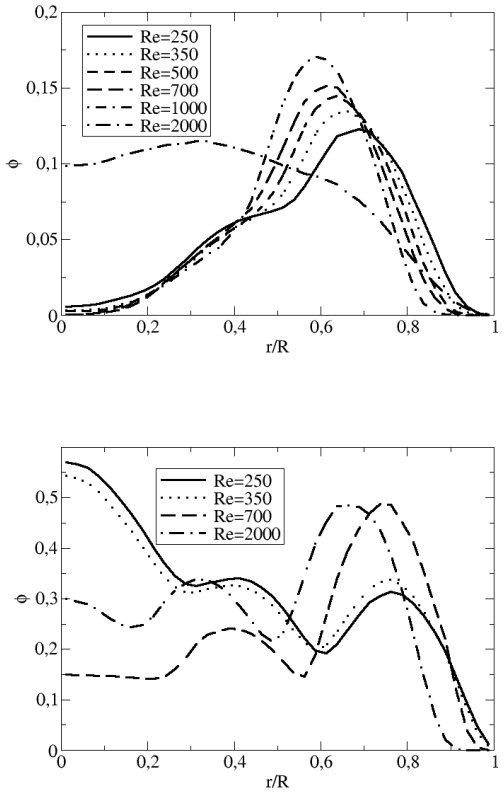

Figure 7. Distribution of particle volume fraction along the pipe radius at $n = 0.4$ for some Reynolds numbers in the laminar regime for $\phi = 0.05$ (upper) and $\phi = 0.20$ (lower)

of increase in resistance depends on the volume fraction as well as the Reynolds number and the degree of shear thinning. In general the effect of volume fraction is larger for a laminar flow with increases in friction factor of up to 100% for 20% particle volume fraction in a Newtonian fluid. A shear thinning fluid will give a smaller resistance than a Newtonian fluid at a given Reynolds number and in the laminar regime this difference increases with increasing Reynolds number. In the turbulent regime there seems to be a threshold effect in as much as a low volume fraction (5%) has no significant effect on the resistance while increasing to 10% increases the resistance significantly. However, at a sufficiently high Reynolds number a low volume fraction will also have a significant effect. Furthermore, it seems that the Reynolds number where this change occurs is lower for a shear thinning fluid. In conclusion, adding large particles to a pipe flow will increase the level of complexity in how that flow behaves. Also, there is a very distinct difference in how the particles alter the flow in the laminar and turbulent regimes, respectively.

ACKNOWLEDGEMENTS

Financial support for this work provided by the Swedish Energy Agency project no. 44266-1 and by Tetra Pak Processing Systems AB. Computational resources were provided by the Swedish National Infrastructure for Computing (SNIC) at NSC and by Lunarc.

REFERENCES

[1] Einstein, A., 1906, "Eine neue Bestimmung der Moleküldimensionen", *Ann Phys*, Vol. 324, pp. 289–306.

[2] Einstein, A., 1911, "Berichtigung zu meiner Arbeit: Eine neue Bestimmung der Moleküldimensionen", *Ann Phys*, Vol. 339, pp. 591–592.

[3] Eilers, H., 1941, "Die Viscosität von Emulsionen hochviskoser Stoffe als Funktion der Konzentration", *Kolloid-Zeitschrift*, Vol. 97, pp. 313–321.

[4] Matas, J.-P., Morris, J., and Guazzelli, E., 2003, "Transition to turbulence in particulate pipe flow", *Phys Rev Lett*, Vol. 90, p. 014501.

Table 1. Darcy friction factor relative to flow without particles

n	ϕ	Re	f/f_s
1	0.05	4000	1.08
1	0.05	8000	1.05
1	0.05	16000	1.29
1	0.10	4000	1.35
1	0.10	8000	1.59
1	0.20	4000	1.56
1	0.20	8000	1.73
0.4	0.05	4000	1.49

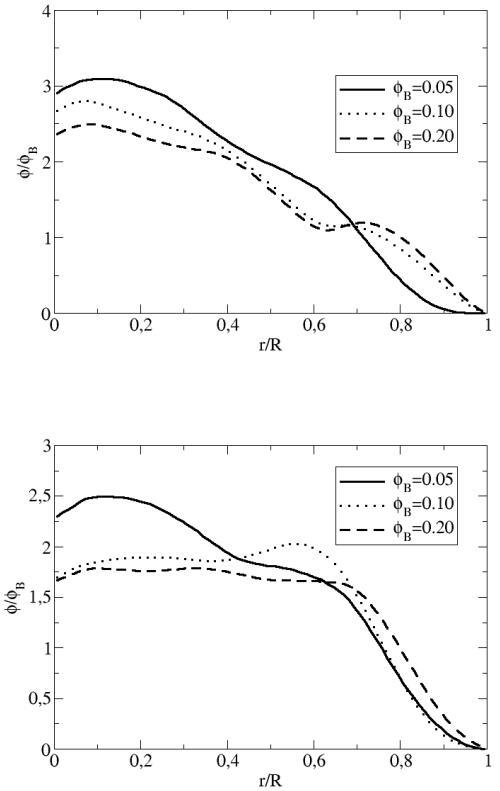

Figure 8. Radial distribution of particle volume fraction for Re = 4000 (upper) and Re = 8000 (lower) for the Newtonian fluid

[5] Agrawal, N., Choueiri, G., and Hof, B., 2019, "Transition to turbulence in particle laden flows", *Phys Rev Lett*, Vol. 122, p. 114502.

[6] Lashgari, I., Picano, F., Breugem, W.-P., and Brandt, L., 2014, "Laminar, turbulent, and inertial shear-tickening regimes in channel flow of neutrally buoyant particle suspensions", *Phys Rev Lett*, Vol. 113, p. 254502.

[7] Wu, T., Shao, X., and Yu, Z., 2011, "Fully resolved numerical simulation of turbulent pipe flows laden with large neutrally-buoyant particles", *J Hydrodynamics*, Vol. 23, pp. 21–25.

[8] Kawamura, T., and Kuwahara, K., 1984, "Computation of high Reynolds number flow around a circular cylinder with surface roughness", *AIAA paper*, Vol. 84-0340.

[9] Revstedt, J., 2013, "Interaction between an incompressible flow and elastic cantilevers of circular cross-section", *Int J Heat Fluid Flow*, Vol. 43, pp. 244–250.

[10] Revstedt, J., 2004, "A virtual boundary method with improved computational efficiency using a multi-grid method", *int J Num Meth Fluids*, Vol. 45 (7), pp. 775–795.

[11] Fadlun, E., Verzicco, R., Orlandi, P., and Modh-Yusof, J., 2000, "Combined Immersed-boundary finite-difference methods for three-dimensinal complex flow situations", *J Comput Phys*, Vol. 161, pp. 35–60.

[12] Fuchs, L., and Zhao, H.-S., 1984, "Solution of three-dimensional viscous incompressible flows by a multi-grid method", *int J Num Meth Fluids*, Vol. 4, pp. 539–555.

[13] Gullbrand, J., Bai, X.-S., and Fuchs, L., 2001, "High-order Cartesian grid method for calculation of incompressible turbulent flow", *int J Num Meth Fluids*, Vol. 36, pp. 539–555.

[14] Costa, P., Boersma, B., Westerweel, J., and Breugem, W.-P., 2015, "Collision model for fully-resolved simulations of flows laden with finite-size particles", *Phys Rev E*, Vol. 92, p. 053012.

[15] Metzner, A., and Reed, J., 1955, "Flow of non-newtonian fluids-correlation of the laminar, transition, and turbulent-flow regions", *AIChE Journal*, Vol. 1, pp. 434–440.

[16] El Khoury, G., Schlatter, P., Noorani, A., Fischer, P., Brethouwer, G., and Johansson, A., 2013, "Direct nulerical simulation of pipe flow at moderately high Reynolds numbers", *Flow Turbul Combust*, Vol. 91, pp. 475–495.

[17] Wilson, K., and Thomas, A., 1985, "A new analysis of the turbulent flow of non-newtonian fluids", *Canadian J of Chem Eng*, Vol. 63, pp. 539–546.

[18] Hamedi, N., and Revstedt, J., 2018, "Dynamic simulation of sedimentation of cubical particles in a power law fluid", J. Vad (ed.), *Proceedings of the 17th Conference on Fluid Flow Technologies*, paper no. CMFF18-051.

Conference on Modelling Fluid Flow (CMFF'22)
The 18th International Conference on Fluid Flow Technologies
Budapest, Hungary, August 30 -September 2, 2022

STUDY ON THE EFFECT OF SUDDEN DUCT DIAMETER CHANGE ON THE PERFORMANCE OF AN AXIAL FLOW FAN

Bálint LENDVAI[1], Tamás BENEDEK[2]

[1] Corresponding Author. Department of Fluid Mechanics, Faculty of Mechanical Engineering, Budapest University of Technology and Economics. Bertalan Lajos u. 4 – 6, H-1111 Budapest, Hungary. Tel.: +36 1 463 2546, E-mail: lendvai.balint@gpk.bme.hu
[2] Department of Fluid Mechanics, Faculty of Mechanical Engineering, Budapest University of Technology and Economics. E-mail: benedek.tamas@gpk.bme.hu

ABSTRACT

The installation of ducted fans has a major impact on their operation. However, axial flow fans are occasionally installed in larger diameter ducts for their small space requirement. This type of installation results in a forward-facing step and a backward-facing step closely upstream and downstream of the fan respectively. These sudden diameter changes cause massive annual separations at the diameter changes, which increases losses in itself, furthermore, the inflow condition is also altered especially close to the tip region of the rotor. The modified inflow condition might result in an increased pressure gradient through the tip gap of the fan, which promotes backflow in the annular region close to the casing. In this paper, we investigate the developed flow field and its effect on the fan performance in the case of an axial flow fan installed in a larger diameter duct at different operating points through computational fluid dynamics simulations.

Keywords: axial flow turbomachinery, backward-facing step, CFD, diameter change, ducted fan, forward-facing step

NOMENCLATURE

c_{mid}	[m]	mid-chord
D	[m]	duct diameter
M	[Nm]	the momentum acting on the rotating surfaces
n	[1/min]	rotation speed
Δp_t	[Pa]	total pressure rise
Q_V	[m^3/s]	flow rate
Re_C	[-]	mid-chordbased Reynolds-number
r_b	[m]	blade tip radius
η	[-]	efficiency
ρ	[kg/ m^3]	density
Φ	[-]	global flow coefficient
φ	[-]	dimensionless axial velocity
φ_c	[-]	dimensionless circumferential velocity
φ_r	[-]	dimensionless radial velocity
Ψ	[-]	total pressure rise coefficient
ψ_t	[-]	dimensionless total pressure

1. INTRODUCTION

Axial flow fans are commonly used in ventilation systems if a relatively high flow rate and low-pressure rise are needed. Based on the application, this type of fan can be installed in various setups, from free-inlet free-exhaust to fully ducted. The inflow conditions of the impeller are heavily impacting the aerodynamic behavior of the fan [1-3]. In the case the inlet velocity profile differs from that prescribed in the design (i.e., free or controlled vortex design [1,4]) or realized during the catalog data measurements, the efficiency may decrease, and the operating point can differ from what was expected.

In the case of free-inlet setup, the inlet flow conditions can be influenced by the intake geometry, for example, bellmouth inlets [5-7]. If the fan is ducted, the developed duct flow determines the inlet velocity profile if the diameter of the duct and the fan casing match. However, in ventilation systems, the diameter of the duct and the fan casing may differ, or the shape of the duct is rectangular instead of a circle. In that case, the inflow conditions are influenced by the flow phenomena induced by the size or shape change. In the case of limited space, the transition between the different sizes or shapes is carried out with sudden changes, which involves the appearance of the boundary layer separation and stagnation zones at the outer radii [8].

Due to the pressure difference between the pressure and suction side of the blade tip, an inevitable tip leakage flow occurs in the gap between the blade tip and the fan casing. The leakage flow is one of the major aerodynamic loss and noise sources of axial flow fans. This leakage flow often rolls up in a tip leakage vortex, which passes through the blade passage in the downstream direction. The strength of

the leakage flow is affected by the tip gap size, if the gap size is relatively large, the leakage flow becomes more dominant, and the resulted aerodynamic noise and loss (blockage effect of the extended leakage flow and the thickened boundary layer on the annular wall) are increased [9-11]. In case of increased tip gap and decreased axial velocity in the tip region, the exit angle of the leakage vortex measured to the axial direction can be increased, which may result that the leakage vortex impinges on the pressure side of the following blade. In that case, an increased sound emission can be experienced, and the aerodynamic losses are increasing as well as the increased blockage effect of the leakage flow [9, 11]

Based on the above, the disturbed flow at the outer radii caused by the diameter or duct shape change in the vicinity of the fan can amplify the negative effects of the tip leakage flow. In the present paper, the effect of the sudden duct diameter change on the flow behavior of an axial flow is investigated in various operation points using steady-state computational fluid dynamics simulations with special attention to the tip region.

2. SETUP OF CASE STUDY

The investigated low-speed fan (Fig 1.) has 5 forward-skewed controlled vortex design blades with circular arch profiles. The radius of the fan blade tips was $r_b = 0.15\ m$ with a hub-to-tip ratio of 0.3. The fan had no inlet or outlet guide vanes. It was installed in a short duct section (casing) of $0.6\ r_b$ length for all cases. The tip clearance of the fan was set to 5%. The chord length of the blades at mid-span was $c_{mid} = 1.09\ r_b$.

Figure 1: Fan of case study

In the simulations $10\ r_b$ long inlet and outlet ducts were connected to the casing of the fan. This was proved enough for the boundary layer to develop fully. Five inlet and outlet duct diameter were investigated, which was as follows respectively: $D = 315; 400; 500; 630; \infty\ mm$. The duct diameter changes were resolved with forward and backward-facing steps. In the case of the unducted arrangement 1 meter long cylindrical fluid volumes with 1 meter diameter were modeled upstream and downstream of the fan. The schematic drawing is shown in Fig 2.

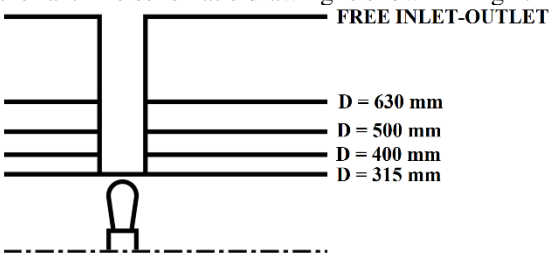

Figure 2: Schematic drawing of the investigated sudden diameter changes

The fan was investigated at $n = 1400\ RPM$ rotational speed. The operation of the fan at different operating points was examined under six flow rates: $\Phi = 0.14; 0.18; 0.22; 0.26; 0.30; 0.34$. Where the flow coefficient was calculated as follows:

$$\Phi = \frac{Q_V}{r_b^3 \cdot \frac{n}{60} \cdot \pi^2 \cdot 2} \tag{2.1}$$

According to the rotational speed and the flow rates, the mid-chord-based Reynolds number of the fan blades varied between $Re_C = 100000 - 110000$.

3. METHODOLOGY

The simulations were carried out in ANSYS Fluent 21R1 software. The Reynolds-averaged Navier Stokes simulations were supplemented with the k-ω shear stress transport turbulence model [12]. The simulation setup is shown in Fig. 3. The axial fan was modeled with the frozen rotor model. The inlet and outlet ducts had a stationary frame of reference. For the ducted arrangements at the duct inlet surface uniform axial velocity profile was prescribed, with velocity magnitude calculated from the flow rate. In order to calculate the turbulence properties at the inlet, turbulence intensity of 5% and the duct hydraulic diameter were set. The outflow was modeled as free exhaust with constant static pressure. Due to the moderate pressure rise and low Mach-number, the fluid was considered incompressible.

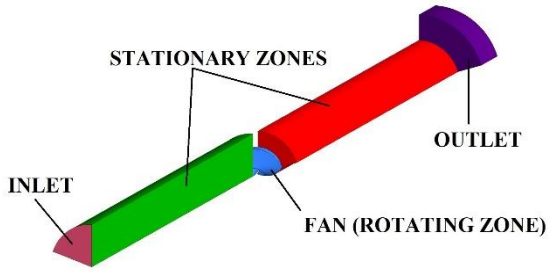

Figure 3: The simulation setup

The numerical meshes (Fig. 4) were constructed utilizing the same rotor mesh and exchanging the different diameter inlet and outlet ducts. The

structured O-grid mesh of the rotor contained 1.5 million cells, the blade was resolved with 85 by 105 cells in axial and radial directions respectively with more refined mesh near the blade leading edge, trailing edge, blade tip, and near the hub. The tip clearance was divided into 25 cells radially, while the blade tip thickness was modeled with 10 cells. The H-grid duct meshes contained 1.1-2.9 million cells depending on their diameter with high-resolution boundary layer and shear layer meshes. Mesh sensitivity analysis showed the mesh was adequate.

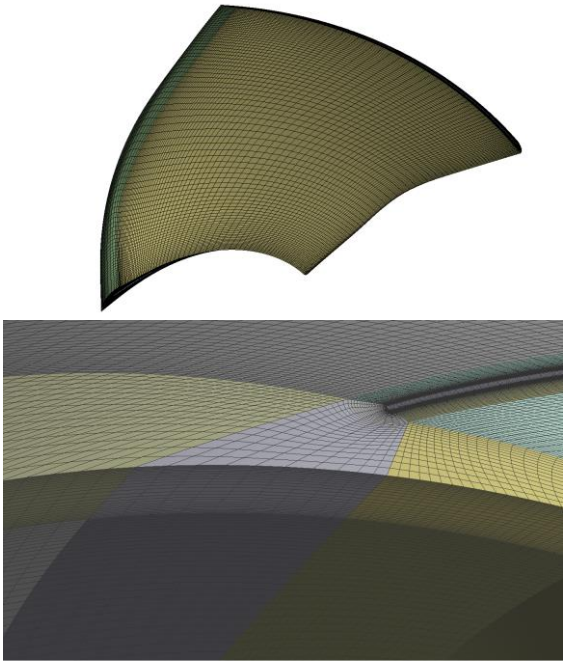

Figure 4: The numerical mesh

From the simulation results, dimensionless characteristic curves (flow coefficient - Φ vs. total pressure rise coefficient - Ψ and flow coefficient – Φ vs. efficiency – η) were derived. The dimensionless quantities were calculated as follows:

$$\Psi = \frac{\Delta p_t}{\rho \cdot r_b^2 \cdot \left(\frac{n}{60}\right)^2 \cdot \pi^2 \cdot 2} \tag{3.1}$$

$$\eta = \frac{Q_V \cdot \Delta p_t}{M \cdot \frac{n}{60} \cdot \pi \cdot 2} \tag{3.2}$$

Besides the characteristic curves, the circumferentially averaged dimensionless velocity (the velocity components are nondimensionalized with the blade tip speed), and total pressure (nondimensionalized with dynamic pressure calculated from the tip speed) profiles in the inlet and outlet cross-section of the casing are also presented, and the typical flow phenomena are visualized.

4. RESULTS

The total pressure rise coefficient and efficiency curves of the fan can be seen in Fig 5. for the investigated duct diameters. It can be concluded that the appropriate diameter ducting clearly outperforms the arrangements with diameter changes in the case of higher flow rates: the total pressure rise and efficiency are lower if the duct size is larger. Furthermore, it can be said in general that the larger the diameter change, the less efficiently the fan operates. It also can be seen the point of maximum efficiency is moving toward the lower flow rates if the duct diameter is increasing. In the case of the lower flow rates, the differences between the curves of different duct diameters are moderate, except for the smallest duct, because the negative effects of the high angle of attack of the blades become more dominant than the losses due to the diameter change.

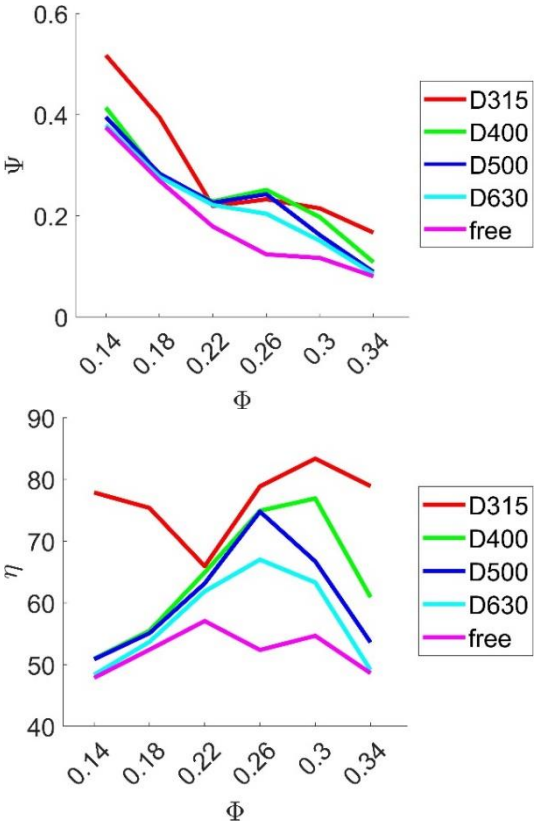

Figure 5: Performance curves

The operation of the fan is also analyzed through pressure and velocity component distributions along the normalized span. The derived curves are shown in Figs. 6-9. for the flow rates of $\Phi = 0.14; 0.22; 0.34$. The distributions of the further investigated flow rates can be found in the appendix. The inlet side distributions are sampled close downstream of the forward-facing step and the outlet side distributions are sampled close upstream of the backward-facing step. This way the immediate effect of the fan blade is reduced. Therefore, a less noisy distribution is obtained. The pressure values were circumferentially averaged based on mass flow rate, and the velocity distributions were area averaged.

Let us investigate the inlet and outlet surfaces separately. The dimensionless axial velocity (φ) profiles are depicted in Fig 6. At the highest

investigated flow rate the inlet axial velocity, according to the controlled vortex design, constantly increases along the span, until the friction on the duct wall decelerates the flow. In the case of the smallest duct, this decrease in the axial velocity begins at 70% of the span, and in the cases of sudden diameter change, it appears around 95% of the span. The maximum inlet axial velocity moves towards lower radii with the decrease of the flow rate in all of the cases. At the lowest flow rates, a recirculation zone is experienced in the tip region of the inlet, and the backflow intensity increases with the duct diameter increase. In Fig 10. the boundary of the recirculation zones is highlighted for different cases. In this figure, the extension of the recirculation zone with the decrease of the flow rate can be observed in the case of the $400\,mm$ duct diameter. In the case of high flow rate operation, apart from the inevitable separation in the corner of the connection of the duct and the fan casing, backflow does not appear in the inlet duct.

The dimensionless circumferential velocity (φ_c) distributions are shown in Fig 7. In the case of the highest flow rate, the circumferential velocity is nearly zero along the span for all of the ducts. With the decrease of the flow rate, the tangential velocity increases near the casing, and that rotating zone becomes more extensive with the further reduction of the flow rate. This increased circumferential velocity reveals that the backflow originates from the tip region of the blade. In Fig 10. it can be seen in the cases of sudden diameter change, the recirculation zone in the corner of the duct connection and the recirculation from the blade tip interact and form a complex recirculation structure.

The dimensionless radial velocity (φ_r) distributions are depicted in Fig 8. At the highest investigated flow rate, the radial velocity is nearly zero in the case of the smallest duct; however, in the other cases, an intensive downward flow is experienced due to the sudden diameter change. The extension of above mentioned the recirculation zone influence the inlet radial velocity distribution as well: with the appearance of the backflow (i.e., the decrease of the flow rate), the downward flow at the inlet section of the blades becomes more intensive in all of the cases. Besides that, due to the increased tangential and radial velocity, the total pressure also increases near the casing in the inlet section of the impeller, as can be seen in Fig 9.

At the outlet section of the blading, the axial velocity distribution (Fig 6.) is nearly similar in all of the cases at the highest investigated flow rate: the axial velocity is moderate in the boundary layer of the annulus walls and farther from the walls a radially increasing axial velocity can be seen. The maximum axial velocity moves toward the casing wall with the increase of the duct diameter. With the decrease in the flow rate, the boundary layer is thickening on the annulus walls. At the lowest investigated flow rate, if there is no change in the diameter, highly reduced axial velocity is experienced in the wall regions, and the maximum axial velocity can be found around the midspan. In the cases of sudden diameter change, the flow pattern differs from that: in the vicinity of the hub, a recirculation zone forms, which extends until 40% of the span. Due to this recirculation zone, the highest axial velocity values appear in the 70-100% interval of the span. In Fig 10. the formation of more and more dominant hub recirculation zone with the decrease of the flow also can be observed in the case of $400\,mm$ duct diameter. In this figure, the appearance of a recirculation zone at the outlet duct connection corner also can be seen in case of sudden diameter changes. It also can be observed that the size of this corner recirculation zone is increasing with the extension of the hub recirculation zone.

The dimensionless circumferential velocity distribution (Fig 7.) in the outlet section shows a maximum at the border of the hub boundary layer, and moderate values can be seen in the vicinity of the hub at the highest investigated flow rate. Farther from the walls, a slight radial increase is experienced in the case of the smallest duct. The slope of the distribution becomes higher with the increase of the duct diameter. However, the average circumferential velocity decreases with the increase of the duct diameter, which gives an explanation for the poorer performance of the higher diameter setups at the higher flow rates. In the case of the lower flow rates, the circumferential velocity decreases in the forming recirculation zone near the hub if the casing at the duct diameter does not match. From the circumferential velocity distribution, it can also be seen that at the lowest flow rate, the extension of this recirculation zone is extended to 40% of the span. This phenomenon explains the outperformance of the matching duct setup in the cases of lower flow rates. At higher radii, the outlet circumferential velocity increases at moderate flow rates in the low axial velocity zone.

In accordance with the circumferential velocity distribution, at the highest investigated flow rate, outside the annular wall boundary layer, a radially increasing total pressure (Fig 9.) is experienced. If the flow rate is decreased, the total pressure is nearly constant farther from the walls, and at the lowest flow rate significantly decreased total pressure values can be seen in the hub recirculation zone in the cases of sudden diameter change.

In the dimensionless radial velocity distributions (Fig 8.), it can be observed that the radial velocity increases with the increase of the duct diameter due to the displacing effect of the hub recirculation zone. If the flow rate decreases, the maximum values move towards to highest radii, which explains the decreasing size of the corner recirculation zone in the cases of sudden diameter change.

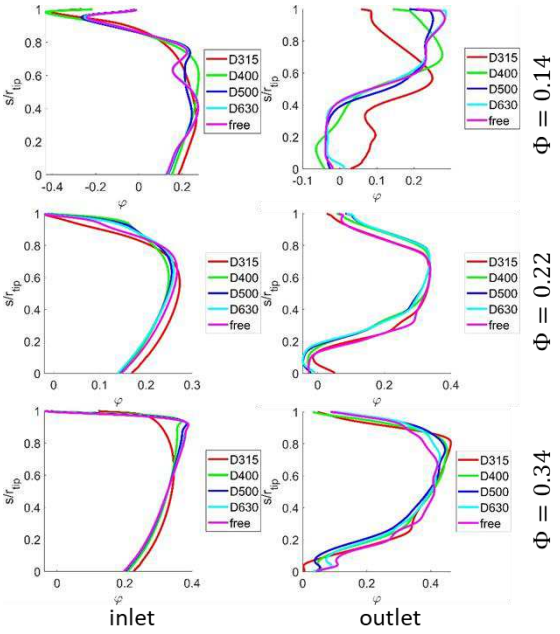

Figure 6: Radial distribution of dimensionless axial velocity at different flow rates close to the forward and backward-facing steps

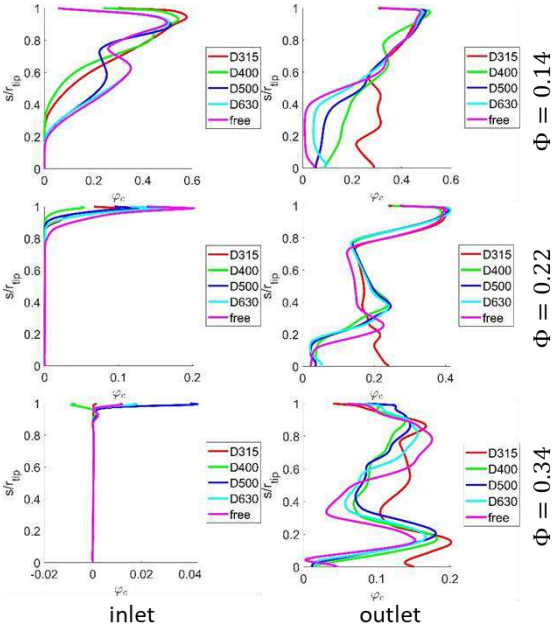

Figure 7: Radial distribution of dimensionless circumferential velocity at different flow rates close to the forward and backward-facing steps

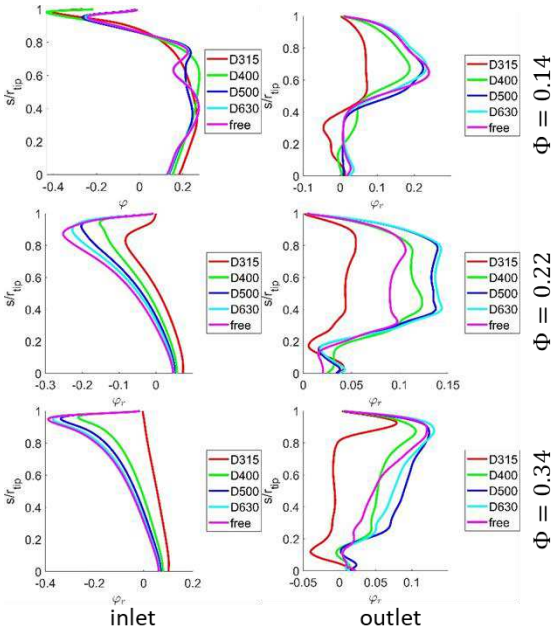

Figure 8: Radial distribution of dimensionless radial velocity at different flow rates close to the forward and backward-facing steps

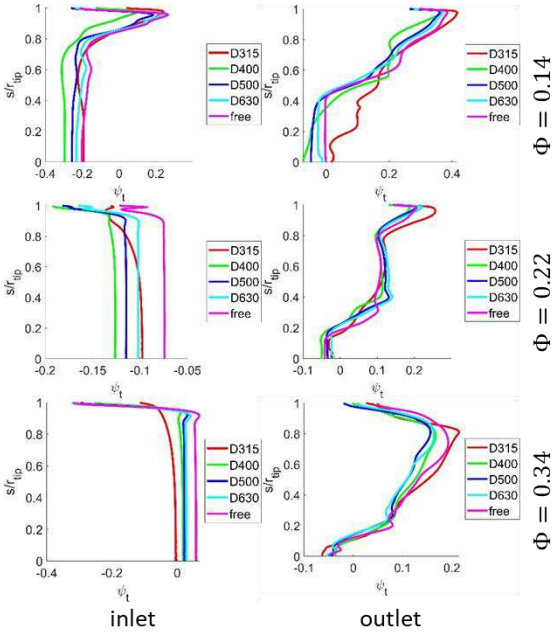

Figure 9: Radial distribution of dimensionless total pressure at different flow rates close to the forward and backward-facing steps

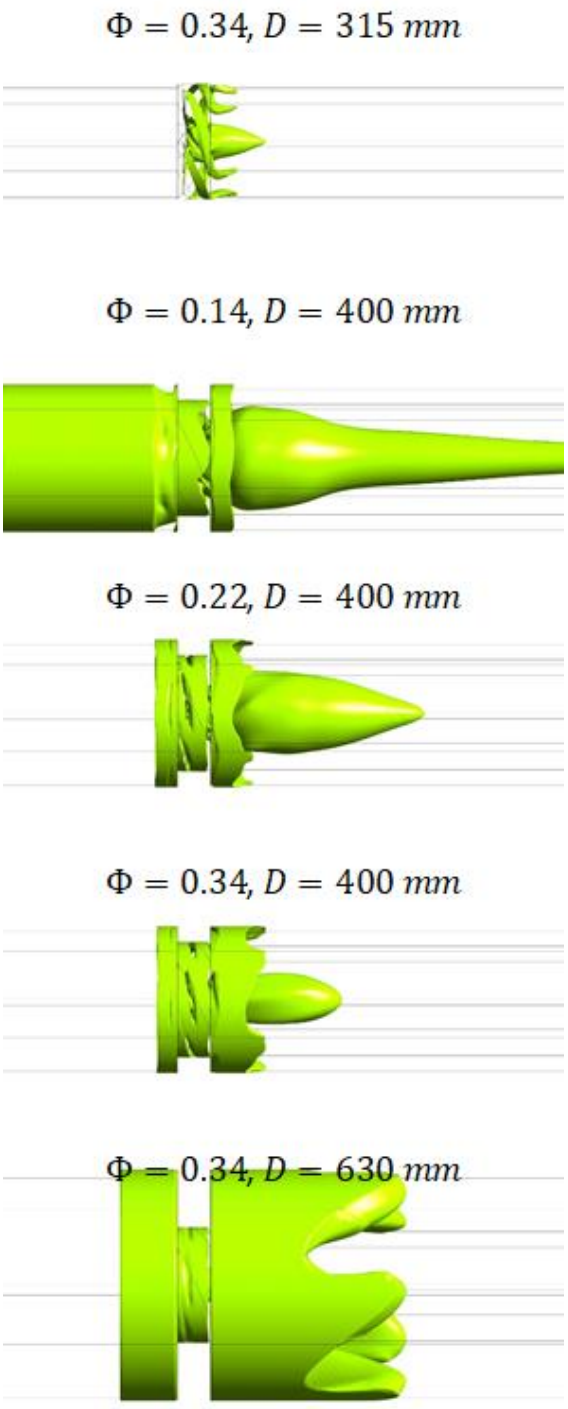

Figure 10. The zero axial velocity iso-surfaces for different duct diameters and operating points

5. SUMMARY

In the present paper, the effect of the sudden diameter changes on the performance of an axial flow fan was investigated using computational fluid mechanics simulations. The fan was placed in a short casing with a diameter of $315\ mm$. The diameter of the connecting ducts varied between $315 - \infty\ mm$. The fan was investigated at constant rotational speed in the $\Phi = 0.14 - 0.34$ flow rate interval. The mid-chord-based Reynolds number of the blades varied between $Re_C = 100000 - 110000$.

In accordance with the expectations, the calculated total pressure rise and efficiency curves showed that the setup without sudden diameter changes outperforms the other cases in the investigated flow rate interval. At the higher investigated flow rates, the total pressure rise, and the efficiency decreased with the increase of the connecting duct diameter. At the lower investigated flow rates, there was no significant difference between the curves of different duct diameters.

The circumferentially averaged velocity and total pressure profiles in the inlet and outlet surface of the blading were also investigated. Based on these profiles and flow visualization, four recirculation zones were found in the cases of sudden diameter changes (see Fig 11): two in the corners of the duct connections, one in the tip region, and one in the vicinity of the hub. The simulation showed that the blade tip recirculation zone becomes more dominant and interacts with the inlet corner recirculation zone with the decrease of the flow rate. In the outlet section, the hub recirculation zone expanded to 40% span at lower flow rates in the cases of sudden diameter changes. In this recirculation zone, the tangential velocity and the total pressure were moderate. The hub recirculation zone was less dominant in the case of the matching duct diameter which explains the outperformance of this setup in the lower flow rate interval. The results also showed that due to the displacing effect of the hub recirculation zone a significant outward flow forms in the cases of sudden diameter change, which cause the contraction of the corner recirculation zone in the outlet duct.

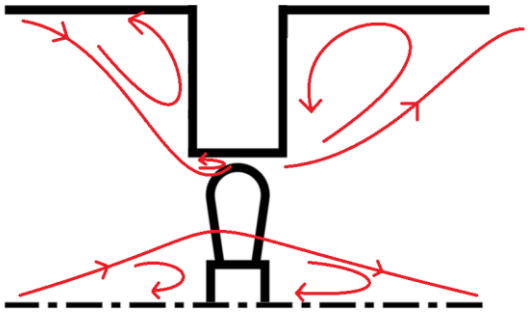

Figure 11: The structure of the separation zones

ACKNOWLEDGEMENTS

This work has been supported by the Hungarian National Research, Development, and Innovation Fund under contract NKFI K 129023.

APPENDIX

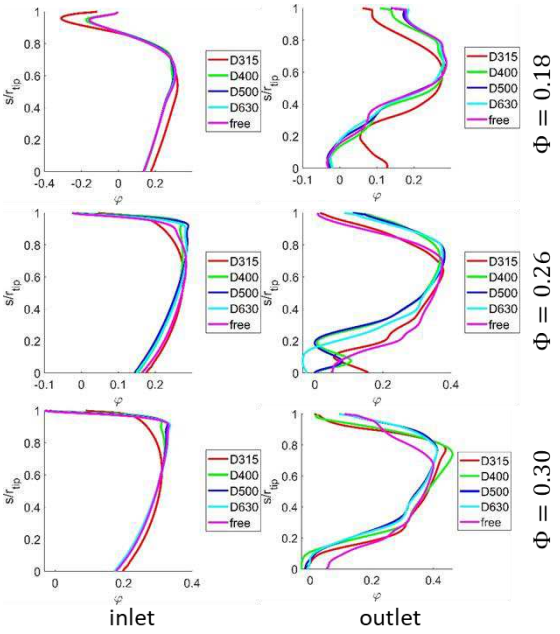

Figure 12: Radial distribution of dimensionless axial velocity at different flow rates close to the forward and backward-facing steps

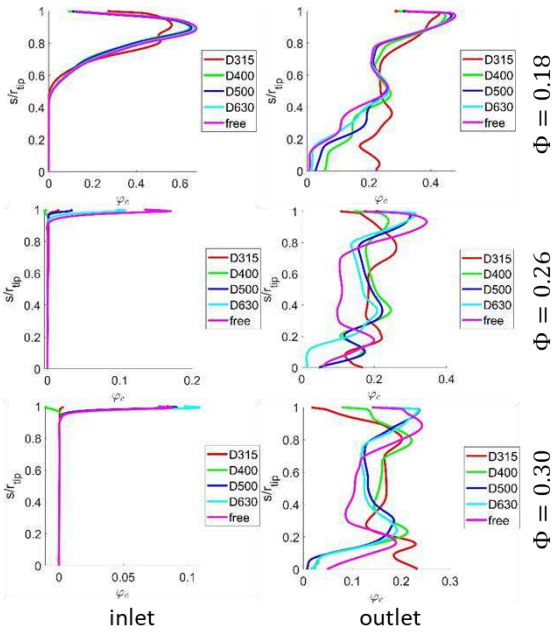

Figure 13: Radial distribution of dimensionless circumferential velocity at different flow rates close to the forward and backward-facing steps

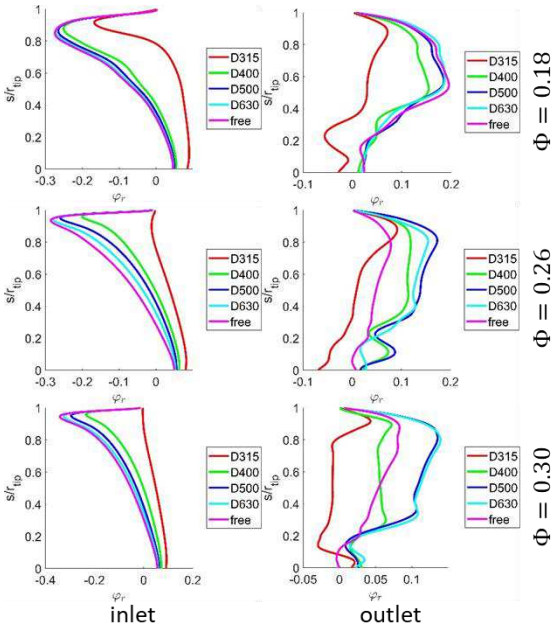

Figure 14: Radial distribution of dimensionless radial velocity at different flow rates close to the forward and backward-facing steps

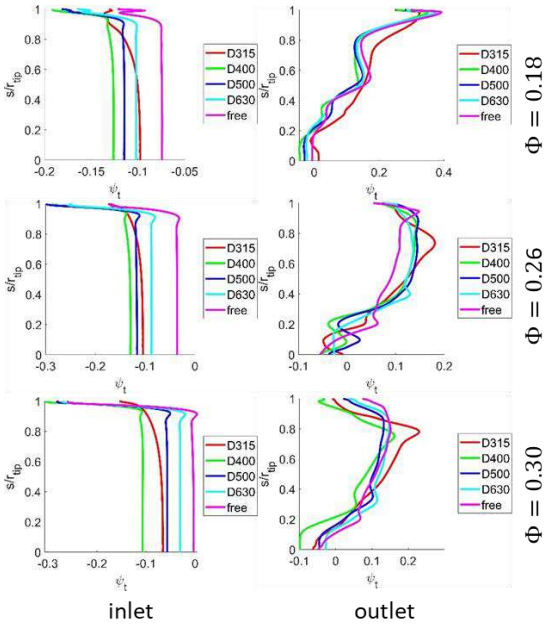

Figure 15: Radial distribution of dimensionless total pressure at different flow rates close to the forward and backward-facing steps

REFERENCES

[1] Carolus, T., 2003, *Ventilatoren* [Fans], 3rd Edition, Teubner Verlag, Germany

[2] Wallis, R. A., 1961, *Axial Flow Fans: Design and Practice*, George Newnes Limited, London, UK

[3] Daly, B. B., 1992, *Woods Practical Guide to Fan Engineering* (sixth impression), Woods of Colchester Ltd., UK

[4] Vad, J., 2013, "Forward blade sweep applied to low-speed axial fan rotors of controlled vortex design: an overview", *Journal of Engineering for Gas Turbines and Power Transactions of the ASME,* Vol. 135(1), Paper: 012601

[5] Benedek, T., Vad, J., and Lendvai, B., 2022, "Combined acoustic and aerodynamic investigation of the effect of inlet geometry on tip leakage flow noise of free-inlet free-exhaust low-speed axial flow fans", *Applied Acoustics* Vol. 187, Paper: 108488

[6] EN ISO 5801:2018 - Fans - Performance testing using standardized airways (ISO 5801:2017), Standard, International Organization for Standardization, Geneva, CH

[7] Stütz, W., 1996, „Untersuchungen zu der wechselwirkung zwischen einlaufduese und axialventilator" [investigations on the interaction between entry geometry and axial fan], *Tech. Rep*. VDI Berichte Nr. 1249, Verein Deutscher Ingenieure

[8] Lukács, E., and Vad, J., 2021, "Flow topology and loss analysis of a square-to-square sudden expansion relevant to HVAC systems: A case study", *Journal of Building Engineering,* Vol. 41, Paper: 102802

[9] Fukano, T., and Jang, C.-M., 2004, "Tip clearance noise of axial flow fans operating at design and off-design condition", *Journal of Sound and Vibration,* Vol. 275(3), pp. 1027-1050.

[10] Hah, C., 2017, Effects of double-leakage tip clearance flow on the performance of a compressor stage with a large rotor tip gap, *Journal of Turbomachinery Transactions of the ASME,* Vol. 139, Paper: 061006.

[11] Mao, X., Liu, B., and Zhao, H., 2019, "Effects of tip clearance size on the unsteady flow behaviors and performance in a counter-rotating axial flow compressor", *Proceedings of the Institution of Mechanical Engineers, Part G: Journal of Aerospace Engineering,* Vol. 233(3), pp. 1059-1070.

[12] Menter, F. R., 1993, "Zonal Two Equation k-ω Turbulence Models For Aerodynamic Flows", *23rd Fluid Dynamics, Plasmadynamics, and Laser Conference*

Conference on Modelling Fluid Flow (CMFF'22)
The 18th International Conference on Fluid Flow Technologies
Budapest, Hungary, August 30-September 2, 2022

MUSHROOM SHAPED BUBBLES AND THE JET OF 1000 M/S

Max KOCH[1], Christiane LECHNER[2,3], Werner LAUTERBORN[2], Robert METTIN[2]

[1] Corresponding Author. Third Physical Institute, Georg-August University Göttingen. Friedrich-Hund-Platz 1, 37077 Göttingen, Germany.
E-mail: max.koch@phys.uni-goettingen.de
[2] Third Physical Institute, Georg-August University Göttingen. Friedrich-Hund-Platz 1, 37077 Göttingen, Germany.
[3] Institute of Fluid Mechanics and Heat Transfer, TU Wien, Getreidemarkt 9, 1060 Vienna, Austria

ABSTRACT

The dynamics of a single, laser-induced cavitation bubble on top of a solid cylinder is studied both experimentally and numerically. When the bubble is generated close to the flat top along the axis of the cylinder and its maximum radius exceeds the one of the flat top surface, it collapses in the form of a mushroom with a footing on the cylinder, a long stem and a hat-like cap typical for a mushroom head. The head may collapse forming a thin, fast liquid jet into the stem, depending on bubble size and bubble distance to the top of the cylinder. The parameter space of initial distance to the cylinder, bubble size and cylinder radius is scanned numerically, partly compared to experiments and evaluated for the resulting jet velocity and jet length and other features. The results represent a contribution to understand the behavior of bubbles collapsing close to structured surfaces, in particular, how thin, fast jets are generated. An indication how the fast jet plays a role for erosion is given, as well.

Keywords: single cavitation bubble, CFD, high-speed imaging, laser-induced, rigid cylinder, fast jet

NOMENCLATURE

D	$[m]$	distance bubble – object
R	$[m]$	bubble radius
p	$[Pa]$	pressure
$\boldsymbol{U}$	$[m/s]$	velocity
α	$[-]$	phase parameter
λ	$[m]$	wavelength
μ	$[Pa\,s]$	viscosity
ρ	$[kg/m^3]$	density

Subscripts and Superscripts

max	maximum
eq	equivalent
init	initial
*	normalized quantity
n,∞	quantity at normal conditions

1. INTRODUCTION

The phenomena described in this manuscript are explained in detail in [1]. This manuscript is to be understood as a summary of the main aspects from this publication, plus a small extension. For a full comprehension it is advisable to read the open access article [1] as well. The present manuscript is written with the assumption of familiarity of the reader with the single bubble cavitation phenomenon. If a text part in this manuscript is cited directly from [1] it is denoted by "([1])" at the end of the paragraph.

Despite considerable efforts to elucidate the erosion process by cavitation bubbles, the precise mechanisms are still under discussion. The dynamics of the bubble is highly influenced by many factors: The properties of the surrounding liquid (density, viscosity), the bubble contents (gas, vapour), the bubble–liquid interface (surface tension, coating), outer factors (pressure, temperature, gravity) and, in particular, the large class of geometrical constraints, i.e., boundaries or objects nearby with different properties from flat to curved or smooth to corrugated and solid to soft. For systematic studies on geometrical constraints, isolated single bubbles are required. The liquid breakdown induced by a focused laser light pulse has been used for this purpose ([1]).

In the past, investigation of bubble dynamics near structured objects got less attention than studies on flat or smooth surfaces. However, it is known that cavitation bubbles can reach, clean and also damage crevices, holes, trenches and other complicated surface features (see, e.g., [2]). Up to now, owing to the large variety of structures and constraints, only a few cases were already investigated for single bubble dynamics. Among the solid boundaries and objects, there are a small hole [3], blind holes/crevices [4], rectangular channels [5], convex surfaces [6], a thin gap (parallel plates) [7, 8], rigid spheres [9, 10], a pencil-like electrode [11], ridges and grooves [12], a micro structured riblet [13], edges [14, 15] and corners [16]. ([1]).

The investigation of the dynamics of a bubble

close to the top of a rigid cylinder, both experimental and numerical, is described in this manuscript. The bubble is generated on the symmetry axis of the cylinder. Therefore, three independent parameters describe the geometrical arrangement as shown in Figure 1: l_p — the length of the cylinder (height above a planar, solid boundary), r_p — the radius of the cylinder and D_{init} — the distance of the bubble to the top of the cylinder at $t = 0$ (i.e. the spot of optical breakdown, hence the plasma spot). The energy of the bubble, given a certain atmospheric pressure, is classified by the maximum radius $R_{max,unbound}$ the bubble would attain in an unbounded liquid. When the bubble is generated close to an object, the maximum, volume-equivalent radius $R_{max,eq}$ will differ from the unbounded one, depending on the structure of the object and D_{init} (see also [17]).

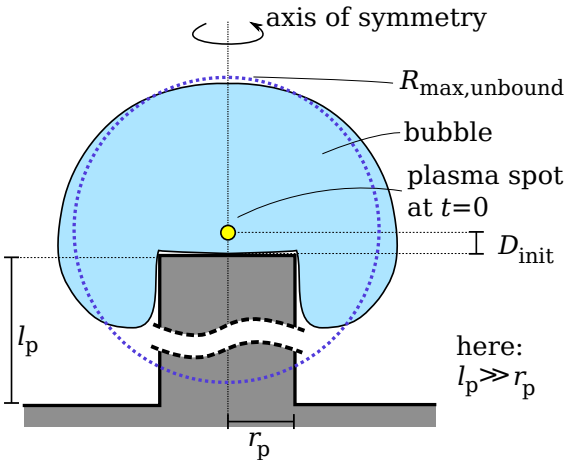

Figure 1. Sketch of the parameters for classification of bubbles close to a solid cylinder [1].

The dynamics of the bubble scale with the non-dimensionalized parameters

$$D^* = \frac{D_{init}}{R_{max,unbound}}, \quad r_p^* = \frac{r_p}{R_{max,unbound}}, \tag{1}$$

for $l_p \gg r_p$. With the reference to $R_{max,unbound}$, the temporal normalization is uniquely defined by the Rayleigh collapse time t_{Rc} given by

$$t_{Rc} = 0.91468 \cdot R_{max,unbound} \sqrt{\rho_\infty / p_\infty}, \tag{2}$$

where $\rho_\infty = 998.2\,kg/m^3$ and $p_\infty = 101315\,Pa$. ([1]).

The case where $l_p = 0$ or $r_p \to \infty$ was and still is heavily studied, it is the case of a bubble close to a flat, rigid boundary. In this case, the bubble will involute and produce a liquid jet towards the solid. Historically, values for $D^* > 0.3$ were investigated, where the jet is called *micro-jet* and exhibits speeds in the order of $100\,m/s$.

Recently, the work by Lechner et al. [18, 19] predicted and described in detail that for $D^* \leq 0.2$, $l_p = 0$ the jet speeds are of one order of magnitude higher. In this parameter subspace, a different jetting mechanism occurs, producing the *fast jet*. The fast jets reach speeds in the order of $1000\,m/s$. They are produced by annular inflow with self-impact and by squeezing the liquid into two opposite directions [20]. The findings are in agreement with the simulations by Pishchalnikov et al. [21] and experiments as early as by Benjamin and Ellis [22]. A comparison with very good agreement of the velocities of numerical simulations with experiments of laser-induced bubbles for both the micro-jet and for the fast jet, as well, can be found in the works of Koch [23] and Koch et al. [24].

Thus, the question arises, whether there are other geometrical configurations where the fast jet is produced. This is indeed the case for the bubble close to the top of a rigid cylinder. The dynamics of the bubble in this case provoke the association with a mushroom shape. The present work investigates the details of the dynamics in the parameter range $0.047 < D^* < 2.009$ and $0.251 < r_p^* < 0.893$.

2. EXPERIMENTAL METHODS

The observation of the laser-induced bubble in the experiment is described briefly here. For a detailed explanation, the reader is referred to [1].

The bubble is produced in the center of a rectangular cuvette of edge length $1\,cm \times 5\,cm \times 4\,cm$ (width, depth, height), filled with de-ionized water. The laser for bubble seeding is an Nd:YAG Litron nano PIV, operated at $\lambda = 532\,nm$ with a single pulse duration of $10\,ns$. The laser light is fist widened and then focused into the center of the cuvette by a lens of $35\,mm$ focal distance.

For the rigid cylinder, a sewing needle was ground to flat top. The needle radius was measured to be $r_p = 272.8\,\mu m$.

Two cameras are applied for observing the bubble, each equipped with a long distance microscope objective (K2 Infinity). For Mega-frames per second recording of the collapse of the bubble the Imacon 468 was used (8 images in total) and for kilo-frames per second recording of the overall dynamics the Photron APS-RX was used. The record trigger for the Imacon Camera has to be known with $1\,\mu s$ precision. This was accomplished with a continuous wave Helium-Neon laser that points onto a photodiode through the site of bubble generation.

Backlight illumination was done with a xenon-flash (*Mecablitz*).

3. BUBBLE MODEL AND NUMERICAL METHODS

The bubble model consists of two phases, one gas phase (air) and one liquid phase (water) that do not exchange mass. Viscosity of both phases is included, while surface tension and gravity are neglected in this case, as well as evaporation or condensation processes. The two phases are considered isentropic, which is valid up to shock waves of $\approx 3\,GPa$ [25, page 40]. Therefore, the energy equation for the set of momentum equations for the compressible

phases can be omitted and can be substituted by two equations of state: the adiabatic gas equation and the Tait-equation

$$\text{gas: } \frac{p}{p_\infty} = \left(\frac{\rho}{\rho_n}\right)^\gamma, \quad \text{liquid: } \frac{p+B}{p_\infty+B} = \left(\frac{\rho}{\rho_\infty}\right)^{n_\mathrm{T}}, \tag{3}$$

where $\gamma = 1.4$ is the polytropic exponent of air, $\rho_n = 1.204\,kg/m^3$, $B = 305\,MPa$ a constant and $n_\mathrm{T} = 7.15$, the Tait-exponent.

The model is implemented in a finite volume solver running in the open source `foam-extend` software package for computational fluid dynamics. This solver is maintained and developed since 2013 (for an extended description, including validation, see e.g. [26, 27, 19, 23]).

The governing equations are the Navier-Stokes equation and the continuity equation

$$\frac{\partial(\rho\boldsymbol{U})}{\partial t} + \nabla\cdot(\rho\boldsymbol{U}\otimes\boldsymbol{U}) = -\nabla p + \nabla\cdot\left[\mu\left(\nabla\boldsymbol{U} + (\nabla\boldsymbol{U})^T - \frac{2}{3}(\nabla\cdot\boldsymbol{U})\,\mathbb{I}\right)\right], \tag{4}$$

$$\frac{\partial\rho}{\partial t} + \nabla\cdot(\rho\boldsymbol{U}) = 0\,, \quad \frac{\partial\alpha_i\rho}{\partial t} + \nabla\cdot(\alpha_i\rho\boldsymbol{U}) = 0\,, \tag{5}$$

where $\boldsymbol{U}$ denotes the velocity, $\otimes$ the tensorial product, ∇ the gradient and $\nabla\cdot$ the divergence, μ the dynamic viscosity and $\mathbb{I}$ the unit tensor. The two phases are distinguished by a phase parameter $\alpha \in [0,1]$ such that, e.g., $\mu = \alpha\mu_l + (1-\alpha)\mu_g$ with μ_l, μ_g the viscosities of the liquid and the gas respectively. The subscript i denotes either l (liquid) or g (gas), where $\alpha_l = \alpha$ and $\alpha_g = 1-\alpha$.

The computational domain is discretized with the finite volume method and the equations are solved in a segregated manner by the PISO algorithm (pressure implicit with splitting of operators).

3.1. Initial data

The calculations have been performed mainly in axial symmetry. Distinct simulations in full 3D have been made for a qualitative comparison, as well. The size of the computational domain for the axisymmetric calculations was chosen to be $52\,mm$, while the maximum radii in unbounded liquid $R_{\mathrm{max,unbound}}$ of the bubbles tested ranged from $224\,\mu m$ to $636\,\mu m$. At $t = 0$ the liquid is at rest and the bubble is compressed to $20\,\mu m$ in all of the 89 cases studied. The cells of the mesh are oriented in the radial direction, only the core of the mesh is in cartesian orientation. The cylinder with a radius of either $200\,\mu m$ or $160\,\mu m$ was cut out of the mesh. The boundary condition at the cylinder is set to no-slip and $\alpha = 1$ (= liquid). The outer boundary of the mesh is set to be wave transmissive. Details for the mesh are found in [1].

3.2. Hardware

The simulations in axial symmetry were done on a dual Xenon Silver 4216 machine with 32 cores and 93.1 *GB* RAM. Each simulation comprised about 125 000 cells and 30 000 time steps, consuming about 1h15min of computational time for $110\,\mu s$.

4. RESULTS

Before describing the results of the bubbles on top of a cylinder, the case for $l_\mathrm{p} = 0$ is recapitulated. In Figure 2 the pressure and velocity field of an axisymmetric simulation of a bubble at $D^* = 0.04$, $l_\mathrm{p} = 0$ are shown for six times shortly before minimum bubble volume in order to elucidate the different jetting mechanism. An annular jet forms on the top of the bubble. The liquid impacts onto itself before the bubble could involute like it would do for $D^* \geq 0.24$. Within a fraction of a microsecond a small part of the liquid is accelerated to, here, more than $1200\,m/s$. More information about this phenomenon is found in [18, 19, 23, 24, 1], as well as in the CMFF'22 article by C. Lechner.

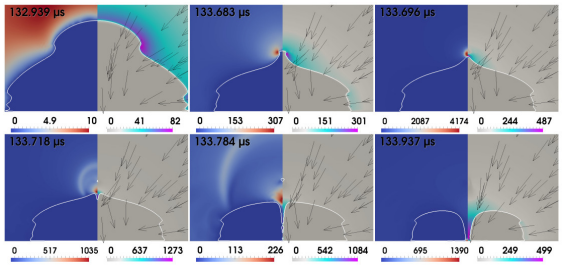

Figure 2. Simulation showing the fast-jet mechanism. Reprinted from [23, Fig. 5.1]. Left part of the frames: pressure field in bar, right part of the frames: velocity field in m/s.

Figure 3 shows the recording of a bubble at $D^* = 0$, $l_\mathrm{p} \gg r_\mathrm{p}$, $r_\mathrm{p}^* \approx 0.32$ with the photron camera. Radius of the cylinder top is $r_\mathrm{p} = 272.8\,\mu m$. Exposure time is $1\,\mu s$. The sequences of four recordings at 21 kfps each were stacked and interleaved. The times for one of the sequences are given and the frames without a time tag are from different sequences used for interpolation. The bubble has a maximum horizontal width of $1689\,\mu m \pm 18\,\mu m$ at $95.2\,\mu s$.

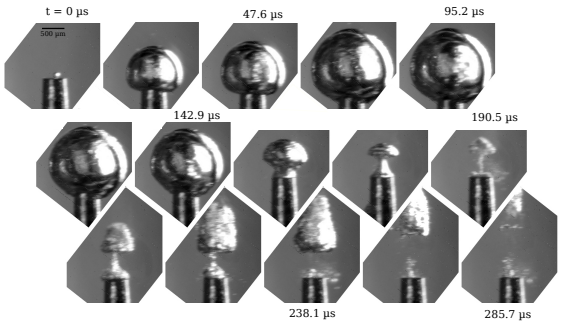

Figure 3. Image sequence of a typical mushroom bubble generated at $D^* \approx 0$, $l_\mathrm{p} \gg r_\mathrm{p}$, recorded with the photron camera. Reprinted from [1].

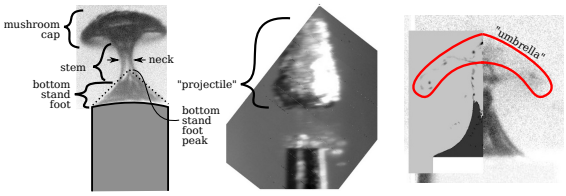

Figure 4. Terminology for mushroom-shaped bubbles. [1]

In order to classify the different parts of the shape of the bubble at different times, the terminology given in Figure 4 is applied. The dynamics of the bubble in Fig. 3 can now be described in the following way: At first, the bubble expands to a radius about 3 times larger than the cylinder radius. Before minimum volume during collapse, the lower part seems to form a waist and the bottom of the bubble forms the *bottom stand foot* (two frames before 190.5 μs). When the neck tapers (one frame before 190.5 μs), the mushroom cap of the bubble becomes even more evident. During bubble volume minimum (190.5 μs), the shape becomes cloudy by fragmentation into many small gas parts and subsequently the mushroom cap grows and detaches as a *projectile*.

In order to gain insight into why the mushroom shape of the bubble is formed and whether it is persistent to a wider range of the $[D^*, r_p^*]$ parameter space, 89 simulations in axial symmetry have been performed, out of which 68 showed the mushroom shape. 18 frames of one simulation with typical dynamics are shown in Figure 5 with arrows indicating the main flow. The color indicates the magnitude of the velocity of the liquid in m/s. The characteristic values of the bubble are: $R_{\mathrm{max,unbound}} = 472.57\,\mu m$, $D^* = 0.063$, $r_p^* = 0.423$, $t_{\mathrm{Rc}} = 42.90\,\mu s$. Cylinder radius is 200 μm. Frames 1–9 show the expansion and the begin of the collapse, while frames 10–18 show the moment of jetting with a *fast jet*, the bubble minimum volume and rebound with the detaching of the projectile.

During the expansion phase, shown in the first 3 frames the bubble interface crosses the cylinder rim, it swirls around it (frame 2), ejecting liquid droplets (in axial symmetry torus ring drops) into the bubble body. Once passed, these droplets hit the outer bubble wall, inducing surface waves there (dashed circles in frame 3). Due to the boundary layer around the cylinder, the bubble never touches the solid, but "swims" on the boundary layer. ([1]).

When the bubble starts collapsing, the outer waist is lifted almost parallel to the cylinder. This flow produces the two annular inflows that form a) a neck and b) the extreme curvatures at the mushroom cap rim. As denoted by the red arrows and circles in frame 7, Fig. 5, the flow that forms the mushroom neck has also a component upwards that tapers the cap to a thin gas film. The phenomenon of *flow focusing* comes into play [28, 19], flow focusing generating strongest acceleration where curvatures are highest. An annular jet is formed that runs along the top part of the shrinking mushroom cap, leaving trails of dim remnant gas that form a thin umbrella (see e.g. Fig. 4, right frame). Numerically, this results into a tearing of the interface, leaving areas where $0.9 < \alpha < 1$. In the end, this annular liquid jet impacts in the zenith of the umbrella, producing a *fast jet*. The fast jet actually is the reason, why the neck will not impact onto itself . It can be seen that the fast jet here reaches values of more than 700 *m/s* (see dashed rectangle on top of the velocity scale in frame 11). In some cases, it is more than 2000 *m/s*, as will be shown later. The liquid inflow from the top now, starting from frame 10 on, makes all sideways inflows at the neck negligible, changing the subsequent dynamics to a zipper-like collapse. The neck is tapered from inside rather than from outside flows. In the experiment, only the aforementioned "bottom stand foot" is observed here, because the outside bubble surface has too many wrinkles to see the jet inside. The minimum volume happens from top-down, thus the top gas fragments are already in the rebound phase, when the lower ones collapse and emit shock waves (not seen here – taking place in frame 16, as indicated by the dashed red circle in the frame). Therefore, the upper bubbles are "kicked" and squeezed upwards. Thereby, a layered structure of (torus) bubbles is observed. ([1]).

Experimental insight into the moment of mushroom bubble jetting can be gained with the Imacon camera. Figure 6 shows such a record of 8 frames at a time during ring jet impact at the top of the mushroom cap. The times denote the delay to the camera trigger. The background of the experimental images was subtracted. The recorded images are compared to a simulation via an overlay with the volume fraction field α on the left side of each frame (mind that the numerical simulation is represented by a cut through the bubble). The characteristic values for the bubble of the simulation are $D^* = 0.057$ and $r_p^* = 0.306$. The frame width for the experiment is $766\,\mu m \pm 10\,\mu m$. The cylinder radius r_p in the experiment is 272.8 μm, in the simulation r_p is 200 μm. It is seen that the simulation and the experiment match very well, even the torus-shaped mushroom cap rim is reproduced by the simulation. It is also evident from the simulation that the stem/neck of the bubble is pierced by the fast jet, producing the top-down zipper-like collapse that is also seen in the experiment. For more comparisons, 3D simulations and experimental recordings, the reader again is referred to [1].

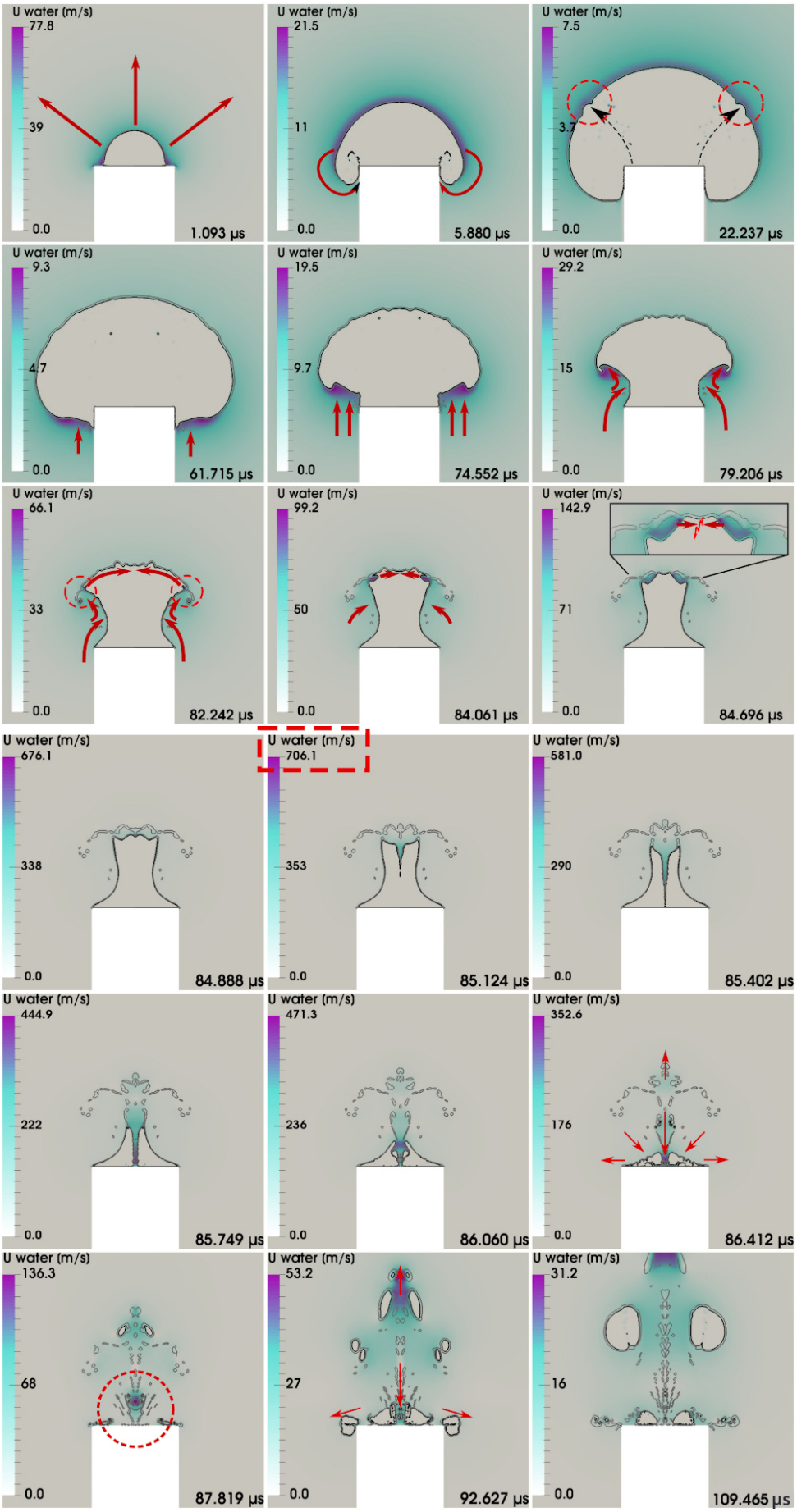

Figure 5. General dynamics of the mushroom bubble. [1]

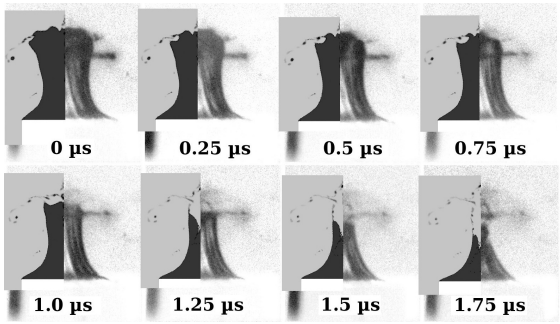

Figure 6. Imacon camera frame sequence of a mushroom bubble at a time during ring jet impact at the top of the mushroom cap. [1]

With the figures given in this manuscript, the main line of reasoning concerning the link between the mushroom shape and the fast jet is sketched.

4.1. Parameter study

The 89 simulations were evaluated and distinct quantities were extracted to be plotted into an interpolated heat map with isocurves within the [D^*, r_p^*] parameter space. Two of the graphs from [1] are shown in Figure 7. Each data point represents one simulation. The data points are plotted in their respective colors that represent their values. White data points denote cases, where either the bubble dynamics was different from the mushroom case, the annular jet impact happens later than the neck closure or a standard jet by involution of the bubble wall was observed.

The jet speed (top graph) was calculated by the distance of the spot of the annular jet impact to the top of the cylinder divided by the time the liquid needs to traverse this distance. This speed, however, did not converge yet for any mesh and time resolution (see explanation in [19, 1]). Therefore, the values ranging from 189 *m/s* to 2164 *m/s* are given as tentative results. The corresponding water hammer pressures ($\rho\, c\, v_{\mathrm{jet}}$) would range from 0.3 GPa to 3 GPa. The heat map suggests that the faster jets are found for low values of r_p^* and higher values of D^*.

In the bottom graph the length of the jet is given, measured from the point of formation to the point of impact onto the pillar surface. When the jet length is compared to the cylinder radius , the jet becomes longer for smaller r_p^* as well (for a fixed r_p). The jet length varied by less than 10 % with grid alterations. It could be an interesting quantity from an experimental point of view, when photographing the jet is planned. ([1]).

5. FURTHER STUDIES

In addition to the material from [1] a glimpse into a probable reason for erosion, first assessed in [23], is given here. For the case of $l_p = 0$ the pressure signal in the symmetry point below the bubble at the solid wall, gained by an axisymmetric simulation, was compared to the dynamics of the bubble:

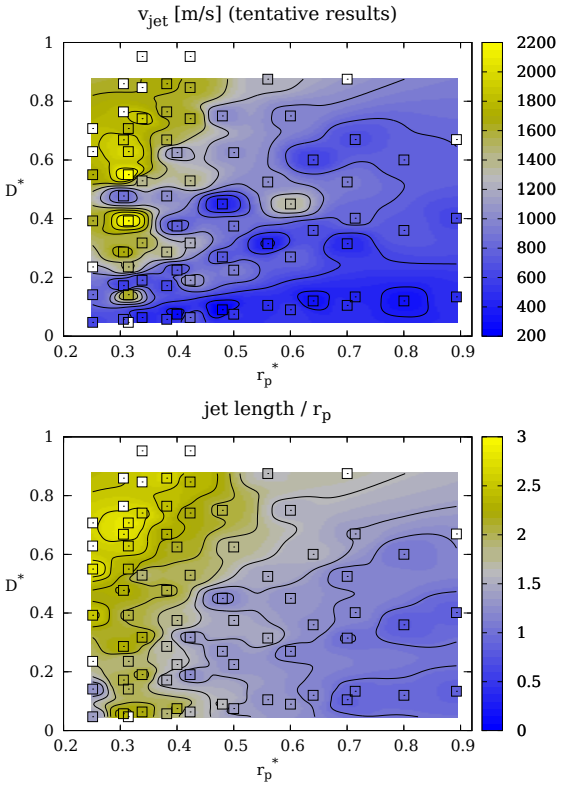

Figure 7. Part of the parameter study (see [1]). Reprinted with different colors.

It is most likely that the main erosion (for $l_p = 0$) happens around $D^* = 0.1$, where peak values of close to 4 GPa are observed. A first evaluation for the reason of this pressure peak is given in Figure 8 for $D^* = 0.1$. Shown is the bubble with the pressure field in bar during and after fast jet impact, as well as the aforementioned pressure signal. The fast jet has already impacted onto the solid boundary before the main pressure peak at 111.65 μs. The main peak roots from the focusing of the toroidal shockwave from the collapse of the bubble directly on the solid boundary. From this simulation, it can be said that one single, laser generated bubble of $R_{\max} \approx 500\,\mu m$ might be able to erode an alloy when generated at a distance of $D^* = 0.1$. ([23]). Detailed experimental studies on erosion tests have been performed by [29, 30].

6. SUMMARY

A laser-induced bubble on top of a long cylinder with a radius at maximum volume larger than the radius of the cylinder shows a dynamics very different from a bubble on an extended flat surface. After having embraced the cylinder top upon expansion, upon collapse it develops a mushroom shape with a head, a long stem and a footing. The special fluid flow leading to the mushroom shape could be reproduced in numerical studies by solving the Navier-Stokes equations for a Tait-compressible liquid with OpenFOAM (precisely the foam-extend fork). The

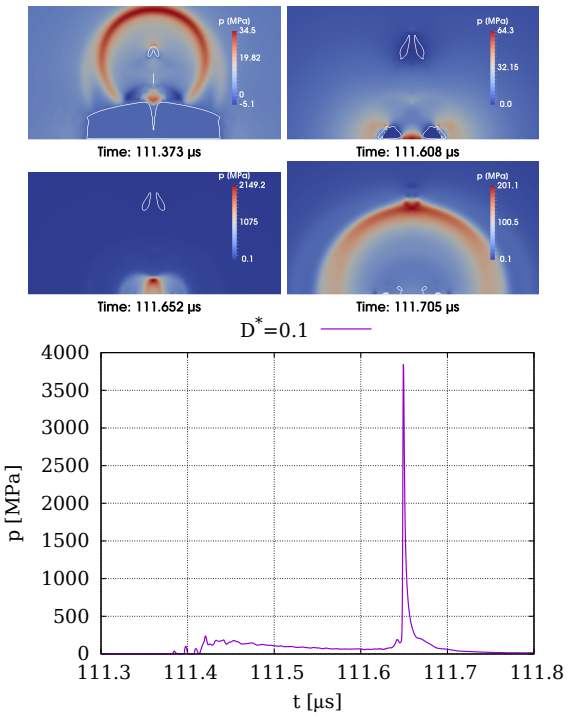

Figure 8. Towards shock waves as reason for erosion. [23]. Top four frames: pressure field [bar] around a bubble at $D^* = 0.04$, $l_p = 0$ at times of fast jet formation and minimum volume. Bottom Frame: Pressure signal [MPa] in the symmetry point below the bubble at the solid boundary showing the large pressure peak from the focusing of the torus shock wave, generated at torus-bubble collapse on the surface.

simulations were carried out in axial symmetry . The simulation code has been validated again by comparison of an experimental with a numerical mushroom shape (Fig. 6). A quite large range of parameters has been studied ($0.047 \leq D^* \leq 2.009$ and $0.251 \leq r_p^* \leq 0.893$). In 68 of 89 cases investigated, the bubble forms a mushroom shape and the mushroom head collapses with forming a fast jet (velocity ranging from 189 m/s to 2164 m/s) into the gaseous stem from the self-impact of an annular inflow by two-dimensional flow focusing. The existence of the fast jet in the experiments has been proven by comparing the experiments with the numerical simulations with respect to stem stability. The range of parameters shows that fast jets of annular-inflow type (studied numerically in [18, 21, 19] and experimentally in [23, 24] for bubbles close to a plane solid boundary) are not a singular phenomenon, but a robust phenomenon. It is expected to occur in many other configurations, too, and to alter the view on cleaning and erosion of surfaces. It may find applications in laser-induced ablation in liquids with pillars of various shapes as targets for laser synthesis and processing of colloids [31]. The fast jet phenomenon also bears a clear potential for erosion of solids. ([1]).

The indication that another cause for erosion might stem from the toroidal shockwave of the bubble collapse has been shown as well for one data point in the parameter subset.

ACKNOWLEDGEMENTS

The work was supported in part by the German Science Foundation (DFG) under contracts ME 1645/8-1, ME 1645/8-3 and ME 1645/5-2 and the Austrian Science Fund (FWF) (Grant No. I 5349-N).

References

[1] M. Koch, J. M. Rosselló, C. Lechner, W. Lauterborn and R. Mettin. “Dynamics of a laser-induced bubble above the flat top of a solid cylinder — mushroom-shaped bubbles and the fast jet”. In: *Fluids* 7.1 (2022).

[2] M. Kauer, V. Belova-Magri, C. Cairós, G. Linka and R. Mettin. “High-speed imaging of ultrasound driven Cavitation bubbles in blind and through holes”. In: *Ultrason. Sonochem.* 48 (2018), pp. 39–50.

[3] B. Karri, K. S. Pillai, E. Klaseboer, S.-W. Ohl and B. C. Khoo. “Collapsing bubble induced pumping in a viscous fluid”. In: *Sensors and Actuators A: Physical* 169.1 (2011), pp. 151–163.

[4] T. Trummler, S. H. Bryngelson, K. Schmidmayer, S. J. Schmidt, T. Colonius and N. A. Adams. “Near-surface dynamics of a gas bubble collapsing above a crevice”. In: *J. Fluid Mech.* 899 (July 2020), A16-1–21.

[5] E. D. Andrews, D. F. Rivas and I. R. Peters. “Cavity collapse near slot geometries”. In: *J. Fluid Mech.* 901 (Sept. 2020), A29-1–22.

[6] Y. Tomita, P. B. Robinson and R. P. Tong. “Growth and collpase of cavitation bubbles near a curved rigid boundary”. In: *J. Fluid Mech.* 466 (2002), pp. 259–283.

[7] E. W. Quah, B. Karri, S.-W. Ohl, E. Klaseboer and B. C. Khoo. “Expansion and collapse of an initially off-centered bubble within a narrow gap and the effect of a free surface”. In: *International Journal of Multiphase Flow* 99 (2018), pp. 62–72.

[8] S. R. Gonzalez-Avila, A. C. van Blokland, Q. Zheng and C.-D. Ohl. “Jetting and shear stress enhancement from cavitation bubbles collapsing in a narrow gap”. In: *J. Fluid Mech.* 884 (2020), A23-1 –A32-23.

[9] S. Li, A.-M. Zhang, R. Han and Q. Ma. “3D full coupling model for strong interaction between a pulsating bubble and a movable sphere”. In: *J. Comput. Phys.* 392 (Sept. 2019), pp. 713–731.

[10] J. Zevnik and M. Dular. “Cavitation bubble interaction with a rigid spherical particle on a microscale”. In: *Ultrasonics Sonochemistry* 69 (2020), p. 105252.

[11] D. Palanker, A. Vankov, J. Miller, M. Friedman and M. Strauss. “Prevention of tissue damage by water jet during cavitation”. In: *J. Appl. Phys.* 94.4 (Aug. 2003), pp. 2654–2661.

[12] D. Kim and D. Kim. “Underwater bubble collapse on a ridge-patterned structure”. In: *Phys. Fluids* 32.5 (May 2020), p. 053312.

[13] E. Kadivar, O. el Moctar, R. Skoda and U. Löschner. “Experimental study of the control of cavitation-induced erosion created by collapse of single bubbles using a micro structured riblet”. In: *Wear* 486-487 (2021), p. 204087.

[14] Y. Zhang, X. Qiu, X. Zhang, N. Tang and Y. Zhang. “Collapsing dynamics of a laser-induced cavitation bubble near the edge of a rigid wall”. In: *Ultrason. Sonochem.* 67 (Oct. 2020), p. 105157.

[15] M. Senegačnik, K. Kunimoto, S. Yamaguchi, K. Kimura, T. Sakka and P. Gregorčič. “Dynamics of laser-induced cavitation bubble during expansion over sharp-edge geometry submerged in liquid – an inside view by diffuse illumination”. In: *Ultrason. Sonochem.* 73 (May 2021), p. 105460.

[16] Q. Wang, M. Mahmud, J. Cui, W. R. Smith and A. D. Walmsley. “Numerical investigation of bubble dynamics at a corner”. In: *Phys. Fluids* 32.5 (May 2020), p. 053306.

[17] W. Lauterborn, C. Lechner, M. Koch and R. Mettin. “Bubble models and real bubbles: Rayleigh and energy-deposit cases in a Tait-compressible liquid”. In: *IMA J. Appl. Math.* 83 (2018), pp. 556–589.

[18] C. Lechner, W. Lauterborn, M. Koch and R. Mettin. “Fast, thin jets from bubbles expanding and collapsing in extreme vicinity to a solid boundary: A numerical study”. In: *Phys. Rev. Fluids* 4 (2 Feb. 2019), p. 021601.

[19] C. Lechner, W. Lauterborn, M. Koch and R. Mettin. “Jet formation from bubbles near a solid boundary in a compressible liquid: Numerical study of distance dependence”. In: *Phys. Rev. Fluids* 5.9 (Sept. 2020), p. 093604.

[20] O. V. Voinov and V. V. Voinov. “On the process of collapse of a cavitation bubble near a wall and the formation of a cumulative jet”. In: *Sov. Phys. Dokl.* 21 (1976), pp. 133–135.

[21] Y. A. Pishchalnikov, W. M. Behnke-Parks, K. Schmidmayer, K. Maeda, T. Colonius, T. W. Kenny and D. J. Laser. “High-speed video microscopy and numerical modeling of bubble dynamics near a surface of urinary stone”. In: *J. Acoust. Soc. Am.* 146 (2019), pp. 516–531.

[22] T. B. Benjamin and A. T. Ellis. “The Collapse of Cavitation Bubbles and the Pressures thereby Produced against Solid Boundaries”. In: *Philos. Trans. R. Soc. London, Ser. A* 260 (1966), pp. 221–240.

[23] M. Koch. “Laser cavitation bubbles at objects: Merging numerical and experimental methods”. http://hdl.handle.net/21.11130/00-1735-0000-0005-1516-B. PhD thesis. Georg-August-Universität Göttingen, Third Physical Institute, 2020.

[24] M. Koch, J. M. Rosselló, C. Lechner, W. Lauterborn, J. Eisener and R. Mettin. “Theory-assisted optical ray tracing to extract cavitation-bubble shapes from experiment”. In: *Exp. Fluids* 62.3 (Mar. 2021), p. 60.

[25] R. H. Cole. *Underwater explosions*. Princeton, New Jersey: Princeton University Press, 1948.

[26] M. Koch. “Numerical modelling of cavitation bubbles with the finite volume method”. English. https://doi.org/10.25625/JVCJVW. Master thesis. Georg-August Universität Göttingen, Drittes Physikalisches Institut, C. D. Labor für Kavitation und Mikro-Erosion, 2014.

[27] M. Koch, C. Lechner, F. Reuter, K. Köhler, R. Mettin and W. Lauterborn. “Numerical modeling of laser generated cavitation bubbles with the finite volume and volume of fluid method, using OpenFOAM”. In: *Comput. Fluids* 126 (2016), pp. 71–90.

[28] W. Lauterborn. “Cavitation bubble dynamics — new tools for an intricate problem”. In: *Appl. Sci. Res.* 38.1 (1982), pp. 165–178.

[29] A. Philipp and W. Lauterborn. “Cavitation erosion by single laser-produced bubbles”. In: *J. Fluid Mech.* 361 (1998), pp. 75–116.

[30] M. Dular, T. Požar, J. Zevnik and R. Petkovšek. “High speed observation of damage created by a collapse of a single cavitation bubble”. In: *Wear* 418-419 (2019), pp. 13–23.

[31] D. Zhang, B. Gökce and S. Barcikowski. “Laser synthesis and processing of colloids: fundamentals and applications”. In: *Chem. Rev.* 117.5 (Feb. 2017), pp. 3990–4103.

Conference on Modelling Fluid Flow (CMFF'22)
The 18th International Conference on Fluid Flow Technologies
Budapest, Hungary, August 30-September 2, 2022

Turbulent mixing simulation using the Hierarchical Parcel Swapping (HiPS) model

Tommy Starick[1], Masoomeh Behrang[2], David O. Lignell[2], Heiko Schmidt[1], Alan Kerstein[3]

[1] Corresponding Author. Chair of Numerical Fluid and Gas Dynamics, Institute of Transport Technology, Brandenburg University of Technology Cottbus-Senftenberg, Siemens-Halske-Ring 15a, D-03046 Cottbus, Germany. Tel.: +49 355 69 4813, Fax: +49 355 69 4891, E-mail: Tommy.Starick@b-tu.de, Heiko.Schmidt@b-tu.de
[2] Department of Chemical Engineering, Brigham Young University Provo, UT, 84602, USA. E-mail: m.behrang2015@gmail.com, davidlignell@byu.edu
[3] Consultant, 72 Lomitas Road, Danville, CA, 94526, USA. E-mail: alan.kerstein@gmail.com

ABSTRACT

A computationally efficient and novel turbulent mixing model termed Hierarchical Parcel-Swapping (HiPS) was introduced by A.R. Kerstein [J. Stat. Phys. 153, 142-161 (2013)]. HiPS simulates the effects of turbulence on time-evolving, diffusive scalar fields. The interpretation of the diffusive scalar fields or a state space as a binary tree structure is an alternative approach compared to existing mixing models. The characteristic feature of HiPS is that every level of the tree corresponds to a specific length and time scale, which is based on inertial range scaling. The state variables reside only at the base of the tree and are understood as fluid parcels. The effects of turbulent advection are represented by stochastic swaps of sub-trees at rates determined by turbulent time scales associated with the sub-trees. The mixing of adjacent fluid parcels is done at rates consistent with the prevailing diffusion time scales. We present an overview of the HiPS model for the simulation of passive scalar mixing and show the generated scalar power spectra with forced turbulence. Additionally, preliminary results for the mean square displacement and scalar dissipation rate will be presented as well as a model extension to account for variable Schmidt number effects.

Keywords: differential diffusion, hierarchical parcel swapping, HiPS, mixing model, passive scalar mixing

NOMENCLATURE

L_0	$[m]$	integral length scale
L_i	$[m]$	length scale of level i
L_η	$[m]$	Kolmogorov length scale
Re	[-]	Reynolds number
Sc	[-]	Schmidt number
Y	[m]	displacement
k_i	$[m^{-1}]$	wavenumber at level i
n	[-]	number of levels
u	[m/s]	velocity
χ	[1/s]	scalar dissipation rate
ϵ	$[m^2/s^3]$	dissipation rate
Γ	$[m^2/s]$	scalar diffusion constant
ϕ	[-]	variable value
ϕ^{**}	[-]	variable value before a swapping event
ϕ^{*}	[-]	variable value after a swapping event
τ	$[s]$	time
τ_0	$[s]$	integral time scale
τ_i	$[s]$	time scale of level i
τ_{mix}	$[s]$	time since last mixing process

1. INTRODUCTION

Turbulent mixing plays an important role in our daily life and ranges, as [1] suggests, "from supernovae to cream in coffee". As of today, there is a large number of mixing models which can be found in the literature [2]. Most of them are formulated in the context of transported Probability Density Function (PDF) methods. The most distinctive representatives are the Interaction by Exchange with the Mean (IEM) model [3], the Euclidean Minimum Spanning Trees (EMST) model [4], Curl's model [5], and the Fokker-Planck type models [2].

The central challenge of these stochastic models is the representation of the mixing processes in a way that is computationally efficient, and which is able to retain a significant level of physics. The constraints for a good mixing model can be derived directly from the statistical analysis of the conditional fluctuating diffusion flux in the composition PDF transport equation, see [2]. Among others, we mention that the molecular mixing model must not modify the scalar mean $\langle\phi\rangle$, and yield the correct joint scalar dissipation rate $\chi_{\alpha\beta}$ (for scalars α and β). Additionally, [2] also lists some desirable properties for good mix-

ing models, among which we mention the bounding of scalars to the so-called allowable region (e.g. positivity), the locality of the mixing in composition space, dependence of the mixing rate on scalar length scales and the incorporation of parametric dependencies such as Reynolds *Re* and Schmidt number *Sc* dependencies.

In Curl's model [5], pairs of particles are randomly selected from an ensemble of particles and their compositions are fully mixed. An alternative to Curl's model is the IEM model [3] and the Linear Mean Square Estimation model (LMSE) [6]. In the IEM mixing model, all of the individual particles gradually evolve to an average state. In terms of desirable properties, Curl's and the IEM model have some serious limitations. The biggest deficiency of these models becomes apparent when considering reactive flows. The constraint that scalar mixing should be local in composition space is violated by both models [2]. The violation of the localness principle of Curl's model produces a discontinuous jump of the fluid-particle composition during a mixing event [2]. This is a clear limitation of the model and causes unphysical conditions in flame sheet simulations. Cold fuel can enter into regions of cold oxidizer without reacting. In reality, the fuel must pass the high temperature region of the flame sheet and is reacting before it can reach the cold oxidizer. The IEM mixing model also violates the locality principle, since it predicts that composition variables vary continuously in composition space under the influence of the mean composition. The Euclidean minimum spanning tree (EMST) mixing model is local in composition space and seeks to address the problems encountered in flows with simultaneous mixing and reactions [4]. However, as in Curl's and IEM mixing models, EMST does not address the problem of the dependency on scalar length scales directly. Note that [7] attempted to introduce length scale dependency in the IEM model by means of a spectral model for the scalar dissipation rate. However, this introduces additional modeling assumptions and complications.

The understanding of the construction mechanism of the PDF of scalar concentrations, and of its time evolution is vital [8]. As [8] explains, "history matters", in the sense that, stirring and diffusion being two distinctive phenomena, it is an urgent need to account for the advection of fluid parcels in the mixing modeling. Statistically, this is a multi-time or multi-point correlation for the diffusion and dispersion of individual fluid parcels [9]. Consider a key issue affecting the IEM and Curl's models: the fact that two fluid parcels that are relatively close to each other are generally in a similar chemical composition state. How can it be that these two parcels are in relatively similar chemical composition if they never mixed before? Therefore, "history matters" [8, 9]. However, multi-point correlations are not considered in pure composition-space stochastic mixing models such as the Curl, IEM or EMST models.

At this point, the Hierarchical Parcel Swapping (HiPS) [10] model provides an efficient mixing model which is able to incorporates the correct physics, including the dynamics of the small scales in physical space. HiPS uses a hierarchical and stochastic mechanism of swapping fluid parcels to incorporate turbulence. Unlike other purely stochastic composition-space mixing models typically used in chemical reaction engineering, HiPS incorporates, by construction, multi-point or multi-parcel correlations. This will allow the understanding of issues such as scaling laws on different regimes of scalar turbulence, structure functions, high order statistics, as well as multi-point Lagrangian statistics.

HiPS as a flexible mixing model could be incorporated in the future as a closure for higher fidelity stochastic turbulence models, hybrid stochastic and Large Eddy Simulation (LES) approaches, or as a subgrid closure in hybrid LES or Reynolds-averaged Navier–Stokes (RANS) methods.

In this work, the functionality of a stand-alone HiPS formulation is first detailed. Preliminary results for passive scalar mixing with forced turbulence are shown. This includes the scalar power spectrum, the mean square displacement and the scalar dissipation rate. Additionally, a model extension of HiPS to take into account differential diffusion (variable Schmidt numbers) is given in the Outlook.

2. HIPS MODEL

HiPS was developed as a turbulent mixing model [10] by A.R. Kerstein. The core principle of HiPS is based on the representation of effects of turbulence on time-evolving scalar fields by a binary tree structure. Interestingly, this idea of the binary tree was postulated by Obukhov [11], according to his considerations on discrete models of turbulence. As in the discrete representation suggested by [11], dynamic parcels are tracked, allowing a consistent Lagrangian treatment. Variable values reside at the base level of the tree, the leaf level, which is a representation of the physical solution. An exemplary representation of the HiPS binary tree with 4 levels is detailed in Fig. 1a. Assuming that every node has exactly 2 children, there are 8 leaves at the leaf level. The number of levels n determines the number of leaves 2^{n-1}. In Fig. 1a, each leaf is understood as a fluid parcel and contains a variable value ϕ_α, where α is an index between 0 and 7. The variable values only reside at the base of the tree.

Every level i of the tree is associated with a specific length scale L_i and time scale τ_i. The length scale of a sub-node is simply half the length of the considered node, though other so-called scale reduction factors may be used. The associated time scales follow Kolmogorov's inertial range scaling law [12],

$$\epsilon \sim \frac{u^2}{\tau} \sim \frac{L^2}{\tau^3}. \tag{1}$$

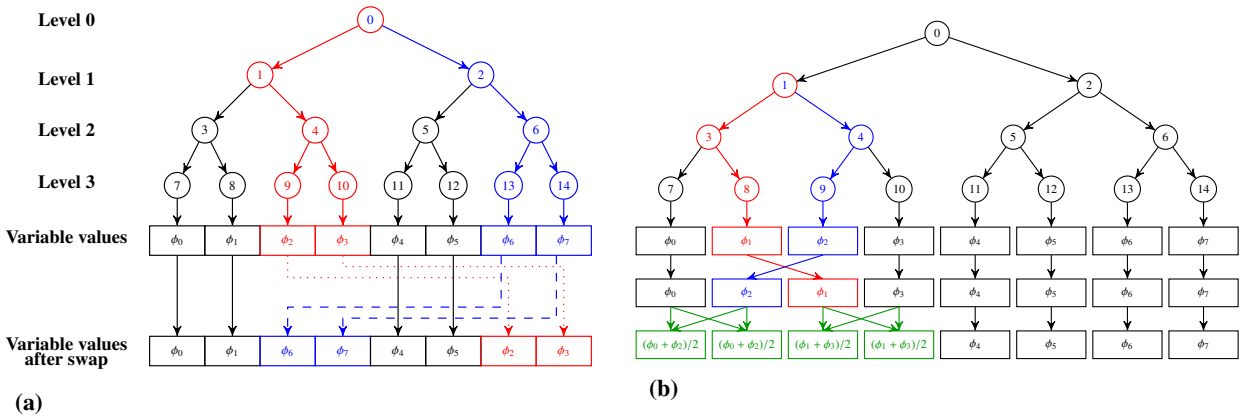

Figure 1. (a) Schematic illustration of a 4 level binary tree used in HiPS with a swapping event originated at node 0 with select grandchildren 4 and 6. (b) Schematic illustration of a swapping event originated at node 1 and a subsequent mixing process. The swapping event changes the proximity of adjacent fluid parcels and requires a subsequent mixing event, which is simply done by intermixing the contents of two adjacent fluid parcels.

In Eq. 1, u stands for the velocity and ϵ for the dissipation rate which is taken to be constant in the inertial range. Table 1 lists the length and time scales for an n level binary tree.

Table 1. Length and time scales of the binary tree used in HiPS.

level	length scale	time scale
0	L_0	τ_0
1	$L_0/2$	$\tau_0/2^{2/3}$
2	$L_0/4$	$\tau_0/4^{2/3}$
i	$L_0/2^i$	$\tau_0/(2^i)^{2/3}$
...	...	...
$n-1$	$L_0/2^{n-1}$	$\tau_0/(2^{n-1})^{2/3}$

The model rules for the representation of the effects of turbulence, which we will refer to as swapping events, are implemented by first selecting a grandparent node. A grandparent node is characterized by its children and grandchildren, such that only node 0 on level 0, as well as nodes 1 and 2 on level 1, can be considered grandparent nodes in Fig. 1a. The grandparent nodes are sampled in time as a Poisson process with a mean rate $\lambda_i = 2^i/\tau_i$, set by time scales assigned to each level i of the tree, based on Kolmogorov's inertial range scaling law [12],

$$\tau_i = \tau_0 \left(\frac{L_i}{L_0} \right)^{(2/3)} . \tag{2}$$

In this scaling law, L_0 and τ_0 are the integral length and time scales assigned to level 0 of the tree, and L_i and τ_i are the length and time scales of the i-th level of the tree. Based on Kolmogorov's hypothesis [13], the Reynolds number represented by the HiPS tree is defined by the tree size,

$$Re^{3/4} = \frac{L_0}{L_\eta}. \tag{3}$$

L_η stands for the Kolmogorov length scale, which is the length scale of the leaf level for the case of unity Schmidt number. The handling of variable Schmidt numbers is outlined in Section 4. After the grandparent node is selected, the swapping event is performed. For this purpose, a grandchild node is randomly selected from each of the left and right branches (children) of the grandparent node. The grandchildren of the grandparent node are then exchanged, or swapped along with their respective subtrees.

Fig. 1a shows this process at the selected parent node 0 with grandchildren 4 and 6. Note that nodes 3 and 5 could also have been selected as grandchildren. The exchange of fluid parcels taking place at the leaf level, the only physically relevant level of the tree, and the only level of the tree which is computationally stored, is an abstraction for the scale-reduction and advective rearrangement of fluid parcels in real turbulent mixing. Fluid properties stored at parcels located at the leaf level, undergo local modifications in their scalar gradients constructed from the discrete fluid properties stored at the leaf level. Considering one velocity component as a scalar, this would be the model analogy of increased strain due to turbulent advection. This complies with a local wavenumber increase, as in Kolmogorov turbulence [10].

The example in Fig. 1a shows a swap involving grandchildren at tree levels higher than the leaf level. Another situation occurs when the grandparent node 1 is selected, and, as an example, grandchildren nodes 8 and 9 are selected accordingly. The swapping event takes place at the leaf level, which corresponds to the smallest represented physical length scale. The parcel swapping changes the proximity within a fluid parcel pair and causes a mixing process. This is the case of Fig. 1b. A similar swapping event could occur if node 2 were selected as the grandparent node.

The mixing process, which is termed mixing

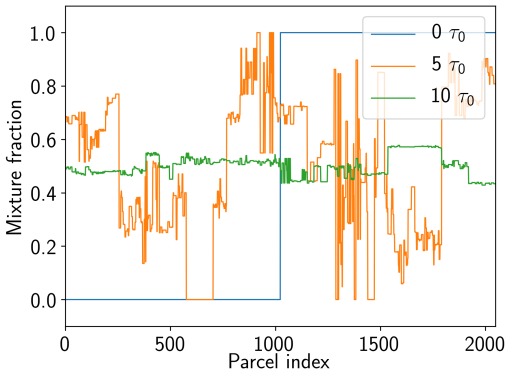

Figure 2. Illustration of passive scalar mixing in HiPS. The mixture fraction of the passive scalar is given at three different times along the fluid parcels.

event, is represented by intermixing the contents of two adjacent fluid parcels (constituting a node-joined pair). Mixing events can be implemented either instantaneously or at rates consistent with the prevailing diffusion time scales. Instantaneous mixing is a particularly efficient way to perform mixing. In the binary tree in Fig. 1a, an instantaneous mixing event would result in the scalar values of the adjacent parcels being replaced with the mean of the two parcels.

One salient feature of HiPS is that the mixing process itself is not restricted to a specific operation or rule. In [10, 14], and in the example presented in Fig. 1b, the mixing rule is equivalent to Curl's model. With this, HiPS effectively incorporates all features of Curl's model, plus the desired scale locality, representation of the correct joint scalar dissipation rate and the dependency of the mixing rate on scalar length scales. The mixing process could also be adapted to implement any existing mixing rule, e.g., IEM, without loss of generality. Additionally, the binary tree representation of the model allows the most efficient way to treat parcel advection from a computational point of view. That is, parcel movements can be simply represented by a bit shift in an index array pointing to locations in the various variable arrays. The efficient implementation of HiPS and its physical basis opens the door for the evaluation of higher order statistics in scalar turbulence in large parameter investigations, e.g., the skewness and hyperskewness of the scalar derivative required in order to discuss anomalous behavior of scalar structure functions [1].

In Fig. 2, the temporal evolution of a scalar mixing simulation is shown. The binary tree used for this simulation spans 12 levels. The plot illustrates the mixture fraction of the scalar against the fluid parcel indices. The scalar profile is initialized with a step function. All scalar values in the parcels at the left-hand sub-tree of the root node 0 are set to the value of 0 and all scalar values in the parcels at the right-hand sub-tree of the the root node 0 are set to the value of 1. This is indicated in Fig. 2 by the blue solid line ($0\tau_0$). At a later time ($5\tau_0$), the effects of the swapping and mixing events on the mixture fraction can be seen. The mixture fraction approaches the mean value of 0.5 with increasing time. After sufficiently long time ($>10\tau_0$), the flow is nearly mixed (approaching the mean value of 0.5) and only minute fluctuations can be seen compared to the orange curve ($5\tau_0$). After a time of $>30\tau_0$ (not shown here), everything is completely mixed and fluctuations can no longer be seen.

3. RESULTS

The following section shows preliminary results of a passive scalar mixing HiPS simulation. For all shown results, the same settings were used. The binary tree spans 16 levels with an associated Reynolds numbers of approximately one million. The represented Schmidt number is unity. This causes that the momentum and mass diffusivity is equal and the Kolmogorov and Batchelor length scales are located on the same level. In the Outlook, the treatment of variable Schmidt numbers is described. The scalar profile is initialized with a step function profile. All scalar values in the parcels at the left-hand sub-tree of the root node 0 are set to the value of 0 and all scalar values in the parcels at the right-hand sub-tree of the the root node 0 are set to the value of 1. The simulation considers turbulent forcing, which means that each time there is a top-level swapping event (swapping at grandparent node 0), a constant is added to the parcels in a given half of the domain so that their average is either 0 (left half) or 1 (right half). This turbulent forcing procedure doesn't change the overall mean and leaves the statistical variance of the subtrees unaffected.

3.1. Scalar spectrum

In HiPS, the generation of a scalar spectrum is not obvious and is reviewed in [10]. The tree structure induces a reduction of the length scales L_i with increasing levels i of the tree. Every step towards to the base of the tree results in an increase in the implied wavenumber $k_i = \frac{2\pi}{L_i}$. The mean variance across all sub-trees 2^i at a given level i is defined as $var_i\phi$, where ϕ denotes the scalar field. The HiPS analog of a scalar power spectrum can be calculated by $E(k) \sim \frac{1}{k_i}(var_{i-1}\phi - var_i\phi)$. In this context, $E(k)$ can be interpreted as scalar energy.

In Fig. 3a, the scalar power spectrum for passive scalar mixing with forced turbulence is shown. The dotted line marks the HiPS generated scalar power spectrum averaged over a time range of $100\tau_0$. The markers indicate the scalar $E(k)$ and the associated wavenumber k_i for the levels of the tree. A normalization with the maximum scalar energy E_0 and maximum wavenumber k_0 is carried out. For comparison purposes, the red line indicates a slope of -5/3 which represents the inertial power spectrum scaling

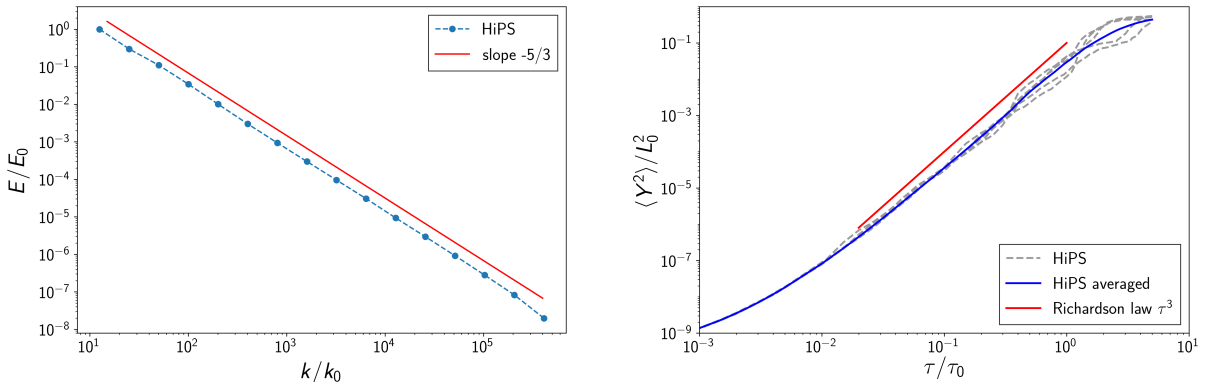

(a) **(b)**

Figure 3. (a) Scalar power spectrum of a passive scalar mixing HiPS simulation with forced turbulence using a step function initial condition (scalar value of 1 in all parcels at left-hand sub-tree and scalar value of 0 in all parcels of right-hand sub-tree). The dotted line shows the scalar power spectrum averaged over a time range of $100\tau_0$. The solid red line demonstrates -5/3 slope for comparison. (b) Mean square displacement of a passive scalar mixing HiPS simulation with forced turbulence. The blue solid line shows ensemble averaged HiPS results for the mean square displacement with a sample size of 100 realizations. The 5 gray dotted lines mark the mean square displacement for 5 independent HiPS realizations. The red solid line shows the Richardson-scaling law of τ^3 for comparison.

$E(k) \sim k^{-5/3}$. Fig. 3a demonstrates Kolmogorov's inertial range scaling law that is one of the core principles of HiPS. Additionally, the fundamental scaling relation in Kolmogorov turbulence of $E(k) \sim k^{-5/3}$ in the inertial range can be reproduced.

3.2. Richardson dispersion

The dispersion of particles under the influence of turbulence still poses challenges in fluid dynamics [15]. The dispersion describes how far initially adjacent particles are spatially separated from each other. Predictions for the dispersion under the influence of turbulence of particle pairs dates back to 1926 when Richardson [16] published an empirical approach where the mean square dispersion grows in time as τ^3.

In Fig. 3b, the mean square displacement $\langle Y^2\rangle$ versus time τ is presented for passive scalar HiPS simulations. A simple procedure to determine the dispersion Y of a parcel pair in HiPS is based on the length scale of the nearest shared parent. As in Fig. 1a shown, for the fluid parcels at nodes 9 and 10, the nearest shared parent has a length scale of L_2 (length scale of level 2). Similar to this procedure, for the fluid parcels at nodes 8 and 10, the nearest shared parent has a length scale of L_1 and for the fluid parcels at nodes 7 and 13, the nearest shared parent has length scale L_0.

In Fig. 3b, the mean square displacement $\langle Y^2\rangle$ is normalized by the square of the integral length scale L_0 and the time τ is normalized by the integral time scale τ_0. The blue solid line shows ensemble averaged HiPS results for the mean square displacement with a sample size of 100 realizations. The 5 gray dotted lines mark the mean square displacement for 5 different and independent HiPS realizations. The deviations of the gray lines from the blue line shows the randomness of the swapping events which is also influencing the mean square displacement. The red solid lines shows the Richardson-scaling law of τ^3 for comparison. It can be seen after a sufficiently long time the mean square displacement follows Richardsons dispersion law. Batchelor [17] predicted that the mean square displacement for times shorter than a characteristic timescale grows as τ^2. The characteristic timescale depends on the initial separation of the considered parcel pair. An investigation of the τ^2-scaling in HiPS is planned next. A finer temporal resolution of the initial phase and a wider range of length and time scales may be necessary for a detailed consideration of the Batchelor scaling. All in all, it is remarkable that such a simple and efficient mixing model is able to reproduce the Richardson dispersion law for the mean square displacement.

3.3. Scalar dissipation rate

The mixing of scalars in turbulent flows is a very interesting problem which provides a fundamental understanding of the basic processes involved. A key quantity in turbulent mixing that directly indicates the rate of decay of scalar fluctuations is the scalar dissipation rate χ.

The scalar dissipation rate is defined by [2],

$$\chi = \left\langle 2\Gamma \frac{\partial \phi'}{\partial x_i} \frac{\partial \phi'}{\partial x_i} \right\rangle \tag{4}$$

In Eq. 4, Γ is the diffusion coefficient of the scalar and $\frac{\partial \phi'}{\partial x_i}$ is the fluctuating scalar gradient. In

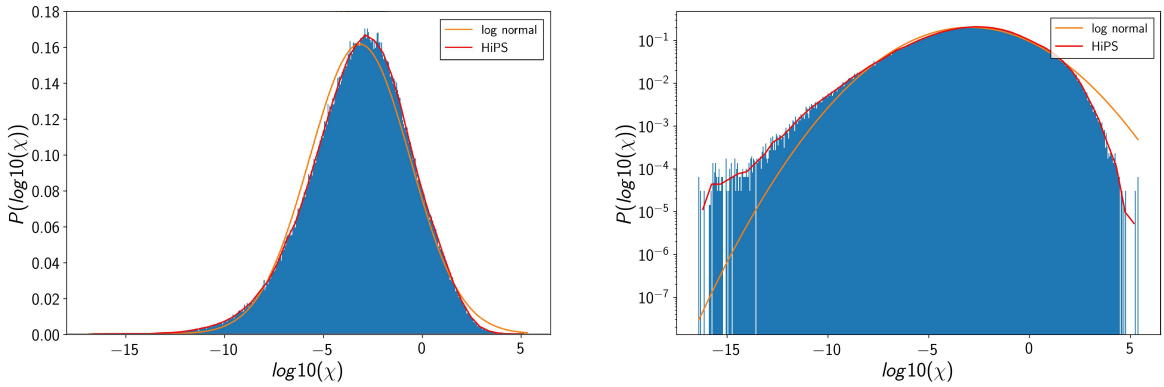

(a) **(b)**

Figure 4. (a) Probability Density Function (PDF) of the logarithmic scalar dissipation rate for a passive scalar mixing simulation in HiPS with a linear y-axis. The orange curve presents a normal distribution with the mean and standard deviation calculated from the HiPS results. (b) PDF of the logarithmic scalar dissipation rate for a passive scalar mixing simulation in HiPS with a logarithmic y-axis.

this context, ϕ is often taken as the mixture fraction. Since HiPS uses fluid parcels with proximities defined by the binary tree structure, a suitable formulation of the scalar dissipation rate in HiPS is needed. The definition of the scalar dissipation rate in HiPS is based on a similar scaling approach as in Eq. 1. For the diffusion coefficient $\Gamma \sim L^2/\tau$. The analogy to the fluctuating scalar gradient is given by the changes of the scalar field by the occurrence of swapping events. $\Delta\phi$ is computed by $\Delta\phi = \phi^{**} - \phi^{*}$. ϕ^{**} is the mixture fraction of the scalar before a swapping event and ϕ^{*} is the mixture fraction of the scalar after a swapping event.

This results in following relationship for the definition of the scalar dissipation rate in HiPS.

$$\chi = 2\frac{(\Delta\phi)^2}{\tau_{mix}} \tag{5}$$

In Eq. 5, τ_{mix} is the time since the last occurrence of a mixing process at the fluid parcel.

In Fig. 4a and 4b, the PDF of the log of the scalar dissipation rate is shown. For comparison purposes, a normal distribution with the mean and standard deviation calculated from the HiPS results is illustrated. Figs. 4a and 4b indicates that the commonly accepted log-normal distribution of the scalar dissipation rate χ is preserved. Additionally, HiPS exhibits a negative skewness in Fig. 4b, which is also seen in experiments and DNS [18].

4. OUTLOOK

In the current HiPS formulation, only unity Schmidt number passive scalars can be considered. This means that the Kolmogorov and Batchelor length scales are located on the same level. Arbitrary Schmidt number effects can be incorporated in the model by modifying the micromixing and swapping procedure, effectively allowing the creation of additional and intermediate levels in the binary tree. For the case of $Sc < 1$, the scalar has a very high diffusivity and the Batchelor length scale is larger than the Kolmogorov length scale. In this case, the mixing process can take place on levels above the leaf level (above the Kolmogorov scale).

The contrary is the case if $Sc > 1$. The diffusivity of the scalar is low and the Batchelor length scale is smaller than the Kolmogorov length scale. For the binary tree representation, this implies the existence of additional tree levels below the existing leaf level, which are turbulently advected, but only by swapping events with grandchildren on Kolmogorov or larger length scales. This implies that the nodes at these levels may be swapped as a consequence of a swapping event on upper tree nodes, but they can not be selected as children nodes themselves. Mixing processes, nonetheless, given by the set of mixing rules implied in the model, may still take place at these nodes below the leaf level.

The model extension for the treatment of variable Schmidt numbers opens the door for the investigation of differential diffusion effects, i.e., simultaneous mixing of scalars with different Schmidt numbers. Differential diffusion effects could be simulated in practice by specifying different mixing rules for each scalar in the binary tree. This allows investigation of multi-parcel correlations and scaling laws at very large or small Reynolds and Schmidt numbers.

5. SUMMARY

HiPS is a novel, computationally efficient and physics-based mixing model which at the same time fulfills constraints for good mixing models and several desirable properties of mixing models like locality of mixing in composition space, dependence of the mixing rate on scalar length scales and the incorporation of parametric dependencies such as Reynolds and Schmidt number dependencies. Additionally, the possibility to consider a large range of scales

while being computationally tractable is a significant advantage.

The results show noticeable agreement with known theories in passive scalar mixing. Given the simplicity of the model, a reproduction of the Richardson dispersion in passive scalar mixing and the preservation of a log-normal distribution of the PDF of the scalar dissipation rate are remarkable results. The extension to variable Schmidt numbers as described in the outlook is a necessary next step in the stand-alone HiPS formulation to investigate multi-parcel correlations and scaling laws at very large or small Reynolds and Schmidt numbers.

It is noted that HiPS has also been formulated as a turbulence model in [14], by means of the incorporation of momentum equations, and the use of a stochastic sampling procedure for swapping events analogous to the implementation of eddy events in the One-Dimensional Turbulence model [19]. A future application of HiPS could be the coupling with LES or RANS in a top-down or bottom-up approach, or by means of a sub-grid mixing model in PDF transport methods.

REFERENCES

[1] Sreenivasan, K. R., 2019, "Turbulent mixing: A perspective", *Proc Natl Acad Sci*, Vol. 116 (37), pp. 18175–18183.

[2] Fox, R. O., 2003, *Computational models for turbulent reacting flows*, Cambridge university press.

[3] Villermaux, J., and Devillon, J. C., 1972, "Représentation de la coalescence et de la redispersion des domaines de ségrégation dans un fluide par un modèle d'interaction phénoménologique", *Chem React Eng, Proc Int Symp, 2nd*, Vol. 2, pp. 1–13.

[4] Subramaniam, S., and Pope, S. B., 1998, "A mixing model for turbulent reactive flows based on Euclidean minimum spanning trees", *Combust Flame*, Vol. 115 (4), pp. 487 – 514.

[5] Curl, R. L., 1963, "Dispersed phase mixing: I. Theory and effects in simple reactors", *AIChE J*, Vol. 9, pp. 175–181.

[6] Dopazo, C., and O'Brien, E. E., 1974, "An approach to the autoignition of a turbulent mixture", *Acta Astronaut*, Vol. 1 (9), pp. 1239 – 1266.

[7] Tsai, K., and Fox, R. O., 1996, "Modeling the scalar dissipation rate for a turbulent series-parallel reaction", *Chem Eng Sci*, Vol. 51 (10), pp. 1929 – 1938.

[8] Villermaux, E., 2019, "Mixing Versus Stirring", *Annu Rev Fluid Mech*, Vol. 51 (1), pp. 245–273.

[9] Shraiman, B. I., and Siggia, E. D., 2000, "Scalar turbulence", *Nature*, Vol. 405 (6787), pp. 639 – 646.

[10] Kerstein, A. R., 2013, "Hierarchical parcel-swapping representation of turbulent mixing. Part 1. Formulation and scaling properties", *J Stat Phys*, Vol. 153 (1), pp. 142–161.

[11] Obukhov, A. M., 1983, "Kolmogorov flow and laboratory simulation of it", *Russian Mathematical Surveys*, Vol. 38 (4), pp. 113–126.

[12] Kolmogorov, A. N., 1991, "The local structure of turbulence in incompressible viscous fluid for very large Reynolds numbers", *Proc R Soc London, Ser A*, Vol. 434 (1890), pp. 9–13.

[13] Pope, S. B., 2011, *Turbulent Flows*, Cambridge University Press, 11th edn.

[14] Kerstein, A. R., 2014, "Hierarchical parcel-swapping representation of turbulent mixing. Part 2. Application to channel flow", *J Fluid Mech*, Vol. 750, pp. 421–463.

[15] Elsinga, G., Ishihara, T., and Hunt, J., 2022, "Non-local dispersion and the reassessment of Richardson's t3-scaling law", *Journal of Fluid Mechanics*, Vol. 932, p. A17.

[16] Richardson, L., 1926, "Atmospheric diffusion shown on a distance-neighbour graph", *Proceedings of the Royal Society of London Series A, Containing Papers of a Mathematical and Physical Character*, Vol. 110 (756), pp. 709–737.

[17] Batchelor, G. K., 1950, "The application of the similarity theory of turbulence to atmospheric diffusion", *Quarterly Journal of the Royal Meteorological Society*, Vol. 76 (328), pp. 133–146.

[18] Watanabe, T., and Gotoh, T., 2004, "Statistics of a passive scalar in homogeneous turbulence", *New J Phys*, Vol. 6, pp. 1–37.

[19] Kerstein, A., 1999, "One-dimensional turbulence: model formulation and application to homogeneous turbulence, shear flows, and buoyant stratified flows", *J Fluid Mech*, Vol. 392, pp. 277–334.

Conference on Modelling Fluid Flow (CMFF'22)
The 18th International Conference on Fluid Flow Technologies
Budapest, Hungary, August 30-September 2, 2022

IMPROVING THE INCOMPRESSIBILITY CONDITION OF THE EXPLICIT SPH METHOD USING THE CONTROL THEORY

Balázs HAVASI-TÓTH'[1],

[1] Corresponding Author. Department of Fluid Mechanics, Faculty of Mechanical Engineering, Budapest University of Technology and Economics. Bertalan Lajos u. 4 - 6, H-1111 Budapest, Hungary. Tel.: +36 1 463 2463, E-mail: havasi-toth.balazs@gpk.bme.hu

ABSTRACT

The conventional smoothed particle hydrodynamics (SPH) method is inherently an explicit scheme; the modeling of weakly compressible flows must imply an equation of state to link the mass density with the pressure. Unfortunately, the SPH scheme has an outstandingly high computational performance requirement, especially in the case of small time step sizes applied due to the large stiffness. Therefore in practice, the speed of sound is usually reduced artificially to meet the requirements of the given fluid flow problem in terms of the compressibility rate. Unfortunately, this approach still demands very low time step sizes in most cases. In this paper, we introduce an excessively simple improvement of the weakly compressible variant of the SPH scheme to achieve a considerably stiffer fluid without the demand for a smaller time step size and additional computational requirement. The present work's motivation was to eliminate the remnant density variance under constant pressure by introducing an integral and differential term in the equation of state analogously with ProportionalâĂŞIntegralâĂŞDerivative (PID) controls. The model was tested through simple two-dimensional hydrostatic and dam break cases.

Keywords: control theory, incompressibility, particle methods, smoothed particle hydrodynamics, SPH

NOMENCLATURE

K_d	$[m^2/s]$	Differential gain
K_i	$[m^2/s^3]$	Integral gain
K_p	$[m^2/s^2]$	Proportional gain
V	$[m^3]$	Particle volume
W	$[1/m^2]$	Smoothing kernel function
Δt	[s]	Time step size
c	[m/s]	Speed of sound
h	[m]	Smoothing distance
m	[kg]	Particle mass
n_b	[−]	Number of neighbours
p	[Pa]	Pressure
q	[−]	Dimensionless distance
$\underline{a}$	$[m/s^2]$	Particle acceleration
$\underline{g}$	$[m/s^2]$	Gravitational acceleration
$\underline{r}$	[m]	Particle position
$\underline{v}$	[m/s]	Particle velocity
γ	[−]	Specific heat ratio
ν	$[m^2/s]$	Kinematic viscosity
ρ	$[kg/m^3]$	Mass density
ρ_0	$[kg/m^3]$	Reference density

Subscripts and Superscripts

i	Index of the particle in interest
j	Index of neighbouring particles
n	Time level

1. INTRODUCTION

Smoothed Particle Hydrodynamics (SPH) is a Lagrangian particle-based meshless collocation scheme introduced by Gingold and Monaghan in 1977 [1] and independently by Lucy [2]. The motivation was the accurate modeling of self-gravitating interstellar gases without boundary conditions. Later, in 1994 Monaghan presented the simulation of coastal free surface flows using the SPH method [3], providing a novel approach of fluid flow modeling in the field of coastal engineering. Since then, SPH has been used successfully in many engineering and scientific areas of solid and fluid mechanics [4, 5, 6, 7, 8]. During the past decades, the conventional SPH method has been significantly improved in terms of the artificial diffusion [9, 10], adaptive spatial resolution [11, 12], and the treatment of undesired compressibility [13, 14].

Due to the lack of kinematic relation between the pressure and the velocity fields, the conventional explicit SPH scheme requires a suitable equation of state [13], that allows small density variations of fluids fulfilling the requirements of the given engineering problem. In most cases, the speed of sound is artificially reduced so that the density variance becomes larger than in real fluids but kept below a de-

sired threshold [15]. However, higher speed of sound results in stiffer systems with the need for smaller time step sizes, which is known to be a significant bottleneck of the weakly compressible variant of SPH.

Using the pressure projection method for incompressible fluids introduced in [16] is widely used in conventional computational fluid dynamics (CFD). Some of the earliest models of truly incompressible SPH (ISPH) schemes implying Chorin's decomposition were introduced and improved in the late 1990s and 2000s [17, 18, 19, 20, 21]. Although the ISPH scheme facilitates the modeling of incompressible fluid flows by avoiding the small time step size of weakly compressible models, the computational requirement per time step is significantly larger, not to mention the implementation issues that came with the semi-implicit solution of the elliptic pressure Poisson equation (PPE) over the continuously changing particle configuration [22].

Due to the large neighbourhood of each particle and changing interparticle distances, one of the drawbacks of the SPH method in general or other particle-based schemes is the high computational performance requirement, which made them too expensive for practical applications for decades. However, recently, the more and more frequent presence of massively parallel architectures made these methods more capable for the computations of some specific problems compared to the finite volume method (FVM) [23]. Although there are numerous techniques for the SPH scheme that imply the solution of the PPE, this approach is less straightforward than in the case of the mesh-based FVM. On the one hand, the assembly of the linear system of the PPE is computationally expensive due to the changing particle configurations, while on the other hand, the efficient solution of the sparse linear system is a challenging task on massively parallel devices. Due to the loss of efficient massive parallelization, the latter appears to be an essential difficulty of the ISPH method.

As an alternative approach, the recent advances made in ISPH computations are frequently subjects of techniques maintaining the explicit solution to utilise the massively parallel devices but reducing the compressibility rate or allowing larger time step size beside the same or smaller density variance. These methods are often referred to as explicit ISPH (EISPH) [22, 24, 25, 26]. Similarly to the truly incompressible SPH schemes, EISPH methods are based on Chorin's decomposition but avoid the solution of the PPE with a computationally intensive implicit algorithm such as the biconjugate gradient stabilized method (BiCGSTAB). Instead, they deal with iterative algorithms, which provide lower accuracy but cheaper solution at the same time.

In the present paper, we introduce a simple and efficient improvement of the weakly compressible SPH scheme allowing the simulation of incompressible fluids with a significantly reduced density error but without the direct or iterative solution of the PPE.

2. THE CONVENTIONAL SPH METHOD

As a fully meshless Lagrangian scheme, the convective and local terms of the changing of any quantity can be expressed by a single term as

$$\frac{d\varphi}{dt} = \frac{\partial\varphi}{\partial t} + \underline{v}\nabla\varphi, \tag{1}$$

where φ is any function and $\underline{v}$ is the velocity field. Using (1), an inviscid fluid is governed by

$$\begin{aligned} \frac{d\underline{v}}{dt} &= -\frac{1}{\rho}\nabla p + \underline{g} \\ \frac{d\rho}{dt} &= -\rho\nabla\underline{v}, \end{aligned} \tag{2}$$

where p and ρ are the pressure and density fields of the fluid and $\underline{g}$ is the gravitational acceleration. As a relation between the the density and the pressure fields, we apply a barotropic equation of state

$$p = p(\rho). \tag{3}$$

2.1. The numerical scheme

Similar to the Finite Difference Methods (FDM), the SPH scheme converts a set of partial differential equations (PDEs) to a larger set of coupled ordinary differential equations (ODEs). The coupling between the equations is determined by the interparticle interactions, where the particles are considered as the smallest and atomic volumes of the discretized matter.

A fundamental step in the discretization process is the choice of the discrete differential operators, to fulfill specific requirements such as conservativity or a given order of consistency. Using the discrete convolution

$$< f >_i = \sum_i^{n_b} V_j f_j W_{ij}, \tag{4}$$

where f is an arbitrary function over a set of particles, V_j is the volume of the jth particle and $W_{ij} = W(|\underline{r}_j - \underline{r}_i|, h)$ is the radially symmetric smoothing kernel function. Throughout the present paper we use the fifth order polynomial Wendland kernel function [27] defined in two dimensions as

$$\begin{aligned} W(|\underline{r}_j - \underline{r}_i|, h) &= \frac{7}{4\pi h^2}\left(1 - \frac{q}{2}\right)(2q+1), \\ q &= \frac{|\underline{r}_j - \underline{r}_i|}{h}, \end{aligned} \tag{5}$$

with h being the smoothing radius. After a few simple steps presented in [28], one can see that the derivatives of an arbitrary function can be approximated by replacing the derivative on the smoothing kernel function, hence we obtain

$$< \nabla f >_i = \sum_j^{n_b} V_j f_j \nabla W_{ij}. \tag{6}$$

However, the operator (6) turns out to be a bad choice

for most problems, due to the low order of consistency, the sensitivity to particle layout and the lack of conservativity. To address these issues, the fluid equations are usually discretized using the operators

$$
\begin{aligned}
(\mathrm{grad}p)_i &= <\nabla p>_i = \rho_i \sum_j^{n_b} \left(\frac{p_i}{\rho_i^2} + \frac{p_j}{\rho_j^2}\right) m_j \nabla W_{ij}, \\
(\mathrm{div}\underline{v})_i &= <\nabla \cdot \underline{v}>_i = \sum_j^{n_b} V_j (\underline{v}_j - \underline{v}_i) \nabla W_{ij},
\end{aligned}
\tag{7}
$$

for the pressure gradient and the divergence of the velocity [28]. Thus the discretized form of (2) yields

$$
\begin{aligned}
\frac{d\underline{v}}{dt} &= -\sum_j^{n_b} \left(\frac{p_i}{\rho_i^2} + \frac{p_j}{\rho_j^2}\right) m_j \nabla W_{ij} + \underline{g}, \\
\frac{d\rho}{dt} &= -\rho_i \sum_j^{n_b} V_j (\underline{v}_j - \underline{v}_i) \nabla W_{ij}.
\end{aligned}
\tag{8}
$$

In the case of weakly compressible flows, the most frequently used equation of state is the Tait's equation written as

$$
p_i = \frac{c^2 \rho_0}{\gamma} \left(\left(\frac{\rho_i}{\rho_0} \right)^\gamma - 1 \right), \tag{9}
$$

where γ and ρ_0 are the specific heat ratio and the reference density respectively. For water, γ is often set to be 7, which results in a stiffer behaviour in terms of compressibility.

2.2. Integration in time

As a meshless particle based method, the discretisation (7) converts the governing PDE's into a set of ODE's, which can be solved by numerical integration. Here we use the velocity-Verlet scheme [29], which is expressed as

$$
\begin{aligned}
\underline{r}_i^{n+1} &= \underline{r}_i^n + \underline{v}_i^n \Delta t + \frac{1}{2} \underline{a}_i^n \Delta t^2, \\
\underline{v}_i^{n+1} &= \underline{v}_i^n + \frac{\underline{a}_i^n + \underline{a}_i^{n+1}}{2} \Delta t,
\end{aligned}
\tag{10}
$$

where the superscript n denotes the time level, $\underline{a}_i$ is the acceleration of the ith particle and Δt is the time step size. For the integration of the continuity equation we use the simple explicit Euler scheme:

$$
\rho_i^{n+1} = \rho_i^n + \left.\frac{d\rho}{dt}\right|_i^n \Delta t. \tag{11}
$$

The adaptive time stepping scheme applied in the present paper is written as

$$
\Delta t = CFL \cdot \min\left(\sqrt{\frac{h}{\max_i |\underline{a}|_i}}, \frac{h}{c} \right), \tag{12}
$$

where $CFL = 0.2$ is the Courant-Friedrichs-Lewy number.

3. MODIFIED EQUATION OF STATE

Apart from a few exceptions, the objective of liquid simulations in SPH reads as

$$
\mathrm{div}\underline{v} = 0. \tag{13}
$$

Unfortunately, the application of the equation of state (9) results in a remnant density deviation even in the case of hydrostatic problems. The reason is that the interparticle pressure forces can be considered as spring forces with complicated spring coefficients deduced from the equation of motion. Although the desired density field is

$$
\rho_i = \rho_0, \tag{14}
$$

it can never be reached using (9), because the corresponding pressure vanishes. This problem is in strong analogy with a simple mass-spring system, where the spring has to be deformed to compensate any constant forces acting on the mass, leading to a remnant offset of the position. It is obvious that the offset can be reduced by increasing the spring coefficient, but it cannot be eliminated without knowing the history of the motion.

One of the simplest techniques for the elimination of the remnant offset is the application of a controller with an integration term. Let us consider an error $\epsilon(t) = \phi(t) - \phi_0$, where ϕ_0 is the desired value for $\phi(t)$. The output of a PID-controller to minimise $\epsilon(t)$ can be written as

$$
u(t) = K_p \epsilon(t) + K_i \int_0^t \epsilon(\tau) d\tau + K_d \frac{d\epsilon(t)}{dt}, \tag{15}
$$

where the K coefficients are the proportional, integral and differential gains (cf. [30]). After rewriting (15) for the density and pressure, we obtain

$$
p_i = K_p(\rho_i - \rho_0) + K_i \int_0^t (\rho_i - \rho_0) d\tau + K_d \left.\frac{d\rho}{dt}\right|_i. \tag{16}
$$

It is worth remarking that the first term is identical with the right-hand side of the conventional SPH equation of state (9) when $\gamma = 1$ and $K_p = c^2$. The second term accumulates the density deviation in time and tunes the pressure value so that the density error becomes smaller. Finally, using (2) and the third term of (16) pressure gradient

$$
(\mathrm{grad}p)_i = \mathrm{grad}(\mathrm{div}\underline{v})_i \tag{17}
$$

becomes a bulk viscosity term. This term might also be used as an artificial viscosity in the momentum equation without the computation of any other particle interaction operator. Since the computation of the artificial viscosity proposed by Morris [31] can be eliminated, the computational cost per time step can be significantly reduced.

3.1. Setting the gain coefficients

For the sake of simplicity, we set the proportional term to be the same as in Tait's equation (9). However, to ensure numerical stability and efficiency in terms of density variance reduction, we propose

the gains for the integral and differential terms as

$$K_i = 0.001c^3/h, \qquad K_d = ch \tag{18}$$

which provide numerically stable simulation regardless of the particle size and artificial speed of sound. Thus the complete equation of state reads as

$$p_i = \frac{c^2\rho_0}{\gamma}\left(\left(\frac{\rho_i}{\rho_0}\right)^{\gamma} - 1\right) + \frac{c^3 h}{10^3}\int_0^t (\rho_i - \rho_0)d\tau + ch\left.\frac{d\rho}{dt}\right|_i, \tag{19}$$

where the numerical integration of the second term on the right hand side is computed using the explicit Euler scheme

$$R_i^{n+1} = R_i^n + \Delta t(\rho_i^n - \rho_0), \tag{20}$$

where

$$R_i^n \approx \int_0^{n\Delta t} (\rho_i - \rho_0)d\tau. \tag{21}$$

It can be seen that the pressure computed using the improved equation of state (19) does not require any significant additional operations. The temporal derivative of the density is computed in (8) regardless of the modification, while the integral term sums the error per particle without the computation of any particle interactions.

4. RESULTS

In this section, we present simple SPH benchmark cases using the conventional Tait's equation (9) and the modified equation of state (19), including the integral and differential terms.

4.1. 2D hydrostatic problem

The first test case has been chosen as the simplest verification of the improved model by monitoring the temporal density variation of the fluid and the steady-state density distributions compared to the conventional equation of state. The investigated hydrostatic problem is shown in Figure 1.

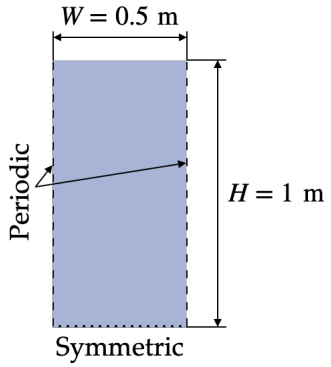

Figure 1. Geometry of the hydrostatic problem. The boundary conditions are periodic at the vertical and symmetric at the bottom boundaries.

The initial condition of the discretisation is chosen to be a relaxed particle layout but with a spatially constant density distribution $\rho = \rho_0$. As a weakly compressible fluid, the density distribution changes in time due to the gravitational forces until a steady-state is reached, when the weight of the liquid and the pressure forces counterbalance each other. The time series of the average density in the case of the original and improved models can be seen in Figure 2. The oscillations of the density are similar; however, the improved equation of state provides a more accurate steady-state density with virtually zero deviation from the reference density. The spatial distributions of the density and pressure are shown in Figure 3. As expected, the pressure distributions are similar, but the densities are different. This is because the density and pressure fields are no longer in total correspondence with the novel equation of state. Using the integral term in (19) the density becomes constant in case of a hydrostatic problem. However, the modified equation of state is accountable for the small fluctuations in the pressure distribution caused by the slightly less uniform particle layout of the hydrostatic case.

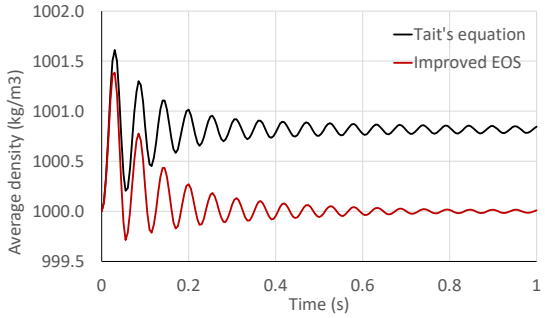

Figure 2. Time series of the average density in case of *a*. Tait's equation and *b*. the improved equation of state (EOS).

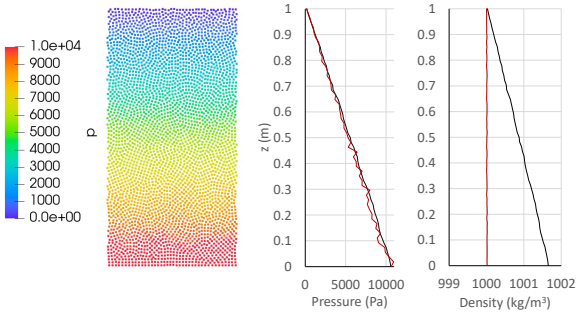

Figure 3. Density and pressure distributions along the vertical axis. Black and red lines show the distributions obtained from the original and modified equation of states respectively.

4.2. 2D dam break

The dam break problem is one of the most frequently referred benchmark cases of the SPH method. Here we present the results of a two-

dimensional case adopted from the DualSPHysics examples [32]. The geometry and the initial layout are presented in Figure 4. The fluid column is initially at rest at the bottom left corner and released at $t = 0$. Like the hydrostatic case, we performed the computations with both the conventional and the improved equation of states. The total number of particles was 21000, while the average time step size was $4.741 \cdot 10^{-5}$ s in both cases, resulting in the same computational time. In Figure 5, the time series

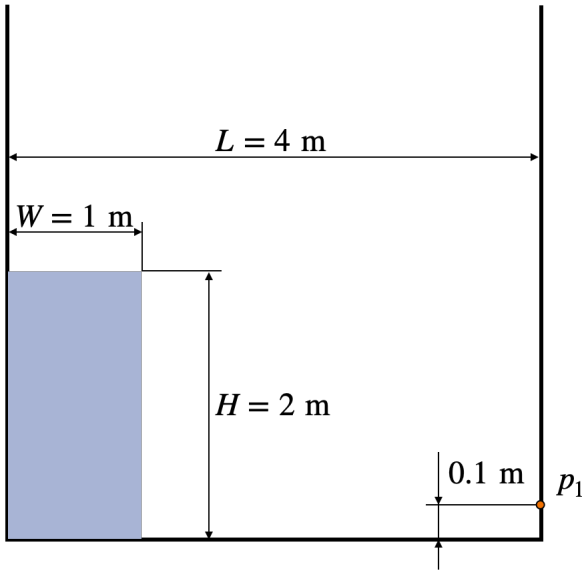

Figure 4. Initial layout of the dam break problem. The p_1 point marks the location of the pressure probe.

of the pressure at the p_1 probe shows that the original and the improved model are in good agreement. However, as expected, due to the additional integral term in (19), the proposed scheme provides consistently higher pressure values at the wall in order to force the density values closer to the reference density. The same behaviour can be observed in terms of the global average of the density in Figure 6. Although the qualitative behaviour is similar, the density approaches the reference value more accurately than the original simulation. The instantaneous

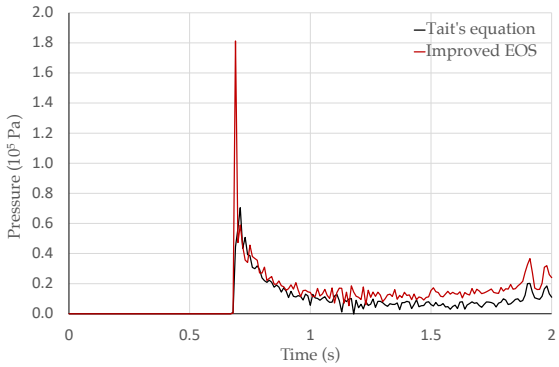

Figure 5. Pressure time series at point p_1.

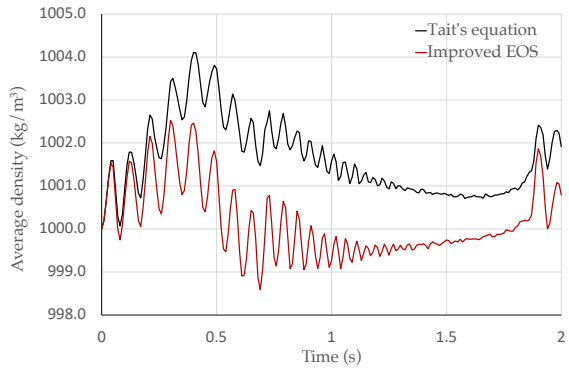

Figure 6. Average density of the fluid particles in the function of time.

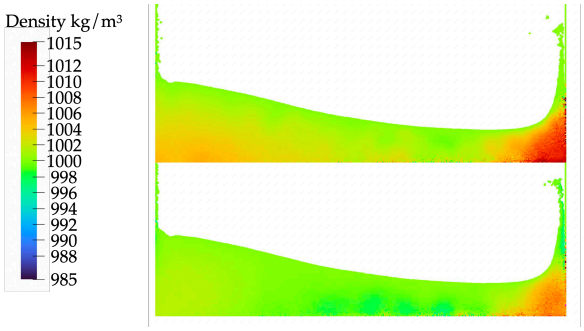

Figure 7. Instantaneous density distribution of the fluid after the collision with the right hand side of the tank wall at t=0.8 s. Top: Tait's equation, bottom: Modified eqaution of state.

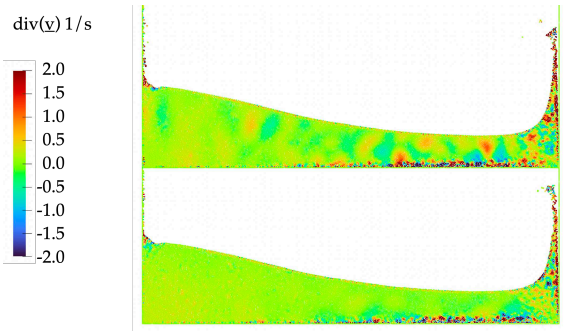

Figure 8. Divergence of the velocity at t=0.8 s. Top: Tait's equation, bottom: Modified eqaution of state.

density distribution after the collision with the tank wall is shown in Figure 7. Another valuable marker of the incompressibility is the divergence of the velocity field, which is presented at the same time instant in Figure 8. Apart from the near-wall fluctuations, it can be seen that the oscillations with long wavelengths are almost completely eliminated in the fluid. Although the constant density and divergence-free velocity field cannot be achieved by an explicit scheme, both of them are significantly improved without any additional computational time.

5. CONCLUSIONS

Motivated by the PID control theory, the present paper introduces a simple improvement of the weakly compressible SPH scheme by implying an integral and differential term in the conventional Tait's equation of state. Since the additional terms only use collocation-dependent quantities that are already computed in most SPH solvers, the computational requirement of the proposed modification is negligible. We present the efficiency of the improvement by two simple test cases of a hydrostatic and a dam break problem. Although the simulations are not truly incompressible, as in the case of an ISPH technique, the density and velocity divergence fields are considerably closer to the desired distributions in both cases. Moreover, in the case of the hydrostatic problem, the fluid reaches the desired reference density over the whole fluid domain. Since the motion of the particles is dependent on the instantaneous local configuration, the model could be further improved by choosing the differential and integral gains adaptively.

ACKNOWLEDGEMENTS

The research reported in this paper and carried out at BME has been supported by the NRDI Fund (TKP2020 NC,Grant No. BME-NCS) based on the charter of bolster issued by the NRDI Office under the auspices of the Ministry for Innovation and Technology. The research reported in this paper is part of project no. BME-NVA-02, implemented with the support provided by the Ministry of Innovation and Technology of Hungary from the National Research, Development and Innovation Fund, financed under the TKP2021 funding scheme.

REFERENCES

[1] R.A. Gingold and J.J. Monaghan. "Smoothed particle hydrodynamics theory and application to non-spherical stars". In: *Mon. Not. R. Astron. Soc.* vol. 181 (1977), pp. 375–389.

[2] L.B. Lucy. "A numerical approach to the testing of the fission hypothesis". In: *Astron. J.* vol. 82 (1977), pp. 1013–1024.

[3] J.J. Monaghan. "Simulating Free Surface Flows with SPH". In: *J. Comput. Phys.* 110 (1994), pp. 399–406.

[4] D. Violeau et al. "Numerical modelling of boom and oil spill with SPH". In: *Coastal Engineering* 54.12 (2007), pp. 895–913.

[5] C. Altomare et al. "Numerical modelling of armour block sea breakwater with smoothed particle hydrodynamics". In: *Computers & Structures* 130 (2014), pp. 34–45.

[6] H.H. Bui et al. "Soil cracking modelling using the mesh-free SPH method". In: *arXiv preprint arXiv:1503.01172* (2015).

[7] R. Chen et al. "Applications of shallow water SPH model in mountainous rivers". In: *Journal of Applied Fluid Mechanics* 8.4 (2015), pp. 863–870.

[8] J.P. Gray, J.J. Monaghan and R.P. Swift. "SPH elastic dynamics". In: *Comput. Methods Appl. Mech. Eng.* 190 (2001), pp. 6641–6662.

[9] D. Molteni and A. Colagrossi. "A simple procedure to improve the pressure evaluation in hydrodynamic context using the SPH". In: *Computer Physics Communications* 180.6 (2009), pp. 861–872.

[10] M. Antuono et al. "Free-surface flows solved by means of SPH schemes with numerical diffusive terms". In: *Computer Physics Communications* 181.3 (2010), pp. 532–549.

[11] R. Vacondio et al. "Variable resolution for SPH in three dimensions: Towards optimal splitting and coalescing for dynamic adaptivity". In: *Computer Methods in Applied Mechanics and Engineering* 300 (2016), pp. 442–460.

[12] B. Havasi-Tóth. "Particle coalescing with angular momentum conservation in SPH simulations". In: *Computers & Fluids* 197 (2020), p. 104384.

[13] J.J. Monaghan and A. Kos. "Solitary waves on a Cretan beach". In: *Journal of waterway, port, coastal, and ocean engineering* 125.3 (1999), pp. 145–155.

[14] S. Shao and E.Y.M. Lo. "Incompressible SPH method for simulating Newtonian and non-Newtonian flows with a free surface". In: *Advances in water resources* 26.7 (2003), pp. 787–800.

[15] J.J. Monaghan. "Smoothed particle hydrodynamics". In: *Rep. Prog. Phys.* vol. 68 (2005), pp. 1–34.

[16] A.J. Chorin. "A numerical method for solving incompressible viscous flow problems". In: *Journal of computational physics* 135.2 (1997), pp. 118–125.

[17] S.J. Cummins and M. Rudman. "An SPH projection method". In: *Journal of computational physics* 152.2 (1999), pp. 584–607.

[18] R. Xu. "An improved incompressible smoothed particle hydrodynamics method and its application in free-surface simulations". PhD thesis. University of Manchester, 2010.

[19] A. Khayyer, H. Gotoh and S.D. Shao. "Corrected incompressible SPH method for accurate water-surface tracking in breaking waves". In: *Coastal Engineering* 55.3 (2008), pp. 236–250.

[20] X.Y. Hu and N.A. Adams. “An incompressible multi-phase SPH method”. In: *Journal of computational physics* 227.1 (2007), pp. 264–278.

[21] S.M. Hosseini and J.J. Feng. “Pressure boundary conditions for computing incompressible flows with SPH”. In: *Journal of Computational physics* 230.19 (2011), pp. 7473–7487.

[22] D.A. Barcarolo et al. “Adaptive particle refinement and derefinement applied to the smoothed particle hydrodynamics method”. In: *Journal of Computational Physics* 273 (2014), pp. 640–657.

[23] S. Li and W.K. Liu. *Meshfree particle methods*. 2007.

[24] E. Daly, S. Grimaldi and H.H. Bui. “Explicit incompressible SPH algorithm for free-surface flow modelling: A comparison with weakly compressible schemes”. In: *Advances in water resources* 97 (2016), pp. 156–167.

[25] M. Bayareh et al. “Explicit incompressible SPH algorithm for modelling channel and lid-driven flows”. In: *SN Applied Sciences* 1.9 (2019), pp. 1–13.

[26] D. Morikawa, H. Senadheera and M. Asai. “Explicit incompressible smoothed particle hydrodynamics in a multi-GPU environment for large-scale simulations”. In: *Computational Particle Mechanics* 8.3 (2021), pp. 493–510.

[27] H. Wendland. “Piecewise polynomial, positive definite and compactly supported radial functions of minimal degree”. In: *Advances in computational Mathematics* 4.1 (1995), pp. 389–396.

[28] D. Violeau. 2012.

[29] L. Verlet. “Computer" experiments" on classical fluids. I. Thermodynamical properties of Lennard-Jones molecules”. In: *Physical review* 159.1 (1967), p. 98.

[30] Gene F. Franklin, J. David Powell and Abbas Emami-Naeini. *Feedback Control of Dynamic Systems (8th Edition) (What’s New in Engineering)*. Pearson, 2018.

[31] J.P. Morris, P.J Fox and Y. Zhu. “Modeling low Reynolds number incompressible flows using SPH”. In: *Journal of computational physics* 136.1 (1997), pp. 214–226.

[32] A.J.C. Crespo et al. “DualSPHysics: Open-source parallel CFD solver based on Smoothed Particle Hydrodynamics (SPH)”. In: *Computer Physics Communications* 187 (2015), pp. 204–216.

Conference on Modelling Fluid Flow (CMFF'22)
The 18th International Conference on Fluid Flow Technologies
Budapest, Hungary, August 30 -September 2, 2022

NUMERICAL ANALYSIS OF THE FLOW BY USING A FREE RUNNER DOWNSTREAM THE FRANCIS TURBINE

Alin BOSIOC[1], Raul SZAKAL[2], Adrian STUPARU[3], Romeo SUSAN-RESIGA[4]

[1] Corresponding Author. Department of Mechanical Machines, Equipment and Transportation, Politehnica University Timișoara, Timișoara, Romania, E-mail: alin.bosioc@upt.ro
[2] Romanian Academy – Timisoara Branch, Bv. Mihai Viteazu, No. 24, Ro-300223, Timișoara, Romania. E-mail: raul.szakal@student.upt.ro
[3] Department of Mechanical Machines, Equipment and Transportation, Politehnica University Timișoara, Timișoara, Romania, E-mail: adrian.stuparu@upt.ro
[4] Department of Mechanical Machines, Equipment and Transportation, Politehnica University Timișoara, Timișoara, Romania, E-mail: romeo.resiga@upt.ro

ABSTRACT

Current requirements of the industrialized countries impose to use as much renewable energy as possible. One meaningful problem of renewable energy is that the produced power is fluctuating. Currently, the only available method for energy compensation in the shortest time is given by hydroelectric power plants. Instead, the hydroelectric power plants (especially the plants equipped with hydraulic turbines with fixed blades) are designed to operate in the vicinity of the optimum operating point with a maximum ±10% deviation. The energy market requires that hydraulic turbines operate in an increasingly wide area between -35 - 20% from the optimum operating point. Operation of hydraulic turbines far from the optimum operating point involves the appearing downstream from the turbine of a decelerated swirling flow with hydraulic instabilities (known in the literature as the vortex rope).

The main purpose of the paper is to investigate numerically a new concept by using a free runner downstream on the main hydraulic runner turbine more precisely in the draft tube cone. The free runner concept supposes that rotates at the runaway speed with vanishing mechanical torque. The main purpose is to redistribute between the shaft and the periphery the total pressure and the moment. Moreover, the free runner does not modify the operating point of the main hydraulic turbine runner.

Keywords: Free Runner Concept, Hydraulic Turbines, Numerical Simulation, LDA

NOMENCLATURE

V_m	[m/sec]	meridional velocity
V_u	[m/sec]	circumferential velocity
V_{ref}	[m/sec]	reference velocity

1. INTRODUCTION

In last decades, the market policy was focused on renewable energy development. The renewable energy (solar and wind) introduces a large fluctuating component in the electrical grid. As consequence, many hydroelectric power plants are operated at for flattening wind and solar power fluctuation [1]. While operated at off-design condition for grid services (part load and high load), hydraulic turbines with fixed blades experience an abrupt decrease in terms of efficiency [4]. An excess of residual swirl is ingested by the draft tube, downstream the turbine runner. The residual swirl that occurs at off-design conditions is a consequence of the mismatch between the flow generated by the wicked gates and the angular momentum extracted by the turbine runner [5]. The most harmful phenomena developed in the draft tube of hydraulic turbine are those at part-load operating conditions. At these regimes, the residual swirl ingested by de conical diffuser of the draft-tube leads to development of so-called vortex rope [6-10]. Vortex rope is a self-induced hydrodynamic instability which can be characterized by a well-defined predominant fundamental frequency. In general, the vortex ropes fundamental frequency varies 0.2 – 0.4 times of the turbine runner rotational frequency, Ciocan et al. [11]. The vortex rope leads to harsh pressure fluctuations that interrupts the safe operation of the hydraulic turbine [12-14]. Many approaches have been considered for mitigation the undesirable effect of the vortex rope or to deeply understand the flow behaviour. Both passive (not require auxiliary power) and active (require auxiliary power and control loop) technics were studied. One of the earlier passive techniques was proposed back

in 80`s by Thicke [15]. Later, many other passive technics as J-grooves mounted on the cone wall [16], fins [17], runner cone extensions [18], diaphragm mounted downstream the conical diffuser [19], radial protrusion of solid bodies [20], flow-feedback method [21] and stator mounted downstream the runner [22] were investigated. Active control technics as air or water injections through various zones of the hydraulic turbine [23-27] and magneto-rheological control technique [28, 29] were also investigated. However, both passive and active control technics have some advantages and drawbacks as presented by Kougias et al. [1]. Together with these control technics various measuring and observing systems were used to quantify the control technics impact on hydrodynamic phenomena developed in the conical diffuser. The most common type of investigations on the hydrodynamic flow filed generated at part load conditions are the pressure measurements at the wall of the conical diffuser and the 2D Laser Doppler Velocimetry (LDV) measurements. Besides these, high speed camera observations and 2D or 3D particle image velocimetry (PIV) were used. The 2D LDV systems is a non-invasive method that allow measuring the velocity profiles in the conical diffusers offering a wide image of the entire flow fields. In contrast, the tools used for measuring the pressure are hard to fit inside the flow and for this reason are often used at the wall of the conical diffuser [23, 30-32]. As consequence, the 2D LDV velocity profile together with the pressure measurements at the wall of the conical diffuser complete each other strengthen a solid base for a deeply understanding of hydrodynamic field in conical diffuser of hydraulic turbines operation at part-load condition. Hence, the two measuring systems are suitable to also investigate the impact of an approached control technique on the vortex rope and its effects.

The analysis combined with the numerical simulation is able to provide a full image of the flow from the hydraulic machinery. Accordingly, the paper presents and analyses the flow in the conical diffuser by combining the experimental investigation and the numerical simulation. The experimental investigations performed in this paper consist by measurements of velocity profiles with Laser Doppler Velocimetry (LDV) and pressure pulsations respectively. The numerical simulation performed in the paper, first is validated from the numerical simulation, and second the vortex rope is extracted for the investigated cases. From the experimental and numerical analysis, the new concept of the free runner mounted downstream the main runner is analysed.

2. EXPERIMENTAL SETUP

In order to analyse the decelerated swirling flow from the conical diffusers of the hydraulic turbines, can be used model turbines or surrogate model turbines. In our case, we have chosen a surrogate model – a swirl generator – capable to offer at the inlet in the conical diffuser a decelerated swirling flow similar with the flow outlet of a real hydraulic turbine, [26].

The swirl apparatus is mounted on an experimental test rig developed in the laboratory, which serves by investigating different control methods of diminishing the flow instabilities associated with the vortex rope. The swirl apparatus which is mounted on the main hydraulic circuit on the test rig has two main components: the swirl generator and the test section. The swirl generator has three components: the ogive, the stator and the main runner, which are mounted on a cylindrical Plexiglas section at an interior diameter of 0,150 m, as presented in Figure 1. The stator and the main runner generate at the inlet in the conical diffuser a rotating flow similar with the flow downstream of a Francis runner operated at 70% discharge from the nominal flow rate, [11].

Downstream the main runner, on the experimental test rig was mounted the free runner concept, see Figure 1 (right). The free runner concept supposes that rotates at the runaway speed with vanishing mechanical torque. The main purpose is to redistribute between the shaft and the periphery the total pressure and the momentum such that the flux of total pressure and the momentum are not altered. Moreover, the free runner does not modify the operating point of the main hydraulic turbine runner. The benefits of the free runner downstream the main runner turbine approach is:

i. reducing the pressure pulsations (synchronous or asynchronous) from the draft tube cone,

ii. optimal configuration for the swirling flow ingested by the draft tube cone,

iii. minimum draft tube losses and maximum pressure recovery.

The concept has been presented by Susan - Resiga et al. [5] by using a Francis turbine with tandem runners. Similar approach can be found at Gokhman [22] by using a stay apparatus downstream the Francis runner. The free runner concept (see the sketch in Figure 1) downstream the main turbine will add the required flexibility for the Francis turbine regulation and avoid the deterioration of hydraulic turbine components.

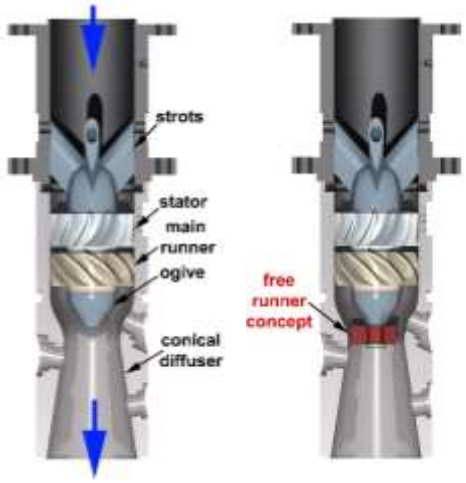

Figure 1. Swirl apparatus and the test section from experimental test rig. The original configuration (left) and the configuration with the free runner concept implemented on the test rig (right).

The main dimensions of the components from the swirl apparatus together with the dimensions of the free runner concept are presented in below table.

Table 1. Hydraulic parameters for the test rig components.

Parameter	Value	Unit
Nominal discharge Qn	0,03	[m^3/s]
Main runner - rotational speed n	940	[rpm]
Main runner - tip diameter D_t	0,150	[m]
Main runner - hub diameter D_h	0,06	[m]
Main runner - blade number z	10	[-]
Free runner - rotational speed n_{fr}	850	[rpm]
Free runner - tip diameter $D_{t\text{-}fr}$	0,100	[m]
Free runner - hub diameter $D_{h\text{-}fr}$	0,03	[m]
Free runner - blade number z_{fr}	3	[-]

During the measurements, the nominal discharge in the main hydraulic circuit was 0,03 m^3/s. The speed for the main runner was measured with the acquisition system existed in the laboratory, while the speed for the free runner was established with the help of the stroboscope.

3. NUMERICAL SETUP

The numerical domain was represented full 3D and consists of 5.8 million mixed cells. First the numerical results were obtained without taking into account the presence of the free runner, and after the vortex rope was developed, the free runner with three blades was activated.

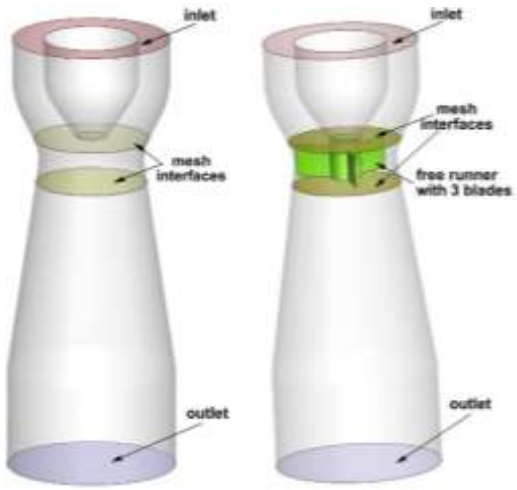

Figure 2. Full 3D domain: without free runner (left), with free runner (right)

The numerical simulation was performed with the help of ANSYS Fluent 2021R1. The unsteady solver was employed, together with the Generalised k-ω (GEKO) model for modelling the turbulence parameters. The velocity components together with the turbulence parameters, from the exit section of the swirl generator, obtained from experimental measurements, were imposed on the inlet boundary of the domain. On the outlet boundary the outflow condition was imposed. For all the wall boundary conditions the default set-up of the Fluent was retained, with No slip shear condition and standard roughness model, [33-34].

In order to compute the interaction between the rotating domain, containing the free runner with 3 blades, and the static domain, the sliding mesh technique was employed, and two mesh interfaces were defined with the matching option activated, upstream and downstream of the free runner. The rotational speed imposed on the rotating domain was 850 rpm, corresponds to the free movement of the runner and was experimentally determined.

To generate the vortex rope, first the presence of the free runner was "hidden" by defining the boundary condition on the blades as interior, and the volume was set as water. After the vortex rope was

generated, the free runner was activated by imposing the wall boundary condition on the blades, and the volume was set as solid.

As solution methods, the scheme of SIMPLEC was employed for computing the pressure-velocity coupling. The spatial discretization was set to Second Order Upwind for pressure, momentum and turbulence parameters and to Least Squares Cell Based for the gradient. The transient formulation was set to Bounded Second Order Implicit.

The time step was set as 0.001 seconds, corresponding to a movement of the free runner of approximately 5°, and 15 iterations were considered for each time step. The numerical simulation was carried out for a flow time of 4.458 seconds for the case without the free runner and for a flow time of 2.505 seconds for the case with the free runner.

4. VALIDATION OF THE RESULTS

A first step in the analysis of the new concept is the validation of the velocity profiles obtained from the 3D numerical simulation against the experimental results. The measurements have been validated in the convergent part of the test section on survey axis W0.

The comparison between the experimental analysis and the 3D numerical simulation, shows that the numerical results are in very good agreement with the experimental values. The comparison was focused on two velocity components: the meridional velocity and the circumferential velocity. Note that the experimental velocity components were used to validate the results from numerical simulations, not as boundary conditions

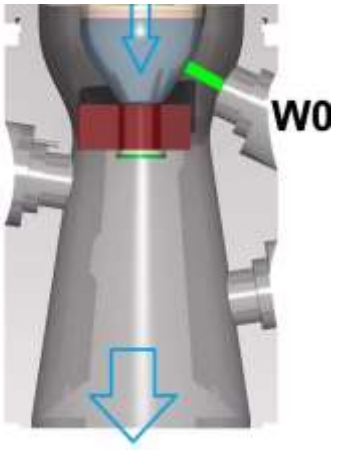

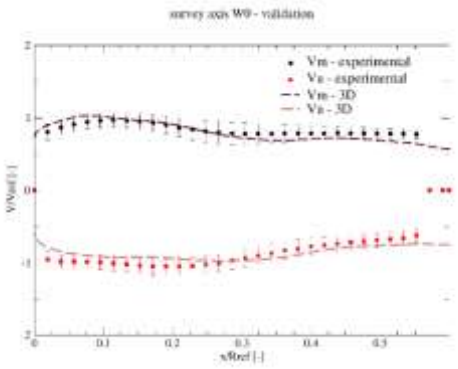

Figure 3. Validation of the velocities measured experimentally with the LDV on survey axis W0 with the velocity profiles obtained from the 3D numerical simulation

5. RESULTS AND ANALYSIS

Taking into account the good validation of the numerical investigation, a next step is the analysis of the flow and of the pressure from the numerical simulation for the investigated cases: without and with free runner. Figure 4 present the flow evaluation in the conical diffuser for both cases, by analysing the formation of the vortex rope. To visualize the vortex rope, a constant pressure iso-surface was plotted, with green colour, and the vortex cores of the flow filed were calculated and plotted, the red coloured spheres. The pictures show that the vortex rope is present in the conical diffuser in the case without free runner (left part of the images). Is forming close to the ogive and continues 2/3 from the length of the conical diffuser. When the free runner is inserted in the extension of the ogive, the vortex rope starts to diminish in length and thickness. Is forming at the end of the shaft of the free runner and continues approximately 1/3 from the length of the conical diffuser.

Formation of the vortex rope in the conical diffuser without free runner

Formation of the vortex rope in the conical diffuser with the free runner

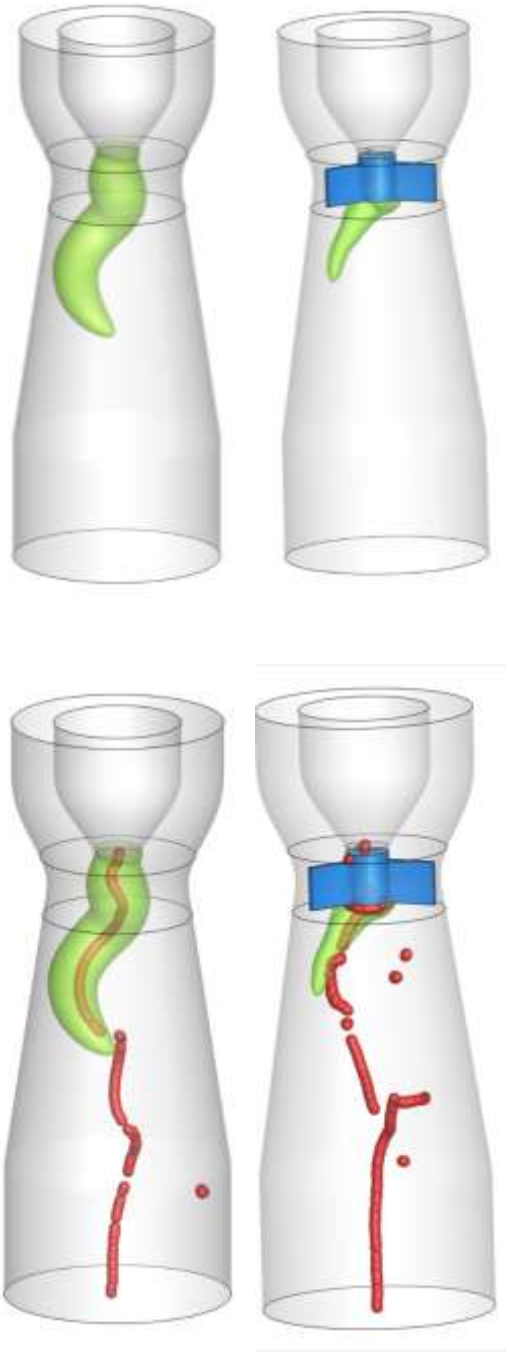

Figure 4. Visualisation of the vortex rope for the case: without and with free runner.

Another analysis consists on the evaluation of the unsteady pressure registered 100 mm downstream from the inlet in the conical diffuser, as shown in Figure 5. The unsteady pressure is registered from the numerical simulation and after was performed the FFT. The analysis of the FFT shows the main frequency of the vortex rope (15.6 Hz). In the case without free runner, the maximum amplitude reaches a value of 2000 Pa. When the free runner is introduced, the maximum amplitude reaches at a value of 1500 Pa, which it means a reduction of 25 %. Nevertheless, is pointed out that in this case is tested a simple free runner with only three straight blades.

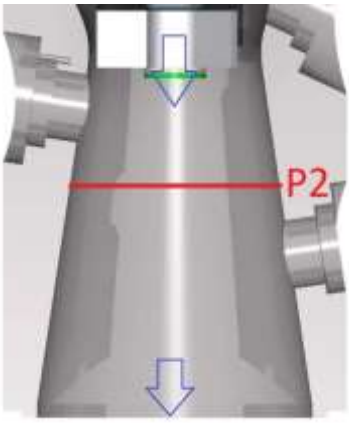

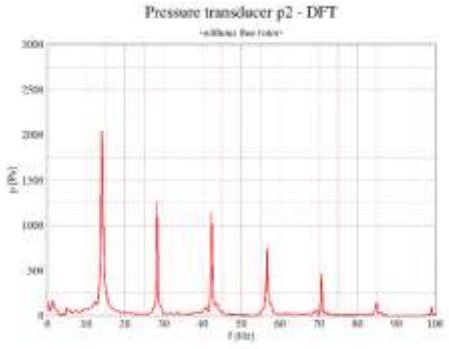

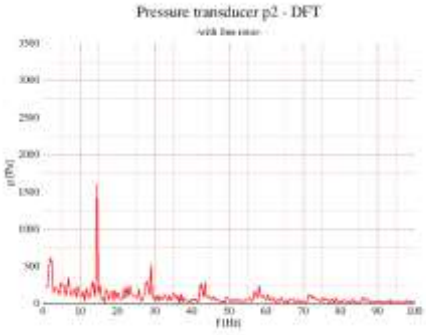

Figure 5. Evaluation of the Fourier transform on the point P2, 100 mm downstream of the inlet in the conical diffuser, for the cases without and with free runner from the numerical simulation.

6. CONCLUSIONS

The paper proposes a new method in order to increase the flexibility in operation for hydraulic turbines by using a free runner mounted downstream the main hydraulic runner. In doing so, on the experimental investigation and numerical simulation, was implemented the new concept. First, was tested a simple free runner, with three straight blades only. The ogive which closes the swirl generator, was modified such that the free runner can be attached and rotated freely with minimum friction. The measurements and the numerical simulation have been performed without and with free runner (at a speed of 850 rpm of the free runner). The vortex rope was evaluated from the 3D numerical simulation for both cases. It was observed clearly that when the free runner is installed, the vortex rope is diminishing in length and thickness. This conclusion can also be supported by the Fourier analysis of the unsteady pressure signals, when the amplitude diminishes with approximately 25% when the free runner is used. Nevertheless, the free runner concept investigated in this paper has used a simple runner with three straight blades only. The further investigations (free runner with more blades and hydrodynamically designed) which are in progress, will confirm that the new concept could reduce the unsteadiness produced by the vortex rope.

ACKNOWLEDGEMENTS

This work was supported by a grant of the Romanian Ministry of Education and Research, CNCS - UEFISCDI, project number PN-III-P1-1.1-TE-2019-1594, within PNCDI III. The second author acknowledge the support of the Romanian Academy – Timișoara Branch thru the research programs of Hydrodynamic, Cavitation and Magnetic Liquid Division from Center for Fundamental and Advanced Technical Research.

REFERENCES

[1] Kougias I., Aggidis G., Avellan F., Deniz S., Lundin U., Moro A., Muntean S., Novara D., Pérez-Díaz J.I., Quaranta E., Schild P., Theodossiou N., Analysis of emerging technologies in the hydropower sector, Renewable and Sustainable Energy Reviews 113 (2019) 109257.

[2] Iliescu M.S., Ciocan G.D., Avellan F., Analysis of the cavitating draft tube vortex in a francis turbine using particle image velocimetry measurements in two-phase flow, J Fluid Eng-T Asme 130(2) (2008).

[3] Neidhardt T., Magnoli M., Gummer J., High part-load fluctuations in Francis turbines and the applicability of model test data, 2017.

[4] Vu T.C., Retieb S., Accuracy assessment of current CFD tools to predict hydraulic turbine efficiency hill chart, Proceedings of the 21st IAHR Symposium on Hydraulic Machinery and Systems, Lausanne, Switzerland, 2002, pp. 193-198.

[5] Susan-Resiga R., Stuparu A., Muntean S., Francis turbine with tandem runners: a proof of concept, IOP Conference Series: Earth and Environmental Science 240 (2019) 022012.

[6] Kumar S., Cervantes M.J., Gandhi B.K., Rotating vortex rope formation and mitigation in draft tube of hydro turbines – A review from experimental perspective, Renewable and Sustainable Energy Reviews 136 (2021) 110354.

[7] Mohammadi M., Hajidavalloo E., Behbahani-Nejad M.J.J.o.F.E., Investigation on combined air and water injection in francis turbine draft tube to reduce vortex rope effects, 141(5) (2019).

[8] Pasche S., Avellan F., Gallaire F., Part Load Vortex Rope as a Global Unstable Mode, Journal of Fluids Engineering 139 (2017).

[9] Nicolet C., Zobeiri A., Maruzewski P., Avellan F., On the upper part load vortex rope in Francis turbine: Experimental investigation, IOP Conference Series: Earth and Environmental Science 12 (2010) 012053.

[10] Stuparu A., Resiga R., The Complex Dynamics of the Precessing Vortex Rope in a Straight Diffuser, IOP Conference Series: Earth and Environmental Science 49 (2016) 082013.

[11] Ciocan G.D., Iliescu M.S., Vu T.C., Nennemann B., Avellan F., Experimental study and numerical simulation of the FLINDT draft tube rotating vortex, J Fluid Eng-T Asme 129(2) (2007) 146-158.

[12] Cassidy J.J., Falvey H.T., Observations of unsteady flow arising after vortex breakdown, Journal of Fluid Mechanics 41(4) (1970) 727-736.

[13] Falvey H.T., Cassidy, J.J., Frequency and amplitude of pressure surges generated by swirling flows, International Association of Hydraulic Research Symposium on Hydraulic Machinery and System, Stockholm, Sweden, 1970.

[14] [14] Jacob T., Prenat J.E., Francis turbine surge: Discussion and data base, Hydraulic Machinery and Cavitation, Vols I and II (1996) 855-864.

[15] Thicke R.H., Practical solutions for draft tube instability, Water Power Dam Constructions 33(2) (1981) 31-37.

[16]Kurokawa J., Imamura H., Choi Y.-D., Effect of J-groove on the suppression of swirl flow in a conical diffuser, Journal of Fluids Engineering 132(7) (2010).

[17]Nishi M., Wang X., Yoshida K., Takahashi T., Tsukamoto T., An experimental study on fins, their role in control of the draft tube surging, Hydraulic machinery and cavitation, Springer1996, pp. 905-914.

[18]Qian Z.-d., Li W., Huai W.-x., Wu Y., The effect of runner cone design on pressure oscillation characteristics in a Francis hydraulic turbine, Proceedings of the Institution of Mechanical Engineers, Part A: Journal of Power and Energy 226 (2012) 137-150.

[19]Tănasă C., Bosioc A., Muntean S., Susan-Resiga R., A Novel Passive Method to Control the Swirling Flow with Vortex Rope from the Conical Diffuser of Hydraulic Turbines with Fixed Blades, Applied Sciences 9(22) (2019).

[20]Shiraghaee S., Sundström J., Raisee M., Cervantes M.J., Mitigation of Draft Tube Pressure Pulsations by Radial Protrusion of Solid Bodies into the Flow Field: An Experimental Investigation, IOP Conference Series: Earth and Environmental Science 774(1) (2021) 012004.

[21]Tanasa C., Susan-Resiga R., Muntean S., Bosioc A.I., Flow-Feedback Method for Mitigating the Vortex Rope in Decelerated Swirling Flows, J Fluid Eng-T Asme 135(6)(6) (2013) .

[22]Gokhman A., Hydraulic turbine and exit stay apparatus therefor, Patent US 6 918 744 B2, 2005.

[23]Kjeldsen M., Olsen K., Nielsen T., Dahlhaug O., Water injection for the mitigation of draft tube pressure pulsations, IAHR international meeting of WG on cavitation and dynamic problems in hydraulic machinery and systems, 2006.

[24]Adolfsson S., Expanding operation ranges using active flow control in Francis turbines, 2014.

[25]Blommaert G., Prenat J., Avellan F., Boyer A., Active control of Francis turbine operation stability, Proceedings of the 3rd ASME/JSME joint fluids engineering conference, 1999, pp. 1-8.

[26]Susan-Resiga R., Vu T.C., Muntean S., Ciocan G.D., Nennemann B., Jet control of the draft tube vortex rope in Francis turbines at partial discharge, 23rd IAHR Symposium Conference, 2006, pp. 67-80.

[27]Bosioc A.I., Susan-Resiga R., Muntean S., Tanasa C., Unsteady Pressure Analysis of a Swirling Flow With Vortex Rope and Axial Water Injection in a Discharge Cone, J Fluid Eng-T Asme 134(8) (2012).

[28]Bosioc A.I., Muntean S., Tanasa C., Susan-Resiga R., Vékás L., Unsteady pressure measurements of decelerated swirling flow in a discharge cone at lower runner speeds, IOP Conference Series: Earth and Environmental Science 22(3) (2014) 032008.

[29]Szakal R.A., Doman A., Muntean S., Influence of the reshaped elbow on the unsteady pressure field in a simplified geometry of the draft tube, Energies 14(5) (2021).

[30]Kirschner O., Ruprecht A., Göde E., Riedelbauch S., Experimental investigation of pressure fluctuations caused by a vortex rope in a draft tube, IOP Conference Series: Earth and Environmental Science 15(6) (2012) 062059.

[31]Bosioc A.I., Tanasa C., Muntean S., Susan-Resiga R.F., Pressure Recovery Improvement in a Conical Diffuser with Swirling Flow Using Water Jet Injection, P Romanian Acad A 11(3) (2010) 245-252.

[32]Kirschner O., Ruprecht A., Göde E., Experimental investigation of pressure pulsation in a simplified draft tube, (2009).

[33]Anton A.A., Reconstruction of a space-time window in a transient simulation of the breaking of a dam, P 6th IEEE Int Symp Applied Computational Intelligence and Informatics (SACI), (2011) 335-340.

[34]Anton A.A., Numerical Investigation of Unsteady Flows using OpenFOAM, Hidraulica, (2016) 7-12.

Conference on Modelling Fluid Flow (CMFF'22)
The 18th International Conference on Fluid Flow Technologies
Budapest, Hungary, August 30 -September 2, 2022

EFFECTS OF VALVE CHARACTERISTICS AND FLUID FORCE ON VALVE STABILITY

Gergely KESZTHELYI[1], Jürgen SCHMIDT[2], Jens DENECKE[3]

[1] Corresponding Author. CSE Center of Safety Excellence gGmbH. Joseph-von-Fraunhofer-Str. 9, D-76327 Pfinztal, Germany. Tel.: +49 721 6699 4837, E-mail: gergely.keszthelyi@cse-institut.de
[2] CSE Center of Safety Excellence gGmbH., e-mail: juergen.schmidt@cse-institut.de
[3] Hochschule Karlsruhe; CSE Center of Safety Excellence gGmbH. e-mail: jens.denecke@cse-institut.de

ABSTRACT

More than 10 models are available in the literature to protect emergency relief lines against valve instabilities and are proposed for the replacement of the 3% rule. They differ in assumptions and simplifications. Literature models to evaluate the stability of spring-loaded safety valves in gas service that can be used to predict an allowable inlet line length are classified, and a representative example of them is introduced more deeply to the readers.

The change in the fluid force acting on the disk is introduced, and two methods of modelling are shown, including measurement results from both literature and from the authors. The effect of the changing of the fluid force during the opening is described in relation to the models investigated, and it is shown that not all models are capable of taking the changes in the fluid force into account.

Two models are expanded to consider the effects of the changing fluid force during the opening of the valve and are compared to simulation results, which show that the expanded models are capable of predicting the effect of the change, unlike their original forms.

Keywords: chatter, fluid force, safety valve, valve instability

NOMENCLATURE

API	American Petroleum Institute	
A_{eff}	[m^2]	effective area
$\hat{A}_{eff}$	[m^2]	normalised effective area
F	[N]	force
L	[m]	inlet line length
a	[m/s]	speed of sound
c	[Ns/m]	damping
k	[N/m]	spring stiffness
m	[kg]	moving mass
$\dot{m}$	[kg/s]	mass flow
t	[s]	time
t_{open}	[s]	opening time
w	[m/s]	fluid velocity
x	[m]	current position of the disk
x_0	[m]	spring pre-compression
ρ	[kg/m]	density
θ	[°]	discharge angle
ω_n	[rad/s]	natural frequency

Subscripts and Superscripts

close	closed the safety valve
f	fluid
face	disk face
open	fully open safety valve
n	nozzle

1. INTRODUCTION

Safety valves serve the purpose of protecting against overpressure, and as such their stable operation is necessary for the safety of the protected system. Experimental evidence has shown that stable operation is not guaranteed in all conditions, and instability can appear in the forms of chatter and flatter [1].

One of the sources of these instabilities is the piping connected to the safety valve, especially the inlet line leading up to it. Models to avoid chatter caused by the inlet line have been researched since Sylvander and Katz's [2] initial research for the API in 1948. Their research has evolved into the three percent rule, which is currently in both the API 520 Part II [3] and ISO4126-9 [4] standards. This rule in its current form limits the non-recoverable pressure loss in the inlet line to three percent of the set pressure of the safety valve. It is based on steady state flow through the valve and was not originally intended to avoid dynamic instabilities.

Research into other methods of determining stability has been ongoing since the adoption of the

three-percent rule, with Darby [5] finding more than 50 publications regarding the stability of the safety valve. Even as many of these do not contain new stability models, or contain models that have been later on improved by their authors, the CSE Institute [6] has identified more than 10 stability models.

In this paper the scope of investigation is limited to models capable to size safety valves for gas service and that do not solve the whole transient movement of the safety valve. The latter means that there will be no Computational Fluid Dynamics (CFD) models reviewed, as they are typically too time consuming for industrial purposes.

2. MODEL DESCRIPTION AND COMPARISON

Models can be categorised based on the assumed source of the instability. Reviewing models from the last 30 years, four main categories of models have been identified:

Balance-based models are based on a pressure balance on the valve disk, consisting of the losses in the inlet line, the set pressure and the reseating pressure. The models of Singh [7] and Melhem's simple force balance [8] are examples of this category, along with of course the three-percent rule itself.

The *pressure wave* models limit the size of the initial waves in the system, based on either the reseating pressure or the set pressure. This category includes the pressure surge model of Frommann and Friedel [9], later improved by Cremers et al. [10].

Stability analysis models operate based on the assumption that a working point exists. A stability analysis in the complex frequency domain is then conducted to determine if the working point is stable. Such models have been previously created by MacLeod [11] and Kastor [12] back in the 80ies, and more recently by Izuchi [13].

The quarter wave model of Hős [14] models the pressure distribution according to the first harmonic of the system, and evaluates the system based on that.

All the models listed above except for the MacLeod model (which is for systems without an inlet line) share the assumption or have such a result, that safe operation of a safety valve can be secured by proscribing a maximum permissible inlet line length.

The various models within a category are rather similar, and as such only the most precise representative will be chosen from them. As such this paper will limit its scope the to the Melhem's [8] *simple force balance* method, the *improved surge model* by Cremers [10], the *Izuchi* model [13] and the *quarter-wave model* of Hős [14].

2.1 Basic equations of the system

The movement within the valve is modelled by all models as a simple spring-mass-damper system moved by the fluid force:

$$F_f = m \cdot \ddot{x} + c \cdot \dot{x} + k \cdot (x + x_0) \tag{1}$$

with x_0 being the length of spring pre-compression necessary for the valve to open at the given set pressure, and as such can be calculated from it. On the right side of the equation, the moving mass m and the spring stiffness k, while not directly available in the manufacturer's catalogues, can be measured directly, without mounting the safety valve on a test rig. The fluid force F_f and the damping c however are affected by many hard to measurable, or changing variables during even the installation, for example the damping containing the friction forces acting upon the disk or the spindle.

Another assumption shared between models is the size of the initial pressure wave in the system. E.g., in the pressure wave models, and some balance-based models, it is calculated as a Joukowsky shock wave, and its maximum value is:

$$\Delta p_{max} = \rho \cdot a \cdot w \tag{2}$$

with the ρ being the density in the upstream vessel, and a the speed of sound in the same location. w is the velocity of the fluid in the pipeline system, which is calculated from the mass flux flowing through the fully open safety valve.

The wave pressure considered to linearly increase with time, starting on the set pressure, up until reaching the return time of a wave in the inlet line. The return time is calculated as twice of the length of the inlet line L divided by the stagnation speed of sound in the upstream vessel. This means that at the time of the valve has fully opened, the wave pressure above the set pressure is:

$$\Delta p\left(t_{open}\right) = \Delta p_{max} \cdot \frac{t_{open}}{\frac{2 \cdot L}{a}} \tag{3}$$

The opening time is usually not provided by the manufacturer and can only be measured if the safety valve is connected to a system. To avoid this, various empirical correlations exist for the determination of the opening time [8].

2.2 Description of models

The *improved surge* model is based on limiting the initial Joukowsky wave of the opening to the difference between the set pressure and the blowdown. This is done by rearranging the terms found in Eqs. (2) and (3) to solve for the initial inlet line length. The model also provides an empirical method of calculating the opening time, which as

mentioned previously is not available in manufacturer catalogues.

The *simple force balance* method is based on calculating the pressures acting on the safety valve disk and comparing them to the blowdown pressure. Reaching the blowdown pressure, the valve is assumed to close. The included pressures are the set pressure, the back pressure, the pressure loss in the inlet line due to friction, and the wave pressure traveling through the inlet line with the speed of sound. As such, it includes more variables than the *improved surge* model, but as the wave pressure is significantly larger than the pressure loss, it is the more important factor in the stability, leading to both models dependent just on the initial wave, i.e., neglecting the frictional losses.

The *Izuchi* model is based upon on the wave equation for the pressure change in the inlet line, while neglecting the effects of the friction in the inlet line, and assuming the system is undamped. Based on this equation, combined with the spring-mass-damper equation seen in Eq. (1), a transfer function is created for the movement of internals in the safety valve. This transfer function is then used for a traditional stability analysis. The final formulation of the Izuchi equation published in [13] is:

$$L = \frac{\pi a}{2\omega_n \sqrt{\frac{x + x_0}{x}}} \tag{4}$$

where ω_n is the natural frequency of the safety valve, calculated as the square root of the spring stiffness divided by the mass considered to be moving. The lift of the safety valve is an input leading to an increasing maximum length with increasing lift. The lift is either calculated by assuming that the safety valve is stable, with the fluid force in Eq. (1) being in balance with the spring forces, or a full lift is assumed.

The *quarter wave model* has formulations of various complexity. Taking one that does not take into account the friction loss in the inlet line, and also assumes the system has no damping (which are assumptions shared with Izuchi), the following closed form equation can be derived:

$$L = \frac{\pi a}{2\omega_n \sqrt{2 \cdot \frac{x + x_0}{x} + 1}} \tag{5}$$

Note that even though the initial idea is different, the final forms of the equations are similar, only differing in constants in the divisor. This means that of these two models the *quarter wave* model will always predict a shorter allowable inlet line length.

3. CHANGES IN THE FLUID FORCE

The fluid force acting on the valve disk is changing during the opening of the safety valve and is the source of the pop opening of the safety valve. This variable is however otherwise not explicitly included in the models listed previously.

This means that the fluid force of Eq. (1) is not a constant force but varies during the opening of the safety valve. The change in fluid force is experimentally proven to be dependent on the valve type (e.g., disk geometry), the valve lift and as a minor effect on the pressure in the vessel and fluid properties. Physically, it is expected to be affected by the spindle friction, flow separation below the valve disk, fluid contraction and redirection within the valve, deflection angle of the fluid at the valve disk, turbulence and vortex creation in the valve housing and several other parameters.

Simplifying the effects on the fluid force, two main models of describing the change in force exist, the *discharge angle* and the *effective area*.

In the discharge angle model, the changes due to flow separation, contraction and redirection are modelled by an average angle representing the fluid force acting on the lower side of the disk. Such definitions of force were used by Singh [7], and most recently Darby [5], though with slightly different formulations. Using the formulation of Darby, the equation for the fluid force is described as:

$$F_f = (p_{in} - p_{back}) \cdot A_n + \\ + \dot{m}^2 \left(\frac{sin(\Theta)}{\rho \pi (x - x_0)} + \frac{1}{\rho \cdot A_{face}} \right) \tag{6}$$

where Θ is the angle between the horizontal and the direction of the fluid, A_n is cross sectional area of the nozzle, and A_{face} the area is the downward facing side of the valve disk,

To increase the precision of the model, a linear change in the discharge angle with valve lift is assumed, where the current angle can be calculated as a linear interpolation between the angles when the valve is closed and is fully open

$$\Theta(x) = \Theta_{closed} + \frac{x}{x_{max}} \cdot \left(\Theta_{open} - \Theta_{\text{closed}}\right) \tag{7}$$

With this linear correlation for the angle the correlation between the force and the lift is a part of a sinusoidal curve.

Another option is to define the force simply as the pressure difference between the pressures at the inlet and the outlet of the safety valve acting on a theoretical, so-called effective area. In this case the fluid force is defined as:

$$F_f = A_{eff}(x) \cdot (p_{in} - p_{out}) \tag{8}$$

with the effective area usually only considered dependent on the current position of the valve disk. To simplify comparisons, the effective area is often converted to a dimensionless variable by dividing it by the flow area of the nozzle:

$$\hat{A}_{eff}(x) = \frac{A_{eff}(x)}{A_n} \quad (9)$$

Herewith, relative effective areas are independent of the size of the safety valve.

The effective area contains all parameters not covered by the 1D ideal spring-mass system equation, as described above. Both the pressures, and the force acting on the disk can be directly measured, and hence the effective area may be deduced from experiments – at least under steady conditions. Generally, this are global measurements where the parameter affecting the relative effective area covered only implicitly.

An advantage of the model is that to calculate the lift of the stable solution, a single-variate ordinary equation can be written for the lift, by combining Eq. (1) in steady state with Eq. (8).

The relative effective area curve always starts at one as it is assumed that when the valve is closed, the forces directly act on the closed disk. To ensure a pop open, all other values of an effective area curve are taken larger than unity.

3.1. Measurements of the changing fluid force

An average discharge angle of the fluid below the valve disk is not provided by the manufacturers of safety valves. In the literature, such values were determined in dynamic experiments by Darby [15]. In his measurements, the Θ_{close} and Θ_{open} angles were obtained by fitting the measurement results to the equations, and assuming a linear change in discharge angle seen in Eq. (3).

As it can be seen in a visualisation of Darby's published measurement data [16] in Figure 1, the results are not conclusive, with the opening and closing angles being dependent not only on the set pressure, but also e.g. on the inlet line length.

This shows that the discharge angle varies with multiple parameters and is difficult for define for every specific valve size and type. Predictions, without a fit to measured values are not feasible.

The effective area is not included in the catalogues provided by the manufacturers, and there are few examples ([12],[13], [14]) in literature of it being depicted from experiments or simulated.

The earliest experimental determination of the effective area conducted by Kastor. A linear equation for the effective area was provided by the author in the appendix, along with the raw measurement data. Visualising the results, there is no real correlation, and the best linear fit had an $R^2 = 0{,}072$ error. This resulted in the author not using the linear fit due to its low accuracy, and instead opted for a constant value in their calculations.

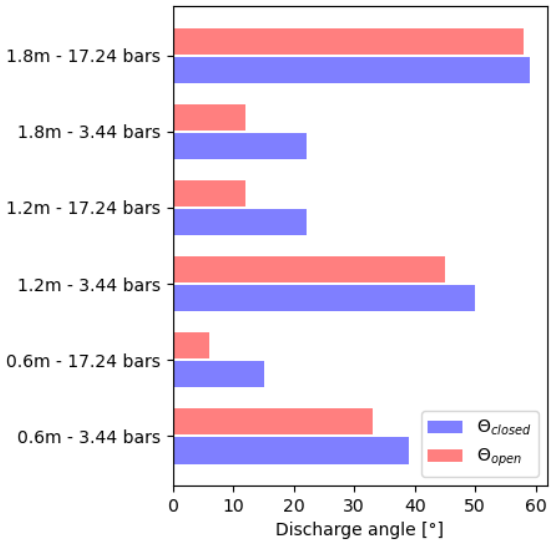

Figure 1. Discharge angles measured by Darby [16]

Izuchi [17] conducted his measurements with a removed spring, and a force measurement to determine the force acting on the disk, at fixed heights. The measurements were repeated with different fittings at the outlet of the safety valve, finding that the curve was highly dependent on the outlet size, with the effective area going below a value of one in case of large reducers.

Similar measurements [18] have also been conducted by the authors the at the CSE Test Loop on a DN25x40 European safety valve, using air as test fluid. In this these measurements, two set pressures (2 bar(g) and 10 bar(g)) and various backpressures, up to 60% of the set pressure were tested, going even beyond the back pressure allowed by the manufacturer.

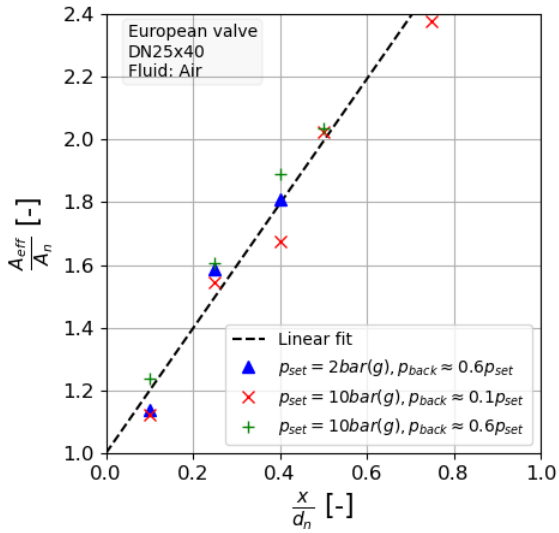

Figure 2. Effective area values measured at the CSE with different set and back pressures

The measurements were conducted with a steady flow, and a fixed lift of the valve disk, with the spring being removed, and replaced by a force sensor. It should be noted that during these kinds of measurements, the setup makes it impossible to measure the average fluid force at full lift, including the force acting on top of the disk in the valve housing.

In the measurements it was found that the effective area curve of the system developed from measurements was independent of both the back pressure of the system, and the set pressure, as the relative errors compared to the fitted curve lay below 16%, and the average error was below 10%. Some representative measurement data, along with the linear fit of the results can be seen in Figure 2.

The measurement results also line up with simple static, two-dimensional CFD simulations [19] conducted on the same valve geometry. Example results for simulations with different back pressures at 10 bar(g) set pressure can be seen in Figure 3, along with a second order fit. These simulations show good correlation with the measured results and were not dependent on the pressures the simulations conducted at. This is in line with the findings of Hős, who also had low variance in the effective area curves in his simulations.

None of the measurements or simulations of the effective area were conducted with a moving disk. This means that the measured values are possibly only approximations compared to a moving valve, as it could also be affected by other parameters, such as the speed of the disk. Further measurements need to be conducted to determine if the measurements with a fixed lift and a load cell are representative of the fluid force.

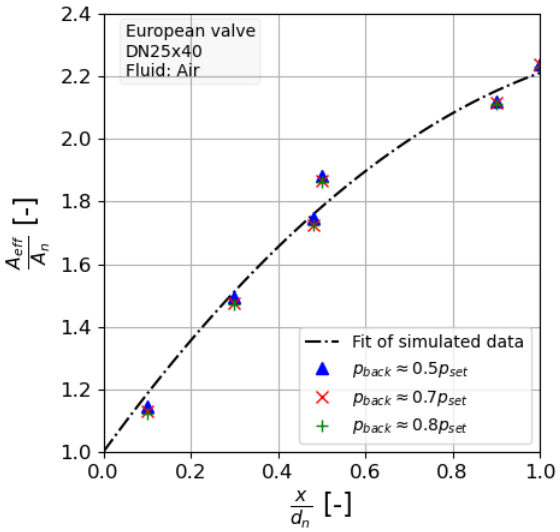

Figure 3. Results of two-dimensional CFD simulations with 10 bar(g) set pressure compared to the curve fitted on measurement values

As the effective area is more easily reproducible by measurements, and it has been used by authors whose models are being compared, it will be used further on as the model for the changing force of the fluid.

3.2. Effects of the changing fluid force on stability models

The change in fluid force depends mainly on two contradicting parameters - the enlargement of the area where the pressure acts on while opening the valve, and the decrease of the pressure below and the increase above the valve disk. At the beginning of the valve opening, the pressure decrease is dominating, hence, the fluid force typically decreases. With further increasing lift, the area increase becomes dominate and lead to larger fluid forces with lift. Typically, a fluid force curve is a 90° turned "s"-shaped to allow for an initially stable, proportional opening of the valve, where mainly spring and fluid forces are in equilibrium. Further opening to the so-called pop-point of the valve would lead to a tremendous excess force compared to the spring and a non-equilibrium of the forces pushing the valve disk to open. The acceleration of the moving masses in the valve heavily depends on the amount of excess force above the pop-point. The disk typically moves up either to a lift where forces become equal or to a geometrical lift limit, where the valve stays open. In case of a stable open of a safety valve, that is not at full lift, these fluid forces are in equilibrium with the spring force acting on the valve disk. Therefore, to properly predict the lift of a safety valve, it is important to know the forces acting on the valve disk.

In case the fluid force is calculated by the effective area model in a safety valve model, the relative effective area used must have values above one to explain the phenomena described in the previous paragraph. Calculating the opening with an effective area that is smaller than in reality would result in a partial opening of the safety valve.

The lift is a direct input for the *Izuchi* and *quarter wave models*, and as such the change of fluid force needs to be taken into account to determine this input parameter. An input of a smaller lift with these models predicts a shorter inlet line, meaning that using the maximum lift would not be conservative.

During the derivation of both models, the effective area was included during the initial phase of the derivations but was later simplified out. This means that both models can be revisited to include the relative effective area curves not just in the lift, but also as an input in itself. The Izuchi formulation in this case takes the form of:

$$L = \frac{\pi a}{2\omega_n \sqrt{\frac{x + x_0}{x} + 1 - \frac{\partial \hat{A}_{eff}(x)}{\partial x} \cdot x}} \tag{10}$$

The original paper [13] does not explain the reason for not including the additional term compared to Eq. (4). According to both personal correspondence with Izuchi, and the white paper of Melhem [20], the reason for the simplification was that the effective area curves were of a shape that the $\frac{\partial \hat{A}_{eff}}{\partial x} \cdot x$ part was close to unity at the full lift of the valve, allowing for a simplification of the equation.

During the derivation of the final formula of the quarter wave model shown in Eq. (5), the relative effective area was assumed to be equal to one, simplifying the calculations, which would not explain a real pop open of a valve. In case of continuing the derivation without this simplification, one arrives at the solution:

$$L = \frac{\pi a}{2\omega_n \sqrt{2 \cdot \frac{x + x_0}{x} \cdot \hat{A}_{eff} + 1}} \tag{11}$$

Note that the two calculation methods, even though they used the same inputs in their simpler forms, they use the effective area curves differently, with the *Izuchi* model using the derivative, and the *quarter wave* using the actual value.

To investigate the theoretical effects of the effective area on the calculated stability of safety valves, one-dimensional CFD simulations with various constant $\hat{A}_{eff}$ values ranging from 1.0 to 2.0 were carried out. The CFD simulations represent an precise solution of an ideal system without the simplifications made in the different models and may be taken to evaluate the assumptions and simplifications implicitly given in the models and also in the expended models seen in equations (10) and (11).

The CFD simulations were based on ideal gas with friction, using a Lax-Wendroff solver in the inlet line. The safety valve was modelled by solving Eq. (1) with a variable step Runge-Kutta method, and the fluid force was calculated using the effective area as described in Eq. (8). Choking was assumed in the smallest cross section in the safety valve to calculate the mass flow leaving the system. The vessel pressure was kept constant during the simulations. Inlet line friction was neglected.

The tested valve was a DN50x80 valve from a European manufacturer, with a nozzle diameter of 46 mm, and a maximum lift of 15.5 mm. This valve had been previously measured at the CSE Institute, and had allowable measurement length results for comparison [21], having started to chatter with an inlet line length of one meter. The released fluid was air at 5.8 bar(g) and 300 K.

The CFD simulations were run in 5-centimetre steps between 0.4 and 1.4 meters of inlet line length. As some simulations might be stable, even if a simulation with a lower line length was unstable, all simulation results are plotted, with the stable and unstable simulations being marked separately, a red plus, and a green x respectively.

The simulation results are compared against the compared to the expanded *Izuchi* and *quarter wave models* described in Eqs.(10) and (11). The lift as an input for these cases was calculated with the vessel pressure to keep with the assumption of the models regarding the lack of friction in the inlet line.

The results of the comparison can be seen in Figure 4. The simulations show that in case of a relative effective area of 1.6 and 1.8, there is an area of instability, but higher inlet line lengths were simulated as stable. Full lift was reached with a relative effective area of 1.8. This influenced the inlet line lengths calculated from the expanded *Izuchi* and *quarter wave models*. It is also the reason for the increase in the permissible inlet line in case of effective areas below 1.8, following the simulated trend.

After the full lift was reached, the predicted inlet line length of *quarter wave model* was decreasing as the effective area appears in the divisor for this model. This highlights, that even after reaching full lift, the chosen effective area model does have an effect on the allowable inlet line length predicted by the model.

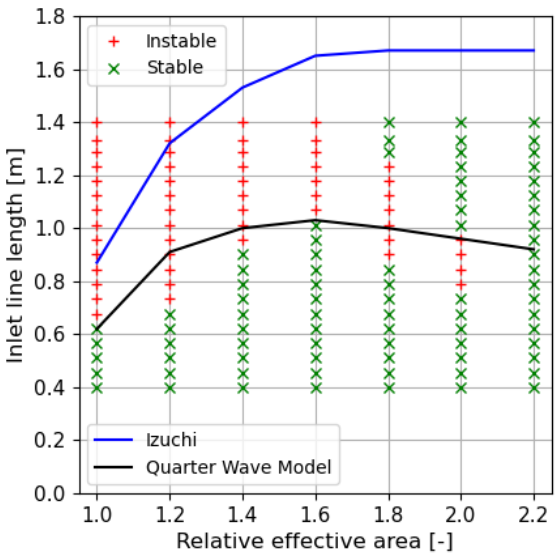

Figure 4. The allowable inlet lines according to the Izuchi and QWM models compared to one-dimensional simulations, with a constant effective area

To test the effect of different effective area curves, simulations and calculations with a constant effective area slope were also conducted, with the relative effective area curve taking the form:

$$\hat{A}_{eff}(x) = 1.0 + slope \cdot \frac{x}{x_{max}} \tag{12}$$

The slopes tested ranged from 0, to 1.0, meaning that the maximum dimensionless effective areas

ranged between 1.0 and 2.2, covering the same range as the constant effective areas in the simulations shown in Fig. 4. The maximum lift was reached with a slope of 0.8, after which the lift for the models was taken as the maximum available lift. The results of the simulations and the extended Izuchi and quarter wave models with an effective area changing linearly can be seen in Figure 5.

Noticeably, in this case, there are no simulations that predicted stable valve movement when a simulation with a smaller inlet line length predicted instability. The trends are similar as with the constant inlet line lengths, with larger effective areas meaning a stabler opening.

Note that in this case, both models predicted a lower allowable inlet line length as the maximum opening was reached. As the derivative of the effective area curve being calculated was positive, not only the *quarter wave* but also the *Izuchi* model decreased by higher effective areas, which appeared after full lift was reached.

The *simple force balance*, *pressure surge models* and the *three percent rule* were not compared to the simulations. These models evaluate the stability based on empirical relations at the nominal lift given by the manufacturer or are experimentally evidenced conventions like the three precent rule. A true lift based on the force balance on the valve disk is not considered.

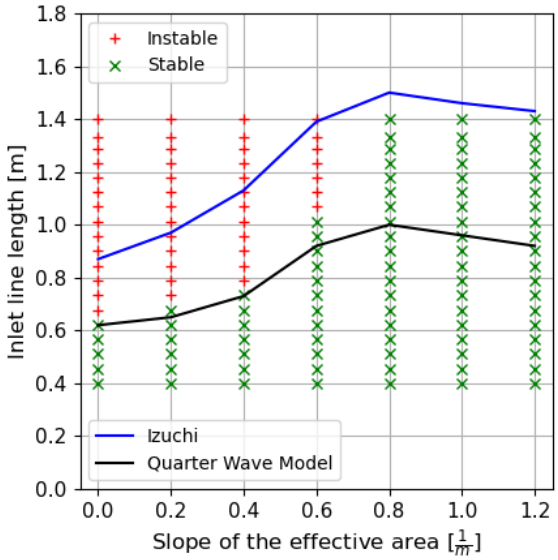

Figure 5. The allowable inlet lines according to the Izuchi and QWM models compared to one-dimensional simulations, with a linearly changing effective area

The results show that in general, a larger effective area increased the stability of the calculated system in the case of both the constant and the linearly changing effective area. This was the case even if full lift was reached, as the effective area or its derivative appear in the *quarter wave* and the *Izuchi* models respectively.

Looking at Figs. 4 and 5 in both cases the minimum length is reached at a constant relative effective area of one. In this case, the expanded *Izuchi* model would take a form similar to the one published in [13], but have an additional term of plus one under the square root in the divisor, predicting a lower inlet line length than the currently published model. In the case of a constant effective area of one, the *quarter wave* model would be unchanged, resulting in only one constant multiplicator difference for the two models.

Note however, that a relative effective area of constant one does not guarantee that the minimum predicted allowable inlet line length of the models will be minimal, that is also dependent on other parameters of the system such as the maximum lift, the set pressure and the spring stiffness. These results show that the effective area is a parameter that needs to be taken into account before calculating using these methods.

4. CONCLUSIONS

Four different categories of models have been introduced, with the classification based on the initial assumptions of the authors of models. A representative example of all four models has been sought out, and their working methods compared, highlighting the differences in their approaches.

The change in fluid force during the opening was introduced and shown to be a necessary component of the operation of pop open safety valves. Only three independent effective area measurements were found in literature however, and as such the parameter is deemed to be under investigated, and its dependencies on factors other than the lift have not been fully examined.

The ways it can affect the various stability models has been shown. The results showed that the *simple force balance*, *improved pressure surge* and the *three-percent rule* are all unaffected in their current formulations, as in the models a full lift is assumed during the calculation of the stability criterion.

The Izuchi and quarter wave however use the lift of the safety valve as an input parameter. Therefore, these models were expanded from their derivations to include the effective area, and using these forms, the effect of the effective area on their predictions were calculated and were compared to one-dimensional CFD simulations. The expansion of the *Izuchi* and *quarter wave models* managed to follow the trends that were simulated. These simulations have also shown that the effective area influences the calculated stability of the safety valve,

As such it can be determined that the changes in fluid force cannot be neglected and needs to be taken into account for the predictions to be precise. Further measurements are needed to determine if the effective area is dependent upon other parameters as well, or only the lift as it is currently assumed.

REFERENCES

[1] American Petroleum Institute (API), *Sizing , Selection , and Installation of Pressure-Relieving Devices in Refineries Part I — Sizing and Selection*, 6th ed., vol. 1, no. July 2014. 2014.

[2] N. E. Sylvander and D. L. Katz, "The Design and Construction of Pressure Relieving Systems," Ann Arbor, 1948. doi: 10.1038/087240a0.

[3] American Petroleum Institute (API), *Sizing, Selection, and Installation of Pressure-relieving Devices; Part II—Installation*, 6th ed., no. March. 2015.

[4] International Organization for Standardization, "ISO 4126-9 Safety devices for protection against excessive pressure - Application and installation of safety devices excluding stand-alone bursting disc safety devices," vol. 2008. 2008.

[5] R. Darby, "The dynamic response of pressure relief valves in vapor or gas service, part I: Mathematical model," *J. Loss Prev. Process Ind.*, vol. 26, no. 6, pp. 1262–1268, Nov. 2013, doi: 10.1016/j.jlp.2013.07.004.

[6] G. Keszthelyi, J. Schmidt, and J. Denecke, "Evaluation and comparison of safety valve chatter prediction models." *DIERS Spring meeting* 2021.

[7] A. Singh, "On the Stability of a Coupled Safety Valve-Piping system," in *Testing and Analysis of Safety / Relief Valve Performance*, 1982, pp. 29–37.

[8] G. A. Melhem, "Analysis of PRV Stability In Relief Systems Part II - Screening," Salem, 2016.

[9] O. Frommann and L. Friedel, "Analysis of safety relief valve chatter induced by pressure waves in gas flow," *J. Loss Prev. Process Ind.*, vol. 11, no. 4, pp. 279–290, Jul. 1998, doi: 10.1016/S0950-4230(97)00040-5.

[10] J. Cremers, L. Friedel, and B. Pallaks, "Validated sizing rule against chatter of relief valves during gas service," *J. Loss Prev. Process Ind.*, vol. 14, no. 4, pp. 261–267, Jul. 2001, doi: 10.1016/S0950-4230(00)00054-1.

[11] G. MacLeod, "Safety Valve Dynamic Instability: An Analysis of Chatter," *J. Press. Vessel Technol.*, vol. 107, no. 2, p. 172, 1985, doi: 10.1115/1.3264430.

[12] K. A. Kastor, "Chatter Instability of Spring Loaded Relief Valves," University of Delaware, 1986.

[13] H. Izuchi, "Stability Analysis of Safety Valve," *Proc. Dyn. Des. Conf.*, vol. 2008, no. 0, pp. 238-1-238–6, 2008, doi: 10.1299/jsmedmc.2008._238-1_.

[14] C. J. Hős, "Direkt rugóterhelésű biztonsági szelepek dinamikus viselkedése és stabilitása," Budapest University of Technology and Economics, 2019.

[15] A. A. Aldeeb, R. Darby, and S. Arndt, "The dynamic response of pressure relief valves in vapor or gas service. Part II: Experimental investigation," *J. Loss Prev. Process Ind.*, vol. 31, no. 1, pp. 127–132, Sep. 2014, doi: 10.1016/j.jlp.2014.06.002.

[16] R. Darby and A. A. Aldeeb, "The dynamic response of pressure relief valves in vapor or gas service. Part III: Model validation," *J. Loss Prev. Process Ind.*, vol. 31, pp. 133–141, Sep. 2014, doi: 10.1016/j.jlp.2014.06.001.

[17] H. Izuchi, "Chatter Of Safety Valve," *API 2008 Fall Meeting*. pp. 1–60, 2008.

[18] C. B. Dinh, "Modellentwicklung zur Untersuchung des Flatterns eines Sicherheitsventils," Hochschule Karlsruhe, 2021.

[19] S. Kempf and S. Kinalicukur, "Experimente zu Hubbegrenzung und Gegendruck," Hochschule Karlsruhe, 2020.

[20] G. A. Melhem, "PRV Stability Inlet Line Critical Length." Salem, pp. 1–11, 2021.

[21] J. Schmidt and J. Denecke, "European Program on Investigation of Valve Instabilities (EuroValve) Part I: Experimental investigation," *Joint US and European DIERS User Group Meeting* 2019.

Conference on Modelling Fluid Flow (CMFF'22)
The 18th International Conference on Fluid Flow Technologies
Budapest, Hungary, August 30 -September 2, 2022

DYNAMIC PRESSURE PROPAGATION IN PIPES: MODELLING AND MEASUREMENT

Goran PAVIĆ[1], Fabien CHEVILLOTTE[2]

[1] Corresponding Author. Vibration-Acoustics Laboratory, National Institute of Applied Science. 20 av. A. Einstein, 69621 Villeurbanne, France. Tel.: +33 472438707, E-mail: goran.pavic@insa-lyon.fr
[2] Matelys Research Lab, 7 rue des Maraîchers, 69120 Vaulx-en-Velin, France. Tel.: +33 972509316, E-mail: fabien.chevillotte@matelys.com

ABSTRACT

Several basic dynamical features of fluid-filled pipes are recalled. The fluid-wall coupling, the key factor governing the pipe dynamics, is outlined. The pressure propagation is shown to consist of a multitude of different waves, moving at different speeds. Both the low- and higher-order pressure waves are discussed. Attention is paid to the most important wave type associated with energy transfer: the plane wave. Several advanced techniques of pipe analysis concerning plane waves are discussed in some depth. These include 1) measurement of dynamic pressure and energy flow in the fluid using non-intrusive external wire sensors, 2) measurement of pressure pulsations at remote positions and 3) prediction of pressure pulsations within a coupled source-circuit assembly. Each technique is illustrated by examples obtained in real operating conditions.

Keywords: dynamic pressure, fluid-filled pipe, fluid waves, measurement, modelling.

NOMENCLATURE

B	[Pa]	fluid bulk modulus
E	[Pa]	Young's modulus
$\underline{I}$	[-]	identity matrix
J	[-]	Bessel function
P	[Pa]	pressure amplitude
U,V,W	[m]	x-,θ-,r- displacement amplitudes
Z	[Ns/m^3]	fluid impedance
b	[-]	wave type indicator
d	[m]	mean pipe diameter
h	[m]	thickness of pipe wall
n	[-]	circumferential order
p	[Pa]	dynamic pressure
x,r	[m]	axial and radial coordinate
t	[s]	time
u,v,w	[m]	x-,θ-,r- displacement components
Δ	[-]	Laplacian operator
Γ	[-]	coupling factor
Ω	[-]	normalised frequency
Ξ	[-]	shell operator
α	[rad]	polarisation angle
ε	[-]	strain
φ	[rad]	phase angle
κ	[-]	normalised wavenumber
ν	[-]	Poisson's coefficient
θ	[rad]	polar angle
ρ	[-]	mass density
ω	[rad/s]	angular frequency

Subscripts and Superscripts

C	belonging to circuit
S	belonging to source
b	wave type index
c	cut-on
f	fluid borne
n	circumferential order index
s	solid borne (wall)
x, r,θ	axial, radial and polar directions

1. INTRODUCTION

A dynamically excited pipe propagates vibration along its wall and pressure pulsations within the contained fluid (gas or liquid). Due to the coupling between the fluid and the wall the axial component of propagation velocity is common to the two media. The velocity depends on the elasticity and mass distribution of both the fluid and the wall. A straight pipe will be considered having uniform properties in the direction of its axis.

Pressure pulsations propagate in an unbounded fluid at the speed of sound. Due to the coupling with the wall, the sound speed in the fluid decreases in comparison with the speed in the unbounded fluid. If the fluid is heavy (water, oil...) the decrease of sound speed can be quite substantial.

The fluid-wall coupling in pipes has been studied since more than a century ago. A simple coupling model was developed at the end of 19th

century by Korteweg [1]. Zhukovskii published shortly after a study of water hammer propagation in pipes, [2]. In subsequent works one of the key issues was the modelling of pipe walls. Simplified formulae of sound speed for various external pipe conditions were published in papers [3,4], and books, [5,6].

The pipe motion becomes increasingly complex with the frequency rising. One of the earliest pipe models involving frequency dependence has been produced by Lin et al using a thin-wall theory applied to a fluid-filled cylindrical shell, [7]. It has been shown that the shell motion can be formulated in terms of waves of different frequency-dependent speeds of propagation. The cross section is then modelled in terms of natural modes while the motion in the axial direction is treated by the wave approach. Using such a dual formulation the response under a point source excitation located in the internal fluid has been found, [8]. The complex modelling has been further extended to the subject of pulsation and vibration energy, [9].

Basic pipe dynamic features are nowadays well understood. It became clear that a comprehensive analysis of pipe behaviour cannot fully rely on either computation or measurement alone. As a rule, the measurements have to be accompanied by adapted modelling if meaningful data are to be produced. The objective of this paper is to outline possibilities of hybrid, i.e. measurement + modelling pipe analysis and the conditions which allow for it.

2. ELASTIC WAVES IN A PIPE

At lower frequencies the pressure pulsations in a pipe dominantly propagate in the form of plane sound waves which travel along the pipe axis in opposite directions. However, at higher frequencies the propagation is far from being simple. The cross section may deform in a very complex manner and the distribution of pulsations may become intricate.

Pipe waves can be either propagating, quasi propagating or evanescent. The amplitude of the latter two types exponentially decreases from pipe discontinuities. The propagating waves dominate away from terminations or discontinuities.

Any wall deformation of the pipe cross section can be decomposed into circumferential harmonics of orders n. The deformation of the order n=0 is called “breathing mode”, that of the order n=1 “flexural mode”. Associated to each order n is a (theoretically infinite) number of propagating, quasi-propagating and evanescent wave types labelled by integer b. Thus each wave can be labelled by two indices: n and b, with n=0,1,2.. and b=1,2… Owing to the coupling each wave simultaneously coexists in the fluid and the wall. A wave of a particular type can propagate, and thus carry energy, only above a certain "cut-on" frequency which depends on the pipe and fluid properties. Below this frequency the wave is of evanescent or quasi-propagating type.

Three wave types of order 0 have zero cut-on, i.e. these waves can propagate at any frequency: the “pulsation”, “extensional” and “torsional” wave. All other wave types, including the remaining ones of order 0, have non-zero cut-on frequencies. The torsional wave is fully decoupled from the fluid and travels entirely in the wall. The energy of the pulsation wave is largely confined to the fluid while that of the extensional one is largely confined to the wall. Besides the three mentioned wave types the n=1 “flexural” wave propagates at any frequency too. Its energy is essentially located in the wall.

It can be safely assumed that at frequencies up to the first cut-on pipe frequency only the pulsation wave effectively governs the dynamical pressure in the fluid. This wave is strongly coupled to the pipe wall which vibrates when subjected to fluid excitation. The pulsation wave is responsible for some key phenomena, such as water hammer.

3. THE PIPE MODEL

The pipe is usually modelled as a circular cylindrical shell filled with a homogeneous fluid, [7-11]. Fig. 1 shows the coordinate system, the pipe geometry and the wall displacements.

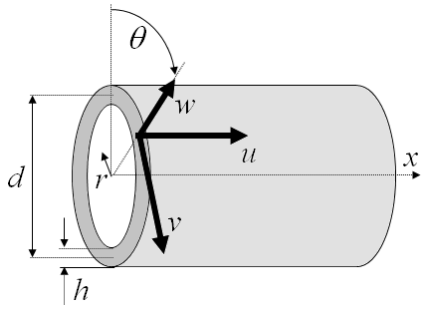

Figure 1. Coordinates and pipe displacements

As shown in [9] the coupled fluid-wall motion can be expressed using the equations of motion of the fluid, Eq. 1, that of the wall, Eq. 2, and the continuity condition at the fluid-wall interface, Eq. 3:

$$B\,\Delta p - \rho_f \frac{\partial^2 p}{\partial t^2} = 0 \tag{1}$$

$$\left(\frac{4Eh}{d^2(1-\nu^2)} \Xi - h\rho_s \frac{\partial^2}{\partial t^2} \underline{\underline{I}} \right) \begin{bmatrix} u \\ v \\ w \end{bmatrix} = \begin{bmatrix} 0 \\ 0 \\ p \end{bmatrix} \tag{2}$$

$$\frac{\partial p}{\partial r} + \rho_f \frac{\partial^2 w}{\partial t^2} = 0 \tag{3}$$

In this work the 3×3 differential operator of wall elasticity, Ξ, uses Flügge’s model, [12], but other models can be used too.

Assuming harmonic pipe motion with angular frequency ω=2πf the solution to Eqs. 1-3 can be

found by factorization. This leads to a pressure pulsation distribution which is in the radial sense governed by Bessel function of order n, J_n, in the circumferential sense by cosine function of the same order and in the axial sense by the exp function. For any given n and b the spatial pressure distribution obeys:

$$p(r,\theta,x) = P\,J_n(k^r_{n,b} r)\cos\left(n\theta+\vartheta\right)e^{\mp jk^x_{n,b}x} \qquad (4)$$

The – and + signs in the exp term respectively denote the wave directions relative to the pipe axis (x axis). Here k^x and k^r stand for the axial and radial components of wavenumber k which make the vector sum of the two components equal to k:

$$(k^x)^2+(k^r)^2 = k^2 = \omega^2/c_f^2, \quad c_f = \sqrt{B/\rho_f} \qquad (5)$$

The three components of wall displacements of amplitudes U, V and W, satisfying Eq. 2 read:

$$\begin{bmatrix} u(\theta,x) \\ v(\theta,x) \\ w(\theta,x) \end{bmatrix} = \begin{bmatrix} U \\ V \\ W \end{bmatrix} \cos\left(n\theta+\alpha+\varphi\right)e^{\mp jk^x x} \qquad (6)$$

with φ=0 for u and w components and φ=-π/2 for v component.

By resolving Eqs. 1-6 a polynomial equation is obtained the roots of which lead to multiple solutions of k^r. Thus, a series of wavenumbers k^r and k^x are obtained for each wave type n,s and each frequency ω. Given any particular value of k^r the relationship between the radial displacement amplitude of the wall W and the fluid pressure amplitude P can be obtained in terms of a "coupling factor" Γ, Eq. 7:

$$\frac{P}{W} = \frac{4Eh}{d^2(1-\nu^2)}\Gamma, \quad \Gamma = \frac{\Omega^2 J_n(\kappa^r)}{\kappa^r\,\partial J_n(\kappa^r)/\partial\kappa^r} \qquad (7)$$

with the wavenumber and frequency expressed in a normalized (non-dimensional) form:

$$\kappa^r = \frac{k^r d}{2}, \quad \Omega = \omega\frac{d}{2}\sqrt{\frac{\rho_s(1-\nu^2)}{E}} \qquad (8)$$

The factor Γ represents the effect of coupling between the fluid and the pipe wall. This factor can be computed once the relationship between the radial wavenumber k^r and frequency ω is known.

For a particular pipe its wavenumber–frequency dependence relative to an order n and type b is called the dispersion law. It is usually presented in terms of normalized axial wavenumber $\kappa^x=k^x\,d/2$. Fig. 2 shows the dispersion diagram of a steel pipe of the 2.5% thickness-to-diameter ratio. The results are given for propagating waves only as these waves are of most interest in usual applications. The two groups of curves correspond to water-filled and empty cases. Empty pipes contain only 3 types of waves, b=1,2,3.

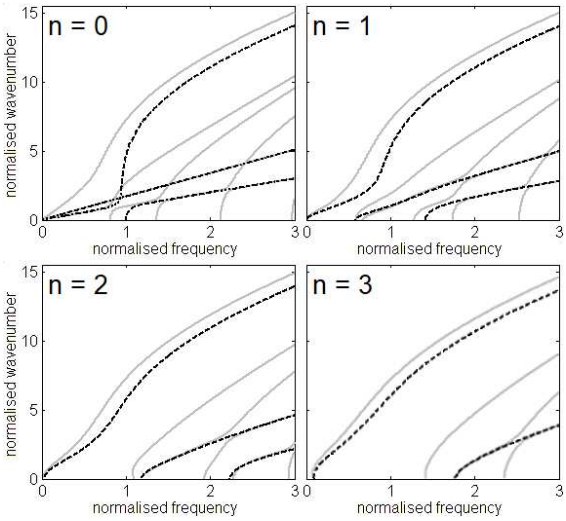

Figure 2. Dispersion diagrams for propagating waves in steel pipe. Full line: water filled; dashed line: empty.

The radial wavenumber component k^r defines the variation of pressure pulsations in the radial sense. Together with the order n it fully specifies the distribution of pressure in the cross section of a pipe due to the corresponding wave. In the same way the axial wavenumber component k^x together with the order n fully specifies the distribution of pressure pulsations in the axial sense. In addition to this the tandem k^x-n fully governs the distribution of wall vibratory displacement components u,v,w via Eq. 6 and thus the distribution of axial and tangential wall strains:

$$\varepsilon_{xx} = \frac{\partial u}{\partial x}, \quad \varepsilon_{\theta\theta} = \frac{2}{d+h}\left(\frac{\partial v}{\partial\theta}+w\right) \qquad (9)$$

The tangential strain $\varepsilon_{\theta\theta}$ is of particular meaning in this study as its measurement will be used for the detection of internal fluid pressure.

3. THE CUT-ON FREQUENCY

As mentioned in §2 a wave of a particular type can propagate and thus carry energy only above its own "cut-on" frequency. This transition frequency decreases with the pipe diameter but rises with its thickness. The cut-on frequencies increase with the increase of order n. Of a particular importance is the first cut-on frequency of n=2 order as this one has the lowest non-zero value. Below this specific frequency only 4 simple waves can propagate, as mentioned, and the analysis simplifies.

If a measurement is carried out below the lowest cut-on frequency a fairly basic sensor array suffices in view of only four wave types being capable to propagate. These are pulsating, extensional, torsional

and flexural waves. In such a case the measurement can be done by employing piezo sensors to detect pressure pulsation and accelerometers to detect wall vibration. The latter can be configured in difference and sum schemes and oriented conveniently such to extract only one type of wave: either extensional, torsional or flexural. The problem may occur if the pipe diameter is large, resulting in a high frequency Ω, Eq. 8. For example, a 16mm thick steel pipe of 2m diameter has its first non-zero cut-on frequency of only 5.2 Hz if water-filled and of 10.5 Hz if filled with methane at 10b static pressure. Most of dynamic phenomena of such a pipe may involve propagating waves of higher-orders which would considerably penalise its analysis.

The analysis can be simplified if the selected sensor can itself respond to the wave of interest only. Where pulsation waves in a pipe are concerned these can be extracted out by using a strain sensor wrapped around the pipe. Such a sensor measures in fact the hoop strain due to breathing, i.e. the n=0 order. Still the pulsating wave is not the only wave type of the n=0 order. The extensional wave is of the same order too, but this wave generates weak hoop strains due to its dominantly axial motion. However, other waves of the n=0 order propagate at frequencies above the higher cut-on frequencies. The lowest non-zero cut on frequency of n=0 order defines thus the range of the effective measurement of pulsating wave using a hoop strain sensor. This frequency is considerably higher than the lowest cut-on of n=2 order. E.g. for a 2m/16mm steel pipe as mentioned above the lowest non-zero cut on frequency of n=0 order is 621 Hz if water-filled and of 281 Hz if filled with methane. Thus, by using a sensor which is sensitive to the n=0 order only the simplified analysis can be done within an extended frequency range.

For a pipe of given material and contained fluid the cut-on frequency normalised using Eq. 8, Ω_c, can be obtained as a sole function of the thickness-to-diameter ratio.

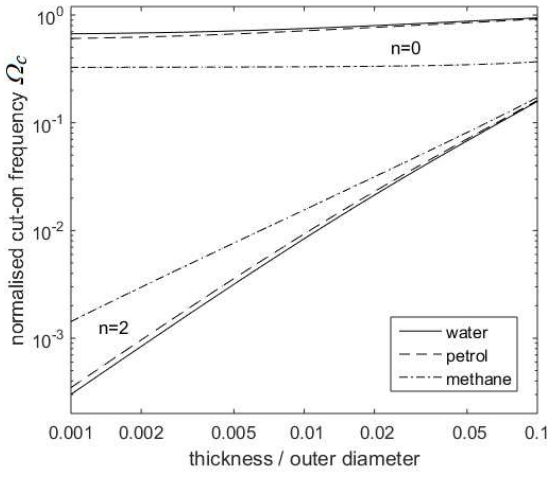

Figure 3. First normalised cut-on frequency of a steel pipe.

Fig. 3 displays the lowest non-zero values Ω_c of a steel pipe for three types of fluid. The difference between the lowest non-zero cut-on frequencies of n=2 and n=0 orders is seen to increase with the thickness/diameter ratio decreasing. The plot on Fig. 3 thus gives the upper frequency limit of a simplified experimental analysis of a straight pipe. The curves belonging to n=2 cut-on refer to the limit below which only the four basic waves can propagate. The n=0 curves refer to the basic breathing waves, the b=1 pulsating and the b=2 extensional wave, which can be measured using the integrating strain sensors as outlined above.

4. NON-INTRUSIVE MEASUREMENT

A piezo-electric wire wrapped around the pipe wall, demonstrated in [13], has been used in this study as a strain sensor. If firmly wrapped around the pipe wall, it directly measures the mean tangential strain around the circumference. This quantity can be related to the internal pressure using Eqs. 7 and 9 which account for the fluid-wall coupling. By applying one or several complete wraps around the pipe wall only the n=0 order of pipe motion is picked up, the other orders being suppressed by the integrating effect of the sensor. The advantage of using such a sensor is triple: it is non-intrusive, it is reusable and it filters out only the desired pipe deformation.

The wire produces an electrical charge which is proportional to its elongation. When connected to a charge amplifier the output voltage signal becomes thus proportional to the mean hoop strain. Fig. 4 shows the PVDF sensor mounted on a 1¼" steel pipe, a part of oil pumping circuit. In view of very high cut-on frequencies of this small pipe, 4.6 kHz for n=2 and 38.6 kHz for n=0, the measurement was safely carried out up to high frequencies.

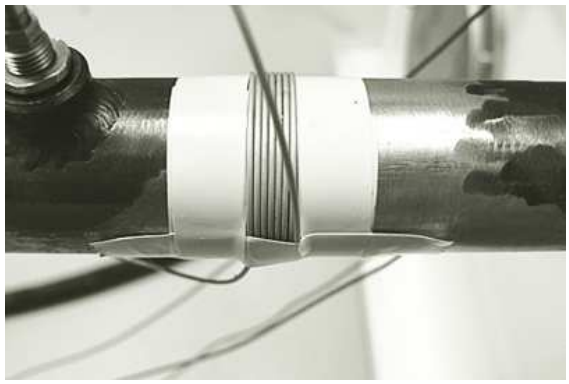

Figure 4. The PVDF wire sensor.

Fig. 5 compares the RMS levels of pressure pulsations obtained via the PVDF wire sensor and the classical intrusive piezo sensor. Quite remarkable matching between the two can be observed at not too high frequencies (top). At high frequencies (bottom) a discrepancy in levels becomes visible as some n=0

order waves other than the pulsation wave begin to propagate thus affecting the sensor output.

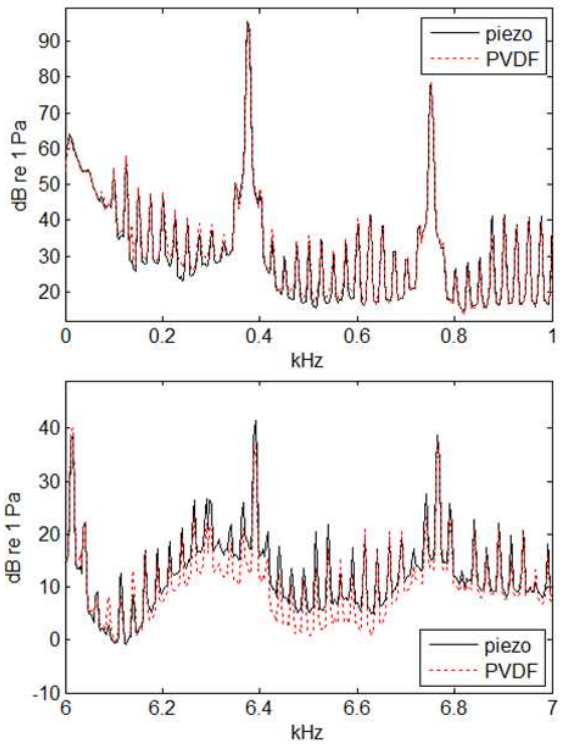

Figure 5. Comparison of pressure pulsation levels. Top: 0-1 kHz; bottom: 6-7 kHz.

5. SPEED OF PRESSURE WAVES

Advanced measurement analysis of pulsation waves, by using either intrusive pressure sensors or strain integrating sensors, allows a comprehensive pipe analysis. Such an analysis requires the precise knowledge of the actual wave speed in the pipe, which can itself be measured by an advanced technique. The following results can be obtained:

- velocity of pulsation waves (velocity of sound) in a given pipe
- flow speed using acoustical Doppler effect
- amount of damping in the fluid
- energy flow of pipe pulsations
- impedance of a hydraulic circuit
- reconstruction of pressure, vibration and strains along the pipe
- pipe thickness using vibration array
- characterisation of a source of pressure pulsation using a hydraulic "multi-charge" technique.

It has been shown that the velocity of sound can be obtained using a cost function computed from the frequency cross-spectra of measured signals, [14]. The method uses an array of 3 sensors. A modified two-parameter cost function can be obtained which indicates by its maximum both the sound velocity and the flow speed of the fluid. Fig. 6 shows the cost function obtained from a measurement on a pipe transporting compressed air: it indicates the speed of sound of 346 m/s and the flow velocity of 17 m/s.

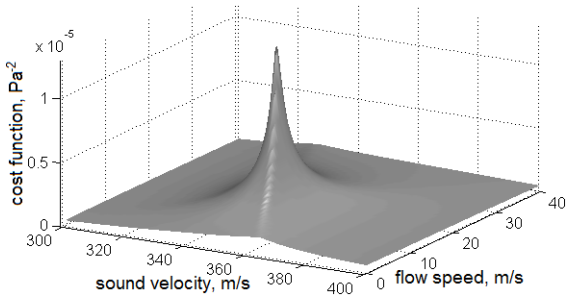

Figure 6. Cost function indicating the sound velocity and the flow speed.

6. APPLICATIONS

The knowledge of the true sound velocity in the pipe can be used to inversely compute the reference sound speed of the fluid itself and thus monitor the state of the fluid in operation. Any change in sound velocity of the fluid, produced e.g. by the presence of gas of impurities, will affect the sound speed and can thus be used as a warning to the operator.

The knowledge of true sound velocity can be further employed for the decomposition of wave components propagating along the pipe in opposite directions. The decomposed wave components can in turn be used for the reconstruction of pressure pulsations, vibrations and dynamical stresses at positions away from the measurement section. The same sensor array used for the measurement of wave speed can be employed to this end. If the pressure measurement is done by employing the external strain sensors, the reconstruction can be made for the strains and the corresponding stresses as well.

6.1. Intensity of pressure pulsations

Fig. 7 illustrates one of possible applications: measurement of energy flow of pipe pulsations. The energy flow per unit surface, the intensity, is shown as a function of frequency. The total intensity is then the frequency integral of the intensity spectrum shown. It is seen that the intensity measured using non-intrusive external sensors matches very well that obtained by classical sensors.

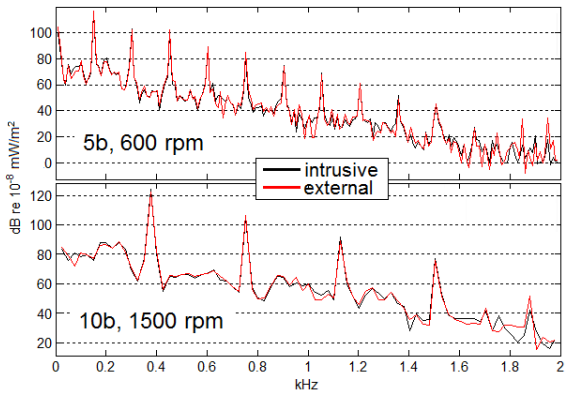

Figure 7. Intensity of pipe pressure pulsations. Top: 5b, 600rpm; bottom: 10b, 1500 rpm.

6.2. Remote pressure reconstruction

Fig. 8 shows the pressure pulsations measured directly and reconstructed from a 1.5m distant array of 3 sensors. The 6" 3mm thick pipe was filled with oil. The reconstruction was done by using the array data to decompose the pressure into positive- and negative-travelling wave components and by retro-propagating these components to the 4th remote point where the reference measurement was carried out in parallel. In this example intrusive piezo sensors were used. Very good matching is observed between the pressure measured directly and reconstructed; the mismatch shown by a grey line is relatively low. The processing of sensor signals was done in time domain using numerical filtering to account for the frequency-dependent coupling factor Γ.

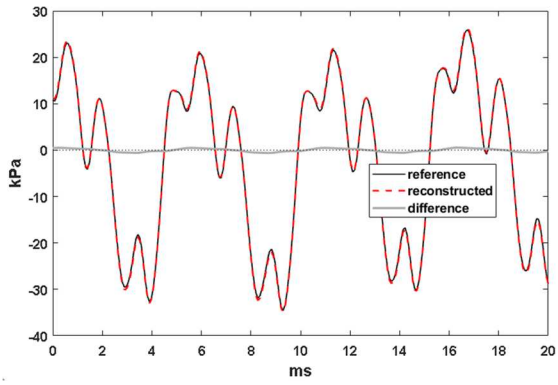

Figure 8. Comparison of pipe pressure pulsations measured directly and remotely.

The example shown in Fig. 8 was obtained in laboratory conditions. But the same technique was successfully applied to in-situ conditions too, e.g. on a dia 2m penstock of a hydraulic power plant, using strain PVDF sensors. Moreover, it has been shown in [15] how the pressure profile along an entire pipe can be reconstructed using the reconstruction technique.

6.3. Source characterisation

Owing to the technique of wave decomposition a pipe can be used for the characterisation of sources of pressure pulsations, such as pumps, compressors, hydro-motors etc. Analysis of hydraulic components by modelling and measurement has been in use since a long time ago. In [16] the authors have made a review of several available analysis techniques.

If the pipe conducts effectively only plane waves, as is often the case, a simple relationship can be established in frequency domain between the pressure at the outlet of the source, p_C, and the intrinsic pressure of the source p_S. The latter denotes the source pressure which would have been produced had the outlet been shut. When the coupling between the source and the circuit is strong, the coupled pressure p_C could be quite different from the intrinsic source pressure p_S. Expressed in terms of frequency pressure amplitudes P, the relationship between the two pressures depends on the impedance of the hydraulic circuit at the coupling position, Z_C, and the impedance of the source at the same position, Z_S:

$$P_C = Z_C/(Z_S + Z_C)\,P_S \qquad (10)$$

Eq. 10 shows that the source is characterised by two parameters: its intrinsic pressure, P_S, and its own impedance, Z_S. By connecting the source to two or more circuits of different impedances these two quantities can be retrieved from the measurement data. This characterisation principle has been first conceived for application on engine exhaust lines, [17-19], but can be readily extended to hydraulic sources [20]. The circuit impedance can also be modelled using the impedance continuity principl.

Fig. 9 shows the comparison between the levels of pressure pulsations in an oil circuit obtained by direct measurements and by prediction. The latter used the separately characterised source pressure and impedance and applied to Eq. 10. The source was a gear electro-pump producing periodic pulsations which are consequently represented by the associated harmonic indices 1, 2…. The total levels of pulsations are indicated by the right column. The circuit impedance Z_C needed for the characterisation was measured by the technique outlined in [21]. A fairly good matching of the measured and predicted results can be seen.

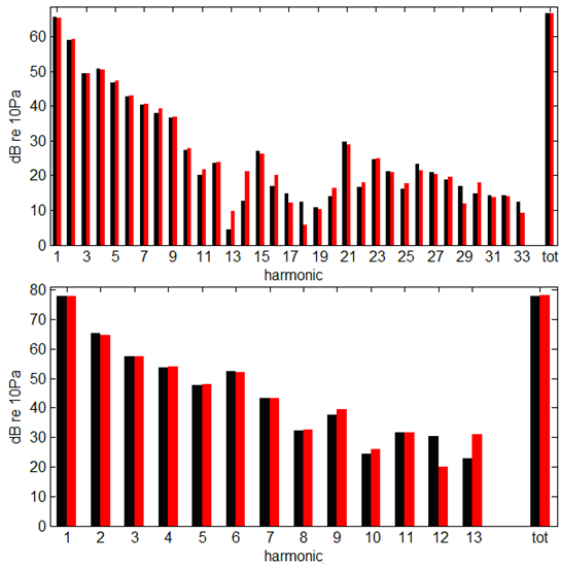

Figure 9. Comparison of levels measured directly (in black) and using Eq. 10 (in red). Top: 5b, 600 rpm (first harmonic 150 Hz); bottom: 10b, 1500 rpm (first harmonic 375 Hz).

7. CONCLUSIONS

A fluid-filled pipe exhibits a complex dynamic behaviour which can be conveniently analysed using multi-point measurements combined with analytical modelling. The motion in any cross section of the

pipe is a sum of circumferential orders n=0,1,2… which govern the deformation of pipe wall and the dynamic pressure distribution within the pipe. To each of these orders is associated a number of pipe waves of different kinds, each having its own wave speed and pressure distribution.

Where the pressure pulsations are concerned one of the waves of the order n=0, called the pulsation wave, is of a particular importance as it transports most of the energy of pressure pulsations along the pipe. An external, non-intrusive strain sensor made of piezo wire was shown to provide a simple means of the measurement of pulsation waves.

The hybrid approach of pipe analysis, i.e. the multi-sensor measurements of pressure pulsations combined with fluid wall modelling, enable one to carry out advanced pipe analysis. Several examples of such analysis based on measurements in operating conditions are outlined in the paper: measurement of fluid energy flow using wire sensors, measurement of pressure pulsations at remote positions, prediction of pressure pulsations of a coupled circuit. These examples show the potential of hybrid approach for prediction, monitoring and diagnostic purposes.

REFERENCES

[1] Korteweg, D. J., 1878, "On the velocity of propagating sound in elastic tubes" (in German), *Physics Annals*, Vol. 174, pp. 525-542.

[2] Zhukovsky, N. E., 1899, *On hydraulic shock in water-conducting pipes* (in Russian), Bulletin of Technical Society, No. 5.

[3] Pearsall, I. S., 1965, "The velocity of water hammer waves", *Proc. Inst. Mech. Eng*., Vol.180, pp. 12-20.

[4] Halliwell A. R., 1963, "Velocity of a water hammer wave in an elastic pipe", *Proc. Amer. Soc. Civil Engrs - J. Hydraulics Division*, Vol. 89, pp. 1-21.

[5] Jaeger, C., 1977, *Fluid transients in hydro-electric engineering practice*, Blackie and Son.

[6] Parmakian, J., 1963, *Water hammer analysis*, Dover.

[7] Lin, T. C. and Morgan, G. W., 1956, "Wave propagation through fluid contained in a cylindrical elastic shell", *J. Acoust. Soc. Amer.*, Vol. 28, pp. 1165-1176.

[8] Merkulov, V. N., Prikhodko, V. Yu. and Tyutekhin, V. V., 1978, "Excitation and propagation of normal modes in a thin cylindrical elastic shell filled with fluid" (in Russian), *Akusticheskii Zhurnal*, Vol. 24, pp. 723-730.

[9] Fuller, C. R. and Fahy, F. J., 1982, "Characteristics of wave propagation and energy distributions in cylindrical elastic shells filled with fluid", *J. Sound Vibration*, Vol. 81, pp. 501-518.

[10] Sorokin, S. V., Nielsen, J. B. and Olhoff, N., 2004, "Green's matrix and the boundary integral equation method for the analysis of vibration and energy flow in cylindrical shells with and without internal fluid loading", *J. Sound Vibration*, Vol. 271, pp. 815–847.

[11] Ledet, L. S. and Sorokin, S. V., 2018, "Bi-orthogonality relations for fluid-filled elastic cylindrical shells: Theory, generalisations and application to construct tailored Green's matrices", *J. Sound Vibration*, Vol. 417, pp. 315-340.

[12] Flügge, W., 1973, *Stresses in shells, 2nd ed.* Springer.

[13] Pinnington, R. J. and Briscoe, A., 1994, "Externally applied sensor for axisymmetric waves in a fluid-filled pipe", *J. Sound Vibration*, Vol. 173, pp. 503-516.

[14] Pavić, G., 2003 "Acoustical analysis of pipes with flow using invariant field functions", *J. Sound Vibration*, Vol. 263, pp. 153-174.

[15] Chevillotte, F., Pavić, G., Dubois, G., Proulx, G., Gagnon, M., 2021 "Novel techniques for the analysis of dynamic pressure in penstocks", *30th IAHR*, Lausanne, Switzerland.

[16] Johnston, D. N. and Edge, K. A., 1989, "Simulation of the pressure ripple characteristics of hydraulic circuits", *Proc. Inst. Mech. Engrs., Part C: Mechanical Engineering Science*, Vol. 203, pp. 275-282.

[17] Kathuriya, M. L. and Munjal, M. L., 1976, "A method for the experimental evaluation of the acoustic characteristics of an engine exhaust system in the presence of mean flow", *J. Acoust. Soc. Amer.*, Vol. 60, pp.745-751.

[18] Prasad, M. G., 1987, "A four load method for evaluation of acoustical source impedance in a duct", *J. Sound Vibration*, Vol. 114, pp. 347-356.

[19] Bodén, H., 1995, "On multi-load methods for measuring the source data of acoustic one-port sources", *J. Sound Vibration*, Vol. 180, pp. 725-743.

[20] Pavić, G. and Chevillotte, F., 2010, "Noise characterization of pulsating hydraulic sources", Proc. *Int. Conf. on Noise and Vibration Eng. ISMA 2010*, Leuven, Belgium, pp. 73-83.

[21] Chung, J. Y. and Blaser, D. A., 1970 "Transfer function method of measuring in-duct acoustic properties. I. Theory", *J. Acoust. Soc. Amer.*, Vol. 68, pp. 907-913.

Conference on Modelling Fluid Flow (CMFF'22)
The 18th International Conference on Fluid Flow Technologies
Budapest, Hungary, August 30 -September 2, 2022

DROPLET SPREADING BEHAVIOUR OVER A SOLID SUBSTRATE MEDIATED BY SURFACE WETTABILITY AND INTERFACIAL TENSION

Dhrijit Kumar DEKA[1], Sukumar PATI[2], László BARANYI[3]

[1] Department of Mechanical Engineering, National Institute of Technology Silchar, Silchar, India-788010, E-mail: dhrijitdeka@gmail.com
[2]Department of Mechanical Engineering, National Institute of Technology Silchar, Silchar, India-788010, E-mail: sukumar@mech.nits.ac.in
[3] Corresponding Author. Department of Fluid and Heat Engineering, Institute of Energy Engineering and Chemical Machinery, University of Miskolc, 3515, Miskolc-Egyetemváros, Hungary. E-mail: laszlo.baranyi@uni-miskolc.hu

ABSTRACT

The present study investigates the fluid-solid interaction phenomenon when a spherical droplet falls on the surface of a solid substrate. Numerical investigations were carried out in a 2D framework to analyse the influence of the wettability of the substrate and interfacial tension of the liquid droplet. The 2-D solver establishes a good agreement with the reported experimental results. The droplet is considered to fall on the solid surface under the influence of a minimal velocity imposed on it. The results are presented in terms of droplet interface morphology and the spreading distance over the solid substrate. It is observed that the spreading tendency of a droplet is much more significant with a hydrophilic surface compared to a hydrophobic surface. It is also established that with the decrease in Weber number the droplet spreading increases. However, droplet spreading on a hydrophobic surface increase with the decrease in Weber number up to a certain limit, after which the droplet starts to contract, reducing the droplet spreading on the surface.

Keywords: Droplet spreading, hydrophilic, hydrophobic, solid substrate, Weber number, wettability.

NOMENCLATURE

D	[mm]	diameter of the droplet
L_s	[-]	non-dimensional spreading length
We	[-]	Weber number
θ	[degree]	contact angle
μ	[Pa s]	viscosity
ρ	[kg/m^3]	density
σ	[N/m]	surface tension
τ	[-]	non-dimensional time
$\phi(x,t)$,	[-]	level-set function

1. INTRODUCTION

When a droplet impacts on a solid surface, the dynamics of interfacial characteristics becomes complex. Researchers have found the dynamics of a droplet impacting on a substrate a topic of interest owing to its appealing physics and versatile applications like ink-jet printing [1], pesticide depositions [2], impact erosion [3], anti-icing [4], etc.

Droplet impact on a solid substrate takes many forms (e.g., spreading, bouncing, fingering, splashing, etc.) [5] based on different properties of the surface as well as different physiochemical and flow properties of the fluid. These include the surface properties of roughness [6] and wettability [7], while fluid properties such as interfacial tension, viscosity, density, and impact velocity [8-10] are some of the key determinants of droplet impact over a solid surface.

The spreading of a liquid droplet on a specifically wetted surface has drawn attention from the research community for bearing remarkable potential within the domain of biomedical research, microfluidics, lab-on-chip applications, etc. The key parameters that govern the phenomenon of spreading over a solid substrate are dynamic contact angle, impact velocity of the droplet and topology of the solid-liquid contact line. Researchers have reported that the dynamic contact angle is dependent upon the physical structure of the impacting surface [11], interfacial characteristics of the participating liquid [12] and also the method by which the droplet is let to impact over the surface [13, 14]. Wildeman et al. [15] investigated numerically and analytically the spreading behaviour of droplet over a smooth surface when the droplet impacts the surface at a high velocity. They found that during the spreading of a liquid droplet over the free-slip surface one-half of the kinetic energy is converted to interfacial energy, irrespective of any other flow parameters. Lann et al.

[16] experimentally explored the influence of impacting droplet diameter on spreading over a solid surface. They reported that the spreading characteristics of the droplet not only depend on the inertia, viscous or capillary force, but also on the droplet size and provide an accurate scaling of droplet spreading behaviour. Léopoldès and Bucknall [17] identified three distinct regimes of droplet spreading when a solid surface is differentiated with two micro-stripes having definite wettability contrast. In their study, different spreading behaviours of droplet were analysed with the variation of wettability contrast. In another study carried out by Kuznetsov et al. [18], three different spreading regimes were identified for a distilled water droplet impacting a solid superhydrophobic and copper substrate.

The dynamics of a droplet when it is imposed with a certain velocity can be characterised by a non-dimensional similarity number called Weber number (*We*), which represents the relative importance of velocity with respect to the surface tension of the liquid. Liu et al. [19] investigated the spreading characteristics of a droplet over a surface at low Weber numbers. Shang et al. [20] explored the spreading of a droplet for a range of Weber numbers on a solid surface maintained at a very low temperature. They reported that a low Weber number leads to a decrease in spreading length, with spreading length first decreasing and then increasing with subsequent cooling at higher Weber numbers.

Most of the recent studies on the spreading of a liquid droplet over a solid surface have explored the influence of surface wettability and a few key determinants like impact velocity, viscosity or surface tension. However, the combined effect of surface wettability with a low Weber number on the spreading characteristics is yet to be studied. Thus, the present study aims to investigate the spreading behaviour of a liquid droplet on a solid surface of different wettability conditions for a specific range of Weber numbers.

2. THEORETICAL FORMULATION

2.1. Problem formulation

The present study numerically investigates the spreading behaviour of a liquid droplet over solid substrate under the combined influence of the wettability condition of the substrate surface, the initial velocity of the droplet and the interfacial tension. A two-dimensional computational domain is used (see Fig. 1) in the present investigation in order to reduce the cost of computation, and is justified by the fact that the present 2D computational results agree well with reported experimental work, as discussed in Section 3.

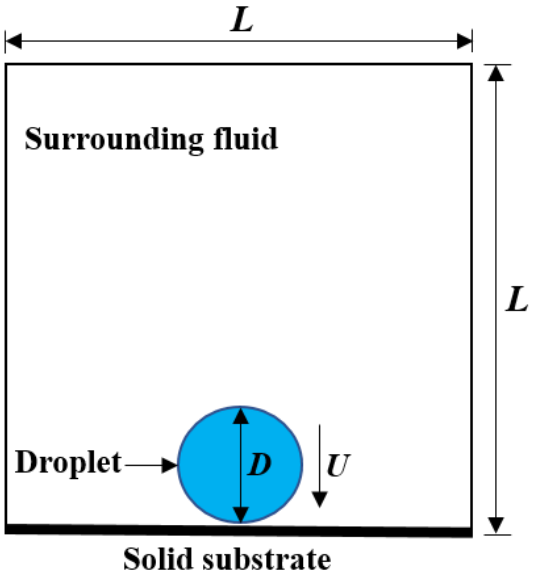

Figure 1. Computational domain of the physical model

The diameter of the droplet (D) is considered to be 2 mm, and based on this, the other dimensions of the computational domain are set. The diameter of the droplet (D) is considered to be 2 mm, and based on this, the other dimensions of the computational domain are set. The side length of the square domain is considered to be L=10D. The droplet is set to fall on the substrate from a distance of 0.01D. The liquid droplet is considered to be water (fluid 1) with density (ρ) and viscosity (μ) of 1000 kg/m^3 and 0.001 Pas, respectively. The water droplet is surrounded by air (fluid 2) (ρ=1.22 kg/m^3, μ=1.98×10^{-5} Pas). The side boundaries are imposed with free-slip boundary conditions, whereas the top boundary of the domain is considered to be of constant pressure identical with the ambient pressure and no-slip boundary conditions are prescribed at the bottom. The effect of gravity is neglected as the size of the droplet is very small [21]. The initial velocity of the droplet is U= 0.001 m/s and the surrounding air is assumed to be stationary. The study puts emphasis on investigating the spreading behaviour changes with different wettability conditions of the wall combined with the interfacial tension of the droplet. Two specific wettability conditions were imposed on the surface: hydrophilic and hydrophobic with a contact angle (θ) of 78^o and 150^o, respectively. The influence of surface tension (σ) with respect to imposed velocity is measured with a non-dimensional parameter called the Weber number (We=$\rho U^2 D/\sigma$) which was varied within a range of 0.001-0.0028.

2.2. Governing equations

The present study adopts the two-phase laminar flow level-set formalism for accurate capturing of interface based on finite element method. For this purpose, an implicit scalar function, the level-set

function, is defined to describe the minimum distance of any location from the interface as

$$\phi(x,t) = \begin{cases} 1 & \text{in the domain of fluid 1} \\ 0 < \phi < 1 & at \text{ the interface} \\ 0 & \text{in the domain of fluid 2} \end{cases} \quad (1)$$

After defining the level-set function $\phi(x,t)$, a generalised transport equation is solved to track the position of the interface throughout the domain as follows

$$\frac{\partial \phi}{\partial t} + \boldsymbol{u}.\nabla\phi = \nabla \cdot \left(\lambda \nabla\phi - \phi(1-\phi)\frac{\nabla\phi}{|\nabla\phi|} \right), \quad (2)$$

where t denotes time, $\boldsymbol{u}$ represents the velocity field, and λ is the diffusion coefficient, which is the product of the parameter controlling interface thickness ($\in_{ls}$) and a re-initialization parameter (γ) .

Next, the level-set function is coupled with the velocity field in order to obtain the coupled Navier-Stokes equation, which can be expressed as

$$\rho\left[\frac{\partial \boldsymbol{u}}{\partial t} + \boldsymbol{u}.\nabla\boldsymbol{u}\right] = -\nabla P + \nabla \cdot \left[\mu\left(\nabla\boldsymbol{u} + \nabla\boldsymbol{u}^T\right)\right] + \sigma\kappa\hat{\boldsymbol{n}}\delta_s\left(r - r_\Gamma\right) \quad , \quad (3)$$

where P is the pressure, μ is the dynamic viscosity, σ is the fluid to fluid interfacial tension, κ is the curvature of the interface, $\delta_s\left(r - r_\Gamma\right)$ is a delta distribution function that is zero everywhere except at the interface, and $\hat{\boldsymbol{n}}$ represents the normal direction to the drop surface. Equations (2) and (3) are solved with the continuity equation given by

$$\nabla \cdot \boldsymbol{u} = 0 \ . \quad (4)$$

3. NUMERICAL METHODOLOGY AND MODEL VALIDATION

A finite element method-based solver was employed to solve the governing equations (1)–(4). The mesh used for the present computational investigation is presented in Fig. 2, where the fluid-to-solid interacting zone is configured with very fine elements. Using the Galerkin weighted method and

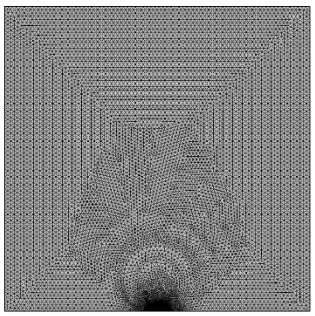

Figure 2. Computational mesh used for the present study

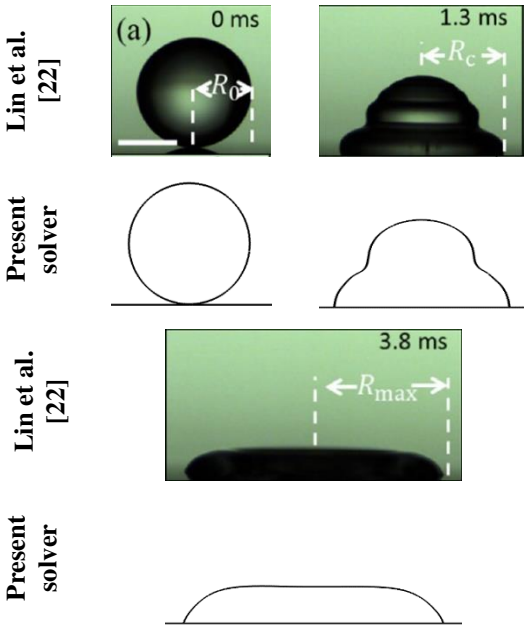

Figure 3. Comparison of results of Lin et al. [22] and the present solver

weak form transformation, the highly non-linear set of transport equations can be solved. The variables are solved iteratively up to a pre-set residual limit of 10^{-6}. The present solver was tested for grid independence. Grid independent results were obtained for a grid with 59262 elements. For this grid, the variation of spreading length (L_s) shows a maximum 0.02% relative difference compared to the preceding grid system (with 47220 elements).

To test whether the solver accurately captures the interfacial dynamics it was used to solve the flow dynamics reported by Lin et al. [22] in their experimental study, where the impact of a droplet over a solid surface with different wettability conditions is extensively analysed. The flow conditions employed in the solver exactly replicated the experimental conditions of Lin et al. [22]. Figure 3 compares the results from the present solver with those reported by Lin et al. [22] and finds good agreement. Thus, the present solver is considered to be capable of capturing the interfacial dynamics.

4. RESULTS AND DISCUSSION

The present study investigates the spreading behaviour of droplet on a surface of a solid substrate. The main aim was to investigate how the spreading characteristics differ with varying wettability conditions of the surface and Weber number. Droplet interface morphology and droplet spreading length are determined for two different surface wettability conditions and a range of Weber numbers. The present study considers only two specific contact angles to represent the two wettability conditions: θ=150° for hydrophobic wettability and θ =78° for hydrophilic wettability.

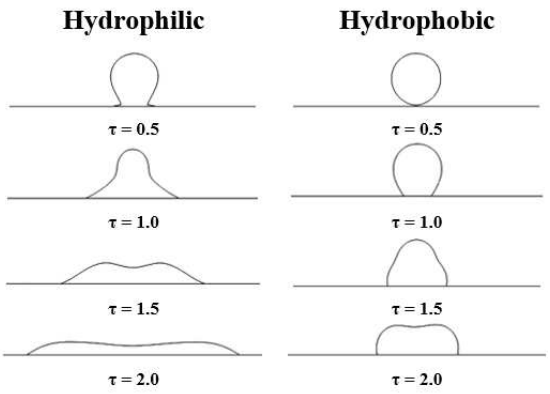

Figure 4. Dynamic evolution of droplet spreading on the solid substrate for two different wettability conditions at *We* = 0.0028

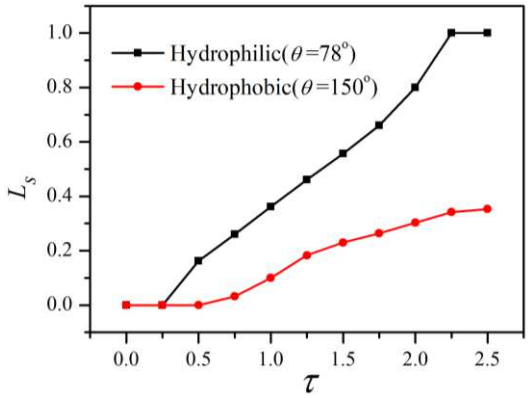

Figure 5. Variation of spreading length (L_s) evolution for hydrophilic and hydrophobic surfaces at *We* = 0.0028

Figure 4 shows how the droplet interface evolves when it comes in contact with the hydrophilic surface or hydrophobic surface of the solid substrate for the specific Weber number (*We*) of 0.0028. It can be observed from the figure that the droplet spreads more widely on the hydrophilic surface compared to the hydrophobic surface. On the hydrophilic surface the droplet starts spreading at dimensionless time τ (=Ut/D) = 0.5 and the solid- liquid interface elongates monotonically. Eventually at τ = 1.5, a capillary wave is formed, which further helps the droplet to spread over the surface and generates a wavy interface, as can be seen at τ = 1.5. Subsequently the wave brings the interface almost parallel to the surface. The hydrophobic surface, however, resists spreading of the droplet on the surface. The initiation of droplet-to-surface contact lags appreciably, as the droplet is yet to form the liquid-solid interface at τ = 0.5. Once the contact is established, the droplet spreads over the surface with time, although, the spreading length is much smaller than for the hydrophilic surface. This can be illustrated by the fact that the hydrophobic surface has a minimal tendency to accumulate the liquid over it, as the solid surface does not promote spreading of the liquid phase and as a consequence, sideways movement of the droplet over the surface is restricted. In contrast, on the hydrophilic surface, there is a great affinity of the droplet to stick on the surface, due to which the interface spreads along the surface easily.

Figure 5 shows the temporal evolution of droplet spreading length on hydrophilic and hydrophobic surfaces. The spreading length (L_s) is normalised by the length of the solid substrate. It is seen in Fig. 5 that the spreading length of the droplet for both wettability conditions monotonically increase with time. However, as described in the previous paragraph, for the hydrophobic surface the spreading length is significantly smaller than that for the hydrophilic surface. This is due to the fact that the hydrophilic surface favours for the droplet to spread the surface, whereas, the hydrophobic surface tends to repel the interface from the liquid to solid attachment.

The spreading behaviour of droplet over a solid surface is highly influenced by the interfacial energy possesses by the droplet. Thus, the present study also explored the different scenarios considering the relative importance of inertia as well as surface tension force that can be expressed through the Weber number. Figure 6 describes the spreading characteristics of a droplet over a hydrophilic surface for three different *We* numbers. For *We*=0.0028, the droplet starts spreading at τ = 0.5 (Fig. 6(a)) and subsequently the spreading length increases as the generated capillary wave pulls the interface laterally. The tip of the droplet shell (seen in Fig. 6(b)) becomes smaller under the effect of the capillary wave, and forms a crest in the middle, as can be observed at τ = 1.5 (Fig. 6(c)). The wavy interface gradually becomes parallel to the solid substrate, with further spreading along the surface as seen at τ = 2.0 (Fig. 6d). The trend remains similar when the Weber number decreases (*We*=0.002, *We*=0.001). However, it can clearly be seen in the figure that with the decrease in Weber number (increasing the surface tension), the spreading tendency increases. It is observed that at any given instant the spreading length is higher for lower values of Weber number. This is due to the fact that the interfacial force aids to the hydrophilicity of the surface and as a cumulative consequence the droplet interface spreads further over the surface. For a hydrophilic surface the droplet interface tends to move towards the surface; when the surface tension increases as *We* decreases, the droplet interface again maintains the tension in the inward direction and retracts. Thus, as a cumulative consequence, the interface spreads further over the hydrophilic solid surface with decreasing Weber number. It is interesting to observe that at *We*=0.001, the droplet spreads the most compared to the other Weber numbers and strikes the boundary wall at τ = 2.0 (Fig. 6(l)).

Droplet behaviour differs when the solid surface is hydrophobic (with all other conditions kept the

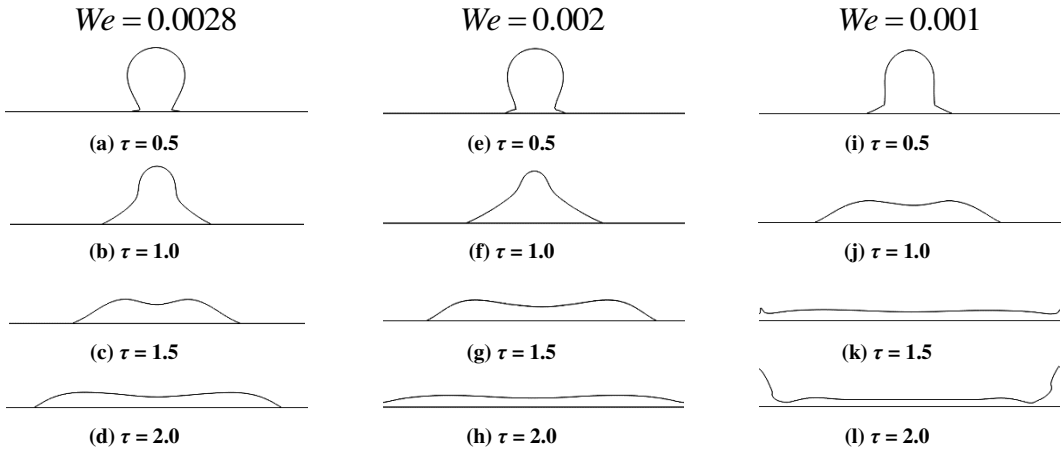

Figure 6. Spreading characteristics of a droplet in terms of interfacial evolution shown at specified instants over a hydrophilic surface for three different *We* numbers

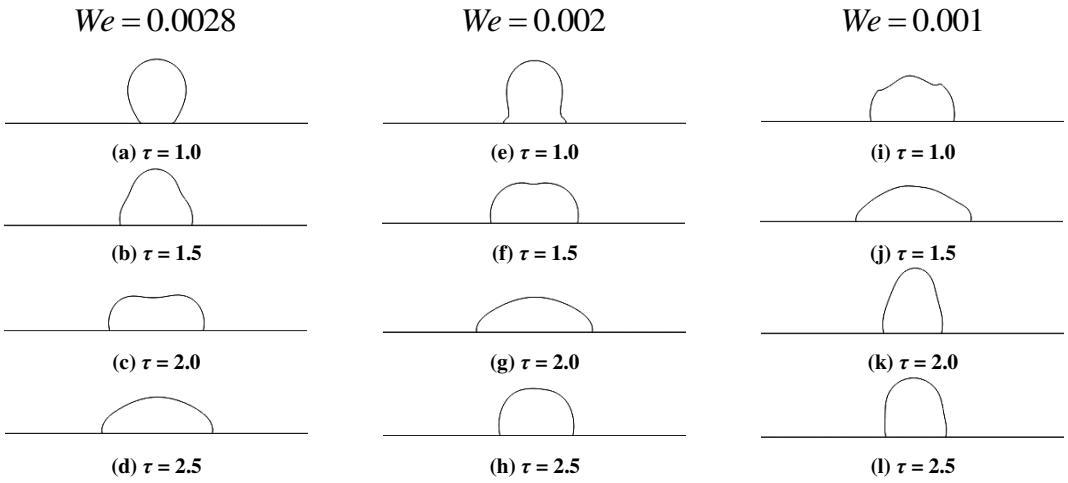

Figure 7. Spreading characteristics of a droplet in terms of interfacial evolution shown at specified instants over a hydrophobic surface for three different *We* numbers

same), shown in Fig. 7. In a generalised framework it can be observed that for the hydrophobic surface the effect of the capillary wave propagating through the droplet interface is significantly suppressed by the repelling effect of the hydrophobic surface. As a consequence, the crest produced at the middle of the interface is not that remarkable, compared to hydrophilic surface. The concave interface formed in Figs. 7(c) & 7(f) quickly diminishes, forming a convex interface. It is well known that in case of a hydrophobic surface, the droplet interface is repelled from the surface and thus spreads less, whereas the increasing interfacial tension favours wider spreading of the liquid over the surface. In other words, two forces oppose to each other, meaning that the droplet interface exerts a resisting effect on the way of its expansion over the hydrophobic surface. Although the increasing interfacial tension due to decrease in Weber number provides favourable conditions for spreading, the repelling action of a hydrophobic surface also supresses expansion. Thus, at *We* (=0.0028) value, the droplet spreads gradually over the surface. However, with the decrease in *We*, the droplet spreads up to a critical limit, a point at which the interfacial tension prevails over the surface repelling of the hydrophobic surface and causes the droplet to retract, thus decreasing the length of spread. The retraction occurs as the hydrophobicity of the surface prevails over the interfacial tension. It can be observed from Fig. 7 that for *We* =0.002, the droplet spreads up to τ = 2.0, and then starts retracting, as can be observed at τ = 2.5. The rebounding of droplet begins earlier, and with further decrease in *We* as it begins even earlier, at τ = 2.0 for *We* =0.001 (Fig. 7(k)).

The behaviour is summarised in Fig. 8. With the decrease in *We* the evolution of spreading length (L_s) increases as the increasing interfacial tension helps the droplet to spread more over the hydrophilic surface, as shown in Fig. 8(a). On the contrary, for

the hydrophobic surface shown in Fig. 8(b), the spreading length increases up to a critical limit and then starts decreasing as the droplet interface starts to retract with the decrease in Weber number. The initiation of retraction appears to occur earlier as Weber number decreases.

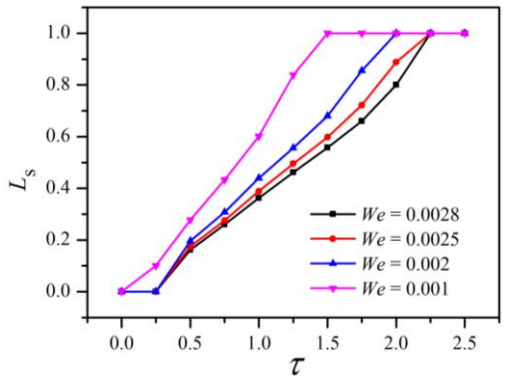

(a) Hydrophilic

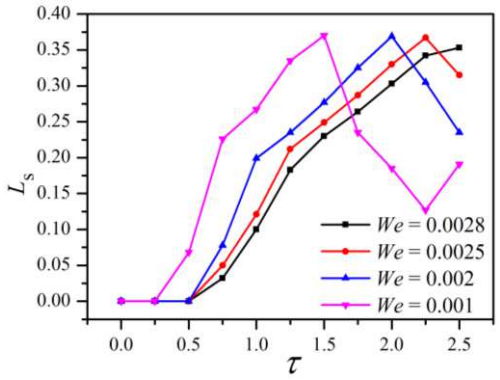

(b) Hydrophobic

Figure 8. Evolution of spreading length with different Weber numbers (*We*) over (a) hydrophilic and (b) hydrophobic surface

5. CONCLUSIONS

Two-dimensional numerical investigations were performed to explore droplet spreading characteristics over a solid substrate of different wettability conditions with varying Weber numbers. The outcomes of the study are presented in terms of droplet interface morphology and spreading length evolution under two wettability conditions – hydrophilic and hydrophobic – along with parametric variations of Weber number. The main findings of the study are as follows.

- The spreading tendency of a droplet over the hydrophilic surface is more prominent compared to the hydrophobic surface. The spreading length of the droplet over hydrophilic surface is significantly larger than hydrophobic surface.
- Decreasing the Weber number results in larger spreading over the hydrophilic surface.
- In the case of the hydrophobic surface, spreading of the droplet increases with decreasing Weber number up to a critical limit, and then the droplet starts to retract. The initiation of retraction over the hydrophobic surface occurs earlier with the decrease in Weber number.

REFERENCES

[1] van Dam, D. B., and Le Clerc, C., 2004, "Experimental study of the impact of an ink-jet printed droplet on a solid substrate", *Phys. Fluids*, Vol. 16, pp. 3403-3414.

[2] Massinon, M., and Lebeau, F., 2012, "Experimental method for the assessment of agricultural spray retention based on high-speed imaging of drop impact on a synthetic superhydrophobic surface", *Biosyst. Eng*., Vol. 112, pp. 56-64.

[3] Oka, Y. I., S. Mihara, and H. Miyata, 2007, "Effective parameters for erosion caused by water droplet impingement and applications to surface treatment technology", *Wear*, Vol. 263, pp. 386-394.

[4] Antonini, C., Innocenti, M., Horn, T., Marengo, M., and Amirfazli, A., 2011, "Understanding the effect of superhydrophobic coatings on energy reduction in anti-icing systems", *Cold Reg. Sci. Technol.*, Vol. 67, pp. 58-67.

[5] Yarin, A.L., 2006, "Drop impact dynamics: splashing, spreading, receding, bouncing", *Annu. Rev. Fluid Mech.,* Vol. 38, pp. 159–192.

[6] Xu, L., 2007, "Liquid drop splashing on smooth, rough, and textured surfaces", *Phys. Rev. E Stat. Nonlin. Soft Matter Phys.*, Vol. 75, pp. 056316.

[7] Aboud, D. G., and Kietzig, A. M., 2015, "Splashing threshold of oblique droplet impacts on surfaces of various wettability", *Langmuir*, Vol. 31, pp. 10100-10111

[8] Stevens, C.S., Latka, A., and Nagel, S.R., 2014, "Comparison of splashing in high- and low viscosity liquids", *Phys. Rev. E Stat. Nonlin. Soft Matter Phys.*, Vol. 89, pp. 063006.

[9] Roisman, I. V., Berberović, E., and Tropea, C., 2009, "Inertia dominated drop collisions. I. On the universal flow in the lamella", *Phys. Fluids*, Vol. 21, pp. 052103.

[10] Pasandideh- Fard, M., Qiao, Y. M., Chandra, S., and Mostaghimi, J., 1996, "Capillary effects during droplet impact on a solid surface", *Phys. Fluids*, Vol. 8, pp. 650-659.

[11] Krishnan, A., Liu, Y. H., Cha, P., Woodward, R., Allara, D., and Vogler, E. A., 2005, "An evaluation of methods for contact angle measurement", *Colloids Surf. B: Biointerfaces*, Vol. 43, pp. 95-98.

[12] Strobel, M., and Lyons, C. S., 2011, "An essay on contact angle measurements", *Plasma Process Polym.,* Vol. 8, pp. 8-13.

[13] Pierce, E., Carmona, F. J., and Amirfazli, A., 2008, "Understanding of sliding and contact angle results in tilted plate experiments", *Colloids Surf. A: Physicochem. Eng. Aspects*, Vol. 323, pp. 73-82.

[14] Brutin, D., Zhu, Z., Rahli, O., Xie, J., Liu, Q., and Tadrist, L., 2009, "Sessile drop in microgravity: creation, contact angle and interface", *Microgravity Sci. Technol*., Vol. 21, pp. 67-76.

[15] Wildeman, S., Visser, C. W., Sun, C., and Lohse, D., 2016, "On the spreading of impacting drops", *J. Fluid Mech*., Vol. 805, pp. 636-655.

[16] Laan, N., de Bruin, K. G., Bartolo, D., Josserand, C., and Bonn, D., 2014, "Maximum diameter of impacting liquid droplets", *Phys. Rev. Appl*., Vol. 2, p. 044018.

[17] Leopoldes, J., and Bucknall, D. G., 2005, "Droplet spreading on microstriped surfaces", *J. Phys. Chem. B.*, Vol. 109, pp. 8973-8977.

[18] Kuznetsov, G. V., Feoktistov, D. V., and Orlova, E. G., 2016, "Regimes of spreading of a water droplet over substrates with varying wettability", *J. Eng. Phys. Thermophys.*, Vol. 89, pp. 317-322.

[19] Liu, X., Zhang, X., and Min, J., 2019, "Spreading of droplets impacting different wettable surfaces at a Weber number close to zero", *Chem. Eng. Sci.*, Vol. 207, pp. 495-503.

[20] Shang, Y., Zhang, Y., Hou, Y., Bai, B., and Zhong, X., 2020, "Effects of surface subcooling on the spreading dynamics of an impact water droplet", *Phys. Fluids*, Vol. 32, p. 123309.

[21] Ristenpart, W. D., McCalla, P. M., Roy, R. V., and Stone, H. A., 2006, "Coalescence of spreading droplets on a wettable substrate", *Phys. Rev. Lett.*, Vol. 97, p. 064501.

[22] Lin, S., Zhao, B., Zou, S., Guo, J., Wei, Z., and Chen, L., 2018, "Impact of viscous droplets on different wettable surfaces: Impact phenomena, the maximum spreading factor, spreading time and post-impact oscillation", *J. Colloid Interface Sci.*, Vol. 516, pp. 86-97.

Conference on Modelling Fluid Flow (CMFF'22)
The 18th International Conference on Fluid Flow Technologies
Budapest, Hungary, August 30 -September 2, 2022

IDENTIFICATION OF LOW FREQUENCY FLUCTUATION IN CENTRIFUGAL FAN

Magdalena STANIK[1], Dominika JASKÓŁA[1], Dominik DEDA[1]

[1] Department of Power Engineering and Turbomachinery, Silesian University of Technology, Konarskiego 18, 44-100 Gliwice, Poland
* magdalenastanik1@gmail.com

ABSTRACT

Centrifugal fans are the most common turbomachines used in technical applications. Many efforts have been made to find the most efficient numerical method of modelling flow in such turbomachines. However, only a few publications focus on the unsteadiness that may have an impact on device efficiency and noise generation. The main goal of this study was to develop an experimental method to investigate or investigate the frequency of oscillation inside the radial fan that can affect the noise. The focus was on measuring pressure changes inside the fan casing, which defined the non-stationary fluctuations in the airflow. The geometry of the fan and the volute were modelled together. The geometric model allowed for the generation of the fluid domain, discretization of space and the construction of a mathematical model describing flow and non-stationary phenomena occurring inside the fan machine. The geometrical model was created using the Solid Works software and the numerical investigation was done using the ANSYS Fluent solver. Computer calculations were compared with the results of experimental research carried out on a 3D printed model. Further, the numerical analysis was validated against the experimental results. Graphs of the dependence of the amplitude (pressure) as a function of time and frequency were obtained. Characteristic frequencies for the largest pressure amplitudes and other relationships describing acoustic phenomena in the centrifugal fan were obtained. The above-mentioned results are the results of a preliminary banking study, which lay a solid basis for subsequent research that is to be taken.

Keywords: Acoustics, Centrifugal fan; CFD; Fourier analysis.

NOMENCLATURE

$\dot{V}$	m^3/s	volumetric flow rate
Δp	Pa	pressure increase
t	°C	temperature
n	rpm	rotational speed
b	-	blades number minute
d	m	diameter
f	Hz	frequency
$\dot{m}$	kg/s	mass flow rate

INTRODUCTION

Fans, blowers, and flow compressors are working machines designed to transport or compress the gas, one of these activities may dominate the other. Blowers, unlike compressors, compress the medium to relatively low pressure, the contractual limit is circa 0.29 MPa. In many cases, overcoming the resistance is the main task of the fan, not the delivery of compressed gas. External work put on the rotor shaft forces the gas, at the same time giving it an increase in kinetic energy. As the energy transfer process takes place continuously during the flow through the rotating fan channels, it is classified as a continuous flow machine. The name of the radial fan tested in the project comes from the radial outflow of the medium from the rotor. It takes place approximately in a plane perpendicular to the axis of rotation, and the meridional components have radial velocities or are slightly deviated from this direction. The centrifugal fan folds up from the rotor mounted on the motor drive shaft. In the centrifugal fan, the rotors are made of two discs (supporting and covering), between which the blades are fixed [1]. The main source of sound in the ventilation system is the fan. Fan noise has different origins. The primary factor is the fan design itself, the number of blades and their shape takes a significant role. Performance, pressure, air velocity, size, and shape of the casing are other significant factors. A general breakdown of noise can be made into noise due to aerodynamic and mechanical factors. The

aerodynamic noise is directly related to airflow through the vane system and the accompanying changes in the surface pressure in the blade-to-blade channel. The sources of mechanical noise are influenced by: imbalance of the rotor, incorrect operation of the bearings, operation of the electric motor, and possible mechanical vibrations of components caused by stiffness of the structure. The area, where acoustic vibrations occur is called the acoustic field. This field describes the propagation of sound in an idealized space in which the influence of the bonding surfaces and the items in it. The distribution of this field is negligible. Under certain conditions, when the influence of the surfaces limiting the movement of the acoustic wave is insignificant, noise measurements can be made assuming that the acoustic field has the characteristics of a free field. A diffuse sound field is an area where a sound wave reflects so many times that it moves in all directions with the same amplitude and probability. The most frequently measured size of the acoustic field is the acoustic pressure, which is the difference between the environmental pressure at a given moment and static pressure. On its basis, it is determined, by sound intensity or sound power. Fan tests on fans can be carried out by two main methods, i.e. quantitative (balance) and qualitative (structure test of flow). Quantitative research includes mass and energy balance, and qualitative research includes invasive and non-invasive measurements. The numerical research (CFD) mentioned in the article belongs to both groups simultaneously. [7] Significant advances in gas flow design methods using numerical fluid mechanics and increases in the computational efficiency of computers have enabled the development of research perspectives in the field of fluid flows. This method gives the possibility of imaging taking into account the flow and fluctuations in the design process of the radial fans. [9] Thanks to the numerical method it is possible to consider complex flow phenomena occurring in rotating machinery. From the results obtained employing the CFD tools, a frequency analysis was performed, and the Furrier transformation made it possible to change the signal into an amplitude spectrum[8]. Hydraulic losses and pressure drops are influenced by many factors, such as the housing structure or the impeller itself[10]. As it is known from the research, even such trivial aspects as the gap between the inlet and the rotor influence pressure losses and machine efficiency [10]. Poor design can lead to unwanted flow interruptions and the formation of turbulence that will adversely affect the performance of the entire machine. [11]

CENTRIFUGAL FAN MODELS

The studies were conducted simultaneously at the Department of Power Engineering and Turbomachinery (DPET) at the Silesian University of Technology (SUT) and the Institute of Thermal Turbomachinery (ITT) at Karlsruhe Institute of Technology (KIT). The models were designed for a similar design point, however, they differ in dimensions. Nevertheless, they can be compared according to fan similarity theory. Real radial fans were built, the design of which was based on a series of calculations carried out by A. Get [2]. The number of rotor blades was calculated, and the length, central as well as outlet angle and the skeleton radius of the blade were calculated according to mentioned reference. Further, they were designed in Solid Works and manufactured employing Nouvel fast prototyping tools, i.e. 3D printing. The table presents the design parameters for which the system elements were designed. Figure 1 shows the SUT fan geometry.

Table 1. Fans design parameters

Variable	KIT	SUT
V, m^3 /s	0,05	0,05
Δp, Pa	63	50
t, °	20	20
n, rpm	600	1000
b, -	9	8
d, m	0.325	0.25

Figure 1. 3D geometry from SUT

EXPERIMENTAL TEST RIG

Both experimental stands have been created to conduct acoustic tests of the fan model. Advanced printing methods were used to create an experimental model. The test rig in Karlsruhe is illustrated in Figure 2.

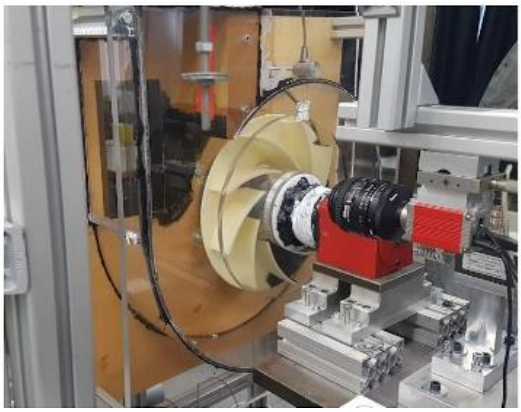

Figure 2. The centrifugal fan test rig of KIT

The hub, the spiral casing as well as the sidewall of the housing hub are made of acrylic glass for optical accessibility. To record the performance curve of the centrifugal fan, pressure values are taken upstream and downstream of the fan what allowed for determining the total pressure increase. Pressure measurement in the straight pipe gives the volume flow rate according to DIN EN ISO 5167. Additionally, the temperature sensor at the inlet as well as the outlet pressure and temperature sensor were mounted. The working point can be shifted along the performance curve by either closing the throttle or powering the auxiliary fan. The inlet section of the test fan was designed to allow determining boundary conditions for the numerical simulations.

The SUT test rig was designed to meet similar flow parameters of the KIT fan. The rig was manufactured employing 3D printing. An electric motor powered by 24 V DC with a 10:1 gear ratio was selected. The stand was also equipped with basic measuring elements: a tachometer and an anemometer. The acoustic measurements were carried out using a probe by PCB PIEZOTRONICS [3]. It is a compact sound pressure measuring device that allows measuring the pressure fluctuation in the flow field that is a source of the noise. The probe is constructed with a detachable stainless steel tub, whose task is to provide an acoustic signal into the microphone inside the probe housing. The microphone with the ICP probe, model 377B26, was placed in the two measuring points shown in the figure below. Measurements were carried out in the area of the air outlet of the impeller as the highest velocity and pressure values are expected there, see Figure 3. Point 1 is halfway between the impeller and the casing, point 2 is offset from the impeller by the same distance. Point 2 is also near the volute tongue, where the greatest turbulent movements happen.

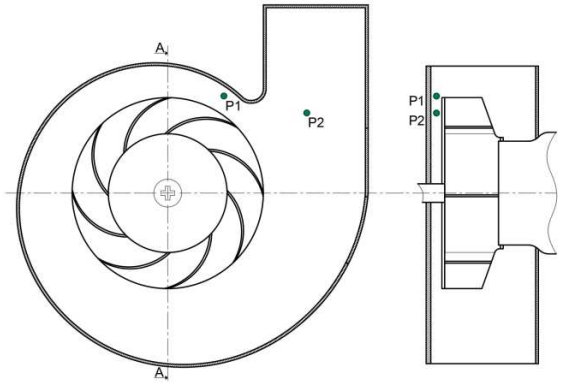

Figure 3. Measuring points in a model of SUT.

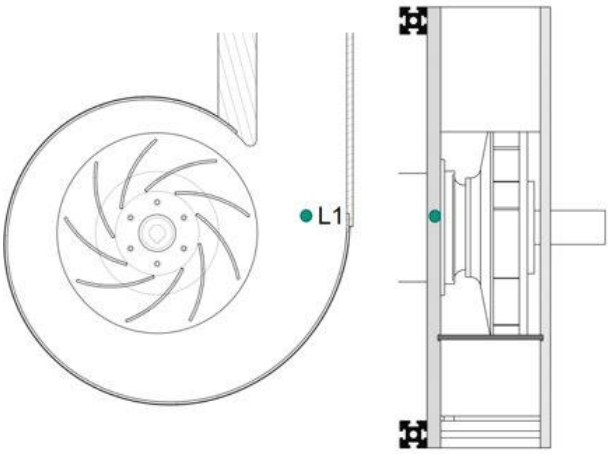

Figure 4 Measuring points in a model of KIT.

NUMERICAL EXPERIMENT

For both models, the simulations were carried out in an unsteady state. Direct numerical simulation (DNS) methods solve the Navier-Stokes equation without any simplifications and predict the unsteady flow including all fluctuations spectra in space and time, and thereby the acoustic field. However, such methods are very demanding in terms of computational time and are not available for technical applications at the moment. Similarly, large eddy simulation (LES) methods are not practical for these applications either, because the requirement regarding the numerical mesh resolution is extremely difficult to meet. Therefore, it was decided that the appropriate method will be unsteady Reynolds-averaged Navier-Stokes (URANS) complemented with Metner shear stress transport (k-ω SST) and the scale adaptive simulation (SAS-SST) turbulence models will be used and compared. The computation domain is split into two parts, the flow field in the volume containing the fan is computed in a rotating frame, and the inlet and the discharge duct are set as stationary. It is important to note that the frequency range is also limited by the mesh spacing. The boundary conditions for the KIT model were selected for the fan nominal load, i.e. the volume flow rate of 0.0637 kg/s. This value was set up at the outlet, whereas at the inlet total parameters were

assumed, i.e. total pressure of 1 bar and total temperature of 300 K. The rotor rotational speed is 600 rpm. The simulations are conducted on a coarse and a fine mesh. The numerical mesh for the case under analysis contains about 0.65×10^6 elements for the rotor domain and 0.8×10^6 elements for the stator domain, which gives almost 1.5×10^6 elements in total. The numerical mesh is of a tetrahedral type with prisms in boundary layers. The y^+ value ranged from 1 for the rotor blades to 3 for the outlet port of the volute.

Figure 5 shows the fan characteristics as the relationships between the pressure rise, efficiency, and the volume flow rate for the rotor constant speed (600 rpm). Results were obtained experimentally and from steady-state CFD simulations with the SST turbulence model on the coarse mesh. It is noticeable that there is a very good convergence between the experimental and numerical results. The adopted numerical method well captures the operating conditions of the centrifugal fan under consideration.

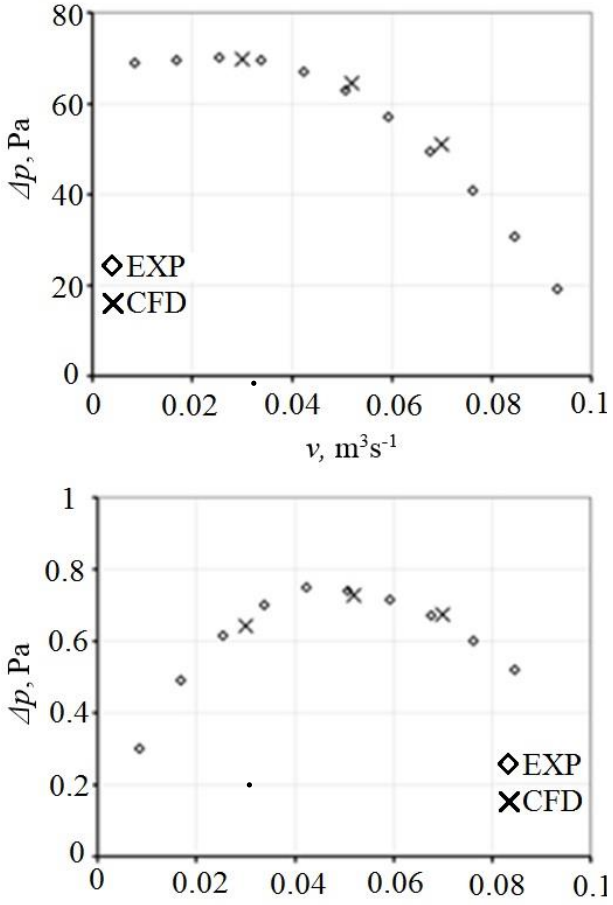

Figure 5. Fan characteristic – comparison of the experiment with CFD modelling

The document presents the results of the transient state from SUT. The experiment was based on the pressure difference between the inlet and outlet of the domain. The fan is designed for a pressure difference of 50 Pa. The design pressure value was also used as a boundary condition for the calculation. The rotor rotational speed is 1000 rpm. The domain of the chasing and rotor consists of 2.1×10^6 elements in total. Results of CFD analysis do not show full agreement with the experiment. This may be due to insufficient mesh quality. However, a more likely reason is the rotor design itself. The applied computational model allowed for an approximate construction of the rotor but did not include all the exact parameters allowing for a sufficient accuracy of the representation of the blades. A coarse mesh sensitivity analysis was conducted to identify if the under-densified mesh is the source of the failure to achieve the required accuracy. Each of the prepared meshes was characterized by the different number of elements or approaches to element size distribution. A feature of the coexistence of all used numerical grids was the application of cells of specific shapes inside the computational domain. It showed that the further increment of the mesh elements gives no meaningful change in occurring flow phenomena. The time step is set to equal 1° displacement of the rotor.

The numerical analysis allowed us to determine the speed inside the fan housing. It is visible that the highest speeds occur in the vicinity of the vanes runoff and at the impeller outlet, see Figure 7. Undesirable air movement is observed which is returned from the volute to the impeller, see Figure 7. This is due to the gap between the rotor and the outlet. Regions of increased velocity coincide with regions of increased pressure

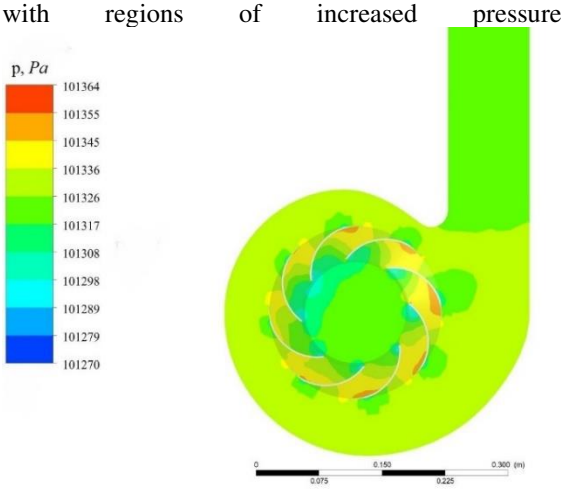

Figure 6 Total pressure contours in SUT fan.

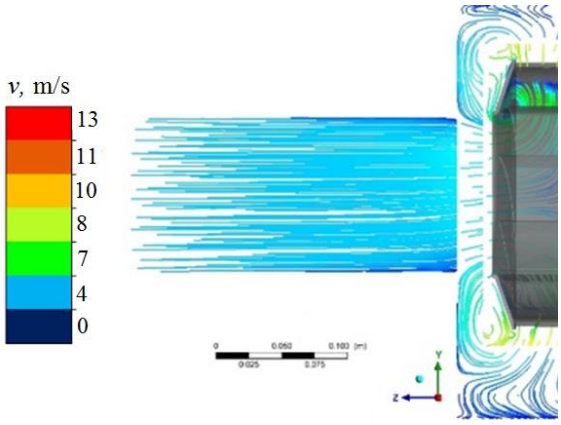

Figure 7. Velocity contours for model form SUT.

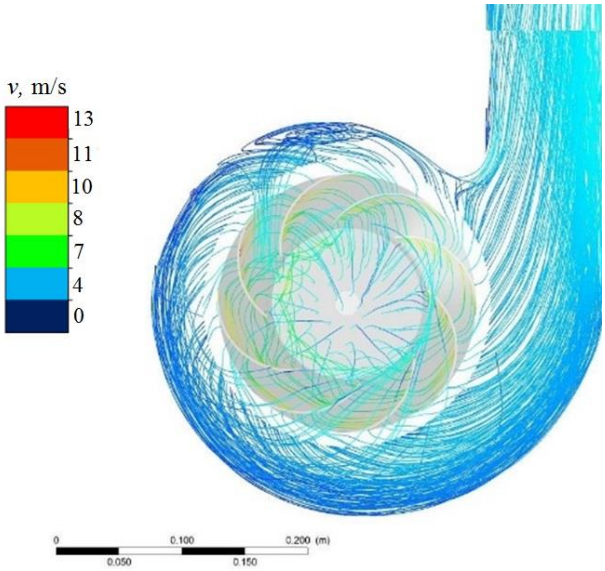

Figure 8 Velocity counts for the model from SUT.

FREQUENCY ANALYSIS OF PRESSURE FLUCTUATIONS.

Measurement conducted in KIT, and SUT allowed for obtaining several different waveforms, being the dependence of the voltage signal (mV) on time (ms). The obtained voltage signal was converted into a pressure value according to the conversion factor included in the device manual further, the Fourier analysis was performed for selected 1024 time samples. Graphs of the dependence of the amplitude (pressure) as a function of time and frequency were obtained. Figures 9 and 10 show the obtained spectrum of pressure fluctuation based on the experiment whereas. Figures 11 and Figure 12 depict the pressure fluctuation spectrum based on the numerical experiment. As it can be seen in the experiment, there appears a tonal noise with a frequency lower than Blade Passing Frequency (BPF).

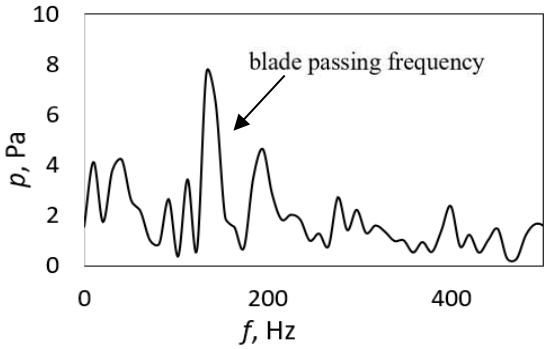

Figure 9. Pressure fluctuation spectrum based on the experiment, point 1, SUT

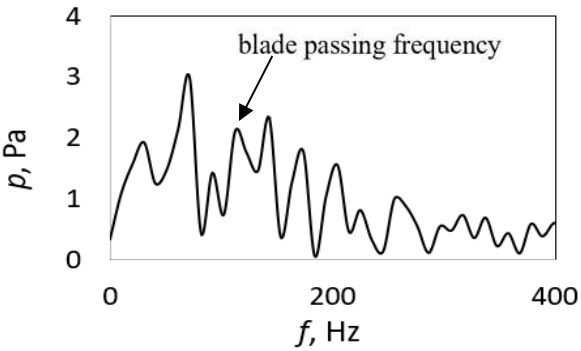

Figure 10. Pressure fluctuation spectrum based on the experiment, point 1, SUT

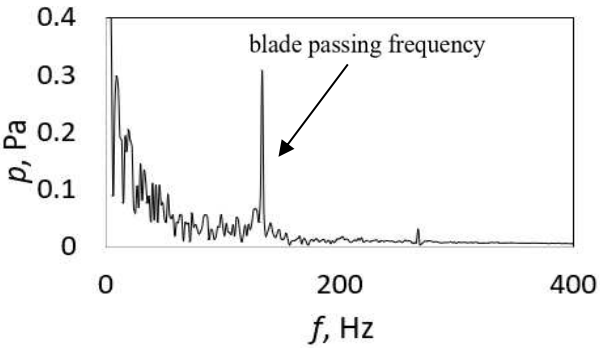

Figure 11 Pressure fluctuation spectrum based on the CFD, point 1, SUT

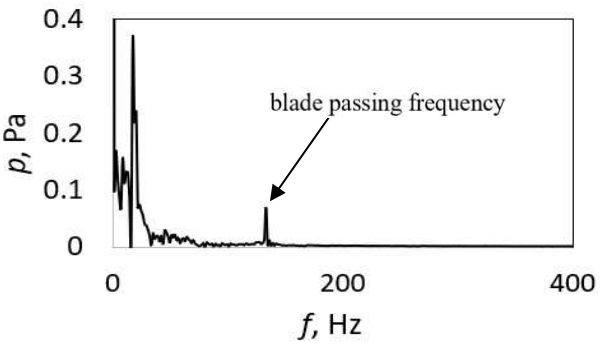

Figure 12 Pressure fluctuation spectrum based on the CFD, point 2, SUT

Presented FFT analysis from SUT shows that for both experiment and CFD analysis it is possible to distinguish blade passage frequency. However, this phenomenon is much more noticeable in point 1 located closer to the rotor. It can be seen that in point 2, the frequency of the passing blades is less significant, while other pressure peaks become more pronounced and rach the value of blade passing frequency at this part of the model. Given the location of the point, it can be concluded that the observed fluctuations are associated with increased tidal turbulence. This may be due to interactions with the casing, which would confirm the study.

Figure 13 depicts the pressure fluctuations obtained numerically. The BPF obtained from the URANS simulations with the SST and the SAS turbulence model totals 97 Hz, which seems to be a bit too high. In the result of the simulation based on the SAS turbulence model, there is a frequency that is half the BPF value. Additionally, significant differences appear between the two models for higher frequencies, exceeding 1.5 kHz. The maximum amplitude of the pressure fluctuations is about 0.7 Pa. It corresponds to the blade passing frequency (BPF) and shows harmonic features.

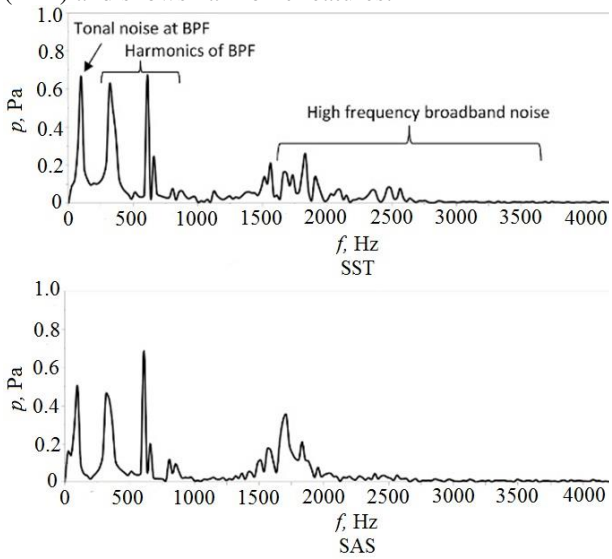

Figure 13. Pressure fluctuation spectrum based on CFD, KIT [4]

CONCLUSIONS

The main objective of the presented research is to find a research workshop. The results of collaboration recently started between the Department of Power Engineering and Turbomachinery of the Silesian University of Technology and the Institute of Thermal Turbomachinery of Karlsruhe Institute of Technology to investigate the flow field with a focus on the noise emission within a centrifugal fan is presented in this paper. The research is both experimental and numerical. Although a complete method for identifying noise sources in flow machines has not been fully developed, the results seem promising. The numerical model has the potential for deep investigation of noise emission due to the pressure fluctuation in centrifugal fans. Studies conducted by the two universities, despite their differences, show considerable similarity in FFT analysis. In both, the KIT and SUT experiments it can be seen that not only blade passing frequency but also the low frequency fluctuation is present. However, its sources, due to different ranges of values, have not been found.

The presented centrifugal fans have been designed for nominal load and operating conditions. Taking into account the similar results of both party studies, the opportunities for improvement are identified which may lead to a deeper understanding of flow phenomena in the most popular turbomachinery. It is also worth remembering that due to the interaction with the piping system, temporary drops in the flow rate may occur. The main aim of that paper was to extend numerical calculations so that they illustrate low frequency flow fluctuations. Achieved results show that numerical methods were correctly chosen and allowed the presentation of phenomena which are the topic of the paper. It has to be emphasized that this was a primary experiment to prove the research gap that has to be studied to provide more sustainable machines.

REFERENCES

[1] S. Kuczewski, Wentylatory Promieniowe, Warszawa, 1966.

[2]A. Gjeta, L. Malka “Outlet Surface Area Influence in Spiral Casing Design on Centrifugal Fan Performance,” European Journal of Engineering Research and Science, January 2020.

[3] Probe Microphone ICP®, Installation and Operating Manual

[4] B. Pritz et al. Identification of unsteady effects in the flow through a centrifugal fan using CFD/CAA methods.

[5] S. Dykas et al., “Numerical method for modelling acoustic waves propagation.”.Arch.Acoust.35(2010),.

[6] S. Fortuna, K. Sobczak; “Numerical and experimental investigations of the flow in the radial fan.”.Mechanics 27(2008), 4,138–143.

[7] T.Siwek,”Badania przepływów w wentylatorze z wirnikiem promieniowym o zabudowie osiowej”, Kraków 2017

[8] G.Szwoch „Analiza częstotliwościowa na procesach sygnałowych”, Politechnika Gdańska

[9] S.Boroń, P.Kubica, „Zastosowanie numerycznej mechaniki płynów CFD do modelowania zabezpieczania pomieszczeń stałymi urządzeniami gaśniczymi gazowymi”, CNBOP-PIB 2016

[10] A.Gejta, „Effect of Clearance Gap in Spiral Casing Design of a Centrifugal Fan with Optimized Impellers”, European Journal of Engineering Research and Science · September 2019
[11] Yu-Tai Lee, „Impact of fan gap flow to the centrifugal impeller aerodynamics”, Glasgow 2012

Conference on Modelling Fluid Flow (CMFF'22)
The 18th International Conference on Fluid Flow Technologies
Budapest, Hungary, August 30-September 2, 2022

LES OF A NON-PREMIXED HYDROGEN FLAME STABILIZED BY WAVY-WALL BLUFF-BODY

Agnieszka WAWRZAK[1], Robert KANTOCH[2], Artur TYLISZCZAK[3]

[1] Department of Thermal Machinery, Faculty of Mechanical Engineering and Computer Science, Czestochowa University of Technology. Al. Armii Krajowej 21, 42-201 Czestochowa, Poland. Tel.: +48 34 3250 590, Fax: +48 34 3250 555, E-mail: agnieszka.wawrzak@pcz.pl
[2] Department of Thermal Machinery, Faculty of Mechanical Engineering and Computer Science, Czestochowa University of Technology. E-mail: robert.kantoch@pcz.pl
[3] Department of Thermal Machinery, Faculty of Mechanical Engineering and Computer Science, Czestochowa University of Technology. E-mail: artur.tyliszczak@pcz.pl

ABSTRACT

Numerical analysis of non-premixed hydrogen flames stabilized by specially designed bluff-bodies is presented. The response of the flame on the different wall topologies (flat or wavy, with the waviness oriented streamwise) is studied using large-eddy simulations (LES) and applying a two-stage procedure involving commercial ANSYS software and an in-house academic high-order code. The chemical source terms are calculated with the help of the 'no-model' approach. In addition, the study attempts to compare the obtained results with the solutions predicted by the Eulerian Stochastic Fields method. Dynamics of flames is found to be strongly dependent on geometrical shaping. In the case of the bluff-body with wavy walls the temperature isosurfaces reflect the bluff-body shape due to large-scale intense vortices induced in the outer shear-layer. The effect of change in wall topology is justified and quantified through time averaged mean and fluctuating quantities. It is the most pronounced in local entrainment of the fuel stream and flame radial position. When the waviness is applied to the bluff-body walls, the mixing is enhanced, the flame is noticeably shifted towards the axis and inlet plane, and slightly stretched in the radial direction compared to the flat wall. m

Keywords: bluff-body, Eulerian Fields, hydrogen, LES, non-premixed flames

NOMENCLATURE

D	$[mm]$	diameter
R	$[J/K\ mol]$	universal gas constant
T	$[K]$	temperature
U_b	$[m/s]$	bulk velocity of the co-flow
Y_α	$[-]$	species mass fractions
D_α	$[m^2/s]$	molecular diffusivity
h	$[J]$	enthalpy
p	$[Pa]$	hydrodynamic pressure
p_0	$[Pa]$	thermodynamic pressure
$\mathbf{S}$	[]	rate of strain tensor
$\boldsymbol{\tau}$	[]	stress tensor
$\mathbf{u}$	$[m/s]$	velocity vector
Δ	$[m]$	LES filter size
$\dot{\omega}_k$	$[mol/m^3\ s]$	reaction rate
μ	$[Pa\ s]$	molecular viscosity
ρ	$[kg/m^3]$	density
$\tilde{\phi}_\alpha$	$[-]$	reactive scalar
ξ^n_α	$[-]$	stochastic representation of the scalar

Subscripts and Superscripts

α	indices of the species
SGS, t	related to sub-grid or turbulent
t	time

1. INTRODUCTION

A better understanding of mutual interactions between turbulent flow and flame occurring downstream the bluff-body geometries limit the further progress in improvements in the efficiency and safety of various combustion applications (burners, chambers, engines). Moreover, a suitable control of turbulent flames dynamics is required for establishment of low-emissions devices according to current international regulations. Such a control can be achieved by applying passive and/or active flow control techniques.Both provide modulation of the multi-scale mixing processes (enhancement/suppression) by the intensification of interactions between large and small turbulent scales.

Using the bluff-body as a part of the injection system constitutes the prominent example of the passive flame control. The bluff-body generates recirculation zones improving the mixing and stabilizing the flame position [1]. Tyliszczak et al. [2] examined a non-premixed flame stabilized in a central recirculation zone produced by a conical/cylindrical bluff-body. They showed that the flame is approach-

ing extinction due to even small changes in simulation parameters. Combination of the passive and active control methods can be applied for optimization of the combustion process in bluff-body burner as it was shown by Kypraiou et al. [3]. The researchers performed the experimental studies on the premixed, partially-premixed and non-premixed methane flames showing that the impact of acoustic oscillations on the bluff-body flames is directly related to the fuel injection system.

The complexity of turbulent mixing and combustion processes raises many important questions that still remain unanswered, despite the great interest of the scientific community in this field. For instance, to what extend does the mixing of the fuel and oxidizer downstream the bluff-body depend on the shape and roughness of the bluff-body? As it was recently demonstrated by [4], the wavy wall, with carefully selected waviness parameters, can effectively enhance the effect of amplitude modulation and hence increase wall shear stress and postpone turbulent separation.

The present paper aims at numerical simulations of non-premixed hydrogen flame stabilized by specially designed bluff-bodies with corrugated surfaces. Computational fluid dynamics (CFD) tools have been widely used for the flame control analyses providing the results related to the global characteristics and deep insight into flame structure and dynamics. In this work we use the Large Eddy Simulation approach and the 'no model' approach where the chemical sources terms are calculated directly from the Arrhenius formula using the filtered variables [5]. The response of the flame on different wall topologies (flat or wavy, with the waviness oriented streamwise) is thoroughly discussed based on instantaneous and time averaged results. For the selected cases we performed the calculations using the Eulerian Stochastic Fields (ESF) method [6] which in the past proved to be able to correctly capture the dynamics of turbulent flames [7, 8] and strongly non-stationary events like the blow-off of bluff-body flames [9]. Results obtained from these computations will be compared with predictions of 'no model' calculations to demonstrate that the sub-grid physics ignored by the no-model approach does not have significant impact on the results and presented during the conference.

2. MODELLING

2.1. LES Approach

In the present study we use two different numerical LES solvers applying two-stage approach. In the first stage, the second order ANSYS Fluent LES solver is involved to model the flow inside the inlet section of the bluff-body burner. The further calculations are performed using a in-house high-order numerical algorithm based on the projection methods[10]. It solves the Favre filtered set of the governing equations assuming the low Mach number approximation [11]:

$$\partial_t \bar{\rho} + \nabla \cdot (\bar{\rho}\widetilde{\mathbf{u}}) = 0 \tag{1}$$

$$\bar{\rho}\partial_t \widetilde{\mathbf{u}} + (\bar{\rho}\widetilde{\mathbf{u}} \cdot \nabla)\widetilde{\mathbf{u}} + \nabla \bar{p} = \nabla \cdot \left(\boldsymbol{\tau} + \boldsymbol{\tau}^{\mathrm{SGS}}\right) \tag{2}$$

$$\bar{\rho}\partial_t \widetilde{Y}_\alpha + (\bar{\rho}\widetilde{\mathbf{u}} \cdot \nabla)\widetilde{Y}_\alpha = \nabla \cdot \left(\bar{\rho}(D_\alpha + D_\alpha^{\mathrm{SGS}})\nabla \widetilde{Y}_\alpha\right) + \overline{\dot{w}}_\alpha \tag{3}$$

$$\bar{\rho}\partial_t \widetilde{h} + (\bar{\rho}\widetilde{\mathbf{u}} \cdot \nabla)\widetilde{h} = \nabla \cdot \left(\bar{\rho}(D + D^{\mathrm{SGS}})\nabla h\right) \tag{4}$$

$$p_0 = \overline{\rho} R \widetilde{T} \tag{5}$$

where the bar and tilde symbols denote filtered quantities, u_i are the velocity components, p is the hydrodynamic pressure, ρ is the density and h stands for the total enthalpy. The symbols p_0 and R are the thermodynamic pressure and gas constant, respectively. The subscript α is the index of the species $\alpha = 1, \ldots,$ N-species whereas the variables Y_α represent species mass fractions. An unresolved sub-grid stress tensor, resulting from the filtering of the non-linear advection terms is defined as $\boldsymbol{\tau}^{\mathrm{SGS}} = 2\mu_{\mathrm{t}}\mathbf{S}$, where $\mathbf{S}$ is the rate of strain tensor of the resolved velocity field and μ_{t} is the sub-grid viscosity computed according to the model proposed by Vreman [12]. The sub-grid diffusivities in Eqs. 3, 4 are computed as $D^{\mathrm{SGS}} = \mu_t/(\bar{\rho}\sigma)$ where σ is the turbulent Schmidt/Prandtl number assumed equal to 0.7 [7].

The chemical sources terms $\overline{\dot{w}_\alpha}$ in Eq. 3 involve the filtered reaction rates of species α, which are strongly non-linear functions of the species mass fractions and enthalpy:

$$\overline{\dot{w}_\alpha(\mathbf{Y}, h)} = \dot{w}_\alpha(\widetilde{\mathbf{Y}}, \widetilde{h}) + \mathcal{F}(\widetilde{Y_\alpha Y_\alpha}'', \widetilde{Y_\alpha}''\widetilde{T}, \ldots) \tag{6}$$

They are computed applying the 'no model' approach, i.e., they are calculated directly from the Arrhenius formula using the filtered variable $\overline{\dot{w}_\alpha(\mathbf{Y}, h)} = \dot{w}_\alpha(\widetilde{\mathbf{Y}}, \widetilde{h})$ [5] or eigth or four ESF [6]. In the ESF combustion model the scalar Equations (3) and (4) are replaced by an equivalent evolution equation for the density-weighted filtered PDF function, which is solved using the stochastic field method proposed by Valiño [6]. Each scalar $\tilde{\phi}_\alpha$ is represented by $1 \le n \le N_s$ stochastic fields ξ_α^n such that

$$\tilde{\phi}_\alpha = \frac{1}{N_s}\sum_{n=1}^{N_s} \xi_\alpha^n \tag{7}$$

The stochastic fields evolve according to:

$$\begin{aligned} \mathrm{d}\xi_\alpha^n = &- \widetilde{\mathbf{u}} \cdot \nabla \xi_\alpha^n \mathrm{d}t + \nabla \cdot \left(\left(D_\alpha + D_\alpha^{SGS}\right) \nabla \xi_\alpha^n\right) \mathrm{d}t \\ &+ \sqrt{2D_\alpha^{SGS}}\, \nabla \xi_\alpha^n \cdot \mathrm{d}\mathbf{W} - 0.5\tau^{-1}\left(\xi_\alpha^n - \tilde{\phi}_\alpha\right)\mathrm{d}t \\ &+ \dot{w}_\alpha(\xi_\alpha^n)\mathrm{d}t \end{aligned}$$

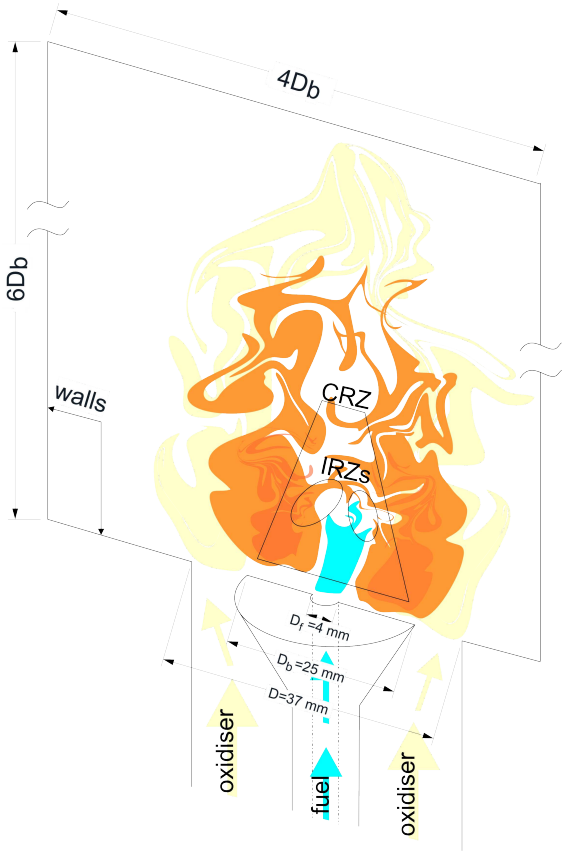

Figure 1. Schematic view on the computational configuration.

(8)

where the micro-mixing time scale equals to $\tau = \bar{\rho}\Delta^2/(\mu + \mu_t)$ [7] with $\Delta = V_{\text{cell}}^{1/3}$ being the LES filter width and d**W** represents a vector of Wiener process increments different for each field. The impact of the modelling of the chemical source terms will be discussed during the conference. In this paper we limit to the cases simulated using the 'no model' approach.

2.2. Test case

In the present work we consider a typical combustion chamber with the conical bluff-body similar to the one studied experimentally by Kypraiou et al. [3] but instead of methane, we use the hydrogen diluted with nitrogen, which is an alternative zero-carbon fuel. The hydrogen mass fraction in the fuel stream is equal to 0.05. Schematic view on the problem considered is presented in Figure 1. The cold (300 K) fuel is injected to the chamber through the 4mm slot in a fuel pipe ended with a bluff-body with the axial velocity assumed equal to 10 m/s. Inside the chamber the fuel ignites in hot (1000 K) co-flowing air. The combustion power is 0.5 kW and the equivalence ratio is equal to 0.047. Unlike in the original configuration of Kypraiou et al. [3] we do not add the swirl to the oxidiser stream and the dominant effect on the flame is due to the changing geometry of the

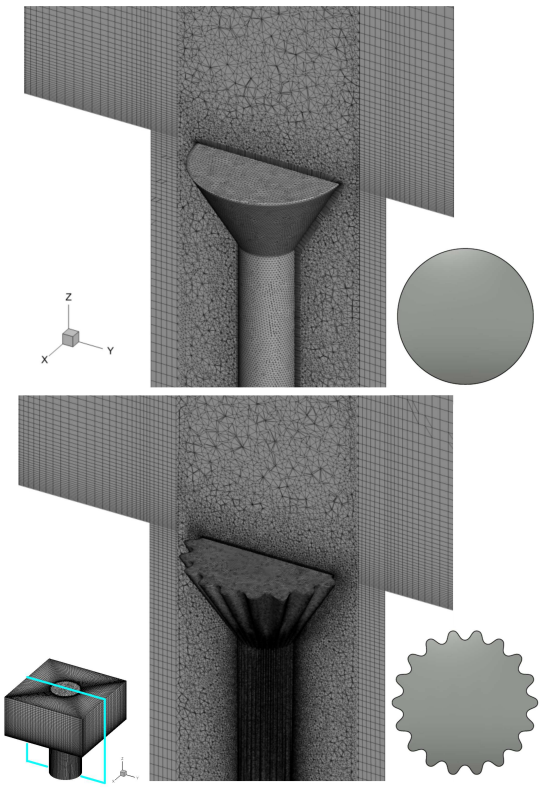

Figure 2. Bluff-body geometries and computational meshes (ANSYS Meshing).

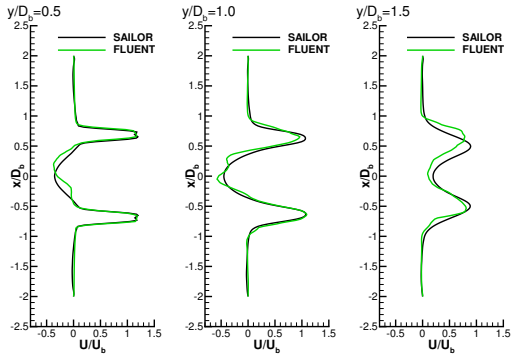

Figure 3. Axial velocity profiles at three different heights above the bluff-body obtained using Fluent and SAILOR codes.

bluff-body. Thus, a comparison with experimental results, even qualitative, is impossible.

Concerning the dynamics of the bluff-body stabilized flames, directly above the bluff-body a central recirculation zone (CRZ in Fig. 1) is formed. Its dimensions and inner structure depend on the bluff-body size and flow parameters. Inside CRZ may exist smaller inner recirculation zones (IRZs). The bluff-bodies investigated in the paper are characterised by the equivalent diameter $D_b = 2\sqrt{S/\pi}$=25 mm (S - actual area of bluff body) and they are placed in a circular duct of diameter D=37 mm. Two different

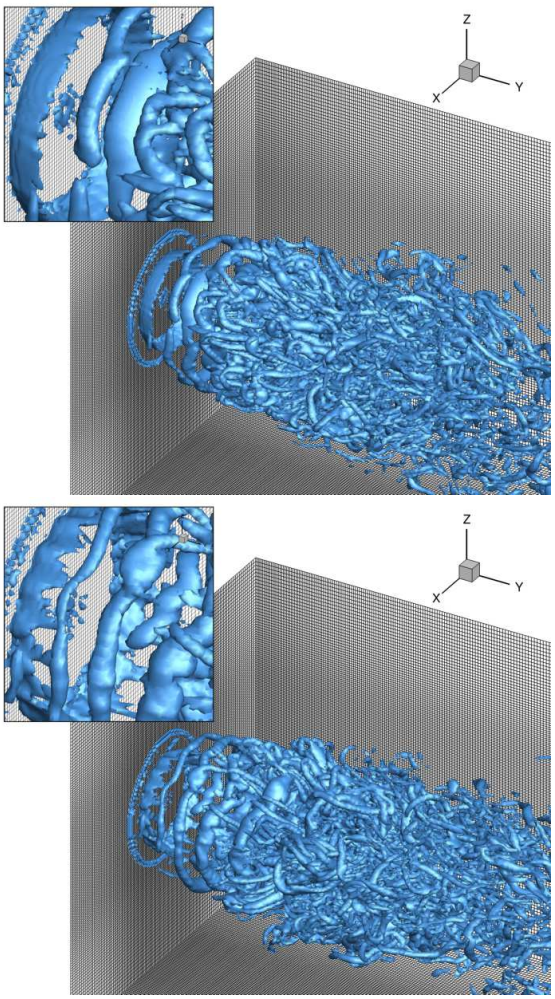

Figure 4. Visualization of the vortex structures. Instantaneous Q-parameter isosurfaces for bluff-bodies with different wall topologies (flat wall - upper row, wavy wall - bottom row). Computational mesh (SAILOR).

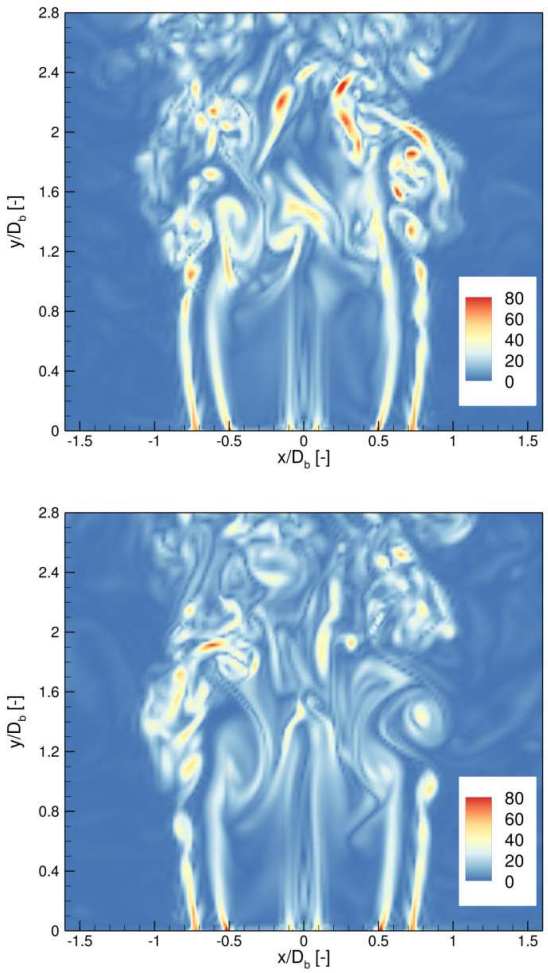

Figure 5. Instantaneous vorticity contours (flat wall - upper row, wavy wall - bottom row).

bluff-bodies are considered, with flat and wavy wall with the waviness oriented streamwise. Both geometries are displayed in Figure 2 along with the computational meshes prepared in the ANSYS Meshing module.

2.3. Numerical details

As mentioned before, the simulations are performed using a two-stage approach. In the first stage we involve the ANSYS Fluent LES solver to model flow through the entrance duct and around the bluff-bodies. In these preliminary calculations we acquire unsteady velocity signals at the end of the inlet section for a period of $150D_b/U_b$ (U_b- bulk velocity of the co-flow). In Fig. 2 the computational grids are presented generated in ANSYS Meshing module. They are block-structured and precisely fitted to the shape of each bluff-body. All geometries are discretized in this way that a near-wall cell height allows for a proper resolution of the turbulent boundary layers ($y+ \approx 1$). The minimum element size is assumed at the level of 0.5 mm for the case with flat wall, whereas in the case of the wavy-wall bluff-body a finer mesh (0.25 mm) in the near-wall region is needed. The overall numbers of cells in the inlet duct are equal to 3.6×10^5 and 3.7×10^5 for the cylindrical bluff-body with the smooth and wavy wall, respectively.

In the second part of the calculations a numerical code SAILOR [10], based on a high-order compact difference algorithm for low Mach number reactive flows, is used to predict the combustion process. Number of studies devoted to number of combustion problems in jet type flames [13, 14] and mixing layers [15, 16] verified the SAILOR codes confirming its accuracy. The extracted velocity fields are imposed onto the inlet plane of the computational domain involving only the outer section of the burner. The computational domain extends $6D_b$ in the axial direction and $4D_b$ in the radial and tangential directions (see Fig. 1). Grid independent solution is obtained at a grid size $N_x \times N_z \times N_y = 144 \times 144 \times 192$ nodes. The nodes are compacted axially and ra-

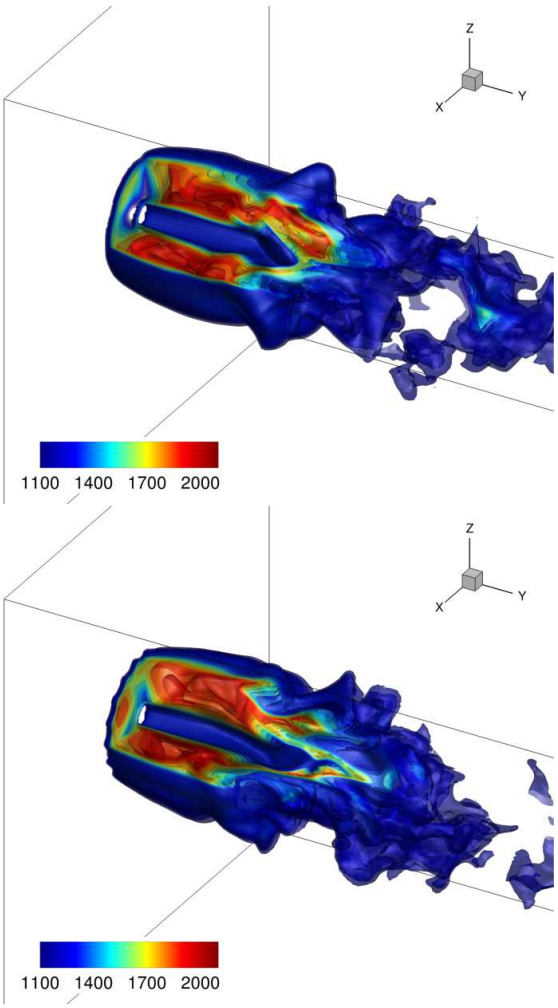

Figure 6. Visualization of flames stabilised by bluff-bodies with different wall topologies (flat wall - upper row, wavy wall - bottom row). Instantaneous temperature isosurfaces.

dially such that almost a uniform grid nodes distribution is ensured at the inlet section (see Figure 4. Maximum cell volume is equal to 1.7×10^{-9} m^3, that corresponds to the minimum cell volume of the computational meshes used in ANSYS software. The time-step is computed according to the Courant-Friedrichs-Lewy (CFL) condition with the maximum CFL number equal to 0.25. Concerning the boundary conditions at the side boundaries, the velocity is set to zero and the species and enthalpy are computed form the Neumann condition, i.e., $\partial Y_\alpha/\partial n = 0$ and $\partial h/\partial n = 0$. The pressure is computed from the Neumann condition ($\partial p/\partial n = 0$) both at the side boundaries as well as at the inlet plane. At the outlet boundary, all velocity components, species and enthalpy are computed from the convective boundary condition $\partial C/\partial t + V_c \partial C/\partial y = 0$, where C represents a general variable and V_c is the calculated as the mean velocity in the outlet plane. To avoid back-flow the velocity V_c is limited such that $V_c = \max(V_c, 0)$. The pressure at the outflow is assumed constant $p = 101325$ Pa.

The SAILOR code uses the projection method for pressure-velocity coupling [10] combined with a predictor-corrector method (Adams-Bashforth / Adams-Moulton) applied for the time integration. The spatial discretization is performed on half-staggered meshes by the 6th order compact finite difference approximation for the momentum and continuity equations. The second-order TVD (Total Variation Diminishing) scheme with Koren limiter is used for the transport equations for chemical species and enthalpy. The time integration of the chemical source is performed with the help of the VODPK (Variable-coefficient Ordinary Differential equation solver with the Preconditioned Krylov method) solver [17] that is well suited for stiff systems. The chemical reaction terms are computed using the CHEMKIN interpreter. The chemical reactions are computed using detailed mechanism of Mueller et al. [18] involving 9 species and 21 reactions for the hydrogen oxidation.

Preliminary simulations performed using ANSYS Fluent and the SAILOR code for the air stream flowing in the duct around the cylindrical bluff-body were conducted to verify the solution strategy. The comparison of the velocity profiles behind the bluff-body revealed that an interpolation of the velocity components related to two-stage procedure does not introduce significant errors. As can be seen in Fig. 3 both solvers provided similar velocity evolution downstream of the bluff-body. However, the results obtained using the SAILOR code seem to be more accurate, at least qualitatively, as they reflect the symmetric shape of the bluff-body. Furthermore, the applied two-stage approach was proven to yield correct results in previous studies devoted to passively controlled jet flames issuing from polygonal nozzles [19].

3. RESULTS

As the streams of fuel and oxidiser are ejected from the inlet plane into quiescent surroundings, the flow undergoes a Kelvin-Helmholtz instability due to a velocity gradient. The vortex rings are generated and detached from the shear layer generated near the bluff body edge. Their shape is respective to the bluff-body shape and in case of the wavy wall the wavy shaped rings are generated. This can be verified from Q-parameter isosurfaces presented in Fig. 4. Since the initial vortices are considerably different when the wall topology varies, their distortion changes as they travel in the downstream direction. An earlier formation of streamwise structures is seen for the flat wall, whereas stronger vortex rings in case of the wavy wall are observed further downstream revealing more complex flow structure. This can be further verified with the help of the vorticity magnitude plotted on the central cross-section and presented in Figure 5. Comparison of the vorticity contours reveals that flow inside CRZ is more intense

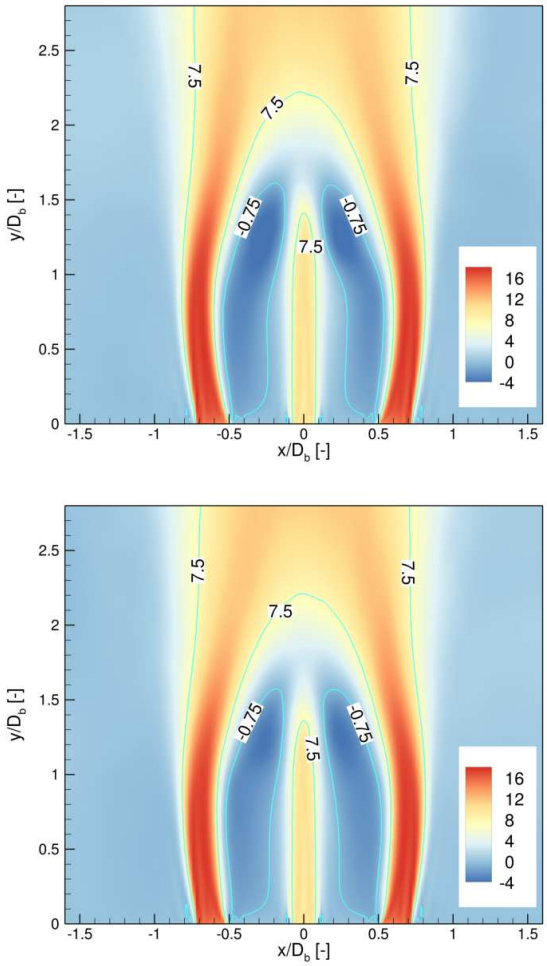

Figure 7. Time averaged axial velocity (mean) contours and isolines (flat wall - upper row, wavy wall - bottom row).

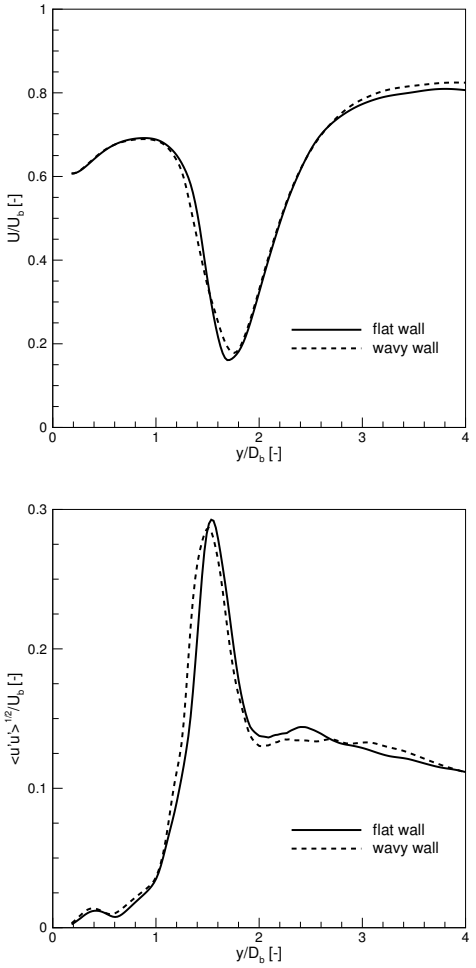

Figure 8. Time averaged axial velocity (mean and rms) along the centreline.

for the case with the wavy wall. With complex wall topology, isolevels seem more wrinkled in an earlier axial location. Similar observation can also be made by comparing isosurfaces of temperature in Figure 6 visualizing topology of the flame. Moreover, the flames reflect the shapes of the bluff-bodies attaching the inlet plane. Therefore, the effect of large-scale intense vortices induced in the outer shear-layer is prominent on the flame structure and shape.

Detailed analysis of the flame dynamics in central recirculation zone has been carried out based on time averaged results presented in Figures 7-10. The time-averaged procedure have been started after the flames had fully developed and continued for $250D_b/U_b$ resulting in fully convergent statistics. Form Fig. 7 it is evident that location of the recirculation zone is only slightly affected by the bluff-bodies geometries compared to the CRZ size and shape. The isoline of negative axial velocity in the case with wavy wall bluff-body is nearly parallel to the fuel stream contrary to the case with flat walls. It results in enhanced mixing manifested by more uniform velocity field inside CRZ. It is also visible in Fig. 7 that the fuel stream velocity decay earlier downstream in case of wavy wall. This confirms the fuel entrainment and enhancement of the fuel/oxidiser mixing. The reduction of the axial velocity along the centreline due to the application of the wavy wall is affected by the earlier growth of the fluctuations as presented in Figure 8. The local entrainment of the fuel stream can be deduced from the radial distribution of the mean hydrogen mass fraction at different distances behind the bluff-body presented in figure 9. The obtained profiles demonstrate the enhancement of the mixing for the case with wavy wall compared to the flat wall. It is manifested by reduced fuel mass fraction already behind the bluff-body (one diameter from the inlet).

In order to examine the impact of the wavy wall of the bluff-body on the flame structure the time-averaged temperature is compared along the radial direction at various axial distances in Figure 10. Increased ($\approx$ 45K) temperature is found at the axis and y/D_b=1.5, i.e, in the region where the recirculation

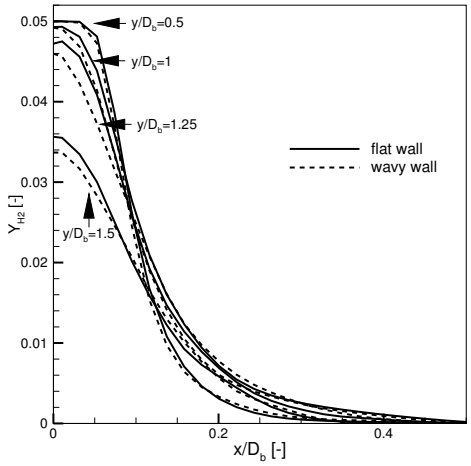

Figure 9. Radial distribution of the time averaged hydrogen mass fraction (mean) at different axial locations.

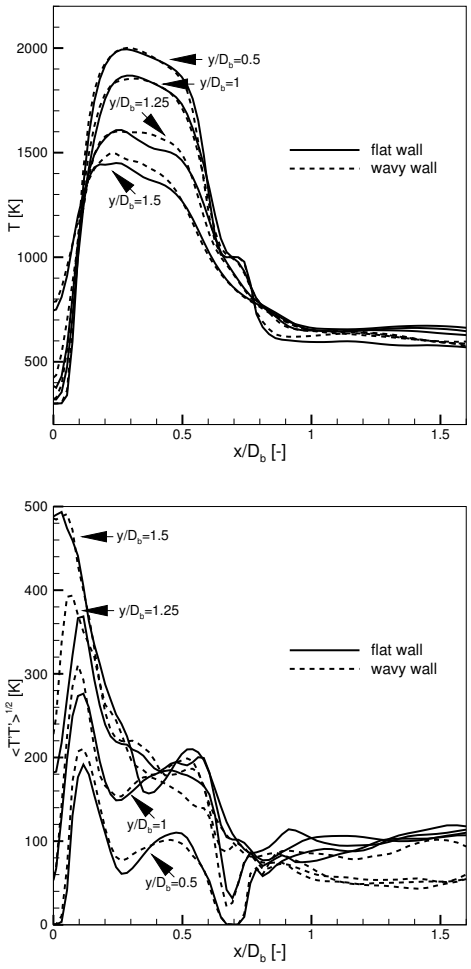

Figure 10. Radial profiles of the time averaged temperature (mean and rms) at different axial locations.

zone ends. This means that the flame appears further upstream compared to case with the flat wall. The increasing of the temperature for wavy wall is also observed in further radial locations respectively for various axial distances. The temperature is 40 K higher compared to the flat wall for radial distance x/D_b=0.1-0.2 and close the inlet plane (y/D_b=0.5-1) and 60 K higher at x/D_b=0.2-0.5 further downstream (y/D_b=1-1.25). Apparently, when the waviness is applied to the bluff-body walls, the flame is noticeably shifted towards the axis and the inlet plane. This is in line with the observation made for the velocity field and CRZ structure. Moreover, the flame is slightly stretched in the radial direction compared to the flat wall. However, the overall flame width does not change. Even more pronounced differences in the flame position are observed in axial distribution of the fluctuating component. One can observed in Fig. 10 that local maximum of the temperature fluctuations persists at x/Db=1 up to y/D_b=1 and shifts $0.05D_b$ towards axis at y/D_b=1.25 when the wavy wall is considered. Moreover, the contribution of the fluctuating component is considerably higher close the inlet plane and is transferred further downstream with 90 K higher values than for the flat wall. Such increase in the fluctuating quantities consistently affects the mean component.

4. SUMMARY

LES simulations of the bluff-body stabilized hydrogen non-premixed flame were carried out. The impact of wall topology (flat or wavy, with the waviness oriented streamwise) on the flame structure was studied for conventional bluff-body burner configuration with the help of second order LES solver provided by ANSYS and an in-house academic high-order code SAILOR. The solution procedure involved the generation of the set of the velocity profiles at the tip of bluff-body by simulating only the inlet section and simulations of the flames performed with the help of the acquired inlet velocity profiles. The chemical source terms were calculated with the help of the 'no-model' approach and comparison the obtained results with the Eulerian Stochatic Fields method will be presented during the conference.

The effect of geometrical shaping was manifested by the flame surfaces reflecting the strong vortex induced in the outer shear-layer which in turn were effectively shaped by wavy walls. Application of the wavy walls enhanced the mixing processes in CRZ comparing to the conventional flat walls. The impact of change in wall topology observed in instantaneous results were justified and quantified with the help of time averaged plots of mean and fluctuating velocity and temperature. The time averaged velocity distributions revealed the fuel entrainment earlier downstream and enhancement of the fuel/oxidiser mixing for the wavy walls applied. Moreover, the time averaged temperature was noticeably higher inside the central recirculation zone at x/D_b=0.2-0.5

and y/D_b=1-1.25 whereas the local maximum of the temperature fluctuations was shifted towards axis when the wall topology was changed. These observations allow to deduce that in case of wavy wall the fuel stream is earlier entranced and flame is shifted towards the centreline.

ACKNOWLEDGEMENTS

This work was supported by the National Science Center in Poland (Grant 2020/39/B/ST8/02802) and statutory founds (BS/PB-1-100-3011/2022/P). The computations were carried out using the PL-Grid Infrastructure.

REFERENCES

[1] Docquier, N., and Candel, S., 2002, "Combustion control and sensors: a review", *Prog Energy Combust Sci*, Vol. 28 (2), pp. 107–150.

[2] Tyliszczak, A., Cavaliere, D., and Mastorakos, E., 2014, "LES/CMC of blow-off in a liquid fueled swirl burner", *Flow Turbul Combust*, Vol. 92 (1-2), pp. 237–267.

[3] Kypraiou, A., Allison, P., Giusti, A., and Mastorakos, E., 2018, "Response of flames with different degrees of premixedness to acoustic oscillations", *Combust Sci Technol*, Vol. 190 (8), pp. 1426–1441.

[4] Dróżdż, A., Niegodajew, P., Romańczyk, M., Sokolenko, V., and Elsner, W., 2021, "Effective use of the streamwise waviness in the control of turbulent separation", *Exp Therm Fluid Sci*, Vol. 121, p. 110291.

[5] Duwig, C., Nogenmyr, K.-J., Chan, C.-k., and Dunn, M. J., 2011, "Large Eddy Simulations of a piloted lean premix jet flame using finite-rate chemistry", *Combust Theory Model*, Vol. 15 (4), pp. 537–568.

[6] Valino, L., Mustata, R., and Letaief, K. B., 2016, "Consistent behavior of Eulerian Monte Carlo fields at low Reynolds numbers", *Flow Turbul Combust*, Vol. 96 (2), pp. 503–512.

[7] Jones, W., and Navarro-Martinez, S., 2007, "Large eddy simulation of autoignition with a subgrid probability density function method", *Combust Flame*, Vol. 150 (3), pp. 170–187.

[8] Bulat, G., Jones, W., and Marquis, A., 2014, "NO and CO formation in an industrial gas-turbine combustion chamber using LES with the Eulerian sub-grid PDF method", *Combust Flame*, Vol. 161 (7), pp. 1804–1825.

[9] Hodzic, E., Jangi, M., Szasz, R.-Z., and Bai, X.-S., 2017, "Large eddy simulation of bluff body flames close to blow-off using an Eulerian stochastic field method", *Combust Flame*, Vol. 181, pp. 1–15.

[10] Tyliszczak, A., 2016, "High-order compact difference algorithm on half-staggered meshes for low Mach number flows", *Comput Fluids*, Vol. 127, pp. 131–145.

[11] Geurts, B., 2004, *Elements of Direct and Large-eddy Simulation*, R.T. Edwards.

[12] Vreman, A., 2004, "An eddy-viscosity subgrid-scale model for turbulent shear flow: Algebraic theory and applications", *Phys Fluids*, Vol. 16 (10), pp. 3670–3681.

[13] Tyliszczak, A., 2015, "LES–CMC study of an excited hydrogen flame", *Combust Flame*, Vol. 162 (10), pp. 3864–3883.

[14] Rosiak, A., and Tyliszczak, A., 2016, "LES-CMC simulations of a turbulent hydrogen jet in oxy-combustion regimes", *Int J Hydrog Energy*, Vol. 41 (22), pp. 9705–9717.

[15] Wawrzak, A., and Tyliszczak, A., 2019, "A spark ignition scenario in a temporally evolving mixing layer", *Combust Flame*, Vol. 209, pp. 353–356.

[16] Wawrzak, A., and Tyliszczak, A., 2020, "Study of a Flame Kernel Evolution in a Turbulent Mixing Layer Using LES with a Laminar Chemistry Model", *Flow Turbul Combust*, Vol. 105, pp. 807–835.

[17] Brown, P.N., and Hindmarsh, A.C., 1989, "Reduced Storage Matrix Methods in Stiff ODE Systems", *J Appl Math Comput*, Vol. 31, pp. 40–91.

[18] Mueller, M., Kim, T., Yetter, R., and Dryer, F., 1999, "Flow reactor studies and kinetic modeling of the H2/O2 reaction", *Int J Chem Kinet*, Vol. 31 (2), pp. 113–125.

[19] Kuban, L., Stempka, J., and Tyliszczak, A., 2021, "Numerical Analysis of the Combustion Dynamics of Passively Controlled Jets Issuing from Polygonal Nozzles", *Energies*, Vol. 14 (3), p. 554.

Conference on Modelling Fluid Flow (CMFF'22)
The 18th International Conference on Fluid Flow Technologies
Budapest, Hungary, August 30-September 2, 2022

On the Effect of Mass Fraction of Frozen Mixture Flow on the Dynamic Performance of a Direct Spring Operated Safety Valve

Csaba Hős[1], G. Burhani[2]

[1] Corresponding Author. Department of Hydrodynamic Systems, Faculty of Mechanical Engineering, Budapest University of Technology and Economics. Bertalan Lajos u. 4 - 6, H-1111 Budapest, Hungary. Tel.: +36 1 463 2216, E-mail: hos.csaba@gpk.bme.hu
[2] Department of Fluid Hydrodynamic Systems, Faculty of Mechanical Engineering, Budapest University of Technology and Economics. E-mail: gburhani@hds.bme.hu

ABSTRACT

We study the effect of frozen mixture (constant mass fraction) flow through a pressure relief valve with upstream piping. DIER's omega technique is employed to cope with the mixture parameters, notable sonic velocity and choked/non-choked flow via the nozzle. By means of one-dimensional simulation, we show that the change in sonic velocity play a fundamental role in both the valve opening time and the its stability. Due to the extremely low sonic velocities e.g. in the case of water-air mixture, such valves will have a poor response time (slow opening) and will also chatter even for short inlet pipings.

Keywords: safety vale, frozen mixture, sonic velocity, valve chatter, valve opening time

NOMENCLATURE

$\mathcal{G}$	$[-]$	dimensionless mass flux
A_s	$[m^2]$	seat area
C_d	$[-]$	discharge coefficient
f	$[Hz]$	frequency
k	$[Ns/m]$	viscous damping coefficient
m	$[kg]$	mass of the valve
p	$[Pa]$	pressure
R	$[J/(kgK)]$	specific gas constant
s	$[N/m]$	spring stiffness
T	$[K]$	temperature
V	$[m^3]$	volume
x	$[m]$	valve displacement
x_0	$[m]$	spring pre-compression
$\dot{m}$	$[kg/s]$	mass flow rate
c	$[m/s]$	speed of sound
p	$[Pa]$	pressure
x	$[-]$	mass fraction
α	$[-]$	volume fraction
ω	$[rad/s]$	eigenfrequency
ρ	$[kg/m^3]$	density

Subscripts and Superscripts

a	ambient
b	back (pressure)
ft	flow-through (area)
g	gas
l	liquid
m	mixture
r	reservoir
ref	reference
set	set (pressure)
u	upstream
v	valve

1. INTRODUCTION

Pressure relief valves (PRV) are devices that protect the pipeline system and reservoirs from excess pressure by venting the unnecessary amount of fluid if needed. As such, they are safety-critical devices; inadequate operation (such as insufficient venting capacity, vibration, the inability of opening due to stuck parts) leads to catastrophic consequences.

These valves are essentially 1 DoF oscillators coupled with the fluid dynamics inside the piping system, resulting in a surprisingly rich dynamical behaviour, see e.g. [1] for an overview. It is well-known that such valves are prone to self-excited oscillations ([2, 3, 4, 5, 6]) and a significant effort was devoted to predicting such oscillations in the phase of design (see [7, 8, 9, 10]). One of the cornerstones of such an analysis is the high-fidelity, yet relatively simple description of the flow force on the valve body and the mass flow rate through the PRV. Although there are standard approaches of describing these forces – e.g. the 'effective area' technique introduced in [11] or the use of the jet angle as in [7, 12] – mostly single-phase cases (either pure gas or liquid) are addressed. [13, 14, 15, 12, 16] report on the effect of the two-phase flow on the *static* characteristics (flow force and mass flux) of the valve, however, the authors are unaware of any study trying to capture the effect of multiphase flow on the *dynamic* behaviour of the PRV, notably opening and closing characteristics.

This paper addresses the problem of predicting the dynamic behaviour of a PRV in the presence of two-phase flow of constant mass fraction. As such, we do not consider phase change and the model will not be (directly) applicable for systems where interphase mass transfer is present (e.g. flashing flows). However, for multicomponent applications, in the absence of mass transfer between the components, our model will provide a possible description of the dynamics, for example in the case of bubbly flows [17, 18, 19], where, even though the void fraction changes if pressure changes, the mass fraction remains constant. Another example with constant mass fraction would be applications in which the humidity content of air is important, see e.g. [20] or [21], especially Figure 8 therein.

In what follows, we start by providing a brief literature overview in section 2, then present our model in section 3. Next, we present our simulation results on the estimation of valve opening time in section 4 and valve stability in section 5. Finally, in section 6 concludes the study.

2. LITERATURE OVERVIEW

Industrial pressure relief valves are sized and chosen based on their capacity, that is the vented mass flow rate at full opening and 110% of the set (opening) pressure. For simple cases such as ideal gas or incompressible liquid, it is straightforward to compute the mass flow rate if the valve lift (flow-through area) and the pressure difference (or, in the case of choked flow, the upstream pressure) are known, together with the discharge coefficient (provided by the manufacturer). However, in the case of wet steam, non-ideal gases or mixtures, or flashing (partial evaporation of saturated liquid due to pressure drop via the valve), predicting the mass flow rate is challenging. DIER's ω technique is one attempt to cope with this problem, that assumes both thermal and mechanical homogeneous case and also neglects the velocity difference between the phases (no slip). Due to its popularity, we will employ this model, even though there are other, more accurate (and complex) models, such as TPHEM, HNE, and HDI methods (see [22] for details).

In contrast to the single-phase flow, the two-phase case has one additional degree of freedom, that is the mass fraction of one of the phases; that is gas mass fraction $x_g = m_g/(m_g + m_l)$ and the liquid mass fraction $x_l = \dot{m}_l/(\dot{m}_g + \dot{m}_l)$.

Leung published a series of papers on the development and use of the ω technique. In [23] he presented the generalised correlation for one-component homogeneous equilibrium model (HEM) for flashing choked flow validated against measurement results for eleven fluids with different properties. The key idea was that the flashing two-phase mixture was considered as a single-phase compressible fluid, and then the use of the ω parameter already defined by Epstein at al. in [24] for all-liquid mixtures. In [25] the same author with Grolmes extended the previous correlation for the flashing choked flow of an initially sub-cooled liquid (for both high and low sub-cooling regions), neglecting the effects of non-equilibrium effects and obtained design charts that were useful for practical applications. Leung discussed similarities between flashing and non-flashing two-phase flow in [26] and showed that, by simply redefining the dimensionless ω parameter, a unified treatment could be obtained.

In another study ([27]), Leung and Nazario reviewed three methods; (a) DIERS' ω method, (b) a technique used by the American Petroleum Institute (API) and (c) an ASME method, to compare the two-phase flashing flow prediction tools, which are highly used in various engineering applications. Their comparison showed that the ASME and DIERS (homogeneous equilibrium) models are in close agreement (these approaches assume isentropic expansion in the nozzles). Moreover, the API method gives significantly higher theoretical mass flux values since it neglects momentum, heat and mass transfer during the flashing process.

Leung summarised his previous work in [28], covering the ω method for mass flux estimation both for ideal nozzle flow and pipe flow with different orientations (horizontal and inclined pipe flows), for flashing, non-flashing, inlet sub-cooled and non-condensible gas. Nine years later, in 2004, Leung applied the ω method for safety relief valves in [29]. It was also shown how the discharge coefficient varies depending on the flow regime, and it was revealed that for the non-flashing flow case, the discharge coefficient lies between the liquid coefficient and the gas coefficient. Moreover, he also observed a higher discharge coefficient value in the case of flashing flow, compared to the single-gas case. In [30], the same author proposed techniques for employing the ω model based on the stagnation conditions of fluid in the vessel and discussed four main cases; saturated liquid, two-phase (gas-liquid mixture), low sub-cooled liquid, and high sub-cooled liquid.

In [31], Lenzing et al. studied the effect of two-phase flow (flashing and non-flashing) on the capacity (i.e. at maximum lift) of safety relief valve experimentally. They compared the measured data against several theoretical predictions; namely the Isentropic Homogeneous Equilibrium Model, DIERS' ω technique, Nastoll's Homogeneous Frozen Flow model and the Goßlau-Weyl model. One of the outcomes of this work is that for non-flashing two-component air/water flow Leung's, extended by the weighted discharge coefficient, can be used (see Figure 1. in [31] and the corresponding text).

Another experimental validation of the technique was reported by Gino Boccardi *et al.* in [32]. The authors compared the test data for steam-water flow in a safety relief valve against three prediction techniques, namely HEM (homogeneous equilibrium model), HNE (thermodynamic non-equilibrium) and

HNE-DS (proposed by the ISO working group), to predict the theoretical mass flux. The results revealed that, even though the HNE-DS method provided the best results, it was not conservative in the sense that in some cases, it predicted higher flow rates compared to the measurements. In contrast, the HEM technique gave poor accuracy, but it was conservative. The same author in a later work [13] discussed another set of experimental data on (steam/water) flashing system through a PRV with a wide range of the operating parameters (such as vapour quality, inlet pressure, mass flow rate, and backpressure). These measurements were also tested against the predictions of the HEM ω method, and the results showed that the mass flow rates provided by the theoretical model and the actual (measured) flow rates correlated reasonably.

Based on the theoretical and experimental work published in the above reports, Leung's ω technique provides a reasonable compromise between modelling complexity and prediction accuracy and we will employ this approach in this paper.

3. MODELLING

3.1. Frozen mixture model

Consider the frozen mixture of an ideal gas and a liquid, that is the gas *mass* fraction $x_g = \frac{m_g}{m_m} = \frac{\dot{m}_g}{\dot{m}_m}$ is constant, where $\dot{m}_m = \dot{m}_g + \dot{m}_l$ and, clearly, $x_l = 1 - x_g$.

We assume that the gas obeys the ideal gas law, that is $p/\rho_g = RT$. For an isentropic change of state, the sonic velocity for *pure gas* ($x_g = 1$) is $c_g = \sqrt{\kappa RT}$. The equation of state of the liquid phase is

$$\rho_l = \rho_{ref} + \frac{1}{c_l^2}\left(p - p_{ref}\right), \tag{1}$$

where the reference values are $p_{ref} = 1\text{bar}$ and $\rho_{ref} = 1000\,kg/m^3$ and c_l is the sonic velocity measured in pure liquid.

The α volume fraction is

$$\alpha_g = \frac{V_g}{V_g + V_m} = \frac{m_g}{m_g + m_l\frac{\rho_g}{\rho_l}} = \frac{x_g}{x_g + (1 - x_g)\frac{\rho_g}{\rho_l}}, \tag{2}$$

with which the mixture density $\rho_m(p, T, x_g)$ becomes

$$\begin{aligned}\rho_m &= \frac{m_m}{V_m} = \frac{\rho_g V_g + \rho_l V_l}{V_g + V_l} = \alpha\rho_g + (1 - \alpha)\rho_l \\ &= \frac{p\left(p - p_{ref} + c_l^2\rho_{ref}\right)}{(p_{ref} - p)RTx_g + c_l^2\left(p(x_g - 1) - RTx_g\rho_{ref}\right)}\end{aligned} \tag{3}$$

It is easy to check that $\rho_m(x_g = 0) = \frac{p}{RT}$ and setting $x_g = 1$ recovers (1). We will also need the pressure as a function of temperature, (mixture) density and gas mass fraction $p(\rho_m, T, x_g)$, which is

$$\begin{aligned}p &= \frac{1}{4}\left(-b + \sqrt{b^2 - 4c}\right), \quad \text{width} \\ b &= -\left(p_{ref} + RTx_g\rho_m + c_l^2\left(\rho_m(1 - x_g) - \rho_{ref}\right)\right) \quad \text{and} \\ c &= RTx_g\rho_m\left(p_{ref} - c_l^2\rho_{ref}\right).\end{aligned} \tag{4}$$

Now we are in the position of computing the mixture sonic velocity, that will play a central role in our later analyses. First, we eliminate the temperature dependence from (3) by assuming isentropic change of state for the gas, and then compute

$$\begin{aligned}c_m^2 &= \left(\frac{\mathrm{d}\rho_m(p, x_g)}{\mathrm{d}p}\right)^{-1}\Bigg|_{isentropic} \\ &= \frac{\kappa(a_0 + a_1)^2}{b_0 + b_1 + b_2 + b_3} \quad \text{where} \\ p &= p_{ref,g}\left(\frac{T}{T_{ref,g}}\right)^{\frac{\kappa}{\kappa-1}} \\ a_0 &= (p - p_{ref})RTx_g \\ a_1 &= c_l^2\left(p(1 - x_g) + RTx_g\rho_{ref}\right) \\ b_0 &= -p^2RTx_g \\ b_1 &= c_l^2p^2(x_g - 1) \\ b_2 &= 2pRTx_g\left(p_{ref} - c_l^2\rho_{ref}\right) \\ b_3 &= -RTx_g\left(p_{ref} - c_l^2\rho_{ref}\right)^2\end{aligned} \tag{5}$$

It straightforward again to check that $c_s^2(x_g = 0) = c_l^2$ and $c_s^2(x_g = 1) = \kappa RT$. Figure 1 depicts the change of sonic velocity (solid line) and gas void fraction α_g (dashed line) as a function of gas mass fraction. These results are in good agreement with the literature data, see [33] for example. The sonic velocity will a play a central role in our further analysis, hence we highlight two well-known facts, namely that (a) it can be as low as 20-50 m/s and (b) a relatively small amount of air (say, $x_g = 10^{-6}$, $\alpha_g = 8.3 \times 10^{-4}$) changes the sonic velocity drastically.

3.2. Pipe flow modelling

The governing equations for the 1D, unsteady flow of an arbitrary fluid in a tube of constant cross section (that is, a pipe) can be written as

$$\frac{\partial\mathcal{U}}{\partial t} + \frac{\partial\mathcal{F}}{\partial x} = \mathcal{S}, \tag{6}$$

with

$$\mathcal{U} = \begin{pmatrix}\rho_m \\ \rho_m v \\ \rho_m v e_{tot}\end{pmatrix}, \quad \mathcal{F} = \begin{pmatrix}\rho_m v \\ \rho_m v^2 + p \\ \rho_m v e_{tot} + pv\end{pmatrix}, \quad \text{and} \tag{7}$$

$$\mathcal{S} = \begin{pmatrix}0 \\ -\frac{\lambda}{2d}v|v| \\ 0\end{pmatrix}. \tag{8}$$

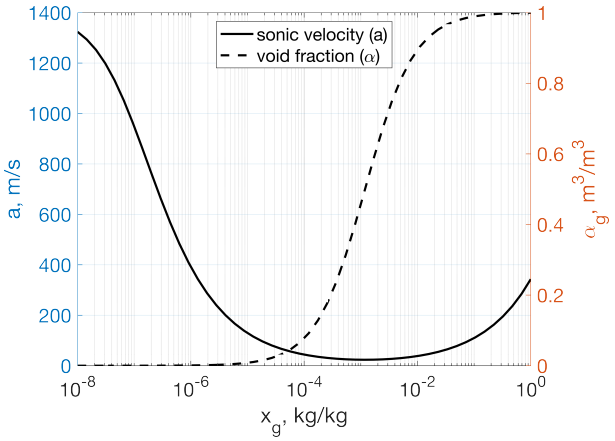

Figure 1. Sonic velocity (left axis) and gas void fraction (right axis) as a function of gas mass fraction.

where $e_{tot} = e + \frac{v^2}{2}$ and the mixture internal energy is $e_m = e_g + e_l = c_{V,g} T x_g + c_l T(1 - x_g) = c_{V,m} T$, where the mixture specific heat capacity at constant volume is $c_{V,m} = x_g c_{V,g} + c_l(1 - x_g)$.

3.3. Valve model

The valve is modelled by a simple 1 DoF oscillatory system, whose governing equation is given by

$$m_v \ddot{x} + k\dot{x} + s\,(x + x_0) = \tilde{A}_{eff}(x) A_s\,(p_u - p_b)\,. \quad (9)$$

$\tilde{A}_{eff}$ is the dimensionless *effective area* curve, which models the force component due to the momentum of the fluid (see [34, 35] for more details). The pressure difference $p_u - p_b$ contains the upstream pressure and the backpressure, which does not necessarily equal the ambient pressure p_a. By adjusting the x_0 spring pre-compression, one can change the opening or *set pressure* p_{set}, which, by definition, is a gauge pressure: $p_{set} = \frac{s x_0}{A_s} - p_a$. Pressure relief valves in oil and gas industry typically contain no artificial damping mechanism but only natural damping, hence we will set $k = 0.01 k_{crit} = 0.01 \times 2\sqrt{sm}$.

The mass flow rate through the valve is $\dot{m} = C_d A_{ft}(x)\sqrt{p_u \rho_u}\mathcal{G}(\eta)$. The *dimensionless* mass flux $\mathcal{G}$ is ($\eta = p_d/p_u$)

for an incompressible fluid:

$$\sqrt{2\,(1 - \eta)} \quad (10)$$

for an un-chooked, single-phase ideal gas:

$$\sqrt{2\frac{\kappa}{\kappa - 1}\left(\eta^{2/\kappa} - \eta^{(\kappa+1)/\kappa}\right)} \quad (11)$$

for a choked, single-phase ideal gas:

$$\sqrt{\kappa\left(\frac{2}{\kappa + 1}\right)^{\frac{\kappa+1}{\kappa-1}}} \quad (12)$$

for an un-choked frozen mixture fluid:

$$\frac{(-2(\omega \ln \eta + (\omega - 1)(1 - \eta))^{1/2}}{\omega(\frac{1}{\eta} - 1) + 1} \quad (13)$$

for a choked frozen mixture fluid:

$$\frac{\eta_c}{\sqrt{\omega}}, \quad (14)$$

where the critical pressure ratio $\eta_c = \frac{p_c}{p_0}$ can be calculated by solving the following implicit equation:

$$\eta_c^2 + (\omega^2 - 2\omega)(1 - \eta_c)^2 + 2\omega^2 \ln \eta_c + 2\omega^2(1 - \eta_c) = 0. \quad (15)$$

and $\omega = \alpha_g/\kappa$, see [28].

3.4. Reservoir model

The rate of change of pressure inside a reservoir is

$$\dot{p}_t = \frac{a_r^2}{V}\left(\dot{m}_{in} - \dot{m}_{out}\right). \quad (16)$$

We shall assume constant inlet flow rate $\dot{m}_{in}$ and variable outlet flow rate, typically, through a pipeline. The reservoir sonic velocity a_r depends on the reservoir temperature, which is connected to the reservoir pressure p_r by an arbitrary, user-defined change of state (e.g. isentropic, isotherm, etc).

3.5. Numerical solution procedure

We use a standard Lax-Wendroff scheme for updating the pipe. The boundary conditions are implemented with the help of Method of Characteristics (MoC, see [36]), the details can be found in [37]. The valve and reservoir model are integrated by a standard 5th-order adaptive Runge-Kutta solver. Special care is devoted to the proper handling of the valve impingement on the seat or upper stopper. The time step is chosen by the CFL criteria, with a CFL number of 0.7-0.9. The whole framework is implemented in Matlab 2021b.

4. VALVE OPENING TIME

In [34], an approximate formula was derived for 'fast' valves. Let the timescale of the valve be $t_{valve} = 2\pi/\omega_v = 2\pi\sqrt{m/s}$. We define the opening time t_{op} as the time needed for a *closed* valve to reach the 95% of the equilibrium lift x_e for a prescribed mass flow rate $\dot{m}_{in}$. If $t_{op} \ll t_{valve}$, we have

$$t_{op} \approx 2 \times 0.95 x_e \omega_v^2 \frac{m \sum V}{A_s a^2 \dot{m}_{in}}. \quad (17)$$

(The condition $t_{op} \ll t_{valve}$ or, equivalently, $\omega_v t_{op} \ll 2\pi$ must be checked a posteriori.) The above equation was derived by assuming a valve mounted directly to the reservoir. Intuitively, a pipe between the valve and reservoir would add addition volume and, if long enough, it will give rise to wave phenomena that also increases the valve opening time, hence we have $\sum V = V_r + A_p L_p$.

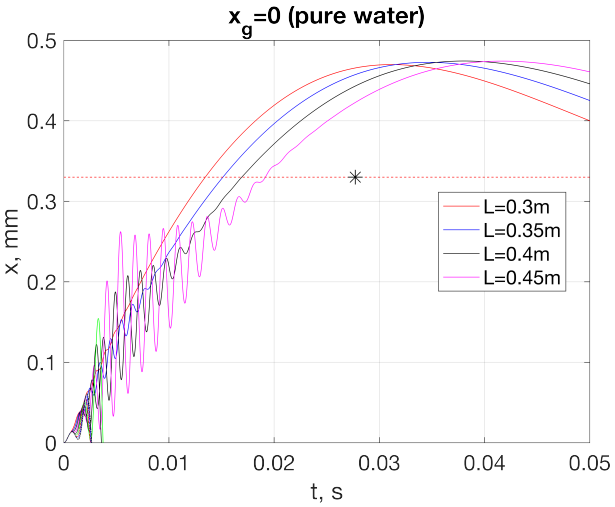

Figure 2. Valve openings with different pipe lengths, for pure water. The dashed line represents the equilibrium lift, the asterisk depict the opening time estimates by (17)**.**

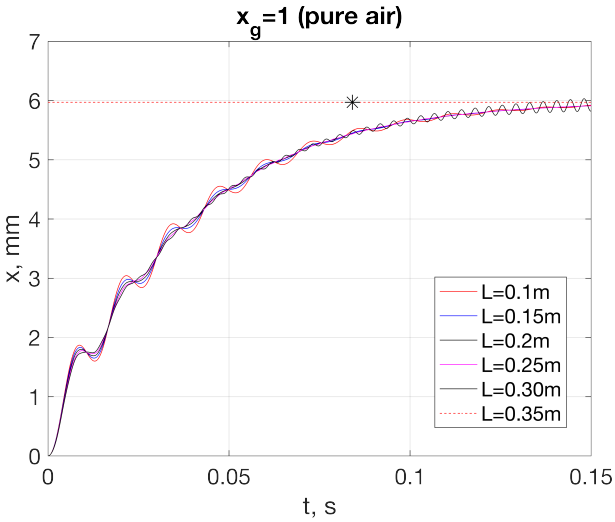

Figure 3. Valve openings with different pipe lengths, for pure air. The dashed line represents the equilibrium lift, the asteriks depict the opening time estimates by (17)**.**

We have run several computations to analyse the effect of mass fraction on the valve opening time with the parameter values provided in Table 1. For the water case, we have set $V = 2\text{m}^3$ and the equilibrium position was $x_e = 0.33$mm and $p_e = 4.11$ bara. This gives (by virtue of (17)) $t_{op} = 0.0278$ s for opening time. Figure 2 depicts the first 0.05 s of the opening process with three different pipe lengths. The dashed horizontal line represents the equilibrium valve lift and the asterisk is the estimates opening time. We observe a slightly increasing opening time due to the increasing pipe length, which changes the overall volume (capacity) in the system. The change in the opening time ((17)) due to the increasing pipe length is less than 1%. We also experienced "opening instability" (see [11] for details). From the mechanical point of view, this case is underdamped as the maximum of the valve lift is 50% higher than the equilibrium position.

Table 1. Parameters

valve mass	m	0.2 kg
spring stiffness	s	47.3 kN/m
valve eigenfreq.	f_v	77 Hz
valve timescale	t_v	0.013 s
set pressure	p_{set}	3 barg
pipe diameter	D_p	45.5 mm
pipe friction coeff.	λ	0.02
inlet mass flow rate	$\dot{m}_{in}$	0.77 kg/s

In the case of pure air, we have $V = 0.02\text{m}^3$, $x_e = 5.97$mm and $p_e = 5.9$bara. This case is overdamped, even though the viscous damping parameter was unchanged and the reservoir volume is smaller. Again, the dashed line represents the equilibrium lift, the asterisk depict the opening time estimates by (17). In this case, we do not experience opening instability.

In both cases, the simulations with longer pipe lengths resulted in unstable valve motion, leads us to our next section.

5. STABILITY AND VALVE CHATTER

In [38], the authors derived an analytical criteria for computing the critical inlet pipe length, that is

$$L_{crit} = \frac{\pi a}{2\omega_v} \frac{1}{\sqrt{2\frac{A_v p_e}{x_e s} + 1}}, \tag{18}$$

where x_e and p_e are the equilibrium valve lift and (absolute) pressure at the valve inlet. Beyond the critical pipelength defined by the above equation, self-excited oscillations will be born, whose dominant frequency will coincide with the pipe's first natural 'organ-mode' eigenfrequency, $f_p = a/(4L)$.

Izuchi in [9] provided a similar equation, that is

$$L^*_{crit} = \frac{\pi a}{2\omega_v} \frac{1}{\sqrt{\frac{x_e + x_0}{x_e}}}. \tag{19}$$

We notice that due to the force equilibrium of the valve, we have $s\,(x_e + x_0) = A_v\,(p_u - p_b)$, hence, if p_u is measured as a *relative* (gauge) pressure above p_b (which is often the ambient pressure), and the momentum forces can be neglected ($A_{eff} = 1$ in (9)), we have $\frac{A_v p_e}{x_e s} = \frac{x_e + x_0}{x_e}$, which is similar to Izuchi's equation, but still, the factor of 2 and the +1 terms are missing.

We have run simulations with two set pressure, that is $p_{set} = 3$ barg and 10 barg. Figures 4 and 5 depict the result. As it can be seen by virtue of (18), the critical pipe length depends on the equilibrium lift and pressure (x_e and p_e) and the sonic velocity. The uppermost panels show the equilibrium lift: it remains constant up to $x_g \approx 0.01$, beyond which it

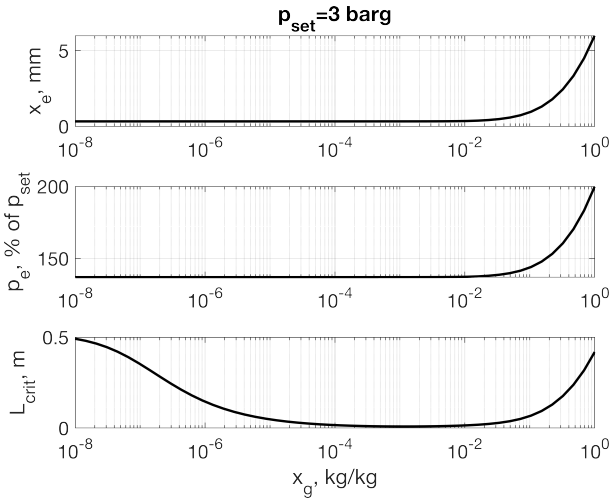

Figure 4. Equilibrium lift, pressure and critical pipe length for p_{set} = 3 barg and $\dot{m}_{in}$ = 0.77 kg/s.

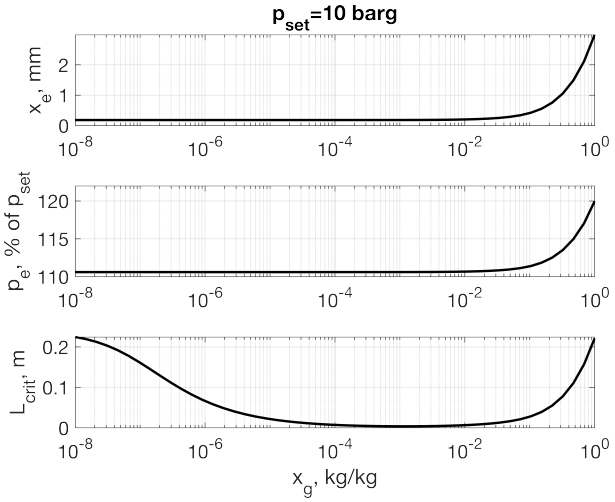

Figure 5. Equilibrium lift, pressure and critical pipe length for p_{set} = 10 barg and $\dot{m}_{in}$ = 0.77 kg/s.

increases due to the fact that the density of the mixture decreases but the overall vented mass flow rate is kept constant. We observe a similar trend in the case of the equilibrium pressure.

However, the shape of the critical pipe length (bottom panels) resembles on the shape of the sonic velocity, see Figure 1. More importantly, in the range of $x_g < 10^{-2}$, the equilibrium lift and pressure are constant yet the critical pipe length changes. This is another observation supporting the importance of the sonic velocity. Again, in the range of the low sonic velocity, the valve will be unstable basically for any (small) pipe length.

6. SUMMARY AND CONCLUSION

We have shown the importance of sonic velocity on valve stability and opening time. Lower sonic velocities will result in slow valve motions and highly unstable valve operation. Our numerical tests has shown that both formulae (opening time (17) and critical pipe length (18)) provide simple means for an order-of-magnitude estimation even in the case of mixture flow. This study was the precursor of further investigation towards exploring the possibility of predicting valve dynamics and stability in the case of non-ideal and/or flashing fluids.

REFERENCES

[1] Hős, C. J., Champneys, A. R., Paul, K., and McNeely, M., 2017, "Dynamic behaviour of direct spring loaded pressure relief valves connected to inlet piping: IV review and recommendations", *Journal of Loss Prevention in the Process Industries*, Vol. 48, pp. 270–288.

[2] Kasai, K., 1968, "On the Stability of a Poppet Valve with an Elastic Support", *Bulletin of JSME*, Vol. 11 (48).

[3] Bazsó, C., and Hős, C., 2013, "An experimental study on the stability of a direct spring loaded poppet relief valve", *Journal of Fluids and Structures*, Vol. 42, pp. 456–465.

[4] Moussou, P., Gibert, R. J., Brasseur, G., Teygeman, C., Ferrari, J., and Rit, J. F., 2010, "Instability of Pressure Relief Valves in Water Pipes", *Journal of Pressure Vessel Technology*, Vol. 132 (4), p. 041308.

[5] Singh, A., 1983, "On the stability of a coupled safety valve-piping system.", *IN: Thermal-hydraulics of nuclear reactors, paper presented at the second int topical meeting on nuclear reactor thermal-hydraulics*.

[6] Singh, A., 1982, "An analytical study of the dynamics and stability of a spring loaded safety valve", *Nuclear Engineering and Design*, Vol. 72 (2), pp. 197–204.

[7] Darby, R., 2012, "The dynamic response of pressure relief valves in vapour or gas service. Part 1: mathematical model", Proprietrary report for PERF 99-05.

[8] Hős, C., Champneys, A., Paul, K., and McNeely, M., 2014, "Dynamic behavior of direct spring loaded pressure relief valves in gas service: Model development, measurements and instability mechanisms", *Journal of Loss Prevention in the Process Industries*, Vol. 31, pp. 70–81.

[9] Izuchi, H., 2010, "Stability Analysis of Safety Valve", American Institute of Chemical Engineers, *10th Topical Conference on Natural Gas Uitilization ISBN: 9781617384417*.

[10] Melham, G., 2014, "Analysis of PRV Stability in Relief Systems, Part I. Detailed Dynamics", An ioMosaic Corporation White Paper.

[11] Hős, C. J., Champneys, A. R., Paul, K., and McNeely, M., 2014, "Dynamic behavior of direct spring loaded pressure relief valves in gas service: Model development, measurements and instability mechanisms", *Journal of Loss Prevention in the Process Industries*, Vol. 31 (1), pp. 70–81.

[12] Narabayashi, T., Nagasaka, H., Niwano, M., and Ohtsuki, Y., 1986, "Safety relief valve performance for two-phase flow", *Journal of Nuclear Science and Technology*.

[13] Boccardi, G., Bubbico, R., Celata, G., and Mazzarotta, B., "Two-phase flow through pressure safety valves. Experimental investigation and model prediction", *Chemical Engineering Science*, (19), pp. 5284–5293.

[14] Dempster, W., and Alshaikh, M., 2015, "An Investigation of the Two Phase Flow and Force Characteristics of a Safety Valve", Tu, ST and Chen, X (ed.), *Pressure Vessel Technology: Preparing For the Future*, Vol. 130 of *Procedia Engineering*, pp. 77–86.

[15] Kourakos, V., Rambaud, P., Buchlin, J. M., and Chabane, S., 2013, "Flowforce in a safety relief valve under incompressible, compressible, and two-phase flow conditions (PVP-2011-57896)", *Journal of Pressure Vessel Technology, Transactions of the ASME*.

[16] Dempster, W., and Alshaikh, M., 2015, "An Investigation of the Two Phase Flow and Force Characteristics of a Safety Valve", *Procedia Engineering*, Vol. 130, pp. 77 – 86.

[17] van Lookeren Campagne, C., Nicodemus, R., de Bruin, G. J., and Lohse, D., 2002, "A Method for Pressure Calculation in Ball Valves Containing Bubbles ", *Journal of Fluids Engineering*, Vol. 124 (3), pp. 765–771.

[18] Ng, K., and Yap, C., 1989, "An investigation of pressure transients in pipelines with two-phase bubbly flow", *International journal for numerical methods in fluids*, Vol. 9 (10), pp. 1207–1219.

[19] Alimonti, C., Falcone, G., and Bello, O., 2010, "Two-phase flow characteristics in multiple orifice valves", *Experimental thermal and fluid science*, Vol. 34 (8), pp. 1324–1333.

[20] Meena, P., Rittidech, S., and Poomsa-ad, N., 2007, "Application of closed-loop oscillating heat-pipe with check valves (CLOHP/CV) air-preheater for reduced relative-humidity in drying systems", *Applied Energy*, Vol. 84 (5), pp. 553 – 564.

[21] Kim, D. K., Min, H. E., Kong, I. M., Lee, M. K., Lee, C. H., Kim, M. S., and Song, H. H., 2016, "Parametric study on interaction of blower and back pressure control valve for a 80-kW class PEM fuel cell vehicle", *International Journal of Hydrogen Energy*, Vol. 41 (39), pp. 17595 – 17615.

[22] Darby, R., 2005, "Size safety-relief valves for any conditions", *Chemical Engineering*, Vol. 112 (9), pp. 42–50.

[23] Leung, J., 1986, "A generalized correlation for one-component homogeneous equilibrium flashing choked flow", *AIChE Journal*, Vol. 32 (10), pp. 1743–1746.

[24] Epstein, M., Henry, R., Midwidy, W., and Pauls, R., 1983, "One-Dimensional Modeling of Two-Phase Jet Expansion and Impingement", *Proc. of the 2nd Int. Topical Meet. Nuclear Reactor Thermal-Hydraulics*.

[25] Leung, J. C., and Grolmes, M. A., 1988, "A generalized correlation for flashing choked flow of initially subcooled liquid", *AIChE Journal*, Vol. 34 (4), pp. 688–691.

[26] Leung, J. C., 1990, "Similarity between flashing and nonflashing two-phase flows", *AI Ch E Journal (American Institute of Chemical Engineers);(USA)*, Vol. 36 (5).

[27] Leung, J., and Nazario, F., 1990, "Two-phase flashing flow methods and comparisons", *Journal of Loss Prevention in the Process Industries*, Vol. 3 (2), pp. 253–260.

[28] Leung, J., 1995, "The Omega Method for Discharge Rate Evaluation", *International symposium, Runaway reactions and pressure relief design*, DIERS, AICHE, The address of the publisher, pp. 367–393, iSBN: 0816906769.

[29] Leung, J., "A theory on the discharge coefficient for safety relief valve", *Journal of Loss Prevention in the Process Industries*, (4), pp. 301–313.

[30] Lees, F., 2012, *Lees' Loss prevention in the process industries: Hazard identification, assessment and control*, Butterworth-Heinemann.

[31] Lenzing, T., Friedel, L., Cremers, J., and Alhusein, M., 1998, "Prediction of the maximum full lift safety valve two-phase flow capacity", *Journal of Loss Prevention in the Process Industries*, Vol. 11 (5), pp. 307–321.

[32] Boccardi, G., Bubbico, R., Celata, G. P., Di Tosto, F., and Trinchieri, R., 2010, "Comparison among three prediction methods for safety valves design in two-phase flow in the case of a small valve", *Chemical Engineering Transactions*, Vol. 19, pp. 175–181.

[33] Nguyen, D., Winter, E., and Greiner, M., 1981, “Sonic velocity in two-phase systems”, *International Journal of Multiphase Flow*, Vol. 7 (3), pp. 311–320, URL https://www.sciencedirect.com/science/article/pii/0301932281900240.

[34] Burhani, M. G., and Hős, C., 2020, “Estimating the opening time of a direct spring operated pressure relief valve in the case of multiphase flow of fixed mass fraction in the absence of piping”, *Journal of Loss Prevention in the Process Industries*, Vol. 66, pp. 104–169, URL https://www.sciencedirect.com/science/article/pii/S095042302030022X.

[35] 2021, “An Experimental Study on the Force Coefficient and the Discharge Coefficient of a Safety Valve in Air-water Mixture Flow”, *PERIODICA POLYTECHNICA-MECHANICAL ENGINEERING*, Vol. 65, pp. 326–336.

[36] Anderson, J., 1995, *Computational Fluid Dynamics*, Computational Fluid Dynamics: The Basics with Applications, McGraw-Hill Education, ISBN 9780070016859, URL https://books.google.hu/books?id=dJceAQAAIAAJ.

[37] Erdődi, I., and Hős, C., 2017, “Prediction of quarter-wave instability in direct spring operated pressure relief valves with upstream piping by means of CFD and reduced order modelling”, *Journal of Fluids and Structures*, Vol. 73, pp. 37–52, URL https://www.sciencedirect.com/science/article/pii/S0889974616303784.

[38] Hős, C., Champneys, A., Paul, K., and McNeely, M., 2016, “Dynamic behaviour of direct spring loaded pressure relief valves: III valves in liquid service”, To appear in *Journal of Loss Prevention in the Process Industries*.

Conference on Modelling Fluid Flow (CMFF'22)
The 18th International Conference on Fluid Flow Technologies
Budapest, Hungary, August 30-September 2, 2022

DISCRETE ELEMENT MODELLING OF NON-SPHERICAL PARTICLES IN TURBULENT GAS-SOLID FLOWS

Berend van Wachem[1], Victor Chéron[2], Fabien Evrard[2,3]

[1] Corresponding Author. E-Mail: berend.vanwachem@ovgu.de. Chair of Mechanical Process Engineering, Faculty of Process and Systems Engineering, Otto-von-Guericke University Magdeburg, Universitätsplatz 2, 39106 Magdeburg, Germany
[2] Chair of Mechanical Process Engineering, Faculty of Process and Systems Engineering, Otto-von-Guericke University Magdeburg, Universitätsplatz 2, 39106 Magdeburg, Germany
[3] Sibley School of Mechanical and Aerospace Engineering, Cornell University, Ithaca, NY 14853, United States of America.

ABSTRACT

In this contribution, a CFD/DEM framework is introduced to predict the behaviour of non-spherical particles in (turbulent) flows. This computational framework comprises different elements. Firstly, the drag, torque and lift relations of each particle shape is determined by means of true *direct numerical simulation*, where the particle is represented by a highly accurate immersed boundary method. Secondly, to deal with particle-particle and particle-wall interactions, a collision model is derived to deal with the collisions between non-spherical particles and the particles and a wall. The discrete element framework is constructed based upon a Quaternion approach. Finally, the framework is tested on two different test-cases: the first is a horizontal channel flow with fibers and the second one is a fluidized bed with ellipsoidal particles. In general, the results show that there is a big effect of particle shape and particle-orientation, which can be accurately captured by the presented framework.

Keywords: CFD/DEM, Direct numerical simulation, Discrete element method, Immersed boundary method, Non-spherical particles

NOMENCLATURE

$\bar{\bar{I}}$	$[kg\,m^2]$	moment of inertia
$\boldsymbol{F}_D$	$[N]$	particle drag force
$\boldsymbol{F}_L$	$[N]$	particle lift force
$\boldsymbol{F}_n$	$[N]$	normal collision force
$\boldsymbol{F}_t$	$[N]$	tangential collision force
K	[]	spring constants
V_p	$[m^3]$	particle volume
$\boldsymbol{a}_c$	$[m/s^2]$	particle acceleration due to collisions
$\boldsymbol{a}_p$	$[m/s^2]$	net particle acceleration
$\boldsymbol{g}$	$[m/s^2]$	gravity acceleration
e	[-]	coefficient of restitution
q	[-]	quaternion
t	$[s]$	time
δ	$[m]$	displacement
ω	$[rad/s]$	particle rotation
ρ_p	$[kg/m^3]$	particle density
$\boldsymbol{\tau}$	$[N\,m]$	torque

Subscripts and Superscripts

b	body space

1. INTRODUCTION

The knowledge of the dynamics of turbulent gas-solid flows has an even increasing importance for the successful design, improvement and operation of numerous industrial applications in process industry, such as fixed and fluidized bed reactors, pneumatic conveying, cyclones, biomass combustors, to just name a few. Such systems exhibit very complex flow dynamics and interactions between the particles and the gas-phase turbulence, also including particle-particle and particle-wall interactions.

The majority of studies involving gas-particle flows assume that particles are perfect spheres. This assumption is very convenient because of several factors: perfect spheres are simple to model, their behavior is well known, and there is a large availability of models in the literature which describe the particle-fluid interactions *e.g.*[1]. However, assuming the particles are perfect spheres may be unrealistic, because most applications deal with non-spherical particles. Analysis of flows with non-spherical particles is considerably more complicated than flows with spherical particles. While a sphere is characterized by its diameter only, even a very simple non-spherical particle such as a disc or a fiber needs at least two parameters to be uniquely defined. This makes the rigid body dynamics of non-spherical particles more complex than that of spherical ones. Moreover, additional complexities arise in describing the interaction of a non-spherical particle with a fluid.

In a uniform flow, the dominant force on a sphere is the drag force, whereas a non-spherical body can also be affected by a transverse lift force, a pitching torque and a counter-rotational torque [2]. Moreover, all of these forces acting on a non-spherical body depend not only on the Reynolds number, but also on the angle between the axes of the particle and the direction of the incoming flow. Additionally, the framework for describing collisions requires a different approach compared to the one used for perfect spheres; for instance, it needs to take into account the orientation of the particle.

The aim of this contribution is to present a framework, based on computational fluid dynamics (CFD) and the discrete element method (DEM), to be able to predict the behavior of non-spherical particles in (turbulent) fluid flows. This framework consists of multiple numerical aspects: first, we will use a novel immersed boundary method (IBM) framework to determine the hydrodynamic behavior of a single non-spherical particle under varying conditions. Secondly, we will propose a DEM framework to model the behavior of non-spherical particles based upon the concept of *Quaternions*. Finally, we will bring together the resulting drag, lift and torque model obtained from the IBM simulations and the DEM framework into a single CFD/DEM framework to predict the behavior of non-spherical particles. To show the ability of the complete framework, two test-cases are presented: the first is the flow of non-spherical particles in turbulent channel flow, and the second is a small fluidized bed with non-spherical particles.

2. IMMERSED BOUNDARY METHOD

The immersed boundary method (IBM) is a popular and efficient way to mimic the behaviour of a boundary condition on a fixed Eulerian mesh. There are a number of implementations of the IBM, falling into, broadly speaking, three categories: cut-cell IBM [3], the ghost-cell IBM [4], and the direct forcing IBM [5]. In this contribution, we adopt the direct forcing IBM as described in [5], which uses an efficient and strong flow-particle coupling scheme. This implementation includes a stabilisation strategy, which scales the forcing weights automatically, in order to create an optimal forcing, minimizing the transpiration error whilst remaining stable.

For each particle shape, many simulations are carried out, where the particle Reynolds number is varied between 0.1 and 500, and the angle of attack is varied. Examples of such simulations are shown in Figure 1 for an ellipsoid and Figure 2 for a fiber. For each simulation, the forces and torques are computed. These forces and torques are then used to design shape-specific correlations, that describe the interactions between the fluid and the particles. The equations are used as a base of large-scale analysis of complex flows with non-spherical particles.

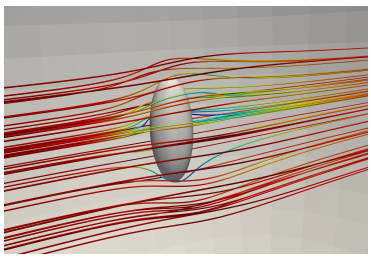

Figure 1. A snapshot of the resolved flow around an ellipse.

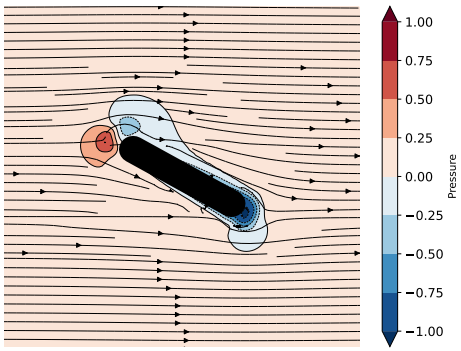

Figure 2. A snapshot of the instantaneous velocity (stream plots) and pressure field (color) in a flow past a fiber of aspect ratio 5 **at particle Reynolds number** 300 **and angle of attack** $\phi = 30$**.**

3. DEM: DYNAMICS OF NON-SPHERICAL PARTICLES

Although the motion or dynamics of a spherical particle is relatively straightforward [6], the dynamics of a non-spherical particle are more complicated. The rigid body dynamics of a non-spherical particle concern its motion and behaviour during one or more collisions. The ordinary differential equation describing the translational position and velocity are the same as for a spherical particle (Newton's second law), as given in the framework of DEM [7]:

$$\frac{D\boldsymbol{v}_p}{Dt} = \boldsymbol{a}_p \tag{1}$$

$$\rho_p V_p \boldsymbol{a}_p = \underbrace{\boldsymbol{F}_D}_{\text{drag}} + \underbrace{\boldsymbol{F}_L}_{\text{lift}} + \underbrace{V_p \rho_p \boldsymbol{g}}_{\text{gravity}} + \underbrace{V_p \nabla P}_{\text{Archimedes}} + \underbrace{\rho_p V_p \boldsymbol{a}_c}_{\text{collisions}} \tag{2}$$

where V_p is the volume of the particle, ρ_p the density, $\boldsymbol{v}_p$ the velocity of the particle in the *Lagrangian* framework, and $\boldsymbol{a}_c$ represents the acceleration of the force arising from collisions between particles. The added mass and history forces are neglected in the equation, as they are not significant in the case studied in this contribution.

The rotational motion of a non-spherical particle is very different compared to that of a spherical particle. For a non-spherical particle the orientation is important, unlike for a spherical particle. To derive

the rotational equations of motion for a non-spherical particle, it is convenient to introduce two types of Cartesian space: body space and world space. Calculations are performed in either space. These two Cartesian spaces are shown in Figure 3.

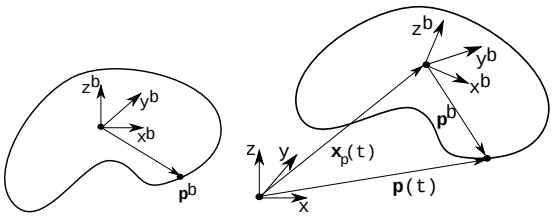

(a) body space (b) world space

Figure 3. The relation between body space (a) and world space (b). The fixed axes of body space, x^b, y^b and z^b are indicated in both figures. The position of a fixed point in body space, $\boldsymbol{p}^b$ is transformed to world space, $\boldsymbol{p}(t)$.

Due to the absence of singularity and Gimbal lock problems [8], unit Quaternions are increasingly popular to represent the rotation of a non-spherical particle. General Quaternions do not only change the orientation of a vector, but also scale the length of a vector. Therefore, the equation for representing rotation cannot be a simple Quaternion multiplication, as the length of the vector could change. To represent rotation by Quaternions, the length of the Quaternions must be exactly unity. Rotation without scaling is performed by unit Quaternions [9].

3.1. Quaternions

A quaternion consists of 4 numbers and represents the rotation and scaling of a body [10]. A quaternion with unit length represents an arbitrary rotation without scaling in 3D space. The condition of the unit length reduces the number of degrees of freedom from 4 to 3. The ODE of a quaternion is similar to that of a rotation matrix,

$$\dot{q}(t) = \frac{1}{2}\omega(t)q(t) \tag{3}$$

The rotation of a body can be seen as the subsequent application of two rotations, given by a pair of quaternions. Thus, the quaternion at the new time level can be interpreted as the quaternion of the previous time level multiplied by the rotational displacement during the time step. The infinitesimal displacement during the time step, is evaluated at the intermediate time level to comply with the mid-point rule and is determined as

$$q'_{n+\frac{1}{2}} = \left[\cos\frac{\|\omega_{n+\frac{1}{4}}\|\delta t}{4}, \sin\frac{\|\omega_{n+\frac{1}{4}}\|\delta t}{4}\frac{\omega_{n+\frac{1}{4}}}{\|\omega_{n+\frac{1}{4}}\|}\right] q_n \tag{4}$$

Hence, it is necessary to determine the mid-point angular velocity between two adjacent time steps. To get an estimate of the angular velocity for a general non-spherical particle, the equation for angular acceleration can be approximated in body space by

$$\dot{\boldsymbol{\omega}}^{\boldsymbol{b}} = \overline{\overline{I^b}}^{-1}\left(\boldsymbol{\tau}^{\boldsymbol{b}} - \boldsymbol{\omega}^{\boldsymbol{b}} \times \overline{\overline{I^b}}\boldsymbol{\omega}^{\boldsymbol{b}}\right) \tag{5}$$

The moment of inertia in body space is constant, and is expressed as $\overline{\overline{I}}_o$, and the relation between the moment of inertia in body space and world space can be represented in quaternion space as

$$\overline{\overline{I}}^{-1} = \left[q(t)\left(q(t)\overline{\overline{I}}_0 q(t)^{-1}\right)^T q(t)^{-1}\right]^T \tag{6}$$

3.2. Collision detection

At sufficient high particle loading, both particle-particle and particle-wall collisions are important for predicting the behaviour of the flow. Therefore, all potential collisions must be correctly detected in order to determine their contribution. Moreover, the particle-wall collisions are required to keep the particles in the domain. There are various frameworks to describe particle collisions. In the hard-sphere, or event driven, framework the collisions are dealt with using global conservation of momentum and energy [6]. In the soft-sphere framework, the dynamics of the actual collision are resolved, using approximations from elasticity theory [7].

In this contribution, we consider the soft-sphere approach, thus contact forces and torques are determined for particles which are actually slightly overlapping. This overlap is a representation for the local deformation, or displacement, and a Hertzian force model can be used to predict the resulting repellent force. Therefore, each pair of near-neighbour particles is checked for overlap. In this contribution, we have chosen to represent each particle as a collection of spheres [11]. This is achieved by 'filling' each body with a number of overlapping fictitious spheres, typically with varying radii, where the number of fictitious spheres determines the accuracy of the surface representation of the body. An example is shown in Figure 4. This framework allows for a similar contact detection approach as for spherical particles, as described, for instance, in [12].

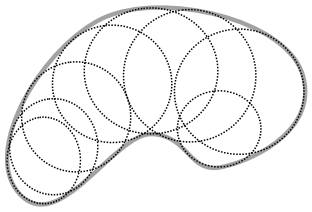

Figure 4. An example of the body shown in Figure 3 filled with 8 spheres. The spheres are used to find potential contact points with neighbouring particles or walls.

3.3. Collision forces

Once a collision is detected, the overlap, or the displacement, between two particles or a particle and a wall is determined. This overlap is used as a meas-

ure to estimate the local deformation of the particle at the point of collision, by assuming the contact point is locally axi-symmetric with a constant local radius, and leads to normal and tangential forces based upon [13],

$$\boldsymbol{F}_n(t) = K_n(t)\delta_n^{\frac{3}{2}}(t)\boldsymbol{n}(t)$$
$$\boldsymbol{F}_t(t) = \min\left(\mu\boldsymbol{F}_n(t), K_t(t)\boldsymbol{\delta}_t(t)\right)$$

where μ is the coefficient of friction, $\delta_n(t)$ is the scalar representing the normal displacement, $\boldsymbol{\delta}_t(t)$ is the vector representing the accumulated tangential displacement over the duration of the collision, mapped onto the current reference frame. The tangential displacement vector is determined by integrating the successive tangential displacements and mapping this into the current frame of reference of the collision. K_n and K_t are the spring constants for the normal and tangential forces respectively, as predicted Hertzian contact theory [13]

$$K_{n,l}(t) = \frac{4}{3}E^*\sqrt{r(t)}$$
$$K_t(t) = 8G^*\sqrt{r(t)\delta_t(t)}$$

where E^* represents the Young's modulus of the pair of colliding particles, G^* is the ratio of the Young's modulus and Poisson's ratio plus one for the pair of colliding particles, $r(t)$ represents the local radius of the particle (the distance from the centre of mass of the particle to the contact point) and the subscript l represents the loading, *i.e.* the particles moving towards each other. When the particles move away from each other, the subscript u, representing unloading are used. To account for the dissipative nature of the collision, a coefficient of restitution is introduced to determine the spring constant value for unloading, represented by the subscript u, following [14]

$$e = \sqrt{\frac{K_{n,u}}{K_{n,l}}} \tag{7}$$

The total force on the body is determined by adding the gravity force, the fluid force, and summing the force contributions of all collisions of each particle

$$\boldsymbol{a}_p(t) = \boldsymbol{g} + \frac{\boldsymbol{F}_f(t)}{m_p} + \sum_{c=\text{contacts}} \frac{\boldsymbol{F}_{n,c}(t) + \boldsymbol{F}_{t,c}(t)}{m_p} \tag{8}$$

where m_p indicates the mass of the particle, $\boldsymbol{g}$ represents the gravitational acceleration, $\boldsymbol{F}_f$ represents the total interaction force with the fluid, and $\boldsymbol{F}_{n,c}$ and $\boldsymbol{F}_{t,c}$ represent the normal and tangential forces from the collision of the particle.

The torque on the body is determined by adding the torque arising from the fluid and the contributions of all collisions of each particle

$$\boldsymbol{\tau}(t) = \boldsymbol{\tau}_f(t) + \sum_{c=\text{contacts}} \Big(\boldsymbol{p}_c - \boldsymbol{x}_p(t)\Big) \times \left(\boldsymbol{F}_{n,c}(t) + \boldsymbol{F}_{t,c}(t)\right) \tag{9}$$

where $\boldsymbol{p}_c$ is the point of contact of the particle with another particle, and $\boldsymbol{x}_p$ is the centre of mass of the particle.

3.4. Hydrodynamic forces and torques

The fluid exerts two types of forces on the particle: drag force in the direction of the flow velocity and a transverse lift force. Additionally, a pitching and counter-rotational torques are present. These interactions are given by the following equations [2]:

$$F_D = C_D\frac{1}{2}\rho\tilde{v}^2\frac{\pi}{4}d_p^2 \tag{10}$$

$$F_L = C_L\frac{1}{2}\rho\tilde{v}^2\frac{\pi}{4}d_p^2 \tag{11}$$

$$\tau_P = C_T\frac{1}{2}\rho\tilde{v}^2\frac{\pi}{8}d_p^3 \tag{12}$$

$$\boldsymbol{\tau}_R = C_R\frac{1}{2}\rho\left(\frac{d_p}{2}\right)^5 |\boldsymbol{\Omega}|\boldsymbol{\Omega} \tag{13}$$

where F_D are the drag force, F_L is the lift force, τ_P is the pitching torque, τ_R is the rotational torque, C_D, C_L, C_T and C_R are the shape specific force and torque coefficients, $\tilde{v} = \widehat{v}^f - v_p$ is the velocity of the particle relative to the local undisturbed fluid velocity, ρ is the fluid density, and d_p the equivalent particle diameter, *i.e.* the diameter of a sphere with the same volume as the considered particle. The relative rotation of the particle with respect to the fluid is given by

$$\boldsymbol{\Omega} = \frac{1}{2}\nabla\times\tilde{\boldsymbol{v}} - \boldsymbol{\omega}_p \tag{14}$$

with ω_p representing the angular velocity of the particle. The total fluid induced force is determined by adding the drag and lift forces and the total fluid induced torque is determined by adding the two torques.

4. CFD: FLUID PHASE MODELLING

The simulations are carried out with our in-house multiphase CFD code Multiflow, which is a transient, three-dimensional, fully coupled parallel computational fluid dynamics (CFD) code based on finite volume discretisation [15, 16] and various types of particle and fluid models. It has shown to be a robust solving framework for viscous multiphase flows in the presence of large source terms and large gradients in density and volume-fraction.

4.1. Large eddy simulation (LES) modelling

The filtering procedure for LES can be found in [17]. The equations arising from filtering are very similar to the Navier-Stokes equations, except for the addition of one term, which describes the behaviour of the sub-grid scale stresses, namely τ_{ij}^a

$$\tau_{ij}^a = \rho_f(\widetilde{v_{f,i}v_{f,j}} - \widetilde{v}_{f,i}\widetilde{v}_{f,j}) \tag{15}$$

To close the sub-grid-scale stresses, the Smagorinsky model [18] is used. The Smagorinsky model assumes that the local SGS stresses are proportional to the

local rate of strain of the resolved flow [19]. The stresses are given as

$$\tau_{ij}^{a} = -2\mu_{SGS}\widetilde{S}_{ij} + \frac{1}{3}\tau_{ll}\delta_{ij} \tag{16}$$

where $\widetilde{S}_{ij} = \frac{1}{2}\left[\frac{\partial \widetilde{v}_{f,i}}{\partial x_j} + \frac{\partial \widetilde{v}_{f,j}}{\partial x_i}\right]$. and μ_{SGS} is the sub-grid scale eddy viscosity. By analogy to Prandtl's mixing-length hypothesis [20], μ_{SGS} can be estimated as

$$\mu_{SGS} = \rho_f (C_{SGS}\Delta)^2 \sqrt{2\widetilde{S}_{ij}\widetilde{S}_{ij}} \tag{17}$$

where C_{SGS} is the Smagorinsky constant and Δ is the LES filter width.

It is well-known that the Smagorisnky model is not suitable for accounting for the effect of walls. This is because the no-slip boundary condition at the wall causes a strong velocity gradient (i.e. the Reynolds number near the wall decreases since the velocity drops). From Prandtl's mixing-length hypothesis this would create unrealistic non-zero sub-grid viscosity values and hence shear stresses near the wall [20]. Therefore, a damping function is used to turn-off the μ_{SGS} near the wall; C_{SGS} is modified as

$$C_{vD} = C_{SGS}\Delta(1 - e^{-y^+/A_o^+}) \tag{18}$$

Note that $y^+ = \frac{u_\tau y}{\nu_f}$; where y^+ is the dimensionless distance to the wall, u_τ is the friction velocity and A_o^+ is a constant normally taken to be 25. μ_{SGS} is modified as

$$\mu_{SGS} = \rho_f C_{vD}^2 \sqrt{2\widetilde{S}_{ij}\widetilde{S}_{ij}} \tag{19}$$

The model has proved to be quite successful in many types of wall bounded turbulent flows with steady boundary layers [21]. However, a DNS resolution is required in the wall region.

5. CFD/DEM: COUPLING BETWEEN CFD AND DEM

As the particles move in a Lagrangian framework and the fluid is solved in a fixed Eulerian framework, the coupling between these frameworks requires special attention. The fluid velocity as determined on the Eulerian mesh must be accurately interpolated to each of the Lagrangian particles. Some properties of interpolation schemes between the Eulerian and the Lagrangian frameworks are discussed in [22]. A frequently used interpolation scheme is the tri-linear interpolation, which has a number of favourable properties, such as continuity and ease of implementation, but suffers from a strong filtering of higher frequency velocity fluctuations and is probably not suitable for accurate computations. Therefore, we have used a polynomial spline interpolation, where a property of the fluid at the particle is approximated by

$$\phi_{f@p} = \sum_{n=1}^{N}\sum_{i,j,k}^{I,J,K} a_{n,ijk}\Delta x^i \Delta y^j \Delta z^k \phi_{f,n} \tag{20}$$

where the summation over n is over the independent points and the summation over (i, j, k) is over the polynomial integer values, and $a_{n,ijk}$ is the constant coefficient corresponding to independent point n and the polynomial powers of (i, j, k) for the three independent directions. The number of independent fluid velocity points, N, used to evaluate the spline is 27, and the order of the polynomial used is, therefore $(I, J, K) = (3, 3, 3)$.

6. SIMULATIONS

6.1. Test-case 1: Turbulent channel flow

In this work, the properties of the fluid phase and the computational domain are the same as in the work of Marchioli et al. [23], who have studied this channel case for spherical and ellipsoidal particles. The size of the channel computational domain is $4\pi h \times 2\pi h \times h$ in the x, y, and z directions, respectively, in which $h = 0.02$ m is the half height of the channel, and the mean flow is in the x direction. There are solid walls in the low and high y directions, and in all other directions, periodic boundaries are applied. Within the turbulent channel flow, fibers with a Stokes number of 5 are released.

In this abstract we show the fluid velocity in the stream-wise velocity in a plane close to one of the walls in Figure 5. Full results are presented during the presentation.

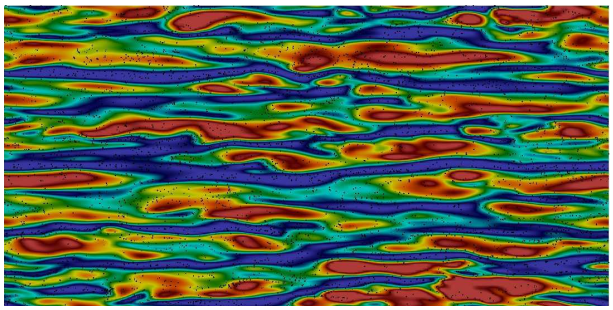

Figure 5. The instantaneous fluid velocity (indicated by colour) in the stream-wise direction and the distribution of ellipsoids with $St = 5$ and an aspect ratio of 5 near the cross-sectional x-z plane at $y^+ = 8$.

6.2. Test-case 2: Fluidized Beds

The fluidized bed test-case is from [6] and consists of a quasi-two dimensional fluidized bed of 500 mm high, 90 mm wide, and 8 mm deep filled with ellipsoidal particles of around $d_p \approx 1.75$ mm. The experiments as well as the simulations with spherical particles has been described in [6]. Figure 6 shows a shapshot of the ellipsoidal particles being fluidized in

the bed. Full results are presented during the presentation.

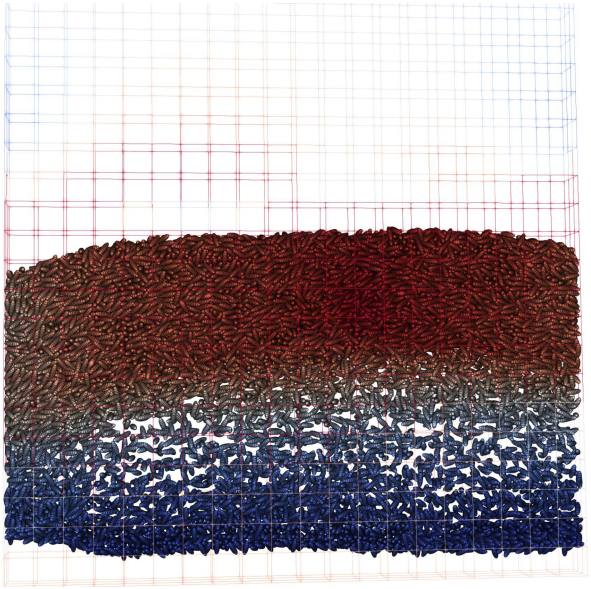

Figure 6. An instantaneous snapshot of the position of the ellipsoids in the fluidized bed. The ellipsoids are coloured by their velocity.

7. CONCLUSIONS

In this contribution we present a fully coupled CFD/DEM framework to predict the behaviour of non-spherical particles in flows. We first use a state-of-the-art immersed boundary method to determine the drag, torque and lift of the non-spherical particle shape. We then use a discrete element model to predict the collisions between two particles and particles and a wall. The orientation of the particle in the discrete element model is described in the framework of Quaternions. Finally, two different applications of the coupled CFD/DEM framework are presented: the flow of fibers in turbulent channel flow, and the behaviour of ellipsoidal particles in a fluidized bed. In both simulations, there is a clear preferred orientation of the particles, leading to a significantly different behaviour of the system compared to the system with spherical particles.

ACKNOWLEDGEMENTS

This research was funded by the Deutsche Forschungsgemeinschaft (DFG, German Research Foundation) - Project-ID 422037413 - TRR 287 and Project-ID 448292913.

REFERENCES

[1] Fan, L. S., and Zhu, C., 1998, *Principles of Gas-Solid Flows*, Cambridge Univ. Press.

[2] Zastawny, M., Mallouppas, G., Zhao, F., and van Wachem, B., 2012, "Derivation of Drag and Lift Force and Torque Coefficients for Non-Spherical Particles in Flows", *International Journal of Multiphase Flow*, Vol. 39, pp. 227–239.

[3] Mark, A., and van Wachem, B., 2008, "Derivation and Validation of a Novel Implicit Second-Order Accurate Immersed Boundary Method", *Journal of Computational Physics*, Vol. 227, pp. 6660–6680.

[4] Majumdar, S., Iaccarino, G., and Durbin, P., 2001, "RANS Solvers with Adaptive Structured Boundary Non-Conforming Grids", *Center for Turbulence Research Annual Research Briefs*, pp. 353–366.

[5] Abdol Azis, M. H., Evrard, F., and van Wachem, B., 2019, "An Immersed Boundary Method for Incompressible Flows in Complex Domains", *Journal of Computational Physics*, Vol. 378, pp. 770–795.

[6] van Wachem, B., Van der Schaaf, J., Schouten, J., Krishna, R., and van den Bleek, C., 2001, "Experimental Validation of Lagrangian-Eulerian Simulations of Fluidized Beds", *Powder Technology*, Vol. 116 (2), pp. 155–165.

[7] Cundall, P., and Strack, O. D. L., 1979, "A Discrete Numerical Model for Granular Assemblies", *Géotechnique*, Vol. 29 (1), pp. 47–65.

[8] Evans, D., and Murad, S., 1977, "Singularity Free Algorithm for Molecular Dynamics Simulation of Rigid Polyatomics", *Molecular Physics*, Vol. 34 (2), pp. 327–331.

[9] Zhao, F., and van Wachem, B., 2013, "A Novel Quaternion Integration Approach for Describing the Behaviour of Non-Spherical Particles", *Acta Mechanica*, Vol. 224 (12), pp. 3091–3109.

[10] Hamilton, W. R., 1844, "On Quaternions; or on a New System of Imaginaries in Algebra", *The London, Edinburgh and Dublin Philosophical Magazine and Journal of Science(3rd Series)*, Vol. 15–36, pp. 1–306.

[11] Langston, P. A., Al-Awamleh, M. A., Fraige, F. Y., and Asmar, B. N., 2004, "Distinct Element Modelling of Non-Spherical Frictionless Particle Flow", *Chemical Engineering Science*, Vol. 59 (2), pp. 425–435.

[12] Allen, M. P., and Tildesley, D. J., 1989, *The Computer Simulation of Liquids, Vol 42*, Oxford University Press.

[13] Mindlin, R. D., and Deresiewicz, H., 1953, "Elastic Spheres in Contact under Varying Oblique Forces", *J of Appl Mech*, Vol. 20, pp. 327–344.

[14] Walton, O. R., and Braun, R. L., 1993, "Simulation of Rotary-Drum and Repose Tests for Frictional Spheres and Rigid Sphere Clusters", *5th Joint DOE/NSF Workshop on Flow of Particulates, Ithaca, NY, 1993 (Lawrence Livermore National Laboratory, Livermore, CA).*, 5th Joint DOE/NSF Workshop on Flow of Particulates, Ithaca, NY, 1993 (Lawrence Livermore National Laboratory, Livermore, CA).

[15] Bartholomew, P., Denner, F., Abdol-Azis, M., Marquis, A., and van Wachem, B., 2018, "Unified Formulation of the Momentum-Weighted Interpolation for Collocated Variable Arrangements", *Journal of Computational Physics*, Vol. 375, pp. 177–208.

[16] Xiao, C.-N., Denner, F., and van Wachem, B., 2017, "Fully-Coupled Pressure-Based Finite-Volume Framework for the Simulation of Fluid Flows at All Speeds in Complex Geometries", *Journal of Computational Physics*, Vol. 346, pp. 91–130.

[17] Sagaut, P., 2005, *Large Eddy Simulation for Incompressible Flows*, third edn., ISBN 1434-8322.

[18] Smagorinsky, J., 1963, "General Circulation Experiments with the Primitive Equations. I: The Basic Experiment.", *Month Weath Rev*, Vol. 91 (3), pp. 99–165.

[19] Versteeg, H. K., and Malalasekera, W., 2007, *An Introduction to Computational Fluid Dynamics: The Finite Volume Method*, Pearson Education, second edn., ISBN 978-0-13-127498-3.

[20] Pope, S. B., 2000, *Turbulent Flows*, Cambridge University Press, Cambridge, sixth edn., ISBN 978-0-521-59886-6.

[21] Germano, M., Piomelli, U., Moin, P., and Cabot, W. H., 1991, "A Dynamic Subgrid-Scale Eddy Viscosity Model", *Physics of Fluids A*, Vol. 3 (7), pp. 1760–1765.

[22] Franklin, J., and Lee, J. S., 2010, "A High Quality Interpolation Method for Colocated Polyhedral/Polygonal Control Volume Methods", *Computers & Fluids*, Vol. 39 (6), pp. 1012–1021.

[23] Marchioli, C., Soldati, A., Kuerten, J. G. M., Arcen, B., Taniere, A., Goldensoph, G., Squires, K. D., Cargnelutti, M. F., and Portela, L. M., 2008, "Statistics of Particle Dispersion in Direct Numerical Simulations of Wall-Bounded Turbulence: Results of an International Collaborative Benchmark Test", *International Journal of Multiphase Flow*, Vol. 34 (9), pp. 879–893.

Conference on Modelling Fluid Flow (CMFF'22)
The 18th International Conference on Fluid Flow Technologies
Budapest, Hungary, August 30 -September 2, 2022

MACHINE LEARNING-BASED CLOSURE DEVELOPMENT FOR MODELING OF COHESIVE GAS-PARTICLE FLOWS

Josef TAUSENDSCHÖN, Mohammadsadegh SALEHI, Stefan RADL

[1] Institute of Process and Particle Engineering, Graz University of Technology. Corresponding Author E-mail: josef.tausendschoen@tugraz.at

ABSTRACT

Coarse-grid simulations of large-scale gas-solid flows using a filtered two-fluid model (fTFM) require appropriate sub-grid closure models to approximate unresolved physical phenomena. Such a sub-grid closure should be accurate enough to account for the effects of the inhomogeneous particle distribution. Several constitutive models are available in the literature for non-cohesive gas-solid flows, while they are not applicable for cohesive flows. Therefore, we aim to investigate the dependency of the drag force closure on the cohesion level, and integrate it into a drag correction concept based on machine learning (ML).

To do so, the results of fully-resolved CFD-DEM simulations of cohesive gas-particle flow are filtered with different filter sizes to develop a new drag closure. In detail, we simulated different systems by changing the cohesion level from cohesionless to highly cohesive, and the size of the systems, via coarse-graining. Afterwards, a dataset for the ML algorithm was created, and various markers were analyzed. Subsequently, a neural network-based drag correction model was created, trained, and tested with the identified markers. Finally, we benchmark the accuracy of the developed models for a range of cohesion levels.

Keywords: Multiphase Flows, Cohesive Gas-Particle Flows, Data-driven Modelling, Machine Learning

NOMENCLATURE

Bo	[-]	Bond number
Ca	[-]	Capillary number
$\underline{\underline{D}}$	[$1/s$]	Symmetric velocity gradient tensor
G	[$1/m^3$]	Filter kernel
$\underline{F}$	[N]	Force
Fr	[-]	Froude number
H_d	[-]	Drag correction function
H_{DNN}	[-]	DNN-based drag function
d	[m]	Particle diameter
f_{DNN}	[-]	Neural network function value
h	[-]	Activation function
h_{ij}^*	[-]	Dimensionless separation distance
$\underline{g}, g$	[m/s^2]	Gravitational acceleration
R	[m]	Particle radius
$\underline{r}$	[m]	Predefined spatial position
$\underline{n_{ij}}$	[-]	Unit normal vector betw. particles
p	[Pa]	Pressure
t	[s]	Time
$\underline{u}, \underline{v}$	[m/s]	Eulerian velocity vector
u, v	[m/s]	Individual component of the velocity vector
u_t	[m/s]	Terminal settling velocity
V_b^*	[-]	Dimensionless bridge volume
$\underline{w}$	[-]	Neural network weight vector
w_0	[-]	Neural network bias
$\underline{x}$	[m]	Spatial position on grid
α	[-]	Coarse-graining ratio
β	[kg/m^3s]	Drag coefficient
Δ_f	[m]	Fluid filter size
Δ_G	[m]	Fluid grid size
ϕ	[-]	Volume fraction
Λ	[-]	Liquid loading level
$\underline{\Phi_d}$	[N/m^3]	Interphase drag force
ρ	[kg/m^3]	Density
θ	[rad]	Contact angle of the liquid bridge
μ_l	[Pa s]	Liquid dynamic viscosity
σ	[N/m]	Surface tension
ψ	[-]	Neural network input
$\dot{\gamma}$	[$1/s$]	Shear rate
$\underline{\underline{\tau}}$	[kg/ms^2]	Phase stress tensor

Subscripts and Superscripts

cap	Capillary
DNN	Deep Neural Network
d	Drift
g	Gas
ref	Reference
P	Particle

s	Solid
sl	Slip
sgs	Sub-grid contribution
tot	Total
max	Maximum
min	Minimum
vis	Viscous
z	Z-direction
Eul	Eulerian
Micro	Microscopic
−	Filtered
~	Filtered and phase-weighted
*	Scaled dimensionless quantity

1. INTRODUCTION

Fine particles are widely used in various industrial sectors as these particles features high specific surface area, which increases the rate of heat and mass transfer [1]. In the petrochemical industry, small particles are used as reacting powders for pulverized coal combustion and gasification. Another example is fluid catalytic cracking process, in which fine particles are used as FCC catalysis [2]. In the pharmaceutical industry, active pharmaceutical ingredients (API) are typically fine, which can improve the dissolution and release rate in the body [3]. In the food industry, due to their high specific surface area, fine powders are desirable [4]. However, the effect of cohesive force on powder flowability becomes more important for fine powder, compared to coarse particles.

Powders with cohesive interactions force can be categorized from mildly cohesive to highly cohesive. The level of cohesion can be quantified based on the Bond number, which describes the ratio of cohesion forces to the gravitational force. In addition to van der Waals forces, particle can become cohesive due to presence of liquid bridge between the particles in the gas-solid systems. This cohesive force is associated with viscous and surface tension forces, quantified by a Bond and capillary number [5]–[7].

As these phenomena occur at a particle level, quantification of these forces is not easy to investigate through experimental approaches. However, detailed numerical simulation can be of significant help in analyzing the contribution of different forces in the strength of granule and powder flowability. Typically, two different approaches can be used in this regard: i) computational fluid dynamic (CFD) through Two-Fluid Method (TFM) approach[8]; ii) CFD coupled with Discrete Element Method (CFD-DEM)[9]. These approaches can be used in highly-resolved and un-resolved scales. However, the computational cost for the highly-resolved one is extremely high when simulating industrial scale systems. Therefore, application of filtered approaches as un-resolved method are desired especially for industrial-scale systems [10], [11].

Simulations of industrial-scale gas-particle flows based on the filtered Two-Fluid model (fTFM) approach, and therefore with coarse grids, depend critically on constitutive models that account for the effects of inhomogeneous structures at the sub-grid level [12]. The complexity of accounting for inhomogeneous structures increases when considering cohesive gas-particle flows [13].

Previously, an artificial neural network-based drag correction model was developed by Jiang et al. [14], [15] for non-cohesive gas-particle systems. However, the question persists if this model is useful for cohesive systems or not. Therefore, in our current contribution, we aim to analyze the influence of cohesion on the drag force closure and integrate it into a machine learning-based drag correction concept. Prior studies [16] identified the sub-grid drift velocity as the crucial quantity for modeling the filtered drag coefficient. Unfortunately, the drift velocity is unavailable in filtered simulations. To correctly reproduce mesoscale structures, and since the drift velocity is also computable, we start with detailed CFD-DEM-based (Computational Fluid Dynamics-Discrete Element Method) simulations, and filter them with different filter sizes to emulate quantities available in an fTFM simulation.

2. MODEL DESCRIPTION AND FILTERING PROCEDURE

We perform fully resolved CFD-DEM simulations of a 2D periodic box over a wide range of different setups. Subsequently, these simulations are filtered (i.e., spatially averaged) with different filter sizes. Coarse-grained CFD-DEM simulations are used to perform simulations with larger system sizes to limit the computational expense. The CFD part is realized within the framework of OpenFOAM® [17], and the DEM part is solved using LIGGGHTS® [18]. The coupling between these two tools is performed with CFDEM® [18].

2.1. Simulation setups

The fluid grid size Δ_G was chosen equal to three times the particle (or parcel in case of coarse-grained simulations) diameter. The domain size is 16 Δ_G x 2 Δ_G x 64 Δ_G in each respective regime. The coarse-graining ratio α is defined as the ratio of the parcel and primary particle diameter (simulations featuring primary particles are indicated by $\alpha = 1$). Coarse-grained parameters are scaled from the primary to the coarse system according to [19]. Cohesion results from liquid bridges between the particles. These liquid bridges are modelled after Wu et al. [20]. The liquid loading level Λ is unchanged over all cohesive simulations. The cohesion level is varied from cohesionless to highly cohesive. For detailed information about the used cohesion models see Append A. In Table 1 an overview of all performed simulation and their system parameters is given.

Table 1. Overview simulation regimes

	$\alpha = 1$	$\alpha = 3$	$\alpha = 5$
d_P [m]	150e-6	450e-6	7.5e-4
Δ_G [m]	450e-6	1.35e-3	2.25e-3
$\phi_{s,tot}$		0.10	
Domain size		16 Δ_G x 2 Δ_G x 64 Δ_G	
Primary particles	10,561	285,147	1,320,125
Parcels	-	10,561	10,561
Bo	0-20	0-100	0-100
Λ		0.001	
Ca		0.01	
Δ_f		3 Δ_G; 4 Δ_G; 5 Δ_G	

The calculated terminal settling velocity u_t for the primary particle is 0.8562 [m/s]. The reference time is $t_{ref} = u_t/g$ and therefore equal to 0.0873 [s]. In [19] comparable simulations needed 5 times t_{ref} to reach a statistical steady-state. Therefore, simulations are performed for nearly $30 \cdot t_{ref}$ in our present study. The time frame in which data was sampled ranged from $18 \cdot t_{ref}$ to $30 \cdot t_{ref}$, with sampling performed every 0.25 t_{ref}.

2.2 Filtering Procedure

Filtering operations are performed via CPPPO [21]. The filtered solid volume fraction is:

$$\bar{\phi}_s(\underline{x},t) = \iiint \phi_s(\underline{r},t)\, G(\underline{r}-\underline{x})\, d\underline{r} \qquad (1)$$

where $\underline{x}$ is the spatial position (any position in the grid), $\underline{r}$ is the predefined spatial position. The filtered gas volume fraction is then $\bar{\phi}_g = 1 - \bar{\phi}_s$.The box filter kernel or top-hat kernel $G(\underline{r}-\underline{x})$ is normalized so that $\iiint G(\underline{r}-\underline{x})\, d\underline{r} = 1$ and is defined by the fluid filter size Δ_f after:

$$G(\underline{r}-\underline{x}) = \begin{cases} \frac{1}{\Delta_f^3}, \text{if } |\underline{r}-\underline{x}| \le \frac{\Delta_f}{2} \\ 0, \text{otherwise} \end{cases} \qquad (2)$$

The filtered gas and solid velocity are then:

$$\underline{\tilde{u}_g} = \frac{1}{\bar{\phi}_g} \iiint G(\underline{r}-\underline{x})\, \phi_g(\underline{r},t)\, \underline{u_g}(\underline{r},t)\, d\underline{r} \qquad (3)$$

$$\underline{\tilde{u}_s} = \frac{1}{\bar{\phi}_s} \iiint G(\underline{r}-\underline{x})\, \phi_s(\underline{r},t)\, \underline{u_s}(\underline{r},t)\, d\underline{r} \qquad (4)$$

The filtered gas pressure is:

$$\bar{p}(\underline{x},t) = \iiint G(\underline{r}-\underline{x})\, p(\underline{r},t)\, d\underline{r} \qquad (5)$$

The mass and momentum conservation balances for filtered CFD-DEM equations of the gas and the solid phase can be found in Appendix B.

2.3. Closure for the interphase drag force

In our contribution we focus on the closure for the interphase drag and the mesoscale interphase force. The mesoscale interphase force is typically referred to as the sub-grid contribution of the interphase drag force, and denotated as $\underline{\Phi_{d,sgs}}$ in what follows. It is defined as the difference between the filtered Eulerian drag force $\underline{\bar{\Phi}_d}$ and the interphase drag force $\underline{\tilde{\Phi}_d}$ calculated based on the filtered slip velocity and the microscopic drag coefficient:

$$\begin{aligned} \underline{\Phi_{d,sgs}} &= \underline{\bar{\Phi}_d} - \underline{\tilde{\Phi}_d} \\ &= \overline{\beta^{Eul}\left(\underline{u_g} - \underline{u_s}\right)} \\ &\quad - \beta^{Micro}(\underline{\tilde{u}_g} - \underline{\tilde{u}_s}) \end{aligned} \qquad (6)$$

where β^{Eul} is the Eulerian drag coefficient. β^{Eul} is equal to the momentum exchange term in the performed CFD-DEM simulations. β^{Micro} is the drag coefficient evaluated based on filtered quantities using specific drag law, e.g. Beetstra et al. [22]. Analogously as in [16] the filtered Eulerian drag force (since not available in filtered simulations) is modelled by:

$$\begin{aligned} &\overline{\beta^{Eul}(\underline{u_g} - \underline{u_s})} \approx \beta^{Micro}(\underline{\tilde{u}_g} - \underline{\tilde{u}_s} + \underline{\tilde{v}_d}) \\ &= \overline{\beta^{Eul}}(\underline{\tilde{u}_g} - \underline{\tilde{u}_s}) \end{aligned} \qquad (7)$$

$\overline{\beta^{Eul}}$ is the filtered Eulerian drag coefficient. The sub-grid drift velocity $\underline{\tilde{v}_d}$ is defined by:

$$\underline{\tilde{v}_d} = \frac{\overline{\phi_s u_g}}{\bar{\phi}_s} - \underline{\tilde{u}_g} \qquad (8)$$

When rearranging Eqs. (6) and (7) one can describe the mesoscale interphase force by $\underline{\Phi_{d,sgs}} = \beta^{Micro}\, \underline{\tilde{v}_d}$. Using this definition and Eq. (6) we can finally model the filtered Eulerian drag force by:

$$\underline{\bar{\Phi}_d} = \underline{\tilde{\Phi}_d} \left(1 + \frac{\underline{\tilde{v}_d}}{\underline{\tilde{u}_g} - \underline{\tilde{u}_s}}\right) = \underline{\tilde{\Phi}_d}\, \underline{H_d} \qquad (9)$$

Where $\underline{H_d}$ is the so-called drag correction function, which must fulfil the following properties:

- $\underline{H_d} \to 1$ for sufficiently small filter sizes (i.e., "well-resolved" simulations).
- $\underline{H_d} \to 1$ in the dilute (i.e., a single particle sedimenting at its terminal speed) and dense limit (i.e., a closely-packed, hence homogeneous, particle suspension sedimenting at steady state).

If we rearrange Eqs. (7) and (9) on can see that the drag correction function can also be approximated by:

$$\frac{\bar{\beta}^{Eul}}{\beta^{Micro}} = 1 + \frac{\underline{\tilde{v}_d}}{\underline{\tilde{u}_g} - \underline{\tilde{u}_s}} = \underline{H_d} \qquad (10)$$

3. DEEP NEURAL NETWORK

Jiang et al. [14], [15] introduced the usage of a Deep Neural Network (DNN) instead of a correlation function to predict the sub-grid drift velocity and subsequently the drag correction function. We evolve this idea into cohesive systems. From this section on, note that the term 'scaled' is used in the manner typical of fTFM to describe dimensionless parameters. In contrast, the term 'normalized' describes the feature normalization (or "scaling") related to the DNN induced data preparation. In order to develop a correct and accurate DNN-based drag correction function, the target for the training, which of course also represents the prediction, must be defined first. Subsequently, the transformation of the prediction into the actual drag correction is specified.

3.1. Target scaling

Since dimensionless quantities are preferred, a direct prediction of the drift velocity is not provided and is unusual. Deep Neural Networks often require target normalization. This demands knowledge or a search of minimum or maximum values. The first one is often not available or ties the prediction to certain preconditions, the latter comes with high computational effort and is often not possible. Therefore, scaling the target with known and available system quantities is preferred. Preliminary tests showed that scaling and additional normalization of the target is not beneficial to the prediction quality. Subsequently, we simply scale the target and do not use any additional normalization. In the present contribution, we focus on the vertical drag correction, represented by the z-direction in our simulations. Thus, only the z-components of the velocities and the drag coefficients were used for our analysis.

Jiang et al. [14] scaled the drift velocity with the filtered solid volume fraction, creating $\bar{\phi}_s\,\tilde{v}_{d,z}$ as the target. In a preceding publication [15], they adapted the target to $\frac{\bar{\phi}_s\,\tilde{v}_{d,z}}{\phi_{s,max}\,u_t}$, making it dimensionless. Two other options appear to be possible dimensionless targets, (i) the drift velocity relative to the terminal settling velocity $\tilde{v}_{d,z}/u_t$, and (ii) the direct prediction of $\frac{\tilde{v}_{d,z}}{\tilde{u}_{g,z}-\tilde{u}_{s,z}}$ from Eq. (10). The first option gave worse results in preliminary tests, and the second option could lead to numerical problems. Finally, $\frac{\bar{\phi}_s\,\tilde{v}_{d,z}}{\phi_{s,max}\,u_t}$ is selected as the target. Using the example of a single-layer neural network, the prediction is then:

$$\frac{\bar{\phi}_s\,\tilde{v}_{d,z}}{\phi_{s,max}\,u_t} = f_{DNN} = h(\underline{w}^T\,\underline{\hat{\psi}} + w_0) \qquad (11)$$

Where $\underline{\hat{\psi}}$ is the normalized input of the neural network, and h is the activation function. $\underline{w}$ the weights of the layer and w_0 is the bias.

3.2. DNN-based drag correction function

To build the DNN-based drag function Eq. (11) is rearranged to:

$$H_{DNN} = \frac{\phi_{s,max}\,u_t}{\bar{\phi}_s(\tilde{u}_{g,z}-\tilde{u}_{s,z})}\,f_{DNN} \qquad (12)$$

In order to meet the requirements stated in Section 2.3, and to be consistent with Jiang et al. [15], H_{DNN} is corrected. If the filtered solid volume fraction $\bar{\phi}_s$ is outside the range of 0.01 to 0.55, the DNN-based drag function is set to zero. Within the specified range, the function value is used. The actual drag correction function is then:

$$H_{d,z} = 1 + \begin{cases} H_{DNN}\,, & 0.01 \le \bar{\phi}_s \le 0.55 \\ 0\,, & else \end{cases} \qquad (13)$$

3.3. Marker selection

All Eulerian quantities available in the simulation are in question as a marker or input quantity of the neural network. Also, system parameters like the Bond number or the filter length can be used. In addition, combinations of the available Eulerian quantities as well as markers calculable with small computational effort, e.g., the gradient of the pressure field, are applicable. Jiang et al. [15] used the dimensionless filter length Δ_f^* and the particle Reynolds number as system parameters. In our simulation dataset, the particle Reynolds number is not changing for a single sedimenting particle, hence it is replaced by the Bond number since it accounts for cohesion.

The relative slip velocity in z-direction $\tilde{u}_{sl,z}/u_t$, the filtered solid volume fraction relative to the maximum solid fraction $\bar{\phi}_s/\phi_{s,max}$, and the scaled gradient in the z-direction of the filtered gas pressure field $\overline{\nabla p_z^*}$ are used equally as in [15]. We add the scaled shear rate of the filtered slip velocity $\overline{\dot{\gamma}^*}$. The input vector $\underline{\psi}$ of the DNN is then defined like:

$$\underline{\psi} = \left(\Delta_f^*, \frac{\bar{\phi}_s}{\phi_{s,max}}, \frac{\tilde{u}_{sl,z}}{u_t}, \overline{\nabla p_z^*}, Bo, \overline{\dot{\gamma}^*}\right) \qquad (14)$$

For the detailed calculation of each marker, see Appendix C. All markers are scaled to be dimensionless. Since different orders of magnitudes are present within the input values and DNNs typically require normalization [23], markers are additionally normalized.

3.4. Marker normalization

The normalization process of the input vector follows:

$$\underline{\hat{\psi}} = (\underline{\psi} - \psi_{min})/(\psi_{max} - \psi_{min}) \qquad (15)$$

Where ψ_{min} and ψ_{max} are the minimum and maximum values of the respective marker. Before normalization, the available data is separated into training, validation, and testing data sets. The

respective min and max values are then searched in the training data and used to normalize (and denormalize) the validation and the testing data to avoid data leakage [24]. If a pre-trained neural network is used for prediction based on a new dataset, the applied normalization strategy offers two options: (i) normalize with min-and max-values based on the new input data, requiring a search over all values, or (ii) normalize with min-and max-values based on the model derivation. In the present contribution, we use the known values from the model derivation as its computationally less demanding.

3.5. Deep Neural Network Design

We use a DNN with three hidden layers, where the respective number of hidden nodes are 128, 64, and 32. Each hidden layer is followed by a Rectifying Linear Unit (ReLu) as the activation function. Regularization is ensured by adding a dropout layer after each hidden layer. The dropout rate for all is 0.05. Mini-batch training and Adam [25] are combined for optimizing the network. The minibatch size is 2048, equal to the number of CFD cells. The output layer has no (or a linear) activation function, typical for regression tasks [23]. Weights are initialized based on the "he uniform" distribution [26].

4. RESULTS

4.1. Filtering results

Before performing and filtering cohesive simulations, the filtering procedure is validated in the cohesionless setup with literature data from Ozel et al. [16]. Figure 1 shows the filtered Eulerian drag coefficient scaled by the microscopic drag coefficient over the relative drift velocity. This comparison only considers representative data, meaning that only $\overline{\beta_z^{Eul}}$ values higher or equal to zero are accepted. Eqs. (7) and (10) show then that -1 is the lower limit for the $\tilde{v}_{d,z}/\tilde{u}_{sl,z}$. From [16] no data over their the upper limit, defined where $\overline{\beta_z^{Eul}}$ and β_z^{Micro} are equal, is available. Within this range, the filtered data agrees very well with the literature data. One has to note that the literature data origins in 3D simulations, while the shown data is from pseudo-2D simulations.

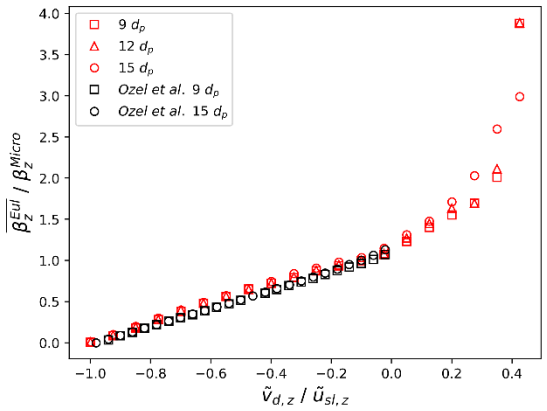

Figure 1. Scaled filtered Eulerian drag coefficient over the scaled drift velocity.

4.2. Prediction of the DNN

Figure 2 depicts an actual random snapshot of a simulation compared to the emulated one based on the DNN prediction. Here the actual target and output value of the DNN is shown (see Eq. (11)). As can be seen, regions of high negative values are qualitatively well predicted, while for positive values the prediction deviates.

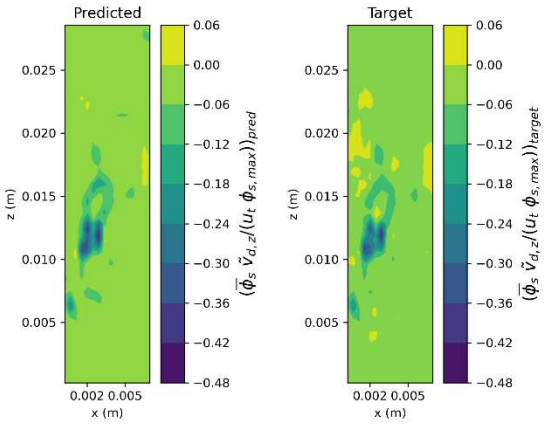

Figure 1. Contour plot of the scaled drift velocity. The left panel: DNN prediction. Right panel: target (ground truth).

For the quantitative perspective, Figure 3 shows a correlation plot for the DNN prediction and the target. The data points shown represent a single test dataset, while the displayed quality measures are from the entire test dataset. As can be seen, the coefficient of determination R^2 is equal to 0.9055, the means squared error is 2.613e-4, and the mean absolute error 8.997e-3.

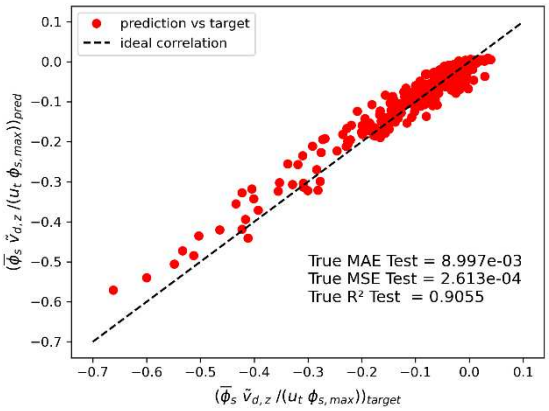

Figure 3. Correlation plot of the DNN prediction and the target for a single random test dataset.

Figure 4 shows the binned statistics of the DNN target over the filtered solid volume fraction. The shown data is based on the highly cohesive coarse-grained simulation with $\alpha = 5$ and $Bo = 90$. All filtered timesteps defined in Section 2.1 are considered. The prediction is depicted here separately for each filter length. As it can be seen, for the two smaller filter lengths the prediction is very accurate in medium to dense regions. In dilute regions, i.e. $\overline{\phi}_s$ smaller 0.1, the predictions of all filter lengths show higher deviations. The higher filter length leads to higher deviations over all solid volume fractions.

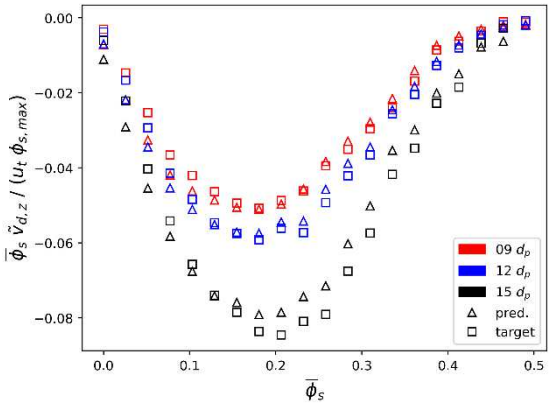

Figure 4. Target and prediction of the DNN binned with respect to the filtered solid volume fraction.

4.3. Drag correction function

After the detailed look on the DNN prediction in Figure 4, the focus here is shifted to the actual drag correction function. Based on the same highly cohesive data, Figure 5 shows the drag correction function over the filtered solid volume fraction. The aspect of Figure 4, that the highest deviations appear in the dilute regions is also found in Figure 5. In dilute regions, up to 0.1 solid volume fraction, a clear underprediction can be detected. Above and up to a filtered solid volume fraction of 0.40 the predictions are very close the target. In dense regions, the forecasts are sometimes very accurate, but also deviate in part. However, the prediction is more accurate than in dilute regions. The influence of the filter length is clearly visible.

In contrast to the direct prediction of the DNN shown in Figure 4 the big filter length does not lead to higher deviations.

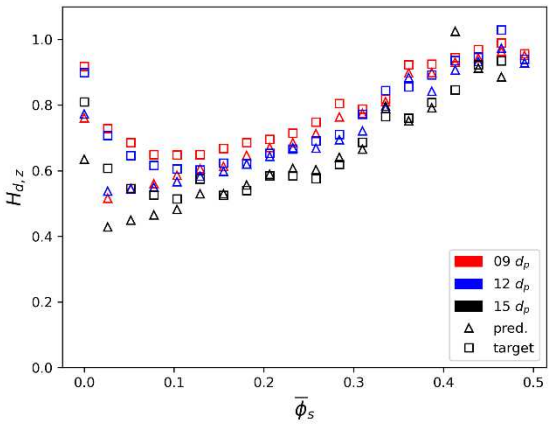

Figure 5. Drag correction function versus filtered solid volume fraction for different filter lengths.

5. SUMMARY

We performed fully-resolved CFD-DEM simulations in a 2D domain as the basis of a machine learning-based closure development for the modeling of cohesive gas-particle flows. These simulations were then filtered with different filter sizes to be able to develop such a drag closure for cohesive systems required for the fTFM approach. In detail, we simulated different systems by changing the cohesion level from cohesionless to highly cohesive, and the size of the systems, via coarse-graining. The filtering routine was successfully validated against literature data.

Then from the markers that are available in a basic fTFM simulation the ones with a high correlation to the defined target value, were selected. It has been shown that scaling the target to a dimensionless quantity is sufficient and that this avoids problems with respect to normalization. Nevertheless, that the input variables were also made dimensionless via scaling, an additional normalization is necessary. With the identified markers we then created, trained, and tested the neural network-based drag correction model.

The overall accuracy of the trained DNN is sufficient in terms of a robust drag correction prediction for a wide range of cohesion levels and system sizes. We additionally showed a detailed analysis of a highly cohesive simulation in a comparably large system. Three different ranges of particle volume fraction in terms of prediction

quality were observed. In dilute regions a clear underprediction was observed. For medium-dense areas, the predictions are very close to the target. In dense regions, the drag correction function varies between very accurate and less accurate. The influence of the filter length is clearly visible.

In our ongoing work the extension to 3D simulations is followed. These fully periodic systems will provide additional insights regarding drag correction. Specifically, investigations towards the anisotropy of the drag coefficient, and the associated corrections, can be expected from our 3D data.

APPENDIX A: COHESION MODELING

The cohesive force in the performed CFD-DEM simulations is the sum of the viscous and capillary force. The viscous force is described after Pitois et al. [27] by:

$$\underline{F_{vis}} = -\frac{3\,\pi}{2}\,\mu_l\,\frac{R}{h_{ij}^*}\,\underline{v_{n,0}}\,X_v^2\,\underline{n_{ij}} \tag{A.1}$$

$$X_v = 1 - \frac{1}{\sqrt{1+\frac{2\,V_b^*}{\pi\,h_{ij}^{*\,2}}}} \tag{A.2}$$

where μ_l is the liquid viscosity, R is the particle radius, $\underline{v_{n,0}}$ the impact velocity, $\underline{n_{ij}}$ the unit normal vector between the colliding particles and V_b^* the dimensionless bridge volume. The dimensionless separation h_{ij}^* is taken to be $h_{ij}^* = \max(h_{\varepsilon,eff}/R\,, h_{ij}^*)$, where $h_{\varepsilon,eff}$ is an effective roughness length of the particle. The capillary force model provided by Mikami et al. [28] is adopted in our present work:

$$\underline{F_{cap}} = \pi\,R\,\gamma\left[\exp\left(\mathrm{A}\,h_{ij}^* + \mathrm{B}\right) + \mathrm{C}\right]\underline{\mathrm{n}_{ij}} \tag{A.3}$$

$$A = -1.1\,(V_b^*)^{-0.53} \tag{A.4}$$

$$B = [-0.34\,\ln(V_b^*) - 0.96]\cdot\theta^2 - 0.019\,\ln(V_b^*) + 0.48 \tag{A.5}$$

$$C = 0.0042\,\ln(V_b^*) + 0.078 \tag{A.6}$$

θ is the contact angle of the liquid bridge. The dimensionless surface-surface separation distance is here defined as $h_{ij}^* = h_{ij}/R$. If particles overlap in a collision, the dimensionless separation distance is set to zero. The capillary number Ca is:

$$Ca = \frac{\mu_l\,u_t}{\sigma} \tag{A.7}$$

APPENDIX B: FILTERED EQUATIONS

For filtered CFD-DEM simulations the mass conservation balances for the gas and solid phase are:

$$\frac{\partial(\rho_g\bar{\phi}_g)}{\partial t} + \nabla\cdot\left(\rho_g\bar{\phi}_g\underline{\tilde{u}_g}\right) = 0 \tag{B.1}$$

$$\frac{\partial(\rho_s\bar{\phi}_s)}{\partial t} + \nabla\cdot\left(\rho_s\bar{\phi}_s\underline{\tilde{u}_s}\right) = 0 \tag{B.2}$$

The momentum conservation balance for the gas and solid phase are then:

$$\begin{aligned}&\frac{\partial(\rho_g\bar{\phi}_g\underline{\tilde{u}_g})}{\partial t} + \nabla\cdot\left(\rho_g\bar{\phi}_g\underline{\tilde{u}_g}\,\underline{\tilde{u}_g}\right)\\ &= -\bar{\phi}_g\nabla\bar{p} - \nabla\cdot(\rho_g\overline{\phi_g\underline{u_g''}\,\underline{u_g''}}) - \nabla\cdot\underline{\underline{\bar{\tau}_g}}\\ &+ \rho_g\bar{\phi}_g\underline{g} - \underline{\widetilde{\Phi}_d} - \overline{\phi_g'\nabla p'}\end{aligned} \tag{B.3}$$

$$\begin{aligned}&\frac{\partial\left(\rho_s\bar{\phi}_s\underline{\tilde{u}_s}\right)}{\partial t} + \nabla\cdot\left(\rho_s\bar{\phi}_s\underline{\tilde{u}_s}\,\underline{\tilde{u}_s}\right)\\ &= -\bar{\phi}_s\nabla\bar{p} - \nabla\bar{p}_s - \nabla\cdot(\rho_s\overline{\phi_s\underline{u_s'}\,\underline{u_s'}})\\ &- \nabla\cdot\underline{\underline{\bar{\tau}_s}} + \rho_s\bar{\phi}_s\underline{g} + \underline{\widetilde{\Phi}_d} - \overline{\phi_s'\nabla p'}\end{aligned} \tag{B.4}$$

Note that a single prime is used for the fluctuation from an algebraic average, e.g. $\underline{u_s'} = \underline{u_s} - \underline{\bar{u}_s}$ and a double prime for the fluctuation from a phase-weighted average, e.g. $\underline{u_g''} = \underline{u_g} - \underline{\tilde{u}_g}$.

APPENDIX C: CFD-DEM SIMULATION PARAMETERS

In Table C.1 all parameters of the performed CFD-DEM simulations, that are not included in Table 1, are summarized.

Table C.1. Simulation parameters

Particle density	2000 [kg/m³]
Gas Density	1.3 [kg/m³]
Gas Viscosity	1.44e-5 [Pa]
Young's modulus	4e6 [Pa]
DEM time step	1e-6 [s]
CFD time step	1e-5 [s]
Coeff. of restitution	0.4
Coeff. of friction	0.9
Coeff. of rolling friction	0.2

APPENDIX D: MARKER DEFINITIONS

The dimensionless filter length Δ_f^* is defined by:

$$\Delta_f^* = \frac{\Delta_f}{d_P\,Fr^{1/3}} \tag{D.1}$$

Where the Froude number Fr is ${u_t}^2/(g\,d_P)$. The scaled gradient of the gas pressure field in z-direction is:

$$\overline{\nabla p_z^*} = \frac{1}{\rho_s\,g}\frac{\partial\bar{p}}{\partial z} \tag{D.2}$$

The Bond number is:

$$Bo = \frac{6\,\sigma}{d_p^2\,g\,\rho_p} \tag{D.3}$$

Where σ is the surface tension. The dimensionless shear rate is:

$$\bar{\dot{\gamma}} = \frac{u_t}{g}\sqrt{2\cdot\underline{\underline{D}}:\underline{\underline{D}}} \tag{D.4}$$

Where $\underline{\underline{D}}$ is the symmetric velocity gradient tensor of the slip velocity. The scaled filtered slip velocity is

the difference between the filtered gas and filtered solid velocity:

$$\frac{\tilde{u}_{sl,z}}{u_t} = \frac{\tilde{u}_{g,z} - \tilde{u}_{s,z}}{u_t} \qquad \text{(D.5)}$$

REFERENCES

[1] F. Raganati, R. Chirone, and P. Ammendola, "Gas-solid fluidization of cohesive powders," *Chem. Eng. Res. Des.*, vol. 133, pp. 347–387, 2018.

[2] J. E. Galvin and S. Benyahia, "The Effect of Cohesive Forces on the Fluidization of Aeratable Powders," *AIChE J.*, vol. 60, no. 2, pp. 473–484, 2014.

[3] K. A. Mehta, G. S. Rekhi, and D. M. Parikh, *Handbook of Pharmaceutical Granulation Technology*. 2016.

[4] B. Cuq *et al.*, "Advances in Food Powder Agglomeration Engineering," vol. 69, J. B. T.-A. in F. and N. R. Henry, Ed. Academic Press, 2013, pp. 41–103.

[5] C. M. Boyce, A. Ozel, J. Kolehmainen, and S. Sundaresan, "Analysis of the Effect of Small Amounts of Liquid on Gas – Solid Fluidization Using CFD-DEM Simulations," vol. 63, no. 12, 2017.

[6] B. Buck, Y. Tang, N. G. Deen, H. Kuipers, and S. Heinrich, "Experimental investigation and force balance modelling of wet particle collisions," in *Particle Interactions 2018-Topical at the 8th World Congress on Particle Technology*, 2018, pp. 151–157.

[7] B. Buck and S. Heinrich, "Collision dynamics of wet particles: Comparison of literature models to new experiments," *Adv. Powder Technol.*, vol. 30, no. 12, pp. 3241–3252, 2019.

[8] M. Askarishahi, M. S. Salehi, and S. Radl, "Capability of the TFM Approach to Predict Fluidization of Cohesive Powders," *Ind. Eng. Chem. Res.*, vol. 61, no. 8, pp. 3186–3205, 2022.

[9] P. Grohn, D. Weis, U. Bröckel, S. Heinrich, and S. Antonyuk, "Contact models and dem simulation of micrometer-sized particles and agglomerates at static loading based on experimental characterization," in *Particles in Contact*, Springer, 2019, pp. 115–163.

[10] S. Radl and S. Sundaresan, "A drag model for filtered Euler–Lagrange simulations of clustered gas–particle suspensions," *Chem. Eng. Sci.*, vol. 117, pp. 416–425, 2014.

[11] M. Girardi, S. Radl, and S. Sundaresan, "Simulating wet gas–solid fluidized beds using coarse-grid CFD-DEM," *Chem. Eng. Sci.*, vol. 144, pp. 224–238, 2016.

[12] Y. Igci and S. Sundaresan, "Constitutive models for filtered two-fluid models of fluidized gas-particle flows," *Ind. Eng. Chem. Res.*, vol. 50, no. 23, pp. 13190–13201, 2011.

[13] M. H. Zhang, K. W. Chu, F. Wei, and A. B. Yu, "A CFD-DEM study of the cluster behavior in riser and downer reactors," *Powder Technol.*, vol. 184, no. 2, pp. 151–165, 2008.

[14] Y. Jiang, J. Kolehmainen, Y. Gu, Y. G. Kevrekidis, A. Ozel, and S. Sundaresan, "Neural-network-based filtered drag model for gas-particle flows," *Powder Technol.*, vol. 346, no. December, pp. 403–413, 2019.

[15] Y. Jiang, X. Chen, J. Kolehmainen, I. G. Kevrekidis, A. Ozel, and S. Sundaresan, "Development of data-driven filtered drag model for industrial-scale fluidized beds," *Chem. Eng. Sci.*, vol. 230, p. 116235, 2021.

[16] A. Ozel, Y. Gu, C. C. Milioli, J. Kolehmainen, and S. Sundaresan, "Towards filtered drag force model for non-cohesive and cohesive particle-gas flows," *Phys. Fluids*, vol. 29, no. 10, 2017.

[17] H. G. Weller, G. Tabor, H. Jasak, and C. Fureby, "A tensorial approach to computational continuum mechanics using object-oriented techniques," *Comput. Phys.*, vol. 12, no. 6, p. 620, 1998.

[18] C. Kloss, C. Goniva, A. Hager, S. Amberger, and S. Pirker, "Models, algorithms and validation for opensource DEM and CFD-DEM," *Prog. Comput. Fluid Dyn. An Int. J.*, vol. 12, no. 2/3, p. 140, 2012.

[19] J. Tausendschön, J. Kolehmainen, S. Sundaresan, and S. Radl, "Coarse graining Euler-Lagrange simulations of cohesive particle fluidization," *Powder Technol.*, vol. 364, pp. 167–182, 2020.

[20] M. Wu, J. G. Khinast, and S. Radl, "The Effect of Liquid Bridge Model Details on the Dynamics of Wet Fluidized Beds," *Am. Inst. Chem. Eng. J.*, vol. 62, no. 6, pp. 1877–1897, 2016.

[21] F. Municchi, C. Goniva, and S. Radl, "Highly efficient spatial data filtering in parallel using the opensource library CPPPO," *Comput. Phys. Commun.*, vol. 207, no. June, pp. 400–414, 2016.

[22] R. Beetstra, M. A. van der Hoef, and J. A. M. Kuipers, "Drag Force of Intermediate Reynolds Number Flow Past Mono- and

Bidisperse Arrays of Spheres," *AIChE J*, vol. 53, no. 2, pp. 489–501, 2007.

[23] J. Heaton, *Artficial Intelligence For Humans, Volume 3: Deep Learning and Neural Networks*. Heaton Research, Inc., 2015.

[24] S. Kaufman, S. Rosset, and C. Perlich, "Leakage in data mining: Formulation, detection, and avoidance," *Proc. ACM SIGKDD Int. Conf. Knowl. Discov. Data Min.*, pp. 556–563, 2011.

[25] D. P. Kingma and J. L. Ba, "Adam: A method for stochastic optimization," *3rd Int. Conf. Learn. Represent. ICLR 2015 - Conf. Track Proc.*, pp. 1–15, 2015.

[26] K. He, X. Zhang, S. Ren, and J. Sun, "Delving deep into rectifiers: Surpassing human-level performance on imagenet classification," *Proc. IEEE Int. Conf. Comput. Vis.*, vol. 2015 Inter, pp. 1026–1034, 2015.

[27] O. Pitois, P. Moucheront, and X. Chateau, "Liquid bridge between two moving spheres: An experimental study of viscosity effects," *J. Colloid Interface Sci.*, vol. 231, no. 1, pp. 26–31, 2000.

[28] T. Mikami, H. Kamiya, and M. Horio, "Numerical simulation of cohesive powder behavior in a fluidized bed," *Chem. Eng. Sci.*, vol. 53, no. 10, pp. 1927–1940, 1998.

Conference on Modelling Fluid Flow (CMFF'22)
The 18th International Conference on Fluid Flow Technologies
Budapest, Hungary, August 30 -September 2, 2022

LOCAL FLOW RESOLUTION WITH THE BLOCKED-OFF METHOD IN DEM-CFD: GASEOUS FUEL JET DISPERSION AND COMBUSTION IN A PARTICLE ASSEMBLY

Enric ILLANA[1,2], Max BRÖMMER[2], Siegmar WIRTZ[2] and Viktor SCHERER[2]

[1] Corresponding Author. Tel.: +49 234 / 32-25340. E-mail: illana@leat.rub.de
[2] Institute of Energy Plant Technology, Ruhr-University Bochum, Universitätsstraße 150, 44780 Bochum, Germany

ABSTRACT

DEM-CFD simulation of reacting flows inside large-scale granular assemblies remains a challenging task. Resolving the flow field within the voids is required to obtain correct conversion rates but due to the computational resources required, this high resolution cannot be employed on the device-scale. In the current work, a combined approach is employed: the so-called blocked-off method is used to resolve the voids between particles within a prescribed refinement region, while the volume-averaged method is applied to the rest of the domain because of its low computational effort. This approach is firstly tested in a case where nitrogen is injected into an air cross-flow. A good agreement with oxygen concentration measurements is obtained when applying the blocked-off method to the whole domain and locally, whereas the volume-averaged method under-predicts the local oxygen concentration since jet dispersion is too low. The latter is also observed in a second case where methane is injected in cross-flow into an air stream with subsequent reaction of the methane. As a result, the locally resolved approach predicts significantly larger reaction rates associated with higher maximum temperatures as well a larger spread of the area with high temperatures than the volume-averaged method.

Keywords: Dispersion, Bulk, Blocked-Off, AVM, DEM-CFD

NOMENCLATURE

A	$[m^2]$	area
d	$[m]$	characteristic face size
Nu	[-]	Nusselt number
Pr	[-]	Prandtl number
Re	[-]	Reynolds number
S	[-]	source term
T	$[K]$	temperature
U	$[m/s]$	velocity
Y	[-]	mass fraction
$\dot{Q}$	$[J/s]$	rate of heat transferred
h	$[W/(m^2\ K)]$	heat transfer coefficient
k_r	$[10^{16}\ /s]$	reaction rate
$\dot{m}$	$[mg/s]$	mass flow
p	$[Pa]$	pressure
w	[-]	weighting factor
ϕ	[-]	solution variable
κ	$[W/(m\ K)]$	thermal conductivity
H	$[m]$	height
W	$[m]$	width
L	$[m]$	length
n	[-]	number of CVs

Subscripts and Superscripts

CV	control volume
N	neighbour
face	triangle of the polyhedron surface
fluid	interpolated from the fluid phase
air	at the air inlet boundary
CH4	at the methane inlet boundary
part	related to the particles
L	lance
B	bottom
AVM	averaged-volume method
BO	blocked-off method

1. INTRODUCTION

A gaseous fluid passing the bulk as a heating or cooling agent or as a system-specific reactant adds a second phase to the system. Its general flow direction may be counter-, parallel- or cross-flow with respect to the solid movement, depending on the system and the product properties pursued. Large forces accompanying the movement of the bulk, high temperatures and a generally poor accessibility from outside of the reactor render the measurement of temperature or concentration profiles within those technical systems nearly impossible. Thus, detailed investigation of the

processes within the bulk and in vicinity of the fluid injection must resort to numerical simulations of the tightly coupled two-phase problem. In principle, coupled DEM-CFD simulations provide the framework for a comprehensive numerical description of the transport and reaction processes. For a more detailed overview on the status on DEM-CFD simulations of reactive particle systems, we refer to [1-4].

Considering the large number of actual particles in many industrial reactors, the numerical description is typically constrained to the so-called unresolved methods, where the bulk particles are represented as a porosity field within the volume-averaged Navier-Stokes equations of the fluid phase (acronym AVM for Averaged Volume Method [1]). Although this approach is applicable to industrial-scale shaft kilns [5], it lacks a detailed description of the flow field within the voids between the particles, thus cannot directly determine effects related to the unresolved scales.

To be specific, in lime shaft kilns the gaseous fuel enters through nozzles at the tip of lances extending into the descending bulk material and releases heat and combustion products in vicinity of the nozzle outlet where the moving lime particles partially block the passage. Discretizing the voids and their temporal development locally in front of the nozzles can solve this issue but must be embedded in a larger, device-spanning AVM solution to capture air preheating and stone cooling in a reasonable fashion. As a consequence, a combined method exploiting both, resolved voids in vicinity of the inlets and the cost-effective AVM in the remaining domain is pursued.

2. PRIMARY OBJECTIVES AND MODEL DESCRIPTION

The long-term scientific objective of the current work is the numerical description of a configuration, where a secondary combustive gas stream is injected orthogonally into a confined flow, only that the flow domain is additionally obstructed by a moving, heat-exchanging and reacting solid bulk. Mixing of the injected fuel flow with the preheated cooling air occurs within the void space between the particles. In comparison to an unconstrained conventional cross-flow situation, length scales of mixing are severely limited and local residence times are short, both requiring much higher local resolution than on the overall device scale.

As a first step towards this goal, AVM-based momentum, heat and mass transfer, tightly coupled with a locally void-resolving method are employed with OpenFOAM (fireFoam, v2012) and an in-house DEM code in order to evaluate the feasibility of the blocked-off method (BO) for this purpose.

2.1. DEM and particle flow

Assuming spherical particles with constant properties instead of employing the actual shape of the limestone objects allows to simplify the geometric complexity of the current study. In case of spheres, a conventional linear spring-dashpot model, which connects a virtual overlap of the spheres with a repulsion force, is employed as the contact force model in the current Discrete Element (DEM) code.

The code used in this study is an ongoing development within the collaborative research centre Bulk-Reaction, which is funded by the German Research foundation [6]. In this code, position vectors (centres of gravity) and quaternions (orientations) are the solid's transport variables while detailed information (if required) on the highly resolved particle shape (triangulated surface) is stored separately in so-called prototypes. This hierarchical structure, besides other advantages, avoids the continuous position update of all corner-points of the objects and restricts it to the required points. At the same time this allows a fast identification of the CVs to be blocked such that the remaining CVs correctly represent a discretisation of the voids between the particles.

2.2. AVM for device-spanning transport

The AVM considers any particle in the flow domain, respectively the discrete elements as their conceptual representations, as a Lagrangian object interacting with one or several CVs. In the current implementation, each element determines the dependence of its properties and source terms on averaged fluid properties ϕ from the closest CVs as

$$\phi_{elem} = \sum w_{CV} \phi_{CV} \quad (1)$$

$$\sum w_{CV} = 1 \quad (2)$$

with volume-related weights depending on a Gaussian kernel function. The source terms determined for the particles must be distributed in the same way to the respective CVs. A similar smoothing method is described in [7], where the volume of a particle is distributed outwards from the cell containing the particle's centre of gravity so that the porosity value of all cells is above a threshold. These processes of weighting, averaging and spatial smoothing are particularly important as they determine energy and mass conservation as well as the required computational effort. If the particles are distinctively smaller than the CVs, the mapping between the particle sources and the CVs is unambiguous, while the assignment of fluid properties to spatial positions within the CV still requires spatial interpolation, since linear profiles of state variables within the CVs are a core assumption of finite volume methods. Therefore, AVM is best suited for CVs larger or of comparable size than the

particles and where a low flow resolution is sufficient since flow gradients are small. The computational effort of this method is low because of the little amount of particle-CV interactions.

2.3. Blocked-off method for locally resolved void space

In vicinity of the inlets, the local mesh resolution must be high enough to sufficiently resolve the voids between particles. A straightforward choice would be a tetrahedral body-conformal discretisation resolving the space available for the fluid as employed by [8] to investigate the effect of different approximations of the particle contact representation in a static assembly of spheres. If moving particles have to be considered, where the voids deform and thus change volume and shape over time, a continuous re-meshing and value interpolation would be required which is tedious and time consuming. A simpler, and especially with respect to computational efficiency cheaper method, is the BO method, initially proposed by Patankar [9]. It enforces artificial boundary conditions within a static mesh and appropriately blocks the control volumes (CVs) partially or fully obstructed by the boundaries of steady or moving objects. The respective CVs are dynamically identified and excluded from the solution by linearizing the source terms in the discretised transport equations of a CFD solver.

In finite volume methods, this requires the solution of a system of equations resulting from the balance of fluxes across the surfaces of control volumes. These balances lead to discretized transport equations for a solution variable ϕ which, in their generic form, are:

$$a_c \phi_c + \sum_{N_{c,c}} a_N \phi_N = S_\phi \tag{3}$$

where *N* refers to the control volumes adjacent to the CVs while a_c and a_N are matrix coefficients containing the information related to the mesh and discretisation scheme. S_ϕ, the source term, combines all terms resulting from the temporal change of ϕ. Non-linear terms on the left hand side of Eq. (3) as well as the boundary values are moved to the right hand side of the equation, but are not shown here for brevity. For stability reasons, the general source term S_ϕ is implemented in a linearized form:

$$S_\phi = S_c - S_p \phi \tag{4}$$

This allows to move the product $S_p \phi$ to the left hand side of Eq. (3), where it enters the matrix on the diagonal, thus increasing diagonal dominance.

$$(a_c + S_p)\, \phi_c + \sum_{N_{c,c}} a_N \phi_N = S_c \tag{5}$$

The field values S_c and S_p exist for every CV and are readily accessible outside the underlying solution procedure. Therefore, they can be employed to prescribe the value of a solution variable ϕ in any control volume of a given mesh without changes to the matrix itself or the associated coefficients. Thus, they provide an efficient interface to reflect boundaries of moving discrete objects within the domain.

At the position of any object larger than the local mesh size (for simplicity a homogenous Cartesian mesh is employed here), its presence within the flow domain can be represented by a cluster of core-CVs and surface-CVs. The solution variable ϕ is forced to the value of S_c by setting S_p to a large number (e.g. 1e20). For fluid flows, as momentum is undefined in the core-CVs, $S_c = 0$ essentially blocks momentum transport, while the pressure based continuity equation automatically enforces mass conservation in the remaining CVs which form the voids. Further details on the implementation of this approach are given in [10] and explained for radiative heat transfer in [11].

2.4. Heat transfer model

In any reacting system, the heat transfer is essential as it often controls the reaction processes via temperature. Considered here are the heat released in the gas phase due to fuel combustion, convective enthalpy transport within the gas phase, convective transport within the solid phase and the mutual enthalpy exchange between the two phases. To keep things simple in this first conceptual test, outer boundaries (except inflow and outflow) are considered adiabatic and heating of the particles is suppressed by a constant particle temperature of 850 °C, corresponding to the calcination temperature of lime. Thus, the plausible assumption is that all heat transferred to the particles is consumed for calcination. Note that radiative heat transfer among particles has been neglected in this preliminary study. Considering non-moving particles corresponds to the situation of solid residence times being much larger than the gas residence time. This is a reasonable simplification which is valid for many shaft kiln applications.

Convective heat exchange between particles and the surrounding fluid flow is calculated on the DEM side by applying the Newton's law of cooling to the total surface of the particle:

$$\dot{Q}_{face} = A_{face}\, h\, (T_{fluid} - T_{face}) \tag{6}$$

where h is the heat transfer coefficient. As the sphere's surface is represented by a triangulated immersed mesh, it is computed locally from the

Nusselt number correlation for flat plates under laminar conditions:

$$Nu = \frac{h\,d}{\kappa_{fluid}} = 0.664\,\sqrt{Re_{face}}\sqrt[3]{Pr_{face}} \qquad (7)$$

The characteristic length L of the transfer is computed from the face area. In the case that a particle is outside the blocked-off region, h and T_{fluid} are equal for all the faces. The overall heat transferred is equally distributed as an energy source to the CVs that are in contact with the particle. If the particle is however inside the BO region, the $\dot{Q}_{face}$ is distributed to the closest CVs that are not blocked.

2.5. Combustion model

A laminar combustion regime is assumed in this work. The following single-step irreversible reaction is considered for modelling the chemical process:

$$CH_4 + 2\,O_2 \rightarrow CO_2 + 2\,H_2O \qquad (8)$$

All species mass fractions are transported except Y_{N2}, which is calculated so that the sum of all mass fractions equals unity. The reaction rate k_r is defined by [12]:

$$k_r = 5.2\,e^{-\frac{14906}{T}} \qquad (9)$$

The fluid thermophysical and transport properties are calculated from the resulting composition and temperature fields.

3. INVESTIGATED TEST CASES

Two different test cases have been considered in the current feasibility study. The first one is based on an experimental study from literature, investigating the injection of a nitrogen flow through a lance into a static regular simple cubic (sc) packing of spheres vertically passed by air [8] and the resulting mixing profiles. The second test case comprises the injection of fuel into a similar generic section of a lime shaft kiln, where it mixes and reacts with the air passing through the assembly. Strictly laminar flow is assumed and the particles are considered non-moving for simplicity.

3.1. Verifying mixing in isothermal cross-flow

The experimental setup has been taken from literature [8] and it is sketched in Figure 1. Particle diameter is 52 mm and the immersion depth of the lance into the bed is 156 mm. The experiments were performed by introducing nitrogen through the lance into the vertically passing laminar air flow. The concentration of oxygen in the passing airflow is obtained as a measure of the mixing. Further details on flow parameters and experimental conditions can be found in the original paper [8].

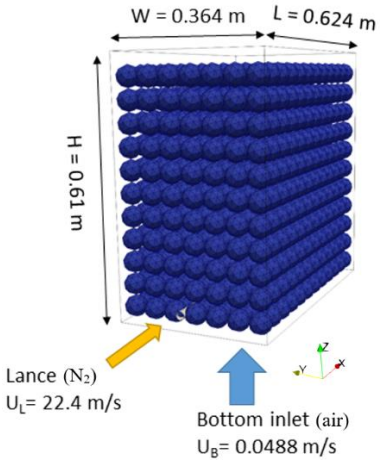

Figure 1. Arrangement of spheres (sc) and location of the lance.

When simulating this arrangement, a major disadvantage of conventional body-conforming tetrahedral meshes resolving the voids space in the whole domain would be the large number of small control volumes required and the challenge to generate a mesh with good properties for an arbitrary arrangement of spheres. Additionally, an adaption to the large difference in length scales (wide inflow with small velocities at the bottom versus comparably high velocity at the tip of the lance) requires considerable effort in this approach.

As an alternative, a structured Cartesian mesh with three different cell size levels, as sketched in the middle of Figure 2, is employed in the current work. The AVM method is applied to the red zone of the domain where the spheres have a similar size as the CVs, while BO is used within the turquoise refinement area and allows to better resolve the flow in vicinity of the lance tip. Furthermore, one pure AVM simulation as well as a fully resolved BO simulation were conducted.

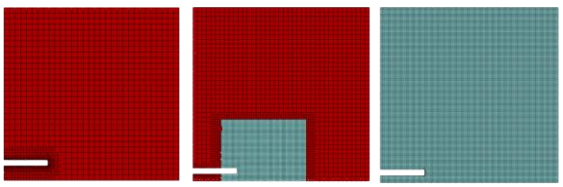

Figure 2. Vertical cut through the mesh at the position of the injection lance for pure AVM (left), locally refined AVM/BO (middle) and fully refined BO approach (right). For the AVM/BO approach, particles are resolved at the region with the lowest cell size level.

The associated meshes are depicted in Figure 2 and the respective numbers of CVs are $n_{AVM} = 29{,}466$ cells, $n_{AVM/BO} = 250{,}688$ cells and $n_{\mathrm{BO}} = 2{,}175{,}408$ cells. Taking computational time with the AVM as the reference, the AVM/BO approach requires 8 times more and the fully refined case 48 times more for the same simulated time.

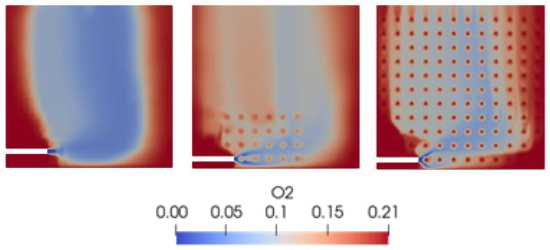

Figure 3. Oxygen mass fraction at the vertical cut for AVM (left), BO (right) and combined AVM-BO methods (middle)

The oxygen mass fraction distribution at the same vertical cut is plotted in Figure 3 for the three approaches considered. In general, the AVM simulation shows a higher oxygen mass fraction in comparison to the two other configurations, indicating that the mixing in crosswise direction of the lance is under-predicted.

Note that since a uniform air composition has been imposed at the start time, and equal to the cross-flow composition, the blocked cells keep in this case an oxygen mass fraction of 0.21. Thus, small dots (representing a part of the particles) are visible within the resolved regions.

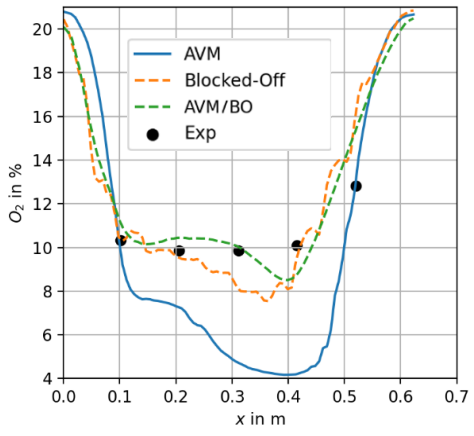

Figure 4. Oxygen mass fraction profiles at a line located 0.468 *m* above the lance

In Figure 4, the mass fraction profiles of oxygen obtained from the different approaches at a height of 0.468 m above the lance axis, i.e. a line along the x direction in the vertical cut, are compared with the measurements from [8]. It can be observed that the use of the AVM method results in low O_2 concentrations due to the reduced mixing of the nitrogen flow with the vertical airflow, while the BO approach is able to reproduce the oxygen concentration level obtained in the measurements. A similar agreement, exhibiting an even higher resolved structure, is observed if the whole domain has the same resolution as the region near the injection. The combined AVM/BO approach in particular, delivers a reasonably smooth and comparable solution for a lower computational cost.

3.2. Combustion of methane injected into a generic shaft kiln section

The previous example has confirmed that the combined AVM/BO approach is able to capture the mixing of a flow introduced through a lance into a crossflow passing through a bulk. The aim of this test case is to determine the influence of the mixing resolution on the combustion process, in terms of flame location and temperature distribution, as occurring in the heating section of lime shaft kilns.

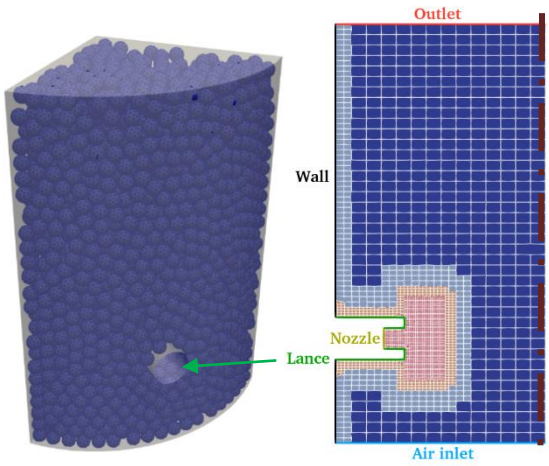

Figure 5. Vertical cut of the mesh at the lance position (left) and particle distribution (right) of the generic lime shaft.

Figure 5 sketches the simulated geometry, which shows the particle assembly as well as a cut of the CFD mesh at the injector, and the relevant dimensions are included in Table 1.

Table 1. Geometric measures of the generic shaft in meters

Radius	1
Height	2
Nozzle diameter	0.1
Lance diameter	0.2
Lance immersion length	0.3
Largest cell size	0.05
Particle diameter	0.08

Table 2. Boundary conditions imposed for both the AVM and locally resolved methods

p_{outlet}	101325
$\dot{m}_{CH4}$	0.028
$\dot{m}_{air}$	0.46
T_{CH4}	300
T_{air}	300
T_{part}	850

For this test case, in order to have a clear comparison between the methods when a reacting flow is computed, the same mesh is used. To do so, since the cells are significantly smaller than the particle size, a uniform porosity level of 0.4 is applied in the regions where AVM is applied. For the simulation with the combined AVM/BO approach, particles are resolved when they lie within the second refinement level (i.e. orange and red cells in Fig. 5, where the cell size is 0.0125 or lower) and a porosity value of 1 is set. The conditions imposed at the boundaries and to the particles can be found in Table 2. The imposed mass flows lead to a cross flow velocity of 0.5 m/s and a jet velocity of 5.5 m/s. The overall equivalence ratio is 1.05.

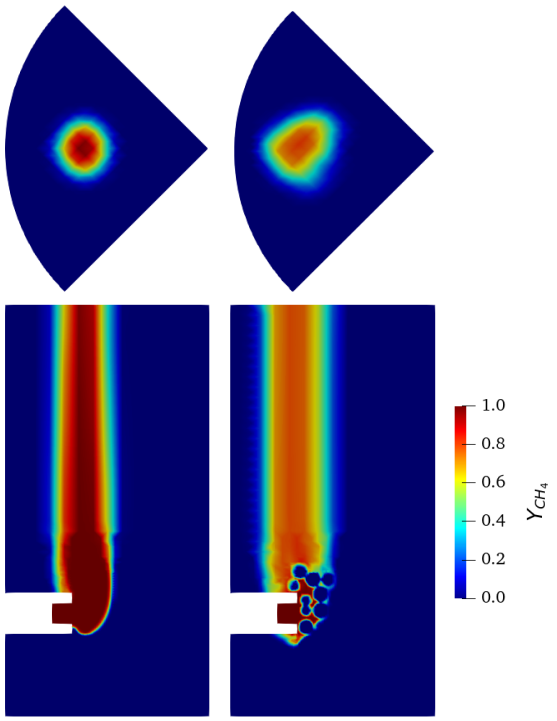

Figure 6. Y_{CH4} distribution at the outlet (top) and middle plane (bottom), AVM (left) and locally resolved (right) AVM/BO method.

The comparison of the methane distribution is performed in Figure 6. It clearly shows that, as stated in the previous test case, the AVM solution presents a reduced amount of mixing and dispersion when compared to the AVM/BO solution. Additionally, since local combustion regime is in this case diffusion-dominated, due to the locally rich conditions at the reaction zone, the amount of burned CH_4 is also highly influenced by the flow mixing. Simulation results indicates that with the AVM only 4.24% of the injected fuel is actually converted to CO_2, while the 10.88% of methane has reacted when using the local refinement by AVM/BO. The latter has in turn a large impact on the temperature field, displayed in Figure 7, where the maximum temperature as well as the area with high temperatures are larger with the combined AVM/BO method. The spatial average at the outlet boundary results in a mean exit temperature of 384.8 K for the AVM and 534.6 K for the locally resolved AVM/BO method.

Regarding the flame shape, a smaller flame surface and thinner flame brush are obtained with the AVM. The stabilization point also differs between both simulations since with the AVM/BO approach it is located below the lance, further upstream of the cross flow.

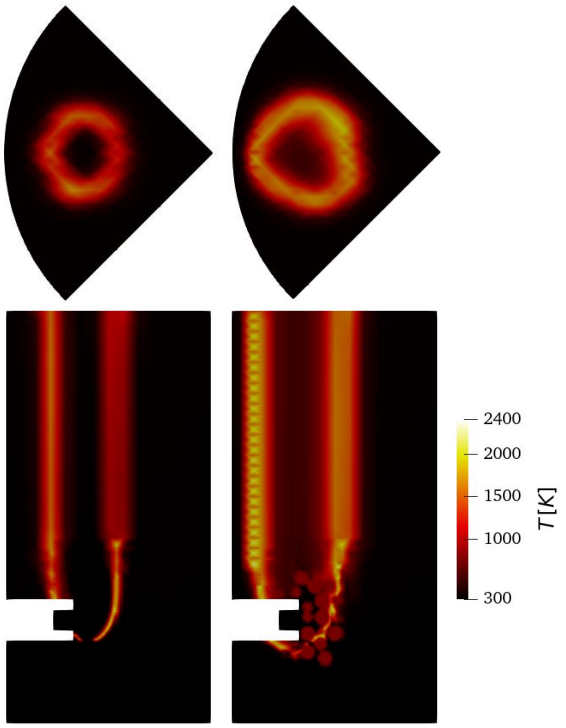

Figure 7. Temperature distribution with the AVM (left) and locally resolved AVM/BO (right) method at the outlet (top) and middle plane (bottom).

4. SUMMARY

The Averaged Volume Method (AVM) is widely used in DEM-CFD approaches to simulate large-scale systems, due to the low computational effort required. It is however limited to meshes with large cell sizes, larger

than the particle size, which does not allow for local flow resolution in the voids among particles. A reduced jet dispersion is a consequence. To properly capture the mixing and reaction processes of gaseous flows and, hence, the associated particle reaction in a particle assembly it is crucial to resolve the voids between particles in critical areas, i.e. in areas with high gradients. For such configurations, the combination of the AVM with the blocked-off (BO) approach presented in this work has shown good agreement with oxygen concentrations measured experimentally in a jet (nitrogen)-crossflow (air) arrangement for a packed bed with spherical particles. The importance of the local flow resolution using the AVM/BO approach is stressed in a reacting flow simulation of a similar jet (methane)-crossflow (air) arrangement: the amount of methane burnt is doubled in the combined AVM/BO solution and thus the averaged exit temperature is around 150 degrees higher.

Although the computing time for the AVM/BO approach is higher (for the current case 8 times) such investment in computing time might be needed to reliably predict lime quality as the quality (reactivity) of the lime depends on material temperature (and residence time).

Note that the method presented can also be applied to turbulent conditions and with moving particles of irregular shape.

ACKNOWLEDGEMENTS

This work has been funded by the Deutsche Forschungsgemeinschaft (DFG, German Research Foundation) – Project-ID 422037413 – TRR 287.

Gefördert durch die Deutsche Forschungsgemeinschaft (DFG) – Projektnummer 422037413 – TRR 287.

REFERENCES

[1] Golshan, S., Sotudeh-Gharebagh, R., Zarghami, R., Mostoufi, N., Blais, B., and Kuipers, J., 2020, "Review and implementation of CFD-DEM applied to chemical process systems", *Chemical Engineering Science*, 221, 115646.

[2] V. Scherer, S. Wirtz, B. Krause, and F. Wissing, 2017, "Simulation of reacting moving granular material in furnaces and boilers an overview on the capabilities of the discrete element method," *Energy Procedia*, 120, 41–61.

[3] B. Peters *et al.*, 2019, "XDEM multi-physics and multi-scale simulation technology: Review of DEM–CFD coupling, methodology and engineering applications," *Particuology*, 44, 176–193.

[4] Z. Peng, E. Doroodchi, and B. Moghtaderi, 2020, "Heat transfer modelling in Discrete Element Method (DEM)-based simulation of thermal processes: Theory and model development," *Prog. Energy Combust. Sci.*, 79, 100847.

[5] Krause, B., Liedmann, B., Wiese, J., Bucher, P., Wirtz, S., Piringer, H., and Scherer, V., 2017, "3D-DEM-CFD simulation of heat and mass transfer, gas combustion and calcination in an intermittent operating lime shaft kiln", *International Journal of Thermal Sciences*, 117, 121-135.

[6] "Bulk Reaction", https://bulk-reaction.de (accessed Jan. 05, 2022).

[7] Spijker, C., Pollhammer, W. R., and Raupenstrauch, H., 2020, "Coupled Computational Fluid Dynamics and Discrete Element Method modelling of shaft furnace, including nitrogen emissions", *12th European Conference on Industrial Furnaces and Boilers*, Portugal.

[8] Alkhalaf, A., Refaey, H. A., Al-durobi, N., and Specht, E., 2018, "Influence of contact point treatment on the cross flow mixing in a simple cubic packed bed: CFD simulation and experimental validation", *Granular Matter*, 20, 22.

[9] Patankar, S., 1980, "Numerical heat transfer and fluid flow", *CRC Press*.

[10] Buss, F., Wirtz, S., and Scherer, V., 2020, "Simulation of a reacting agitated bed of straw pellets by a resolved coupled DEM/CFD method using a blocked-off approach", *International Journal of Thermal Sciences*, 152, 106332.

[11] Jaeger, B., Schlag, M., Scherer, V., Wirtz, S., and Schiemann, M., 2021, "Radiative heat transfer with a blocked-off approach for application in the discrete element method", *Powder Technology*, 392, 558-569.

[12] reactingFoam tutorial, www.openfoam.com (accessed Mar. 10, 2022).

Conference on Modelling Fluid Flow (CMFF'22)
The 18th International Conference on Fluid Flow Technologies
Budapest, Hungary, August 30-September 2, 2022

MULTIMODAL HEMODYNAMIC EVALUATION OF VESSEL WALL ENHANCED CEREBRAL DRAINING VEINS FOR THE ASSESSMENT OF ARTERIOVENOUS MALFORMATIONS

Janneck Stahl[1], Sylvia Saalfeld[2], Laura Stone McGuire[3], Denise Brunozzi[3], Ali Alaraj[3], David Hasan[4], Philipp Berg[1]

[1] Corresponding Author. Department of Fluid Dynamics and Technical Flows, Research Campus *STIMULATE*, University of Magdeburg, Universitätsplatz 2, 39106 Magdeburg, Germany. E-mail: janneck.stahl@ovgu.de
[2] Department of Simulation and Graphics, Research Campus *STIMULATE*, University of Magdeburg, Germany. E-mail: sylvia.saalfeld@ovgu.de
[3] Department of Neurosurgery, University of Illinois, Chicago, USA. E-mail: alaraj@uic.edu
[4] Duke Neurological Disorders Clinic, Durham, NC, USA. E-mail: david.hasan@duke.edu

ABSTRACT

Cerebral arteriovenous malformations (AVMs) are a neurovascular disease where the arteries directly connecting to the veins via a nodular nidus. This study investigates the relationship between wall enhancement, referring to a local increase of the intensity in vessel wall magnetic resonance imaging (VW-MRI), and hemodynamics along AVM draining veins. Image-based blood flow simulations using computational fluid dynamics (CFD) were conducted based on 3D models of the venous domain for eight AVM cases. The areas of the vessel wall enhancement were manually extracted from VW-MRI data, co-registered and mapped onto the luminal surface models. Hemodynamic results of draining veins containing enhancement are compared with non-enhanced draining veins of the AVM cases. Global comparison of shear-related draining vein hemodynamics reveals a mean decrease of time-averaged wall shear stress and oscillatory shear index, while the relative residence time demonstrates an increase in draining veins harboring vessel wall enhancement. Furthermore, the enhanced walls are assessed locally in terms of shear-related hemodynamic parameters and related to the non-enhancing area of the corresponding draining veins. In conclusion, this initial multimodal investigation of hemodynamics in AVM draining veins allows for precise prediction of occurring shear-related phenomena, especially in areas of vessel wall enhancement and improves the understanding of this complex neurovascular pathology.

Keywords: arteriovenous malformations, cerebral blood flow, CFD, hemodynamics, wall enhancement

NOMENCLATURE

$AWSS$	$[Pa]$	time-averaged wall shear stress
OSI	$[-]$	oscillatory shear index
RRT	$[1/Pa]$	relative residence time

1. INTRODUCTION

Cerebral arteriovenous malformations (AVMs) contain a complex vasculature. Instead of a capillary bed, a tangle-like nidus occurs locally, directly connecting the arterial and venous vascular system. The challenging neurovascular disease shows a prevalence of 18 per 100,000 and is responsible for 2% of all hemorrhagic strokes [1, 2]. Due to the lack of microcirculation structures between the vascular systems, hemodynamic stressors such as steep pressure gradients and increased flow might alter brain vasculature. Additionally, these undesired physiological conditions might cause a further weakening of the vessel walls resulting in hemorrhage, which can be found in 50% of cerebral AVMs [3].
While most research studies only assess the morphology and hemodynamics of AVM arteries and the nidus, knowledge with respect to the hemodynamics for the venous areas is limited [4, 5, 6]. Already existing studies have simulated blood flow in cerebral veins and investigated various hemodynamic aspects, however, they are not related to existing pathologies such as AVMs [7, 8]. Therefore, this study particularly focusses on the AVM draining veins.
Due to improvements in medical imaging the complex morphologies of AVMs could be diagnosed more precisely. These include vessel wall magnetic resonance imaging (VW-MRI), which can provide indications of histologic changes in the vessel wall by enhanced intensity values in these areas, which

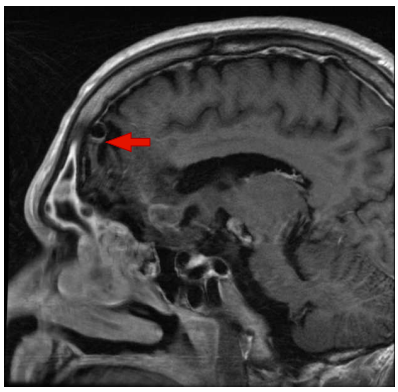

Figure 1. VW-MRI from saggital view of an AVM draining vein. The red arrow indicates signal enhancement in the vessel wall.

is called wall enhancement (see Figure 1). Furthermore, studies have shown that wall enhancement could be assumed as a possible biomarker for vessel wall inflammation [9, 10, 11].
The present study aims to investigate blood flow along the vessel wall of signal-enhanced AVM draining veins by multimodal hemodynamic modeling. Through an interdisciplinary approach, initial observations of various hemodynamic parameter changes in these areas are carried out. The simulation results based on computational fluid dynamics (CFD) will then be correlated with the enhanced local vascular areas.

2. MATERIAL AND METHODS

2.1. Image Data

Eight AVM patients are included in the study. Of the total 15 identified draining veins, seven draining veins (46.7 %) show a local vessel wall signal enhancement in the VW-MRI data. Multimodal medical image data are provided for all patients. First, 3D rotational angiography (3DRA) image data are available, which have a high spatial resolution of the arterial area as well as the nidus. The focus is especially on the draining veins, exiting from the nidus and merging into the deep veins. For this reason, magnetic resonance venography (MRV) data, which particularly resolves the venous vascular area, is used for the morphological studies. In addition to imaging data depicting patient-specific vascular anatomy, intravascular flow measurements based on 2D phase contrast magnetic resonance imaging (2D PC MRI) are available. Flow quantifications perpendicular to the corresponding vessel axis were acquired using non-invasive optimal vessel analysis (NOVA) software (VasSol Inc, River Forest, IL) [12]. These flow rates can be used for realistic boundary conditions of the hemodynamic simulations.

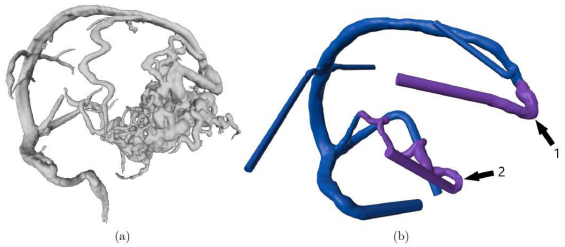

Figure 2. Segmented 3D models of vascular anatomy of an exemplary case: (a) Initial segmentation from the MRV data including nidus. (b) Processed model without nidus with the two draining veins colored in purple and labeled.

2.2. Multimodal Image Segmentation and 3D Model Extraction

The image segmentation and surface mesh generation was carried out using MeVisLab 3.4.1 (MeVis Medical Solutions AG, Bremen, Germany). As the focus of this study is on the venous region and in particular on the draining veins of the AVM, the segmentations of the vascular structures are primarily realized based on the MRV data. By using threshold-based segmentation before converting the segmentation masks into triangulated surface meshes, initial 3D models are provided (see Figure 2).
To perform a successful hemodynamic simulation, the surface mesh should be as free of artefacts as possible. For this reason, manual corrections on the initial segmentations are necessary, which are performed with the 3D modeling software Blender 2.9 (Blender Foundations, Amsterdam, Netherlands). Initially, the nidus are removed using boolean cuts, since this is not the focus of the study, but rather the veins that drain out of it. Fused vessel areas are separated and artifacts appearing on the surface mesh are removed. Since edged vessel areas are created during these post-processing steps local laplaician smoothing is conducted to maintain a realistic vessel shape in these regions. Furthermore, the vascular 3D models are prepared for the subsequent hemodynamic simulations by cutting and extruding the in- and outlet cross-sections perpendicular to the vessel axis (see Fig. 2).

2.3. Segmentation and Co-Registration of the Wall Enhancement

To identify the enhanced areas VW-MRI images from coronal, axial and sagittal planes were marked by an experienced neurosurgeon. Based on the markers, these areas are manually extracted in MeVisLab using the CSO (Contour Segmentation Object) library before converting them into 3D models. In order to visualize the enhanced areas on the vascular surface of the previously segmented venous models, co-registration is required, since VW-MRI and MRV data are not located in the same coordinate system. The registration is performed using a rigid body 3D

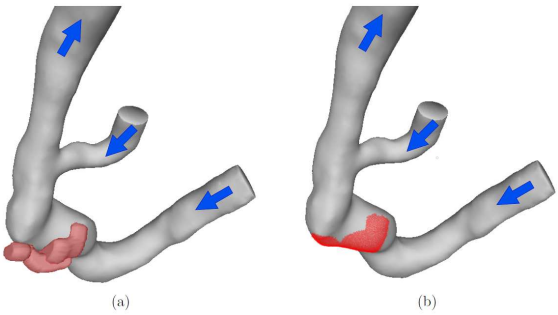

Figure 3. Mapping of the segmented structures of the wall enhancement shown in red (a) to the vessel surface of the draining vein (b). The blue arrows indicate the direction of the blood flow.

image-based registration pre-implemented in MeVisLab. By shifting the VW-MRI data into the space of the MRV data, a corresponding transformation matrix results, which is subsequently applied to the enhancement models. Thus, the wall enhancement extraction moves exactly to the luminal vessel wall. Since the venous models only indicate luminal information, the areas of enhancement are mapped exactly to the venous surface. This results in an area of enhancement lying exactly on the venous vessel wall, where the hemodynamics can be examined locally (see Figure 3).

2.4. Hemodynamic Simulation

Based on the presented segmentation results, hemodynamic simulations are carried out to assess the individual flow situation and enable a precise evaluation at wall enhanced areas, respectively. Here, numerical simulations are acquired with a CFD approach using a finite-volume-based solver.

In a first step, spatial discretization is perfomed using STAR-CCM+ 2020.1 (Siemens Product Lifecycle Management Software Inc., Plato, TX, USA). Specifically, polyhedral as well as prism cells with a base size of 0.25 mm were used for the generation of the underlying volume meshes resulting in a number of elements ranging from 1.5 to 3.7 million depending on the respective vascular domain. The creation of three prism layers with a growth rate of 1.3 is of particular importance to account for the occurring velocity gradients especially due to narrow vessel courses.

To realize the time-dependent blood flow simulations, patient-specific in- and outflow boundary conditions are defined for each model. For all cases, flow quantifications are available for the main in- and outflow vessels as well as for the draining veins by means of 2D PC MRI measurements of the time-dependent volume rate.

At the vessel cross sections, where no flow quantification measurements are available, constant pressure values are assumed based on the literature [13]. Blood is treated as an incompressible ($\rho = 1055\ \frac{\mathrm{kg}}{\mathrm{m}^3}$), Newtonian ($\eta = 4\ \mathrm{mPa} \cdot \mathrm{s}$) fluid and laminar flow

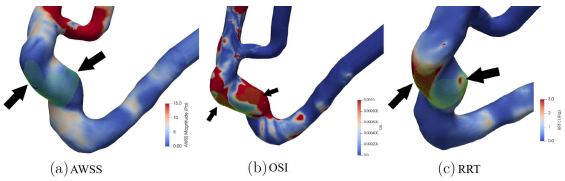

Figure 4. Qualitative representation of AWSS (a), OSI (b), RRT (c) on the vessel surface in the area of draining veins for an exemplary case with overlaid wall enhancement (green, recall Fig. 3) and marked areas showing a local hemodynamic change compared to the surrounding area.

conditions were assumed. Furthermore, the vessel walls follow the rigid wall condition, as no further information is available. For all patient-specific models, two cardiac cycles are simulated. The first cycle represents the initialization of the simulation, while the second provides the periodic solutions. Consequently, only the last cycle is included in the following consideration.

2.5. Analysis

For hemodynamic evaluation, three shear-related parameter are calculated using the 3D post-processing software EnSight 10.2.8 (ANSYS, Inc., Canonsburg, PA, USA).

- Time-averaged Wall Shear Stress (AWSS) describes the tangential shear stress along the luminal vessel wall.
- Oscillatory Shear Index (OSI) is a metric to describe the change in magnitude and direction of wall shear stress throughout one cardiac cycle.
- Relative Residence Time (RRT) provides information about the blood flow distribution at the vessel wall.

3. RESULTS

3.1. Qualitative Results

For the qualitative analysis, the calculated parameters were displayed on the vessel wall of the 3D venous models. Since the signal ehancement extracted from the VW-MRI data is present on the vessel wall as well, visual characteristics of local hemodynamic properties can thus be detected in these areas. For all the draining veins with wall enhancement, initial qualitative tendencies can be observed, as exemplified in Figure 4. In the area of the enhancement, a locally decreased AWSS and locally increased RRT can be recognized. In contrast, the OSI shows no clear hemodynamic tendency in this area.

3.2. Quantitative Results

In addition to the qualitative observations, quantifications are performed along the vessel surface. First, all identified draining veins for the eight patient

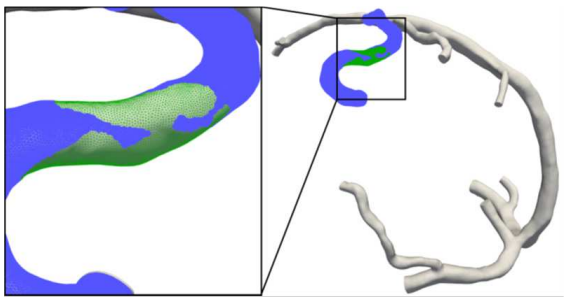

Figure 5. Illustration of enhanced area (green) on the remaining draining vein without enhancement (blue) for an exemplary case.

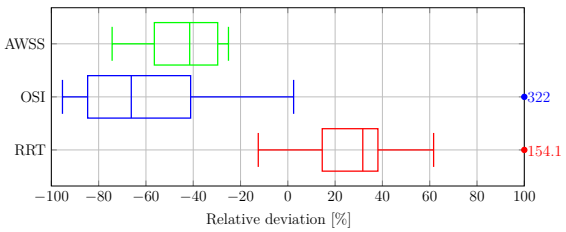

Figure 6. Boxplots of the mean relative deviations of the shear-related parameters within enhanced areas compared to areas of the draining vein without enhancement. The respective outliers for the OSI and RRT, which were removed due to the scaling from -100 % to 100 %, are indicated on the right side of the boxplot.

models are included in the analysis and a global comparison is carried out. The three calculated hemodynamic parameters (AWSS, OSI and RRT) averaged over all seven veins showing wall enhancement were compared with those averaged over all eight veins with no wall enhancement (see Table 1). Global comparison of shear-related hemodynamics of total draining veins thus shows a mean decrease in AWSS (-72.8 %) and OSI (-89.5 %), whereas RRT in draining veins with wall enhancement of the vessel wall shows an increase (+86.9 %).

Table 1. Results of the global hemodynamic comparison

Parameter	Enhanced	Non-enhanced
AWSS [Pa]	1.75	6.42
OSI	$1.43 \cdot 10^{-3}$	$1.36 \cdot 10^{-2}$
RRT [1/Pa]	0.98	0.53

In addition to the global quantification, particular consideration is given to the local hemodynamic characteristics in the area of extracted signal enhancement. For this purpose, the parameters are calculated both directly locally in the enhanced areas and on the areas of the draining veins, which present with no enhancement (see Figure 5). The calculations of the relative deviations of the hemodynamic parameters in the area of enhancement compared with the rest of the venous vascular surface indicate a mean reduction of AWSS (-44.5 %) and OSI (-13.0 %) whereas RRT (+40.0 %) shows an increase. These local quantitative investigations confirm the initial qualitative observations and are visualized in the boxplots (see Figure 6).

4. DISCUSSION

The hemodynamics of draining veins of cerebral AVMs are presently not well understood. In particular, local enhancements in the vessel walls of these veins, which are detected in the VW-MRI data, have not been analyzed with respect to underlying hemodynamics. This interdiciplinary approach investigates time-dependent hemodynamic information at local signal enhancements in vessel walls of draining veins to improve the understanding of cerebral AVMs. Patient-specific 3D models of venous vascular anatomy could be generated based on multimodal imaging data for eight patients whose AVMs showed different complexities with respect to their courses and number of draining veins.

The time-dependent blood flow simulations based on the segmented 3D models provide the basis for the qualitative and quantitative haemodynamic observations of the draining veins. By obtaining patient-specific flow quantification measurements using 2D PC MRI on the draining veins and the main veins, it is possible to define patient-specific boundary conditions at almost all inlets and outlets for each model. The combination of patient-specific vascular models with a high number of venous vessels with the corresponding *in vivo* measured flow data enable the performance of realistic simulations.

To investigate the impact of hemodynamics along the vessel wall, especially locally in the area of a present signal enhancement, the three shear-related parameters AWSS, OSI and RRT are chosen. These parameters are considered to be of special relevance in neurovascular research and can provide information about possible pathological changes [14, 15, 16]. Accordingly, these parameters can provide information about vascular alteration processes, allowing conclusions to be drawn about the states of vessel walls. In blood vessels, WSS acts mainly on the endothelium, the innermost layer of the vessel wall, and is considered a critical parameter affecting vascular changes [17]. While numerous hemodynamic studies for cerebral aneurysms show the influence of WSS on rupture risk [18], the effects of WSS in AVMs are poorly understood. Some studies analyzed WSS in the feeding arteries of AVMs. These reveal increased WSS in the feeding arteries compared with the contralateral ones [16], with this effect being particularly evident in symptomatic AVMs [19]. However, no such observations have been made for draining veins, so that it is not possible to compare these results with the findings of this work. The OSI and RRT are also considered critical parameters for rupture risk analysis of cerebral aneurysms [20, 21]. Specifically,

WSS, OSI and RRT could already be investigated for signal-enhanced aneurysms. In particular, low shear stress and increased OSI and RRT values have already been correlated with signal amplifications in the vessel walls of cerebral aneurysms [22, 23, 24].
The qualitative results of the hemodynamic simulations show the local expressions of these shear-related parameters in the area of the identified signal amplifications. For most patients, especially low AWSS and high RRT values are found in the enhanced areas. In contrast, no clear tendencies can be identified for the OSI on the basis of the qualitative analyses. Since the qualitative representations only provide a visual impression of the distributions of the hemodynamic parameters on the vessel wall, the tendencies were examined more precisely on the basis of quantitative investigations. The global comparison of the 15 draining veins also shows that enhanced draining veins have overall lower AWSS and OSI and higher RRT values. These results confirm previous studies in which signal enhancement was found in the vessel wall, especially in aneurysms with low global AWSS [22]. However, it is critical to associate global hemodynamic investigations with highly localized signal enhancement. The areas of enhancement cover only a very small part of the vascular surface in draining veins. For this reason, the quantitative analysis is also performed in the locally limited areas of enhancement. The relative parameter deviations within these areas show a clear tendency, especially for the AWSS and confirm the initial qualitative observations of the local behavior. With the lowest variation around the mean value, this parameter is characterized as the most stable in its behavior in the signal enhancement. For the RRT, the observed qualitative characteristics are also confirmed by the relative deviations. Here, the distribution around the average value is higher compared to the AWSS. For the OSI, the quantitative observations must be critically evaluated. Due to the very small range of values in both the enhanced and the non-enhanced regions, there are high variations in the relative deviations. Therefore, the behavior of the OSI cannot be associated with the occurrence of vessel wall enhancement. For the AWSS, on the other hand, a relationship from locally low shear stress to the occurrence of enhancement can be established. These have been increasingly associated with inflammatory processes in the vessel wall using VW-MRI [25, 26] and low shear stress can be associated with vessel wall inflammation [27]. Accordingly, this supports the findings of the study. Due to the indirect proportionality of the RRT to the AWSS [28], it is possible to attribute the locally increased RRT values to the occurrence of local signal amplifications as well.
The key findings of this study confirm existing observations regarding the behaviour of AWSS and RRT for enhanced vascular structures. By applying these findings to venous areas of AVMs that have been poorly studied so far, new possibilities arise in the risk assessment of this disease. Inflammatory processes in the vessel walls, which often cause further pathological diseases, can be attributed to low tangential forces and high residence times of the blood on the vessel wall.

Limitations: The presented approach has several limitations. First, numerous manual image processing steps are necessary to generate the patient-specific 3D models. In particular, the local smoothing operations can artificially alter the model and cause it to deviate from the patient-specific morphology. To avoid this, continuous comparison with various angiographic data is necessary, which is time-consuming.
Furthermore, the enhanced areas projected onto the venous models are not fully representing the real wall enhancement. Due to the manual registration method, there may be slight deviations in the exact position. Due to the contour-based segmentation method, the enhanced structures are extracted as areas of constant intensity. This makes it impossible to show different intensity levels of signal amplification on the vessel wall of the draining veins. For this reason, the areas on the vein could only be divided into enhanced and non-enhanced areas, thus the calculated hemodynamic parameters could only be correlated with the occurrence of an enhancement and not with an intensity level. Within the hemodynamic simulations, several simplifications are made, such as the use of constant pressure values at unknown vessel cross-sections or the assumption of rigid walls. In particular, model simplification to rigid wall conditions is a well-known problem in numerical flow simulation for neurovascular vessels. Especially, for the consideration of shear-related parameters on the vessel wall, an integration of information such as patient-specific wall properties would be beneficial. However, the modelling of vessel wall boundary conditions is only advantageous if corresponding reliable wall information from the respective patient exists. Since such information could not be obtained from the available image data, no modelling of vessel wall boundary conditions was performed in this work. Simplified assumptions such as constant wall thicknesses, on the other hand, can lead to erroneous results [29].
Finally, the lack of consideration of the nidus for the hemodynamic considerations must be mentioned. Existing studies already modelled realistic nidus vessels for the validation of CFD simulations [30]. For the investigations of this work, however, the exclusion of the nidus can be considered acceptable. Measured patient-specific flow rates were defined at the inlets of the draining veins and thus the hemodynamic influence of the nidus was included. In addition, this reduced the calculation times for the numerical simulations.
Despite these limitations, this study provides initial insights into the hemodynamic characteristics of AVM draining veins. The developed approach,

which is performed for eight patients, forms a basis for the investigation of further patients with signal-enhanced veins of AVMs. This can strengthen hemodynamic understanding and thus provide further insight into the relationship between promising biomarkers in imaging data and the underlying physical cause.

5. CONCLUSION

The study addresses the hemodynamic investigation of draining veins of cerebral AVMs with local wall enhancement detectable in the VW-MRI data. The developed approach allows to process multimodal medical image data. Previously verified local vessel wall signal enhancements are manually extracted and mapped onto the surface of these models after appropriate co-registration with the luminal vessel models. Based on the venous vessel models, time-dependent numerical blood flow simulations are carried out. Due to the availability of patient-specific blood flow quantifications, these could be defined as in- and outlet boundary conditions for the haemodynamic simulations, thus ensuring reliable blood flow prediction. By visualizing the simulation results with overlaid wall enhancement, qualitative trends in hemodynamic behavior could be observed within the enhanced regions. These tendencies could also be demonstrated with the help of a quantitative analysis. Thus, it is possible to consider potential correlations between signal-enhanced vascular regions and local decreases (AWSS, OSI) or increases (RRT) of hemodynamic parameter values.

ACKNOWLEDGEMENTS

This work is partly funded by the Federal Ministry of Education and Research within the Forschungscampus *STIMULATE* (grant no. 13GW0473A) and the German Research Foundation (BE 6230/6-1). The authors state no conflict of interest.

REFERENCES

[1] Choi, J. H., Mast, H., Sciacca, R. R., Hartmann, A., Khaw, A. V., Mohr, J. P., Sacco, R. L., and Stapf, C., 2006, "Clinical Outcome After First and Recurrent Hemorrhage in Patients With Untreated Brain Arteriovenous Malformation", *Stroke*, Vol. 37 (5), pp. 1243–1247.

[2] Lin, T. M., Yang, H. C., Lee, C. C., Wu, H. M., Hu, Y. S., Luo, C. B., Guo, W. Y., Kao, Y. H., Chung, W. Y., and Lin, C. J., 2020, "Stasis Index from Hemodynamic Analysis using Quantitative DSA correlates with Hemorrhage of Supratentorial Arteriovenous Malformation: A Cross-sectional Study", *Journal of Neurosurgery*, Vol. 132 (5), pp. 1574–1582.

[3] Mohr, J. P., Kejda-Scharler, J., and Pile-Spellman, J., 2013, "Diagnosis and Treatment of Arteriovenous Malformations", *Current Neurology and Neuroscience Reports*, Vol. 13 (2).

[4] Takeda, Y., Kin, T., Sekine, T., Hasegawa, H., Suzuki, Y., Uchikawa, H., Koike, T., Kiyofuji, S., Shinya, Y., Kawashima, M., and Saito, N., 2021, "Hemodynamic Analysis of Cerebral AVMs with 3D Phase-Contrast MR Imaging", *American Journal of Neuroradiology*, Vol. 42 (12), pp. 2138–2145.

[5] Frey, S., Cantieni, T., Vuillemin, N., Haine, A., Kammer, R., von Tengg-Kobligk, H., Obrist, D., and Baumgartner, I., 2018, "Angioarchitecture and Hemodynamics of Microvascular Arterio-Venous Malformations", *PLOS ONE*, Vol. 13 (9), p. e0203368.

[6] Chenoune, Y., Tankyevych, O., Li, F., Piotin, M., Blanc, R., and Petit, E., 2019, "Three-dimensional Segmentation and Symbolic Representation of Cerebral Vessels on 3DRA Images of Arteriovenous Malformations", *Computers in Biology and Medicine*, Vol. 115, p. 103489.

[7] Ho, H., Mithraratne, K., and Hunter, P., 2013, "Numerical Simulation of Blood Flow in an Anatomically-Accurate Cerebral Venous Tree", *IEEE Transactions on Medical Imaging*, Vol. 32 (1), pp. 85–91.

[8] Miraucourt, O., Salmon, S., Szopos, M., and Thiriet, M., 2016, "Blood Flow in the Cerebral Venous System: Modeling and Simulation", *Computer Methods in Biomechanics and Biomedical Engineering*, Vol. 20 (5), pp. 471–482.

[9] Edjlali, M., Guédon, A., Hassen, W. B., Boulouis, G., Benzakoun, J., Rodriguez-Régent, C., Trystram, D., Nataf, F., Meder, J.-F., Turski, P., Oppenheim, C., and Naggara, O., 2018, "Circumferential Thick Enhancement at Vessel Wall MRI Has High Specificity for Intracranial Aneurysm Instability", *Radiology*, Vol. 289 (1), pp. 181–187.

[10] Larsen, N., Flüh, C., Saalfeld, S., Voß, S., Hille, G., Trick, D., Wodarg, F., Synowitz, M., Jansen, O., and Berg, P., 2020, "Multimodal Validation of Focal Enhancement in Intracranial Aneurysms as a Surrogate Marker for Aneurysm Instability", *Neuroradiology*, Vol. 62 (12), pp. 1627–1635.

[11] Küker, W., Gaertner, S., Nagele, T., Dopfer, C., Schoning, M., Fiehler, J., Rothwell, P. M., and Herrlinger, U., 2008, "Vessel Wall Contrast Enhancement: A Diagnostic Sign of Cerebral Vasculitis", *Cerebrovascular Diseases*, Vol. 26 (1), pp. 23–29.

[12] Alaraj, A., Amin-Hanjani, S., Shakur, S. F., Aletich, V. A., Ivanov, A., Carlson, A. P., Oh, G., and Charbel, F. T., 2015, "Quantitative Assessment of Changes in Cerebral Arteriovenous Malformation Hemodynamics After Embolization", *Stroke*, Vol. 46 (4), pp. 942–947.

[13] Guglielmi, G., 2008, "Analysis of the Hemodynamic Characteristics of Brain Arteriovenous Malformations using Electrical Models", *Neurosurgery*, Vol. 63 (1), pp. 1–11.

[14] Cebral, J., Mut, F., Weir, J., and Putman, C., 2010, "Association of Hemodynamic Characteristics and Cerebral Aneurysm Rupture", *American Journal of Neuroradiology*, Vol. 32 (2), pp. 264–270.

[15] Xiang, J., Tutino, V., Snyder, K., and Meng, H., 2013, "CFD: Computational Fluid Dynamics or Confounding Factor Dissemination? The Role of Hemodynamics in Intracranial Aneurysm Rupture Risk Assessment", *American Journal of Neuroradiology*, Vol. 35 (10), pp. 1849–1857.

[16] Alaraj, A., Shakur, S. F., Amin-Hanjani, S., Mostafa, H., Khan, S., Aletich, V. A., and Charbel, F. T., 2015, "Changes in Wall Shear Stress of Cerebral Arteriovenous Malformation Feeder Arteries After Embolization and Surgery", *Stroke*, Vol. 46 (5), pp. 1216–1220.

[17] Epstein, F. H., Gibbons, G. H., and Dzau, V. J., 1994, "The Emerging Concept of Vascular Remodeling", *New England Journal of Medicine*, Vol. 330 (20), pp. 1431–1438.

[18] Meng, H., Tutino, V., Xiang, J., and Siddiqui, A., 2013, "High WSS or Low WSS? Complex Interactions of Hemodynamics with Intracranial Aneurysm Initiation, Growth, and Rupture: Toward a Unifying Hypothesis", *American Journal of Neuroradiology*, Vol. 35 (7), pp. 1254–1262.

[19] Chang, W., Loecher, M., Wu, Y., Niemann, D., Ciske, B., Aagaard-Kienitz, B., Kecskemeti, S., Johnson, K., Wieben, O., Mistretta, C., and Turski, P., 2012, "Hemodynamic Changes in Patients with Arteriovenous Malformations Assessed Using High-Resolution 3D Radial Phase-Contrast MR Angiography", *American Journal of Neuroradiology*, Vol. 33 (8), pp. 1565–1572.

[20] Berg, P., and Beuing, O., 2017, "Multiple Intracranial Aneurysms: A Direct Hemodynamic Comparison between Ruptured and Unruptured Vessel Malformations", *International Journal of Computer Assisted Radiology and Surgery*, Vol. 13 (1), pp. 83–93.

[21] Neyazi, B., Swiatek, V. M., Skalej, M., Beuing, O., Stein, K.-P., Hattingen, J., Preim, B., Berg, P., Saalfeld, S., and Sandalcioglu, I. E., 2020, "Rupture Risk Assessment for Multiple Intracranial Aneurysms: Why there is no Need for Dozens of Clinical, Morphological and Hemodynamic Parameters", *Therapeutic Advances in Neurological Disorders*, Vol. 13, p. 175628642096615.

[22] Zhang, M., Peng, F., Tong, X., Feng, X., Li, Y., Chen, H., Niu, H., Zhang, B., Song, G., Li, Y., Liu, P., Liu, A., and Li, R., 2021, "Associations between Haemodynamics and Wall Enhancement of Intracranial Aneurysm", *Stroke and Vascular Neurology*, Vol. 6 (3), pp. 467–475.

[23] Veeturi, S. S., Rajabzadeh-Oghaz, H., Pintér, N. K., Waqas, M., Hasan, D. M., Snyder, K. V., Siddiqui, A. H., and Tutino, V. M., 2021, "Aneurysm Risk Metrics and Hemodynamics are Associated with Greater Vessel Wall Enhancement in Intracranial Aneurysms", *Royal Society Open Science*, Vol. 8 (11).

[24] Lv, N., Karmonik, C., Chen, S., Wang, X., Fang, Y., Huang, Q., and Liu, J., 2020, "Wall Enhancement, Hemodynamics, and Morphology in Unruptured Intracranial Aneurysms with High Rupture Risk", *Translational Stroke Research*, Vol. 11 (5), pp. 882–889.

[25] Young, C. C., Bonow, R. H., Barros, G., Mossa-Basha, M., Kim, L. J., and Levitt, M. R., 2019, "Magnetic Resonance Vessel Wall Imaging in Cerebrovascular Diseases", *Neurosurgical Focus*, Vol. 47 (6), p. E4.

[26] Lehman, V. T., Brinjikji, W., Mossa-Basha, M., Lanzino, G., Rabinstein, A. A., Kallmes, D. F., and Huston, J., 2018, "Conventional and High-resolution Vessel Wall MRI of Intracranial Aneurysms: Current Concepts and New Horizons", *Journal of Neurosurgery*, Vol. 128 (4), pp. 969–981.

[27] Traub, O., and Berk, B. C., 1998, "Laminar Shear Stress: Mechanisms by which Endothelial Cells Transduce an Atheroprotective Force", *Arteriosclerosis, Thrombosis, and Vascular Biology*, Vol. 18 (5), pp. 677–685.

[28] Himburg, H. A., Grzybowski, D. M., Hazel, A. L., LaMack, J. A., Li, X.-M., and Friedman, M. H., 2004, "Spatial Comparison between Wall Shear Stress Measures and Porcine Arterial Endothelial Permeability", *American Journal of Physiology-Heart and Circulatory Physiology*, Vol. 286 (5), pp. H1916–H1922.

[29] Voß, S., Glaßer, S., Hoffmann, T., Beuing, O., Weigand, S., Jachau, K., Preim, B., Thévenin, D., Janiga, G., and Berg, P., 2016, "Fluid-Structure Simulations of a Ruptured Intracranial Aneurysm: Constant versus Patient-Specific Wall Thickness", *Computational and Mathematical Methods in Medicine*, Vol. 2016, pp. 1–8.

[30] Kaneko, N., Ullman, H., Ali, F., Berg, P., Ooi, Y. C., Tateshima, S., Colby, G. P., Komuro, Y., Hu, P., Khatibi, K., Mejia, L. L. P., Szeder, V., Nour, M., Guo, L., Chien, A., Vinuela, F., Nemoto, S., Mashiko, T., Sehara, Y., Hinman, J. D., Duckwiler, G., and Jahan, R., 2020, "In Vitro Modeling of Human Brain Arteriovenous Malformation for Endovascular Simulation and Flow Analysis", *World Neurosurgery*, Vol. 141, pp. e873–e879.

Conference on Modelling Fluid Flow (CMFF'22)
The 18th International Conference on Fluid Flow Technologies
Budapest, Hungary, August 30-September 2, 2022

EFFECT OF DIFFERENT CHEMICAL MECHANISMS IN SONOCHEMICAL MODELLING

Csanád KALMÁR[1], Ferenc HEGEDŰS[2]

[1] Corresponding Author. Department of Hydrodynamic Systems, Faculty of Mechanical Engineering, Budapest University of Technology and Economics. Műegyetem rkp. 3., H-1111 Budapest, Hungary. E-mail: cskalmar@hds.bme.hu
[2] Department of Hydrodynamic Systems, Faculty of Mechanical Engineering, Budapest University of Technology and Economics. Műegyetem rkp. 3., H-1111 Budapest, Hungary. E-mail: fhegedus@hds.bme.hu

ABSTRACT

Quantitative modelling of chemical processes inside an acoustically driven gas bubble has been a keen interest in sonochemistry. Presumably the most difficult task of chemical modelling is that the rate of every single chemical reaction has to be calculated precisely. The complications originate from the fact that the reaction rates depend exponentially on the temperature. It follows that correct validation of the model parameters is essential in reaction kinetics.

In the present paper, a precisely validated, up-to-date chemical mechanism is introduced for a single sonochemical bubble with initial content of pure oxygen and water vapour. The model properly includes specified third-body coefficients, pressure-dependency, reaction duplication, and it works with up-to-date, validated Arrhenius-constants.

The chemical yield is compared to three other, widely applied chemical mechanisms in the literature. The results point out that apart from some moderately good agreement in some cases, the chemical yield can vary between several orders of magnitude amongst the various mechanisms in a wide parameter range. Additionally, qualitative validation is performed with H_2O_2 measurements from the literature, as well.

As a consequence, we can certainly state that applying an up-to-date chemical mechanism is mandatory in order to make quantitatively correct conclusions about chemical activity.

Keywords: bubble dynamics, chemical modeling, chemical reactions, reaction mechanisms, sonochemistry

NOMENCLATURE

$\dot{Q}_{th}$	$[W]$	heat flux
$\sum \dot{Q}$	$[W]$	total heat
A	$[m^2]$	bubble surface
A_i	[1]	pre-exponential factor of reaction i
C_v	$[J/molK]$	specific heat on constant volume
E_i	$[mol/cm^3 s]$	activation energy of reaction i
I	[1]	number of chemical reactions
K	[1]	number of chemical species
M	$[mol/cm^3]$	total concentration
P_∞	$[bar]$	ambient pressure
R	$[\mu m]$	bubble radius
R_g	$[J/kgK]$	universal gas constant
T	$[K]$	internal temperature
T_∞	$[K]$	ambient temperature
V	$[m^3]$	bubble volume
b_i	[1]	temperature exponent of reaction i
c_k	$[mol/cm^3]$	concentration of species k
c_L	$[m/s]$	sound speed in liquid
f	$[kHz]$	ultrasound frequency
k_f, k_b	[1]	forward/backward reaction rate constant
l_{th}	$[m]$	thermal boundary layer thickness
n_t	$[mol]$	total amount of substance
p	$[bar]$	internal pressure
p_A	$[bar]$	pressure amplitude
q_i	$[mol/cm^3 s]$	net rate of reaction i
t	$[s]$	time
α_{ki}	[1]	third-body efficiencies
χ	$[m^2/s]$	thermal diffusivity
χ_k	[1]	chemical symbol of species k
$\dot{\omega}$	[1]	production rate
λ	$[W/mK]$	heat flux coefficient
μ_L	$[Pas]$	liquid dynamic viscosity
ν	[1]	stochiometric coefficient
ρ_L	$[kg/m^3]$	liquid density
σ	$[N/m]$	surface tension
τ	[1]	dimensionless time

Subscripts and Superscripts

L	liquid
∞	far-field value
f, b	forward, backward

i	reaction index
k	component index

1. INTRODUCTION

In a liquid domain, excited by high intensity and high frequency ultrasound, the dissolved gas content forms bubble clusters that consist of millions of micron-sized bubbles [1, 2]. If the pressure amplitude exceeds Blake's critical threshold [3], the bubbles can grow even 100 times their equilibrium size in the negative pressure phase. This is followed by a rapid compression in the positive pressure phase due to the high inertia of the liquid (inertial cavitation). During the strong collapse, the peak pressure and temperature can reach up to hundreds of bar and thousand of Kelvins, respectively [4]. With these conditions, the bubbles act as tiny chemical reactors, as the gas components dissociate and several different molecules are created. The new species are later applied in various areas of engineering, i.e. polymer synthesis [5], producing nanoparticles [6], or degradation of wastewater [7, 8].

Quantitative modeling of chemical reactions inside oscillating bubbles has been studied continuously since the mid-1990s [9, 10, 11]. However, some major difficulties have emerged during the years. Presumably, the reason of the biggest challenge in sonochemical modelling is that the rates of most chemical reactions have *exponential* dependence on the temperature. This fact results in an extreme sensitivity on the model parameters and demands a precise and up-to-date validation process (e.g. for the Arrhenius constants). Most of the applied chemical mechanisms in the sonochemical literature tend to lack an advanced validation method, and the applied model parameters are often outdated.

Besides using up-to-date parameters in the reaction mechanism, there are other modelling issues which are usually neglected during the computation of a chemically active bubble. For example, the so-called three-body reactions are occasionally taken into account, but *enhanced* third-body efficiencies for specific molecules are rarely specified. In addition, pressure-dependence of reaction rates is seldom included in the mechanisms, although it can change the chemical rates significantly due to the high compression ratio inside a bubble. Finally, the rate constants of some specific reactions can have a more complex dependence on the temperature than exponential; this also needs a special care.

In the present study, *a precisely validated, up-to-date chemical mechanism* for a single, chemically active bubble is introduced [12], which takes into account all the mentioned modelling issues. It is compared numerically to 3 widely applied chemical mechanisms in the sonochemistry literature at various driving parameter (ultrasound amplitude and frequency) values.

2. MATHEMATICAL MODEL

The mathematical model of a chemically active bubble is divided into two main parts: physical and chemical. The physical part of the model describes the temporal evolution of the bubble radius, temperature and pressure, while the chemical part focuses on the chemical processes and the rates of the chemical reactions. By this separation, the difference between the chemical mechanisms can be examined precisely, since the physical part of the model is kept the same during the simulations.

It is important to mention that in this article, most parameter values are not given, only the governing equations are presented. The interested reader is referred to our recent publication [13], where a detailed description can be found with all the necessary constants and model parameters.

2.1. Physical model

In our model, the following assumptions are made. A single, spherically symmetric gas bubble is considered that initially contains non-condensable gas (oxygen) and water vapour. The gas content is treated as an ideal mixture of ideal gases. The concentrations of species, the pressure and the temperature are considered as spatially uniform except a thermal boundary layer, which is necessary to calculate heat fluxes with the bulk liquid. Non-equilibrium evaporation and condensation are also included.

The radial dynamics of an oscillating bubble is described by the modified Keller–Miksis equation [14] in the form of

$$\left(1-\frac{\dot{R}}{c_L}\right)R\ddot{R}+\left(1-\frac{\dot{R}}{3c_L}\right)\frac{3}{2}\dot{R}^2 = \left(1+\frac{\dot{R}}{c_L}+\frac{R}{c_L}\frac{d}{dt}\right)\frac{(p_L-p_\infty(t))}{\rho_L}, \quad (1)$$

where $R(t)$ is the radius of the bubble, t is the time, c_L is the sound speed in the liquid and ρ_L is the density of the liquid. p_L is the liquid pressure at the bubble wall which is related to the internal pressure (p) via the boundary condition

$$p = p_L + \frac{2\sigma}{R} + 4\mu_L\frac{\dot{R}}{R}\,. \quad (2)$$

Here, σ is the surface tension and μ_L is the dynamic viscosity of the liquid. The dots stand for derivatives with respect to time. The far field pressure p_∞ contains the harmonic ultrasound excitation as

$$p_\infty(t) = P_\infty + p_A \sin(2\pi f t), \quad (3)$$

where P_∞ is the ambient pressure, p_A and f are the ultrasound pressure amplitude and frequency, respectively; these two are the driving parameters that will be investigated later.

For calculating the internal pressure p in Eq. (2), the ideal gas law is applied as

$$p = MR_gT, \quad (4)$$

where M is the total concentration of the mixture, R_g is the universal gas constant and T is the internal temperature. It is calculated by solving the first law of thermodynamics in the time-dependent form of

$$\dot{T} = \frac{-p\dot{V} + \sum \dot{Q}}{n_t \overline{C}_v}, \tag{5}$$

where $V = 4R^3\pi/3$ is the volume of the bubble, $\sum \dot{Q}$ is the sum of heat flux and reaction heats. n_t is the total amount of substance of the mixture in moles and $\overline{C}_v$ is the average molar heat capacity of the mixture at constant volume. The heat capacities and other thermodynamic quantities are approximated with polynomials via the NASA chemical equilibrium code [15]. Again, see Ref. [13] for details.

Heat conduction between the fluid and the bubble interior is modelled with the approach used by several authors in the past [16, 17]. In a thermal boundary layer, the temperature changes linearly from the bubble mean temperature T to the ambient liquid temperature T_∞, which is kept constant. In this approach, the amount of heat transfer is approximated as

$$\dot{Q}_{th} = A\overline{\lambda} \left.\frac{\partial T}{\partial r}\right|_{r=R} \approx A\overline{\lambda} \frac{T_\infty - T}{l_{\text{th}}}, \tag{6}$$

where A is the area of the bubble surface, $\overline{\lambda}$ is the averaged thermal conductivity of the mixture and l_{th} is the thickness of the thermal boundary layer calculated as

$$l_{\text{th}} = \min\left(\sqrt{\frac{R\overline{\chi}}{\dot{R}}}, \frac{R}{\pi}\right), \tag{7}$$

where $\overline{\chi}$ is the averaged thermal diffusivity of the mixture. Non-equilibrium evaporation and condensation of water are considered here as a net substance flow rate into the liquid, with the method of Fujikawa [18].

As a summary, the physical part of the model results in a set of ordinary differential equations: the Keller–Miksis equation (1) is of second order for the bubble radius $R(t)$, and Eq. (5) is of first order for the internal temperature $T(t)$. The internal pressure is obtained form Eq. (4) as and algebraic equation.

2.2. Chemical model

The chemical part of the model focuses on calculating the rate of chemical reactions and temporal evolution of the molecule numbers of each chemical species. First, let us consider the following reversible chemical reactions involving K chemical species in the general form of

$$\sum_{k=1}^{K} \nu_{ki}^f \chi_k \Leftrightarrow \sum_{k=1}^{K} \nu_{ki}^b \chi_k \qquad (i = 1, ..., I), \tag{8}$$

where ν_{ki} are the stoichiometric coefficients, χ_k is the chemical symbol for the kth species, and I is the total number of reactions. The superscripts f and b indicate forward and backward directions, respectively. The net rate of reaction i (q_i) is calculated as the difference of forward and backward rates as

$$q_i = k_{f_i} \prod_{k=1}^{K} {c_k}^{\nu_{ki}^f} - k_{b_i} \prod_{k=1}^{K} {c_k}^{\nu_{ki}^b}, \tag{9}$$

where c_k is the concentration of species k, k_{f_i} and k_{b_i} are the forward and backward reaction rate constants of reaction i, respectively (defined later). The basic equation for calculating the forward reaction rate constants is the modified Arrhenius-equation in the form of

$$k_{f_i} = A_i T^{b_i} \exp\left(\frac{-E_i}{R_g T}\right), \tag{10}$$

where A_i is the pre-exponential factor, b_i is the temperature exponent, and E_i is the activation energy. The backward rate constants k_{b_i} are calculated via proper thermodynamic conditions, see [13] for details. With all q_i values, the production rate of each species is expressed as

$$\dot{\omega}_k = \sum_{i=1}^{I} \nu_{ki} q_i, \qquad (k = 1, ..., K), \tag{11}$$

where $\nu_{ki} = \nu_{ki}^b - \nu_{ki}^f$. $\dot{\omega}_k$ represents the rate of change of c_k due to chemical reactions. The complete system of ordinary differential equations is completed as

$$\dot{c}_k = \dot{\omega}_k - c_k \frac{\dot{V}}{V}, \tag{12}$$

with the amount of water vapour being adjusted with the net evaporation rate.

In our presented model, the above described method is complemented with possible third-body efficiency and pressure-dependency of certain reactions. In the former case, q_i in Eq. (9) is modified as $q_i' = q_i[M]$, where $[M]$ is the effective total concentration of the third-body species, expressed as $[M] = \sum_{k=1}^{K} \alpha_{ki} c_k$. Here, α_{ki} is the matrix of the third-body efficiencies. Usually, most α_{ki} is assumed to be 1, and only those that differ from 1 are highlighted in [13].

A detailed explanation of reaction rates in the case of pressure-dependent reactions is omitted here. Nonetheless, in a state-of-the-art chemical mechanism, they play an essential role, especially if the pressure varies by orders of magnitude. The forward rate constant of a pressure-dependent reaction is shown at constant temperature in Figure 1. It is apparent that the reaction rate changes multiple orders of magnitude in the pressure interval that emerges during strong bubble collapses (from one to around hundreds of bars). This implies the necessity of taking into account pressure dependency. It should be noted here that depending on the model parameters, the trend of pressure-dependency can be highly different for each reaction.

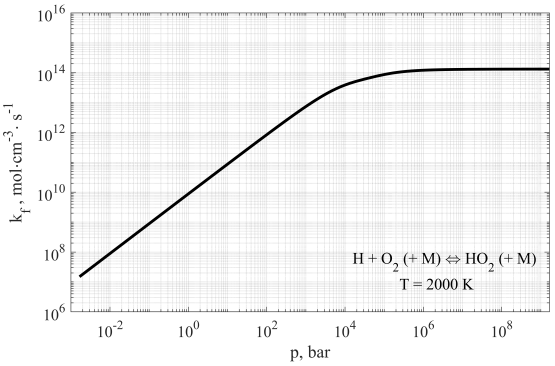

Figure 1. Forward rate constant of a pressure-dependent reaction $H + O_2 (+M) \Leftrightarrow HO_2 (+M)$ as a function of pressure, at $T = 2000$ K.

3. METHOD OF COMPARISON

The main aim of the present study is to show the importance of appropriate chemical mechanism in sonochemical calculations. As a process, we make numerical simulations with 3 different, widely applied chemical mechanisms in sonochemistry, and compare the results with our newly introduced mechanism. All of the models have been used for bubbles containing initially only O_2 and water vapour. Our mechanism will be labeled as ELTE/HDS2022, and it will be considered as the most precise one.

The three other mechanisms are labeled in this paper as Kamath1993 [19, 20], Yasui2003 [21] and Merouani2014 [22]. The names and years refer to the first appearance in sonochemical simulations. These mechanisms tend to work with outdated Arrhenius coefficients, and the backward rate constants k_{b_i} are calculated by prescribed *backward* Arrhenius coefficients, rather then precise thermodynamic equilibrium conditions. Some third-body efficiencies are occasionally indicated, but pressure-dependency is not taken into account in either model. The exact values of the applied Arrhenius coefficients can be found in the aforementioned papers; however, it can be observed that some of these constants can vary even by multiple orders of magnitudes. Conceivably, this may result in remarkably different results, see later sections.

In our work, we perform numerical simulations at different driving parameters (pressure amplitude and frequency). For each parameter combination, the *chemical yield* is defined, see Sec. 4.1. The simulations are made with all 4 different mechanisms at the whole examined parameter regime, with the physical part of the model being kept the same. The models are compared by the chemical yields of some specific chemical species.

4. RESULTS

4.1. Definition of chemical yield

After solving the complete system of ordinary differential equations at a given parameter combination numerically, one would get the time curves of bubble radius $R(t)$, internal temperature $T(t)$, and concentration profile $c_k(t)$ for each species. The convergent part of the result is shown on Figure 2 at $p_A = 1.6$ bar, $f = 50$ kHz and $R_E = 4\,\mu$m. Note that the time axes are in dimensionless form of $\tau = t \cdot f$, which means that $\tau = 1$ belongs to one excitation cycle.

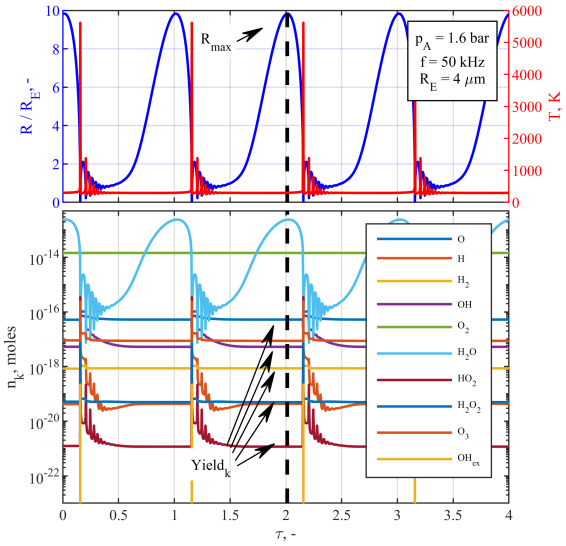

Figure 2. Time curves at $p_A = 1.6$ bar, $f = 50$ kHz and $R_E = 4\,\mu$m with the ELTE/HDS2022 model. The bubble radius (blue) and temperature (red) curves are on the top chart, the amount of substance of each species are on the bottom chart (on logarithmic scale).

Chemical yield is the numerical metric that quantifies the chemical activity of the bubble. In our work, it is defined for each chemical species as the amount of substance at the maximum bubble radius. In Fig. 2, the vertical dashed lines represent the maximum radius, and the chemical yields for some components are marked with arrows. During further evaluation, the chemical yields of hydrogen-peroxide (H_2O_2) and OH radical will be compared as two of the important molecules in sonochemical applications [23, 24].

4.2. Difference among the chemical mechanisms

Our strategy to compare the examined mechanisms is to perform the numerical simulations at different driving parameters with the four model, and examine the chemical yields. In Figure 3, the yields of H_2O_2 are show as a function of pressure amplitude (between 1 and 2 bars) at $R_E = 4\,\mu$m at four different driving frequencies with the 4 models. The vertical axes are on logarithmic scales.

It is apparent from the charts that large variance emerges between all four models, in almost all the amplitude domain. For example, the yield

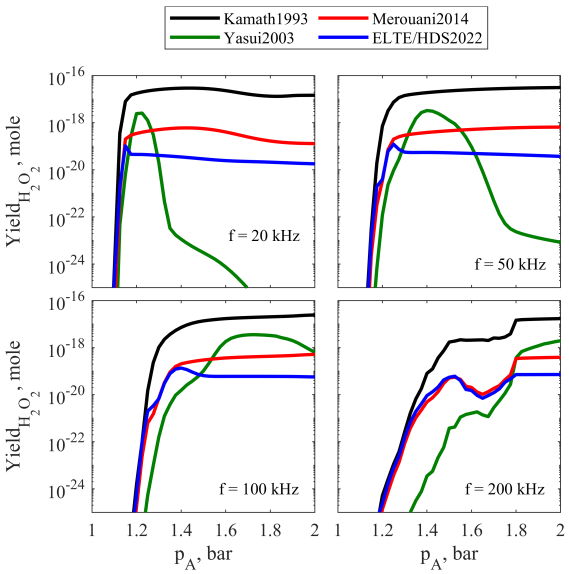

Figure 3. The chemical yield of H_2O_2 as a function of pressure amplitude at $R_E = 4\,\mu$m at four different driving frequencies with the 4 models.

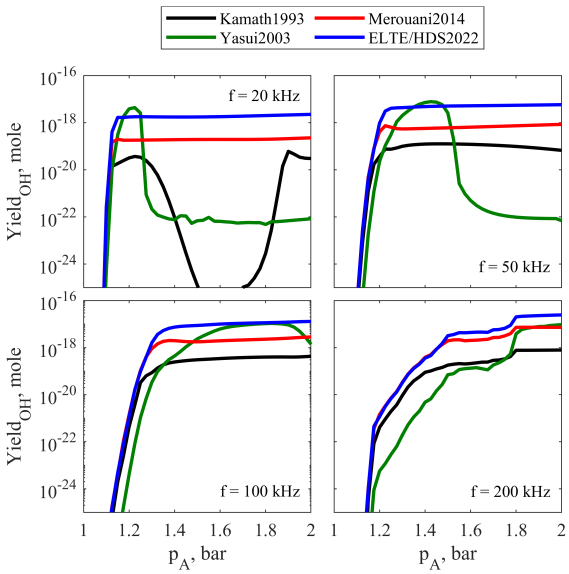

Figure 4. The chemical yield of OH as a function of pressure amplitude at $R_E = 4\,\mu$m at four different driving frequencies with the 4 models.

of H_2O_2 with Kamath1993 is the largest, by more then one order of magnitude then the others. Especially at lower frequencies, there is an immense amount of difference between the results. Considering ELTE/HDS2022 as the best chemical mechanism, Merouani2014 (red lines) shows the closest yield values, but the numerical values can differ by a factor of 3-5. The model of Yasui2003 behaves even qualitatively differently than the other three; it shows a visible peak of H_2O_2 yield at lower pressure amplitude values for all driving frequencies, followed by a steep decrease as p_A increases (except for $f = 200\,$kHz). This can lead to the identification of false optimal operating conditions.

Similar conclusions can be taken in the case of OH radical, see Figure 4. Here, the chemical yield of OH is plotted at the same parameter domain as of H_2O_2. It can be observed that even the trends with Yasui2003 and Kamath1993 are rather different from the others, especially on lower frequencies. Merouani2014 is at least qualitatively similar to ELTE/HDS2022, but the 3 to 5 times differences are appear here, as well.

As a consequence, it is clear that the calculated chemical yields usually differ by several orders of magnitudes; thus, the *proper modelling of the chemical reactions is mandatory* for drawing meaningful conclusions.

4.3. Qualitative validation of the chemical mechanism

Due to the complex behaviour of chemical reactions, the validation of different chemical mechanisms are possibly the most difficult task in the topic. As a qualitative validation, we compare the results to the measurements of Brotchie et al. [25], where they measured the chemical output of H_2O_2 as a function of driving frequency. Their results showed that there exist an optimal driving frequency (regarding H_2O_2 outcome) at around $f \approx 200 - 300\,$kHz.

We performed numerical simulations at constant $R_E = 8\,\mu$m and $p_A = 2\,$bar, on various driving frequencies between 20 and 350 kHz with all four examined mechanisms. The chemical yields of H_2O_2 are show on Figure 5, with logarithmic yield axis. The maximum yield values are marked with circles for each mechanism. It can be observed that only ELTE/HDS2022 model predicts the maximum yield correctly over the domain of [25]. The other three ones underestimate the optimal frequency by even 100 - 200 kHz. This result also confirms our presupposition that our up-to-date chemical mechanism is the most precise one – at least regarding H_2O_2 outcome.

5. SUMMARY

The present paper focuses on the chemical modelling of an ultrasound driven gas bubble. An up-to-date chemical mechanism is presented for a bubble initially containing only oxygen and water vapour. The model includes accurately validated Arrhenius-coefficients and third-body efficiency factors, takes into account pressure-dependent reactions, and calculates the backward rate constants from accurate equilibrium equations.

The mechanism is compared to three other chemical models that are widely used in sonochemistry with the physical part of the models kept the same. The analysis is made via a well-defined chemical yield. The results showed that there are orders of magnitude differences between the yields of H_2O_2 and OH as calculated from the various chem-

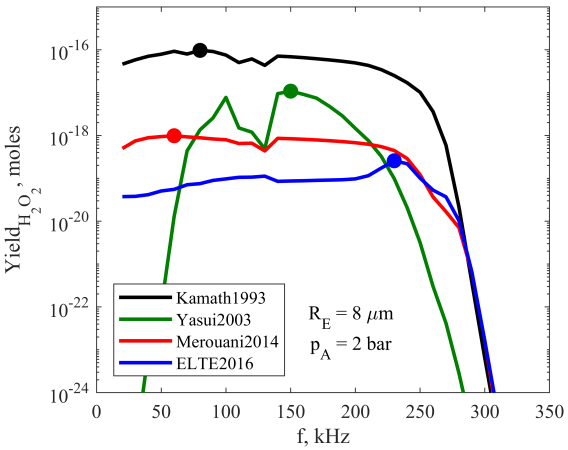

Figure 5. The chemical yield of H_2O_2 as a function of frequency at $R_E = 8\,\mu$m and $p_A = 2$ bar with the 4 models. The maximum yield values are marked with circles for each mechanism.

ical models in a wide parameter range. In addition, the trends of the yield as a function of control parameters can have different characteristics; thus, one can identify false optimal operating conditions.

Additionally, the models were compared to the H_2O_2 measurements of Brothcie et al. [25]. It turned out that only ELTE/HDS2022 mechanism estimates the optimal driving frequency range properly.

The presented results imply that in order to make qualitatively and quantitatively correct conclusions about the chemical activity, *it is essential to employ a state-of-the-art, properly validated chemical mechanism* for a given sonochemical task.

ACKNOWLEDGEMENTS

The research reported in this paper is part of project no. BME-NVA-02, implemented with the support provided by the Ministry of Innovation and Technology of Hungary from the National Research, Development and Innovation Fund, financed under the TKP2021 funding scheme.

The research was also supported by the János Bolyai Research Scholarship of the Hungarian Academy of Sciences and by the New National Excellence Program of the Ministry of Human Capacities (project no. ÚNKP-21-5-BME-369).

REFERENCES

[1] Mettin, R., 2007, "From a single bubble to bubble structures in acoustic cavitation", *Oscillations, Waves and Interactions: Sixty Years Drittes Physikalisches Institut; a Festschrift*, Universitätsverlag Göttingen, Göttingen, Germany.

[2] Rosselló, J., Lauterborn, W., Koch, M., Wilken, T., Kurz, T., and Mettin, R., 2018, "Acoustically induced bubble jets", *Physics of Fluids*, Vol. 30 (12), p. 122004.

[3] Blake, F. G., 1949, "The onset of cavitation in liquids", *Tech Memo*, (12).

[4] Klapcsik, K., 2021, "GPU accelerated numerical investigation of the spherical stability of an acoustic cavitation bubble excited by dual-frequency", *Ultrasonics Sonochemistry*, Vol. 77, p. 105684.

[5] Kanmuri, S., and Moholkar, V. S., 2010, "Mechanistic aspects of sonochemical copolymerization of butyl acrylate and methyl methacrylate", *Polymer*, Vol. 51 (14), pp. 3249–3261.

[6] Choudhury, H. A., Choudhary, A., Sivakumar, M., and Moholkar, V. S., 2013, "Mechanistic investigation of the sonochemical synthesis of zinc ferrite", *Ultrasonics Sonochemistry*, Vol. 20 (1), pp. 294–302.

[7] Gole, V. L., Fishgold, A., Sierra-Alvarez, R., Deymier, P., and Keswani, M., 2018, "Treatment of perfluorooctane sulfonic acid (PFOS) using a large-scale sonochemical reactor", *Sep Purif Technol*, Vol. 194, pp. 104–110.

[8] Sivasankar, T., and Moholkar, V. S., 2009, "Physical insights into the sonochemical degradation of recalcitrant organic pollutants with cavitation bubble dynamics", *Ultrasonics Sonochemistry*, Vol. 16 (6), pp. 769–781.

[9] Yasui, K., Tuziuti, T., Kozuka, T., Towata, A., and Iida, Y., 2007, "Relationship between the bubble temperature and main oxidant created inside an air bubble under ultrasound", *The Journal of Chemical Physics*, Vol. 127 (15), p. 154502.

[10] Stricker, L., Prosperetti, A., and Lohse, D., 2011, "Validation of an approximate model for the thermal behavior in acoustically driven bubbles", *The Journal of the Acoustical Society of America*, Vol. 130 (5), pp. 3243–3251.

[11] Kalmár, C., Klapcsik, K., and Hegedűs, F., 2020, "Relationship between the radial dynamics and the chemical production of a harmonically driven spherical bubble", *Ultrasonics Sonochemistry*, Vol. 64, p. 104989.

[12] Varga, T., Olm, C., Nagy, T., Zsély, I. G., Valkó, É., Pálvölgyi, R., Curran, H. J., and Turányi, T., 2016, "Development of a joint hydrogen and syngas combustion mechanism based on an optimization approach", *International Journal of Chemical Kinetics*, Vol. 48 (8), pp. 407–422.

[13] Kalmár, C., Turányi, T., Zsély, I. G., Papp, M., and Hegedűs, F., 2022, "The importance of chemical mechanisms in sonochemical modelling", *Ultrasonics Sonochemistry*, p. 105925.

[14] Sojahrood, A., Haghi, H., Karshafian, R., and Kolios, M. C., 2021, "Classification of the major nonlinear regimes of oscillations, oscillation properties, and mechanisms of wave energy dissipation in the nonlinear oscillations of coated and uncoated bubbles", *Physics of Fluids*, Vol. 33 (1), p. 016105.

[15] Gordon, S., 1976, *Computer program for calculation of complex chemical equilibrium compositions, rocket performance, incident and reflected shocks, and Chapman-Jouguet detonations*, Vol. 273, Scientific and Technical Information Office, National Aeronautics and Space Administration.

[16] Toegel, R., Gompf, B., Pecha, R., and Lohse, D., 2000, "Does water vapor prevent upscaling sonoluminescence?", *Physical Review Letters*, Vol. 85 (15), p. 3165.

[17] Pandit, A. V., Sarvothaman, V. P., and Ranade, V. V., 2021, "Estimation of chemical and physical effects of cavitation by analysis of cavitating single bubble dynamics", *Ultrasonics Sonochemistry*, Vol. 77, p. 105677.

[18] Fujikawa, S., and Akamatsu, T., 1980, "Effects of the non-equilibrium condensation of vapour on the pressure wave produced by the collapse of a bubble in a liquid", *J Fluid Mech*, Vol. 97 (3), pp. 481–512.

[19] Kamath, V., Prosperetti, A., and Egolfopoulos, F., 1993, "A theoretical study of sonoluminescence", *The Journal of the Acoustical Society of America*, Vol. 94 (1), pp. 248–260.

[20] Egolfopoulos, F., and Law, C. K., 1991, "An experimental and computational study of the burning rates of ultra-lean to moderately-rich $H_2/O_2/N_2$ laminar flames with pressure variations", *Proc Combust Inst*, Vol. 23, pp. 333–340.

[21] Yasui, K., Tuziuti, T., Iida, Y., and Mitome, H., 2003, "Theoretical study of the ambient-pressure dependence of sonochemical reactions", *Journal of Chemical Physics*, Vol. 119 (1), pp. 346–356.

[22] Merouani, S., Hamdaoui, O., Rezgui, Y., and Guemini, M., 2014, "Theoretical estimation of the temperature and pressure within collapsing acoustical bubbles", *Ultrason Sonochem*, Vol. 21 (1), pp. 53–59.

[23] Kanthale, P., Ashokkumar, M., and Grieser, F., 2008, "Sonoluminescence, sonochemistry (H_2O_2 yield) and bubble dynamics: frequency and power effects", *Ultrasonics Sonochemistry*, Vol. 15 (2), pp. 143–150.

[24] Pétrier, C., and Francony, A., 1997, "Ultrasonic waste-water treatment: incidence of ultrasonic frequency on the rate of phenol and carbon tetrachloride degradation", *Ultrason Sonochem*, Vol. 4 (4), pp. 295–300.

[25] Brotchie, A., Ashokkumar, M., and Grieser, F., 2008, "Sonochemistry and sonoluminescence under simultaneous high-and low-frequency irradiation", *The Journal of Physical Chemistry C*, Vol. 112 (22), pp. 8343–8348.

Conference on Modelling Fluid Flow (CMFF'22)
The 18th International Conference on Fluid Flow Technologies
Budapest, Hungary, August 30 -September 2, 2022

CFD-DEM MODELLING OF SHAFT FURNACES, USING THE VOLUME FRACTION SMOOTHER APPROACH

Christoph Spijker[1], Harald Raupenstrauch[2]

[1] Corresponding Author. Chair of Thermal Processing Technology, Montanuniversitaet Leoben. Franz-Josef-Str. 18, A-8700 Leoben, Austria. Tel.: + 43 3842 402 5818, E-mail: christoph.spijker@unileoben.ac.at
[2] Chair of Thermal Processing Technology, Montanuniversitaet Leoben. Franz-Josef-Str. 18, A-8700 Leoben, Austria. Tel.: + 43 3842 402 5800, E-mail: harald.raupenstrauch@unileoben.ac.at

ABSTRACT

Shaft furnaces are widely used in high processing granular materials at high temperatures due to their high energy efficiency. The modelling of those furnaces is challenging. Small geometric details like the burner nozzles demand a fine Computational Fluid Dynamic (CFD) grid that requires a resolved Discrete Element Method (DEM) approach. The long process time of the granular material and the huge amount of particles make a resolved DEM approach not manageable in terms of computing resources. Therefore, two techniques were developed, the Volume Fraction Smoother (VFS) where the particle size can be independent of the cell size and the Timescale Splitting Method (TSSM) which allows to separate the fluid and DEM time scales to speed up the simulation.

Keywords: CDF, DEM, Shaft furnace, Timescale Splitting Method, Volume Fraction Smoother

NOMENCLATURE

C_p	[-]	static pressure coefficient
$\underline{U}$	[m/s]	relative velocity
S_{comb}	[J/m^3s]	enthalpy combustion source term
$S_{comb,Yi}$	[kg/m^3s]	combustion species source term
S_p	[J/m^3s]	enthalpy particle source term
$S_{p,Yi}$	[kg/m^3s]	particle species source term
S_μ	[kg/m^2s^2]	viscosity term
Y_i	[kg/m^2s]	mass fraction of the species i
c	[-]	force coefficient
d	[m]	diameter
g	[m/s^2]	gravity
h	[J/kg]	relative enthalpy
p	[Pa]	absolute pressure
t	[s]	time
$\underline{u}$	[m/s]	gas phase velocity
α	[W/mK]	thermal conductivity
δ	[-]	Kronecker delta
ε	[-]	gas volume fraction
μ	[Pas]	gas phase viscosity
ρ	[kg/m^3]	gas phase density

Subscripts and Superscripts

comb	combustion
p	particle
eff	effective, from the turbulence model
i, j,m	direction index

1. INTRODUCTION

Shaft furnaces use off-gas to preheat the granular product in the top part of the furnace and use the hot product after the burning zone to preheat the combustion air. This direct heat exchange leads to energy efficiency and wide use in high-temperature processes handling granular materials. Due to the constantly moving granular material, measurements inside shaft furnaces are difficult and often the temperature profile, one of the key parameters for energy efficiency of those furnaces is unknown in industrial processes.

To model the temperature profile of shaft furnaces, the movement of the granular phase in combination with combustion, flow, and heat transfer by convection and radiation must be considered. The combustion and geometry of the burner nozzles need an according mesh resolution, often smaller than the particles. To avoid the computing-intensive resolved Discrete Element Method (DEM) approaches, the Volume Fraction Smoother (VFS) was created by Pollhammer [1]. This approach shifts the volume fraction in the grid to neighbour cells to create the structure of the particle bed. To further reduce the transient calculation time of the furnace, Timescale Splitting Method (TSSM) was introduced. This method corrects fluxes to different time scales for the heat up of the particles.

2. MODEL DESCRIPTION

2.1. Granular phase

2.1.1 Particle flow

For the particle movement and collisions, the in OpenFOAM 2.4.0 [2] implemented "basicKinematicCollidingCloud" was used. This model calculates the particle contact forces with the Pair–Spring–Slider–Dashpot Model by Cundall and Strack [3]. To increase the collision time step, the Young's modulus of the particles was decreased from $2.00 \cdot 10^{11}$ Pa to $3.77 \cdot 10^{8}$ Pa so that the particles at the bottom of the furnace overlap by max. 2 %. Höhner [4] showed that an overlap of 2 % has no significant impact on the granular flow. The fluid-particle interaction forces on the particles were modelled by the Ergun–Wen–Yu–Drag model implemented in OpenFOAM [2].

2.1.2 Particle-particle heat transfer

For modelling the conductive heat transfer between individual particles, the thermal resistance between overlapping particles was modelled based on the approach of Zhang et al. [5]. Because the particles were softened, the contact areas were calculated by the forces, using the unsoftened Young's modulus. To evaluate the sub-model, the heat flux between two steel particles, with a diameter of 19.8 mm and fixed contact forces, was compared to the measurements by Kuwagi et al. [6] (Figure 1). The given implementation in the model underestimates the rate of heat flow between paricles slightly for high contact forces.

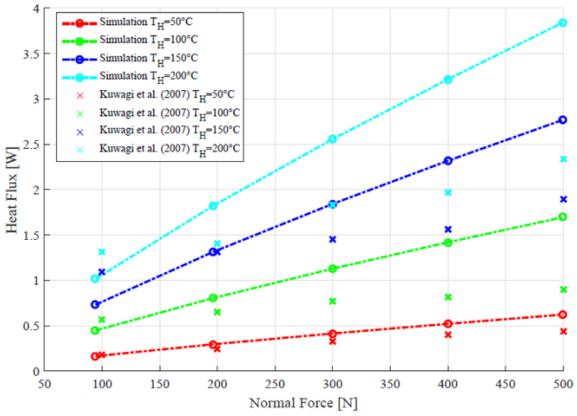

Figure 1. Comparison of the rate of heat flow for different normal forces between the presented model and the measurements of Kuwagi et al. [6]

The dominating mechanism for particle-particle heat transfer in a shaft furnace is radiation. To model the radiation between particles in a packed bed, shadowing must be considered. Feng and Han [7] calculated the view factors between individual particles in a monodispersed packed bed, considering shadowing effects. These results are implemented by a fitted function in the model. The assumption of a monodisperse bed is valid for a refractory shaft furnace due to its narrow size distribution. Yagi and Kunii et al. [8] measured the effective heat conductivity of 11 mm iron spheres in a packed bed. This setup was used to evaluate the particle-particle heat transfer by radiation and conduction. The comparison in Figure 2 shows that the model can predict the effective heat conductivity inside the uncertainty of different measurements from 400 K to 1100 K.

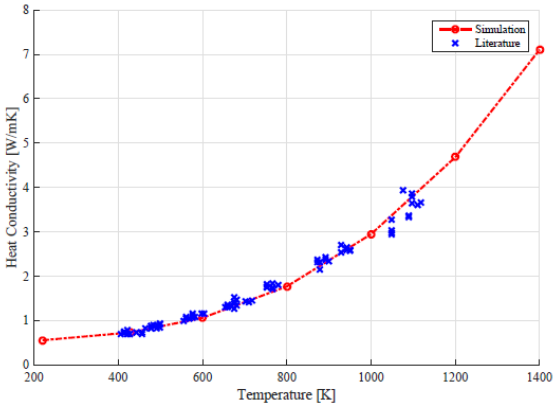

Figure 2. Comparison of the model to the measurements of Yagi and Kunii [8].

2.2. Gas phase

2.2.1 VFS

In the presented model, the particles are none resolved in the CFD grid and lager than the cells. This could lead to a particle volume fraction larger than 1 in certain cells. The rest of the cells have a volume fraction of 0 (Figure 3 a.)). To obtain a physical correct volume fraction, Pollhammer [1] developed the VFS. The basic idea is to displace the volume fraction in neighbour cells, over a pre-defined volume fraction threshold of 0.9. (Figure 3 b.)). The neighbour cells reach in this step a volume fraction over the threshold and the smoothing and the process is continued, till all cells have a volume fraction smaller than the defined threshold. The smoothing algorithm is used at the beginning of each time step.

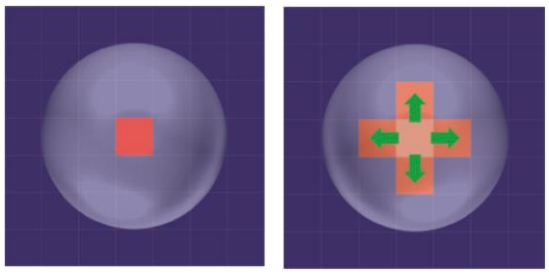

a.) Initial volume fraction

b.) First smoothing iteration

c.) Second smoothing iteration

d.) Final smoothing iteration

Figure 3. Schematic explanation of the Volume Fraction Smoother algorithm [1]

2.2.2 Flow

Shaft furnaces are only partially filled with particles. So, the gas phase momentum balance equation must differentiate between the packed bed and free fluid flow. If the particle volume fraction in a cell is higher than 0.1 the approach for the packed bed is used. The momentum equation (equation 1) uses different viscosity terms S_μ based on the regime.

$$\frac{(\partial \rho \varepsilon u_i)}{\partial t} + \frac{\partial}{\partial x_j}(\rho \varepsilon u_j u_i) + S_\mu = -\frac{\partial p}{\partial x_i}\varepsilon + \rho g_i \varepsilon \tag{1}$$

For the free flow regime, a turbulence-based viscosity pressure drop equation (equation 2) is used. To model the effective viscosity μ_{eff}, sum of laminar viscosity and turbulent viscosity, the standard k-ε model [9] is used.

$$S_\mu = -\mu_{eff}\left(\frac{\partial u_i}{\partial x_j}\varepsilon + \frac{\partial u_j}{\partial x_i}\varepsilon\right) + \frac{2}{3}\mu_{eff}\frac{\partial u_m}{\partial x_m}\varepsilon\delta_{ij} \tag{2}$$

In the packed bed regime, the Ergun equation (equation 3) is used to model the pressure drop.

$$S_\mu = \left[150\frac{(1-\varepsilon)^2}{\varepsilon^3}\frac{\eta_f U_{sf,i}}{d_P^2} + 1.75\frac{1-\varepsilon}{\varepsilon^3}\frac{\rho_f U_{sf,i}|\vec{U_{sf}}|}{d_P}\right]\frac{1}{\varepsilon(1-\varepsilon)} \tag{3}$$

To evaluate the implemented model, an experiment was set up, using a 145 mm high packed bed of 14 mm glass speres and a 155 mm free flow region. The pressure drop for different superficial velocities was measured. This bed was modelled using the VFS and a resolved DEM approach. As shown in Figure 4 both models show a good comparison to the experimental data. The Ergun equation deviates at higher superficial velocities, due to wall effects on the volume fraction.

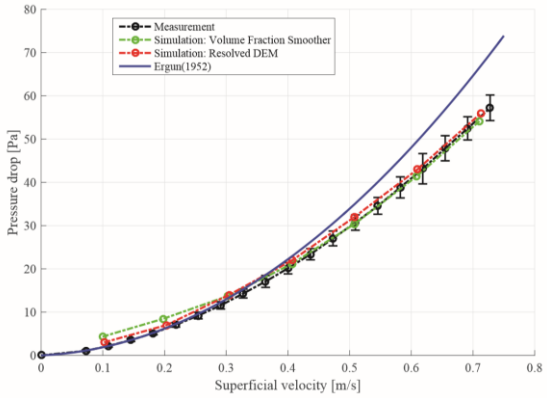

Figure 4. Comparison of the pressure drop as function of superficial velocity between measurements, the Volume Fraction Smoother, resolved DEM and the Ergun equation in a packed bed of 14 mm glass spheres.

2.2.3 Enthalpy

The equation for the enthalpy (equation 4) is adapted for the gas phase volume fraction ε and has a source term for the heat of combustion S_{comb} modelled from the combustion model, corrected by the gas phase volume fraction and the source for the practice-gas heat transfer S_p. This source term is modelled using a heat exchange model by Gunn et al. [10].

$$\frac{\partial}{\partial t}(\rho\varepsilon h) + \nabla\cdot(\rho\varepsilon u h) - \nabla\cdot(\alpha_{eff}\varepsilon\nabla h) = S_p + \varepsilon S_{comb} \tag{4}$$

2.2.4 Species

The species equations (equation 5) have a similar structure as the energy equation (equation 5). The particle source term $S_{p,Yi}$ describes the emitted or consumed gas from a particle due to drying or chemical reaction. The source term for the combustion $S_{comb,yi}$ calculated by the combustion model and must be corrected by the gas phase volume fraction ε.

$$\frac{\partial}{\partial t}(\rho\varepsilon Y_i) + \nabla\cdot(\rho\varepsilon u Y_i) - \nabla\cdot(\mu_{eff}\varepsilon\nabla Y_i) = S_{p,Y_i} + \varepsilon S_{comb,Y_i} \tag{5}$$

2.2.5 Combustion

To model the chemical reactions of the combustion process, the in OpenFOAM [2] implemented Partially Stirred Reactor model (PaSR) by Peng and Kärrholm [11] is used. To ensure reasonable computing effort the 4-step global mechanism by Jones and Lindstedt [12] is in use.

2.3 TSSM

The model of the shaft furnace is transient. In the industrial process, the particles have a residence time of approx. 6 hours in the furnace. To reach a quasi-steady state condition in the furnace, Pollhammer [1] developed the TSSM. The unaccelerated timestep is used for the gas phase equations and the collision substyles for the granular phase. For the particle fluxes, an accelerated timescale is introduced. The relation between the timescales is called the acceleration factor and all particle fluxes like heat, species, and the mass flow of particles into the furnace are multiplied by this pre-defined factor.

To evaluate the TSSM, the heat-up of a fixed bed, with a hight of 150 mm was simulated, with and without time scale splitting. The particles in his bed have a diameter of 10 mm, and a temperature of 300 K as the initial condition. Air with a superficial velocity of 0.5 m/s and a temperature of 400 K is injected from the bottom of the bed. Figure 5 compares the particle temperatures at 20 mm, 50 mm, and 100 mm bed height, between the unaccelerated case and by using the TSSM with an acceleration factor of 200. The maximum deviation between the cases is 8 % for the particles at 100 mm. The calculation time using the TSSM with a factor of 200 can be reduced to 2 % in this test case.

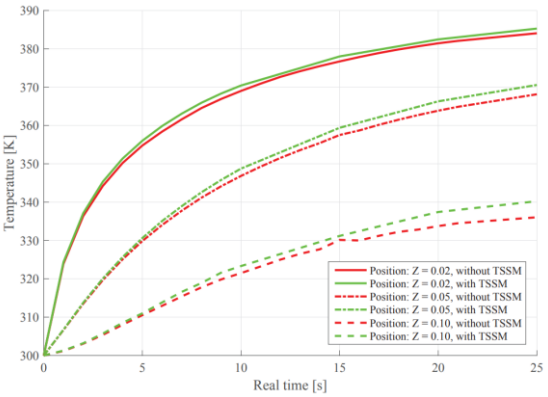

Figure 5. Comparison of the temperatures in a packed bed, with and without using the TSSM.

3. SHAFT FURNACE

The presented shaft furnace is used for spinel production, where the crystal structure is changed at 2130 K and no heterogeneous reactions occur. The furnace has a hight of 10 m and an inner diameter of 0.85 m. 3000 kg/h particles with a diameter range from 16 mm to 19.5 mm feed from the top by hopper (Figure 6). The off-gas is extracted with a side pipe under the hopper. At the height of 8 m, 12 premixed air-natural gas burners with a diameter of 15 mm are installed, flush fitting to the wall in a circular arrangement (Figure 6). The particles are extracted at the bottom of the shaft, and 2000 Nm³/h secondary air is fed into the furnace.

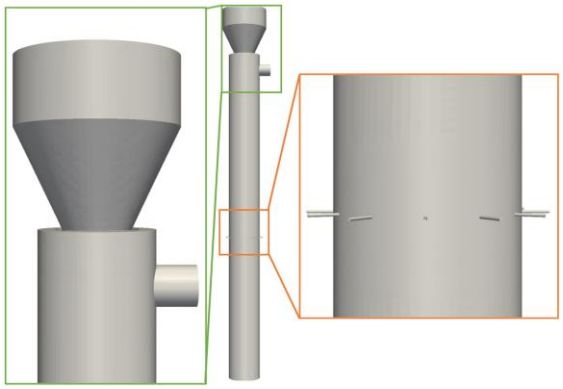

Figure 5. The geometry of the shaft furnace. At the top the feeding hopper and the exhaust pipe are shown (green). In the middle section 12 premixed burners are installed (orange).

The mesh of the furnace consists of 6.3 million hexahedral cells. The furnace is filled with approx. 1.8 million particles. For the simulation an acceleration factor of 678 for the TSSM was used.

4. RESULTS

The temperature profiles of the gas and particle phase (Figure 6) show a nearly identical profile due to the high heat transfer coefficients, ranging from 120 W/m²K to 300 W/m²K. The particles reach a maximum temperature of 2243 K at the reaction zone of the burners. In the centre of the furnace, at same height the temperature reaches 2209 K. These results agree with the operation window of the furnace. The minimum temperature for changing the crystal structure is 2130 K and the maximum temperature is limited by the solidus temperature of the particle at 2320 K. The dominant heat transfer mechanism in the hotter sections of the furnace is particle-particle radiation, leading to a low radial temperature gradient. The radial temperature profiles form in the top and bottom sections, where the temperatures are lower and particle-particle radiation is less dominant. The particle-particle conduction has no significant impact on the temperature profile due to the low heat fluxes in comparison to the radiation at the high temperatures in the furnace.

The pressure drop between the exhaust duct and the secondary air inlet, at the bottom of the furnace, is predicted with 67×10^3 Pa. The control system of

the furnace measures an average pressure drop of 62×10^3 Pa.

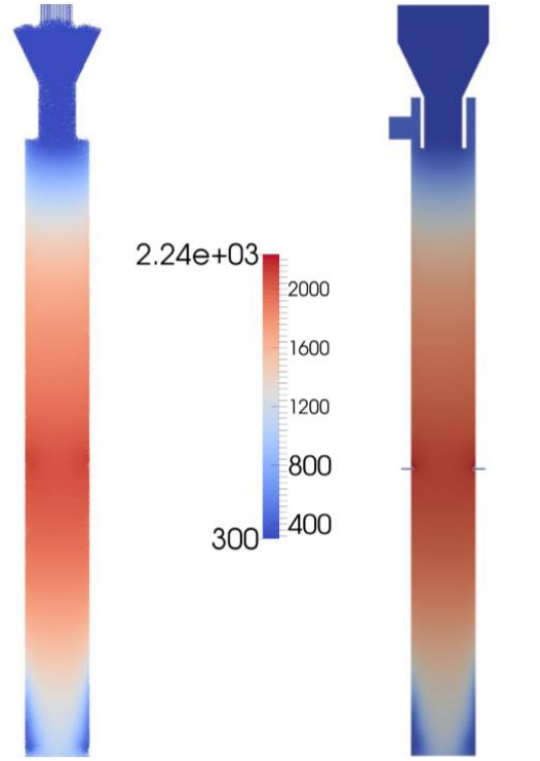

Particle temperature [K]

Gas phase temperature [K]

Figure 6. Left, modelled particle temperature in the furnace. Right, modelled gas phase temperature in the furnace.

5. SUMMARY

Modelling an industrial shaft furnace with a CFD-DEM approach is challenging due to the large number of particles and long process times. The granular phase in the presented spinel shaft furnaces is modelled by 1.8 million particles. To avoid using a resolved DEM approach, the VFS was developed. This approach is able to predict the pressure drop and fluid flow in the packed bed. This was shown by modelling lab-scale test and the industrial furnace. To avoid the transient modelling of long process times, the TSSM was developed. This method separates the timescales and corrects the fluxes accordingly. This allows to reduce the processing time that has to be modelled by a factor of up to 680. The method showed up to an 8 % temperature difference for the transient heat up of particles compared to DEM without TSSM. This difference should decrease when a quasi-steady-state condition is achieved, like in the shaft furnace. The model predicted maximal temperatures inside the operation window of the furnace from 2130 K to 2320 K. A weak point of the model presented is the implementation of combustion. The combustion model considered is basically valid for turbulent combustion in an unconfined space. However, in the void spaces among the particles the heat released by the combustion process is absorbed quickly by the neighbouring particles. This effect should be considered in the combustion model and is part of our future work. For the shaft furnace, this assumption is not a significant impact. The heat of combustion process is rapidly distributed due to the particle-particle radiation. In the future, an improvement of the combustion model is intended.

REFERENCES

[1] Pollhammer, W. R., 2019, „A CFD–DEM model for nitrogen oxide prediction in shaft furnaces using OpenFOAM", *PhD Thesis, Montanuniversitaet Leoben, Chair of Thermal Processing Technology*

[2] The OpenFOAM Foundation Ltd., Openfoam 2.4.x, 2015 , URL https://github.com/OpenFOAM/OpenFOAM-2.4.x.

[3] Cundall, P. A., and Strack, O. D. L., 1979 "A discrete numerical model for granular assemblies", *Geotechnique*, Vol. 29, pp. 47–65

[4] Höhner, D., Wirtz, S., and Scherer, V., 2013, „Experimental and numerical investigation on the influence of particle shape and shape approximation on hopper discharge using the discrete element method", *Powder Technology, Vol.* 235, pp: 614–627

[5] Zhang, X., Cong, P., Fujiwara, S., and Fujii, M., 2002, *Thermal Science and Engineering*, pp. 11–12

[6] Kuwagi, K., Mokhtar, M. A. B., Takami, T., and Horio, M., 2007 "Analysis of heat transfer between two particles for dem simulations", *12th international conference on fluidization*, New York, pp. 241–248

[7] Feng, Y. T., and Han, K., 2012 "An accurate evaluation of geometric view factors for modelling radiative heat transfer in randomly packed beds of equally sized spheres", *International Journal of Heat and Mass Transfer*, Vol. 55, pp. 6374–6383

[8] Yagi, S., and Kunii, D., 1957 "Studies on effective thermal conductivities in packed beds" *AIChE Journal*, Vol. 3, pp. 373–381

[9] Launder, B. E.; and Spalding, D.B., 1974, "The numerical computation of turbulent flows". *Computer Methods in Applied Mechanics and Engineering*. Vol. 3, pp. 269–289

[10]Gunn, D. J.,1978, “Transfer of heat or mass to particles in fixed and fluidised beds”, *International Journal of Heat and Mass Transfer*, Vol. 21, pp. 467–476

[11]Kärrholm, P. F., 2008, “Numerical modelling of diesel spray injection, turbulence interaction and combustion”. *PhD Thesis, University Göteborg*

[12]Jones, W. P., and Lindstedt, R. P., 1988, “Global reaction schemes for hydrocarbon combustion”, *Combustion and Flame*, Vol. 73, 1988, pp. 222–233

Conference on Modelling Fluid Flow (CMFF'22)
The 18th International Conference on Fluid Flow Technologies
Budapest, Hungary, August 30 -September 2, 2022

EXAMINATION OF SAHARAN BOUNDARY LAYER BY A SINGLE-COLUMN AND 3D WRF MODEL – A CASE STUDY FOR FENNEC CAMPAIGN

Árpád BORDÁS[1], András Zénó GYÖNGYÖSI[2], Tamás WEIDINGER[2]

[1] Corresponding Author. Department of Meteorology, Institute of Geography and Earth Sciences Faculty of Sciences, Eötvös Loránd University, Pázmány Péter sétány 1/A, H-1117 Budapest, Hungary. Tel.: +36 1 372 2545, E-mail: bordas.arpad@gmail.com
2 Department of Meteorology, Institute of Geography and Earth Sciences Faculty of Sciences, Eötvös Loránd University, Pázmány Péter sétány 1/A, H-1117 Budapest, Hungary. Tel.: +36 1 372 2545, E-mail: gyzeno@caesar.elte.hu, weidi@staff.elte.hu

ABSTRACT

Understanding of the atmospheric boundary layer (ABL) processes, as well as description of the layer characteristics and vertical structure above deserts is very important for investigation of effects of deserts on weather, climate and transport of mineral dust. According to high insolation and lack of moisture Saharan boundary layer is the one of the deepest on the Earth. The aim of our study is to examine structure of the Saharan boundary layer and temporal evolution of the ABL height employing a single-column ABL model and the 3D Weather Research and Forecasting (WRF) model. WRF runs were done using the telescopic nesting method and 4 different ABL parameterization setups. Model outputs were compared with radiosonde data obtained during Fennec campaign (2011).

Keywords: Saharan boundary layer, shallow convection, single-column ABL model, 3D WRF model, Fennec campaign

1. INTRODUCTION

Sahara, the largest hot desert on the Earth, plays a key role in regional and global climate process [1], and represents the largest source of mineral dust on the planet [2,3]. North African dust hot spots located in the Sahara and Sahel contribute to 50–70% of the global mineral dust budget [4,5]. The dust travels through the Atlantic Ocean to North and South America, but it also affects Europe's air pollution conditions. In the 40-year time period from 1979 to 2018 more than 200 North African dust events were detected in the Carpathian Basin (Central Europe) [5].

As a result of the extreme near-surface temperatures the Saharan ABL commonly reaches 5–6 km [6] making it probably the deepest on the Earth. The Saharan boundary layer is characterized with a particular structure [7]. The morning and midday, relatively shallow, convective layer is capped by a narrow (about 100 m deep) temperature inversion. The inversion layer separates convective layer from a deep near neutral residual layer formed by the previous day's completely developed convective boundary layer. The three-layered (well-mixed convective layer, weak inversion and weakly stable residual layer) potential temperature structure allows detrainment of the warmest plumes across the weak temperature inversion, which slows down the growth of the convective layer. As the boundary layer grows overshooting plumes can also entrain the free atmosphere. The convective layer often reaches its full extent only in the late afternoon. Observations show that the residual layer sometimes persist over large areas throughout the day, the boundary layer depth varies by up to 100% over horizontal distances of a few kilometers [8]. This effect can be connected with subsidence, caused by circulations induced by albedo variations [9], or by effects of orography [10].

The goal of our work is to examine vertical structure of the Saharan boundary layer and the layer's diurnal variation employing a simple single-column (1D) ABL model [11] and the 3D WRF model [12]. WRF runs were done by 4 different boundary layer parameterization setups using telescopic nesting method. Modelled vertical profiles and estimated boundary layer depths were compared with radiosonde measurement data obtained in Fennec campaign [13]. The Fennec program is a large-scale, international observational and modelling project that aimed to produce the most comprehensive dataset of the central Saharan atmosphere. The goals of the program are to derive a definitive dataset for central Sahara from ground, aircraft and satellite observations, to characterize structure of the central Sahara's atmosphere, to

quantify weather prediction and climate model errors, as well as to establish mechanisms of mineral dust emissions in 2011 and 2012.

2. INVESTIGATION METHODS

2.1. Observations – The Fennec Program

Despite the Sahara's importance to Earth's climate, routine meteorological measurements are one of the sparsest of any landmass and the few data that exists is mostly from the periphery of the desert [14]. During the intensive Fennec observation periods (June 2011 and June 2012) two grounds based manned supersites and an automatic weather station network, containing eight stations across the Sahara [15], were provided the measurement data. The supersites were located at Bordj Badji Mokhtar (BBM) (in the very south of Algeria, circa 300 km northwest from the triple point of Algeria, Mali and Niger – 21.37°N 0.93°E, see Figure 1.) close to the climatological location of the Saharan heat low [7,8], as well as farther west at Zouérat (Mauritania – 22.68°N 12.47°W) [16]. Instrumentation at supersites included a flux tower, aerosol sampling equipment, 4 to 8 radiosondes daily, lidar and sodar. Radiosondes were also released at higher frequency across the Algerian network.

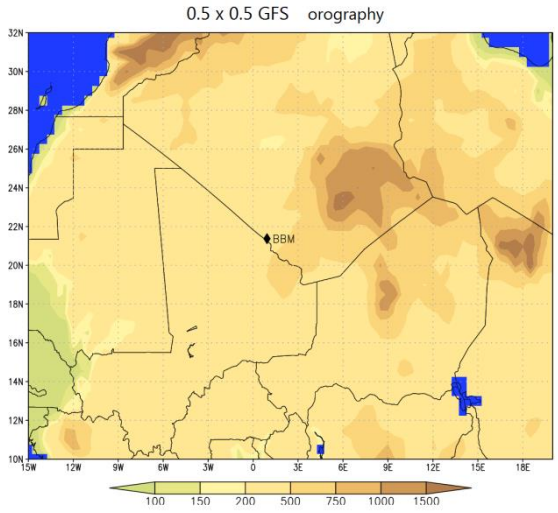

Figure 1. Location of the BBM supersite on the high resolution model orographic map.

The ground based campaign was complemented by several aircraft campaigns. The instrumented UK FAAM BAe-146 aircraft flew into the central Sahara from Morocco in April 2011 and from the Fuerteventura base in June 2011 and June 2012. The June 2011 campaign also included the instrumented French Falcon F20. Over all campaigns, more than 200 hours of science flights were conducted, included the first-ever flights to sample vertical structure of the Saharan ABL using an extensive suite of onboard instrumentation. Approximately 300 dropsondes were also released [7, 13].

2.2. The Single-Column Model

Single-column models (SCM) are very useful tools in ABL investigation. Such models are comprehensive enough to illustrate basic ABL characteristics, describe vertical structure and model turbulent boundary layer processes. The used single-column model [11, 17] employs a first order turbulence closure and a combined (local and nonlocal) mixing scheme [18]. In stable and neutral static conditions, turbulent mixing is simulated as a subgrid (local) process. During unstable conditions, depending on the calculated ratio between local and nonlocal mixing of heat, the model simulates turbulent mixing of sensible heat, moisture, and momentum as a split between small scale and large scale processes. The height of the ABL, one of the mean characteristics of the boundary layer, shows a strong diurnal variation. The model determines the ABL height by specifying a critical value of the bulk Richardson number. The model was verified by controlled offline numerical experiments and the Wangara database [19]. Employing the single-column model vertical potential temperature profiles were calculated and the height of the Saharan boundary layer was estimated.

2.3. The 3D WRF Model

The WRF model [12] developed by UCAR (University Corporation for Atmospheric Research) is a well-established, tested, and documented, non-hydrostatic, mesoscale meteorological model, applicable for both atmospheric research and weather forecasting purposes ranging from micro to global scales. Its modularity and flexibility together with its detailed documentation, as well as a possibility to compare different parameterization processes suited well for the needs of our purposes.

Advanced Research WRF (ARW) core, versions 3.5 (release April 18, 2013), later version 3.9 have been applied to generate numerical input for our NWP system. Input geographical dataset have been generated from USGS (United States Geological Survey) dataset originally used by WRF in 0.5° × 0.5° resolution (see Figure 1.). According to our previous WRF investigations [20] three level telescopic nesting was applied ranging from 27 km in the coarsest domain (d01) through 9 km in the intermediate domain (d02) to 3 km horizontal resolution in the high resolution lowest nested domain (d03) that is located in BBM. The aim behind the nesting is to increase spatial resolution just in the central model domain with the idea to optimise computing time. Telescopic nesting is shown in Figure 2. The number of vertical levels was 30, the top level was on 50 hPa. GFS data with

0.25º × 0.25º resolution was applied as initial and boundary conditions for the limited area integration of the outermost domain in every 3 hours, with no additional data assimilation. Using the same physical parameterizations and four different ABL parameterizations vertical potential temperature profiles and diurnal variation of the ABL height were obtained and examined.

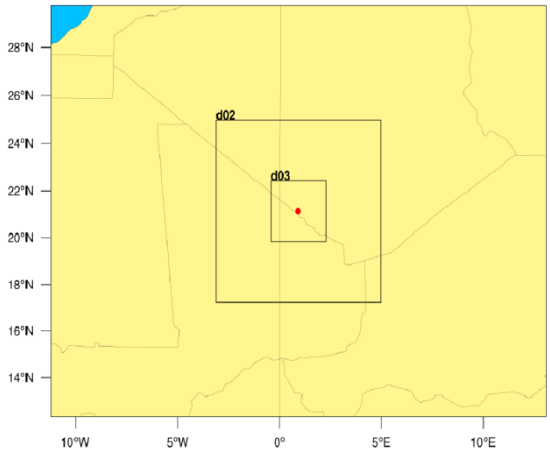

Figure 2. The telescopic three level nested model domains.

3. RESULTS

The SCM was initialized with a 0.5 Hz radiosonde data (potential temperature, water vapor mixing ratio and horizontal wind components) obtained at 0900 UTC 20 June 2011 from the BBM supersite using Vaisala RS92 sonde. This day was chosen because the midday temperature profile was representative of a typical Saharan ABL and the height of the boundary layer exceeds 5000 m by the end of the day, with little influence from synoptic processes [7]. The time variation of the observed quantities at the lowest model level was set explicitly as a lower boundary condition in the model.

Due to the available Fennec data the model was run from 0900 to 1800 UTC. According to previous single-column model investigations [7] calculations were done by a 50 m vertical model resolution and 1 minute time step. ABL depth was calculated every 10 minutes. The model determines the ABL height by specifying a critical value of the bulk Richardson number which was set to 0.25.

Figure 3. compares measured and modelled virtual potential temperature profiles. As it was expected [7] the simple SCM predicts more slowly grow of the ABL in the morning period from 0900 to 1200 UTC. Very rapid growth of the ABL is obtained from 1200 to 1400 UTC. The convective boundary layer reaches maximum height about 1500 UTC and shows no significant structural changes before the evening collapse.

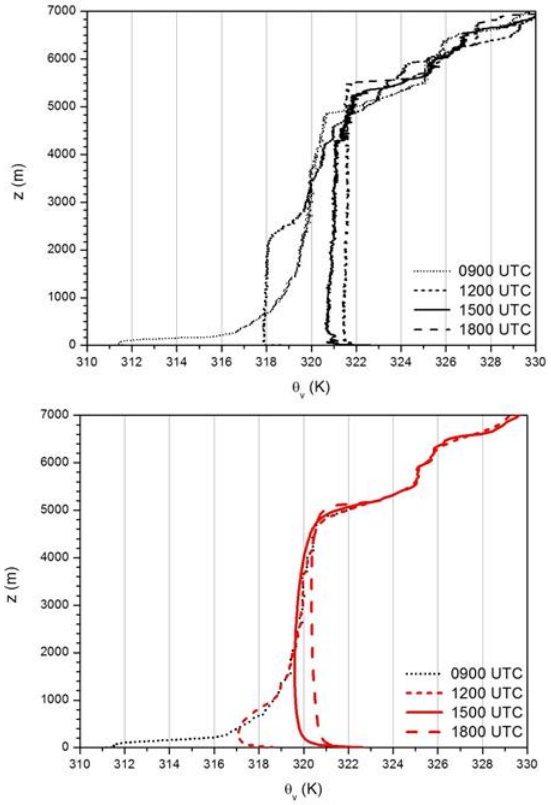

Figure 3. Radiosonde (above) and SCM (below) virtual potential temperature (θ_v) profiles.

Figure 4. represents ABL heights estimated using radiosonde data and calculated by SCM. Due to slowly morning growth of the convective layer our model failed to reproduce the fine vertical structure of the particular boundary layer and underestimates ABL height in the morning period. In the afternoon when the deep Saharan boundary layer was formed the SCM slightly underestimates ABL height.

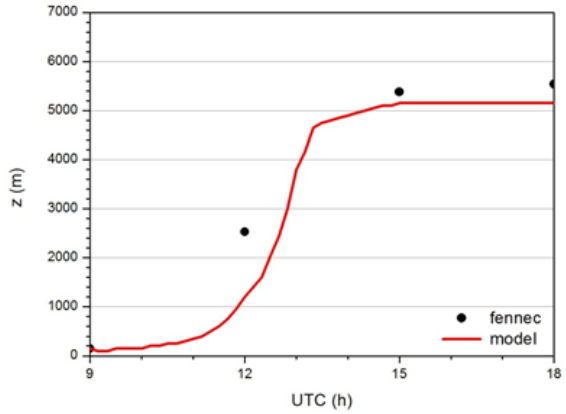

Figure 4. Temporal evolution of the estimated (radiosonde) and predicted (SCM) height of the ABL.

3D WRF runs were performed using the following settings [12]: WRF single–moment 3–class and 5–class schemes for microphysics (option 4), RRTMG shortwave and longwave schemes (option 4), Unified Noah land surface model (option 2), Kain–Fritsch scheme for cumulus parameterization (option 1) expect the high resolution telescopic domain (d03) where the cumulus parameterization was turned off (option 0). We used 4 different boundary layer schemes with the idea to compare potential temperature profiles obtained by different types of description of the mixing processes in the boundary layer. Model runs were done by the following schemes: Yonsei University Scheme (option 1, T1), Mellor-Yamada-Janjic scheme (option 2, T2), Mellor-Yamada Nakanishi Niino level 2.5 scheme (option 5, T3) and asymmetric convection model 2 (option 7, T4).

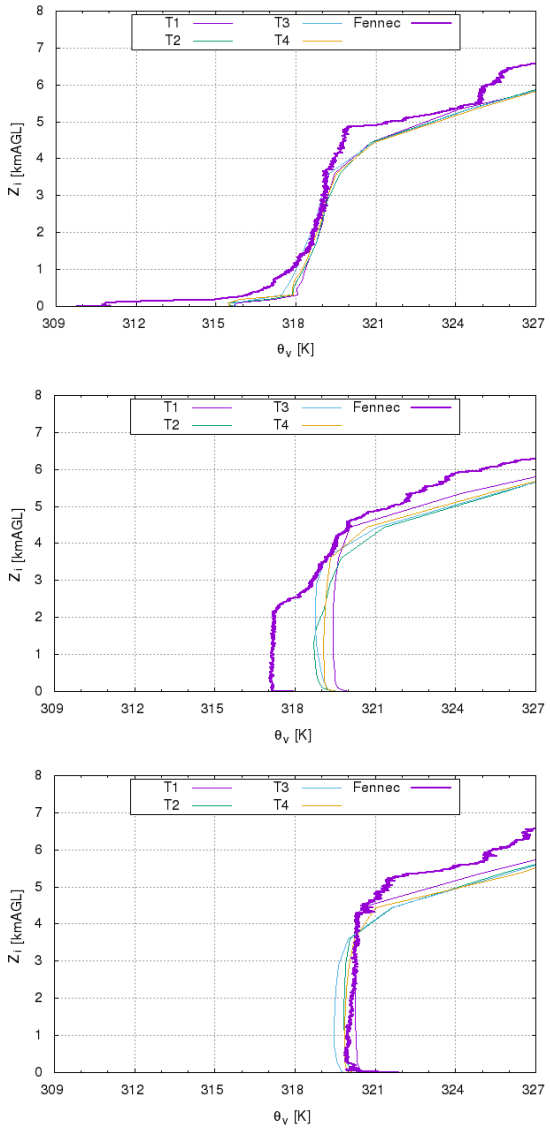

Figure 5. Modelled (3D WRF for BBM) and measured (radiosonde) potential temperature (θ_v) profiles for 0900 UTC (above), 1200 UTC (in the middle) and 1500 UTC (below).

Figure 5. presents comparison between potential temperature profiles for BBM simulated by WRF model using different mixing schemes and measured radiosonde data. Due to higher near surface temperatures at 0900 UTC modelled profiles show earlier formation of the convective layer and overestimate ABL height at 1200 UTC. Furthermore, predicted profiles for 1500 UTC are very close to observations, but underestimate the ABL height.

Figure 6. shows diurnal course of the modelled WRF ABL heights from 0600 to 2100 UTC, and compares model results with radiosonde data estimations. Using all the ABL mixing schemes WRF runs predict rapid formation of the convective ABL from 0900 to 1100 UTC, the layer reaches its full extent to 1200 UTC. Period from 1200 to 1700 UTC is characterized by minor changes in ABL height estimation. Collapse of the boundary layer is predicted around 1800 UTC by all the used schemes. Comparing to observational radiosonde data the model runs predict earlier timing of formation of the convective layer and collapse of the Saharan boundary layer, as well as underestimate maximum ABL height.

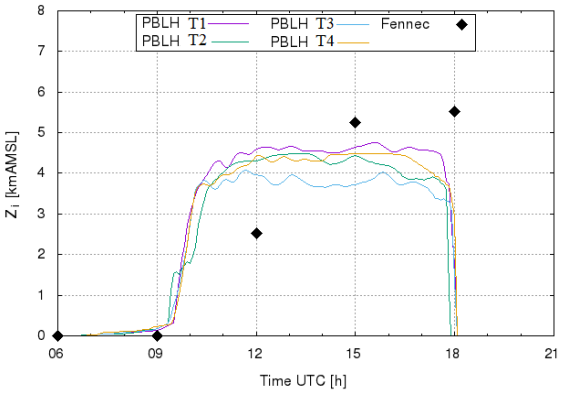

Figure 6. Courses of the estimated (radiosonde) and modelled (3D WRF for BBM) ABL heights.

5. SUMMARY AND CONCLUSIONS

Sahara desert plays crucial role in our climate system. Description of Saharan ABL and simulation of boundary layer processes is very important for weather prediction and environmental modelling. We examined one of the deepest ABL on the Earth employing SCM and 3D WRF model (by telescopic nesting and 4 different mixing schemes). Modelled virtual potential temperature profiles were compared to radiosonde data obtained in Fennec campaign (20 June 2011).

During the formation of the convective layer (from 0900 to 1200 UTC) our SCM failed to reproduce rapid grow and the fine vertical structure of the particular Saharan ABL, as well as underestimates ABL height. In the afternoon when the convective ABL was formed compared to

radiosnde measurements underestimation of ABL height is negligible.

3D WRF model runs predict very early grow of the convective ABL and overestimate ABL height in the morning period. During the afternoon model predictions underestimate ABL heights and show early collapse of the boundary layer. Our plan is to perform further WRF simulations with different model setups for the defined Sahara region.

ACKNOWLEDGEMENTS

The authors would like to thank Douglas Parker (University of Leeds) for provided radisonde data, as well as the first author thanks EUfar for the financial support and opportunity to join the June 2011flight campaign.

REFERENCES

[1] Haywood, J., and O. Boucher, 2000, „Estimates of the direct and indirect radiative forcing due to tropospheric aerosols: A review", *Rev. Geophys.*, Vol. 38, pp. 513-543.

[2] Prospero, J.M., Ginoux, P., Torres, O., Nicholson, S.E., and Gill, T.E., 2002, "Environmental characterization of global sources of atmospheric soil dust identified with the Nimbus 7 Total Ozone Mapping Spectrometer (TOMS) absorbing aerosol product", *Rev. Geophys.*, Vol. 40, 1002.

[3] Carlson, T.N., 2016, "The Saharan Elevated Mixed Layer and its Aerosol Optical Depth" The *Open Atmospheric Sci. J.*, Vol. 10, pp. 26-38.

[4] Ginoux, P., Chin, M., Tegen, I., Prospero, J. M., Holben, B., Dubovik, O., and Lin, S.-J., 2001, "Sources and distributions of dust aerosols simulated with the GOCART model", *J. Geophys. Res. Atmos.*, Vol. 106, pp. 20255-20273.

[5] Varga, Gy., 2020, "Changing nature of Saharan dust deposition in the Carpathian Basin (Central Europe): 40 years of identified North African dust events (1979–2018)", *Environ. Int.*, Vol. 139, 105712.

[6] Gamo, M., 1996, "Thickness of the dry convection and large-scale subsidence above deserts", *Boundary-Layer Meteorol.*, Vol. 79, pp. 265-278.

[7] Garcia-Carreras, L., Marsham, J. H., Parker, D. J., Bain, C. L., Milton, S., Saci, A., Salah-Ferroudj, M., Ouchene, B., and Washington, R., 2013, "The impact of convective cold pool outflows on model biases in the Sahara", *Geophys. Res. Lett.*, Vol. 40, pp. 1647-1652.

[8] Marsham, J. H., Hobby, M., Allen, C. J. T., Banks, J. R., Bart, M., Brooks, B. J., Cavazos-Guerra, C., Engelstaedter, S., Gascoyne, M., Lima, A. R., Martins, J. V., McQuaid, J. B., O'Leary, A., Ouchene, B., Ouladichir, A., Parker, D. J., Saci, A., Salah-Ferroudj, M., Todd, M. C., and Washington, R., 2013, "Meteorology and dust in the central Sahara: Observations from Fennec supersite-1 during the June 2011 intensive observation period", *J. Geophys. Res. Atmos.*, Vol. 118, pp.4069-4089.

[9] Marsham, J. H., Parker, D. J., Grams, C. M., Johnson, B. T., Grey, W. M. F., and Ross, A. N., 2008, "Observations of mesoscale and boundary-layer scale circulations affecting dust transport and uplift over the Sahara", *Atmos. Chem. Phys.*, Vol. 8, pp. 6979-6993.

[10] Birch, C. E., Parker, D. J., Marsham, J. H., and Devine, G. M., 2012, "The effect of orography and surface albedo on stratification in the summertime Saharan boundary layer: Dynamics and implications for dust transport", *J. Geophys. Res.*, Vol. 117, D05105.

[11] Bordás, Á., and Weidinger, T., 2015, "Combined closure single-column atmospheric boundary layer model", *Időjárás*, Vol. 119, pp. 379-398.

[12] Skamarock, W. C., Klemp, J. B., Dudhia, J., Gill, D. O., Barker, D. M., Duda, M. G., Huang, X-Y. Wang, W., and Powers, J. G., 2008, "A description of the Advanced Research WRF Version 3." *NCAR Technical Note 475*, 113 pp.

[13] Washington, R., Flamant, C., Parker, D., Marsham, J., McQuaid, J., Brindley, H., Todd, M., Highwood, E., Ryder, C., Chaboureau, J.-P., Kocha, C., Bechir, M., and Saci, A., 2012, "Fennec – the Saharan climate system" *CLIVAR* Exchanges, Vol. 60, pp. 31-33.

[14] Marsham, J. H., Parker, D. J., Todd, M. C., Banks, J. R., Brindley, H. E., Garcia-Carreras, L., Roberts, A. J. and Ryder, C. L., 2016, "The contrasting roles of water and dust in controlling daily variations in radiative heating of the summertime Saharan heat low", *Atmos. Chem. Phys.*, Vol. 16, pp. 3563-3575.

[15] Hobby, M., Gascoyne, M., Marsham, J. H., Bart, M., Allen, C., Engelstaedter, S., Fadel, D. M., Gandega, A., Lane, R., McQuaid, J., Ouchene, B., Ouladicher, A., Parker, D., Rosenberg, P., Sallah-Ferroudj, M., Saci, A., Seddik, F., Todd, M., Walker, D., and Washington, R., 2013, "The Fennec automatic weather station (AWS) network: monitoring the Saharan climate system", *J. Atmos. Ocean. Tech.*, Vol. 30, pp. 709-742.

[16] Todd, M. C., Allen, C. J. T., Bart, M., Bechir, M., Bentefouet, J., Brooks, B. J., Cavazos-Guerra, C., Clovis, T., Deyane, S., Dieh, M., Engelstaedter, S., Flamant, C., Garcia-Carreras, L., Gandega, A., Gascoyne, M., Hobby, M., Kocha, C., Lavaysse, Marsham, J. H., Martins, J. V., McQuaid, J. B., Ngamini, J. B., Parker, D. J., Podvin, T., Rocha-Lima, A., Traore, S., Wang, Y., and Washington, R., 2013, "Meteorological and dust aerosol conditions over the western Saharan region observed at Fennec Supersite-2 during the intensive observation period in June 2011" *J. Geophys. Res. Atmos.*, Vol. 118, pp. 8426-8447.

[17] Bordás, Á., and Weidinger, T., 2012, "Analysis of the local versus nonlocal behaviuor of the mixing of heat in the convective boundary layer", *15th Conference on Modelling Fluid Flow*, Budapest, Hungary

[18] Bordás, Á., 2008, "One-column vertical turbulent mixing model for the atmospheric convective layer", *Phys. Scr.*, Vol. T132, 5.

[19] Hess, G. D., Hicks, B. B., and Yamada, T., 1981, "The impact of the Wangara Experiment", *Boundary-Layer Meteorol.*, Vol. 20, pp. 135-174.

[20] Bottyán, Zs., Gyöngyösi, A.Z., Wantuch, F., Tuba, Z., Kurunczi, Z., Kardos, P., Istenes, Z., Weidinger, T., Hadobács, K., Szabó, Z., Balczó, M., Varga, Á., Bíróné Kircsi, A., and Horváth, Gy., 2015, „Measuring and modeling of hazardous weather phenomena to aviation using the Hungarian Unmanned Meteorological Aircraft System (HUMAS)", *Időjárás*, Vol. 119, pp. 307-335.

Conference on Modelling Fluid Flow (CMFF'22)
The 18th International Conference on Fluid Flow Technologies
Budapest, Hungary, August 30 -September 2, 2022

HIGH RESOLUTION EXPERIMENTS WITH THE AROME NUMERICAL WEATHER PREDICTION MODEL OVER HUNGARY

Balázs SZINTAI[1*], Kristóf SZANYI[1]

1 Corresponding Author. Hungarian Meteorological Service (OMSZ), Kitaibel Pál utca 1. H-1024 Budapest, Hungary. Tel.: +36 1 346 4705 E-mail: szintai.b@met.hu
2 Hungarian Meteorological Service (OMSZ), Kitaibel Pál utca 1. H-1024 Budapest, Hungary. E-mail: szanyi.k@met.hu

ABSTRACT

This paper summarizes the developments related to the spatial and temporal upgrade of the AROME non-hydrostatic numerical weather prediction model run at the Hungarian Meteorological Service. Horizontal and vertical resolution of the model is increased from 2.5 km to 1.3 km and from 60 to 90 vertical levels, respectively. Changes in the physical parameterizations related to the resolution increase are described and their impact is demonstrated by verification results from long time periods. It is shown that simulation of cloud cover is highly sensitive to the setting of the microphysical parameterization. The data assimilation system was also adapted to better represent severe weather events. The three hourly assimilation cycle of AROME was increased to an hourly Rapid Update Cycle. Results show that in the case of precipitation and temperature, the use of the hourly assimilation leads to some improvement which is especially useful for the purpose of short-range forecasting and nowcasting.

Keywords: data assimilation, cloud microphysics, numerical weather prediction, physical parameterization, rapid update cycle, verification

1. INTRODUCTION

For this study, the AROME non-hydrostatic high resolution model was used [1]. The development of AROME (Application of Research to Operations at Mesoscale) was initiated at Meteo-France [2] at the beginning of the 2000's and is currently further developed in the ACCORD NWP modelling consortia. The AROME model has three main components: the non-hydrostatic ALADIN dynamical core [3, 4], the atmospheric physical parameterizations, which are taken from the French Meso-NH research model [5] and the SURFEX land-surface model [6]. A mesoscale data assimilation system with a three-dimensional variational (3D-VAR; [7]) scheme for the upper-air and an optimum interpolation [8] technique for the surface analyses provides reliable local initial conditions for the AROME model.

At the Hungarian Meteorological Service (OMSZ) the AROME model is run operationally since 2010 [9]. The model is integrated at 2.5 km horizontal resolution with 60 vertical levels and uses lateral boundary conditions from the IFS (Integrated Forecasting System) model of ECMWF. The AROME assimilation system, using conventional observations (SYNOP, radiosoundings, AMDAR), was operationally implemented in 2013 [10].

Currently, the AROME model is running eight times a day with lead times out to +48 h. The assimilated measurements are extended with Mode-S and GNSS data [11]. On the medium term it is planned to further increase both the model resolution (to 1.3 km) and the frequency of the runs (to hourly forecasts). In this way OMSZ can serve its users with more accurate weather forecasts at higher spatial and temporal resolutions and more frequent updates during the day. Such users are on the one hand internal users (forecasters) responsible for issuing warnings of severe weather and on the other hand external users mainly from the renewable energy industry (operating solar and wind power plants).

2. CHOICE OF PHYSICAL PARAMETERIZATIONS

To reflect users' needs both higher horizontal and vertical resolution of the AROME model was tested. In the horizontal, the resolution was increased from 2.5 km to 1.3 km by keeping the original physical size of the domain, resulting in about four times as much horizontal gridpoints. The number of vertical levels was increased from 60 to 90, resulting in more vertical levels in the Planetary Boundary Layer (PBL) and with the height of the first model level decreasing from 10 m to 5 m. Most of the settings in the dynamical core and physical

parameterizations of this new 1.3 km AROME version are identical with the operational AROME run at Meteo-France [12]. To improve model performance some tuning regarding the microphysics scheme was performed which is described in the following. The goal of these first experiments with the higher model resolution was to get a comparable model performance to the operational 2.5 km AROME. Later, these high resolution model settings were serving as a basis for the high resolution data assimilation experiments (described in Section 3).

2.1. Experimental Setup

The 2.5 km AROME version run operationally at OMSZ applies a diagnostic formulation [13] for the subgrid statistical cloud scheme, while at Meteo-France a prognostic one [14] is used. The two schemes produce a significantly different cloud cover: the diagnostic formulation simulates smooth cloud fields while the prognostic formulation tends to produce a cloud cover value with two categories ("zero or one"), with lower average values.

As in the operational AROME the diagnostic formulation has a positive bias for cloud cover, it was decided that the prognostic formulation is tried for the 1.3 km version (further referred to as "vsig2"). However, this resulted in too low cloud cover, consequently some tuning was applied for the VSIGQSAT parameter. VSIGQSAT is a parameter from the subgrid condensation scheme that is linked to the width of the probability density function (PDF) of the subgrid variance of the saturation departure. This parameter is only used in the case of the prognostic formulation of the statistical cloud scheme. The higher the VSIGQSAT is, the larger the variance of the PDF and it is easier for the model to condense water in a fraction of the grid, thus simulation more clouds. The default value of VSIGQSAT is 0.02 and in the sensitivity experiments a value of 0.06 was tested (referred to as "vsig6").

The first experiments with the higher vertical and horizontal resolution were not using data assimilation, as this would require the recomputation of the background error covariance matrix which in turn needs the running of the model. Atmospheric initial conditions for the 1.3 km AROME runs were interpolated from the IFS forecasts of ECMWF. Initial soil fields (soil moisture and temperature) were interpolated from the operational AROME model on the first day of the experiment and soil was running freely (i.e. without soil assimilation) during the whole experimental interval.

These experimental 1.3 km runs (with 90 levels) were compared to the operational AROME run at 2.5 km and 60 levels (using data assimilation, referred to as "oper") and to a reference 2.5 km run with 90 levels and no data assimilation (referred to as "ref_2.5km90L"). To assess the impact of the subgrid statistical cloud scheme, a run with 1.3 km resolution and the diagnostic cloud scheme was also completed (referred to as "losig_F"). Main settings of these experiments are summarized in Table 1.

Table 1. Main settings of the experiments related to physical parameterizations.

Experiment	oper	ref_2.5 km90L	losig_F	vsig2	vsig6
Resolution	2.5 km	2.5 km	1.3 km	1.3 km	1.3 km
Vertical levels	60	90	90	90	90
Data assimilation	yes	no	no	no	no
Statistical cloud scheme	diag	diag	diag	prog	prog
VSIGQSAT	-	-	-	0.02	0.06

Three longer time periods were run (around 25 days each): in January 2021, in May 2021 and in July 2021. During these periods, 30-hour long forecasts were made starting at 00 UTC each day. Results were basically similar in the three time periods, consequently, in the following only results from the July period are shown. This summer period (from 7 to 28 July) was abounded with high precipitation and other severe weather events.

2.2. Verification

In order to assess the impact of the resolution increase and the physical parameterization tuning to the quality of the forecast, pointwise verification was carried out using the Objective Verification System (OVISYS), which is a software developed by OMSZ. OVISYS compares the forecast to the observations measured by the national synoptic stations and calculates different indices (e.g. root mean square error, bias) that can be used to evaluate the quality of the forecast.

Figure 1 shows the impact of the different configurations on the simulation of cloud cover. If we compare "oper" with "ref_2.5km90L" we can note that increasing the vertical resolution increases the cloud cover. If we increase the horizontal resolution as well using the same parameterization settings (comparing "ref_2.5km90L" with "losig_F"), then cloud cover is overestimated even more. If we use the prognostic cloud scheme with the default value of VSIGQSAT ("vsig2") then cloud cover is significantly underestimated. This can be improved by tuning the VSIGQSAT parameter (comparing "vsig2" and "vsig6"). If we compare the "ref_2.5km90L" and "vsig6" experiments, we can conclude that increasing the horizontal resolution and applying the new physical parameterization settings at the same time improves the quality of cloud cover forecasts.

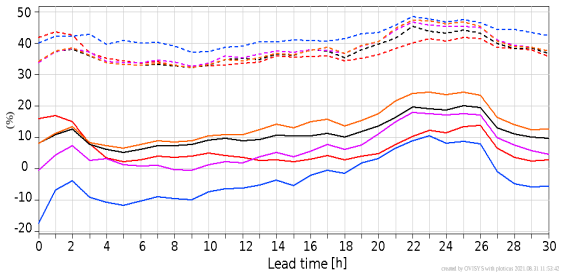

Figure 1. Bias (solid lines) and Root Mean Square Error (dashed lines) of cloud cover from different AROME experiments computed by OVISYS. Experiments: red: "oper"; black: "ref_2.5km90L"; orange: "losig_F"; blue: "vsig2"; purple: "vsig6".

Figure 2 shows the verification scores for 2 metre temperature. For this parameter the "oper" configuration is clearly the best, however, we have to note that this version uses such a 2 metre diagnostic which is not recommended for 90 vertical levels. If we compare only the 90 level configurations, we can conclude that "ref_2.5km90L" is the best, so for 2 metre temperature the higher horizontal resolution does not bring any benefit.

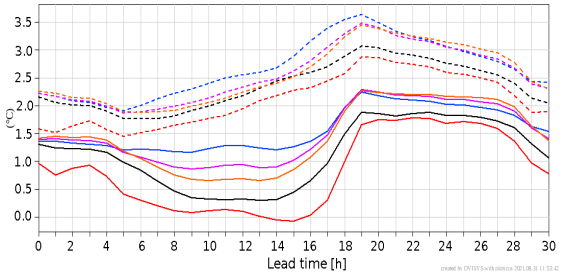

Figure 2. Same as Fig. 1 but for 2 metre temperature.

For the assessment of precipitation forecasts next to the computation of pointwise verification scores (not shown here) a spatial verification method using radar measurements was also applied [13, 14]. For summer convective precipitation, initial conditions are highly important in the first 6-8 hours of the forecast, so we should only compare the experiments without data assimilation (i.e. all experiments except for "oper").

Figure 3 shows the daily evolution of the average intensity of the three strongest precipitation objects. It can noted that the 2.5 km resolution AROME tends to overestimate convective precipitation in the morning hours and during nighttime, while it is more accurate during the afternoon hours. The 1.3 km resolution experiments are close to each other and all of them are underestimating convective precipitation in the afternoon. All model versions simulate the onset of convective precipitation fairly well.

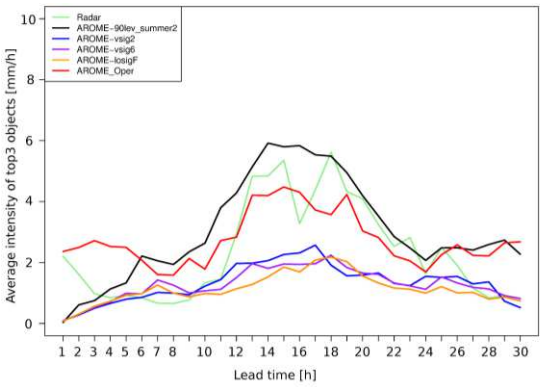

Figure 3. Daily evolution of the average intensity of the three strongest precipitation objects computed from radar measurements (green) and AROME experiments (same colour notation as in Fig. 1).

3. EXPERIMENTS WITH 1-HOURLY CYCLING IN DATA ASSIMILATION

With the introduction of a finer spatial resolution in the AROME numerical weather prediction model, it is possible to improve the quality of some forecast parameters as demonstrated in the previous section. However, there are several examples of specific weather events (especially the ones linked to convection) that demonstrate not only the need to model small-scale phenomena, but also to the need to adapt the time scale of the data assimilation to better represent these events. In addition, the growing number of observations with sub-hourly frequency (e.g. radars, wind profilers, Mode-S datasets) motivates the use of 1-hourly cycling in data assimilation, as it enables the use of the most recent observations in the forecast.

3.1. The Rapid Update Cycle

The Rapid Update Cycle (RUC) is an assimilation method developed by Benjamin et al. [17, 18] with the primary purpose of addressing the above mentioned issues. The 1-hourly RUC is designed to use the most recent observations each hour, which are then combined with the forecast from the previous hour in order to produce a new analysis as an estimate of the current state of the atmosphere. This estimate is then used to produce the background field for the next hour.

In theory, this approach of high-frequency data assimilation is highly beneficial for the purpose of short-range forecasting, however in practice, the use of the 1-hourly RUC does not guarantee more accurate forecasts, especially if the quantity or quality of the high-frequency observations to be used in the RUC are not adequate (see [18] for a detailed description of the potential issues).

3.2. Experimental Setup

Two experimental setups were used in order to assess the impact of applying the 1-hourly RUC. The first experiment (EXP_1.3) was created with 1.3 km horizontal resolution and 90 vertical levels as explained in the previous section, while the second experiment (EXP_2.5) used 2.5 km horizontal resolution with 60 levels. Both experiments were based on the current operational AROME model (OPER) with the common difference being the use of the 1-hourly RUC which is not present in the operational setup. EXP_1.3 was also modified to use the VSIGQSAT value of 0.06 instead of the default value of 0.02 to match the 'vsig6' experiment described in the previous sections which yielded the best results compared to the operational forecast. Based on earlier experiments, a symmetrical assimilation window was chosen: –30 and +30 minutes in hourly RUC experiments, –90 and +90 minutes in the 3-hourly operational forecasts.

The most important parameters for each setup are provided in Table 2.

Table 2. Main parameters of the two experimental setups and the operational AROME model.

Experiment	EXP_1.3	EXP_2.5	OPER
Resolution	1.3 km	2.5 km	2.5 km
Vertical levels	90	60	60
Cycling	1-hourly	1-hourly	3-hourly
Assimilation window	–30 min/+30 min	–30 min/+30 min	–90 min/+90 min
VSIGQSAT	0.06	0.02	0.02

Both experimental setups were run on the three week period (i.e. between 7 and 28 July 2021 with a spin-up period between 1 and 7 July) studied in the previous sections, as the summer forecast may benefit the most from the application of 1 hourly cycling. During this period, 30 hour long forecasts were made at 00 UTC each day.

3.3. Verification

In order to assess the impact of implementing the 1-hourly RUC on the quality of the forecast, pointwise verification was carried out using OVISYS.

It can be concluded that both experiments using the 1-hourly RUC yield somewhat better forecasts than the operational model, albeit the results vary greatly for different meteorological parameters. For instance, Figure 4 illustrates the quality of the 21 hour long forecast of the 6-hourly sum of precipitation using the Equitable Threat Score (ETS). The ETS is an index that compares the given forecast to a fictional random forecast in relation to pre-defined threshold values and by definition gives a value on a scale between –1/3 and 1, where 1 would indicate a perfect forecast and 0 a random forecast (negative values indicate that the given forecast is even worse than a random one). As demonstrated in Fig. 4, the ETS scores for precipitation are the highest for EXP_1.3, while in the case of EXP_2.5 only the scores for the higher precipitation thresholds are improved compared to the OPER. Using different indices and forecast lengths show similar results, therefore it can be concluded that the combination of the high resolution model and the 1-hourly RUC can be expected to improve the quality of the forecast the most, at least in the case of precipitation.

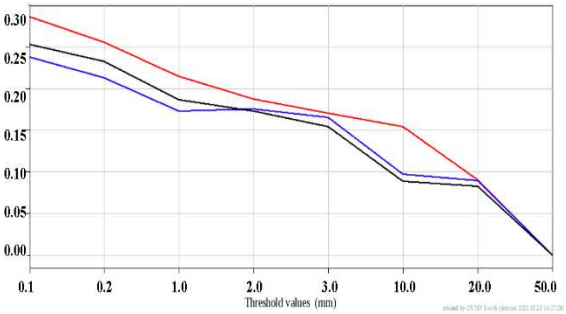

Figure 4. Equitable Threat Scores (ETS) for 21 hour long forecasts of 6 hour sum of precipitation in the EXP_1.3 (red) and EXP_2.5 (blue) experiments and the OPER model (black) in relation to the pre-defined thresholds for precipitation.

Regarding three other parameters, a substantial improvement can be observed in the case of 2 metre temperature (Figure 5), especially in the EXP_1.3 setup.

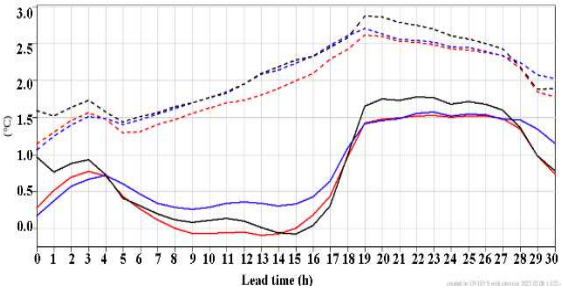

Figure 5. Bias (solid line) and RMSE (dashed line) scores of 2 metre temperature for different forecast lengths in the EXP_1.3 (red) and EXP_2.5 (blue) experiments and the OPER model (black).

In contrast, the cloudiness and 10 metre wind parameters and also the upper level wind forecasts demonstrate much greater errors in both experiments than those observed in the OPER model (Figure 6). Further investigation is needed in

order to determine the cause of this deterioration of wind forecast quality in the 1-hourly RUC setups.

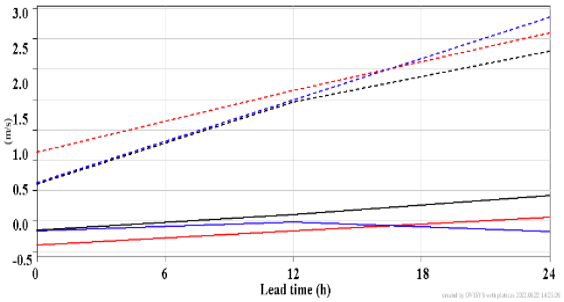

Figure 6. Bias (solid line) and RMSE (dashed line) scores of 925 hPa wind speed for different forecast lengths in the EXP_1.3 (red) and EXP_2.5 (blue) experiments and the OPER model (black).

4. CONCLUSIONS AND PLANS

The present paper describes the experiments of the AROME NWP model using higher horizontal and vertical resolution and associated developments in the data assimilation system.

Regarding the model settings it can be concluded that the resolution increase alone does not necessarily improve the forecasts, however, if certain changes and tunings are applied in the parameterization of microphysical processes then some improvement can be obtained as compared to the operational AROME version.

Based on the verification results, it can be concluded that combining the high resolution AROME model with 1-hourly cycling in data assimilation is a potentially effective way of improving the quality of the forecast. The results shown in this paper suggest that in the case of some meteorological parameters, such as precipitation and temperature, the use of the 1-hourly RUC already leads to some improvement which is especially useful for the purpose of short-range forecasting and nowcasting. However, in order to effectively adapt the RUC into the operational setup, the experimental settings need to be further tweaked to reduce or eliminate the negative impact to cloudiness and wind forecasts. After finding an optimal RUC setup, it may also be beneficial to add more types of observations (e.g. radar and Mode-S datasets) in order to utilise the full potential of the 1-hourly RUC.

ACKNOWLEDGEMENTS

This work has been financed by the Ministry of Innovation and Technology in Hungary. The authors are grateful to Florian Suzat (Meteo-France) for his help in setting up the high resolution model domain for AROME and to Gabriella Szépszó (OMSZ) for useful suggestions about the manuscript.

REFERENCES

[1] Termonia P., C. Fischer, E. Bazile, F. Bouyssel, R. Brožková, P. Bénard, B. Bochenek, D. Degrauwe, M. Derková, R. El Khatib, R. Hamdi, J. Mašek, P. Pottier, N. Pristov, Y. Seity, P. Smolíková, O. Španiel, M. Tudor, Y. Wang, C. Wittmann, and A. Joly, 2018: The ALADIN System and its canonical model configurations AROME CY41T1 and ALARO CY40T1, Geosci. Model Dev., 11, 257-281.

[2] Seity, Y., P. Brousseau, S. Malardel, G. Hello, P. Bénard, F. Bouttier, C. Lac, and V. Masson, 2011: The AROME-France Convective-Scale Operational Model. Mon. Wea. Rev., 139, 976-991.

[3] Bubnová, R., G., Hello, P. Bénard, J.-F. Geleyn, 1995: Integration of the fully elastic equations cast in the hydrostatic pressure terrain-following in the framework of the ARPEGE/ALADIN NWP system. Mon. Wea. Rev., 123, 515-535.

[4] Benard, P., J. Vivoda, J. Masek, P. Smolikova, K. Yessad, C. Smith, R. Brozkova, and J.-F. Geleyn, 2010: Dynamical kernel of the Aladin-NH spectral limited-area model: Revised formulation and sensitivity experiments. Quart. J. Roy. Meteor. Soc., 136, 155-169.

[5] Lafore, J.-P., and Coauthors, 1998: The Meso-NH atmospheric simulation system. Part I: Adiabatic formulation and control simulations. Ann. Geophys., 16, 90-109.

[6] Masson, V., P. Le Moigne, E. Martin, S. Faroux, A. Alias, R. Alkama, S. Belamari, A. Barbu, A. Boone, F. Bouyssel, P. Brousseau, E. Brun, J.-C. Calvet, D. Carrer, B. Decharme, C. Delire, S. Donier, K. Essaouini, A.-L. Gibelin, H. Giordani, F. Habets, M. Jidane, G. Kerdraon, E. Kourzeneva, M. Lafaysse, S. Lafont, C. Lebeaupin Brossier, A. Lemonsu, J.-F. Mahfouf, P. Marguinaud, M. Mokhtari, S. Morin, G. Pigeon, R. Salgado, Y. Seity, F. Taillefer, G. Tanguy, P. Tulet, B. Vincendon, V. Vionnet, and A. Voldoire, 2013: The SURFEXv7.2 land and ocean surface platform for coupled or offline simulation of earth surface variables and fluxes. Geosci. Model Dev., 6, 929-960.

[7] Fischer, C., T. Montmerle, L. Berre, L. Auger, and S. E. Stefanescu, 2005: An overview of the variational assimilation in the Aladin/FranceNWP system. Quart. J. Roy. Meteor. Soc., 131, 3477-3492.

[8] Giard, D., and E. Bazile, 2000: Implementation of a new assimilation scheme for soil and

surface variables in a global NWP model. Mon. Wea. Rev., 128, 997-1015.

[9] Szintai, B., M. Szűcs, R. Randriamampianina, and L. Kullmann, 2015: Application of the AROME non-hydrostatic model at the Hungarian Meteorological Service: physical parametrizations and ensemble forecasting. Időjárás, 119, 2, 241-265.

[10] Mile, M., G. Bölöni, R. Randriamampianina, R. Steib, and E. Kucukkaraca, 2015: Overview of mesoscale data assimilation developments at the Hungarian Meteorological Service. Időjárás, 119, 2, 215-241.

[11] Tóth, H., Homonnai, V., Mile, M., Várkonyi, A., Kocsis, Zs., Szanyi, K., Tóth, G., Szintai, B., and Szépszó, G., 2021: Recent developments in the data assimilation of AROME/HU numerical weather prediction model. Időjárás, 125, 521-553.

[12] Brousseau, P., Seity, Y., Ricard, D. and Léger, J., 2016: Improvement of the forecast of convective activity from the AROME-France system. Q.J.R. Meteorol. Soc., 142, 2231-2243.

[13] Sommeria G. and J.W. Deardorff, 1977: Subgrid scale condensation in models for non precipitating clouds. J. Atmos., Sci., 34, 344-355.

[14] Chaboureau, J.-P., J.-P. Cammas, P. J. Mascart, J.-P. Pinty, and J.-P. Lafore, 2002: Mesoscale model cloud scheme assessment using satellite observations. J. Geophys. Res., 107(D16), 4301.

[15] Wernli, H., Paulat, M., Hagen, M. and Frei, Ch., 2008: SAL - A novel quality measure for the verification of Quantitative Precipitation Forecast. Mon. Wea. Rev., 136, 4470-4487.

[16] D Řezáčová, B Szintai, B Jakubiak, J -I Yano, S Turner, 2015,: Verification of high-resolution precipitation forecast with radar-based data. In R. S. Plant and J.-I. Yano, editors, Parameterization of Atmospheric Convection. Volume 2. Imperial College Press, 2015.

[17] Benjamin, S. G., Brundage, K. J., Miller, P. A., Smith, T. L., Grell, G. A., Kim, D., Brown, J. M., and Schlatter, T. W., 1994: The Rapid Update Cycle at NMC. 10th Conference on Numerical Weather Prediction, AMS, Portland, OR, 566-568.

[18] Benjamin, S. G., Dévényi, D., Weygandt, S. S., Brundage, K. J., Brown, J. M., Grell, G. A., Kim, D., Schwartz, B. E., Smirnova, T. G., and Smith, T. L., 2003: An Hourly Assimilation/Forecast Cycle: The RUC. Mon. Wea. Rev., 132, 495-518.

Conference on Modelling Fluid Flow (CMFF'22)
The 18th International Conference on Fluid Flow Technologies
Budapest, Hungary, August 30 -September 2, 2022

SIMULATION OF REACTING AND MOVING GRANULAR ASSEMBLIES OF THERMALLY THICK PARTICLES BY DEM/CFD
A BRIEF OVERVIEW

Enric ILLANA[2], Maximilian BRÖMMER[2], Siegmar WIRTZ[2], Viktor SCHERER[1,2]

[1] Corresponding Author. Tel.: +49 234 / 32-26328. E-mail: scherer@leat.rub.de
[2] Institute of Energy Plant Technology, Ruhr-University Bochum, Universitätsstraße 150, 44780 Bochum, Germany

ABSTRACT

This paper briefly summarizes the potential and the limitations of the Discrete Element Method (DEM) coupled with Computational Fluid Mechanics (CFD) to simulate chemically reacting, moving granular material passed by fluid flow. A special focus is set on thermally thick particles, which requires to resolve the intra-particle transport and reaction processes. The aspect of complex particle shape is addressed as shape may dominate the particle movement in densely packed granular assemblies even more than details of contact force laws. The fluid flow in the granular assembly is assumed to be a gas, i.e. solid-liquid systems are not considered.

The potential of DEM/CFD will be highlighted presenting three illustrative examples: a large-scale lime shaft kiln with intermittent operation, an industrial-size grate firing system for the incineration of municipal waste, and a small-scale straw pellet stove. In the summary, an outlook is given on open questions and further research needs.

Keywords: Chemical reactions, DEM-CFD, Granular assemblies, Thermally thick particles

NOMENCLATURE

A	$[m^2]$	area
A_g	$[m^2]$	exposed surface
E	$[J]$	total energy
E_y	$[N/m^2]$	Young's modulus
F	$[N]$	force
$\underline{J}$	$[kg/m^2s]$	diffusion flux of species
M	$[Nm]$	moment
N_S	[-]	number of species
R_c	$[K/W]$	thermal constriction resistance
R_g	$[K/W]$	stagnant gas zone resistance
R_i	$[kg/m^3s]$	species production by reaction
T	$[K]$	temperature
S_m	$[kg/m^3s]$	mass source
$\underline{S_{int}}$	$[kg/m^2s^2]$	interaction force
$S_{i,R}$	$[kg/m^3s]$	species creation from particles
S_P	$[W/m^3]$	heat source from particles
S_R	$[W/m^3]$	heat sources from reaction
Y	$[kg/kg]$	mass fraction of species
g	$[m/s^2]$	gravitational acceleration
h	$[J/kg]$	enthalpy
k^n	$[N/m]$	normal spring stiffness
k^t	$[N/m]$	tangential spring stiffness
k	$[W/mK]$	thermal conductivity
l_g	$[m]$	average distance
m	$[kg]$	mass
$\underline{n}$	[-]	normal vector
p	$[Pa]$	pressure
q	$[W]$	heat transfer
r	$[m]$	radius
r_c	$[m]$	contact radius of contact zone
$\underline{t}$	[-]	tangential vector
v	$[m/s]$	velocity
γ	$[N/m]$	damping coefficient
ε_m	[-]	emissivity
θ	$[kg/m^2]$	moment of inertia
θ_{hm}	[-]	harmonic mean Poisson's ratio
μ_{dyn}	[-]	friction coefficient
ξ	$[m]$	overlap
ρ	$[kg/m^3]$	density
σ	$[W/m^2K^4]$	Stefan-Boltzmann const.
τ	$[N/m^2]$	stress tensor
φ	$[rad/s]$	angular velocity
ψ	[-]	porosity

Subscripts and Superscripts

diss	dissipative
eff	effective
el	elastic
f	fluid
g	gas
hm	harmonic mean

n	normal
p	related to the particles
rad	radiation
surf	surface
t	tangential

1. INTRODUCTION

Thermochemical treatment of particles is a core unit operation in process industry. If the particles are large, i.e. must be treated as being thermally thick, this gives rise to additional difficulties in the description. Examples of processes with thermally thick particles are the treatment of minerals in multiple hearth furnaces, the calcination of limestone or magnesite and the reduction of iron oxide by hydrogen in shaft kilns, the production of foamed clay in rotary kilns, the combustion of wood chips or municipal waste on grate firing systems but also the roasting of coffee beans in drum roasters. The difficulty in the description of those kind of systems arises from the facts that:

- particles size is in the cm-range, i.e. particle-internal gradients of temperature and composition must be accounted for,
- with large particles the movement is dominated by shape,
- particles may underlie a particle size distribution leading to segregation,
- particles can change their shape and size,
- phase change (solid-gas) may occur during conversion,
- product quality (calcination degree, reactivity, porosity) depends of the time-temperature history of each individual particle in the reactor.

Virtually always a gas flow is present in the granular assembly. The gas flow can be a gas released by the particles (volatiles from solid fuels, CO_2 from calcination), a gaseous fuel which delivers heat for endothermic particle processes (e.g. calcination) or acts as a reducing media (CO and H_2 in blast furnaces/direct iron ore reduction) or simply air for cooling or combustion purposes.

DEM coupled with CFD is able to describe the above mentioned physical and chemical effects. In DEM, the movement of each particle in a granular assembly is tracked and its interaction with other surrounding particles or walls. Cundall and Strack [1] were the first to introduce DEM for spherical particles in the late 1970s. Considering complex particle shape in DEM is still not standard and is part of ongoing research [2]. Many of the DEM codes like the commercial software Rocky, XDEM, an in-house code of the University of Luxembourg, or LIGGGHTS, a former open source code, can be coupled with CFD. For non-reacting gas-particle system, like fluidized beds, many examples exist for DEM/CFD simulation [3]–[7]. A good overview on non-reacting DEM/CFD including complex particle shape, particle breakage, attrition and force laws considering adhesion is given by Guo and Curtis [8].

In recent years, chemically reacting systems became of interest in DEM/CFD development. Complexity increases as processes like heat and mass transfer, homogeneous and heterogeneous reactions have to be described in addition. A comprehensive review on heat transfer modelling in DEM/CFD is given by Peng et al. [9] in 2020. An overview on the application of DEM/CFD in process engineering has been presented by Kieckhefen et al. [10] and to chemical process systems by Golshan et al. [11], both in 2020. The last two reviews, however, are mainly limited to small particles (mm-range, thermally thin), with the typical application being fluidized beds. An early overview on the DEM/CFD simulation of thermally thick particles is given by Scherer et al. in 2017 [12].

In our opinion, the real strength of DEM/CFD lies in the description of chemically reacting granular assemblies employing larger particles in the cm-range as intra-particle process can easily be considered in DEM and coupled with the surrounding gas phase. Furthermore, as with size also the mass of the particles becomes large, particle movement is typically dominated by gravitation or mechanical agitation and the influence of fluid flow on the particle movement can be neglected. In addition, the large size of the particles limits particle numbers making the simulation of some industrial-scale systems feasible without employing coarse graining concepts, which cluster a number of particles into parcels, a concept frequently used for fluidized bed simulations [13].

A pioneer in the description of systems with chemically reacting, large particles by DEM/CFD is Peters [14], who presented early work already in the late 1990's. Examples of his current work are the simulation of iron ore reduction in blast furnaces using spherical particles [15] or the combustion of wood pellets, approximating the pellet shape by clustered spheres [16]. He also published a review paper on DEM/CFD which contains further examples [17]. Recently, Gao et al. [18] presented a DEM/CFD study on the pyrolysis of cubic biomass particles using superquadrics for shape representation. Radl et al. [19] presented PARSCALE, an extension to LIGGGHTS, to account for intra-particle heat and mass transfer. They used the oxidation of porous spherical copper particles as an example. In Kuwagi et al. [20], an approach to describe the incineration of nuclear waste (spherical particles) in a fixed bed reactor can be found. A DEM/CFD study on shaft kilns for the production of spinel, using spherical particles, is presented at the current CMFF'22 conference by Spijker and Raupenstrauch [21]. Our own group did use DEM/CFD to simulate the calcination of limestone in shaft kilns [22][23] and the combustion of municipal waste on grate firing systems [24],

where the particles are represented by spheres. The drying of wood chips (cuboids) in a rotary kiln [25] and the combustion of wood pellets (cylinders and sphero-cylinders) in small-scale heating systems [26], [27] are examples for complex particle shape.

Note that the current brief overview on the simulation of reacting and moving granular assemblies by DEM/CFD can only touch a few specific subjects of thermally thick particles and can't replace the comprehensive reviews mentioned above [8]–[11], [17] .

2. METHODS

2.1. Mechanics

In DEM, Newton's Eq. (1) and Euler's equations Eq. (2) describe the translational and rotational movement of particles. The tangential and normal contact forces and moments acting on the particles must be known to solve these equations.

$$\frac{d}{dt}\left(m_i \cdot \frac{d\underline{x_i}}{dt}\right) = \frac{dm_i}{dt} \cdot \frac{d\underline{x_i}}{dt} + m_i \cdot \frac{d^2\underline{x_i}}{dt^2} = \sum_{j=1}^{N} \underline{F_{ij}} + m_i\,\underline{g} = \underline{F_i} + m_i\,\underline{g} \tag{1}$$

$$\frac{d}{dt}\left(\theta_i \cdot \frac{d\underline{\varphi_i}}{dt}\right) = \frac{d\theta_i}{dt} \cdot \frac{d\underline{\varphi_i}}{dt} + \theta_i \cdot \frac{d^2\underline{\varphi_i}}{dt^2} = \sum_{j=1}^{N} \underline{M_{ij}} + \underline{M_i^r} = \sum_{j=1}^{N} \underline{r_i} \times \underline{F_{ij}} + \underline{M_i^r} = \underline{M_i} \tag{2}$$

There a numerous force laws available. An overview is given by Kruggel-Emden et al. for normal [28] and tangential [29] forces. The simplest and still common approach for the normal force is a linear spring-dashpot model [30], where $\underline{n}$ represents the normal vector (Eq. (3)). The first term is the elastic repulsion which is proportional to the overlap ξ between the impacting partners. The second term, the dissipation, is proportional to the normal relative velocity $\underline{v^n}$. The required contact parameters are the stiffness of a linear spring k^n and the damping coefficient γ^n.

$$\underline{F^n} = \underline{F_{el}^n} + \underline{F_{diss}^n} = \left(-k^n\,\xi - \gamma^n |\underline{v^n}|\right) \cdot \underline{n} \tag{3}$$

Eq. (4) gives a typical tangential force law with $\underline{t}$ being the tangential vector, k^t being the tangential stiffness of a linear spring and ξ^t the tangential spring elongation. The force is limited by Coulomb's law.

$$\underline{F^t} = -\min\left(|k^t\,\xi^t|, |\mu_{dyn}\,\underline{F^n}|\right) \cdot \underline{t} \tag{4}$$

The material parameters are typically derived from single particle measurements and/or are adapted to measurements of static and dynamic angle of repose [31]. For reacting particle systems, the particle surface can get hot and, hence, sticky due to softening or sintering effects, i.e. adequate models for adhesive forces are needed [32]. An example of such force laws is the model introduced by Wissing et al. [24] for municipal waste, where the adhesive force magnitude is based on remaining carbon content in the particle.

The contact time of a collision has to be resolved with a sufficient number of numerical time steps (approx. 20) for a correct temporal description of the evolution of the contact forces. For particles with high elastic modulus, like lime stones or iron ore, this can lead to very short integration time steps and, hence, high computational costs. Therefore, sometimes particles are made artificially softer, i.e. spring stiffness k^n is reduced. This, however, may influence the characteristics of bulk movement but also can alter the gas phase flow field in the packed bed as void spaces among particles change. So far, there is no real universal law how soft particles are allowed to be made and experiments are strongly recommended to check whether DEM with soft particles reproduces the experimental findings. A rule of thumb has been given by Cleary et al. [33] by recommending to limit the maximum overlap ξ_{max} to 0.1 to 0.5 % of the particle radius.

The laws of motion can be integrated by different numerical schemes [34]. For reacting DEM, it is recommended to integrate the product of mass (inertia) and velocity (angular velocity) as mass and inertia may change in parallel with chemical conversion.

In our opinion, contact force models currently seem not to be the bottleneck for reacting DEM as they are able to reproduce the major effects, and this although the force laws are only an approximation of a collision as they do not account for the three dimensional deformation of the particles occurring in reality.

2.2. Particle shape approximation

The major methods to represent particle shape in DEM are depicted in Figure 1. Spheres allow for easy and fast contact detection, and, hence, are sometimes the only solution in case of high particle numbers. The reproduction of the bulk behavior of particles of complex shape by spheres needs an artificial adaption of contact parameters, i.e. the identified contact parameters are then problem specific and can't be transferred to other applications.

Clusters of spheres are the next step of complexity. This approach has the advantage that contact detection still relies on simple algorithms for the collisions of spheres. Cluster of spheres are a good solution as long as just bulk movement is of

interest. However, reacting DEM of large particles requires discretization of the particle interior to account for inner particle processes, which is difficult with clustered spheres. Other methods for particles of complex shape are superellipsoids [35][36] or superquadrics [37][38] which are less computationally demanding than polyhedrons but not as general in shape representation. Polyhedrons (polytopes) allow for the representation of very complex particle shape. Combined with surface triangulation, intra-particle discretization is straightforward. Standard polyhedrons are sharped-edged which very often does not really occur in nature. Therefore, so-called dilated polyhedrons with rounded edges have been suggested by Ji et al. [39] and Desphande et al. [40]. In the very end, it is a problem specific decision which computational effort can be afforded and which details in shape representation is required.

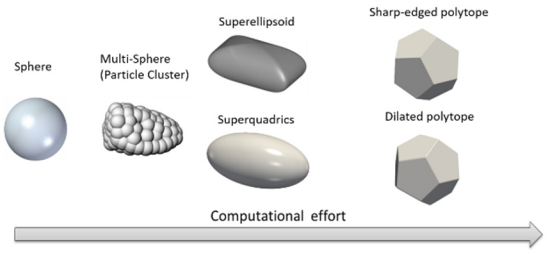

Figure 1. Approximation of particle shape by different methods.

Contact detection in DEM is subdivided into two steps. In a first step, the next neighbors of particles are determined. Fast methods of neighborhood search are hierarchical grids, as used in MercuryDPM [41][42], or octree based approaches [43]. The actual contact detection is the second step and can be very time consuming for complex particle shape. To save computing time, a newer class of contact detection methods pre-computes the relevant parameters of a particle-particle contact (for a given pair of shapes) in dependence of their individual rotation and distance and stores the parameters in a table. Examples are the Orientation Discretization [44] or our own suggestion called Directional Tabulation [40].

2.3. Intra-particle processes

The description of intra-particle processes has to include the diffusive and convective transport of heat and mass as well as source or sink terms for chemical reactions. An overpressure might evolve in the particles due to the generation of a gas within a particle (e.g. volatile release during pyrolysis of wood) [22]. To solve the respective partial differential equations (for brevity not listed here), a discretization of the particle volume is needed. For surface triangulated objects, the discretization is straightforward based on a tetrahedron segmentation. Other discretization approaches, as cartesian grids or unstructured and non-orthogonal meshes are also possible [45].

For materials which show material anisotropy (e.g. fibrous biomass), 3D particle discretization and the knowledge of directional material parameters are mandatory. An example how important the effect of anisotropy can be, is shown in Figure 2 [46].

The figure shows the simulation of convective drying of silica gel spheres which possess isotropic material properties (left) and beech wood spheres with anisotropic properties (middle and right). For silica gel, the particle shows the highest temperatures in vicinity of the stagnation point, where the highest heat transfer coefficients occur. However, when fiber direction (and moisture transport direction) is parallel to the gas flow, the stagnation point stays cool, as the moisture leaves (and cools) the particle at the stagnation point. As expected, when fiber direction and gas flow are perpendicular to each other, the stagnation point is at higher temperature again.

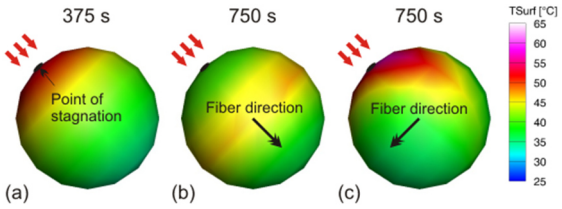

Figure 2. Simulation result for surface temperature: (a) silica gel; (b) beech wood sphere with airflow in fiber direction (c) airflow perpendicular to fiber direction [46].

The complexity of single particle models can vary. For example, drying can be described based on a very simple approach describing just water vapor diffusion or in a more complex manner based on a multi-phase model which resolves the transport of water vapor, free water and bound water [45]. If such complex single particle models as the latter are needed to resolve the underlying physical/chemical effects, single particle models can become a bottleneck in corresponding DEM/CFD simulations.

A remedy can be provided by model reduction. Scherer et al. [25] derived for the anisotropic drying of wood chips spatial modes with corresponding time-dependent coefficients. The coefficients are described by ordinary differential equations A linear combination of just five modes was sufficient to reproduce the transient solution of the corresponding partial differential equation. A reduction of computing time in the order of 100 could be obtained.

The quality of the single particle model depends on the exact knowledge of physical properties like anisotropic thermal conductivity, diffusion coefficients, permeability or species source terms

like gas release by pyrolysis, parameters which are often not known with sufficient accuracy. Hence, calibration and validation of single particle models by experiments, typically by thermogravimetry, are required (e.g. [45]).

2.4. Contact heat transfer

The appropriate description of contact heat transfer is still a weak point in DEM. To describe contact heat transfer, the contact area must be known. But as contact mechanics in DEM is based on simplified force laws, particle deformation is not really described and, hence, the contact area is not exactly known. For spheres, the approach by Vargas and McCarthy [47] (Eq. (5)) is still very common. Heat is transferred by the direct contact of the two spheres (R_c) and by conduction through the stagnant interstitial gas layer (R_g). The theory of Hertz [48] is used to calculate the contact area between two particles whereby the contact radius r_c of the circular contact zone is utilized to determine the thermal constriction resistance R_c in Eq. (6). For the stagnant gas zone resistance R_g, the exposed surface area $A_g$of the spheres and average distance l_g between spheres have to be known in Eq. (7). Additionally, care has to be taken to use the real particle stiffness (material parameter) for the calculation of the contact area and not the reduced stiffness often used to solve the equations of motion of the particles.

$$q_{con} = \left(\frac{1}{R_c} + \frac{1}{R_g}\right) \cdot (T_{surf,2} - T_{surf,1}) \qquad (5)$$

with

$$R_c = \frac{1}{2 \cdot k_{hm} \cdot r_c} \quad \text{with} \quad r_c = \left(\frac{3 \cdot (1 - \theta_{hm}^2) \cdot |F_n| \cdot r_{hm}}{2 \cdot E_{y,hm}}\right)^{\frac{1}{3}} \qquad (6)$$

and

$$R_g = \frac{l_g}{k_g \cdot A_g} \quad \text{with} \quad A_g = 2 \cdot \pi \cdot r^2 - \pi \cdot r_c^2 \quad \text{and} \quad l_g = \frac{r_{hm}^2 \cdot \left(1 - \frac{\pi}{4}\right)}{r_{hm} - r_c} \qquad (7)$$

As contact heat transfer is also dependent on surface roughness, Tsori et al. [49] present an extension of the approach of Vargas and McCarthy by considering an average slope of particle surface roughness.

The situation gets much more complex for particles of complex shape, as point contacts, line contacts and contacts of planes can occur. A recent suggestion has been made by Joulin et al. [50] combining DEM with FEM for a realistic modelling of contact area for complex shaped particles. However, easy and fast methods for complex shaped particles to describe contact heat transfer are still missing.

Note that contact heat transfer is important for certain processes as rotary kilns. However, when the granular assembly is passed by a gas very often convection dominates over conduction making an exact knowledge of contact heat transfer less important. The same holds true at high temperature when radiation becomes the dominating effect.

2.5. Radiative heat transfer

For thermally thick, heavy particles, the granular assembly is typically densely packed, i.e. the void spaces among particles are rather small. This allows to neglect gas radiation in the voids as the optical path length is accordingly small.

The most simplest approach to account for bed internal short-range radiation among particle is depicted in Figure 3. This method is based on the assumption that all particles within a volume of radiation influence, the radiation control volume, are in exchange with the target particle. Typically, a control volume of 2-3 particle diameters including the immediate neighbors is sufficient, as this is the approximate viewing distance in a dense bed (at least for granular assemblies with narrow particle size distribution). By this approach, the net heat flux for each particle can be calculated with Eq. (8).

$$q_{rad} = \sigma \cdot \varepsilon_m \cdot A_{surf} \cdot \left(T_{rad,p}^4 - T_{surf}^4\right) \qquad (8)$$

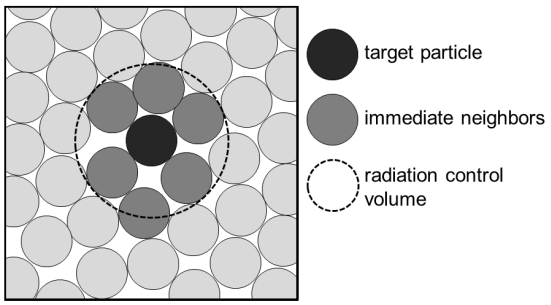

Figure 3. Sketch of the radiation control voume around a target particle [26].

The radiation temperature $T_{rad,p}$ is described by Eq. (9). It is defined as the sum over all emitted heat fluxes of j particles inside the radiation control volume weighted by the surface and emissivity of each particle. This model is highly simplified but fast, especially for moving granular assemblies, and did show reasonable results in comparison with experimental data [51].

$$T_{rad} = \left(\frac{\sum_j \sigma \, A_j \, \varepsilon_j \, T_{S,j}^4}{\sum_j \sigma \, A_j \varepsilon_j} \right)^{0.25} \quad (9)$$

Note that emissivity ε is often unknown and even can change during a chemical reaction (for example, during decomposition of $CaCO_3$ to CaO [52]). Hence, appropriate assumptions are needed here.

For a more detailed modelling of radiation exchange between particles, the view factors in all spatial directions from each particle have to be determined. There exist a couple of approaches to derive approximations for the view factors for packings of spherical particles. Methods for monodisperse granular assemblies have been presented by Cheng et al. [53] and Wu et al. [54] and for spherical particle that underlie a particle size distribution by Chen et al. [55]. For monodisperse spheres, an approach has been presented by Forberg and Radl which allows to account for shadowing effects. Finally, Tausendschön and Radl [56] just recently presented a paper on a Deep Neural Network (DNN)-based view factor model to calculate radiative heat transfer between particles. For more detailed insight into these models, we refer to the very good and comprehensive overview on heat transfer modelling in DEM by Peng et al. [9].

The models above assume a uniform temperature of the particle surface of the spheres. Wiese et al. [57] presented an approach to account for particle surface temperature distribution based on surface triangulation.

$$F_{ij} = \frac{\cos\alpha \cos\beta}{\pi \, |\underline{v}|^2} \, A_j \quad (10)$$

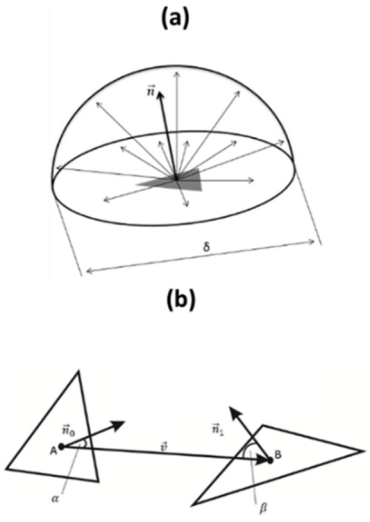

Figure 4. Sketch of the triangle-triangle radiation model [26].

They assumed that every single triangle exchanges thermal radiation with the particles (triangles) in its associated hemisphere (Figure 4a). In addition, the influence of the distance and the orientation of the triangles (Figure 4b) are taken into account by simplified view factors (Eq. (10)).

Figure 5 shows a DEM-simulation using the triangle-triangle radiation model. The bed consisting of cylindrical pellets is heated up by a hot cylindrical wall surrounding the bed (not shown in Figure 5). Temperature gradients on the particles are clearly visible.

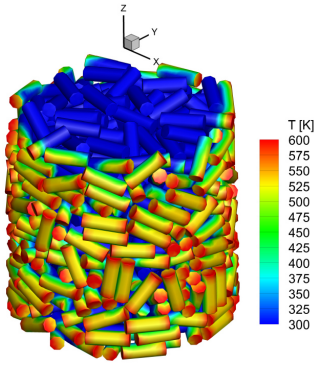

Figure 5. Surface temperature of pellets. The particle bed is heated up by a surrounding cylinder (not shown in the figure) at a radiation temperature of 923 *K* [57].

The view factor approaches are very helpful, but for moving granular assemblies difficult to handle because view factors must be continuously updated which increases the numerical effort. In addition, for granular assemblies with a wide particle size distribution, the number of surrounding neighboring particles can get very large. Effective, simple models are missing here.

2.6. Particle-Fluid coupling

For the coupling of DEM with CFD, two basic approaches are common. First, a so-called non-resolved DEM/CFD where the particles on the CFD side are just represented by a porosity distribution, i.e. the gas phase is not aware of the details of the particle shape. Typically, the CFD cell size is in the same order of magnitude as the particle size. Second, the flow field around each particle is fully resolved, which leads to CFD cell sizes well below the particle size.

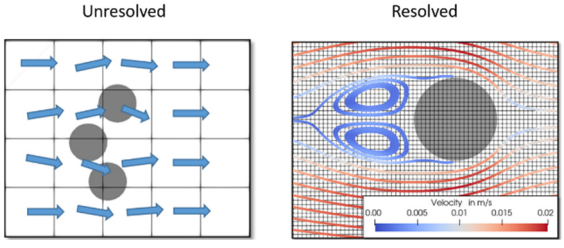

Figure 6. Possible approaches for a gas flow around a particle: (a) Simplified approach with a coarse CFD mesh and a porous medium. (b) Fully resolved flow field around the particle.

The first, unresolved approach is the method of choice or even the only method with affordable computing times for large-scale systems with many particles. The partial differential equations (mass, momentum, species, energy) for the gas phase are based on a porous media approach:

$$\frac{\partial}{\partial t}(\psi\rho_f) + \nabla\cdot(\psi\rho_f \underline{u_f}) = S_m \tag{11}$$

$$\frac{\partial}{\partial t}(\psi\rho_f \underline{u_f}) + \nabla\cdot(\psi\rho_f \underline{u_f}\,\underline{u_f}) = -\psi\nabla p + \nabla\cdot(\psi\,\underline{\underline{\tau}}) + \psi\rho_f \underline{g} - \underline{S_{\text{int}}} \tag{12}$$

$$\frac{\partial}{\partial t}(\psi\rho_f Y_i) + \nabla\cdot(\psi\rho_f \underline{u_f} Y_i) = -\nabla\cdot(\psi \underline{J_i}) + R_i + S_{i,R} \quad i \in [1, N_S] \tag{13}$$

$$\frac{\partial}{\partial t}(\psi\rho_f E_f) + \nabla\cdot(\psi \underline{u_f}(\rho_f E_f + p)) = \nabla\cdot(\psi k_{eff}\nabla T_f + (\underline{\underline{\tau}}\cdot(\psi \underline{u_f}))) + S_R + S_P \tag{14}$$

As shown in Eq. (11) to (14), the coupling between granular and gas phase is primarily based on porosity or void space ψ. The porosity, which varies in space and time for moving granular assemblies, is calculated by DEM and transferred to the gas phase. As the gas phase is not aware of the details of the particle geometry, heat and mass transfer have to be described by Nu, respectively, Sh number correlations. Similarly, momentum transfer (e.g. pressure drop) is represented by correlations, such as the approaches of Ergun [58] and Di Felice [59]. These correlations are reliable for spherical particles, but respective correlations for non-spherical particles are still a topic for ongoing research [60][61][62]. Eq. (13) and (14) also contain source terms to account for chemical reactions, which have to be described by respective models. For gas phase conversion, many models such as Eddy Break Up, Eddy Dissipation Model, Eddy Dissipation Concept or Flamelets exist and can be applied in DEM/CFD. Here, it is more the question how these models, typically reliable or flame propagation in larger combustion chambers, can be applied to the conditions in the tiny void spaces of granular assemblies, where catalytic and/or wall-quenching effects are present and the development of large-scale turbulence structures is suppressed by the length scales of the voids. In addition, for most of the above mentioned models, the reaction progress is based on fuel-oxidizer mixing, but as the flow field is not fully resolved in the porous media approach this puts limitations on the accuracy of the description of gas phase conversion.

For resolved DEM/CFD, immersed boundary methods (IBM) are common. An example is presented at the CMFF'22 by van Wachem et al. [63]. IBM allows for the resolution of particle shape on the fluid-side and, hence, resolution of local flow structures and the associated transfer processes without continuous remeshing as necessary for body fitted CFD simulations of moving particle assemblies. However, although the IBM method is quite powerful, it sets limitations to the number of particles which can be handled due to computational costs., i.e. for large-scale industrial systems the application of IBM is at least critical.

However, in many industrial applications of full resolution of the whole reactor domain is often not required. For example, the lime shaft kiln presented in section 3.1 can be simulated by the non-resolved porous media approach with good accuracy with the exception of the area where gaseous fuel jets enter the packing of lime stones. In this area, a locally resolved simulation would be very helpful as fuel jet penetration and local fuel conversion dominate the temperature field in the reactor (and hence conversion of lime stone to CaO). Therefore, a combination of resolved and unresolved DEM/CFD simulation in one computational domain would be a good solution. Such an approach is suggested by Illana et al. at the current CMFF'22 [64], by using the so-called blocked-off (BO) approach of Patankar [68] for local resolution. The BO method enforces artificial boundary conditions within a static mesh and appropriately blocks the control volumes (CVs) partially or fully obstructed by the boundaries of steady or moving objects. The respective CVs are dynamically identified and excluded from the solution by linearizing the source terms in the discretised transport equations of a CFD solver. For more detail see [64].

The BO method has been applied to an experimental jet in a crossflow setup from literature [65] which is sketched in Figure 7. Particle diameter is 52 *mm* and the immersion depth of the lance into the bed is 156 *mm*. The experiments were performed by introducing nitrogen through the lance into the vertically passing laminar air flow. The concentration of oxygen in the passing airflow is obtained as a measure of the gas mixing. For this arrangement, a simulation with the non-resolved porous media approach has been carried out and a simulation where the near-field of the lance has been resolved by the BO method (for details see [64]).

In Figure 8, the concentrations profiles of oxygen obtained from the two approaches at a height of 0.468 *m* above the lance axis, i.e. a line along the x direction in the vertical cut, are compared with the measurements. It can be observed that the use of the porous media approach results in low O_2 concentrations due to the reduced mixing of the nitrogen flow with the vertical airflow, while the locally resolved approach is able to reproduce the

oxygen concentration level obtained in the measurements. Assuming the N_2 jet would be a gaseous field such an under-prediction of mixing by the porous media approach would of course drastically influence the local heat release by combustion and, as a consequence, the gas phase temperature field and the corresponding local progress of calcination.

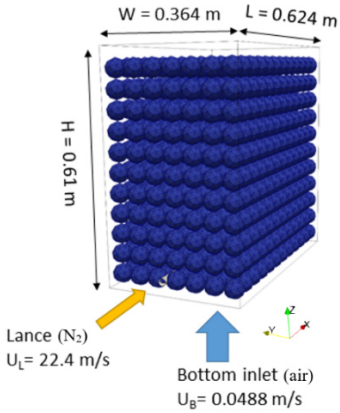

Figure 7. Arrangement of spheres (simple cubic packing) and location of the lance [64].

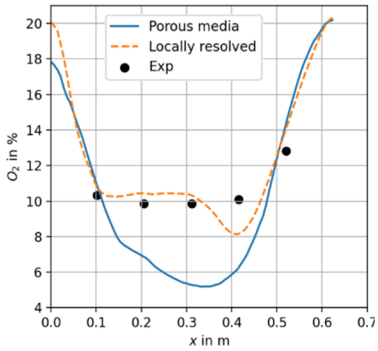

Figure 8. Oxygen concentration profiles at a line located 0.468 *m* above the lance [64].

Note that at the current CMFF'22 Spijker and Raupenstrauch present a simplified approach, called volume smoother approach, to provide more realistic structure of the particle bed on the CFD side. This approach shifts/smears the volume fraction in the CFD grid to neighbouring cells until a certain threshold. For more details, see [21].

3. SIMULATION EXAMPLES

In the following, three examples of DEM/CFD simulations of a reacting granular assembly with thermally thick particles are presented. First, a lime shaft kiln for the production of CaO from $CaCO_3$, second, a grate firing system for the incineration of municipal waste and third, a straw pellet stove. Whereas in the first two examples the particles are represented as spheres, in the third example sphero-cylinders are used for pellet shape approximation. In addition, in the first two examples non-resolved DEM/CFD simulations with the porous media approach were carried out. In contrast, the last example shows a resolved DEM/CFD simulation using the blocked-off approach to represent the particles in the fluid flow. We have taken the three examples from our own group, but of course further important work on DEM/CFD simulation of reacting thermally thick particles have been carried out by others (e.g. [14]–[16], [18]–[21]). Note that the simulations presented here were carried out with our in-house code called LEAT-DEM coupled with FLUENT.

3.1. Lime shaft kiln

In the calcination process, limestone is converted at high temperatures (T > 900 °C) into calcium oxide and carbon dioxide. The current example is based on a so-called parallel-flow regenerative lime shaft kiln (PFR-kiln) [66]. The example is based on an existing industrial kiln, part of the product portfolio of the Maerz Ofenbau AG, Switzerland. A PFR-kiln consists of two vertical shafts and a connecting crossover channel (see Figure 9). The lime stones move through the shafts due to gravitation. While in one shaft the calcination takes place in parallel flow of particles (the necessary heat is provided by the combustion of methane), the other shaft preheats the lime stone in counter flow. It is a transient process since the two shafts periodically switch their function at cycles of 15 min. Due to the regenerative process, PFR-kilns show the lowest heat consumption of lime kilns available today.

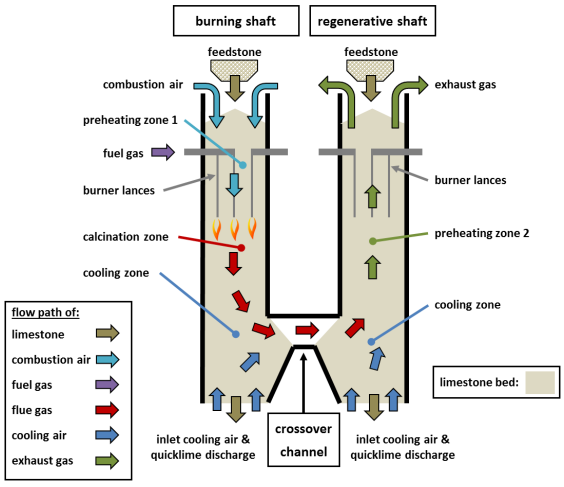

Figure 9. Operation principle of a rectangular PFR-kiln – gas flow and limestone movement [66].

In the simulation, contact heat transfer, radiative heat transfer among particles and convective heat transfer are considered. The single particle calcination model includes diffusion and advection (Stefan flow) of CO_2. Gas phase combustion of

methane is considered by a two-step mechanism including the intermediate formation of CO. The lime stones, represented by spheres, underlie a particle size distribution (50-90 *mm*). The total height of a single shaft is 18 *m*, and its width is 1.6 *m*. The end of the burner lances is 5.8 *m* below the limestone inlet.

Figure 10 shows the gas temperature and CH_4 mass fraction at the end of one cycle in the plane of symmetry. The left shaft is the burning shaft. The highest temperature occurs close to the burner lances where the methane is combusted. The heat of calcination act as a heat sink and, therefore, areas of higher temperatures diminish fast. Gas temperature in the calcination zone of the burning shaft is between 1000 °*C* and 1200 °*C*. In the right shaft, the regenerative shaft, the maximum temperature in is around 900 °*C*. The right image shows the mass fraction of methane. Methane is converted just before the exhaust gases reach the crossover channel. A too long flame is undesired as combustion in the crossover channel would generate high temperatures possibly damaging the refractory lining in that area.

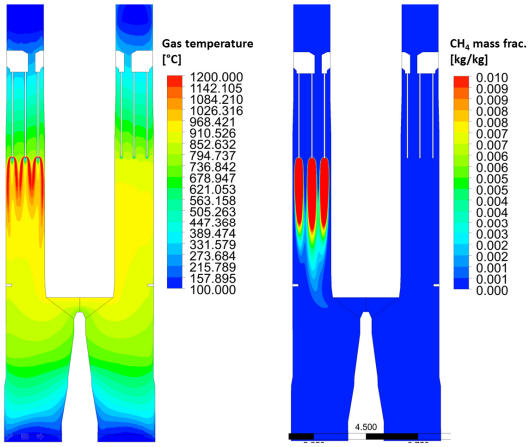

Figure 10. Fluid temperature and CH_4 mass fraction in the fluid phase (plane of symmetry). Results taken from the CFD-simulation at the end of one cycle. The left shaft represents the burning shaft [66].

Figure 11 left shows the particle residence times. The mean residence is about 20 *h* and identical in burning and regenerative shaft. The particles near the inner cooling zone wall have longer residence times caused by the shaft slope. In the upper shaft, the radial residence time distribution shows almost no gradients, i.e. no core flow exists. The second image shows the degree of calcination of each individual particle. Smaller particles are completely calcined, whereas larger particles show a lower degree of conversion. Furthermore, the kiln operates with a reduced conversion efficiency near the outer wall, because the hot flue gas flows towards the crossover channel and thus closer to the inner wall. In total, the mass averaged calcination degree of the exiting limestone is about 95 %. Note that industrial PFR-kilns operates at conversion degrees over 99.9 %, which could be achieved in the simulations too by increasing the thermal input.

In the paper [66], we also show a comparison with temperature measurements. A thermocouple lance was used, which travels with the limestone bed through the kiln. Agreement was fair, keeping in mind that just a single thermocouple reading was available in the large kiln. This also highlights an important research need for further work. Measurement is such in kind of high temperature reactors are scarce and extremely challenging. However, for DEM/CFD calibration such data are urgently needed.

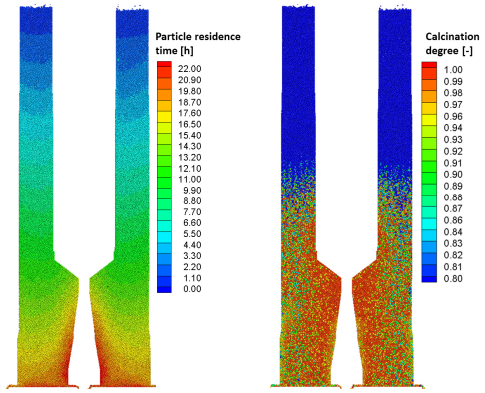

Figure 11. Particle residence times and calcination degrees (plane of symmetry). Results taken from the DEM-simulation at the end of one cycle. The left shaft represents the burning shaft [66].

3.2. Waste incineration plant

The second example is based on municipal waste incineration plant in Germany [24]. The MHKW Frankfurt has a thermal load of 57 MW_{th}. The grate consists of two sections (see Figure 12**,** bottom). The first one is inclined by an angle of 10°, has a length of 7.3 *m*. The second grate section is located 0.54 *m* below the first section. The length of this horizontally arranged section is 3.06 *m*, the width of the grate is 7.36 *m*. To save computing time just a strip of 50 *cm* width has been simulated. The waste bed is supplied by primary air (in crossflow to the waste bed) through six primary air zones. The waste transport is due to movable (forward-acting) stoking bars. The mean residence time on the grate is approximately 90 minutes. Above the grate, the released volatiles are converted in the combustion chamber. Secondary air is injected for conversion of the volatiles in a gas flame. The gas flame exchange radiative with the fuel bed, an important mechanism for waste ignition and conversion.

The waste particles are represented as spheres. Of course, waste particles are not spherical, hence, the sphere dimensions represent the area of

mechanical influence of a specific fuel particle rather than its actual geometry. The fuel is subdivided in up to 11 fractions such as plastics, organics, textiles, sanitary products etc. Each fraction has its own fuel characteristics, i.e. chemical composition, heating value, particle size distribution and, hence, shows different combustion behavior. Maximum particle size is 0.27 m. Drying, pyrolysis and char combustion and gasification are modelled. Pyrolysis gas combustion is modelled by a one-step reaction based on a volatile surrogate species. Particle size changes (shrinks) during conversion due to fuel conversion. A model which accounts for adhesive forces is implemented. The adhesive forces become lower with increasing fuel conversion; a linear decrease with remaining fuel carbon content is assumed.

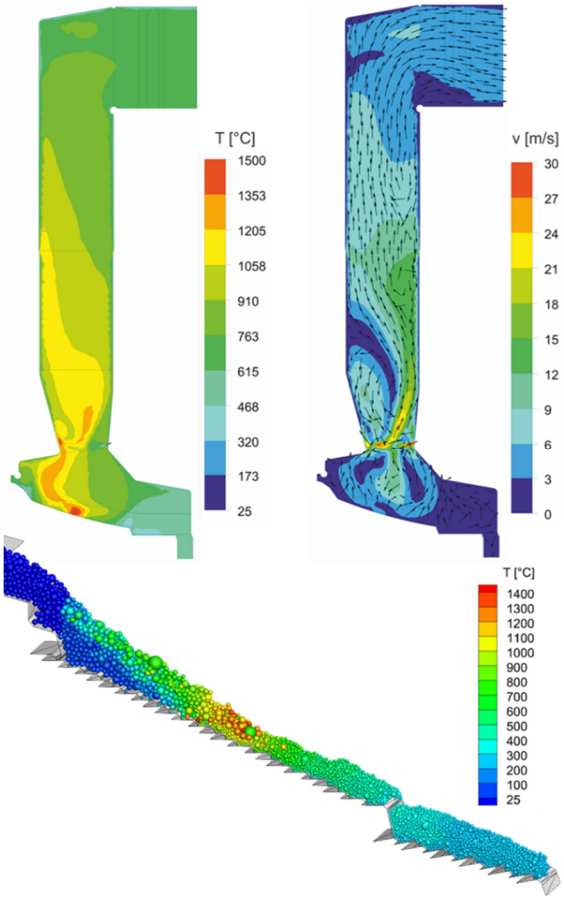

Figure 12. Temperature (top left) and velocity (top right) distribution in the furnace; surface temperature of waste particles (bottom) [24].

Examples of results are shown in Figure 12. The upper figures depict the temperature and velocity distribution of the gases in the symmetry plane of the combustion chamber. The lower figure shows the corresponding particle surface temperature of the waste particles. Waste enters the grate form the left and is transported to the right. The maximum surface temperature of the particles is up to 1400 °C, typically at 50% traveling distance. Further downstream, with proceeding conversion, the temperature decreases due to cooling by the primary air. The particles leave the grate with temperatures in the order of 200 °C to 300 °C.

The maximum of the gas temperature (top left) reaches its maximum at the same position as the maximum waste temperature. The gas temperature of approx. 1500 °C is 100 °C higher than the waste temperature, which is due is due to the conversion of CO and volatiles above the waste bed. A temperature asymmetry occurs, as the temperature close to the boiler front wall (left) is higher than the temperature at the back wall (right).

The absolute velocity and the velocity vectors (top right) clearly depict the location of secondary air injection, which is injected from the front and the back wall, inducing strong mixing and a recirculation zone close to the front wall. Downstream of the secondary air injection, a streak can be observed that stretches from the front to the back wall and again to the front wall inducing a recirculation zone at the back wall.

Another important information that can be derived from such simulation is the change in the volume of the waste fraction due to conversion. This is depicted in Figure 13 for the 11 fractions simulated. The largest change in volume occurs for wood (low ash content, high volatile content) and plastics (low ash content, high volatile), whereas the smallest change (with the exception of inerts) can be observed for fines as they contain a large amount of ash.

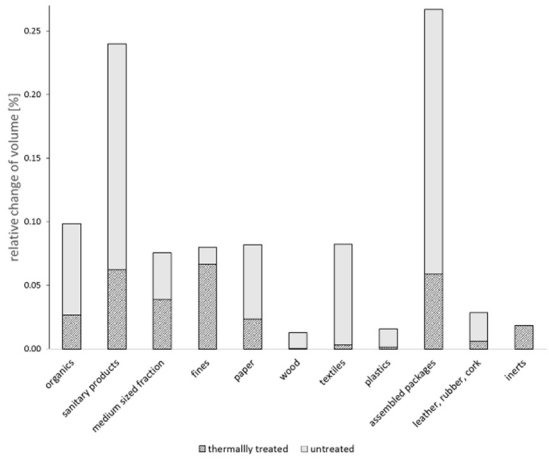

Figure 13. Relative change of volume before and after thermal treatment for the 11 waste fractions considered [24].

3.3. Straw pellet stove

As a last example, a simulation for non-spherical particles is presented with a resolved DEM/CFD approach based on the blocked-off method introduced earlier [27]. The test case is sketched in Figure 14 a. It consists of a cylindrical combustion chamber for gas phase combustion and a cylindrical

burner bowl filled with straw pellets. The wall of the combustion chamber is electrically heated to 1000 *K*. It provides the radiative heat for pellet ignition. Primary air is passing the fuel bed through the grate located at the burner bowl bottom. Secondary air is added to the combustion chamber above the pellet bed. Primary to secondary air mass flow ratio is set to 20 %. Details of the burner bowl with the grate formed by three stoking rings are shown in Figure 14. The stoking rings allow for mechanical agitation of the pellet bed (see Figure 14 b and c: initial position b, fully traversed stoking rings c). The inner stoking ring as well as the outer stoking ring can be moved vertically. The central element is static. Different stoking pattern can be carried out.

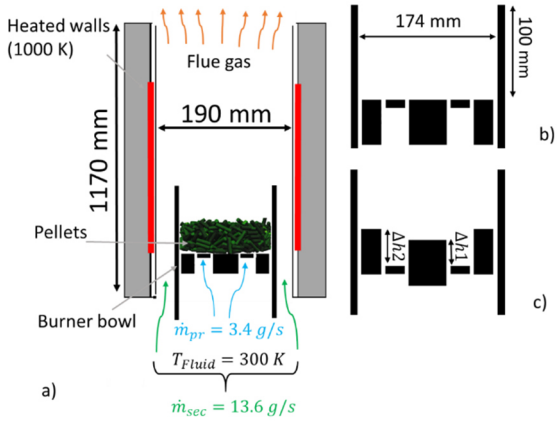

Figure 14. a) Sketch of the test rig, b) static burner bowl and c) burner bowl with fully traversed stoking elements [27].

The particles in the DEM/CFD simulation are represented by surface triangulated sphero-cylinders. The number of intra-particle cells is in the order of 500. Pellets shrink during volatile release but keep their shape during char burnout (the ash of straw tends to agglomerate and forms a stable skeleton). The pellets underlie a length distribution from 9 to 25 *mm*. Radiation is modelled by the discrete ordinate model (DOM) which has been combined with the blocked-off method, hence also bed internal radiation is modelled by DOM. To account for the turbulence structure of the gas phase above the bed, very large eddy simulation (VLES) has been applied. The particle reaction model includes drying, pyrolysis and char conversion. Pyrolysis gas combustion is modelled by a two-step reaction based on a pyrolysis gas surrogate and the intermediate formation of CO.

Figure 15 shows the temperatures and water contents of the pellets after 400 *s* of operation (top static bed, bottom agitated bed). At this moment in time already volatile release occurs, but no volatile flame is present. Thus, the energy supply to the bed occurs due to radiation by the electrically heated combustion chamber walls. In the static case, particles with high temperatures (top, left) are located in the top layer. Radiative heat from the walls is absorbed at the surface of the pellets but cannot reach pellets in deeper layers. In case of bed agitation, this is considerably different. Here, the number of hot particles at the surface is smaller. This can be explained by the fact that hot pellets from the top layer are transported into the bulk where radiative heat exchange with the heated walls above the burner bowl is blocked and convective cooling of pellets by primary air occurs. For the static mode, the absence of pellet mixing leads to a typical separation layer between raw pellets inside the bed and dry pellets at the bed surface (top, right), whereas for the agitated case pellet mixing leads to a much more homogeneous drying of the bulk.

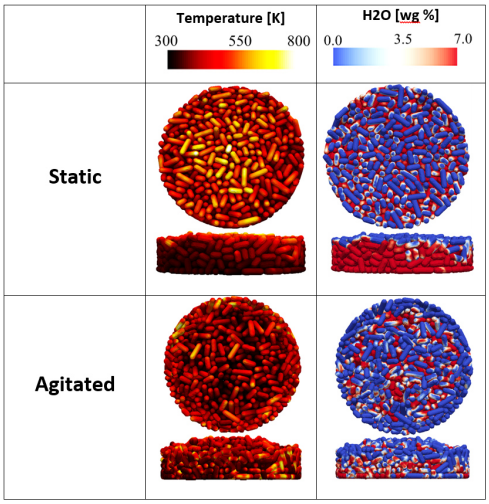

Figure 15. Distribution of temperature and water content in the bulk after 400 *s* [27].

Figure 16 shows a cross-sectional view through the center of the burner bowl for the static (left) and the agitated (right) operation after 600 *s* of operation. Merged contour plots of the gas temperatures and temperature distribution inside each individual pellet are depicted at the top in a logarithmic scale. Respective plots of the oxygen mass fraction of the gas phase are shown below.

At this point, a significant amount of volatiles has been released to the gas phase for the static case, leading to a gas flame above of the bed. Therefore, the maximum temperature level is significantly higher compared to the agitated case. Maximum temperatures (1000 *K*) occur at the bed surface due to conversion of volatiles as well as heterogeneous char combustion at the pellet surface. This leads to regions of lower oxygen mass fractions directly downstream of the fuel bed.

In agitated operation, the temperature level is significantly lower. Mixing of the bulk leads to a homogeneous but overall reduced heating of gas phase and pellets. This leads to less volatile products in the gas phase and only minor consumption of

oxygen by gas phase (no volatile flame present) and heterogeneous char reaction.

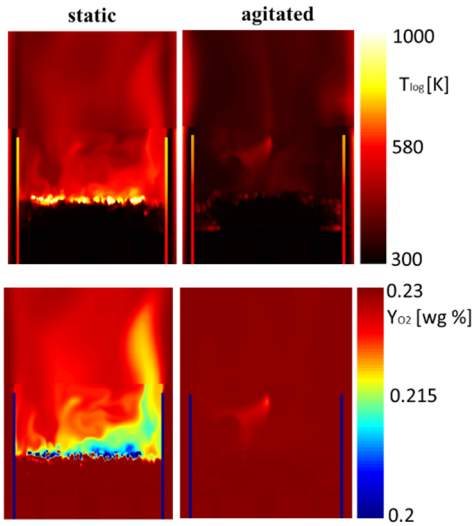

Figure 16. Contours of gas phase temperature and oxygen mass fraction after 600 *s* for a static bed (left) and an agitated bed (right) [27].

4. SUMMARY AND CONCLUSION

An overview is given on DEM/CFD simulation of reacting and moving granular assemblies passed by gas flow with a focus on thermally thick particles. The approaches to represent complex particle shape, heat and mass transfer, intra-particle process and chemical conversion are briefly summarized. Three examples are presented, namely a large-scale lime shaft kiln with intermittent operation, an industrial-size grate firing system for the incineration of municipal waste, and a small-scale straw pellet stove. These examples demonstrate the deep insight that can be gained by DEM/CFD into the chemical/physical processes in densely packed, chemically reactive granular assemblies with gas flow. For example, DEM/CFD allows for the prediction of particle product quality (e.g. calcination degree in lime shaft kilns) as intra intra-particle processes are resolved. When complex particle shapes are considered, a realistic description of effects like bridging, arching or segregation in moving granular assemblies is possible, which is very difficult to achieve with continuum approaches.

Despite of these advantages, there are still limitations of DEM/CFD for actual technical systems. Computing time for large-scale systems is still high, especially for particles with complex shape. Therefore, for many large-scale systems, like lime shaft kilns with number of particles in the order of one million, still simplifications, like representing the lime stones by spheres, are necessary. Even then, computing times are significant. Very typical, the bottleneck in term of computing times is particle mechanics (neighbourhood search and contact resolution) and often not the thermochemical processes. This allows for some freedom in selecting rather sophisticated methods to represent thermochemical conversion without influencing overall computing time to a large extend.

In summary, important research needs to make reacting DEM/CFD a standard engineering tool are:

- Fast neighbourhood and contact detection algorithms, especially for polydisperse granular assemblies with particles of complex shape,
- Improvement of contact heat transfer models for particles of complex shape,
- Reliable and fast particle-particle radiation models for moving polydisperse granular assemblies with particles of complex shape,
- Detailed single particle models, e.g. based on pore network simulations, to derive directional transport properties to formulate simpler single particle continuum models,
- Model reduction to provide fast single particle models based on ordinary differential equations,
- Methods to improve the spatial and directional representation of granular structure on the CFD side for the DEM/CFD porous medium approach for a more accurate prediction of the flow field,
- Effective methods which allow for a self-adaptive switch between locally resolved simulation of the particle shape on the CFD side and the porous media approach in the same computational domain,
- Validated gas phase combustion models which are able to describe the scale sensitivity of turbulence chemistry interaction as well as catalytic and quenching effects in the void space of the granular assembly,
- and, most important, experimental data sets for particle motion, gas phase velocity and homogeneous and heterogeneous reaction progress in high temperature granular assemblies to validate DEM/CFD simulations.

Note that many of these topics are currently addressed by the Collaborative Research Center 287 Bulk-Reaction, a larger-scale (10 million €) project funded by the German Research Foundation (DFG). For more details, see [67].

ACKNOWLEDGEMENTS

Funded by the Deutsche Forschungsgemeinschaft (DFG, German Research Foundation) – Project-ID 422037413 – TRR 287.

Gefördert durch die Deutsche Forschungsgemeinschaft (DFG) – Projektnummer 422037413 – TRR 287.

REFERENCES

[1] P. A. Cundall and O. D. Strack, 1979, “A discrete numerical model for granular

assemblies," *Geotechnique*, vol. 29, pp. 47–65.

[2] L. Zhan, C. Peng, B. Zhang, and W. Wu, 2021, "A surface mesh represented discrete element method (SMR-DEM) for particles of arbitrary shape," *Powder Technol.*, vol. 377, pp. 760–779.

[3] L. Fries, S. Antonyuk, S. Heinrich, and S. Palzer, 2011, "DEM-CFD modeling of a fluidized bed spray granulator," *Chem. Eng. Sci.*, vol. 66, pp. 2340–2355.

[4] L. Fries, S. Antonyuk, S. Heinrich, D. Dopfer, and S. Palzer, 2013, "Collision dynamics in fluidised bed granulators: A DEM-CFD study," *Chem. Eng. Sci.*, vol. 86, pp. 108–123.

[5] V. Salikov, S. Antonyuk, S. Heinrich, V. S. Sutkar, N. G. Deen, and J. A. M. Kuipers, 2015, "Characterization and CFD-DEM modelling of a prismatic spouted bed," *Powder Technol.*, vol. 270, pp. 622–636.

[6] N. G. Deen, M. V. S. Annaland, M. A. Van der Hoef, and J. A. M. Kuipers, 2007, "Review of discrete particle modeling of fluidized beds," *Chem. Eng. Sci.*, vol. 62, pp. 28–44.

[7] G. Lian, W. Zhong, and X. Liu, 2021, "CFD–DEM Investigation of Fuel Dispersion Behaviors in a 3D Fluidized Bed," *Ind. Eng. Chem. Res.*, vol. 60, pp. 13272–13285.

[8] Y. Guo and J. S. Curtis, 2015, "Discrete element method simulations for complex granular flows," *Annu. Rev. Fluid Mech.*, vol. 47, pp. 21–46.

[9] Z. Peng, E. Doroodchi, and B. Moghtaderi, 2020, "Heat transfer modelling in Discrete Element Method (DEM)-based simulations of thermal processes: Theory and model development," *Prog. Energy Combust. Sci.*, vol. 79, p. 100847.

[10] P. Kieckhefen, S. Pietsch, M. Dosta, and S. Heinrich, 2020, "Possibilities and limits of computational fluid dynamics–discrete element method simulations in process engineering: A review of recent advancements and future trends," *Annu. Rev. Chem. Biomol. Eng.*, vol. 11, pp. 397–422.

[11] S. Golshan, R. Sotudeh-Gharebagh, R. Zarghami, N. Mostoufi, B. Blais, and J. A. M. Kuipers, 2020, "Review and implementation of CFD-DEM applied to chemical process systems," *Chem. Eng. Sci.*, vol. 221, p. 115646.

[12] V. Scherer, S. Wirtz, B. Krause, and F. Wissing, 2017, "Simulation of reacting moving granular material in furnaces and boilers an overview on the capabilities of the discrete element method," *Energy Procedia*, vol. 120, pp. 41–61.

[13] A. Di Renzo, E. S. Napolitano, and F. P. Di Maio, 2021, "Coarse-Grain DEM Modelling in Fluidized Bed Simulation: A Review, 9, 279," *Processes*, vol. 9, p. 279.

[14] B. Peters, 1999, "Numerical simulation of the motion and combustion of granular material," *Ind. Heat Eng.*, vol. 21, pp. 109–113.

[15] B. Peters, M. Baniasadi, and M. Baniasadi, 2018, "The extended discrete element method (XDEM): An advanced approach to model blast furnace," *Iron Ores and Iron Oxide Materials,* IntechOpen.

[16] M. Mohseni, B. Peters, and M. Baniasadi, 2017, "Conversion analysis of a cylindrical biomass particle with a DEM-CFD coupling approach," *Case Stud. Therm. Eng.*, vol. 10, pp. 343–356.

[17] B. Peters, M. Baniasadi, M. Baniasadi, X. Besseron, A. E. Donoso, M. Mohseni, and G. Pozzetti, 2019, "XDEM multi-physics and multi-scale simulation technology: Review of DEM–CFD coupling, methodology and engineering applications," *Particuology*, vol. 44, pp. 176–193.

[18] X. Gao, J. Yu, L. Lu, and W. A. Rogers, 2021, "Coupling particle scale model and SuperDEM-CFD for multiscale simulation of biomass pyrolysis in a packed bed pyrolyzer," *AIChE J.*, vol. 67, p. 17139.

[19] S. Radl, T. Forgber, A. Aigner, and C. Kloss, 2015, "ParScale - An Open-Source Library for the Simulation of Intra-Particle Heat and Mass Transport Processes in Coupled Simulations," *IVth International Conference on Particle-based Methods*, Barcelona, Spain.

[20] K. Kuwagi, T. Takami, A.B. Alias, D. Rong, H. Takeda, S. Yanase, T. Kouchi, T. Hyakutake, K. Yokoyama, Y. Ohara, N. Takahashi, and N. Sugitsue, 2016, "Development of DEM–CFD Simulation of Combustion Flow in Incinerator with the Representative Particle Model," *J. Chem. Eng. Jpn.*, vol. 49, pp. 425–434.

[21] C. Spijker and H. Raupenstrauch, 2022, "CFD-DEM Modelling of shaft furnaces, using the volume fraction smoother approach," *Conference on Modelling Fluid Flow*, Budapest, Hungary.

[22] B. Krause, B. Liedmann, J. Wiese, S. Wirtz, and V. Scherer, 2015, "Coupled three dimensional DEM-CFD simulation of a lime shaft kiln - Calcination, particle movement and gas phase flow field," *Chem. Eng. Sci.*, vol. 134, pp. 834–849.

[23] T. Bluhm-Drenhaus, E. Simsek, S. Wirtz, and V. Scherer, 2010, "A coupled fluid dynamic-discrete element simulation of heat and mass transfer in a lime shaft kiln," *Chem. Eng. Sci.*, vol. 65, pp. 2821–2834.

[24] F. Wissing, S. Wirtz, and V. Scherer, 2017, "Simulating municipal solid waste incineration with a DEM/CFD method–

Influences of waste properties, grate and furnace design," *Fuel*, vol. 206, pp. 638–656.
[25] V. Scherer, M. Mönnigmann, M. O. Berner, and F. Sudbrock, 2016, "Coupled DEM-CFD Simulation of Drying Wood Chips in a Rotary Drum - Baffle Design and Model Reduction," *Fuel*, vol. 184, pp. 896-904.
[26] J. Wiese, F. Wissing, D. Höhner, S. Wirtz, V. Scherer, U. Ley, and H.M. Behr, 2016, "DEM/CFD modeling of the fuel conversion in a pellet stove," *Fuel Process. Technol.*, vol. 152, pp. 223–239.
[27] F. Buss, S. Wirtz, and V. Scherer, 2020, "Simulation of a reacting agitated bed of straw pellets by a resolved coupled DEM/CFD method using a blocked-off approach," *Int. J. Therm. Sci.*, vol. 152, p. 106332.
[28] H. Kruggel-Emden, E. Simsek, S. Rickelt, S. Wirtz, and V. Scherer, 2007, "Review and extension of normal force models for the Discrete Element Method," *Powder Technol.*, vol. 171, pp. 157–173.
[29] H. Kruggel-Emden, S. Wirtz, and V. Scherer, 2008, "A study on tangential force laws applicable to the discrete element method (DEM) for materials with viscoelastic or plastic behavior," *Chem. Eng. Sci.*, vol. 63, pp. 1523–1541.
[30] E. Simsek, B. Brosch, S. Wirtz, V. Scherer, and F. Krüll, 2009, "Numerical simulation of grate firing systems using a coupled CFD/discrete element method (DEM)," *Powder Technol.*, vol. 193, pp. 266–273.
[31] F. Elskamp, H. Kruggel-Emden, M. Hennig, and U. Teipel, 2017, "A strategy to determine DEM parameters for spherical and non-spherical particles," *Granul. Matter*, vol. 19, pp. 1–13.
[32] S. Luding, K. Manetsberger, and J. Müllers, 2005, "A discrete model for long time sintering," *J. Mech. Phys. Solids*, vol. 53, pp. 455–491.
[33] P. W. Cleary, 2010, "DEM prediction of industrial and geophysical particle flows," *Particuology*, vol. 8, pp. 106–118.
[34] H. Kruggel-Emden, M. Sturm, S. Wirtz, and V. Scherer, 2008, "Selection of an appropriate time integration scheme for the discrete element method (DEM)," *Comput. Chem. Eng.*, vol. 32, pp. 2263–2279.
[35] X. Lin and T. NG, 1995, "Contact Detection Algorithms for Three-Dimensional Ellipsoids in Discrete Element Modelling," *Int. J. Numer. Anal. Methods Geomech.*, vol. 19, pp. 653–659.
[36] H. Ouadfel and L. Rothenburg, 1999, "An algorithm for detecting inter-ellipsoid contacts," *Comput. Geotech.*, vol. 24, pp. 245–263.
[37] P. W. Cleary and N. Stokes, 1997, "Efficient collision detection for three dimensional super-ellipsoid particles," *8th International Computational Techniques and Applications Conference,* Adelaide, Australia.
[38] P. W. Cleary and M. L. Sawley, 2002, "DEM modelling of industrial granular flows: 3D case studies and the effect of particle shape on hopper discharge," *Appl. Math. Model.*, vol. 26, pp. 89–111.
[39] S. Ji, S. Sun, and Y. Yan, 2015, "Discrete element modeling of rock materials with dilated polyhedral elements," *Procedia Eng.*, vol. 102, pp. 1793–1802.
[40] R. Deshpande, E. Illana Mahiques, S. Wirtz, and V. Scherer, accepted, "Resolving particle shape in DEM simulations from tabulated geometry information," *Powder Technol.*.
[41] T. Weinhart, A. R. Thornton, S. Luding, and O. Bokhove, 2012, "From discrete particles to continuum fields near a boundary," *Granul. Matter*, vol. 14, pp. 289–294.
[42] A. Thornton, S. Luding, and O. Bokhove, 2012, "Modeling of particle size segregation: calibration using the discrete particle method," *Int. J. Mod. Phys. C*, vol. 23, p. 1240014.
[43] G. Stein, S. Wirtz, and V. Scherer, 2016, "Performance improvements of polydisperse DEM simulations using a loose octree approach," *Parallel Comput. Road Exascale*, vol. 27, p. 53.
[44] K. Dong, C. Wang, and A. Yu, 2015, "A novel method based on orientation discretization for discrete element modeling of non-spherical particles," *Chem. Eng. Sci.*, vol. 126, pp. 500–516.
[45] F. Sudbrock, 2014, "DEM/CFD Analyse der konvektiven Trocknung von bewegten Schüttungen," *Dissertation Ruhr-Universität Bochum.*
[46] F. Sudbrock, H. Kruggel-Emden, S. Wirtz, and V. Scherer, 2015, "Convective Drying of Agitated Silica Gel and Beech Wood Particle Beds—Experiments and Transient DEM-CFD Simulations," *Dry. Technol.*, vol. 33, pp. 1808–1820.
[47] W. L. Vargas and J. J. McCarthy, 2002, "Conductivity of granular media with stagnant interstitial fluids via thermal particle dynamics simulation," *Int. J. Heat Mass Transf.*, vol. 45, pp. 4847–4856.
[48] H. Hertz, 1881, "Über die Berührung fester elastischer Körper," *J. Für Reine Angew. Mech.*, vol. 92, pp. 156–171.
[49] T. Tsory, N. Ben-Jacob, T. Brosh, and A. Levy, 2013, "Thermal DEM–CFD modeling and simulation of heat transfer through packed bed," *Powder Technol.*, vol. 244, pp. 52–60.
[50] C. Joulin, J. Xiang, J.-P. Latham, C. Pain, and P. Salinas, 2020, "Capturing heat transfer for

complex-shaped multibody contact problems, a new FDEM approach," *Comput. Part. Mech.*, vol. 7, pp. 919–934.
[51] S. Yagi and D. Kunii, 1957, "Studies on effective thermal conductivities in packed beds," *AIChE J.*, vol. 3, pp. 373–381.
[52] J. Gorewoda and V. Scherer, 2016, "Influence of carbonate decomposition on normal spectral radiative emittance in the context of oxyfuel combustion," *Energy Fuels*, vol. 30, pp. 9752–9760.
[53] G. J. Cheng and A. B. Yu, 2013, "Particle scale evaluation of the effective thermal conductivity from the structure of a packed bed: radiation heat transfer," *Ind. Eng. Chem. Res.*, vol. 52, pp. 12202–12211.
[54] H. Wu, N. Gui, X. Yang, J. Tu, and S. Jiang, 2016, "Effect of scale on the modeling of radiation heat transfer in packed pebble beds," *Int. J. Heat Mass Transf.*, vol. 101, pp. 562–569.
[55] L. Chen, C. Wang, M. Moscardini, M. Kamlah, and S. Liu, 2019, "A DEM-based heat transfer model for the evaluation of effective thermal conductivity of packed beds filled with stagnant fluid: Thermal contact theory and numerical simulation," *Int. J. Heat Mass Transf.*, vol. 132, pp. 331–346.
[56] J. Tausendschön and S. Radl, 2021, "Deep neural network-based heat radiation modelling between particles and between walls and particles," *Int. J. Heat Mass Transf.*, vol. 177, p. 121557.
[57] J. Wiese, 2015, "Experimentelle und numerische Untersuchungen an Holzpelletfeuerungen," *Dissertation Ruhr-Universität Bochum.*
[58] S. Ergun, 1952, "Fluid flow through packed columns," *Chem Eng Prog1*, vol. 48, pp. 89–94.
[59] R. Di Felice, 1994, "The voidage function for fluid-particle interaction systems," *Int. J. Multiph. Flow*, vol. 20, pp. 153–159.
[60] J. E. Hilton and P. W. Cleary, 2011, "The influence of particle shape on flow modes in pneumatic conveying," *Chem. Eng. Sci.*, vol. 66, pp. 231–240.
[61] Z. Y. Zhou, D. Pinson, R. P. Zou, and A. B. Yu, 2011, "Discrete particle simulation of gas fluidization of ellipsoidal particles," *Chem. Eng. Sci.*, vol. 66, pp. 6128–6145.
[62] H. Kruggel-Emden and T. Oschmann, 2014, "Numerical study of rope formation and dispersion of non-spherical particles during pneumatic conveying in a pipe bend," *Powder Technol.*, vol. 268, pp. 219–236.
[63] B. G. M. van Wachem, V. Chéron, and F. Evrard, 2022, "Discrete element modelling of non-spherical particles in turbulent gas-solid flows," *Conference on Modelling Fluid Flow*, Budapest, Hungary.
[64] E. Illana Mahiques, M. Brömmer, S. Wirtz, and V. Scherer, 2022, "Local flow resolution with the Blocked-Off method in DEM-CFD: Gaseous fuel jet dispersion and combustion in a particle assembly," *Conference on Modelling Fluid Flow*, Budapest, Hungary.
[65] A. Alkhalaf, H. A. Refaey, N. Al-durobi, and E. Specht, 2018, "Influence of contact point treatment on the cross flow mixing in a simple cubic packed bed: CFD simulation and experimental validation," *Granul. Matter*, vol. 20, p. 22.
[66] B. Krause *et al.*, 2017, "3D-DEM-CFD simulation of heat and mass transfer, gas combustion and calcination in an intermittent operating lime shaft kiln," *Int. J. Therm. Sci.*, vol. 117, pp. 121–135.
[67] "Bulk-Reaction." https://bulk-reaction.de/ (accessed Jun. 13, 2022).

Conference on Modelling Fluid Flow (CMFF'22)
The 18th International Conference on Fluid Flow Technologies
Budapest, Hungary, August 30 -September 2, 2022

PAST, PRESENT, AND NEW CHALLENGES FOR COMPUTATIONAL HEMODYNAMICS OF CEREBRAL CIRCULATION

Marie OSHIMA[1], Changyoung YUHN [2], Masaharu KOBAYASHI[3]

[1] Corresponding Author. Interfaculty Initiative in Information Studies, the University of Tokyo, 4-6-1 Komaba, Meguro-ku, Tokyo, Japan 153-8505 Tel.: +81 3 5452 6205, E-mail: marie@iis.u-tokyo.ac.jp
[2] Institute of Industrial Science, the University of Tokyo (Currently, Toyota Central R&D Labs., INC.). E-mail: yuhn@iis.u-tokyo.ac.jp
[3] Institute of Industrial Science, the University of Tokyo (Currently, Chi Co., LTD). E-mail: mkoba@iis.u-tokyo.ac.jp

ABSTRACT

A patient-specific simulation has been widely used not only for scientific study to elucidate mechanism between hemodynamics and cardiovascular diseases such as stroke but also for clinical applications to predict post-operative blood flow situation. Since carotid artery stenosis is a major cause of a stroke, patients with severe carotid artery stenosis often undergo revascularization surgery such as carotid artery stenting to prevent a stroke from happening in the future. However, some patients suffer from complications like cerebral hyperfusion syndrome (CHS), which leads to hemorrhage due to a sudden increase in a flow rate in the brain. Therefore, predicting the blood flow in the brain after the surgery is very important to determine the most suitable surgery for an individual patient to avoid complications like CHS after the surgery.

The paper reviews the patient-specific simulation. In order to predict the post-operative flow in the brain after the surgery, it is necessary to consider the entire circulatory system because the surgery affects the blood flow in the brain as well as in the entire circulatory system. Therefore, the authors have been developing a multi-scale blood flow simulation by combining 1D (One-dimensional) and 0D (Zero-dimensional) models.

The patient-specific simulation utilizes geometric and physiological parameters derived from clinical data for the region of interest, i.e. the circle of Wills (CoW) in this paper as well as the literature data for the rest of circulatory system. These data contain uncertainties, which affect the simulation results by propagating through mathematical models and the simulation. Thus, quantifying an impact of uncertainties in medical images on simulated quantities is an essential task to obtain reliable results. In general, uncertainty quantification requires a large number of case studies to investigate the effects of uncertainties in a probabilistic manner. Thus, a surrogate model based on a machine learning technique was developed and applied to three patients for investigation of CHS risk after the surgery.

Keywords: patient-specific simulation, multi-simulation, 1D-0D models, quantification of uncertainties, machine learning, cerebral circulation

1. INTRODUCTION

Stroke is the second cause of death in the world [1]. It is not only fatal because of high mortality rate but also low quality of life in case of severe complications such as parallelization or impaired consciousness. There are two types of strokes: ischemic and hemorrhage strokes. The ischemic strokes are mainly caused by severe arterial stenosis, which is resulted from progression of atherosclerosis. The arterial stenosis is a serious cardiovascular disease-causing large pressure drop and an abrupt decrease in a flow rate. If stenosis becomes highly sever, a surgery such as carotid artery stenting (CAS) or carotid endarterectomy (CAE) is performed to prevent those fatal situations[2,3]. However, the surgery sometimes causes the postoperative syndrome such as intracranial hemorrhage caused by cerebral hyper fusion (CHS) [4] . Thus, it is important to examine the effects of surgery on a patient and to understand changes in the distributions of blood flow and pressure after the surgery.

The patient-specific modeling and numerical simulations have been widely applied to investigate the hemodynamics for an individual patient [5, 6]. In this method, the simulation is performed in the three-dimension for the patient's vasuclar geometry, which is constructed from the medical images such as computed tomography (CT) or magnetic resonance imaging (MRI). It can provide the detailed hemodynamic information but limited only to the region of interest due to resolution of the medical images. The surgery influences hemodynamics not only in a localized region around the stenotic region,

in which medical images are available but also throughout the peripheral areas to the entire circulatory system. The objective of the paper is to develop a simulation system to examine the hemodynamics locally as well as globally in the circulatory system. Thus, a multi-scale approach has been developed to consider the effects of peripheral vascular network as well as the entire circulatory system using combined reduce models of one-dimension (1D) and zero-dimension (0D) [7-9]. The 1D-0D simulation is an appropriate method to capture primary hemodynamics information such as flow rate or pressure with less computing time and better portability comparing to three-dimensional (3D) simulation.

The Patient-specific blood flow simulation is performed by applying vascular geometry and velocity information from medical images of an individual patient to obtain hemodynamic factors such as blood flow velocity, pressure, and wall shear stresses, which are important indicators for cardiovascular diseases. The pipeline of the patient-specific simulation system consists of three steps: 1) vascular geometric modeling, 2) multi-scale blood simulation using multi-modal data of medical images, and 3) visualization of simulation results as illustrated in Figre1[8].

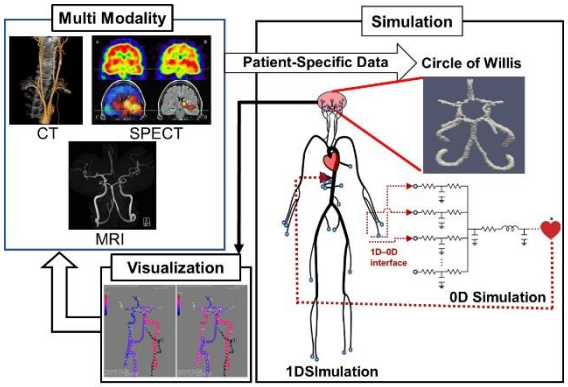

Figure1. Schematic illustration of patient-specific simulation

In the first step for vascular geometric modeling, the 3D vascular geometry is constructed from either CT or MRI. The information on the radius and the length of artery can be obtained as well as the vascular parameter such curvature and torsion from the 3D vascular geometry data and it is applied to a part of 1D domain in order to perform the patient-specific 1D-0D simulation. In the second step for multi-scale blood simulation using multi-modal data of medical images, the simulation can be conducted in either 1D-0D or 3D-1D-0D depending on how detail the hemodynamic information is required. Since the 1D-0D simulation is carried out with consideration of the entire circulatory system incorporating the patient-specific geometry constructed from the medical images, it is quite effective to examine the influences of surgery for each patient. In the last step for visualization, it is important to present the simulation results in an effective way for better understanding of hemodynamics or for an appropriate diagnosis to provide a suitable surgical planning. However, the current visualization tools are generally available for the 3D simulations but not for the 1D-0D simulation. Therefore, the authors have been developing a visualization system for the 1D domain where the patient-specific geometry is applied.

The present simulation system was applied to investigate the blood flow in the Circle of Willis (CoW), which is a vital region of cerebrovascular circulation. The paper presents each process in the pipeline of patient-specific simulation using 1D-0D simulation with multimodal data of medical images. The results were compared between pre- and post-operative flows to examine the effects of revascularization surgery on cerebral circulation[8].

Since the patient-specific simulation is generally carried out using patient data, the uncertainties in the data propagate throughout mathematical models as well as the simulation and affect the simulations results. Therefore, uncertainty quantification (UQ) is an important issue, particularly for clinical applications. In the paper, the UQ is performed using a machine-learning surrogate model based on the 1D-0D simulation of the cerebral circulation with consideration of the entire circulatory system to estimate the flow rates in the Circle of Willis (CoW) for prediction of CHS risk. The CHS occurs when the post-operative flow rate becomes larger than 100% of the pre-operative one, in which the post-operative flow rate becomes twice the pre-operative one [4]. Thus, in this study, a difference in flow (ΔQ) between before and after the surgery was predicted. Since the UQ requires a large size of simulations, a surrogate model has been developed using deep neural network (DNN) with the datasets obtained from the 1D-0D simulation. The accuracy of surrogate model was investigated by varying hyperparameters and the number of training data. The present surrogate models were applied to three patients including one patient with high risk of CHS. The results showed that the surrogate model predicted probabilistic distribution of ΔQ in each artery of CoW with drastic reduction in computer time from twenty- minutes of 1D-0D simulation to milliseconds.

2. VASUCULAR GEOMETRIC MODELING

The vascular geometric modelling plays an important role in the patient-specific simulations. The authors have been developing a vascular geometric modelling system, V-Modeler [10,11]. The vascular geometry is extracted from the medical images of DICOM data format such as CT or MRA. V-Modeler conducts the modeling procedure according to the

five processes: (I) segmentation of arterial lumen, (II) extraction of luminal centerlines, (III) reconstruction of surfaces, (IV) calculation of geometrical parameters, and (V) registration and tracking of centerlines and surfaces. If there are series of medical images in time, the temporal changes in geometry can be captured in a parametric manner.

The arterial lumen is segmented from each slice of medical images in process I. After the centerlines are extracted from the segmented regions in the process II, they are converted into spline functions. In the process III, the 3D surfaces of the lumen are constructed. The process IV provides the geometric parameters of the lumen and its centerlines such as the length of centerline, radius of the lumen on each cross section perpendicular to the centerlines. The 3D geometric parameters of curvatures and the torsions are also calculated along the centerlines. In the process V, registration is performed so as to determine a geometrical transformation by aligning corresponding points between two sets of the same modality of medical images.

The development environment of V-Modeler is based on Visual Studio 2010 Professional (C++ programming language) on Windows 7 Professional 64bit. The image processing libraries are MIST (Media Integration Standard Toolkit, Nagoya University, Japan) and OpenCV 2.2, visualization library is OpenGL. The GUI of V-Modeler is designed to perform each process interactively and user-friendly, and to visualize the results of CoW as described in Figure 2. The vascular geometry of Figure 2 was extracted from MRA of the patient, who was a 70 years old male with 73%(NASCET) stenosis on the left ICA(Internal Carotid Artery) and had CAS surgery for revascularization treatment.

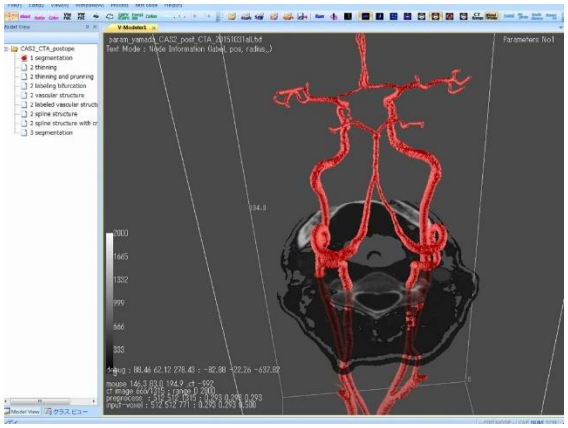

Figure2. The circle of Willis constructed from MRA using V-modeler

In order to derive a smooth centerline against noises intrinsic to the medical images for calculation for curvature and torsion, the authors developed a new penalized SFM, "geo-SFM". The present method enables us to optimize geometrical parameters such as curvature and torsion along arterial centerlines extracted from medical images using a penalty term with a higher-order degree of spline as well as Akaike indices to determine the unknown coefficients associated with penalty terms.

For a B-spline curve and its derivatives, let $\mathbf{P}(t)=(x,y,z)$ be a position vector along a curve as a function of a parameter t as follows:

$$\boldsymbol{P}(t)=\sum_{i=1}^{n} B_{i,k}(t)\boldsymbol{x}_i, \tag{1}$$

where $B_{i,k}(t)$ is the i-th normalized B-spline function of order k (degree k-1), and $\mathbf{x}_i=(x_i, y_i, z_i)$ is the position vector of the n control polygon vertices. $B_{i,k}(t)$ is defined by the Cox-de Boor recursion formulas,

$$\boldsymbol{B}_{i,1}(\boldsymbol{t})=\begin{cases}\mathbf{1} & \boldsymbol{t_i \le t < t_{i+1}}\\ \mathbf{0} & \boldsymbol{otherwise}\end{cases}$$

$$\boldsymbol{B}_{i,k}(\boldsymbol{t})=\frac{(\boldsymbol{t-t_i})\boldsymbol{B}_{i,k-1}(\boldsymbol{t})}{\boldsymbol{k-1}}+\frac{(\boldsymbol{t_{i+k}-t})\boldsymbol{B}_{i+1,k-1}(\boldsymbol{t})}{\boldsymbol{k-1}}. \tag{2}$$

The N-th derivative of the B-spline curve $\mathbf{P}^{(N)}(t)$ with t is obtained from the N-th derivative of the B-spline function, $B_{i,k}{}^{(N)}(t)$.

$$\boldsymbol{P}^{(N)}(\boldsymbol{t})=\sum_{\boldsymbol{i=1}}^{\boldsymbol{n}}\boldsymbol{B}_{\boldsymbol{i,k}}{}^{(\boldsymbol{N})}(\boldsymbol{t})\boldsymbol{x}_i \tag{3}$$

The geometric parameters on the spline curve, such as curvature κ and torsion τ, are given respectively by

$$\boldsymbol{\kappa}=\frac{\mathbf{1}}{\boldsymbol{s'^2}}\sqrt{(\boldsymbol{x''})^2+(\boldsymbol{y''})^2+(\boldsymbol{z''})^2}$$
$$\boldsymbol{\tau}=\frac{1}{\boldsymbol{\kappa^2 s'^6}}\begin{vmatrix}\boldsymbol{x'} & \boldsymbol{y'} & \boldsymbol{z'}\\ \boldsymbol{x''} & \boldsymbol{y''} & \boldsymbol{z''}\\ \boldsymbol{x'''} & \boldsymbol{y'''} & \boldsymbol{z'''}\end{vmatrix}, \tag{4}$$

where x', x'', and x''' are the 1st, 2nd, and 3rd derivative of x in terms of t, and y', y'', y''', z', z'', and z''' are as well. The variable s' is defined as,

$$s'=\sqrt{(x')^2+(y')^2+(z')^2}. \tag{5}$$

The geo-SFM uses the 5th degree spline basis function and penalty terms of both the 3rd and 4th derivatives to optimize curvature and torsion along the fitted curve. The degree of spline basis function requires the 5th degree spline basis function at minimum in order to assure continuity and smooth connectivity of piecewise polynomials with respect to the 3rd derivative along the B-spline curve. The penalty terms require the 3rd and 4th derivatives in order to control the 2nd and 3rd derivatives of the fitted curve used to calculate the curvature and torsion in (4).

The objective function S_{geo} of geo-SFM is defined by

$$S_{geo} = \sum_{j=1}^{m}\{y_j - P(t_j)\}^2 + \lambda_3 \int_{t_{min}}^{t_{max}} \left\{\frac{d^3P(t)}{dt^3}\right\}^2 dt + \lambda_4 \int_{t_{min}}^{t_{max}} \left\{\frac{d^4P(t)}{dt^4}\right\}^2 dt, \quad (6)$$

where $\mathbf{P}(t)$ is the fitted curve, $\mathbf{y}_j$ are m data points, λ_3 and λ_4 are the coefficients of the penalty terms determined to minimize the objective function S_{geo}, and $t_{\min}$ and $t_{\max}$ are integral intervals of the parameter t of the fitted curve.

The AIC is used to identify optimal penalty terms as a measure of the relative quality of statistical models for a given set of data. Let L be the Gaussian log-likelihood; AIC is then given by

$$\boldsymbol{AIC} = \sum_{j=1}^{m} \frac{1}{\sigma^2}\left(y_j - \sum_{i=1}^{n} B_{i,k}(t_j)x_i\right)^2 + 2m\,ln\,\sigma + 3m\,ln\,2\pi + 3 \cdot 2 \cdot trace(\boldsymbol{H}), \quad (7)$$

where $\mathbf{H}$ is defined as

$$\boldsymbol{H} = \boldsymbol{B}\left(\boldsymbol{B}^T\boldsymbol{B} + \lambda_3 \boldsymbol{B}_3{}^T\boldsymbol{B}_3 + \lambda_4 \boldsymbol{B}_4{}^T\boldsymbol{B}_4\right)^{-1}\boldsymbol{B}^T \quad (8)$$

and $trace(\mathbf{H})$ in (7) represents the effective dimension.

3. NUMERICAL METHOD OF MULTI-SCALE BLOOD SIMULATION

The 1D-0D simulation consists of the closed loop to represent the entire circulatory system in a way that the outflow boundaries of the 1D domain are connected to the inflow boundaries of the 0D domain while the.outflow boundaries of the 0D domain are connected to the inflow boundaries of the 1D domain. The 1D simulation is conducted for the blood flow in large arteries while the 0D is for small arteries, arterioles, capillaries, veins, and heart. In the 1D-0D simulation, the statistical data are used for the geometry such as the radius and the length and for the physiological properties such as resistance, compliance, and inductance. The patient-specific geometry is also applied to a part of 1D domain, in this paper, CoW in order to obtain the hemodynamic information for individual patients.

The 1D simulation is applied to a total of 83 arteries which consists of 55 arteries based on Liang model[7] and newly added 27 arteries of cerebrovascular and neck circulations[8]. The governing equations of the 1D simulation can be obtained by integrating the continuity and Navier-Stokes equations over an artery cross-section and are given by [12]:

$$\frac{\partial A}{\partial t} + \frac{\partial Q}{\partial z} = 0 \quad (9)$$

$$\frac{\partial Q}{\partial t} + \frac{\partial}{\partial z}\left(\frac{Q^2}{A}\right) + \frac{A}{\rho}\frac{\partial P}{\partial z} + 8\pi\frac{\mu}{\rho}\frac{Q}{A} = 0 \quad (10)$$

where A, Q and P are the cross-sectional area, the flow rate and the pressure, respectively. In addition, the following pressure-area relationship is used:

$$P - P_0 = \frac{Eh_0}{r_0(1-\sigma^2)}\left(\sqrt{\frac{A}{A_0}} - 1\right) \quad (11)$$

where E, h, r, and s represent the Young's modulus, the wall thickness and arterial radius, and the Poisson ratio. The subscript 0 means a value at the reference state. Since the artery is an incompressible material, the Poisson ratio in the paper is taken to be 0.5. The Lax-Wendorff method is used to solve equations (1)-(3).

In this study, the patient-specific geometry was applied to the part of CoW. The 1D simulation used the configuration of vascular network in the CoW and the geometric information of the arterial radius and length, in which could be provided easily by the 3D geometric information of V-Modeler.

The 0D simulation is applied to the peripheral vascular network, which consists of arteries smaller than one used for the 1D simulations, capillaries, venous system, and heart. The 0-D simulation is given by lumped parameter models as follows[7,8]:

$$C\frac{dP_i}{dt} + Q_{i+1} - Q_i = 0 \quad (12)$$

$$L\frac{dQ_{i+1}}{dt} = -(P_{i+1} - P_i) - RQ_{i+1} \quad (13)$$

where C, L, and R represent the compliance, the inductance, and the resistance of the blood vessel. The 4th order Runge-Kutta method is used to solve equations (4) and (5).

The 1D model can not capture a pressure drop (ΔP) in a stenosis region caused by separation due to an abrupt change in a cross-sectional area because separation is a three-dimensional phenomenon. Therefore, the following 0D stenosis model by Young and Tsai is applied to the stenosis region [13.14]:

$$\Delta P = R_v Q + K_t \frac{8\rho}{\pi^2 D_n^4}\left\{\frac{1}{(1-SR)^2} - 1\right\}^2 Q|Q| + K_u \frac{4\rho L_s}{\pi D_n^2}\dot{Q}, \quad (14)$$

where R_v, D_n, SR, L_s, and $\dot{Q}$ are the viscous resistance of the stenosis, the maximum diameter distal to the stenosis, a stenosis ratio defined as the percentage reduction in diameter $(1 - D_s/D_n)$ with the minimum stenosis diameter D_s, the stenosis length, and the time derivative of Q, respectively. The first, second, and third terms in Eq. (14) describe pressure drop by viscous friction, flow separation, and pulsatility, respectively. In this paper, R_v was given

by Bessems [15] with consideration of the diameter change along the axial direction as follows:

$$R_{\mathrm{v}} = \int_0^{L_{\mathrm{s}}} \frac{128\mu}{\pi D^4(x)} dx\,, \qquad (15)$$

where a parabolic velocity profile (i.e., Poiseuille flow) was assumed throughout the stenosis. The coefficients K_{t} and K_{u} depend on the stenosis geometry. They were assumed to be 1.52 and 1.2, respectively according to the literature [14,16] while K_{u} was fixed as 1.2 due to its negligible influence on ΔP. However, in the UQ study, K_{t} was regarded as an uncertain parameter ranging between 1.0 and 2.699 [17].

When the patient-specific geometry is applied to the 1D-0D simulation, it is also necessary to adjust the differences in the physiological parameters such as the peripheral resistances from the literature data to the patient-specific ones. In this study, the SPECT data were used as the reference data to adjust the peripheral resistances in the 0D domain downstream from the region where the patient-specific geometry region were applied since they represented a map of the peripheral flow rates in the brain. The PC-MRA data were also used together with the SPECT data in order to predict the flow rate more accurately[8]. In the present method, the peripheral resistance of each efferent artery of the CoW, R was adjusted in every cardiac cycle to match with the corresponding reference flow rate by the SPECT data Q_s as follows[8] :

$$R_i^{n+1} = R_i^n \cdot \left(1 - \alpha \cdot \frac{Q_{s\_i} - Q_i^n}{Q_{s\_i}}\right) \qquad (16)$$

where the subscript i and the superscript n denote the efferent arterial segment number and the number of the cardiac cycle, respectively. The parameter α is a relaxation coefficient.

4. VISUALIZATION OF 1D SIMULATION

The commercial software for visualization of results is generally available for the 3D simulation but not for the 1D-0D simulation. In the present simulation, the patient-specific 3D geometry was applied to the CoW region as a part of the 1D simulation. Thus, the paper has developed a visualization system for the 1D simulation where the patient-specific data are used.

The visualization part is incorporated into V-Modeler as described in Figure 3 since the 1D simulation uses the information of the radius and length extracted from the medical image data by V-Modeler [9]. V-Modeler has also the information about the centreline of vascular lumen, which is expressed by a spline-function. First of all, the grid point used for the 1D simulation is allocated in the three-dimensional coordinates using the information of the centreline in the 3D. Since the radius can be obtained from the area resulted from 1D simulation, the pressure and the flow rate were remapped onto the 3D geometry.

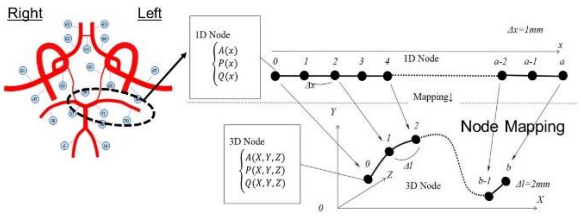

Figure 3. Schematic illustration of mapping 1D simulation results onto 3D vascular geometry

Visualization can be carried out not only for the changes in the flow rates, the pressures, and the cross-sectional areas but also for the wall shear stresses, which are post calculated from the results of 1D simulation. The results can be also presented as movie to see dynamic changes of flow. Figure 4 shows the simulation results of pre-operative (Figure 4.A)) and post-operative (Figure 4.B)) flow rates for the same patient, whose vascular geometry is described in Figure 2.

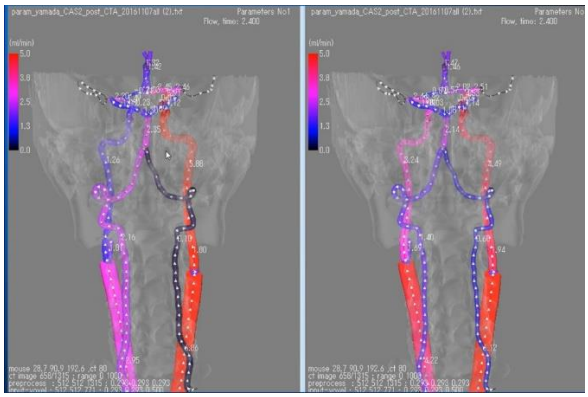

A)Pre-operative case B) Post-operative case

Figure 4. Visualisation of flow rates in CoW from the posterior view

Since there was stenosis on the left ICA, the flow rate on the left side was lower than that on the right side while the flow rate on both sides became the same after the surgery. In general, the flow rates for a healthy person are about equal on both sides so that revascularization surgery was successful.

5. UNCERTAINTY QUNTAIFICATION

Even though patient-specific simulations are verified and validated, there is an intrinsic limit to accuracy due to uncertainties in clinical data. For example, a size of each arterial diameter or length in the CoW can be different depending on a person who perform segmentation. These uncertainties come not only from segmentation but also from various sources such as spatial and temporal resolution of medical images. measurement errors, and so on. Therefore, it is necessary to evaluate the simulation results not in a

deterministic but in a stochastic manner by considering uncertainties in clinical data and their non-linear influences through the simulation on results.

However, if such uncertainties are included in the simulation, the computational cost would increase dramatically due to a large number of simulations by varying simulation conditions with may combinations of uncertainties. In order to perform UQ within a reasonable computational, reduction of computational cost is essential. There are two approaches: reduction in the number of simulations or in the cost of an individual simulation. The first one puts an emphasis on the efficiency of the stochastic space using techniques such as stochastic collocation methods [18] or multi-resolution stochastic expansion [19,20] to achieve a faster convergence of statistics. The second one employs reduced-order (1D–0D) models [21,22]. However, UQ still faces a challenge even with reduced order models since individual simulations usually involve iterative calculations to assimilate the data or to obtain converged solutions, which still requires a large amount of time and computational resources.

Due to recent advancement in machine-leaning technique, one effective way is to construct a data-driven surrogate model by fitting a regression model to the simulation data. The surrogate model can predict the results based on simple input-output relationships from verified and validated cardiovascular models, which leads to significant acceleration of predictions with sufficient accuracy. Recently, a data-driven machine learning method has been develped using deep neural networks (DNNs) [23-25]. DNNs is effective to map high-dimensional data with complex and highly non-linear relationships. Even thogh incoopertaing machine learning techniques to cardiovascular simulations has been an active area of research in the last few years [25-27], most of them have been developed to predict fractional flow reserve in coronary arteries. In this paper, the surrogate model was developed to conduct UQ efficetly even on a PC compter for cerebral circulation, which has complex blood flow patterns because of collateral pathways forming a ring-like structureof CoW.

5.1. Surrogate Model based on Machine Learning

The DNN was employed for the surrogaste model based on machine learning as a regression model and was fitted to the training data to obtain an input-output relationship from the 1D-0D somulation. After contructiong the surrogate model, UQ was condcuted folloing the pipelien described in Figure 5 [28].

In order to develop the surogate model, aquasition of trainging data is an imprtant task by defining inputs and outputs. In this study, input data were a total of 60 parameters as follows:

- Diameters of 22 carotid and cerebral arteries in the 1D model (22 parameters).

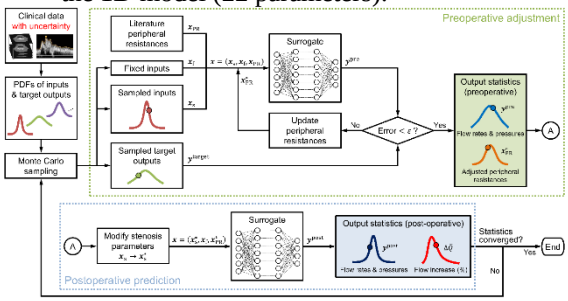

Figure 5. Schematic pipeline of uncertainty quantification [28]

- Lengths of 22 carotid and cerebral arteries in the 1D model (22 parameters).
- R_{v}, D_{n}, K_{t} ,and SR in Eqs. (14) and (15) for each of the left and right ICA stenoses (8 parameters).
- PRs at the six outlets of the CoW (7 parameters).
- Scaling factor for the total PR (1 parameter).
- Age (1 parameter).

A total of 60 parameters characterized the patient's anatomical and physiological conditions and also became as inputs to the surrogate model for investigation of UQ in the cerebral circulation. In this paper, variation of stenosis length, L_{s}, was ignored because the third term of Eq. (14) was negligible compared to the other terms. However, the effect of L_{s} on the viscous resistance of the stenosis was included in R_{v}, as seen in Eq. (15).

After the simulation results such as A, Q, and P were obtained by the present 1D-0D, the following output data were selected for the surrogate model:

- Cycle-averaged flow rates, $\bar{Q}$, in the middle of the carotid and cerebral arteries (22 quantities).
- Cycle-averaged pressures, $\bar{P}$, in the middle of the carotid and cerebral arteries (22 quantities).
- Mean arterial pressure, i.e., the cycle-averaged pressure in the middle of the left subclavian artery (1 quantity).

A total of 45 output parameters above were the primary clinically relevant quantities of cerebral circulation in this study. Therefore, the surrogate model defined a mapping from the inputs $\boldsymbol{x} \in \mathbb{R}^{60}$ to the outputs $\boldsymbol{y} \in \mathbb{R}^{45}$.

After the 1D-0D simulation was performed to create a total of 200,000 sets of input-output varying 60 input parameters, the data set was divided into three groups: 1) training , 2) validation, and test data in a ratio of 6:2:2. The surrogate model was developed using the DNN with 120,000 training data and validated with 40,000 test data. The hyperparameters of DNN such as N_{layer}, N_{mode}, B, and l_{r} were set to be 7,200, 3,00, and $10^{-2.5}$, respectively.

5.2. Patient Characteristics

A total of three patients were selected for this study. The characteristic of each patient is summarized in Table 1 and the vascular geometry of each patient is also described in Figure 6.

Table 1 Characteristics of patients[28]

		Patient 1	Patient 2	Patient 3
Age/Sex		82/M	63/M	72/M
Mean arterial pressure		109.0 mmHg	112.0 mmHg	118.3 mmHg
Stenosis	Location	Rt. ICA	Lt. ICA	Rt. ICA
	SR	59%	83%	91%
	R_v	0.5 mmHg s mL^{-1}	11.3 mmHg s mL^{-1}	66.6 mmHg s mL^{-1}
Treatment		Endarterectomy	Staged stenting	Endarterectomy
Geometry		CT	CT	CT
Flow data	Inflow rate	PC-MRI	Doppler ultrasound	PC-MRI
	Outflow rate	SPECT	SPECT	SPECT
Circle of Willis structure		Complete	One artery may be absent	Complete

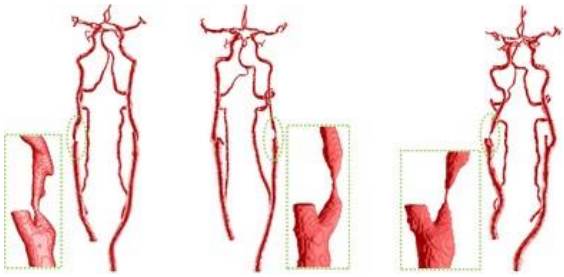

A)Patient 1 B) Patient 2 3)Patient 3

Figure 6. Vascular geometry{28}

For all patients, CT data were used to constrcut vascular geometry while PC-MRI or ultrasound data were used for inflows we well as SECT data for outflows. The mean arterial pressure in the upper arm were measured before the surgery. The stenosis ratios (SR) for Patients 1–3 were measured as 59%, 83%, and 91%, respectively, which result in the respective values of R_v as 0.5 mmHg s mL^{-1}, 11.3 mmHg s mL^{-1}, and 66.6 mmHg s mL^{-1}, respectively. Patient 1 and Patient 3 had a complete CoW while Patient 2 was difficult to confirm an anterior communicating artery (ACoA) from CT data. In addition, Patient 2 was identified by the surgeon aa high risk for CHS, based on the collected data. In fact, Patient 2 underwent staged surgery, where the stenosis was pre-dilated with a balloon, followed by complete dilation with a stent after two weeks.

5.3. Uncertainty Quantification for risk prediction of CHS

The risk of CHS is identified as a drastic increase (>100%) in cerebral blood flow (CBF) CBF immediately after an ICA stenosis surgery [4]. Therefore, if a difference ΔQ in flowrates between per-operative and post-operative flows becomes more that 100 %, a patient can be assumed to have high risk of cerebral hyperfusion status. Therefore, the following quantity is evaluated as an indicator:

$$\Delta\bar{Q}_i = \frac{\bar{Q}_i^{\text{post}} - \bar{Q}_i^{\text{pre}}}{\bar{Q}_i^{\text{pre}}} \times 100\%, i = 1, 2, \ldots, 6 \qquad (17)$$

where $\bar{Q}_i^{\text{pre}}$ and $\bar{Q}_i^{\text{post}}$ denote the cycle-averaged flow rates at the six outlets of the CoW before and after dilating the stenosis, respectively.

Since the arterial diameter or length was obtained from CT, its uncertainty associated with CT was defined with ±2 pixels (±0.702–0.936 mm, depending on image resolution) with respect to the arterial diameter obtained from segmentation. The uncertainty in the stenosis parameters was considered to be a 2-pixel except Patient 2, whose the anterior communicating artery (ACoA) was too difficult to be segmented from CT images. Hence, we assumed its diameter had an uncertainty of 0.1–2.6 mm, which included the possibility that the artery was absent. .

The uncertainties in the measured flow rates were determined depending on the modality. The uncertainty in each modality was defined as ±16% for PCR-MRI, ±35% for ultrasound, and ±16% for SPECT. These ranges were determined based on the literature [8] .

The Monte-Carlo method was used to evaluate propagation of uncertainties and their influences on the predicted $\Delta\bar{Q}_i$. The surrogate model reduced significantly the time and computational costs required for UQ to several milliseconds on a single core of the CPU (Intel Core i9-9900K). In this study, a GPU machine (NVIDIA GeForce RTX2080 Ti) was used to perform 10,000 parallel predictions on a GPU, which resulted in more significant reduction of computer time.

Figure 7 summarizes ΔQ, an increase in flow rate from pre- to post-operation at the middle cerebral artery n the stenosis side.

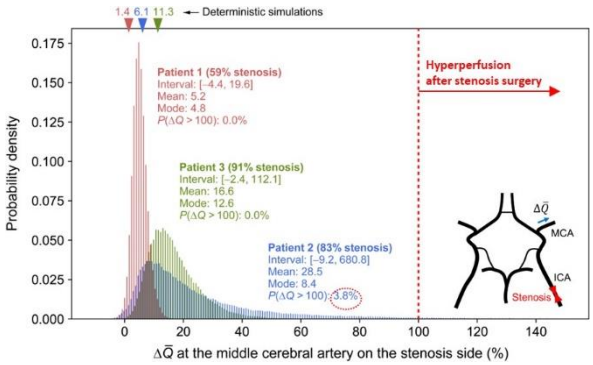

Figure 7. Comparison of probability density of an increase in flow rate from pre-operative to the post-operation (ΔQ) for Patient 1-3[28]

As shown in Figure 7, large variations were found in the predicted $\Delta\bar{Q}$ by considering uncertities.

The distribution of $\Delta\bar{Q}$ showed more extensive spread, especially to high values, in Patients 2 and 3 with more severe stenosis (83% and 91% stenosis, respectively) than in Patient 1 (59% stenosis). Since Patient 2 had a large uncertainty in the diameter of the ACoA, a pronounced variability of $\Delta\bar{Q}$ (up to 681%) was observed, which implied that $\Delta\bar{Q}$ was significantly affected by this artery. In addtion, Patient 2 might have a 3.8% chance of $\Delta\bar{Q}$ exceeding 100% while the corresponding estimates for Patients 1 and 3 were 0% and 0.001% (only one sample), respectively.

6. SUMMARY

The paper presented a multi-scale 1D-0D simulation method with multimodal medical images. In order to conduct uncertainty quantification, a data-driven surrogate model was developed using a machine learning technique. The risk of CHS was predicted by training a DNN with 1D-0D simulation data. The surrogate model reduced the time required for a prediction to a few milliseconds. The present surrogate model was applied to the UQ problem by evaluating the impact of uncertainties in the arterial diameters, stenosis parameters, and measured flow rates on the predicted increase in CBF ($\Delta\bar{Q}$) following carotid artery stenosis surgery. Due to the excellent parallelization performance, the surrogate model enabled UQ with 100,000 predictions to be performed in less than a minute. A high $\Delta\bar{Q}$ of more than 100% was observed when the stenosis ratio was high and the ACoA had a small diameter, which suggested that severe stenosis with insufficient collateral circulation may be a risk factor for CHS.

Even though the paper showed only CHS case, the surrogate model can be applicable more broadly to prediction of cerebral circulation. The proposed surrogate modeling approach will facilitate the execution of not only UQ but also other computationally expensive tasks such as sensitivity analysis and extensive case studies to advance applying simulation to clinical study.,

ACKNOWLEDGEMENTS

This work was supported by the Japan Society for the Promotion of Science through Grants-in-Aid for Scientific Research (Grant Nos. 16H04264 and 18J21374). The authors would like acknowledge Dr. Shigeki at Shiga University of Medical Science and Motoharu Hayakawa at Fujita Health University for their support to provide medical images.

REFERENCES

[1] WHO (World Health Organization) , ''The top cause of death'', https://www.who.int/news-room/fact-sheets/detail/the-top-10-causes-of-death.

[2] North American Symptomatic Carotid Endarterectomy Trial Collaborators, Barnett HJM, Taylor DW, et al. , 1991, ''Beneficial Effect of Carotid Endarterectomy in Symptomatic Patients with High-grade carotid stenosis'', . *N Engl J Med*. Vol. 325, pp.445-453.

[3] Brott, T. G., Hobson, R.W. 2nd, Howard, G., et al., 2010, '' Stenting versus Endarterectomy for Treatment of Carotid-Artery Stenosis''. *N Engl J Med*. Vol.363, pp.11-23.

[4] van Mook, W. N., Rennenberg, R. J., Schurink, G. W., et al. 2005, ''Cerebral Hyperfusion Syndrome''. *Lancet Neurol*., Vol.4, pp.877-888.

[5] Oshima, M., Torii, R., Tokuda, S., Yamada, S., Koizumi, A.,2012, "Patient-Specific Modeling and Multi-ScaleBlood Simulation for Computational Hemodynamic Study on the Human Cerebrovascular System", Current Pharmaceutical Biotechnology, Vol.13, pp. 2153-2165.

[6] Grinberg, L., Cheever, E., Anor, T., Madsen, J. R., Karniadakis, G. E., 2011, '' Modeling Blood Flow Circulation in Intracranial Arterial Networks: a Comparative 3D/1D Simulation Study'', *Ann Biomed Eng*. Vol. 39, **pp.**297-309.

[7] Liang, F., Oshima, M., Huang, H., Liu, H., Takagi, S., 2015, "Numerical Study of Cerebroarterial Hemodynamic Changes Following Carotid Artery Operation: A Comparison Between Multiscale Modeling and Stand-Alone Three-Dimensional Modeling", Journal of Biomechanical Engineering, Vol.137, DOI: 10.1115/1.403145.

[8] Zhang, H., Fujiwara, N., Kobayashi, M., Yamada, S., Liang, F., Takagi, S., Oshima, M., 2016, "Development of a Numerical Method for Patient-Specific Cerebral Circulation using 1D-0D Simulation of the Entire Cardiovascular System with SPECT Data", Annals of biomedical engineering, Vol.44, pp. 2351-2363.

[9] Yuhn, C., Hoshina, K., Miyahara, K., Oshima, M. , 2019, "Computational Simulation of Flow-Induced Arterial Remodeling of the Pancreaticoduodenal Arcade Associated with Celiac Artery Stenosis", Journal of Biomechanics, Vol.92, pp. 146-154.

[10] Kobayashi, M., Hoshina, K., Nemoto, Y., Takagi, S., Shojima, M., Hayakawa, M., Yamada, S., Oshima, M., 2020, "A Penalized Spline Fitting Method to Optimize Geometric Parameters of Arterial Centerlines Extracted from Medical Images", Computerized Medical Imaging and Graphics, Vol.84, pp. 101746..

[11] Kobayashi, M., Hoshina, K., Yamamoto, S., Nemoto, Y., Akai, T., Shigematsu, K., Watanabe, T., Oshima, M., 2015, "Development of an Image-Based Modeling System to Investigate Evolutional Geometric Changes of a Stent Graft in an Abdominal Aortic Aneurysm", Circulation

Journal, Vol.79, pp. 1534-1541.
[12] Olufsen, M. S., Peskin, C. S., Kim, W. Y., Pedersen, E. M., Nadim, A., Larsen, J.,2003,'' Numerical Simulation and Experimental Validation of Blood Flow in Arteries with Structured-Tree Outflow Conditions'', *Ann Biomed Eng*. Vol.28, pp.1281-1299.
[13] Young, D. F., Tsai, F. Y., 1973, '' Flow Characteristics in Models of Arterial Stenoses—i. Steady Flow. *J Biomech*. Vol.6., pp.395-402.
[14] Young, D. F., Tsai, F. Y., 1973, '' Flow Characteristics in Models of Arterial Stenoses—ii. Unsteady Flow'', *J Biomech*., Vol.6, pp.547-559.
[15] Bessems, D., 2007, ''On the Propagation of Pressure and Flow waves through SWthe patient-specific arterial system*",* PhD Thesis, Technische Universiteit Eindhoven, Eindhoven, Netherlands.
[16] Seeley, B. D, Young, D. F., 1976, '' Effect of Geometry on Pressure Losses across Models of Arterial Stenoses''. *J Biomech*., Vol.9, pp.439-446.
[17] Heinen S. G. H, van den Heuvel D. A. F., de Vries J. P. P. M., van de Vosse, F. N, Delhaas, T. , Huberts, W. A., 2019, ''Geometry-Based Model for Non-Invasive Estimation of Pressure gradients over iliac artery stenoses. *J Biomech*, Vol.92, pp.67-75.
[18] Sankaran, S., Marsden, AL., 2011," A stochastic collocation method for uncertainty quantification and propagation in cardiovascular simulations", *J Biomech. Eng*., Vol. 133, pp.031001.
[19] Schiavazzi, D.E., Doostan, A., Iaccarino, G., Marsden, A.L., 2017, "A generalized multi-resolution expansion for uncertainty propagation with application to cardiovascular modeling", *Comput. Methods Appl. Mech. Eng.*, Vol.314, pp.196-221.
[20] Seo, J, Schiavazzi, D.E., Kahn, A.M., Marsden, A.L., 2020, "The effects of clinically-derived parametric data uncertainty in patient-specific coronary simulations with deformable walls", *Int. J Numer. Method Biomed Eng.*, Vol.36, DOI: 10.1002/cnm.3351.
[21] Xiu D, Sherwin S.J., 2007, "Parametric uncertainty analysis of pulse wave propagation in a model of a human arterial network", *J Comput. Phys.*, Vol.226, pp.1385-1407.
[22] Chen, P., Quarteroni, A., Rozza, G., 2013, "Simulation-based uncertainty quantification of human arterial network hemodynamics", *Int. J Numer. Method Biomed Eng.*, Vol.29(6), pp.698-721.
[23] Zhu, Y., Zabaras, N., 2018, "Bayesian deep convolutional encoder–decoder networks for surrogate modeling and uncertainty quantification", *J Comput. Phys.*, Vol.366, pp.415-447.
[24] Tripathy, R.K., Bilionis, I., 2018, "Deep UQ: learning deep neural network surrogate models for high dimensional uncertainty quantification", *J Comput. Phys*., Vol. 375, pp.565-588.
[25] Liang, L., Mao, W., Sun, W., 2020, "A feasibility study of deep learning for predicting hemodynamics of human thoracic aorta", *J Biomech*., Vol.99, pp.109544.
[26] Sankaran, S., Grady, L., Taylor, C.A., 2015, "Impact of geometric uncertainty on hemodynamic simulations using machine learning", *Comput. Methods Appl. Mech. Eng*., Vol.297, pp.167-190.
[27] Itu, L., Rapaka, S., Passerini, T., et al., 2016, "A machine-learning approach for computation of fractional flow reserve from coronary computed tomography", *J Appl Physiol*., Vol.121, pp.42-52.
[28] Yuhn, C., Oshima, M., Chen, Y., Hayakawa, M., Yamada, S., 2022, "Uncertainty Quantification in Cerebral Circulation Simulation Focusing on Collateral Flow: Surrogate Model Approach with Machine Learning", *PLOS Comput. Biol.*, DOI: 10.1371/journal.pcbi.1009996.

Conference on Modelling Fluid Flow (CMFF'22)
The 18th International Conference on Fluid Flow Technologies
Budapest, Hungary, August 30-September 2, 2022

State of Art and Challenges in Computational Aeroacoustics

Manfred KALTENBACHER[1], Stefan SCHODER[1], Clemens FREIDHAGER[1]

[1] Institute of Fundamentals and Theory in Electrical Engineering , Graz University of Technology (TU Graz). Inffeldgasse 18, 8010 Graz, Austria. E-mail: manfred.kaltenbacher@tugraz.at

ABSTRACT

Aeroacoustics is a young physical and engineering discipline and a topic of strong ongoing research. Basically, all physical phenomena of flow induced sound are described by the set of compressible flow equations. To achieve a deeper physical understanding of the sound generation phenomena, the sound propagation and its interaction, physical models and appropriate numerical simulation schemes are needed. In doing so, the physics of the famous inhomogeneous wave equation of Lighthill and its extensions, as well as perturbation equations based on systematic decomposition of physical field properties are discussed. Furthermore, three different benchmark cases are presented, which serve as important building blocks for the development of new physical models and numerical simulation schemes.

Keywords: Aeroacoustics, analogies, perturbation equations, Helmholtz decomposition

NOMENCLATURE

c	[m/s]	speed of sound
H	[m^2 / s^2]	total enthalpy
$\underline{L}$	[m/s^2]	Lamb vector
l_{ch}	[m]	characteristic length scale
Ma	[-]	Mach number
$\underline{n}$	[-]	unit normal vector
p	[Pa]	total pressure
$\overline{p}$	[Pa]	time mean pressure
p'	[Pa]	fluctuating pressure
p^{a}	[Pa]	acoustic pressure
p^{ic}	[Pa]	incompressible pressure
$\underline{\underline{T}}$	[Pa]	Lighthill tensor
u_{ch}	[m/s]	characteristic flow velocity
$\underline{u}$	$[m/s]$	total velocity vector
$\overline{\underline{u}}$	$[m/s]$	time mean velocity vector
$\underline{u}^{\mathrm{a}}$	$[m/s]$	acoustic particle velocity vector
$\underline{u}^{\mathrm{ic}}$	$[m/s]$	incompressible velocity vector
$\underline{x}$	[m]	observer coordinate vector
$\underline{y}$	[m]	source coordinate vector
δ	[-]	Kronecker delta
λ	[m]	wavelength
ρ	[kg/m^3]	total density
ρ'	[kg/m^3]	fluctuating density
ρ^{a}	[kg/m^3]	acoustic density
$\underline{\underline{\tau}}$	[N/m^2]	viscous stress tensor
φ	[m^2/s]	scalar flow potential
ψ	[m^2/s]	scalar acoustic potential
$\underline{\omega}$	[1/s]	vorticity vector

Subscripts and Superscripts

a	acoustic
c	compressible
ch	characteristic
ic	incompressible
ref	reference
-	temporal mean
0	constant physical value

1. INTRODUCTION

The sound generated by a flow in an unbounded fluid is usually called *aerodynamic sound*. Most unsteady flows in technical applications are of high Reynolds number, and the acoustic radiation is a very small by-product of the motion. Thereby, turbulence is usually produced by fluid motion over a solid body and/or by flow instabilities.

Since the beginning of computational aeroacoustics (CAA) several physical models and numerical schemes have been developed, each of these trying to overcome the challenges for an effective and accurate computation of the radiated sound. The challenges that have to be considered for the simulation of flow induced sound include [1, 2, 3, 4]:

- *Energy disparity and acoustic inefficiency:* There is a large disparity between the energy in the flow and the radiated acoustic energy. In general, the total radiated power of a turbulent jet scales with $O(u_{\mathrm{ch}}^8/c^5)$ (u_{ch} is the characteristic flow velocity and c the speed of sound), and

pressure fluctuations on surfaces inside the flow scales with $O(u_{\mathrm{ch}}^6/c^3)$.

- *Length scale disparity:* Large disparity also occurs between the size of an eddy in the turbulent flow and the wavelength of the generated acoustic sound. Eddies with characteristic length scale l_{ch}, velocity u_{ch}, lifetime l_{ch}/u_{ch}, and frequency f radiate acoustic waves of the same characteristic frequency, but with a much larger length scale being the acoustic wavelength

$$\lambda \propto c\,\frac{l_{ch}}{u_{\mathrm{ch}}} = \frac{l_{ch}}{\mathrm{Ma}}. \tag{1}$$

  In Eq. (1) Ma denotes the Mach number computed by the ratio of the characteristic velocity u_{ch} over the speed of sound c.

- *Dispersion:* Numerical discretization in space and time converts the original non-dispersive system into a dispersive discretized one. As such, this error has to be kept as small as possible by the numerical schemes, in which both the amplitude and phase of the wave are of crucial importance.

- *Simulation of unbounded domains:* A main issue for the simulation of unbounded domains using volume discretization methods remains the boundary treatment, which needs to be applied to avoid reflections of outgoing vortical structures as well as reflections of waves at the boundary of the computational domain.

In general, aeroacoustic formulations may be categorized as follows: (1) direct numerical simulations resolving all vortical and acoustic scales; (2) aeroacoustic analogies; (3) perturbation equations based on systematic decomposition of physical field properties. In this contribution, the focus is on aeroacoustic analogies and perturbation equations. Direct numerical simulations by solving the full set of compressible flow equations and resolving both vortical and wave components become more and more attractive, due to the increase of computer resources [5, 6, 7, 8]. Still, the application to industrial relevant problems is limited.

2. PHYSICAL MODELING

2.1. Lighthill's analogy and extensions

Lighthill transformed the general equations of mass and momentum conservation to an exact inhomogeneous wave equation whose source terms are important only within the turbulent region [9]. In doing so, the in-homogeneous wave equation was derived

$$\left(\frac{1}{c_0^2}\frac{\partial^2}{\partial t^2} - \frac{\partial^2}{\partial x_i^2}\right) c_0^2(\rho-\rho_0) = \frac{\partial^2 T_{ij}}{\partial x_i \partial x_j}\,. \tag{2}$$

It has to be noted that $(\rho-\rho_0) = \rho'$ is a fluctuating density not being equal to the acoustic density ρ^{a}, but a superposition of flow and acoustic parts within flow regions. Far away form the flow, the fluctuating density ρ' approaches the acoustic density ρ^{a}. Furthermore, the right hand side of (2) contains the *Lighthill stress tensor*, and computes by

$$T_{ij} = \rho u_i u_j + \Big((p-p_0) - c_0^2(\rho-\rho_0)\Big)\,\delta_{ij} - \tau_{ij}\,. \tag{3}$$

In Eqs. (2) and (3) ρ denotes the total density, ρ_0 the ambient density, c_0 the mean speed of sound, p the total pressure, p_0 the ambient pressure, $\underline{u}$ the total velocity, δ the Kronecker delta and τ_{ij} the components of the viscous stress tensor. In the definition of the Lighthill tensor according to Eq. (3) the term $\rho u_i u_j$ are called the Reynolds stresses. The second term $\Big((p-p_0) - c_0^2(\rho-\rho_0)\Big)\,\delta_{ij}$ represents the *excess of* moment transfer by the pressure over that in the ideal fluid of density ρ_0 and speed of sound c_0. This is produced by wave amplitude nonlinearity, and by mean density variations in the source flow. The viscous stress tensor τ_{ij} properly accounts for the attenuation of the sound. Please note that the terms in T_{ij} not only account for the generation of sound, but also includes acoustic *self modulation* caused by

- acoustic nonlinearity,
- the convection of sound waves by the flow velocity,
- refraction caused by sound speed variations,
- and attenuation due to thermal and viscous actions.

The influence of acoustic nonlinearity and thermoviscous dissipation is usually sufficiently small to be neglected within the source region. Convection and refraction of sound within the flow region can be important, e.g., in the presence of a mean shear layer (when the Reynolds stress will include terms like $\rho u_{0i} u'_j$, where $\underline{u}_0$ and $\underline{u}'$ respectively denote the mean and fluctuating components of $\underline{u}$). Such effects are described by the presence of unsteady linear terms in T_{ij}. Furthermore, since for practical applications, T_{ij} is obtained by numerically solving the full set of compressible flow equations, the question of how accurate these terms are resolved, is always present.

In summary, Lighthill's inhomogeneous wave equation equipped with appropriate boundary conditions (e.g., sound hard at solid walls) correctly models all physical flow-acoustic effects. However, the whole set of compressible flow dynamics equations has to be solved in order to be able to calculate Lighthill's tensor. This means that both the flow structures and acoustic waves have to be resolved, which is an enormous challenge for any numerical scheme and the computational noise itself may strongly disturb the physical radiating wave components [10]. Therefore, in the theories of Phillips and Lilley interaction effects have been, at least to some extent, moved to the wave operator [11, 12]. These equations predict

certain aspects of the sound field surrounding a jet quite accurately, which are not accounted in Lighthill's equation due to the restricted numerical resolution of T_{ij} [13]. Please note that Lighthill was initially interested in solving the problem illustrated in Fig. 1a, of the sound produced by a turbulent nozzle flow. However, at this time a volume discret-

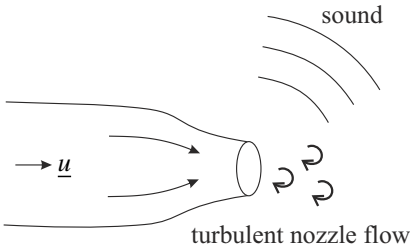

(a) Turbulent nozzle flow.

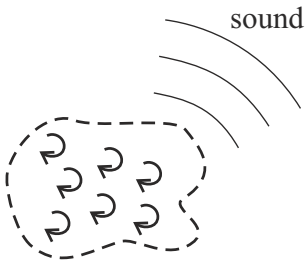

(b) Isolated turbulent region.

Figure 1. Sound generation by turbulent flows.

ization by numerical schemes was not feasible and so a transformation of the inhomogeneous wave equation into an integral representation was performed by Green's function of free radiation, resulting in

$$c_0^2\rho'(\underline{x},t) = \frac{1}{4\pi}\frac{\partial^2}{\partial x_i \partial x_j}\int_{-\infty}^{\infty}\frac{T_{ij}(\underline{y},t-|\underline{x}-\underline{y}|/c_0)}{|\underline{x}-\underline{y}|}\,\mathrm{d}\underline{y}\,. \tag{4}$$

Thereby, $\underline{y}$ defines the source coordinate and $\underline{x}$ the coordinate at which the acoustic density fluctuation is computed. Therefore, Lighthill's integral formulation just applies to the simple situation as given in Fig. 1b. This avoids complications caused by the presence of the nozzle. Curle investigated the effects of surfaces at rest on the integral solution in terms of Green's function on Lighthill's theory [14]. The extension uses the known facts of distribution theory, and the formulation reads as

$$\begin{aligned} c_0^2\rho'\,H(f) \;=\; & \frac{\partial^2}{\partial x_i \partial x_j}\int_{\Omega}\frac{\left\langle T_{ij}\right\rangle}{4\pi|\underline{x}-\underline{y}|}\,\mathrm{d}\underline{y} \\ & -\frac{\partial}{\partial x_i}\oint_{\Gamma_s}\frac{\left\langle (p-p_0)\delta_{ij}-\tau_{ij}\right\rangle}{4\pi|\underline{x}-\underline{y}|}\,\mathrm{d}s_j(\underline{y})\,, \end{aligned} \tag{5}$$

where $<\star>$ denotes the evaluation of the term at retarted time and $H(f)$ the Heaviside function of f describing the solid (scatterer) surface Γ_s by

$$f(\underline{x}) = \begin{cases} 0 & \text{for } \underline{x} \text{ on } \Gamma_s \\ <0 & \text{for } \underline{x} \text{ within the surface} \\ >0 & \text{for } \underline{x} \text{ in } \Omega \end{cases}. \tag{6}$$

Ffowcs Williams and Hawkings [15] generalized Curle's integral representation towards accounting for the effects of arbitrary moving bodies in the source domain, extending Kirchhoff's formula derived in [16]. The aeroacoustic analogy of Ffowcs Williams and Hawkings[15] is probably one of the most used analogies for free radiation today[17, 18]. However, the integral solution has the restriction that the integration surface must surround all reflection walls and the mean flow field must be constant or zero. The surface may be a physical boundary of a solid or a transparent surface that encloses a fluid body.

For practical applications of Lighthill's analogy, it would be quite beneficial to know the leading order term of Lighthill's tensor. This analysis has been done in [19] for low Mach number flows in an isentropic medium by applying the method of matched asymptotic expansion (see, e.g., [10]). Sound emission from an eddy region involves three length scales: the eddy size l, the wavelength λ of the sound, and a dimension L of the region. The problem is solved for $\mathrm{Ma} \ll 1$ and $L/l \sim 1$ by matching the compressible eddy core scaled by l to a surrounding acoustic field scaled by λ. Thereby, Lighthill's solution is shown to be adequate in both regions, if T_{ij} is approximated by

$$T_{ij} \approx \rho_0 u_i^{ic} u_j^{ic}\,, \tag{7}$$

with $\underline{u}^{ic} = \nabla\times\underline{\psi}(\underline{\omega})$ and vorticity $\underline{\omega} = \nabla\times\underline{u}^{ic}$. Such a flow field is described by solving the incompressible flow dynamics equations. Thereby, an incompressible flow velocity $\underline{u}^{ic}$ and pressure p^{ic} are obtained. For an incompressible flow, the divergence of $\underline{u}^{ic}$ is zero, which allows to rewrite the second spatial derivative of Eq. (7) by

$$\frac{\partial^2}{\partial x_i x_j}(\rho_0 u_i^{ic} u_j^{ic}) = \rho_0 \frac{\partial u_j^{ic}}{\partial x_i}\frac{\partial u_i^{ic}}{\partial x_j}\,. \tag{8}$$

Furthermore, applying the divergence to the conservation of momentum and neglecting viscous stresses provides the following equivalence

$$\frac{\partial^2 p^{ic}}{\partial x_i^2} = -\rho_0 \frac{\partial^2 u_i^{ic} u_j^{ic}}{\partial x_i \partial x_j}\,. \tag{9}$$

In doing so, the flow is totally separated from the acoustic field, which also means that any influence of the acoustic field on the flow field is neglected. Such an approach belongs to hybrid schemes separating the flow from the acoustic computations [4]. Thereby, an optimal computational grid can be used for each individual physical field achieving highest accuracy. As a result, the two grids may be quite different according to the following criteria: (1)

near walls, the flow grid needs refinement to resolve boundary layers; (2) the flow grid is mostly coarsened towards outflow boundaries to dissipate vortices; (3) the acoustic grid has to transport waves and therefore needs an uniform grid size all over the computational domain. Thereby, any feedback of the acoustic field on the flow field can just be modeled, when the compressible flow equations are solved to resolve all vertical and wave structures.

2.2. Perturbation equations

The acoustic/viscous splitting technique for the prediction of flow induced sound was first introduced in [20], and afterwards many groups presented alternative and improved formulations for linear and nonlinear wave propagation [21, 22, 23, 24]. These formulations are all based on the idea, that the flow field quantities are split into compressible and incompressible parts.

For the following derivation, a generic splitting of physical quantities is applied to the conservation equations

$$p = \bar{p} + p^{ic} + p^{c} = \bar{p} + p^{ic} + p^{a} \quad (10)$$

$$\underline{u} = \underline{\bar{u}} + \underline{u}^{ic} + \underline{u}^{c} = \underline{\bar{u}} + \underline{u}^{ic} + \underline{u}^{a} \quad (11)$$

$$\rho = \rho_0 + \rho_1 + \rho^{a} \,. \quad (12)$$

Thereby the field variables are split into mean and fluctuating parts just like in the LEE (Linearized Euler Equations). In addition the fluctuating field variables are split into acoustic and non-acoustic components. Finally, the density correction ρ_1 is build in as introduced above. This choice is motivated by the following assumptions

- The acoustic field is a fluctuating field.
- The acoustic field is irrotational, i.e. $\nabla \times \underline{u}^{a} = 0$.
- The acoustic field requires compressible media and an incompressible pressure fluctuation is not equivalent to an acoustic pressure fluctuation.

By doing so, the perturbation equations[1] assuming an incompressible flow are derived

$$\frac{\partial p^{a}}{\partial t} + \underline{\bar{u}} \cdot \nabla p^{a} + \rho_0 c_0^2 \nabla \cdot \underline{u}^{a} = -\frac{\partial p^{ic}}{\partial t} - \underline{\bar{u}} \cdot \nabla p^{ic} \quad (13)$$

$$\rho_0 \frac{\partial \underline{u}^{a}}{\partial t} + \rho_0 \nabla(\underline{\bar{u}} \cdot \underline{u}^{a}) + \nabla p^{a} = 0 \quad (14)$$

with spatial constant mean density ρ_0 and speed of sound c_0. This system of partial differential equations is equivalent to the previously published ones [22]. The source term is the substantial derivative of the incompressible flow pressure p^{ic}. Using the acoustic scalar potential ψ^{a} and assuming a spatial constant mean density ρ_0 and speed of sound c_0, Eq. (14) may be rewritten by

$$\nabla \left(\rho_0 \frac{\partial \psi^{a}}{\partial t} + \rho_0 \underline{\bar{u}} \cdot \nabla \psi^{a} - p^{a} \right) = 0 \,, \quad (15)$$

resulting in

$$p^{a} = \rho_0 \frac{\partial \psi^{a}}{\partial t} + \rho_0 \underline{\bar{u}} \cdot \nabla \psi^{a} \,. \quad (16)$$

Now, substituting Eq. (16) into Eq. (13) leads to

$$\frac{1}{c_0^2} \frac{D^2 \psi^{a}}{Dt^2} - \Delta \psi^{a} = -\frac{1}{\rho_0 c_0^2} \frac{Dp^{ic}}{Dt} \,; \quad \frac{D}{Dt} = \frac{\partial}{\partial t} + \underline{\bar{u}} \cdot \nabla \,. \quad (17)$$

This convective wave equation fully describes acoustic sources generated by incompressible flow structures and its wave propagation through flowing media. In addition, instead of the original unknowns p^{a} and $\underline{u}^{a}$ just the scalar unknown ψ^{a} has to be computed. In accordance with the acoustic perturbation equations (APE), this resulting wave equation for the acoustic scalar potential has been named *Perturbed Convective Wave Equation* (PCWE) [26, 27].

Finally, it is of great interest that by neglecting the mean flow $\underline{\bar{u}}$ in Eqs. (13) and (14), one arrives at the linearized conservation equations of acoustics with $\partial p^{ic}/\partial t$ as a source term

$$\frac{1}{\rho_0 c_0^2} \frac{\partial p^{a}}{\partial t} + \nabla \cdot \underline{u}^{a} = \frac{-1}{\rho_0 c_0^2} \frac{\partial p^{ic}}{\partial t} \quad (18)$$

$$\frac{\partial \underline{u}^{a}}{\partial t} + \frac{1}{\rho_0} \nabla p^{a} = 0 \,. \quad (19)$$

Again using the scalar potential ψ^{a}, one arrives at

$$\frac{1}{c_0^2} \frac{\partial^2 \psi^{a}}{\partial t^2} - \nabla \cdot \nabla \psi^{a} = \frac{-1}{\rho_0 c_0^2} \frac{\partial p^{ic}}{\partial t} \,. \quad (20)$$

Furthermore, as done in the standard acoustic case, one may apply $\partial/\partial t$ to (18) and $\nabla\cdot$ to (19) and subtract the two resulting equations to arrive at

$$\frac{1}{c_0^2} \frac{\partial^2 p^{a}}{\partial t^2} - \nabla \cdot \nabla p^{a} = \frac{-1}{c_0^2} \frac{\partial^2 p^{ic}}{\partial t^2} \,. \quad (21)$$

Please note, that this equation can also be obtained by starting at Lighthill's inhomogeneous wave equation for incompressible flow, where the second spatial derivative of Lighthill's tensor is substituted by the Laplacian of the incompressible flow pressure (see (9)). Using the decomposition of the fluctuating pressure

$$p' = p^{ic} + p^{a} \,,$$

results again into (21). It has to be mentioned that Eq. (21) was originally derived by a different approach in [28], and is known as Ribner's dilatation equation.

[1] For a detailed derivation of perturbation equations both for compressible as well as incompressible flows, see [25]

2.3. Towards general aeroacoustics

A general aeroacoustic formulation composes a hyperbolic left hand side defined by a wave operator $\Box$ and a generic right hand side $RHS(\star)$ [29]

$$\Box p' = RHS(p, \underline{u}, \rho, ...) . \tag{22}$$

To this end, Lighthill's inhomogeneous wave equation perfectly fits to this class. It is obvious that the right hand side $RHS(\star)$ of Lighthill's inhomogeneous wave equation contains not only source terms, but also nonlinear and interaction terms between the sound and flow field, which includes effects such as convection and refraction of the sound by the flow (see Sec. 2.1).

In 2003, Goldstein proposed a method to split flow variables $(p, \underline{u}, ...)$ into a base flow (non-radiating) and a remaining component (acoustic, radiating fluctuations) [30]

$$\star = \tilde{\star} + \star' . \tag{23}$$

Applying the decomposition to the right hand side of the wave equation (the left hand side of the equation is already treated in this manner during the derivation of the acoustic equation) leads to

$$\Box p' = RHS(\tilde{p}, \tilde{\underline{u}}, \tilde{\rho}, p', \underline{u}', \rho', ...) . \tag{24}$$

Now, interaction terms can be moved to the differential operator to take, e.g., convection and refraction effects into account, and even nonlinear interactions can be considered. Therefore, three steps to relax the Mach number constraint imposed by the incompressible flow simulation are proposed:

1. Perform a compressible flow simulation, which incorporates two-way coupling of flow and acoustics.
2. Filtering of the flow field, such that one obtains a pure non-radiating field from which the acoustic sources are computed.
3. Solve with an appropriate wave operator for the radiating field

$$\Box p' = RHS(\tilde{p}, \tilde{\underline{v}}, \tilde{\rho}, ...) . \tag{25}$$

Naturally, the incompressibility condition (regarding the concept of a non-radiating base flow of Goldstein) leads to the Helmholtz decomposition of the flow field. An additive splitting on the bounded problem domain Ω of the velocity field $\underline{u} \in \mathrm{L}^2(\Omega)$ in L^2-orthogonal velocity components reads as [31]

$$\underline{u} = \underline{u}^{\mathrm{ic}} + \underline{u}^{\mathrm{c}} + \underline{u}^{\mathrm{h}} = \nabla \times \underline{A}^{\mathrm{ic}} + \nabla \phi^{\mathrm{c}} + \underline{u}^{\mathrm{h}} , \tag{26}$$

where $\underline{u}^{\mathrm{ic}}$ represents the solenoidal (non-radiating base flow) part, $\underline{u}^{\mathrm{c}}$ the irrotational (radiating) part and $\underline{u}^{\mathrm{h}}$ the harmonic (divergence-free and curl-free) part of the flow velocity. The scalar potential ϕ^{c} is associated with the compressible part and the property $\nabla \times \underline{u}^{\mathrm{c}} = 0$, whereas the vector potential $\underline{A}^{\mathrm{ic}}$ describes the solenoidal (vortical) part of the velocity field, satisfying $\nabla \cdot \underline{u}^{\mathrm{ic}} = 0$.

Based on the decomposition Eq. (26), the actual computation of the additive velocity components for a bounded domain is formulated, where the total flow field $\underline{u}$ and its derivatives do not decay towards or vanish at the boundaries of the decomposition domain. Thus, one has to include the harmonic part $\underline{u}^{\mathrm{h}}$ of the decomposition, which physically speaking is the potential flow solution of the configuration. Thereby, a domain as depicted in Fig. 2 is considered, with the flow boundaries $\Gamma_{1,...,4}$. Applying the curl to Eq. (26), the vector valued curl-curl equation with the vorticity $\underline{\omega} = \nabla \times \underline{u}$ as forcing is obtained

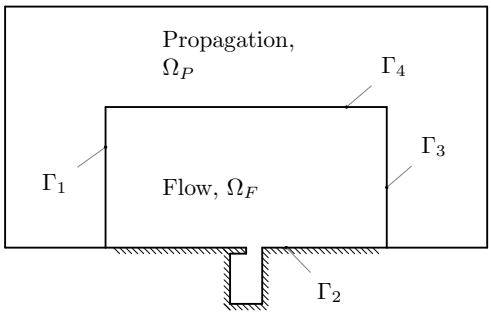

Figure 2. The flow domain Ω_{F} is a subdomain of the acoustic domain Ω_{A}, which includes the flow domain as its source domain and the propagation domain Ω_{P}.

$$\nabla \times \nabla \times \underline{A}^{*,\mathrm{ic}} = \nabla \times \underline{u} = \underline{\omega} . \tag{27}$$

The star denotes the joint function of both parts, the incompressible and the harmonic one. The function space $\mathcal{W}$ for the vector potential

$$\mathcal{W} = \{\underline{\varphi} \in H(curl, \Omega) | \underline{n} \times \nabla \times \underline{\varphi} = \underline{n} \times \underline{u} \text{ on } \Gamma_{1,2,3,4}\}$$

requires a finite element discretization with edge elements (Nédélec elements) [32]. Due to the space $\mathcal{W}$ and the orthogonality condition, the decomposition fulfills along the boundary

$$\int_{\Gamma} \underline{A}^{*,\mathrm{ic}} \cdot (\underline{u}^{\mathrm{c}} \times \underline{n}) \mathrm{d}s = 0 , \tag{28}$$

ensuring the orthogonality of the components and an unique decomposition. Finally, the non-radiating component, which contains all divergence-free components, computes by

$$\tilde{\underline{u}} := \underline{u}^{*,\mathrm{ic}} = \nabla \times \underline{A}^{*,\mathrm{ic}} = \nabla \times \underline{A}^{\mathrm{ic}} . \tag{29}$$

For the computation of the wave propagation, the equation of vortex sound [33] based on the total enthalpy

$$H = \int \frac{\mathrm{d}p}{\rho} + \frac{u^2}{2} \tag{30}$$

as primary variable, with $u^2 = \underline{u} \cdot \underline{u}$, is applied. The acoustic analogy for homentropic flow reads as

$$\frac{1}{c^2} \frac{\mathrm{D}^2}{\mathrm{D}t^2} H - \nabla \cdot \nabla H = \nabla \cdot \left(\underline{\omega} \times \tilde{\underline{u}} \right) = \nabla \cdot \underline{L}(\tilde{\underline{u}}) . \tag{31}$$

The wave operator is of convective type, where the total derivative is defined as

$$\frac{\mathrm{D}\star}{\mathrm{D}t} = \frac{\partial \star}{\partial t} + (\underline{u} \cdot \nabla) \star \ . \tag{32}$$

The aeroacoustic source term is known as the divergence of the Lamb vector $\underline{L}$

$$\underline{L}(\underline{u}) = \left(\underline{\omega} \times \underline{\tilde{u}}\right) . \tag{33}$$

3. BENCHMARKS

In the following, three benchmark case are discussed, which are already established or become a standard in the near future to test aeroacoustic formulations.

3.1. Vortex Pair

The rotating vortex pair has been frequently used to determine the capabilities of aeroacoustic methodologies [34, 35, 36]. This arrangement has the nature of a quadrupolar sound field. Figure 3 illustrates the configuration of the vortex pair. Both vortices are delta distributions and oppose each other at a distance of $2r_0$. The strength of each vortex is characterized by the circulation intensity Γ. The vortices rotate around the origin with a period of $T = 8\pi^2 r_0^2/\Gamma$ imposing an angular rotating speed $\underline{\omega}_r = \Gamma/(4\pi r_0^2)\,\underline{e}_3 = \omega_r\,\underline{e}_3$. Each vortex convects the other vortex by a velocity of $\underline{u}_\theta = \Gamma/(4\pi r_0)\,\underline{e}_t$, where $\underline{e}_t$ is the unit vector in tangential direction. The Mach number in the circumferential direction is given by $M_\theta = u_\theta/c = \Gamma/(4\pi r_0 c)$. The potential flow theory can be used to determine the fundamental solution of the spinning vortex pair in terms of the complex flow potential function. In doing so, one introduces the transformation from Cartesian coordinates (x_1, x_2) to the complex plane with the complex coordinate $z = r\exp^{i\theta} = x_1 + ix_2$. The location of each vortex over time t is defined by $b = r_0 \exp^{i\omega t}$. Using these definitions, the incompressible, inviscid flow potential $\varphi(z,t)$ computes by

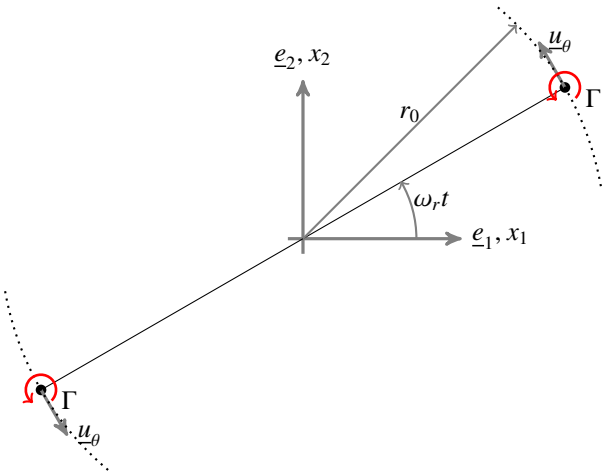

Figure 3. Schematic of the co-rotating vortex pair defining the main geometrical and physical characteristics.

$$\varphi(z,t) = \frac{\Gamma}{2\pi i}\ln(z-b) + \frac{\Gamma}{2\pi i}\ln(z+b) = \frac{\Gamma}{2\pi i}\ln(z^2-b^2) . \tag{34}$$

The incompressible velocity field $\underline{u}^{\mathrm{ic}} = (u_1, u_2)^{\mathrm{T}}$ of the spinning vortex pair is obtained by differentiating Eq. (34) with respect to the complex coordinate z

$$u_1 - iu_2 = \frac{\partial \varphi(z,t)}{\partial z} = \frac{\Gamma}{\pi i}\frac{z}{z^2 - b^2} . \tag{35}$$

The incompressible fluid dynamic pressure p^{ic} is obtained by applying the unsteady form of Bernoulli's principle

$$p^{\mathrm{ic}} = p_0 - \rho_0 \frac{\partial \mathrm{Re}\{\varphi(z,t)\}}{\partial t} - \frac{1}{2}\rho_0 (u_1^2 + u_2^2) . \tag{36}$$

Müller and Obermeier [37] derived an analytic solution of the acoustic far-field, based on matched asymptotic expansion of the potential solution. Starting from the solution in form of a complex potential Eq. (34), matching the inner and the outer solution yields the pressure fluctuation p' of the co-rotating vortex pair

$$p' = \frac{\rho_0 \Gamma^4}{64\pi^3 r_0^4 c^2}\Big(J_2(2kr)\cos(2\omega t) - Y_2(2kr)\sin(2\omega t)\Big) . \tag{37}$$

In Eq. (37) $k = \omega/c$ denotes the wave number, $J_2(\star)$ the second-order Bessel function of first kind and $Y_2(\star)$ the second kind. It should be emphasized that this fluctuating pressure p' is not equal to the acoustic pressure p^{a}; however, $p' \to p^{\mathrm{a}}$ holds in the far-field.

In doing so, the co-rotating vortex pair on a stationary grid with moving sources induced by the vortical structures are simulated. An unstructured mesh is used to discretize the computational domain. In the source region, a characteristic mesh size of $h \approx 90\,\mathrm{cm}$ is used. Each vortex distribution $\Gamma\delta(z-b)$ is approximated by a continuous multivariant normal distribution with equivalent circulation Γ and an isotropic variance of $\sigma^2 = 0.05\,\mathrm{m}^2$.

The analytic field is represented on the flow grid and is based on a circulation strength of $\Gamma = 2\pi\,\mathrm{m}^2/\mathrm{s}$ and a distance of $2r_0 = 2\,\mathrm{m}$ between the vortices. The angular rotation induced by the vortices is $\omega_r = 0.5\,\mathrm{s}^{-1}$, the speed of sound $c = \sqrt{10}\,\mathrm{m/s}$ and density $\rho_0 = 1\,\mathrm{kg/m}^3$. Using this flow field, the source term computation is performed and finally the sound, which is compared to the analytic solution in the far-field (see Eq. (37)), is computed. The first simulation is based on vortex sound equation according to Eq. (31), and the second computation uses the perturbed convective wave equation (PCWE) as presented in Sec. 2.2. Based on the computational methodology of radial basis functions, the following simulation workflow for the computation of the aeroacoustic source terms is performed. First, the incompressible pressure p^{ic}, flow velocity $\underline{u}^{\mathrm{ic}}$, and vor-

ticity $\underline{\omega}$ are computed. Second, if required, derivatives are computed by the radial basis function framework [38]. As a third step, a conservative interpolation to a much coarser mesh for the acoustic computation is performed [39]. The computational domain has a diameter of $5r_0$ (relatively high resolved unstructured triangular mesh, $h \approx 90\,\text{cm}$) is embedded in a propagation region, in which gradually the unstructured mesh size is increased. The propagation region is surrounded by a structured perfectly matched layer (PML) region [40], which absorbs the radiating waves. The wave length $\lambda = \frac{2\pi}{k} \approx 20\,\text{m}$ is resolved (in the propagation region) with approximately 20 linear finite elements per wavelength. For both acoustic simulations, a Newmark scheme with a time step size of $\Delta t = 0.09\,\text{s}$ is applied for the time discretization.

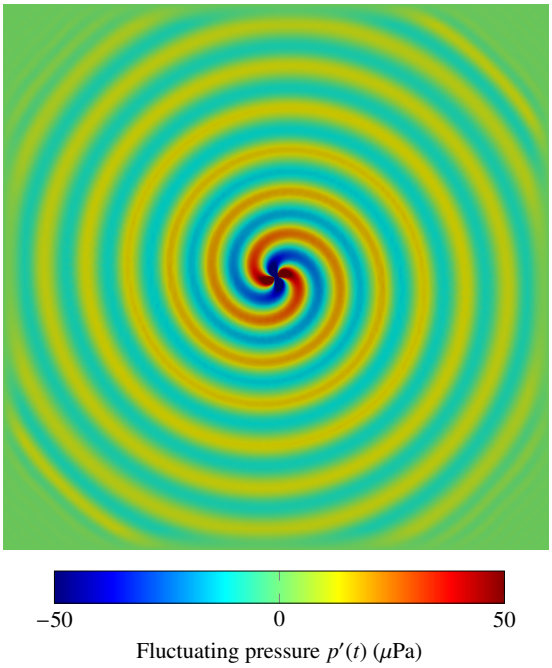

Figure 4. Simulation result solving Eq. (31) with the Lamb vector as source term.

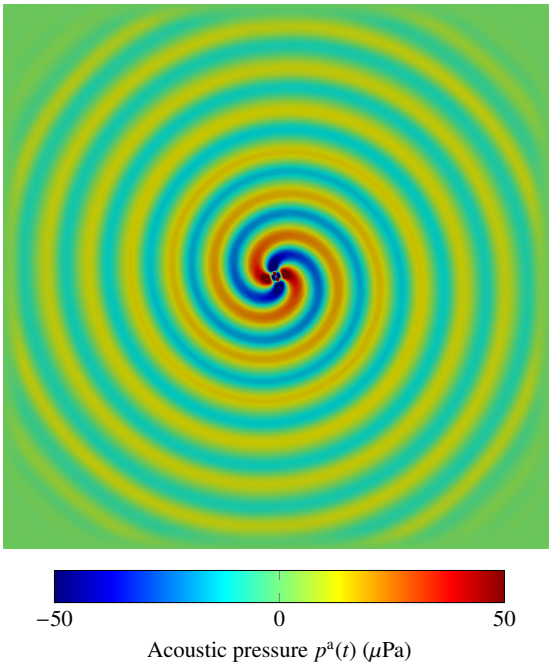

Figure 5. Simulation result solving Eq. (17) with the substantial derivative of the incompressible pressure as source term.

main of $(260\,\text{x}260)\,\text{m}^2$ for the two wave equations is decomposed into three subdomains. The source domain has a diameter of $5r_0$ (relatively high resolved unstructured triangular mesh, $h \approx 90\,\text{cm}$) is embedded in a propagation region, in which gradually the unstructured mesh size is increased. The propagation region is surrounded by a structured perfectly matched layer (PML) region [40], which absorbs the radiating waves. The wave length $\lambda = \frac{2\pi}{k} \approx 20\,\text{m}$ is resolved (in the propagation region) with approximately 20 linear finite elements per wavelength. For both acoustic simulations, a Newmark scheme with a time step size of $\Delta t = 0.09\,\text{s}$ is applied for the time discretization.

Figure 4 shows the fluctuating pressure field of the co-rotating vortex pair obtained by solving Eq. (31). The acoustic field obtained by solving Eq. (17) is displayed in Fig. 5. In the acoustic near-field, differences occur due to the different solution quantities in the two aeroacoustic formulations. Both results have the characteristic radiation pattern of the co-rotating vortex pair.

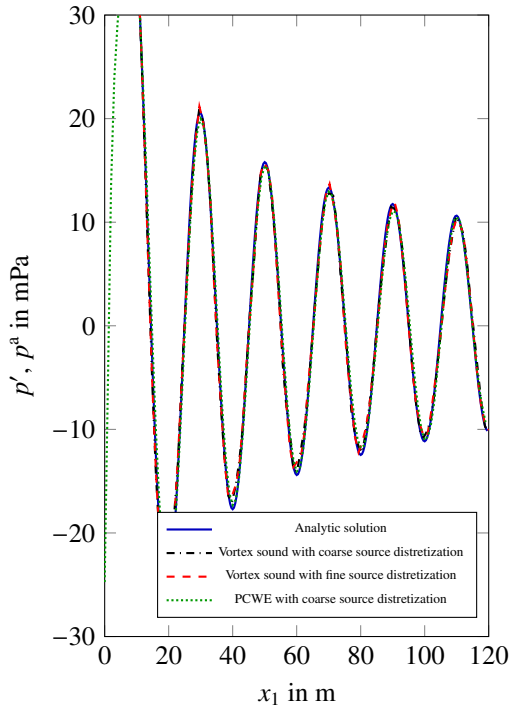

Figure 6. Fluctuating pressure p' and acoustic pressure p^a, respectively, as a function of the coordinate x_1.

The steepest descent of the Gaussian distribution is discretized by 5 linear triangular elements over 2σ. This coarse approximation of the vortical distribution shows the robustness of the radial basis function derivatives. A mesh refinement of the source region (see Fig. 6) causes no significant increase in accuracy compared to the analytic solution. As depicted in Fig. 6, one can clearly see the good accordance of numerical and analytic solution, even for the coarse grid.

3.2. Axial Fan

(a) Axial fan.

(b) Pressure sensors K1 to K6.

Figure 7. Axial fan and position of the pressure sensors.

The investigated axial fan is displayed in Fig. 7 consisting of nine fan blades with a tip diameter of 495 mm. It was installed inside a duct with a diameter of 500 mm, hence the tip gap was 2.5 mm. The fan was embedded in a sound hard tube and all measurements were performed in a standardized inlet test chamber according to ISO 5801. The test chamber has been built as an anechoic chamber with absorbing walls, ceiling, and floor, to enable aeroacoustic measurements. The rotational speed of the fan was about 1500 rpm, which results in a maximum tip speed of 38.89 m/s. The fan was installed in a short duct with a bellmouth on the in- and outlet to resemble a realistic test setup. The fan was driven by a motor inside the duct. Torque and rotational speed were measured with a precision torque meter. To ensure that torque measurements are not compromised by frictional torque of the bearings, an offset measurement was performed with the fan being removed. All details towards the measurements can be found in [41].

For the numerical computation of the flow field, OpenFOAM Toolbox version 2.3.0 has been used to solve the incompressible Navier-Stokes equations based on the finite-volume method and the arbitrary mesh interface (AMI). The AMI allows simulation across disconnected, but adjacent mesh domains, which are especially required for rotating geometries. The computational domain is displayed in Fig. 8a including the axial fan inside the pipe, the inlet chamber, and the outlet region. The flow solu-

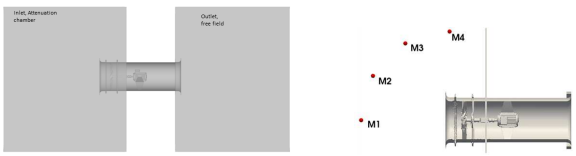

(a) Computational domain for flow computation.

(b) Microphone positions.

Figure 8. Computational domain for flow computation and position of the microphones.

tion is computed using an adapted version of the pimpleDyMFoam solver, which can handle dynamic meshes, with a time step size of $\Delta t = 10\,\mu$s. For the CFD computation, a hexahedron-dominant finite volume mesh consisting of 29.8 million cells was generated with the automatic mesh generator HEXPRESSTM / Hybrid from Numeca, as displayed in Fig. 9a. The transient simulation was carried out by using a detached-eddy simulation based on the Spalart-Allmaras turbulence model to accurately resolve the complex flow field. The applied finite-volume scheme has been second order in space and time, and the convective term has been discretized by a bounded central upwind scheme. In total, the CFD

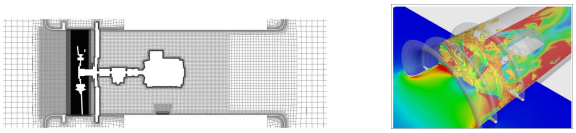

(a) Computational grid.

(b) Flow structure.

Figure 9. Cross section through the computational mesh for CFD and flow structure for a characteristic time step.

computation has been performed for 10 revolutions. After about 6 revolutions, the flow field achieved steady-state and the CFD data of the remaining 4 revolutions have been used for acoustic source and wave propagation computations. Figure 9b displays the flow structure for a characteristic time step.

To validate the flow computation, wall pressure fluctuations were measured with 6 differential miniature pressure transducers XCS-093-1psi D (Kulite Semiconductor Products) with a diameter of 2.5 mm (see Fig. 7b). The sensors were flush mounted and equally spaced along a line on the duct. Exemplary,

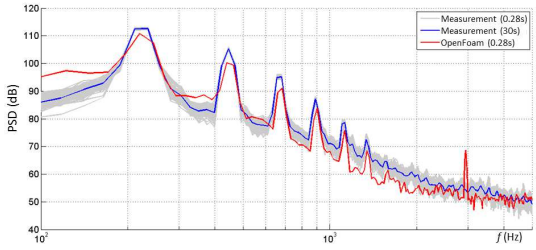

(a) Position 2

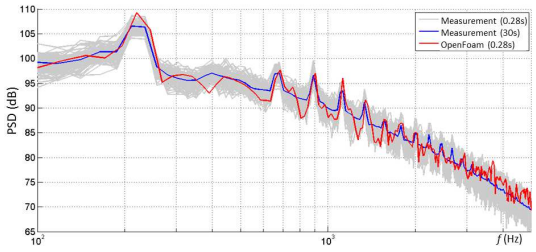

(b) Position 4

Figure 10. Spectral density (relative to 20μPa) of the measured instationary pressures at position K2 and K4.

the spectral density (PSD) of the instationary pressure in Fig. 10 at position K2 and K4 is displayed (for

positions see Fig. 7b). Here, it should be emphasized that especially a good comparison between measured and simulated pressure spectra is of high relevance since the instationary pressure is a key physical quantity within aeroacoustic computations.

In accordance to the flow computation, the rotating domain is embedded into a quiescent propagation region for performing the acoustic simulations (see Fig. 11) [27]. Furthermore, at the inflow and outflow boundaries of the CFD domain two additional regions as PML are added to effectively approximate acoustic free field conditions [40]. To resolve

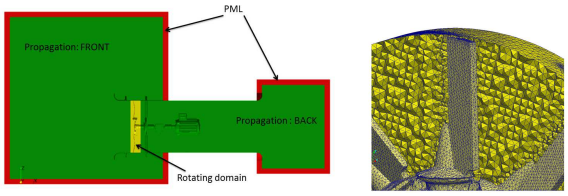

(a) Computational setup **(b) Detail of mesh**

Figure 11. Computational domain for the acoustic calculation and detail of acoustic mesh near the rotor.

accurately the rotor geometry, tetrahedron elements are used as displayed in Fig. 11b. As soon as the inlet as well as the outlet are reached, hexahedron elements are used and the two meshes are coupled by a Nitsche-type mortaring approach. The computational mesh resulted in approximately 2 million cells, which is by a factor of 15 smaller than the flow grid. Thereby, the spatial resolution of the mesh has been chosen to resolve acoustic waves up to 5 kHz (about ten finite elements with linear basis functions per wavelength), which was the main frequency range of interest. The used time-stepping scheme with controlled dispersion (Hilber-Hughes-Taylor) numerically damps waves of higher frequency to avoid numerical artifacts. Therefore, the computed acoustic spectra will strongly decrease above 5 kHz (see Figs. 12a and 12b). The mesh convergence has been studied by placing artificial sources on the rotor blades. The computation of the acoustic sources on the flow grid are interpolated to the acoustic grid via a cut-volume-cell approach [42, 43].

The sound field was measured with four 1/2 inch free-field microphones, type 4189-L-001 (Brüel & Kjaer) arranged in a quarter-circle with a radius of 1 m around the inlet bellmouth in a horizontal plane at the same height as the rotational axis, see Fig. 8b. Thereby, the measurements were made synchronized with the wall pressure fluctuations. Accordingly, measurement time was 30 s with a sampling frequency of 48 kHz. Figures 12 display the computed power spectral density of the acoustic pressure at the two microphone positions (for location see Fig. 8b). Thereby, the smoothed measured spectra obtained from the 30 s recorded acoustic pressure signals as well as the individual spectra by just using measured data of 0.1 s (in gray) are displayed. The computed spectra based on the numerical simulations using openCFS [44] are calculated out of a real-time simulation of 0.06 s. Further details on the numerical

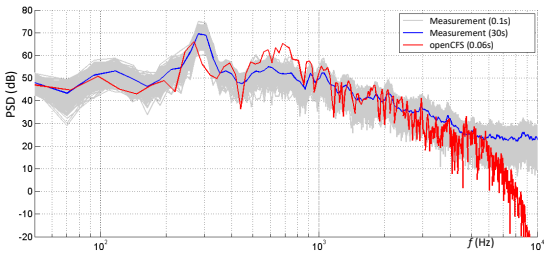

(a) Position M1

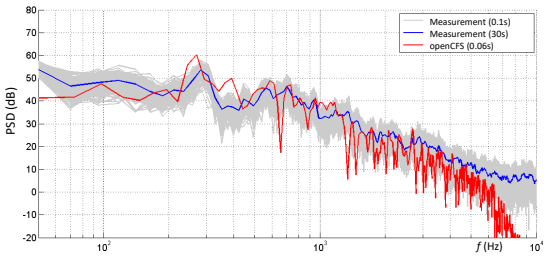

(b) Position M4

Figure 12. Spectral density (relative to 20μPa) of the measured microphone signals at position M1 and M4.

computations can be found in [42].

3.3. Cavity with a lip

This benchmark case by [45] considers a flow - acoustic feedback mechanism. The geometrical properties are given in Fig. 13, with all spatial dimensions in mm. The deep cavity has a reduced

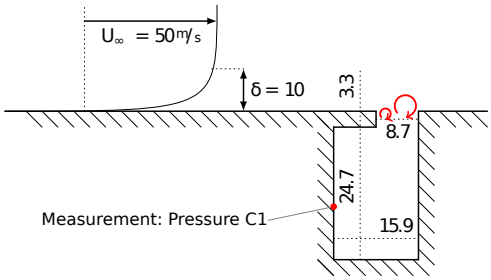

Figure 13. The geometry and the flow configuration of the benchmark problem, cavity with a lip.

cross-section at the orifice and the cavity separates two flat plate configurations. The flow, with a free-stream velocity of $U_\infty = 50$ m/s, develops over the plate up to a boundary layer thickness of $\delta = 10$ mm. For this configuration the first shear layer mode is expected at about $f_{s1} = 1.7$ kHz.

The unsteady, compressible, and laminar flow simulation is performed with a prescribed velocity profile $\underline{u} = \underline{u}_{in}$ at the inlet Γ_1, a no slip and no penetration condition $\underline{u} = \underline{0}$ for the wall Γ_2, an enforced

reference pressure $p = p_{\text{ref}}$ at the outlet Γ_3, and a symmetry condition $\underline{u} \cdot \underline{n} = 0$ at the top Γ_4 (see Fig. 2). Thereby, the commercial CFD software Ansys-Fluent has been used. The compressible flow simulation demonstrates the presence of standing waves due to the boundary conditions of the compressible flow simulation as displayed in Fig. 14. This shows

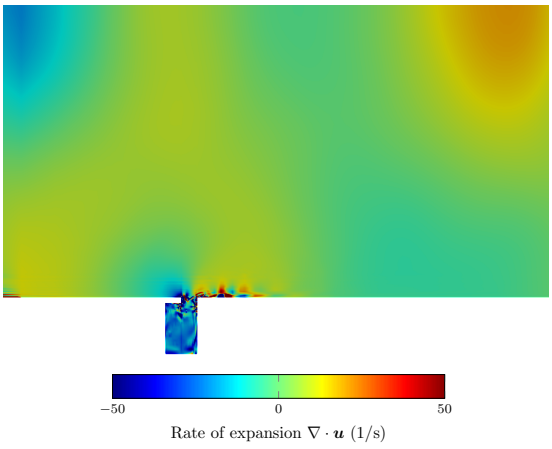

Figure 14. The rate of expansion $\nabla \cdot \underline{u}$ of the compressible flow simulation at a representative time step.

how important it is to model boundaries with respect to the physical phenomena.

For each time step of the compressible flow computation, Eq. (27) is solved with the appropriate boundary conditions

$$\underline{n} \times \nabla \times \underline{A}^{*,\text{ic}} = \underline{n} \times \underline{u} \text{ on } \Gamma_{1,2,3,4}$$

to obtain the pure vortical velocity field according to Eq. (29) (see Fig. 15). This method tackles the

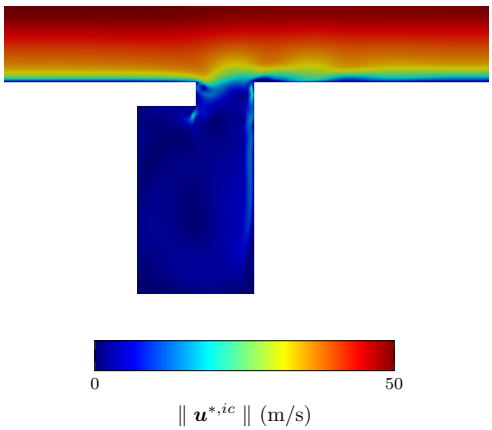

Figure 15. The magnitude of the incompressible component of the flow velocity captures the vortical flow features of the simulation.

compressible phenomena inside the domain Ω_F by filtering the domain artifacts of the compressible flow field such that the computed sources are not corrupted. Figure 16 illustrates the shape and nature of the Lamb vector (Fourier-transformed) at the first shear layer mode, where the difference between the corrected and non-corrected Lamb vector gets visible.

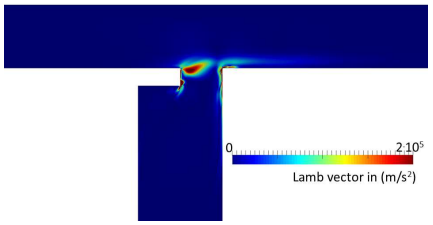

(a) $x-$ component of Lamb vector

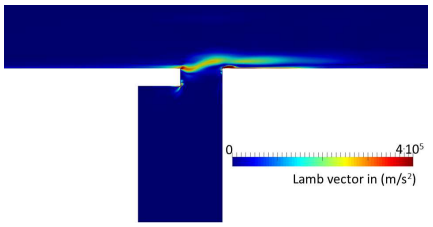

(b) $y-$ component of Lamb vector

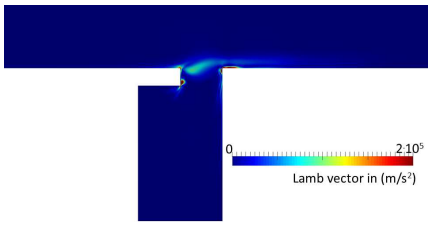

(c) $x-$ component of corrected Lamb vector

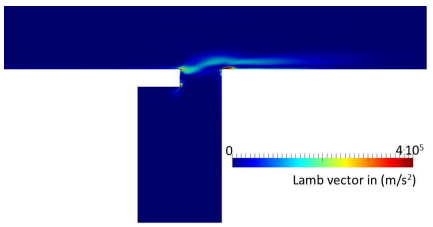

(d) $y-$ component of corrected Lamb vector

Figure 16. Comparison of the Lamb vector for the corrected and the non-corrected calculation at the first shear layer mode.

The acoustic simulations utilizes the equation of vortex sound Eq. (31) to compute the acoustic propagation applying the finite element method by using the in-house solver openCFS [44]. Two different aeroacoustic source variants are investigated, the uncorrected Lamb vector $\underline{L}(\underline{u})$ (field quantities directly from the compressible flow simulation) and the corrected Lamb vector $\underline{L}(\tilde{\underline{u}})$ based on the Helmholtz decomposition in the vector potential formulation. Figure 17 compares the resulting acoustic fields. As expected, the acoustic field computed by the corrected source term is strongly reduced in amplitude and shows a typically wave propagation, whereas Fig. 17a shows perturbations.

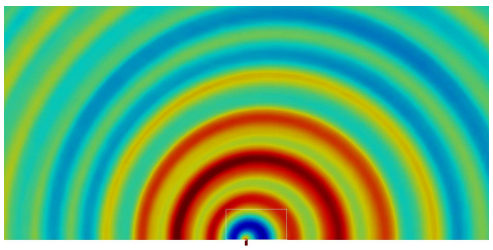

(a) $\underline{L}(\underline{u}) = \underline{\omega} \times \underline{u}$**, not corrected**

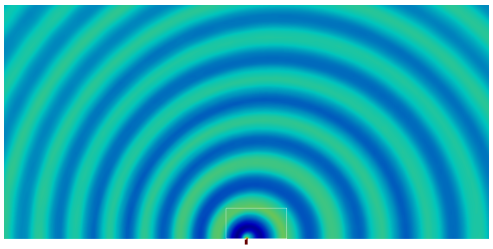

(b) $\underline{L}(\underline{\tilde{u}}) = \underline{\omega} \times \underline{\tilde{u}}$**, corrected**

Figure 17. Field of the total enthalpy fluctuation H at a characteristic time.

The ideal gas law and Eq. (30) serves us a relation between the specific enthalpy H and the sound pressure p^{a}. In its linearized form, the sound pressure level (SPL) computes by

$$SPL = 20 \log \left(\frac{\rho_0 H}{p_{\mathrm{a,ref}}} \right) \tag{38}$$

with $p^{\mathrm{a}}_{\mathrm{ref}}$ being $20\,\mu$Pa. Table 1 quantifies the obtained results for the first shear layer mode in the far field, where the computed 2D acoustic sound pressure has been scaled according to [46] for comparison with the measured data. Thereby, the computations of the non-corrected source terms overestimate the experimental result by 22 dB. In the case of the corrected source terms, the overestimation is just 4 dB.

Table 1. Comparison of the pressure outside the cavity

	f_{s1}/Hz	SPL_{s1}/dB
Experiment	1650	30
Simulation $\underline{L}(\underline{\tilde{u}}) = \underline{\omega} \times \underline{\tilde{u}}$	1660	34
Simulation $\underline{L}(\underline{u}) = \underline{\omega} \times \underline{u}$	1660	52

4. SUMMARY

This article has discussed physical models and numerical schemes for computational aeroacoustics. In doing so, the main challenges for flow induced sound both for low and high Mach number flows have been highlighted. The discussed physical models concentrate on aeroacoustic analogies and perturbation equations based on systematic decomposition of physical field properties. Although main achievements have been obtained within the last twenty years, aeroacoustics is still a topic of ongoing research with many phenomena, which are partially not fully understood or / and needs physical models and numerical computational schemes to support their understanding.

ACKNOWLEDGEMENTS

The authors acknowledge support from the Austria Research Promotion Agency (FFG) under no. 867971 and no. 874784.

REFERENCES

[1] Hardin, J. C., and Hussaini, M. Y. (eds.), 1992, *Computational Aeroacoustics*, chap. Computational aeroacoustics for low Mach number flows, Springer-Verlag, pp. 50–68, new York.

[2] Hardin, J. C., and Hussaini, M. Y. (eds.), 1992, *Computational Aeroacoustics*, chap. Regarding numerical considerations for computational aeroacoustics, Springer-Verlag, pp. 216–228, new York.

[3] Wagner, C., Hüttl, T., and Sagaut, P. (eds.), 2007, *Large-Eddy Simulation for Acoustics*, Cambridge University Press.

[4] Schoder, S., and Kaltenbacher, M., 2019, "Hybrid Aeroacoustic Computations: State of Art and New Achievements", *Journal of Theoretical and Computational Acoustics*, Vol. 27 (04), p. 1950020.

[5] Bailly, C., Bogey, C., and Marsden, O., 2010, "Progress in direct noise computation", *International Journal of Aeroacoustics*, Vol. 9 (1-2), pp. 123–143.

[6] Frank, H., and Munz, C. D., 2016, "Direct aeroacoustic simulation of acoustic feedback phenomena on a side-view mirror", *Journal of Sound and Vibration*, Vol. 371, pp. 132–149.

[7] Fares, E., Duda, B., and Khorrami, M. R., 2016, "Airframe Noise Prediction of a Full Aircraft in Model and Full Scale Using a Lattice Boltzmann Approach", *22nd AIAA/CEAS Aeroacoustics Conference*, p. 2707.

[8] Sanders, L., Manoha, E., Murayama, M., Yokokawa, Y., Yamamoto, K., and Hirai, T., 2016, "Lattice-Boltzmann Flow Simulation of a Two-Wheel Landing Gear", *22nd AIAA/CEAS Aeroacoustics Conference*, p. 2767.

[9] Lighthill, M., 1952, "On sound generated aerodynamically I. General theory", *Proc Roy Soc Lond*, (A 211), pp. 564–587.

[10] Crighton, D. G., Dowling, A. P., Ffowcs-Williams, J. E., Heckl, M., and Leppington,

F. G., 1992, *Modern methods in analytical acoustics*, Springer Lecture Notes.

[11] Phillips, O. M., 1960, "On the generation of sound by supersonic turbulent shear layers", *J Fluid Mech*, Vol. 9, pp. 1–18.

[12] Lilley, G. M., 1974, "On the noise from jets", *Tech. rep.*, AGARD CP-131.

[13] Goldstein, M. E., 1976., *Aeroacoustics*, McGraw-Hill.

[14] Curle, N., 1955, "The Influence of Solid Boundaries upon Aerodynamic Sound", *Proceedings of the Royal Society of London A: Mathematical, Physical and Engineering Sciences*, Vol. 231 (1187), pp. 505–514.

[15] Williams, J. E. F., and Hawkings, D. L., 1969, "Sound Generation by turbulence and surface in arbitratry motion", *Philosophical Transactions of the Royal Society of London, Series A, Mathematical and Physical Sciences*, Vol. 264, pp. 321–342.

[16] Morgan, W. R., 1930, "The Kirchhoff Formula Extended to a Moving Surface", *Philosophical Magazine*, Vol. 9, pp. 141–161.

[17] Prieur, J., , and Rahier, G., 2001, "Aeroacoustic integral methods, formulation and efficient numerical implementation", *Aerospace Science and Technology*, Vol. 5 (7), pp. 457–468.

[18] Astley, R. J., Sugimoto, R., Achunche, I. M., Kewin, M. F., Mustafi, P., and Deane, E. P., 2010, "Reprint of: A review of CAA for fan duct propagation and radiation, with application to liner optimisation", *Procedia IUTAM*, Vol. 1, pp. 143–152.

[19] Crow, S. C., 1970, "Aerodynamic sound emmission as a singular perturbation problem", *Studies of Applied Mathematics*, Vol. 49, pp. 21–44.

[20] Hardin, J. C., and Pope, D. S., 1994, "An acoustic/viscous splitting technique for computational aeroacoustics", *heoretical and Computational Fluid Dynamics*, pp. 323–340.

[21] Shen, W. Z. and Sørensen, J. N., 1999, "Aeroacoustic Modelling of Low-Speed Flows", *Theoretical and Computational Fluid Dynamics*, Vol. 13, pp. 271–289.

[22] Ewert, R., and Schröder, W., 2003, "Acoustic perturbation equations based on flow decomposition via source filtering", *Journal of Computational Physics*, Vol. 188, pp. 365–398.

[23] Seo, J., and Moon, Y., 2005, "Perturbed Compressible Equations for Aeroacoustic Noise Prediction at Low Mach Numbers", *AIAA Journal*, Vol. 43, pp. 1716–1724.

[24] Munz, C., Dumbser, M., and Roller, S., 2007, "Linearized acoustic perturbation equations for low Mach number flow with variable density and temperature", *Journal of Computational Physics*, Vol. 224, pp. 352 – 364.

[25] Hüppe, A., 2013, "Spectral Finite Elements for Acoustic Field Computation", Ph.D. thesis, University of Klagenfurt, Austria.

[26] Hüppe, A., Grabinger, J., Kaltenbacher, M., Reppenhagen, A., and Kühnel, W., 2014, "A non-conforming finite element method for computational aeroacoustics in rotating systems", *American Institute of Aeronautics and Astronautics Conference 2014*.

[27] Kaltenbacher, M., Hüppe, A., Reppenhagen, A., Zenger, F., and Becker, S., 2017, "Computational aeroacoustics for rotating systems with application to an axial fan", *AIAA journal*, pp. 3831–3838.

[28] Ribner, H. S., 1962, "Aerodynamic Sound from Fluid Dilatations - A Theory of the Sound from Jets and Other Flows", *Tech. rep.*, Institute for Aerospace Studies, University of Toronto.

[29] Schoder, S., Roppert, K., and Kaltenbacher, M., 2020, "elmholtz's decomposition for compressible flows and its application to computational aeroacoustics", *SN Partial Differ Equ Appl*, Vol. 1 (46), pp. 1–20.

[30] Goldstein, M. E., 2003, "A generalized acoustic analogy", *Journal of Fluid Mechanics*, Vol. 488, pp. 315–333.

[31] Schoder, S., Roppert, K., and Kaltenbacher, M., 2020, "Postprocessing of Direct Aeroacoustic Simulations Using Helmholtz Decomposition", *AIAA Journal*, Vol. 58 (7), pp. 3019–3027.

[32] Kaltenbacher, M., 2015, *Numerical Simulation of Mechatronic Sensors and Actuators*, Springer, Berlin, 3rd edn.

[33] Howe, M. S., 2003, *Theory of Vortex Sound*, Cambridge Texts in Applied Mathematics.

[34] Lee, D. J., and Koo, S. O., 1995, "Numerical study of sound generation due to a spinning vortex pair", *AIAA Journal*, Vol. 33 (1), pp. 20–26.

[35] Slimon, S. A., Soteriou, M. C., and Davis, D. W., 1999, "Computational aeroacoustics simulations using the expansion about incompressible flow approach", *AIAA journal*, Vol. 37 (4), pp. 409–416.

[36] Hardin, J. C., and Pope, D. S., 1994, "An acoustic/viscous splitting technique for computational aeroacoustics", *Theoretical and Computational Fluid Dynamics*, Vol. 6 (5), pp. 323–340.

[37] Müller, E. A., and Obermeier, F., 1967, "The spinning vortices as a source of sound", *AGARD CP-22*, pp. 22–1.

[38] Schoder, S., Roppert, K., Weitz, M., Junger, C., and Kaltenbacher, M., 2020, "Aeroacoustic source term computation based on radial basis functions", *International Journal for Numerical Methods in Engineering*, Vol. 121 (9), pp. 2051–2067.

[39] Kaltenbacher, M., 2018, *Computational Acoustics*, CISM International Centre for Mechanical Sciences, Springer International Publishing, ISBN 9783319590387.

[40] Kaltenbacher, B., Kaltenbacher, M., and Sim, I., 2013, "A modified and stable version of a perfectly matched layer technique for the 3-d second order wave equation in time domain with an application to aeroacoustics.", *Journal of Computational Physics*, Vol. 235, pp. 407–422.

[41] Zenger, F., Junger, C., Kaltenbacher, M., and Becker, S., 2016, "A Benchmark Case for Aerodynamics and Aeroacoustics of a Low Pressure Axial Fan", *SAE Technical Paper*, SAE International.

[42] Schoder, Stefan, Junger, Clemens, and Kaltenbacher, Manfred, 2020, "Computational aeroacoustics of the EAA benchmark case of an axial fan", *Acta Acustica*, Vol. 4 (5), p. 22.

[43] Schoder, S., Wurzinger, A., Junger, C., Weitz, M., Freidhager, C., Roppert, K., and Kaltenbacher, M., 2021, "Application Limits of Conservative Source Interpolation Methods Using a Low Mach Number Hybrid Aeroacoustic Workflow", *Journal of Theoretical and Computational Acoustics*, Vol. 29 (01), p. 2050032.

[44] Kaltenbacher, M., 2022, "openCFS - Finite Element solver for Multiphyics", `http://www.opencfs.org`.

[45] Henderson, B., 2000, "Automobile Noise Involving Feedback- Sound Generation by Low Speed Cavity Flows", *Tech. rep.*, In: Third Computational Aeroacoustic(CAA) Workshop on Benchmark Problems.

[46] Oberai, A., Roknaldin, F., and Hughes, T. J. R., 2002, "Computation of trailing-edge noise due to turbulent flow over an airfoil", *AIAA*, Vol. 40 (11).

Conference on Modelling Fluid Flow (CMFF'22)
The 18th International Conference on Fluid Flow Technologies
Budapest, Hungary, August 30-September 2, 2022

Optical Measurements of Drops in Flows

Cameron TROPEA[1], Bastian STUMPF[1], Can Li[2], Wu ZHOU[3]

[1] Corresponding Author. Institute of Fluid Mechanics and Aerodynamics, Technical University of Darmstadt, Germany. Tel. +49 6151 22175, E-mail: ctropea@sla.tu-darmstadt.de
[2] National Key Laboratory of Transient Physics, Nanjing University of Science and Technology, Nanjing 210094, China
[3] School of Energy and Power Engineering, University of Shanghai for Science and Technology, China

ABSTRACT

This article reviews recent developments of three selelcted techniques for the measurement of drops in fluid flows. In all cases the developments extend the capabilities and achievable measurement accuracy of the respective technique.
The first technique is the two-camera Depth from Defocus (DFD), in which drops within a volume are imaged onto two cameras with differing degrees of out-of-focus. This allows both drop size and position to be determined, yielding drop size distributions and volume concentration. The notable feature is the very well-defined detection volume, leading to high accuracy of the volume concentration measurement, a quantity which is very elusive with other measurement techniques.
The second technique is also an imaging technique in which the volume fraction of two-component drops of immiscible fluids can be determined. This technique is novel and has applications where drops and/or sprays of one fluid impact onto a film of another fluid and the mixture fraction of the resulting splashed, secondary droplets is sought.
The third technique is an extension of rainbow refractometry to a planar configuration, allowing drop size and temperature (refractive index) to be determined over an illuminated plane. Of particular interest is a novel approach to calibrating the scattering angle over the entire plane, an important input parameter for the inversion of the rainbow pattern into size and refractive index.

Keywords: sprays, atomization, drop imaging, rainbow refractometry, depth from defocus

1. DEPTH FROM DEFOCUS

There exist numerous implementations of depth from defocus imaging systems, starting from the introduction of the concept by Pentland [1] and Kratkov [2]. Some are based on single-sensor imaging [3, 4] or two-sensor imaging [5, 6]. A variation on DFD for particle tracking is astigmatism particle image velocimetry, using a cylindrical lens to distinguish whether the object is behind or in front of the object plane [7]. A more comprehensive summary of DFD techniques can be found in Zhou et al. [8]. In the present study two cameras are used, each imaging the same volume but with different degrees of out-of-focus. The principle of DFD is illustrated in Fig. 1.

Each drop/particle is therefore imaged out of focus

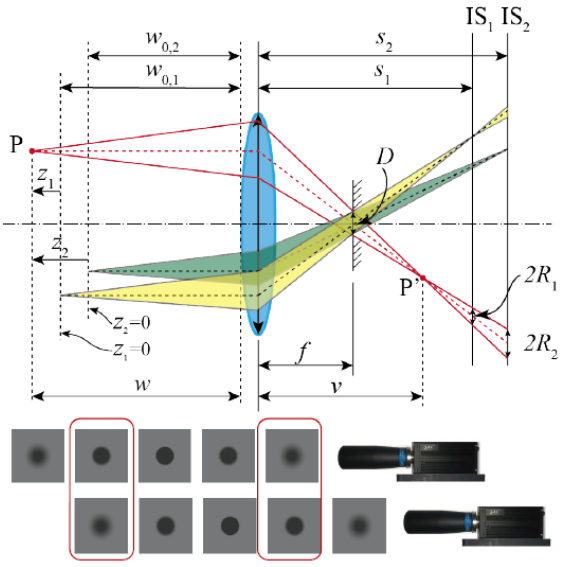

Figure 1. Principle of Depth from Defocus. a) Cameras are adjusted to be in focus at planes removed z_1 (yellow) and z_2 (green) from the object plane; b) Depending on drop position and camera, the image can be in or out of focus

and the aim of the processing is to mathematically describe the out of focus image such that the position and size of the drop can be extracted from the two images. The out of focus image is blurred and this image (I_i) can be described by the convolution of the

in-focus image (I_S) with a blur kernel h_i, i.e.

$$I_i = I_S * h_i \qquad (i = 1, 2 \text{ for cameras 1 and 2}) \quad (1)$$

The blur kernel is typically assumed to be Gaussian in nature with a standard deviaton σ, i.e.

$$h = \frac{1}{2\pi\sigma^2} \exp^{\frac{-r_h^2}{2\pi^2}} = \frac{1}{2\pi\sigma^2} \exp^{\frac{-r^2+r_t^2-2rr_t\cos\theta}{2\pi^2}} \quad (2)$$

where r_h is a radial coordinate, as defined in Fig. 2 This allows the gray level g_t in the blurred imaged

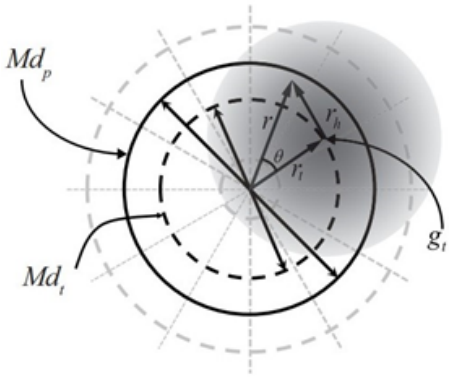

Figure 2. Schematic of the blur convolution in the image. M is the magnification; d_p is the true particle/drop size; d_t is the particle image size using the gray threshold level g_t.

to be computed as a function of the true drop size d_0, and rearranging into dimensionless quantities this takes the form

$$g_t = \frac{1}{4\pi} \int_0^{2\pi} \int_0^{\left(\frac{d_0}{2\sigma}\right)} \exp^{\frac{-\left(\left(\frac{r}{\sigma}\right)^2+\left(\frac{r_t d_0}{d_0\sigma}\right)^2-2\frac{rd_0r_t}{\sigma\sigma d_0}\cos\theta\right)}{2}} d\left(\frac{r}{\sigma}\right)^2 d\theta \quad (3)$$

By involving a thresholding process on the blurred image with a fixed threshold g_t, a circular image with the measured diameter d_t can be obtained. Although the resulting integral of Eq. 3 cannot be calculated explicitly, it indicates a fixed functional relationship f between the dimensionless ratios $d_{t,i}/d_p$ and $(z - z_i)/d_p$ for a given threshold gray level g_t, where d_p is the true particle/drop diameter and $d_{t,i}$ is the directly measured diameter on the image, using the g_t gray level.

With two cameras, this leads to a classical problem of two unknowns (d_p and z) and two equations, namely:

$$\frac{d_{t,i}}{d_p} = f_i\left(\frac{z - z_i}{d_p}\right) \qquad (i = 1, 2) \quad (4)$$

The functions f_i are determined using a calibration reticule plate traversed through different z values. The bounds of the measurement depth range for each camera ($z_{i,min}, z_{i,max}$) correspond to the limit when $d_{t,i}$ goes to zero, i.e. when the particle can no longer be detected with a certain grey level threshold g_t on the image. The magnification must also be chosen such that the expanded and blurred images of individual drops do not overlap with one another. The processing is depicted graphically in Fig. 3. A comprehensive study investigating the sensitivity of various optical parameters on the accuracy of the position and size determination of the drop can be found in [9]. Experience has shown that a normalized threshold gray level of 0.5-0.6 is a very good choice. One of the unique features of this imaging technique is the almost linear dependence of depth range with particle size, i.e. larger particles can be detected on the image for a larger variation of position z, or $\Delta w = z - z_i$. For instance, Fig. 4 shows a scatter diagram of approx. 20000 drops extracted from 2005 image pairs taken from a flat fan spray. The linear relationship between drop diameter and depth position (Δw) is evident from this diagram. The measurement volume is a function of particle size, but is approximately 4.5 x 3.5 x 25 mm^3 (Width x Height x Depth) for the largest drops observed (240μm diameter). The backlight LED was set to pulse mode with a pulse width of 1 μs.

Knowing the linear dependence of measurement depth on drop size, allows computation of the number density (number of drops per m^3). Practically the volumetric number density is computed by first dividing the entire size range into sub-ranges, for example $N_{bin} = 100$ equal bins. There are n_i drops in the ith bin. The width (W) and height (H) are estimated as the image area minus the area containing truncated drop images, which cannot be processed, i.e. $W_i = W - d_i$, $H_i = H - d_i$, using the values of W and H for the camera with the smallest field of view. The depth of the measurement volume is equal to the effective depth of field for size $\overline{d}_i$, i.e. Δw_i. The number density $\overline{N}$ can then be expressed as

$$\overline{N} = \frac{1}{N_{\text{imag}}} \sum_{i=1}^{N_{\text{bin}}} \frac{n_i}{W_i H_i \Delta w_i} \quad (5)$$

where N_{imag} is the number of processed images. The number density computed for the above-mentioned measurement of a spray from a flat fan nozzle is 357 drop/cm^3. Further examples of laboratory measurements with this depth from defocus system can be found in the articles [8, 9].

2. VOLUME FRACTION OF TWO-COMPONENT DROPLETS

To illustrate the purpose of this technique, Fig. 5 illustrates the splash resulting when a red-colored water drop impacts onto a clear film of silicone oil of 600μm thickness. The ejected secondary drops often have a mixture of water and silicone oil and the aim is to determine the volume fraction of the inner drops compared to the bulk drops. Such a measurement capability is interesting (and necessary) when examining the impact of fuel drops onto an oil film [10] in a combustion chamber or a water-urea drop onto an enriched urea film on the wall of a SCR sys-

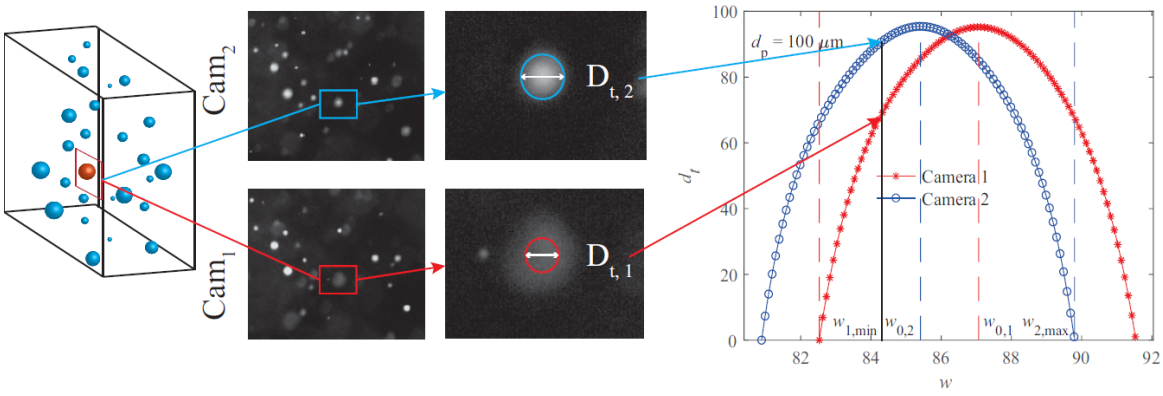

Figure 3. Two images of the same particle/drop and the measured diameters on the images, d_t. The calibration functions f_1 and f_2 are shown on the right diagram, from which the size and position of the particle can be determined by solving Eqs. 4.

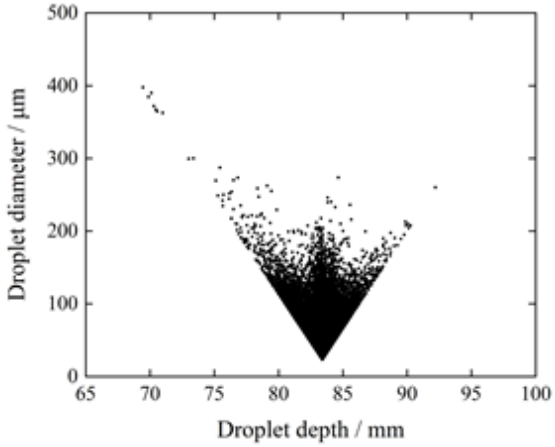

Figure 4. Sampled drop diameters and corresponding depths

tem (Selective Catalytic Reduction). Thus, this technique applies to drop impact onto films of dissimilar liquids [11, 12].

The technique determines the volume fraction of the

Figure 5. Photograph of a red-colored water drop (D=3mm, u=3.3 m/s) impinging onto a film of silicone oil of 600μm thickness, illustrating the generated secondary droplets; b),c) Time sequence of secondary droplets ejected from finger jets.

inner droplet to the outer drop ($V_{\text{frac}} = V_{\text{inner}}/V_{\text{outer}}$) by examining the area ratio on the image of red area to total area of each drop ($A_{\text{frac}} = A_{\text{inner}}/A_{\text{outer}}$). This however cannot be a direct correspondence, since the (red) area of the inner drop depends on the observation perspective. For instance, Fig. 6 illustrates images of such a two-component drop rotating freely in an acoustic levitator at different time instances. The area ratio A_{frac} changes dramatically, although the volume fraction V_{frac} remains constant. To understand this effect, a simple ray-tracing approach can be considered, illustrated in Fig. 7. It is obvious from these simple considerations, that the area ratio on a planar image will also depend on the relative refractive index of the outer drop to the surrounding medium, usually gas.

The application of this simple ray-tracing exercise

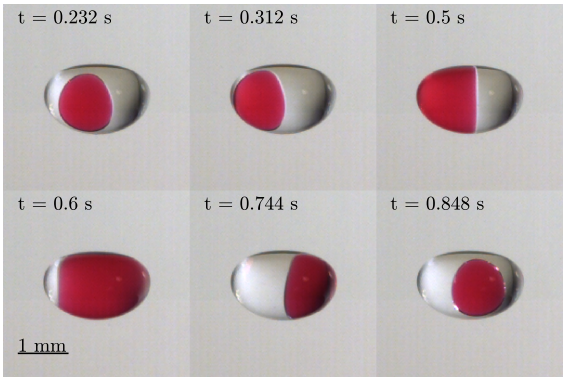

Figure 6. Levitated two-component droplet (V_{frac}=0.13) of red colored water and silicone oil at various time instances.

leads to a relation between A_{frac} and V_{frac} as illustrated in Fig. 8, indicating that, depending on the position of the inner droplet in the outer drop with respect to the viewing angle, the maximum discernible volume fraction is a little as 0.08 when the inner drop

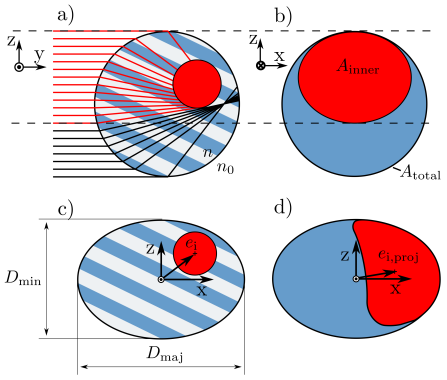

Figure 7. a) Schematic representation of ray paths refracted in a two-component droplet in a sectional view; b) projected image onto a camera; c) definition of coordinate system origin; d) definition of projected eccentricity vector.

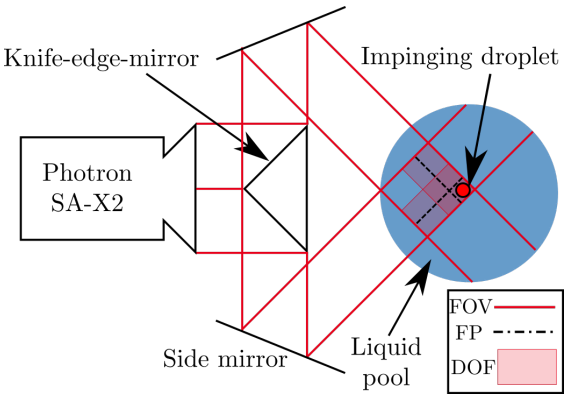

Figure 9. Sketch of the splashing setup showing the respective fields of view (FOV), focal planes (FP) and depth of field (DOF).

is at the rear of the outer drop, and 0.58 when the inner droplet is at the front of the outer drop. This maximum is reached when the area ratio becomes unity. To alleviate this limitation, it is therefore necessary either to observed the droplet for a longer period of time, during which the observation perspective may change and the area ratio may sometimes be smaller than unity, or to observe the droplet simultaneously from more than one perspective. The latter approach has been used in the present study, realized in a one-camera configuration, as shown in Fig. 9. In this configuration, two orthogonal views of the drop are imaged simultaneously onto different portions of the camera chip using mirrors and a prism in front of the camera.

It becomes apparent that due to the influence of re-

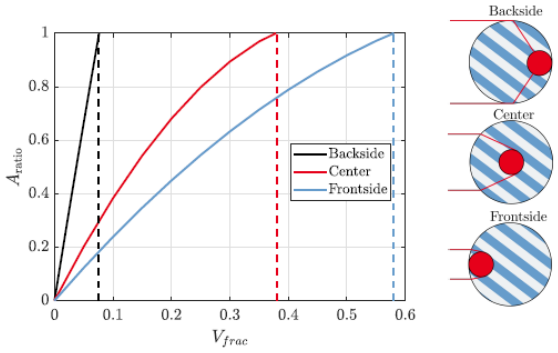

Figure 8. a) Relation between V_{frac} and A_{frac} in dependence of the relative position of the inner droplet. Dashed lines represent the V_{frac} for which $A_{\text{frac}} = 1$; b) Light ray paths within a two-component droplet in sectional view, resulting in varying A_{frac}.

fraction inside the two-component droplet the real position of the enclosed droplet cannot be determined unambiguously. Only the projected eccentricities $\vec{e}_{i,\text{proj}}$ can be measured directly from the recordings. This makes direct solution of the inverse problem difficult. On the other hand, the projected A_{ratio} in combination with $\vec{e}_{i,\text{proj}}$ do include information about V_{frac}. In order to utilize this information to determine the V_{frac} a support vector machine (SVM) is used. The SVM is a methodology from the field of machine learning, first introduced by [13], which has become widely used for solving classification problems [14]. The aim of using a SVM in the context of this study is to provide an algorithm, which is able to predict a volume fraction $\hat{V}_{\text{frac}}$ based on experimentally observable features, summarized in an observation vector $\vec{b}$.

To train a SVM with the aim to predict $\hat{V}_{\text{frac}}$, first a set of classes has to be defined. It becomes apparent from Fig. 8 that the projected A_{ratio} is close to unity for high V_{frac} even if the inner droplet is positioned on the side facing the observer. The V_{frac} of cases with $A_{\text{ratio}} \approx 1$ cannot be determined unambiguously, since the projected image of the droplet contains limited information. A reasonable trade off is to limit the measuring range of V_{frac} between 0 and 0.5. This measuring range is then divided into equal bin sizes of 0.025 resulting in 21 discrete classes each representing 5% intervals of the upper measuring range limit.

The projected A_{ratio} depends on V_{frac}, the refractive index n, the relative position e_i of the inner drop and the aspect ratio ε of the two-component drop. With the aim to determine V_{frac}, the information of A_{ratio}, n, ε and e_i must therefore be taken into account. Since it is not possible to directly determine the exact position of the inner droplet from the recordings, its position is estimated by considering the centre of the projected area of the inner droplet in each perspective image $e_{i,\text{proj}}$, with $e_{i,\text{proj}}$ being a two-dimensional vector as depicted in Fig. 7d. Thus the observation

vector $\vec{b}$ becomes

$$\vec{b} = [\varepsilon, A_{\text{ratio},1}, A_{\text{ratio},2}, e_{x,\text{proj},1}, e_{z,\text{proj},1}, e_{y,\text{proj},2}, e_{z,\text{proj},2}]. \quad (6)$$

The area ratios can be summarized in $A_{\text{ratio, p}}$ and the eccentricities in $e_{i,\text{proj},p}$, where the subscript $p \in [1, 2]$ denotes the respective perspective 1 or 2 and the subscript i denotes the components of the eccentricity vector. The classification is based on these seven features.

In the next step the algorithm needs to be trained, i.e. the hyperplanes for the l= 210 binary classifiers need to be found. For this purpose 67500 synthetic observations $\vec{b}$ were generated. For each observation two orthogonal projections are generated. The V_{frac} and the position of the inner droplet e_i are randomly varied, whereby V_{frac} is limited to the interval $[0, 0.5]$ and e_i is constrained by the condition that the inner droplet must be wholly within the outer droplet. An image processing script based on the Matlab image processing toolbox is then used to extract $A_{\text{ratio,p}}$, ε and $e_{i,\text{proj},p}$ from the synthetically generated image pairs. These quantities are then combined in $\vec{b}$ and each observation is labeled with the V_{frac} it was generated with. Further details of the SVM implementation can be found in [15].

This section closes with sample measurements to illustrate the achievable accuracy. These measurements were conducted on drops held in an acoustic levitator. Two types of experiments were conducted. In the first experiments, solid particles of known and precise size were injected into the outer drop; hence, the exact volume fraction is known once the volume of the outer drop is determined through shadowgraphy. This offers a ground truth as a benchmark and moreover, the solid particles cannot deform under influence of the acoustic pressure. The second experiments was then a drop-in-drop experiments, in which the volume of both the inner (colored) and outer drop was carefully controlled during injection with precision needles. Again, the volume fraction is therefore known. These experiments allow the accuracy of the technique under well-controlled conditions to be explored.

The results of these two experiments are shown in Fig. 10. These results indicate, that particularly for volume fractions < 0.3, the measurement accuracy is very good. For larger values of volume fraction the measurements performed with particles embedded in the outer drop are significantly better that for the drop-in-drop experiments. This is likely due to the deformation of the inner drop due to acoustic pressure, an effect which was not considered in the SVM training data.

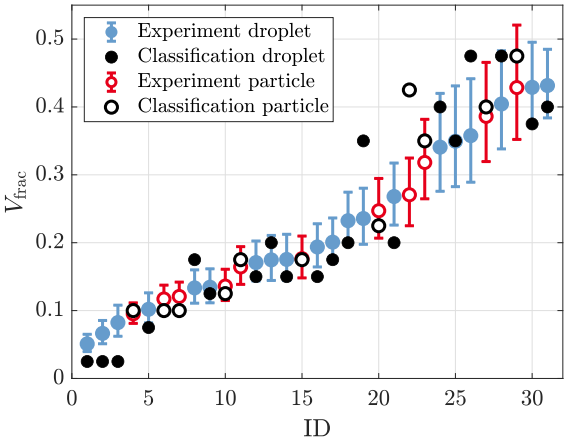

Figure 10. Comparison between experimental and classification based volume fraction V_{frac} determination. Blue markers indicate drop-in-drop experiments with red colored water inside silicone oil, whereas red markers indicate spherical particles (D=1mm) inside silicone oil drops. The black symbols correspond to the estimated volume fraction from the experimental images. ID (Identification number) is simply a counter for the various experiments, arranged sequentially in order of increasing V_{frac}.

3. PLANAR RAINBOW REFRACTOMETRY

Roth et al. [16] first proposed standard rainbow refractometry (SRR) to simultaneously measure the temperature (refractive index) and size of individual droplet (or monodisperse droplets), however, SRR is very sensitive to any departure from sphericity. With a similar optical system, van Beeck et al. [17] developed global rainbow refractometry (GRR) for the measurement of size distribution and average refractive index (or temperature) of an ensemble of spray droplets; GRR is relatively insensitive to non-sphericity droplets. Further to these conventional and partially commercially available techniques, the capability of rainbow refractometry to measure the following quantities has been demonstrated: size of droplets in air [18] and in liquid-liquid flows [19], non-sphericity [20], heat & mass transfer parameters (refractive index [21], temperature [22], transient evaporation rate [23]), often simultaneously. Recently, the technique has been extended to characterize oscillating [24] and colloidal droplets [25, 26]. In the following, some recent developments to extend rainbow refractometry from a point measurement to a planar measurement will be discussed, in particular with reference to advances outlined in [27, 28].

The optical configuration for a planar rainbow refractometer is shown in Fig. 11 and the experimental setup is pictured in Fig. 12. The illumination is with a vertically polarized laser light sheet, similar to that used in particle image velocimetry (PIV). The detector must now be aligned at an angle, such that the primary rainbow pattern for the particular relative refractive index of the drops will be captured on the camera chip. There are several complicating

factors in doing this and resolving these factors is the substance of the present contribution.

To begin, the angular position a particular pixel on the camera chip represents depends on the position of the scattering drop in the illumination plane. Therefore, the angle calibration must be carried out throughout the entire plane. This will be accomplished using a chain of monodispersed droplets, as described below. Second, for several reasons the relative refractive index of the drop may not be known. This would be the case if there were a mixture of different fluids, and then the refractive index must be determined simultaneously with the size and position of the drop. Another situation would be if the drops were two or multi-component and one component was more volatile, such that evaporation would lead to a change of relative refractive index. The objective in analysing the rainbow pattern arising from each individual drop is therefore to determine the size, refractive index (temperature) and position in each recorded image. This analysis is often referred to as the 'inversion' of the rainbow pattern, since it represents an inverse problem to be solved.

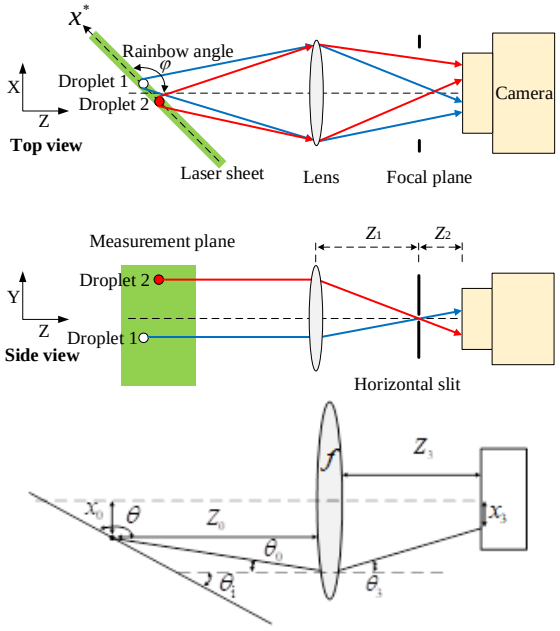

Figure 11. Optical configuration for planar rainbow refractometry

An important element in the optical configuration is the insertion of a horizontal slit at the back focal plane of the focusing lens, in front of the camera. With the horizontal slit, rainbow patterns of drops at different heights and horizontal positions in the illuminated measurement plane are separately recorded on different row and column pixels of the camera. A typical image obtained from a spray using the planar rainbow refractometer is pictured in Fig. 13. From this image it is apparent, that the planar rainbow refractometry will be limited in measurable number density, since at higher concentration the rainbow patters will overlap excessively and can not be analysed. This is similar to limitations in interferometric particle imaging (IPI) [29]. Furthermore, it is also apparent that determination of the position of the particle is not straightforward, since the rainbow pattern is by nature more intense for the primary fringe (Airy) and less for the supernumerary fringes. More details regarding this difficulty can be found in [27].

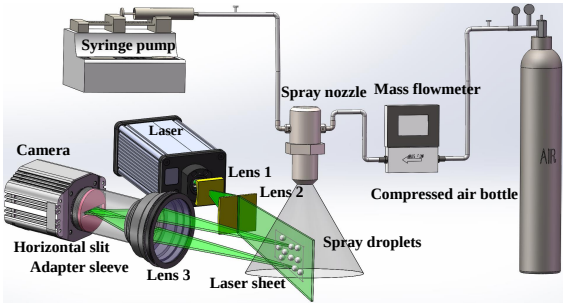

Figure 12. Experimental setup to demonstrate planar rainbow refractometry

A novel development in implementing the planar

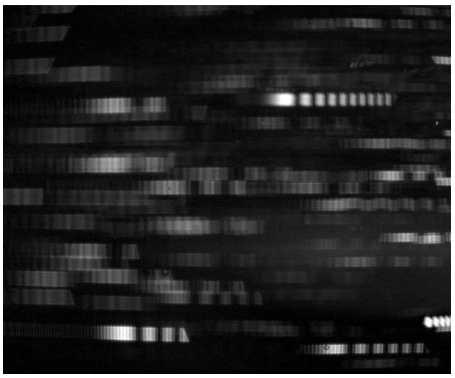

Figure 13. Typical image obtained from a spray using the planar rainbow refractometer.

rainbow refractometer is the method of calibrating the scatter angle. For this a monodisperse droplet generator is used (vibrating orifice) [30] and traversed through a number of positions in the illumination plane, as shown in Fig. 14a. The resulting rainbow patters received for three different positions are pictured in Fig. 14b, directly next to one another. This image shows the rainbow pattern with supernumerary bows and also the ripple structure for the droplet stream, superimposed on the rainbow patterns for clarity. Knowing the position and size of the drops, it is then possible to compute the expected rainbow pattern using a Lorenz-Mie code (e.g. [31]) and then match the expected pattern with the experimentally observed pattern. The matching parameters are the transform matrix of physical drop position to pixel position on the camera chip (ABCD matrix).

Further details of this procedure can be found in [28]

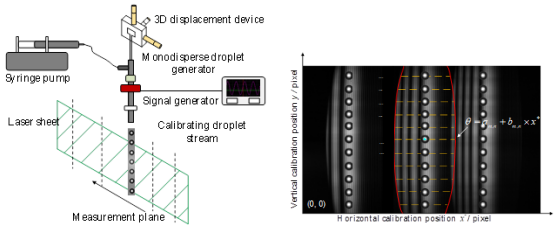

Figure 14. a) Scattering angle calibration of the measurement plane using a traversing monodisperse droplet stream; b) Rainbow patterns of a monodispersed droplet stream at three different positions within the illuminated plane, taken separately but superimposed onto one image.

4. SUMMARY

This has been an intentionally brief review of selected recent developments in the field of particle/drop measurements in flows, because more comprehensive descriptions and analyses are available elsewhere. Nevertheless, each of the three techniques discussed, feature either extended measurement capabilities or improved measurement range/accuracy. For instance, the Depth from Defocus imaging technique increases the depth of field in resolving particles/drops and exhibits a well-defined detection volume, allowing reliable volumetric number densities to be computed; a capability which no other method presently offers adequately. The measurement of volume fraction of two-component drops is equally unique in its measurement capability, and incorporates an innovative approach to image processing, using a support vector machine (SVM). Finally, the planar version of rainbow refractometry extends conventional rainbow refractometry to an entire plane, a capability especially welcome when measuring in sprays.

None of the discussed techniques are yet to be offered commercially and there are certainly many limitations of each technique in application, which have not been thoroughly elaborated here. On the other hand, discussing these innovations may promote further developments and advances in measuring drops/particles in flows. No doubt the accuracy and reliability of each technique will also improve with advancing technology in hardware components, especially with respect to spatial and temporal resolution and sensitivity of imaging cameras.

ACKNOWLEDGEMENTS

The technique for measuring the volume fraction of two-component drops was financially supported be the Deutsche Forschungsgemeinschaft through SFB/TRR 150, Subproject A02.

REFERENCES

[1] Pentland, A. P., 1987, “A new sense for depth of field”, *IEEE transactions on pattern analysis and machine intelligence*, (4), pp. 523–531.

[2] Krotkov, E., 1988, “Focusing”, *International Journal of Computer Vision*, Vol. 1 (3), pp. 223–237.

[3] Willert, C., and Gharib, M., 1992, “Three-dimensional particle imaging with a single camera”, *Experiments in Fluids*, Vol. 12 (6), pp. 353–358.

[4] Saxena, A., Chung, S. H., and Ng, A. Y., 2008, “3-d depth reconstruction from a single still image”, *International Journal of Computer Vision*, Vol. 76 (1), pp. 53–69.

[5] Ghita, O., and Whelan, P. F., 2001, “A video-rate range sensor based on depth from defocus”, *Optics & Laser Technology*, Vol. 33 (3), pp. 167–176.

[6] Murata, S., and Kawamura, M., 1999, “Particle depth measurement based on depth-from-defocus”, *Optics & Laser Technology*, Vol. 31 (1), pp. 95–102.

[7] Cierpka, C., Segura, R., Hain, R., and Kaehler, C. J., 2010, “A simple single camera 3C3D velocity measurement technique without errors due to depth of correlation and spatial averaging for microfluidics”, *Measurement Science and Technology*, Vol. 21 (4), p. 045401.

[8] Zhou, W., Tropea, C., Chen, B., Zhang, Y., Luo, X., and Cai, X., 2020, “Spray drop measurements using depth from defocus”, *Measurement Science and Technology*, Vol. 31 (7), p. 075901.

[9] Zhou, W., Zhang, Y., Chen, B., Tropea, C., Xu, R., and Cai, X., 2021, “Sensitivity analysis and measurement uncertainties of a two-camera depth from defocus imaging system”, *Experiments in Fluids*, Vol. 62 (11), pp. 1–14.

[10] Kubach, H., Weidenlener, A., Pfeil, J., Koch, T., Kittel, H., Roisman, I. V., and Tropea, C., 2018, “Investigations on the Influence of Fuel Oil Film Interaction on Pre-ignition Events in Highly Boosted DI Gasoline Engines”, *Tech. rep.*, SAE Technical Paper.

[11] Geppert, A., Chatzianagnostou, D., Meister, C., Gomaa, H., Lamanna, G., and Weigand, B., 2016, “Classification of impact morphology and splashing/deposition limit for N-Hexadecane”, *Atomization and Sprays*, Vol. 26 (10).

[12] Kittel, H. M., Roisman, I. V., and Tropea, C., 2018, "Splash of a drop impacting onto a solid substrate wetted by a thin film of another liquid", *Physical Review Fluids*, Vol. 3 (7), p. 073601.

[13] Cortes, C., and Vapnik, V., 1995, "Support-Vector Networks", *Machine Learning*, (20), pp. 273–297.

[14] Awad, M., and Khanna, R., 2015, *Efficient Learning Machines : Theories, Concepts, and Applications for Engineers and System Designers*, Apress, Berkeley, CA, 1st ed. 2015 edn., ISBN 9781430259909, URL `https://doi.org/10.1007/978-1-4302-5990-9`.

[15] Stumpf, B., Ruesch, J. H., Roisman, I. V., Tropea, C., and Hussong, J., 2022, "An imaging technique for determining the volume fraction of two-component droplets of immiscible fluids", *Experiments in Fluids*, Vol. 63 (7), pp. 1–13.

[16] Roth, N., Anders, K., and Frohn, A., 1990, "Simultaneous measurement of temperature and size of droplets in the micrometer range", *Journal of Laser Applications*, Vol. 2 (1), pp. 37–42.

[17] Van Beeck, J., Giannoulis, D., Zimmer, L., and Riethmuller, M., 1999, "Global rainbow thermometry for droplet-temperature measurement", *Optics Letters*, Vol. 24 (23), pp. 1696–1698.

[18] Rosebrock, C. D., Shirinzadeh, S., Soeken, M., Riefler, N., Wriedt, T., Drechsler, R., and Mädler, L., 2016, "Time-resolved detection of diffusion limited temperature gradients inside single isolated burning droplets using Rainbow Refractometry", *Combustion and Flame*, Vol. 168, pp. 255–269.

[19] Ouattara, M., Lamadie, F., Sentis, M. P., and Onofri, F. R., 2017, "Droplet sizing and mixture fraction measurement in liquid–liquid flows with rainbow-angle diffractometry", *Applied Optics*, Vol. 56 (29), pp. 8109–8120.

[20] Onofri, F. R., Ren, K. F., Sentis, M., Gaubert, Q., and Pelcé, C., 2015, "Experimental validation of the vectorial complex ray model on the inter-caustics scattering of oblate droplets", *Optics Express*, Vol. 23 (12), pp. 15768–15773.

[21] Ouboukhlik, M., Godard, G., Saengkaew, S., Fournier-Salaün, M.-C., Estel, L., and Gréhan, G., 2015, "Mass transfer evolution in a reactive spray during carbon dioxide capture", *Chemical Engineering & Technology*, Vol. 38 (7), pp. 1154–1164.

[22] Verdier, A., Santiago, J. M., Vandel, A., Saengkaew, S., Cabot, G., Gréhan, G., and Renou, B., 2017, "Experimental study of local flame structures and fuel droplet properties of a spray jet flame", *Proceedings of the Combustion Institute*, Vol. 36 (2), pp. 2595–2602.

[23] Li, C., Lv, Q., Wu, Y., Wu, X., and Tropea, C., 2020, "Measurement of transient evaporation of an ethanol droplet stream with phase rainbow refractometry and high-speed microscopic shadowgraphy", *International Journal of Heat and Mass Transfer*, Vol. 146, p. 118843.

[24] Lv, Q., Wu, Y., Li, C., Wu, X., Chen, L., and Cen, K., 2020, "Surface tension and viscosity measurement of oscillating droplet using rainbow refractometry", *Optics Letters*, Vol. 45 (24), pp. 6687–6690.

[25] Li, C., Wu, X., Cao, J., Chen, L., Gréhan, G., and Cen, K., 2018, "Application of rainbow refractometry for measurement of droplets with solid inclusions", *Optics & Laser Technology*, Vol. 98, pp. 354–362.

[26] Li, C., Wu, Y., Wu, X., and Tropea, C., 2020, "Simultaneous measurement of refractive index, diameter and colloid concentration of a droplet using rainbow refractometry", *Journal of Quantitative Spectroscopy and Radiative Transfer*, Vol. 245, p. 106834.

[27] Li, C., Lv, Q., Li, N., Wu, Y., Wu, X., Weng, C., and Tropea, C., 2021, "Planar rainbow refractometry", *Optics Letters*, Vol. 46 (23), pp. 5898–5901.

[28] Li, C., Lv, Q., Wu, X., and Tropea, C., 2022, "Planar rainbow refractometry for size, refractive index and position measurement of droplets in a plane", *Proceedings of 20th Int. Symp. on the Appl. of Laser and Imaging Techn. to Fluid Mech.*, Lisbon, Portugal.

[29] Damaschke, N., Nobach, H., and Tropea, C., 2002, "Optical limits of particle concentration for multi-dimensional particle sizing techniques in fluid mechanics", *Experiments in Fluids*, Vol. 32 (2), pp. 143–152.

[30] Berglund, R. N., and Liu, B. Y., 1973, "Generation of monodisperse aerosol standards", *Environmental Science & Technology*, Vol. 7 (2), pp. 147–153.

[31] Laven, P., 2004, "Simulation of rainbows, coronas and glories using Mie theory and the Debye series", *Journal of Quantitative Spectroscopy and Radiative Transfer*, Vol. 89 (1-4), pp. 257–269.

Conference on Modelling Fluid Flow (CMFF'22)
The 18th International Conference on Fluid Flow Technologies
Budapest, Hungary, August 30 -September 2, 2022

RECENT ADVANCES IN CFD-DEM SIMULATION OF FLUIDIZED BEDS

Babak Aghel[1,2], Falah Alobaid[1], Christoph Graf[1], Bernd Epple[1]

[1]Corresponding author, Technical University of Darmstadt, Institute for Energy Systems and Technology, Otto-Berndt-Straße 2, 64287 Darmstadt, Germany, Tel.: +49 (0) 6151 16 23004, Fax: +49 (0) 6151 16 22690, E-mail: falah.alobaid@est.tu-darmstadt.de

[2]Department of Chemical Engineering, Faculty of Energy, Kermanshah University of Technology, Kermanshah, Iran, E-mail: babak.aghel@est.tu-darmstadt.de

ABSTRACT

For many decades, experimental measurements, usually at the lab scale, have been considered the main basis for developing and designing commercial-scale gas-solid equipment. However, it is difficult to describe the hydrodynamic characteristics of this flow, despite the extensive experimental work carried out by many researchers. Due to the increasing development of computational performance, numerical simulations are gaining particular importance in the prediction of gas-solid flows, studying design modifications, and complementing experimental data. Although real-time simulations will require substantial progress in the accuracy, capability, and efficiency of numerical models, future developments could herald a new era of so-called virtual reality for process engineering, featuring interactive simulations instead of stepwise experimental scale-up studies and cost-intensive empirical trial-and-error methods. This review provides a significant body of knowledge on the developments of CFD-DEM models and how they can be applied in various gas-solid systems, mainly fluidized beds. Current research trends, as well as research gaps and opportunities for future CFD-DEM applications to chemical and energy processes based on fluidized bed systems, are presented.

Keywords: Gas-Solid Flows; Fluidized Bed; CFD-DEM Model

1. INTRODUCTION

Chemical and energy systems are complex processes that include several phenomena such as thermochemical reactions and multiphase flows. Diverse materials lead to different two-phase flows. In practice, there are gas-fluid, fluid-solid, and gas-solid flows. In gas-fluid flows, one of the phases is in a dispersible form, while in the fluid-solid and gas-solid flows the solid always remains in the dispersed phase.

Experimental measurements enable a fundamental understanding of the hydrodynamic behavior of reactive gas-solid flows, but detailed experimental data is hard to get hold of due to the harsh environment (high temperature, high pressure, and/or toxic gases), and the costs of measuring devices.

Numerical simulation makes it possible to bypass a long process of planning and constructing experiments, providing a quick evaluation of local and global flow field variables (e.g. the temperature, velocity, and concentration) at the industrial scale. However, the reliable simulation of large-scale systems is hindered by a failure to accurately understand the fundamentals of gas-solid flows (e.g. gas-particle, particle-particle, and particle-wall interactions) [1].

Taking into account how the gas phase influences the solid phase and vice versa, as well as how particles influence other particles and walls (gas-particle, particle-particle, and particle-wall interactions), one can differentiate between various coupling approaches, mainly two-way coupling and four-way coupling. There is also a three-way coupling scheme, in which the gas and particle affect each other and the particle wakes and other gas-phase disturbances affect the motion of other particles, e.g. drafting of a trailing particle.

For the representation of gas-solid flows, there are different computational fluid dynamic (CFD) models available, namely the two-fluid model, the discrete-particle model, the hybrid model, and the direct numerical simulation model [2].

2. THEORY

In the discrete-particle method, the gas phase is modeled as a continuum and the solid phase is treated as a dispersed phase, in which individual particles are tracked transiently in the computational domain. The discrete-particle method is distinguished by its particle collision detection methodology, either stochastic or deterministic. The detection of particle-particle and particle-wall collisions is crucially

important in terms of both the computational effort and the simulation accuracy.

The idea behind the stochastic collision models is that the motion of each particle is calculated independently of the remaining particles. However, information on other particles should be available to generate virtual collision partners, whose properties are derived from the local average values of these particles. The probability of a collision occurring between the investigated particle and the virtual particle can then be calculated using random numbers. In the deterministic collision detection models, each particle is tested for a possible collision with other partners (particle or wall) [3].

For the discrete-particle simulations with stochastic or deterministic collision detections, two models are widely used for particle-particle and particle-wall collisions, namely hard-sphere and soft-sphere models. The hard-sphere model allows instantaneous and single binary collisions between the collision partners, which are considered to be rigid spheres (or ideal spheres) so that there is no deformation of the particles during the collision. Properties of the particles after the collision (e.g., velocity, position, and temperature) are related to the properties of the particles before the collision through momentum and energy balances.

In the so-called soft-sphere model, also known as the discrete element method (DEM), the particles can overlap each other or penetrate the wall (see Figure 1.) Depending on the penetration depth, a contact force is determined, changing the motions of particles. In this model, a particle-particle collision takes place when the distance between the center points of two particles is smaller than the sum of both radii. Likewise, a particle-wall collision occurs if the distance between the particle center point and the wall surface is smaller than the particle radius. Depending on the penetration depth, the resulting contact force is modeled using a spring-damper-slider system. The most important advantage of the DEM model is that multiple particle-particle and particle-wall collisions can be calculated simultaneously. In addition to contact forces, other short-range forces such as adhesive forces can be taken into consideration in the context of the DEM model.

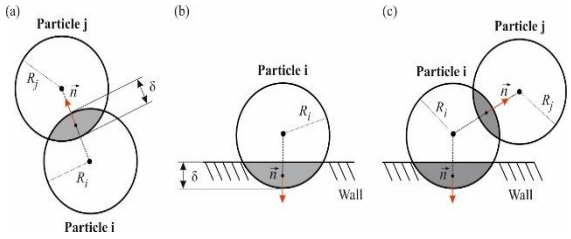

Figure 1. Collision occurrence in the DEM model [4]

In the following sections, we will review the existing literature on the soft-sphere model within the framework of the discrete-particle model, applied to chemical and energy processes based on fluidized bed systems. The CFD-DEM studies found in the literature (with and without chemical reaction) have been evaluated, with a special focus on works that include validation, comparison with other numerical approaches, and their application to real systems.

3. DEVELOPMENT STATUS

Although the DEM model was originally developed by Cundall and Strack [5], in 1993 Tsuji et al. [6] presented one of the first successful DEM simulation studies on the hydrodynamic behavior of gas-solid flows in a lab-scale fluidized bed system. They calculated the trajectory of each particle, taking into account the influence of the gas phase on the solid phase and vice versa, in addition to the particle-particle and particle-wall collisions. This approach is also known in the literature as the DDPM-DEM or CFD-DEM model.

In recent years, significant advances have been achieved in this field of research. Many authors have also compared the simulation results of the DEM model with measurements and with the results of the two-fluid model and the hybrid model, among others, in the works of Chiesa et al. [7]. The DEM model shows better agreement with experimental data compared to other numerical approaches. However, the DEM simulation is computationally expensive when tracking particles in gas-solid flows due to the high computational effort required to detect particle-particle and particle-wall collisions.

A review of the literature on the DEM model reveals that a significant number of published papers are related to cold gas-solid flows, focusing at the early stage of development on 2D and quasi-2D simulations and recently on 3D simulations at the lab scale. Although many authors mention industrial applications in their works, non-reactive gas-solid flows with spherical particles are assumed in most DEM simulations. This simplification is usually accompanied by neglecting a certain number of volume and surface forces, as well as the forces that act on the particles (e.g. Basset, Saffman, Magnus, and electrostatic forces)[8–10].

The drag force makes up a considerable part of all works on DEM and remains one of the major challenges faced in simulations of gas-solid flows. Numerous DEM studies have been carried out using several conventional drag models, such as those developed by Wen and Yu, Syamlal, O'Brien, and Gidaspow. As these conventional drag models have been proven to overestimate the momentum transfer between the gas and solid phases [4], several modifications have been made.

For example, a three-zone or a four-zone drag model calculates the interphase momentum transfer coefficient by selecting universal drag laws for each

zone to match the experimental data [11]. Advanced drag models based on flow structures have also been developed, such as the energy minimization multi-scale (EMMS) model or the drag model as described by Kuipers, showing more accurate results regarding the modeling of circulating fluidized bed systems [12–14].

The contact forces are of particular relevance in fluidization systems and are therefore taken into account in all DEM simulations. The contact force is determined using the Voigt-Kelvin model, which describes the viscoelastic and time-dependent behavior of collision[15]. Part of the kinetic energy is irreversibly dissipated in the form of deformation energy and can be taken into consideration by employing restitution coefficients. At higher collision velocities or for a particle with non-spherical shapes, the restitution coefficients decrease and thus cannot be considered constant [16].

However, the restitution coefficients are set as constant in previous DEM studies due to the relatively low particle velocities and the assumption of spherical particles. Although the non-linear contact models show an accurate distribution of the contact force curve, the linear contact model, which consists of a linear spring model and a linear visco-elastic damping element, has frequently been applied [17].

In the literature on DEM, the effect of the adhesive forces without physical contact (e.g., van der Waals and electrostatic forces) is rarely investigated [18]. This is since these forces are of relevance for micro-size particles. Accordingly, the number of fine particles per volume unit is enormous, which in turn makes the DEM simulation of fluidized bed systems with finer particles extremely expensive.

Furthermore, the electrostatic effect significantly decreases at higher temperatures, and parameters such as particle sizes are not used in most fluidized bed applications. At a high moisture level, the adhesive force due to liquid bridging can have a particularly significant influence on the hydrodynamic behavior of gas-solid flows in fluidized bed systems. The simulation of this adhesive force with and without the liquid transport process due to liquid bridge separation has been widely discussed in the literature on DEM[19,20].

Notwithstanding the great efforts and progress made in recent years in the discrete-particle model with DEM, basic flow properties (e.g. segregation, agglomeration, and attrition) are still not taken into consideration sufficiently. Furthermore, real particulate systems include particles of different chemical compositions, densities, shapes, and sizes (e.g. wood pellets or wood chips) that may change during the transient simulation due to chemical reactions.

Most DEM studies in the literature are restricted to circular particles in 2D cases, or spherical particles in 3D cases, which are of constant diameter (monodisperse) and have the same material properties [9]. The fluidization behavior of particles with complex geometries and different material properties is significantly more complicated than that of spherical particles. Furthermore, the heat and mass transfer rates largely depend on particle geometry. Relatively big particles imply larger temperature gradients and have longer residence times. Despite this, limited numbers of CFD-DEM studies on fluidized bed systems with non-spherical particles can be found in the literature [21].

4. LITERATURE REVIEW

The challenges for the simulation of chemical and energy process systems are to combine the gas flow and the homogeneous reactions with the motions of particles with complex geometries and heterogeneous reactions, taking into consideration the temperature distribution inside the particles as well as the momentum, heat, and mass transfer rates between the gas and solid phases. However, work has only just begun on the chemical reaction mechanism in the discrete-particle model with DEM.

Most works found in the literature are dedicated to heat transfer between the gas and solid phases. Few studies are also found on the gasification or combustion process of solid fuels (including biomass or coal), while CO_2 capture technologies and metallurgical or mining processes are much less frequent.

Since 2006, Scherer et al. have been working on the simulation of biomass and waste combustion in a grate firing system by hooking an in-house DEM code with a chemical reaction mechanism in the commercial CFD code “ANSYS-FLUENT” [22,23]. The numerical results show satisfactory agreement with measurements, even though the model has faced a few challenges, making assumptions such as spherical particles and constant temperature distribution inside the particles.

In 2009, Oevermann et al. [24] presented one of the first DEM studies on the wood gasification process in a 2D fluidized bed system. This study was followed in 2013 by the work of Alobaid [25], who developed an in-house CFD/DEM code, known as “DEMEST”, for the numerical simulation of biomass conversion in fluidized beds. Here, gas-particle interactions are studied using new procedures, known as the offset method and the two-grid method. This improves the simulation accuracy by up to one order of magnitude and allows the fluid grid resolution to be varied independently of the particle size. Within the last seven years, there has been only a moderate increase in DEM studies on reactive gas-solid flows in fluidized bed systems [26].

4.1 NON-REACTIVE SIMULATION

4.1.1 Two-dimensional Applications

Since the successful works by Tsuji et al. [6], the number of manuscripts dealing with the fluidized bed simulation using the DEM model has increased sharply. According to the authors, the CFD-DEM model they developed can provide detailed dynamic information at different levels, from the processing equipment to the individual particle. Mikami et al. [27] developed a numerical simulation model to study the fluidization behavior of dry and wet cohesive powder in a two-dimensional fluidized bed system with 14,000 spherical particles. The results showed that the fluidization of wet powder forms agglomerates. Furthermore, the fluctuations in the pressure drop and the minimum fluidizing velocity were lower for dry particles than for wet powder.

The work by Link [8] was extended by Sutkar et al. [28] to investigate the hydrodynamics of gas-solid spouted, fluidized beds with draught plates and liquid injection. The result indicates that for glass particles under dry and wet conditions, the time-averaged particle velocities are similar to quasi-steady-state behavior. Compared to dry systems, lower particle velocities were observed for the wet systems in both the spout and annulus.

Götz [29] developed a parallel DEM simulation code, in which the computational domain is divided into several decompositions and each sub-block is allocated one processor. Based on the model developed by Götz, Alobaid et al. [30] extended the program to include the numerical simulation of gas-solid flow in a fluidized bed. The particle-particle, particle-wall, and gas-particle interactions are modeled by tracking all individual particles. The results showed that the DEM model can accurately predict the hydrodynamic behavior of the gas-solid flow in the fluidized bed. The simulated spatial distribution of solid, the bed height, and the equivalent bubble diameter agree very well with the experiments (see Figure 2).

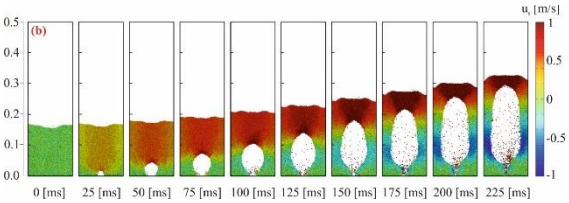

Figure 2. Snapshots of the spatial distribution of solid [30]

Lu et al. [31] investigated how different numerical parameters such as the grid resolution, the drag models (homogeneous and heterogeneous), and the parcel size affected the hydrodynamic behavior of gas-solid flows in a bubbling fluidized bed. The numerical results indicate that the selected drag model has a significant influence on bubble sizes and solid distributions. Progress in recent years was achieved by supplying a pulsed gas mass flow rate to the fluidized bed, the so-called pulsed-fluidized bed (PFB). Wu et al. [32] investigated the dynamic bubble patterns in a quasi-2D pulsed-fluidized bed using the CFD-DEM model. The developed model was validated through experiments, showing quantitative agreement.

Finally, it is worth mentioning that the pseudo-2D CFD-DEM simulations represent a crucial approach for converting the velocity data obtained from particle image velocimetry measurements to the solid flux that provides the most important information for the solid motion in gas-solid fluidized beds.

4.1.2 Three-dimensional Applications

According to the literature, the differences in the solid motions in the 2D and 3D beds are prominent at the beginning of the fluidization process. During fluidization, flow patterns such as the period of bubble formation agree in both simulations, except for the motion of particles near the corners of the bed.

Saidi et al. [33] analyzed the hydrodynamic behavior of gas-solid flows in rectangular spouted, fluidized bed systems of different thicknesses (ranging from pseudo-2D to 3D) using the CFD-DEM model. The results showed that the gas flow fields calculated in the 3D cases have a narrower peak with a higher magnitude of central particle flux compared to the pseudo-2D cases, consistent with measurements. According to the authors, the walls have a considerable impact on the hydrodynamic behavior of gas-solid flows, and this effect becomes insignificant once the thickness increases.

Nikolopoulos et al. [34] compared the coarse-grained discrete-element CFD-DEM with the two-fluid model when both are applied to simulate a semi-industrial riser. The authors explained that the EMMS model and its respective theory were developed and validated based on two-fluid simulations, and it was directly applied to the coarse-grained CFD-DEM model without any modification. The higher accuracy of the EMMS drag model compared with the Gidaspow model was also confirmed.

In most of the studies mentioned above, one component was generally selected for the CFD-DEM simulations, e.g. a riser or a cyclone. The investigated parallelization strategy shows excellent accuracy, good stability, and high efficiency using different processors and under different operating conditions. However, the speed-up ratio and efficiency slightly decrease when the numbers of computational grids and particles are increased.

In this context, Norouzi et al. [35] presented a new parallel CFD-DEM solver that uses both CPU and GPU resources. Using a desktop computer with a 4-core CPU, a frequency of 3.6 GHz, and an NVIDIA GeForce® 660Ti GPU, two different simulation cases were carried out. According to the authors, it took about 6 hours (with two CPU cores) to complete one second of simulation in the case of a large system with 870,000 particles. For the smaller

system with 47,000 particles, only 30 minutes (with one CPU core) were required for one second of simulation.

Yang et al. [36] applied the CFD-DEM model for the three-dimensional simulation of a full-loop CFB with six parallel cyclones (see Figure 3). The authors stated that there is a need for full-loop simulations in future works, rather than focusing on a specific component (i.e. the riser) due to the heterogeneous solid loading in the cyclones.

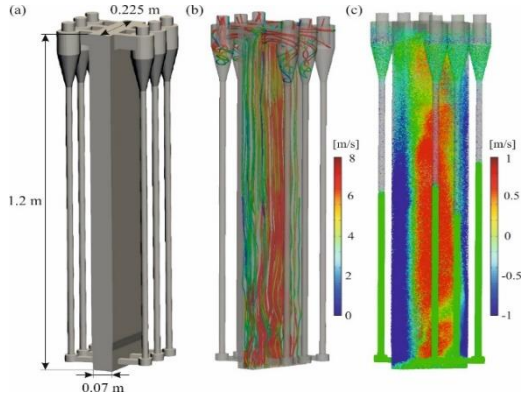

Figure 3. Fluidization behaviour of the gas-solid flow in the full-loop CFB with six parallel cyclones [36]

4.2 REACTIVE SIMULATION

4.2.1 Heat and Mass Transfer Models

In the literature on DEM, there has been broad discussion on specific thermal processes such as the modeling of heat and mass transfer or the consideration of high-temperature adhesive force (metallic solid bridging) in fluidized bed systems. At a sufficiently elevated temperature (60 % of absolute melting temperature), stable solid bridges can be formed between collided particles [37]. The building of sintered bridges depends strongly on the surrounding pressure and the interfacial energies.

Only a few other descriptions were found in the DEM literature, contributing to the agglomeration process. The modeling of heat and mass transfer, by contrast, was discussed in detail. A comparison between the numerical model and the experimental data shows that CFD-DEM simulations are capable of accurately predicting the hydrodynamic behavior of gas-solid flows at elevated temperatures. One example of CFD-DEM simulations with the heat transfer mechanism was presented by Kuipers [38] (see Figure 4).

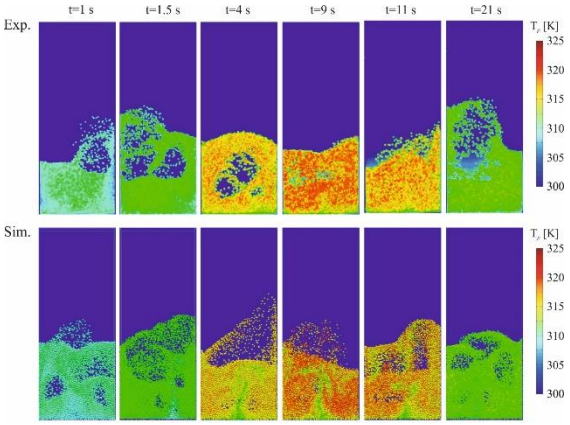

Figure 4. CFD/DEM simulation of a pseudo-2D fluidized bed taking into consideration the heat transfer mechanism [38]

The DEM model that was previously developed to study the heat transfer of spherical particles was extended to evaluate the heat transfer of non-spherical particles. For example, Gan et al. [39] studied the heat transfer in the gas fluidization of ellipsoids. Three heat transfer models (convection, conduction, and radiation) were modified to consider the particle shape and the contact geometry.

The authors claimed that the convective heat transfer coefficients of prolate particles are greater than those of spheres and oblate particles. Wang et al. [40] coupled the CFD-DEM model with a heat exchange model for a single particle, firstly validated for a pseudo-2D bubbling fluidized bed, and secondly applied to a circulating fluidized bed. The numerical results agree with the experimental data in a bubbling fluidized bed. The authors also reported that the gas velocity and particle diameter have a more noteworthy influence on convective heat transfer than on conductive heat transfer.

4.2.2 Combustion and Gasification

Despite the considerable progress in recent years, the CFD-DEM simulation of reactive gas-solid flows in fluidized beds remains a major challenge and is still at an early stage of development. One of the first contributions to this field of research was presented by Zhou et al. [41] in 2004. Here, the DEM model with a large eddy simulation was used to model coal combustion in a 2D bubbling fluidized bed system. The chemical reaction mechanism comprises the heterogeneous reactions of char with O_2, CO, CO_2, NO, and N_2O, along with the homogeneous reactions including CO, O_2, NO, and N_2O. The heat transfer model used took into account particle-gas convective heat transfer, particle-bed radiation heat transfer, the heating rate of a particle, and particle-particle heat transfer.

To reduce the computational cost, Bruchmüller et al. [42] carried out a parallel CFD-DEM simulation on a high-end multiprocessor computer. According to the authors, the superficial fluidization

velocity is crucial, while the biomass moisture content is less important for the final bio-oil yield. Alobaid [25] developed a 3D in-house program, "DEMEST", for the numerical simulation of biomass combustion in a bubbling fluidized bed system (including drying, pyrolysis, and combustion of the char and volatile matter). The numerical results achieve coupling between the CFD-DEM model and the thermochemical reaction mechanism model. The author mentions that the use of other solid fuels such as coal or a mixture of coal and biomass can also be handled with the program.

In another study, Zhao et al. [43] investigated glucose gasification in a supercritical water fluidized bed reactor using the CFD-DEM model. The authors applied a simplified reaction kinetic model, including glucose decomposition, the water-gas shift reaction, and methanation reactions. The numerical results showed good agreement with measurements. It was found that the high wall temperature, the low flow mass rate, and the high initial bed height support the gasification process. At a mass flow rate below the minimum fluidization, the gasification efficiency and thus the H_2 yield decreases.

Directly-irradiated fluidized bed reactors are a promising technology for solar applications (e.g. thermochemical energy storage, solar gasification of hydrocarbons (e.g. coal, biomass, and RDF), and production of solar fuels). Several experimental studies investigated this technology and recently numerical CFD-DEM studies were also performed.

4.2.3 CO_2 Capture Technologies

Various carbon capture processes based on fluidized bed technology are currently being developed (e.g. carbonate-looping process and chemical-looping combustion), but most of them have the consequence of relatively high energy consumption. In the literature on DEM, few studies have been conducted to simulate the chemical-looping combustion process.

The major focus of these works was on investigating the hydrodynamic behavior of cold gas-solid flows in lab-scale systems, while the chemical reaction model was not taken into consideration, e.g.[44,45]. The same applies to CFD-DEM studies used for the carbonate-looping process, with very few exceptions, such as the work of Stroh et al. [46]. According to the authors, the challenges for research lie in the complex hydrodynamics in fluidized beds and the accurate prediction of reactive gas-solid mixtures. They studied the carbonator of the 1 MW_{th} carbonate-looping test facility erected at the Technical University of Darmstadt. The carbonate-looping process, also known as calcium looping, has the potential to significantly reduce the efficiency loss of a conventional steam cycle since the process operates at high temperatures, allowing heat to be used for energy production in a steam cycle. The process can be retrofitted in existing fossil or biomass-fired power plants to remove CO_2 from the flue gas. Furthermore, the technology is particularly suitable for efficiently capturing CO_2 from other industrial sources such as cement or steel plants. Furthermore, different homogeneous drag models (Tang, Gidaspow, Wen and Yu, Syamlal and O'Brien and Gibilaro) and a heterogeneous drag model (EMMS) were applied and evaluated. The authors recommended using the heterogeneous EMMS drag model to improve the accuracy of the simulation result.

For the time being, only a limited number of experimental research works for large or semi-industrial test facilities are available. This is due to the operational challenges in terms of their complexity and the costly measurement apparatus required to obtain the flow characteristics. Therefore, the validated coarse-grained CFD-DEM model at the megawatt scale is of high relevance to upscale the carbonate-looping process.

5. CONCLUSION

A fluidized bed is a bulk of solid particles, with gas flowing into the reactor from the bottom via a porous plate or nozzles. Experimental measurement is usually carried out at a lab scale and provides basic knowledge of the investigated process to underpin design and development. However, the lower costs, the adaptability and the possibility to obtain detailed information are the main reasons why CFD is applied to fluidized bed systems.

Although, CFD-DEM simulations have proven computationally expensive when particles in gas-solid flows due to the high computational cost required to detect particle-particle and particle-wall collisions. A review of the literature on the CFD-DEM model shows that a considerable number of published papers are related to cold gas-solid flows, focusing at the early stage of development on 2D and quasi-2D simulations and recently on 3D simulations at the lab scale. While many authors mention industrial applications in their works, the modeling of turbulence, chemical reaction, and heat transfer is not a part of the CFD-DEM simulation in most cases.

This simplification is usually accompanied by taking into consideration spherical particles and neglecting a certain number of volume and surface forces, as well as the forces that act on the particles. Examples of studies have been reported on fluidization behavior, mixing, and segregation of spherical and non-spherical particles, considering adhesive forces.

It was found that the hydrodynamic behavior of gas-solid flows largely depends on the particles with their complex geometries, size distributions, and material properties. The assumption of monodisperse spherical particles is therefore not valid for the CFD-DEM simulations. However, the CFD-DEM simulations applied to large or semi-industrial test

facilities still face major challenges due to the complexity of the process and the computational cost.

All in all, the CFD-DEM model in combination with chemical reactions, heat, and mass transfer may become a standard tool for the design and development of fluidized bed systems. Nevertheless, significant research efforts are required to make the CFD-DEM model as competitive as the present status of the two-fluid model.

REFERENCES

[1] Alobaid F. Computational Fluid Dynamics. Numerical Simulation for Next Generation Thermal Power Plants, Springer; 2018, p. 87–204.

[2] Kuerten J. G. M. Point-Particle DNS and LES of Particle-Laden Turbulent flow-a state-of-the-art review. Flow Turbul Combust 2016;97:689–713.

[3] Hoomans BPB, Kuipers JAM, Briels WJ, van Swaaij WPM. Discrete particle simulation of bubble and slug formation in a two-dimensional gas-fluidised bed: a hard-sphere approach. Chemical Engineering Science 1996;51:99–118.

[4] Alobaid F, Almohammed N, Farid MM, May J, Rößger P, Richter A, et al. Progress in CFD Simulations of Fluidized Beds for Chemical and Energy Process Engineering. Progress in Energy and Combustion Science 2021:100930.

[5] Cundall PA, Strack ODL. A discrete numerical model for granular assemblies. Geotechnique 1979;29:47–65.

[6] Tsuji Y, Kawaguchi T, Tanaka T. Discrete particle simulation of two-dimensional fluidized bed. Powder Technol 1993;77:79–87.

[7] Chiesa M, Mathiesen V, Melheim JA, Halvorsen B. Numerical simulation of particulate flow by the Eulerian–Lagrangian and the Eulerian–Eulerian approach with application to a fluidized bed. Comput Chem Eng 2005;29:291–304.

[8] Link JM. Development and validation of a discrete particle model of a spout-fluid bed granulator 2006. Ph.D. Thesis, University of Twente, Enschede.

[9] Mahmoodi B, Hosseini SH, Ahmadi G. CFD–DEM simulation of a pseudo-two-dimensional spouted bed comprising coarse particles. Particuology 2019;43:171–80.

[10] Van Buijtenen MS, Deen NG, Heinrich S, Antonyuk S, Kuipers JAM. A discrete element study of wet particle–particle interaction during granulation in a spout fluidized bed. The Canadian Journal of Chemical Engineering 2009;87:308–17.

[11] Gao X, Wu C, Cheng Y, Wang L, Li X. Experimental and numerical investigation of solid behavior in a gas–solid turbulent fluidized bed. Powder Technol 2012;228:1–13.

[12] Yang Y, Zi C, Huang Z, Wang J, Lungu M, Liao Z, et al. CFD-DEM investigation of particle elutriation with electrostatic effects in gas-solid fluidized beds. Powder Technology 2017;308:422–33.

[13] Agrawal V, Shinde Y, Shah MT, Utikar RP, Pareek VK, Joshi JB. Effect of drag models on CFD–DEM predictions of bubbling fluidized beds with Geldart D particles. Advanced Powder Technology 2018;29:2658–69.

[14] Koralkar N.V, Bose M. Performance of drag models for simulation of fluidized beds with Geldart D particles. Advanced Powder Technology 2016;27:2377–98.

[15] Sommerfeld M. Kinetic simulations for analysing the wall collision process of non-spherical particles. Fluids Engineering Division Summer Meeting, vol. 36169, 2002, p. 539–47.

[16] Sommerfeld M. Kinetic simulations for analysing the wall collision process of non-spherical particles. Fluids Engineering Division Summer Meeting, vol. 36169, 2002, p. 539–47.

[17] Kruggel-Emden H, Simsek E, Rickelt S, Wirtz S, Scherer V. Review and extension of normal force models for the discrete element method. Powder Technology 2007;171:157–73.

[18] Okhovat-Alavian SM, Shabanian J, Norouzi HR, Zarghami R, Chaouki J, Mostoufi N. Effect of interparticle force on gas dynamics in a bubbling gas–solid fluidized bed: a CFD-DEM study. Chemical Engineering Research and Design 2019;152:348–62.

[19] Shi D, McCarthy JJ. Numerical simulation of liquid transfer between particles. Powder Technology 2008;184:64–75.

[20] Anand A, Curtis JS, Wassgren CR, Hancock BC, Ketterhagen WR. Predicting discharge dynamics of wet cohesive particles from a rectangular hopper using the discrete element method (DEM). Chemical Engineering Science 2009;64:5268–75.

[21] Zhong W, Yu A, Liu X, Tong Z, Zhang H. DEM/CFD-DEM modelling of non-spherical particulate systems: theoretical developments and applications. Powder Technol 2016;302:108–52.

[22] Wiese J, Wissing F, Höhner D, Wirtz S, Scherer V, Ley U, et al. DEM/CFD modeling of the fuel conversion in a pellet stove. Fuel Processing Technology 2016;152:223–39.

[23]Bambauer F, Wirtz S, Scherer V, Bartusch H. Transient DEM-CFD simulation of solid and fluid flow in a three dimensional blast furnace model. Powder Technology 2018;334:53–64.

[24]Oevermann M, Gerber S, Behrendt F. Euler–Lagrange/DEM simulation of wood gasification in a bubbling fluidized bed reactor. Particuology 2009;7:307–16.

[25]Alobaid F. 3D modelling and simulation of reactive fluidized beds for conversion of biomass with discrete element method 2013. Ph.D. Thesis, Technische Universität Darmstadt, Germany.

[26]Stroh A, Daikeler A, Nikku M, May J, Alobaid F, von Bohnstein M, et al. Coarse grain 3D CFD-DEM simulation and validation with capacitance probe measurements in a circulating fluidized bed. Chemical Engineering Science 2019;196:37–53.

[27]Mikami T, Kamiya H, Horio M. Numerical simulation of cohesive powder behavior in a fluidized bed. Chem Eng Sci 1998;53:1927–40.

[28]Sutkar VS, Deen NG, Patil A v, Peters EAJF, Kuipers JAM, Salikov V, et al. Experimental study of hydrodynamics and thermal behavior of a pseudo-2D spout-fluidized bed with liquid injection. AIChE Journal 2015;61:1146–59.

[29]Götz S. Gekoppelte CFD/DEM-simulation blasenbildender wirbelschichten. Shaker; 2006.

[30]Alobaid F, Epple B. Improvement, validation and application of CFD/DEM model to dense gas–solid flow in a fluidized bed. Particuology 2013;11:514–26.

[31]Lu L, Konan A, Benyahia S. Influence of grid resolution, parcel size and drag models on bubbling fluidized bed simulation. Chemical Engineering Journal 2017;326:627–39.

[32]Wu K, de Martín L, Coppens M-O. Pattern formation in pulsed gas-solid fluidized beds–the role of granular solid mechanics. Chemical Engineering Journal 2017;329:4–14.

[33]Saidi M, Tabrizi HB, Grace JR, Lim CJ. Hydrodynamic investigation of gas-solid flow in rectangular spout-fluid bed using CFD-DEM modeling. Powder Technology 2015;284:355–64.

[34]Nikolopoulos A, Stroh A, Zeneli M, Alobaid F, Nikolopoulos N, Ströhle J, et al. Numerical investigation and comparison of coarse grain CFD–DEM and TFM in the case of a 1 MWth fluidized bed carbonator simulation. Chemical Engineering Science 2017;163:189–205.

[35]Norouzi HR, Zarghami R, Mostoufi N. New hybrid CPU-GPU solver for CFD-DEM simulation of fluidized beds. Powder Technology 2017;316:233–44.

[36]Yang S, Wang S, Luo K, Fan J, Chew JW. Numerical investigation of the back-mixing and non-uniform characteristics in the three-dimensional full-loop circulating fluidized bed combustor with six parallel cyclones. Applied Thermal Engineering 2019;153:524–35.

[37]Schubert H. Grundlagen des agglomerierens. Chemie Ingenieur Technik 1979;51:266–77.

[38] Kuipers J. Multi-scaling Modelling of Mass, Momentum and Heat Transfer in Dense Gas-Particle Flows. Workshop on Fluidized Bed Modeling. Freiberg, Germany: TU Bergakademie Freiberg; 2017. p. 1-51.

[39]Gan J, Zhou Z, Yu A. Particle scale study of heat transfer in packed and fluidized beds of ellipsoidal particles. Chem Eng Sci 2016;144:201–15.

[40]Wang S, Luo K, Hu C, Lin J, Fan J. CFD-DEM simulation of heat transfer in fluidized beds: Model verification, validation, and application. Chemical Engineering Science 2019;197:280–95.

[41]Zhou H, Flamant G, Gauthier D. DEM-LES simulation of coal combustion in a bubbling fluidized bed Part II: coal combustion at the particle level. Chemical Engineering Science 2004;59:4205–15.

[42]Bruchmüller J, van Wachem BGM, Gu S, Luo KH, Brown RC. Modeling the thermochemical degradation of biomass inside a fast pyrolysis fluidized bed reactor. AIChE Journal 2012;58:3030–42.

[43]Zhao L, Lu Y. Hydrogen production by biomass gasification in a supercritical water fluidized bed reactor: a CFD-DEM study. The Journal of Supercritical Fluids 2018;131:26–36.

[44]Fulchini F, Ghadiri M, Borissova A, Amblard B, Bertholin S, Cloupet A, et al. Development of a methodology for predicting particle attrition in a cyclone by CFD-DEM. Powder Technology 2019;357:21–32.

[45]Banerjee S, Agarwal RK. Computational fluid dynamics simulations of a binary particle bed in a riser-based carbon stripper for chemical looping combustion. Powder Technology 2018;325:361–7.

[46]Stroh A, Alobaid F, von Bohnstein M, Ströhle J, Epple B. Numerical CFD simulation of 1 MWth circulating fluidized bed using the coarse grain discrete element method with homogenous drag models and particle size distribution. Fuel Processing Technology 2018;169:84–93.

Sponsors and Partners:

ERCOFTAC European Research Community On Flow, Turbulence And Combustion
www.ercoftac.org

Budapest University of Technology and Economics, Faculty of Mechanical Engineering, Department of Fluid Mechanics
www.ara.bme.hu

The Japan Society of Mechanical Engineers
www.jsme.or.jp

The Visualization Society of Japan
www.vsj.jp

FLUID-LAB.HU Flow Technology Kft.
www.fluid-lab.hu

DAAL-CON Kft.
www.exandair.com

Hungaro-Ventilátor Kft.
www.hungaro-ventilator.hu

Knorr-Bremse Vasúti Jármű Rendszerek Hungária Kft.
www.rail.knorr-bremse.com/en/hu/

Szellőző Művek Kft.
www.szellozomuvek.hu

Wienerberger Téglaipari Zrt.
www.wienerberger.hu

KNORR-BREMSE

ERCOFTAC
European Research Community On Flow, Turbulence And Combustion

HV-VENT THE FAN FACTORY

JSME

Wienerberger

V.S.J.

EXANDAIR TEXTILE AIR DUCT

SZELLŐZŐ művek

Department of Fluid Mechanics

FLUID-LAB.HU FLOW TECHNOLOGY LTD

www.cmff.hu